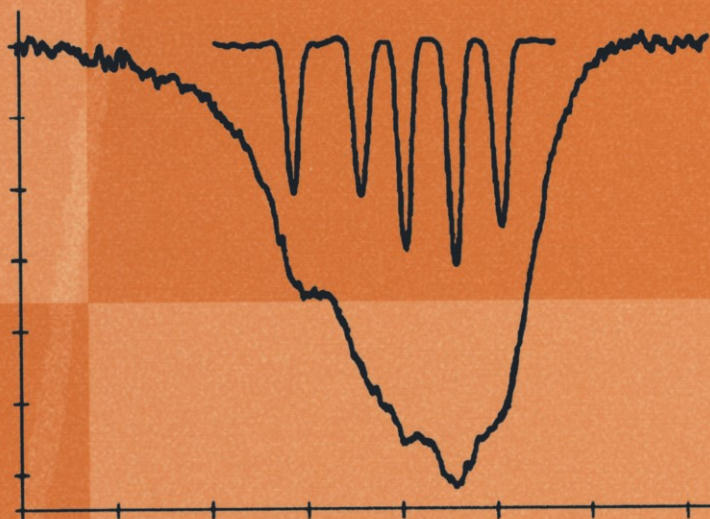


S. Svanberg

Atomic and Molecular Spectroscopy

Basic Aspects and
Practical Applications

Fourth Edition



Springer

Atomic and Molecular Spectroscopy

Advanced Texts in Physics

This program of advanced texts covers a broad spectrum of topics which are of current and emerging interest in physics. Each book provides a comprehensive and yet accessible introduction to a field at the forefront of modern research. As such, these texts are intended for senior undergraduate and graduate students at the MS and PhD level; however, research scientists seeking an introduction to particular areas of physics will also benefit from the titles in this collection.

**Springer-Verlag
Berlin Heidelberg
GmbH**

Physics and Astronomy

springeronline.com



Sune Svanberg

Atomic and Molecular Spectroscopy

Basic Aspects and Practical Applications

Fourth, Revised Edition
With 404 Figures and 14 Tables



Springer

Professor Sune Svanberg

Department of Physics
Lund Institute of Technology
P.O. Box 118
221 00 Lund
Sweden
E-mail: sune.svanberg@fysik.lth.se

ISSN 1439-2674

ISBN 978-3-540-20382-7

Library of Congress Cataloging-in-Publication Data

Svanberg, S. (Sune), 1943-

Atomic and molecular spectroscopy: basic aspects and practical applications/

Sune Svanberg. – 4th, rev. ed.

p. cm. – (Advanced texts in physics, ISSN 1439-2674)

Includes bibliographical references and index.

ISBN 978-3-540-20382-7 ISBN 978-3-642-18520-5 (eBook)

DOI 10.1007/978-642-18520-5

1. Atomic spectroscopy. 2. Molecular spectroscopy. I. Title. II. Series.

QC454.A8S85 2004 539'.6'0287 – dc22 2003063954

This work is subject to copyright. All rights are reserved, whether the whole or part of the material is concerned, specifically the rights of translation, reprinting, reuse of illustrations, recitation, broadcasting, reproduction on microfilm or in any other way, and storage in data banks. Duplication of this publication or parts thereof is permitted only under the provisions of the German Copyright Law of September 9, 1965, in its current version, and permission for use must always be obtained from Springer-Verlag. Violations are liable for prosecution under the German Copyright Law.

springeronline.com

© Springer-Verlag Berlin Heidelberg 1991, 1992, 2001, 2004

Originally published by Springer-Verlag Berlin Heidelberg New York in 2004

The use of general descriptive names, registered names, trademarks, etc. in this publication does not imply, even in the absence of a specific statement, that such names are exempt from the relevant protective laws and regulations and therefore free for general use.

Typesetting: Data conversion by LE-T_EX Jelonek, Schmidt & Vöckler GbR, Leipzig

Cover design: *design & production* GmbH, Heidelberg

Printed on acid-free paper SPIN 10963869 57/3141/di 5 4 3 2 1 0

To Katarina, Emilie, Kristina,
my Mother
and the memory of my Father

Preface

The present book – *Atomic and Molecular Spectroscopy – Basic Aspects and Practical Applications* – has been developed over a long time. The Third Edition, which appeared in 2001, was fully revised and updated to the state of the field at that time. The book appeared in hard cover well suited for individual and library use. However, the book is basically a text, also well suited as a base for a course on the topic. A lower-cost paper-back edition better serves such purposes, as did the Second (paper-back) Edition of the book. The Fourth Edition presented has now been corrected for misprints and contains some additional text. A number of important literature references up until mid-2003 have been added to provide a fully updated account of the dynamic field of Atomic and Molecular Spectroscopy.

Lund, October 2003

Sune Svanberg

Preface to the Third Edition

Atomic and molecular spectroscopy – both in its basic and in its applied aspects – is in a dynamic state of development. It continues to provide new fascinating possibilities for a deeper understanding of the fundamental properties of the building blocks of matter and their interaction with electromagnetic irradiation. It generates new possibilities for practical applications in industry, chemistry, astronomy, geosciences, biology, medicine and information technology.

Ten years after the appearance of the first edition there was a need for a thorough revision of the book, again bringing it up to the leading edge in the new millennium. This has led to a considerable extension of the material and thus of the size of the book. As previously, the focus has been on the physical understanding of the processes and phenomena, and on providing a broad overview of the possibilities of atomic and molecular spectroscopy. Thus, the mathematical description is frequently superficial – for the benefit of students and scientists in other natural sciences without a rigorous physics background. My belief is that the physical (and intuitive) understanding, when possible, is also the most important aspect for the hard-core physicist. The reader will find ample references to textbooks, review articles and research papers providing all the details on almost any topic in the field, and the reference list was, with considerable effort, updated till mid-2000 and in some cases till early 2001. This could still mean that important references are lacking, and I apologize to the authors for unfortunate omissions.

The reader who already knows the previous editions will notice that new material is added, particularly in the following fields: clusters, satellite remote sensing, astrophysical applications, the generation of ultrafast and ultraintense laser radiation, diode laser spectroscopy, ultrafast spectroscopy, femtochemistry, high-power laser–matter interaction, laser cooling and trapping, Bose–Einstein condensation, and lasers in environmental and medical research. Thus, it is felt that the book provides a rather extensive overview of the major spectroscopy fields.

In order to improve the usefulness of the book as a text for a course on the topic at the pre- or postgraduate level, a section of questions and exercises has been added. The material is presented following the chapters, and, in addition, material connecting wider areas is supplied. A detailed subject index

is also provided, helping the reader to easily find an entry to the introduction of a subfield and references to the relevant literature.

The author benefited a lot from the interaction with students and colleagues when developing this book. He is very grateful for comments and corrections.

Finally, I would like to thank Gertrud Dimler, Adelheid Duhm and Claus Ascheron at Springer-Verlag for their professional work, and Helmut Lotsch for his encouragement throughout this book project.

Lund, June 2001

Sune Svanberg

Preface to the First Edition

Atomic and molecular spectroscopy has provided basic information leading to the development of quantum mechanics and to the understanding of the building blocks of matter. It continues to provide further insight into the statics and dynamics of the microcosmos, and provides the means for testing new concepts and computational methods. The results of atomic and molecular spectroscopy are of great importance in astrophysics, plasma and laser physics. The rapidly growing field of spectroscopic applications has made considerable impact on many disciplines, including medicine, environmental protection, chemical processing and energy research. In particular, the techniques of electron and laser spectroscopy, the subjects of the 1981 Nobel prize in physics, have contributed much to the analytical potential of spectroscopy.

This textbook on *Atomic and Molecular Spectroscopy* has been prepared to provide an overview of modern spectroscopic methods. It is intended to serve as a text for a course on the subject for final-year undergraduate physics students or graduate students. It should also be useful for students of astrophysics and chemistry. The text has evolved from courses on atomic and molecular spectroscopy given by the author since 1975 at Chalmers University of Technology and at the Lund Institute of Technology. References are given to important books and review articles which allow more detailed studies of different aspects of atomic and molecular spectroscopy. No attempt has been made to cover all important references, nor have priority aspects been systematically considered.

It is assumed that the reader has a basic knowledge of quantum mechanics and atomic physics. However, the completion of a specialized course on atomic and molecular physics is not required. The present treatise (disregarding Chap. 4) is not particularly mathematical, but emphasizes the physical understanding of the different techniques of spectroscopy. In the course given by the author, the time for solving calculational problems has been reduced to allow a more complete overview of the field in the time available. Particular emphasis has been given to technical applications. However, by increasing the allotted problem-solving time or by omitting certain areas of spectroscopy, a more problem-oriented course can easily be taught based on this book. In his courses, the author has combined lectures with a number of 5-hour

laboratory experiments (performed on research equipment) and a number of 1-2 hour visits to local research groups in physics, chemistry and astronomy.

Part of the material is reworked from the Swedish textbook *Atomfysik* by I. Lindgren and S. Svanberg (Universitetsförlaget, Uppsala 1974). The author is very grateful to his teacher Prof. I. Lindgren for contributions and support through the years. He would also like to thank many colleagues, including Prof. D. Dravins, Dr. Å Hjalmarsson, Prof. I. Martinson, Prof. J. Nordgren, Prof. C. Nordling, Dr. W. Persson, Prof. A. Rósen, Prof. H. Siegbahn and Dr. C.-G. Wahlström for valuable suggestions and corrections.

Special thanks are due to Mrs. C. Holmqvist for typing numerous versions of the manuscript and Dr. H. Sheppard for correcting the English and assisting with the figures. Mr. Å. Bergqvist and Mr. G. Romerius helped by drawing some of the figures. Finally, the kind help and support of Dr. H. Lotsch of Springer-Verlag is gratefully acknowledged.

Lund, September 1990

Sune Svanberg

Contents

| | |
|----------------------------------------------------|----|
| 1. Introduction | 1 |
| 2. Atomic Structure | 5 |
| 2.1 One-Electron Systems | 5 |
| 2.2 Alkali Atoms | 7 |
| 2.3 Magnetic Effects | 8 |
| 2.3.1 Precessional Motion | 8 |
| 2.3.2 Spin-Orbit Interaction | 9 |
| 2.4 General Many-Electron Systems | 10 |
| 2.5 The Influence of External Fields | 17 |
| 2.5.1 Magnetic Fields | 18 |
| 2.5.2 Electric Fields | 21 |
| 2.6 Hyperfine Structure | 23 |
| 2.6.1 Magnetic Hyperfine Structure | 23 |
| 2.6.2 Electric Hyperfine Structure | 25 |
| 2.7 The Influence of External Fields (hfs) | 26 |
| 2.8 Isotopic Shifts | 29 |
| 3. Molecular Structure | 31 |
| 3.1 Electronic Levels | 32 |
| 3.2 Rotational Energy | 35 |
| 3.3 Vibrational Energy | 36 |
| 3.4 Polyatomic Molecules | 37 |
| 3.5 Clusters | 39 |
| 3.6 Other Molecular Structures | 40 |
| 4. Radiation and Scattering Processes | 41 |
| 4.1 Resonance Radiation | 41 |
| 4.2 Spectra Generated by Dipole Transitions | 51 |
| 4.2.1 Atoms | 52 |
| 4.2.2 Molecules | 55 |
| 4.3 Rayleigh and Raman Scattering | 61 |
| 4.4 Raman Spectra | 63 |
| 4.4.1 Vibrational Raman Spectra | 63 |

| | | |
|-----------|------------------------------------------------------------------------------|-----------|
| 4.4.2 | Rotational Raman Spectra | 64 |
| 4.4.3 | Vibrational–Rotational Raman Spectra | 64 |
| 4.5 | Mie Scattering | 65 |
| 4.6 | Atmospheric Scattering Phenomena | 66 |
| 4.7 | Comparison Between Different Radiation and Scattering Processes | 69 |
| 4.8 | Collision-Induced Processes | 70 |
| 5. | Spectroscopy of Inner Electrons | 71 |
| 5.1 | X-Ray Spectroscopy | 71 |
| 5.1.1 | X-Ray Emission Spectroscopy | 73 |
| 5.1.2 | X-Ray Absorption Spectroscopy | 79 |
| 5.1.3 | X-Ray Imaging Applications | 82 |
| 5.2 | Photoelectron Spectroscopy | 85 |
| 5.2.1 | XPS Techniques and Results | 87 |
| 5.2.2 | Chemical Shifts | 90 |
| 5.3 | Auger Electron Spectroscopy | 95 |
| 6. | Optical Spectroscopy | 97 |
| 6.1 | Light Sources | 97 |
| 6.1.1 | Line Light Sources | 98 |
| 6.1.2 | Continuum Light Sources | 106 |
| 6.1.3 | Synchrotron Radiation | 108 |
| 6.1.4 | Natural Radiation Sources | 113 |
| 6.2 | Spectral Resolution Instruments | 114 |
| 6.2.1 | Prism Spectrometers | 114 |
| 6.2.2 | Grating Spectrometers | 117 |
| 6.2.3 | The Fabry–Pérot Interferometer | 121 |
| 6.2.4 | The Fourier Transform Spectrometer | 126 |
| 6.3 | Detectors | 128 |
| 6.4 | Optical Components and Materials | 134 |
| 6.4.1 | Interference Filters and Mirrors | 134 |
| 6.4.2 | Absorption Filters | 138 |
| 6.4.3 | Polarizers | 141 |
| 6.4.4 | Optical Materials | 143 |
| 6.4.5 | Influence of the Transmission Medium | 144 |
| 6.5 | Optical Methods of Chemical Analysis | 148 |
| 6.5.1 | The Beer–Lambert Law | 149 |
| 6.5.2 | Atomic Absorption/Emission Spectrophotometry | 151 |
| 6.5.3 | Burners, Flames, Sample Preparation and Measurements | 155 |
| 6.5.4 | Modified Methods of Atomization | 156 |
| 6.5.5 | Multi-Element Analysis | 157 |
| 6.5.6 | Molecular Spectrophotometry | 158 |
| 6.5.7 | Raman Spectroscopy | 160 |

| | | |
|-------|-----------------------------------------------------------------------|-----|
| 6.6 | Optical Remote Sensing | 162 |
| 6.6.1 | Atmospheric Monitoring with Passive Techniques | 164 |
| 6.6.2 | Land and Water Measurements with Passive Techniques | 171 |
| 6.7 | Astrophysical Spectroscopy | 176 |
| 7. | Radio-Frequency Spectroscopy | 187 |
| 7.1 | Resonance Methods | 187 |
| 7.1.1 | Magnetic Resonance | 187 |
| 7.1.2 | Atomic-Beam Magnetic Resonance | 189 |
| 7.1.3 | Optical Pumping | 197 |
| 7.1.4 | Optical Double Resonance | 200 |
| 7.1.5 | Level-Crossing Spectroscopy | 203 |
| 7.1.6 | Resonance Methods for Liquids and Solids | 209 |
| 7.2 | Microwave Radiometry | 218 |
| 7.3 | Radio Astronomy | 222 |
| 8. | Lasers | 227 |
| 8.1 | Basic Principles | 227 |
| 8.2 | Coherence | 230 |
| 8.3 | Resonators and Mode Structure | 231 |
| 8.4 | Fixed-Frequency Lasers | 236 |
| 8.4.1 | The Ruby Laser | 236 |
| 8.4.2 | Four-Level Lasers | 238 |
| 8.4.3 | Pulsed Gas Lasers | 241 |
| 8.4.4 | The He–Ne Laser | 243 |
| 8.4.5 | Gaseous Ion Lasers | 244 |
| 8.5 | Tunable Lasers | 246 |
| 8.5.1 | Dye Lasers | 246 |
| 8.5.2 | Colour-Centre Lasers | 255 |
| 8.5.3 | Tunable Solid-State Lasers | 256 |
| 8.5.4 | Tunable CO ₂ Lasers | 257 |
| 8.5.5 | Semiconductor Lasers | 259 |
| 8.6 | Nonlinear Optical Phenomena | 262 |
| 8.7 | Ultra-short and Ultra-high-Power Laser Pulse Generation | 276 |
| 8.7.1 | Short-Pulse Generation by Mode-Locking | 276 |
| 8.7.2 | Generation of Ultra-high Power Pulses | 282 |
| 9. | Laser Spectroscopy | 287 |
| 9.1 | Basic Principles | 287 |
| 9.1.1 | Comparison Between Conventional Light Sources and Lasers | 287 |
| 9.1.2 | Saturation | 287 |
| 9.1.3 | Excitation Methods | 289 |

| | | |
|-------|--------------------------------------------------------------------------------------------|-----|
| 9.1.4 | Detection Methods | 290 |
| 9.1.5 | Laser Wavelength Setting | 292 |
| 9.2 | Doppler-Limited Techniques | 294 |
| 9.2.1 | Absorption Measurements | 294 |
| 9.2.2 | Intracavity Absorption Measurements | 296 |
| 9.2.3 | Absorption Measurements on Excited States | 297 |
| 9.2.4 | Level Labelling | 298 |
| 9.2.5 | Two-Photon Absorption Measurements | 299 |
| 9.2.6 | Opto-Galvanic Spectroscopy | 301 |
| 9.2.7 | Single-Atom and Single-Molecule Detection | 304 |
| 9.2.8 | Opto-Acoustic Spectroscopy | 304 |
| 9.3 | Optical Double-Resonance and Level-Crossing Experiments with Laser Excitation | 306 |
| 9.4 | Time-Resolved Atomic and Molecular Spectroscopy | 311 |
| 9.4.1 | Generation of Short Optical Pulses | 312 |
| 9.4.2 | Measurement Techniques for Optical Transients | 312 |
| 9.4.3 | Background to Lifetime Measurements | 318 |
| 9.4.4 | Survey of Methods of Measurement for Radiative Properties | 319 |
| 9.4.5 | Quantum-Beat Spectroscopy | 325 |
| 9.5 | Ultrafast Spectroscopy | 331 |
| 9.5.1 | Ultrafast Measurement Techniques | 332 |
| 9.5.2 | Molecular Reaction Dynamics (Femtochemistry) | 336 |
| 9.5.3 | Coherent Control | 338 |
| 9.6 | High-Power Laser Experiments | 339 |
| 9.6.1 | Above Threshold Ionization (ATI) | 340 |
| 9.6.2 | High Harmonic Generation | 342 |
| 9.6.3 | X-Ray Laser Pumping | 347 |
| 9.6.4 | Broadband X-Ray Generation | 348 |
| 9.6.5 | Relativistic Effects and Laser Accelerators | 351 |
| 9.6.6 | Laser-Nuclear Interactions and Laser-Driven Fusion | 351 |
| 9.7 | High-Resolution Laser Spectroscopy | 351 |
| 9.7.1 | Spectroscopy on Collimated Atomic and Ionic Beams | 352 |
| 9.7.2 | Saturation Spectroscopy and Related Techniques | 359 |
| 9.7.3 | Doppler-Free Two-Photon Absorption | 368 |
| 9.8 | Cooling and Trapping of Ions and Atoms | 374 |
| 9.8.1 | Introduction | 374 |
| 9.8.2 | Ion Traps | 376 |
| 9.8.3 | Basic Laser Cooling in Traps | 377 |
| 9.8.4 | Trapped Ion Spectroscopy | 379 |
| 9.8.5 | Atom Cooling and Trapping | 379 |
| 9.8.6 | Sub-Recoil Cooling | 382 |
| 9.8.7 | Atom Optics | 384 |
| 9.8.8 | Bose-Einstein Condensation and “Atom Lasers” | 384 |
| 9.8.9 | Ultracold Fermionic Gases | 387 |

| | |
|-------------------------------------------------------------------------------------------|-----|
| 10. Laser-Spectroscopic Applications | 389 |
| 10.1 Diagnostics of Combustion Processes | 389 |
| 10.1.1 Background | 389 |
| 10.1.2 Laser-Induced Fluorescence and Related Techniques | 392 |
| 10.1.3 Raman Spectroscopy | 398 |
| 10.1.4 Coherent Anti-Stokes Raman Scattering | 398 |
| 10.1.5 Velocity Measurements | 403 |
| 10.2 Laser Remote Sensing of the Atmosphere | 406 |
| 10.2.1 Optical Heterodyne Detection | 407 |
| 10.2.2 Long-Path Absorption Techniques | 408 |
| 10.2.3 Lidar Techniques | 414 |
| 10.3 Laser-Induced Fluorescence and Raman Spectroscopy in Liquids and Solids | 425 |
| 10.3.1 Hydrospheric Remote Sensing | 426 |
| 10.3.2 Vegetation Monitoring | 429 |
| 10.3.3 Monitoring of Surface Layers | 430 |
| 10.4 Laser-Induced Chemical Processes | 435 |
| 10.4.1 Laser-Induced Chemistry | 435 |
| 10.4.2 Laser Isotope Separation | 436 |
| 10.5 Spectroscopic Aspects of Lasers in Medicine | 441 |
| 10.5.1 Thermal Interaction of Laser Light with Tissue | 441 |
| 10.5.2 Photodynamic Tumour Therapy | 443 |
| 10.5.3 Tissue Diagnostics with Laser-Induced Fluorescence | 447 |
| 10.5.4 Scattering Spectroscopy and Tissue Transillumination . | 454 |
| Questions and Exercises | 461 |
| References | 473 |
| Index | 575 |

1. Introduction

By *spectroscopy* we usually mean experimental charting of the energy-level structure of physical systems. For that purpose, the transition processes, spontaneous or induced, between different energy states are studied and spectroscopy therefore normally means analysis of various types of radiation – electromagnetic or particle emission. Spectroscopic investigations can be of a fundamental or an applied nature. In fundamental spectroscopy experimentally determined energy levels, transition probabilities, etc. are employed for obtaining an understanding of the studied systems using adequate theories or models. Usually, certain primary quantities (wavelengths, intensities, etc.) are measured in spectroscopic investigations. These quantities are then used to evaluate more fundamental quantities. This process is schematically illustrated in Fig. 1.1.

Fundamental quantities, such as wavelengths and transition probabilities, determined using spectroscopy, for atoms and molecules are of direct importance in several disciplines such as astrophysics, plasma and laser physics. Here, as in many fields of applied spectroscopy, the spectroscopic information can be used in various kinds of analysis. For instance, optical atomic absorption or emission spectroscopy is used for both qualitative and quantitative chemical analysis. Other types of spectroscopy, e.g. electron spectroscopy methods or nuclear magnetic resonance, also provide information on the chemical environment in which a studied atom is situated. Tunable lasers have had a major impact on both fundamental and applied spectroscopy. New fields of applied laser spectroscopy include remote sensing of the environment, medical applications, combustion diagnostics, laser-induced chemistry and isotope separation.

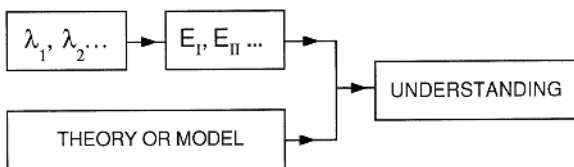


Fig. 1.1. The spectroscopic process

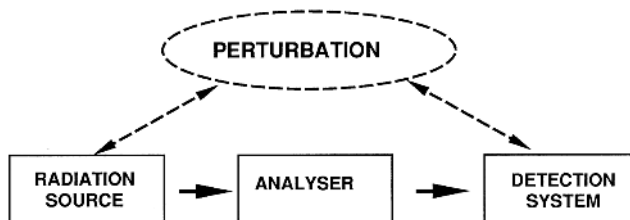


Fig. 1.2. Basic arrangement of a spectroscopic set-up

Dynamic properties of atomic and molecular systems can be studied by time-resolved spectroscopy. The recent availability of compact high-power lasers has allowed a quickly expanding research activity in ultra-intense laser-matter interaction, also offering many new challenges for theory.

In principle, a set-up for spectral studies consists of three components: a radiation source, an analyser and a detection system. In many modern techniques the system under investigation is subjected to different types of static or oscillatory fields and the influence of these fields on the system is studied in order to obtain a more complete picture of the system. Resonance methods are of special importance since they provide high accuracy in the determination of small energy splittings. The basic arrangement of a spectroscopic set-up is shown in Fig. 1.2.

The choice of spectroscopic method is primarily determined by the energy range of the phenomenon to be studied. In Fig. 1.3 the spectral ranges that

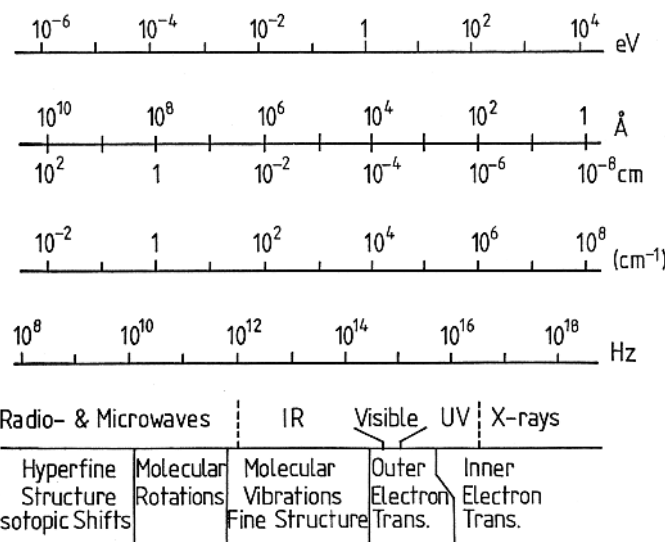


Fig. 1.3. Energy scales and spectroscopic phenomena

Table 1.1. Conversion factors between different energy units

| Unit | Joule | cm^{-1} | Hz | eV |
|---------------------|---------------------------|---------------------------|--------------------------|---------------------------|
| 1 Joule (1 J) | 1 | 5.03378×10^{22} | 1.50919×10^{33} | 6.24150×10^{18} |
| 1 cm^{-1} | 1.98658×10^{-23} | 1 | 2.99792×10^{10} | 1.23992×10^{-4} |
| 1 Hz | 6.62608×10^{-34} | 3.33565×10^{-11} | 1 | 4.13567×10^{-15} |
| 1 eV | 1.60218×10^{-19} | 8.06502×10^3 | 2.41799×10^{14} | 1 |

are of interest in atomic and molecular spectroscopy are shown. The energy ranges for different types of structures and transitions are also indicated. Using the simple relations

$$\Delta E = h\nu, \quad \lambda = c/\nu, \quad 1/\lambda = \nu/c, \quad \nu = c(1/\lambda), \quad (1.1)$$

| | | | |
|--------|------------|------------|-----------|
| Energy | Wavelength | Wavenumber | Frequency |
|--------|------------|------------|-----------|

(h : Planck constant, c : velocity of light) an energy interval ΔE can be uniquely expressed in eV (energy), nm ($=10 \text{ \AA}$) (wavelength), cm^{-1} (wavenumber) or Hz (frequency). 1 cm^{-1} is sometimes called 1 Kayser. In Table 1.1 conversion factors between different units are given. The general field of scientific unit conversion is treated in [1.1]. The conversion factors are clearly connected to the values of the fundamental constants [1.2].

The choice of unit depends, to a great extent, on the energy region and on traditional factors:

| | |
|------------------------|--------------------------------------------------|
| X-ray region | keV , |
| Visible and UV regions | nm , \AA (in solid-state physics: eV) , |
| Infrared region | μm , cm^{-1} , |
| Radio-frequency region | MHz , cm^{-1} . |

It is practical to memorize the following approximate relations

$$1 \text{ eV} \longleftrightarrow 8000 \text{ cm}^{-1} \longleftrightarrow 1200 \text{ nm} ,$$

$$1 \text{ cm}^{-1} \longleftrightarrow 30 \text{ GHz} ,$$

and kT at $T = 300 \text{ K}$ (room temperature)

$$kT_{300} \simeq 1/40 \text{ eV} .$$

(k is the Boltzmann constant, and T is the absolute temperature).

Transitions between inner electron orbitals normally occur in the keV range (X-rays) while the energies for transitions between outer orbitals are in the eV region (visible or near-UV and IR regions). The fine structure of atoms is of the order of 10^{-3} eV ($\sim 10 \text{ cm}^{-1}$) and hyperfine structures are typically about 10^{-6} eV ($\sim 300 \text{ MHz}$). Molecular vibrational energies splittings are of the order of 10^{-1} eV , while rotational splittings are typically 10^{-3} eV . Of course, these energies vary widely and the above values are given only to provide a first estimate of typical orders of magnitude.

As a background to atomic and molecular spectroscopy a survey of atomic and molecular structure is given in Chaps. 2 and 3. Chapter 4 deals with the fundamental radiative and scattering processes that are encountered in spectroscopy. Chapter 5 is devoted to the study of inner electrons while the techniques of basic and applied optical spectroscopy are treated in Chap. 6. The precision methods of radio-frequency spectroscopy are described in Chap. 7. Finally, the last three chapters deal with lasers and their application to fundamental and applied spectroscopy.

2. Atomic Structure

In this chapter a brief description of the energy-level structure of atomic systems will be given. This will not include a rigorous quantum-mechanical treatment, but will deal with more qualitative aspects. The atomic structures that are explored with the spectroscopic techniques discussed in this text will be described. For a more complete treatment the reader is referred to standard textbooks on atomic physics and quantum mechanics [2.1–2.22].

2.1 One-Electron Systems

In hydrogen and hydrogen-like systems a single electron moves around the nucleus of charge Ze at a distance r in a *central field*, and its potential energy is given by

$$V(r) = -\frac{Ze^2}{4\pi\epsilon_0 r}. \quad (2.1)$$

The Hamiltonian of the system is then

$$\mathcal{H}_0 = \frac{1}{2m}\mathbf{p}^2 + V(r) \quad (2.2)$$

(\mathbf{p} is the momentum operator, m is the electron mass) and the energy eigenvalues are obtained by solving the Schrödinger equation

$$\left[-\frac{\hbar^2}{2m}\Delta + V(r) \right] \psi = E\psi \quad (2.3)$$

(Δ is the Laplace operator, and $\hbar = h/2\pi$). The eigenvalues depend only on the principal quantum number n and are independent of the azimuthal quantum number ℓ and its projection m_ℓ

$$E_n = -hc\text{Ry} \frac{Z^2}{n^2} (n = 1, 2, 3, \dots), \quad (2.4)$$

where

$$\text{Ry} = \frac{me^4}{4\pi(4\pi\epsilon_0)^2 c\hbar^3}. \quad (2.5)$$

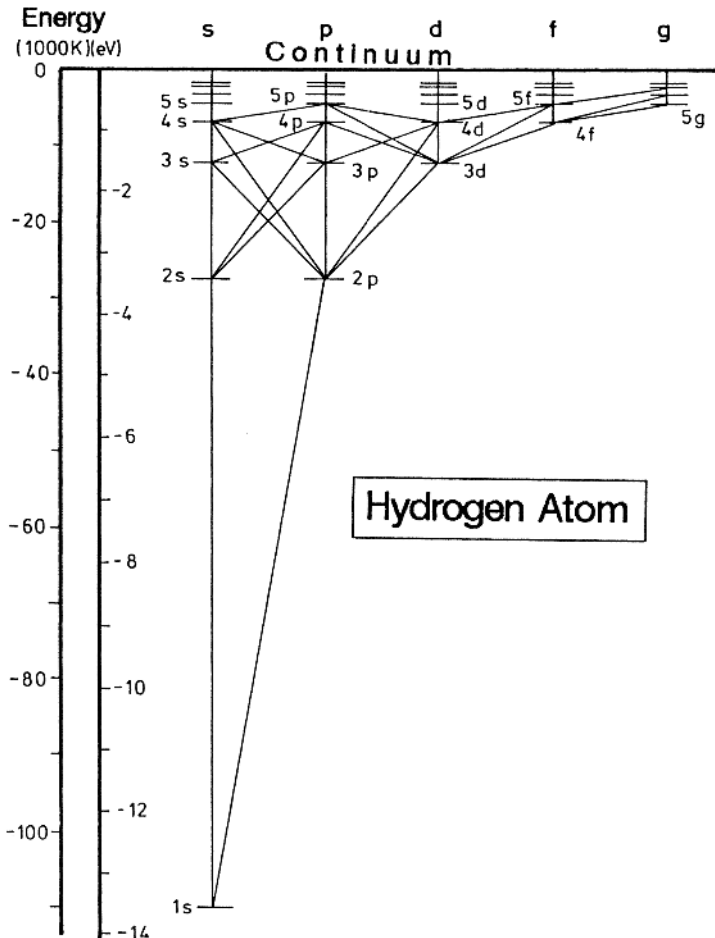


Fig. 2.1. Energy level diagram of the hydrogen atom

However, the ℓ value specifies the wavefunctions and the states are characterized according to

$$\ell = \begin{matrix} 0 & 1 & 2 & 3 & 4 & 5 \end{matrix} \quad \begin{matrix} s & p & d & f & g & h \end{matrix}.$$

If relativistic and quantum electrodynamic (QED) effects are considered, the far-reaching degeneracy for hydrogen-like systems is lifted. In Fig. 2.1 the simple energy-level diagram of hydrogen is shown.

Besides hydrogen, hydrogen-like ions [2.23] and positronium (positron + electron) and muonium (proton + muon) [2.24] have been much studied since they constitute good testing grounds for advanced theories.

2.2 Alkali Atoms

In alkali atoms there is a single electron outside a spherically symmetric inner electron cloud (core). The field in which the outer electron moves is not Coulombic, but is still essentially central. The energy for such a system can be written

$$E = -\frac{hc \text{ Ry}}{n_{\text{eff}}^2}, \quad (2.6)$$

where $n_{\text{eff}} = n - d$ is called the *effective quantum number*, and d the *quantum defect*. The s electrons may penetrate into the core (they can even be found at the surface or actually inside the nucleus) thus experiencing an increased force from the less shielded nucleus, which results in a stronger binding. This behaviour is reflected in the quantum defect, which for s electrons is of the

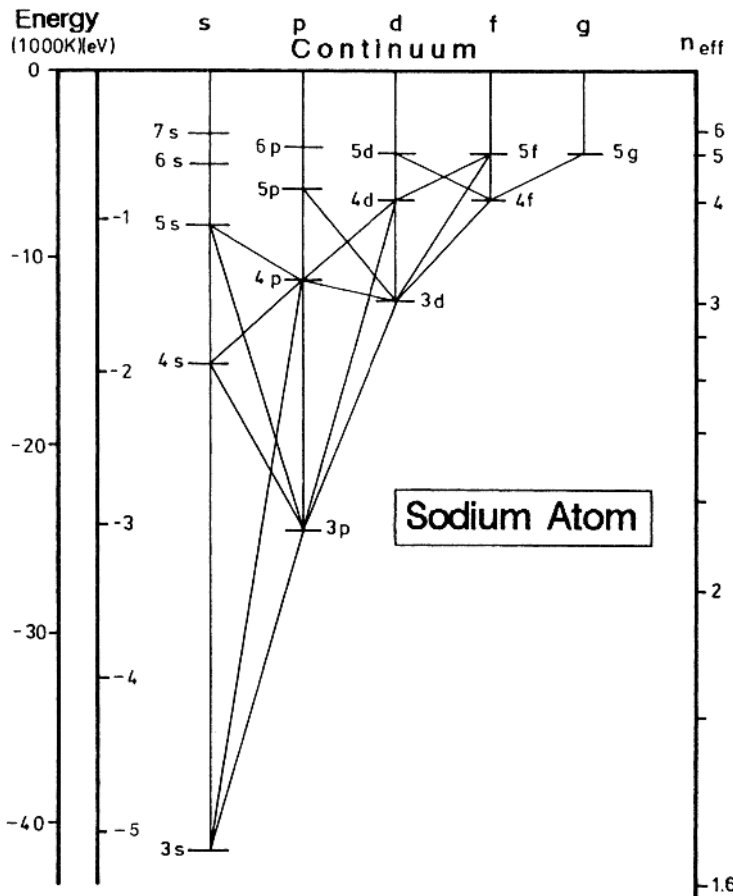


Fig. 2.2. Energy level diagram of the sodium atom

order of 2. For high- ℓ orbits (*non-penetrating electrons*) the quantum defect approaches zero. These effects are illustrated for the case of sodium in Fig. 2.2.

2.3 Magnetic Effects

2.3.1 Precessional Motion

An angular momentum vector \mathbf{L} , associated with a magnetic moment μ_L will precess in a magnetic field, as illustrated in Fig. 2.3. Frequently we encounter this phenomenon in the description of atomic and molecular processes. To demonstrate the phenomenon, imagine magnetic poles q in analogy with the electrical case, for which we have the same mathematical description. For the mechanical moment \mathbf{M} we then have

$$|\mathbf{M}| = qB \frac{d}{2} \sin \theta + qB \frac{d}{2} \sin \theta = qBd \sin \theta, \quad (2.7)$$

that is

$$\mathbf{M} = \mu_L \times \mathbf{B} \text{ with } |\mu_L| = qd. \quad (2.8)$$

But

$$\mu_L = -g\mu_B \mathbf{L}, \quad (2.9)$$

where μ_B is the *Bohr magneton* and g is a positive constant of proportionality. (Throughout this book we use dimensionless angular momentum vectors. μ_B has the dimension of a magnetic moment.) The laws of motion then yield

$$\frac{d\mathbf{L}}{dt} = \mathbf{M} = -g\mu_B \mathbf{L} \times \mathbf{B}. \quad (2.10)$$

Thus

$$d\mathbf{L} = -(g\mu_B \mathbf{L} \times \mathbf{B})dt, \quad (2.11)$$

showing that the tip of \mathbf{L} moves perpendicularly to both \mathbf{L} and \mathbf{B} , i.e. \mathbf{L} precesses with an angular frequency $\omega = g\mu_B B$.

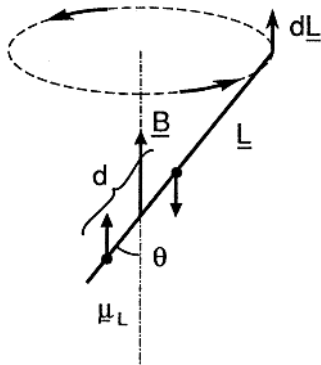


Fig. 2.3. Precession of an angular momentum vector and an associated magnetic moment in the magnetic field

2.3.2 Spin-Orbit Interaction

The electron has a spin angular momentum \mathbf{s} and an associated magnetic moment $\boldsymbol{\mu}_s$ i.e.,

$$\boldsymbol{\mu}_s = -g_s \mu_B \mathbf{s}. \quad (2.12)$$

As the electron moves in the electric field of the nucleus it is subject to a magnetic field \mathbf{B}_ℓ , which is proportional to the angular momentum \mathbf{l} of the electron (Fig. 2.4). The electron then has an orientational energy E_{so} in the field

$$E_{\text{so}} = -\boldsymbol{\mu}_s \cdot \mathbf{B}_\ell = \zeta \mathbf{l} \cdot \mathbf{s}, \quad (2.13)$$

where ζ is a constant of proportionality. \mathbf{l} and \mathbf{s} couple and precess about their mutual resultant \mathbf{j} with a frequency proportional to the strength of the field. We have

$$\mathbf{j} = \mathbf{l} + \mathbf{s}. \quad (2.14)$$

For the corresponding quantum numbers describing the length of the vector (e.g., $|j| = [j(j+1)]^{1/2}$, dimensionless angular momentum! The normally occurring \hbar in the length expression of an angular momentum vector is included in ζ !) we have

$$\begin{aligned} s &= 1/2, \\ \ell &= 0, 1, 2, \dots, \\ j &= \ell \pm 1/2. \end{aligned}$$

Using the vector cosine theorem

$$\mathbf{j}^2 = (\mathbf{l} + \mathbf{s})^2 = \mathbf{l}^2 + \mathbf{s}^2 + 2\mathbf{l} \cdot \mathbf{s}$$

we obtain

$$E_{\text{so}} = \zeta [j(j+1) - \ell(\ell+1) - s(s+1)]/2. \quad (2.15)$$

Here we have inserted the “quantum-mechanical squares” or, to use a more modern term, used first-order perturbation theory. The so-called *fine-structure splitting* between the two possible j levels is given by

$$\Delta E_{\text{so}} = \zeta(\ell + 1/2). \quad (2.16)$$

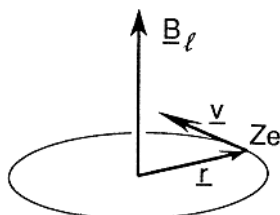


Fig. 2.4. Magnetic field associated with orbital motion

Table 2.1. Fine-structure splittings in 2P states of the alkali atoms [cm^{-1}]

| <i>n</i> | Na | K | Rb | Cs |
|----------|-----|-----|-----|-----|
| 3 | 17 | | | |
| 4 | 5.6 | 58 | | |
| 5 | 2.5 | 19 | 238 | |
| 6 | 1.2 | 8.4 | 78 | 554 |
| 7 | 0.7 | 4.5 | 35 | 181 |
| 8 | 0.4 | 2.7 | 19 | 83 |
| 9 | | 1.7 | 11 | 45 |
| 10 | | 1.2 | 7 | 27 |

In a simple calculation, ζ is found to be a positive quantity, scaling as $1/n_{\text{eff}}^3$. The high- j level then has a higher energy than the low- j level. This is found to be true for p -states of alkali atoms, and in Table 2.1 some experimentally determined fine-structure splittings are given. For $\ell > 1$ *level inversion* sometimes occurs, i.e. the high- j level has the lower energy. This is due to *core polarization*. The outer electron polarizes the closed shells so that a dominating, oppositely directed magnetic field contribution is obtained from these shells. In Fig. 2.5 the level ordering for the alkali atoms doublets is indicated.

ALKALI ATOM FINE-STRUCTURE

| | Li | Na | K | Rb | Cs |
|--------------|----|----|---|----|----|
| ^2P | ↑ | ↑ | ↑ | ↑ | ↑ |
| ^2D | ↑ | ↓ | ↓ | ↑* | ↑ |
| ^2F | ↑ | ↑ | ↓ | ↓ | ↓ |
| ^2G | ↑ | ↑ | | | |

NORMAL: \uparrow
 INVERTED: \downarrow

Fig. 2.5. Level ordering in alkali atom doublet series. (The asterisk* indicates that the lowest member of the Rubidium series is inverted)

2.4 General Many-Electron Systems

The structure of the general many-electron system with i electrons is obviously much more difficult to calculate. As a starting point the following approximate Hamiltonian is used

$$\mathcal{H} = \sum_i \left(\frac{1}{2m} \mathbf{p}_i^2 - \frac{Ze^2}{4\pi\epsilon_0 r_i} \right) + \sum_{i < j} \frac{e^2}{4\pi\epsilon_0 r_{ij}} + \sum_i \zeta_i(r_i) \mathbf{l}_i \cdot \mathbf{s}_i. \quad (2.17)$$

Here r_{ij} is the distance between the electrons i and j . As an approximation to (2.17) we assume that every electron moves independently of the other electrons in an average field, generated by the nucleus and the other electrons (the *independent particle model*). The field is assumed to be *central* (dependent only on r). This is the *central-field approximation*. The assumption of a central field combined with the Pauli exclusion principle results in a shell structure for the electrons and successively heavier elements can be constructed using the building-up principle (the total energy is minimized). The atom can be characterized by its *electron configuration*, e.g. for the lowest state of sodium we have

$$1s^2 2s^2 2p^6 3s.$$

In Table 2.2 the ground configurations of the atoms are listed. Obviously, the field in atoms is only approximately central. Besides a *central* part, the electrostatic repulsion between electrons causes a *non-central* contribution, which can be treated as a perturbation. The spin-orbit interaction must also be taken into account. If the non-central electrostatic part strongly dominates over the spin-orbit interaction, the latter is neglected as a first approximation. A coupling between the individual angular momenta is then obtained

$$\mathbf{L} = \sum_i \mathbf{l}_i, \mathbf{S} = \sum_i \mathbf{s}_i. \quad (2.18)$$

Depending on which values are possible for the corresponding quantum numbers L and S for a certain configuration, a number of electrostatically split *terms* are obtained. Such terms are designated

$$2S + 1_X.$$

The quantity $2S+1$ is called the *multiplicity*. In analogy with the one electron case we have

$$\begin{array}{llllll} L & = & 0 & 1 & 2 & 3 & 4 \\ X & = & S & P & D & F & G \end{array}.$$

This type of coupling is called *LS coupling*.

The spins of two electrons can be arranged such that $S = 0$ (singlet state) or $S = 1$ (triplet state). In Fig. 2.6 the energy-level diagram for helium is shown (ground configuration $1s^2$). The alkaline-earth atoms Be, Mg, Ca, Sr and Ba in their ground configuration all have two s electrons in the outer shell and thus have similar energy-level diagrams. As an example, the energy-level diagram for calcium is given in Fig. 2.7. Zn, Cd and Hg also have similar energy-level schemes as they also have two electrons in the outer shell.

Table 2.2. Ground configurations of atoms [2.1]

| Atomic number Z | Element | Shells | | | | | LS configuration of the ground state | First ionization potential [eV] | | | | | | | |
|--------------------|-------------|--------|---|-------|---|---|--------------------------------------|---------------------------------|---|---|----|-------------|-------------|-------------|-------|
| | | K | | L | | M | N | O | | | | | | | |
| | | n = 1 | s | n = 2 | s | p | d | n = 3 | s | p | d | n = 4 | s | p | |
| 1 | Hydrogen | H | 1 | | | | | | | | | $^2S_{1/2}$ | 13.60 | | |
| 2 | Helium | He | 2 | | | | | | | | | 1S_0 | 24.58 | | |
| 3 | Lithium | Li | 2 | 1 | | | | | | | | $^2S_{1/2}$ | 5.39 | | |
| 4 | Beryllium | Be | 2 | 2 | | | | | | | | 1S_0 | 9.32 | | |
| 5 | Boron | B | 2 | 2 | 1 | | | | | | | $^2P_{1/2}$ | 8.30 | | |
| 6 | Carbon | C | 2 | 2 | 2 | | | | | | | 3P_0 | 11.26 | | |
| 7 | Nitrogen | N | 2 | 2 | 3 | | | | | | | $^4S_{3/2}$ | 14.54 | | |
| 8 | Oxygen | O | 2 | 2 | 4 | | | | | | | 3P_2 | 13.61 | | |
| 9 | Fluorine | F | 2 | 2 | 5 | | | | | | | $^2P_{3/2}$ | 17.42 | | |
| 10 | Neon | Ne | 2 | 2 | 6 | | | | | | | 1S_0 | 21.56 | | |
| 11 | Sodium | Na | 2 | 2 | 6 | 1 | | | | | | $^2S_{1/2}$ | 5.14 | | |
| 12 | Magnesium | Mg | 2 | 2 | 6 | 2 | | | | | | 1S_0 | 7.64 | | |
| 13 | Aluminium | Al | 2 | 2 | 6 | 2 | 1 | | | | | $^2P_{1/2}$ | 5.98 | | |
| 14 | Silicon | Si | 2 | 2 | 6 | 2 | 2 | | | | | 3P_0 | 8.15 | | |
| 15 | Phosphorous | P | 2 | 2 | 6 | 2 | 3 | | | | | $^4S_{3/2}$ | 10.55 | | |
| 16 | Sulphur | S | 2 | 2 | 6 | 2 | 4 | | | | | 3P_2 | 10.36 | | |
| 17 | Chlorine | Cl | 2 | 2 | 6 | 2 | 5 | | | | | $^2P_{3/2}$ | 13.01 | | |
| 18 | Argon | Ar | 2 | 2 | 6 | 2 | 6 | | | | | 1S_0 | 15.76 | | |
| 19 | Potassium | K | 2 | 2 | 6 | 2 | 6 | 1 | | | | $^2S_{1/2}$ | 4.34 | | |
| 20 | Calcium | Ca | 2 | 2 | 6 | 2 | 6 | 2 | | | | 1S_0 | 6.11 | | |
| 21 | Scandium | Sc | 2 | 2 | 6 | 2 | 6 | 1 | 2 | | | $^2D_{3/2}$ | 6.56 | | |
| 22 | Titanium | Ti | 2 | 2 | 6 | 2 | 6 | 2 | 2 | | | 3F_2 | 6.83 | | |
| 23 | Vanadium | V | 2 | 2 | 6 | 2 | 6 | 3 | 2 | | | $^4F_{3/2}$ | 6.74 | | |
| 24 | Chromium | Cr | 2 | 2 | 6 | 2 | 6 | 5 | 1 | | | 7S_3 | 6.76 | | |
| 25 | Manganese | Mn | 2 | 2 | 6 | 2 | 6 | 5 | 2 | | | $^6S_{5/2}$ | 7.43 | | |
| 26 | Iron | Fe | 2 | 2 | 6 | 2 | 6 | 6 | 2 | | | 5D_4 | 7.90 | | |
| 27 | Cobalt | Co | 2 | 2 | 6 | 2 | 6 | 7 | 2 | | | $^4F_{9/2}$ | 7.86 | | |
| 28 | Nickel | Ni | 2 | 2 | 6 | 2 | 6 | 8 | 2 | | | 3F_4 | 7.63 | | |
| 29 | Copper | Cu | 2 | 2 | 6 | 2 | 6 | 10 | 1 | | | $^2S_{1/2}$ | 7.72 | | |
| 30 | Zinc | Zn | 2 | 2 | 6 | 2 | 6 | 10 | 2 | | | 1S_0 | 9.39 | | |
| 31 | Gallium | Ga | 2 | 2 | 6 | 2 | 6 | 10 | 2 | 1 | | $^2P_{1/2}$ | 6.00 | | |
| 32 | Germanium | Ge | 2 | 2 | 6 | 2 | 6 | 10 | 2 | 2 | | 3P_0 | 7.88 | | |
| 33 | Arsenic | As | 2 | 2 | 6 | 2 | 6 | 10 | 2 | 3 | | $^4S_{3/2}$ | 9.81 | | |
| 34 | Selenium | Se | 2 | 2 | 6 | 2 | 6 | 10 | 2 | 4 | | 3P_2 | 9.75 | | |
| 35 | Bromine | Br | 2 | 2 | 6 | 2 | 6 | 10 | 2 | 5 | | $^2P_{3/2}$ | 11.84 | | |
| 36 | Krypton | Kr | 2 | 2 | 6 | 2 | 6 | 10 | 2 | 6 | | 1S_0 | 14.00 | | |
| 37 | Rubidium | Rb | 2 | 2 | 6 | 2 | 6 | 10 | 2 | 6 | 1 | $^2S_{1/2}$ | 4.18 | | |
| 38 | Strontium | Sr | 2 | 2 | 6 | 2 | 6 | 10 | 2 | 6 | 2 | 1S_0 | 5.69 | | |
| 39 | Yttrium | Y | 2 | 2 | 6 | 2 | 6 | 10 | 2 | 6 | 1 | 2 | $^2D_{3/2}$ | 6.38 | |
| 40 | Zirconium | Zr | 2 | 2 | 6 | 2 | 6 | 10 | 2 | 6 | 2 | 2 | 3F_2 | 6.84 | |
| 41 | Niobium | Nb | 2 | 2 | 6 | 2 | 6 | 10 | 2 | 6 | 4 | 1 | $^6D_{1/2}$ | 6.88 | |
| 42 | Molybdenum | Mo | 2 | 2 | 6 | 2 | 6 | 10 | 2 | 6 | 5 | 1 | 7S_3 | 7.13 | |
| 43 | Technetium | Tc | 2 | 2 | 6 | 2 | 6 | 10 | 2 | 6 | 6 | 1 | $^6D_{9/2}$ | 7.23 | |
| 44 | Ruthenium | Ru | 2 | 2 | 6 | 2 | 6 | 10 | 2 | 6 | 7 | 1 | 5F_5 | 7.37 | |
| 45 | Rhodium | Rh | 2 | 2 | 6 | 2 | 6 | 10 | 2 | 6 | 8 | 1 | $^4F_{9/2}$ | 7.46 | |
| 46 | Palladium | Pd | 2 | 2 | 6 | 2 | 6 | 10 | 2 | 6 | 10 | | 1S_0 | 8.33 | |
| 47 | Silver | Ag | 2 | 2 | 6 | 2 | 6 | 10 | 2 | 6 | 10 | 1 | $^2S_{1/2}$ | 7.57 | |
| 48 | Cadmium | Cd | 2 | 2 | 6 | 2 | 6 | 10 | 2 | 6 | 10 | 2 | 1S_0 | 8.99 | |
| 49 | Indium | In | 2 | 2 | 6 | 2 | 6 | 10 | 2 | 6 | 10 | 2 | 1 | $^2P_{1/2}$ | 5.79 |
| 50 | Tin | Sn | 2 | 2 | 6 | 2 | 6 | 10 | 2 | 6 | 10 | 2 | 2 | 3P_0 | 7.33 |
| 51 | Antimony | Sb | 2 | 2 | 6 | 2 | 6 | 10 | 2 | 6 | 10 | 2 | 3 | $^4S_{3/2}$ | 8.64 |
| 52 | Tellurium | Te | 2 | 2 | 6 | 2 | 6 | 10 | 2 | 6 | 10 | 2 | 4 | 3P_2 | 9.01 |
| 53 | Iodine | J | 2 | 2 | 6 | 2 | 6 | 10 | 2 | 6 | 10 | 2 | 5 | $^2P_{3/2}$ | 10.44 |
| 54 | Xenon | Xe | 2 | 2 | 6 | 2 | 6 | 10 | 2 | 6 | 10 | 2 | 6 | 1S_0 | 12.13 |

Transition elements

Transition elements

| Atomic number <i>Z</i> | Element | Shells | LS config- uration | | | | | | | | First ionization potential [eV] | | | |
|---------------------------|--------------|--------|-----------------------|----------|----------|----------|----------|----------|----------|----------|---------------------------------|----------|--------------|-------|
| | | | N | | | O | | | P | | Q | | | |
| | | | n = 4 | | n = 5 | | n = 6 | | n = 7 | | | | | |
| | | | <i>s</i> | <i>p</i> | <i>d</i> | <i>f</i> | <i>s</i> | <i>p</i> | <i>d</i> | <i>f</i> | <i>s</i> | <i>p</i> | <i>d</i> | |
| 55 | Cesium | Cs | 2 | 6 | 10 | | 2 | 6 | | | 1 | | $^2S_{1/2}$ | 3.89 |
| 56 | Barium | Ba | 2 | 6 | 10 | | 2 | 6 | | | 2 | | 1S_0 | 5.21 |
| 57 | Lanthanum | La | 2 | 6 | 10 | | 2 | 6 | 1 | | 2 | | $^2D_{3/2}$ | 5.61 |
| 58 | Cerium | Ce | 2 | 6 | 10 | | 2 | 6 | | | 2 | | 3H_4 | 5.6 |
| 59 | Praseodymium | Pr | 2 | 6 | 10 | | 3 | 2 | 6 | | 2 | | $^4I_{9/2}$ | 5.46 |
| 60 | Neodymium | Nd | 2 | 6 | 10 | | 4 | 2 | 6 | | 2 | | 5I_4 | 5.51 |
| 61 | Promethium | Pm | 2 | 6 | 10 | | 5 | 2 | 6 | | 2 | | $^6H_{5/2}$ | |
| 62 | Samarium | Sm | 2 | 6 | 10 | | 6 | 2 | 6 | | 2 | | 7F_0 | 5.6 |
| 63 | Europium | Eu | 2 | 6 | 10 | | 7 | 2 | 6 | | 2 | | $^8S_{7/2}$ | 5.67 |
| 64 | Gadolinium | Gd | 2 | 6 | 10 | | 7 | 2 | 6 | 1 | 2 | | 9D_2 | 6.16 |
| 65 | Terbium | Tb | 2 | 6 | 10 | | 9 | 2 | 6 | | 2 | | — | 5.98 |
| 66 | Dysprosium | Dy | 2 | 6 | 10 | | 10 | 2 | 6 | | 2 | | 5I_8 | 6.8 |
| 67 | Holmium | Ho | 2 | 6 | 10 | | 11 | 2 | 6 | | 2 | | $^4I_{15/2}$ | |
| 68 | Erbium | Er | 2 | 6 | 10 | | 12 | 2 | 6 | | 2 | | 3H_6 | 6.08 |
| 69 | Thulium | Tm | 2 | 6 | 10 | | 13 | 2 | 6 | | 2 | | $^2F_{7/2}$ | 5.81 |
| 70 | Ytterbium | Yb | 2 | 6 | 10 | | 14 | 2 | 6 | | 2 | | 1S_0 | 6.22 |
| 71 | Lutetium | Lu | 2 | 6 | 10 | | 14 | 2 | 6 | 1 | 2 | | $^2D_{3/2}$ | 6.15 |
| 72 | Hafnium | Hf | 2 | 6 | 10 | | 14 | 2 | 6 | 2 | 2 | | 3F_2 | 5.5 |
| 73 | Tantalum | Ta | 2 | 6 | 10 | | 14 | 2 | 6 | 3 | 2 | | $^4F_{3/2}$ | 7.7 |
| 74 | Tungsten | W | 2 | 6 | 10 | | 14 | 2 | 6 | 4 | 2 | | 5D_0 | 7.98 |
| 75 | Rhenium | Re | 2 | 6 | 10 | | 14 | 2 | 6 | 5 | 2 | | $^6S_{5/2}$ | 7.87 |
| 76 | Osmium | Os | 2 | 6 | 10 | | 14 | 2 | 6 | 6 | 2 | | 5D_4 | 8.7 |
| 77 | Iridium | Ir | 2 | 6 | 10 | | 14 | 2 | 6 | 9 | | | $^2D_{5/2}$ | 9.2 |
| 78 | Platinum | Pt | 2 | 6 | 10 | | 14 | 2 | 6 | 9 | 1 | | 3D_3 | 9.0 |
| 79 | Gold | Au | 2 | 6 | 10 | | 14 | 2 | 6 | 10 | 1 | | $^2S_{1/2}$ | 9.22 |
| 80 | Mercury | Hg | 2 | 6 | 10 | | 14 | 2 | 6 | 10 | 2 | | 1S_0 | 10.43 |
| 81 | Thallium | Tl | 2 | 6 | 10 | | 14 | 2 | 6 | 10 | 2 | 1 | $^2P_{1/2}$ | 6.11 |
| 82 | Lead | Pb | 2 | 6 | 10 | | 14 | 2 | 6 | 10 | 2 | 2 | 3P_0 | 7.42 |
| 83 | Bismuth | Bi | 2 | 6 | 10 | | 14 | 2 | 6 | 10 | 2 | 3 | $^4S_{3/2}$ | 7.29 |
| 84 | Polonium | Po | 2 | 6 | 10 | | 14 | 2 | 6 | 10 | 2 | 4 | 3P_2 | 8.43 |
| 85 | Astatine | At | 2 | 6 | 10 | | 14 | 2 | 6 | 10 | 2 | 5 | | 9.5 |
| 86 | Radon | Rn | 2 | 6 | 10 | | 14 | 2 | 6 | 10 | 2 | 6 | 1S_0 | 10.75 |
| 87 | Francium | Fr | 2 | 6 | 10 | | 14 | 2 | 6 | 10 | 2 | 6 | 1 | 4 |
| 88 | Radium | Ra | 2 | 6 | 10 | | 14 | 2 | 6 | 10 | 2 | 6 | 2 | 5.28 |
| 89 | Actinium | Ac | 2 | 6 | 10 | | 14 | 2 | 6 | 10 | 2 | 6 | 1 2 | |
| 90 | Thorium | Th | 2 | 6 | 10 | | 14 | 2 | 6 | 10 | 2 | 6 | 2 2 | |
| 91 | Protactinium | Pa | 2 | 6 | 10 | | 14 | 2 | 6 | 10 | 2 | 2 | 6 1 2 | |
| 92 | Uranium | U | 2 | 6 | 10 | | 14 | 2 | 6 | 10 | 3 | 2 | 6 1 2 | |
| 93 | Neptunium | Np | 2 | 6 | 10 | | 14 | 2 | 6 | 10 | 4 | 2 | 6 1 2 | |
| 94 | Plutonium | Pu | 2 | 6 | 10 | | 14 | 2 | 6 | 10 | 6 | 2 | 6 | 2 |
| 95 | Americium | Am | 2 | 6 | 10 | | 14 | 2 | 6 | 10 | 7 | 2 | 6 | 2 |
| 96 | Curium | Cm | 2 | 6 | 10 | | 14 | 2 | 6 | 10 | 7 | 2 | 6 | 1 2 |
| 97 | Berkelium | Bk | 2 | 6 | 10 | | 14 | 2 | 6 | 10 | 8 | 2 | 6 | 1 2 |
| 98 | Californium | Cf | 2 | 6 | 10 | | 14 | 2 | 6 | 10 | 10 | 2 | 6 | 2 |
| 99 | Einsteinium | Es | 2 | 6 | 10 | | 14 | 2 | 6 | 10 | 11 | 2 | 6 | 2 |
| 100 | Fermium | Fm | 2 | 6 | 10 | | 14 | 2 | 6 | 10 | 12 | 2 | 6 | 2 |
| 101 | Mendelevium | Md | 2 | 6 | 10 | | 14 | 2 | 6 | 10 | 13 | 2 | 6 | 2 |
| 102 | Nobelium | No | 2 | 6 | 10 | | 14 | 2 | 6 | 10 | 14 | 2 | 6 | 2 |
| 103 | Lawrencium | Lw | 2 | 6 | 10 | | 14 | 2 | 6 | 10 | 14 | 2 | 6 | 1 2 |
| 104 | Kurchatovium | | 2 | 6 | 10 | | 14 | 2 | 6 | 10 | 14 | 2 | 6 | 2 2 |
| 105 | Hahnium | | 2 | 6 | 10 | | 14 | 2 | 6 | 10 | 14 | 2 | 6 | 3 2 |

Actinides

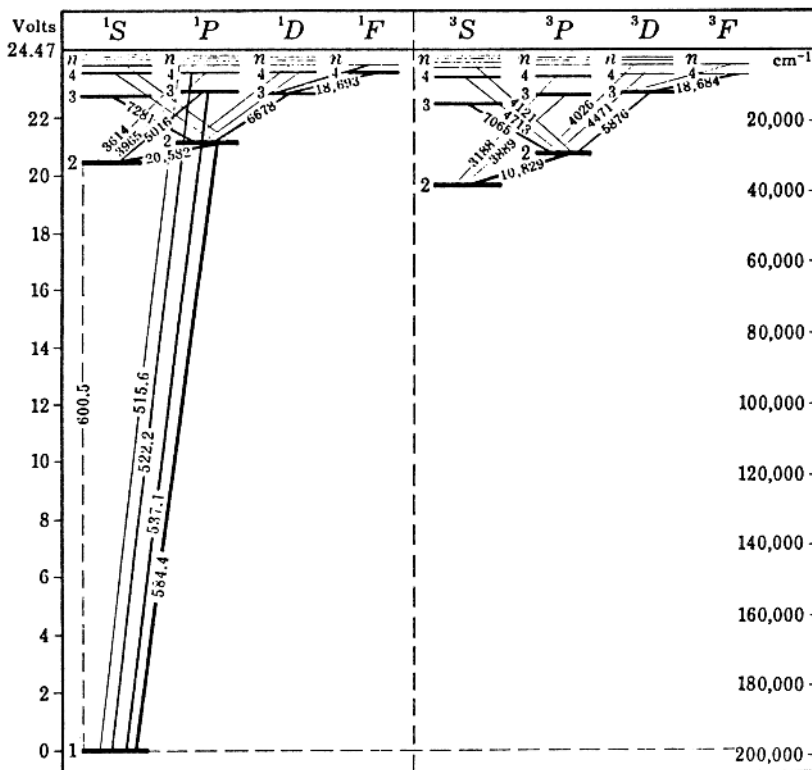


Fig. 2.6. Energy level diagram for the helium atom [2.12]

For atoms with more electrons in the outer shell, coupling the individual orbital and spin angular momenta to the resultants L and S is more complicated. For electrons of the same type (e.g. p electrons) it is important to distinguish between *equivalent* electrons (n quantum numbers also the same) or *non-equivalent* electrons. In the former case the Pauli principle strongly reduces the number of possible states. In Table 2.3 the LS terms obtained for different electron configurations are listed.

The description LS coupling may be somewhat confusing as there is primarily no spin-orbit interaction. However, we can now introduce this interaction as an additional, small perturbation. Through this perturbation, \mathbf{L} and \mathbf{S} couple to produce a resulting \mathbf{J} . As magnetic fields and magnetic moments can be associated with both \mathbf{L} and \mathbf{S} , there should, according to Sect. 2.3.1, be a precession of \mathbf{L} about \mathbf{S} and of \mathbf{S} about \mathbf{L} . As none of the vectors is fixed in space, a precession about the resultant \mathbf{J} occurs as shown in Fig. 2.8. For the corresponding J quantum number we have the relation

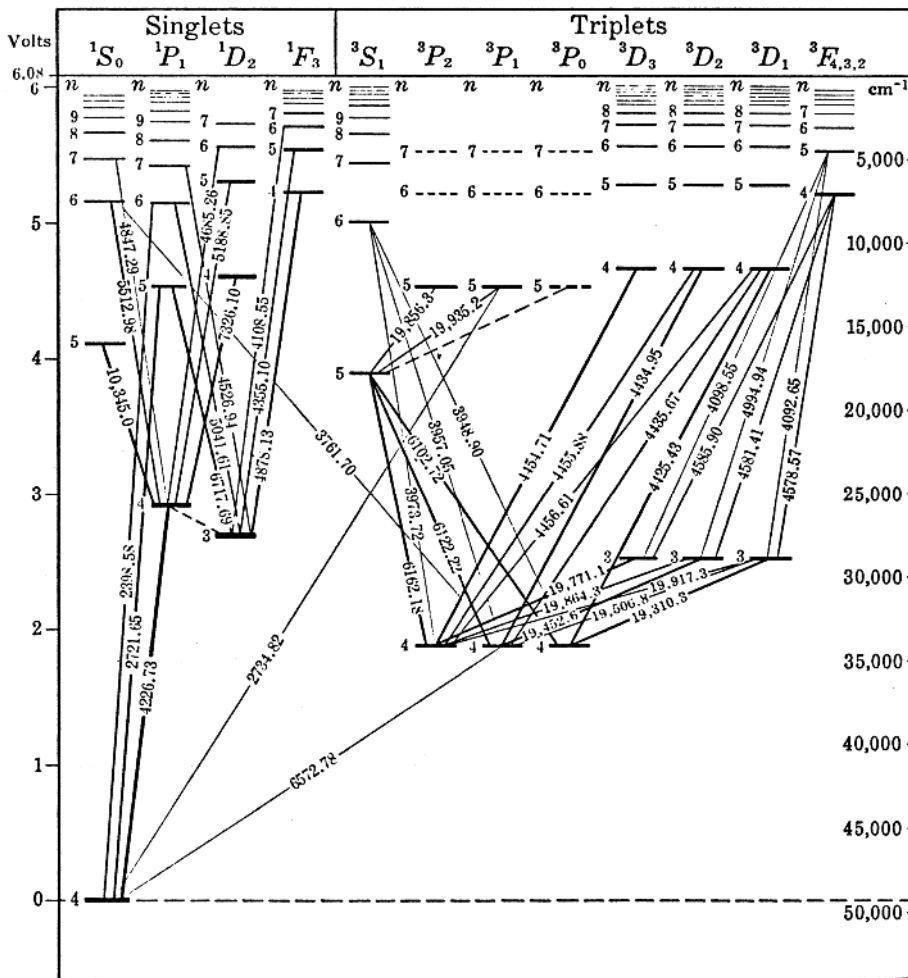


Fig. 2.7. Energy level diagram for the calcium atom [2.12]

$$J = L + S, L + S - 1, \dots, |L - S|. \quad (2.19)$$

In analogy with the one-electron case we have

$$E_{\text{so}} = A(L, S)[J(J + 1) - L(L + 1) - S(S + 1)]/2. \quad (2.20)$$

For the interval ΔE_{so} we have the *Landé interval rule*

$$\Delta E_{\text{so}(J, J-1)} = AJ. \quad (2.21)$$

The resulting energy levels for the case of two equivalent p electrons in LS coupling is shown in the left-hand part of Fig. 2.9.

If, contrary to what was assumed above, the spin-orbit interaction dominates over the non-central electrostatic interaction, we obtain primarily

Table 2.3. Examples of LS terms for some configurations. The designation ${}^1D(2)$ means that there are two 1D terms [2.12]

| Electron Configuration | Terms |
|------------------------|-----------------------------------------------------------------------------------------------|
| Equivalent | |
| s^2 | 1S |
| p^2 | ${}^1S, {}^1D, {}^3P$ |
| p^3 | ${}^2P, {}^2D, {}^4S$ |
| p^4 | ${}^1S, {}^1D, {}^3P$ |
| p^5 | 2P |
| p^6 | 1S |
| d^2 | ${}^1S, {}^1D, {}^1G, {}^3P, {}^3F$ |
| d^3 | ${}^2P, {}^2D(2), {}^2F, {}^2G, {}^2H, {}^4P, {}^4F$ |
| d^4 | ${}^1S(2), {}^1D(2), {}^1F, {}^1G(2), {}^1I, {}^3P(2), {}^3D, {}^3F(2), {}^3G, {}^3H, {}^5D$ |
| d^5 | ${}^2S, {}^2P, {}^2D(3), {}^2F(2), {}^2G(2), {}^2H, {}^2I, {}^4P, {}^4D, {}^4F, {}^4G, {}^6S$ |
| Non-equivalent | |
| $s\ s$ | ${}^1S, {}^3S$ |
| $s\ p$ | ${}^1P, {}^3P$ |
| $s\ d$ | ${}^1D, {}^3D$ |
| $p\ p$ | ${}^1S, {}^1P, {}^1D, {}^3S, {}^3P, {}^3D$ |
| $p\ d$ | ${}^1P, {}^1D, {}^1F, {}^3P, {}^3D, {}^3F$ |
| $d\ d$ | ${}^1S, {}^1P, {}^1D, {}^1F, {}^1G, {}^3S, {}^3P, {}^3D, {}^3F, {}^3G$ |

a coupling between the orbital and spin angular momenta of the individual electrons

$$\mathbf{j}_i = \mathbf{l}_i + \mathbf{s}_i . \quad (2.22)$$

In this case we talk about *jj coupling*. If the weaker electrostatic interaction is then applied, the individual \mathbf{j}_i momenta couple to form a resultant \mathbf{J} . The resulting energy-level diagram is quite different compared with the case of LS coupling (i.e., there is no interval rule). In the right-hand part of Fig. 2.9 the jj structure for two equivalent p electrons is shown. In the outer

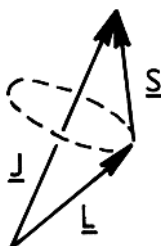


Fig. 2.8. Precession of \mathbf{L} and \mathbf{S} about \mathbf{J}

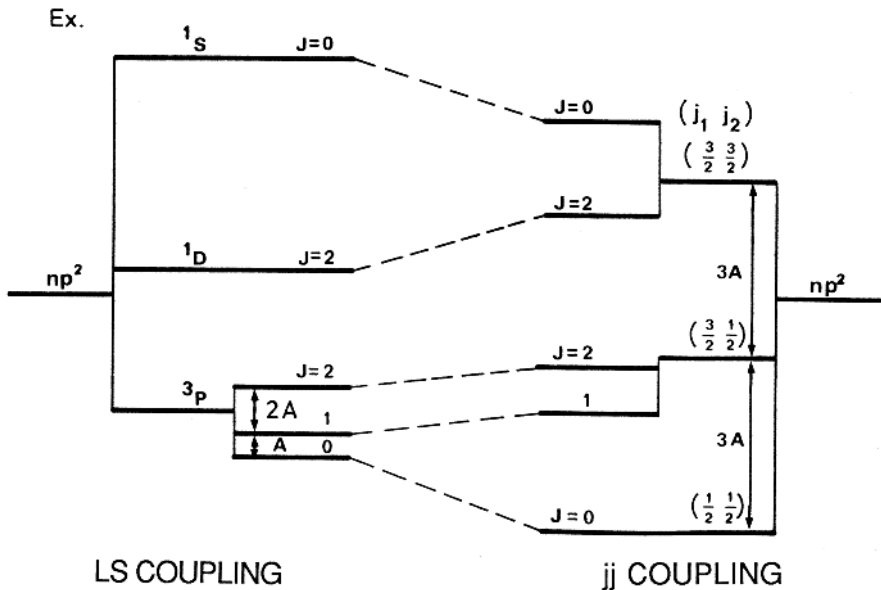


Fig. 2.9. Coupling conditions for two equivalent p electrons

shells of light elements there is generally *LS* coupling, whereas *jj* coupling is typically exhibited by inner shells of heavy atoms. In general, the situation is an intermediate of the two cases described and *intermediate coupling* arises. By experimentally determining the relative positions of the energy levels of a given configuration using spectroscopy, the coupling conditions can be investigated. The energy-level diagrams and level designations of atoms and singly and multiply ionized atoms have been determined in a process that is still continuing. A lot of this material is collected in [2.25–2.31]. Theoretical calculations, employing *self-consistent field* methods and other advanced techniques for describing the basic atomic energy-level structure, have been described in [2.13, 2.32–2.37]. The energy-level structure for atoms with two outer electrons is frequently parametrized using the so-called *multichannel quantum defect theory* (MQDT) [2.38–2.40].

2.5 The Influence of External Fields

Since the particles making up the atoms have magnetic moments, and since the charged electrons describe “orbits” around the nucleus, the atom as a whole has magnetic properties and is influenced by external magnetic fields. In the same way, the negatively charged electron cloud must be displaced with regard to the positive nuclear charge under the influence of an external electric field.

2.5.1 Magnetic Fields

First consider an atom with only one electron outside the closed shells. The atom is situated in a homogeneous magnetic field \mathbf{B} , which is *weak*. The meaning of the word “weak” will be clarified later. Associated with the orbital and spin motions there are magnetic moments, see (2.9), i.e.,

$$\mu_s = -g_s \mu_B \mathbf{s}, \quad (2.23)$$

$$\mu_\ell = -g_\ell \mu_B \mathbf{l}. \quad (2.24)$$

It has been found that $g_s = 2$ (apart from a 0.1% correction due to quantum electrodynamics) and $g_\ell = 1$. The spin-orbit interaction causes a precession of \mathbf{s} and \mathbf{l} about \mathbf{j} , which results in a magnetic moment μ_j precessing around \mathbf{j} with a time-averaged value $\langle \mu_j \rangle$ and in the opposite direction to \mathbf{j} . As shown in Fig. 2.10, the averaged moment will now precess slowly around an external field \mathbf{B} which may be generated, for example, by fixed coils. In the vector model we can project the contribution of μ_j in the \mathbf{j} direction

$$\langle \mu_j \rangle = -\mu_B \frac{3j^2 - l^2 + s^2}{2j^2} = -\mu_B g_j j \quad (2.25)$$

$$g_j = 1 + \frac{j(j+1) - \ell(\ell+1) + s(s+1)}{2j(j+1)} \quad (\text{Landé formula}). \quad (2.26)$$

To obtain these expressions we have utilized the relations

$$\mathbf{l} \cdot \mathbf{j} = (j^2 + l^2 - s^2)/2 \quad (2.27)$$

and

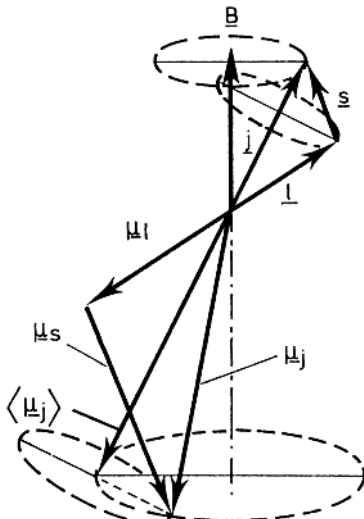


Fig. 2.10. Vector model for the Zeeman effect

$$\mathbf{s} \cdot \mathbf{j} = (j^2 - l^2 + s^2)/2 \quad (2.28)$$

and have inserted the “quantum-mechanical squares”. For the orientational energy E_m in the external field we then obtain

$$E_m = -\langle \mu_j \rangle \cdot \mathbf{B} = \mu_B B g_j m_j, \quad (2.29)$$

where the effect is seen of the space quantization m_j ($m_j = j, j-1, \dots -j$). The equidistant splitting of the m_j sublevels described by (2.29) is called the *Zeeman effect*. The Zeeman effect is obtained in magnetic fields of sufficiently low strengths that the orientational energy E_m of the atom in the external field is negligibly small compared with the internal orientational energy, the spin-orbit interaction energy. In such cases the coupling between \mathbf{l} and \mathbf{s} remains strong. According to (2.10) and (2.29) the precession velocity is proportional to the coupling energy. Another way of expressing the Zeeman effect condition is then to state that the precession movement about the external field is very slow compared with the internal ($\mathbf{j} = \mathbf{l} + \mathbf{s}$) precession velocity. If we have the opposite condition, i.e. a *strong* field, more energy is associated with the individual coupling of μ_ℓ and μ_s to the external field \mathbf{B} than with the internal coupling. The coupling between \mathbf{l} and \mathbf{s} therefore breaks up and \mathbf{l} and \mathbf{s} precess independently about the field with separate space quantizations (Fig. 2.11). This is the *Paschen-Back effect*. For this condition we have

$$E_m = \mu_B B (m_\ell + g_s m_s) + \zeta m_\ell m_s, \quad (2.30)$$

where ζ is the fine-structure interaction constant from (2.13). Of course, all intermediate situations are also possible and the mathematical treatment then becomes more complicated. Still restricting ourselves to cases with only one outer electron, a general expression for the magnetic field dependence of

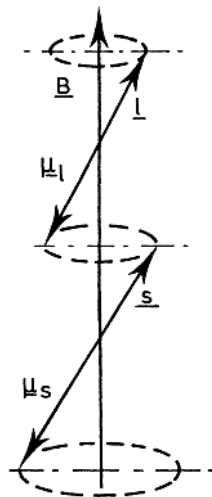


Fig. 2.11. Vector model for the Paschen-Back effect

the sublevels of a fine-structure doublet can be given, which describes the Zeeman, Paschen–Back and the intermediate field regions (the *Breit–Rabi formula* for the fine structure)

$$E(J, m_j) = -\frac{\Delta E_{\text{so}}}{2(2\ell + 1)} + \mu_B B m_j \pm \frac{\Delta E_{\text{so}}}{2} \sqrt{1 + \frac{4m_j x}{2\ell + 1} + x^2} \quad (2.31)$$

with

$$x = (g_s - 1) \frac{\mu_B B}{\Delta E_{\text{so}}} \quad \text{and} \quad \Delta E_{\text{so}} = (\ell + 1/2)\zeta.$$

The plus sign corresponds to the sublevels originating in the higher J level. In Fig. 2.12 the magnetic field behaviour of a 2P state with a fine-structure splitting ΔE of 110 cm^{-1} is shown. In the Zeeman region ($E_m \ll 110 \text{ cm}^{-1}$)

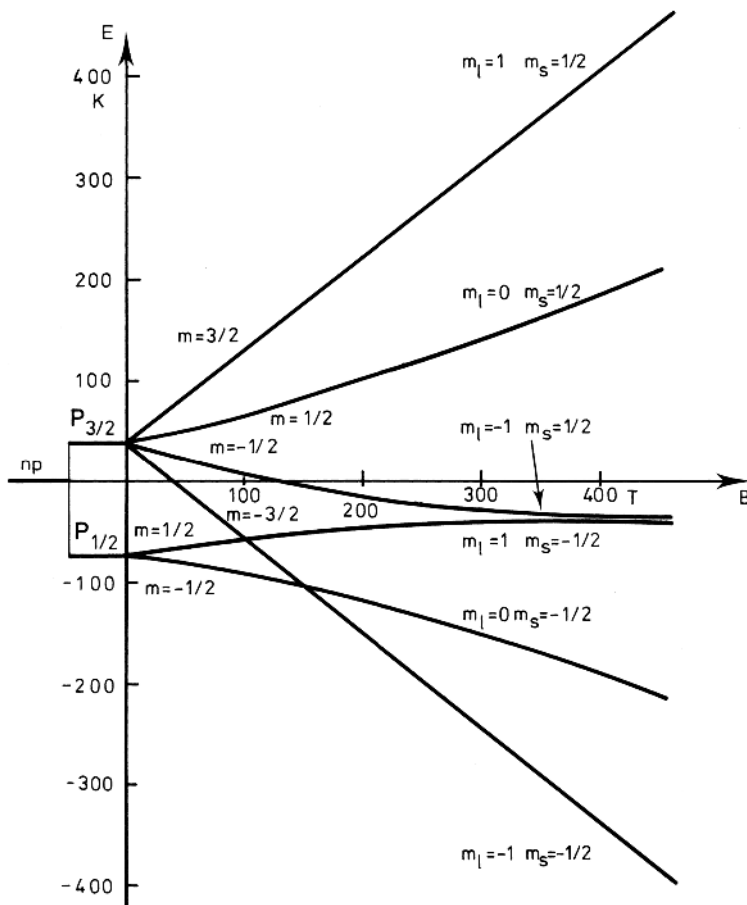


Fig. 2.12. Energy level diagram for a 2P state with fine-structure splitting 110 cm^{-1}

the energies are linear functions of the field B which is also the case in the Paschen–Back region ($E_m \gg 110 \text{ cm}^{-1}$), which is not fully reached in the figure. For the quantum numbers m_j in the Zeeman region and m_ℓ and m_s in the Paschen–Back region we have $m_j = m_\ell + m_s$ (as $j_z = \ell_z + s_z$ is a constant of motion). This relation in connection with the *non-crossing rule* (levels with the same $m_j = m_\ell + m_s$ cannot cross) prescribes which Zeeman level should be connected to which Paschen–Back level. (The non-crossing rule can be understood considering the signs of the second-order perturbation terms.) Equation (2.31) describes how sublevels with the same m_j value mix, resulting in nonlinear field dependencies. As the $m = 3/2$ and $-3/2$ levels have no mixing partner they remain linear in the magnetic field. (The expression under the square root becomes $(1 \pm x)^2$.)

For many-electron systems a similar description can be given for the magnetic field influence. For the Zeeman effect we have

$$E_m = g_J \mu_B \mu_J B. \quad (2.32)$$

The Landé formula for g_J , (2.26), in the many-electron case is only valid for pure LS coupling. For jj coupling of two electrons the following expression for the g -factor can be derived

$$g = \frac{J(J+1) + j_1(j_1+1) - j_2(j_2+1)}{2J(J+1)} g_1 + \frac{J(J+1) + j_2(j_2+1) - j_1(j_1+1)}{2J(J+1)} g_2. \quad (2.33)$$

Here g_1 and g_2 are g -factors for electrons 1 and 2 according to the Landé formula (2.26). By measuring the g -factors for all states of a given configuration it is possible to determine the degree of intermediate coupling, i.e. to determine the coefficients c_i in the expansion $\psi' = \sum c_i \psi_i(LS, (jj))$ of a real state ψ' in pure LS or jj states.

2.5.2 Electric Fields

In a homogeneous electric field \mathcal{E} an atom becomes *polarized*, i.e. the centre of the electronic cloud no longer coincides with the nucleus. The field induces an electric dipole moment \mathbf{d} , which is proportional to the field

$$\mathbf{d} = \alpha \mathcal{E}. \quad (2.34)$$

The orientation energy of the induced dipole is given by $E_e = -\mathbf{d} \cdot \mathcal{E}$. This so-called *Stark effect* thus generally increases as the square of the applied electric field strength. For hydrogen and hydrogen-like systems special conditions prevail due to the level degeneracy and hence a *linear* Stark effect is obtained. For the normal quadratic case it can be shown, that a common displacement of all sublevels (the *scalar* effect) is obtained as well as a differential displacement, depending on the m_j^2 value (the *tensor* effect). For a fine-structure level with quantum number J we have

$$E_s = -\frac{1}{2} \left(\alpha_0 + \alpha_2 \frac{3m_J^2 - J(J+1)}{J(2J-1)} \right) \mathcal{E}^2, \quad (2.35)$$

where α_0 and α_2 , being the *scalar* and *tensor polarizability constants*, respectively, can be determined experimentally and calculated theoretically. For $J = 0$ or $1/2$, for which the formula breaks down, there is only a scalar effect. The Stark effect can be seen as an admixture of other states into the state under study. Perturbing states are those for which there are allowed electric dipole transitions (Sect. 4.2) to the state under study. Energetically close-lying states have the greatest influence. A theoretical calculation of the constants α_0 and α_2 involves an evaluation of the matrix elements of the electric dipole operator (Chap. 4). Investigations of the Stark effect are therefore, from a theoretical point of view, closely related to studies of transition probabilities and lifetimes of excited states. (Sects. 4.1 and 9.4). In Fig. 2.13 an example of the Stark effect is given; different aspects of this phenomenon have been treated in [2.41].

Highly excited atoms with large principal quantum numbers n (*Rydberg atoms*) [2.42, 2.43] are very sensitive to electric fields since they have large α_0 and α_2 values. Clearly, the loosely bound outer electron is strongly influenced by an electric field. If the field strength is sufficiently high, the electron can be swept away (*field ionization*). For Rydberg atoms the critical field for field ionization is proportional to n^{-4} . Whereas ground-state atoms can be field-ionized only at field strengths of the order of some MV/cm, an atom in an $n = 30$ state only requires a few V/cm. The phenomenon of field ionization is illustrated by a potential diagram in Fig. 2.14, showing the possibility of electron tunnelling through the potential barrier and the conversion from bound to unbound states. For a more detailed discussion of field ionization the reader is referred to [2.44, 2.45]. It should be noted, that (2.35) is valid only for low electric field strengths far from the region of field ionization. Stronger fields must be handled with a different mathematical approach [2.46].

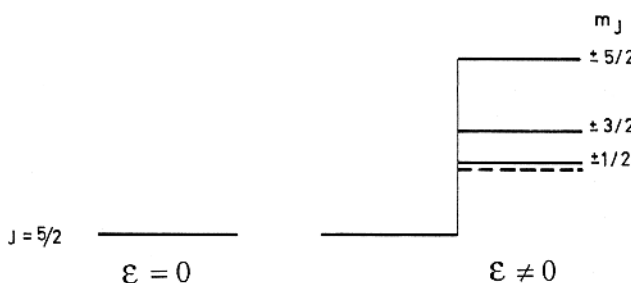


Fig. 2.13. Stark effect for a $J = 5/2$ state

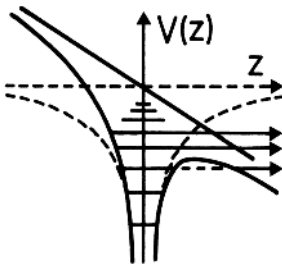


Fig. 2.14. Atomic field ionization

2.6 Hyperfine Structure

Hyperfine structure (hfs) in optical spectra was discovered independently by A. Michelson, and Ch. Fabry and A. Pérot at the end of the 19th century. The effect is explained by the presence of nuclear magnetic and electric moments, interacting with the electronic shell.

2.6.1 Magnetic Hyperfine Structure

Associated with its spin angular momentum \mathbf{I} , a nucleus has a magnetic dipole moment μ_I

$$\mu_I = g_I \mu_N \mathbf{I} = g'_I \mu_B \mathbf{I}. \quad (2.36)$$

In this expression, which is analogous to (2.9, 2.23, 2.24), the *nuclear magneton* $\mu_N = \mu_B/1836$, and g_I (g'_I) is a constant of proportionality with positive or negative sign. At the site of the nucleus the electron shell exhibits an effective magnetic field \mathbf{B}_J directed along the atomic “axis of rotation” \mathbf{J} , i.e.,

$$\mathbf{B}_J = k \mathbf{J}. \quad (2.37)$$

There will be a magnetic coupling (orientational energy) between the nucleus and the electron shell, and the interaction is described by

$$H_{\text{mhfs}} = a \mathbf{I} \cdot \mathbf{J} \quad (2.38)$$

with

$$a = -k g_I \mu_N. \quad (2.39)$$

Note that the *magnetic dipole interaction constant* a is a product of a nuclear quantity g_I , which is proportional to the moment, and an electronic quantity k , which is proportional to the internal magnetic field strength. \mathbf{I} and \mathbf{J} precess about their resultant \mathbf{F} , as shown in Fig. 2.15. We have

$$\mathbf{F} = \mathbf{I} + \mathbf{J}, \quad F = I + J, \quad I + J - 1, \dots |I - J|. \quad (2.40)$$

The energy contribution is calculated from (2.38) in the same way as the spin-orbit interaction (2.15)

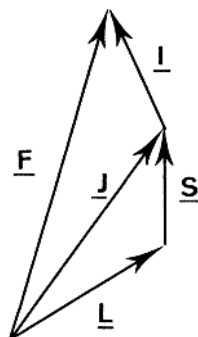


Fig. 2.15. Coupling of angular momentum vectors

$$E_{\text{mhfs}} = \frac{a}{2} [F(F+1) - I(I+1) - J(J+1)]. \quad (2.41)$$

As for the fine structure, the Landé interval rule is also valid for the magnetic hyperfine structure

$$\Delta E_{\text{mhfs}}(F, F-1) = aF. \quad (2.42)$$

In Fig. 2.16 hyperfine structures for two cases are displayed, one for the case of a positive a value ("normal" structure) and one for the case of a negative a value (*inverted* structure). Clearly, both signs can occur, since the sign of the g_J factor varies for different nuclei. (The sign of k can also vary.)

The magnetic dipole interaction constant a can frequently be determined accurately with precise methods which will be discussed in Chaps. 7 and 9. As we have mentioned, it represents a quantity in the field between atomic and nuclear physics. If the nuclear moment is known, the measurement yields an experimental value of the magnetic field at the nucleus that can be compared with the results of atomic calculations. If, on the other hand, the field can be

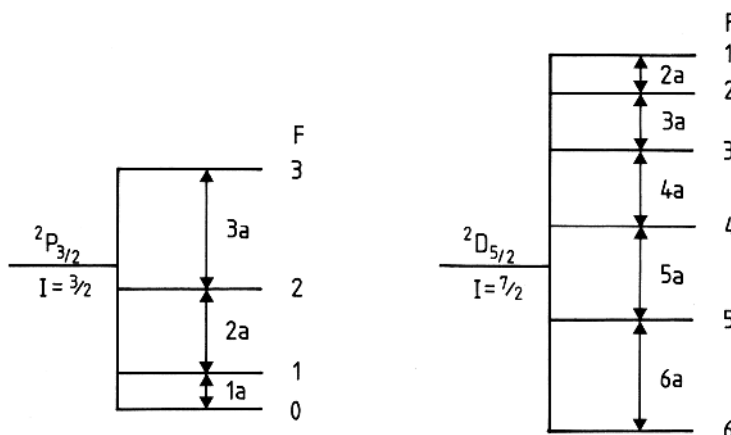


Fig. 2.16. Examples of hyperfine structure

calculated reliably, information on unknown nuclear moments can be obtained. The hyperfine structure will be particularly large if the atom contains an unpaired s electron, giving rise to the *Fermi contact interaction*, caused by the large probability of the s electron being found inside the nucleus.

The field strength at the nucleus is of the same order of magnitude as that exerted on the electron in its spin-orbit interaction. Since typical magnetic moments for nuclei are about 1000 times smaller than corresponding moments for the electron shell ($\mu_B/\mu_N = 1836$) the magnetic hyperfine structure is correspondingly smaller compared with the fine structure. As mentioned in Chap. 1, typical splittings are of the order of 10^{-6} eV ($\sim 10^{-2}$ cm $^{-1}$).

2.6.2 Electric Hyperfine Structure

In the same way as a magnetic dipole acquires an orientational energy in a magnetic field, a non-spherically symmetric charge distribution will acquire such an energy in an electric field gradient (Fig. 2.17).

Atomic nuclei can be stretched like cigars (prolate shape) or compressed like discs (oblate shape). The deformation is described by the *electric quadrupole moment* Q (prolate: $Q > 0$; oblate: $Q < 0$). The principal interaction is, of course, the normal electrostatic (Coulomb) force on the charged nucleus (*monopole* interaction). The differential interaction, which depends on the structure of the nucleus and on the variation of the field across its finite extension, is of course very much smaller (*quadrupole* interaction). It gives rise to an electric hyperfine structure. The energy contribution depends on the direction of the nuclear spin in relation to the electric field gradient. For the electric hyperfine interaction one obtains

$$E_{\text{ehfs}} = b \frac{(3C/4)(C+1) - I(I+1)J(J+1)}{2I(2I-1)J(2J-1)} \quad (2.43)$$

with

$$C = F(F+1) - I(I+1) - J(J+1) \quad \text{and} \quad b = \frac{e^2}{4\pi\epsilon_0} q_J Q. \quad (2.44)$$

In analogy with the magnetic dipole interaction constant a the *electric quadrupole interaction constant* b is a product of a nuclear quantity Q , the electric

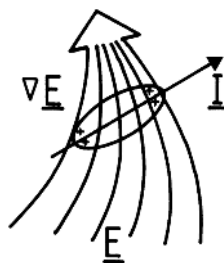


Fig. 2.17. Orientation energy of an electric quadrupole in an electric field gradient

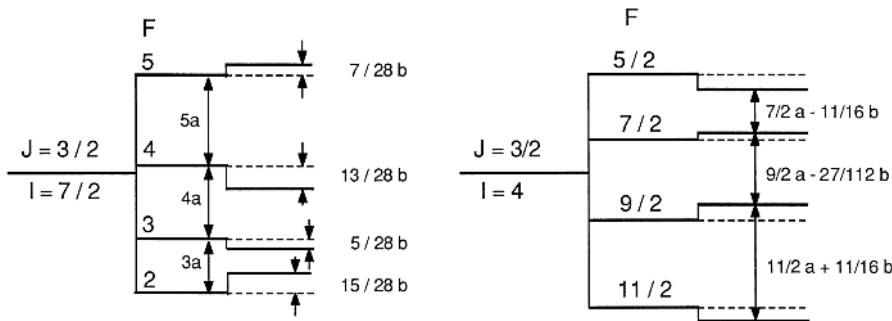


Fig. 2.18. Examples of magnetic and electric hyperfine structure

quadrupole moment, and an electronic quantity q_J , which is proportional to the electric field gradient. Thus, with the b factor experimentally determined, information on the nucleus *or* the electronic shell can be obtained. The electric hyperfine structure is of the same order of magnitude as the magnetic one, but generally somewhat smaller. It exhibits itself as a deviation from the Landé interval rule. In Fig. 2.18 two examples of the combined action of magnetic and electric hyperfine structure are shown.

If the nucleus has no spin, i.e. $I = 0$, there is neither a magnetic nor an electric hyperfine structure. For $I = 1/2$ only a magnetic interaction is possible, whereas the occurrence of electrical hyperfine structure requires $I \geq 1$ and $J \geq 1$. Hyperfine structure and the determination of nuclear moments have been discussed in [2.47]. Extensive data on nuclear moments have been listed in [2.48, 2.49]; hfs data for the extensively studied alkali atoms have been compiled in [2.50] and the theoretical aspects of atomic hyperfine interactions have been covered in [2.51–2.54].

2.7 The Influence of External Fields (hfs)

In a weak external magnetic field \mathbf{B} there will be a splitting of magnetic sublevels for the hyperfine structure (hfs) case as for the previously discussed case, where the influence of the nucleus was omitted. However, also in the hyperfine structure case the electronic shell is responsible for the interaction. Because of the coupling between \mathbf{I} and \mathbf{J} , these vectors precess about \mathbf{F} . Thus, the direction in relation to \mathbf{B} of the electronic magnetic moment, which is associated with \mathbf{J} , is influenced. The situation is illustrated in Fig. 2.19.

As the nuclear magnetic moment is negligibly small in comparison with that of the electronic shell, the direct interaction of the nuclear moment with the field is normally negligible. The coupling in the inner, extremely strong field (the magnetic hyperfine coupling) is, however, much larger and, as a matter of fact, the *Zeeman effect for the hyperfine structure* demands

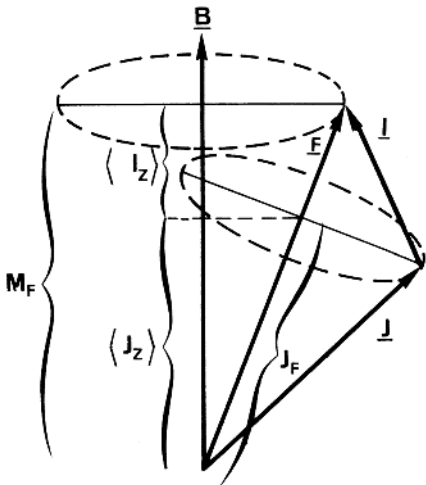


Fig. 2.19. Vector diagram for the Zeeman effect of the hyperfine structure

that the external interaction be negligible compared with the internal one. Using the vector model, we obtain, as in the fine structure case,

$$E_m = \mu_B B g_J \frac{F(F+1) - I(I+1) + J(J+1)}{2F(F+1)} M_F = \mu_B B g_F M_F. \quad (2.45)$$

In the presence of hyperfine structure, g_F now takes the place of g_J in describing the “gear ratio” between the magnetic energy contribution and field strength. Although again there is an *electronic* magnetic moment, the influence is modified by the nuclear coupling resulting in a different angle of $\langle \mu_J \rangle$ with respect to the magnetic field. If J and g_J are known, a measurement of g_F gives information on the nuclear spin I .

In strong magnetic fields, the *Paschen-Back effect for the hyperfine structure* will result. As for the fine structure case the mathematical expression is simple, i.e.,

$$E_m = \mu_B B (g_J M_J - g'_I M_I) + a M_I M_J. \quad (2.46)$$

In *intermediate fields* the calculation is more complicated. For I or $J = 1/2$, the *Breit-Rabi formula* can be expressed in analogy with the fine structure case, see (2.31). For $J = 1/2$ we have

$$E(F, M_F) = -\frac{\Delta E}{2(2I+1)} - g'_I \mu_B B M_F \pm \frac{\Delta E}{2} \sqrt{1 + \frac{4M_F x}{2I+1} + x^2} \quad (2.47)$$

with

$$x = (g_J + g'_I) \frac{\mu_B B}{\Delta E} \quad \text{and} \quad \Delta E = (I + \frac{1}{2})a.$$

Here the plus sign refers to the higher F value. In Fig. 2.20 the dependence of the sublevels on the magnetic field for a $J = 1/2$, $I = 3/2$ state is shown.

The Zeeman and Paschen–Back regions can be identified and the relevant quantum numbers M_F , M_I , and M_J , are indicated ($M_F = M_I + M_J$). The $M_F = \pm 2$ levels have no mixing partner and proceed linearly into the Paschen–Back region.

For the general case a computer calculation, in which the quantum-mechanical energy matrix is *diagonalized*, is required. Atoms with hfs in external magnetic fields have been discussed in [2.47]. Hyperfine structures are normally given in MHz. Using this unit for energy and expressing B in Gauss (10^{-4} Tesla), μ_B/h has the numerical value of 1.400 (MHz/Gauss).

In the presence of an external electric field a Stark effect for the hyperfine structure occurs. The theory which applies to this situation has been given in [2.55, 2.56].

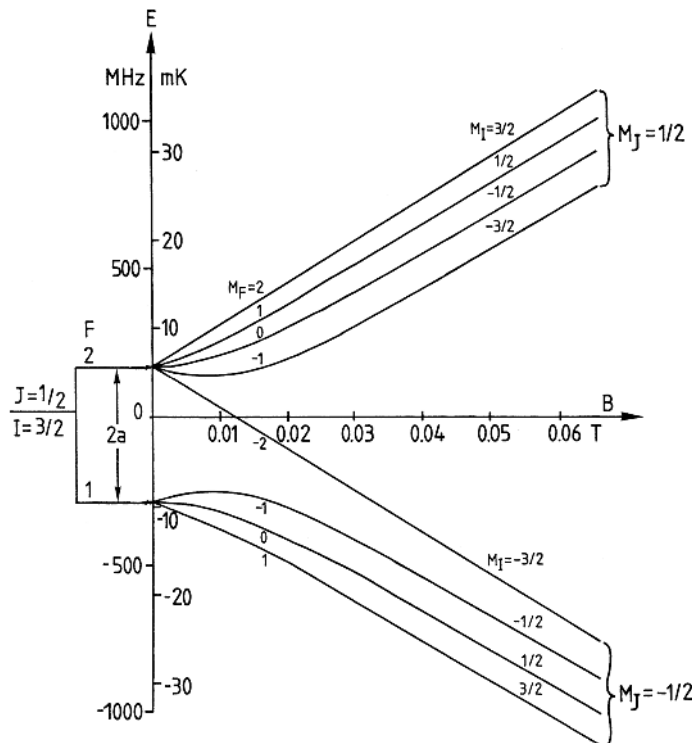


Fig. 2.20. Breit–Rabi diagram for an alkali state with $J = 1/2$ and $I = 3/2$. (Ground state of ^{39}K)

2.8 Isotopic Shifts

Isotopes with $I = 0$ have no hyperfine structure, but in transitions between energy levels in a mixture of $I = 0$ isotopes of the same element, a line structure may still be obtained. This effect is called the *isotopic shift*. It has two origins and a distinction is made between the *mass effect* and the *volume effect*. The mass effect can be divided up into the *normal* and the *specific* mass effects. The normal mass effect is due to the movement of the nucleus, which is due to the fact that it is not infinitely heavy. For hydrogenic systems it is possible to take this into account by using the *reduced mass* μ instead of m

$$\mu = \frac{mM}{m + M} \quad (2.48)$$

(m : electron mass, M : nuclear mass). For a transition in hydrogenic systems one finds that the mass shift between two isotopes of mass M and $M + 1$ decreases with M according to

$$\Delta\nu \propto M^{-2}. \quad (2.49)$$

The specific mass effect is due to the interactions (correlations) between the different outer electrons. The mass effect is very prominent for hydrogen/deuterium but is quickly reduced for heavier elements. For such elements the volume effect becomes important. It is particularly prominent when the electron configuration contains unpaired s electrons. The nucleus has a charge density ρ_n over a finite volume. The s electron with a charge probability distribution $\rho_e(r)$ can penetrate the nucleus and is then no longer

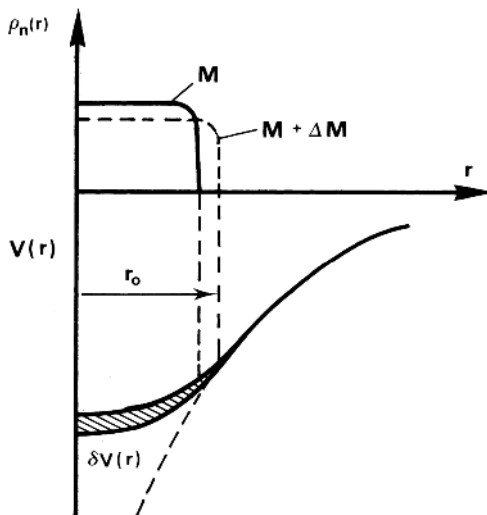


Fig. 2.21. The origin of the volume isotopic shift

under the influence of the pure Coulomb field. A nucleus of mass M has a smaller radius r than one with the mass $M + \Delta M$, and thus the potential begins to deviate from a Coulombic one at smaller values of r . The situation is illustrated in Fig. 2.21. There will be an energy shift described by

$$\Delta E = \int_0^{r_0} \rho_e(r) 4\pi r^2 \delta V(r) dr. \quad (2.50)$$

Studies of the volume effect yield information on the charge distribution in the nucleus. Hyperfine structure and isotopic shifts are of the same order of magnitude. Isotopic shifts can be studied in the visible region as well as in the X-ray region. Particularly prominent isotopic shifts are obtained for muonic atoms, in which, for example, a μ meson ($m_\mu = 209m_e$) has taken the place of an electron. The classical radius of the orbit is reduced by a factor of 209, and thus the nuclear influences are much greater than those pertaining to the electrons. Isotope shifts and their interpretation have been discussed in [2.57–2.59].

Different aspects of current atomic physics research are covered in the proceedings of a series of international atomic physics conferences [2.60–2.75]. Further reviews may be found in [2.76, 2.77].

3. Molecular Structure

A molecule is formed by the binding of two or more atoms in such a way that the total energy is lower than the sum of the energies of the constituents. The bonds are normally of *ionic* or *covalent* nature. Particularly weak bonds occur in *van der Waals* molecules. The energy-level diagrams of molecules are significantly more complicated than those of atoms since, apart from energy levels corresponding to different electronic arrangements, there are also different states corresponding to vibrational and rotational motion. The structure is schematically shown in Fig. 3.1. This chapter will mainly be concerned with *diatomic* molecules.

For a more detailed description of molecular structure the reader is referred to [3.1–3.14].

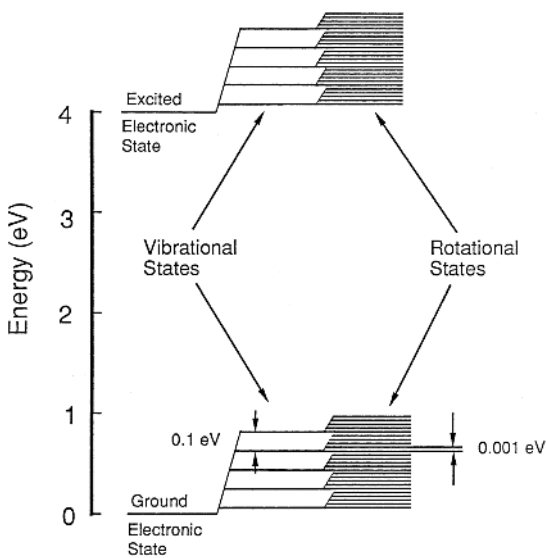


Fig. 3.1. Schematic molecular energy level diagram with electronic, vibrational and rotational levels

3.1 Electronic Levels

In the mathematical treatment of atoms it has been found that the interactions, especially electron–electron interactions, are rather complicated. Theoretical studies of molecules are also more complicated than those of atoms because we do not have any given centre but many centres, one for each atom in the molecule. As for atoms, the theoretical treatment of molecules starts with the Schrödinger equation and, as in the case of atoms, it is useful to consider the independent-particle model. In this approximation one assumes that each electron moves independently of the others in the field generated by the nuclei and the other electrons. For an atom the central field approximation is then a natural further step. However, as there are many centres in a molecule, such a model does not apply here. In order to facilitate the calculations one generally tries to utilize other symmetry properties of the molecule. In the treatment of diatomic molecules we have *cylindrical symmetry* and it is then possible to separate the Schrödinger equation into equations corresponding to different absolute values of the angular momentum projection onto the symmetry axis. Electronic orbitals denoted by σ , π , δ , ... are obtained corresponding to the m_ℓ values 0, 1, 2, ... (m_ℓ is the quantum number for the orbital angular momentum projection). In molecules with two atoms of the same kind (homo-nuclear molecules) there is a centre of symmetry. For such molecules the states are further classified by indicating the parity of the wavefunction: even, g (German “gerade”) or odd, u (German “ungerade”), e.g., σ_g , σ_u , π_g , π_u , ...

Electrons are much lighter than nuclei and move much faster. Thus the electrons can adjust to the movement of the nuclei, which means that the electronic states are at any moment essentially the same as if the nuclei were fixed. This is the basis of the *Born–Oppenheimer approximation*, which assumes fixed nuclei. The wave function can be expressed as a product of an electronic wave function with the nuclei assumed fixed and a nuclear wave function describing the relative nuclear motion. Energy eigenvalues for the electronic Schrödinger equation, solved for different nuclear separations, form a potential, that is inserted into the nuclear Schrödinger equation together with the nuclear repulsion term.

In order to further describe the molecular wavefunctions or the molecular orbitals, Linear Combinations of Atomic Orbitals (LCAO) are normally used (*LCAO method*). Such a method of solution is possible since the directional dependence of the spherical-harmonic functions for the atomic orbitals can be used. The Pauli principle can be applied to the single-electron molecular orbitals and by filling the states with the available electrons the molecular electron configurations are attained. Coupling of the angular momenta of the open shell then gives rise to molecular terms.

The total angular momentum of the electrons in a molecule is not a constant of motion, since the electrons do not move in a central field. The coupling

of angular momenta for the electrons will therefore be different from the atomic case.

Let us consider a diatomic molecule which has an axial symmetry with regard to the axis through the two nuclei (i.e., cylindrical symmetry). Only the component of the electron orbital angular momentum L_z along the symmetry axis will be a constant of motion. The total angular momentum \mathbf{L} will precess about the symmetry axis, as shown in Fig. 3.2.

The projected component is characterized by the quantum number M_L

$$M_L = L, L-1, \dots, -L. \quad (3.1)$$

However, since the internuclear field is of electric nature rather than magnetic, the energy is not changed for the exchange $M_L \rightarrow -M_L$. (Compare the Stark effect with the Zeeman effect). Since the field is very strong the energy separation between states with different M_L values is quite substantial. The absolute value for M_L is designated Λ

$$\Lambda = |M_L|, \Lambda = 0, 1, 2, \dots, L. \quad (3.2)$$

The states are given the following symbols

$$\begin{array}{cccc} \Lambda = & 0 & 1 & 2 & 3 \\ \Sigma & \Pi & \Delta & \Phi. \end{array}$$

The states are doubly degenerate apart from Σ states because of the $M_L \leftrightarrow -M_L$ symmetry.

The resulting spin quantum number \mathbf{S} of the electrons is also needed to characterize the molecular states. In diatomic molecules with $\Lambda > 0$ \mathbf{S} precesses about the internuclear axis and can have $2S + 1$ well-defined projections. The quantum number for S_z is called Σ . As for the atomic case the *multiplicity*, $2S + 1$, is placed as an index of the Λ symbol, e.g. $^3\Pi$, $^1\Delta$.

The total electronic angular momentum along the internuclear axis is designated Ω and is obtained from Λ and Σ

$$\Omega = \Lambda + \Sigma, \Lambda + \Sigma - 1, |\Lambda - \Sigma|. \quad (3.3)$$

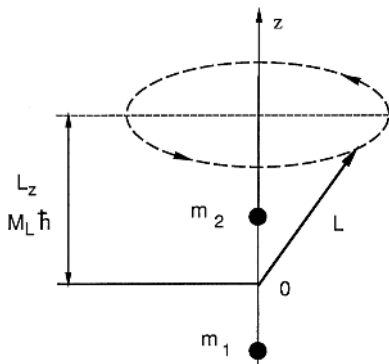


Fig. 3.2. Precession of \mathbf{L} in a diatomic molecule

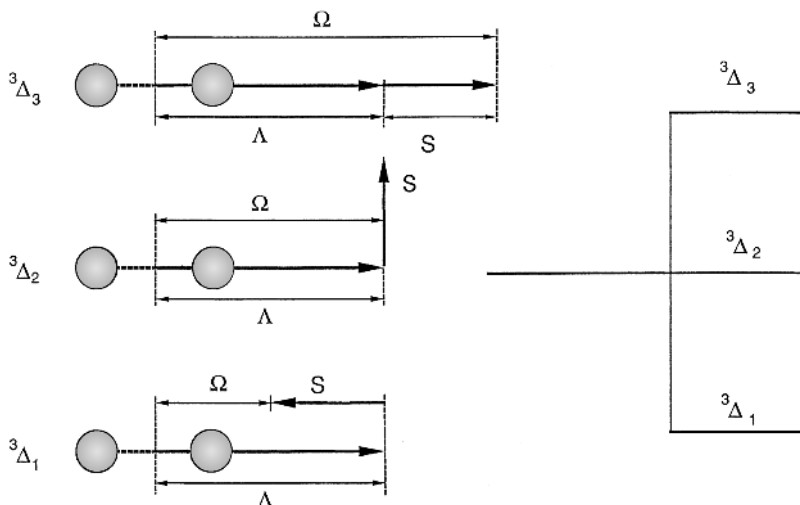


Fig. 3.3. Term splitting for molecules

For $\Lambda > 0$ the $(2S + 1)$ values of Ω with different energies are obtained. In Fig. 3.3 the possible states for $\Lambda = 2$ and $S = 1$ are shown.

The strength and type of bonding between two atoms depend on the tendency of the participating atoms to donate, attract and share electrons. The variation of the electronic energy with the bond length r between the nuclei is schematically shown in Fig. 3.4 for the OH (hetero-nuclear) and O₂ (homo-nuclear) molecules. The curve with the lowest energy corresponds to the ground state while the other curves represent different electronic states,

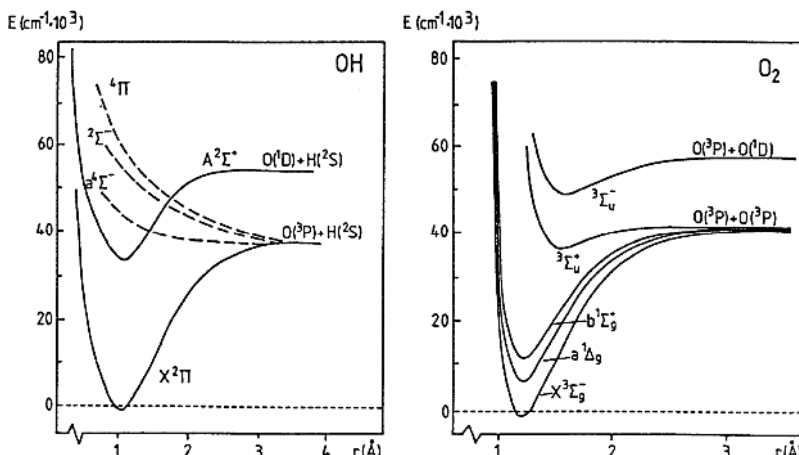


Fig. 3.4. Energy level diagram for OH (left) and O₂ (right)

which may also be unbound. The ground state is designated X , and the excited states are conventionally called A, B, C etc.

3.2 Rotational Energy

Consider a rotating diatomic molecule, as shown in Fig. 3.5, with the atomic masses m_1 and m_2 at distances r_1 and r_2 from the centre of gravity. The moment of inertia with respect to the rotational axis is \mathbf{I} . We have

$$\begin{aligned} r &= r_1 + r_2, \\ m_1 r_1 &= m_2 r_2, \\ I &= m_1 r_1^2 + m_2 r_2^2. \end{aligned}$$

We then obtain

$$I = \frac{m_1 m_2}{m_1 + m_2} (r_1 + r_2)^2 = \mu r^2, \quad (3.4)$$

where μ is the reduced mass. Classically, the angular momentum \mathbf{L} and the energy E are given by

$$\left. \begin{aligned} \mathbf{L} &= I \omega / \hbar \\ E &= I \omega^2 / 2 \end{aligned} \right\} \Rightarrow E = \frac{\mathbf{L}^2 \hbar^2}{2I}$$

where ω is the angular frequency vector. Quantum mechanically, \mathbf{L} is given by

$$|\mathbf{L}| = \sqrt{J(J+1)} \hbar, \quad J = 0, 1, 2, \dots \quad (3.5)$$

and thus the quantized energy of the rotator is given by

$$E_J = J(J+1) \hbar^2 / 2I = B J(J+1). \quad (3.6)$$

This energy expression leads to energy levels such as those in Fig. 3.6.

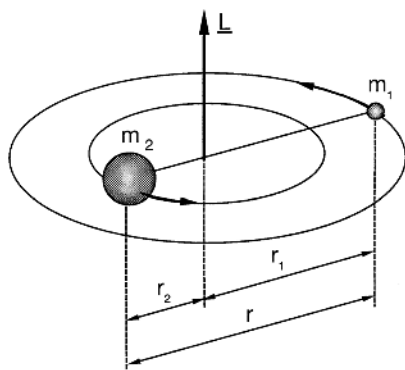


Fig. 3.5. Rotation of a diatomic molecule

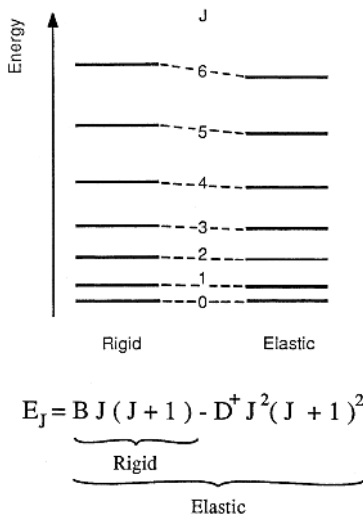


Fig. 3.6. Rotational levels for a rigid rotator (left) and an elastic rotator (right)

If the rotator is not completely rigid it is slightly extended in higher rotational states. Then I increases and E_J will decrease. This results in a successive downward movement of the upper energy levels. The elastic rotator is described by

$$E_J = B J (J + 1) - D^+ J^2 (J + 1)^2. \quad (3.7)$$

Here D^+ is a positive constant and $D^+ / B \ll 1$. In Fig. 3.6 the modified rotational levels are also included. The energy separation between rotational levels is of the order of 10^{-3} eV.

In molecules with an open electron shell there is a coupling between the angular momentum of the electrons and the molecular rotation. The situation is described by the *Hund coupling cases* a, b, c or d. (This complication, which sometimes leads to the absence of the first rotational levels, will not be treated in this book.) The coupling between \mathbf{L} and \mathbf{J} can lead to a splitting of each J level into two states (Λ doubling) breaking the M_L degeneracy.

3.3 Vibrational Energy

The potential energy of a diatomic molecule depends on the internuclear distance r . In Fig. 3.7 a typical potential curve is shown. The so-called *Morse potential* is often used

$$V(r) = D \left(1 - e^{-\alpha(r-r_0)} \right)^2. \quad (3.8)$$

Here r_0 corresponds to the bottom of the potential curve, and D is the dissociation energy. One atom oscillates with regard to the other in this potential. A Taylor expansion of $V(r)$ close to $r = r_0$

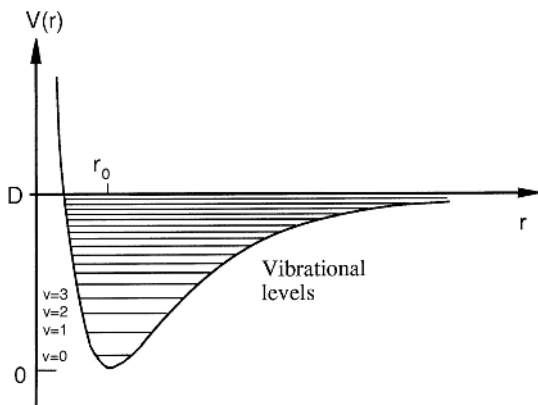


Fig. 3.7. Vibrational potential and energy levels

$$V(r) = D\alpha^2(r - r_0)^2 + \dots \quad (3.9)$$

shows that the bottom of the potential curve may be approximated by a parabola and the molecule is then called a *harmonic oscillator*. The classical vibrational frequency ν_c is given by

$$\nu_c = \frac{1}{2\pi} \sqrt{\frac{k}{\mu}}, \quad (3.10)$$

where μ is the reduced mass and k is the force constant (defined by the force expression $F = -k(r - r_0)$). Thus $k = 2D\alpha^2$ according to (3.9)). Quantum mechanically

$$E_v = (v + 1/2)h\nu_c, \quad v = 0, 1, 2, \dots \quad (3.11)$$

leading to *equidistant* vibrational levels and the presence of a *zero-point energy* $h\nu_c/2$. For higher-lying vibrational levels the harmonic oscillator model is obviously not valid, since the higher terms of $V(r)$ become important. For a non-harmonic oscillator the energy eigenvalues are given approximately by

$$E_v = (v + 1/2)h\nu_c - (v + 1/2)^2 x_e h\nu_c. \quad (3.12)$$

Here x_e is a small positive constant. Increasingly closer-lying energy levels are obtained, developing into a continuum at $E = D$. The separation between low-lying vibrational levels is typically 0.1 eV.

3.4 Polyatomic Molecules

While the energy-level structure of diatomic molecules can be divided up reasonably easily, the degree of complexity is greatly increased for polyatomic molecules. Such molecules have several nuclear distances, several

force constants, several dissociation energies etc., which must normally be determined simultaneously. While for diatomic molecules it is possible to start from empirical regularities in the spectra and arrive at a theoretical interpretation, such a procedure is difficult for polyatomic molecules. Instead it is more advantageous to first develop the theory and then use the theory to interpret the observed spectra. An important point to consider is the *shape* of the molecule, i.e. the internal arrangement of the atoms, as certain qualitative features are associated with a certain shape. The study of *symmetry properties* is thus very important in the understanding of complicated molecules [3.15–3.17]. The symmetry is described in group theory in terms of *point groups*. For example, carbon tetrachloride CCl_4 , which has a tetrahedral structure, belongs to a point group called T_d .

The vibrational motion of a polyatomic molecule is described by *fundamental frequencies (modes)*, corresponding to different types of vibration. Every atom has 3 degrees of freedom (the 3 dimensions of space) leading to $3N$ degrees of freedom for an N -atomic molecule. Of these degrees of freedom, three describe rotation around a centre of mass, which does not correspond to any vibrational motion. A further three degrees of freedom describe a translational motion which does not either give rise to any vibrational movement. Thus, in general an N -atomic molecule has $3N - 6$ vibrational modes. For a *linear* molecule there is one more mode ($3N - 5$) because only two independent rotational movements exist. The different vibrational modes in the molecule represent stretching, where the distance between the atoms

| | STRETCHING | | BENDING | |
|---------------|------------|------------|---------|---|
| | SYMMETRIC | SCISSORING | WAGGING | - |
| AX_2 | | | | |
| | | | | |

| | STRETCHING | | BENDING | |
|---------------|------------|-----------|---------|--|
| | SYMMETRIC | SYMMETRIC | | |
| AX_3 | | | | |
| | | | | |

Fig. 3.8. Stretching and bending modes for the molecular groups

in the molecule is changed, or bending, where the angle between the atoms in the molecule is changed. In Fig. 3.8 examples of stretching and bending modes for AX_2 and AX_3 molecular groups are given.

The possibilities of understanding even complicated molecular structure have much improved with advanced theoretical development. The result is the firm establishment of *quantum chemistry* as a discipline, culminating in the award of the Nobel prize in chemistry in 1998 to *W. Kohn* and *J.A. Pople* [3.18–3.24].

3.5 Clusters

Clusters are polyatomic molecules, generally consisting of atoms of the same kind. Many elements spontaneously evaporate as molecules, e.g., arsenic (As_4), tellurium (Te_2) and Bi (Bi_x). If an element is evaporated into a supersonic jet of an inert gas, e.g., by laser ablation, clusters are formed in the rapidly expanding and adiabatically cooling gas [3.25–3.28]. Mass spectrometric studies can be performed showing the distribution of masses in the cluster formation. In studies of carbon, it was found that C_{60} and C_{70} were overabundant. It has been shown (Nobel prize in chemistry 1996 to *R.F. Curl Jr.*, *H. Kroto*, and *R.E. Smalley*) that C_{60} corresponds to a particularly symmetric arrangement of the atoms in the form of a soccerball (20 hexagons, 12 pentagons) as shown in Fig. 3.9, where also carbon cluster mass spectra for different running conditions are shown. The symmetric structure is normally referred to as *buckminsterfullerene* (after R. Buckminster Fuller, an American architect who constructed a dome of this shape for the 1967 Montreal World Exhibition). The structures are cage-like, and other atoms can be trapped inside, giving rise to *endohedral fullerenes*. Clusters and fullerenes have very interesting physical and chemical properties, which are much studied. They may become of great technological use for catalysts, lubricants etc. It has been shown that more complicated structures can be obtained with carbon atoms, such as tubes [3.30, 3.31]. Complex molecules of these kinds are of considerable interest for nanometer technology.

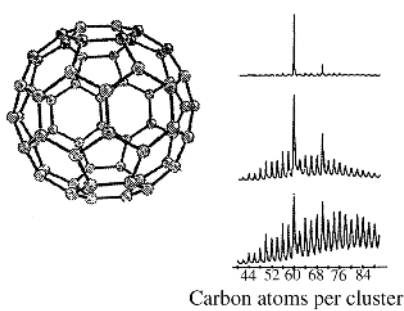


Fig. 3.9. Carbon cluster mass spectra and the structure of C_{60} [3.29]

3.6 Other Molecular Structures

Apart from the energy-level structures discussed above, molecules exhibit both the Zeeman and Stark effects. Further, hyperfine structure and isotopic shifts also occur. The occurrence of isotopic shifts is particularly simple to understand considering the substantially altered values of the reduced mass found in the vibrational and rotational energy expressions.

4. Radiation and Scattering Processes

After the brief survey of atomic and molecular energy structures in Chaps. 2 and 3 we will now consider radiation and scattering processes by which atoms and molecules change their energy state. The processes are accompanied by the absorption or release of radiation, giving rise to spectra. These spectra can be used to clarify the structure of atoms and molecules and for a wealth of analytical purposes. We will first consider the case of transitions at a frequency corresponding to given energy separations (resonance radiation) and then discuss Rayleigh, Raman and Mie scattering. A detailed presentation of the theory of radiation and scattering processes can be found in [4.1–4.13]. Several of the books on atomic, molecular and quantum mechanics, cited earlier, also discuss this topic in more detail.

4.1 Resonance Radiation

Consider an atomic or molecular system with energy levels E_k subject to a time-dependent perturbation \mathcal{H}' , e.g., the oscillating electric field of incoming monochromatic light (Fig. 4.1). In this section we will consider in what state a system, initially in a given state, will be found after having interacted with an electromagnetic field for a time t . We start with the time-dependent Schrödinger equation

$$i\hbar \frac{\partial \Psi(t)}{\partial t} = (\mathcal{H}_0 + \mathcal{H}')\Psi(t). \quad (4.1)$$

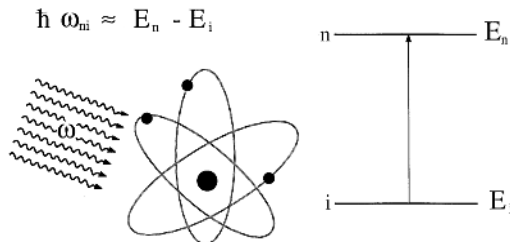


Fig. 4.1. Interaction between electromagnetic radiation and an atom

The time-independent eigenfunctions of \mathcal{H}_0 (describing the non-perturbed system) and the eigenvalues E_k are assumed to be known:

$$\mathcal{H}_0 \psi_k^0 = E_k \psi_k^0. \quad (4.2)$$

The eigenfunctions are supposed to be normalized and those with the same eigenvalues have been orthogonalized. These eigenfunctions have the time dependence

$$\Psi_k^0(t) = \psi_k^0 \exp(-i\omega_k t) \quad (4.3)$$

with $\omega_k = E_k/\hbar$. Since the functions constitute a complete system, an arbitrary time-dependent function can be expanded according to

$$\Psi(t) = \sum_k c_k(t) \Psi_k^0(t) = \sum_k c_k(t) \psi_k^0 \exp(-i\omega_k t). \quad (4.4)$$

Inserting this expression into the Schrödinger equation (4.1) gives

$$i\hbar \sum_k \frac{dc_k}{dt} \exp(-i\omega_k t) \psi_k^0 = \mathcal{H}' \sum_k c_k \exp(-i\omega_k t) \psi_k^0.$$

Multiplication by Ψ_n^{0*} and integration yield

$$\frac{dc_n}{dt} = -\frac{i}{\hbar} \sum_k \exp(i\omega_{nk} t) \langle \psi_n^0 | \mathcal{H}' | \psi_k^0 \rangle \quad (4.5)$$

with

$$\omega_{nk} = \omega_n - \omega_k = \frac{1}{\hbar} (E_n - E_k).$$

The set of equations (4.5), written for the various values of n , constitutes a set of coupled linear differential equations. The coupling between these equations arises solely from the existence of the perturbation \mathcal{H}' , which has non-zero off-diagonal matrix elements. Assume that the system is in an eigenstate of \mathcal{H}_0 , say E_i , at $t = 0$. Thus, with the probability interpretation of the wave function we have

$$c_i(0) = 1, \quad c_k(0) = 0, \quad k \neq i. \quad (4.6)$$

The first-order result is now obtained by integration of (4.5), using the condition (4.6) in the integral also for $t > 0$, i.e.,

$$c_n(t) = -\frac{i}{\hbar} \int_0^t \exp(i\omega_{ni} t') \langle n | \mathcal{H}' | i \rangle dt', \quad n \neq i, \quad (4.7)$$

where $|i\rangle$ abbreviates $|\psi_i^0\rangle$ and correspondingly for $\langle n |$. The transition probability from state i to state n is then $|c_n(t)|^2$. In order to calculate this quantity we must consider the time-dependent perturbation \mathcal{H}' more explicitly.

We start by considering a one-electron system influenced by an electromagnetic field. In a source-free region this field can be expressed by the magnetic

vector potential \mathbf{A} , fulfilling the condition $\nabla \cdot \mathbf{A} = 0$ according to the Lorentz condition $\nabla \cdot \mathbf{A} + c^{-1} \partial \phi / \partial t = 0$. The Hamiltonian of the system is

$$\begin{aligned}\mathcal{H} &= \frac{1}{2m}(\mathbf{p} + e\mathbf{A})^2 + V(r), \\ \mathcal{H} &= \frac{1}{2m}(-i\hbar\nabla + e\mathbf{A})^2 + V(r),\end{aligned}\quad (4.8)$$

where $V(r)$ is the static potential. But $\nabla \cdot (\mathbf{A}f) = (\nabla \cdot \mathbf{A})f + \mathbf{A} \cdot (\nabla f) = \mathbf{A} \cdot (\nabla f)$, since $\nabla \cdot \mathbf{A} = 0$ according to the Lorentz condition, i.e., \mathbf{A} and ∇ commute. Thus

$$\mathcal{H} = -\underbrace{\frac{\hbar^2}{2m}\nabla^2 + V(r)}_{\mathcal{H}_0} - i\frac{\hbar e}{m}\mathbf{A} \cdot \nabla + \frac{e^2}{2m}\mathbf{A}^2. \quad (4.9)$$

For weak fields the last quadratic term can be neglected (it is important for two-photon transitions, see Sect. 9.1.3). If the radiation is of frequency ω , $\mathbf{A} = \mathbf{A}_0 \cos \omega t$ and the quadratic term is neglected, then

$$\mathcal{H}' = -i\frac{\hbar e}{m}\mathbf{A} \cdot \nabla = C \cos \omega t \quad (4.10)$$

with

$$C = -i\frac{\hbar e}{m}\mathbf{A}_0 \cdot \nabla. \quad (4.11)$$

Using the Eulerian formulae, (4.7) now becomes

$$\begin{aligned}c_n(t) &= -\frac{1}{2\hbar} \langle n | C | i \rangle \left(\frac{\exp[i(\omega_{ni} - \omega)t] - 1}{\omega_{ni} - \omega} \right. \\ &\quad \left. + \frac{\exp[i(\omega_{ni} + \omega)t] - 1}{\omega_{ni} + \omega} \right).\end{aligned}\quad (4.12)$$

The case when $\Delta\omega = \omega_{ni} - \omega$ is close to zero is of special interest. This is when the irradiation frequency ω is close to the energy difference between states i and n . Then the second term in (4.12) can be neglected and, using the Eulerian formulae, the first term becomes

$$c_n(t) = -\frac{i}{2\hbar} \langle n | C | i \rangle e^{i\Delta\omega t/2} \frac{\sin(\Delta\omega t/2)}{\Delta\omega t/2}. \quad (4.13)$$

The time-dependent probability of an $i \rightarrow n$ transition is thus

$$|c_n(t)|^2 \propto \left(\frac{\sin(\Delta\omega t/2)}{\Delta\omega t/2} \right)^2 t^2. \quad (4.14)$$

The transition probability is plotted in Fig. 4.2 as a function of $\Delta\omega$ for a given value of t . The function has a prominent maximum for $\Delta\omega = 0$, i.e. when the photon energy of the radiation field exactly matches the energy difference between the final and initial states

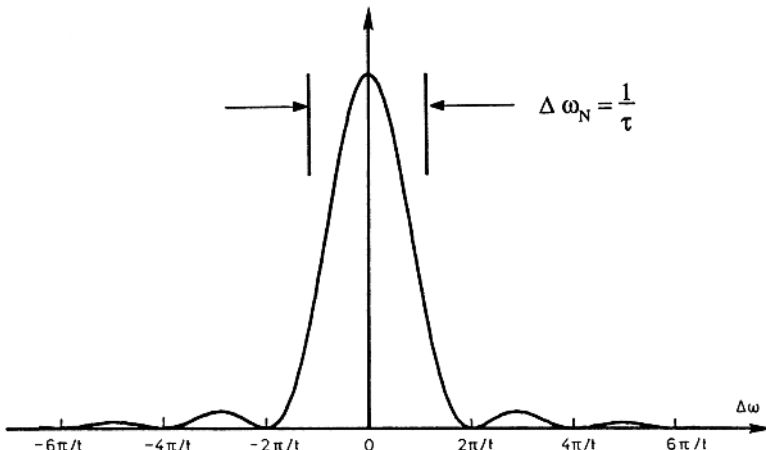


Fig. 4.2. Transition probability for absorption and stimulated emission

$$\hbar\omega = \hbar\omega_{ni} = E_n - E_i. \quad (4.15)$$

This condition is called *resonance*. We have assumed that a transition to a state with higher energy occurs, i.e. *absorption* of radiation. However, exactly the same result is obtained if

$$\hbar\omega = \hbar\omega_{in} = E_i - E_n, \quad (4.16)$$

where the final state n is below the initial state. In this case the first term in (4.12) is neglected instead of the last. The situation where the perturbation causes the system to emit a photon of the same energy as that of the incoming photons is called *stimulated emission*. From completely equivalent mathematics it follows that the probabilities for absorption and stimulated emission are the same. Furthermore, a stimulated photon is emitted in the same direction and the wave has the same phase as that of the incoming photon (coherence). This can be seen in a semiclassical picture of these radiative processes where the two processes are considered essentially equivalent. The coherence properties of the stimulated photon result in a strengthening of the incoming beam, a process that is the exact counterpart of the attenuation of a well-defined beam by absorption processes under other circumstances. We will consider later which process dominates.

According to (4.14) the maximum transition probability ($\Delta\omega = 0$) is proportional to t^2 , where t is the time during which the system is subject to the perturbation. This seems unphysical; one would expect the transition probability to increase linearly with t . However, we must consider that the energy levels are not infinitely sharp, but have a certain width, associated with the natural lifetime (τ) of the state. This point will be considered later in this chapter. If the perturbation is applied for a time $t \gg \tau$, the resonance curve of Fig. 4.2 will be much narrower than this level width. The

maximum value of the curve then has no significance; instead the area below the curve yields the transition probability. Since the half-width of the curve is proportional to t^{-1} and its maximum value to t^2 (the internal shape being independent of t) the area under the curve is proportional to t , as expected. This is called the *Fermi Golden Rule*.

At this point we should recall that a prerequisite for any process to take place at all is that the matrix element $\langle n|C|i\rangle$ in (4.12) is non-zero. We will now consider this matrix element more closely, namely

$$\langle n|C|i\rangle = -i\frac{\hbar e}{m}\langle n|\mathbf{A}_0 \cdot \nabla|i\rangle. \quad (4.17)$$

Transitions involving outer electrons normally occur in the optical or UV region, which means that the wavelength of the radiation ($\lambda > 100$ nm) is much greater than the dimensions of the atom (~ 0.1 nm). Thus, the spatial variation of the amplitude over the atom can be neglected and we can write

$$\langle n|C|i\rangle = -i\frac{\hbar e}{m}\mathbf{A}_0\langle n|\nabla|i\rangle. \quad (4.18)$$

Using the relations

$$i\frac{\hbar(\mathbf{d}\mathbf{r})}{dt} = [\mathbf{r}, \mathcal{H}_0]$$

and

$$\mathbf{p} = m\frac{d\mathbf{r}}{dt} = -i\hbar\nabla$$

we obtain

$$\nabla = -\frac{m}{\hbar^2}[\mathcal{H}_0, \mathbf{r}]$$

and thus

$$\langle n|\nabla|i\rangle = -\frac{m}{\hbar^2}\langle n|\mathcal{H}_0\mathbf{r} - \mathbf{r}\mathcal{H}_0|i\rangle = -\frac{m}{\hbar^2}(E_n - E_i)\langle n|\mathbf{r}|i\rangle.$$

Here the Hamiltonian operator \mathcal{H}_0 , being Hermitian, acts to the left in the first term and to the right in the second term. We then obtain

$$\langle n|C|i\rangle = i\omega_{ni}\mathbf{A}_0 \cdot \langle n|\mathbf{r}|i\rangle. \quad (4.19)$$

Thus we have shown that the transition probability $|c_n(t)|^2$ is proportional to the square of the matrix element between the initial and final state formed with the atomic *electric dipole operator*

$$\mathbf{p} = -e\mathbf{r}. \quad (4.20)$$

So far we have treated absorption and stimulated emission of radiation. However, it is well known that an atom can emit radiation even when it is not externally perturbed, i.e. *spontaneous emission*. It is not possible to treat this process fully here, since consideration of the quantization of the electromagnetic field as described by *quantum electrodynamics* (QED) is

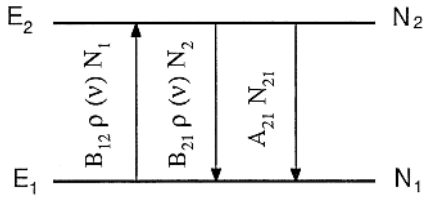


Fig. 4.3. Radiative processes connecting energy levels E_1 and E_2

necessary. According to QED a coupling between the atom and the “vacuum state” of the field is responsible for the emission.

A simple relation will be derived between the probabilities for spontaneous and stimulated emission and absorption of radiation using wellknown statistical distribution laws. Consider a system such as that illustrated in Fig. 4.3 with two energy levels, E_1 and E_2 , populated by N_1 and N_2 atoms, respectively. Three radiative processes can occur between the levels, as discussed above. In the figure the processes are expressed using the so-called *Einstein coefficients*, B_{12} , B_{21} and A_{21} , which are defined such that the rate of change in the population numbers is

$$\frac{dN_1}{dt} = -\frac{dN_2}{dt} = -B_{12}\rho(\nu)N_1 + B_{21}\rho(\nu)N_2 + A_{21}N_2, \quad (4.21)$$

where $\rho(\nu)$ is the energy density of the radiation field per frequency interval, and $\nu = (E_2 - E_1)/h$. At equilibrium we have

$$\frac{dN_1}{dt} = \frac{dN_2}{dt} = 0 \quad (4.22)$$

yielding

$$\rho(\nu) = \frac{A_{21}}{B_{12}(N_1/N_2) - B_{21}}. \quad (4.23)$$

We now assume the system to be in thermodynamic equilibrium with the radiation field. The distribution of the atoms is governed by Boltzmann’s law

$$\frac{N_1}{N_2} = \exp\left(\frac{h\nu}{kT}\right), \quad (4.24)$$

where T is the absolute temperature of the system and k is the Boltzmann constant. By identifying the expression for ρ given above with the Planck radiation law

$$\rho(\nu) = \frac{16\pi^2\hbar\nu^3}{c^3} \frac{1}{\exp(h\nu/kT) - 1} \quad (4.25)$$

we obtain the following relations between the three coefficients

$$B_{12} = B_{21}, \quad (4.26)$$

$$\frac{A_{21}}{B_{21}} = \frac{16\pi^2\hbar\nu^3}{c^3}. \quad (4.27)$$

The first relation shows that the probabilities for absorption and stimulated emission are the same for a transition between states 1 and 2. This is in accordance with the result obtained above using first-order perturbation theory. Note, that the result (4.26) is independent of the strength of the radiation field. It was in discussions of this kind that A. Einstein, in 1917, found it necessary to introduce the concept of stimulated emission in order to obtain agreement with the statistical laws known at that time [4.14].

From (4.27), (4.13) and (4.19) the spontaneous transition probability between the states i and k is found to be

$$A_{ik} = \frac{32\pi^3}{3} \frac{\nu^3}{4\pi\epsilon_0\hbar c^3} |\langle i | e\mathbf{r} | k \rangle|^2. \quad (4.28)$$

The most important result here is that this transition probability is determined by the same matrix elements as the induced transitions. Thus there are common *selection rules* for all three types of transitions.

So far we have only treated electric dipole radiation. In a more detailed treatment the radiation field can be described by electric and magnetic “*multipoles fields*”, i.e. magnetic dipole radiation, electric quadrupole radiation etc. Magnetic dipole radiation is analogous to electric dipole radiation and it depends on the magnetic dipole moment of the atom

$$\boldsymbol{\mu}_J = -\mu_B \sum_i (\mathbf{l}_i + 2\mathbf{s}_i) = -\mu_B (\mathbf{L} + 2\mathbf{S}). \quad (4.29)$$

If electric dipole radiation is allowed, i.e. if the matrix element of \mathbf{p} between the two states is non-zero, this type of radiation strongly dominates over the other types. If, however, an electric dipole transition is not allowed, other types of radiation become important.

The total spontaneous transition probability per unit time for an atom, in a specific state i , can be expressed as

$$A_i = \sum_k A_{ik}, \quad (4.30)$$

where the summation is over all levels of the atom having energies less than E_i and A_{ik} is the spontaneous transition probability for a single process. This means that the number of atoms, N , in a certain state i will decrease exponentially with time

$$N = N_0 \exp(-t/\tau_i) \quad (4.31)$$

with

$$\tau_i = 1/A_i. \quad (4.32)$$

Here we have assumed that the considered level is not re-populated by decay from higher-lying levels.

On average, the time elapsed before an atom in the upper state decays to another state is

$$\bar{t} = \frac{\int_0^\infty t \exp(-t/\tau) dt}{\int_0^\infty \exp(-t/\tau) dt} = \tau \quad (4.33)$$

and therefore τ is called the *mean lifetime*. It is also possible to calculate the *variance* Δt of the lifetime of the atom in the state of interest

$$(\Delta t)^2 = \frac{\int_0^\infty (t - \tau)^2 \exp(-t/\tau) dt}{\int_0^\infty \exp(-t/\tau) dt} = \tau^2. \quad (4.34)$$

Thus, the “uncertainty” in the lifetime is also equal to τ . The corresponding uncertainty (ΔE) in an energy determination of the level must fulfil the Heisenberg uncertainty relation

$$\Delta E \cdot \Delta t \geq \hbar/2. \quad (4.35)$$

Here, mathematically the uncertainties are *variances*. The minimum value of this product yields the minimum energy uncertainty which can never be surpassed

$$\Delta E_{\min} = \hbar \Delta \nu. \quad (4.36)$$

We find that the so-called *natural radiation width* (in frequency units) is given by

$$\Delta \nu_N = 2 \Delta \nu = 1/2\pi\tau. \quad (4.37)$$

It is interesting to compare this “microscopic” treatment of radiative processes with the “macroscopic” treatment of classical physics. In the latter, the atom is considered as an exponentially damped harmonic oscillator with an amplitude (Fig. 4.4)

$$\mathcal{E} = \mathcal{E}_0 e^{-t/2\tau} \cos(2\pi\nu_0 t). \quad (4.38)$$

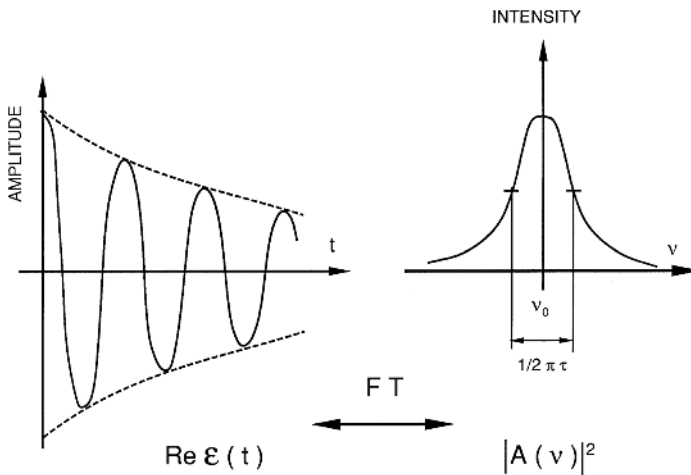


Fig. 4.4. Semiclassical picture of a radiating atom

Because the oscillation is damped the frequency cannot be infinitely sharp. A Fourier analysis allows a determination of the frequency distribution giving rise to this special time dependence for the oscillation. In Fourier analysis it is convenient to work with the complex function

$$\mathcal{E}(t) = \mathcal{E}_0 e^{-t/2\tau} e^{i2\pi\nu_0 t}, \quad (4.39)$$

the real part of which is the function given in (4.38). The *amplitude* distribution is described by the Fourier transform

$$\begin{aligned} A(\nu) &= \frac{1}{2\pi} \int_0^\infty \mathcal{E}_0 e^{t/2\tau} e^{i2\pi(\nu_0 - \nu)t} dt \\ &= \frac{\mathcal{E}_0}{2\pi} \frac{-1}{i2\pi(\nu_0 - \nu) - 1/2\tau}. \end{aligned}$$

The intensity distribution is $|A(\nu)|^2$:

$$\begin{aligned} |A(\nu)|^2 &= A(\nu)A^*(\nu) = \frac{\mathcal{E}_0^2}{4\pi^2} [4\pi^2(\nu - \nu_0)^2 + 1/4\tau^2]^{-1} \\ &= \frac{(\mathcal{E}_0^2\tau^2)}{\pi^2} \left[1 + \left(\frac{\nu - \nu_0}{1/4\pi\tau} \right)^2 \right]^{-1}. \end{aligned} \quad (4.40)$$

This is a Lorentzian curve with a full-width at half-maximum of $\Delta\nu = (2\pi\tau)^{-1}$. This classical approach thus yields the same radiative width as quantum mechanics. The broadening of the transition due to the finite lifetime of the excited state is called the *homogeneous* broadening in contrast to *inhomogeneous* broadening, which will be discussed in Chap. 6.

At the end of this section we would like to mention two kinds of recently investigated phenomena that can influence the natural radiative lifetime. The first is the *ambient black-body radiation* which, even at room temperature, can have a substantial effect on the lifetime of highly-excited, normally long-lived, states. Such states are connected to nearby levels by microwave electric dipole transitions. The substantial black-body radiation in this wavelength region can induce transitions through absorption or stimulated emission, thus effectively reducing the lifetime of the investigated state. The effects can be quite drastic and can only be eliminated by cooling the atomic environment to low temperatures [4.15, 4.16].

The second phenomenon is of a much more fundamental nature, and can be understood in the more detailed treatment of the interaction between matter and light provided by the quantum electrodynamic (QED) theory. As we have seen above, it is frequently sufficient to treat the light/matter interaction by quantizing the matter (atoms/molecules) and to consider the light as an electromagnetic field from which absorption can occur only in quantized energy units (photons). However, many aspects require a more rigorous treatment, where the electromagnetic field is also quantized. We have already discussed the case of spontaneous emission, which can be seen as due to an interaction of the atom with the lowest (vacuum) state of the

quantized field. Based on the theory of spontaneous emission, there is now a possibility of influencing the natural lifetime of an excited state by manipulating the quantized field ground state. This can be done by placing an atom in a cavity whose dimensions are too small to support the vacuum mode of the field (“turning off the vacuum”), leading to a prolonged excited-state lifetime [4.17, 4.18]. In the same way the vacuum mode can be enhanced by using a cavity tuned to resonance with an atomic microwave transition, resulting in an increased spontaneous emission rate and a decreased lifetime [4.19]. Clearly, the *Lamb shift*, which is a pure quantum electrodynamical effect, is also influenced by a cavity.

The quantized nature of the field and its fundamental interaction with atoms lead to many further interesting non-classical phenomena, which are treated in a field generally referred to as *quantum optics* [4.20–4.28]. The field also comprises emerging practical applications such as *quantum computing* and *quantum cryptography*.

The first observation of the non-classical properties of light was made in the *Hanbury-Brown and Twiss experiment* [4.29] which sought to deduce the size of a star from studies of intensity fluctuations in the light. They studied the correlation between intensity fluctuations at two spatially separated detectors. The experiment lead to an increased interest in the quantum-mechanical coherence properties of light. It was shown that partially coherent light exhibits a bunching effect, i.e. photons are not detected equally spread in time [4.30]. This could be understood from the quantum field theory of light [4.31]. The theory also predicted *photon anti-bunching* in the interaction with atoms. This phenomenon in light interaction with a single atom has been observed [4.32] and can be understood in terms of *shelfing* (See Sect. 9.8.4). Because of the finite lifetime of an atom in an excited state there must be some time separation between two emitted photons.

Further interesting quantum-optical experiments have been pursued using a single atom in a cavity of extremely high Q -value (wall reflectivity). Single-atom maser action has been achieved and detailed studies of the interaction between the atom and the field have been pursued [4.19, 4.33–4.38]. Atoms were laser-excited into high Rydberg states and microwave transitions to neighbouring Rydberg states were observed. Single-atom laser action in the visible spectrum has been observed in later studies [4.39, 4.40].

A further aspect of the quantized electromagnetic field is the possibility of generating light in a *squeezed state* [4.41–4.44]. Coherent light can be described as radiation with equal variance (uncertainty) in space and momentum corresponding to a minimum uncertainty state according to the Heisenberg relation. It can also be expressed in a similar manner in terms of intensity and phase. The accuracy of optical measurements is limited by the variances. However, a reduced variance in one observable can be compensated by an increase in the other one, still compatible with the uncertainty principle. This is achieved for squeezed light, for which the phase can be measured

more accurately than primarily expected, at the expense of an increased intensity uncertainty. Squeezed light has been generated in many ways, maybe most conveniently in the optical parametric generation process (Sect. 8.6). It might have important applications for optical communication and precise interferometric measurements of small displacements, e.g. in gravity-wave detection experiments [4.45].

4.2 Spectra Generated by Dipole Transitions

A spectrum is generated by transitions between different energy states according to certain selection rules. The selection rules for allowed transitions essentially reflect the requirement of conservation of angular momentum for the atom/molecule-photon system. Considerations of symmetry for the wave functions describing the states involved are also important. For electric dipole transitions the establishing of selection rules is equivalent to a determination of the conditions under which the matrix element $\langle n|\mathbf{r}|i\rangle$ is non-zero. Since \mathbf{r} is an odd operator, we can immediately state that the two considered states must be of *opposite parity*.

The selection rules will not be derived here, but stated with some comments. We will then see how spectra are generated by allowed transitions between energy levels described in Chaps. 2 and 3. It is best to treat atoms and molecules separately, but first some general features will be discussed in connection with Fig. 4.5.

Spectra of atoms and molecules resulting from absorption or emission can be studied. In *absorption*, a wavelength continuum is used, of which certain wavelengths are absorbed. *Emission* spectra may be generated in a discharge in a light source where the excited levels are populated by, for example, electron collisions. If atoms or molecules are irradiated by light of

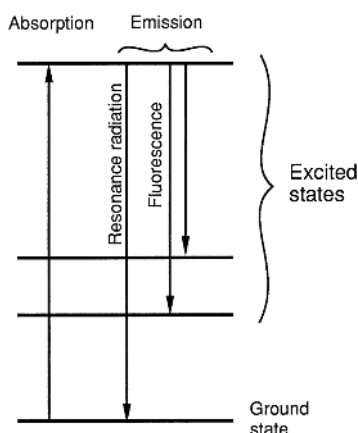


Fig. 4.5. Terminology for radiative processes

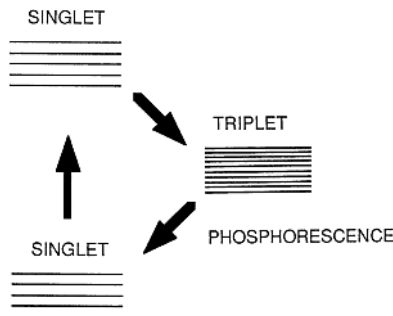


Fig. 4.6. The phosphorescence phenomenon

a wavelength that corresponds to the energy of an allowed transition from the ground state, there will be a *resonance absorption* of photons followed by the release of *resonance radiation* in the decay back to the original level. If the decay occurs to levels above the ground state, the emitted light is called *fluorescence light*.

A special type of emission, *phosphorescence*, can be obtained from certain molecules that are excited from the ground state to a higher-lying state in the normal way. If the molecules make transitions to a lower-lying state of another multiplicity, for example, through collisions, the molecules can accumulate here for a long time, since the transition to the ground state is normally radiatively forbidden (Fig. 4.6). In phosphorescing substances the state is not depopulated through radiationless transitions and therefore an extremely long lifetime is obtained (seconds or more), and weak light will be emitted long after the excitation has been terminated.

4.2.1 Atoms

For one-electron systems we have the following selection rules

$$\begin{aligned}\Delta\ell &= \pm 1, \\ \Delta j &= 0, \pm 1.\end{aligned}\tag{4.41}$$

For many-electron systems we have

$$\Delta J = 0, \pm 1 \quad 0 \leftrightarrow 0 \quad \text{forbidden}.\tag{4.42}$$

In pure *LS* coupling we also have

$$\begin{aligned}\Delta L &= 0, \pm 1 \quad 0 \leftrightarrow 0 \quad \text{forbidden}, \\ \Delta S &= 0.\end{aligned}\tag{4.43}$$

In Fig. 4.7 allowed transitions between a *p*² and an *sp* configuration are indicated as an example.

Transitions in the H, Na, He and Ca atoms are indicated in Figs. 2.1, 2.2, 2.6, and 2.7, respectively.

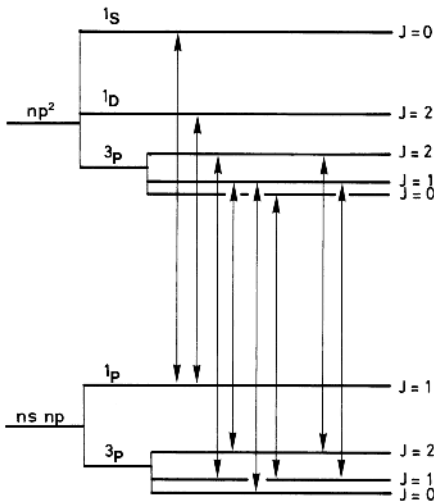


Fig. 4.7. Allowed electric dipole transitions between a p^2 and an sp configuration

Even at small deviations from LS coupling, transitions between states of different multiplicity (*intercombination lines*) are observed. Such lines are indicated for the Ca atoms in Fig. 2.7.

In the presence of hyperfine structure there is a further selection rule:

$$\Delta F = 0, \pm 1 \quad 0 \leftrightarrow 0 \quad \text{forbidden.} \quad (4.44)$$

So far we have only considered transitions of outer electrons giving rise to lines in the IR, visible and UV spectral regions. If a vacancy is created in an inner shell, de-excitation occurs by successive transitions inwards by electrons from outer shells (Chap. 5). In Fig. 4.8 level and transition designations for the inner shells of the copper atom are given.

So far we have not discussed the selection rules for the M quantum number. M describes projections of the *resulting* angular momentum of the atom, which can be \mathbf{J} or \mathbf{F} . The rule is

$$\Delta M = 0, \pm 1. \quad (4.45)$$

The different values of ΔM correspond to different *angular distributions* of the radiation and to different *polarization conditions*. For $\Delta M = 0$ only the z component of $\mathbf{p} = -e\mathbf{r}$ contributes and the radiation can be compared to that of a classical dipole oscillating along the direction of the field (quantization axis). The radiation then has an intensity which is proportional to $\sin^2 \theta$, θ being the angle between the field and the direction of radiation. As for the polarization, the electrical vector oscillates in the plane defined by the field and the direction of the radiation. (The magnetic vector is perpendicular to the electric one and both vectors are perpendicular to the direction of propagation.) In a similar way, it is found that the $x \pm iy$ components

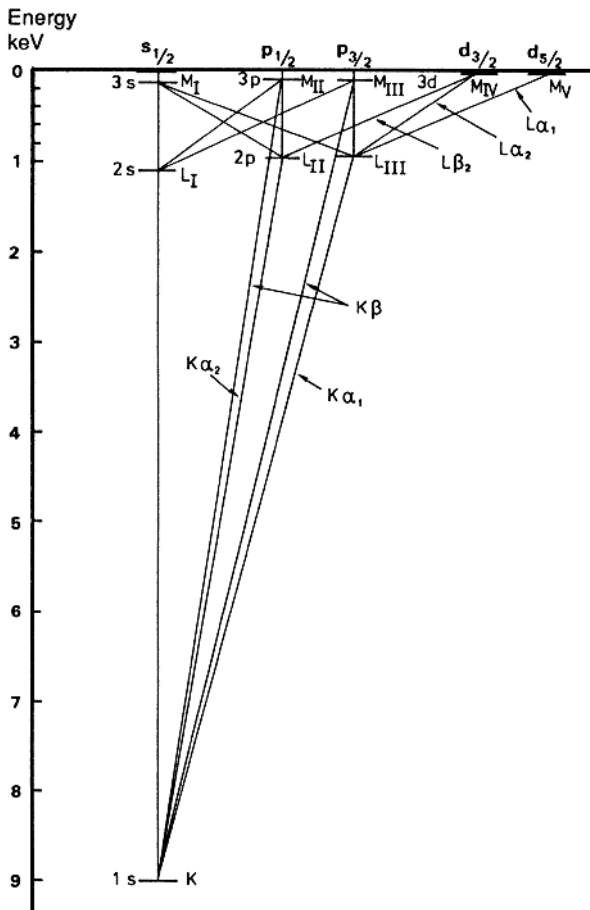


Fig. 4.8. X-ray transitions in the copper atom

of p are responsible for $\Delta M = \pm 1$ transitions corresponding to an electric dipole rotating in the x - y plane, i.e. perpendicularly to the field direction. The intensity is, in this case, proportional to $(1 + \cos^2 \theta)$, and the radiation is generally elliptically polarized. In the z -direction it is circularly polarized and in the x - y plane linearly polarized. The radiation that corresponds to $\Delta M = 0$ is called π radiation and for $\Delta M = \pm 1$ the term σ radiation is used. The intensity and polarization distributions are illustrated in Fig. 4.9.

We have discussed above the distribution of the emitted radiation. Clearly, the process is reversible and the given angular distributions then give the relative probability of absorption of an incoming photon by an atom in the lower energy state.

Radiative transitions in atoms and selection rules have been discussed in more detail in the atomic physics books referred to in Chap. 2.

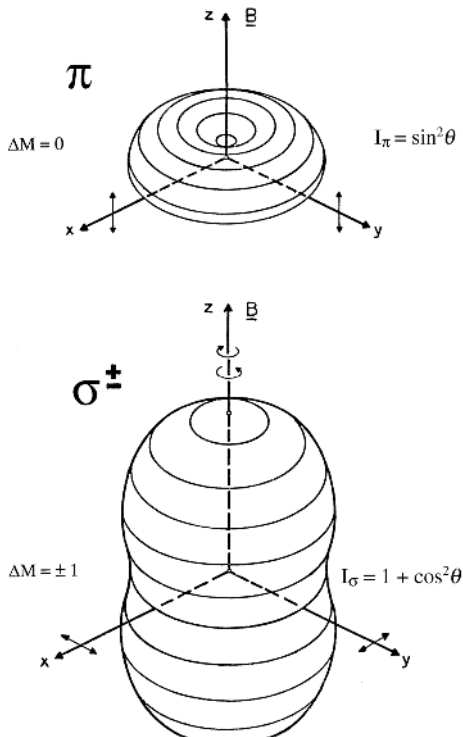


Fig. 4.9. Intensity distributions for π and σ radiation. The marks on the coordinate axes indicate the oscillation direction of the electric field vector

4.2.2 Molecules

Classically, light is emitted by a system only if its electric dipole moment is changed. This rule is also valid quantum mechanically and is of special importance in the consideration of the radiative properties of molecules. We will first treat rotational and vibrational transitions within a given electronic molecular state. Primarily, we only consider ${}^1\Sigma$ states for which the complications, discussed at the end of Sect. 3.2, do not occur since the rotational angular momentum is the only form of angular momentum present.

Rotational Transitions. A diatomic molecule with two different kinds of atoms has a permanent dipole moment in the direction of the symmetry axis. If the molecule rotates the dipole should classically emit radiation (see also Fig. 4.9). Quantum mechanically, radiation occurs when the rotation is changed. For the rotational quantum number J , which was defined in Chap. 3, we have

$$\Delta J = \pm 1. \quad (4.46)$$

Using the energy expression (3.6) for rotational levels we have

$$\nu_{J+1 \leftrightarrow J} = \frac{2B}{h}(J+1), \quad J = 0, 1, 2, \dots \quad (4.47)$$

Thus we obtain equidistant rotational lines in the far IR ($\sim 1000 \mu\text{m}$) as illustrated in Fig. 4.10.

If we take the elasticity of the molecule into account (3.7) we obtain

$$\nu_{J+1 \leftrightarrow J} = \frac{2B}{h}(J+1) - \frac{4D^+}{h}(J+1)^3. \quad (4.48)$$

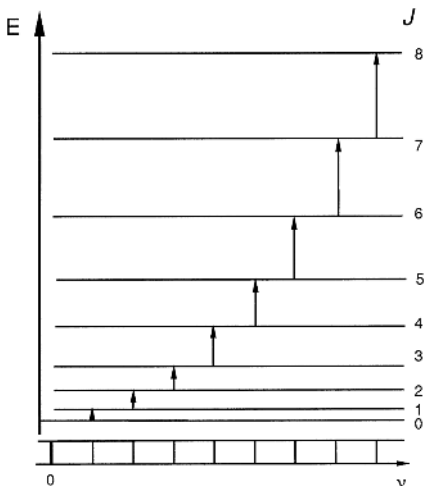


Fig. 4.10. Rotational transitions in a diatomic molecule

Vibrational Transitions. If the molecule has a permanent dipole moment at the equilibrium distance (r_0 in Fig. 3.7) this moment will vary periodically during vibration. Classically, radiation will then be emitted. If a diatomic molecule has a harmonic oscillatory movement we obtain the quantum mechanical selection rule

$$\Delta v = \pm 1. \quad (4.49)$$

Since the energy levels of the harmonic oscillator are equidistant, only one IR vibrational line ($\sim 10 \mu\text{m}$) is obtained. If the potential deviates from the harmonic oscillator, transitions with $\Delta v = \pm 2$, $\Delta v = \pm 3$, etc. can also occur. These transitions, which are generally weak, are called overtones (harmonics). As for rotational motion, molecules of the type O_2 , N_2 (i.e., homonuclear molecules) do not exhibit electric-dipole vibrational lines. However, quadrupole- and pressure-induced transitions of homonuclear molecules can be observed faintly.

Vibrational-Rotational Spectra. If there were no interaction between rotational and vibrational motion, the energy of a rotating vibrator would simply be the sum of its rotational and vibrational energies according to the

above expressions. However, the moment of inertia of the molecule is influenced by molecular vibration during rotation. The vibrational energy is much greater than the rotational energy and we can use the mean value of r^2 (see (3.4), (3.6)) during the vibration to calculate an effective rotational constant B' , which is slightly lower than the one corresponding to the equilibrium separation. Writing the energy of a molecular level as

$$E = (v + 1/2)h\nu_c + B'J(J + 1) \quad (4.50)$$

and using the selection rules $\Delta v = \pm 1$, $\Delta J = \pm 1$ we obtain the absorption spectrum

$$\Delta E = h\nu_c \begin{cases} +2B'(J + 1) & J \rightarrow J + 1 \quad J = 0, 1, \dots \text{ (R branch)} \\ -2B'J & J \rightarrow J - 1 \quad J = 1, 2, \dots \text{ (P branch)} \end{cases} \quad (4.51)$$

Lines corresponding to the upper expression form the so-called *R branch*, while the lower expression yields the *P branch*. In Fig. 4.11 the transitions are indicated for a simple case. Note, that there is no line at $\Delta E = h\nu$, since $\Delta J = 0$ is forbidden for diatomic molecules. As a matter of fact, the value of B' will decrease for higher vibrational states. Designating the rotational constants for the two states B' and B'' (upper and lower states, respectively) we obtain

$$\Delta E = h\nu_c \begin{cases} +2B' + (3B' - B'')J + (B' - B'')J^2 & J \rightarrow J + 1 \quad J = 0, 1, \dots \text{ (R branch)} \\ -(B' + B'')J + (B' - B'')J^2 & J \rightarrow J - 1 \quad J = 1, 2, \dots \text{ (P branch)} \end{cases} \quad (4.52)$$

Both branches can be represented by a single formula

$$\Delta E = h\nu_c + (B' + B'')m + (B' - B'')m^2 \quad (4.53)$$

with

$$m = 1, 2, 3 \dots \text{ for the R branch}$$

and

$$m = -1, -2, -3 \dots \text{ for the P branch.}$$

Since $B' < B''$, because of the averaging over r^2 (see (3.4)) this formula shows that the distance between lines becomes successively smaller in the R branch, while there is a corresponding increase in the P branch, as illustrated in Fig. 4.12.

For sufficiently high values of J there can be an inversion of the R branch, giving rise to the formation of a *band head*. Since the B values differ still more between states belonging to different electronic levels, band heads are more frequently observed in spectra obtained in electronic transitions. Equation

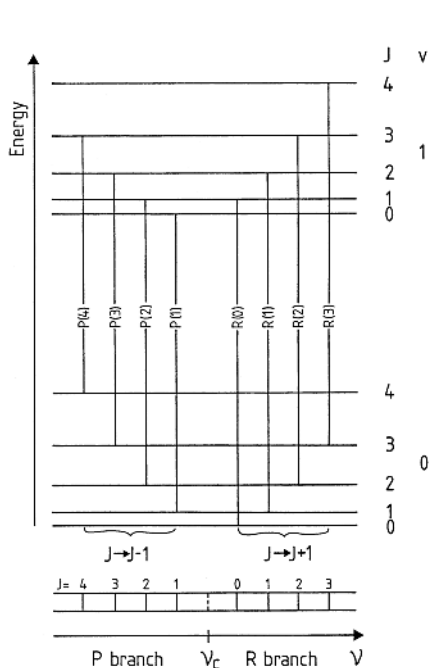


Fig. 4.11. Vibrational-rotational spectrum when the rotational constant B is the same in both vibrational states

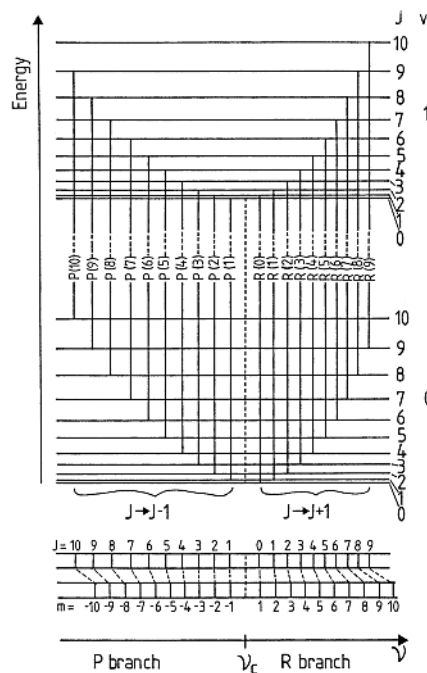


Fig. 4.12. Vibrational-rotational spectrum when the rotational constant is smaller in the upper vibrational state

(4.53) represents a parabola, and a diagram like the one given in Fig. 4.13 is called a *Fortrat parabola*. Depending on the relative sizes of B' and B'' , the parabola has its vertex towards higher or lower frequencies. If $B' < B''$, the band is said to be *shaded to the red*, whereas if $B' > B''$, it is *shaded to the violet*.

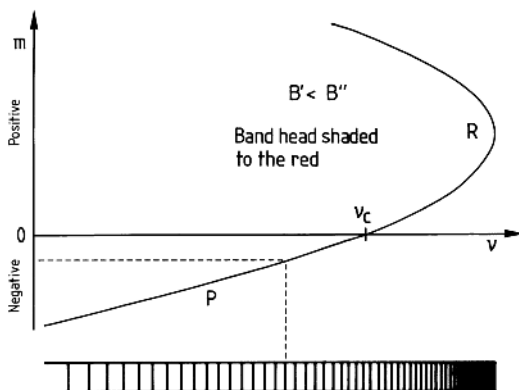


Fig. 4.13. Fortrat parabola

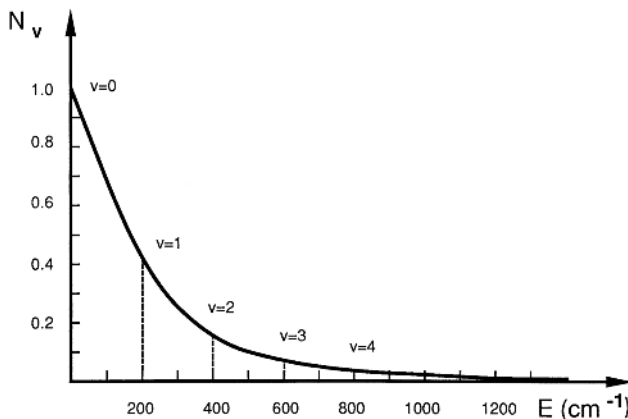


Fig. 4.14. Population distribution on different vibrational levels of I_2 [4.46]

The population of different vibrational levels is given by the Boltzmann distribution. Thus only the state with $v = 0$ is well populated for molecules with a large separation between the vibrational levels, e.g. N_2 and O_2 . The distribution for a molecule with a small value of $h\nu_c/kT$ is shown in Fig. 4.14.

The intensity distribution *within* a vibrational-rotational band is also determined by the Boltzmann distribution. It is then necessary to take the $2J + 1$ magnetic sublevels of a rotational level into account. The distribution factor is

$$N_J \propto (2J + 1)e^{-BJ(J+1)/kT}. \quad (4.54)$$

In the left part of Fig. 4.15 this distribution for the HCl molecule ($B = 10.44 \text{ cm}^{-1}$) is shown for room temperature. This distribution leads to a somewhat higher intensity of the R branch compared with the P branch which is

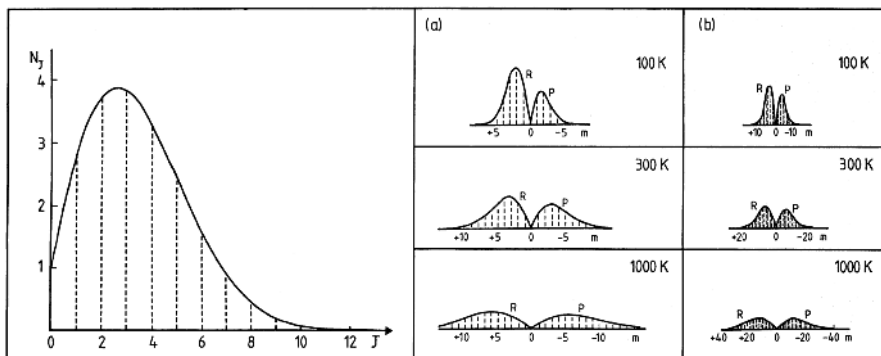


Fig. 4.15. Population distribution on different rotational levels and resulting spectra for different temperatures, (a) $B = 10.44 \text{ cm}^{-1}$, (b) $B = 2 \text{ cm}^{-1}$ [4.46]

also illustrated in the figure for two molecules with large and small B values, respectively. This effect can be utilized for temperature measurements.

Electronic Transitions – The Franck–Condon Principle. Vibrational and rotational spectra arise from the movements of the atomic nuclei of the molecule. In transitions between different electronic configurations much higher energies are involved (\sim eV, visible or UV region). Normally a transition in the electronic shell is accompanied by transitions between different vibrational and rotational levels of the molecule. Therefore *bands* are also obtained in the visible region. The intensities of the components of the observed vibrational structure are explained by the *Franck–Condon principle*. Electronic transitions in molecules occur so quickly that the nuclei do not change their relative positions in vibrational motion. Some cases are illustrated in Fig. 4.16. In part (a) of the figure the equilibrium distances of the two potential curves are the same. Primarily, we then obtain a $v = 0 \rightarrow v = 0$ transition in absorption since the relative positions and velocities of the nuclei are not changed. In (b) transitions occur primarily from the $v = 0$ level to a level with higher v , since the wave function in the excited state has a maximum at the classical turning point. In (c) dissociation primarily occurs, resulting in a continuum in the absorption spectrum. Typical spectra are also shown beside the potential curves.

The transition back to the ground state from an excited electronic state can occur in several ways. Transitions can occur by direct emission of a photon. De-excitation can also occur through successive transitions via the vibrational levels in the excited electron configuration and only after that be followed by a return to the ground state. The light is then shifted towards red compared with the excitation wavelength (*Stokes shifting*). This can be observed, for example, in organic dye molecules.

While $\Delta J = 0$ is forbidden in a pure rotational–vibrational transition, this type of transition is allowed in connection with electronic transitions (still not for ${}^1\Sigma - {}^1\Sigma$ transitions). The new selection rule gives rise to a *Q branch*, in addition to the *R* and *P* branches.

Molecular spectra have been discussed in more detail in the molecular physics books referred to in Chap. 3.

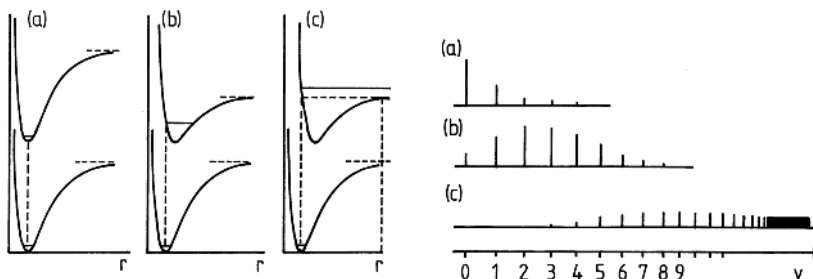


Fig. 4.16. Illustration of the Franck–Condon principle and resulting spectra [4.46]

4.3 Rayleigh and Raman Scattering

As shown in Sect. 4.1, resonant transitions can be obtained if an atomic or molecular system is irradiated by light with an energy corresponding to the energy separation between two levels. Even if the light is not of a resonant frequency, weak scattering effects are still obtained, so-called *Rayleigh* and *Raman scattering*. This scattering can be explained classically as well as quantum mechanically. Detailed descriptions of these phenomena and their utilization can be found in [4.11–4.13].

If a molecule is subject to an electric field \mathcal{E} , an electric dipole moment \mathbf{P} is induced in the molecule (see the Stark effect), i.e.,

$$\mathbf{P} = \alpha \mathcal{E}. \quad (4.55)$$

Generally, \mathbf{P} is not directed along \mathcal{E} since the molecule is frequently asymmetric and α is then replaced by a *polarization tensor*. For an oscillating field

$$\mathcal{E} = \mathcal{E}_0 \sin(2\pi\nu t) \quad (4.56)$$

the polarization will vary at the frequency ν , resulting in a re-radiation of light of the same frequency. This *Rayleigh scattering* is *elastic* in nature. For the total radiated energy I from an oscillating dipole

$$I = \frac{2}{3c^3} \overline{\left(\frac{d^2 P}{dt^2} \right)^2} \quad (4.57)$$

where the bar denotes time averaging. Equations (4.57), (4.56) yield

$$I = \frac{16\pi^4 c}{3\lambda^4} \alpha^2 \mathcal{E}_0^2. \quad (4.58)$$

Here we have used the relation $\overline{(\sin^2 2\pi\nu t)} = 1/2$. As can be seen, Rayleigh scattering strongly increases with diminishing wavelength.

If a molecule vibrates, its polarizability varies. Further, the polarizability depends on the orientation of the molecule with regard to the field, as mentioned in connection with the introduction of the polarizability tensor. Thus the polarizability of the molecule varies as it rotates. We can then state

$$\alpha = \alpha_0 + \alpha_{lv} \sin(2\pi\nu_{vibr} t) \quad \alpha_{lv} \ll \alpha_0 \quad (4.59)$$

for the vibrational motion and

$$\alpha = \alpha_0 + \alpha_{lr} \sin(2\pi 2\nu_{rot} t) \quad \alpha_{lr} \ll \alpha_0 \quad (4.60)$$

for the rotational motion, where the variation occurs at twice the rotational frequency ν_{rot} . This is due to the fact that the polarizability is the same for opposite directions of the field (cf. the Stark effect). If an external oscillating field of frequency ν is applied, there will be a coupling between the applied and the internal oscillation. This coupling becomes evident if (4.59) or (4.60) is inserted into $|\mathbf{P}| = \alpha |\mathcal{E}|$ and simple trigonometric relations are employed.

For vibrational motion

$$P = \alpha_0 \mathcal{E}_0 \sin(2\pi\nu t) + (1/2)\alpha_{\text{lv}} \mathcal{E}_0 [\cos 2\pi(\nu - \nu_{\text{vibr}})t - \cos 2\pi(\nu + \nu_{\text{vibr}})t] \quad (4.61)$$

and for rotational motion

Thus a sideband is obtained on both sides of the Rayleigh line. The sidebands are shifted from the Rayleigh frequency by the vibrational frequency and twice the rotational frequency, respectively. The down- and upshifted components are called the *Stokes* and the *Anti-Stokes* lines, respectively, and their strength is generally $\sim 1/1000$ of the strength of the Rayleigh line. The phenomenon is called the *Raman effect* and was first observed experimentally in 1928 by the Indian scientist *C.V. Raman* (Nobel prize 1930). The Raman effect represents *inelastic scattering*. In the quantum mechanical theory of Raman scattering, *virtual* levels are introduced which mediate the scattering (Fig. 4.17).

In the interaction with a molecule, an amount of energy can be emitted or absorbed by the molecule, corresponding to a change in the frequency of the scattered light quantum. From (4.61) and (4.62) it is evident that the Raman effect occurs only when the polarizability is changed in the process ($\alpha_1 \neq 0$). The Raman scattering increases for shorter wavelengths and also exhibits resonances when real levels are approached.

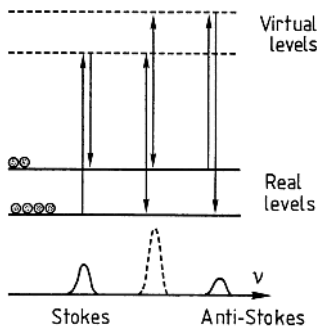


Fig. 4.17. Raman scattering

4.4 Raman Spectra

When a molecular gas is intensely irradiated with monochromatic light, usually from a laser, a spectrum of Raman lines is generated close to the strong elastic Rayleigh component.

4.4.1 Vibrational Raman Spectra

For the Raman effect, vibration in a harmonic oscillator potential leads to the same selection rule as for the normal IR spectrum

$$\Delta v = \pm 1. \quad (4.63)$$

Thus a Stokes and an anti-Stokes component are obtained, shifted by a frequency ν_c from the Rayleigh line. At normal temperatures, most of the molecules are in the lowest state ($v = 0$) and few are in the $v = 1$ state. The intensity of the Stokes line, corresponding to the transition $0 \rightarrow 1$, is thus much greater than that of the anti-Stokes line ($1 \rightarrow 0$). In the quantum-mechanical picture the intensities reflect the populations of the levels. On the other hand, the classical picture falsely predicts components of equal intensity. By comparing the intensities of the Stokes and the anti-Stokes components the temperature can be determined, for example, in a flame. Because of the nonharmonicity of the vibrational potential the spacing between the vibrational levels is not constant. This results in the occurrence of separated Stokes components originating from different vibrational levels. Utilizing the components from higher levels (*hot bands*), the temperature can conveniently be determined as illustrated in Fig. 4.18.

Diatom molecules with identical atoms do not exhibit any IR spectrum because of the absence of a permanent dipole moment. They are, however, *polarizable* and the Raman effect is then observed. In most diatomic molecules the separation between the lowest vibrational levels is so large that only the Stokes line can be observed at room temperature. However, anti-Stokes

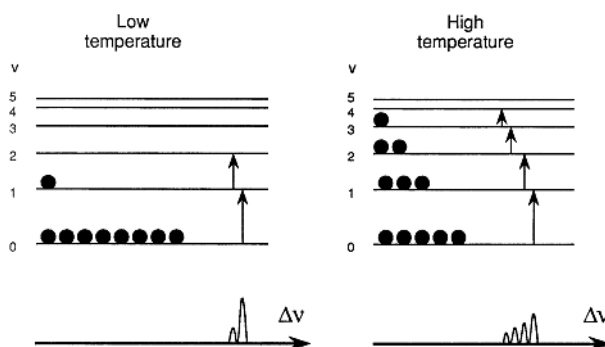


Fig. 4.18. The occurrence of vibrational “hot bands” in Raman spectra

lines can be observed for most polyatomic molecules which exhibit lower vibrational frequencies.

4.4.2 Rotational Raman Spectra

While the vibrational Raman effect has the same selection rule as the IR transitions, different rules apply for the rotational Raman effect (compare with the classical picture!)

$$\Delta J = \pm 2. \quad (4.64)$$

Since several rotational levels with different J values are populated normally, the rotational Raman spectrum consists of several lines. $\Delta J = 0$ corresponds to the Rayleigh line. Stokes and anti-Stokes branches of equidistant lines corresponding to $\Delta J = \pm 2$ are obtained. The branches are called S and O for $\Delta J = +2$ and $\Delta J = -2$, respectively. Utilizing (3.6), we have

$$\nu_{J+2 \leftrightarrow J} = \frac{4B(J + 3/2)}{h}. \quad (4.65)$$

An example of the rotational Raman effect is shown in Fig. 4.19.

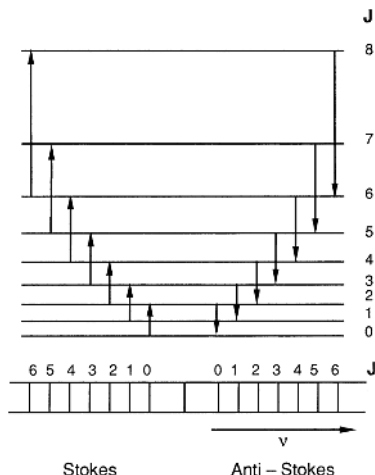


Fig. 4.19. Rotational Raman spectrum

4.4.3 Vibrational–Rotational Raman Spectra

As for dipole transitions, we obtain a combined vibrational–rotational spectrum for Raman scattering. Such a Raman band contains three branches, S , Q ($\Delta J = 0$) and O . Since the rotational constants for the vibrational levels with $v = 0$ and 1 are almost identical, the lines of the Q branch occur almost on top of each other and can frequently not be resolved. Because of this,

a very strong central line occurs. The S and O branches are much weaker since the components are spread out. These branches correspond to the R and P branches in IR spectra, with the exception that the separations in the Raman spectrum are twice as large. In Fig. 4.20 an example of a Raman spectrum is given. The intensity distribution, previously discussed for IR transitions, is illustrated.

As we have seen, IR and Raman spectra frequently yield the same information. Raman spectra can, in many respects, be considered as IR spectra which have been moved into the visible region employing a visible excitation line. However, IR and Raman spectra also complement each other, as different transitions can sometimes be observed.

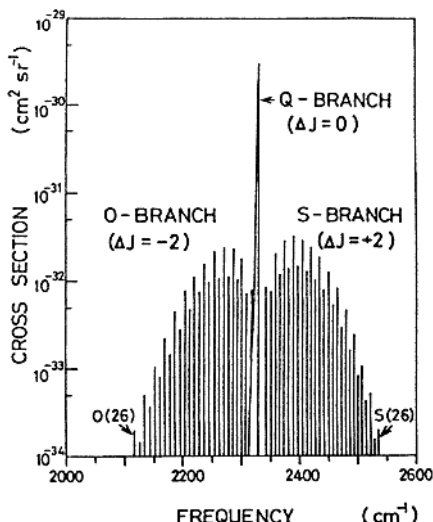


Fig. 4.20. Vibrational-rotational Raman spectrum of N_2 [4.47]

4.5 Mie Scattering

In Sect. 4.3 we discussed Rayleigh scattering, which occurs when a light wave induces a varying polarization in molecules. In this case the wavelength was larger than the molecular diameter. When light falls on particles of a size considerably exceeding the light wavelength, elastic scattering is observed. This type of scattering was investigated as early as 1908 for the case of spherical particles by G. Mie. *Mie scattering* has been discussed in detail in [4.8]. The probability (cross-section) for Mie scattering is a complicated function of wavelength λ , particle radius r , index of refraction and absorption

$$\sigma_{\text{Mie}} = f(x, m_{\text{rel}}), \quad (4.66)$$

where

$$x = \frac{2\pi r}{\lambda}, \quad m_{\text{rel}} = m_1/m_2, \quad (4.67)$$

where m_1 is the complex index of refraction ($m_1 = n - ik$) for the particles and m_2 is the corresponding quantity for the surrounding medium. For air, $m_2 \simeq 1$. σ_{Mie} oscillates rapidly as a function of the parameter x due to interference effects related to surface waves on the particles. For natural particle distributions in the atmosphere the oscillations are smeared out and the scattering intensity varies only slowly with the wavelength. The intensity increases towards shorter wavelengths with an approximate λ^{-2} dependence. In the atmosphere Mie scattering from particles is normally more important than Rayleigh scattering from molecules. The visibility is determined by Mie scattering. In the absence of particles in the atmosphere the visibility would be hundreds of kilometres. A relatively simple relation between the visibility and the effective Mie scattering cross-section exists.

Mie scattering can be used to monitor particles in ambient air and water (Sect. 10.2.3). It is also useful in the laboratory. Measurements in the direction of the probing beam are called *turbidimetry* while measurements in other directions are called *nephelometry*. (Greek *nephele* = cloud). Particle sizes and shape parameters can be determined from the angular and polarization distributions, at least under favourable conditions [4.48, 4.49].

4.6 Atmospheric Scattering Phenomena

The wavelength dependence of Mie and Rayleigh scattering is responsible for the blue of the clear sky and the red of the setting sun. The sun emits essentially “white” light. Blue light is scattered more effectively than red and so red light is transmitted better when the angle at which the sun shines is small (long path length through particle-rich layers). These well-known atmospheric scattering phenomena are illustrated in Fig. 4.21.

Another well-known atmospheric feature is the *rainbow*. This phenomenon can be explained in detail using Mie-scattering theory. However, the general principles of the rainbow can be described considerably more simply. As early as the 17th century R. Descartes explained the most important points of the rainbow phenomenon. The normal, most intense rainbow (the *primary* rainbow) is formed by the rays of the sun being reflected once in the interior of drops of moisture, as illustrated in Fig. 4.22. The colours occur (starting at the outside) in the order red, orange, yellow, green, blue, indigo and violet. Often, a weaker, *secondary* rainbow can be observed outside the primary rainbow. This is formed by light which has been reflected twice in the interior of the droplets, and the colours occur in the reverse order. The angle of deflection for a ray impinging on a drop depends on the index of refraction and the parameter of incidence b , which is the vertical distance between the incoming

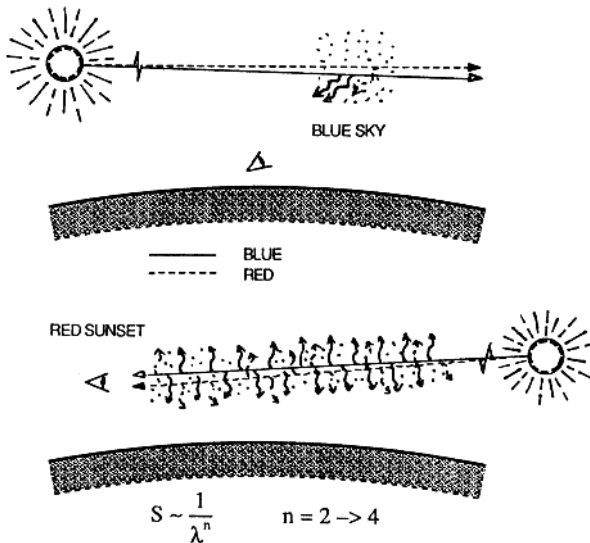


Fig. 4.21. The occurrence of blue sky and red sunset

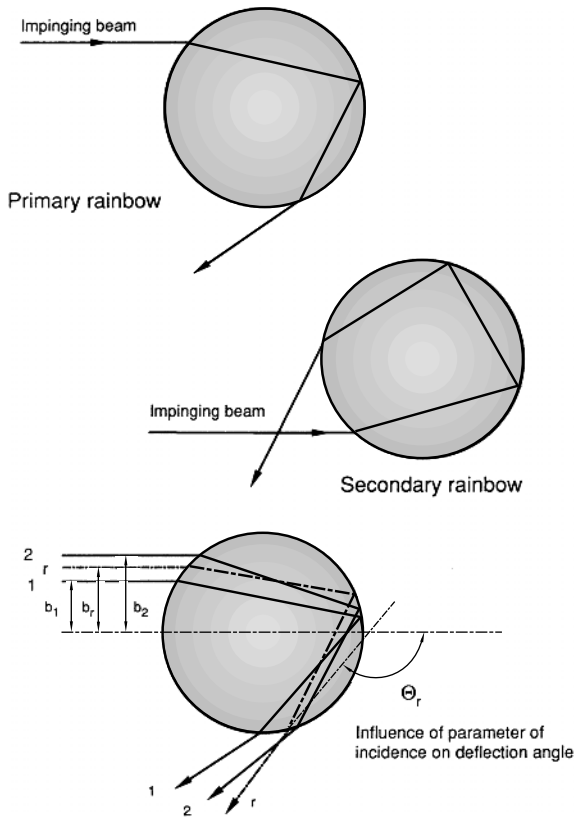


Fig. 4.22. Reflection and refraction in raindrops

ray and an axis drawn through the centre of the drop parallel to the incoming beam (Fig. 4.22). Parallel light rays impinging on a drop are scattered in many directions because all parameters of incidence are represented and because of partial reflection from the drop surface. However, a strong concentration of intensity in a particular direction is obtained. Rays with zero parameter of incidence are reflected, retracing their path and giving a deflection angle of 180° . For increasing values of b , the angle of deflection θ decreases to a certain value, $\theta = \theta_r$, from which it slowly increases again for increasing values of b , as illustrated in Fig. 4.23. Around θ_r the variation of θ with b is slow and all rays with a parameter of incidence close to b_r leave in a narrow angular range, resulting in a high intensity. For water droplets θ_r (the rainbow angle) is 138° for red light and 140° for blue light. The secondary rainbow, corresponding to two inner reflections, can be explained in the same way. A high light intensity is obtained around 130° .

In the range of angles between the two rainbows there will be no rays corresponding to one or two reflections. Therefore the sky brightness is reduced.

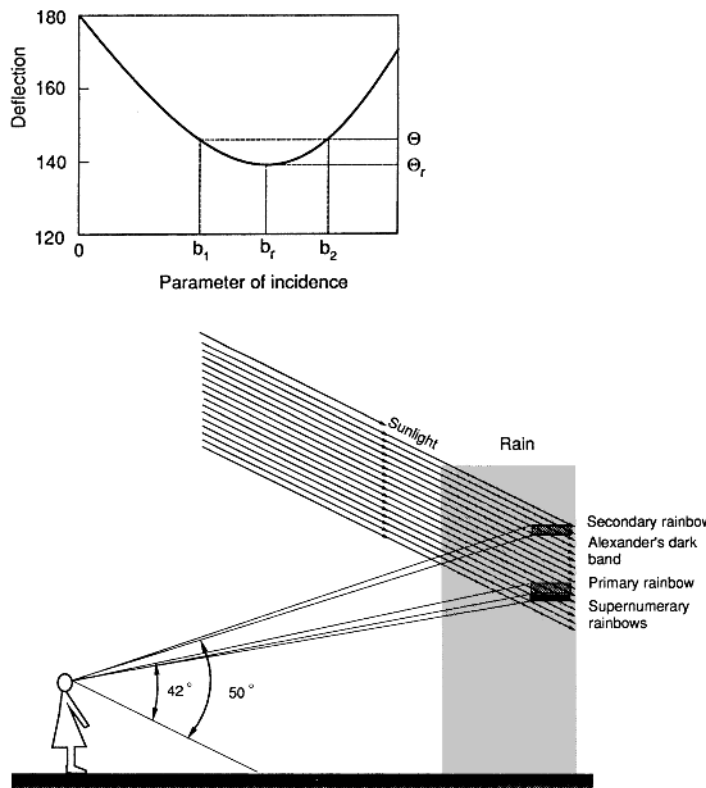


Fig. 4.23. Dependence of deflection angle on the parameter of incidence (above) and observation angles for the rainbow (below)

ced. This darker region is called *Alexander's dark band* (Greek philosopher, 200 B.C.).

On the inner bright side of the primary rainbow (close to the violet primary band) a number of extra bands often occur, alternating in colour between green and pale red. These extra bands are caused by interference between rays with b values slightly higher and slightly lower than b_r being deflected in the same direction (cf. Young's double-slit experiment). Since the interference effect is due to differences in the path length through the drop the appearance of extra bands depends on the drop size. Frequently the bands are most visible below the top of the primary rainbow. The raindrops are smallest at high altitude and increase in size as they fall. The interference effect is smeared out for large drops.

The scattered light in rainbows is almost fully polarized since the angle of incidence for the internal reflection is close to the Brewster angle ($\tan \theta = n$).

The angle of observation for a rainbow is shown in Fig. 4.23. A rainbow is circular due to the spherical symmetry of the drops. From an aeroplane, in principle, a complete rainbow can be seen centred around the shadow of the aeroplane. Common atmospheric scattering phenomena such as the rainbow have been discussed in [4.50]. Other phenomena such as atmospheric haloes, mirages, the "green flash" etc. have been treated in [4.51].

4.7 Comparison Between Different Radiation and Scattering Processes

In Table 4.1 the cross-sections for different radiation and scattering processes are compared. Of course, the strength varies considerably for a particular process, but the numbers give an indication of the relative strengths. Resonance absorption and the associated fluorescence process (electric dipole radiation) are the strongest processes. Strong fluorescence only occurs at low pressures at which collisional processes can be neglected. At atmospheric pressure the return to the lower state usually occurs through collisional processes (*quenching*), see (10.1). The fluorescence intensity can then be reduced by a factor

Table 4.1. Comparison between different radiation and scattering processes

| Process | Cross-section σ [cm ²] |
|-------------------------|-------------------------------------------|
| Resonance absorption | 10^{-16} |
| Fluorescence | 10^{-16} |
| Fluorescence (quenched) | 10^{-20} |
| Rayleigh scattering | 10^{-26} |
| Raman scattering | 10^{-29} |
| Mie scattering | 10^{-26} – 10^{-8} |

of 10^3 – 10^5 . Rayleigh scattering is generally 10^{10} times weaker than resonance absorption. Raman scattering is a further factor of 10^3 weaker. The strength of Mie scattering varies strongly with the particle size.

4.8 Collision-Induced Processes

In this chapter, we have dealt with radiative transfer of atoms and molecules between different energy states rather extensively. However, transitions can also be induced by collisions. Extensive information on the static and dynamic properties of atoms and molecules can be obtained from collision physics. Although this book is centred on the spectroscopy of atoms and molecules, the importance of collisional physics should be clearly pointed out. For studies of these aspects the reader is referred to [4.52–4.58].

5. Spectroscopy of Inner Electrons

In this chapter we will discuss spectroscopic methods that involve inner electrons [5.1, 5.2]. Such electrons are much more strongly bound than outer electrons and the interaction energies become correspondingly high. Two kinds of methods are used to study inner electrons, those that are based on absorbed or emitted X-ray radiation (*X-ray spectroscopy*) and those dealing with energy measurements on emitted photoelectrons (*photoelectron spectroscopy* (XPS or ESCA)).

5.1 X-Ray Spectroscopy

When a solid is bombarded by electrons at an energy of few keV or more, X-rays are emitted. The radiation consists of a continuous part (*Bremsstrahlung*) and a discrete (*characteristic*) part. The Bremsstrahlung is generated by the charged electrons that undergo deceleration and a change in direction of motion when interacting with the atoms of the sample. The maximum energy of the X-ray quanta corresponds to a full utilization of the kinetic energy of the incoming electrons. The discrete radiation is a line spectrum that is characteristic for the material and, as for optical radiation, it is caused by spontaneous transitions between atomic states. As a result of electron bombardment an electron can be knocked out of an inner shell of the atom. The atom is then in a state of high excitation and a transition to a state of lower energy quickly occurs through an electron from an outer shell falling into the vacancy to fill the hole. Thus the electron hole is seen to move outwards towards outer shells. A series of emission lines, corresponding to the successive atomic energy losses, is obtained. The processes are illustrated in Fig. 5.1 in which energy levels corresponding to an electron vacancy in the K , L , M , N etc. shell (see also Table 2.2) are indicated, and emission lines corresponding to transitions between such states are shown. The transitions are denoted $K\alpha$, $K\beta$, $K\gamma$ etc., corresponding to the movement of the electron hole from the K shell to the L , M etc. shell. Correspondingly, $L\alpha$, $L\beta$ etc. lines are emitted when an L-shell vacancy is filled. If fine structure is also considered, energy levels are given a further index L_I , L_{II} , L_{III} etc. and emission lines a further specification $K\alpha_1$, $K\alpha_2$ etc. as already indicated in Fig. 4.8, in which the more commonly used convention of negative level energies was

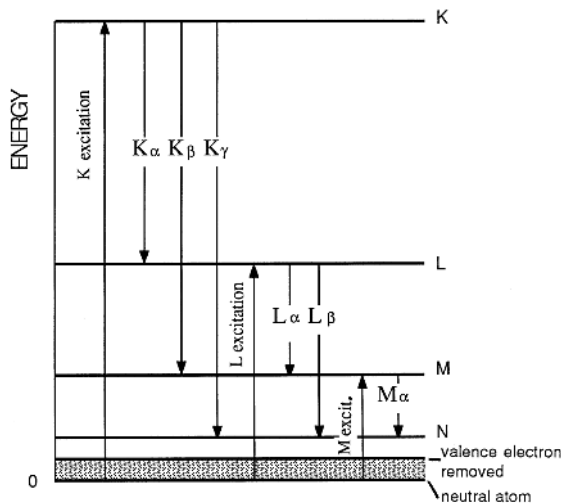


Fig. 5.1. Inner electron energy levels and corresponding X-ray transitions

used. As an example, an X-ray emission spectrum from molybdenum excited by 35 keV electrons is shown in Fig. 5.2 with the continuum Bremsstrahlung and the most energetic characteristic lines.

X-rays were discovered by K. Röntgen in 1895 [5.3], and were shown to be electromagnetic radiation with a wavelength comparable to the distance

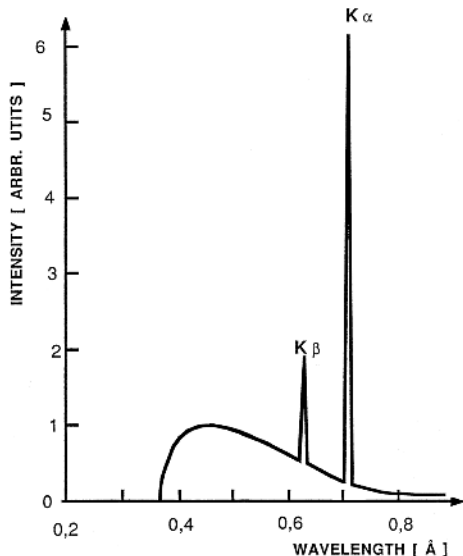


Fig. 5.2. X-ray emission spectrum from molybdenum, obtained for an acceleration voltage of 35 kV. The continuum radiation (Bremsstrahlung) as well as characteristic lines are shown

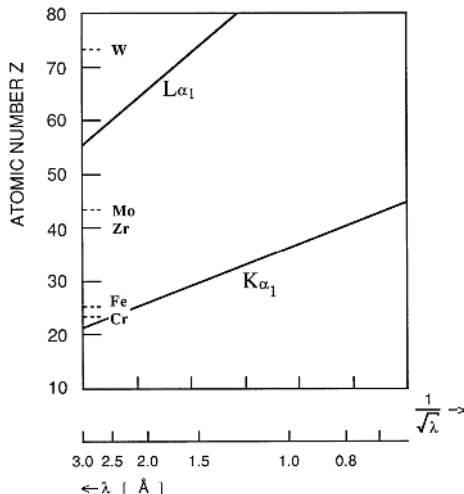


Fig. 5.3. Diagram illustrating Moseley's law

between crystal planes (~ 0.1 nm) in investigations by K. von Laue and W.H. and W.L. Bragg, father and son (1913). More detailed studies of X-ray spectra were performed by H. Moseley and high-precision techniques were introduced by M. Siegbahn. The wavelengths of a large number of emission lines have now been very accurately determined. The atomic X-ray investigations have resulted in a very thorough charting of the energy levels of inner electrons.

The energy levels in the inner electron shells are comparatively little affected by the chemical environment of the atoms. Thus, a spectral analysis of the characteristic X-ray emission is well suited for elemental analysis. The relation between the wavelength λ of a particular X-ray line and the nuclear charge Z of the corresponding atom is given by *Moseley's law*

$$1/\sqrt{\lambda} = C(Z - \sigma). \quad (5.1)$$

Here C and σ are constants characterizing a particular spectral series. Moseley's law can be derived from the simple Bohr atomic model (Sect. 2.1) taking shielding into account. A Moseley diagram for $K\alpha$ and $L\alpha$ emission is shown in Fig. 5.3. Using such a diagram the identification of different elements in a sample is greatly facilitated.

5.1.1 X-Ray Emission Spectroscopy

X-ray emission can be induced in different ways. We have already mentioned the use of energetic electrons. Alternatively, heavier charged particles can be used. It is also possible to create an inner shell vacancy by irradiating the sample with X-ray radiation. We are then dealing with an inner shell photoelectric effect. The characteristic radiation following X-ray absorption is referred to as *X-ray fluorescence* following the terminology in the optical

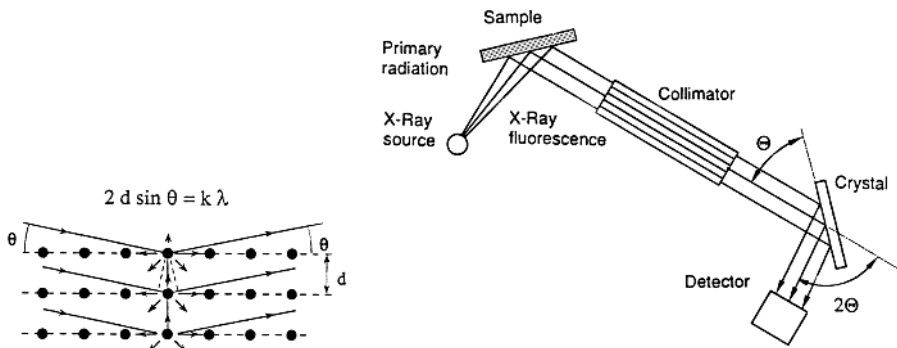


Fig. 5.4. Illustration of Bragg diffraction (left) and a wavelength-dispersive X-ray fluorescence spectrometer (right)

spectral region. The energy (wavelength) of the X-ray quanta can be determined in two basically different ways. Measurement systems are referred to as being *wavelength-dispersive* or *energy-dispersive*. In the former type of instrument an X-ray spectrometer using a crystal for the wavelength analysis is used. In Fig. 5.4 a diagram of a wavelength-dispersive X-ray fluorescence system is shown. An X-ray tube with an anode (also called “anti-cathode”) of tungsten or sometimes chromium, gold or rhodium, is used for exciting X-ray fluorescence in the sample. With the aid of a collimator, parallel beams from the sample are directed towards the flat crystal at an angle of incidence θ . The analysing crystal has been cut to have its crystal planes, separated by d , parallel to the crystal surface. The detector of the spectrometer is placed behind a collimator to receive radiation that has been deflected by 2θ from the original direction. When using the spectrometer the crystal is turned by a motor at a constant angular velocity at the same time as the detector arm is moved at twice the angular velocity. Radiation quanta can pass into the detector when the *Bragg relation* is fulfilled (Fig. 5.4)

$$2d \sin \theta = k\lambda. \quad (5.2)$$

NaCl ($d = 0.56$ nm) or LiF ($d = 0.4$ nm) are frequently used as crystals. The X-rays bundles are collimated using systems of thin metal plates (thickness: 50 μm) arranged parallel to each other at small separations (0.5 mm). In this way the divergence can be limited to one degree or less.

An example of an X-ray fluorescence spectrum of an alloy sample is shown in Fig. 5.5.

A curved crystal can be used: this will cause radiation diverging from an entrance slit to be focused towards an exit slit with a strong intensity advantage. Curved crystals of alkali halides or mica can be used. X-ray spectrometers, where the diffracting crystals operate in transmission (*Laue*) geometry instead of in reflectance (*Bragg*) geometry, can also be constructed. Different spectrometers for the X-ray region are discussed in [5.5]. An example

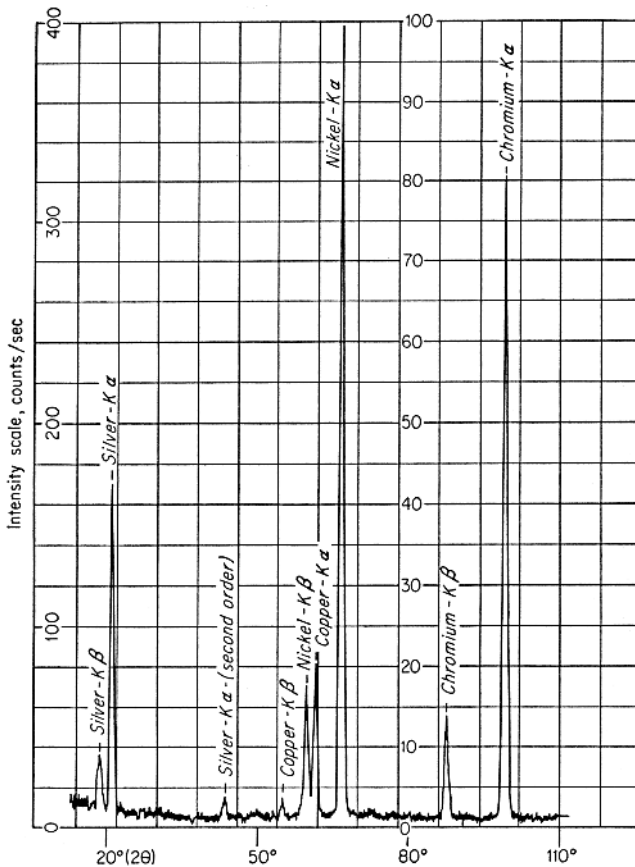


Fig. 5.5. X-ray fluorescence spectrum of chromium-nickel plating on a silver-copper base. The recording was taken with a wavelength-dispersive spectrometer [5.4]

of a recording of the Ta K α, β lines, recorded with a Laue spectrometer, is shown in Fig. 5.6 [5.6]. The X-rays were generated by focusing a high-power laser beam onto a rotating tantalum disc (see also Sect. 9.6.4). Because of the widespread use of synchrotron radiation (Sect. 6.1.3) at short wavelengths, an advanced technology for X-ray monochromators (selecting a narrow band out of a continuum) has been developed [5.7].

A Geiger counter, a proportional counter or a scintillation counter can be used for X-ray detection. The two former types are gas-filled. The incoming X-rays cause the formation of ions which are then detected. Such detectors are mostly used for long-wavelength radiation ($\lambda > 0.2$ nm). For X-rays of shorter wavelengths scintillation counters are used, in which X-ray-induced light flashes in sodium iodide crystals are detected by a photomultiplier tube (Sect. 6.3). Imaging X-ray detectors are also available as discussed below in

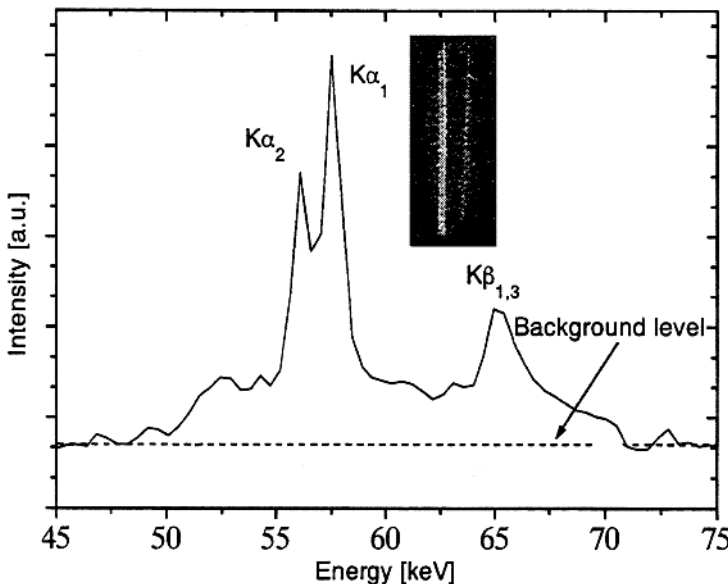


Fig. 5.6. Recording of the K α, β lines from tantalum [5.6]

connection with X-ray imaging. Such detectors are of course very useful for efficient simultaneous spectroscopic recording of a specific X-ray region.

Fluorescence spectrometers are widely used in the metal industry. Frequently, parallel spectrometers are employed. Such an instrument actually consists of a number of crystal spectrometers, each set for a particular emission line. The spectrometers are arranged around the sample, which is irradiated by an X-ray tube. One of the spectrometers is set for a standard sample that is contained in the sample holder. In this way the intensity of the X-ray tube can be monitored. Frequently, a measurement is terminated when a preset number of counts for the reference sample has been obtained. The corresponding number of counts from the other detectors can then be directly used for a parallel assessment of the elemental composition of the sample. With a sequential spectrometer, a number of selected elements are measured sequentially by turning the crystal and the detector to preset positions. With computer steering the measurement process is automatic. This type of instrument is well suited for varying types of analysis, whereas parallel spectrometers are more suited to continuous control operation of, for example, a steel mill in near-real time.

As was mentioned above, X-ray analysis can also be performed using an *energy-dispersive* system. In this case no analysing crystal is needed. Instead the radiation falls directly on an energy-dispersive detector. Normally a lithium-doped silicon detector (Si(Li)) is used, which yields voltage pulses that are proportional to the energy of the X-ray quanta. The pulses are sorted

according to their amplitude (energy) in a multi-channel analyser using an Analogue-to-Digital Converter (ADC). Gradually the full spectrum emerges on the system display. The linewidth obtained with a Si(Li) detector is about 150 eV. Partly overlapping lines can be deconvoluted using computer analysis. It should be noted that an energy-dispersive system of this kind automatically permits multi-element analysis.

It might be expected that the intensity of a spectral line from a sample would be directly proportional to the amount of the corresponding element in the sample. In practice the intensity can deviate considerably from the expected linear relation due to absorption in the matrix material and multiple scattering processes. However, it is possible to correct for such effects and very reliable quantitative analyses can be performed. X-ray fluorescence measurements on alloys have an elemental sensitivity of about 10 ppm (ppm: parts per million, 1:10⁶). The typical penetration depth of the radiation in the metal is about 1 μm and thus, primarily, the surface is analysed. X-ray emission techniques have been discussed in [5.8–5.10].

As we have already mentioned, characteristic X-rays can also be induced using accelerated heavy particles such as protons. This technique is called PIXE (*Particle-Induced X-ray Emission*) [5.11–5.13]. The cross-section for the creation of an inner shell vacancy is very high using protons at an energy of a few MeV, and therefore a sensitivity much better than that typical for X-ray fluorescence is obtained. Most elements except the very light ones ($Z < 14$) can be detected in concentrations below 1 ppb (parts per billion:

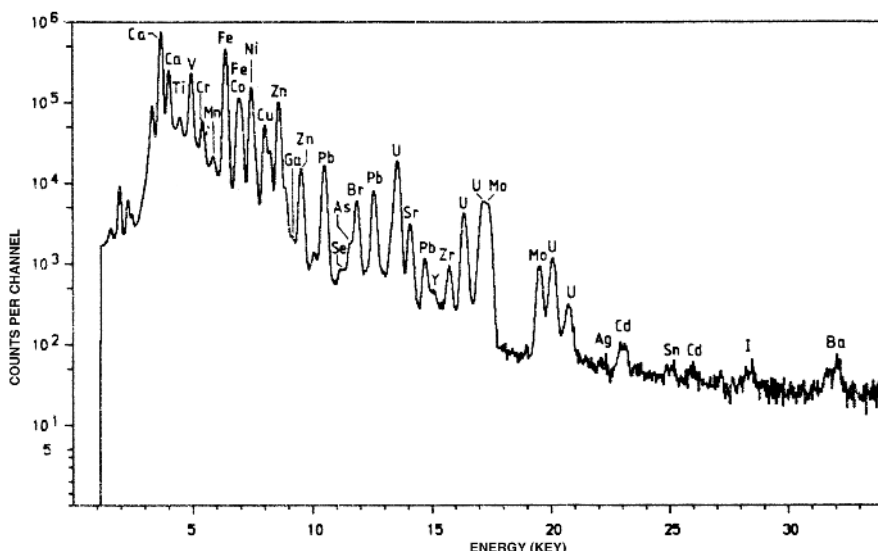


Fig. 5.7. PIXE spectrum of Arctic sea water. An energy-dispersive detector system was utilized [5.11]

$1:10^9$). With a specially focused proton beam (microbeam) quantities of an element as low as 10^{-18} g can be detected. The comparatively large number of small accelerators that are presently less suitable for nuclear physics work are generally very useful for PIXE. As an example of a PIXE spectrum, illustrating the use of an energy-dispersive Si(Li) detector, a spectrum of sea water is shown in Fig. 5.7. Some of the lines are identified.

By using a highly focused proton beam which is scanned over a sample, it is possible to produce elemental imaging of a microscopic specimen, in which the spatial intensities of individual X-ray emission lines are displayed. Clearly, there are many applications of this micro-probe technique to medical, toxicological, environmental, semiconductor and forensic science monitoring. An example of an elemental PIXE image is shown in Fig. 5.8, showing the distribution of different elements in a human hair.

X-ray analysis using different excitation and detection techniques has wide applications in fields ranging from biology and medicine to archaeology and forensic science. One interesting area of application is the measurement of heavy metals in particulate air pollution [5.15]. Airborne particles can be collected in different size fractions using special devices called cascade im-

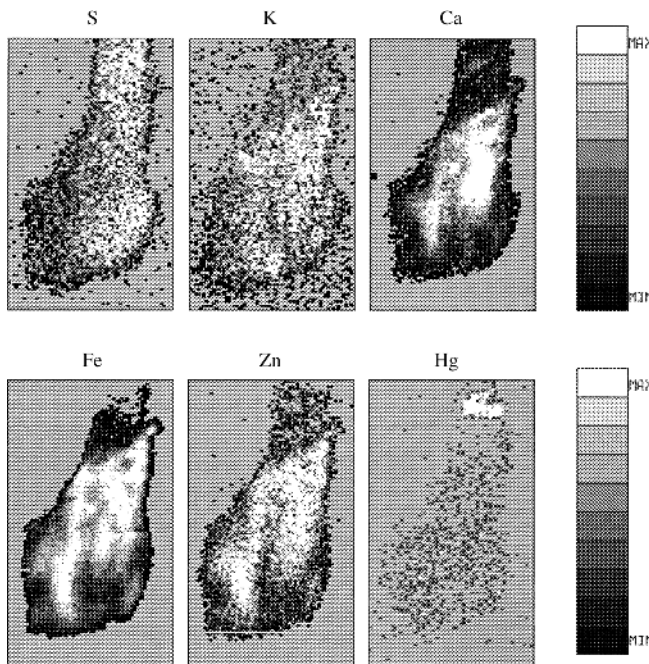


Fig. 5.8. Distributions of different elements in a human hair strand (with root) obtained with the PIXE microbeam technique. The beard hair belonged to the famous astronomer Tycho Brahe (1546-1601), and was retrieved at a tomb opening. Note the uptake of mercury shortly before the death of the bearer [5.14]

particulates. The particles deposited on the foils are then analysed. Small particles with diameters less than $2\text{ }\mu\text{m}$ are particularly important, since they follow inhaled air down into the alveoles of the lung. The human uptake of metals due to general air pollution or due to special working environments (e.g., inhalation of fumes by welders) can be investigated with samples of blood serum.

Our discussion of X-ray emission spectroscopy has so far mainly been focused on the analytical capabilities of systems with moderate resolution. Clearly, X-ray emission spectroscopy is also a field of active research, particularly in the soft X-ray region. Here dipole transitions between well-defined inner orbitals and more diffuse (perturbed) valence orbitals are studied, yielding valuable information on the latter orbitals. In the measurements it is clearly desirable to increase the resolution as much as possible. Wavelength-dispersive instruments are then mandatory. (Above 3 nm two orders of magnitude better resolution than in energy-dispersive systems is attainable). For soft and ultra-soft X-ray wavelengths special organic crystal materials with a large crystal plane separation, such as potassium hydrogen ftalate ($d = 2.7\text{ nm}$) and lead stearate ($d = 10\text{ nm}$), can be used. If the wavelength is not too short the best choice is frequently to use a concave grating at grazing angle of incidence (see also Sect. 6.2.2). Ion-etched holographic X-ray gratings can have an efficiency exceeding 10%. A photographic plate provides parallel detection of many lines. Recently, electronic multichannel techniques for X-ray spectra recording have been introduced (see also Fig. 6.38). If the entrance slit, the plate and a grating with a radius of curvature r are placed on a circle of radius $r/2$ (the *Rowland circle*), sharp spectral lines are obtained without using any collimators (Fig. 6.25).

As an example of a spectrum obtained with a 10 m instrument (grating radius 10 m) a recording of the carbon K emission line from the CO_2 molecule is shown in Fig. 5.9. As can be seen, the high resolution reveals a clear structure due to molecular vibration. Through careful analysis of a spectrum of this kind it is possible to evaluate the C–O bond length very accurately in the core-ionized molecule. It turns out that the bond length is shortened by about 2% when the $1s$ core vacancy has been formed in the carbon atom. From the linewidth it is also possible to evaluate the natural lifetime of the C $1s$ state (Sect. 9.4.4). The lifetime is of the order 10^{-14} s . Atomic structure research using X-ray emission spectroscopy has been discussed in [5.16–5.21].

5.1.2 X-Ray Absorption Spectroscopy

We have seen how measurements of X-ray emission lines have an important analytical potential and also yield fundamental information on the structure of atoms and molecules. An emission line yields information on the *difference* in binding energy between two electronic states. However, from a theoretical point of view the *absolute* binding energies are of even greater interest. In order to determine such energies *absorption* of X-rays, rather than emission,

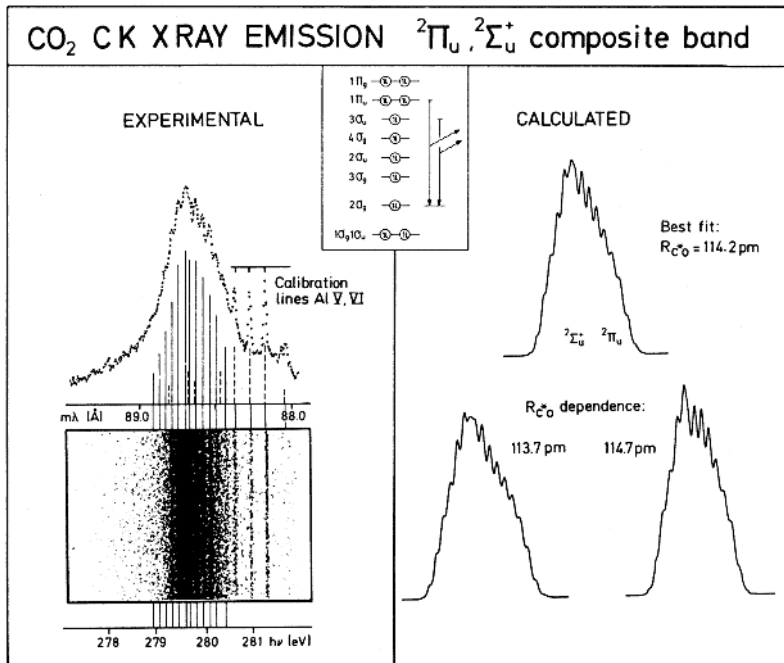


Fig. 5.9. The carbon K emission spectrum from the CO_2 molecule. To the left the photographic plate and a corresponding densitometer trace are shown. Calculated spectra are shown to the right, illustrating the sensitivity of the spectrum to the C–O bond length [5.16]

has to be studied. For such purposes an X-ray continuum is used and the sample absorption as a function of the wavelength is measured. If the energy of the X-ray photons is sufficiently high, an inner electron can be excited to an unoccupied state, either in the discrete or in the continuous part of the spectrum. In the latter case an electron has been released from the system (photoemission). The available empty discrete levels (the excited valence-electron states) are closely spaced in a region of a few eV and converge at the ionization limit. For increasing X-ray energies the absorption is strongly increased at the energy at which an additional, more strongly bound electron is released. An *absorption edge* is observed, from which the approximate binding energy is obtained.

For increasing photon energy the thresholds for photoemission from deeper and deeper shells are reached and additional contributions to the total absorption are obtained, resulting in a number of edges, as illustrated in Fig. 5.10. Apart from the edges there is a general fall-off in absorption due to a ν^{-3} dependence of the absorption coefficient. The absorption edges exhibit fine structure corresponding to the fine structure of the core states (Sect. 5.1). However, even the K edge exhibits a structure, as shown in Fig. 5.11, which

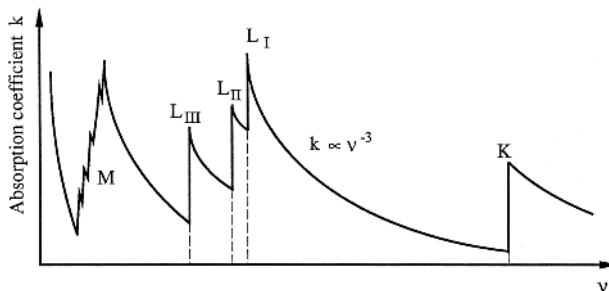


Fig. 5.10. X-ray absorption spectrum with absorption edges

is due to discrete levels close to the series limit. The position of the edges also depends slightly on the chemical composition of the studied material (chemical shifts, Sect. 5.2.2). The shifts are of the order of a few eV, and the difference in position of the edge for a solid and free atoms can be expected to be of the same order of magnitude. A measurement on a solid is in relation to the Fermi level and thus a correction for the work function must be applied in order to allow a comparison with measurements or calculations for free atoms. The different effects discussed above result in an uncertainty of at least 5 eV for atomic binding energies obtained from X-ray absorption data. However, since binding energies are frequently of the order of keV or larger, this uncertainty is frequently of less importance. X-ray absorption data are available for most elements in the solid state. During recent years high-resolution measurements of the edge structures have become possible using synchrotron radiation (Sect. 6.1.3). Such measurements are referred to as EXAFS (Extended X-ray Absorption Fine Structure) studies or NEXAFS (Near-Edge X-ray Absorption Fine Structure) – also termed XANES for

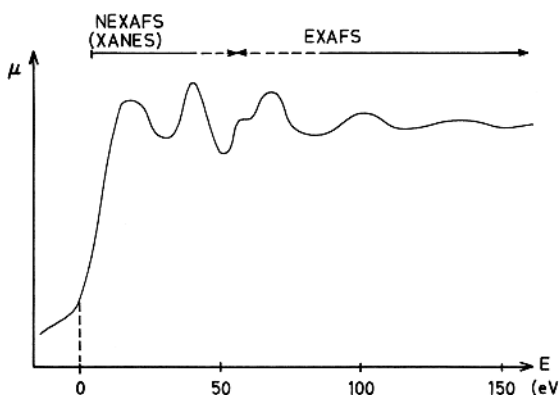


Fig. 5.11. Fine structure at a K absorption edge, observed at high resolution (EXAFS spectrum). [Adapted from a figure by C. Nordling]

X-ray Absorption, Near-Edge Structure – depending on how far from the edge one records and analyses the X-ray absorption spectrum. Information on distances to neighbouring atoms from the studied atoms is obtained from EXAFS spectra.

X-ray absorption and EXAFS spectroscopy has been discussed in [5.22–5.28].

5.1.3 X-Ray Imaging Applications

Medical Imaging. X-ray absorption is extensively used in medical diagnostic imaging. Different aspects of diagnostic radiology are covered in [5.29–5.31]. The energy of the exciting electrons in the X-ray tube (determining the high-energy cut-off; see Fig. 5.2) needed for different medical applications depends on the tissue thickness and is typically 20 keV for mammography and 60 keV for chest radiography. Soft X-ray radiation, which would otherwise be strongly absorbed in the superficial layers, is filtered away by means of an aluminium or copper filter. Bones appear as shadows since they contain heavier elements, primarily calcium, which absorb more strongly. Normal X-ray film is used for the recording, but, more recently image plates with much better sensitivity are employed (Sect. 6.3). The image information stored in metastable states of certain rare-earth salts is read out with a focused laser beam inducing optical fluorescence, and a digitized image is obtained, which allows efficient processing and storage. The quality of X-ray recordings are impaired by Compton-scattered X-ray photons, which give rise to a diffuse background on the plate.

In order to enhance certain structures in the body, contrast agents (biocompatible compounds of higher-*Z* materials) are used. Thus, barium sulphate is normally administered orally to enhance gastro-intestinal radiography. A further very important agent is iodine, which when injected as an organic compound into blood vessels can yield an enhanced contrast for radiography, e.g., of the coronary arteries providing the heart muscle with its blood supply. An example of medical recordings before and after the administration of iodine is shown in Fig. 5.12, where the vessels alone are shown by subtracting two images [5.32].

Blood vessels can be monitored even more efficiently and using lower doses of X-rays if narrow-band radiation, provided from a synchrotron (Sect. 6.1.3) is used. X-rays are applied just above the *K*-absorption edge of iodine (33.2 keV) and then immediately below the same edge, resulting in two images [5.33]. By subtracting or dividing the two images, which can be recorded in a swift sequence after the contrast agent has been supplied, the vessels appear very clear in this differential absorption scheme (See Fig. 5.13 [5.34]). The same philosophy of differential absorption is also used in imaging of air pollutants using laser radar techniques (Sect. 10.2.3). In both cases, division of the data curves/images has the advantage of providing dimensionless data, which is immune to distance, variations in illumination etc.

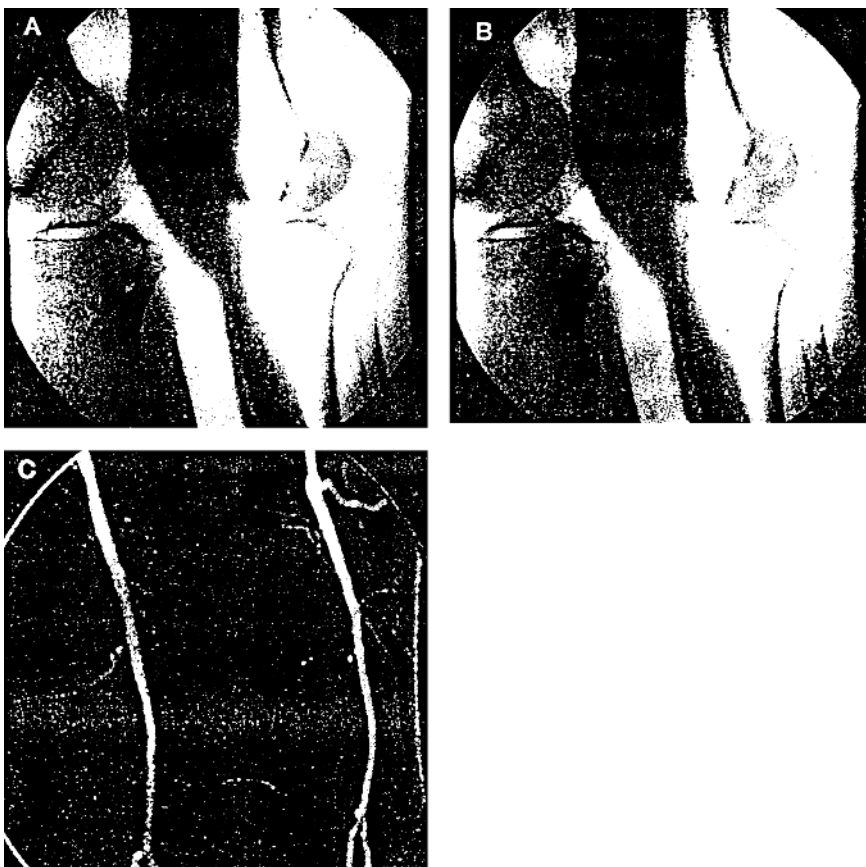


Fig. 5.12. Medical imaging with a contrast agent. A: before contrast injection; B: after contrast injection; C: subtracted images [5.32]

In X-ray transillumination recordings, only “line-of-sight” information is obtained. In order to obtain three-dimensional data it is possible to make the transilluminations in many different directions (projections) and then to use the mathematics of tomographic reconstruction [5.35, 5.36].

Very recently, high-power laser radiation focused to a very small spot on a high- Z material, such as tantalum, has been used to generate X-rays with energies reaching up to the MeV regime and with extremely short temporal duration [5.37–5.39]. (See also Sect. 9.6.4). Such radiation has also been employed for biological and medical imaging [5.39, 5.40]. New possibilities of magnification radiography [5.39], single-shot ultrafast (1 ps) imaging [5.40, 5.41], differential imaging [5.42] and rejection of Compton-scattered, image-blurring photons [5.43, 5.44] are now being explored.

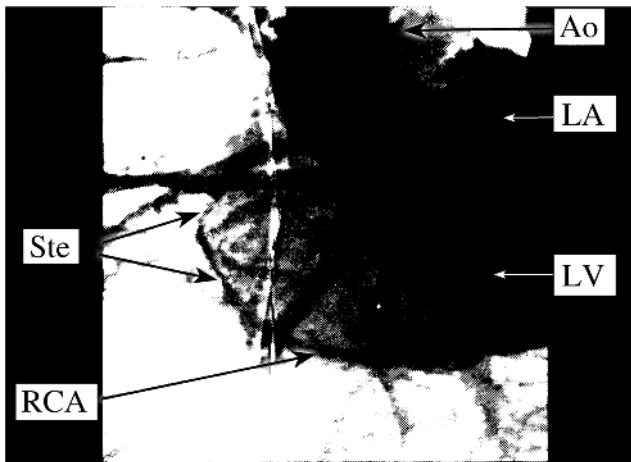


Fig. 5.13. Imaging (subtracted images) with differential absorption across the iodine K edge using synchrotron radiation. RCA denotes the right coronary artery, showing two stenoses (Ste). Ao is the aorta, with very strong differential absorption [5.34]

A large amount of data on the structure of complex organic molecules has been obtained in X-ray diffraction studies on crystalline samples [5.45]. Recently, X-ray pulses have been used for time-resolved diffraction studies, allowing dynamic processes to be investigated [5.46].

X-Ray Microscopy. The resolution of a microscope is limited by diffraction of the radiation used in the instrument. The resolution is proportional to the wavelength, and thus it is attractive to go to the X-ray region for obtaining high resolution [5.47]. A particularly interesting region for X-ray microscopy is the so-called water window ($2.4 \text{ nm} < \lambda < 4.4 \text{ nm}$), corresponding to the wavelength region between the K absorption edges of oxygen and carbon (Fig. 5.14). By choosing the soft X-ray wavelength in this window a natural contrast between water and proteins (containing carbon) is obtained, allowing efficient microscopy of living cells/tissue, and the need for differential imaging using two wavelengths is reduced (see above). As a radiation source for X-ray microscopy, high-intensity pulsed-laser irradiation of liquid micro-droplets seems to be particularly promising [5.48], yielding sharp K -line emission, which can be focused by a microzone plate (Fig. 5.14). X-ray microscopy has the advantage over electron microscopy [5.49] in that, while yielding a lower resolution, fresh, living sample cells can be used in contrast to the need for drying and metal-film coating the cells.

X-Ray Lithography. Lithography is used for patterning, e.g. in the micro-electronics industry [5.50]. X-ray lithography offers the potential advantage over ultraviolet lithography by providing higher resolution, again for reasons of reduced diffraction. In *proximity X-ray lithography* a mask is placed just

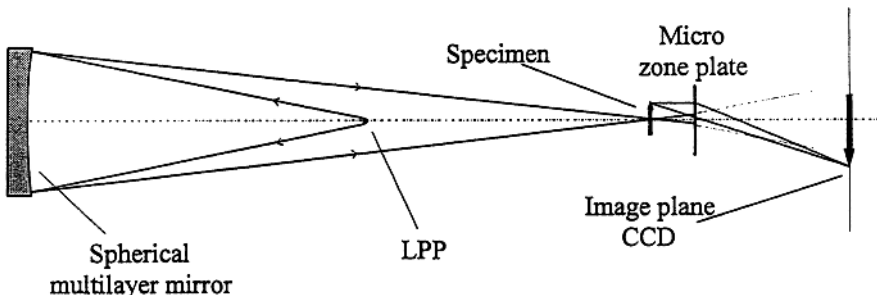
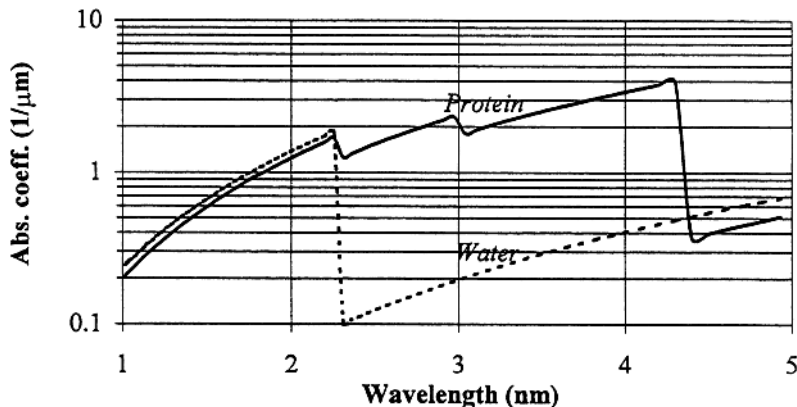


Fig. 5.14. The water window for soft X-ray microscopy, and a set-up for X-ray microscopy. LPP: laser-produced plasma [5.48]

above the substrate (resist), generally consisting of *poly-methyl-meth-acrylate* (PMMA). In *projection X-ray lithography* an X-ray reflecting optical system is used instead. Reasonable reflectivities in the soft X-ray region for perpendicularly incident rays can be achieved using Mo/Si multilayers. Short-wavelength lithography could have important applications for high-density electronics and nano-fabrication [5.51].

5.2 Photoelectron Spectroscopy

In the previous section we described how X-ray absorption measurements can be used to obtain information on energy levels in atoms. In the absorption process an electron can be released and an alternative way of obtaining energy-level information is therefore to study the energies of the emitted electrons (photoelectrons). This technique was applied as early as the beginning of the 20th century, but the instruments used had such a low resolution that little information was obtained. At the same time the optical and X-ray

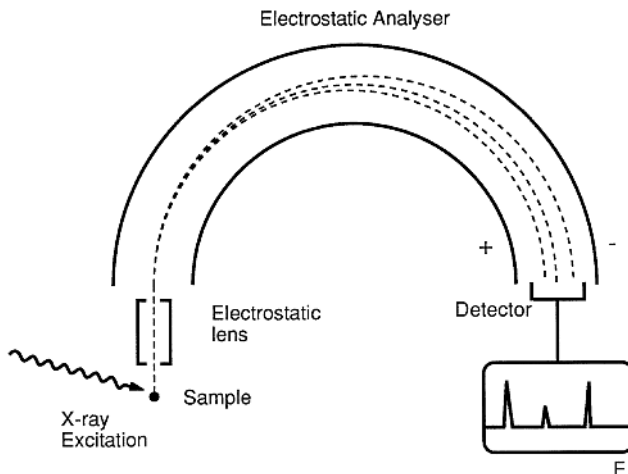


Fig. 5.15. The principles of XPS. The photoelectrons emitted from the sample are analysed for energy in an electrostatic spectrometer

methods of spectroscopy were developed to higher and higher precision and there was little interest in electron spectroscopy for a long time.

While atomic physics developed significantly during the beginning of the 20th century, interest was gradually diverted to nuclear physics. In this field of research new techniques were introduced to allow high precision and some of the techniques developed turned out to be very well suited to atomic physics experiments. This was the case for precision beta-particle spectroscopy that was developed by K. Siegbahn and co-workers. Their doubly focusing iron-free spectrometer with two coaxial coils was found to be very well suited to the analysis of X-ray excited photoelectron spectra and the first results were reported in 1957. This was the starting point for a new type of spectroscopy called XPS (*X-ray Photoemission Spectroscopy*) or ESCA (*Electron Spectroscopy for Chemical Analysis*). This field of research has since developed very rapidly.

The principle of XPS is very simple, as illustrated in Fig. 5.15. Using a characteristic X-ray line from an X-ray tube an electron is ejected from an inner shell in a sample atom, and its kinetic energy E_{kin} is then the difference between the photon energy $h\nu$ and the binding energy E_B of the electron:

$$E_{\text{kin}} = h\nu - E_B. \quad (5.3)$$

(The recoil energy of the atom can normally be disregarded.) The binding energy of the electron is defined as the energy difference between the final and initial states

$$E_B = E_{\text{ion}} - E_{\text{atom}}. \quad (5.4)$$

By analysing the emitted electrons it is possible to determine the binding energies of electrons in different shells. This has been done for most

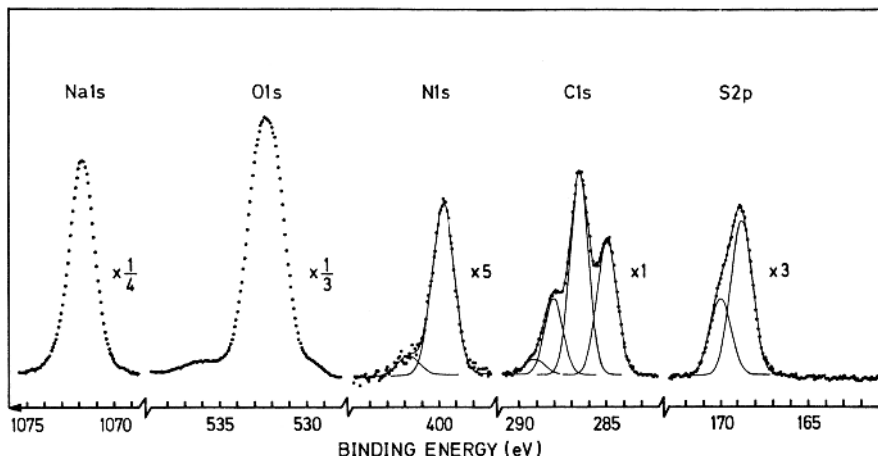


Fig. 5.16. XPS spectrum of a complex organic molecule (heparin) [5.52]

elements and the results are in general more reliable than those obtained by X-ray absorption. In Fig. 5.16 the different peaks obtained in measurements on a complex organic molecule are shown. From the recording the binding energies of 1s and 2p electrons in several light atoms can be deduced. Initially, electron spectroscopy measurements were only made on solids, and uncertainties similar to those discussed in connection with the X-ray absorption technique occurred. Over the last 20 years it has become possible to perform measurements on free atoms and molecules with a corresponding increase in accuracy in binding energy determinations. This is important for comparisons with theoretical calculations, which can presently be performed very accurately.

Electron spectroscopy has been discussed in detail in [5.53–5.61].

5.2.1 XPS Techniques and Results

Presently, electrostatic energy analysers have fully replaced magnetic ones, since the former have many practical advantages. An electrostatic analyser consists essentially of two concentric cylindrical capacitor electrodes that produce a well-defined radial electric field.

The resolution of an instrument will be limited by the monochromaticity of the exciting X-ray radiation. Frequently, the K emission from aluminium at 1486 eV is used. The natural radiation width of the line is about 1 eV and the line is broadened by unresolved fine structure (the overlapping $K\alpha_1$ and $K\alpha_2$ components). *X-ray monochromatization* by filtering out a narrow spectral region can be accomplished by placing the X-ray anode, a spherical single crystal analyser and the sample on a *Rowland circle* (Fig. 6.25). For a certain angle between the three objects the Bragg relation will be fulfilled only for

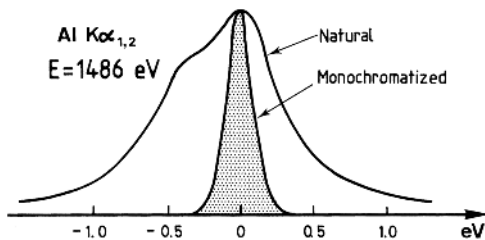


Fig. 5.17. Line profile of the $K\alpha$ line of Al, with and without monochromatization [5.58]

a specific wavelength. Since both the anode and the sample have a finite size the monochromatization has limitations. A typical effect of monochromatization is shown in Fig. 5.17. Although a linewidth below the natural one has been achieved this does not violate the Heisenberg uncertainty relation, since it is still not possible to measure the $K\alpha$ photon energy of Al with a higher precision than before.

For solid samples it is possible to increase the resolution further by compensating for the finite extension of anode and sample by constructing the spectrometer with a certain dispersion. This is illustrated in Fig. 5.18. If the anode has a certain size, the Bragg relation will be fulfilled at slightly different wavelengths for different parts of its surface. These different wavelengths will be focused at slightly different parts on the sample, resulting in

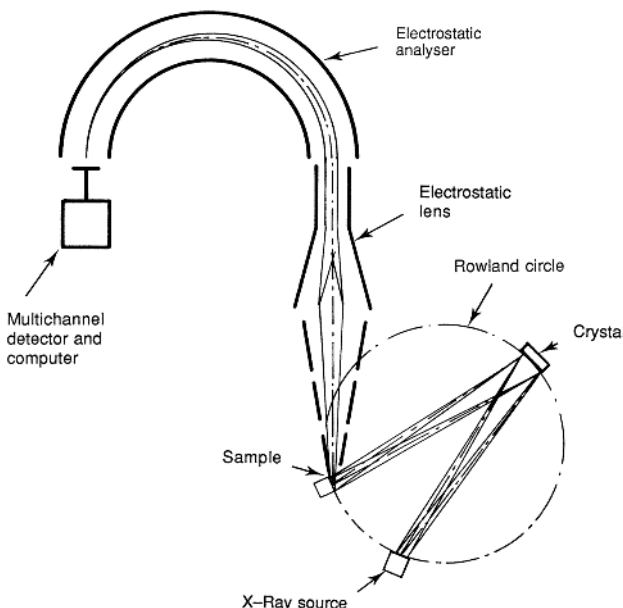


Fig. 5.18. An ESCA instrument with X-ray monochromatization and dispersion compensation

slightly different emitted electron energies from different parts of the sample. By making modifications in the design of the spectrometer, these electrons can be focused to the same point in the detector plane for a given setting of the spectrometer. Unfortunately, this technique does not work for gases which are of particular interest, since the surface of the sample is no longer restrained to the Rowland circle. Instead a *fine-focusing technique* has been developed in which the extension of the X-ray source has been strongly reduced by focusing the exciting electron beam onto a very small surface. In order to avoid overheating, the anode must then be rotated at high speed. The fine-focusing technique provides the most efficient monochromatization in work with gaseous, liquid and solid samples. Monochromatized radiation from synchrotrons is presently widely used in XPS studies (Fig. 6.13) [5.62]. Outer shells can be investigated using special short-wavelength lamps, e.g. strong He lamps emitting the $1s2p-1s^2$ resonance line at 58.4 nm (21.2 eV) [5.63].

In order to be able to measure many electron lines simultaneously a multichannel detector is frequently placed in the detector plane instead of using a detector behind an exit slit. The electrons then impinge on a micro channel plate (see also Fig. 6.38), in which electron multiplication occurs due to secondary emission by the inner wall material in the densely packed tubes in the plate. The original electron line image in the focal plane of the spectrometer is amplified and, by using two channel plates in series, an electron multiplication of 10^8 can be obtained. The electron showers are converted into optical signals on a phosphor screen which is viewed by a diode array or vidicon (TV camera) (Fig. 6.38).

As an example of an atomic photoelectron spectrum a recording for mercury is shown in Fig. 5.19, in which all populated levels in the N , O and P shells ($n = 4, 5$ and 6) can be observed. The common level designations from X-ray spectroscopy (Sect. 5.1; Fig. 4.8) have been used. Thus N_I corresponds to the $4s$ level, N_{II} and N_{III} are the $4p_{1/2}$ and $4p_{3/2}$ fine structure levels, N_{IV} and N_V are the $4d_{3/2}$ and $4d_{5/2}$ levels etc. It can be clearly seen how the spin-orbit interaction decreases with increasing principal quantum number, as for alkali atom valence-electron excited states (Table 2.1). An enlarged section of the spectral region to the left of the N_{VI} and N_{VII} lines (the $4f_{5/2}$ and $4f_{7/2}$ levels) is also included, revealing many weak components. Some of these are referred to as *shake-up lines*. At the same time as a photoelectron is ejected an outer electron can be excited, resulting in a lower photoelectron energy than otherwise, i.e. corresponding to a line for a higher binding energy. The presence of shake-up lines is a fundamental quantum-mechanical phenomenon. The wave function $|\psi_{N-1}^0\rangle$ for the system with a newly created inner shell vacancy can be expanded in the wave function system for the ordinary ion system that is obtained after the relaxation of the electronic shell. The intensity I_i of a shake-up line, corresponding to the state $|\psi_{N-1}^i\rangle$ of the ion is given by

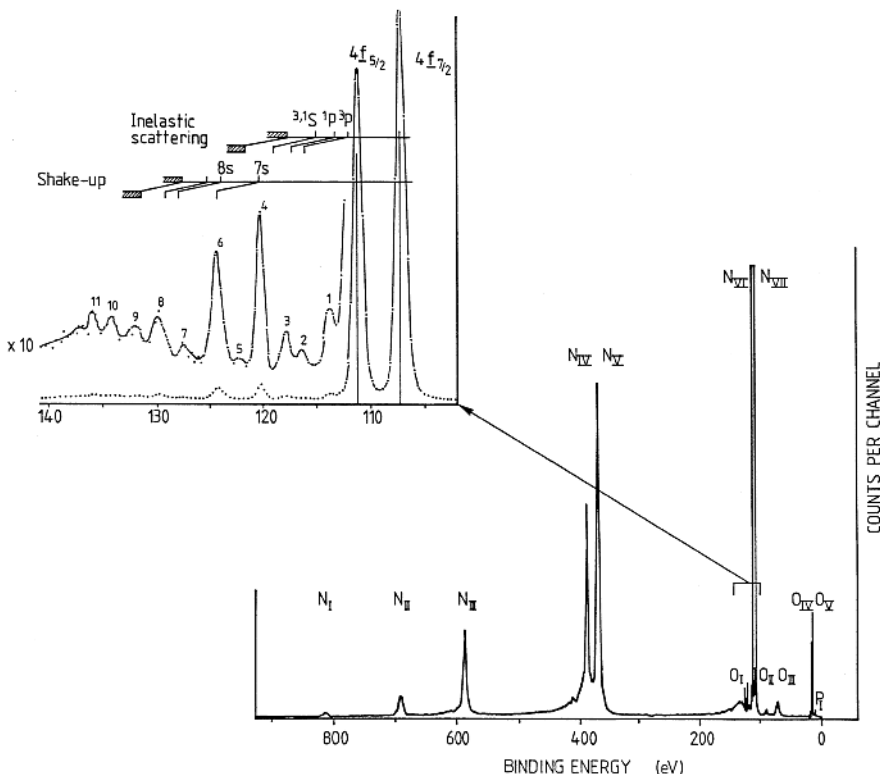


Fig. 5.19. ESCA spectrum of atomic mercury exhibiting shake-up lines [5.64]

$$I_i \propto |\langle \psi_{N-1}^0 | \psi_{N-1}^i \rangle|^2. \quad (5.5)$$

A sulphur *L*-shell XPS spectrum showing valence orbitals of the SF_6 molecule is shown in Fig. 5.20. An ultra-soft X-ray emission spectrum for the same molecule is also included. The figure illustrates how the different selection rules for X-ray emission and XPS lead to complementary information for the interpretation of the valence orbital structure of the molecule.

5.2.2 Chemical Shifts

In this section we will discuss an aspect of electron spectroscopy that is of great importance because of its applications: the presence of *chemical shifts* in the binding energies. Such shifts, which have already been mentioned in connection with X-ray absorption spectroscopy (Sect. 5.1.2), constitute a source of error in the determination of binding energies, but also provide rich information on the atomic chemical environment. It is found that when the binding energy of a particular inner orbital is studied in different chemical environments a variation (chemical shift) of typically a few eV is found. This

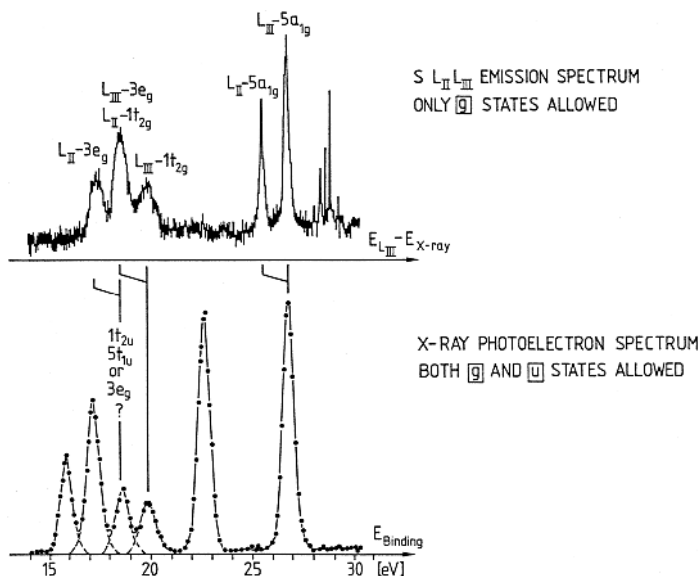


Fig. 5.20. Comparison between an X-ray emission spectrum and an XPS spectrum for SF₆, illustrating different selection rules [5.20]

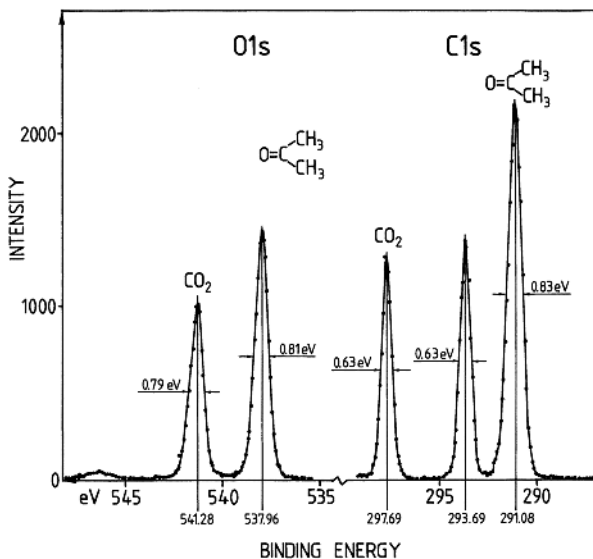


Fig. 5.21. Spectra of the acetone and the carbon dioxide molecules, illustrating chemical shifts [5.65]

is illustrated in Fig. 5.21 for the case of acetone. Whereas the $1s$ electron for oxygen only shows one distinct binding energy, the corresponding electronic state for carbon gives rise to a split line with a $1 : 2$ intensity relation between the two components. The double line reflects the different positions of the three carbon atoms in the acetone molecule; one related to a double bond to oxygen and two equivalent positions in CH_3 groups. For comparison, the corresponding lines in the CO_2 molecule are included in the figure showing still other shifts. Chemical shifts are evident in the already shown Fig. 5.16, where different positions of, for example, the carbon atom in the molecule are reflected in the spectrum. A particularly illustrative example is given for the case of the ethyltrifluoroacetate molecule in Fig. 5.22, featuring four equally strong carbon $1s$ lines corresponding to four different chemical environments. By comparing experimentally determined chemical shifts with theoretical calculations, valuable information on the molecular structure is obtained and at the same time the reliability of different theoretical models can be tested. The shift of the inner energy levels is not due to a deformation of the corresponding orbitals but rather to a change in the electrical potential in the inner part due to the change in the outer orbitals. Detailed calculations using molecular self-consistent-field approaches yield good agreement with experiments. In a simpler approach, the molecule is represented by ions with specific "effective" charges. Using atomic calculations the shift of inner levels can be obtained as a function of this charge. Comparisons with experimentally determined shifts give a description of the charge distribution in the molecule.

As we have pointed out, the presence of chemical shifts has resulted in important applications for electron spectroscopy. Since the positions of the lines depend on the chemical composition, the method can be used for qualitative as well as quantitative chemical analysis. One of the commonly

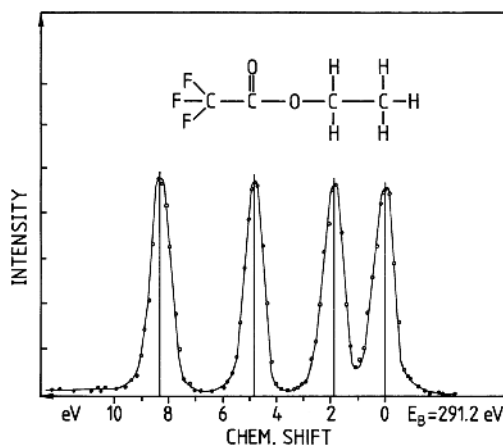


Fig. 5.22. $1s$ electron lines for carbon in ethyltrifluoroacetate [5.65]

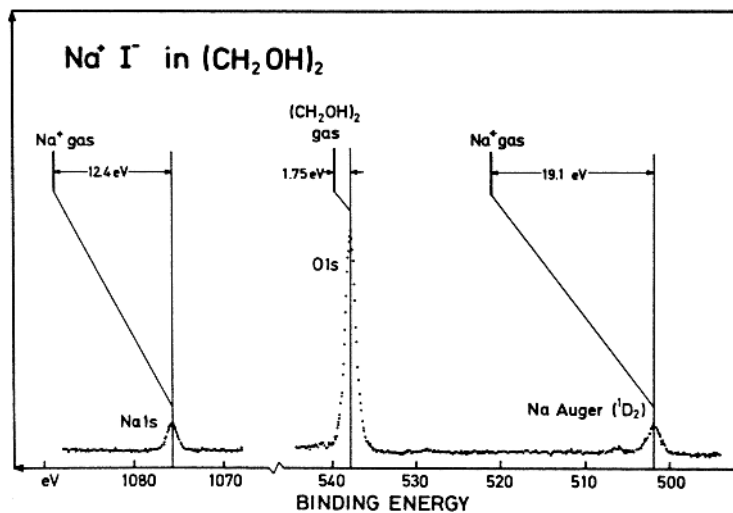


Fig. 5.23. Electron spectrum of a solution of $\text{Na}^+ \text{I}^-$ in glycole. Solvation shifts with respect to the gas phase line positions are observed [5.66]

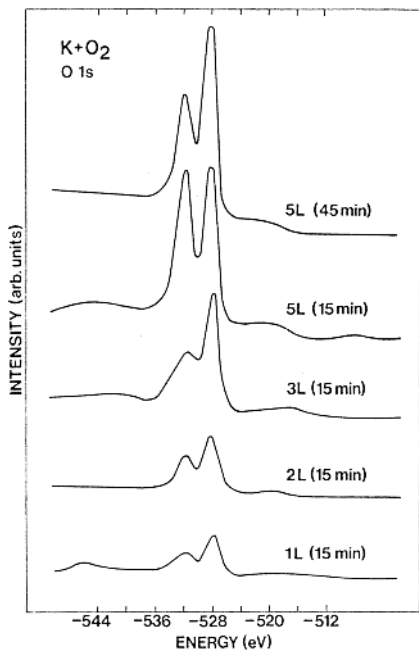


Fig. 5.24. ESCA surface sensitivity illustrated by progressing oxidation of a potassium surface. 1L corresponds to 10^{-6} torr · s of O_2 exposure [5.67]

used names for the XPS method, ESCA (*Electron Spectroscopy for Chemical Analysis*), focuses on this aspect.

One can also use the shift between free atomic or molecular species and the condensed phase to study cohesive properties. An example for a liquid phase system is shown in Fig. 5.23, viz. the photoelectron spectrum of a NaI solution. In this case the free-ion/dissolved-ion shift can be related to the energy of dissolution of the ion in the solution (solvation energy), providing information on the solution structure [5.66].

In the study of condensed phase samples it is the outermost layers which are probed in the photoelectron experiments (down to 1 nm below the surface). The *surface sensitivity* is illustrated in Fig. 5.24 for the case of slow oxidation of a potassium surface. Peaks due to potassium oxide and physisorbed O₂ occur. A further example of surface studies is shown in Fig. 5.25, which shows ESCA spectra for a clean gold foil and for a gold foil contaminated by a faint fingerprint from a finger that had previously been in contact with silicone oil. Surface monitoring has been discussed in [5.68, 5.69].

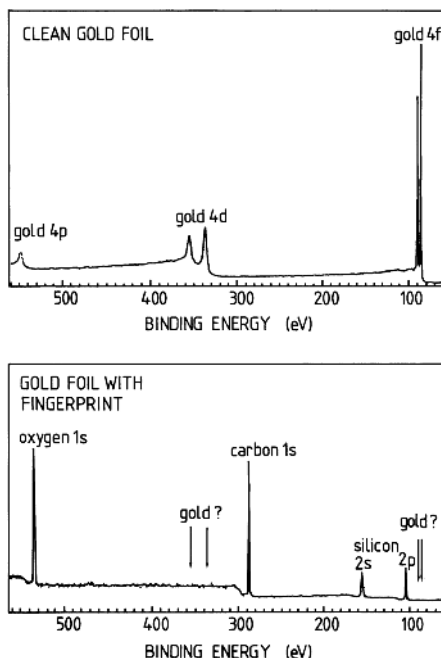


Fig. 5.25. ESCA surface sensitivity illustrated by spectra from a clean and a contaminated gold surface [5.59]

5.3 Auger Electron Spectroscopy

In normal photoelectron spectroscopy, as described above, the energy of the ejected electrons varies according to the energy of the exciting X-ray quanta; see (5.3). However, an emission of electrons with a kinetic energy that does not depend on the excitation energy is also observed. This process is called the *Auger effect* (P. Auger, 1925). The energy that would normally be emitted as, for example, a $K\alpha$ quantum is instead used to release an outer electron, which emerges with a kinetic energy E_{kin} determined by the $K\alpha$ energy $E_{K\alpha}$ and the binding energy of the outer electron E_B :

$$E_{\text{kin}} = E_{K\alpha} - E_B. \quad (5.6)$$

The process is illustrated in Fig. 5.26 for the case of a KLL Auger process, corresponding to the primary removal of a K electron, the infall of an L electron into the hole and the ejection of a further L electron. Clearly, the Auger electron energy must also depend on the coupling of the two holes in the final state. Corresponding Auger spectra from Mg and MgO are shown in Fig. 5.27. The influence of the hole coupling is shown as well as the chemical shift between the metal and the oxide. Additional peaks in the Mg spectrum are due to volume plasmons (a solid-state phenomenon).

Auger electrons can be emitted if the inner-shell vacancy is created by the absorption of an X-ray quantum or by electron bombardment. However, in the latter case an electron continuum due to the scattered electrons tends to mask the frequently weak Auger lines in the case of solid samples. Spectral derivation techniques can then be used to enhance the signals. For gases the background is weak and causes no problems.

The probability of Auger-electron emission dominates over the emission of characteristic X-rays for light elements, while the opposite conditions prevail for heavy elements.

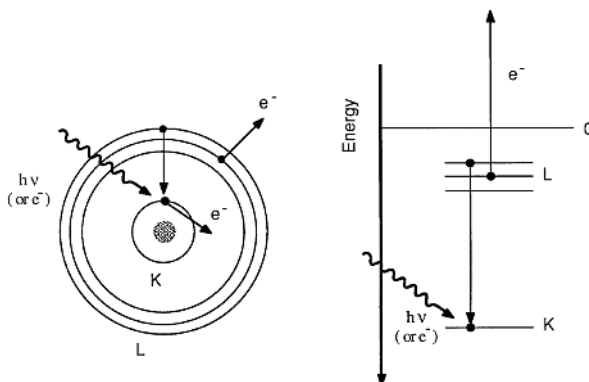


Fig. 5.26. Illustration of the Auger process (KLL Auger process)

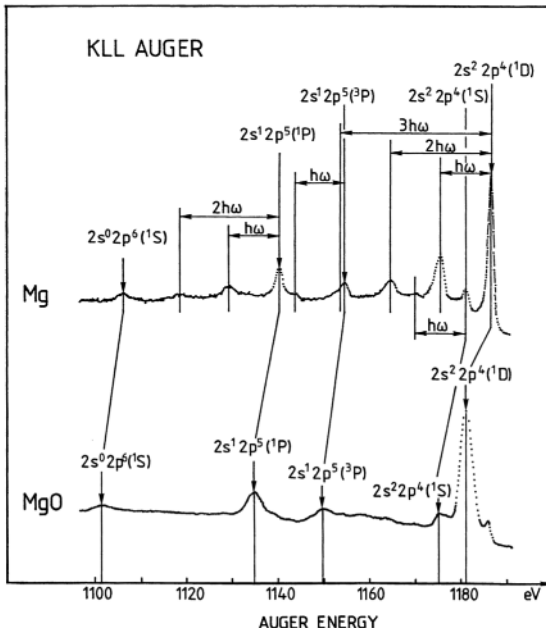


Fig. 5.27. Auger electron spectra for Mg and MgO (solids) illustrating the influence of chemical shifts and electron hole coupling. Additional peaks $n\hbar\omega$ are due to volume plasmons [5.69]

The Auger technique is comparatively simple and it has the same surface sensitivity as XPS. Because of this, Auger spectroscopy is frequently used as a diagnostic tool, e.g., for controlling the cleanliness of a surface in connection with surface physics investigations. A particularly valuable technique is scanning Auger spectroscopy, which can provide surface images with a resolution of 200 nm [5.70].

6. Optical Spectroscopy

The method of spectroscopy, using a suitable light source and spectral apparatus for radiation analysis, has its natural field of application in the determination of the general energy-level structure in the energy range corresponding to UV, visible and IR light. The energy-level scheme for atoms and ions of many different charge states has been established from spectral analysis in different wavelength regions, as discussed in Chap. 2. Many of the observed spectral lines are listed in standard monographs [6.1–6.5]. Hyperfine structure can also be studied in many cases using high-resolution instruments. The first observations of hyperfine structure in optical spectra were made at the end of the 19th century by A. Michelson (1891) and by Ch. Fabry and A. Pérot (1897). An interpretation of the structure was put forward at the end of the 1920s. The optical method for studies of hyperfine structure is particularly suitable when unpaired *s*-electrons are present (large hyperfine structure). A large number of nuclei have been studied with regard to nuclear spin and moments through the years. Many radioactive isotopes have also been studied using very small samples. Although the classical optical method has low accuracy, compared with resonance methods (Chap. 7) or laser techniques (Chap. 9), its field of application is wide. A very large number of excited levels can be studied through the structure in the large number of lines emitted by a light source. The structure in spectral lines, connecting a ground state or a well-populated metastable state with higher-lying, short-lived states, can also be studied in absorption experiments, in which the atomic absorption in a continuous spectral distribution is recorded. The techniques of classical optical spectroscopy have been covered in [6.6–6.8].

6.1 Light Sources

Many different types of light sources (lamps) have been developed for atomic spectroscopy investigations. If the radiation from the source is to be analysed directly, the lamp should, of course, contain the atomic species for which the emission spectrum is to be studied. Such light sources are designated *line light sources*. If the light source is to be used for excitation of atoms that are to be studied with some spectroscopic method, any light source yielding a sufficient intensity at the excitation wavelength can be used: accidental

coincidences between lines from different elements can, for example, be used. Close-lying lines can cause confusion in spectral analysis and have therefore been listed [6.9]. However, such perfect coincidences are rare, considering that the lines normally have to overlap within 0.001 nm. In certain experiments (e.g., in absorption experiments) *continuum light sources*, which do not produce any characteristic line spectrum, can be used. However, such light sources generally yield too low an intensity per spectral interval to be useful for excitation purposes, unless the absorption bands are broad. The opposite is true for the third main group of light sources, *lasers*. Here, the intensity per spectral interval is many orders of magnitude higher than that which is obtained from line sources. For quite some time only laser transitions in fixed-frequency lasers [6.10], or accidentally coincident lines could be studied. However, tunable lasers are now available, making more general applications of the unique properties of laser light possible in spectroscopy. Lasers will be discussed in Chap. 8.

6.1.1 Line Light Sources

The accuracy of a spectroscopic measurement is determined by the sharpness of the lines to be measured. The experimentally recorded width of the lines is due to two contributions: the primary width (from the source) and the instrumental width of the spectral apparatus used. We will first consider the factors contributing to the primary width of the light source. These broadening factors are also relevant in absorption experiments. We have already dealt with the *natural radiation width (homogeneous broadening)* of energy levels in Chap. 4. For most light sources this width is small compared with the *Doppler broadening*. Because of the varying velocities and directions of movement for the atoms under study, light within a certain frequency interval can be emitted or absorbed, as illustrated in Fig. 6.1.

Doppler broadening is an example of *inhomogeneous broadening*, in which different atoms contribute to different parts of the line profile. Light of frequency ν_0 , emitted from a source moving with a thermal velocity v , towards ($v > 0$) or away ($v < 0$) from an observer is recorded with a frequency shift

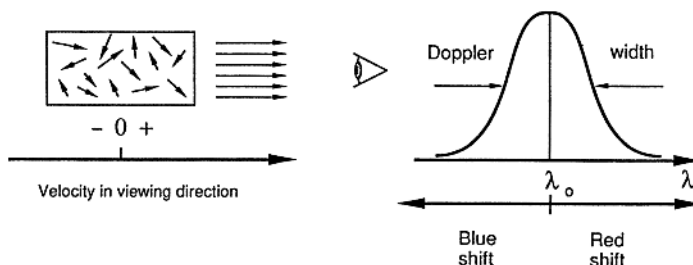


Fig. 6.1. The origin of Doppler broadening of a spectral line

$\Delta\nu$ given by

$$\Delta\nu = \nu - \nu_0 = \nu_0 v/c. \quad (6.1)$$

This expresses the *Doppler effect*.

In a light source or in an absorption cell the velocities of the atoms follow a Maxwell distribution and the number of atoms with velocity components between v and $v + dv$ in the direction of observation is

$$dN = Nf(v)dv, \quad (6.2)$$

where $f(v)$ is the distribution function for the particular velocity component v :

$$f(v) = \sqrt{\frac{M}{2\pi RT}} \exp\left(-\frac{M}{2RT}v^2\right). \quad (6.3)$$

Here N is the total number of atoms, M is the atomic weight and R is the general gas constant. The light power emitted in the frequency interval ν to $\nu + \Delta\nu$ is denoted by $P_\nu d\nu$. This power is proportional to the number of light-emitting atoms in this band, i.e., the atoms with a velocity component v between v and $v + dv$, hence

$$v = c\frac{\nu - \nu_0}{\nu_0} \quad \text{and} \quad dv = c\frac{d\nu}{\nu_0} \quad (6.4)$$

and

$$P_\nu d\nu = KNf\left(c\frac{\nu - \nu_0}{\nu_0}\right)c\frac{d\nu}{\nu_0} \quad (6.5)$$

and

$$P_\nu = K'f\left(c\frac{\nu - \nu_0}{\nu_0}\right) = K'' \exp\left(-\frac{M}{2RT}c^2\frac{(\nu - \nu_0)^2}{\nu_0^2}\right). \quad (6.6)$$

K , K' and K'' are constants of proportionality. Equation (6.6) describes a Gaussian with a half-intensity at $e^{-x} = 1/2$, i.e., when

$$\delta\nu = \nu - \nu_0 = \frac{\nu_0}{c} \sqrt{\frac{2RT}{M} \ln 2}. \quad (6.7)$$

The full-width at half-maximum (FWHM), the *Doppler width*, is then

$$\Delta\nu_D = 2\delta\nu = \frac{2\sqrt{2R\ln 2}}{c} \nu_0 \sqrt{\frac{T}{M}}. \quad (6.8)$$

The value of the constant is $7.16 \times 10^{-7} \text{ K}^{-1/2}$. As an example, for $\lambda = 500 \text{ nm}$, $T = 500 \text{ K}$ and $M = 100$ the Doppler broadening is

$$\Delta\nu_D = 7.16 \times 10^{-7} \frac{3 \times 10^8}{5 \times 10^{-7}} \sqrt{5} = 960 \text{ MHz} \longleftrightarrow 0.001 \text{ nm}.$$

A general rule, which may easily be memorized, is that the typical Doppler width in the visible range for typical light sources is about 0.001 nm or

1000 MHz. In the IR region the width is, of course, proportionally smaller, i.e. about 50 MHz at 10 μm .

If the atoms under study undergo frequent *collisions*, the spectral lines will be broadened. With increasing pressure *Lorentz broadening* (due to collisions between different kinds of atoms) and *Holtsmark broadening* (due to collisions between the same kind of atoms) will be more and more prominent. These two broadening mechanisms are generally treated together as pressure broadening. The collisional width, $\Delta\nu_{\text{coll}}(P_0, T_0)$, of the resulting Lorentzian curve is about 0.5–5 GHz at atmospheric pressure and room temperature. The width can be calculated for any temperature and pressure using the relation

$$\Delta\nu_{\text{coll}}(P, T) = \Delta\nu_{\text{coll}}(P_0, T_0) \frac{P}{P_0} \sqrt{\frac{T_0}{T}}. \quad (6.9)$$

If collisions with electrons and ions occur, as in discharge lamps, *Stark broadening*, due to the strong electrical fields experienced by the atoms during collisions, will also contribute to the total line broadening.

Line broadening mechanisms and resulting lineshapes have been discussed in [6.11–6.14].

In Fig. 6.2 a number of line light sources have been schematically depicted. With a *dc gas discharge* between two electrodes the spectra of most gases can be conveniently produced. The discharge current is generally low, about 100 mA. Considerably stronger currents are used in *dc arcs*. The cathode contains the atomic species for which the spectrum is to be produced. Atoms are brought into the arc, which is burning between the anode and the cathode in an inert-gas atmosphere, through sputtering. This type of lamp has been extensively used for studies of the strengths of spectral lines (transition probabilities) [6.15, 6.16].

The *hollow cathode* is a very useful light source, which produces comparatively narrow spectral lines. A dc discharge of typically 10 to 500 mA runs in an inert-gas atmosphere (pressure: 1–5 torr) between a ring-shaped anode and the cathode, which is made of the element to be studied. A hole, with a typical depth and diameter of 5 mm is drilled in the cathode. Because of the field distribution around the hole the discharge will run down into the hole. Atoms are sputtered into the discharge through the ion bombardment, and the atoms are excited in the discharge. Intense light emission is obtained from the hole. By cooling the hollow cathode with liquid nitrogen, the Doppler width, which is the dominating source of broadening, can be further reduced (Schüler hollow cathode).

In an electric *spark discharge* considerably higher excitation energies are obtained than in the light sources described earlier. A large capacitor ($\sim 0.5 \mu\text{F}$) is discharged through a spark gap between two electrodes of the element to be studied. Sometimes a piece of insulating material is placed between the electrodes to guide the spark (*sliding spark*). Highly ionized atoms with more than 10 electrons removed can be obtained and the cor-

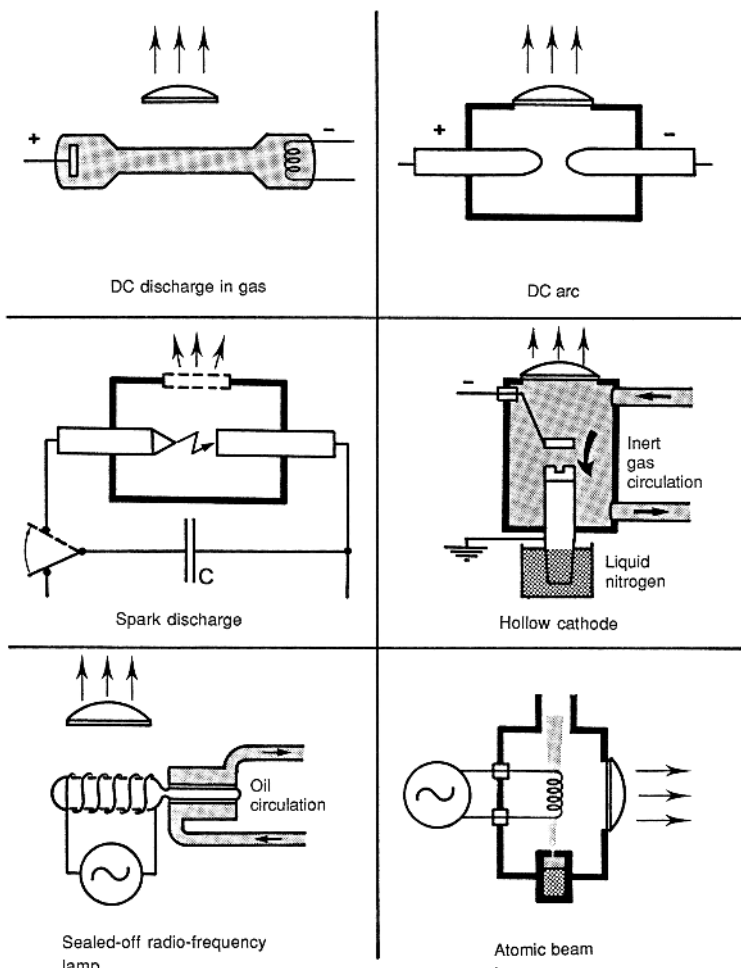


Fig. 6.2. Line light sources of different constructions

responding spectra studied. The intermittent light emission from the spark can best be studied with spectrographs with photographic recording, since the photographic plate is a perfect light integrator. Photoelectric recording, which is otherwise frequently employed, is not suitable when working with this kind of light source. The blackening of photographically recorded plates can conveniently be recorded with photoelectrical methods (microdensitometer).

A sealed *radio-frequency discharge lamp* can be used for most elements which develop a sufficient vapour pressure ($> 10^{-3}$ torr) within the temperature range in which glass or quartz vessels can be employed (below 1000 °C). The lamp vessel is sealed under high vacuum after a small amount of the element of interest has been brought into it by heating a lump of the material

that is kept in a sidearm of the vacuum manifold. The sealed lamp vessel is placed in an RF coil inside an oven, and an RF power of typically 100 W is applied. This kind of lamp is frequently used for alkali atoms. At the low temperatures needed in these cases, the metal vapour pressure can be accurately regulated by circulating oil around a cold finger on the lamp vessel, which is kept at a slightly higher temperature. The coldest point on the vessel will determine the metal vapour pressure.

In the *atomic-beam lamp*, an atomic beam is excited in an RF coil, and light emitted at right angles to the atomic beam is collected. In this way the Doppler broadening of the emission lines will be much reduced. The same principle for linewidth reduction is used in absorption measurements, in which absorption from a continuous wavelength distribution by atoms is recorded at right angles to the collimated beam. The resulting Doppler width when atoms with a preferred direction of motion are used can be calculated in a similar way as for the case with evenly distributed directions of motion. In practical cases, linewidths of tens of MHz are obtained in optical absorption measurements on atomic beams, at thermal velocities (a few hundred m/s).

A special type of light emission is obtained from a *laser-produced plasma* [6.17–6.23]. Here the beam from a high-power laser is focused onto a small spot on the surface of a metallic substrate. Typically a Nd:Glass laser (Chap. 8) is used with a pulse energy of about 10 J and a pulse length of a few ns. Plasma temperatures as high as 10^6 – 10^7 K can be obtained. The ionization occurs very quickly and the low states of ionization do not have time to radiate. The maximum state of ionization (up to 60 electrons removed) can be varied by changing the pulse energy and focusing. The laser-produced plasma spectrum is easier to interpret than the spectrum from a spark, where a large number of ionization stages simultaneously yield spectral lines. In particular, if a high- Z target material is used a strong soft X-ray continuum will also be obtained. This radiation is comparable to that produced by an electron synchrotron (Sect. 6.1.3). Such short-wavelength radiation is very useful both for spectroscopic investigations and for technical applications such as X-ray microscopy and lithography in connection with semiconductor circuit production (see Sects. 5.1.3 and 9.6.4).

In laser-driven fusion research high-power beams are made to impinge on small targets of deuterium and tritium [6.24]. It is also possible to study highly ionized spectra from other plasma generators used in fusion research, such as *Tokamak* machines. A smaller plasma light source is the *theta pinch*, where a strong current pulse in a one-turn coil excites and contracts the plasma. Spectral analysis of the plasma light serves as an important diagnostic tool in fusion research machines [6.25].

Finally, the *beam-foil light* source and its applications will be described. These techniques were introduced in 1963 by *Bashkin* and *Kay* [6.26, 6.27]. The principles of beam-foil spectroscopy are illustrated in Fig. 6.3. Ions of the element to be studied are produced with a well-defined energy (velocity) in

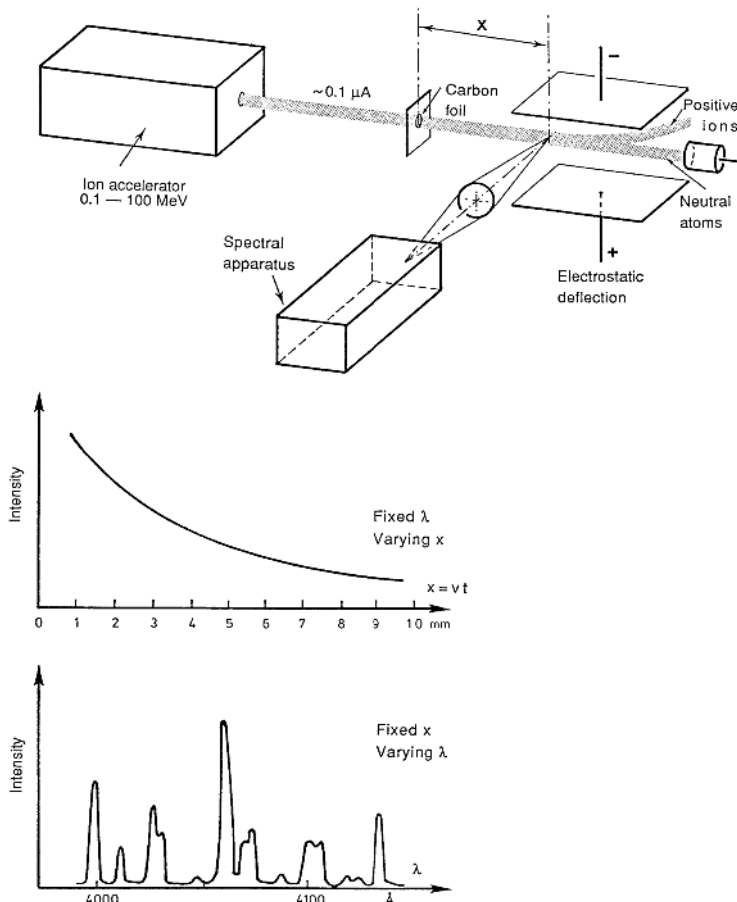


Fig. 6.3. Principles of beam-foil spectroscopy

an ion accelerator. The ions (with a typical velocity of 10^6 m/s) pass a 50 nm thick carbon foil, in which very abrupt excitation occurs (the passage time is $\sim 10^{-14} \text{ s}$). Ions of different charges are formed. An electron can also be picked up and a neutral atom is then formed. The excited states will decay after passing through the foil and the corresponding spectrum can be recorded with a spectrometer. Because of a certain lateral scattering in the foil and since a finite solid angle must be used for the detection of the photons, the Doppler broadening for the fast particles will be large, typically a few 0.1 nm . The linewidth can, however, be reduced using special imaging techniques (refocusing) [6.28]. A typical beam-foil spectrum is shown in Fig. 6.4.

Since the velocity of the particles is known, a well-defined timescale is obtained after the foil and the decay can be observed directly. In such measurements the foil is normally moved back and forth while the detection

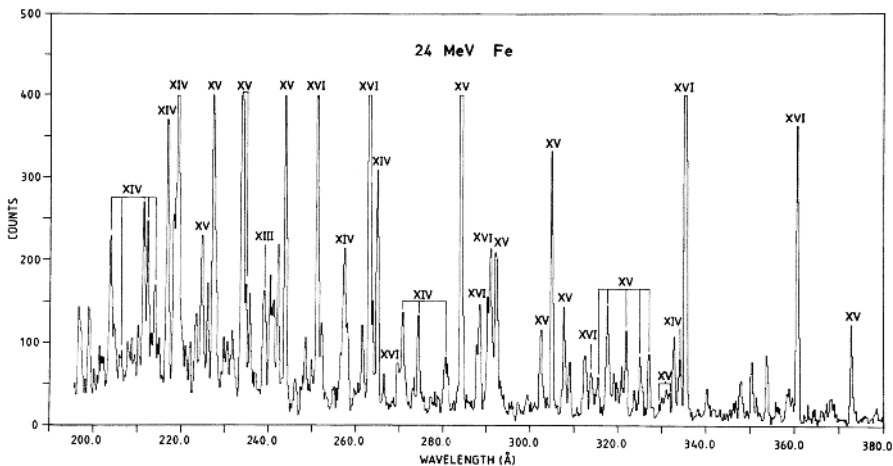


Fig. 6.4. Example of a beam-foil spectrum obtained using an accelerated iron-ion beam [6.29]

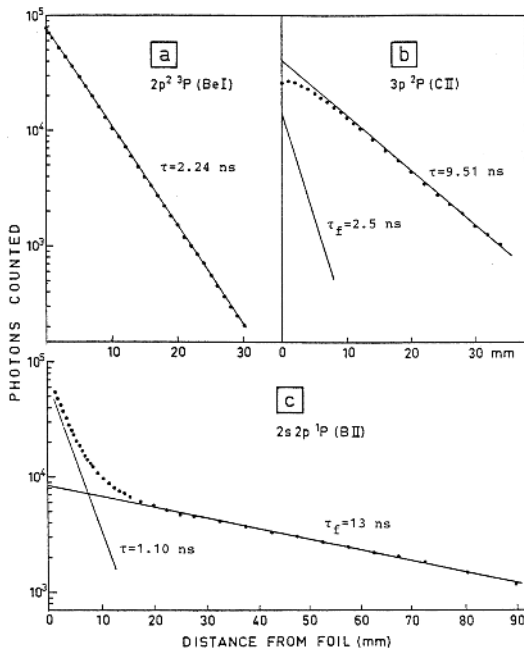


Fig. 6.5. Examples of decay curves obtained with beam-foil spectroscopy [6.32], Curve *a* presents the decay of a Be I level unaffected by cascades. In *(b)* a level in C II is repopulated by a short-lived level, while in *(c)* a level in BII is repopulated by a longer-lived level. τ_f denotes the half-life of the level feeding the level of interest

system remains fixed. A certain energy loss and velocity spread (straggling) is obtained as the ions pass through the foil and these small effects can be studied if an electrostatic velocity analyser is placed after the foil, as is illustrated in the figure. Lifetimes of excited states of atoms and ions can be conveniently measured with the beam-foil method. Since the excitation process is not selective, the decay curve must be carefully analysed so that cascade decays from higher-lying states can be identified and corrected for [6.30, 6.31]. Lifetime measurements using the beam-foil technique are illustrated in Fig. 6.5. The beam-foil method yields low signal strengths, since the particle density in the beam is typically 10^5 ions/cm³. Ion accelerators in different energy ranges can be used: from mass separators yielding 100 keV energy to heavy-ion accelerators yielding particle energies up to 300 GeV. Atoms ionized 90 times have been observed. In order to determine which lines belong to a certain ionization state, a strong electric field can be applied which deflects the beam according to the charge states of the ionic beam constituents.

As a result of the abrupt foil excitation, atoms and ions can be excited into a quantum-mechanical state that is a coherent superposition of eigenstates. By "coherent" we mean in this context that a well-defined relation exists between the phase factors of the different eigenstates. If the sublevels are not equally populated but a certain degree of "alignment" is brought about, some components of the light from the decaying, abruptly excited state will

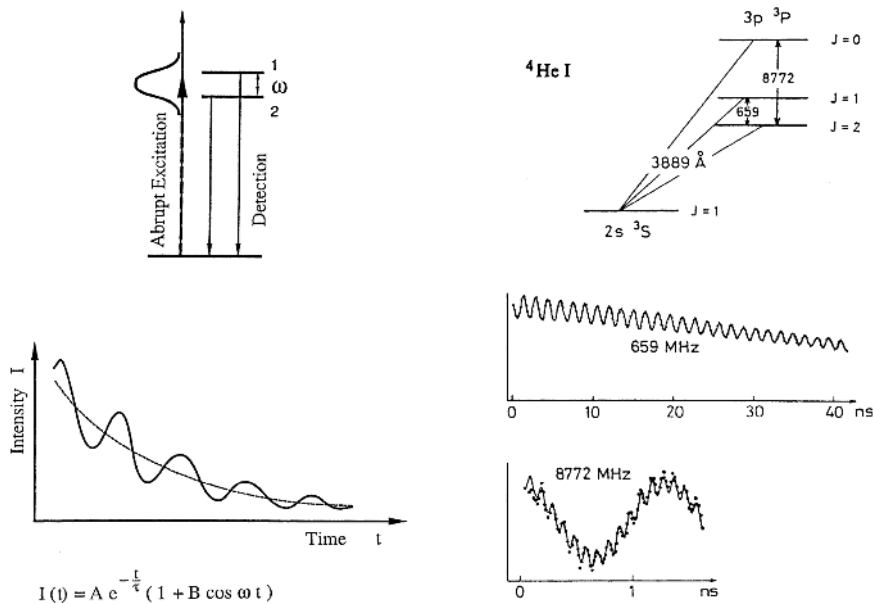


Fig. 6.6. Principle of quantum beats (left) and illustration of fine-structure quantum beats in ${}^4\text{He}$ (right) [6.35]

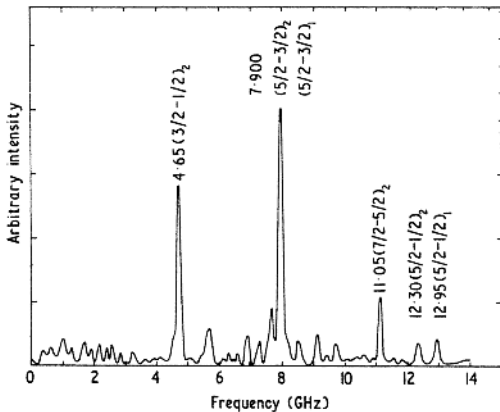


Fig. 6.7. Fourier analysis of hyperfine-structure quantum beats in the $1s2p\ ^3P_{1,2} \rightarrow 1s2s\ ^3S_1$ decay of Be III [$I(^9\text{Be}) = 3/2$] [6.36]

be modulated at frequencies that correspond to the energy splittings between the substates. Such an alignment can be obtained in the beamfoil excitation process, especially if the symmetry is broken by inclining the foil with respect to the ion beam [6.33]. This so-called *quantum-beat spectroscopy*, which was treated theoretically for the beam-foil case in [6.34], is very useful for measuring fine and hyperfine structure separations. The technique is illustrated by a fine-structure determination for ^4He in Fig. 6.6. An example of hyperfine structure quantum beats is given in Fig. 6.7. We will return to quantum-beat experiments in Sect. 9.4.5, where the more well-defined case of optical (laser) excitation is discussed.

As we have seen, the beam-foil light source offers many possibilities for studies of spectra, lifetimes and level separations, and extensive data have been collected during the last 30 years [6.37–6.41]. Comprehensive reviews of the field of beam-foil spectroscopy have been written [6.42–6.48].

6.1.2 Continuum Light Sources

The *black-body emitter* is the simplest type of continuum light source. The radiation from a heated tungsten ribbon approaches that of a Planck emitter. However, for a given temperature only about 30% of the power emitted by a truly black body is obtained (emissivity: 30%). The highest temperature attainable in this way is 3400 K. Normally, the working temperature for a tungsten lamp is about 2900 K. Such a lamp is useful in the wavelength region 320 nm to 2.5 μm . Planck-radiation diagrams for certain characteristic temperatures are shown in Fig. 6.8, which also illustrates the displacement of the wavelength of maximum emission towards shorter wavelengths with increasing temperature (the Wien displacement law: $\lambda_{\max} \propto T^{-1}$). For the IR

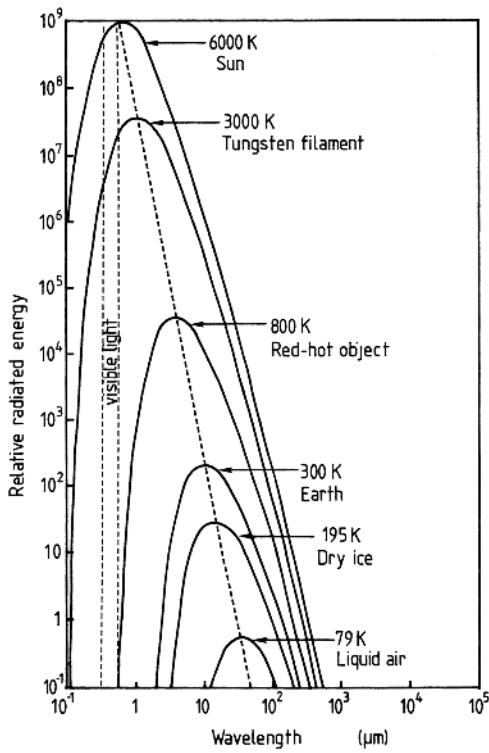


Fig. 6.8. Planck radiation diagrams for different temperatures

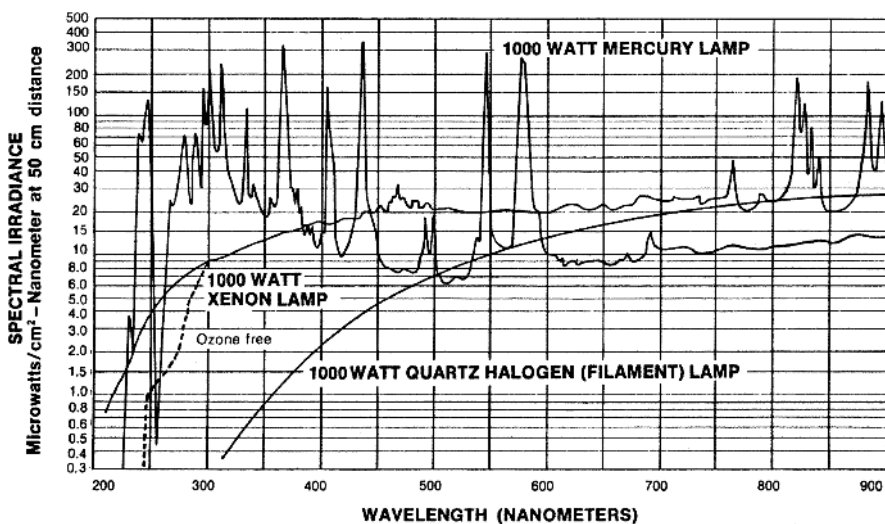


Fig. 6.9. Spectral distributions from some gas-filled lamps (Courtesy: Oriel Corp., Stratford, CT, USA)

region a so-called *Nernst glower* is frequently used. This consists of a heated rod of sintered cerium and zirconium oxides (1500–2000 K).

In the UV and visible regions lamps utilizing a gas discharge are frequently used. In a *deuterium lamp* at a pressure of some tens of torrs, the spectral lines are broadened to a continuum-like spectrum with only certain peaks remaining. The practical region of use is 180–380 nm. Lamps with much higher pressures can also be used. In *xenon* and *mercury lamps* pressures of tens of atmospheres are often used. Spectral distributions of some gas-filled lamps are presented in Fig. 6.9. Although the total output power from a continuum source of this kind can be very high (> 1 kW), the power within a region corresponding to an individual atomic absorption line (0.001–0.005 nm) is always small.

6.1.3 Synchrotron Radiation

During recent years *electron synchrotrons* have been increasingly used as sources of continuum radiation. Originally, the radiation was obtained “parasitically” from machines that were constructed for nuclear physics experiments. Lately, many machines dedicated for light generation have been built. Because of the strong centrifugal acceleration ($\sim 10^{16}$ g for electrons with a velocity close to c in an orbit of 1 m radius), the electrons will emit radiation. At low velocities the emission pattern is a normal $\sin^2 \theta$ dipole distribution with the orbit radius as the symmetry axis (Fig. 6.10). Because of relativistic effects the emission characteristics will be strongly peaked in the momentary flight direction of a high-speed electron [6.49, 6.50]. The opening angle of the emission cone is inversely proportional to the electron energy and is typically a small fraction of a degree. The light is linearly polarized. The total power P of the synchrotron radiation increases as the fourth power of the electron energy E

$$P[\text{W}] = 88.5 \frac{I[\text{mA}](E[\text{GeV}])^4}{R[\text{m}]} , \quad (6.10)$$

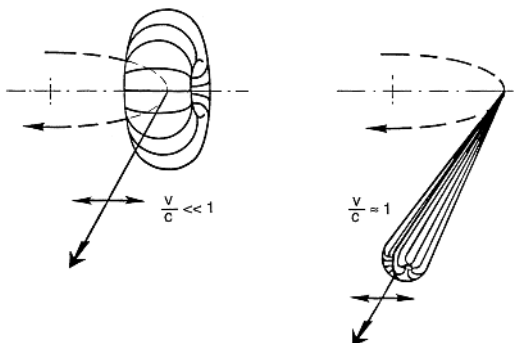


Fig. 6.10. Generation of synchrotron radiation [6.50]

where I is the electron beam current and R is the radius of the electron orbit. Classically, the frequency of the radiation emitted by a circulating electron would be the inverse of the period of revolution and would be typically 10 MHz. However, because of relativistic effects overtones of very high orders are emitted at high powers. Because of the short time for the radiation lobe of an individual electron to sweep over the detector and fluctuations in energy and orbit position, the frequency distribution is smeared out into a continuum which extends down to very short wavelengths. A synchrotron radiation source is normally classified by its *characteristic wavelength* λ_c

$$\lambda_c[\text{\AA}] = 5.6 \frac{R[\text{m}]}{(E[\text{GeV}])^3}. \quad (6.11)$$

The maximum of the intensity distribution is close to λ_c . The characteristic wavelength for typical, large machines is around 1 nm. It is possible to express the distribution of any electron synchrotron radiation in normalized intensity units using the characteristic wavelength as the wavelength unit. The universal distribution function is shown in Fig. 6.11.

In order to achieve high radiation intensities *electron storage rings* are used. The layout of such a ring is shown in Fig. 6.12. In these rings, which are pumped by (filled from) an electron accelerator, circulating currents of the order of 1 A can be obtained. Using radio-frequency fields sufficient energy is delivered to the electrons to compensate for the radiative losses. (Compare with the Bohr atomic model!) In the ring the electrons are arranged in circulating bunches. Thus the emission as seen by a user who is placed tangentially to the orbit will be pulsed with a pulse width in the subnanosecond region and a repetition rate of the order of MHz to GHz. Thus time-resolved experiments can be performed [6.51, 6.52]. Data for a number of facilities producing synchrotron radiation are given in Table 6.1. With synchrotrons of reasonable sizes the intensity per Doppler width that is achievable is comparable to that which is obtained from efficient line light sources. However, the intensity increases towards the extreme UV (XUV) and X-ray regions, where no comparable continuum light sources exist.

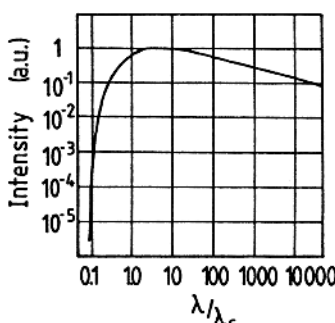


Fig. 6.11. Universal intensity distribution function for synchrotron radiation

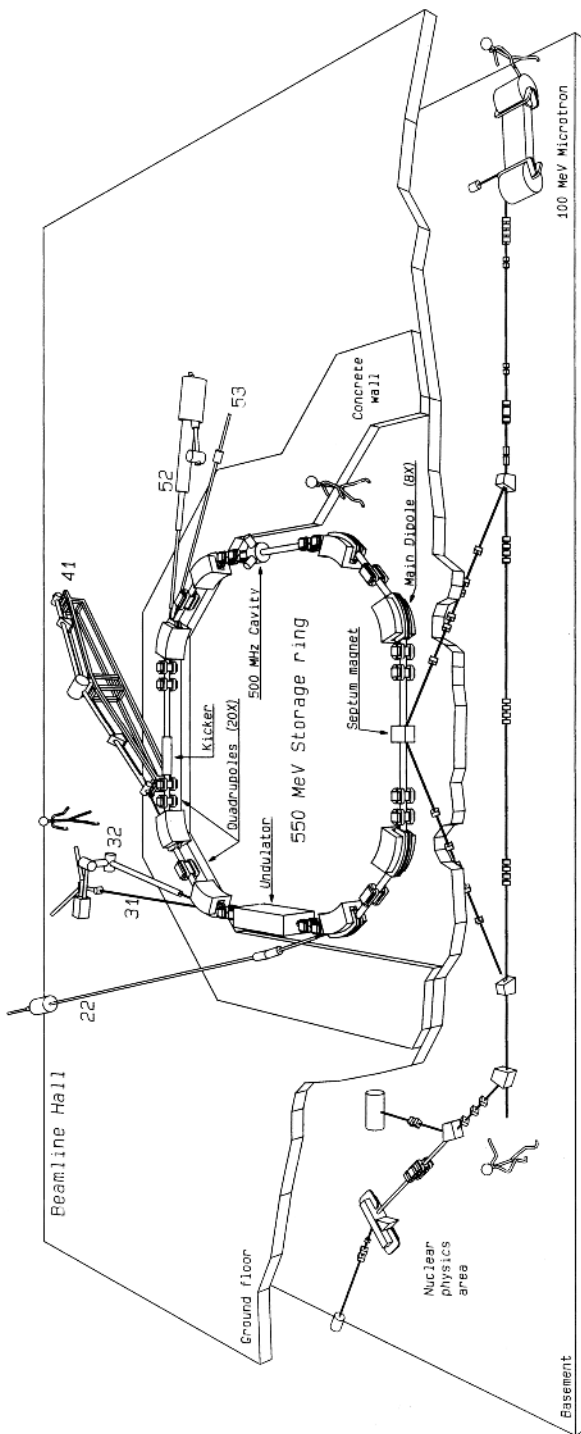


Fig. 6.12. Layout of the MAX storage ring (Lund) for the generation of synchrotron radiation (Courtesy: P. Röjsel, MAX Synchrotron Radiation Laboratory)

Table 6.1. Data for some synchrotron radiation facilities

| Facilities | E [GeV] | Circumference [m] | I [mA] |
|--------------------------|-----------|-------------------|----------|
| MAX II (Lund) | 1.5 | 90 | 200 |
| Bessy II (Berlin) | 1.7 | 240 | 200 |
| ALS (Berkeley) | 1.9 | 197 | 400 |
| Elettra (Trieste) | 2.0 | 259 | 300 |
| Photon Factory (Tsukuba) | 2.5 | 187 | 400 |
| SPEAR II (Stanford) | 3.0 | | 500 |
| ESRF (Grenoble) | 6.0 | 844 | 200 |
| APS (Chicago) | 7.0 | 1104 | 300 |

The performance of synchrotrons and storage rings can be further enhanced by using *wigglers* or *undulators* [6.53]. In the former type of system a number of local, sharp bends in the electron beam are made using strong magnets. In this way a local emission of still shorter wavelength can be obtained, see (6.11). An undulator is a periodical structure of magnets on a straight part of the electron path between the large bending magnets of the machine, where the electrons are bent back and forth resulting in particularly strong radiation in narrow wavelength bands (fundamental band and high overtone bands) and in a well-defined direction. By introducing suitable mirrors laser action can be achieved in a so-called *Free-Electron Laser* (FEL) [6.54–6.62]. Tunable radiation with extremely high powers should ultimately be feasible.

Several FELs are now operating producing tuneable radiation mostly covering the IR spectral region. FEL operation in the visible and UV region has also been demonstrated at several facilities. Coherent light generation from an undulator is possible without using laser mirrors employing the *optical klystron* process [6.63]. In very long undulators with exceedingly high electron-beam quality the *SASE* (Self-Amplified Spontaneous Emission)-*FEL* operation should be possible [6.64]. Such devices, now constructed, e.g., at DESY (Hamburg), have the potential to produce ultra-intense coherent radiation down to the 10 nm range and possibly lower. The *Inverse Free-Electron Laser* (IFEL) action [6.65] can be used to accelerate electrons using intense laser beams.

Synchrotron radiation has many applications in a large number of scientific and industrial areas: physics, chemistry, biology, medicine and electronics. With regard to atomic and molecular spectroscopy, synchrotron radiation is particularly applicable for X-ray and photoelectron studies. In most experiments it is necessary to have monochromatized photons, which can be obtained using specially designed monochromators capable of handling the intense radiation. An arrangement for ESCA studies (Sect. 5.2) using synchrotron radiation is shown in Fig. 6.13. Another important area in which

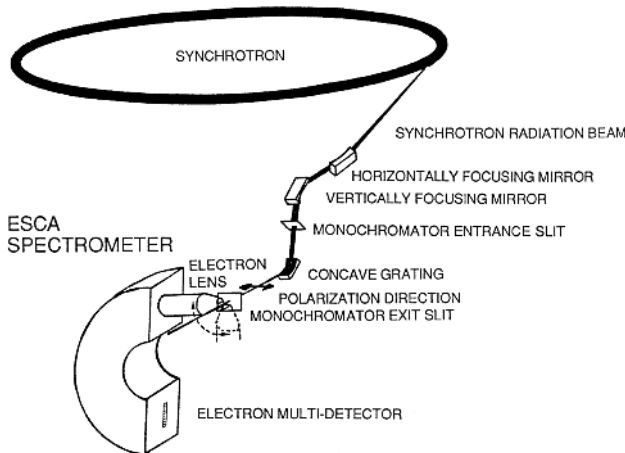


Fig. 6.13. XPS (ESCA) arrangement at a synchrotron radiation source [6.66]

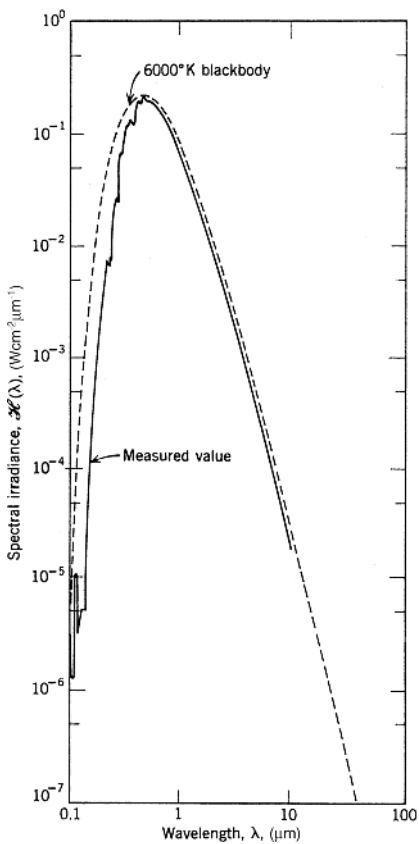


Fig. 6.14. Spectral distribution of sunlight outside the atmosphere [6.73]

synchrotron radiation can be applied is EXAFS (Extended X-ray Absorption Fine Structure spectroscopy, Sect. 5.1.2). A spectrum can be recorded in typically 1/1000 of the time needed when a conventional X-ray source is used. Synchrotron radiation and its applications have been discussed in [6.67–6.72].

6.1.4 Natural Radiation Sources

In connection with continuum light sources we will also consider some natural radiation sources. The sun is clearly our most powerful radiation source and, apart from a large number of absorption and emission lines, it essentially radiates like a Planck radiation source at a temperature of 6000 K (Fig. 6.14). The moon exhibits a similar distribution, although about 10^6 times weaker. The clear sky also yields a continuum-like distribution (Fig. 6.15). The distribution from the sun is enhanced towards the blue region because of the strong wavelength dependence of Rayleigh scattering. Further, there is a general ~ 300 K radiation in the IR region due to the thermal emission of the atmosphere. The spectral distribution of the night sky is determined by scattered starlight, galactic light and zodiacal light (Fig. 6.16).

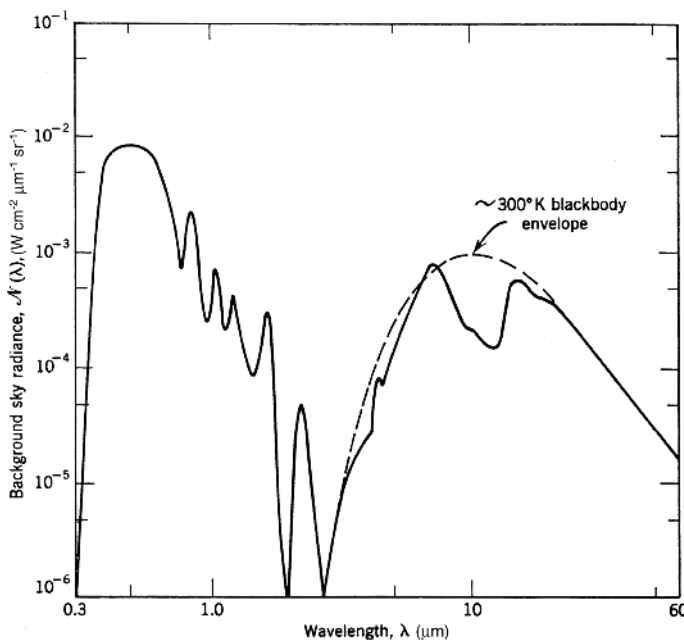


Fig. 6.15. Spectral distribution of the blue sky [6.74]

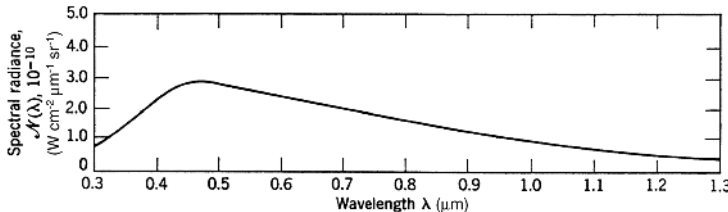


Fig. 6.16. Spectral distribution of the night sky [6.74]

6.2 Spectral Resolution Instruments

Spectral resolution instruments of different kinds are used for resolving the different wavelength components of light. Important factors of merit for such devices are resolving power and light transmission. The resolving power \mathcal{R} is defined by

$$\mathcal{R} = \frac{\lambda}{\delta\lambda}, \quad (6.12)$$

where $\delta\lambda$ is the resulting linewidth of the spectral apparatus when using monochromatic light of wavelength λ .

We will describe four types of instruments: prism and grating instruments, the Fabry-Pérot interferometer and the Fourier transform spectrometer. A large number of varieties of these different types are used in spectroscopic research and various applications. Spectroscopic instruments have been discussed in [6.6, 6.7, 6.75].

6.2.1 Prism Spectrometers

Names such as spectrometer, spectroscope, spectrograph or monochromator are used for basically the same types of instrument, which are, however, applied in different ways. The principle of a prism spectrograph is illustrated in Fig. 6.17. The resolving power \mathcal{R} is determined by the dispersion, $dn/d\lambda$, and the length of the prism base b

$$\mathcal{R} = \frac{\lambda}{\delta\lambda} = b \frac{dn}{d\lambda}. \quad (6.13)$$

If the prism is made of flint glass ($dn/d\lambda = 1200 \text{ cm}^{-1}$ at $\lambda \sim 500 \text{ nm}$) and has a base length of 5 cm, then the resolving power \mathcal{R} will be 6000. For practical reasons the size of the prism must be limited and thus this type of spectrograph will necessarily have a relatively low resolution. The finite width of the slits used will clearly reduce the theoretical resolving power given above. Since the dispersion of a prism strongly increases towards shorter wavelengths, the resolution obtainable with a prism instrument will vary with the wavelength. In Fig. 6.18 the dispersions of different prism materials are

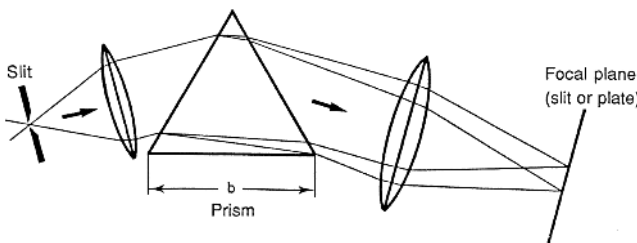


Fig. 6.17. Principle of a prism spectrograph

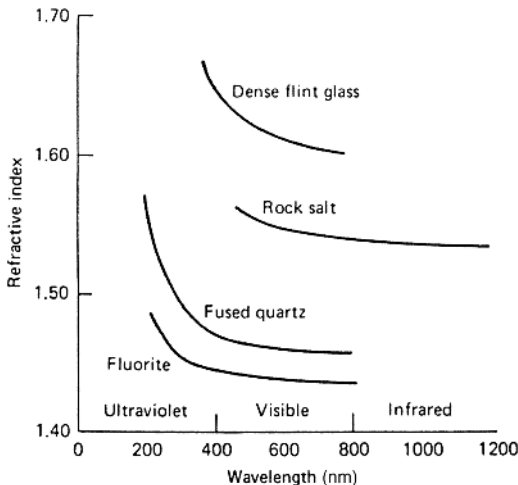


Fig. 6.18. Dispersion of various prism materials [6.76]

shown. Figure 6.19 displays the slit width necessary to achieve a 1 nm band pass for a typical prism spectrometer.

Commercial instruments frequently use a so-called *Littrow* mount. Here a Littrow prism with a 30° angle and one surface silvered, as shown in Fig. 6.20, is used for increased dispersion. Arrangements with lenses or mirrors can be used for collimating the incoming light onto the prism and for focusing the refracted beams towards the photographic plate or the exit slit.

Prisms of different kinds can be used to deflect or deviate a beam of light. They can invert or rotate images and they can be used for separation of different states of polarization. Some prisms that are frequently used in optical and spectroscopic systems will be discussed here. Illustrations are found in Fig. 6.21.

A *right-angle prism* using total internal reflection off the uncoated hypotenuse deviates a beam by 90° , if it impinges perpendicular to one of the entrance surfaces. This type of prism is very useful for deviating high-power laser beams.

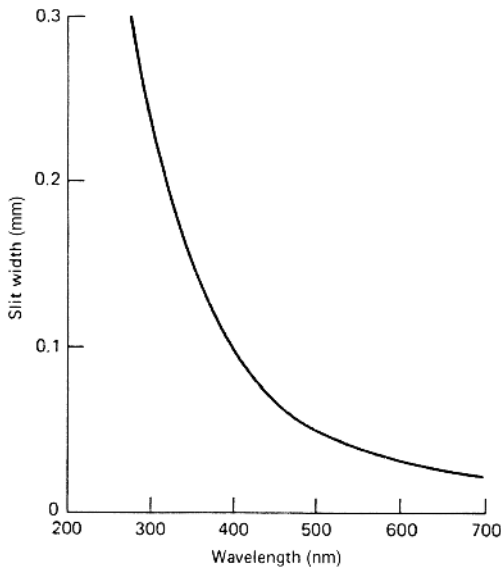


Fig. 6.19. Diagram showing the slit width required to achieve a constant band pass of 1 nm from a prism spectrograph [6.76]

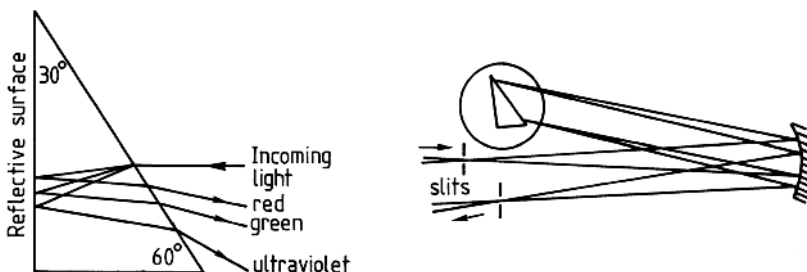


Fig. 6.20. Littrow prism and Littrow prism mount

In the *Amici (roof) prism*, the hypotenuse in the right-angle prism is replaced by two internal reflector surfaces oriented at 90° to each other (a “roof”). This prism also deflects a beam by 90° but at the same time rotates the image by 180° . The *pentaprism* deflects the incoming beams by 90° *regardless* of the angle of incidence and does not invert or reverse the image. This prism does not operate on total internal reflection but requires a mirror coating on two faces.

The *Pellin-Broca* prism also deviates beams by roughly 90° but is a dispersive prism, frequently used to separate laser beams of different colours after nonlinear frequency conversion (Sect. 8.6). By combining four Pellin-Broca prisms, beam separation with maintained direction of propagation can be achieved. In the *straight-view prism* colour dispersion in the forward

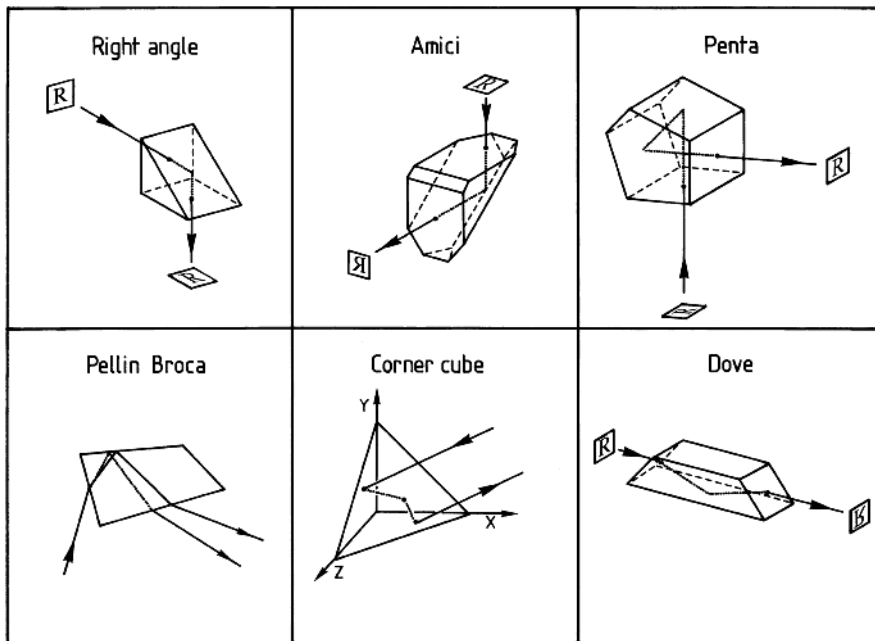


Fig. 6.21. Prisms frequently used in optical and spectroscopic systems (After material from Melles Griot)

direction is instead accomplished. The *dove prism* also transmits light in the forward direction but without dispersion. It has the important property of rotating the image (at twice the angular rate of the prism). A *corner-cube prism*, with three orthogonal total internal reflection faces, acts as a *retroreflector*. A beam entering the corner cube will, after 3 reflections, be sent in the opposite direction regardless of the angle of incidence. Frequently, corner cube reflectors are made from 3 first-surface mirrors rather than from solid glass or quartz.

6.2.2 Grating Spectrometers

A reflection grating is used for the spectral separation in a grating spectrometer. The basic arrangement is shown in Fig. 6.22. Constructive interference is obtained when the optical path difference is an integer number (m) of wavelengths for diffraction at adjacent lines, as expressed by the grating equation

$$m\lambda = d(\sin \alpha + \sin \beta). \quad (6.14)$$

Here d is the line separation and α and β the angles of incidence and reflection, respectively. The resolving power \mathcal{R} of the grating is determined by the total number of illuminated lines N and by the diffraction order m , i.e.,

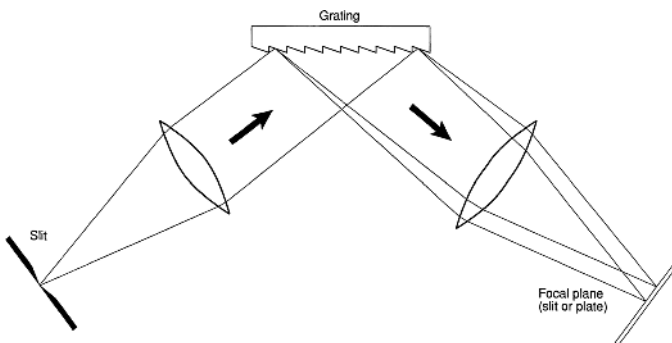


Fig. 6.22. Principle of a grating spectrograph

$$\mathcal{R} = \frac{\lambda}{\delta\lambda} = N \cdot m. \quad (6.15)$$

Thus a 10 cm grating with 3000 lines/cm has a resolving power of 30 000 in the first order.

Gratings were first made by J. Fraunhofer in 1823. Normally, a grating is ruled in a surface layer of aluminum on a substrate by means of a diamond tip. The ruling is performed with high-precision ruling machines, which are interferometrically controlled. *Replica gratings* which are the ones that are marketed, are manufactured by a casting procedure. During recent years *holographic gratings* have been much used. These gratings are produced by recording interference fringes from two crossed laser beams. An Ar⁺ laser acting on photoresist can be used. A density of up to 6000 lines/mm can be attained.

The intensity that is diffracted at a certain wavelength depends on the shape of the lines. Ruled gratings are made with a certain "blaze" angle, chosen according to which wavelength region is to be enhanced through reflective action (Fig. 6.23). The efficiency of a grating can be up to 70% at the blaze angle for a certain order. Recently, it has also become possible to produce gratings with a blaze by the holographic process. From mechanically ruled gratings so-called ghost lines can appear due to periodical errors in the

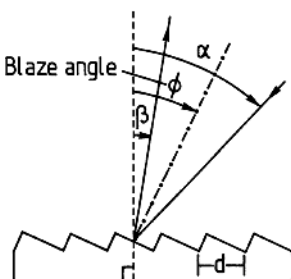


Fig. 6.23. Blaze angle of a grating

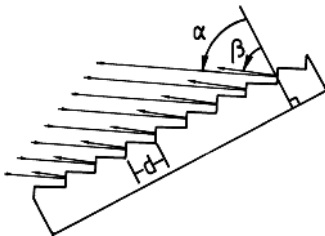


Fig. 6.24. Echelle grating

mechanical feeding of the machine. Such lines do not result from holographic gratings, which also have a lower level of diffusely scattered light (stray light). While the first diffraction order is normally used in small spectrometers, higher diffraction orders are frequently used in large research instruments. One drawback of grating spectrometers is that for a certain grating setting a series of wavelengths ($\lambda_0, \lambda_0/2, \lambda_0/3, \dots$) is diffracted in the same direction (overlapping orders). The problem can be eliminated using filters or a pre-monochromator. An especially high resolution, but also many overlapping orders, is obtained with an echelle grating (Fig. 6.24). Such gratings operate at such a high angle that the steep side of the line is utilized. Echelle gratings have comparatively few lines/mm but operate at a very high diffraction order. A resolving power approaching 10^6 can be achieved with grating instruments. Grating characteristics are discussed in [6.77].

Grating spectrometers are, in general, equipped with mirrors instead of lenses. Some common arrangements are shown in Fig. 6.25. Instruments for the visible region frequently make use of the Ebert or the Czerny–Turner arrangement. A grating in a Littrow mount is frequently used for tuning pulsed dye lasers (Sect. 8.5.1). By using concave gratings the need for collimating and focusing mirrors is eliminated, which is particularly valuable in the VUV (vacuum ultraviolet) and XUV (extreme UV) regions, where conventional mirrors are ineffective.

Frequently an arrangement utilizing the *Rowland circle* is used. The entrance slit, the grating and the spectral image are all on a circle which has a diameter equal to the radius of curvature of the concave grating. For the very short wavelengths that are obtained in spectra from highly ionized atoms or in X-ray spectra, a *grazing angle of incidence* is used to minimize the absorption losses in the grating.

The beam leaving a monochromator always contains small amounts of radiation at wavelengths other than the selected one. This *stray light* is due to reflections and scattering from different parts of the monochromator. The amount of stray light can be much reduced by using a *double monochromator* which consists of two adjacent single monochromators connected only through a common intermediate (exit/entrance) slit.

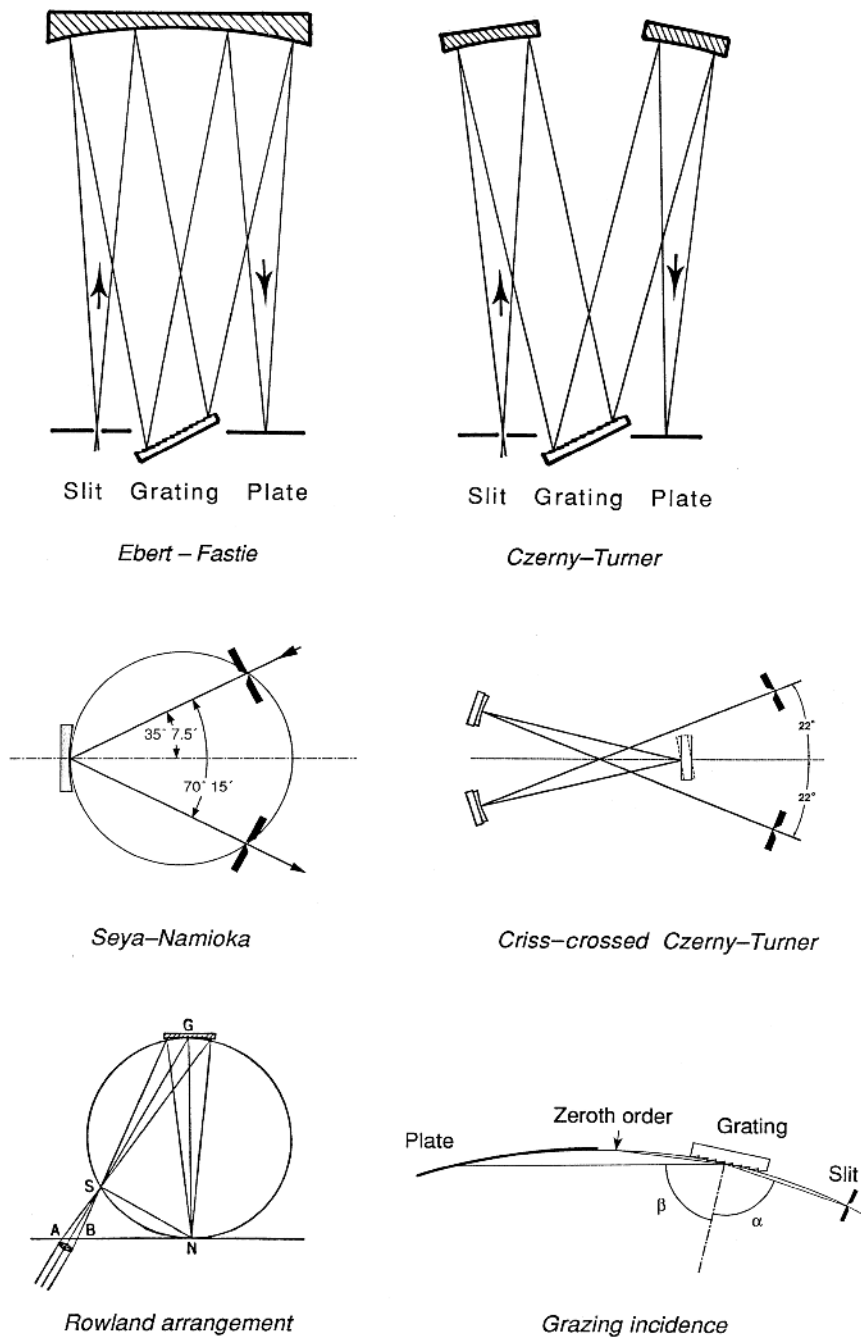


Fig. 6.25. Some common arrangements for grating spectrometers

6.2.3 The Fabry–Pérot Interferometer

The Fabry–Pérot interferometer was introduced by C. Fabry and A. Pérot in 1896. The interferometer consists of two flat, parallel mirrors with high reflectivity and low absorption. Light impinging on the interferometer will undergo multiple reflections between the mirrors whereby part of the light is transmitted (Fig. 6.26). The different components of the transmitted light will interfere at infinity, but the interference pattern can be imaged on a screen using a lens. According to the Fermat principle the relative phases of the different rays will not be changed by their passage through the lens. For the analysis we introduce the following symbols pertaining to light *intensity*:

R : reflectivity of a mirror layer,

T : transmission of a mirror layer,

A : absorption of a mirror layer,

with the relationship

$$R + T + A = 1. \quad (6.16)$$

For the *amplitudes*, the corresponding quantities are r , t , and a , i.e.,

$$r^2 = R, \quad t^2 = T, \quad a^2 = A. \quad (6.17)$$

Further, we introduce

ℓ : distance between the layers,

n : index of refraction between the layers,

θ : angle of incidence of the light,

f : focal length of the lens,

λ : wavelength of the incoming monochromatic light,

ϕ : phase shift between two successively emerging rays, and

s, S : amplitudes.

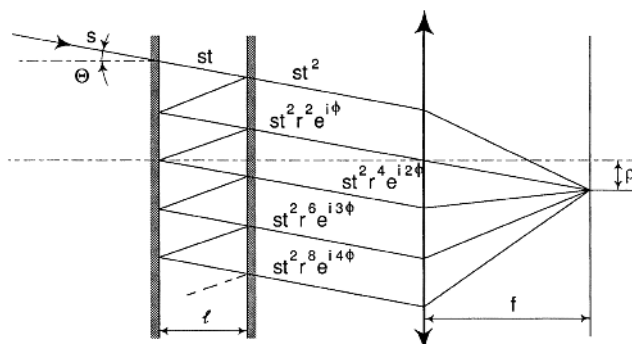


Fig. 6.26. Ray tracing in a Fabry–Pérot interferometer

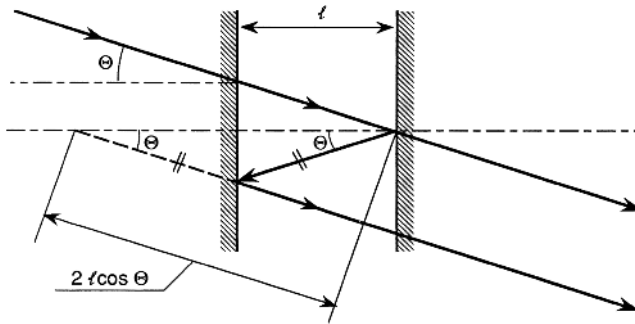


Fig. 6.27. Evaluation of the retardation

We will first calculate the optical path difference Δ (the *retardation*) between two successive rays making use of Fig. 6.27, namely

$$\Delta = 2n\ell \cos \theta. \quad (6.18)$$

Constructive interference requires

$$\Delta = m\lambda, \quad (6.19)$$

where m is normally a large integer ($m \simeq 10^4$). All rays that are incident on a conical surface are equivalent. Thus we will obtain a system of rings on the screen. The radius of a ring is denoted by ρ . For small angles we have $\cos \theta = 1 - \theta^2/2$ and $\theta = \rho/f$, which together with (6.18) and (6.19) yields $2n\ell(1 - \rho^2/2f^2) = m\lambda$ and

$$\rho = f \sqrt{(2n\ell - m\lambda)/n\ell}. \quad (6.20)$$

Thus, for the case when constructive interference occurs on the symmetry axis (the square root is zero for $m = m_0$), rings with $m = m_0 - 1, m_0 - 2, \dots$ will have radii proportional to $\sqrt{1}, \sqrt{2}, \sqrt{3}$ etc.

We shall now study the intensity distribution in more detail. Using Fig. 6.26 we find that the total transmitted amplitude S for the case of $a = 0$, i.e. $t^2 = 1 - r^2$, is given by the geometrical series

$$S = st^2(1 + r^2 e^{i\phi} + r^4 e^{i2\phi} + r^6 e^{i3\phi} + \dots) = \frac{s(1 - r^2)}{1 - r^2 e^{i\phi}}, \quad (6.21)$$

where the phase shift ϕ is given by

$$\phi = \frac{\Delta}{\lambda} 2\pi = \frac{\Delta}{c} 2\pi\nu. \quad (6.22)$$

From the amplitude S we obtain the corresponding intensity I

$$I = |S|^2 = \frac{s^2(1 - r^2)^2}{1 - r^2(e^{i\phi} + e^{-i\phi}) + r^4}.$$

But $(e^{i\phi} + e^{-i\phi})/2 = \cos \phi = 1 - 2 \sin^2(\phi/2)$. With $s^2 = I_0$ we then have

$$I = I_0 \left(1 + \frac{4r^2}{(1-r^2)^2} \sin^2 \phi/2 \right)^{-1}.$$

Finally, if the absorption in the layers is considered we obtain

$$I = \left(\frac{T}{1-R} \right)^2 I_0 \left(1 + \frac{4R}{(1-R)^2} \sin^2 \phi/2 \right)^{-1}. \quad (6.23)$$

This is called the *Airy distribution*, and is illustrated in Fig. 6.28. The maximum intensity

$$I_{\max} = I_0 \left(\frac{T}{1-R} \right)^2 \quad (6.24)$$

is obtained for $\phi = 0, 2\pi, \dots$, while the minimum intensity

$$I_{\min} = I_0 \left(\frac{T}{1+R} \right)^2 \quad (6.25)$$

is obtained for $\phi = \pi, 3\pi, \dots$ etc.

The separation between maxima is called the *free spectral range*. In frequency units it is given by

$$\Delta\nu_{\text{fsr}} = \frac{c}{\Delta} = \frac{c}{2n\ell \cos\theta} = \frac{c}{2n\ell}. \quad (6.26)$$

The half-width of a transmission peak is

$$\delta\nu = \frac{c}{\pi} \frac{1-R}{\Delta\sqrt{R}} \quad (\text{for large values of } R). \quad (6.27)$$

The ratio between these two quantities is called the *finesse* N and is determined only by the reflectivity R of the layers

$$N = \frac{\Delta\nu_{\text{fsr}}}{\delta\nu} = \frac{\pi\sqrt{R}}{1-R}. \quad (6.28)$$

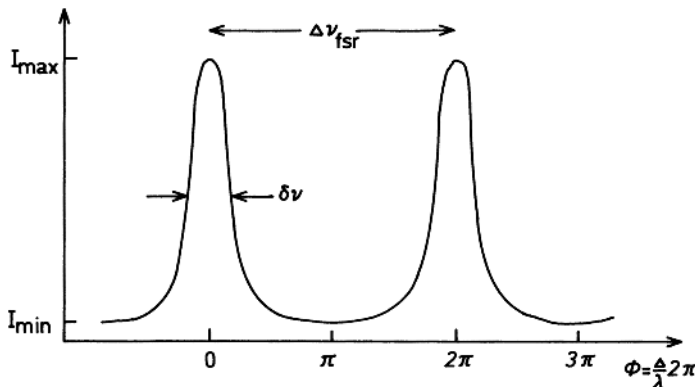


Fig. 6.28. Airy distribution from a Fabry-Pérot interferometer

The resolution of the Fabry–Pérot interferometer is

$$\mathcal{R} = \frac{\lambda}{\delta\lambda} = \frac{\nu}{\delta\nu} = \frac{\nu}{\Delta\nu_{\text{fsr}}} \frac{\Delta\nu_{\text{fsr}}}{\delta\nu} = \nu \frac{2n\ell}{c} N. \quad (6.29)$$

The variable ϕ in the Airy function is

$$\phi = \frac{2n\ell \cos \theta}{\lambda} \cdot 2\pi. \quad (6.30)$$

Thus, for a given wavelength λ we can run through the transmission curve in Fig. 6.28 by varying θ , n or ℓ .

In a photographic recording the ring system is recorded as a function of θ . For a photoelectric recording $\theta = 0^\circ$ is chosen by placing a small hole on the symmetry axis, and the intensity of the central spot is recorded with a photomultiplier tube. Now either ℓ or n is changed. The Fabry–Pérot interferometer normally consists of two flat quartz substrates with reflective coatings and the substrates are precisely separated by Invar spacers. n can then be varied by changing the gas pressure in the Fabry–Pérot housing (pressure scanning). Alternatively, the spacing can be varied by using piezoelectric crystals in the mounts of one of the plates.

As an example, we will consider a Fabry–Pérot interferometer which has a mirror separation of 1 cm (air). The coatings have a reflectivity of 98%. We then have $\Delta\nu_{\text{fsr}} = c/2\ell = 15 \text{ GHz}$, $N \simeq 150$ and $\delta\nu = 100 \text{ MHz}$. If the interferometer is used at $500 \text{ nm} \leftrightarrow 6 \times 10^{14} \text{ Hz}$ then $\mathcal{R} = 6 \times 10^6$. Clearly, for such an interferometer the width of the spectral line from the light source is a limiting factor.

Because of small imperfections and the finite size of the circular aperture the practically achievable resolution is frequently reduced. Because of its high resolution the Fabry–Pérot interferometer has been much used for measuring hyperfine structure and isotope shifts. The spectral line of interest is then first selected by a monochromator or an interference filter. First, a free spectral range of sufficient width to accomodate all the spectral components of the line is chosen to allow the correct order of components to be determined. Then the plates are moved further apart, resulting in an increased resolution but also the inclusion of overlapping orders.

All hyperfine components have their own Airy functions, which are shifted with respect to each other. The Fabry–Pérot pattern repeats itself with a period of the free spectral range, which is used for the frequency calibration. An example of a Fabry–Pérot recording is illustrated in Fig. 6.29. The Fabry–Pérot interferometer was discussed in [6.79].

Interferometers with spherical mirrors can also be used. A frequently used arrangement is used in the *confocal* interferometer, where the mirror separation ℓ equals the radius r of the mirrors (Fig. 6.30). The naming of this interferometer is due to the fact that the focal length f of a mirror of radius r is $f = r/2$. In a confocal interferometer a light ray makes two double passes between the mirrors before the primary and the reflected beams again coalesce at the second mirror and can interfere.

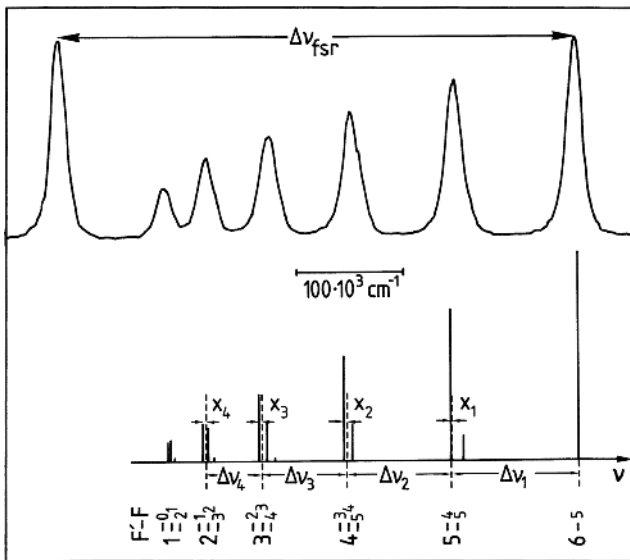


Fig. 6.29. Examples of a Fabry-Pérot recording obtained by pressure scanning. The hyperfine structure of ^{55}Mn ($I = 5/2$) in a $J = 7/2 \leftrightarrow 5/2$ transition at 5395 \AA has been recorded with an instrumental free spectral range of 15 GHz [6.78]

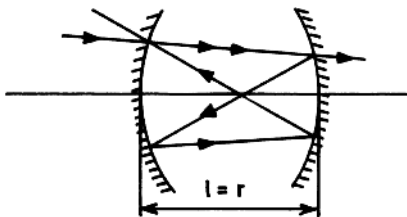


Fig. 6.30. Confocal interferometer [6.80]

Since this corresponds to a planar interferometer with double the mirror separation the free spectral range for a confocal interferometer is given by

$$\Delta\nu_{\text{fsr}} = \frac{c}{4n\ell}. \quad (6.31)$$

This interferometer is a special case of the *multi-pass interferometer*, where N double passes between the mirrors occur before interference. For such an interferometer we have

$$\Delta\nu_{\text{fsr}} = \frac{c}{N \cdot 2n\ell}. \quad (6.32)$$

It can be shown that the mirror radius and the mirror separation must fulfil the relation

$$r = \ell[1 - \cos(\pi/N)]^{-1}. \quad (6.33)$$

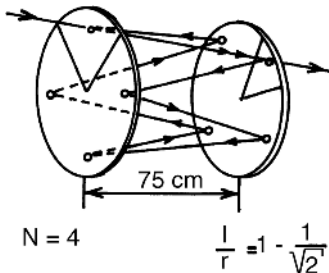


Fig. 6.31. Multi-pass interferometer for $N = 4$ [6.80]

For $N = 2$ we have the special case of the confocal interferometer. As an example, we can choose a multi-pass interferometer with a mirror separation of 0.75 m operating with $N = 4$ (Fig. 6.31). We find $r = 0.75/(1 - 1/\sqrt{2}) = 2.56$ m. The free spectral range for this device is $\Delta\nu_{\text{fsr}} = c/4 \cdot 2 \cdot 0.75$ m = 50 MHz.

Multi-pass interferometers are frequently used for monitoring laser beams of a very sharp frequency. A small free spectral range can be obtained without using a very long interferometer. Using special multilayer techniques it has recently become possible to produce coatings resulting in a finesse of the order of 10^3 ("supercavity"). Clearly, such instruments have important applications for ultra-stable lasers and precision metrology.

6.2.4 The Fourier Transform Spectrometer

The Fourier transform spectrometer (FTS) is a dual-beam interferometer, which is most frequently of the Michelson type, as shown in Fig. 6.32. If the arms of the interferometer have equal lengths, the path difference between the two interfering beams would be 0. If the mirror is moved $\Delta/2$ an optical path difference of Δ is introduced. For the case of monochromatic radiation and equally intense beams the intensity at the detector will be

$$I(\Delta) = I_0 \cos^2(\phi/2). \quad (6.34)$$

with

$$\phi = \frac{\Delta}{\lambda} 2\pi = \frac{\Delta}{c} 2\pi\nu. \quad (6.35)$$

If the light source emits a spectrum $B(\nu)$ we then obtain

$$\begin{aligned} I(\Delta) &= \int_0^\infty B(\nu) \cos^2 \left(\frac{\Delta}{c} \pi\nu \right) d\nu \\ &= \frac{1}{2} \int_0^\infty B(\nu) \left[1 + \cos \left(\frac{\Delta}{c} 2\pi\nu \right) \right] d\nu. \end{aligned} \quad (6.36)$$

The part of the above expression that depends on Δ is called the *interferogram*

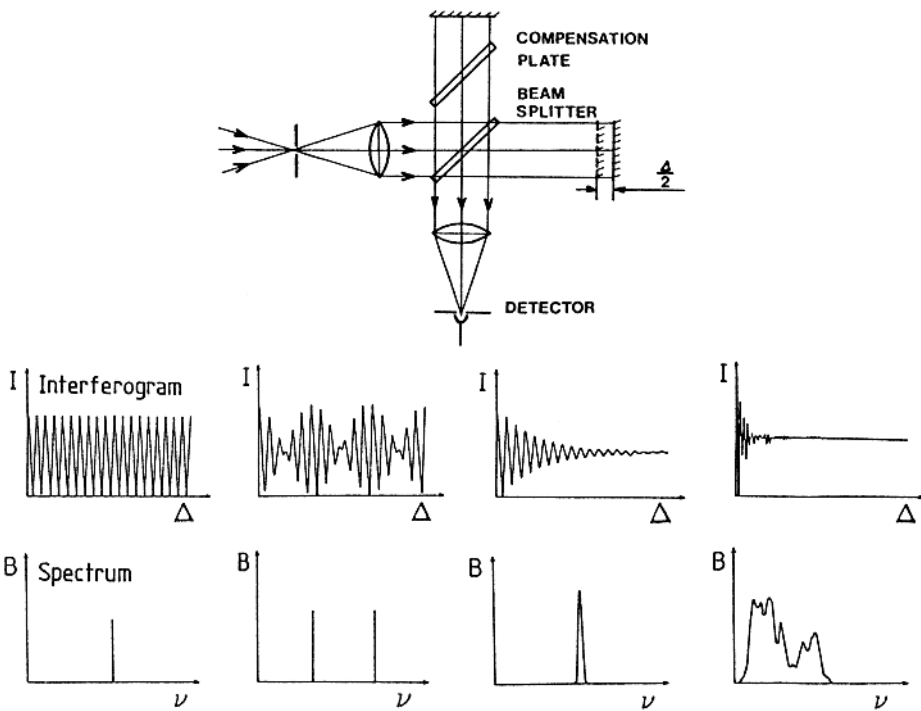


Fig. 6.32. Fourier transform spectrometer and basic signals (Courtesy: Ulf Litzén)

$$J(\Delta) = \frac{1}{2} \int_0^{\infty} B(\nu) \cos \left(\frac{\Delta}{c} 2\pi\nu \right) d\nu. \quad (6.37)$$

The spectrum $B(\nu)$ can be calculated from the interferogram $J(\Delta)$ as its Fourier cosine transform

$$B(\nu) \propto \int_0^{\infty} J(\Delta) \cos \left(\frac{\Delta}{c} 2\pi\nu \right) d\Delta. \quad (6.38)$$

Such a calculation is conveniently performed on a computer [6.81] and special, very fast processors have been constructed. In practice, the movable mirror can only be moved a limited distance ($< 1 \text{ m}$) and therefore the integration must be performed over a finite interval. Such a limited integration gives rise to side maxima on the spectral lines. By using a mathematical trick, which involves the multiplication of the integrand in (6.37) by a particular function, the unwanted maxima can be suppressed. However, this procedure, which is called *apodization*, gives rise to broader spectral lines. The interferogram has many similarities to a *hologram*. Every part of it contains information on the whole structure, but a high resolution is obtained only when a large part of it is utilized. One of the great advantages of Fourier transform spectroscopy is that all spectral lines are recorded at the same time (the *multiplex* or *Felgett advantage*). Unless photographic or array detector recording is used,

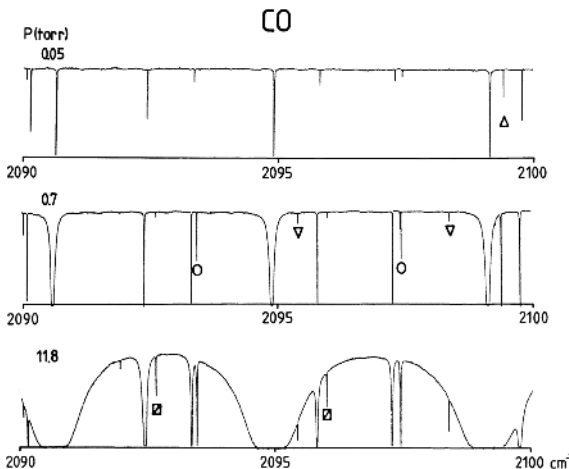


Fig. 6.33. Fourier-transform spectrometer recording for a gas containing different isotopic species of CO at increasing pressures [6.82]

the earlier mentioned types of spectral apparatus only collect information at a particular wavelength at any time. In the IR region, where photographic plates are not available, Fourier instruments are particularly valuable. Further, a Fourier transform spectrometer has a comparatively high light collecting efficiency, since it does not require narrow slits for the above-mentioned reasons (the *Jacquinot advantage*). Instruments of this kind have a very good signal-to-noise ratio and instruments with a resolution of $\mathcal{R} = 10^7$ can be constructed. The movement of the mirror is normally controlled by fringes from a HeNe laser. Examples of FTS spectra are shown in Fig. 6.33. Interferometers and interferometry have been discussed in [6.83–6.91].

6.3 Detectors

Historically, the photographic plate is an important detector of light that has been spectrally decomposed by a spectral apparatus. Photographic emulsions are still important for recording the emission lines from ionized atoms. As we have already mentioned, the *photographic material* has the unique property of being an integrator over the intensity fluctuations of a light source. There are many types of films for spectroscopic use. In Fig. 6.34 regions of sensitivity for some emulsions are shown. The information stored on a plate can be sensed by a *microdensitometer* and transferred to a recorder. For the evaluation of emission spectra, reference lines from a different light source are frequently exposed on the same plate. A *comparator* is used to determine the relative positions of the lines on the plate.

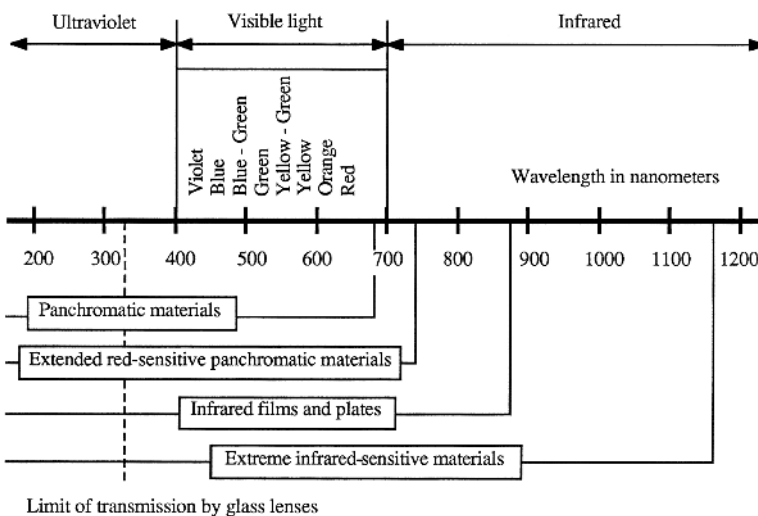


Fig. 6.34. Sensitivity regions for photographic emulsions [6.92]

In modern spectroscopy in the visible or the UV region a *Photomultiplier Tube* (PMT) is normally used. A PMT is an amplifying photocell. The light falls on a photocathode from which electrons are released due to the photoelectric effect. The electrons are accelerated through a chain of secondary electrodes, dynodes, that are held at increasingly higher potential. The dynodes, which are normally covered with CsSb, release secondary electrons and an avalanche amplification is obtained. A current that can be more than 10^6 times stronger than the primary photocurrent is obtained from the collecting anode. In Fig. 6.35 a PMT and its electrical supply are shown. A number of cathode materials with different spectral sensitivities can be chosen. The sensitivity is frequently expressed as the *quantum efficiency*, which is the number of photoelectrons (< 1) that can be obtained per incoming absorbed photon. Two common materials are Na_2KSbCs ("trialkali") and AgOCs . The so called ERMA cathode materials provide an approximatively flat spectral response out to $0.9 \mu\text{m}$. In Fig. 6.36 curves for a number of materials are shown. S designations for the materials are frequently used (e.g., S20).

In many cases it is important to minimize the *dark current* of the PMT. The number of thermally released electrons can be reduced by cooling. For most materials no further improvement is obtained below -30°C , except for red-sensitive materials with, for example, an S1 response, for which dry ice (222K) or liquid nitrogen (77K) cooling is advisable. The dark current in PMTs can be reduced by a factor of 10 or more by cooling.

No detectors of the PMT type exist for the IR region. Other types of detectors are instead used. A *thermocouple* can be a useful detector at long wavelengths. A *bolometer* is a resistance thermometer with a platinum wire

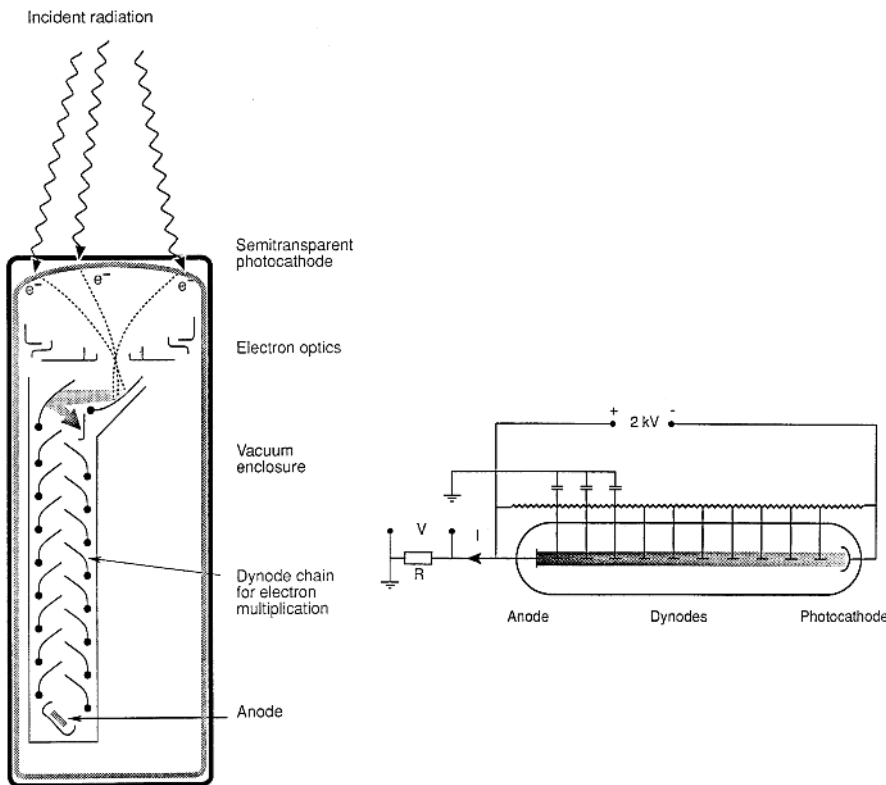


Fig. 6.35. Construction of a photomultiplier tube and its high-voltage supply

or a thermistor as a sensor. Certain crystals are *pyroelectric*, i.e. they give rise to an electrical potential between opposite surfaces when heated. Lithium niobate is used for such purposes. *Photoconducting detectors* are particularly useful in the IR region. Especially common is the *lead sulphide* (PbS) cell, which operates at room temperature, but with a rather slow ($\sim ms$) response time. Detectors made of *indium arsenide* ($InAs$) or *indium antimonide* ($InSb$) are considerably faster and are frequently cooled to liquid nitrogen temperatures (77 K). Further down in the IR region, e.g. around $10\mu m$, cooled *mercury cadmium telluride* ($HgCdTe$) detectors are used. Sensitivity curves for different detector materials are shown in Fig. 6.37.

Since the internal low-noise amplification of PMTs has no counterpart in the IR region (except possibly for the case of *avalanche diodes*) one has to rely on low-noise electronic amplification. Noise is normally a greater problem in the IR region than in the visible region. One remedy in the IR region is to use *heterodyne detection*, as discussed in Sect. 10.2.1. Optical detectors have been discussed in [6.93–6.100].

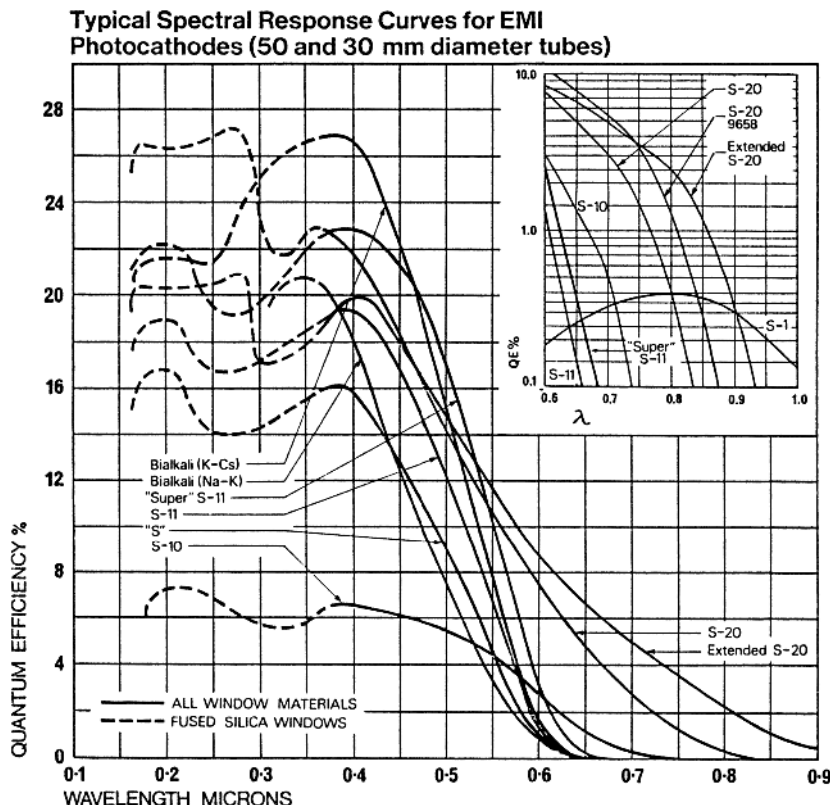


Fig. 6.36. Quantum efficiency curves for various photocathode materials (Courtesy: EMI)

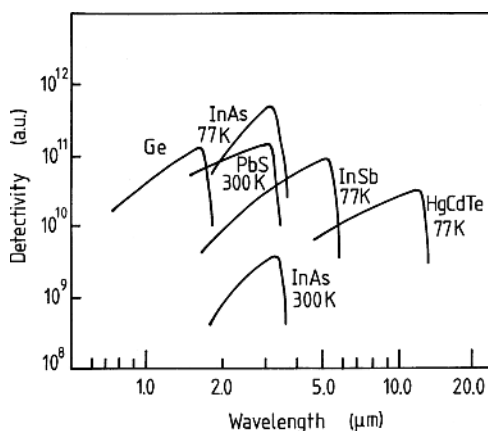


Fig. 6.37. Sensitivity curves for infrared detector materials

We shall conclude this section on detectors by briefly describing *array detectors* which combine the advantages of the integration and multiplexing characteristics of the photographic plate, as well as the electronic read-out of the PMT. In these solid-state devices, a large number of light-sensitive elements (256, 512 or 1024) are closely arranged in a row. Each one is connected to one channel of a multichannel analyser, in which a certain number of counts are stored, proportional to the intensity of the impinging light. If the array of detectors is arranged in the focal plane of a spectrograph, the spectrum is immediately obtained in the multichannel analyser (Optical Multichannel Analyser, OMA). A linear diode array can consist of, for example, 512 optical diodes, each $50\text{ }\mu\text{m}$ wide and 2.5 mm high. The elements then form an “electronic photographic plate” of size $25 \times 2.5\text{ mm}^2$. In order to attain a higher light sensitivity the array can be placed behind an *image intensifier tube*, which is based on a microchannel plate [6.101]. The arrangement is shown in Fig. 6.38. The spectrum illuminates a photocathode in which

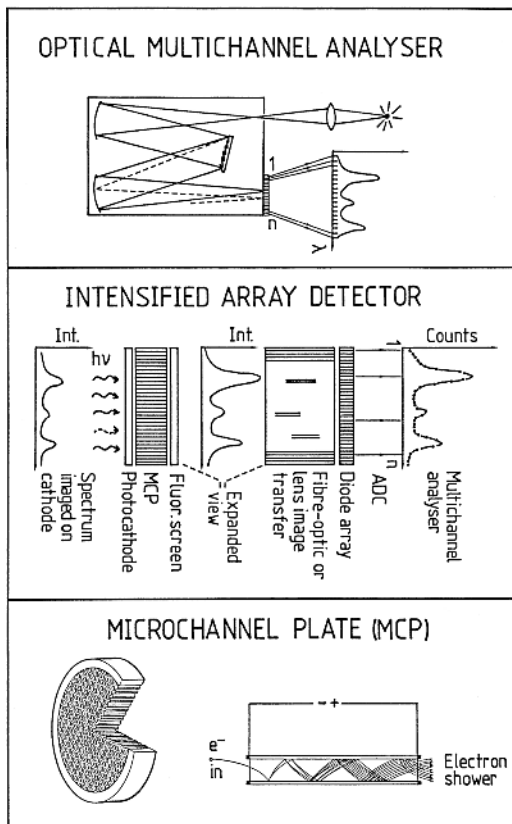


Fig. 6.38. Optical multichannel analyser with microchannel-plate image intensifier

electrons are released. The electrons are sucked into the narrow channels of the microchannel plate. The channels are covered with a material emitting secondary electrons and multiplication occurs as the electrons pass along the channel, propelled by an applied electric field. The showers of electrons, that are spatially arranged corresponding to the primary spectrum, impinge on a phosphor screen that produces an amplified image of the original spectrum. The light is then transferred to the diode array with retained spatial information, sometimes employing bunches of optical fibres. An amplification of more than 10^4 can be obtained. The high voltage for the channel-plate operation can be pulsed rapidly, and thus the whole detector assembly can be gated to be sensitive during time intervals down to 1 ns. This type of operation is of great interest, e.g., for background rejection in connection with spectroscopy using short laser pulses.

Array detectors can also be two-dimensional and can be used for imaging. We will discuss spectroscopic applications of such imaging later. The field of solid-state array detectors is rapidly developing, driven by TV applications. The whole area of CCD (Charge Coupled Device) technology will undoubtedly yield interesting new possibilities for advanced detection of spectroscopic information. Imaging electro-optic detectors have been discussed in [6.102–6.104].

In particular, imaging spectrometers can be constructed, in which different spatial locations along a line across the object are imaged along the entrance slit. In the perpendicular direction the spectrum can be dispersed, and thus the full spectrum in each point along the chosen line is recorded on a two-dimensional detector. This technology is used, for example, in “push-broom” remote-sensing systems installed in airplanes or satellites (Sect. 6.6.2). A further application of such two-dimensional detectors is to provide simultaneous spectral and temporal resolution for an object. In such a system the detector is placed in the focal plane of a streak camera (Sect. 9.5.1) preceded by a spectrometer.

The human eye is a very high resolution detector, which is highly integrated with the brain to perform real-time object detection and identification. The high acuity part of the retina is the approximatively 1.5 mm diameter *fovea* (“yellow spot”), where some 5 million colour-sensitive *cone* receptors capture the scene. More spread across the retina are the much more light-sensitive *rod* receptors, which, however, do not distinguish colours. Thus, at low-ambient-light conditions all objects are only vaguely seen (by the rods) on a grey-scale. Enhanced *night vision* is obtained using an image intensifier tube, where the input photocathode side of the tube is placed in the image plane of the light-collecting optics, and an eyepiece lens is used to observe the thousand-fold intensified image on the phosphor side of the tube. Clearly, any colour perception is lost in the process, and images appear green, since that is the colour of the most efficient phosphors.

However, there is a way to achieve “*colour night vision*” [6.105, 6.106], if blue, green and red filter sectors are used in two synchronously rotated filter wheels placed on either side of an image-intensifier tube which has been equipped with a special broad-band (“white”) phosphor. This phosphor is similar to that used in fluorescent lamp tubes, where the strong UV mercury lines from the heated vapour are converted into white light [6.107]. The three different colours are now intensified separately. For example, when the red-transmitting filter sector is in front of the cathode, the red parts of the image are intensified into a white image, which is observed through a red-transmitting filter. In the same way, the blue and green parts of the object are intensified (with colour preserved!). If the filter wheels rotate fast enough, the brain will see the full colour image without flickering. By proper adjustment of sensitivities and filter transmissions the normal colours are seen, since moon- or star-light basically has a very similar spectral distribution as the sun- or daylight. In principle, the same result is obtained if filtered images are recorded by a black-and-white CCD detector and then co-processed digitally into a colour TV image.

We will finish this section on detector technology by mentioning some new developments in X-ray imaging. Traditionally, photographic films which are blackened by the high-energy X-ray quanta, have been used in medical radiology. A much higher sensitivity is obtained using *image plate technology* [6.108]. Instead of the silver bromide grains the “emulsion” contains microscopic crystals of certain rare-earth salts. The absorbed energy of the X-ray quantum transfers the rare-earth ion into a long-lived metastable state and a “latent” image is formed. The image information is sequentially read out with a scanned and focused He-Ne laser beam, transferring the metastable ions into a higher, short-lived state from which blue fluorescence light is emitted in the decay. A digitized image is obtained, which allows efficient processing and storage. By proper light treatment the plates can be again prepared with the ions in the proper state to allow repeated use of the same image plate.

CCD detectors can also be used for X-ray imaging [6.109], e.g. for dental applications [6.110].

6.4 Optical Components and Materials

6.4.1 Interference Filters and Mirrors

Filters of different kinds are employed to select a certain spectral region. Relatively narrow spectral regions can be isolated using an *interference filter*. Such a filter for a wavelength λ is, in its simplest form, a Fabry-Pérot interferometer with a mirror separation of $\lambda/2$. Transmission maxima are also obtained for the wavelengths $\lambda/2$, $\lambda/3$, $\lambda/4$ etc. Filters for the short wavelength region, $\lambda < 240$ nm, are frequently made in this way with partially reflecting metal

layers on each side of a $\lambda/2$ dielectric layer. Transmission maxima at shorter wavelengths are effectively absorbed by the substrate material (e.g., quartz; see below). The absorption of the metal layers reduces the transmission of the filter. Because of this, *multiple dielectric layers* are used almost exclusively at longer wavelengths. In order to achieve a high reflectivity and low absorption many layers of thickness $\lambda/4$ with alternating high and low refractive indices (e.g., ZnS, $n = 2.3$ and MgF₂, $n = 1.35$) are used. The number of layers used determines the sharpness of the filter. The centre wavelength is determined by the thickness of the spacer layer. By using two or more filters of this kind in series (multicavity filter), with coupling layers to reduce reflection losses, sharper filters can be constructed. Suppression of transmission maxima at shorter wavelengths can easily be achieved by combining the interference filter with a high-pass coloured glass filter (Sect. 6.4.2). Unfortunately there are no simple efficient low-pass filters for suppressing long wavelengths. If such suppression is required a filter with *induced transmission* can be used. Such a filter, which is a hybrid between a metal-dielectric-metal filter and an all-dielectric filter, is characterized by the absence of long-wavelength transmission. In order to obtain a sharp interference filter with complete suppression outside the passband it can be necessary to combine a multicavity filter, an induced transmission filter and a high-pass coloured glass filter to form an integrated composite filter. Examples of individual transmission curves are shown in Fig. 6.39.

The transmission maximum of an interference filter is shifted towards shorter wavelengths if it is used at an inclined angle. The new transmission wavelength λ_θ is related to the nominal wavelength λ_0 by

$$\lambda_\theta = \lambda_0 \frac{\sqrt{n^2 - \sin^2 \theta}}{n}. \quad (6.39)$$

Here θ is the angle of incidence and n is the refractive index of the spacer layer. As an example, for $\theta = 10^\circ$, $n = 1.45$ and a filter wavelength of 600 nm we obtain $\Delta\lambda_\theta = \lambda_0 - \lambda_\theta \simeq 4$ nm. This means that if a filter is used in a converging or diverging beam of light, the transmission profile is somewhat shifted towards shorter wavelengths. For a cone of light with an angle at the apex of 2θ the effective shift is about $\Delta\lambda_\theta/2$.

Mirrors are also made using multiple dielectric layers of thickness $\lambda/4$. The more layers that are added, the better the reflectivity that can be achieved in a certain wavelength region. In Fig. 6.40 the effect of an increase in the number of layers is demonstrated. A reflectivity better than 0.999 can be obtained using 30 layers. Clearly, thin-film techniques of this kind are of great importance for the construction of laser cavities and for interferometers with sharp frequency discrimination characteristics.

We will also briefly discuss *anti-reflection layers*. A surface without any special preparation between an external medium (frequently air), with refractive index n_0 , and an optical component with refractive index n , has a reflectivity R given by

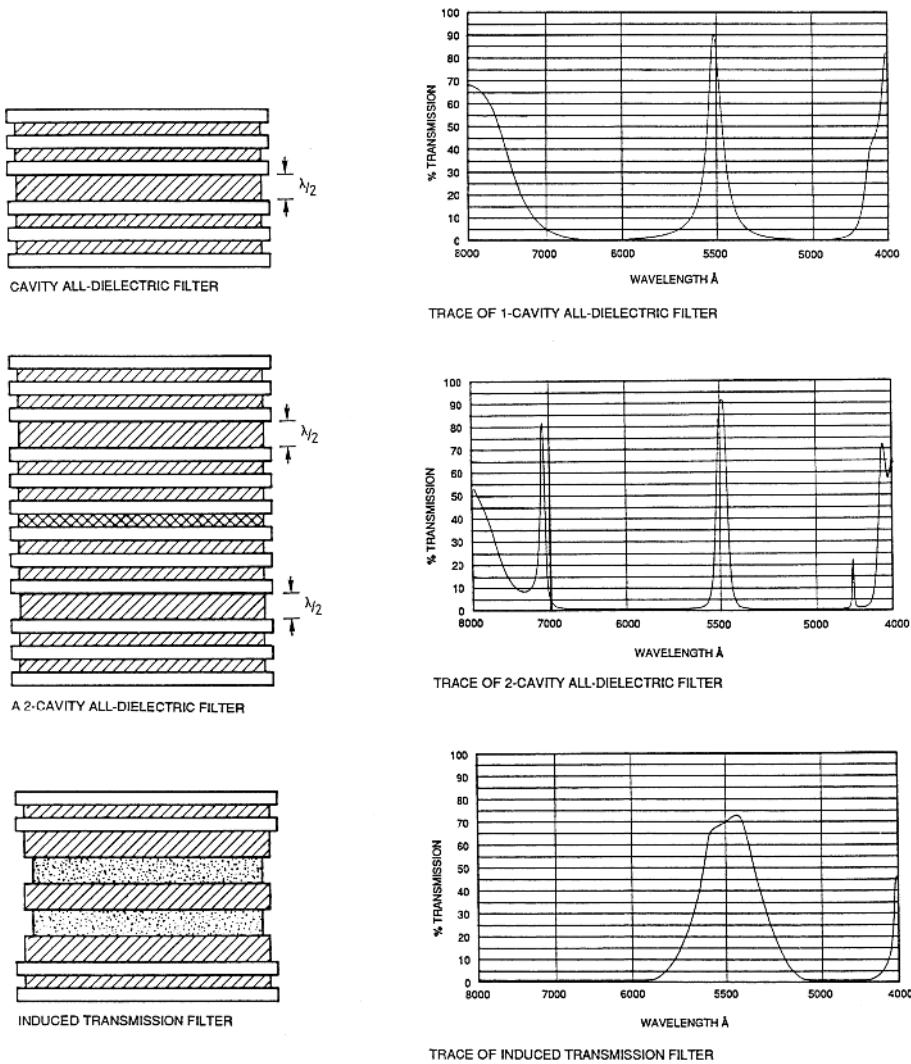


Fig. 6.39. Interference filter layers and resulting transmission curves [6.111]

$$R = \left(\frac{n - n_0}{n + n_0} \right)^2. \quad (6.40)$$

For a quartz-air boundary we have $R = [(1.5 - 1)/(1.5 + 1)]^2 \simeq 4\%$. It can be shown that if a layer of refractive index n_1 and thickness $\lambda/4$ is evaporated onto the optical component the reflectivity will be zero provided that $n_1 = \sqrt{n}$. MgF_2 with $n = 1.35$ is frequently a suitable material. In order to achieve anti-reflection properties in a larger wavelength region, e.g. in the whole visible region, multiple-layer techniques are used,

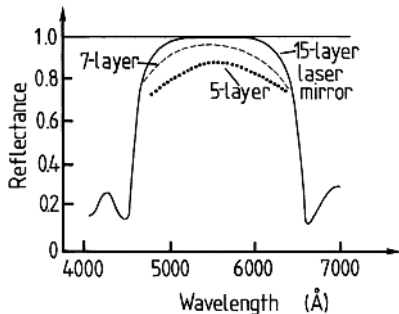


Fig. 6.40. Multiple-layer mirror reflectivity [6.112]

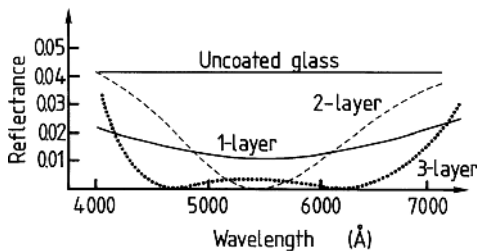


Fig. 6.41. Action of anti-reflection coatings [6.112]

as illustrated in Fig. 6.41. Advanced anti-reflection techniques are clearly a prerequisite for the construction of modern multiple-element lenses, etc., which would otherwise be cluttered by scattered light from the many surfaces.

Mirrors that are intended to be used over a wide range of wavelengths generally consist of *metal coatings* on a substrate. A layer thickness of the order of 150 nm is adequate. Reflectivity curves for some metal coatings are shown in Fig. 6.42. Silver has a reflectivity of 96–98% in the visible and IR regions. Since a silver surface tarnishes, a protective layer of, for example, SiO is needed. Gold is a highly suitable material for the IR region. Aluminum can be used over a wide range of wavelengths from UV to IR. Aluminum coatings are especially useful far down in the UV region, i.e. 200 nm and below. The reflective properties in the UV region can be improved by using a surface layer of SiO₂ or MgF₂, which also allows the otherwise very vulnerable mirror to be cleaned. In techniques involving high-power pulsed laser beams aluminum mirrors have a limited applicability because of the possibility of evaporation of the coating. For such applications dielectric mirrors or totally reflecting 90° prisms are used.

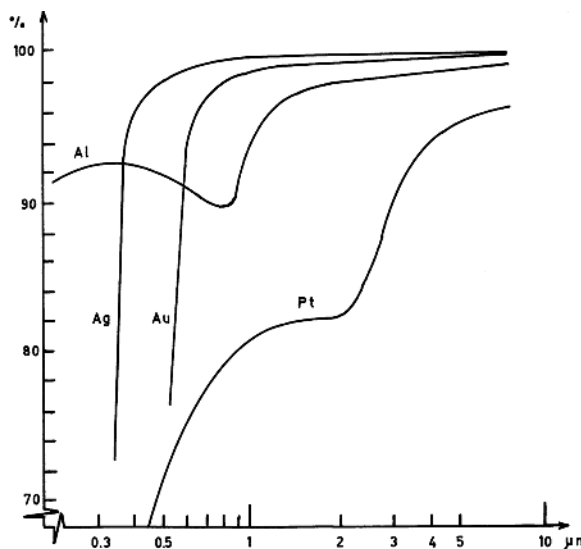


Fig. 6.42. Reflectivity of metal coatings

6.4.2 Absorption Filters

If the narrow region of transmission typical for an interference filter is not required, a simpler and much cheaper absorption filter can frequently be used. In *coloured glass filters* or plastic filters the absorption can be caused by simple or complex ions (e.g., nickel, cobalt, neodymium, praseodymium, uranium). Semiconductor-doped glasses are used as sharp cut-off filters. Using $\text{CdS}_x\text{Se}_{1-x}$ doping the absorption edge moves downwards for increasing x -values. Such filters are very efficient for suppressing short wavelengths. In Fig. 6.43 some transmission curves for coloured glass filters are given.

Sometimes *liquid filters* consisting of a quartz cuvette filled with a particular liquid can be quite useful. Organic liquids can be used as high-pass filters with cut-offs in the UV region, where coloured glass filters cannot be used. The cut-off wavelengths are schematically given in Fig. 6.44 for a number of liquids. Water solutions of inorganic salts are also of interest. For example, a mixture of nickel sulphate and cobalt sulphate is transparent in the UV region over 230–330 nm but completely blocks the visible region. Liquid filters have been discussed in [6.113, 6.114].

Absorption filters, in contrast to interference filters, can be used at any angle of incidence and can thus be used in strongly converging or diverging beams. It should be noted that certain coloured glass filters can exhibit rather strong broadband fluorescence when used to block UV light, which can sometimes cause problems. When a combination of an interference and a coloured glass filter is used, placing the interference filter in front of the fluorescing filter can improve the performance.

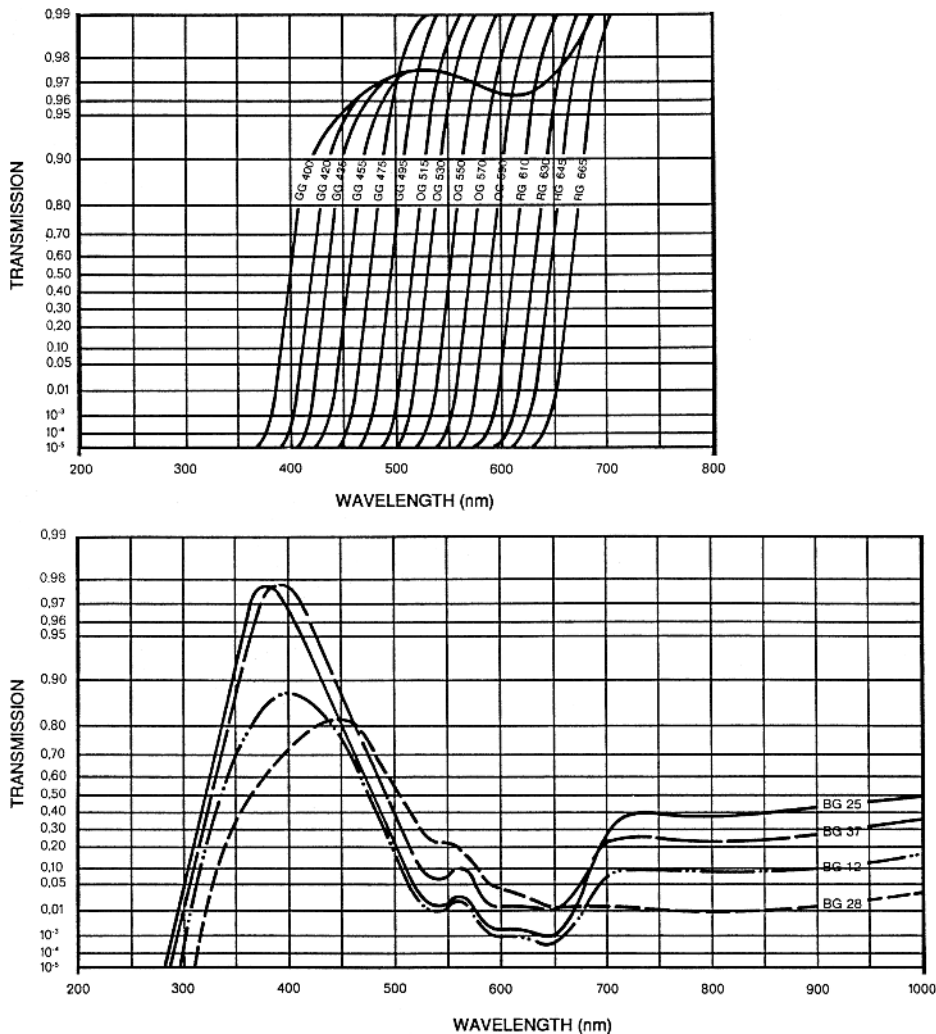


Fig. 6.43. Examples of transmission curves for coloured-glass filters (Courtesy: Schott Glaswerke)

Neutral-density filters are used to reduce the intensity of a light beam in a well-defined way, e.g. for testing the linearity of an optical detector. Filters of this kind should have a constant attenuation over large spectral ranges to facilitate their use. Normally, semitransparent metal films of chromium or nickel on quartz substrates are used. A filter is characterized by its transmittance T , or optical density D . D and T are related according to

$$D = \log_{10}(1/T) . \quad (6.41)$$

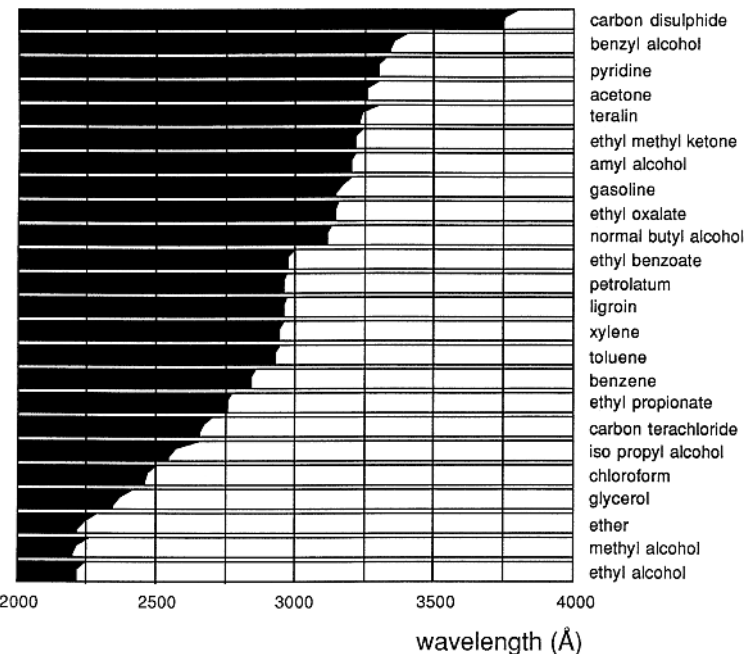


Fig. 6.44. Spectral characteristics for some liquid filters. Black indicates blocked transmission [6.113]

Thus, a filter of optical density $D = 1.0$ has a transmittance T of 0.1 (10%). When two neutral density filters are combined, the transmittances are multiplied, while the optical densities are added. In Table 6.2 some pairs of D and T values are given. For high-power laser beams, bulk absorbing glasses or combinations of inclined quartz plates (Fresnel reflection) must be used [6.115].

Finally in this section we would like to mention the rapidly emerging field of “smart-window” technology [6.116, 6.117], which can provide variable optical properties for windows and mirrors. *Electrochromic films*, which change their transmission or colour when an electric voltage is applied across the film, are used. WO_3 is the most commonly used material, which is influenced by ionic transport through an adjacent ionic film. Transparent electrode films attached to normal glass sheets can be made from tin-doped In_2O_3 . Electrochrome windows have the potential for reducing the need for air-conditioning considerably in hot regions. A mirror preceded by an electrochromic film will have a variable reflectivity. This technology is already commercially available in anti-glare rear mirrors for cars. The related phenomenon of *photochromism* is used in the eyeglasses, which reduces transmission when subjected to sunlight.

Table 6.2. Optical densities D and transmissions T

| D | T[%] | D | T[%] |
|-----|------|-----|------|
| 0.0 | 100 | 0.8 | 16 |
| 0.1 | 79 | 1.0 | 10 |
| 0.2 | 63 | 1.5 | 3.1 |
| 0.3 | 50 | 2.0 | 1.0 |
| 0.4 | 40 | 3.0 | 0.1 |
| 0.5 | 32 | 4.0 | 0.01 |

6.4.3 Polarizers

Polarized light can be obtained or analysed using certain prisms or polarizing films. Reflection at a non-normal angle of incidence at the flat surface of an optical material also results in a certain degree of polarization according to the Fresnel formulae (Fig. 6.45). In particular, at the Brewster angle ($\tan \theta = n$) the reflected light is fully polarized perpendicularly to the plane of incidence (the plane containing the normal to the surface) (S-polarized light). Light components polarized in the plane of incidence (P-polarized light) penetrate into the medium without loss. A stack of glass or quartz plates at the Brewster angle will successively reflect almost all components perpendicular to the plane of incidence, leaving a highly polarized transmitted beam.

A convenient way to attain a very high degree of linear polarization is to use prisms made of the birefringent material calcite (CaCO_3). The arrangements in *Glan-Taylor* and *Glan-Thompson* polarizers are shown in Fig. 6.46. Both these polarizers consist of a combination of two prisms, in the first type air-spaced, in the second case cemented. The prism angle has been chosen such that the ordinary beam is totally internally reflected and absorbed laterally in the prism, while the extraordinary beam is transmitted into the

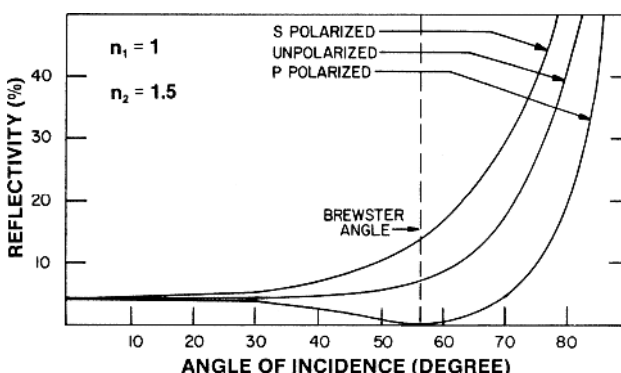


Fig. 6.45. Polarization-dependent reflectivity at an optical surface (Fresnel formulae) [6.112]

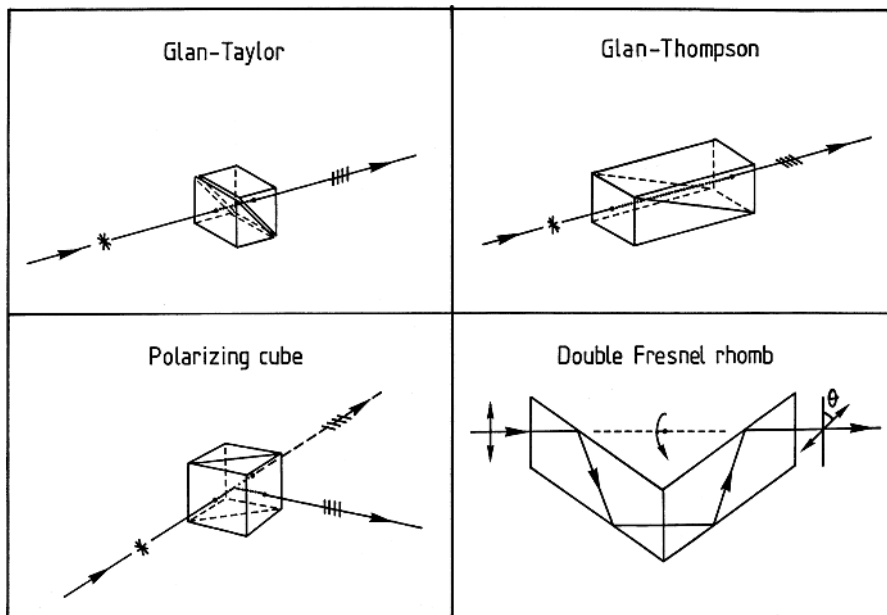


Fig. 6.46. Polarizing prisms (After material from Melles Griot)

next prism and leaves it undeviated. Glan-Thompson prisms have a larger acceptance angle but cannot be used in the UV region because of absorption in the optical cement. Both types of Glan prism exhibit an extinction ratio of better than 10^5 for crossed polarizers.

A *polarizing beam-splitter* is formed by combining two right-angle prisms into a cube. A special multilayer film between the prisms acts as a stack polarizer as described above. An unpolarized beam is thus divided into two perpendicular highly polarized components. Conversely, two polarized beams can be combined into a single beam using this type of component.

Optical retarder plates, of appropriate thicknesses, made of birefringent material, normally crystalline quartz or mica, can be used to rotate the plane of polarization for linearly polarized light or to produce circularly polarized light. To rotate linearly polarized light by an arbitrary angle, a *double Fresnel rhomb* is very useful (Fig. 6.46).

Linear polarizers can also be made of *polyvinyl film* that has been stretched so as to align long chains of molecules. Different kinds of polarizer of this type are available for wavelengths from 200 nm up to the near-IR. In Fig. 6.47 examples of transmission and extinction curves are shown.

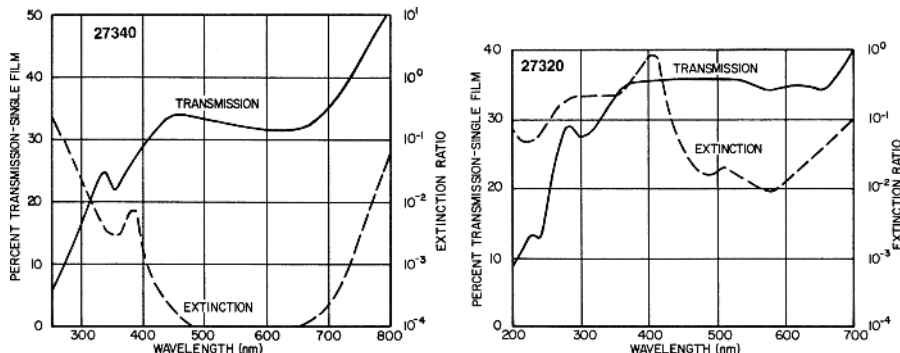


Fig. 6.47. Spectral characteristics of polyvinyl film polarizers (Courtesy: Oriel Corp., Stratford, CT, USA)

6.4.4 Optical Materials

Optical components are manufactured from transparent materials of certain refractive indices. We have already discussed the refractive properties of glass and quartz in Sect. 6.2.1. Here we will consider the transmission properties of optical materials. Optical glass is transparent from about 350 nm to 2.6 μm [6.118]. This region of transmission can be extended by using quartz. In Fig. 6.48 transmission curves for different qualities of quartz are shown. As can be seen, the best quartz has a transmission down to 170 nm. However, strong absorption bands can occur in the near-IR region, particularly at 2.7 μm . These are due to the presence of water (O–H bonds) in the quartz. Water-free quartz can be used up to about 3.5 μm .

The region of UV transmission can be extended down to 125 nm using CaF_2 and to 110 nm using LiF . These materials are also transparent in the

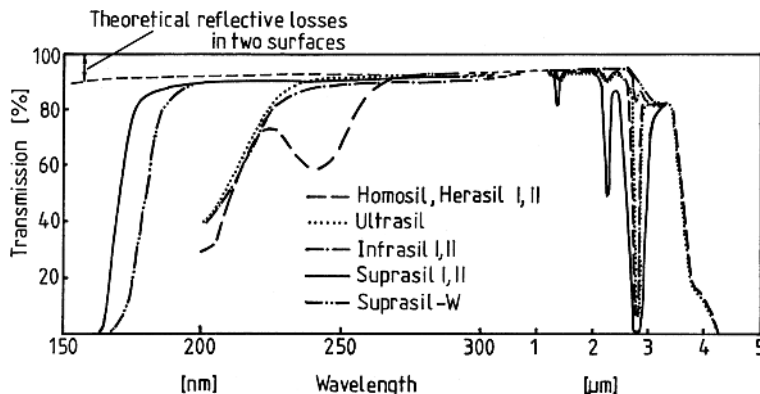


Fig. 6.48. Transmission curves for different qualities of quartz (Courtesy Heraeus Quarzglas GmbH)

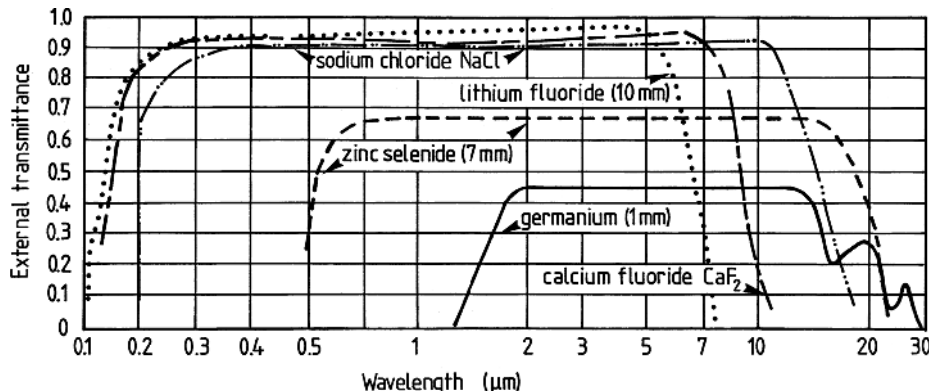


Fig. 6.49. Transmission curves for far-UV and IR-transmitting materials (After material from Oriel Corp., Stratford, CT, USA)

IR region out to 9 and 6 μm , respectively. At still longer wavelengths NaCl can be used. The transmission curves for these materials are shown in Fig. 6.49.

6.4.5 Influence of the Transmission Medium

In discussing the transmission of different optical materials we should also consider the properties of air. For laboratory spectroscopy it is important to note that oxygen, water vapour and carbon dioxide in the air strongly absorb wavelengths below 200 nm. Thus the spectroscopic equipment must be evacuated when working in short-wavelength regions (*vacuum spectroscopy*). Alternatively, for wavelengths above 145 nm the equipment can be flushed with nitrogen. Wavelengths measured in air must be corrected for the refractive index of air to yield *vacuum wavelengths*, which are those used to calculate the positions of energy levels. The wavelength corrections, $\Delta\lambda$, to be *added to an air wavelength* (15 °C, 760 torr) are given by the *Edlén formula* [6.119]

$$\Delta\lambda = (n - 1)\lambda_{\text{air}} > 0 \quad (6.42)$$

$$(n - 1) = 10^{-8} \left(8342.13 + \frac{2\ 406\ 030}{130 - \sigma^2} + \frac{15\ 997}{38.9 - \sigma^2} \right),$$

$$(\sigma = 1/\lambda, \sigma \text{ in } \mu\text{m}^{-1}).$$

The correction is graphically displayed in Fig. 6.50.

Air has strong absorption bands in the IR region, which are mainly due to H_2O and CO_2 . It seems clear that the slowly increasing CO_2 content of the atmosphere will lead to a gradual heating of the atmosphere [6.120]. In astronomical observations very long absorption paths through the atmosphere are obtained. The stratospheric ozone layer, at a height of about 25 km, absorbs strongly in a band around 9.5 μm . More interestingly, it absorbs all

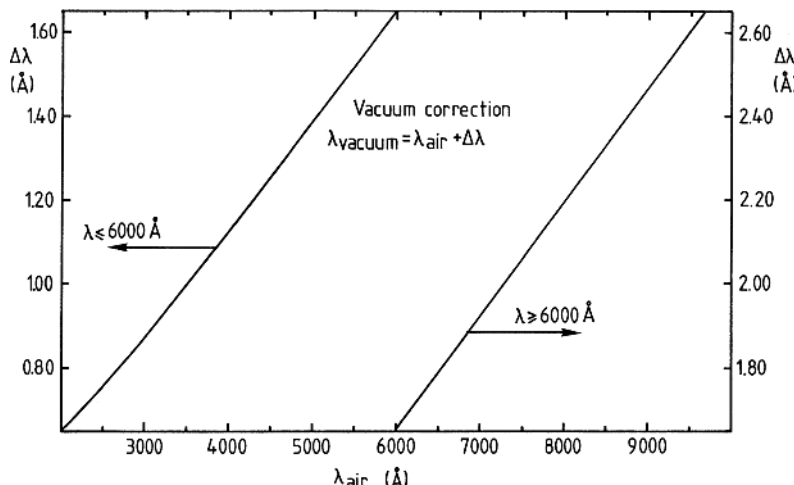


Fig. 6.50. Wavelength correction curve (Courtesy: P. Grafström)

radiation below 300 nm, which is essential for shielding life from mutagenic short UV radiation. In recent years it has become obvious that a depletion of the protecting ozone layer due to human activities is going on. One area of concern is the injection of nitrogen oxides (NO_x) into the stratosphere in the form of exhaust from high-flying, Supersonic Transport (SST) aeroplanes. Tropospheric NO_x is normally washed out as acid rain. More important is the influence of freons (chlorofluoro-carbons), from spray cans and cooling equipment, which are inert with respect to the normal atmospheric gases. Freons diffuse into the stratosphere, where they can react with the ozone molecules. The chemistry behind the ozone formation and depletion was awarded the Nobel prize in chemistry 1995 (*P. Crutzen, M. Molina and F.S. Rowland*). Strong regulations against freons are now being enforced. As the natural variation in the thickness of the ozone layer is quite large, it is difficult to establish trends. However, since the time constants for processes of the kind discussed here are tens of years, it is important to identify trends as early as possible. There is strong evidence for a growing Antarctic "ozone hole" during the (Antarctic) spring months [6.121–6.124]. Spectroscopic ozone-layer monitoring is being performed through absorption measurements from the ground (Dobson instruments) or from satellites and balloons. Ground-based vertical lidar sounding of ozone is also a powerful technique (Sect. 10.2.3). Air pollution and atmospheric chemistry have been discussed in [6.125–6.130].

The spectral distribution of the sun's radiation is shown in Fig. 6.51, both outside the atmosphere and at sea level with different absorption bands indicated. The vertical transmission of the earth's atmosphere, including longer IR wavelengths, is shown in Fig. 6.52. The curve for the whole atmosphere is depicted at the bottom, and individual constituent curves are included, too.

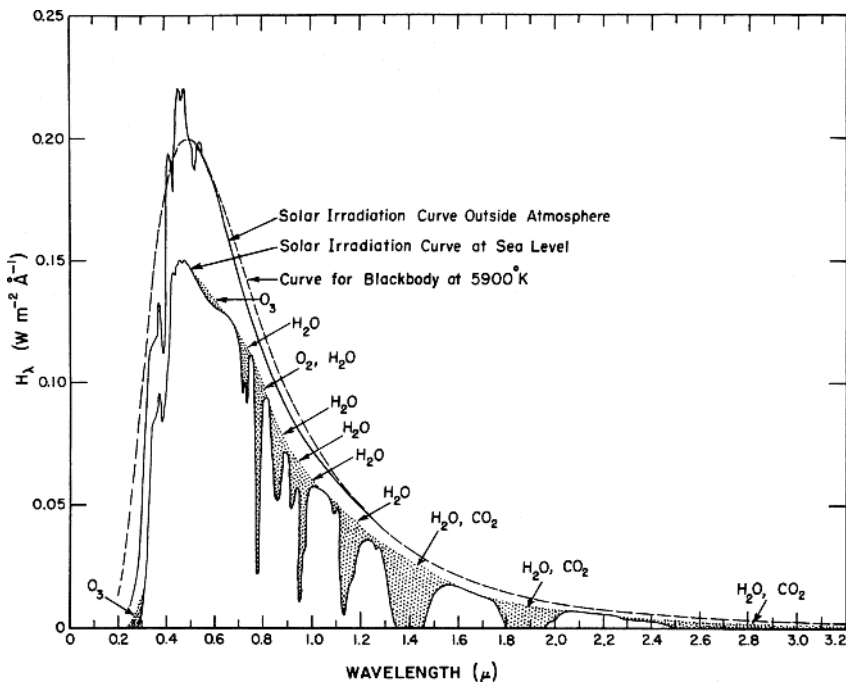


Fig. 6.51. Spectral distribution of the sun's radiation outside the atmosphere and at sea level with absorption bands indicated [6.131]

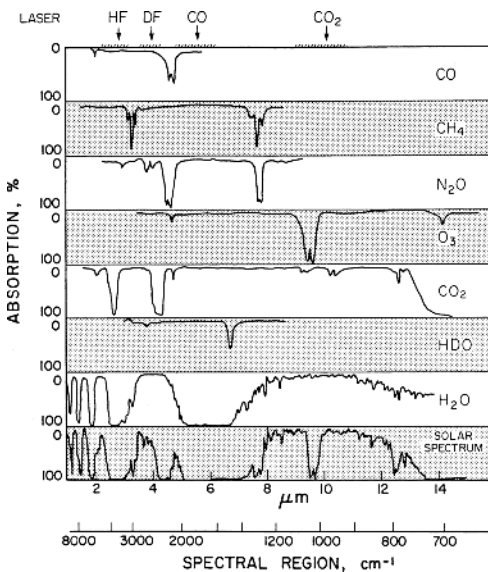


Fig. 6.52. Vertical absorption curve for the earth's atmosphere (bottom), and individual constituent absorptions [6.132]

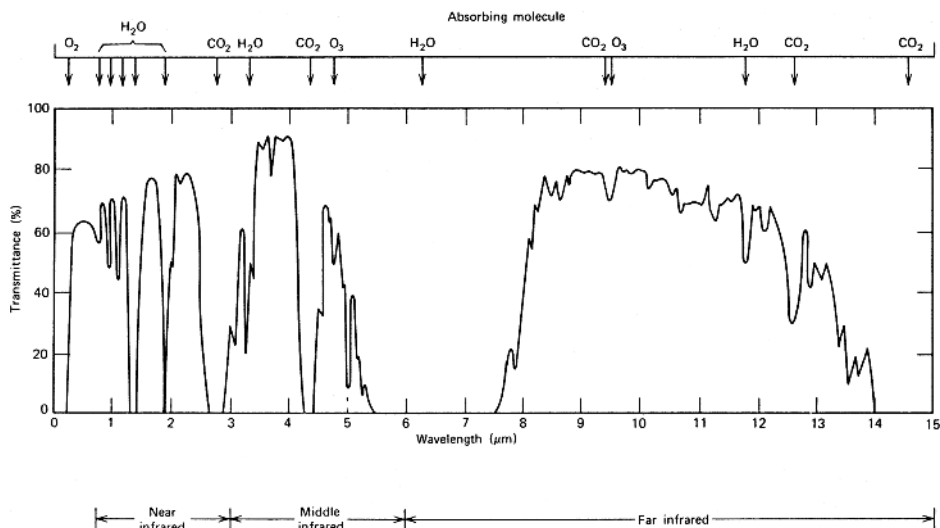


Fig. 6.53. Horizontal atmospheric absorption curve over a distance of 1.8 km at sea level [6.133]

These data will determine the spectral range of ground-based astronomical observations. A corresponding curve for horizontal atmospheric absorption at sea level over a distance of one nautical mile (1.8 km) is given in Fig. 6.53. This curve is of interest when considering free-laser-beam optical communica-

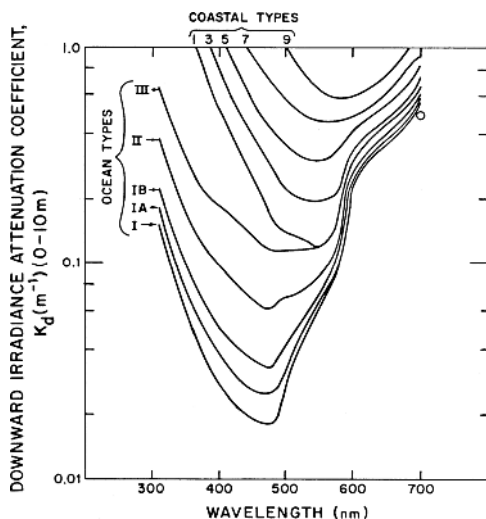


Fig. 6.54. Spectral dependence of the absorption coefficient for different types of sea water (From [6.139], based on data from [6.137, 6.140])

tions or passive and active forms of atmospheric remote sensing (Sects. 6.6.1 and 10.2). The absorption properties of the atmosphere have been discussed in [6.134–6.136].

We will conclude this section by giving the transmission properties of sea water [6.137, 6.138]. In Fig. 6.54 the absorption coefficients for different types of water are given in the visible region [6.139]. The “blue-green window” of water is clearly seen. The curves determine vertical visibility and the possibility of laser bathymetry (Sect. 10.3.1) etc. Communication with submarines using satellite-based blue-green lasers is being considered. The only alternative for such communication purposes is the use of radio waves of extremely long wavelength (VLW).

6.5 Optical Methods of Chemical Analysis

Several highly applicable methods of analysis rely on the interaction between light (UV–visible–IR) and matter. The wavelengths (energies) at which the interactions occur are characteristic for the individual substances (spectral “fingerprint”), and this forms the basis of qualitative analysis using light. Further, the intensities that are measured in such interactions are closely related to the concentration of the particular substance. Therefore quantitative analysis, which is frequently very accurate, can be performed.

The optical methods of analysis, as well as those based on X-ray transitions (Chap. 5) are of great interest for determinations of the presence and concentration of a very large number of substances. The presence of chemical elements can be determined and molecular identification can also be made. Molecular analysis can be performed by IR absorption spectroscopy and also by XPS (Chap. 5) and NMR (Chap. 7). We will briefly describe some applications of optical analysis methods.

In the steel industry, as well as in the chemical and pharmaceutical industries, there are clearly many fields of application for analysis techniques. In the field of medicine, determinations of haemoglobin and metal concentrations in blood and of glucose, albumin and heavy metals in urine are often performed. In the field of agriculture, it is of great interest to determine the concentration of certain trace elements in soil samples to assess the need for the addition of fertilizers. In environmental conservation it is necessary to measure the concentrations of a large number of substances in the air and water in low concentrations. Low concentrations are frequently given in ppm (parts per million: $1 : 10^6$), ppb (parts per billion, $1 : 10^9$) or ppt (parts per trillion, $1 : 10^{12}$). Frequently, it is necessary to be able to perform the analysis on quantities as small as 10^{-15} to 10^{-20} g. Using laser-spectroscopic techniques single atoms can be detected (Sect. 9.2.7).

The development of analytical methods has been in progress since the beginning of the 19th century. J.J. Berzelius (1779–1848) determined the constituents of about 2000 chemical compounds. The periodic table of the

elements was put forward by D. Mendeleyev in 1872. At that time only 67 elements were known. By 1900 the number had increased to 83. Even today the number of elements is increasing, approaching $Z = 114$, due to the possibilities at heavy-ion accelerators [6.141].

Analysis by optical techniques is frequently performed by measuring absorption. It is important to be able to correctly relate the absorption to the concentration. The relation which is called the *Beer–Lambert* law will now be considered.

6.5.1 The Beer–Lambert Law

Consider monochromatic light of intensity P_0 impinging on a sample of thickness b as illustrated in Fig. 6.55. The sample can be a solution in a cuvette or atoms in a flame from a specially designed burner. An intensity P_t is transmitted through the sample. (We disregard possible effects from the sample confinement). We now consider the conditions over a small interval Δx in the sample. Before the considered space interval, the intensity has been reduced to P , and it will be further reduced by ΔP in the interval Δx . The fractional attenuation $\Delta P/P$ is proportional to the number of absorbers, Δn , in the small interval Δx

$$\frac{\Delta P}{P} = -k\Delta n = -k_1 c \Delta x. \quad (6.43)$$

Here k and k_1 are constants and the last equality is valid for a uniform concentration c throughout the sample. When light passes through the sample, P changes from P_0 to P_t , n from 0 to N and x from 0 to b . By integration we obtain

$$\int_{P_0}^{P_t} \frac{dP}{P} = - \int_0^N k dn = - \int_0^b k_1 c dx, \ln \frac{P_0}{P_t} = kN = k_1 bc. \quad (6.44)$$

We now define the *absorbance* A

$$A = \log_{10} \frac{P_0}{P_t} = 0.434 \ln \frac{P_0}{P_t}. \quad (6.45)$$

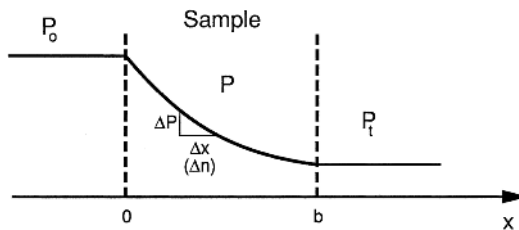


Fig. 6.55. Illustration of the Beer-Lambert law

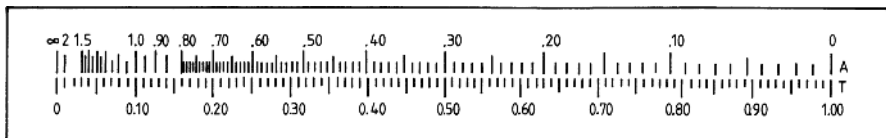


Fig. 6.56. Linear scale for transmittance and corresponding logarithmic scale for absorbance

Thus

$$A = k_2 c \quad (k_2 \text{ proportionality constant}) . \quad (6.46)$$

This is the *Beer–Lambert law*, stating that the absorbance is proportional to the concentration of absorbers in the sample.

The ratio P_t/P_0 is defined as the transmittance T . Thus we have

$$A = \log_{10} T^{-1} = 0.434 \ln T^{-1} . \quad (6.47)$$

We note that the absorbance A , and the optical density D , previously introduced (Sect. 6.4.2) are synonymous concepts.

We will now consider the accuracy of a concentration determined by a measurement of the transmission through the sample. In analytical instruments based on absorption measurements the transmittance or absorbance value is read off directly on a scale or is given digitally. In Fig. 6.56 a linear scale for transmittance and a corresponding logarithmic scale for absorbance are given (compare with Table 6.2). From (6.46) and (6.47) we find

$$\frac{\Delta c}{c} = \frac{\Delta A}{A} = -\frac{0.43}{A} \frac{\Delta T}{T} .$$

The relative accuracy in the concentration determination $\Delta c/c$ depends on the error in reading the scale (or the error in digitizing). Clearly, a small error ΔT in the T reading results in a large uncertainty in the absorbance if T is small (then also $A \cdot T$ is small). In the same way it is important that the full-scale deflection ($T = 100\%$) is suitably set in order to be able to determine small concentrations. If we assume that the uncertainty in the full-scale setting and in measurements is the same, we obtain the resulting relative concentration error by quadratic addition of the errors:

$$\frac{\Delta c}{c} = \frac{\Delta A}{A} = -\frac{0.43}{A} \sqrt{\left(\frac{\Delta T}{T}\right)^2 + \left(\frac{\Delta T}{1}\right)^2} = -\frac{0.43\sqrt{1+T^2}}{AT} \Delta T . \quad (6.48)$$

Hence, the error in the relative concentration depends on ΔT and on the factor $0.43(1+T^2)^{1/2}/AT$. The variation in this factor as a function of A is given in Fig. 6.57. The factor is large for small and large values of A and has a minimum for $A = 0.48$. The analysis performed above reflects the almost self-evident fact that it is much more difficult to measure accurately a concentration corresponding to very little absorption or very little transmission than to measure it in a situation for which about half of the light is absorbed.

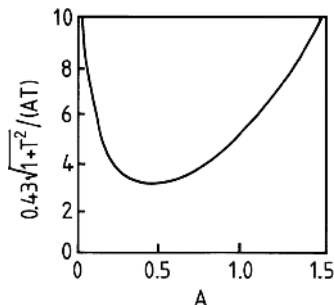


Fig. 6.57. Illustration of error distribution curve

In absorption measurements the atoms or molecules in the ground state are monitored. In contrast, the excited-state population is monitored in *emission* studies. The excitation can be performed in many ways, thermally or in a spark discharge. The intensity of the emitted light clearly depends on the concentration of the substance. If the excitation has been brought about through irradiation with light from an external light source, *fluorescence* light is obtained. The fluorescence light intensity can be directly related to the ground-state population.

6.5.2 Atomic Absorption/Emission Spectrophotometry

The colouring of flames when a metal salt is introduced was studied as early as the 18th century. In 1860 R. Bunsen and G.R. Kirchhoff established the connections between spectral emission lines and certain elements, i.e. *flame emission spectroscopy* was first used for qualitative analysis. Since then flame emission spectroscopy techniques have been further developed, including the construction of special burners into which the sample can be injected and electronic light-measuring equipment. The light emitted by thermally excited atoms is measured. However, only a small fraction of the atoms are excited in the flame, while most of them remain in the ground state. The Boltzmann law describes the relation between the number of excited and ground-state atoms N_{exc} and N_{gr} , respectively:

$$\frac{N_{\text{exc}}}{N_{\text{gr}}} = \frac{g_{\text{exc}}}{g_{\text{gr}}} e^{-\Delta E/kT}. \quad (6.49)$$

Here g_{exc} and g_{gr} are the statistical weights of the states ($g = 2J + 1$ for atomic states characterized by the total electronic angular momentum quantum number J). As an example, at $T = 2500\text{ K}$ we find for Na with the ground state $3s\ 2^1S_{1/2}$ and the first excited state $3p\ 2^3P_{1/2}$ ($\Delta E = 2.1\text{ eV}$, $g_{\text{exc}} = g_{\text{gr}} = 2$) that $N_{\text{exc}}/N_{\text{gr}} = 5 \times 10^{-5}$.

The accuracy and sensitivity in a measurement should be improved if the determination were instead based on the large number of ground-state atoms. Relatively speaking, the number of ground-state atoms does not change

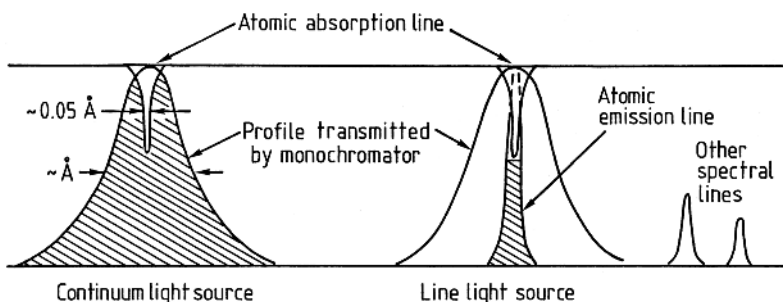


Fig. 6.58. Comparison between the use of a continuum and a line light source in atomic absorption measurements

significantly for a small change in temperature, while, on the other hand, the number of excited-state atoms depends strongly on the temperature. Observations of this kind suggest the introduction of the *atomic absorption method*, which has become a very common standard method for accurate measurements of low concentrations of elements.

Atomic absorption spectroscopy differs from normal spectrophotometry (Sect. 6.5.6) in one important aspect. As we have described before (Sect. 6.1.1), the linewidth of an atomic line is a few thousands of a nm. It is therefore necessary to use a line light source, since a monochromator of reasonable dimensions cannot resolve such a line. With a continuum light source filtered by a monochromator to a passband with a width of a few nm the absorption due to the atoms in the flame would be totally negligible (Fig. 6.58). On the other hand, if a *hollow-cathode lamp* is used, the linewidths for the corresponding element match and strong absorption can be obtained. The monochromator is still necessary to suppress other lines that do not originate in the ground state. The presence of such lines would clearly dilute the absorption by the atoms. Generally, a special hollow-cathode lamp is used for each element to be measured. In certain cases several elements can be combined in one hollow cathode. However, since the burning time of a lamp is limited to about 1000 hours, the advantage is limited. Instead, provisions for rapidly changing the lamps can be utilized. Recommended spectral lines for atomic absorption spectrophotometry are given in Table 6.3. The lines are generally strong resonance lines from the ground state and in some cases lines originating in metastable states.

A basic set-up for atomic emission, as well as absorption spectrophotometry is shown in Fig. 6.59. In the absorption mode it is necessary to modulate the output of the lamp, either by modulating the discharge current or by using a mechanical chopper. The signal at the PMT will then consist of a dc contribution due to the thermally excited atoms emitting the line studied and an ac contribution due to the transmitted hollow-cathode light. By detecting the ac component with a phase-sensitive ac amplifier (lock-in amplifier) it is

Table 6.3. Recommended lines for atomic absorption spectrophotometry

| Element | Wavelength [nm] | Element | Wavelength [nm] |
|------------|-----------------|--------------|-----------------|
| Aluminium | 309.3 | Neodymium | 492.5 |
| Antimony | 206.6 | Nickel | 232.0/341.5 |
| Arsenic | 193.7 | Niobium | 405.9 |
| Barium | 553.5 | Osmium | 290.9 |
| Beryllium | 234.9 | Palladium | 244.8/247.6 |
| Bismuth | 223.1/306.8 | Platinum | 265.9 |
| Boron | 249.8 | Potassium | 766.5 |
| Cadmium | 228.8 | Praseodymium | 495.1 |
| Calcium | 422.7 | Rhenium | 346.0 |
| Caesium | 852.1 | Rhodium | 343.5 |
| Cerium | 520.0 | Rubidium | 780.0 |
| Chromium | 357.9 | Ruthenium | 349.9 |
| Cobalt | 240.7 | Samarium | 429.7 |
| Copper | 324.8 | Scandium | 391.2 |
| Dysprosium | 421.2 | Selenium | 196.0 |
| Erbium | 400.8 | Silicon | 251.6 |
| Europium | 459.4 | Silver | 328.1 |
| Gadolinium | 368.4 | Sodium | 589.0 |
| Gallium | 287.4 | Strontium | 460.7 |
| Germanium | 265.2 | Tantalum | 271.5 |
| Gold | 242.8 | Tellurium | 214.3 |
| Hafnium | 307.3 | Terbium | 432.7 |
| Holmium | 410.4 | Thallium | 276.8 |
| Indium | 303.9 | Thorium | 371.9 |
| Iridium | 208.9 | Thulium | 371.8 |
| Iron | 248.3 | Tin | 224.4/233.4 |
| Lanthanum | 550.1 | Titanium | 364.3 |
| Lead | 217.0/283.3 | Tungsten | 255.1 |
| Lithium | 670.8 | Uranium | 358.5 |
| Lutetium | 336.0 | Vanadium | 318.4 |
| Magnesium | 285.2 | Ytterbium | 398.8 |
| Manganese | 279.5 | Yttrium | 410.2 |
| Mercury | 253.6 | Zinc | 213.9 |
| Molybdenum | 313.3 | Zirconium | 360.1 |

possible to study the absorption without background problems. Frequently a dual-beam system is used (Fig. 6.60). The light is then intermittently sent through the flame (sample beam) or beside it (reference beam). The two beams are balanced on the lock-in amplifier (zero ac component) for the

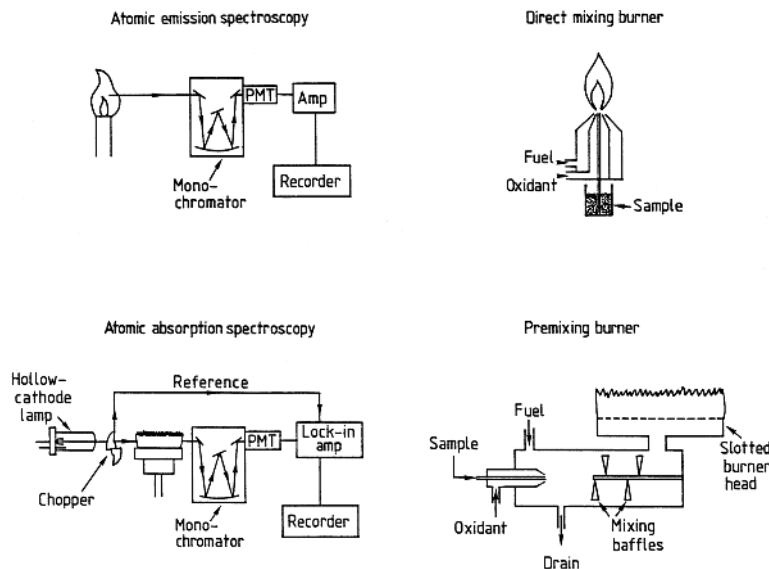


Fig. 6.59. Basic arrangements for atomic emission and atomic absorption spectro-photometry. Burner arrangements are also shown

case of no sample injection into the flame. The presence of atoms to be measured results in an imbalance between the two beams (an ac component), the amplitude of which is proportional to the absorption. Using this method, drifts in the lamp intensity, the sensitivity of the detector and the electronic amplification are compensated for.

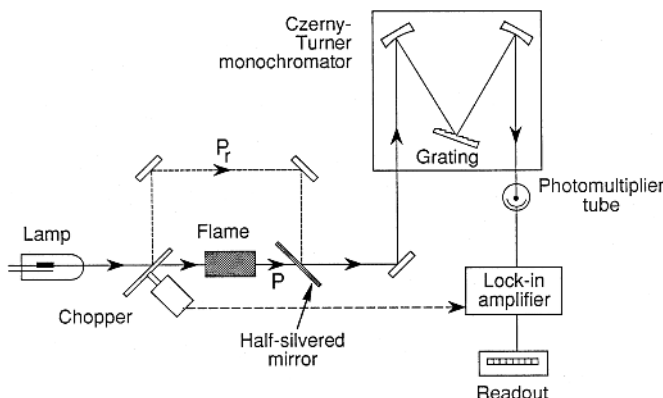


Fig. 6.60. A dual-beam spectroscopic system

6.5.3 Burners, Flames, Sample Preparation and Measurements

Two types of burners are used for flame spectrometry – direct mixing burners and premixing burners. In the former type the gas and the oxidant are mixed immediately before ignition at the burner mouth. The sample, which is kept as a water solution, is sucked into the flame through a thin tube. In premixing burners the gases are mixed in a chamber into which the sample solution is also sprayed. The latter type of burner normally has a slit-shaped head of about 10 cm in length, yielding a long absorption path through the laminar flame obtained with this type of burner. Any gas mixtures can be used in direct-mixing burners while only gas combinations with a burning velocity slower than the gas flow velocity out of the burner can be used in premixing burners to avoid flash-back. This eliminates the hot acetylene/oxygen flame (3100 °C), while acetylene/air (2200 °C) and acetylene/N₂O (2800 °C) can readily be used. In the flame the small sample droplets are dried and then the salt particles are evaporated forming free atoms. The flame temperature must be chosen in a trade-off between the desired high degree of molecular dissociation and undesired atomic ionization, leading to a reduction in the signal. Practical measurements are performed with water solutions containing the sample which has been dissolved, sometimes using an acid. The measurements are performed by comparing the sample solution with standard solutions of known concentrations. Using a number of such standards a calibration curve, which should exhibit linearity in absorbance versus concentration, see (6.46), is obtained. Another possibility is to add known amounts of an element to the sample solution and observe the increase in absorbance (“standard addition method”). Sensitivities obtained are frequently in the ppb region. The use of these techniques is illustrated in Fig. 6.61.

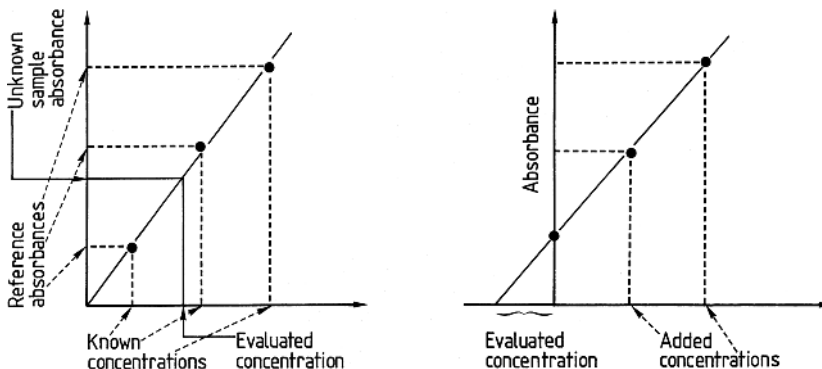


Fig. 6.61. Illustration of concentration evaluations using standard solutions and the standard-addition method

6.5.4 Modified Methods of Atomization

In burners of the types discussed above only about 20% of the solution is atomized, while the rest is lost due to the formation of large droplets that are drained away. Further, the concentration in the flame at any one time is low because of the continuous aspiration of the sample solution. A number of techniques have been developed in which the whole sample is vaporized, at the same time yielding a stronger, transient absorption peak. In the *graphite oven* technique the sample is injected into an electrically heated graphite tube through which inert gas is flowing, as indicated in Fig. 6.62. The heating is performed in three steps. First the sample is dried at a low temperature. Then it is ashed at a higher temperature and is finally evaporated as the heating current is further increased. The measurement is performed during the third stage while the vaporized sample remains in the oven.

As compromises between flame and flameless atomization techniques, the Delves cup and sample boat methods have been developed (Fig. 6.63). In the first of these two techniques the sample is kept in a small cup made of nickel. It is introduced into the flame of an ordinary atomic absorption slit burner. The sample is vaporized and the vapour passes through a hole into a nickel tube that is mounted horizontally in the flame above the cup. The

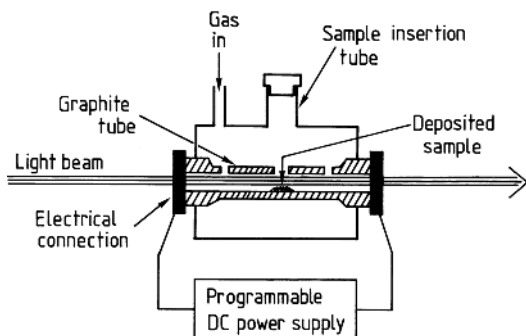


Fig. 6.62. Graphite oven vaporization of analytical samples

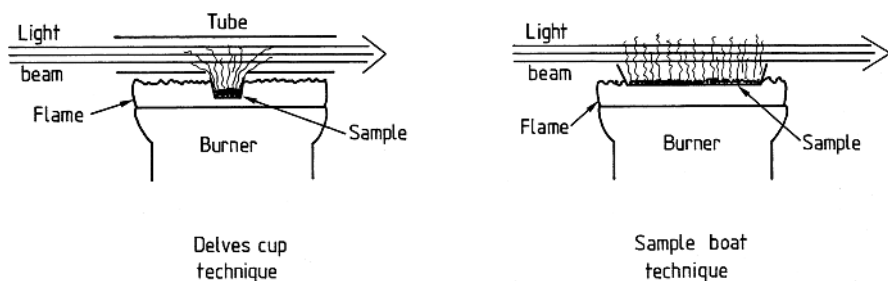


Fig. 6.63. Delves cup and sample-boat arrangements

whole sample is used for the measurement and is present at the same time in the light path. In the sample boat technique the sample is placed in an elongated "boat" made of tantalum. The sample is brought into the flame just below the light path and an absorption peak is recorded for a short time. The modified methods of atomization discussed above allow the detection limit for many elements to be lowered by 1–4 orders of magnitude.

Atomic absorption and emission techniques have been discussed in [6.142–6.144].

6.5.5 Multi-Element Analysis

It is frequently desirable to be able to determine the concentration of several elements simultaneously. Atomic absorption is then impractical, since different hollow-cathode lamps are required. Clearly, the atomic emission method is more suitable. However, a drawback with this technique is that thermal excitation in a flame is relatively poor, but alternative methods of excitation can be used. For a long time arcs or sparks have been used in metallurgical analysis. In this case the sample, which must be solid, forms one of the electrodes.

In order to eliminate the drawback of being limited to solid samples a new type of excitation source, the *Inductively Coupled Plasma* (ICP) source, has been developed. The working principle for this source is illustrated in Fig. 6.64. Three concentric quartz tubes carry flowing gases. An inductance coil fed by an RF generator is placed around the upper end of the outer tube. In the oscillating field argon flowing out between the outer and

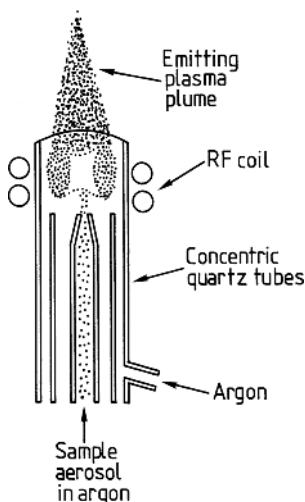


Fig. 6.64. Principle of the inductively coupled plasma source

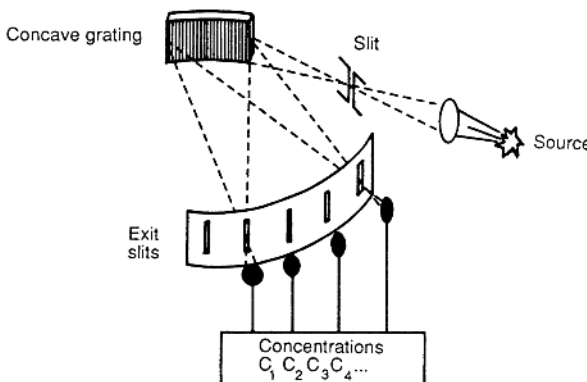


Fig. 6.65. System for multi-element analysis

middle tube will be ionized and forms a plasma at a temperature in the 5000–10 000 K range. Some argon gas also flows between the inner and middle tubes to stabilize the plasma and prevent it from coming into contact with the inner tubes. When the sample is introduced, as fine droplets in the argon stream through the inner tube, complete atomization and efficient thermal excitation are obtained in the hot plasma.

The light emitted from the excitation source is dispersed and recorded by multiple photodetectors placed behind suitably located exit slits (Fig. 6.65). Fibre-optical techniques can also be used to collect light at a suitable location in the spectrometer focal plane for transmission to a battery of PMTs. Calibration can be provided using standard solutions or standard electrodes. Using a computer-controlled data collection system the concentrations of the selected elements can be printed out shortly after the introduction of the sample. A complete system frequently incorporates means for automatic sample exchange.

6.5.6 Molecular Spectrophotometry

In a spectrophotometer the absorption of a molecular sample (gas, liquid or solid) can be measured as a function of the wavelength. The absorption normally occurs in bands that are not too narrow and therefore a continuum light source can be used in connection with a spectral resolving apparatus, which is normally a grating monochromator but can also be a Fourier transform spectrometer [6.145, 6.146]. Spectrophotometers based on grating monochromators are frequently of the dual-beam type, with one beam passing the sample cell and the other one a reference (empty) cell of the same type before the transmitted intensities are compared at the detector. The layout for such an instrument is shown in Fig. 6.66.

Instruments are normally designed for the UV/visible region or the IR region. Tungsten or deuterium lamps (Sect. 6.1.2) are used in the former

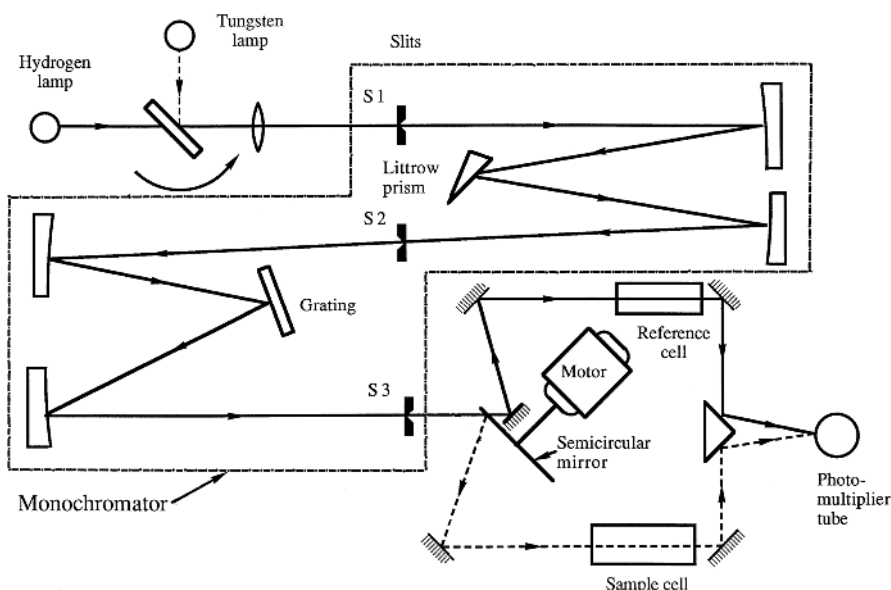


Fig. 6.66. Spectrophotometer of the dual-beam type [6.144]

instruments while, for example, a Nernst glower, is employed in the IR region. Correspondingly, PMTs or PbS cells are used as detectors.

The sample to be studied in the spectrophotometer can be solid, liquid or gaseous. Liquids are investigated in cells or cuvettes made of quartz ($\lambda < 3 \mu\text{m}$) or NaCl ($3 \mu\text{m} < \lambda < 15 \mu\text{m}$). The cell walls and the solvent will affect the measurements, and to correct for these effects a reference cell of the same kind filled with the same solvent but without the sample molecules is used. The transmittance can then be written

$$T = \frac{P_{\text{solution}}}{P_{\text{solvent}}} \simeq \frac{P}{P_0}. \quad (6.50)$$

Commonly used solvents are carbon disulphide CS_2 ($7.5-16 \mu\text{m}$) and carbon tetrachloride CCl_4 ($2.5-7.5 \mu\text{m}$). If highly absorbing solvents are used the length of the cell must be kept short, e.g. 0.01 mm. Solids that cannot be dissolved are ground into fine particles ($< 2 \mu\text{m}$) that are suspended in an oil.

Most inorganic and organic compounds in the liquid or solid phase give rise to broad absorption peaks. Exceptions are ions of the lanthanides and actinides that have sharp, well-defined peaks in the UV and visible regions. The peaks are due to transitions of the optically active $4f$ or $5f$ electrons that are shielded by external electrons. Gaseous samples investigated in multi-pass cells give very sharp absorption features with corresponding demands on spectral resolution. An especially valuable device for gas studies is the *White cell* [6.147], for which multiple reflections can be used to achieve an effective

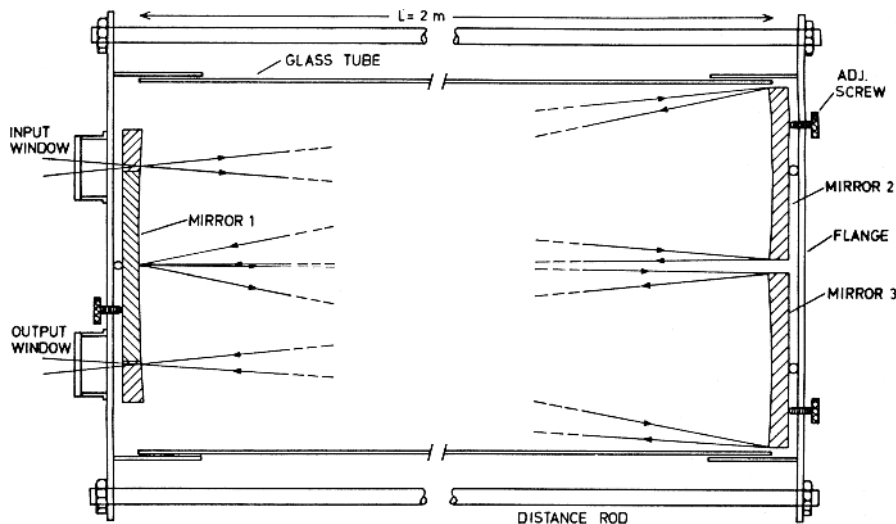


Fig. 6.67. Optical arrangement for a White cell [6.148]

absorption path of more than 100 m even if the physical length of the cell is only 1 to 2 m. The optical arrangement in a White cell is illustrated in Fig. 6.67.

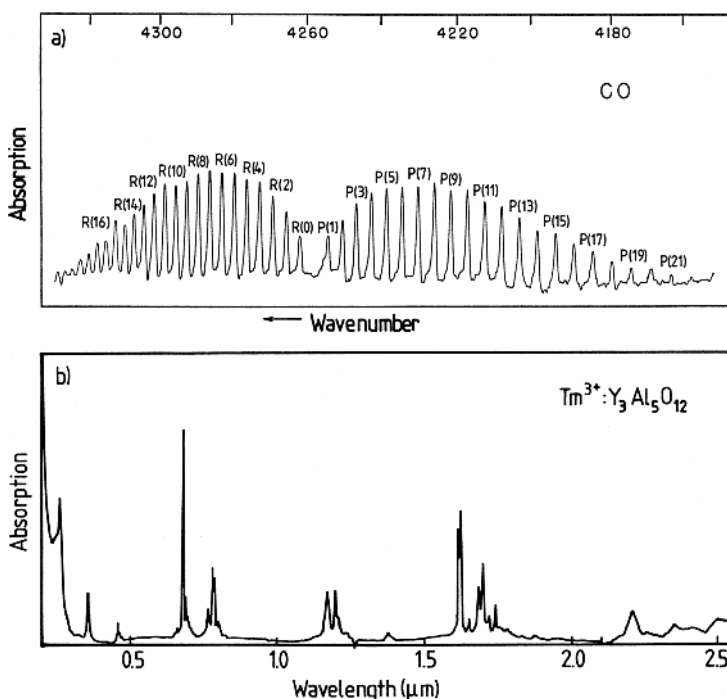
Spectrophotometry in the UV/visible/IR regions can be used for qualitative as well as quantitative analysis. Qualitative analysis is performed by empirically comparing measured spectra with reference spectra that have been catalogued for a large number of compounds [6.149–6.155]. For quantitative analysis the same principles as those used in atomic absorption spectrometry are utilized. The structures observed in the IR region are due to vibrational transitions. These give rise to rather sharp spectral features, even for liquids and solids, in comparison with those obtained for normal electronic transitions observed in the UV/visible regions. The rotational motion is quenched and thus only broadened vibrational transitions are observed. In a complicated molecule many fundamental frequencies, corresponding to different atomic groups, are obtained (Sect. 3.4). This facilitates the identification of substances. In Table 6.4 examples of characteristic frequencies are given. Two examples of IR absorption spectra are given in Fig. 6.68.

6.5.7 Raman Spectroscopy

As we have previously noted, Raman spectroscopy is complementary to IR spectroscopy. A special feature of Raman spectroscopy is that molecules without a dipole moment can be investigated, e.g. H_2 , N_2 , and O_2 . In early Raman spectroscopy measurements a strong Hg lamp was used as a light source. In modern commercial instruments an Ar^+ laser (Sect. 8.4.5) with an

Table 6.4. Characteristic bond-stretching vibration frequencies of certain molecular groups

| Group | Wave number [cm ⁻¹] | Group | Wave number [cm ⁻¹] | Group | Wave number [cm ⁻¹] |
|---------------------------|------------------------------------|----------------------------|------------------------------------|-----------------------------|------------------------------------|
| $\equiv\text{C}-\text{H}$ | 3300 | $>\text{N}-\text{H}$ | 3350 | $\geq\text{C}-\text{C}\leq$ | 900 |
| $\geq\text{C}-\text{H}$ | 3020 | $>\text{C}=\text{O}$ | 1700 | $\geq\text{C}-\text{F}$ | 1100 |
| $\geq\text{C}-\text{H}$ | 2960 | $-\text{C}\equiv\text{N}$ | 2100 | $\geq\text{C}-\text{Cl}$ | 650 |
| | | $-\text{C}\equiv\text{C}-$ | 2050 | $\geq\text{C}-\text{Br}$ | 560 |
| $-\text{O}-\text{H}$ | 3680 (gas) 3400 (liquid) | $>\text{C}=\text{C}\leq$ | 1650 | $\geq\text{C}-\text{I}$ | 500 |

**Fig. 6.68.** Two examples of IR absorption spectra: (a) carbon monoxide gas [6.154]; (b) thulium ions in a crystalline matrix [6.156]

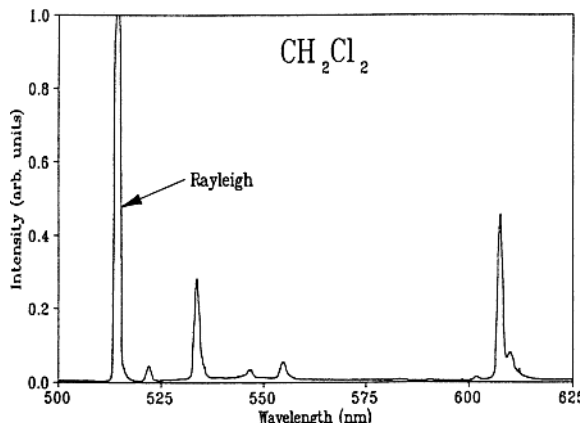


Fig. 6.69. Raman spectrum of liquid CH_2Cl_2 obtained using an argon-ion laser emitting at 515 nm [6.162]

output power of several watts in a single line (normally 514.5 or 488.0 nm) is used. The light scattered from the sample is analysed with a spectrometer. Normally a double or a triple spectrometer is used, since it is of utmost importance to suppress the intense Rayleigh-scattered light. Specifically designed dielectric layer filters which fully transmit the surrounding wavelengths but strongly reject the laser wavelengths (notch filters) are also very helpful in Raman spectroscopy. The polarization of the Raman-scattered light can give valuable additional information on the structure of the investigated molecules. In Raman spectroscopy it is important to work with pure substances in order to avoid the masking of weak Raman components by broadband fluorescence from impurities. (The Stokes components are on the same side of the exciting line as the redshifted fluorescence light). Raman techniques have been discussed in [6.89, 6.157–6.161].

As an example of a Raman spectrum from a liquid a recording for CH_2Cl_2 is shown in Fig. 6.69. Raman spectra for gases will be discussed in Sect. 10.1.3.

The Raman scattering can be enhanced by a factor of the order of 10^6 if the exciting line coincides with an allowed electronic transition (*resonance Raman effect*). In recent years several types of *coherent Raman spectroscopy* [6.163] have been introduced, e.g. *coherent anti-Stokes Raman spectroscopy* (CARS) (Sects. 8.6 and 10.1.4) and *Raman gain spectroscopy*.

6.6 Optical Remote Sensing

In the previous section we have described how optical spectroscopy can be used to analyse samples in the laboratory. In this section we will describe how spectroscopy can provide information on the environment by performing measurements at a distance. *Remote sensing* is a general term used for

techniques by means of which information on physical or chemical conditions at a spatially remote location can be gained using suitable equipment. In the concept of remote sensing the possibility of quickly changing the object of study is included. The principle of remote sensing is illustrated in Fig. 6.70. By means of electromagnetic waves, the remote-sensing equipment (generally called the *sensor*) is in contact with the spatially separated measurement volume, which is characterized by parameters P_1, P_2, P_3 etc. Using the sensor the value of a certain parameter, P_i , in the measurement volume can be read off. The measurement process involves an analysis of the radiation reaching the sensor from the object and can be characterized as a type of applied molecular spectroscopy [6.165].

Remote sensing can be performed using *passive* or *active* techniques. While changes in the spectral distribution of the background radiation (e.g., the sunlight) are analysed using passive techniques, changes in the radiation transmitted by the equipment due to interactions with the measurement volume are studied in active techniques. These concepts can be illustrated by a simple example.

In colour photography of a sunlit object the absorption and reflection properties (the colour) of the object can be assessed knowing the spectral composition of the sun's radiation and the colour sensitivity of the film. The photograph constitutes a remote sensing recording using passive techniques. If instead the object had been photographed in a dark room using a flashlight with a certain spectral distribution (frequently simulating that of sunlight) an active recording would have been obtained. This example illustrates that remote sensing is a very general concept. The information obtained can be of different kinds: geometrical information (maps), natural resources, meteorological information or concentrations of atmospheric pollutants.

Remote-sensing systems can be mounted on different platforms depending on the type of measuring task. A sensor mounted on a satellite can have global coverage. Many of the numerous satellites that orbit above the earth are equipped with sensors for monitoring meteorological conditions, earth resources or for military surveillance. Examples of series of satellites transmitting their information to ground-receiving stations via microwave

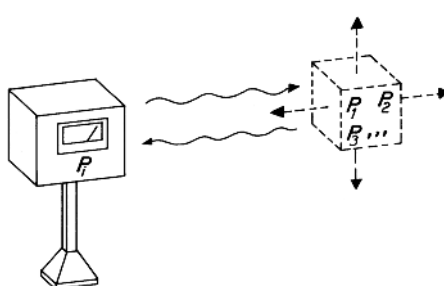


Fig. 6.70. Principle of remote sensing [6.164]

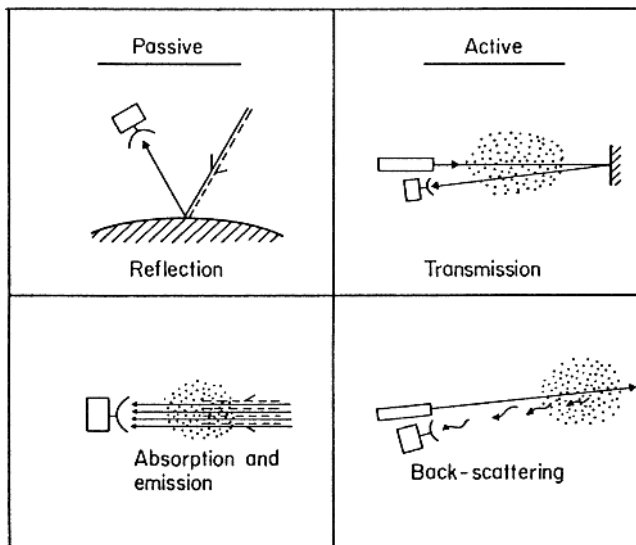


Fig. 6.71. Passive and active remote sensing techniques [6.164]

links are TIROS, LANDSAT, and SPOT. Airborne sensors or mobile land systems can be used for regional remote sensing. Finally, fixed systems are suitable for monitoring urban or industrial areas.

In Fig. 6.71 different passive and active remote-sensing techniques are illustrated. The selective reflection of solar radiation from the earth's surface, the absorption or the thermal emission of the atmosphere can be studied with passive techniques. Active techniques frequently make use of laser or microwave radiation. The transmission or scattering of such radiation can yield information on the atmosphere or the land and sea surface.

6.6.1 Atmospheric Monitoring with Passive Techniques

Some passive atmospheric monitoring techniques will be discussed here, while active techniques for such purposes will be described in Chap. 10. The general principle of passive atmospheric monitoring is illustrated in Fig. 6.72. The absorption of the sun's or sky's radiation, caused by atmospheric constituents, can be measured using a suitable spectrometer. The observed frequencies of absorption are used for gas identification, and the strengths of the absorption lines determine the concentration of absorbing molecules according to the Beer-Lambert law (Sect. 6.5.1). If the absorption coefficient $\sigma(\nu)$ of the gas is known from laboratory measurements, the total number of absorbing molecules can be determined from the ratio between the received radiation intensity $P_t(\nu)$ and the original intensity $P_0(\nu)$. If $N(r)$ is the molecular concentration at the range r we have

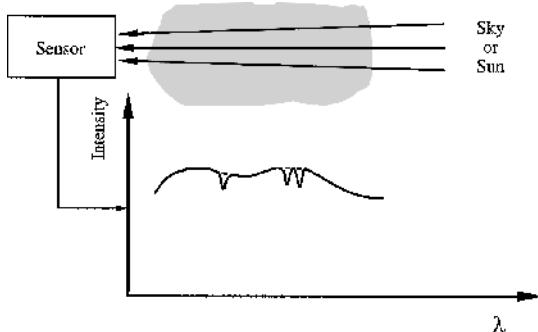


Fig. 6.72. Principle of passive atmospheric monitoring [6.166]

$$\frac{P_t(\nu)}{P_0(\nu)} = \exp \left[-\sigma(\nu) \int_0^{\infty} N(r) dr \right]. \quad (6.51)$$

Thus, range-resolved concentrations cannot normally be obtained using passive techniques since the path of absorption is undefined. If there is a temperature inversion in the atmosphere, no mixing occurs through the inversion layer and a value for the average concentration up to the inversion layer can be obtained in vertical measurements. Using satellites, absorption measurements can be made at sunrise and sunset through varying thicknesses of the atmosphere ("limb" absorption) (Fig. 6.73). A vertical concentration profile can then be calculated from the absorption data. By carefully measuring the line shape of absorption lines it is possible to determine a vertical concentration profile through a deconvolution procedure, taking the pressure broadening (Sect. 6.1.1) at different heights into account [6.167, 6.168] (Sect. 10.2.1). Grating, Fourier transform or heterodyne spectrometers can be used to analyse the spectral distribution. Ground-based monitoring against the sun or moon disc can also be performed [6.169].

A special problem in optical atmospheric monitoring is the ever-present turbulence of the air that makes the recorded light intensity vary substan-

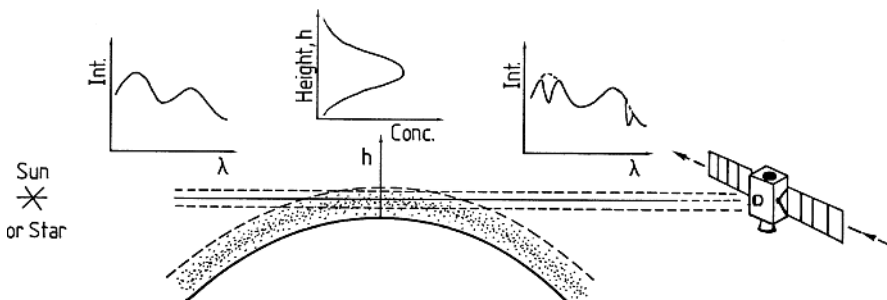


Fig. 6.73. Limb absorption measurements from a satellite

tially (hence the “twinkling” of the stars). However, the amplitude of such fluctuations is negligible for frequencies above 100 Hz. This observation calls for the registration of certain small wavelength regions with peaks and valleys in a time of the order of 10 ms, if small net absorptions are to be detected. This can be performed by exchanging the fixed exit slit of the spectrometer for a rotating disc with radial slits scanning the spectrum in front of a sufficiently large detector surface (e.g., a 5 cm diameter PMT). To ensure a good signal-to-noise ratio thousands of individual scans can be added in a computer, allowing absorption features as small as 0.01 per cent to be detected. With such a sensitivity not only common air pollutants can be detected but also the presence of various low-concentration atmospheric radicals such as HONO and NO_3 . This technique is normally combined with the use of a distant artificial continuum light source such as a high-pressure xenon lamp (Sect. 6.1.2). The technique is then normally referred to as *doas* (differential optical absorption spectroscopy) [6.170–6.174]. The same effect can be obtained by simultaneously recording a high-resolution spectrum and a low-resolution (normalizing) spectrum using a spectrometer with dual output slits and then dividing one signal by the other [6.175]. A doas set-up for urban pollution monitoring is shown in the upper part of Fig. 6.74 and its use for sulphur dioxide measurements is illustrated in four panels in the middle part of the figure [6.172]. In panel (a) the spectral distribution of a xenon lamp 2 km away is recorded in the wavelength region 280–320 nm after the light has passed through the polluted city atmosphere. The small absorption features around 300 nm are magnified in panel (b), where a 5th order polynomial (not being able to follow the fast undulations) is also fitted to the spectrum. In panel (c) the atmospheric spectrum is divided by the fitted curve to give a spectrum normalized to the case of a lamp constant intensity spectral distribution. Finally, in panel (d) a laboratory spectrum for sulphur dioxide (dashed curve) is fitted and we observe an almost perfect fit in a logarithmic representation. An average mixing ratio of 4 ppb is evaluated. In the lower part of the figure experimental doas data for ammonia are shown [6.173]. Again, a laboratory spectrum has been fitted. The NH_3 molecule absorbs at around 210 nm, where the lamp intensity is quite low and where atmospheric scattering also strongly attenuates the beam.

The doas technique can also be employed using sky radiation (scattered sunlight) as the (passive) light source. In Fig. 6.75 the vertically recorded sky spectrum at the side (b) and below (a) the volcanic plume of Mt. Etna is shown [6.176], together with a (logarithmic) curve obtained when dividing the two curves by each other. The SO_2 spectral signature clearly emerges as demonstrated by the almost perfect fit to a laboratory spectrum (see also Fig. 6.74 (*middle*)). Since the atmospheric scattering is complex and occurs not only above the plume but also inside and below, the calculation of the gas column involves some corrections (see also Sect. 10.2.3). In Fig. 6.75 a complex Fraunhofer line pattern intermingled with major atmospheric

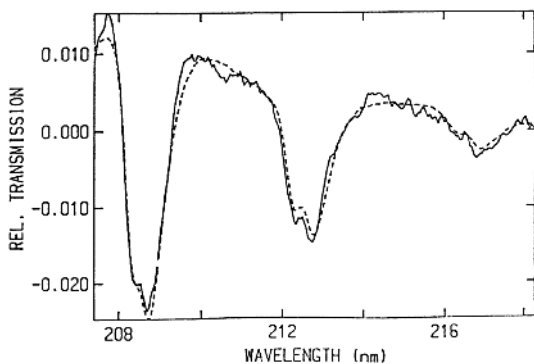
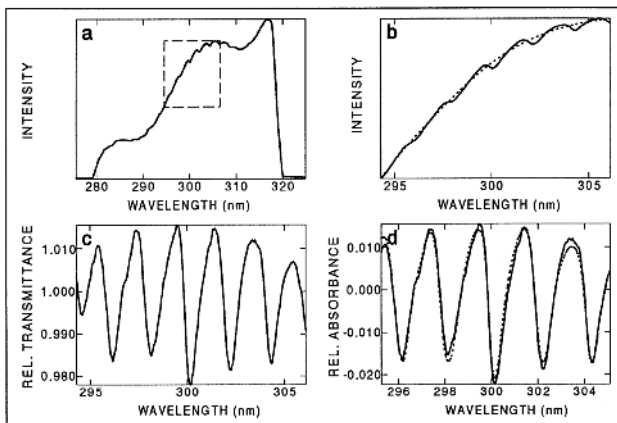
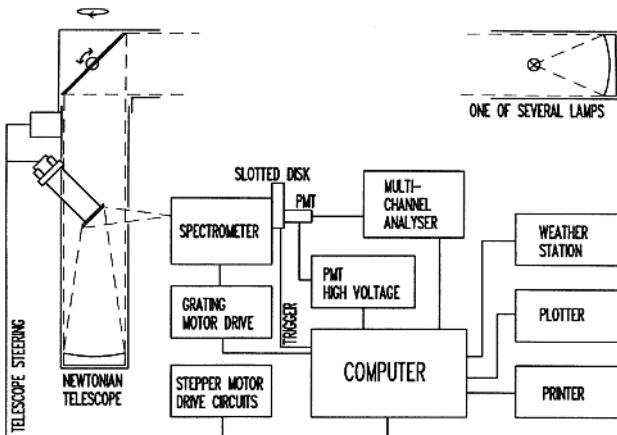


Fig. 6.74. *Top:* Set-up for doas spectroscopy. *Middle:* Measurement example with signals due to an average concentration of 4 ppb of SO₂ over 2000 m [6.172]. *Bottom:* Atmospheric NH₃ spectrum recorded with a doas system over a 265 path 2 meters above a meadow in a rural area [6.173]

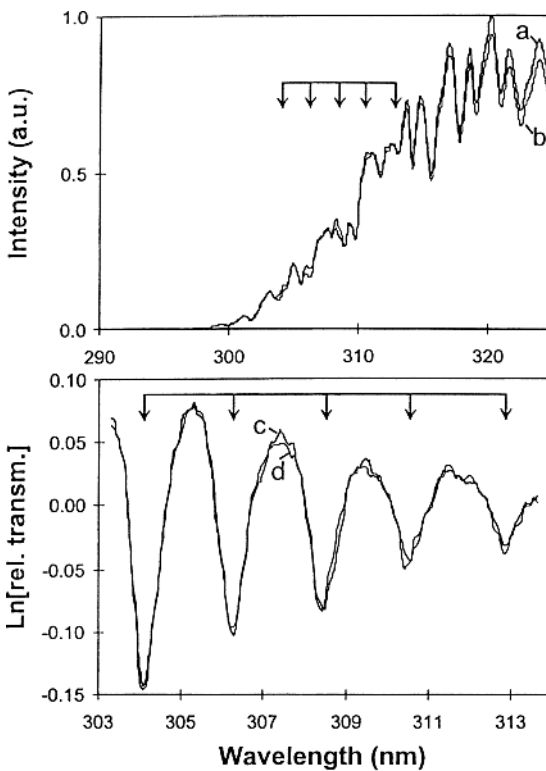


Fig. 6.75. Passive doas recording using blue sky radiation as the illumination source. Sky spectra recorded through the volcanic plume of Mt. Etna (**a**) and at the side of the plume (**b**) are shown together with a divided spectrum clearly showing the SO_2 signature [6.176]

species absorption features is shown. Also, note the cut-off towards shorter wavelengths at about 300 nm due to the stratospheric ozone!

Instruments called *correlation spectrometers* can also be used for passive gas analysis. In these systems a spectrum stored in the instrument is compared (correlated) with the spectrum of the incoming light and a signal that is proportional to the number of absorbing molecules of a particular kind is generated. The correlation can be performed in different ways. In a dispersive, photoelectrically recording spectrometer a metal mask with slits made for the lines of a particular gas can be vibrated back and forth in the image plane and the ac component of the transmitted intensity can be recorded (Fig. 6.76). If the light does not exhibit the particular lines there will be no correlation, but if the lines are present, systematic increases and decreases in the transmitted intensity are obtained when the mask is moved. The mask pattern can be made as concentric rings deposited on a round quartz disc that is rotated in

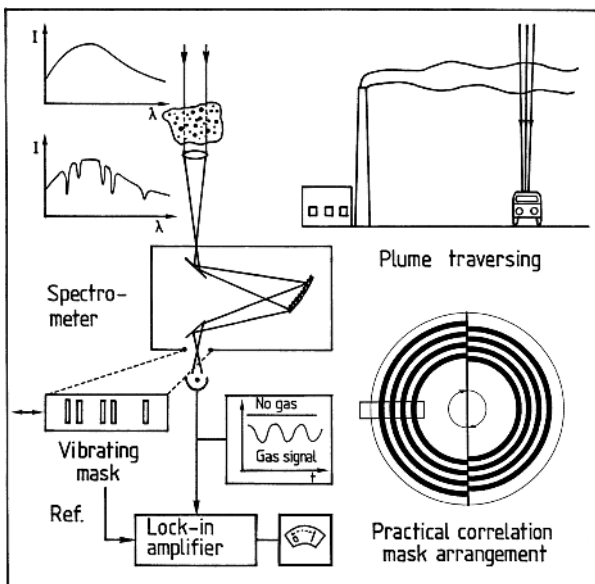


Fig. 6.76. Principle of a dispersive mask correlation spectrometer

the focal plane. For half the circumference the pattern is slightly displaced from the expected spectral lines [6.177].

In a different type of instrument a gas cell is instead used for the correlation [6.178]. A *gas correlation spectrometer* is shown in Fig. 6.77. The incoming light is alternately sent through a cell containing the gas to be studied at such a high concentration that little or no light can pass at the absorption wavelengths, and through an empty reference cell. For the case of no external gas a gray wedge (continuously graded neutral density filter) is adjusted so that equal intensities are obtained through both spectrometer channels in a particular passband isolated by a filter. Now, if an external pollution cloud is present, the signal through the gas correlation cell is not affected, since no higher absorption than full absorption can be obtained. On the other hand, the light through the reference channel is reduced due to the absorption lines of the cloud. Thus an imbalance is recorded at the initially balanced lock-in detector. For calibration purposes a cell with a known (concentration \times length)-value is inserted in the light path in front of the correlation spectrometer.

The gas correlation concept can be extended to the case of imaging, where images are recorded both through a gas cell and directly [6.179]. By subtracting or dividing the images pixel by pixel, only the areas of the scene affected by specific gas absorption will be separated out. Since most gases have their absorption in the IR region, an IR camera operating in a scanning mode with a single detector ("thermovision") or with an IR CCD is employed (Sect. 6.3).

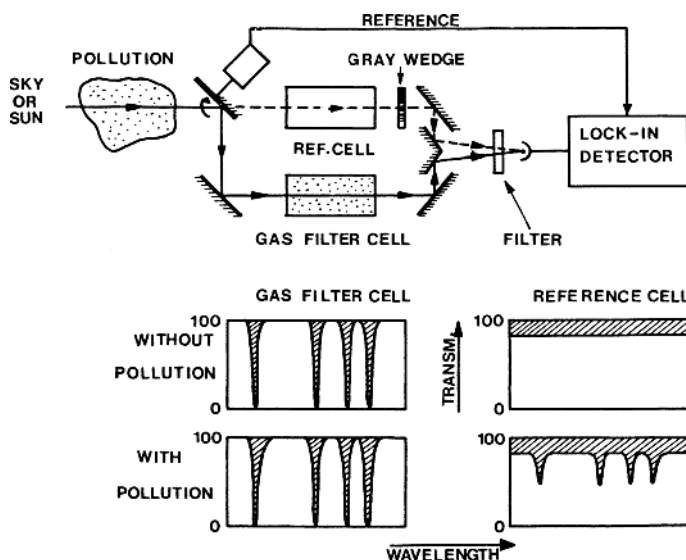


Fig. 6.77. Principle of a gas correlation spectrometer [6.166]

The background distributed radiation source (the sky, walls, ground or an artificial heat blanket) must then have a different temperature than the gas to be imaged (see also Fig. 7.29 and [6.180]).

An enhanced correlation set-up with no moving parts, can be achieved by modulating the absorption spectrum of the gas in a reference cell. Then the optical path does not need to be divided into two paths, but the external gas can be observed through the modulated cell as indicated in Fig. 6.78, where the special case of light transmission over a considerable distance by means of fibre optics is indicated [6.181]. This can be performed using pressure, Stark

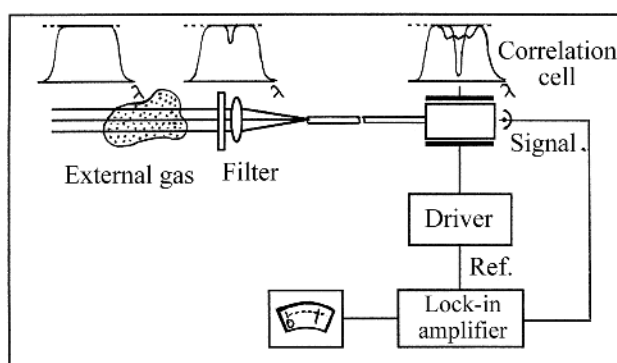


Fig. 6.78. Illustration of modulated gas-correlation spectroscopy for the case of a fibre-optic gas monitoring system

or Zeeman modulation. The modulation at the detector in the presence of the selected gas in the measurement volume is caused by a decreased absorption in the modulation cell, where the perturbation broadens the line, thus reducing the blocking capacity of the cell for the unmodulated gas absorption profile.

A further means of broadband monitoring of gas absorption is to place the measurement cell inside one of the arms of a Michelson interferometer, which for the case of the absence of the trace gas in the cell is adjusted close to the equal armlength setting for a minimum signal transmission to the detector. This is possible in a comparatively large wavelength range, selected by a filter placed after the lamp. If the gas absorptive components are present in the cell, light at the absorbing wavelengths is not cancelled out by exact interference at the detector, and the spectral signal appears in "emission" from a zero background, although it is a weak absorption signal [6.181]. Changes in index of refraction, etc., normally only cause a small effect in these measurements, which rely instead on the optical absorption imbalance between the arms.

6.6.2 Land and Water Measurements with Passive Techniques

In passive monitoring of land or water surfaces the reflective properties or the IR thermal emission are normally used. In earth resource monitoring the selective reflection properties of different types of materials, exposed to sunlight, are used. In Fig. 6.79 some reflectance curves are shown.

Multi-spectral aerial photography represents the simplest type of reflective remote sensing. A number of aligned identical cameras equipped with different filters, are activated at the same time. This technique produces images directly and can be used to monitor land vegetation, and oil, algae and turbidity in water. The sensitivity of photographic materials only extends

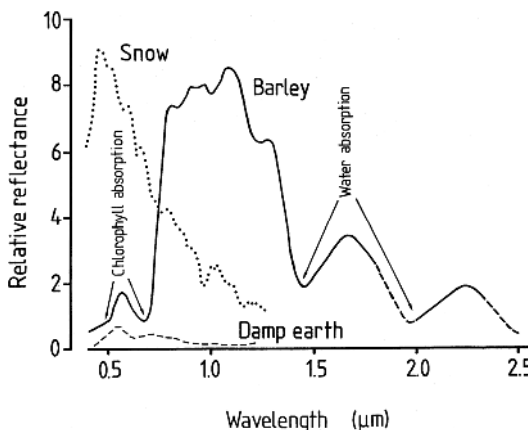


Fig. 6.79. Reflectance curves for different ground surfaces (After L.Wastensson)

into the near-IR region, which limits the possibility of discriminating between different materials.

Many substances and materials have characteristic spectral signatures in that part of the IR region which is not covered by photographic emulsions. As a general-purpose technique in wide wavelength regions *Multi-Spectral Scanning* (MSS) performed from an aeroplane, or better still a satellite, can be used. The principle of this technique is illustrated in Fig. 6.80.

Different points on the earth's surface are sensed sequentially using a scanner mirror placed in front of a light-collecting telescope ("whisk-broom" sensor). As the sensor platform moves forward, a certain strip ("swath") on the surface is covered in a manner resembling the scanning on a TV screen. The radiation is divided up into different wavelength bands that are recorded in parallel detectors. After digitizing, the information is stored on a recorder or transmitted to a receiving station on the ground. Presently, American LANDSAT satellites operate from a height of about 700 km and have a swath of about 185 km. The surface reflectivity is sensed in 7 bands centred at 0.49, 0.56, 0.66, 0.83, 1.65, 2.25 and 11.45 μm . The spatial resolution is $30 \times 30 \text{ m}^2$. The wavelength bands (excluding the thermal 11.45 μm band, denoted band 6) are shown in Fig. 6.81, superimposed on reflectance spectra from leaves (green, yellowing and senescent). The spectral bands in the middle infrared (MIR) region are selected to prevent interference from the strong atmospheric absorption bands due to CO_2 and H_2O (See Fig. 6.51).

Receiving stations are distributed around the globe. The digital data must first be rectified to a normal map grid to eliminate the influence of the

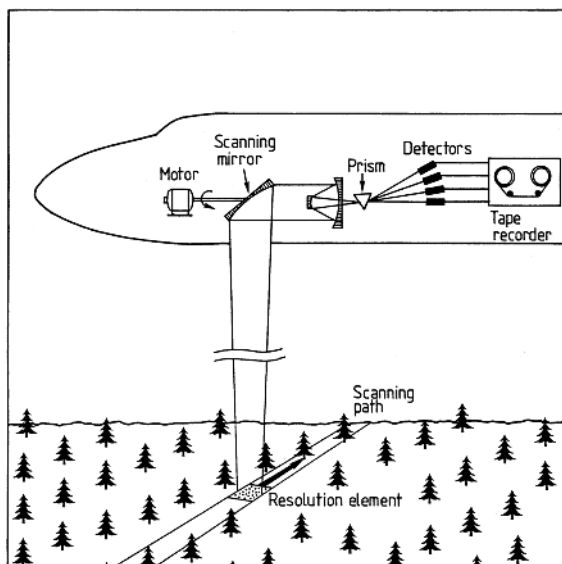


Fig. 6.80. Multi-spectral scanning of the earth's surface

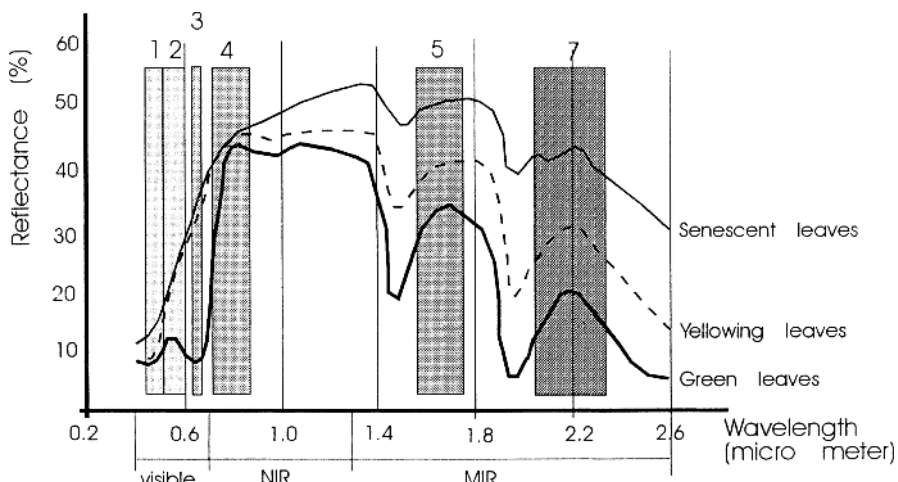


Fig. 6.81. Spectral bands for the LANDSAT Thematic Mapper sensor superimposed of typical reflectance spectra of leaves in different seasonal stages (Courtesy: L. Olsson, Lund University)

observation angle. Packages of data preprocessed in this way, called “*scenes*”, covering a surface of $185 \times 185 \text{ km}^2$, for example, are made available to users. Image processing can then be performed with advanced interactive computer systems. A classification of the information in a scene can be made using stored spectral signatures. Thus maps can be produced showing, for example, different kinds of crops identified by their specific spectral signatures [6.182]. Present trends in digital image processing include an increasing utilization of the geometrical line and granulation patterns (texture). This field is developing very rapidly. Array detectors can be used to eliminate the need for mirror scanning (“push-broom” sensors). Two-dimensional detectors can combine spatial and spectral information (imaging spectrometer; see also Sect. 6.3) [6.183]. This concept is illustrated in Fig. 6.82. For each signal integration on the detector, the spectral data along a swath perpendicular to the satellite flight direction are collected as adjacent columns on the two-dimensional detector. At the next signal integration the satellite has moved forward and data for the next swath on the ground is collected. This type of technology is used on the French SPOT satellites, which have a spatial resolution of about $20 \times 20 \text{ m}^2$. It is also incorporated on several new satellite systems such as LANDSAT 7 (launched 1999). Sensor systems with very high spectral resolution and many spectral bands have also been developed, e.g., the SeaWiFS (Sea-viewing Wide Field-of-view Sensor) on board the SeaSTAR satellite, which was launched 1997. Airborne sensor systems with a hundred closely spaced spectral channels are also operational, performing *hyperspectral imaging*. Figure 6.83 shows a satellite map of the southern part

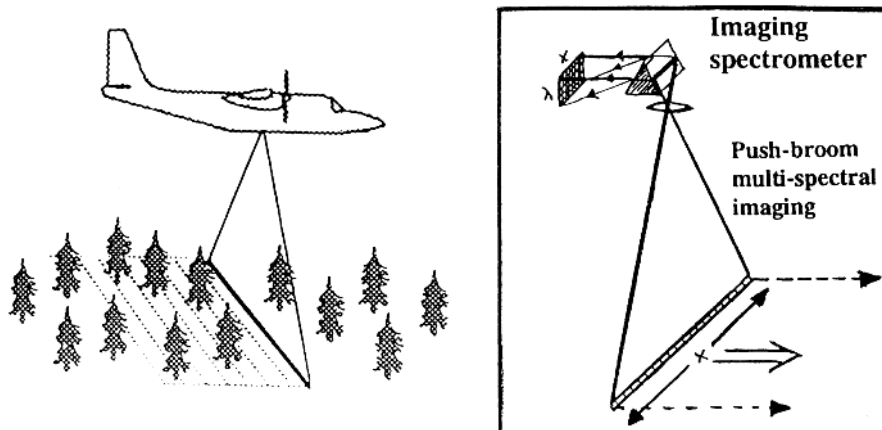


Fig. 6.82. Principle of a push-broom multispectral sensor

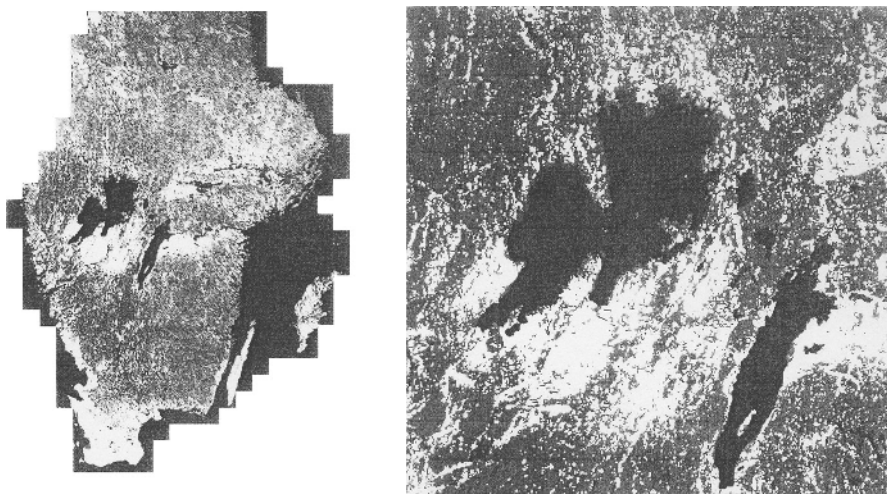


Fig. 6.83. Forest coverage map for southern Sweden, processed from LANDSAT and SPOT satellite imagery. A magnification of the great lakes area is included. Forest pixels are dark in the pictures (Courtesy: Swedish Space Corporation)

of Sweden, where the multi-spectral data has been processed to show forest coverage.

IR measurements for assessing surface temperature are of interest in many contexts. One application is to monitor heat plumes in water adjacent to nuclear power plants. A dramatic example of this concept is shown in Fig. 6.84, documenting the Chernobyl reactor accident as detected by the SPOT and LANDSAT satellites. The accident is manifested in the major

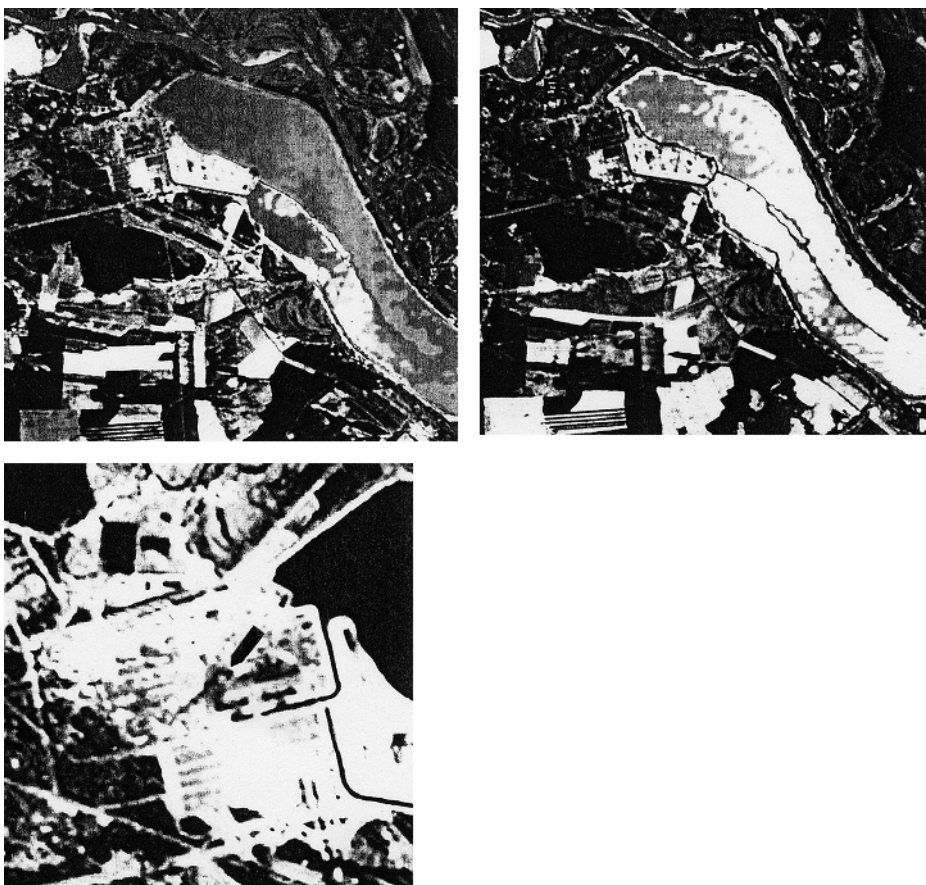


Fig. 6.84. Processed SPOT images of the Chernobyl nuclear power-plant area, before and shortly after the reactor accident (April 26, 1986). *Top left*: before accident. *Top right*: after accident; cooling water stream perturbed. *Left*: magnification showing damaged reactor building as a spectral anomaly, at arrow (Courtesy: Swedish Space Corporation)

change in the distribution of heated water before and after the accident and in the occurrence of a hot spot (one pixel) marking the reactor building.

By monitoring temperature inertia in a diurnal cycle, information on different types of rocks, for example, can be obtained from the heat dynamics. In general, comparing satellite imagery from different times but corrected with precision to the same geometry, a lot of information on changing processes on a local or a global scale can be obtained. The techniques and applications of multi-spectral analysis from space have been discussed, for example, in [6.184–6.188].

Thermal imaging is quite useful in remote sensing, but also has many other applications [6.189]. Thus, “thermovision” cameras can be used to find heat leaks from houses in cold regions or leaks in city heating networks laid down under the streets. The techniques also have applications in finding “coldsolder” joints on printed-circuit boards (joint heating) and have been investigated for tumour localization (tissue temperature rise).

6.7 Astrophysical Spectroscopy

In the same way as in laboratory optical analysis and in remote sensing it is possible to use characteristic wavelengths and line intensities in light from astronomical sources for qualitative and quantitative analysis of the chemical constituents of stars and other objects [6.190–6.195]. The radiation is collected with large telescopes [6.196–6.198]. In this section we will give a few examples illustrating how knowledge can be obtained on astronomical objects by the analysis of electromagnetic radiation in the optical region. The “surface temperature” of a star can be determined from its spectral features. Stars are divided up into classes according to their temperature (highest → lowest): O, B, A, F, G, K and M-type stars. In Fig. 6.85 some classified star spectra are given. Table 6.5 lists special spectral features pertaining to the different classes.

Stellar spectra normally consist of absorption lines which occur when the intense continuum radiation from the hot interior of the star is filtered on passing through the cooler outer stellar atmosphere. The strength of the absorption line is a measure of the abundance of the element. As a measure in the determination of the number of absorbing atoms the so-called *equivalent width* of the spectral line is used. The equivalent width is defined as the width of a square box that covers the same surface as the actual absorption profile of

Table 6.5. Spectral features characterizing different classes of stars

| | |
|---|----------------------------------------------------------------------------------------------------------------|
| O | Lines of neutral and ionized He, and of multiply ionized light elements. |
| B | Lines of He and of singly ionized light elements. Hydrogen Balmer series appears. |
| A | Strong hydrogen Balmer series. Neutral and singly ionized metal lines. |
| F | Hydrogen Balmer series weaker. The Fraunhofer K and H lines due to Ca^+ become very strong. |
| G | Lines of neutral metals dominate the spectrum. Molecular bands of CN and CH appear. |
| K | The lines of neutral metals and the molecular bands become even stronger than in class G. Bands of TiO appear. |
| M | TiO bands become stronger and many other molecular bands are present. |

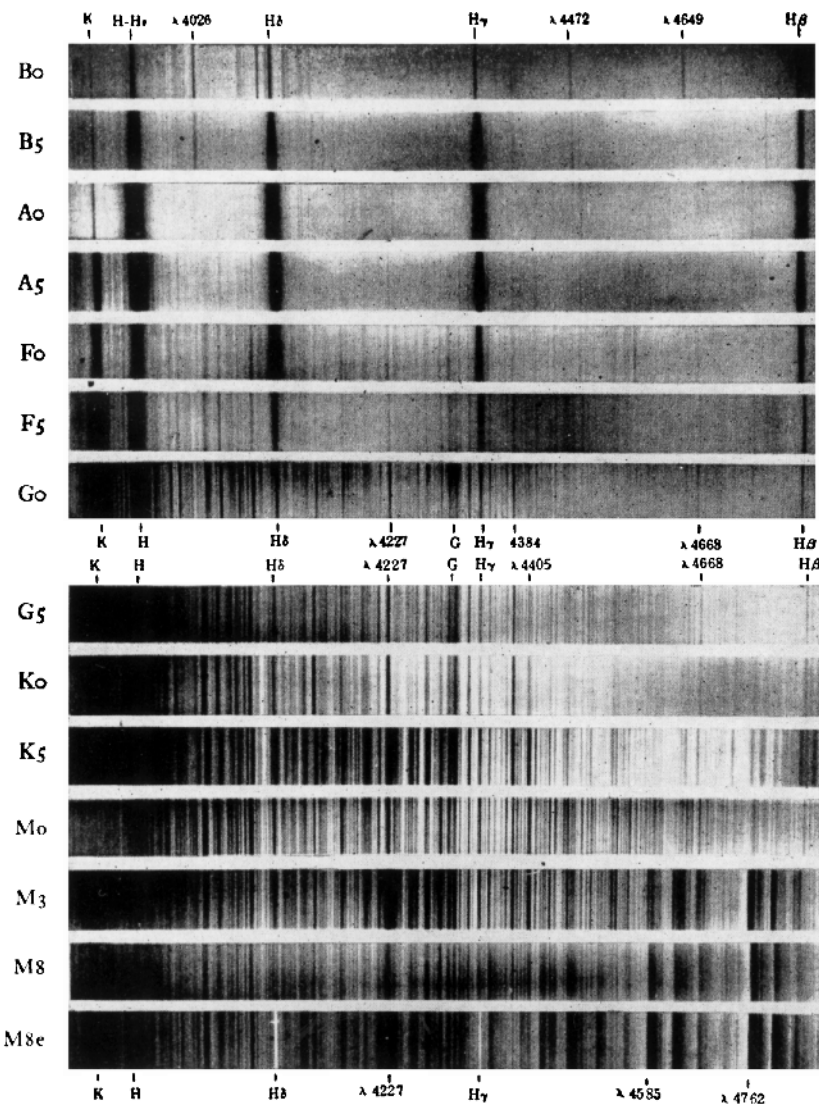


Fig. 6.85. Classified star spectra [6.195]

the line, as illustrated in Fig. 6.86. An example of an experimentally recorded stellar line is included in the figure.

The relation between equivalent width and the number of absorbing atoms is called the *curve of growth*. Clearly, the transition probability for the transition considered is of paramount importance in this context and we will return to this point later (Sect. 9.4.3). In calculations it is necessary to assume a certain model for the stellar atmosphere. In Fig. 6.87 a small wavelength

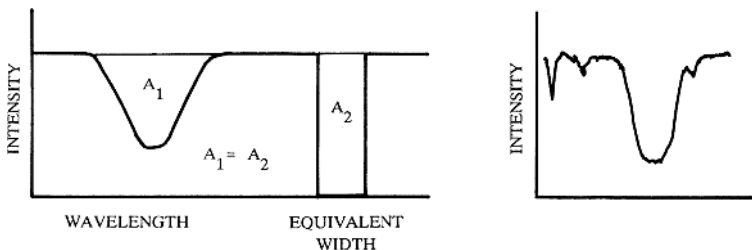


Fig. 6.86. Definition of equivalent width and an experimentally recorded spectral line [6.199]

interval of the sun's spectrum is shown, recorded at a high spectral resolution. The resonance line of Ca II is very prominent. The relative abundances of the elements in the sun, as obtained using spectral analysis, are given in Fig. 6.88.

Emission lines also occur in stellar radiation, especially from hot stars, e.g. from Wolf-Rayet stars. In the solar corona, emission lines from very highly ionized atoms occur. Several of these lines that are observed in the visible or UV regions correspond to "forbidden" transitions within the ionic ground configuration. For example, the 530.3 nm line is due to 13-fold ionized iron. The coronal lines constituted a long-lasting puzzle, which was solved by

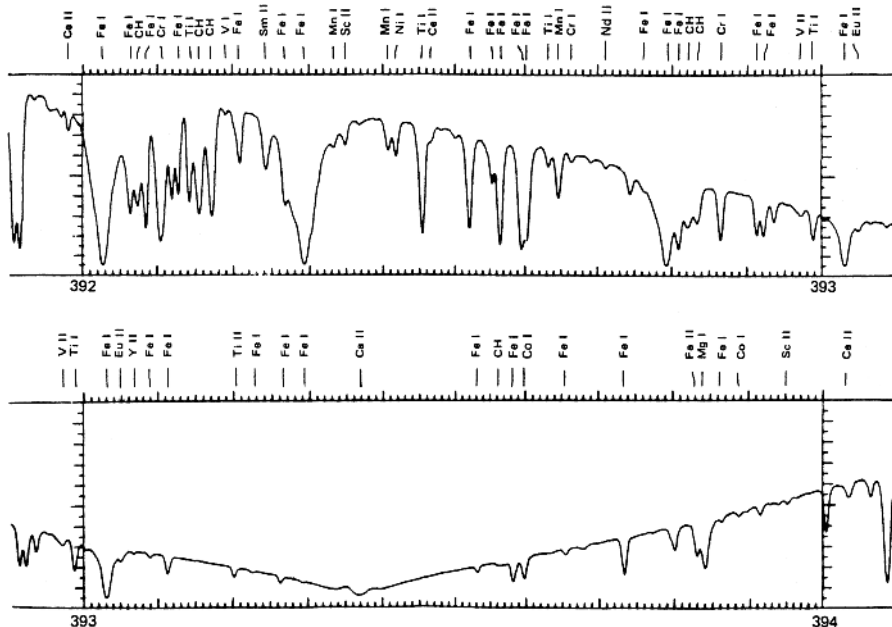


Fig. 6.87. A small interval of the sun's spectrum around the strong CaII resonance line [6.200]

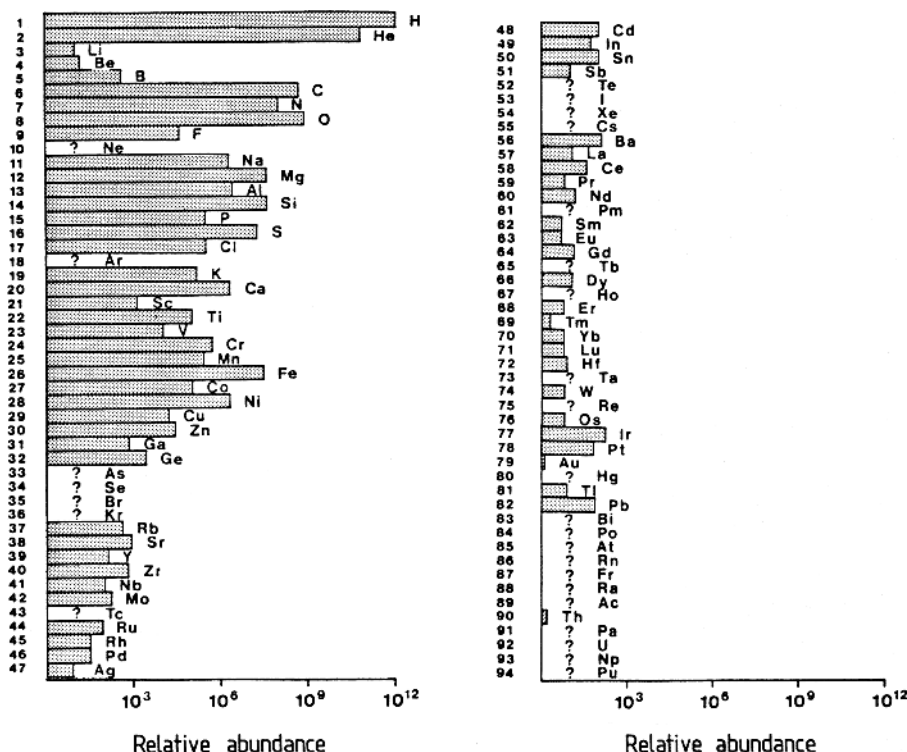


Fig. 6.88. Relative abundances of the elements in the sun, as obtained using spectral analysis [6.201]

B. Edlén [6.202]. A very early problem was the identification of the strong He lines, first attributed to a new and at that time unknown element (named after *Helios*, Gr. for sun), later found in the laboratory. There has always been a very close interaction between astrophysics and atomic physics in terms of identifying observed lines.

Lines from very highly ionized atoms in general fall in the extreme UV region because of the strong excess nuclear charge. Telescopes for X-ray and short UV wavelengths have been placed on astronomical satellites that are controlled from ground observatories. Examples of such astronomical satellites are OSO (Orbiting Solar Observatory), Einstein, Exosat, IUE (International Ultraviolet Explorer) and ROSAT [6.203, 6.204]. Exploration of the sky in the IR region from space is also of great interest [6.205].

The *Hubble Space Telescope* (HST) [6.206], which is the largest space-borne astronomical facility so far, was launched in 1990. The high-resolution echelle spectrometer on board the HST has provided VUV spectra, e.g. of chemically peculiar stars. Such spectra have shown an over-abundance of rare-earth elements, gold, etc. in these stars by a factor of 10^3 – 10^5 , relative

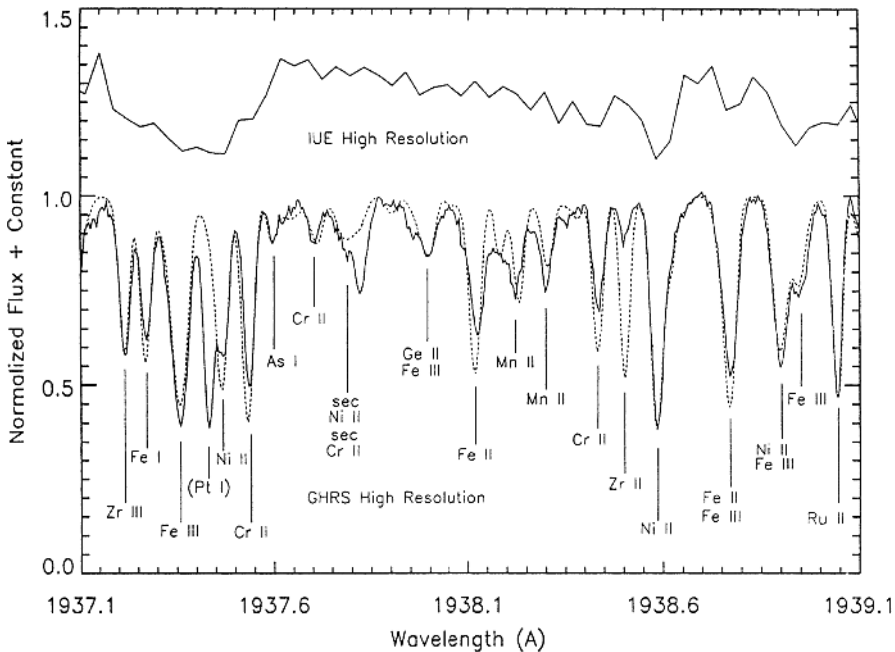


Fig. 6.89. Spectrum of the chemically peculiar star *Chi Lupi*, recorded with the echelle spectrometer of the Hubble Space Telescope [6.207]

to the sun. A representative spectrum for such a star (*Chi Lupi*) is shown in Fig. 6.89, with a calculated model spectrum included as a dashed curve [6.207]. The best previously recorded spectrum, obtained with the IUE satellite, is also included in the figure. Apart from being freed of atmospheric absorption problems (Figs. 6.51, 6.52), HST also, after a service mission in 1993 to correct the faulty optics, provides extremely sharp images, not blurred by atmospheric turbulence. Actually, the HST “Deep Field” camera has seen further into the universe than any other telescope (Fig. 6.90).

While earth-bound astronomical observations are always impaired by atmospheric absorption, the detrimental effects of turbulence can be reduced by choosing telescope sites with particularly good “seeing”, i.e., stable atmospheric conditions. This has lead to the selection of Chilean high-altitude desert locations for the European Southern Observatory (ESO) at La Silla and the new Very Large Telescope (VLT) at Paranal. Nevertheless, there are random fluctuations in the index of refraction. In spectral monitoring this can be handled by fast scanning or parallel (diode-array) detection, as discussed for doas applications, for example (Sect. 6.6.1). However, images will suffer blurring. The technique of adaptive optics, whereby a mirror can be deformed by actuators to compensate for turbulence [6.209], can improve the situation considerably. A bright star must be available within the field



Fig. 6.90. Hubble Space Telescope “Deep Field” image of the most distant part of the universe observed so far. Each blob in the figure is a galaxy at distances ranging out to 10 billion light years [6.208]

of view, which is forced to be recorded as the point source by the fast feedback, adaptive regulation of the mirror surface. If this is achieved, faint and perhaps distributed objects such as remote galaxies will be able to be recorded sharply. Since bright stars are absent in most regions of the sky, a “laser guide star” formed by a strong laser beam inducing sodium fluorescence in the mesospheric sodium layer can be used as a replacement (Sect. 10.2.3).

We will now give a few further examples of interesting observations in astrophysical spectra. Sometimes certain stellar lines appear much brighter than would be expected, considering the temperature, transition probabilities, branching ratios, etc. Such phenomena can be explained as due to accidental coincidences between broadened strong spectral lines of high-abundance elements, resonantly pumping transitions in the elements studied and causing strong fluorescence upon decay. This is the so-called *Bowen mechanism* [6.210], and well-known examples are the 313.4, 304.7 and 344.4 nm lines in O III, pumped by the 30.38 Ly- α line of He II, and the 245.9, 249.2 and 248.1 nm lines in Fe II, pumped by the 154.8 nm line of C IV. Very recently, even optical lasing on Fe II lines around $1.7\text{ }\mu\text{m}$ has been observed in the region of the star *Eta Carinae* [6.211], caused by amplification of spontaneous emission in a cloud of ions. Two Fe II lines around 251 nm are pumped by the hydrogen Ly- α in a Bowen mechanism (See Fig. 6.91), and they feed two long-lived states to inversion (Sect. 8.1) leading to the near-infrared lasing.

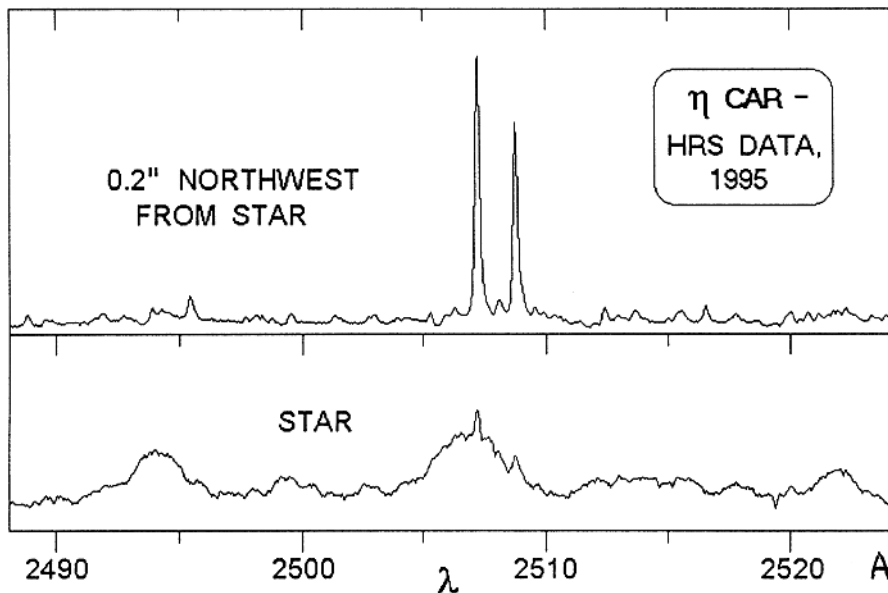


Fig. 6.91. Anomalously bright Fe II fluorescence lines at 250.6 and 250.8 nm, observed in the neighbourhood of *Eta Carinae*. The lines feed two long-lived states, which decay in lasing transitions around $1.7 \mu\text{m}$. As a reference, the stellar spectrum, with normal intensities of the Fe II lines, is also shown [6.211]

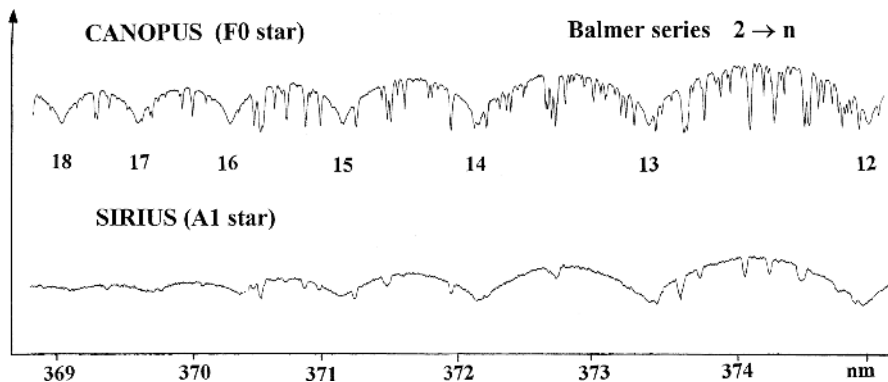


Fig. 6.92. Series of absorption lines corresponding to high Balmer series transitions for the stars Canopus and Sirius. The high Rydberg states are sensitive to collisions. Other sharper absorption lines due to transitions between low-energy states in different elements are shown superimposed on the hydrogen lines. (Courtesy: D. Dravins, Lund Observatory)

The Doppler effect causes displaced spectral lines from objects in motion. The rotation of a star around its axis causes an extra broadening of the spectral lines, as does turbulence in the stellar atmosphere. A detailed analysis

of the line profiles can clearly yield interesting information on the physical condition of the object.

Two spectra of high members of the hydrogen Balmer series ($2s - np$) recorded for identical experimental conditions are shown in Fig. 6.92 for the two bright stars *Alpha Carinae* (Canopus) and *Alpha Canis Majoris* (Sirius). The much higher gas pressures on the dwarf star Sirius broaden the uppermost energy levels of hydrogen, causing a smearing-out of the highest Balmer lines. In the low-pressure atmosphere of the bright giant Canopus, the Balmer series can be followed to around $n = 28$, at 366.5 nm, while for Sirius none can be identified above $n = 18$, around 369 nm. The extent to which lines in the Balmer series can be followed is thus a spectroscopic criterion for stellar surface pressure. The temperatures of the two stars are quite similar, and the rotational broadening is only a negligible fraction of the Balmer line widths.

Distant galaxies exhibit large red shifts. Extremely large red shifts are observed for quasars [6.212]. The red shifts are normally interpreted in terms of radial motion. The largest equivalent velocity observed exceeds $0.9 c$. In Fig. 6.93 a spectrum for a quasar with a velocity of $0.85 c$ is shown. It can be noted how, for example, the Lyman α line, normally at 121.6 nm, has been shifted up to 445.1 nm in the blue spectral region! The study of other extraordinary celestial objects has been further stimulated by the sudden occurrence of the 1987 supernova in the Large Magellanic Cloud [6.214]. It was the first supernova in 383 years that could be seen with the naked eye. A spectrum of the nova recorded 7 days after the explosion is shown in Fig. 6.94. The spectrum exhibits a continuum background and superimposed Balmer α and

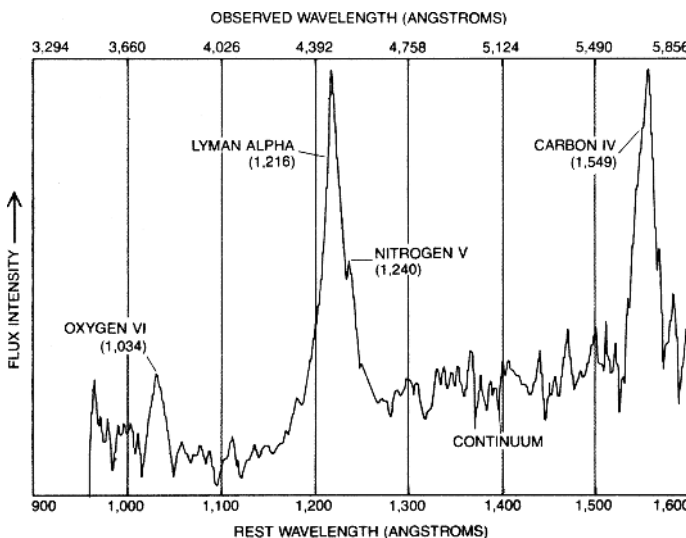


Fig. 6.93. Spectrum of a quasar exhibiting huge Doppler shifts [6.213] (Copyright 1982 by Scientific American, Inc. All rights reserved)

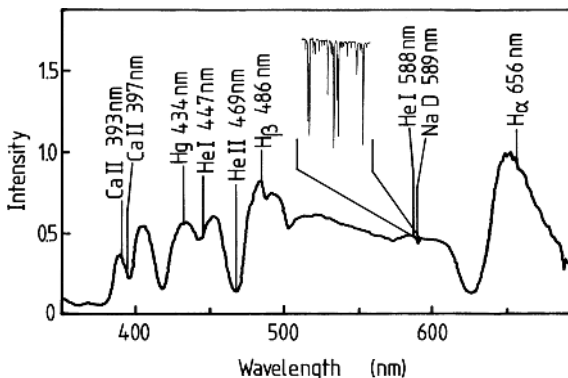


Fig. 6.94. Spectrum of the supernova 1987A in the Large Magellanic Cloud, recorded 7 days after the explosion. The prominent lines are due to the hydrogen Balmer series, Doppler-shifted and broadened due to very high expansion velocities (10 000 km/s). The H_{α} line is partly seen also in emission. An insert shows narrow Na absorption lines due to cold gas clouds moving with different velocities along the line of sight [6.215]

β lines. The hydrogen lines are strongly broadened due to different velocities in the expanding gas shell. Note that both emission and absorption line components occur. By studying Doppler-shifted narrow absorption lines from Na and Ca II with the bright nova continuum as background it has been possible to identify more than 10 cold gas clouds moving at different speeds (see figure insert).

The Zeeman effect of spectral lines can be used to measure magnetic field strengths in the region of line formation. Clear Zeeman patterns occur in lines originating from sunspots, which are characterized by strong magnetic fields.

The study of the planetary atmospheres has become a field of increasing interest during recent years. Terrestrial observations have been complemented by recordings from spacecraft. In Fig. 6.95 terrestrial IR recordings of CO_2 in the atmosphere of Venus are shown, illustrating the increase in information content with increasing spectral resolution. As an example of a spacecraft recording, a spectrum of the atmosphere of one of the Saturn moons, Titan, is shown in Fig. 6.96. The IR recording exhibits lines from many hydrocarbons. Our knowledge of Jupiter, Saturn, Uranus, and Neptune has been vastly extended through the Voyager missions [6.217–6.219]. At the return of Halley's comet in 1986, humankind had also become ready to launch a whole fleet of well-equipped scientific space vehicles towards it, including the European Giotto and the Soviet Vega sondes [6.220]. A $16 \times 8 \times 8 \text{ km}^3$ -sized comet nucleus could be photographed using Giotto's multi-colour camera. Comet spectra are rich in molecular emission bands. A terrestrial photographic recording of a Halley's comet spectrum after the passage of the perihelium is shown in Fig. 6.97. By using a long spectrometer

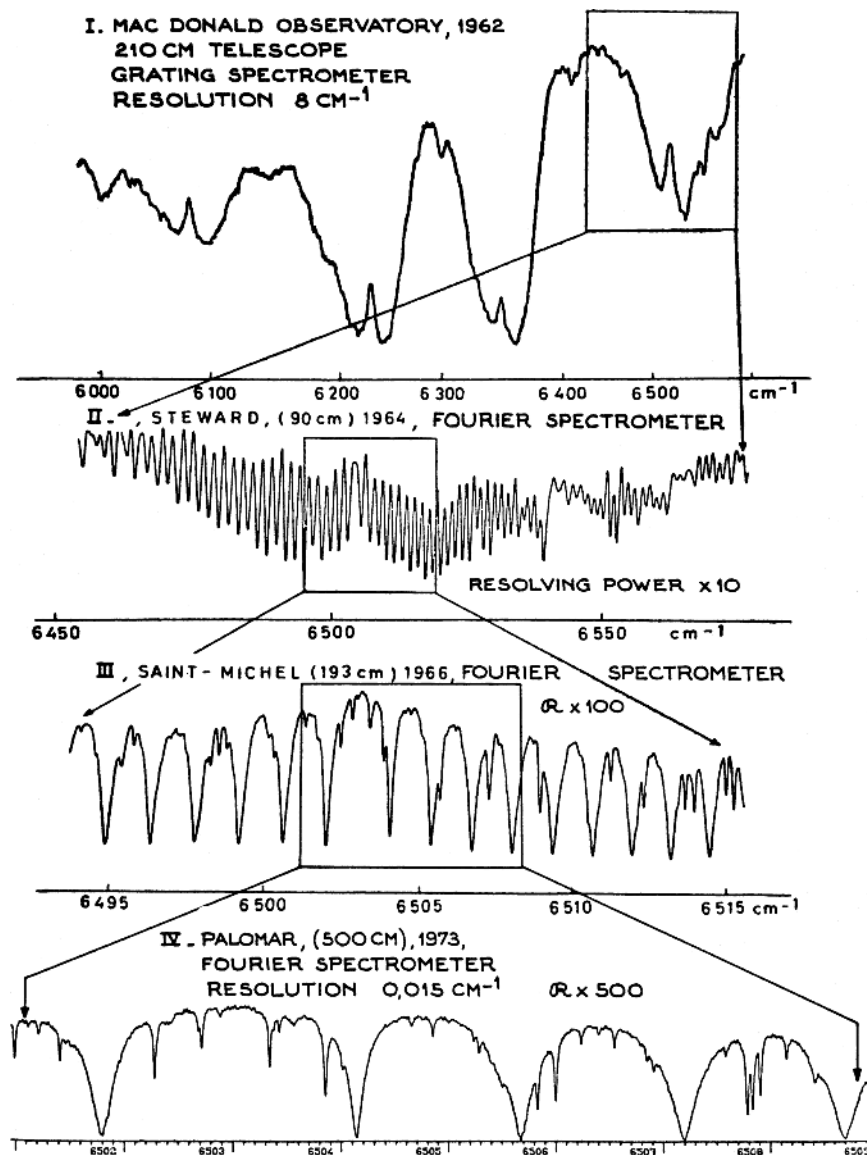


Fig. 6.95. Terrestrial recordings of CO₂ in the atmosphere of Venus illustrating the continuing refinement of the available spectral resolution [6.216]

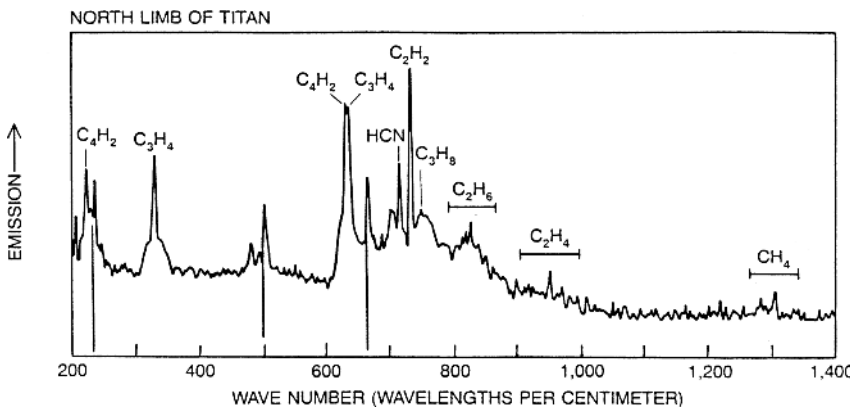


Fig. 6.96. Recording of emission bands in the atmosphere of the Saturn moon Titan, obtained by the spectrometer of the Voyager I spacecraft entering the Saturn-moon system [6.218] (Copyright 1982 by Scientific American, Inc. All rights reserved)

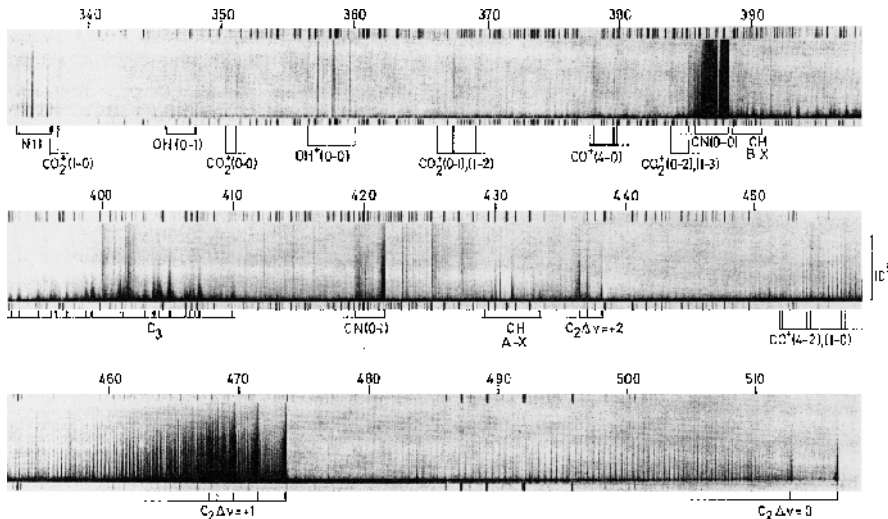


Fig. 6.97. Molecular emission spectrum from Halley's comet on its 1986 return to its perihelion. Along the vertical scale the whole length of the comet tail is imaged using a long spectrometer slit. C₂, C₃ and CN bands are very prominent. Note that the C₃ emission (the "Comet" band) occurs only from a region close to the comet nucleus [6.221]

slit, imaging a distance of 10⁵ km from the nucleus (*bottom*) through the comet tail, the strength of the emission through the comet structure could be recorded.

7. Radio-Frequency Spectroscopy

Whereas the resolution in optical investigations of free atoms is limited by different broadening mechanisms in the light source and the spectral equipment, resonance methods yield a linewidth which is limited essentially only by the Heisenberg uncertainty relation. For investigations of ground- and meta-stable states two methods, *Optical Pumping* (OP) and *Atomic-Beam Magnetic Resonance* (ABMR) can be utilized. In the second method, a spatial deflection of free atoms is used, while the first method is an optical resonance method. For studies of short-lived excited states two additional optical precision methods are available: *Optical Double Resonance* (ODR) and *Level Crossing* (LC) Spectroscopy. Resonance techniques can also be used for investigating liquids and solids. *Nuclear Magnetic Resonance* (NMR), *Electron Spin Resonance* (ESR) and *Electron-Nuclear Double Resonance* (ENDOR) will be discussed. As the radio-frequency techniques make use of *magnetic resonance*, a general description of this phenomenon will be given.

Radiowaves and microwaves also have several other fields of application in spectroscopy. Molecular rotational transitions correspond to this wavelength region. Radiometers can be used for passive remote sensing of, for example, temperature and air humidity, and radar systems can be utilized for active measurements of, for example, oil slicks at sea. Finally, radio astronomy is a fascinating field, yielding information on the most remote parts of the universe.

7.1 Resonance Methods

7.1.1 Magnetic Resonance

We will now study the influence of a rotating magnetic field \mathbf{B}_1 on a magnetic moment $\boldsymbol{\mu}_L$, which precesses with an angular frequency ω_0 in an external magnetic field \mathbf{B}_0 , as illustrated in Fig. 7.1 (Sect. 2.3.1)

$$\boldsymbol{\mu}_L = -g\mu_B \mathbf{L} \quad (7.1)$$

and

$$\omega_0 = g\mu_B \mathbf{B}_0, \quad (7.2)$$

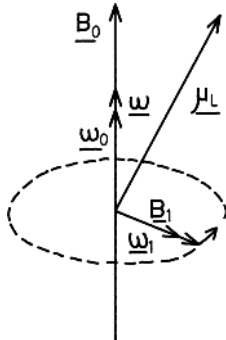


Fig. 7.1. Illustration of magnetic resonance

where \mathbf{L} is the angular momentum vector associated with μ_L . The field \mathbf{B}_1 rotates with an angular frequency ω around \mathbf{B}_0 . If ω and ω_0 are very different, the relative positions of μ_L and \mathbf{B}_1 vary quickly and only a minor influence on μ_L can be expected. However, if $\omega = \omega_0$, the relative positions of μ_L and \mathbf{B}_1 are fixed and it can be seen intuitively that \mathbf{B}_1 will have a large effect on μ_L . We will now show this more rigorously. We have, see (2.10),

$$\frac{d\mathbf{L}}{dt} = \mathbf{M} = \mu_L \times (\mathbf{B}_0 + \mathbf{B}_1), \quad (7.3)$$

and

$$\frac{d\mu_L}{dt} = -\mu_L \times (g\mu_B \mathbf{B}_0 + g\mu_B \mathbf{B}_1) = (\omega_0 + \omega_1) \times \mu_L. \quad (7.4)$$

where we have defined ω_1 by the relation $\omega_1 = g\mu_B \mathbf{B}_1$ in analogy with (7.2). In order to evaluate the influence of the rotating field we now introduce a coordinate system which rotates with \mathbf{B}_1 around \mathbf{B}_0 . We then have

$$\frac{d\mu_L}{dt}|_{\text{lab}} = \frac{d\mu_L}{dt}|_{\substack{\text{rot} \\ \text{syst}}}^{\text{rel}} + \frac{d\mu_L}{dt}|_{\substack{\text{rot} \\ \text{syst}}}^{\text{rot}}, \quad (7.5)$$

$$(\omega_0 + \omega_1) \times \mu_L = \frac{d\mu_L}{dt}|_{\substack{\text{rot} \\ \text{syst}}}^{\text{rel}} + \omega \times \mu_L, \quad (7.6)$$

$$\frac{d\mu_L}{dt}|_{\substack{\text{rot} \\ \text{syst}}}^{\text{rel}} = (\omega_1 + \omega_0 - \omega) \times \mu_L = (\omega_1 - \delta\omega) \times \mu_L. \quad (7.7)$$

When $\delta\omega = \omega_0 - \omega = 0$, μ_L rotates around ω_1 . The projection of μ_L on \mathbf{B}_0 then changes sign periodically and the energy increases and decreases regularly. This is the semiclassical description of *magnetic resonance*. A quantum-mechanical description corresponding to the one given for *electrical* dipole transitions can be given for these *magnetic* dipole transitions.

As we have seen, a resonance will be induced by a rotating field. However, it is easier to produce a linearly oscillating field and such a field can always

be resolved into two counter-rotating components, out of which one can be made resonant. The other component is then very far from resonance and will normally have a negligible effect.

7.1.2 Atomic-Beam Magnetic Resonance

In many spectroscopic techniques, e.g. in ABMR, atomic beams are employed [7.1]. Such beams are generated in a vacuum system by evaporation of atoms. Vacuum techniques are discussed in [7.2, 7.3]. The energy of the atoms will be of the order of kT , normally corresponding to thermal velocities of a few hundred m/s. The temperature needed to produce an atomic beam is determined by the vapour pressure of the element [7.4, 7.5] (typically a value of 10^{-3} torr is used in the evaporating oven). In Fig. 7.2 vapour pressure data for different elements are given.

The first atomic beam experiments were performed between 1910 and 1920. In 1922 O. Stern and W. Gerlach performed their famous experiment, in which they showed that a beam of silver atoms was divided up into two components in an inhomogeneous magnetic field [7.6]. This was the first direct experimental demonstration of space quantization. In order to explain the results of this experiment we will first consider an *electric* dipole placed in an inhomogeneous *electric* field, as illustrated in Fig. 7.3. The dipole is influenced by the force

$$\mathbf{F} = e \mathbf{dE}, \quad (7.8)$$

where $d\mathbf{E}$ has the components dE_x , dE_y and dE_z .

$$dE_x = \frac{\partial E_x}{\partial x} dx + \frac{\partial E_x}{\partial y} dy + \frac{\partial E_x}{\partial z} dz = (\mathbf{dr} \cdot \nabla) E_x. \quad (7.9)$$

Corresponding expressions are obtained for the y and z components. The electric dipole moment is defined as $\mathbf{P} = e \mathbf{dr}$ and thus

$$F_x = (\mathbf{P} \cdot \nabla) E_x, \text{ etc.} \quad (7.10)$$

An analogous expression is valid for a magnetic dipole μ in an inhomogeneous magnetic field \mathbf{B}

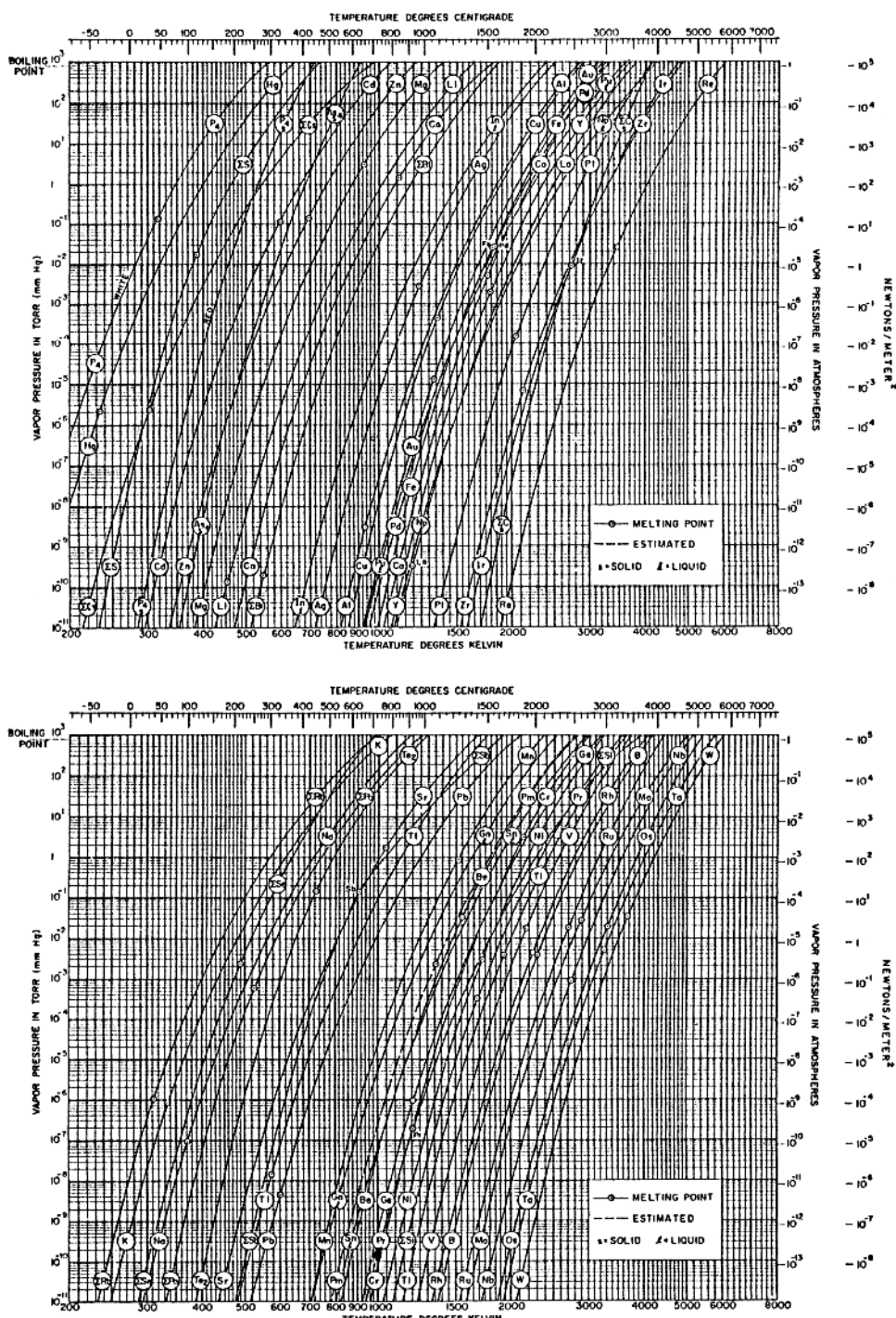
$$F_x = (\mu \cdot \nabla) B_x, \text{ etc.} \quad (7.11)$$

If μ is the dipole moment μ_J of an atom, only the force component in the direction of the field will yield a net effect due to the precessional motion.

If we choose the field direction at the atom to be the z direction, the time-averaged value of (7.11) is reduced to

$$\langle F_x \rangle = \langle F_y \rangle = 0; \langle F_z \rangle = \langle \mu_{Jz} \rangle \frac{\partial B}{\partial z}. \quad (7.12)$$

In the Zeeman region for the fine structure, in which M_J is well defined, we can write



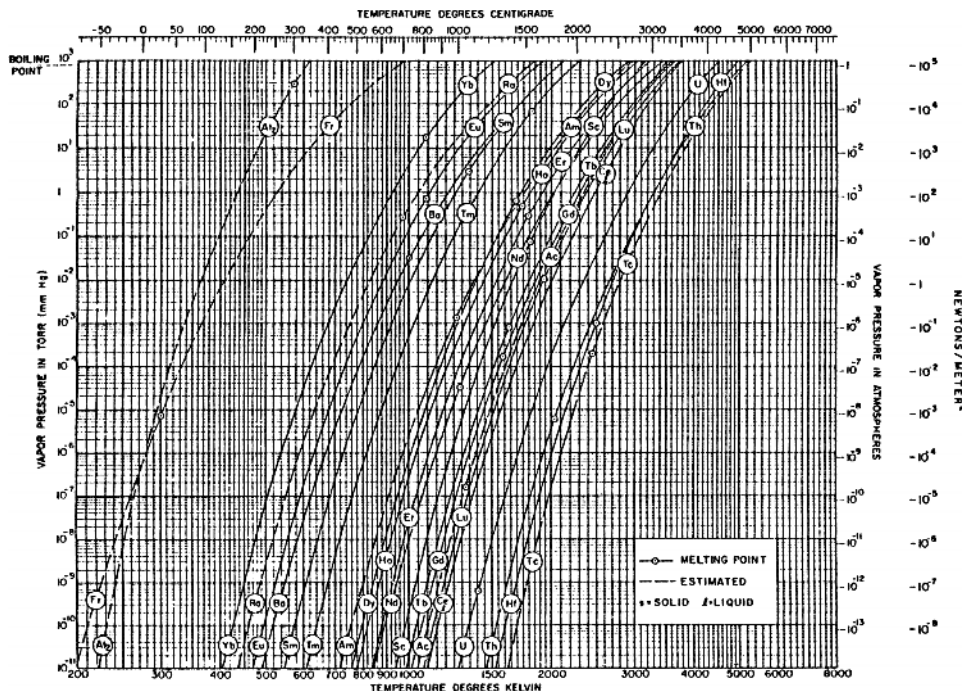


Fig. 7.2. (Continued) Vapour pressure data for the elements [7.5]

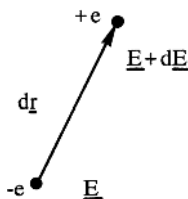


Fig. 7.3. An electric dipole in an inhomogeneous electric field

$$\langle \mu_{J_z} \rangle = -\mu_B g_J M_J, \quad (7.13)$$

i.e., the atom is influenced by a force which is proportional to M_J . Silver atoms have $J = 1/2$ in the ground state and thus the beam is separated into two components, as shown in Fig. 7.4.

If we take the coupling between \mathbf{I} and \mathbf{J} into account, the total magnetic moment (which is essentially due only to the electronic shell) will vary with the field strength because of the successive decoupling of \mathbf{I} and \mathbf{J} which occurs for increasing magnetic fields. The general expression for the force acting on an atom is

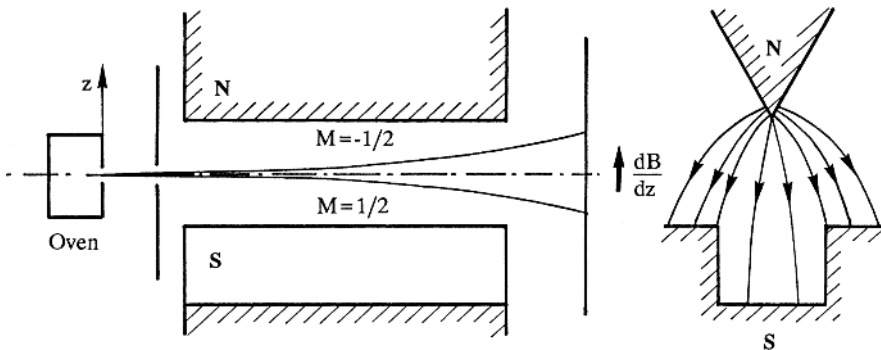


Fig. 7.4. The Stern-Gerlach experiment

$$\mathbf{F} = -\nabla W = -\frac{dW}{dB} \nabla B, \quad (7.14)$$

where W is the atomic energy in the magnetic field, which depends on the absolute value of the magnetic field strength $B = |\mathbf{B}|$. If we compare this equation with (7.12), we can define an effective magnetic moment

$$\mu_{\text{eff}} = -\frac{dW}{dB} \quad (7.15)$$

and the force is still given by (7.12). Figure 2.20 shows an energy-level diagram for an atom with hyperfine structure, subject to an external magnetic field. As can be seen, μ_{eff} varies strongly with the field for certain sublevels. For special values of the field $\mu_{\text{eff}} = 0$ for one or several sublevels ($M_F = -1$ in Fig. 2.20). This was used by Rabi and co-workers for the determination of several nuclear spins and hfs constants (zero-moment method).

A great improvement in the atomic beam technique was made with the introduction of the *ABMR technique* by Rabi and co-workers in 1938 [7.7]. This was the first application of the magnetic resonance principle, which has subsequently been successfully used in many other cases (see below). The ABMR technique is illustrated in Fig. 7.5. An atomic beam produced by an oven passes through two inhomogeneous magnetic fields A and B , which are of the same type as those used in the Stern-Gerlach experiment. If the field gradient is directed upwards in both magnets, an atom with $\mu_{\text{eff}} < 0$ will, according to (7.12), be deflected downwards, as indicated by the full line in the figure. A magnet C is placed between the A and B magnets, generating a homogeneous field, in which an oscillating magnetic field can be applied through an RF loop. If the applied frequency corresponds to the energy difference in the C field between the originally selected state and another higher or lower state of the atom, a transition to such a state can occur through absorption or stimulated emission of the corresponding radiation. This is the resonance phenomenon discussed in Sects. 4.1 and 7.1.1. If the transition occurs to a state with $\mu_{\text{eff}} > 0$ in the B field, the atom will be

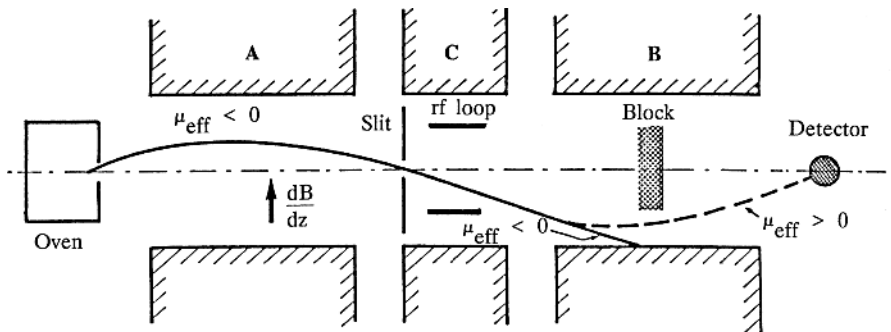


Fig. 7.5. Atomic-beam magnetic-resonance apparatus (flop-in arrangement)

deflected according to the dashed line in the figure and will hit a particle detector. This so-called *flop-in* arrangement produces a strong increase in the signal at resonance. If the *A* and *B* fields have oppositely directed field gradients, the detector normally detects a large signal, which is decreased at resonance (*flop-out* arrangement). Note that the atoms normally experience a strong magnetic field in the *A* and *B* magnetic fields, facilitating the sign determination of μ_{eff} for the Paschen–Back region atoms.

The theoretical linewidth in resonance experiments is determined by the Heisenberg uncertainty relation. In ABMR the width is determined by the time spent by the atoms in the oscillating field and corresponds to 10–50 kHz. The resonance frequency can therefore normally be determined to within a few kHz, whereas the accuracy in conventional optical spectroscopy is of the order of 100 MHz. In a modified method introduced by *Ramsey* (Nobel prize 1989) [7.1, 7.8], two synchronously oscillating RF fields, widely separated in a long *C* field are used to effectively increase the interaction time, and the linewidth can be reduced to a few hundred Hz, enabling extremely accurate hfs determinations. Due to the interference in the two separated interactions, fringe patterns are obtained, as illustrated in Fig. 7.6 (*Ramsey fringe method*) (see also Sect. 9.7.3).

The selection rules and transition probabilities for RF transitions are determined by the magnetic dipole operator for the whole system

$$\mu = \mu_I + \mu_J. \quad (7.16)$$

In a weak field (Zeeman effect of the hfs), the selection rules for RF transitions are

$$\Delta M_F = 0, \pm 1, \quad (7.17)$$

$$\Delta F = 0, \pm 1, \quad F = 0 \leftrightarrow F = 0 \quad \text{forbidden}. \quad (7.18)$$

$\Delta M_F = 0$ transitions are induced by a magnetic RF field parallel to the static field, while $\Delta M_F = \pm 1$ transitions occur for an oscillating field perpendicular

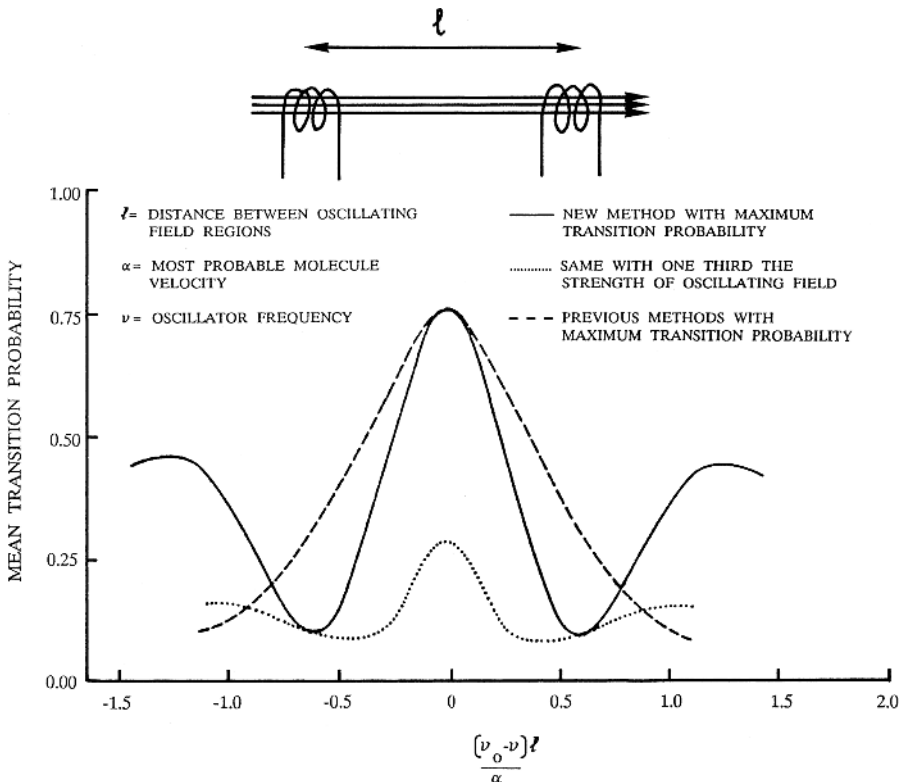


Fig. 7.6. Arrangement and signal for the Ramsey fringe technique [7.8]

to the static field. The transitions are denoted σ and π transitions, respectively. (The magnetic field is perpendicular to the electric field; compare Sect. 4.2.1.) In a strong magnetic field (Paschen–Back effect of hfs), we have the selection rules

$$\Delta M_I = 0, \Delta M_J = 0, \pm 1. \quad (7.19)$$

This means that the RF field can flip the decoupled electronic angular momentum but not the nuclear spin.

According to (2.45) the resonance frequency for a $\Delta F = 0, \Delta M_F = \pm 1$ transition in a weak field is given by

$$\nu = \frac{|\Delta E_m|}{h} = \left| \frac{\mu_B B g_J}{h} \frac{F(F+1) - I(I+1) + J(J+1)}{2F(F+1)} \right|, \quad (7.20)$$

where the small contribution from the nuclear magnetic moment has been neglected. (If ν is expressed in MHz and B in Gauss (1 Gauss = 10^{-4} T), the value of μ/h becomes 1.400 MHz/Gauss). The above expression is used to determine nuclear spins, I , with the ABMR method. Since I is limited to integers or half-integers the g_J value can be determined by the same relation if

an approximate value is known. A prerequisite for the detection of a resonance is that the value of μ_{eff} in strong fields is changed through the transition. (For the flop-in arrangement the sign must also be changed.) Therefore, for $J = 1/2$ only one $\Delta F = 0$ transition can be studied (between $M_F = -1$ and $M_F = -2$ in the example given in Fig. 2.20).

In stronger fields, F is no longer a well-defined quantum number. The influence of the other F states can be calculated using higher-order perturbation theory or matrix diagonalization. The deviation from the linear expression given in (7.20) in this field region thus yields approximate information on the hfs splitting. Using the approximate value as a starting point, a search for $\Delta F = 1$ transitions in low fields can be performed. From the hfs constants a and b , the magnetic dipole moment μ_I and the electric quadrupole moment Q of the nucleus can be determined, provided that reliable theoretical calculations of the electronic magnetic field and the electric field gradient at the nucleus can be performed; see (2.39) and (2.44). If the magnetic moment has been determined by a direct method (like NMR, Sect. 7.1.6) for one isotope it is possible to determine the corresponding moment for another isotope using the ratio between their interaction constants. According to (2.36) and (2.39) we have $a = -kg_I\mu_N$ and $\mu_I = g_I\mu_N I$. The maximum component $\mu_I = g_I\mu_N I$ is defined as the scalar dipole moment of the nucleus. For two isotopes 1 and 2 we then have

$$\frac{\mu_{I_1}}{\mu_{I_2}} = \frac{a_1}{a_2} \frac{I_1}{I_2}. \quad (7.21)$$

This relation is based on the assumption that the k value is the same for both isotopes. Since k , to a first approximation, is only related to the electronic shell, such an assumption is very reasonable. However, small differences in k can occur due to electron penetration into the nucleus (*s*-electrons). This results in a deviation from the relation in (7.21), or a so-called *hyperfine anomaly* [7.9]. However, this anomaly is generally less than 1%. The dipole moment of the nucleus can also be determined directly by high-precision ABMR measurement in high magnetic fields, by observing the small direct contribution from the nucleus.

The first ABMR measurements were performed on alkali atoms, which can easily be detected using a hot wire of W, Pt or some other material with a high work function (Langmuir–Taylor detector). An atom with a low ionization energy is ionized with a high probability when it hits the wire, and the resulting ion current is measured. For elements with a higher ionization potential the ionization can be accomplished through electron bombardment, but the yield is then many orders of magnitude lower. Atoms which have passed the apparatus at resonance can also be detected by observing the fluorescence light which is released upon irradiation with a laser tuned to a strong transition (Sect. 9.7.1). Radioactive isotopes can be detected with a very high sensitivity by using the radioactive decay. The atoms are then collected on a foil which, after exposure, is transferred to a scintillation or

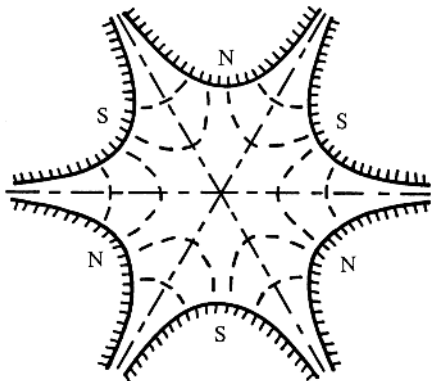


Fig. 7.7. A sextupole magnet

Geiger–Müller detector. For a further increase in sensitivity, focusing sextupole magnets can be used instead of the conventional A and B magnets. In a sextupole magnet, such as the one shown in Fig. 7.7, the field strength is proportional to r^2 (r is the distance from the symmetry axis), which, according to (7.14) and (7.15), means that a focusing force is obtained for $\mu_{\text{eff}} < 0$, while defocusing occurs for $\mu_{\text{eff}} > 0$. A large number of shortlived radioactive nuclei have been studied with regard to spin and moment using the ABMR method [7.10, 7.11]. Such measurements are made possible by placing the ABMR apparatus on-line with an isotope-producing target at an accelerator facility. Nuclear spins for isotopes with a half-life shorter than 1 minute can be determined.

Apart from being applied to atomic ground states, the ABMR method can also be used for investigating metastable states with a lifetime of at least a few milliseconds, a time allowing passage through the apparatus. Metastable levels not higher than 0.5 eV above the ground state are often sufficiently populated thermally [7.12]. For refractory elements, special techniques have been developed for producing atomic beams of elements such as Mo, Ta and W [7.13]. Metastable levels can be efficiently populated with a plasma discharge in the oven [7.14], by light irradiation, etc. It is valuable to study several states belonging to the ground configuration, allowing for a more complete analysis of the hyperfine interactions. ABMR techniques and results are discussed in [7.15, 7.16]. Atoms with $J = 0$ (diamagnetic atoms) cannot be studied by the ABMR method, since they are not deflected in inhomogeneous fields. Spin and moment determinations can then be made only after populating a state with $J > 0$.

The ABMR method has an important application as time and frequency standard. Presently, the hfs splitting between the $F = 4$ and $F = 3$ levels of the $6\ ^2S_{1/2}$ ground state in ^{133}Cs in zero magnetic field is used as a frequency/time standard. This splitting has been determined to be (and then defined as)

$$\Delta\nu(^{133}\text{Cs}) = 9\,192\,631\,770 \text{ Hz}.$$

This value agrees with the astronomical definition based on the tropical year of 1900 within the accuracy of the latter definition. The stability and reproducibility are presently about $1 : 10^{13}$. The Ramsey-fringe technique is used to attain this high degree of accuracy.

7.1.3 Optical Pumping

In magnetic resonance experiments, differences in population between substates are detected using different techniques. In the ABMR method the differences are created by spatially deflecting the atoms. In 1950 *A. Kastler* showed that large differences in population between the sublevels of the ground state can be obtained using polarized light [7.17]. This results in a high sensitivity compared with the case of Nuclear Magnetic Resonance (NMR) and Electron Spin Resonance (ESR), for which methods the normal thermal population differences are used (Sect. 7.1.6). The basic principle for the Optical Pumping (OP) method is illustrated in Fig. 7.8.

Here alkali atoms are considered with a $^2S_{1/2}$ ground state and a first excited $^2P_{1/2}$ state. First we disregard the influence of the nuclear spin. In a weak magnetic field both states are split into two magnetic sublevels with $M_J = \pm 1/2$. If the field is 1 Gauss, the lower of the two levels of the ground state has a thermal population excess of a few parts in 10^7 . The optical pumping is performed on a low-density gas with a vapour pressure of about 10^{-6} torr corresponding to about 10^{11} atoms/cm 3 . At this low pressure the atoms can be considered to be free from the influence of collisions. For example, if we want to study sodium, a resonance cell containing sodium vapour is irradiated with a sodium lamp, preferably of the RF-discharge type (Sect. 6.1.1). Using an interference filter, the transition $3p\ ^2P_{1/2} - 3s\ ^2S_{1/2}$ at 5896 Å (D_1 line) is selected. If the light is circularly polarized with right-hand helicity and if it is radiated along the magnetic field direction, the atoms must take up the angular momentum of the photon upon absorption. The angular momentum is directed in the light propagation direction; σ^+ excitation (Fig. 4.9). This means that the ground-state atoms with $M_J = -1/2$

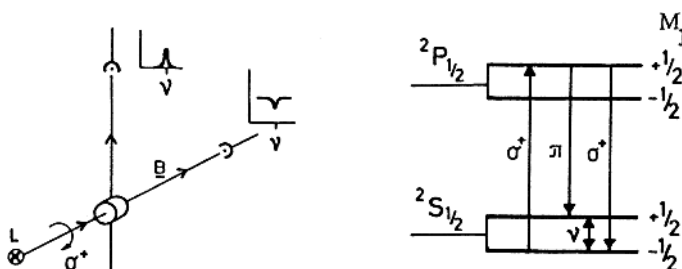


Fig. 7.8. Principles of optical pumping

are transferred to $M_J = +1/2$ ($\Delta M_J = +1$) in the excited state, from which they decay after about 10^{-8} s. The relative probabilities for decays to the $M_J = -1/2$ and $M_J = +1/2$ levels of the ground state are $2/3$ and $1/3$, respectively. Atoms in the $M_J = +1/2$ state cannot be excited, since the angular momentum of the photon cannot be accommodated. Thus atoms which were originally in the $M_J = +1/2$ state remain uninfluenced, whereas the $M_J = -1/2$ atoms are pumped over into the $M_J = +1/2$ ground level after a sufficient number of excitation processes. This is equivalent to an atomic orientation. After the pumping, the gas is totally transparent to the pumping light and a detector placed in the field direction will register a high light intensity. If an RF field, fulfilling the resonance condition for the ground state, is now applied perpendicularly to the static field direction, magnetic dipole transitions $\Delta M_J = \pm 1$ will be induced, transferring atoms into the $M_J = -1/2$ state, where they immediately start to absorb light. At the detector, a decrease in the transmitted intensity is observed. After the excitation, fluorescence light from σ and π transitions is obtained (Fig. 4.9), which can be observed by a detector placed perpendicularly to the magnetic field. The RF resonance, which often occurs at an energy of about 10^{-8} eV, thus results in a release of energetic optical photons (2–3 eV in the visible region) and a strong internal atomic amplification is obtained.

If we take the influence of the nuclear spin into account, we have analogous conditions. With a nuclear spin $I = 3/2$ (e.g., ^{23}Na , ^{39}K or ^{87}Rb) the ground state has an energy-level scheme of the type illustrated in Fig. 2.20. The excited $^2P_{1/2}$ state has a Breit–Rabi diagram of essentially the same appearance as that of the ground state. When σ^+ light is radiated, the magnetic quantum number is increased by one unit in each absorption process, whereas the magnetic quantum number can remain the same or be decreased or increased by one unit in the emission process. The systematic increase in the quantum number in the absorption process results in a final accumulation of atoms in the state with the highest M_F quantum number, after a sufficient number of excitations. (Since $\Delta F = \pm 1$ transitions are also allowed, the hyperfine level groups communicate with each other). When the \mathbf{F} vector has been oriented in this way, there will also be a nuclear orientation due to the coupling between \mathbf{I} and \mathbf{J} . This nuclear orientation can be used for radioactive detection of unstable atoms [7.18]. Oriented β -emitting nuclei will give rise to an anisotropic β -particle intensity distribution. At resonance the orientation is lost and an isotropic angular distribution is obtained. Several short-lived isotopes have been studied with this method, particularly at on-line production facilities [7.19].

If the electronic shell has no angular momentum ($J = 0$), such as in the inert gases, direct nuclear orientation is obtained by pumping. The nuclear moments can then be determined directly, as in NMR experiments (Sect. 7.1.6), but with a much higher sensitivity.

In practice, the optical pumping process is made more difficult by the possibility to leave a pumped state without being affected by an applied resonant field. This phenomenon is called *relaxation* and is primarily caused by collisions with the cell walls. By filling the cell with 10–50 torr of inert gas (buffer gas) the time between wall collisions can be much prolonged due to diffusion. After collisions with inert gas atoms with spherically symmetric electron shells, the orientation of the alkali atom is maintained since the inert gas atoms cannot take up angular momentum. Alternatively, the cell walls can be covered with some suitable organic compound, such as paraffin or teflon. In this way relaxation times longer than one second can be attained. According to the Heisenberg uncertainty principle, this corresponds to a resonance linewidth of less than 1 Hz. A large number of precision determinations of hyperfine structure have been made using optical pumping. Optical pumping experiments are discussed in more detail in [7.20–7.22].

Since extremely narrow resonance lines can be obtained in optical pumping experiments, frequency standards of comparatively simple design can be achieved. The hyperfine transitions used in the atomic-beam clock are also used in the optically pumped frequency standards. However, the resonance frequency is comparatively strongly dependent on the pressure of the buffer gas [7.23]. It is also dependent on the intensity of the pumping light (“light shifts”) [7.21]. Thus, it would seem that an *absolute* frequency standard of maximal precision cannot be achieved. On the other hand, optically pumped systems have proven to be very suitable for relative measurements and as *secondary* standards. By observing sharp $\Delta F = 0$, $\Delta M_F = \pm 1$ transitions, which are strongly magnetic-field dependent, fields can be measured with a very high precision. Optically pumped magnetometers can also be used at low magnetic fields in contrast to NMR devices, which require a field of a few hundred Gauss (0.02 T) to produce a measurable signal.

The *hydrogen maser* provides another way of obtaining an atomic clock [7.24]. The principle of this device is shown in Fig. 7.9. Atomic hydrogen is

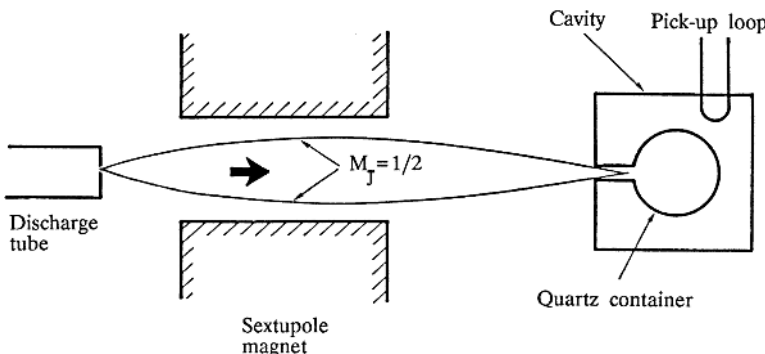


Fig. 7.9. The hydrogen maser

formed through dissociation of hydrogen molecules in an electric discharge. A beam of hydrogen atoms is passed through a sextupole magnet. Atoms in the $M_J = +1/2$ state are then focused, while atoms with $M_J = -1/2$ are defocused (ABMR, Sect. 7.1.2). The former atoms arrive in a quartz container inside a cavity which is tuned to the hfs separation for the ground state of hydrogen, about 1420 MHz. The cavity is subjected to a weak magnetic field, and the $M_J = +1/2$ state is then transformed into the $F = 1$ state, since the nuclear spin is $I = 1/2$. Transitions to the lower state, $F = 0$, can then occur through stimulated emission (c.f. the NH_3 maser, Sect. 8.1). If there is a sufficient number of $F = 1$ atoms in the cavity, self oscillation (maser action) occurs at a frequency corresponding to the hfs separation of hydrogen. The linewidth is influenced by relaxation processes. By coating the walls with teflon, long relaxation times can be achieved. Since buffer gas is not needed in the cavity, there are no pressure shifts. On the other hand, the resonance frequency is slightly dependent on the shape of the cavity and the wall surface, etc. However, these effects are several orders of magnitude lower than the pressure shift in optical pumping. The most accurate determination of the hfs separation in hydrogen is

$$\Delta\nu(H) = 1\,420\,405\,751.7667 \pm 0.0009 \text{ Hz},$$

using the ABMR caesium clock as the reference. The reproducibility of the hydrogen maser does not exceed that of the ABMR Cs clock, which still constitutes the official standard. Atomic clocks have been discussed in [7.25].

Accurate atomic clocks form a core ingredient for the new navigational possibilities provided by the satellite-based *Global Positioning System* (GPS) [7.26]. A GPS device receives the clock-controlled signals from several satellites and interpolates the actual position of the receiver with a precision of typically ten meters. An ultimate precision of few metres seems possible in refined GPS systems. It should be noted that the propagation times of the GPS signals are slightly influenced by the water-vapour content of the atmosphere. High-precision data analysis yields both accurate positions and a global mapping of atmospheric water vapour, which is of the utmost interest for accurate weather prediction [7.27].

7.1.4 Optical Double Resonance

In 1949, *A. Kastler* and *J. Brossel* proposed a resonance method for excited atomic states [7.28]. The principles of this method are best described by discussing an explicit example. A suitable case is the very first experiment of this kind, performed by *Brossel* and *Bitter* for spin-zero mercury isotopes, as illustrated in Fig. 7.10 [7.29]. A resonance cell containing mercury vapour is illuminated with light from a mercury lamp and the released fluorescence light is observed. In an external magnetic field the first excited state, $6s6p\ ^3P_1$, is split up into three magnetic sublevels, while the ground state, $6s^2\ ^1S_0$, is not affected. If the electric field vector of the exciting light is parallel

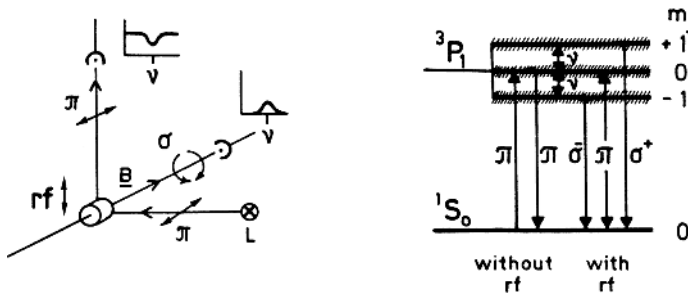


Fig. 7.10. Principles of optical double resonance

to the external field, only π transitions, $\Delta M = 0$, are induced (Fig. 4.9). The fluorescence light, which is emitted after about 10^{-7} s, will also be due to π transitions, with an angular distribution $I_\pi \propto \sin^2 \theta$. Thus, no light is emitted in the field direction. By subjecting the cell to a resonant RF field, transitions to the $M = \pm 1$ levels can be induced and σ components ($\Delta M = \pm 1$) are now obtained in the fluorescent light. Since the σ light has an angular distribution $I_\sigma \propto (1 + \cos^2 \theta)$ with maximum intensity in the field direction, the resonance can be observed as an increase in the light signal at a detector in this direction. Of course, the π emission is correspondingly decreased, and this can be observed at right angles to the field direction through a linear polarizer set to select the π components. The width of the resonance curve will be

$$\Delta\nu = \frac{1}{\pi\tau}, \quad (7.22)$$

since the two sublevels involved both have a natural radiation width of $\Delta\nu_N = (2\pi\tau)^{-1}$. As in optical pumping, the influence of low-energy RF photons is detected using high-energy optical photons. The name double-resonance indicates that both optical and RF resonances are required in the technique. In the chosen example, experimental information on the g_J factor and the natural radiative lifetime is obtained for the excited state. In Fig. 7.11 examples of RF resonance in excited S states of ^{39}K are shown together with the corresponding Breit–Rabi diagram. In this case of hyperfine structure, the signals in the Paschen–Back region yield information on the nuclear spin ($2I + 1$ resonances), the magnetic dipole interaction constant (the signal separations are $a/\mu_B g_J$) and the Landé g_J factor (the centre of gravity of the $2I + 1$ signals corresponds to the pure electronic Zeeman-effect magnetic-field position). Hyperfine structure can also be measured by optical double-resonance, even if the magnetic field is zero. (The direction of the electric field vector of the light is then chosen as the quantization axis.) A schematic example of $\Delta F = 1$ transitions induced in zero field for the $7^2P_{3/2}$ state of ^{133}Cs ($I = 7/2$) is given in Fig. 7.12. The corresponding energy-level diagram can be found in Fig. 2.18 (left; $b(^{133}\text{Cs})$ is almost zero).

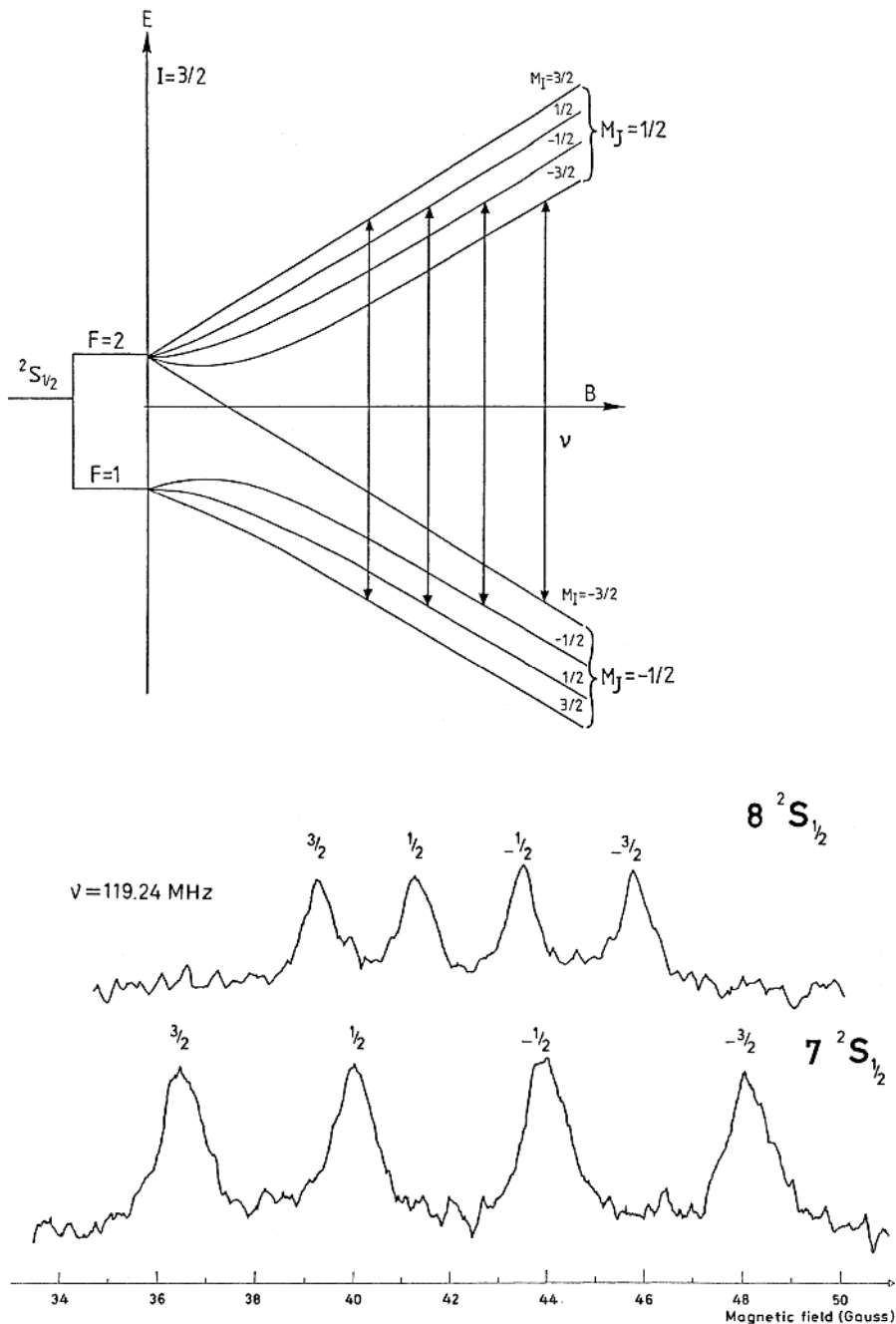


Fig. 7.11. Optical double-resonance signals in the Paschen-Back region for excited S states of ^{39}K ($I = 3/2$). Stepwise excitations from the $4 \ ^2S_{1/2}$ ground state via the $4 \ ^2P_{1/2}$ state with circularly polarized light were used [7.30]

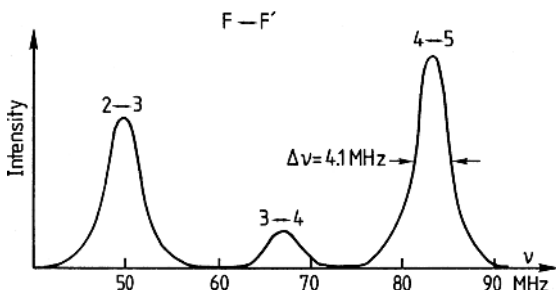


Fig. 7.12. $\Delta F = \pm 1$ ODR signals in the $7p\ 2P_{3/2}$ state of ^{133}Cs

Elements with such a low vapour pressure that a sufficient atomic density cannot be obtained in a quartz resonance cell before the softening point of quartz is reached can be investigated in an atomic beam which is produced in a vacuum system (Sect. 7.1.2). A section of the beam is illuminated with light and is subject to an RF field. The intensity, or polarization distribution, of the fluorescence light is observed. The optical double-resonance technique is a very general one, allowing important information to be extracted for excited states. (See also Sect. 9.3.) Similar information is obtained in experiments using the level-crossing technique, which will be described next. The experimental arrangements are quite similar, too.

7.1.5 Level-Crossing Spectroscopy

In the level-crossing (LC) method interference effects in the fluorescence radiation are studied instead of RF resonances. Since the technique is very closely related to the resonance methods, we will treat it in this context. Level-crossing effects were first observed by *W. Hanle* in 1924, who studied the magnetic-field dependence of mercury fluorescence light close to zero magnetic field [7.31]. A classical description of the effect was given. The phenomenon was investigated again in 1959 in a study of fine-structure level crossings for the $1s2p\ 3P$ multiplet of ^4He , performed by *Colgrove* et al. [7.32].

Let us consider two magnetic sublevels belonging to an excited state of lifetime τ . In a particular field B_0 the two levels cross. We also consider two sublevels belonging to the ground state. In Fig. 7.13 we assume that the magnetic quantum numbers M are 1 and 3 in the excited state and 2 and 3 in the ground state.

The atoms are irradiated with light that is polarized at right angles to the external magnetic field. Such light will induce σ^+ and σ^- transitions ($\Delta M = \pm 1$), as described in Fig. 4.9. First we consider the case where the magnetic field is set far from B_0 . The $M = 3$ level in the excited state is excited from the $M = 2$ level in the ground state, and in the decay σ as well as π light is obtained. The $M = 1$ level can be excited from the $M = 2$

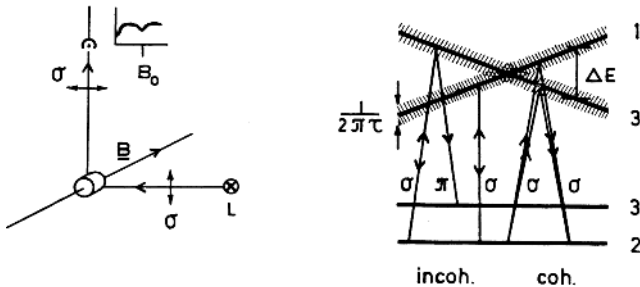


Fig. 7.13. Principles of level-crossing spectroscopy

level, and σ light is emitted in the decay. The scattering processes, in which the two excited levels participate, are completely independent of each other. This is called *incoherent* scattering. In the magnetic field region in which the two excited levels overlap within their natural radiation widths $(2\pi\tau)^{-1}$, a different scattering process can occur. *Cohesive* excitation of the two levels is possible from the $M = 2$ level, since every incoming photon has σ^+ ($\Delta M = +1$) as well as σ^- ($\Delta M = -1$) character. Because of the uncertainty in energy the process is allowed in the overlap region from an energy point of view. The atom is excited into a linear superposition of the two excited substates. The difference in phase in the factors $\exp(-iEt/\hbar)$ for the wave functions of the two states is

$$\Delta\phi = \frac{\Delta Et}{\hbar}. \quad (7.23)$$

Within the overlap region

$$\frac{\Delta E}{h} \leq \frac{1}{2\pi\tau} \quad (7.24)$$

the phase difference will not exceed $\Delta\phi = 1$ during the lifetime τ . Thus, a “phase memory” is retained from the excitation to the decay and we get interference between the amplitudes from the scattering processes involving the two sublevels. The total intensity of the scattered light is independent of the strength of the magnetic field, but in the overlap region the angular distribution of the fluorescence light is changed. The detected intensity change can be used to localize the level-crossing position. Conceptually, there are many parallels between the level-crossing phenomenon and Young’s double-slit experiment. Thus, the levels correspond to the slits. There is interference only when the slits are close to each other, not when they are far apart. The total intensity is constant, and only the distribution changes. The interference effect occurs only if the two slits are illuminated coherently.

The complete theory of resonance scattering is given by *Breit* [7.33] and *Franken* [7.34]. The *Breit formula* from 1933 gives the intensity S of emitted photons with polarization vector e_g obtained after absorption of photons

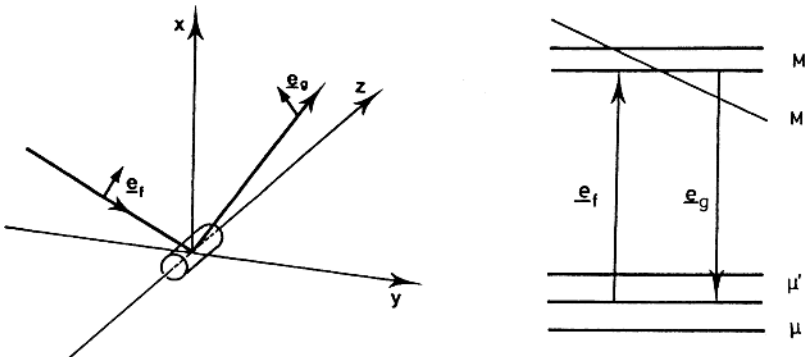


Fig. 7.14. Resonance scattering

with polarization e_f (e_g and e_f are unity vectors) in the interaction with an atomic system (Fig. 7.14).

If the excited state has magnetic sublevels with indices M and M' and the ground state has sublevels with indices μ , and μ' , the *Breit formula* can be written

$$S = C \sum_{\substack{\mu\mu' \\ MM'}} \frac{f_{M\mu} f_{\mu M'} g_{M'\mu'} g_{\mu' M}}{1 + 2\pi i\tau(\nu_M - \nu_{M'})}. \quad (7.25)$$

Here $f_{M\mu}$, $g_{M'\mu'}$ etc. are matrix elements of the type

$$\begin{aligned} f_{M\mu} &= \langle M | \mathbf{e}_f \cdot \mathbf{r} | \mu \rangle, \\ g_{M'\mu'} &= \langle M' | \mathbf{e}_g \cdot \mathbf{r} | \mu' \rangle, \end{aligned} \quad (7.26)$$

where \mathbf{er} is the electric dipole operator. The transition probability per time interval between sublevels with quantum numbers M and μ is proportional to $|f_{M\mu}|^2$. τ is the natural radiative lifetime for the excited state and $\nu_M - \nu_{M'}$ is the energy separation in frequency units between the sublevels with quantum numbers M and M' . In (7.25) the summation should be performed for all pairs of levels in the excited state and in the ground state. To differentiate between summations over the ground-state levels and over excited-state levels we define

$$K_{MM'} = \sum_{\mu\mu'} f_{M\mu} f_{\mu M'} g_{M'\mu'} g_{\mu' M}. \quad (7.27)$$

We then have

$$S = C \sum_{MM'} \frac{K_{MM'}}{1 + 2\pi i\tau(\nu_M - \nu_{M'})}. \quad (7.28)$$

Since the order of summation is immaterial we can write

$$\begin{aligned} S &= C \sum_{MM'} \frac{1}{2} \left(\frac{K_{MM'}}{1 + 2\pi i\tau(\nu_M - \nu_{M'})} + \frac{K_{M'M}}{1 + 2\pi i\tau(\nu_{M'} - \nu_M)} \right) \\ &= C \sum_{MM'} \frac{1}{2} \left(\frac{K_{MM'}}{1 + 2\pi i\tau(\nu_M - \nu_{M'})} + \frac{K_{MM'}^*}{1 - 2\pi i\tau(\nu_M - \nu_{M'})} \right), \end{aligned} \quad (7.29)$$

since $f_{M\mu}^* = f_{\mu M}$, etc. We then have

$$\begin{aligned} S &= C \sum_{MM'} \left(\frac{\operatorname{Re}\{K_{MM'}\}}{1 + 4\pi^2\tau^2(\nu_M - \nu_{M'})^2} \right. \\ &\quad \left. + \frac{\operatorname{Im}\{K_{MM'}\}2\pi\tau(\nu_M - \nu_{M'})}{1 + 4\pi^2\tau^2(\nu_M - \nu_{M'})^2} \right). \end{aligned} \quad (7.30)$$

Because of the selection rule $\Delta M = 0, \pm 1$ we find that $K_{MM'} \neq 0$ only for $|M - M'| = 0, 1$ or 2 . For $|M - M'| = 0$ a level crossing cannot occur because of the non-crossing rule. Instead a related phenomenon, “*anti-crossing*”, can be observed under certain circumstances [7.35]. For the arrangement shown in Fig. 7.13 it can be shown that $K_{MM'} = 0$ for $|M - M'| = 1$. If we now consider the special case where the sublevels of the excited state are linear Zeeman levels, we have $|\nu_M - \nu_{M'}| = 2\mu_B g B / \hbar$ for $|M - M'| = 2$, yielding

$$\begin{aligned} S &= C \left(\sum_M \operatorname{Re}\{K_{MM}\} + \frac{\sum_{MM'} \operatorname{Re}\{K_{MM'}\}}{1 + (2g\mu_B\tau B/\hbar)^2} \right. \\ &\quad \left. + \frac{\sum_{MM'} \operatorname{Im}\{K_{MM'}\}2g\mu_B\tau B/\hbar}{1 + (2g\mu_B\tau B/\hbar)^2} \right). \end{aligned} \quad (7.31)$$

The first term represents the field-independent background, the second denotes a Lorentzian with FWHM $\Delta B = \hbar/g\mu_B\tau$, and the third one describes a dispersion curve with the extrema separation $\Delta B = \hbar/g\mu_B\tau$.

This formula describes the signal around zero magnetic field, the so-called *Hanle effect*. The signal is generally a superposition of a Lorentzian and a dispersion curve on a constant background. The background corresponds to the incoherent excitation processes, in which each level scatters individually. We note that

$$K_{MM} = \sum_{\mu\mu'} |f_{M\mu}|^2 |G_{M\mu'}|^2. \quad (7.32)$$

Depending on the chosen polarization directions, $K_{MM'}$ can be made purely real or purely imaginary. It can be shown that when the polarization of the

detected light is chosen to be parallel or perpendicular to the polarization of the exciting light $K_{MM'}$ will be real, yielding a pure Lorentzian, whereas at 45° $K_{MM'}$ is imaginary. By changing the polarization it is thus possible to choose the signal shape. From (7.31) it can be seen that the signal half-width depends not only on τ but also on g . The g value describes the rate of crossing and it is obvious from Fig. 7.13 that the region of level overlap depends on the crossing angle. For a general level-crossing signal in a field B_0 , where B_0 is non-zero, the signal full-width at half-maximum (FWHM) of a Lorentz-shaped curve is given by

$$\Delta B = \frac{1}{\pi \tau (d\nu/dB)_{B_0}}. \quad (7.33)$$

The Hanle effect is, in general, much stronger than the high-field signals, since many pairs of $|\Delta M| = 2$ levels contribute to the zero-field signal.

While the level-crossing phenomenon in general requires a quantum-mechanical treatment, a simple, semiclassical model can be given for the Hanle effect. We then consider the absorbing atoms as electrical dipoles which oscillate along the horizontal axis, as shown in Fig. 7.15. Such a dipole will radiate in a $\sin^2 \theta$ pattern, where θ is measured relative to the horizontal axis. Thus, no intensity will be observed at the detector shown in the figure. If a magnetic field is applied, the atom seen as a magnetic dipole will precess around the magnetic field with the Larmor frequency ω_L :

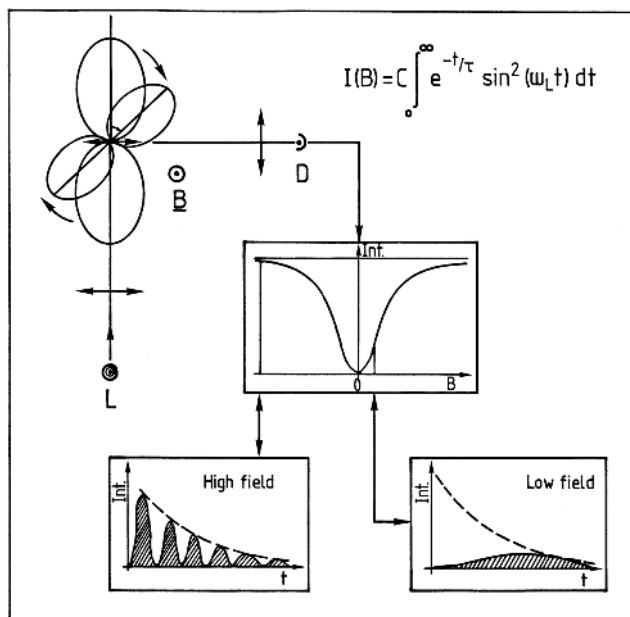


Fig. 7.15. Semiclassical picture of the Hanle effect

$$\omega_L = \frac{g_L \mu_B B}{\hbar}. \quad (7.34)$$

The dipole radiation pattern will then revolve and the direction θ can be replaced by $\omega_L t$, where t is the time after the excitation. Since the dipole radiates energy, a factor $\exp(-t/\tau)$ must be added. τ is the mean lifetime of the state. In level-crossing spectroscopy continuous excitation of dipoles oc-

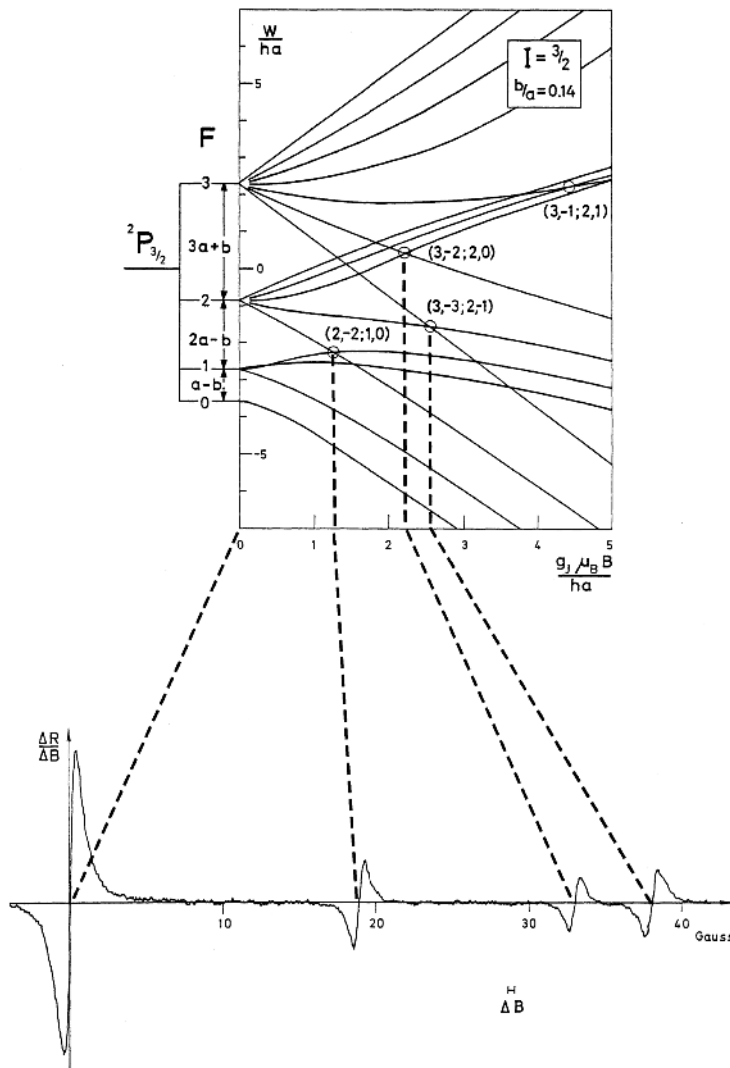


Fig. 7.16. Hfs level diagram for the $6p\ ^2P_{3/2}$ state in ^{87}Rb and corresponding level-crossing signals. $\Delta M = 2$ level-crossings are denoted by the symbol $(F, M; F', M')$ [7.36]

curs and the reradiated light is observed continuously. The observed intensity $I(B)$ will then be the result of an integration from 0 to infinity in time. We thus have

$$I(B) = C \int_0^\infty e^{-t/\tau} \sin^2(\omega_L t) dt, \quad (7.35)$$

where C is a constant. This is a standard integral yielding

$$I(B) = C' \left(1 - \frac{1}{1 + (2g_L \mu_B \tau B / \hbar)^2} \right), \quad (7.36)$$

which is an inverted Lorentzian.

In Fig. 7.16 an example illustrating the use of the level-crossing method for the determination of hyperfine structure is given. The state $6p\ ^2P_{3/2}$ in ^{87}Rb is studied. By employing magnetic field modulation in conjunction with lock-in detection the derivative (approximately) of the $\Delta M = 2$ level-crossing signals is recorded. Clearly, the positions of the crossings depend not only on the factors a and b but also on the g_J factor. As a matter of fact, only the ratios a/g_J and b/g_J can be determined by level-crossing spectroscopy.

Using optical double-resonance and level-crossing spectroscopy much experimental information, particularly on hyperfine structure, has been obtained. To perform a complete hyperfine structure analysis, it is necessary to have data for many states belonging to the same configuration. Using excitation from metastable states and utilizing cascade population of lower states from high-lying states opens up a wide field of application for these methods [7.37]. By using tunable lasers as excitation light sources still further possibilities are created (Sect. 9.3). The consistency of theoretical calculations for evaluating nuclear moments can be tested by studying a large number of levels for the same atom. (Clearly, the nucleus can only have well-defined nuclear moments.) The influence of polarization, correlation and relativistic effects can be investigated in this way.

As we have seen, lifetimes for excited states can be determined using optical double-resonance and level-crossing spectroscopy. The results are very reliable, since these methods are subject to only small systematic errors.

Resonance scattering by atoms has further been discussed in [7.38]. ODR and LC techniques were reviewed in [7.39–7.41] and extensive results for alkali metal atoms have been presented in [7.42].

7.1.6 Resonance Methods for Liquids and Solids

We will now discuss resonance techniques that are useful for studying liquid and solid samples. In these methods the differences in population between magnetically separated sublevels, due to the thermal Boltzmann distribution, are utilized. Magnetic field splittings are always small in comparison to kT , which is about $1/40$ eV at room temperature. Thus population differences will always be small, and the number of atoms required is much larger than for

the optical resonance techniques. However, very sensitive resonance detection techniques based on RF signals have been developed. The field of resonance spectroscopy of non-gaseous media is covered in [7.43–7.45].

When sample atoms are not in a gaseous phase, coupling to the surrounding medium occurs. This has the effect that after a perturbation, e.g., an abrupt magnetic field change, a new equilibrium value $\bar{\mu}_L$ of the macroscopic magnetization, μ_L , is reached in the sample only after a certain time, the relaxation time characterized by the time constant τ . The effect of the relaxation can be taken into account by adding a term $(\bar{\mu}_L - \mu_L)/\tau$ to (7.7). The new mathematical relations, expressed in component form, are known as the *Bloch equations*. The solution reveals that the magnetic resonance curve is a Lorentzian with a half-width inversely proportional to τ . From the equations it also follows that, apart from fast changes of sign for $(\mu_L)_z$ at resonance, there will also be a transverse macroscopic component $(\mu_L)_T$ which rotates at the resonance frequency. Here the relaxation time τ is introduced in a vector relation and thus all components of μ_L will have the same value of τ . However, it is generally necessary to separate the *longitudinal relaxation time* τ_1 for $(\mu_L)_z$ and the *transverse relaxation time* τ_2 for $(\mu_L)_{x,y}$.

Magnetic resonance is normally detected utilizing the transverse component $(\mu_L)_T$, which is formed when the resonance condition is fulfilled. In the detection method devised by *F.B. Bloch*, a detection coil, placed at right angles to the inducing RF coil, is used. A sinusoidal voltage component is induced in the detection coil by the rotating magnetization. Because of the perpendicular arrangement the driving field is not picked up. A simple measurement system based on this principle is shown in Fig. 7.17. In a different detection technique, devised by *E.M. Purcell*, a single coil is employed and a bridge circuit is used to measure the induction changes in the coil that occur at resonance.

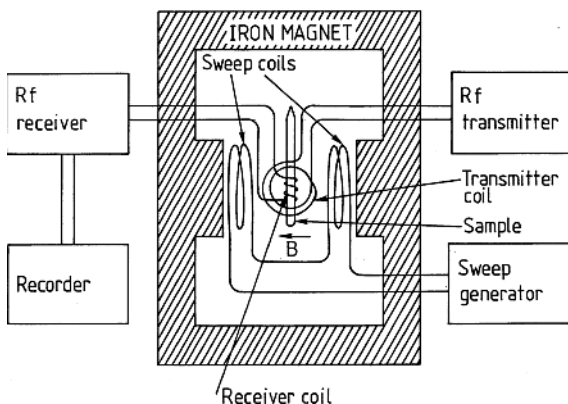


Fig. 7.17. An NMR spectrometer

Nuclear Magnetic Resonance. The NMR technique utilizes the macroscopic magnetic moment resulting from the nuclei in the sample. In an external magnetic field B the nuclear spin I can have $2I + 1$ different orientations. The energy E_m of a magnetic sublevel is given by

$$E_m = -g'_I \mu_B B m_I. \quad (7.37)$$

A macroscopic longitudinal magnetization (μ_I)_z due to the slightly different thermal level populations is obtained. Using an RF field, magnetic dipole transitions between the levels are induced and g_I can be measured. Since the magnetic moments of nuclei are small ($\mu_N = \mu_B/1836$), the resonance frequencies for commonly used field strengths are low. At a field of 1 T, typical for an iron magnet, resonance frequencies of a few tens of MHz are obtained. With superconducting magnetic field coils fields of 10 T corresponding to ~ 500 MHz (for protons) have been attained with a corresponding increase in signal strength.

The nucleus most commonly observed is the hydrogen nucleus (proton). The proton resonance frequency is slightly dependent on the position of the hydrogen atom in the molecule. This is because a varying degree of shielding of the magnetic field occurs, depending on the properties of the neighbouring atoms. Thus, the NMR method can be used for structural determinations and chemical analysis (see ESCA, Sect. 5.2.2). As an example, an NMR spectrum for ethanol C_2H_5OH is shown in Fig. 7.18. The proton resonance frequency is characteristic for each of the structural groups. At higher resolution it is observed that the resonances are broken up into a number of separate signals. This is due to *spin-spin interactions* the different nuclei in the molecule. Further information on the molecule can be obtained from the number of resonances and the size of splittings.

The technique we have discussed so far is the continuous-wave (stationary) method. For a constant magnetic field, the frequency of the oscillator, which generates a field with an amplitude of about 10^{-7} T, is slowly swept and

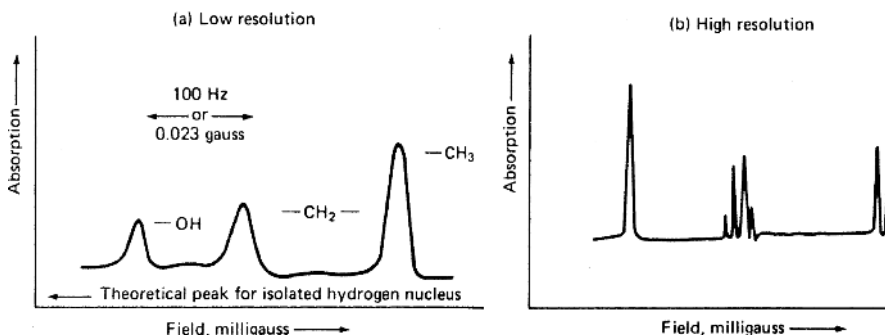


Fig. 7.18. NMR spectra of the protons in C_2H_5OH taken at low and high resolution [7.46]

the signal is recorded as a function of frequency. An NMR spectrum in the *frequency domain* is thus obtained.

Modern NMR spectroscopy frequently uses pulsed RF radiation and the observation is performed instead in the *time domain*. Pulsed NMR can be utilized in different ways. If a short pulse of high field strength B_1 , ($\sim 10^{-3}$ T) and duration t_p is applied, the magnetic moments will be rotated by an angle α around B_1 ,

$$\alpha = g_I' \mu_B B_1 t_p, \quad (7.38)$$

and a macroscopic transverse magnetization is created for nuclei with a resonance frequency covered by the Fourier-broadened frequency distribution, $\Delta\nu$, centred around the nominal oscillator frequency ν_0 ($\Delta\nu \propto 1/t_p$). For each kind of nuclei (e.g., the protons in the ethanol molecule) a rotating macroscopic transverse magnetization will occur that will induce an oscillating voltage in the pick-up coils. The oscillation will die away with the relaxation time constant. The recorded signal is called the *Free Induction Decay* (FID) signal. Every type of nucleus covered by the pulse will give rise to separate FID signals which will interfere with each other. Using a Fourier transform, the individual Larmor precession frequencies $F(\omega)$ (resonance frequencies) can be calculated from the time-domain spectrum (the interferogram) $f(t)$:

$$F(\omega) = 2\pi \int_{-\infty}^{+\infty} f(t) \exp(-i\omega t) dt. \quad (7.39)$$

Clearly, this *Fourier Transform NMR* (FT-NMR) has much in common with optical Fourier transform spectroscopy (Sect. 6.2.4) and quantum-beat spectroscopy (Sect. 9.4.5), including the multiplex advantage, allowing simultaneous detection of the signals from different nuclei. In a mechanical analogy, the sharp pulse can be seen as a stroke that excites several tuning forks, which for some time ring out their eigenfrequencies. A very good signal-to-noise ratio is obtained in FT-NMR, allowing the detection of biologically less abundant nuclei with non-zero spin, e.g., ^{13}C and ^{31}P .

For liquids high-resolution NMR spectra, such as the one shown in Fig. 7.18 for ethanol, can be obtained. Sharp signals, separated due to spin-spin or quadrupole interactions, are obtained. The signals are not broadened since the molecular motion in the liquid averages out the inhomogeneities that would otherwise make the resonance frequency unsharp. This is not the case for solids, in which the constituents are fixed and yield permanent different field distributions broadening the resonance lines. A remedy for the broadening is to simultaneously apply a strong radio-frequency field that is resonant with the nuclei that are not under (resonance) investigation. These nuclei will then rotate and the spin-spin coupling to the studied nuclei will be averaged out. The technique is called *high-power decoupling*. Broadening due to coupling between nuclei of the same kind obviously cannot be eliminated in this way, but this can be accomplished instead by choosing a *magic angle* θ

$(3\cos^2\theta - 1 = 0, \theta = 54.7^\circ)$ between an axis of rapid mechanical sample rotation and the B_0 direction (see also Sect. 9.4.5).

Many NMR techniques that utilize pairs of RF pulses or sequences of pulses have been devised for measurements of τ_1 and τ_2 . The angle of rotation due to the B_1 field can be chosen by varying the length of the pulses; see (7.38). In one technique a “90° pulse” brings the magnetization down into the xy plane from the initial z direction. Because of slight inhomogeneities in the magnetic field, the individual nuclear spins will have slightly different Larmor precession frequencies, and thus the spins, which were initially aligned by the 90° pulse, will dephase leading to a decay of the ac signal picked up from the rotating transverse magnetization. However, if a “180° pulse” is applied after some time T , all the individual spins will be inverted and start precessing in the opposite direction, again with slightly different Larmor frequencies. After a time T the individual spins will again be in phase, creating a macroscopic transverse magnetization that will result in a strong pick-up signal, a *spin echo*, which will begin to die away when the spins begin to be out of phase again. The situation is similar to that in a race between fast and slow runners, where the runners change direction at a second signal and run back to the starting line, which they will all reach at the same time. The height of the spin echo will reflect the true “dephasing time”, τ_2 , due to the spin-spin relaxation, which can now be measured in spite of the unavoidable field inhomogeneities. However, if a molecule moves in a liquid subject to an inhomogeneous field, the amplitude of the echo will be further reduced and diffusion coefficients or even flow velocities can be measured. The spin-echo phenomenon has its counterpart in the optical region, where photon echoes can be induced by laser pulses. Echo techniques have been discussed in [7.47].

NMR techniques are used for studying the chemical composition as well as the detailed structure and bond character of molecules. Kinetic processes, such as rotations and inversions of molecules, can also be studied. NMR has found many industrial applications, especially in measurements on foodstuffs. The strength of the proton signal yields the concentration of a hydrogen-containing substance. The signal of protons in a solid matrix decays faster than that for a liquid sample. This property can be used for fast measurements of moisture content or oil assessment in seeds, etc. NMR spectroscopy has been discussed in [7.45, 7.48–7.50].

A further application of NMR techniques is for magnetic field measurements. A well-defined, small probe sample, e.g. water in an RF coil is used, positioned in the unknown field, which is calculated by inserting the measured frequency in (7.37). Because the population differences are due to thermal effects, fields above 0.02 T are normally necessary. This technique is also frequently used for stabilizing a magnetic field by regulating the magnetizing-coil power supply using a servo-loop locked into the NMR signal.

A diagnostic application of NMR in the medical field has been made possible through the development of the *NMR imaging (tomographic) technique*

[7.51–7.55], frequently referred to as MRI (*magnetic resonance imaging*). Here the object, e.g., the head of a patient, is placed in a magnetic field that has a well-defined field gradient produced by gradient coils in the x , y and z directions. For a given oscillator frequency the resonance condition is fulfilled only in a particular layer, which can be moved in the gradient direction through the object by varying the frequency. By sequentially measuring the signals from layers at different orientations in the object it is possible to reconstruct the proton density of the object in three dimensions by a mathematical algorithm (back-projection) similar to the one used in X-ray tomographic imaging [Computer-Aided Tomography (CAT) scanners]. In this way high-resolution images can be obtained which discriminate between different types of tissues. The diagnostic capability is much increased by using the different relaxation times in different tissues, e.g., in tumours compared with normal tissue. Rather than imaging the proton concentration, images of the local τ_1 and τ_2 values can then be made. Paramagnetic ions such as Gd^{3+} influence relaxation times and can be used as MRI contrast agents [7.56].

Using pulse techniques it is also possible to produce dynamic images of blood flow, etc. Current developments are aimed at increasing the sensitivity, e.g., by using higher fields, so that imaging of other nuclei of high medical interest but low biological abundance (^{43}Ca , ^{31}P , ^{23}Na , ^{19}F , ^{15}N and ^{13}C) may be realized. In Fig. 7.19 an example of an NMR tomographic image and in Fig. 7.20 a corresponding X-ray tomographic image are shown, illustrating the detection of a brain tumour with the two techniques.

Very recently the MRI techniques have been extended to the imaging of gas filling in the lungs [7.57, 7.58]. Lungs are traditionally very difficult to image. In the new technique inert gas atoms are first polarized by optical pumping (Sect. 7.1.3). Metastable ^3He atoms were polarized by optical pumping on the $1s2s\ ^3S_1 - 1s2p\ ^3P_0$ transition, induced by the circularly polarized 1083 nm output from an arc-lamp-pumped LNA ($\text{La}_{1-x}\text{Nd}_x\text{MgAl}_{11}\text{O}_{19}$) laser [7.59]. The orientation is transferred with high efficiency to the $1s^2\ ^1S_0$ ground state by spin-exchange collisions leading to a strong orientation of the $I = 1/2$ nuclei [7.60]. Alternatively, rubidium atoms are first optically pumped (by a powerful diode laser), transferring their orientation to the helium nuclei in spin-exchange collisions [7.61, 7.62]. In this way ground-state ^{129}Xe atoms ($I = 1/2$) can also have their nuclei oriented. The pumping process must occur at low pressures, but it is then possible to compress the gas for convenient transport of reasonable amounts of gas [7.63]. The polarized inert gases can keep their orientation for hours (100 h) [7.64] and thus be brought to the patient, inhaled into the lungs without risk, and kept there for a few seconds during the MRI recording. The high degree of orientation strongly compensates for the low density of spins so that images of diagnostic quality can be obtained. Examples of human lung imaging are shown in Fig. 7.21. Since xenon is absorbed into the blood stream, it is possible to follow the dynamic gas uptake from the lungs, which yields further diagnostic information.

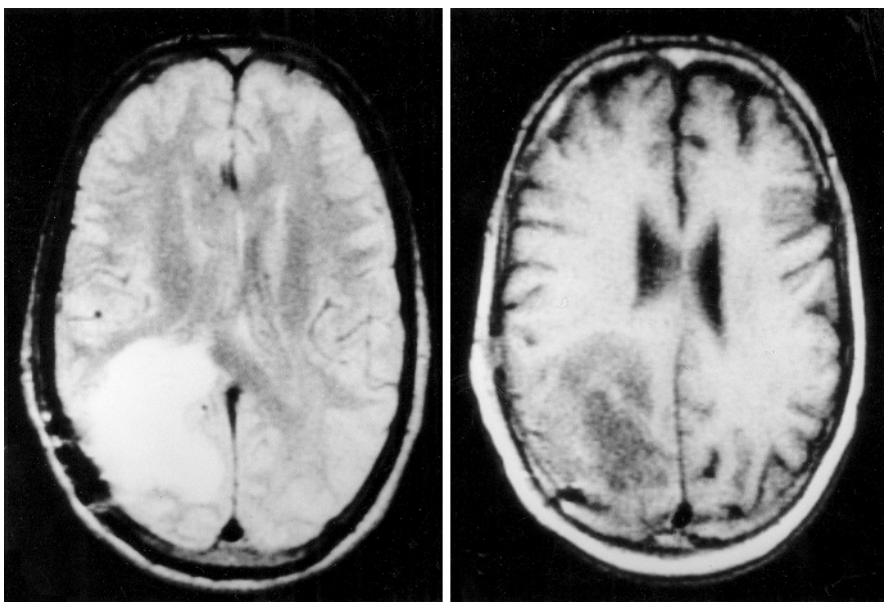


Fig. 7.19. NMR tomographic images of a human brain revealing a malignant tumor in the lower left region. The image to the *left* is τ_2 weighted while the image to the *right* is τ_1 weighted (Courtesy: O. Jarlman)

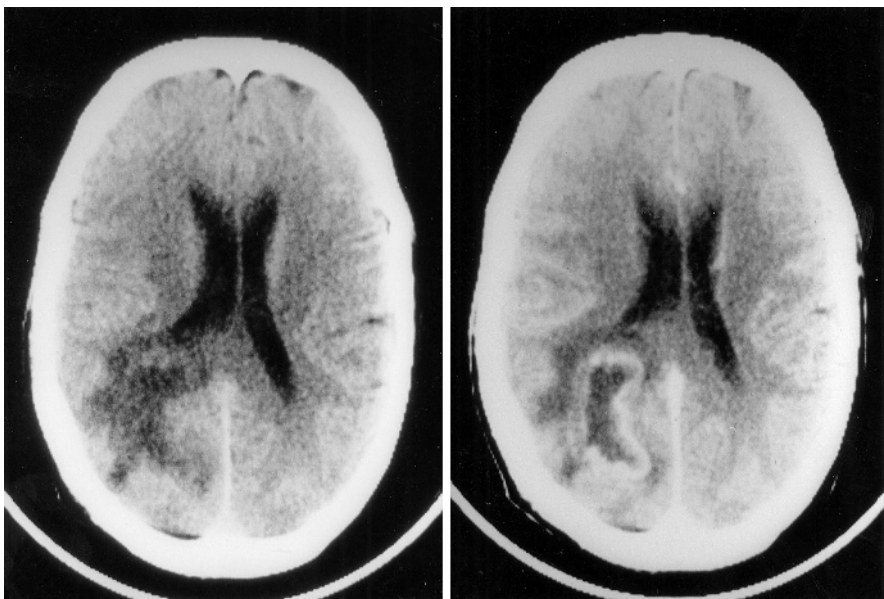


Fig. 7.20. Computerized X-ray tomographic images of the same human head as shown in Fig. 7.19. The image to the *right* is enhanced with an iodine contrast medium. (Courtesy: O. Jarlman)

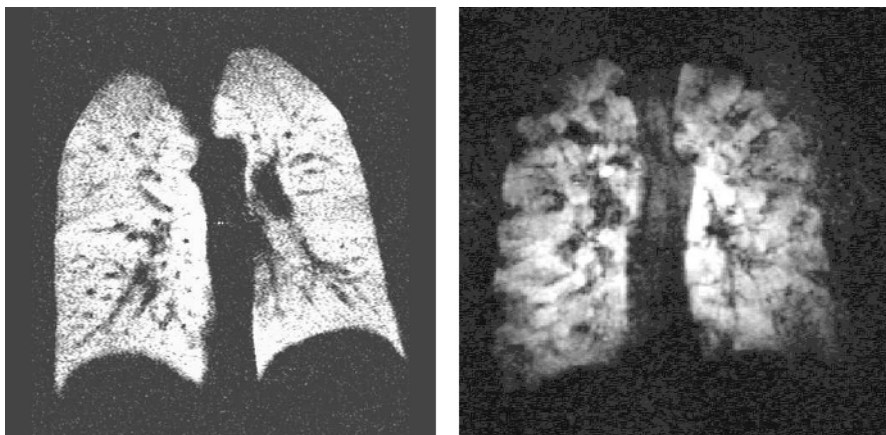


Fig. 7.21. MRI images of human lungs, recorded using spin-polarized helium gas. To the *left* normal lungs are shown, while the lungs of a heavy smoker are shown to the *right* [7.65]

We note that the possibility of providing an ensemble of fully spin polarized He nuclei opens up very interesting possibilities in nuclear physics, providing polarized beam targets, spin analysis in nuclear reactions, etc. [7.65].

Optical pumping in solids also provides new possibilities in material research. Relaxation processes can be studied and optical detection of NMR and ENDOR signals can be obtained [7.66].

Electron Spin Resonance. ESR is the counterpart of NMR, corresponding to magnetic splitting due to *electron* spin rather than *nuclear* spin. In a crystal field the projection of the orbital angular momentum \mathbf{L} on a given direction is frequently averaged to zero. This is called *quenching* and has the effect that orbital angular momentum does not need to be considered when discussing the energy-level splittings in an external field. Thus the splitting will be given only by the magnetic moment due to the total electronic spin \mathbf{S} , as shown in Fig. 7.22. In the simplest case we have

$$E_m = g_s \mu_B B m_s. \quad (7.40)$$

Since the magnetic moment of the electron is large ($g_s \simeq 2$) in comparison with that of the nucleus, much higher resonance frequencies are obtained than for NMR. In commercial instruments it is customary to work at 0.34 T, corresponding to a resonance frequency of about 9.5 GHz. Thus, the experimental technique involves resonant cavities and waveguides for the microwaves used. In the presence of crystal fields the position of the resonance depends on the orientation of the crystal with respect to the magnetic field. The interaction must therefore be described by vectors or tensors rather than by a scalar relation such as (7.40).

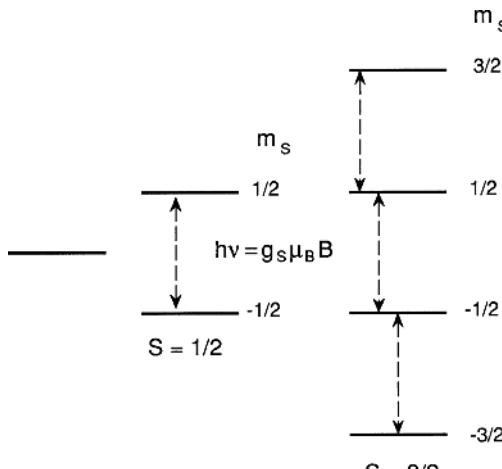


Fig. 7.22. ESR transitions

Because of the larger energy separations in ESR the signals are much stronger than in NMR. ESR can be applied in much the same way as NMR for analytical purposes. A prerequisite is that the net spin is non-zero, which is the case for *paramagnetic* substances. In particular, free radicals and molecular ions can frequently be investigated. ESR techniques have been discussed in [7.67–7.69].

Electron-Nuclear Double-Resonance. In the ENDOR method NMR and ESR are combined. The technique is illustrated in Fig. 7.23, in which a system with $S = 1/2$ and $I = 1/2$ is considered. In the Paschen–Back region we have two m_I values for each m_S value. If a microwave field saturates the ESR transition between the states with $m_I = +1/2$, only a weak absorption signal is obtained when an equilibrium situation is reached. The upper level

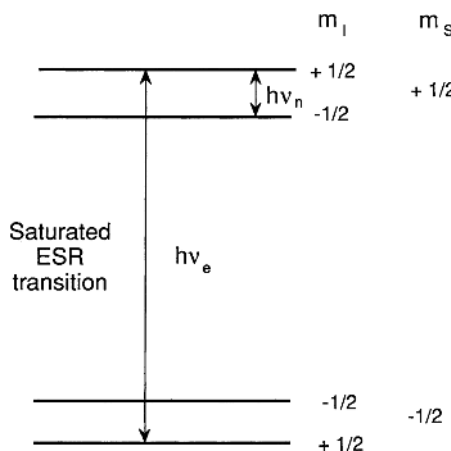


Fig. 7.23. The principle of ENDOR

then has a high excess population compared with the Boltzmann distribution. If an NMR transition is then induced in the upper group of levels, the state with $m_I = +1/2$ is depopulated. This results in a strong increase in the ESR resonance. In an ENDOR experiment the ESR resonance in the microwave region is thus constantly driven and a search is made in the radio-frequency region until the NMR resonance occurs, resulting in a strong increase in the ESR amplitude. Using the ENDOR technique, NMR signals with an intensity typical for ESR signals are thus obtained.

We have discussed earlier the high sensitivity achieved in optical pumping, for which a much more complete orientation is achieved than in the thermal case. As mentioned above, certain solids can also be pumped optically and ESR and NMR signals can be detected optically [7.66, 7.70]. However, the efficiency is reduced due to competing radiationless transitions.

7.2 Microwave Radiometry

Spectroscopy in the microwave region yields valuable information on the rotational structure of molecules [7.71–7.73]. Apart from this type of fundamental experiments, important applications of microwave radiometry include atmospheric and ocean monitoring [7.74–7.80]. Passive as well as active techniques are used for different types of remote sensing. Active microwave techniques are pursued with radar systems.

In Fig. 7.24 the vertical absorption of the atmosphere in the 1–300 GHz region is shown. The absorption bands are due to H_2O and O_2 . The 60 GHz O_2 band consists of about 25 lines, which can be resolved in the stratosphere but which overlap in a single band at low altitudes due to pressure broadening. The atmospheric pressure can be measured by studying pressure-broadening effects. At high altitudes the broadening is given by the Doppler effect, which yields information on the temperature. The water vapour content can be determined using the strong absorption at 22 and 183 GHz. Vertical measurements can be performed from the ground (towards zenith) or from satellites (towards nadir). So-called *limb emission* or *limb absorption* measurements can be made from satellites (see Fig. 6.73). In absorption measurements radiation through the atmosphere at sunrise and sunset is employed. A deconvolution procedure must be used to obtain the vertical profiles of pressure, temperature and humidity. Satellites equipped with microwave radiometers can be used to determine temperatures to an accuracy of better than 1 °C.

Active microwave systems (radar) have many applications apart from the normal ranging applications that are used, for example, for navigation. A weather radar station is capable of locating and quantifying rainfall over considerable distances. To detect the small particles a short operating wavelength is necessary to achieve adequate scattering. Radar systems for environmental applications are air- or satellite-borne. In SLAR (*Side Looking Airborne Radar*) systems the imaging sweep is obtained through the forward movement

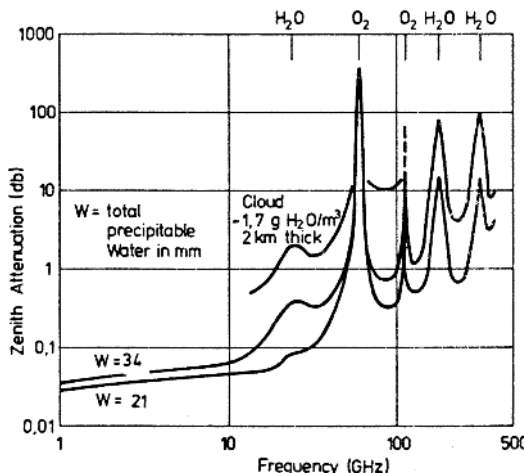


Fig. 7.24. The integrated vertical microwave absorption of the atmosphere with varying water content in the air [7.81]

of the propelling craft. The principle of SLAR is shown in Fig. 7.25. A disc-shaped radiation lobe is transmitted from an elongated antenna. The ground surface is hit at successively later times and the echo from the radar pulse will return to the antenna at different times and a picture line is thus generated. Then a new pulse is transmitted and a new picture line, corresponding to the new position of the aeroplane is obtained. The strength of the return signal depends not only on the distance, which can easily be compensated for, but also on the structure of the surface, water content, etc. Ocean waves, especially, yield echoes whose strength depends on the wavelength of the water waves (sea clutter). A 10 GHz system ($\lambda = 3$ cm) is especially sensitive to the fine capillary waves, which occur at sufficiently large wind speeds (> 8 m/s). If the sea is covered by oil, the capillary waves disappear and the oil slick can be detected as a decrease in the sea clutter. In Fig. 7.26 oil detection with a SLAR system is illustrated. Such a system is also useful for sea ice monitoring.

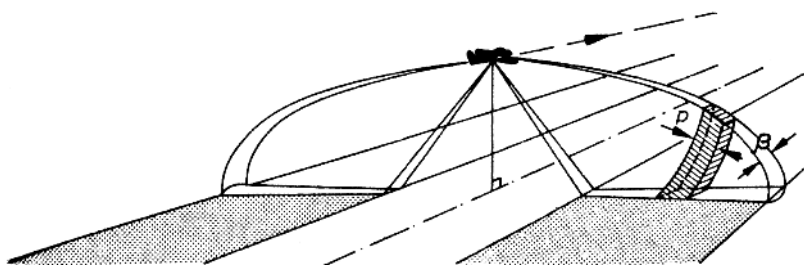


Fig. 7.25. The principle of SLAR [7.82]

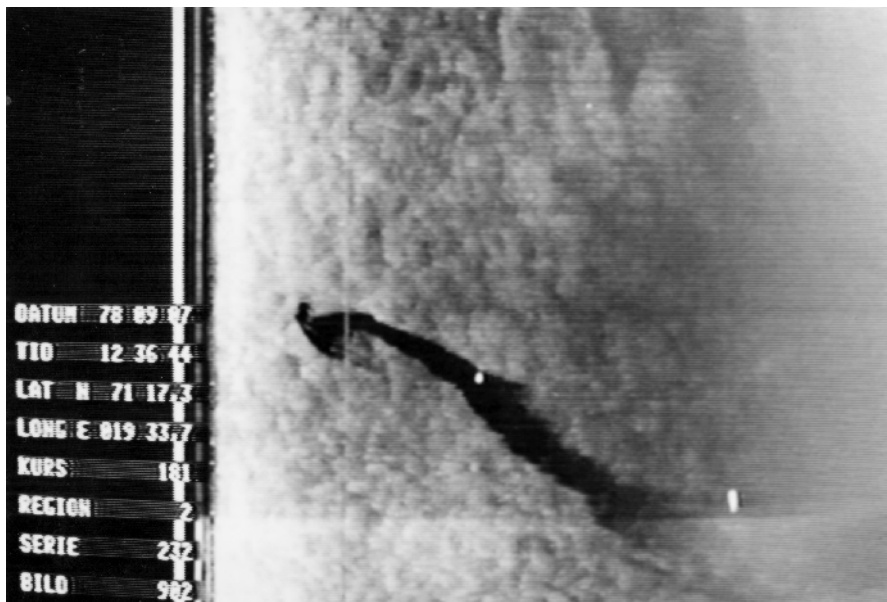


Fig. 7.26. $20 \times 20 \text{ km}^2$ SLAR image of a marine oil slick and ships. 24 hours before the recording 25 tons of crude oil had been dumped. (Courtesy: The Swedish Space Corporation)

Because of the long wavelength of the radar waves a high spatial resolution cannot be obtained for antennas of reasonable size. This is a particular problem for satellite applications, which can, however, be circumvented using so-called SAR (*Synthetic Aperture Radar*) techniques. A high lateral resolution is obtained by using short pulses in the same way as in a SLAR system. In order to obtain a high resolution in the flight line direction, the slightly different Doppler shifts in the back-scattered radiation from the diverging antenna lobe are used to sort the return signals into different spatial channels along the flight line [7.83–7.85].

Several active radar satellites have been launched, e.g., the European ERS-1 (1991–1999) and ERS-2 (launch 1995) satellites, which have circular orbits 785 km above the ground. Radar sensors have the particular advantage of providing data irrespective of cloud layer. The ERS SAR system operating in the C-band (5.3 GHz, 6 cm) yields a ground resolution of about 20 m. An ERS image, showing a polar research vessel in the Arctic ice, is presented in Fig. 7.27 [7.86]. The radar echoes depend on the dielectric properties of the target materials. For example, different types of sea ice and the water content of snow can be evaluated in this way [7.87]. Multi-frequency systems and polarization analysis provide spectral finger-printing at microwave wavelengths and classification of image elements [7.75, 7.78, 7.88].

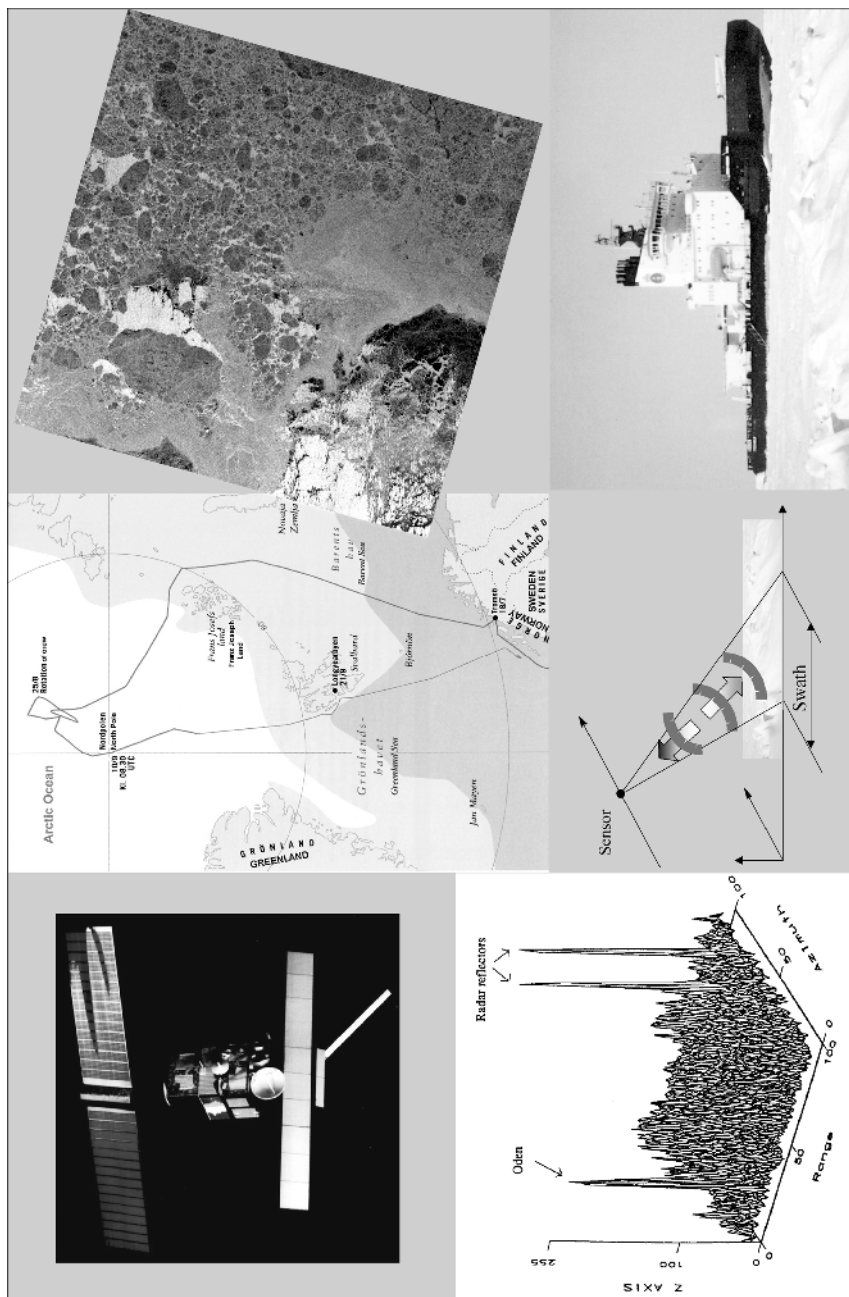


Fig. 7.27. During Arctic expeditions in 1991 and 1996 with the Swedish ice-breaker Oden, data on sea ice and snow were collected and at the same time the ESA ERS-1/2 satellites were used to acquire SAR images (an image over $80 \times 80 \text{ km}^2$ is included). Radar reflectors for calibration were also used [7.86] (Courtesy: J. Askne, CTH)

7.3 Radio Astronomy

In the science of radio astronomy continuum radiation and absorption or emission lines due to celestial phenomena are observed in the frequency region of 1–300 GHz ($300\text{ mm} > \lambda > 1\text{ mm}$). The absorption bands due to the terrestrial atmosphere, as illustrated in Fig. 7.24, will clearly place limitations on such measurements. The diffraction-limited resolution for a telescope is determined by the ratio λ/d , where d is the diameter of the telescope. In a comparison with optical telescopes it can be noted that a radio telescope has 10^4 to 10^5 times worse angular resolution for a given value of d . For practical reasons a telescope diameter of the order of 100 m is an upper limit, especially since a surface precision of about $\lambda/20$ must be maintained. Examples of radio telescopes are the 100 m telescope near Bonn in Germany, which is used in the frequency region 1–45 GHz and the 20 m Onsala telescope in Sweden, which can be used for frequencies up to 120 GHz ($\lambda = 2.5\text{ mm}$). A diagram of the latter telescope is shown in Fig. 7.28.

To amplify the weak radio signals picked up by the telescopes, travelling-wave masers and superconducting mixers are sometimes used. An example

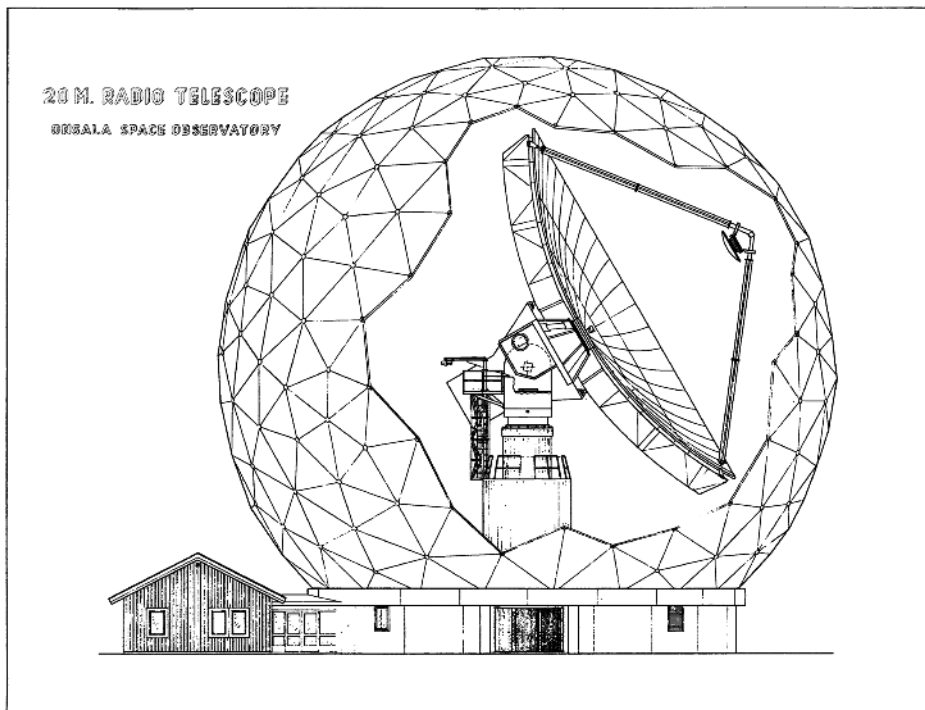


Fig. 7.28. Diagram of the 20 m diameter millimetre-wave telescope at Onsala, Sweden (Courtesy: Onsala Space Observatory)

of a maser medium is iron-doped rutile (TiO_2), which can be magnetically tuned in a certain frequency range. Signal analysis is often performed using autocorrelation techniques, in which the incoming signal is compared with a replica of itself that has been displaced in time by a variable interval. Other signal analysis techniques employ analogue filter banks and acousto-optical spectrometers.

In order to increase the angular resolution in radio astronomy the technique of *aperture synthesis* is used, in which signals from spatially separated antennas are combined, monitoring the correct relative phases. For example, a system of telescopes that can be displaced by up to 5 km relative to each other, due to the fact that they are mounted on rails, is used in Cambridge, Great Britain. The lengths of the connecting cables are known with an uncertainty of 1 mm. The largest such interferometer is the Very Large Array in New Mexico, a Y with 3 arms of length up to 27 km! The mathematical processing of data from different telescope positions to form a high-resolution radio image includes, as its most critical component, a fast Fourier transform, and the fast development of computers has been a prerequisite for high-resolution radio astronomy. As in optical Fourier transform spectroscopy (Sect. 6.2.4), a multiplex advantage is obtained in radio interferometry: information from a solid angle interval, which is determined by the (wide) diffraction lobe of each individual small telescope, is obtained simultaneously. An extreme angular resolution (10^{-4} arcseconds) can be obtained in so-called VLBI (*Very Long Base line Interferometry*) measurements. The first trans-oceanic radio-interferometric measurements were performed in 1968 between telescopes in Sweden, Massachusetts, West Virginia and California. The largest telescope separation was 8000 km. Perfect time synchronization using atomic clocks (Sect. 7.1.3) is needed in order to utilize the detailed phase difference information. VLBI can also be used to obtain precise information on the continuing small displacements of continents. From such measurements it is known that Europe and North America drift apart at a rate of 2 cm/year!

Radio signals are obtained primarily from interstellar gas clouds but also from distinct, localized sources. The gas clouds are observed against the general cosmic background corresponding to black-body radiation of $T_b = 3\text{ K}$. Depending on whether the local radiation temperature T of the cloud is lower or higher than T_b , molecular lines from the cloud are observed as absorption lines in the background radiation or as emission lines, as illustrated in Fig. 7.29. If a population inversion between the molecular levels exists (at least 3 levels must then be involved), the background radiation can be amplified by maser action. Such action can be recognized through the characteristic line narrowing for stimulated emission [7.90–7.92].

Molecular lines observed in the microwave region are due to pure rotational or hyperfine transitions. Hydrogen is the most abundant element in the universe. The H_2 molecule does not possess a dipole moment and therefore no

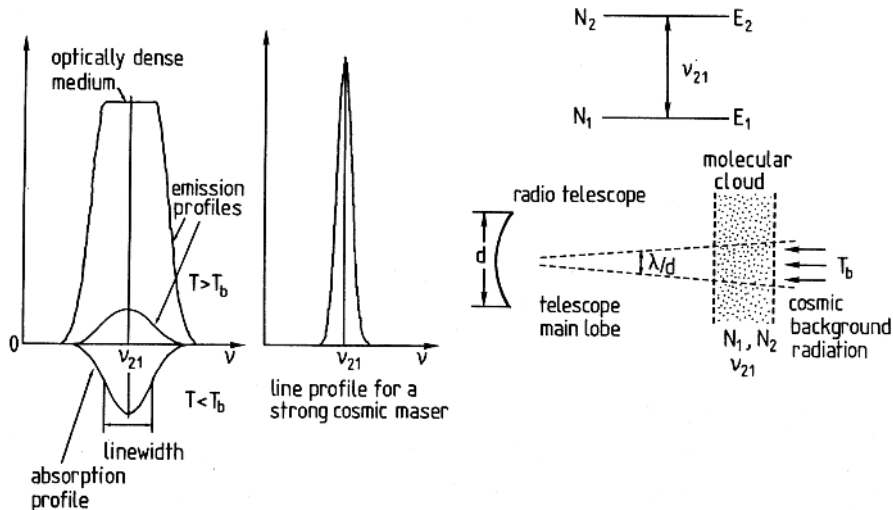


Fig. 7.29. Absorption and emission lines in the microwave region. The narrowing of a maser transition is also illustrated [7.89]

allowed electric dipole transitions are observed. This molecule can, therefore, not be observed.

However, atomic hydrogen can be observed at the magnetic dipole hyperfine transition ($\nu = 1.42$ GHz) between the hyperfine levels $F = 1$ and $F = 0$ of the ground state (Sect. 7.1.3). For example, using the corresponding 21 cm line the spiral structure of our galaxy has been investigated.

A large number of interstellar molecules have been detected. The hydroxyl radical OH has a large dipole moment and was observed in 1963 after necessary laboratory measurements had been made. The OH levels and transitions are depicted in Fig. 7.30. The rotational level is split into two levels (Λ -doubling, Sect. 3.2), each with two hyperfine levels. The observations made were absorption measurements with the strong continuum radio-source Cassiopeia A providing the background. Maser action in OH has been observed in many cases and the pumping is normally due to hot star radiation. The CH radical, also featuring Λ -doubling, was observed at

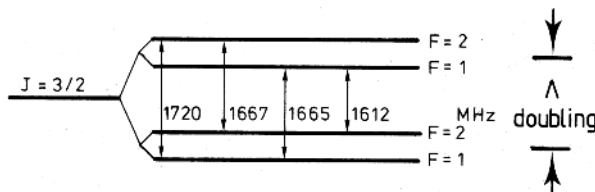


Fig. 7.30. OH molecule substructure and microwave transitions [7.89]

Onsala in 1973. The water molecule H_2O , which has an angle of 105° between the H atoms, has a complex rotational spectrum. Intense maser action has been observed for the 22 GHz transition, which is also seen in atmospheric absorption (Fig. 7.24). High-frequency radio astronomy observations have to be performed on dry days. A large number of other molecules, some of them quite complex, have been observed in space. The (very) remote sensing of the physical conditions in the interstellar clouds has been discussed in [7.93–7.95].

As with any other spectral lines, radio lines exhibit Doppler shifts if the molecular gas is in motion. In Fig. 7.31 velocity distributions are shown based on Doppler observations on OH, CH and HCHO lines observed in the direction of Cassiopeia A. The components around 45 km/s are due to clouds in the Perseus arm of our galaxy, while the components around 0 km/s are due to the Orion arm. While OH and HCHO appear in absorption, CH is seen in (weak) maser emission against the background source.

Apart from the study of interstellar clouds, a large number of “point” sources have also been investigated using radio astronomy. The observation of pulsars (1967) is one of the more spectacular discoveries (Nobel prize to *A. Hewish* in 1994 [7.96]). Pulsars have a pulse period of the order of seconds. They are considered to be rapidly rotating neutron stars, which are very small, dense objects. An example of pulsar signals is given in Fig. 7.32.

The pulsar PSR 1913 +16 is particularly interesting, since it exhibits small periodic changes in its pulse frequency (which is very high; the period is only 59 ms). This means that it has a companion and they orbit, bound

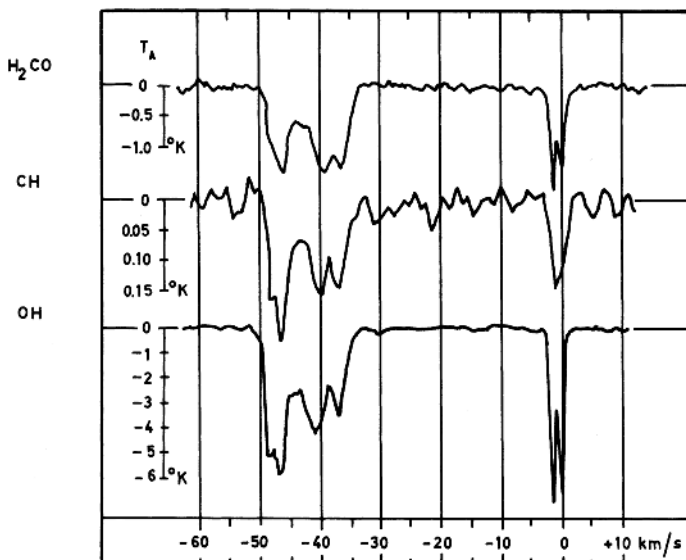


Fig. 7.31. Spiral structure of our galaxy mapped out with Doppler-shifted microwave signals [7.89]

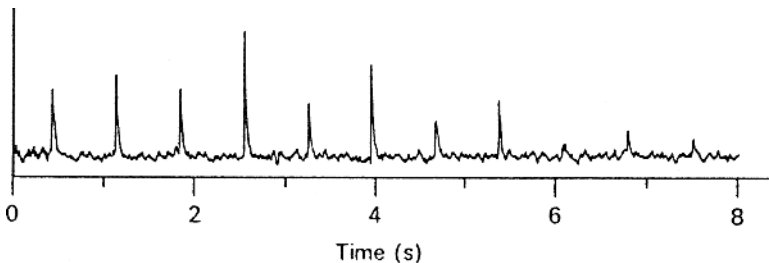


Fig. 7.32. Periodic signals due to a pulsar source (Courtesy: Onsala Space Observatory)

to each other, with a period of 7.8 h, corresponding to a velocity of about $0.001 c$. According to the general theory of relativity, an intensely rotating heavy system should emit gravitational radiation, leading to a slow decrease in the orbit period. This has been accurately observed, fully supporting Einstein's theory [7.97, 7.98]. The 43 arcsecond per century advancement of the perihelion of Mercury was an early confirmation of the theory. For the double pulsar PSR 1913 +16 the corresponding effect is 4 degrees/year! The 1993 Nobel prize in Physics was awarded to *R.A. Hulse* and *J.H. Taylor* for their discovery of this remarkable double pulsar, which constitutes a precise laboratory for relativity research. In particular, the data show that gravitational radiation must exist and should be of a quadrupolar nature. However, the gravitational quanta (*gravitons*) have not yet been observed, although large experimental efforts are under way [7.99].

The enormous energy generation in quasars, probably associated with black holes at cosmological distances, is another fascinating discovery due to radio astronomy. Radio astronomy has been covered in [7.100–7.103].

The somewhat controversial field of the search for extraterrestrial intelligence has been treated in [7.104 7.105]. Radio astronomy tools have been used, but very recently the search has been extended to a search for possible laser flashes from distant objects. The first two space craft to leave the solar system (Pioneer 10 and 11, launched in 1972 and 1973, respectively) carried a plaque with the frequencies of the 14 strongest pulsars, expressed with the hydrogen hfs frequency as a base, and with indications of their relative directions with regard to our solar system, as a sign of our own intelligence [7.106]!

8. Lasers

In this chapter we will discuss the general principles of lasers. Since we mainly consider spectroscopic aspects in this book, we will focus on tunable lasers for laser spectroscopy in the frequency (wavelength) domain and short-pulse lasers for spectroscopy in the time domain. Short-pulse lasers are also required for the generation of ultra-intense laser pulses, the use of which has opened up a new field of spectroscopy: ultra-intense laser/matter interaction. In addition to the many types of spectroscopically interesting lasers, we will also cover a number of the fixed-frequency lasers that are used to pump them. For more detailed accounts of the field of laser physics, frequently also referred to as quantum electronics, we refer the reader to standard textbooks [8.1–8.13].

8.1 Basic Principles

The first operating laser, the ruby laser, was constructed in 1960 by *Maiman* [8.14]. An important step in the development chain resulting in the laser was a theoretical paper from 1958 by *Schawlow* and *Townes* [8.15], who analysed the prerequisites for laser action. The ammonia maser had been introduced as early as 1954 by *Gordon* et al. [8.16]. This device operated in the microwave region, and the laser is the counterpart in the visible wavelength region. As we will see, it is not trivial to bridge the large frequency gap between the microwave and optical regions. The 1964 Nobel Prize in Physics was awarded to *N.G. Basov*, *A.M. Prokhorov* and *Ch.H. Townes* for the development of the maser and the laser [8.17–8.19]. Maser and laser are acronyms for “microwave” and “light”, respectively, “amplification by stimulated emission of radiation”. Stimulated emission is essential for both processes, and we will discuss this phenomenon first. Let us in the same way as in Sect. 4.1 consider a system of atoms with two energy levels E_1 and E_2 (Fig. 8.1). Photons of energy $E_2 - E_1$ are allowed to impinge on the system and we consider which of the two processes, absorption or stimulated emission, is the most probable. In Chap. 4, we showed that $B_{21} = B_{12}$ and therefore the relative probability of the two events is only dependent on the populations of the individual levels. In a system in thermodynamical equilibrium (left in figure), the lower level is strongly overpopulated and therefore the photon is normally absorbed. In order to make the stimulated emission process more probable, we must, in

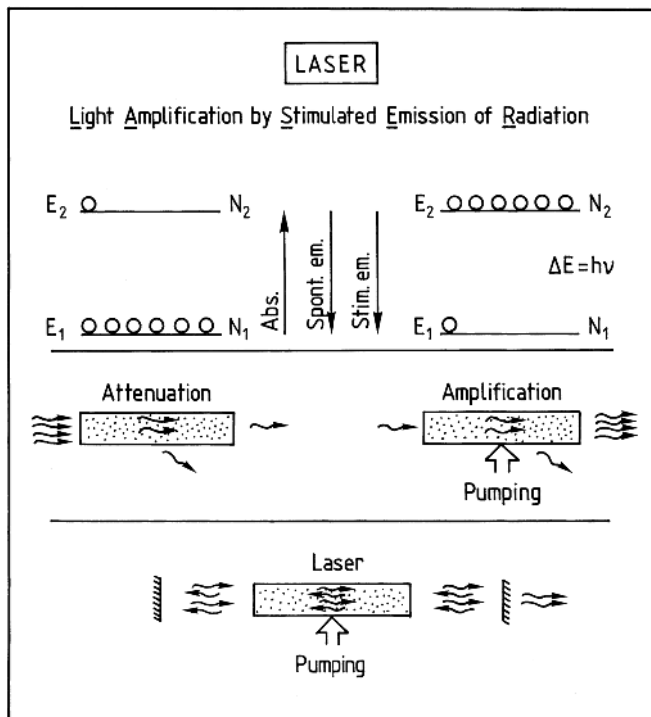


Fig. 8.1. Basic phenomena in laser action

one way or another, induce a greater population in the upper level than in the lower level. Then a greater number of photons are obtained than the number impinging on the medium. These stimulated photons have the same frequency, phase and direction of propagation as the stimulating photons and are described as *coherent*. We have thus shown that *population inversion* is a prerequisite for amplification by stimulated emission of radiation. Note the complete symmetry pertaining to the two processes of absorption and stimulated emission. By arranging a feedback cavity around the amplifying medium a self-oscillating laser can be obtained, as will be discussed in more detail later. A complete discussion of the conditions for reaching the threshold for laser oscillation must also include considerations of linewidths.

The construction of a maser or a laser involves the fundamental task of creating a population inversion. Spontaneous emission is not desired in this case, since it reduces the population difference without leading to the emission of coherent photons. Such decays constitute noise in the amplifier that the inverted system constitutes. A good introduction to laser physics is obtained by considering the mechanism of the ammonia maser. The ammonia molecule is drawn schematically in Fig. 8.2. The nitrogen atom oscillates back and forth through the plane defined by the hydrogen atoms. Two eigenstates are pos-

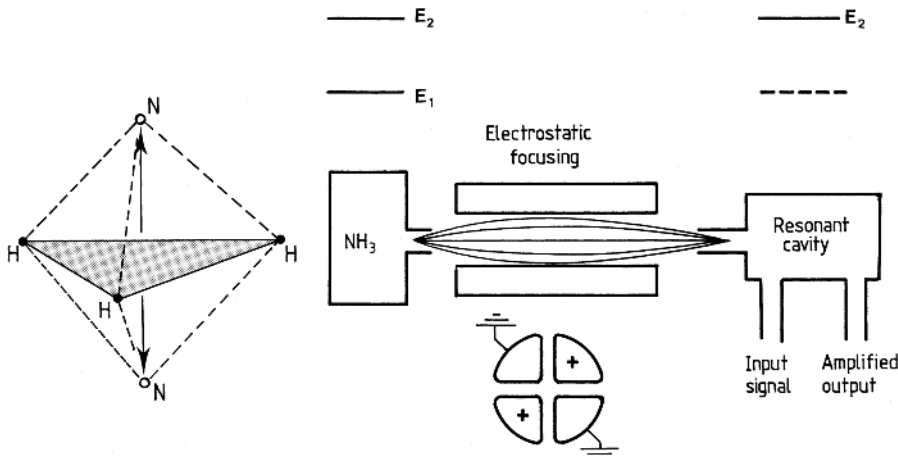


Fig. 8.2. The ammonia molecule and schematics of an ammonia maser

sible for this inversion oscillation, corresponding to a symmetric and an anti-symmetric wave function. The energy separation between these eigenstates corresponds to 23.87 GHz or a wavelength of 1.25 cm for absorbed/emitted photons. In Fig. 8.2 Townes' set-up is also shown (see also Sect. 7.1.3). From the gas reservoir, molecules emerge in both energy states. In passing through an inhomogeneous electric field, molecules in the upper energy level will be focused into the cavity, while lower-level molecules are defocused and filtered away. In this process the molecular induced dipole moment is active (Sect. 7.1.2). The cavity is resonant at the transition frequency between the eigenstates. An inverted population is sustained in the cavity. If a microwave signal of the correct frequency is then fed into the cavity it will give rise to stimulated emission and the signal will be amplified. If a sufficiently large number of molecules in the upper energy state are fed into the cavity, self-oscillation can be initiated by the noise photons also present in the cavity. The ammonia maser was used as a clock before more accurate atomic clocks were developed.

Whereas amplification (oscillation) is obtained comparatively readily at these frequencies, which are of the order of 10^{10} Hz, it is considerably more difficult to achieve a corresponding situation for optical waves with a frequency of 10^{15} Hz. The reason is clear from (4.27):

$$\frac{A_{21}}{B_{21}\rho(\nu)} = 16\pi^2 \frac{\hbar\nu^3}{c^3\rho(\nu)}, \quad (8.1)$$

i.e., the ratio between the number of spontaneous and stimulated decays increases as ν^3 . Thus, the upper level will be comparatively rapidly depopulated by spontaneous decays and a very efficient pumping mechanism for the upper level is necessary to achieve laser action. From this argument it follows that it is very difficult to construct an X-ray laser.

The first demonstration of X-ray lasing was made in 1985 for $3s$ - $3p$ transitions at 20.6 and 21.0 nm in neon-like selenium (Se XXV) [8.20]. Population inversion was created in an elongated plasma created after the impinging of 0.5 ns pulses (0.53 μ m) from part of the NOVA Nd:glass laser facility. Since then much progress has been made [8.21–8.26], facilitated by the development of relatively compact, ultra-intense lasers. These aspects will be covered in Sects. 8.7.2 and 9.6.

8.2 Coherence

Lasers are characterized by light that is highly *coherent* in comparison with light from conventional light sources. There are two types of coherence: *temporal coherence* and *spatial coherence*. The degree of *temporal coherence* of a light source is a measure of the possibility of predicting phase and amplitude for the light at a given location and at a certain time, provided that these quantities were known at an earlier well-defined time, at the same point. As discussed in Chap. 4, there is a time uncertainty τ associated with the spontaneous decay of an excited atom. If the classical wave approach is applied to the light, then the wave will be emitted during $\simeq \tau$ seconds, and therefore the length ℓ_c , the *coherence length* of the connected wave train, will be

$$\ell_c = \tau c. \quad (8.2)$$

Because of the finite emission time in this picture, the wave train is cut off and a Fourier analysis of the train yields a frequency spread of $\Delta\nu = (2\pi\tau)^{-1}$, as previously discussed. From a quantum-mechanical point of view the argument should be given the other way around. The time uncertainty yields a frequency spread and a corresponding associated length of the wave train. Wave trains emitted in different decays are completely unrelated. For $\tau = 10^{-8}$ s a coherence length of 3 m is obtained. Practical gaseous light sources have a Doppler broadening which is considerably larger than the natural radiation width. Because of the increased frequency spread a prediction of the phase is made more difficult. Line light sources have a typical coherence length of $\simeq 10$ cm. Sources emitting a Planck distribution clearly have a very short coherence length.

A light wave is considered to be *spatially coherent* if there is a constant phase difference between *different* points of observation. Light that is emitted from different parts of a conventional light source is not phase-related. Therefore, the light from an extended light source will not be spatially coherent at close distances.

A good measure of the coherence of a light source is its ability to produce stable interference fringes. (An incoherent light source may produce momentary interference but the fringes continuously move swiftly and unpredictably.) The two types of coherence can be illustrated by two examples. If the

path difference in a Michelson interferometer (Sect. 6.2.4) is 1 m no fringes are obtained with a conventional light source because of its poor temporal coherence. If the two slits in Young's experiment are illuminated by light from different parts of a fluorescence tube no fringes are obtained because of the poor spatial coherence of the light source. Lasers have very high temporal and spatial coherence since the photons are produced in chain reactions of stimulated emissions, in which all the generated photons represent waves with a common phase.

8.3 Resonators and Mode Structure

A population-inverted medium will amplify an incoming wave of the correct frequency through stimulated emission. Whereas the maser in the microwave region is an amplifier with a low noise level, finding applications, for example, in radio astronomy (Sect. 7.3) a laser in the visible region is very noisy because of the increasing importance of the spontaneous emission. According to (8.1) the signal-to-background ratio will be reduced by a factor of about 10^{15} for a frequency change of a factor 10^5 , from microwaves to visible light. Therefore, lasers are rarely used for light amplification, except for the case of amplifying laser pulses. Lasers are normally used as *light generators (oscillators)*. An amplifier becomes an oscillator if feedback is introduced. This can be achieved by placing the laser medium in a *resonator* consisting of two mirrors (Figs. 8.1 and 8.3). A spontaneously generated noise photon of the correct frequency and direction of propagation (perpendicular to the end mirror) is amplified and starts the process. The light intensity is substantially increased by reflections back and forth through the laser medium. In order to sustain the laser action, it is necessary to continuously pump in order to maintain the population inversion. In order to obtain a useful external beam, one of the mirrors is made partially transparent. Clearly, the emerging light represents a loss factor and the degree of *output coupling* possible without terminating the laser action depends on the gain of the medium. Ideally, the extracted

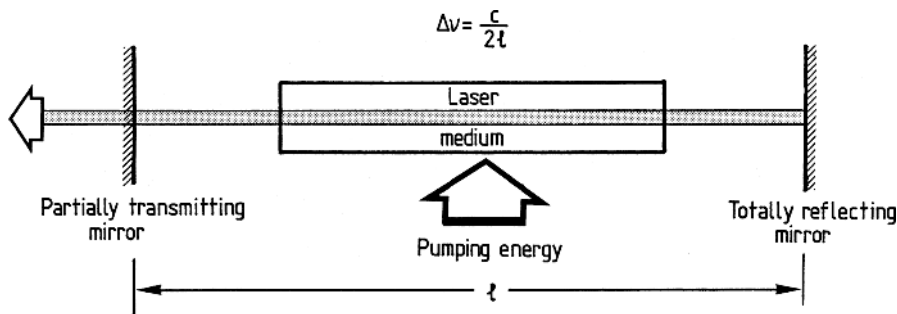


Fig. 8.3. Principal arrangements for a laser

energy would be the only source of loss. By using multiple dielectric layers the absorption losses due to the mirrors can be kept well below 1%. All optical surfaces inside the cavity must be kept very clean since any absorption is amplified by the multiple passes. In the figure the laser mirrors are indicated as plane. For such a system the alignment of the resonator is critical if losses are to be prevented. A considerably more stable configuration is obtained if at least one of the mirrors is slightly curved. In Fig. 8.4 a number of resonator arrangements are illustrated. The relative merits of different configurations have been discussed, e.g. in [8.27, 8.28].

As for a microwave cavity, several types of transverse electromagnetic oscillations or *modes* are possible for a laser cavity. Generally, one tries to isolate the mode that has the highest symmetry. This mode is designated TEM_{00} . Other modes (TEM_{pq} , p, q integers) corresponding to more or less asymmetric radiation fields can be suppressed by making the tube containing the laser medium sufficiently narrow or by introducing an axial aperture. A laser beam due to a laser oscillating in the TEM_{00} mode has a symmetric

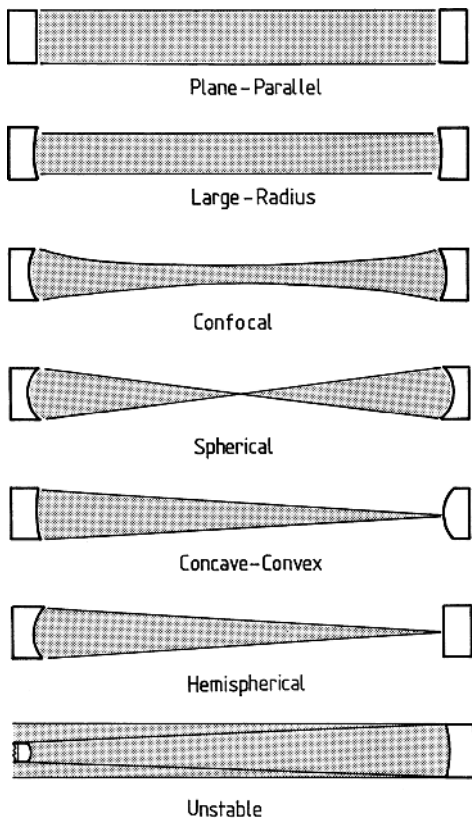


Fig. 8.4. Different resonator arrangements

cross-section and the intensity falls off according to a Gaussian distribution. Laser modes were discussed in [8.28, 8.29].

As a consequence of the coherence, the laser light can be transmitted as an almost parallel bundle. The small divergence is a consequence of the unavoidable influence of diffraction. For radiation in phase and with the same amplitude over a circular aperture of diameter d , the angle θ between the centre of the diffraction pattern and the first dark interference ring is given by

$$\theta = 1.22 \lambda/d. \quad (8.3)$$

A visible diffraction-limited laser with an emerging beam of diameter 1 mm will have a divergence of about 0.5 mrad. Many practical systems have a divergence that is limited only by diffraction. For such a laser the spot at a distance of 1 km has a diameter of about 0.5 m. By first expanding the beam to a larger value of d it is possible to achieve a correspondingly smaller divergence. By focusing a parallel TEM_{00} beam a very small spot diameter δ can be obtained. For a perfect lens of focal length f we obtain

$$\delta = \frac{4}{\pi} f \frac{\lambda}{d}. \quad (8.4)$$

A further useful quantity, related to focused laser beams, is the *confocal parameter* z , defined as the distance between the two locations at each side of the focus at which the intensity has fallen to 50% of the maximum value:

$$z = 2\pi\delta^2/\lambda \quad (8.5)$$

A very high degree of linear polarization can be obtained for a laser with low losses in one direction of oscillation and high losses in the perpendicular direction. For a laser with a gas as the active medium this is accomplished by placing the windows of the gas container at the Brewster angle to the optical axis of the laser (Fig. 8.5). For other lasers some other type of polarizer can be placed inside the cavity.

We have now discussed different characteristics of laser light without dealing with its frequency distribution in detail. It is evident that a stable oscillation mode can be achieved in the resonator only if there is constant

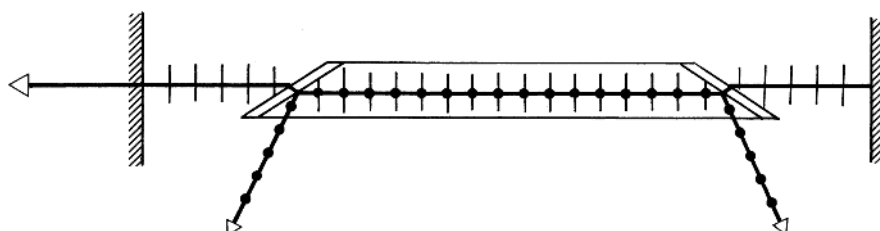


Fig. 8.5. Generation of polarized laser light using intracavity Brewster angle windows

constructive interference, i.e. standing waves. This occurs when an integral number of half-wavelengths fit into the cavity of (optical) path length ℓ . By considering two adjacent modes we obtain the mode separation $\Delta\nu$:

$$\begin{aligned} n \frac{\lambda}{2} &= n \frac{c}{2\nu} = (n+1) \frac{c}{2(\nu + \Delta\nu)} = \ell, \\ \Delta\nu &= c/2\ell. \end{aligned} \quad (8.6)$$

This expression has already been derived; see (6.26). Clearly, the laser cavity is a Fabry–Pérot resonator with a free spectral range given by (8.6). With a cavity length of 1 m the mode separation is 150 MHz.

Let us now consider a gas laser, for which the stimulated emission occurs for a certain spectral line, determined mostly by Doppler and pressure broadening (Fig. 8.6). Modes not falling within the linewidth are impossible since there is no gain for such modes. As a matter of fact, modes that are not close to the peak of the profile (the gain profile) will have too low a gain to compensate for the losses. Clearly, there is a certain threshold for the pump energy below which no modes at all have a sufficient gain. When lasing, only the most favourable modes will oscillate because of the regenerative nature of the laser action (“strong become stronger, weak become weaker”). When several modes oscillate simultaneously we talk about *multi-mode operation*. By introducing a Fabry–Pérot interferometer into the laser cavity with a free spectral range sufficiently large so that only one of its transmission peaks falls in the region for possible laser action, a single cavity mode can be selected (*single-mode operation*). The interferometer is frequently made as a plane-parallel disc with semitransparent dielectric coatings (an “etalon”). The choice of mode is made by inclining the etalon. The transmission maxima of the etalon are also influenced by the temperature. In the absence of temperature stabilization, “mode hopping” can occur.

When the laser is oscillating in only one mode, it produces a beam of very sharp frequency. Because of the generation of light by stimulated emission inside the cavity, the linewidth can become much smaller than the width of the Fabry–Pérot resonance (the Airy function) or the natural radiation width. Using indirect measurement techniques, linewidths of the order of 1 Hz have been established for a He–Ne laser, approaching the Schawlow–Townes limit [8.15]. To obtain narrow lines a careful stabilization of the length of the laser cavity using a servo system is necessary, otherwise vibrations will cause a considerable effective linewidth. Even without such servo stabilization a single-mode laser has very good temporal coherence. In comparison, the coherence length for a multi-mode laser is very small. A high spatial coherence is still maintained due to phase locking in the stimulated emission. Therefore, sharp interference fringes are obtained in most interference experiments.

Now we will study a number of laser types more closely. We distinguish between *fixed-frequency lasers* and *tunable lasers*. In a limited sense, the former type is also tunable since different modes under the gain curve can be selected. In lasers for which the active medium is a solid, the gain curve can

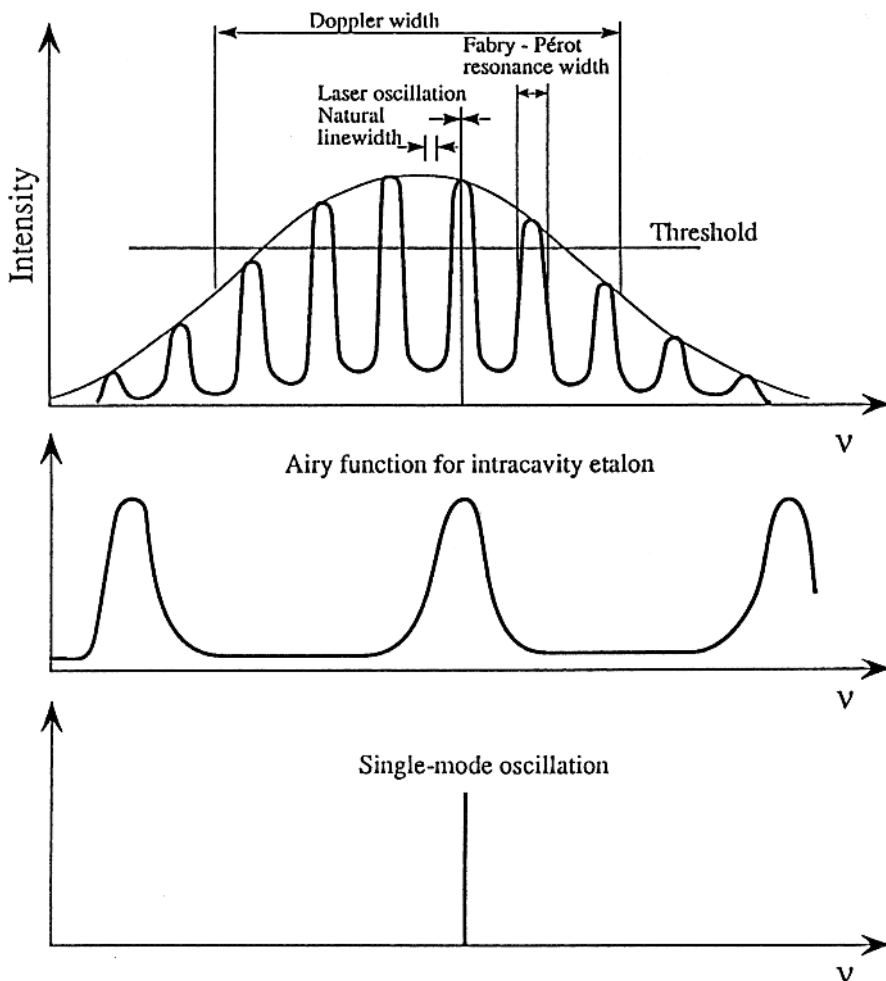


Fig. 8.6. Multi-mode laser action and the generation of single-mode radiation

be moved slightly by changing the temperature. We will primarily discuss fixed-frequency lasers that are used for the pumping of tunable lasers. By a tunable laser we here mean a laser whose wavelength can be varied over a large region ($> 100 \text{ \AA}$). Such lasers, which are of great spectroscopic interest, will be discussed in some detail.

8.4 Fixed-Frequency Lasers

8.4.1 The Ruby Laser

As we have mentioned, laser action was first observed in ruby [8.14]. Ruby is a red crystal of Al_2O_3 with an addition of about 0.05% Cr_2O_3 . Only the Cr^{3+} ions are of interest here since the other ions do not participate in the process. The chromium ion has three d electrons in its unfilled shell and has a 4F term as the ground-state term. The next higher state is a 2G term. The ruby crystal has a weakly rhombic structure. Because of the action of the crystal field, the 4F term will be split into the levels 4F_1 , 4F_2 and 4A_2 , where the designations are no longer the ordinary ones from atomic spectroscopy but are defined in the group-theory treatment of the crystal field problem. The 2G term is split into levels designated 2A_1 , 2F_1 , 2F_2 and 2E . The 4F_1 and 4F_2 levels are strongly broadened into energy bands, whereas 2E has a doublet structure. In Fig. 8.7 the energy levels of Cr^{3+} in ruby that are relevant for laser action are indicated. The ruby crystal has strong, broad absorption bands around 550 and 400 nm. Ions that have been pumped to the 4F bands will fall, within 10^{-7} s, to the 2E levels, in which a population is quickly built up because the lifetime of this level is very long, about 5 ms. Population inversion with regard to the ground state is most easily achieved for the lower of the two

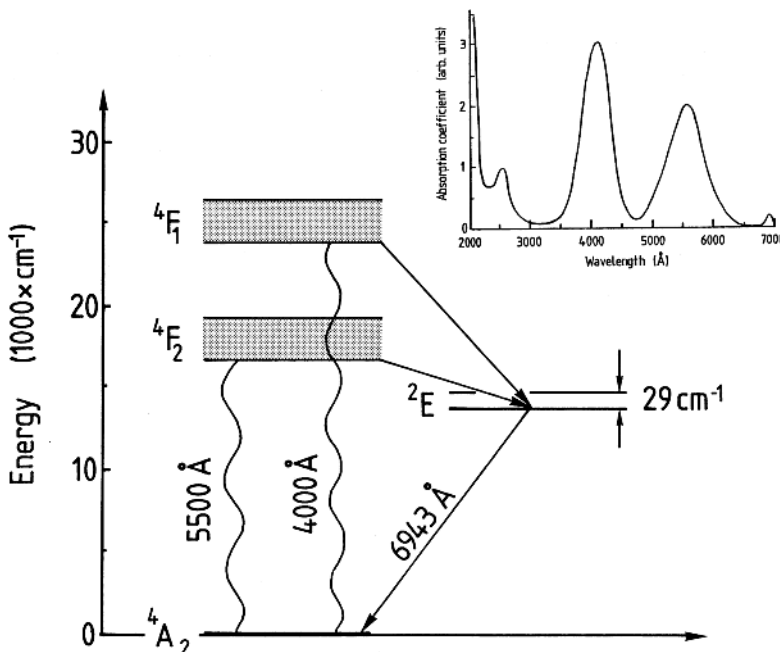


Fig. 8.7. Level diagram and schematic absorption curves for ruby

2E levels. Stimulated emission is obtained at 6943 Å at room temperature. If the crystal is cooled to 77 K (liquid nitrogen temperature) the wavelength is shifted to 6934 Å.

In the ruby laser, which is an example of a *three-level laser*, population inversion must be achieved with regard to the normally well-populated ground state. It is thus necessary to pump the ions very efficiently from the ground state to the 4F levels. In Fig. 8.8 one possible pumping arrangement (also used by Th. Maiman) is shown. A ruby rod, about 5 cm long and with flat, parallel silvered end surfaces, is placed inside a helical flash-lamp, filled with, for example, xenon at high pressure (Sect. 6.1.2). A capacitor of about $100\mu\text{F}$ charged to about 2 kV is discharged through the flash-lamp, which lights up for about 1 ms. Because of the broad absorption bands of ruby a non-negligible part of the light, emitted as a continuum, is absorbed. After about 0.5 ms stimulated emission is transmitted through the one semi-transparent end surface of the rod. The light is emitted as a sequence of short spikes of about 1 μs duration. This is due to the disappearance of the population inversion when stimulated emission has occurred. The flash-lamp is still on and needs some time to restore the population inversion, leading to the emission of a new laser spike. This behaviour, which is frequently not wanted, can be eliminated by *Q-switching* [8.30, 8.31].

In this case, laser mirrors, separated from the rod, are used and the light path between the mirrors is initially blocked. The quality factor or *Q value* of the cavity is then low and stimulated emission is not initiated, although a strong inversion has occurred. If the blocking is quickly removed, the cavity can enhance the light field and the emission occurs in a *giant pulse*. In practice, polarized laser light is used and the Kerr or Pockels effect are employed to rapidly switch the plane of polarization. Giant pulses can have a peak power of 10^8 W and a pulse width of about 10 ns. This technique is referred to as *active Q-switching*. By introducing a *saturable absorber*, which is a nonlinear device with a strong absorption for weak intensities

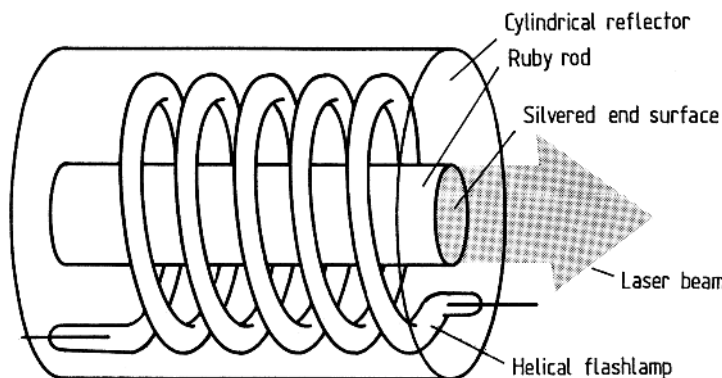


Fig. 8.8. Arrangement for a ruby laser

but showing a good transparency for high intensities, the same effect can be achieved, although not at an equally well-defined time. Saturable absorbers are frequently bleachable dyes, such as BDN (4-dimethyl-aminodithiobenzil-nickel) dissolved in 1,2-dichloroethane for switching of the Nd:YAG laser.

8.4.2 Four-Level Lasers

We have already mentioned the difficulties involved with a three-level laser in which the laser transition is terminated in the continuously well-populated ground state. The successful operation of the ruby laser relies on the very favourable combination of broad absorption bands and the long upper-state lifetime allowing the storage of energy. In a *4-level laser*, a final level, which is not the ground state, is used. The basic diagram is shown in Fig. 8.9a.

Suitable energy-level diagrams of this general type can be found, particularly for ions of the rare-earth elements. The ions can be incorporated into certain crystals such as CaF_2 or CaWO_4 and also in glass. It is important that level 3 (the storage level) has a comparatively long lifetime so that the ions can be accumulated there. On the other hand, level 4 must be depopulated efficiently. In many elements level 4 is so close to the ground state that cooling

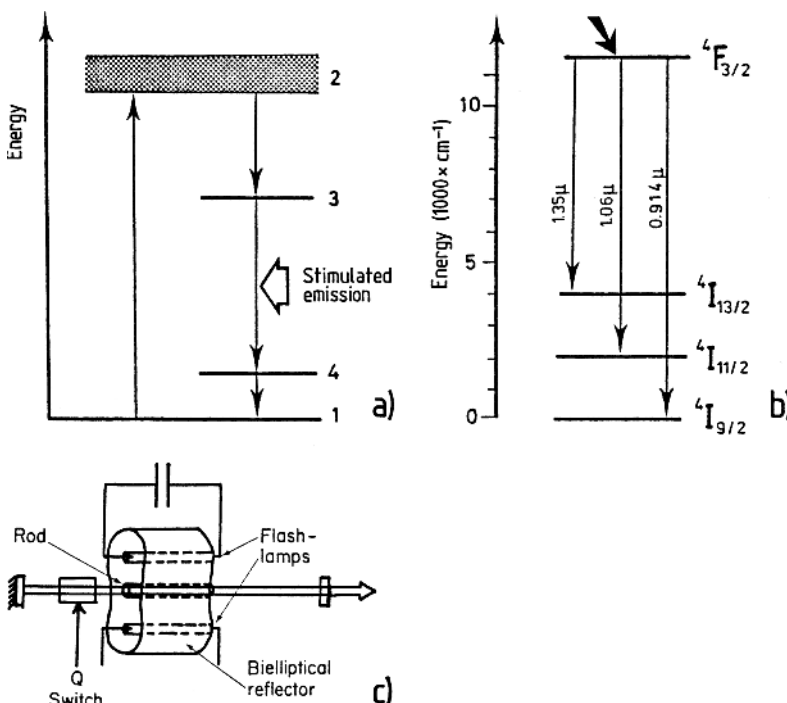


Fig. 8.9. The 4-level laser. (a) Basic energy-level diagram; (b) lasing transitions in the Nd^{3+} :YAG laser; (c) typical practical arrangement for a Nd:YAG laser [8.32]

is necessary to reduce its thermal population. Laser action has been achieved for most of the rare-earth ions. An especially useful type of 4-level laser is the Nd:YAG laser, for which Nd^{3+} ions have been incorporated into an yttrium-aluminum host crystal of garnet type (“Yttrium-Aluminum-Garnet”, $\text{Y}_3\text{Al}_5\text{O}_{12}$). The lasing transitions for this laser are shown in Fig. 8.9b; in particular, the most commonly used one at $1.064\text{ }\mu\text{m}$. In Fig. 8.9c a frequently used Nd:YAG laser arrangement with two linear flash-lamps in a bi-elliptic pumping cavity for efficient pumping of the rod is shown. Nd:YAG lasers with a high output power are constructed with an oscillator followed by one or several amplifier stages. This is a very general construction for pulsed lasers. The oscillator is designed for relatively low power. It is then possible to control the mode structure, linewidth and pulse length precisely. A sharp frequency, a short pulse length and a clean TEM_{00} mode can generally only be achieved at the expense of the output power. A laser amplifier, consisting of a larger flash-lamp-pumped rod, will boost the energy of the pulse without changing the beam quality. The diameter of the amplifying medium is successively increased in the amplifying stages and the laser beam is correspondingly expanded. The technology of solid-state lasers has been discussed in [8.33–8.37]. High-power Nd-glass lasers are used in fusion research based on laser-driven inertial confinement [8.38–8.40]. The generation of ultra-high peak laser power is addressed in Sect. 8.7.

A typical Nd:YAG laboratory laser system for spectroscopic applications is an oscillator-amplifier arrangement yielding $1.06\text{ }\mu\text{m}$ pulses of 10 ns duration and 1 J energy at a repetition rate of 10 Hz . In such systems, a so-called unstable resonator (Fig. 8.4) is sometimes used to allow a more efficient energy extraction from the oscillator rod than that which is possible for a resonator sustaining a TEM_{00} mode. Instead of a semi-transparent output coupler a very small central feedback mirror is used and the output power is extracted in an annulus around this mirror. In rod arrangements, Nd:glass is limited to very low repetition rates because of the poor thermal properties of glass, leading to strong lens effects. However, by using a slab arrangement instead of a rod for the active medium, as illustrated in Fig. 8.10, lensing effects can be shown to self-compensate and it is possible to construct very efficient glass lasers [8.41]. The Nd:YAG and glass materials absorb the pumping radiation in certain spectral regions, as shown in Fig. 8.11. New host materials, such as GGG (Gadolinium–Gallium–Garnet, $\text{Gd}_3\text{Ga}_5\text{O}_{12}$) and GSGG (Gadolinium–Scandium–Gallium–Garnet), in which Cr^{3+} ions have also been incorporated as sensitizers, utilize the available radiation more efficiently and show great promise.

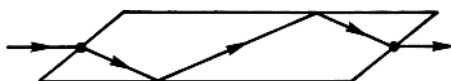


Fig. 8.10. Slab arrangement of the gain medium in a solid-state laser

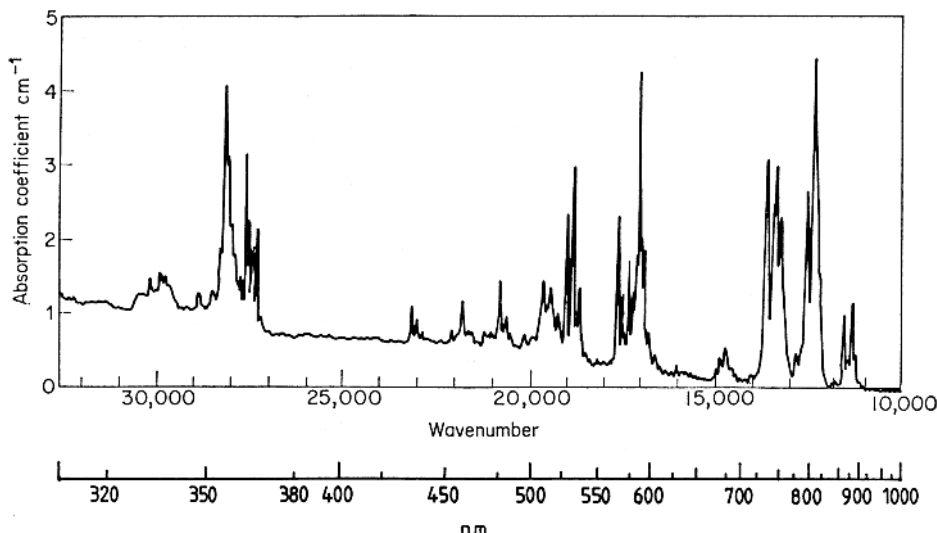


Fig. 8.11. Absorption curve for Nd:YAG [8.42]

Another useful laser material is Nd:YLF (Yttrium–Lithium–Fluoride). The upper state fluorescent lifetime in YLF is about $520\text{ }\mu\text{s}$ as compared with about $230\text{ }\mu\text{s}$ for YAG, which makes Nd:YLF particularly valuable for high-repetition systems (kHz), which can then be efficiently pumped by a CW discharge lamp rather than a flashlamp. After frequency doubling to 527 nm such systems can yield 20 mJ/pulse at 1 kHz, averaging a power in the green of 20 W.

Different laser crystals have been described in [8.35, 8.36]. Increased efficiencies (beyond the 2% wall-plug power to laser power-conversion efficiency typical for a Nd:YAG laser) are attainable by pumping a YAG rod with a suitable frequency-matched diode laser (Sect. 8.5.5) [8.43, 8.44]. Frequently, the diode laser is chosen to operate at the 808 nm absorption peak. In Fig. 8.12 the pumping of a miniature rod is shown, yielding single-mode output at a wall-plug conversion efficiency of better than 5%. Such a laser is ideal as a high-quality oscillator for subsequent amplification. High pumping powers can be obtained using arrays of diode lasers [8.45–8.48]. The cost of such lasers

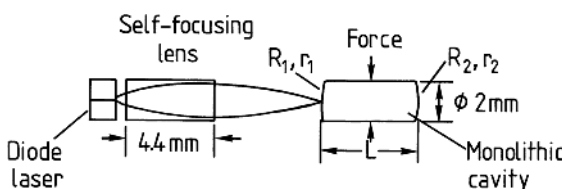


Fig. 8.12. Diode laser pumping of a miniature Nd:YAG laser [8.45]

is rapidly coming down and diode-pumped solid-state lasers of considerable output are now quickly emerging, particularly for CW applications (see also the end of Sect. 8.4.5).

8.4.3 Pulsed Gas Lasers

The lasers we have considered so far have a solid material as the active medium. Generally, flash-lamp pumping is employed and short pulses are obtained at a repetition rate of typically 10 Hz. High peak powers are obtained in the Q-switched mode (MW–GW). Gaseous media can also be used for the generation of short laser pulses. We shall consider here the nitrogen laser, the excimer laser and the copper vapour laser.

The relevant parts of the N_2 molecule level diagram and the basic arrangement for the N_2 laser are given in Fig. 8.13. Pumping is achieved using an electrical discharge of short duration, transversely, in a tube through which N_2 at a pressure of about 100 torr is flowing. The transfer probability at electron impact for $X \rightarrow C$ is much larger than for $X \rightarrow B$. Thus, population inversion occurs at level C with regard to B. However the lifetime of state C is only about 40 ns, whereas the corresponding value for state B is about 10 μ s. A very fast discharge, generated using a *Blumlein circuit*, is utilized, since the upper level cannot store energy (Q-switching is not possible). The population inversion can obviously be achieved only for a short time (self-terminating transition). The pulse length for the nitrogen laser is normally less than 10 ns and emission follows at 337.1 nm. Peak power up to 1 MW can be achieved. Pulse energies are typically a few mJ, and repetition rates exceeding 100 Hz can be obtained. Sealed-off N_2 lasers operating with 0.1 mJ output energy in 3 ns pulses at 10 Hz are also available as very compact units with wide applicability, especially for inducing fluorescence in analytical and diagnostic applications (Chap. 10).

The nitrogen laser has such a high gain that a laser beam can be obtained even without cavity mirrors through amplified spontaneous emission (sometimes the term *super-radiant laser* is used). Normally, a totally reflecting mirror is used at one end of the gain tube while the window at the opposite

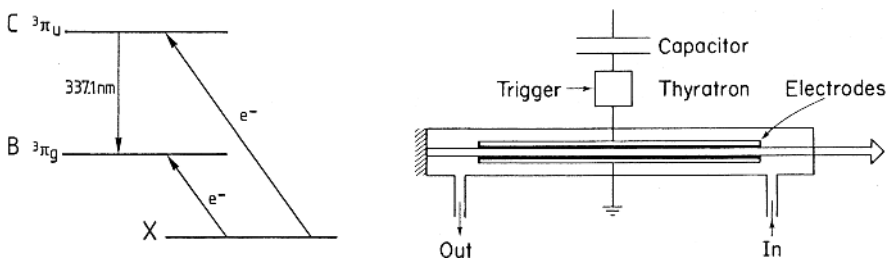


Fig. 8.13. Energy-level diagram and basic arrangements for a nitrogen laser [8.32]

end has a very high transmission. The divergence of the beam is given by the geometry of the discharge channel and is typically 10 mrad.

The construction of an *excimer laser* [8.49–8.51] is similar to that of an N_2 laser. Excimer molecules (“excited dimers”) are characterized by the absence of a stable ground state while short-lived, excited states exist. In excimer lasers, molecules such as KrF and XeCl are used as the active medium. These molecules are formed in the excited state in a fast, electrical discharge in a mixture of the inert gas and F_2 or HCl . The high reactivity of the latter gases makes material selection, gas handling, etc. critical for this type of laser. In Fig. 8.14 an excimer level diagram and laser lines for different excimer molecules are given. Since no ground state exists, excimer molecules constitute the perfect laser medium, with automatic population inversion once a molecule has been created. Important laser emission lines are 249 nm (KrF : yields the highest power), 308 nm (XeCl : best suited for dye laser pumping) and 193 nm (ArF : attractive short wavelength for photochemistry). Pulse energies of hundreds of mJ can be achieved and average powers of 100 W can be reached. Excimer laser technology is quickly maturing and these lasers find many important applications.

Pulsed CO_2 lasers, which were available long before excimer lasers, have a similar construction. These infrared lasers are of great technological importance. CO_2 lasers will be discussed later.

In the *copper vapour laser* the discharge tube must be heated to high temperatures in order to produce a sufficient Cu vapour pressure. This laser emits at 510 and 578 nm, corresponding to the $(4p\ ^2P_{3/2} \rightarrow 4d\ ^2D_{5/2})$ and $(4p\ ^2P_{1/2} \rightarrow 4d\ ^2D_{3/2})$ transitions, respectively. Since the terminal 2D states are metastable, only pulsed operation is possible. High repetition rates can usually be obtained with this laser, up to 10 kHz. The average power can

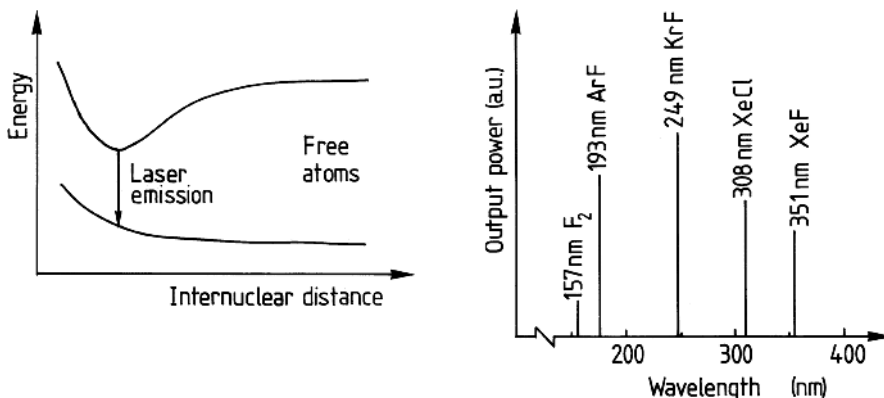


Fig. 8.14. Energy-level diagram for an excimer molecule and laser emission lines from different excimer molecules

exceed 10 W. Exchanging copper for gold results in red emission at 628 nm. Metal-vapour lasers are discussed in [8.52].

Whereas population inversion can often be achieved relatively easily with a pulsed pumping source, it is considerably more difficult, and sometimes impossible, to continuously maintain population inversion while laser action prevails. Clearly, lasing means that excited atoms decay with the emission of stimulated radiation and thus the laser action itself will cause the lasing action to stop. Efficient pumping mechanisms are required. We will now study some important types of continuous fixed-frequency lasers which all work with gaseous laser media.

8.4.4 The He–Ne Laser

The helium–neon laser was the first gas laser and it was designed and built by *A. Javan* and co-workers [8.53] shortly after the introduction of the ruby laser. The He–Ne laser is one of the most common laser types. The construction can be made comparatively simple and cheap, and continuous laser action is obtained. The active medium is a gas mixture of He and Ne (ratio 5:1) in a glass tube at a total pressure of about 1 torr. Energy is added through an electric discharge through the gas. In order to understand the principle of the He–Ne laser, the energy-level diagrams of both He and Ne must be considered (Fig. 8.15). In the discharge (1000 V, 10 mA) He atoms are excited to the metastable $2s\ 3^1S$ and $2s\ 1^1S$ states through electron impact. In Ne the $4s$ and $5s$ level systems have almost the same energies as the metastable He states. Because of this, the probability of Ne excitation through collisions with metastable He atoms is very large. A population inversion between the s states and the lower-lying $3p$ and $4p$ levels is achieved and several laser transitions are possible. Since the lifetimes of the p states are very short ($\simeq 10$ ns) in comparison with the s state lifetimes (~ 100 ns), the population inversion can be maintained and continuous lasing is achieved. The reflection properties

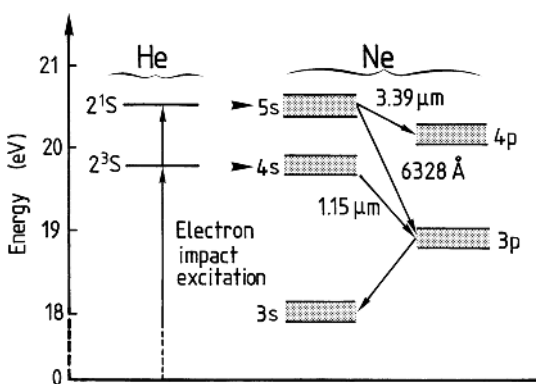


Fig. 8.15. Energy-level diagrams relevant to the He–Ne laser

of the laser mirrors determine which line will lase. The most frequently used line is the red line at 6328 Å, but many other visible and IR lines are possible. The Doppler width of this line is about 1700 MHz. With a typical resonator length of 30 cm a mode separation of 500 MHz is obtained. Such a laser will exhibit 2 or 3 modes. With a sufficiently short laser (10–15 cm), single-mode operation can be attained. He–Ne lasers yield low output powers, typically a few mW.

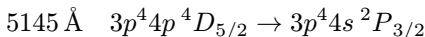
Primary energy storage in He is also used in the *helium–cadmium laser*. Here, a sufficient metal vapour pressure must be achieved by heating. Excited Cd ions are produced by Penning ionization:



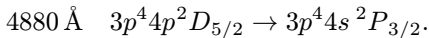
Two short-wavelength lines, 4416 Å ($4d^95s^2 \ 2D_{5/2} \rightarrow 4d^{10}5p \ 2P_{3/2}$) and 3250 Å ($4d^95s^2 \ 2D_{3/2} \rightarrow 4d^{10}5p \ 2P^{1/2}$), are obtained at power levels of 50 and 5 mW, respectively. An alternative way of producing the excited Cd ions is to use soft X-ray photoionization of ground-state $4d^{10}5s^2$ Cd atoms [8.54]. High-power laser pulses impinging on a high-Z material, such as Ta, can be used for soft X-ray production (Sects. 5.1.3 and 9.6). Using soft X-ray pumping, gain has also been demonstrated in In III (185 nm) [8.55] and Xe III (109 nm) [8.56].

8.4.5 Gaseous Ion Lasers

In gaseous ion lasers a population inversion between excited states of ionized argon or krypton is achieved. The pumping is accomplished through a strong dc discharge in low-density gas (~ 0.2 torr). The discharge tube is 1–2 m long and current densities of about 500 A/cm^2 are used. Thus, a high electrical power is needed ($\sim 10 \text{ kW}$) and the discharge tube, which is made of beryllium oxide or graphite, must have an efficient water cooling system. Excited ions are produced in collisions between inert gas atoms and electrons. For ionization of an argon atom an energy of 15.75 eV is needed. The interesting excited ionic states belonging to the configuration $3p^44p$ are located about 20 eV above the ionic $3p^5$ ground state. In Fig. 8.16 a partial level scheme for Ar^+ is given, with laser lines connecting $3p^44p$ levels and $3p^44s$ levels indicated. Several blue and green laser lines are obtained (5145, 5017, 4965, 4880, 4765, 4727, 4658, 4579 and 4545 Å). The strongest lines are



and



When using laser mirrors with a high reflectivity in the blue-green region all the lines are produced simultaneously. Argon-ion lasers with a total output power of up to 30 W are commercially available. In Fig. 8.17 the principal arrangement of an argon-ion laser is shown. By using a prism in front of

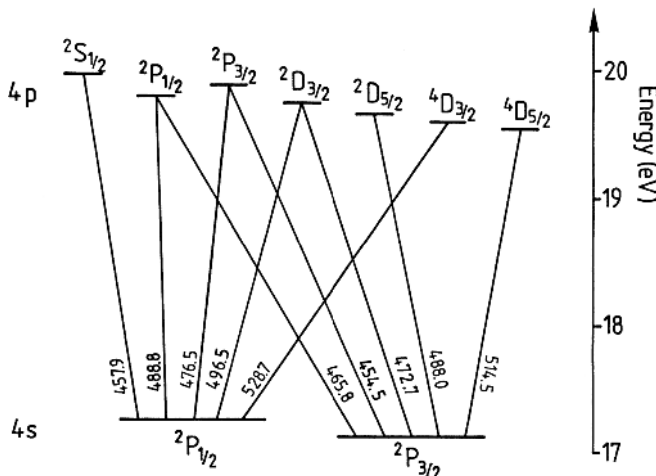


Fig. 8.16. Energy level diagram of the Ar^+ ion, with argon-ion laser lines indicated

the totally reflecting mirror the individual spectral lines can be isolated. For a certain position of the prism only one wavelength is reflected back towards the semi-transparent output coupler, while the other wavelengths are refracted out of the cavity. By introducing an intracavity solid Fabry-Pérot interferometer (etalon), single-mode oscillation can be obtained.

At very high discharge currents laser transitions are also obtained in doubly ionized argon. Several UV lines in the wavelength region 300–386 nm are then obtained with a total power up to 5 W.

The *krypton-ion laser* has the same construction as the *argon-ion laser* but the discharge tube is instead filled with krypton. Apart from blue and green lines, several red lines are also obtained with this laser (7931, 7525, 6764, 6471, 5682, 5309, 5208, 4825, 4762, 4680, 4131 and 4067 Å), as well as strong UV lines (3564, 3507 and 3375 Å). Ion lasers are discussed in greater detail in [8.57].

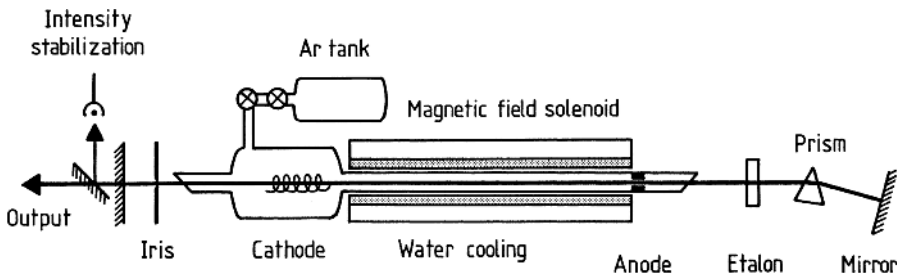


Fig. 8.17. Principal arrangement for an argon-ion laser

Argon-ion lasers are now being replaced by CW solid-state lasers which can be conveniently pumped by diode-laser arrays, leading to a high efficiency and tractable heat dissipation. Thus, CW Nd:YVO₄ (Yttrium-Vanadate; upper-state lifetime 60 µs) lasers with intracavity frequency doubling in LBO (Lithium triborate) yielding up to 10 W output power at 532 nm are increasingly used as pump sources for tunable lasers (see below).

8.5 Tunable Lasers

Whereas fixed-frequency lasers have found important applications in, for example, measurement techniques, information transmission, holography and material processing, tunable lasers are of greatest interest for atomic and molecular spectroscopy. Using different types of tunable lasers the wavelength range 320 nm to tens of µm can be covered by direct laser action, and the tunability region of an individual laser can be considerably extended using nonlinear optical effects. Tunable lasers comprise dye lasers, F-centre lasers, certain solid-state lasers, spin-flip Raman lasers [8.58], parametric oscillators, high-pressure CO₂ lasers and semiconductor lasers. Here we will discuss the most important of these laser types. Overviews of tunable lasers can be found in [8.59–8.62].

8.5.1 Dye Lasers

Laser action in organic dyes was discovered independently by *Sorokin* et al. [8.63] and *Schäfer* et al. [8.64] in 1966. Since then, several hundreds of dyes have been shown to have suitable properties, to greater or lesser degrees, for use as laser media. One of the most common laser dyes is Rhodamine 6G dissolved in methanol or ethylene glycol. The complex structure of organic dyes is illustrated in Fig. 8.18, where the formula for Rhodamine 6G is shown.

The general energy-level structure of an organic dye is shown in Fig. 8.19. The transitions relevant for laser action occur between the two lower electronic singlet states. The ground state, as well as the excited state, is split into a continuous structure of smeared energy sublevels due to the interaction with the solvent. Normally the molecules are Boltzmann-distributed on the lowest sublevels of the ground state. The molecules can be excited to the next singlet band with light. In radiationless transitions the molecules relax very quickly ($\sim 10^{-12}$ s) to the lowest level of the excited state, from where the molecules return to the sublevels of the ground state with a lifetime of about 10^{-9} s, emitting fluorescent light. The resulting absorption and emission curves for Rhodamine 6G are included in Fig. 8.19. Because of the relaxation in the excited singlet band the same fluorescence curve is obtained regardless of the spectral distribution of the absorbed light. For example, the curve given in the figure is obtained regardless of whether a flash-lamp or a fixed-frequency laser is used for the excitation.

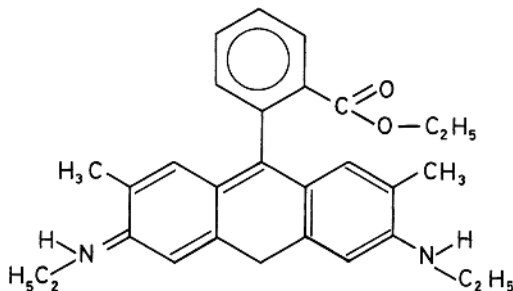


Fig. 8.18. The chemical structure of Rhodamine 6G

The usefulness of an organic dye for laser applications much depends on the position of higher-lying singlet bands and on the influence of the system of triplet levels that is always present in organic dye molecules. If a higher-lying singlet state has an inappropriate energy, a strong absorption of fluorescence light results. Through radiationless transitions, excited dye molecules can be transferred to the triplet system. If a large number of molecules assemble in the lowest triplet state, the fluorescent light from the singlet system can be strongly absorbed by triplet molecules. If the organic dye is pumped sufficiently strongly, a population inversion between the lowest sublevel of the upper singlet state and the sublevels of the ground state is obtained. Amplification by stimulated emission can then be achieved. If a dye solution is contained in a cell, placed in a laser cavity, and sufficient pumping power

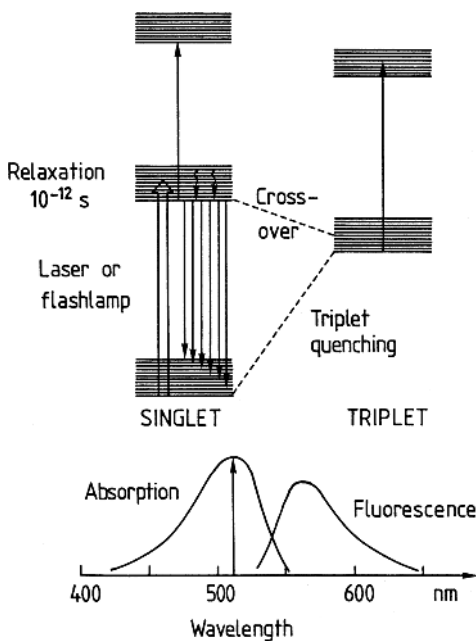


Fig. 8.19. General energy-level structure of an organic dye molecule, and resulting absorption and fluorescence curves

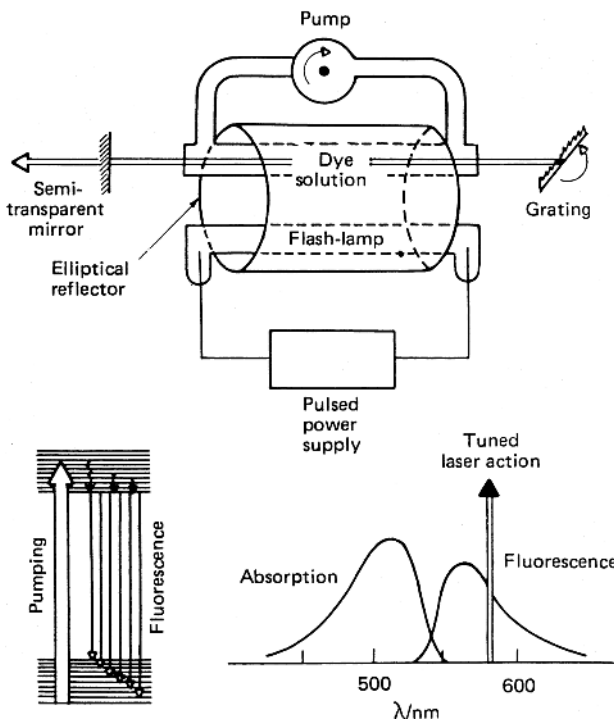


Fig. 8.20. Flash-lamp-pumped dye laser [8.32]

is supplied, laser action will occur (Fig. 8.20). With broadband laser mirrors stimulated emission is obtained in a wavelength range of a few tens of Å close to the peak of the fluorescence band.

A very important step was taken by *Soffer and McFarland* [8.65] in 1967 by replacing the totally reflecting mirror with a grating in a Littrow mount (Fig. 6.20). A frequency-selective feedback was obtained and the bandwidth of the stimulated radiation was reduced to about 0.5 Å. By turning the grating the laser could be continuously tuned over the fluorescence band of the dye. In Fig. 8.20 an arrangement for flash-lamp-pumping of a tunable dye laser is shown. Here, a tube is used for the dye solution, which is pumped with a linear flash-lamp. Laser pulses with a duration of about 1 μs and a peak power of several kW are obtained. The repetition rate is generally about 1 Hz. Pulsed dye lasers are more frequently pumped by a fixed-frequency laser, which is normally a nitrogen, an excimer, a copper or a frequency-doubled Nd:YAG laser. In Fig. 8.21 three different arrangements are shown. In the *Hänsch* design [8.66], an intracavity beam expander is used to widen the diameter of the beam so that more lines of the Littrow-mounted grating are illuminated. This leads to an increased resolution (Sect. 6.2.2) at the same time as the grating is protected from local heating. The linewidth with such

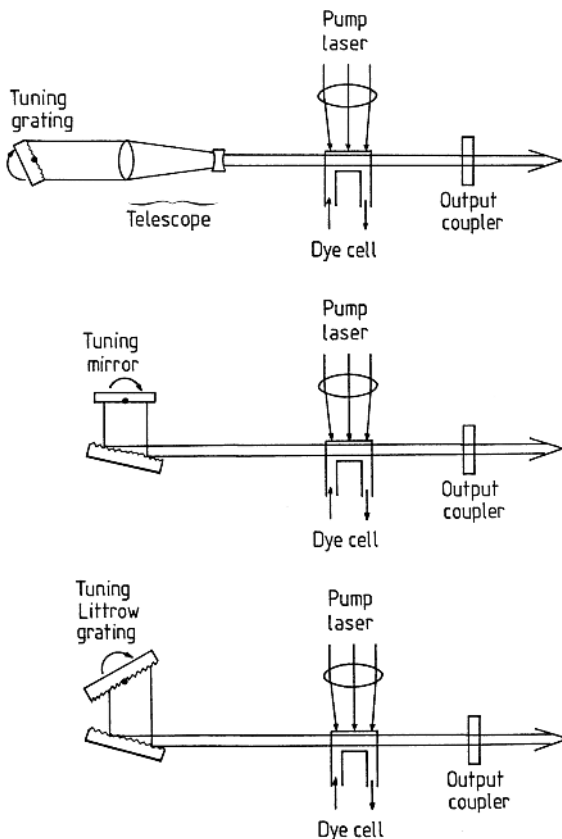


Fig. 8.21. Dye laser cavities of various designs

an arrangement is typically 0.1 \AA . Using an intracavity etalon the linewidth can be reduced by a factor of 10. Instead of using a telescope a multiple-prism arrangement can be used, since expansion *across* the grooves is the only consideration from a resolution point of view. Note that because of the short pumping time (5–10 ns) there is normally no time for a cavity-mode structure to build up in a short-pulse laser. Mode positions are only weakly indicated in the essentially smooth frequency distribution.

In Fig. 8.21 an arrangement is shown in which all the grating lines can be utilized without using any form of beam expansion [8.67]. Here, grazing incidence on a fixed grating is employed. The laser is tuned by turning a mirror reflecting the first order of the grating back on itself. The useful laser beam can be taken out as the zeroth order beam from the grating (reflection) or through a partially transmitting end mirror. The latter arrangement reduces the broadband dye emission. By exchanging the tuning mirror for a grating in a Littrow mount a still higher resolution can be achieved. By eliminating the

telescope the cavity can be made very short. This leads to many round trips during the pulse, a large free spectral range and the possibility of single-mode operation [8.67].

If a high pulse energy is needed while retaining a small linewidth and a high beam quality, it is advisable to utilize an oscillator/amplifier arrangement, as mentioned above. In Fig. 8.22 two examples are given. In order to achieve a very small linewidth (~ 100 MHz) an external Fabry-Pérot interferometer can be used to filter the oscillation output before amplification.

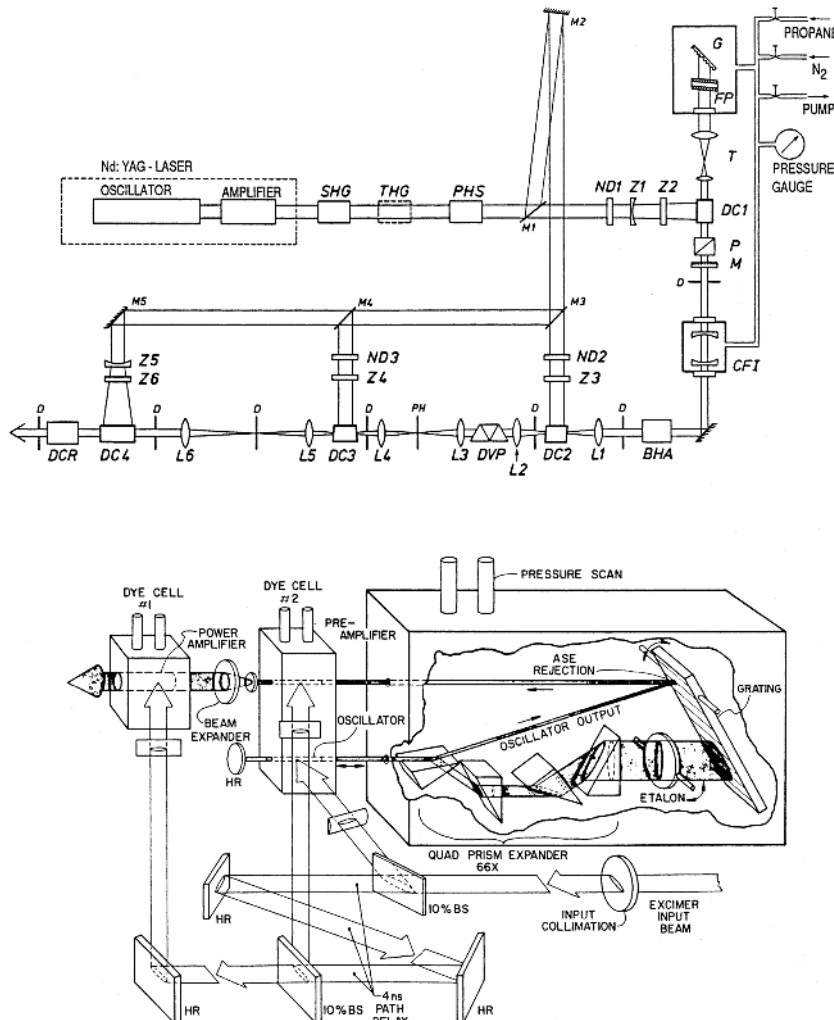


Fig. 8.22. Oscillator/amplifier arrangements for tunable dye lasers ([8.68], and courtesy: Lambda Physik)

In the figure, the possibility of pressure-scanning the laser is also illustrated. Since grating, internal and external Fabry-Pérot interferometer are tuned in the same way when the pressure is changed (the expression nl occurs in all the formulae), all the elements will remain synchronized once they have been correctly adjusted.

Pulsed dye lasers can be operated from 320 to 1000 nm using different dyes. In Fig. 8.23 tuning curves for a dye laser, pumped by an excimer laser or harmonics of the Nd:YAG laser, are shown. An energy conversion of 10–20% is typical for excimer laser pumping. With a frequency-doubled Nd:YAG laser (532 nm) the conversion for Rhodamine dyes can exceed 40%. The frequency range of dye lasers can be extended using nonlinear optics techniques (Sect. 8.6).

As for fixed-frequency lasers, it is considerably more difficult to achieve continuous laser action than pulsed operation with a dye laser. The first continuous dye laser was designed in 1970 by *Peterson et al.* [8.70]. A special problem associated with organic dyes is the building up of a population of molecules in the lowest triplet state. For pulsed pumping, laser light can be obtained for a short time before triplet absorption dominates. To achieve continuous laser action, absorbing triplet molecules must be removed. Certain chemicals, such as cyclo-octatetraene (COT) or even dissolved O₂, are very active in transferring triplet molecules to the ground state without emitting radiation (triplet quenching). An argon or a krypton-ion laser with a power of several watts is used as a pump source for a continuous dye laser. With Rhodamine 6G, a conversion efficiency of 20% can be achieved in the most favourable wavelength region. However, the efficiency is normally lower. At the present time it is possible to cover the wavelength range 375–950 nm with continuous dye lasers. In order to achieve continuous laser action a certain dye must be pumped at a suitable wavelength, for which good absorption occurs. The green, yellow and red regions can be covered by dyes that can be pumped by the blue-green lines of the argon-ion laser. Certain dyes need to be pumped by the violet or red lines from the krypton-ion laser. Blue and violet dyes, e.g. Stilbene, require pumping with the UV lines from an Ar⁺ or Kr⁺ laser. In Fig. 8.24 an example of the arrangement of a continuous, tunable dye laser is given. Using focused argon-ion laser light a continuous population inversion is maintained at a point on a quickly flowing flat jet of dye that is ejected through a specially designed nozzle. Ethylene glycol is used as the dye solvent, because of its high viscosity. This arrangement ensures an efficient cooling of the dye.

The gain volume is at the focal point of a folded cavity, consisting of two spherical mirrors and a flat output coupler. Tuning is accomplished with a birefringent, so-called Lyot filter [8.71]. This consists of one or several crystalline quartz plates mounted at the Brewster angle. The dominant transmission maximum of this filter can be moved by turning the optical axis of the filter with respect to the plane of polarization of the light in the

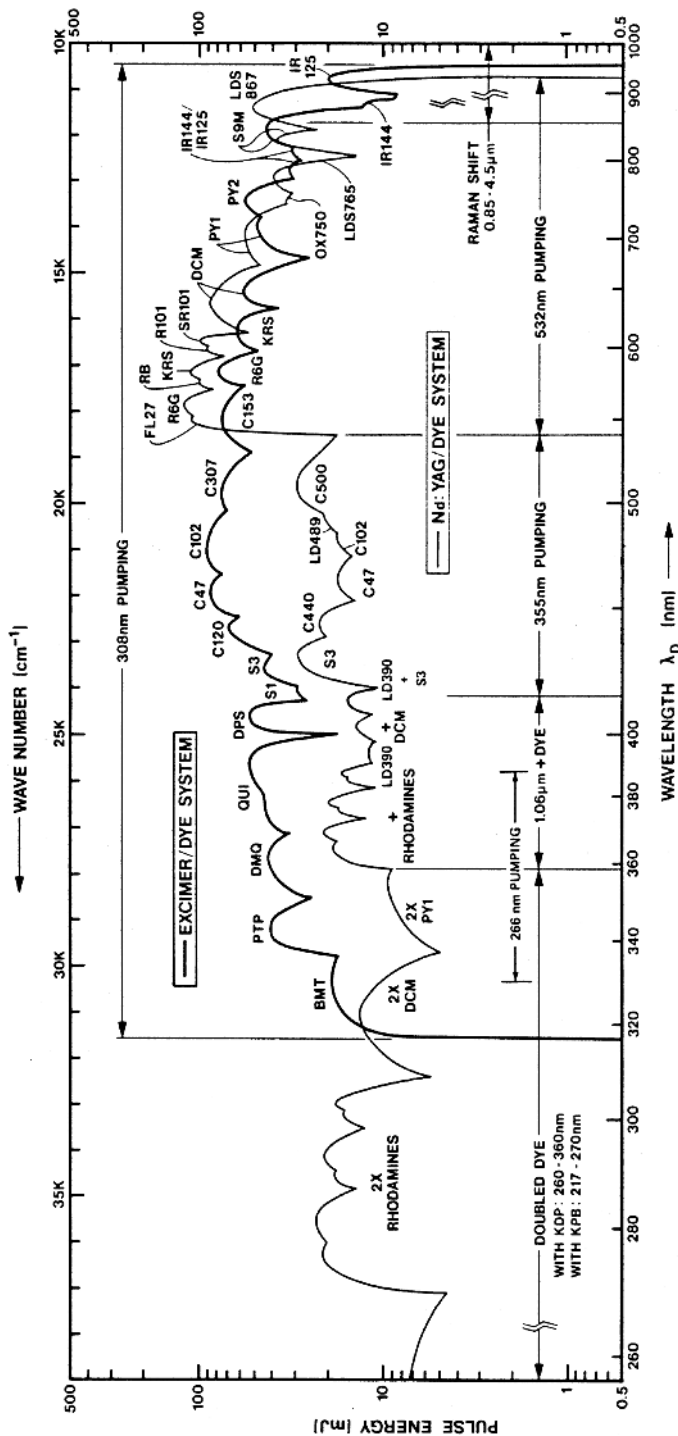


Fig. 8.23. Tuning curves for excimer-pumped and Nd:YAG-pumped dye lasers [8.69]

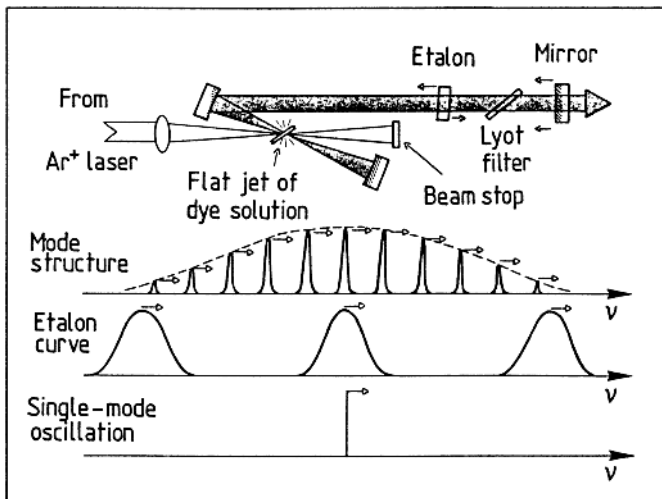


Fig. 8.24. Continuous dye laser using a flat dye-solution jet as the active medium

cavity. A bandwidth of about 0.5 \AA is obtained from a CW dye laser when only a primary tuning element is used. The width of the filter peak is much larger but the laser will only oscillate close to the transmission peak because of the regenerative nature of laser action. With a typical cavity length of 30 cm a mode separation of 500 MHz is obtained, thus permitting several hundreds of modes to oscillate under the gain profile, which is given by the frequency selectivity of the cavity (not by any Doppler broadening as is the case in a gas laser). With an intracavity high-finesse etalon (Sect. 6.2.3), a single-cavity mode can be selected, but the resulting frequency width for the outgoing light will still be several 10's of MHz, since the frequency stability is limited by vibrations, etc. With a frequency stabilization system the linewidth can be reduced to less than 1 MHz. Such a system is shown in Fig. 8.25. Using more advanced systems with active electro-optic phase control, the linewidth can be reduced to the Hz level.

In order to be able to make a system with etalons work over a wide wavelength region, two low-finesse etalons (broadband coatings) are used in series. With a 1 mm thick etalon ($n = 1.5$), a free spectral range of 100 GHz is obtained and, when operated with a transmission maximum close to a maximum of the Lyot filter, some 10 modes may lase. Adjacent etalon maxima occur where the filter has a substantially reduced transmission. If an additional, thicker etalon is introduced, having a substantially reduced free spectral range, say 10 GHz, single-mode operation can be achieved. In Fig. 8.26 the transmission profiles of the different resonator components are shown. In order to achieve a high single-mode power, a ring-laser cavity is frequently used instead of the usual standing-wave linear cavity. This avoids the problem of high non-utilized gain in the standing-wave nodes of the linear

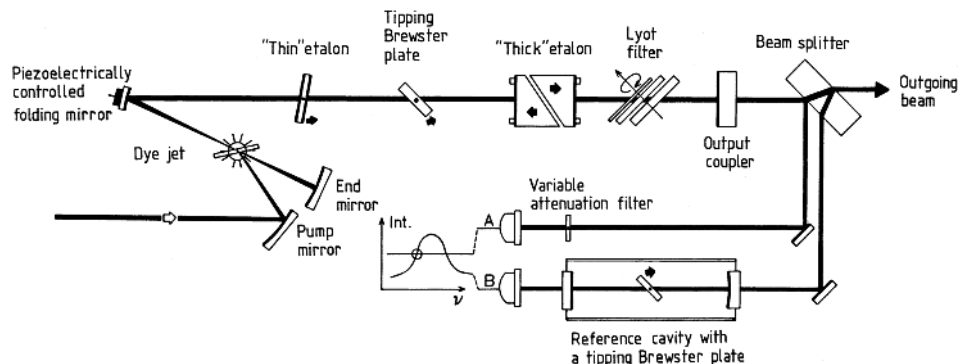


Fig. 8.25. Tunable single-mode dye laser with active frequency stabilization (Courtesy: Coherent, Inc.)

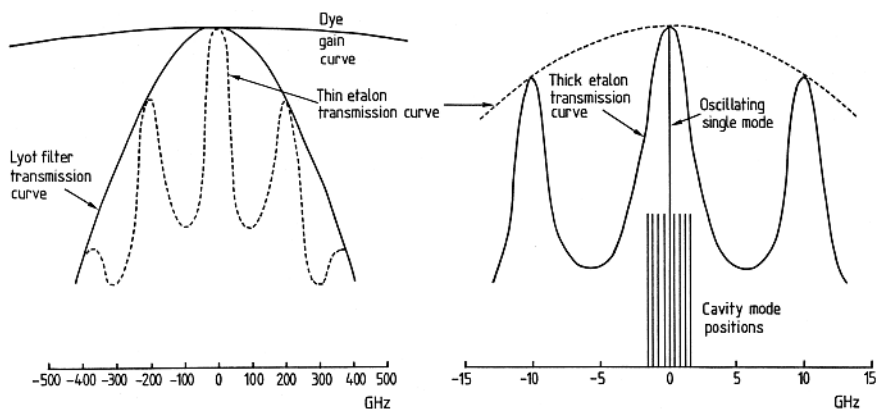
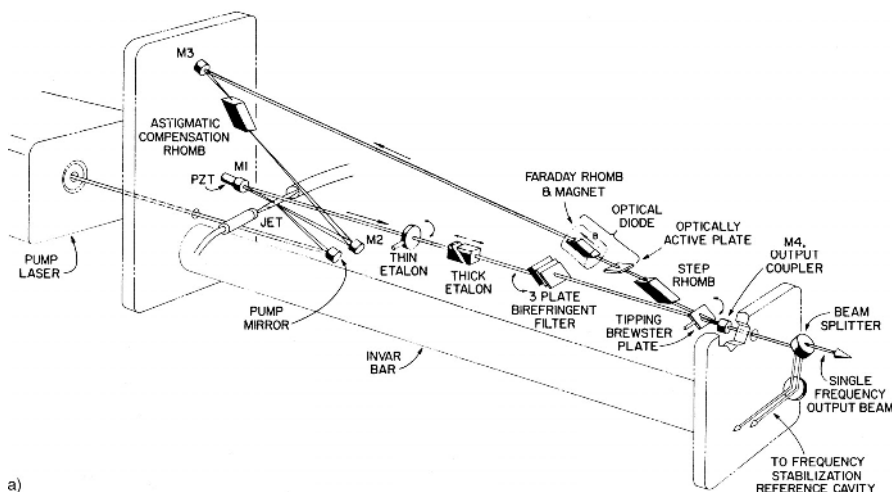
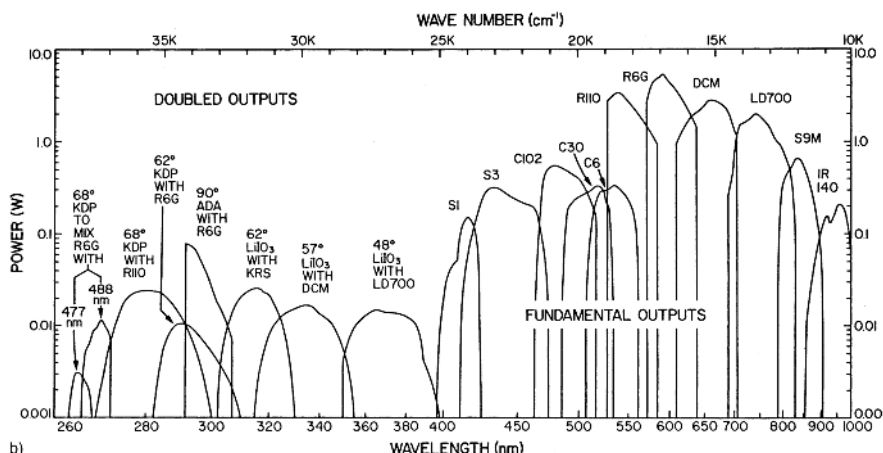


Fig. 8.26. Hierarchic sequence of spectral curves illustrating the narrowing of the frequency domain and the isolation of a single cavity mode for a linear cavity

cavity. This gain will ultimately be utilized by an unwanted second cavity mode, so that at high pumping power it can no longer be suppressed. A ring-laser arrangement is shown in Fig. 8.27a. Tuning curves for a single-mode dye laser are shown in Fig. 8.27b. Dye lasers have been discussed in detail in [8.69–8.73], and laser dyes are covered in [8.74].



a)



b)

Fig. 8.27. (a) Tunable single-mode dye ring laser (Courtesy: Coherent, Inc.)
 (b) Tuning curves for a CW single-mode dye laser (Courtesy: Coherent, Inc.)

8.5.2 Colour-Centre Lasers

In the near-IR region colour-centre (F-centre) lasers can be used [8.75]. These lasers resemble dye lasers with regard to function and construction. Instead of the dye solution a cooled F-centre crystal is used as the active, laser-pumped medium. The colour centre is a defect in a crystal lattice, e.g., KCl. The defect consists of an ion vacancy that has trapped an electron. If impurity ions are close to the vacancy, the optical properties are changed. F-centre

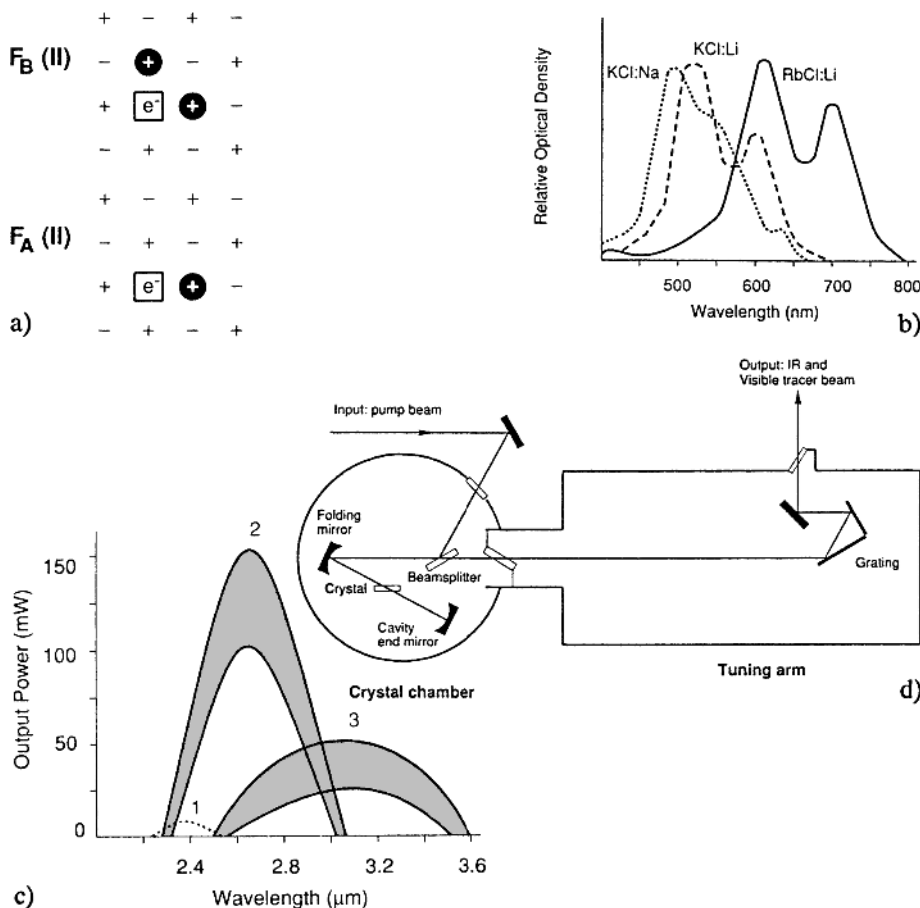


Fig. 8.28. Basics of F-centre lasers. The figure shows (a) F-centre structures, (b) absorption, (c) laser-emission curves, and (d) the cavity arrangement for a commercially available unit (Courtesy: Burleigh Instruments, Inc.)

crystals absorb visible radiation and fluorescence in the near-IR region. Using different crystals, the range $1\text{--}3.5\,\mu\text{m}$ can be covered. In Fig. 8.28 F-centre structures, absorption and lasing curves are shown as well as a practical arrangement in a commercial F-centre laser.

8.5.3 Tunable Solid-State Lasers

Certain solid-state materials with transition-element or rare-earth ions as impurities in a host matrix have rather broad gain curves and can thus be tuned over a certain range. This is the case for the Nd: Glass laser, which can be tuned in the region $1.0\text{--}1.1\,\mu\text{m}$. The alexandrite ($\text{Cr}^{3+}:\text{BeAl}_2\text{O}_4$) and emerald ($\text{Cr}^{3+}:\text{Be}_3\text{Al}_2\text{Si}_6\text{C}_{18}$) lasers that bear a close resemblance to ruby lasers

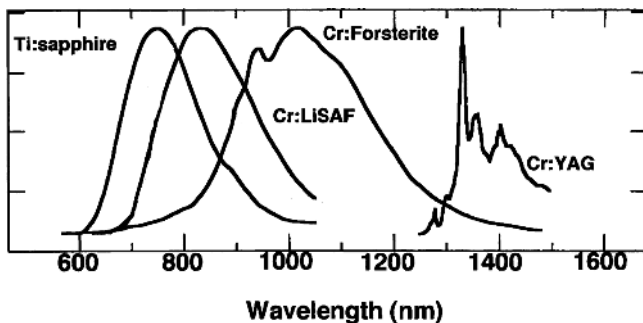


Fig. 8.29. Fluorescence curves for some tunable solid-state laser materials (Adapted from [8.77])

can, in the same way, be tuned in the regions 730–800 nm and 700–850 nm, respectively. Additional chromium-based lasers are LISAF ($\text{Cr}^{3+}:\text{LiSrAlF}_6$) and Forsterite ($\text{Cr}^{4+}:\text{Mg}_2\text{SiO}_4$). All these lasers can be pumped directly with a flash-lamp. Finally, some further transition element lasers should be mentioned. $\text{Co}:\text{MgF}_2$ can be pumped by a simple, non-Q-switched Nd:YAG laser and yields tunable radiation in the region $1.7\text{--}2.3\mu\text{m}$. If the material is instead doped with vanadium, it can be tuned in the region $1.0\text{--}1.1\mu\text{m}$.

During the last few years titanium-doped sapphire (Ti:S , $\text{Ti}^{3+}:\text{Al}_2\text{O}_3$) [8.76] has emerged as a very important tunable solid-state laser material. It has a particularly large tuning range, 660–1100 nm. This broad gain profile also makes it extremely interesting for the generation of ultra-short pulses by mode-locking, as will be discussed in Sect. 8.7. $\text{Ti}:\text{S}$ can be directly pumped by flash-lamps (with short pulse lengths because of the upper state short lifetime of about $3.2\mu\text{s}$), but better by a frequency-doubled Nd:YAG laser (532 nm) and behaves much like a dye laser. The fact that sapphire conducts heat extremely well makes the thermal effects tractable, in spite of it being a solid. CW operation is possible using argon-ion laser pumping, and single-mode tunable laser arrangements similar in construction to what is shown in Fig. 8.27a are available. Fluorescence curves for some tunable solid-state laser materials are given in Fig. 8.29 [8.77]. Tunable solid-state lasers have been discussed in [8.33, 8.78, 8.79].

8.5.4 Tunable CO_2 Lasers

The carbon dioxide laser is the most efficient gas laser, with a wall-plug efficiency of up to 20%. It works in the IR region around $10\mu\text{m}$. In numerous applications a non-tuned CO_2 laser is used. However, from a spectroscopic point of view, the fact that it can be line-tuned and continuously tuned at high gas pressures is very useful. In Fig. 8.30 a level diagram and a practical arrangement for a tuned CO_2 laser are shown, together with a diagram of the available lines. The CO_2 molecule has three fundamental modes of

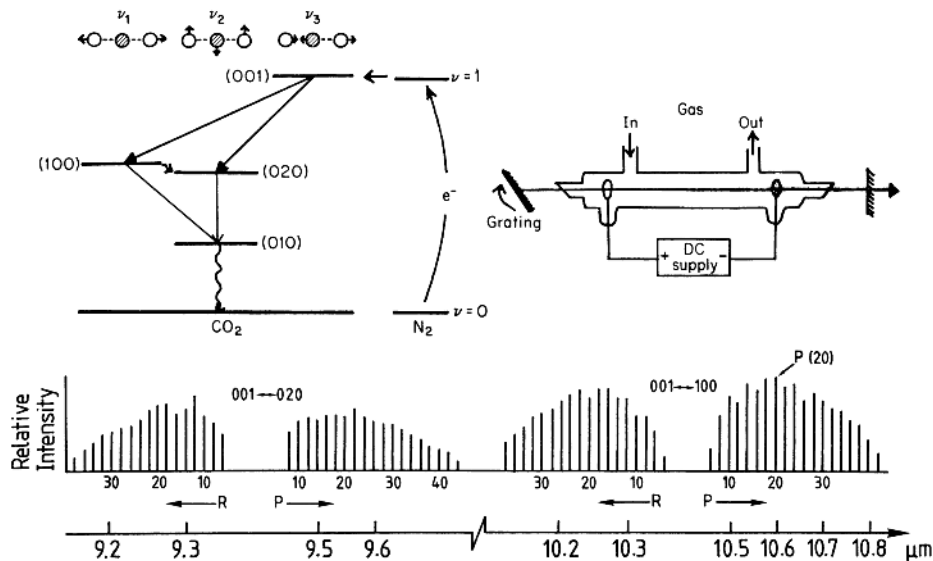


Fig. 8.30. Energy-level diagram relevant to the CO₂ laser with individual vibrational-rotational laser lines and a cavity arrangement illustrated [8.32]

vibration (Sect. 3.4). In the mode that corresponds to symmetric stretching (ν_1), the two oxygen atoms move in opposite directions while the carbon atom is stationary. In the bending mode (ν_2), the molecule is bent back and forth. Finally, in the asymmetric stretching mode (ν_3), the oxygen atoms move together while the carbon atom moves in the opposite direction.

The vibrational state of the molecule is specified by a set of vibrational quantum numbers (ν_1 , ν_2 , ν_3), one for each vibrational mode. In the CO₂ laser the level corresponding to asymmetric stretching (001) is populated efficiently by almost-resonant collisions with excited molecules of nitrogen that have been added to the CO₂ gas. An electric discharge populates the first excited vibrational level in nitrogen. A strong population inversion with respect to the lower-lying CO₂ states (100) and (020) occurs. In a suitably arranged laser cavity, laser emission can occur in the bands 10.2–10.8 μm and 9.2–9.7 μm using a large number of rotational lines. If no special precautions are taken, lasing occurs on the strongest line: P(20) at 10.59 μm.

Using a Littrow-mounted grating other individual P and R branch lines can be chosen. Within every line, fine tuning can be accomplished within about 50 MHz, corresponding to the Doppler width at 10 μm for the CO₂ molecules. By utilizing isotopic molecules, like ¹³CO₂, further fixed wavelengths can be chosen. A continuous CO₂ laser of this type normally has an electric discharge along the tube. However, it is also possible to work at high gas pressures (at atmospheric pressure and up to 10 atmospheres) if a transverse, pulsed discharge is used (TEA, Transverse Electric Atmospheric

laser, see also Sect. 8.4.3). At 10 atmospheres the pressure broadening is about 2 cm^{-1} (60 GHz) and the individual rotational-vibrational lines that are typically separated by $1\text{--}3\text{ cm}^{-1}$ merge. Continuous laser action within the band is then possible. Continuous laser action with a certain tunability can be obtained in *waveguide lasers*, operating at 1 atmosphere pressure.

Non-spectroscopic high-power CO_2 lasers have been constructed with a continuous output of up to tens of kW. Such lasers are used industrially for cutting, welding, hardening, etc. High-power pulsed CO_2 lasers are also used for fusion research. CO_2 lasers were discussed in [8.80–8.82].

Lasers with CO as an active medium can also be constructed. This type of laser type yields a large number of lines in the region $5.1\text{--}5.6\text{ }\mu\text{m}$. In order to achieve efficient operation, the discharge tube must be cooled to low temperatures which complicates practical use. It is simpler to use HF or DF lasers, which give lines in the $2.8\text{--}4.0\text{ }\mu\text{m}$ region. Such lasers are examples of chemical lasers, for which the active molecules are formed in the discharge tube from the supplied gases H_2/D_2 and SF_6 .

As we have seen above, lasing has been achieved for a very large number of atomic and molecular lines. Listings of these lines can be found in [8.83, 8.84].

8.5.5 Semiconductor Lasers

In 1962 several researchers discovered, that laser action can be achieved in certain semiconductor diode arrangements [8.85]. The physics behind this process is different from that discussed so far. However, the fundamental requirement of the creation of a population inversion still exists. A typical diode laser material is gallium arsenide (GaAs) that has been strongly doped. Laser action occurs in the transition zone between p- and n-doped material in a diode subject to a voltage applied in the forward direction. In Fig. 8.31 the basic energy-level diagrams for the cases of voltage off and on are shown. The voltage forces electrons as well as holes into the transition region. Here the conduction-band states have excess population with respect to the empty states of the valence band. Stimulated light emission with a photon energy corresponding to the band gap will result upon the recombination of electrons and holes. Semiconductor lasers are very small, with typical dimensions of less than one mm. In Fig. 8.32 the geometry of a typical early laser diode is shown. Two opposite sides are polished and serve as a cavity. Due to the smallness of the cavity, single-mode oscillation is frequently obtained. Diode lasers with an external cavity can also be used.

The original homojunction systems have successively been replaced by *heterojunction lasers* [8.87, 8.88], which have a complex layered structure (Fig. 8.33), made possible through the development of *MBE* (Molecular Beam Epitaxy) and *MOCVD* (Metal Chemical Vapour Deposition) techniques. $\text{Al}_x\text{Ga}_{1-x}\text{As}$ diode lasers operating at room temperature around 800 nm have obtained great importance for use in CD players, laser printers and bar-

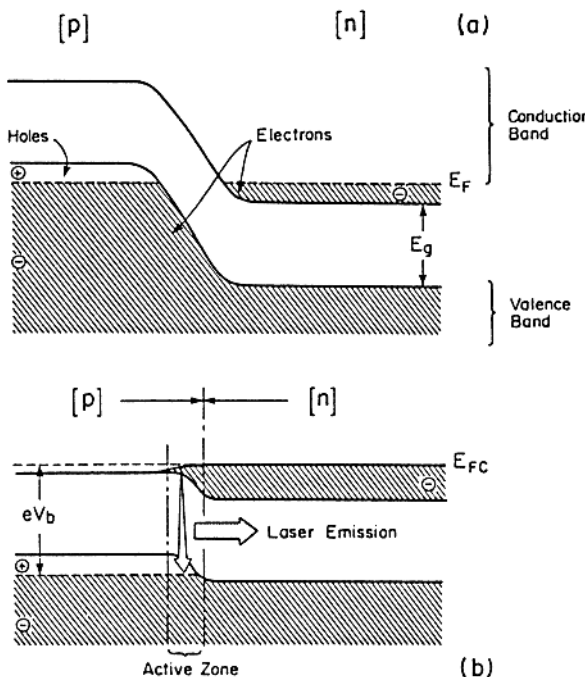


Fig. 8.31. Energy-level diagram for a semiconductor diode laser (a) without voltage and (b) with an applied voltage [8.86]

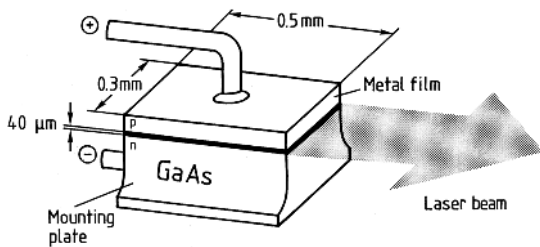


Fig. 8.32. Diode laser

code readers. Such lasers are also high-quality, narrow-band sources for laser spectroscopy. Coarse tuning is performed by thermo-electric change of the junction temperature, which changes the bandgap and index of refraction, while swift scanning over small spectral regions is achieved by current ramping. The resonance lines of K, Rb and Cs are readily accessed in this way. High-power systems, frequently manufactured with many individual units integrated into a “bar” [8.46–8.48], are now widely used for efficient solid-state laser pumping (Sect. 8.4.2). The high diode-laser efficiency (electrical-to-optical power) of up to 80% results in low power consumption and easily tractable thermal problems.

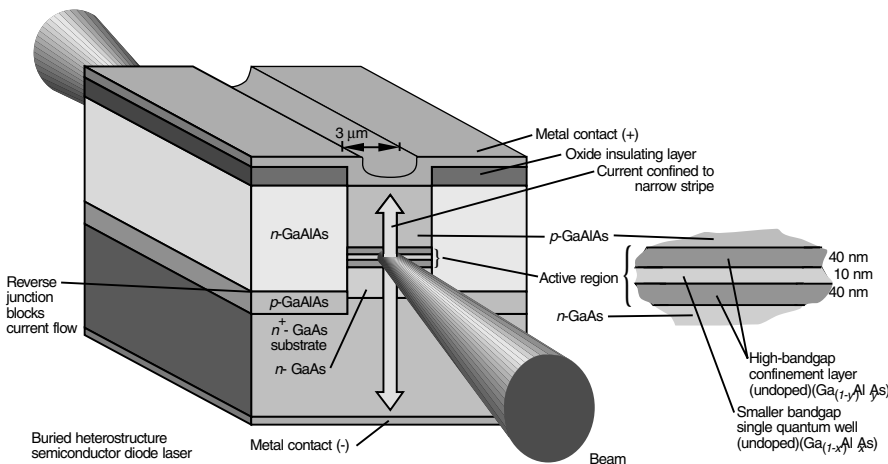


Fig. 8.33. Heterostructure diode laser [8.89]

Diode-laser development is largely driven by optical telecommunication needs. The usefulness of this type of laser in these contexts stems from the ease with which the output can be electrically modulated at an extremely high bit-rate (up to tens of Gb/s). Since low loss wavelength regions for optical fibres are around 1.3 and at 1.55 μm (see Fig. 8.34) governed by the presence of Fe impurities, OH radical absorption and elastic scattering, the most developed diode lasers are found there. An interesting technology employing diode-pumped Er³⁺-doped fibre amplifiers for 1.55 μm has also been developed for long-haul transmission lines [8.91]. While telecommunication lasers are operated at room temperature, laser for longer wavelengths need

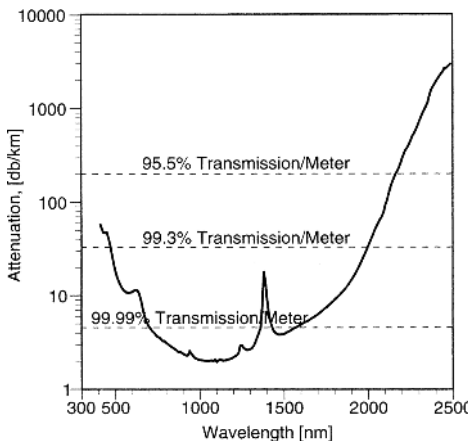


Fig. 8.34. Transmission curve for a quartz optical fibre [8.90]

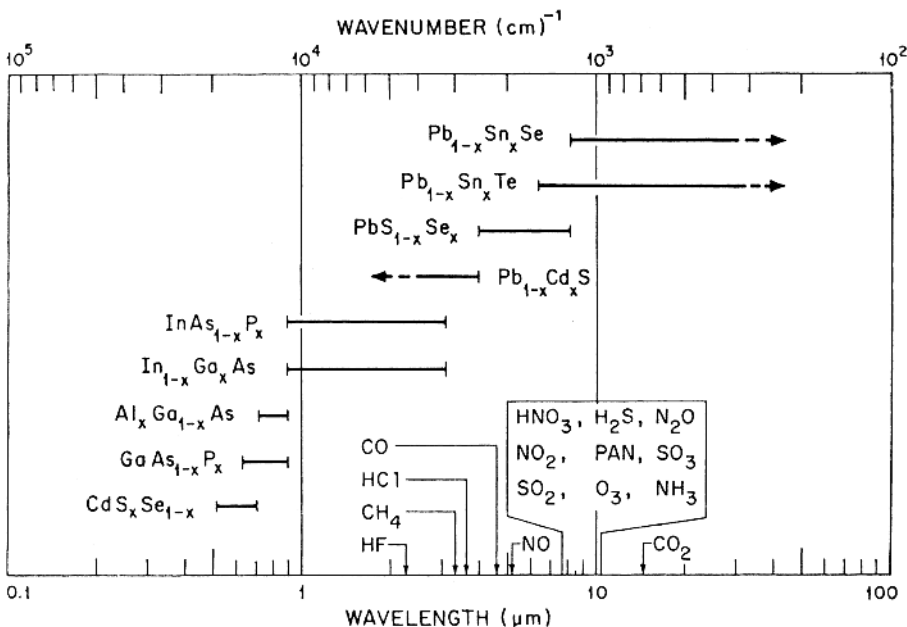


Fig. 8.35. Tuning ranges for different types of semiconductor laser [8.86]

cryogenic cooling. Spectroscopic diode lasers for wavelengths out to $40\text{ }\mu\text{m}$ have been developed as indicated in Fig. 8.35. Material combinations of Pb, S, Sn, Se and Te are used.

Intense research for extending room-temperature diode-laser emission to visible wavelengths has been performed [8.92]. Laser pointers at 670 nm and at 633 nm (where the human eye has a 9 times higher sensitivity) are now readily available. Blue and violet cw laser action in GaN and other materials has even been achieved (printing and lithographic applications) [8.93]. New developments in semiconductor lasers also include vertical cavity surface emitting lasers (VCSEL) [8.94] and quantum cascade lasers (QCL) [8.95], which have interesting properties for spectroscopy. Diode laser technology is described in [8.96–8.99] and spectroscopic applications of diode lasers in [8.100–8.103].

8.6 Nonlinear Optical Phenomena

Several nonlinear optical phenomena can be utilized to extend the available wavelength range for a certain laser type. First we consider *frequency doubling*. In an electric circuit, frequency doubling of an input signal can be achieved by using nonlinear components. The corresponding optical phenomenon, which is an example of *nonlinear optical effects*, can be observed in

certain crystals that are traversed by very intense laser light. Light propagation through a transparent medium can be considered as a process in which electrical dipoles (electrons bound to a nucleus) are made to oscillate by the radiation field, and thus to re-emit the light. Through interference, light in the beam direction only is obtained. As long as the oscillation amplitude is small the dipoles can follow the applied oscillation, but at higher amplitudes nonlinearities occur when the dipoles can no longer reproduce the applied oscillation. Harmonics then occur. If \mathcal{E} is the applied electric field and P is the polarization for the optical medium we can write

$$P = \chi^{(1)}\mathcal{E} + \chi^{(2)}\mathcal{E}^2 + \chi^{(3)}\mathcal{E}^3 + \dots, \quad (8.7)$$

where $\chi^{(i)}$ are polarizability constants (susceptibilities). From the second term in (8.7) we obtain for $\mathcal{E} = \mathcal{E}_0 \sin \omega t$

$$P_2 = \chi^{(2)}\mathcal{E}_0^2 \sin^2 \omega t = \frac{1}{2}\chi^{(2)}\mathcal{E}_0^2(1 - \cos 2\omega t).$$

This term is responsible for the generation of frequency-doubled light. A prerequisite is that the crystal has a non-central symmetric structure. Using symmetry arguments, it can be shown that for a material with a centre of symmetry all even coefficients $\chi^{(2)}$, $\chi^{(4)}$ etc. must vanish. Since $\chi^{(2)}$ is always small, it is necessary for \mathcal{E}_0 to be sufficiently high. With pulsed lasers electric field strengths of a sufficient magnitude ($\sim 10^5$ V/cm) can easily be obtained so that the terms $\chi^{(1)}\mathcal{E}$ and $\chi^{(2)}\mathcal{E}^2$ become comparable in magnitude. The generation of frequency-doubled radiation is hampered by wavelength dispersion for the two waves at frequencies ω and 2ω . Since the waves do not normally propagate with the same velocity, destructive interference occurs with a resulting low yield. By utilizing doubly refractive materials, for which the velocity of propagation for the ordinary ray at ω coalesces with the velocity for the extraordinary ray at 2ω , “phase matching” can be obtained. The phase-matching condition also expresses the requirement for conservation of momentum. By tilting the crystal, and thus selecting the direction of propagation through it, phase matching can be achieved within a certain wavelength range. In Fig. 8.36 the generation of a frequency-doubled wave and the achievement of phase matching are illustrated.

Temperature also influences the phase matching. It is especially advantageous if phase matching for a direction at 90° to the optical axis can be achieved by temperature adjustment. Then the extraordinary ray is not displaced with respect to the ordinary ray, which is otherwise the case, reducing the beam overlap. KDP (potassium dihydrogen phosphate) and KPB (potassium pentaborate) are frequently used crystals. An energy conversion efficiency of tens of per cent can be achieved for the former material, whereas the latter has a substantially smaller efficiency. β -barium-borate (BBO, BaB_2O_4) is a new high-efficiency material, that is replacing KPB. Because of the nonlinear nature of the frequency-doubling process, it is normally used in connection with pulsed lasers. Using tunable dye lasers, doubling down

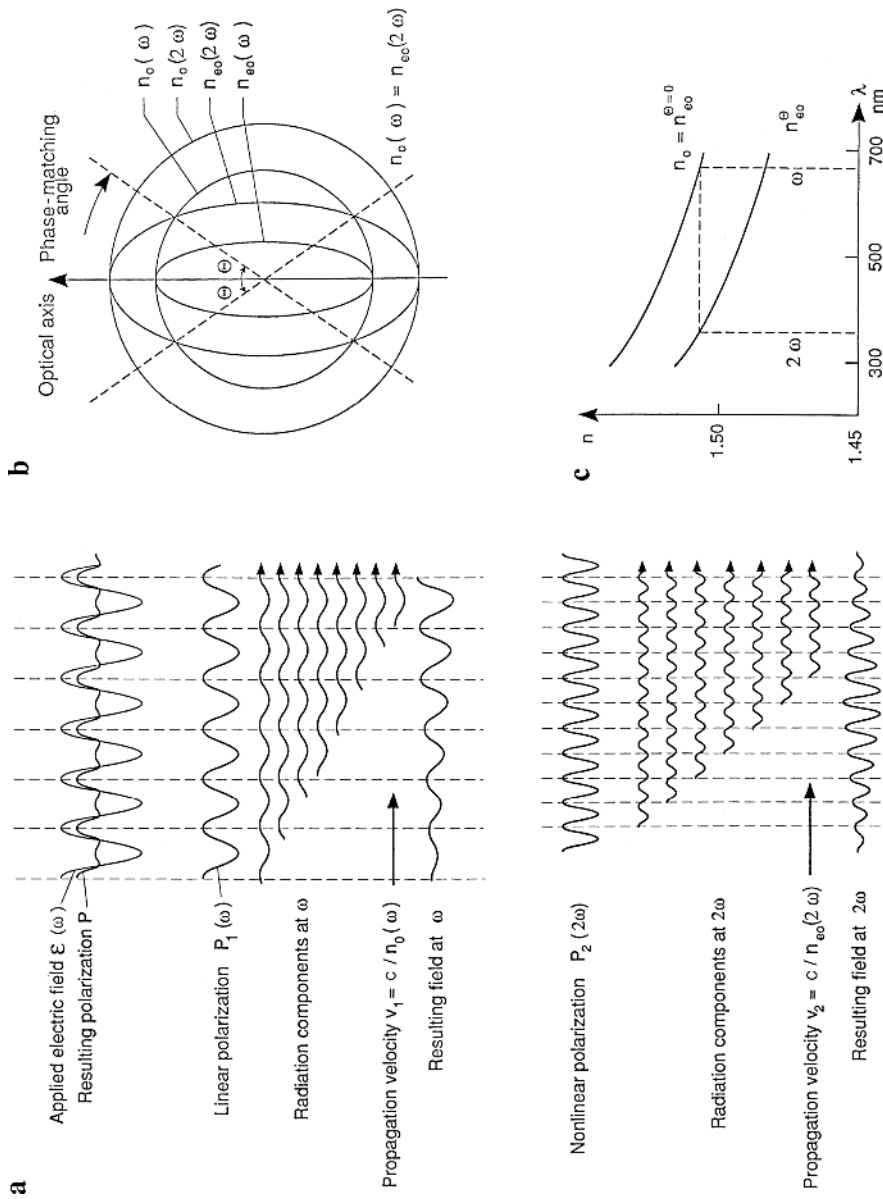


Fig. 8.36. The generation of a frequency-doubled wave in a nonlinear crystal. (a) Fields and polarizations in the crystal; (b) the concept of phase matching is illustrated; (c) dispersion curves for KDP

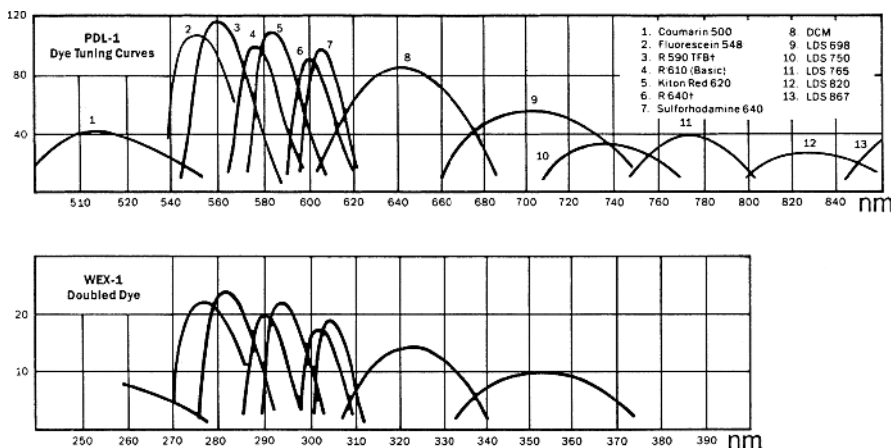


Fig. 8.37. Primary, and frequency-doubled tuning curves for a Nd:YAG-pumped dye laser (Courtesy: Spectra Physics, Inc.)

to about 200 nm can be achieved, with the limit set by material absorption. In Fig. 8.37 frequency-doubling curves for a Nd:YAG-pumped dye laser are given.

By using an intracavity frequency-doubling crystal or an external enhancement cavity [8.104, 8.105] continuous frequency doubling and mixing can also be achieved for CW dye laser radiation. Powers of several mW can then be achieved (Fig. 8.27b).

Frequency doubling can be seen as a *mixing* of two waves of the same frequency in a nonlinear medium. The more general processes, sum and difference-frequency generation, are also possible and can be used to generate new frequencies using two lasers. The process can be explained by expressing the light field as

$$\mathcal{E} = \mathcal{E}_1 \cos \omega_1 t + \mathcal{E}_2 \cos \omega_2 t. \quad (8.8)$$

The quadratic term in (8.7) can then be written

$$\begin{aligned} P_2 &= \chi^{(2)} [\mathcal{E}_1^2 \cos^2 \omega_1 t + \mathcal{E}_2^2 \cos^2 \omega_2 t + 2\mathcal{E}_1 \mathcal{E}_2 \cos \omega_1 t \cos \omega_2 t] \\ &= \chi^{(2)} \left[\frac{1}{2} (\mathcal{E}_1^2 + \mathcal{E}_2^2) + \frac{1}{2} \mathcal{E}_1^2 \cos 2\omega_1 t + \frac{1}{2} \mathcal{E}_2^2 \cos 2\omega_2 t \right. \\ &\quad \left. + \mathcal{E}_1 \mathcal{E}_2 \cos(\omega_1 + \omega_2)t + \mathcal{E}_1 \mathcal{E}_2 \cos(\omega_1 - \omega_2)t \right]. \end{aligned} \quad (8.9)$$

It can be seen that, apart from the doubled frequencies, sum and difference frequencies are obtained. The phase matching is chosen to strongly enhance one of the terms. In Fig. 8.38 curves for sum generation employing a dye laser and the fundamental frequency of the Nd:YAG laser are given.

For difference-frequency generation materials that are transparent in the IR region are needed. In Fig. 8.39 IR generation in LiNbO₃ (lithium niobate) is illustrated employing single-mode Ar⁺ and dye lasers, and output curves

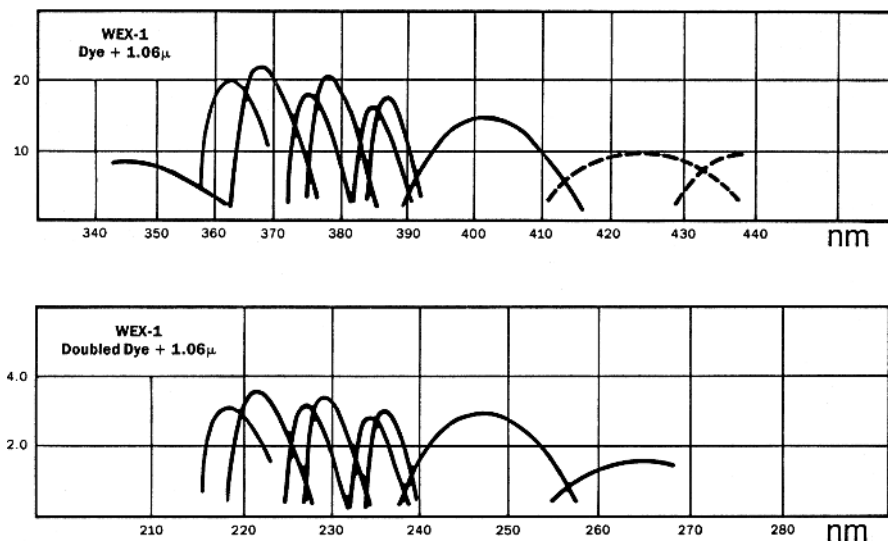


Fig. 8.38. Sum-frequency generation curves for a Nd:YAG-based tunable dye laser (Courtesy: Spectra Physics, Inc.)

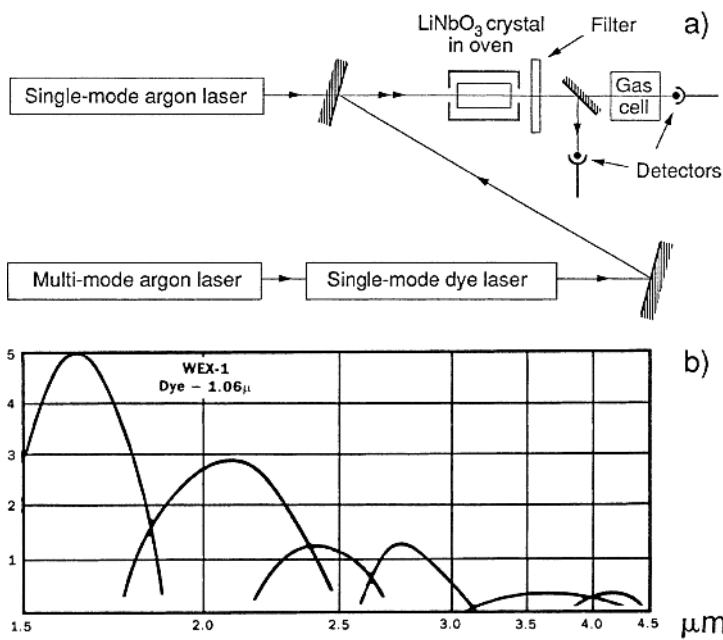


Fig. 8.39. IR radiation by difference frequency generation in LiNbO_3 : (a) A set-up for CW generation [8.106] and (b) curves for pulsed IR radiation obtained using a Nd:YAG-based tunable laser (Courtesy: Spectra Physics, Inc.)

for a Nd:YAG-based difference-frequency generator are also given. Crystals of CdGeAs₂, AgGaS₂ and AgGaSe₂ are also available, allowing frequency doubling and sum-frequency generation for pulsed CO₂ lasers. Nonlinear materials for frequency doubling and mixing have been discussed in [8.107–8.110].

Nonlinear processes require high intensities if they are to be efficient. This limits the applications in the field of diode lasers. However, it is possible to focus the radiation into a narrow waveguide structure of a nonlinear material, such as LiNbO₃. Clearly, phase mismatch will occur after some distance of propagation. By the technique of electric-field-induced *periodic poling* it is possible to regain phase-matching in this *quasi-phase-matching* scheme by periodically switching the sign of the dispersion. Local ferroelectric domain switching occurs and leads to permanent changes in the crystal structure. In this way it has become possible to perform frequency doubling to the blue wavelength region [8.111] and difference-frequency generation to IR wavelengths [8.112], in a similar way to that shown in Fig. 8.39. Recently it has also become possible to perform poling of bulk crystals to allow high-power applications [8.113]. The use of the techniques described here has important advantages over conventional phase-matching. The same polarization can be used on all beams, resulting in typically 10 times higher specific nonlinearity and a corresponding increase in efficiency of the conversion. Further, phase-matching can be achieved over the whole transmission range of the material.

The *Optical Parametric Oscillator* (OPO) process should also be mentioned. Here a nonlinear crystal in a cavity is used to generate two new frequencies (ω_1 and ω_2) from a single one (ω) that is used to pump the crystal (Fig. 8.40). Energy conservation requires $\omega_1 + \omega_2 = \omega$. The frequency division between the two new waves (the *signal* and the *idler*) is chosen by the phase-matching condition. In order to further narrow down the resulting linewidth one of the cavity mirrors can be replaced by a grating, as indicated in the figure. The crystal and grating are tuned synchronously. The parametric process can also be used in *Optical Parametric Amplifiers* (OPA) to boost the output power. Parametric systems have recently been refined with regard to linewidth and output power to present a competitive alternative to dye or other tunable lasers. Large wavelength regions can be spanned, especially since the fundamental, doubled or tripled output of the fixed-frequency pump laser (frequently a Nd:YAG laser) can be employed. Tuning curves for a commercial unit are shown in Fig. 8.41. Parametric light generation was reviewed in [8.114, 8.115].

Frequency mixing can also be achieved in mixtures of metal vapours and inert gases. Since asymmetry is not present in a gas, terms depending on $\chi^{(2)}$ are excluded. Third-order processes ($\chi^{(3)} \neq 0$) can be utilized. Direct frequency tripling and four-wave mixing processes are of this type.

In order to access short VUV wavelengths down to the LiF cutoff (110 nm), the resonant four-wave mixing process is quite efficient. This tech-

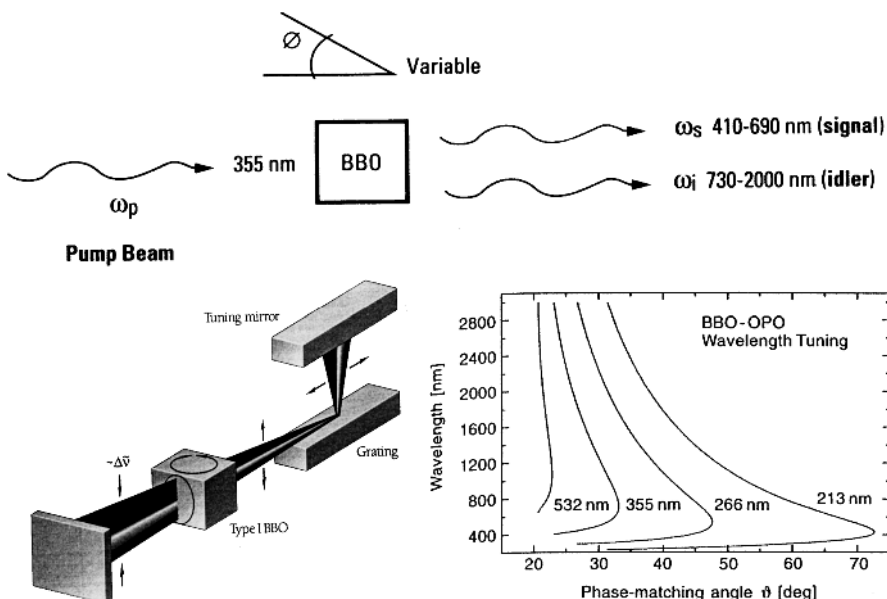


Fig. 8.40. Principle of an optical parametric oscillator (OPO) (Courtesy: Spectra Physics and Continuum, and [6.80])

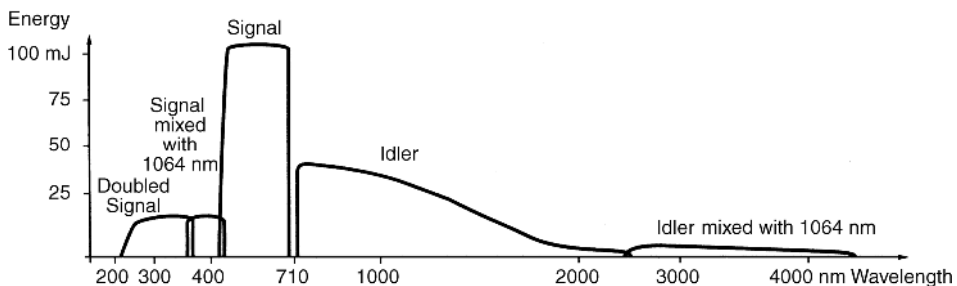


Fig. 8.41. Tuning curves for a commercial pulsed OPO (Courtesy: Spectra Physics)

nique is illustrated for the case of Kr gas in Fig. 8.42a [8.116]. Basically, two UV photons at 212 nm are subtractively mixed with a third, co-propagating tunable photon to generate a short-wavelength tunable photon in a process involving the frequencies ω_R , ω_L and ω_{VUV} :

$$\omega_{VUV} = 2\omega_R - \omega_L. \quad (8.10)$$

Since the process is two-photon resonant, it has a high efficiency. Examples of experimental tuning curves in Kr [8.117] are shown in Fig. 8.42b for different dyes in the tunable laser, which was used with its fundamental output ω_L , its frequency doubled output $2\omega_L$ and its IR frequency mixed output $\omega_L + \omega_{IR}$

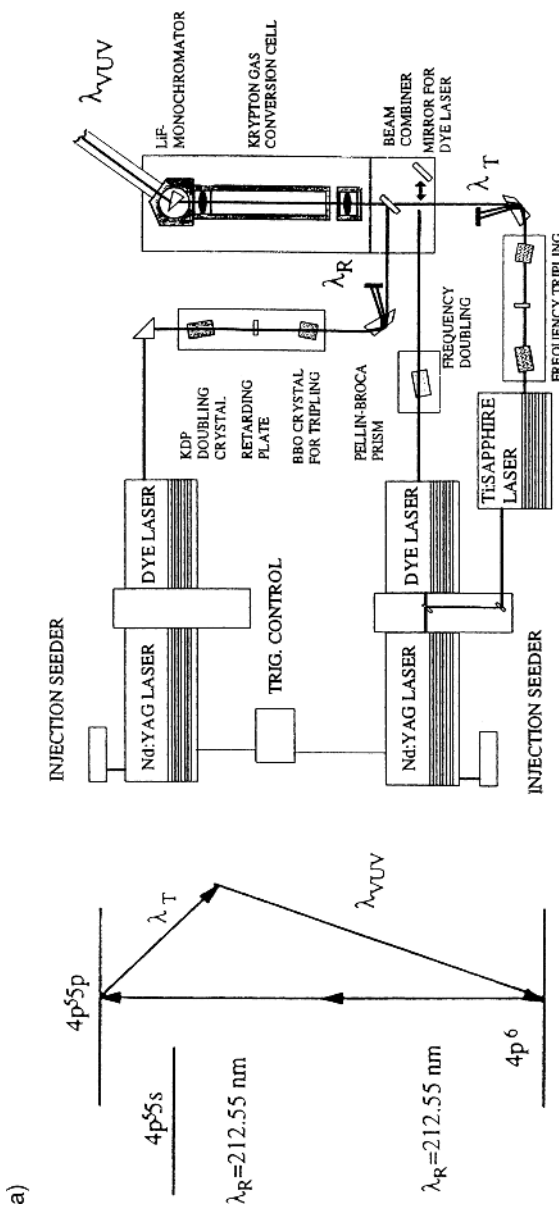


Fig. 8.42a. Illustration of VUV radiation generation using two laser beams interacting in Kr gas [8.116]

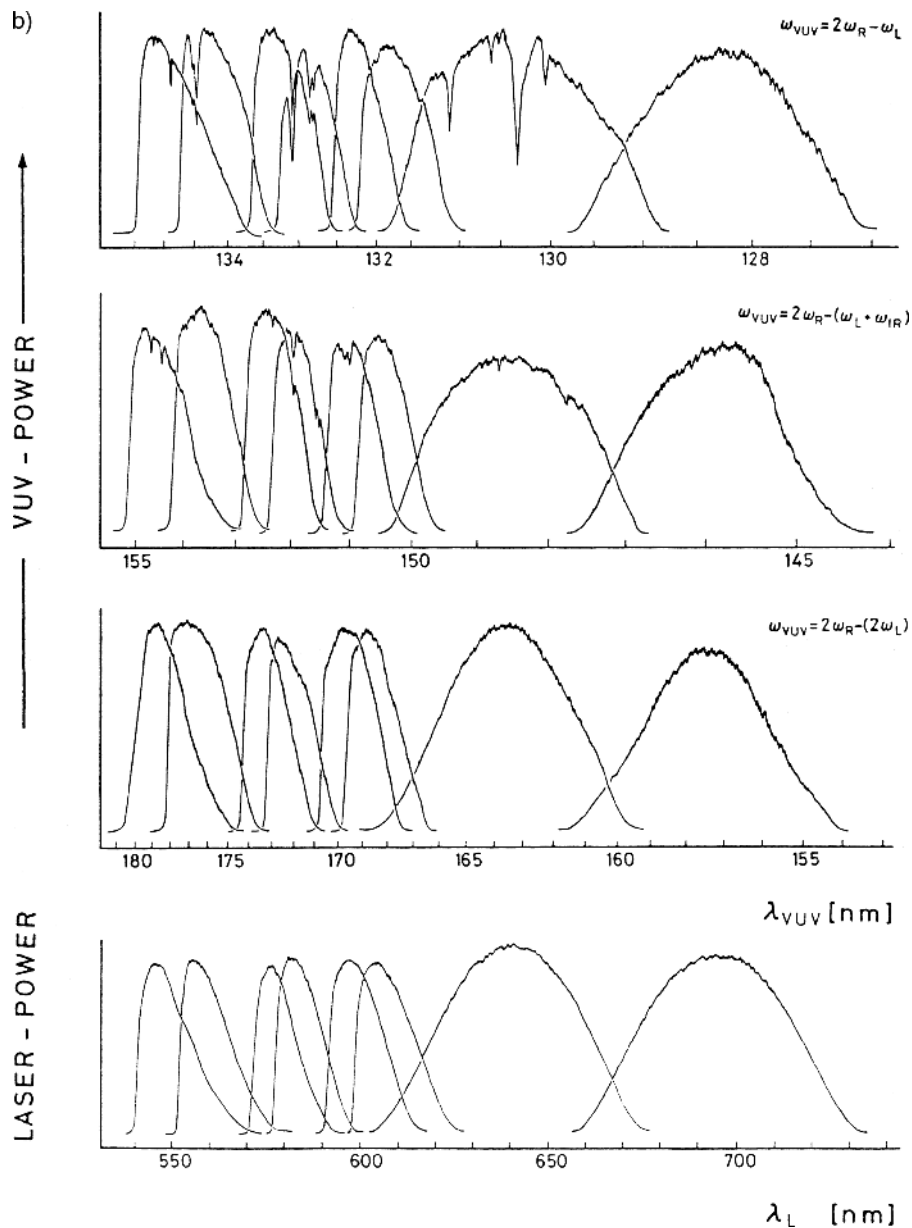


Fig. 8.42b. Tuning curves in the vacuum-ultraviolet spectral region obtained using different mixing processes in Kr [8.117]

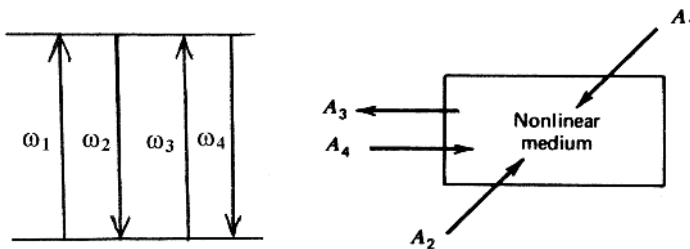


Fig. 8.43. Principle of degenerate four-wave mixing

(see also Fig. 8.38). VUV generation in inert gases and metal vapors and applications of VUV radiation are discussed in [8.117–8.124].

If all photons involved in the mixing process have the same wavelength, the process is referred to as *degenerate four-wave mixing* (DFWM). Clearly, the generated photons are then hard to distinguish from the pumping photons and the process is of little interest. However, a different beam geometry which satisfies the phase-matching condition can be used, allowing the generated photon beam to be readily distinguished (see Fig. 8.43). Two counter-propagating beams are overlapped in the medium, and a third beam, coming in at an angle, is added. The newly generated beam will then propagate backwards and can be isolated by using a beamsplitter. The process can be seen as Bragg scattering (Littrow geometry) by the standing-wave grating set up by the counter-propagating beams. The process occurs in gases, with strong resonant enhancement if the frequency is tuned to an atomic or molecular transition. The presence of a particular species in a gas can be detected in this way (see also Chap. 10). The process also occurs in crystals, where the medium is much denser. The most fascinating aspect of the backward-propagating beam is that it can be shown to be *phase conjugated*, i.e. the wavefront is exactly reversed and in all details retraces the incoming beam. This means that if the incoming beam was first distorted by passing a phase aberrator, such as a turbulent flame or even a piece of ground glass (bathroom window), it will appear undistorted when it reappears through the aberrator again. The result is that a badly distorted image can be reconstructed again. An example is shown in Fig. 8.44, where an argon laser beam was passed through a slide and a piece of ground glass before being reflected back. The images were recorded after reflecting off a normal mirror (*left*) and a phase-conjugator (*right*; BSO self-conjugating crystal). By making one of the mirrors in a laser phase conjugating, the cavity becomes immune to lensing in the laser medium caused by thermal loads. The technique has been incorporated in commercial lasers.

Optical phase conjugation was first observed in connection with *stimulated Brillouin scattering* (SBS) [8.125] and then in four-wave mixing processes [8.126]. It is further discussed in [8.127–8.129].

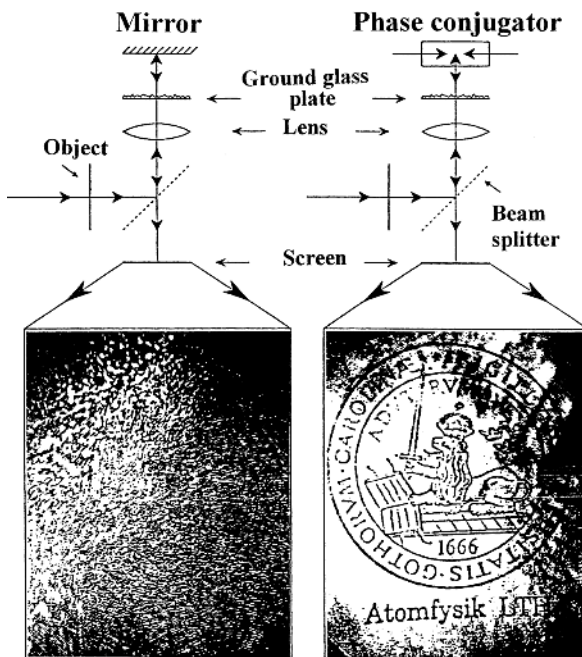


Fig. 8.44. Demonstration of optical phase conjugation. The experimental arrangement, and images with and without a phase conjugator are shown (Courtesy: Sven-Göran Pettersson, LTH)

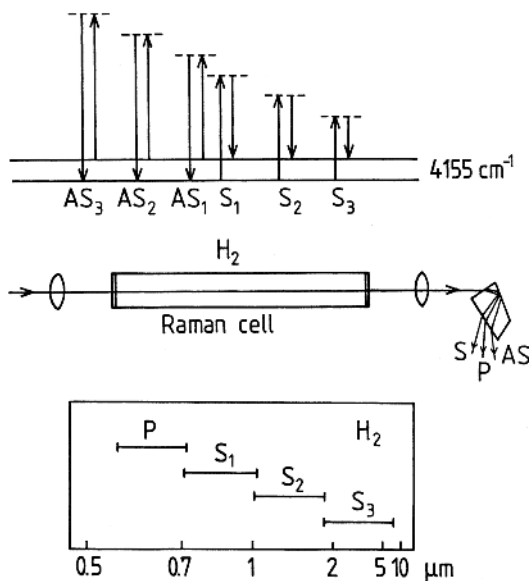


Fig. 8.45. Generation of stimulated Raman scattering

The SBS process has a further interesting property, namely, to provide temporal compression of laser pulses [8.130–8.132].

Stimulated Raman scattering processes are particularly convenient for the generation of new tunable wavelengths. If a gas is irradiated with laser light of sufficiently high power, stimulated Raman scattering occurs. The Stokes-shifted light propagates in the same direction as the pump radiation. In hydrogen gas a vibrational shift of 4155 cm^{-1} ($\sim 0.5\text{ eV}$) is obtained. The process is illustrated in Fig. 8.45 together with an illustration of how higher Stokes components are obtained by further Stokes shifts. Radiation of shorter wavelength can also be obtained (anti-Stokes components) by four-wave mixing between the pump radiation and Stokes-shifted components. A gas pressure of 10 atmospheres is common. There is no phase-matching condition. By using a small number of very efficient dyes in a pulsed dye laser, wavelengths from the vacuum ultraviolet to $10\text{ }\mu\text{m}$ can be achieved by Raman shifting. The efficiency in the conversion to the first Stokes component can exceed 10%, whereas higher-order components are much weaker. In Fig. 8.46, the relation between the primary radiation and the generated wavelengths is illustrated. Besides H_2 , other gases, in particular D_2 (2987 cm^{-1}) and CH_4 (2917 cm^{-1}), can be used in Raman shifters. Raman shifting is discussed in [8.133, 8.134].

High harmonics generation as a means to achieve short-wavelength tunable radiation requires very high peak intensities and will be considered in Sect. 9.6.2.

We end this section on frequency extension techniques by discussing the *CARS* (Coherent Anti-Stokes Raman Scattering) process, which is a special case of four-wave mixing [8.135]. The process is useful for the generation of new frequencies (1st anti-Stokes component in the stimulated Raman scattering discussed above) and also for powerful spectroscopic applications (Sect. 10.1.4). In Fig. 8.47 basic diagrams for the process are given illustrating energy and linear momentum conservation.

In the CARS process the sample is irradiated by two laser beams and the frequency difference between the beams is chosen to correspond to the vibrational (rotational) splitting of the irradiated molecules. The beams are denoted the *pump beam* (at frequency ω_P) and the *Stokes beam* (at frequency ω_S). Two photons of frequency ω_P are mixed with a photon of frequency ω_S , through the third-order susceptibility $\chi^{(3)}$, to generate a stimulated anti-Stokes photon of frequency ω_{AS} (in the anti-Stokes position with regard to the pump beam)

$$\omega_{AS} = 2\omega_P - \omega_S. \quad (8.11)$$

The phase-matching condition can be written

$$\mathbf{k}_{AS} = 2\mathbf{k}_P - \mathbf{k}_S, \quad (8.12)$$

where \mathbf{k} is the wave vector with $|\mathbf{k}| = \omega n/c$.

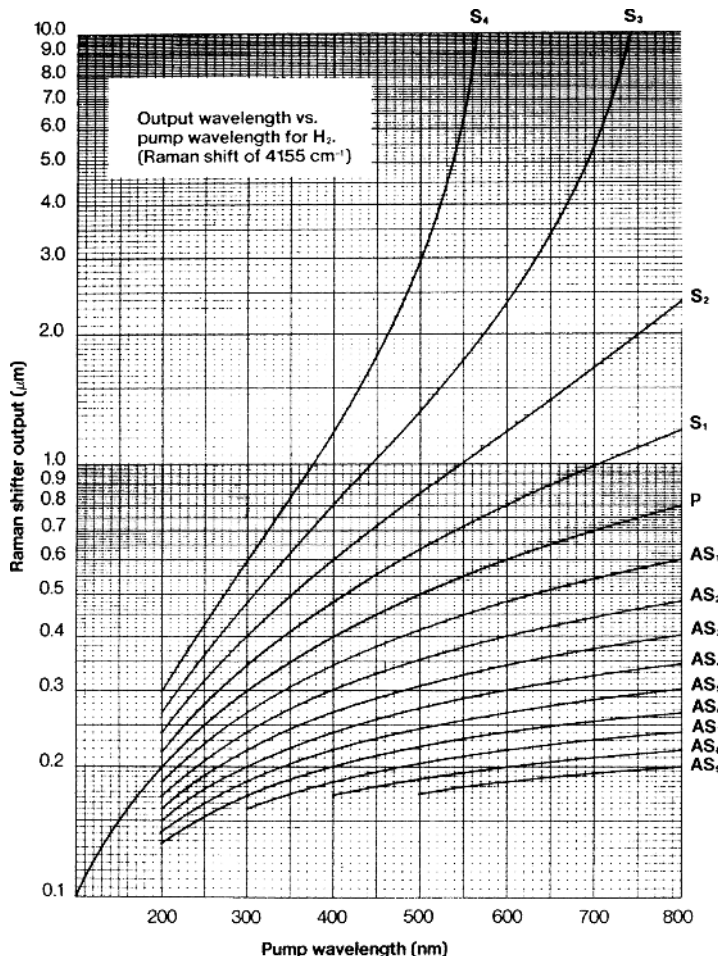


Fig. 8.46. The relation between applied wavelength and generated coherent Raman components using H_2 gas (G. Bjorklund, private communication)

In liquids and solids with a strong wavelength dispersion the two primary laser beams must be crossed at a small angle and the generated CARS beam will emerge at still another angle to fulfil the phase-matching condition (8.12). In a gas with negligible dispersion ($n \simeq 1$), collinear phase matching is possible. In diagnostic applications, the so-called BOXCARS geometry is frequently used to achieve improved spatial resolution [8.137]. The CARS beam is generated only from the region in which the incoming laser beams cross. In this case two pump beams and one Stokes beam are used.

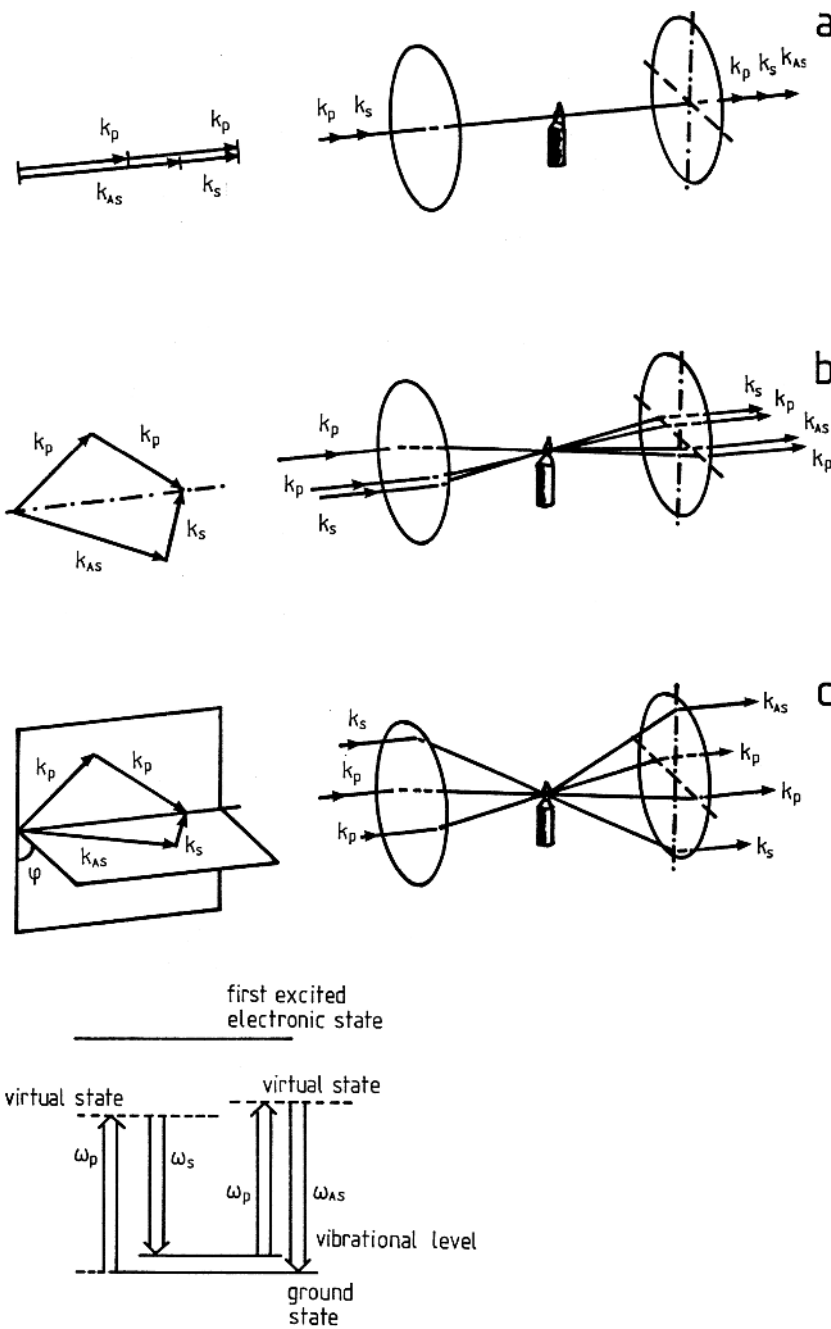


Fig. 8.47. Basic diagram and phase-matching schemes for Coherent Anti-Stokes Raman Scattering (CARS). (a) Collinear, (b) BOXCARS, and (c) folded BOXCARS phase matching [8.136]

When the phase-matching condition is fulfilled, the power P_{AS} of the generated beam is related to the powers P_{P} and P_{S} of the pump and Stokes beams, respectively, through the expression

$$P_{\text{AS}} \simeq \left| \chi^{(3)} \right|^2 \cdot P_{\text{P}}^2 P_{\text{S}}. \quad (8.13)$$

Since $\chi^{(3)}$ is proportional to the molecular number density, N , we make the interesting (and unusual) observation that the generated beam strength is proportional to N^2 rather than to N .

The basis for most nonlinear optical processes has been discussed in [8.138]. Several recent monographs cover the field extensively [8.139–8.145].

8.7 Ultra-short and Ultra-high-Power Laser Pulse Generation

During recent years a particularly fast developing field has been the generation and application of extremely short laser pulses covering the picosecond ($1\text{ ps} = 10^{-12}\text{ s}$) range down to a duration of a few femtoseconds ($1\text{ fs} = 10^{-15}\text{ s}$). Such short pulses can also be amplified to extremely high powers in the terawatt ($1\text{ TW} = 10^{12}\text{ W}$) range, even approaching the petawatt ($1\text{ PW} = 10^{15}\text{ W}$) regime. We will here describe the laser technology for achieving these extreme levels of performance and will defer a discussion of applications to Sects. 9.5 and 9.6.

8.7.1 Short-Pulse Generation by Mode-Locking

We will here describe the use of *mode-locking* [8.146], where we find, perhaps somewhat surprisingly, that the shortest optical pulses are generated by using continuous laser beams! Interference effects are employed and a particularly clear and beautiful illustration of the action of the Fourier transform from the frequency to the time domain is obtained.

For a short description of the mode-locking phenomenon we consider a CW laser system with a cavity length of ℓ . If no frequency discriminating element is present in the cavity, laser operation on an atomic or ionic line will yield only a few cavity modes, whereas a corresponding dye laser with a very broad gain medium will feature a large number of modes. The modes are separated by $\Delta\nu = c/2\ell$, or, in angular frequency, $\Delta\omega = 2\pi(c/2\ell) = \pi c/\ell$, where ℓ is the cavity length. The phases of these modes are completely unrelated. If we assume an idealized situation in which $2N + 1$ modes of equal amplitude \mathcal{E}_0 oscillate with a constant phase relation

$$\phi_k - \phi_{k-1} = \alpha \quad (8.14)$$

between adjacent modes (mode-locking), the resulting light field $\mathcal{E}(t)$ is given by

$$\mathcal{E}(t) = \sum_{k=-N}^N \mathcal{E}_0 \exp\{i[(\omega_0 + k\Delta\omega)t + k\alpha]\}. \quad (8.15)$$

Here ω_0 is the centre angular frequency. The evaluation of this expression involves the same type of mathematics as that used for calculating the spectral intensity distribution from a grating, and we have

$$\mathcal{E}(t) = A(t) \exp(i\omega_0 t) \quad (8.16)$$

with

$$A(t) = \mathcal{E}_0 \frac{\sin[(2N+1)(\Delta\omega t + \alpha)/2]}{\sin[(\Delta\omega t + \alpha)/2]}. \quad (8.17)$$

Equation (8.16) represents an optical sinusoidal carrier wave of frequency ω_0 , which is amplitude-modulated in time according to (8.17). The light intensity is proportional to $A^2(t)$, and in Fig. 8.48 the intensity for the case of seven locked modes is given.

The phase relation (8.14) causes the continuous partial waves to interfere constructively to give short pulses separated in time by

$$\Delta t = 2l/c. \quad (8.18)$$

(The maxima occur when the denominator in (8.17) approaches 0.) The pulse separation is the time taken for light to go back and forth in the cavity (“cavity round-trip time”) and is typically 10 ns (1 ns \leftrightarrow 30 cm). From (8.17) we also obtain the time δt from the pulse maximum to the first zero point

$$\delta t = \frac{2\pi}{(2N+1)\Delta\omega} = \frac{1}{\nu_{\text{osc}}}. \quad (8.19)$$

Thus, δt is the inverse of the oscillation bandwidth ν_{osc} of the laser and we note that a large number of locked modes is needed in order to obtain a short pulse length. Clearly, this is entirely consistent with the uncertainty relation requiring a large frequency uncertainty if the time uncertainty is small. It also reflects the general properties of the Fourier transform between the time and the frequency domains. In a dye laser with a broad frequency selective element (e.g., a single-plate Lyot filter), resulting in a bandwidth of $\sim 5 \text{ \AA}$, mode-locking results in pulses of a few picoseconds ($1 \text{ ps} = 10^{-12} \text{ s}$) duration. From (8.17) it follows that the pulse peak intensity $A^2(t)$ is proportional

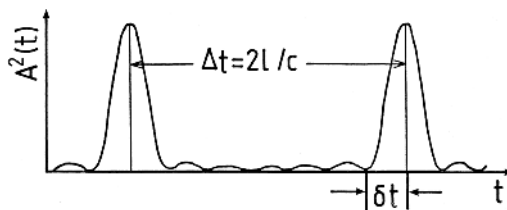


Fig. 8.48. Temporal structure of seven locked modes of equal amplitude

to $(2N + 1)^2 \mathcal{E}_0^2$, whereas the light intensity for non-locked modes would be proportional to $(2N + l) \mathcal{E}_0^2$. This is consistent with the observation that $\Delta t/\delta t = (2N + 1)$. The total time-averaged intensity remains constant but the distribution in time is entirely different. We note that very high peak powers can be obtained with a dye laser that has a high N value [8.147].

We will now describe how mode-locking according to (8.14), can be accomplished. Several approaches can be used: active or passive mode-locking. *Active* mode-locking is obtained by modulating the gain or loss of the laser at a frequency that matches the mode separation $\Delta\omega$. This can be accomplished using a Bragg cell, as illustrated in Fig. 8.49a. Optical side-bands are then generated for every mode. These side-bands coalesce with the neighbouring mode positions and impose their phase on them. In this way all modes are successively locked in phase with each other, i.e. mode-locking. In an alternative way of describing the phenomenon the loss modulation can be seen as a shutter in the cavity. The shutter is only open during certain intervals separated by the cavity round-trip time. Then a multi-mode oscillation with unrelated phases cannot occur since each mode would be strongly attenuated. On the other hand, if the phases are locked as in (8.14), the energy distribution in the resonator is a short pulse that passes the shutter when it is open, which happens at exactly the right times. Because of the “regenerative” nature of the laser action the phases tend to lock in a way leading to low effective losses (at pulse formation).

A common way to mode-lock a dye laser that is pumped by an ion laser is to use *synchronous pumping*. An actively locked ion laser with the same cavity length as the dye laser is then used (the length of the dye-laser cavity is accurately adjusted). Then the laser medium is inverted only during short time intervals, and only a light pulse that bounces back and forth in the cavity passing the gain medium at exactly the right time can be amplified (Fig. 8.49b). By using a second Bragg cell in the dye laser a bouncing pulse can be deflected out of the resonator when it has gained in intensity in the low-loss cavity. Using this *cavity-dumping* technique, stronger picosecond pulses at longer time separations than those from normal mode-locking are obtained. Single picosecond pulses can then be further amplified in successive stages using amplifier cells with dye that is pumped by a high-power pulsed laser, e.g., a frequency-doubled Nd:YAG laser.

In *passive* mode-locking a thin (0.1 mm) *saturable absorber* (special dye) is used in the cavity. For sufficiently high light intensities the absorption of the substance is reduced (bleaching). Such intensities are obtained for mode-locking with associated pulse formation, whereas all unrelated cavity modes are strongly absorbed and quenched. The laser modes then tend to arrange themselves so that oscillation and intensity can build up and passive mode-locking is achieved. The best efficiency is obtained if the absorber is placed in direct connection to the high reflector of the cavity so that a still higher intensity is obtained in the turning pulse (Fig. 8.49c). In a technique using

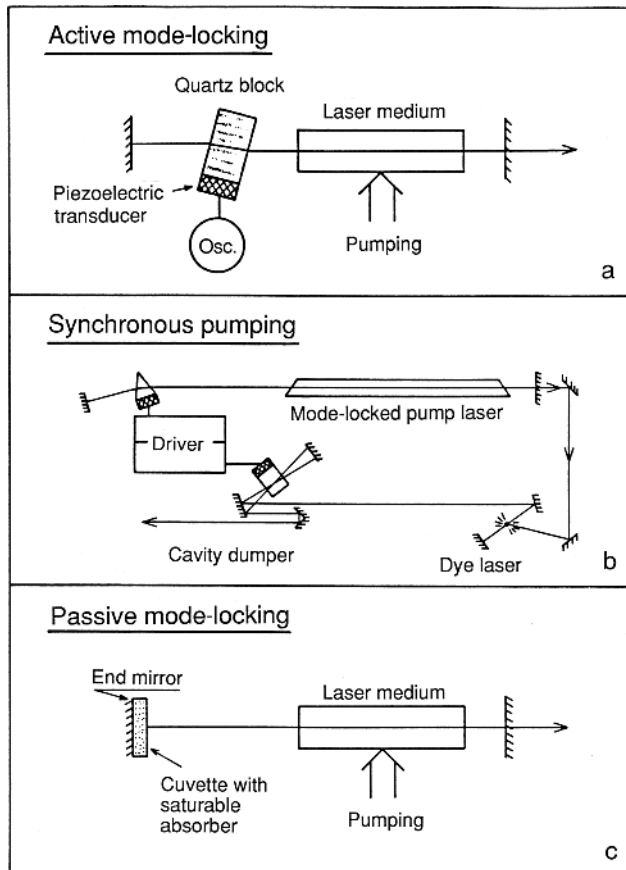


Fig. 8.49. (a) Active mode-locking by acousto-optic modulation. (b) Synchronous pumping of a dye laser equipped with a cavity dumper. (c) Passive mode-locking using a saturable absorber

“colliding” pulses a ring cavity is used with a very thin saturable absorber (normally a bleachable dye jet) [8.148]. In the ring cavity light circulates in both directions. Only if extremely short pulses from both directions simultaneously pass the saturation medium is sufficient bleaching and thus high transmission obtained. In this way pulse lengths of 100 femtoseconds ($1\text{ fs} = 10^{-15}\text{ s}$), corresponding to a spectral width of about 5 nm, can be achieved. The formal mathematical treatment for active and passive mode-locking is rather complex and we give only the above rather crude phenomenological descriptions.

Further reductions in pulse length can be accomplished by *pulse compression*. A femtosecond pulse is then transmitted through an optical fibre, which has an index of refraction that depends on the intensity. The spectral

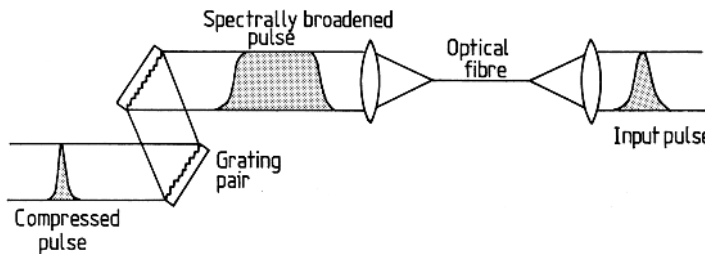


Fig. 8.50. Pulse compression using spectral broadening in an optical fibre and subsequent wavelength-dependent retardation in a grating pair

distribution of the pulse is then broadened by self-phase modulation and the pulse length is shortened by a subsequent passage of the pulse through a wavelength-dependent optical retarder consisting of two gratings, as illustrated in Fig. 8.50. Pulses of 6 fs duration corresponding to only three optical periods could be obtained in this way [8.149].

Very short laser pulses must, as we have seen, contain a broad frequency (wavelength) distribution. Special attention must then be paid to the pulse propagation, since the index of refraction and thus the speed of light in optical materials depends on the wavelength, resulting in different transit time for different colours through an optical component. The spread would typically be tens of fs for a Fourier-limited 100 fs pulse passing through a 1 mm sample of glass. In order to allow a short pulse to build up it is necessary to compensate for this *group-velocity dispersion*. It can conveniently be performed by a pair of prisms, as illustrated in Fig. 8.51. Because of the differential sideways translation of different wavelengths due to the angular dispersion of the prism, the length of the light path in the time-delaying glass is correspondingly different. By proper adjustment of the prisms it is possible to make light of all wavelengths pass through the intracavity optical components in the same time, resulting in ultra-short pulse generation. (The angular deviation in one prism is compensated for by the other one). As an alternative to the prism pair it is possible to use chirped mirrors, with multilayer coatings designed to introduce different delays for the different wavelength components building up the pulse [8.150]. In this way group velocity dispersion compensation can be achieved.

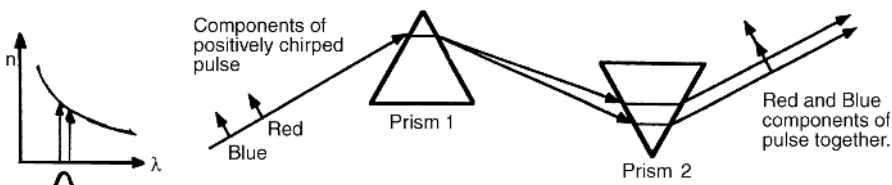


Fig. 8.51. Group velocity dispersion compensation using a prism pair

A particularly powerful femtosecond laser in terms of pulse length, output power and ease of operation is the *self-mode-locked* (or *Kerr-lens mode-locked*) *Ti:sapphire* laser [8.151]. The mechanism of mode-locking is here different from those discussed above and relies on the nonlinear effects of self-focusing. The layout of such a laser is shown in Fig. 8.52. A key aspect is the presence of an iris aperture which is closed to such a small hole, that laser action is almost quenched by intracavity absorption. However, if because of a statistical fluctuation the light intensity is high in a temporal spike, there is a slight focusing of the beam, since the index of refraction n in a medium is intensity-dependent and higher for higher intensities I :

$$n = n_0 + n_2 I. \quad (8.20)$$

This is frequently referred to as the optical Kerr effect. Thus, a beam with a Gaussian cross-section will experience the action of a positive lens causing focusing on passing through a slab of optical material. The intensity spike will experience less loss and will be further amplified. Since the spike can be seen as formed by interference between phase-related equidistant modes, mode-locking has been achieved spontaneously. The lasing action can only occur when there is mode-locking and intense pulse formation; otherwise the light is scraped off by the aperture.

The broad gain medium of Ti:S ($\Delta\nu = 10^{14}$ Hz) allows the build-up of very short pulses with a Fourier limitation of roughly $1/\Delta\nu = 10$ fs. Recently, pulse lengths of about 5.5 fs have been attained directly from a Ti:S laser, corresponding to about two optical cycles [9.152]. Using subsequent compression of pulses which have first been spectrally broadened by self-phase modulation as already discussed in connection with Fig. 8.50, a pulse length of 4.6 fs has been attained [8.153]. Techniques for ultra-short laser-pulse generation are

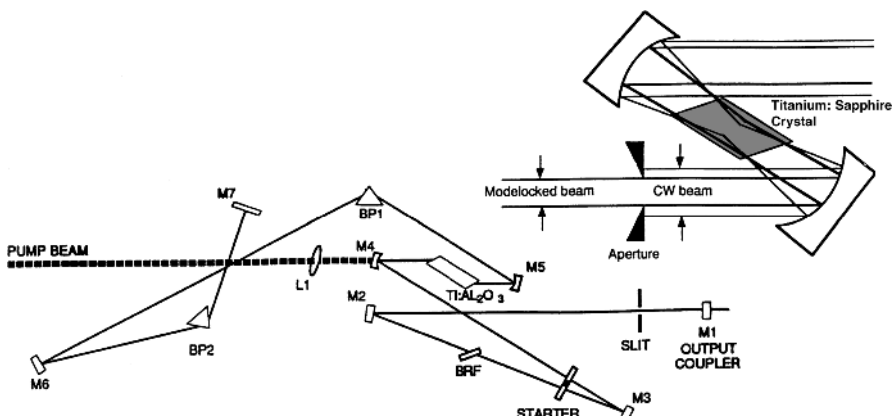


Fig. 8.52. Schematic layout of a mode-locked titanium-doped sapphire laser. The aperture arrangement critical for the self-(Kerr-lens) mode-locking is illustrated separately. (Courtesy: Coherent, Inc.)

discussed in [8.154–8.159]. Measuring techniques for ultra-fast phenomena will be discussed in Sect. 9.5.

8.7.2 Generation of Ultra-high Power Pulses

Ultra-short pulses can be very useful for attaining very high optical power levels, since the pulse energies can still stay modest. As an example, a mode-locked Ti:S laser of the kind illustrated in Fig. 8.52, running at an average power of 1 W, a pulse repetition rate of 100 MHz and a pulse length of 100 fs, yields a peak power of about 10^5 W. To reach terawatt power levels very substantial amplification is needed. Using conventional amplifiers would require the diameter of the beam to be increased substantially, since the damage threshold for many optical components is of the order of 100 GW/cm^2 . Such systems become very expensive and have very low repetition rate and availability. However, the technique of *chirped-pulse amplification* (CPA) [8.160] offers a very elegant way to circumvent these problems. The basics of the CPA technique can be explained considering Fig. 8.53. An oscillator pulse of typically 100 fs duration and 10 nJ energy derived from a laser of the type shown in Fig. 8.52 is first stretched in time by typically a factor of a few thousand. The pulse is then amplified extensively, while still keeping the peak value reasonably low because of the stretching, so that small-diameter beams (typically 5 mm diameter) can be employed. The amplified beam is then expanded to a larger diameter and is temporally compressed back to the original time duration, leading to peak powers in the TW range. The action of the stretcher, which consists of a lens and grating arrangement, is based on different colour components in the Fourier broadened short pulse, as illustrated in Fig. 8.54a. The low-frequency components travel a shorter distance and will come out first after reflection back through the system. The

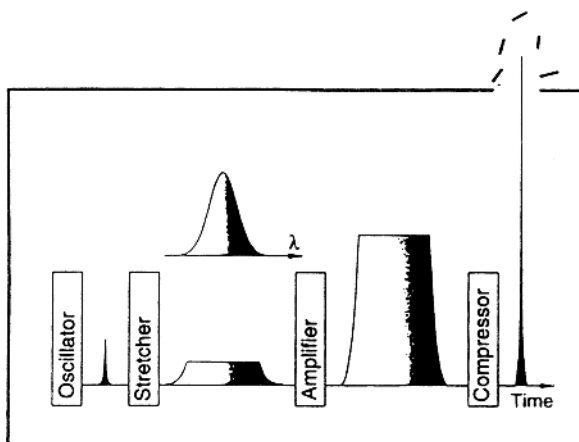


Fig. 8.53. The principle of chirped-pulse amplification [8.161]

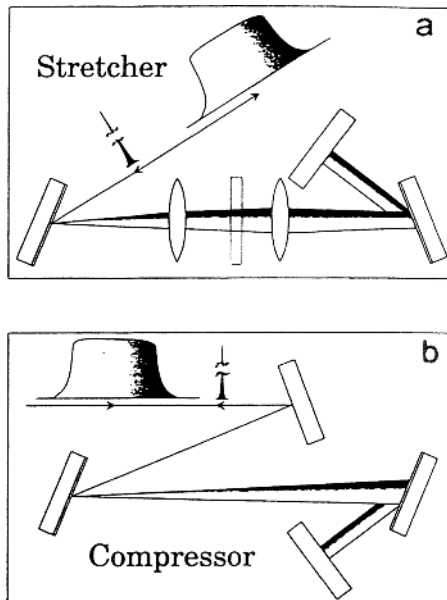


Fig. 8.54. Operational principle of a pulse stretcher (a) and a pulse compressor (b) [8.161]

emerging pulse is thus colour-coded in time in a well-defined way, allowing, in principle, an exact play-back later on. The compressor, handling the strongly amplified pulse, incorporates two gratings (Fig. 8.54b) arranged with tilts in such a way that the high-frequency components are retarded and exit the compressor at the same time as the low-frequency components which entered in the trailing end of the incoming stretched pulse. The situation resembles the conditions in a race between two skaters on a race track, where the “injustice” created in the first lap with one skater taking the inner, shorter course is compensated by interchanging the courses for the second lap, forcing the favoured contestant to now take the longer course.

An illustration of the construction of a multi-terawatt system is given in Fig. 8.55. A 100 fs oscillator pulse, generated in a Ti:S mode-locked laser, is stretched by a factor of 2500 and is injected into a *regen(erative) amplifier*, where it is trapped bouncing back and forth in a resonator containing a Ti:S amplifier crystal. After 12 passes and an amplification of 10^6 the pulse is ejected from the regen. The switching in and out of the cavity is accomplished by a combination of polarizers and a Pockels cell inside the cavity, which switch the plane of linear polarization of the pulse at the proper times. Further boosting of the energy (now about 10 mJ) is achieved in one or more multi-pass Ti:S amplifiers, which like the regen is pumped by frequency-doubled Nd:YAG radiation (532 nm). After compression several TW of peak power is available from systems of this kind.

If a Fourier-limited pulse is amplified, the original pulse length can be obtained after stretching, amplification and compression, provided that all

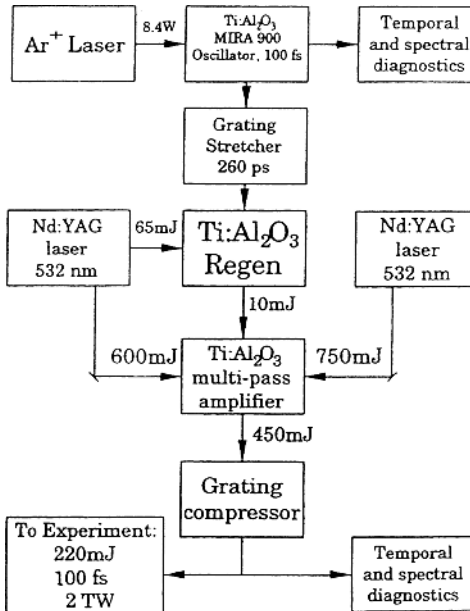


Fig. 8.55. Schematics of a high-repetition-rate terawatt laser system based on chirped pulse amplification [8.161, 8.124]

frequency components of the pulse are handled with the same efficiency in the process. Otherwise, pulse prolongation will occur as well as the formation of a pedestal of intensity surrounding the main pulse. Even if the intensity level is 10^6 times lower in the pedestal, the power may still be enough to ionize the target before the arrival of the main pulse, which is supposed to provide an instantaneous ultra-intense interaction with an unperturbed target.

Chirped-pulse amplification Ti:S systems with a repetition rate of 10 Hz allow convenient high-power laser/matter interaction experiments on normal laboratory scales. Such experiments are discussed in Sect. 9.6. Systems with 10 Hz repetition rate, 30 fs pulse duration and tens of TW output powers are available. In CPA systems using large Nd:glass final amplifiers even PW (1 PW = 10^{15} W) power levels have been reached at very low repetition rates. In order to achieve short pulses and high contrasts, the group-velocity dispersion must be compensated to a high precision (to high orders in the mathematical expansion of the dispersion) [8.162–8.165]. The build-up of a large accumulated optical phase shift (the so called B-integral)

$$\phi_{\text{nonlinear}} = \int (2\pi/\lambda) n_2 I(l) dl \quad (8.21)$$

in the most intense parts of the beam due to the nonlinear index of refraction n_2 (see (8.20)) in optical components and also in air, must also be avoided. This necessitates air evacuation in the compressor area and in the

subsequent beam-transport tubes of high-power systems in order to avoid distortions of the optical pulses. Higher repetition rate CPA lasers operating at 1 kHz or slightly higher and with sub-TW powers can also be constructed. The 1 kHz pump lasers are then normally Nd:YLF units pumped by CW discharge lamps.

9. Laser Spectroscopy

The wide applicability of lasers in spectroscopy is due to several factors. As we have seen, very high intensities can be obtained in a small frequency interval. The favourable spatial properties of laser beams with the possibility of very good focusing is also of great importance. With the advent of tunable lasers, completely new types of experiments have become possible and investigations that were only barely possible with conventional light sources can now be readily performed. It is fair to state that tunable lasers have revolutionized optical spectroscopy. Several monographs and review articles on laser spectroscopy have been published [9.1–9.22]. A wealth of material is presented in the proceedings of International Laser Spectroscopy Conferences [9.23–9.36].

9.1 Basic Principles

9.1.1 Comparison Between Conventional Light Sources and Lasers

A comparison is made in Table 9.1 between a conventional line light source and a continuous single-mode dye laser, with representative data for both sources. In many spectroscopic experiments a decisive factor is by what power per unit area and spectral interval a sample can be irradiated. The designation $I(\nu)$ is used for this power density/frequency unit. In the comparison in Table 9.1 the value of $I(\nu)$ is 10^9 times higher for the laser. With a pulsed laser $I(\nu)$ may be increased by many more orders of magnitude.

9.1.2 Saturation

A very high population in short-lived excited states can be obtained using the high values of $I(\nu)$ that are available with lasers. For a two-level system (Sect. 4.1) with populations N_1 and N_2 in the lower and upper states, respectively, we obtain using (4.21) and (4.22)

$$\frac{N_2}{N_1 + N_2} = \frac{1/2}{1 + A/2B\rho(\nu)} . \quad (9.1)$$

For $B\rho(\nu) \gg A$ we have

Table 9.1. Comparison between a conventional light source (RF discharge lamp) and a single-mode dye laser

| | Conventional line source (RF discharge lamp) | Continuous single-mode dye laser |
|-------------------------------------------|----------------------------------------------------|-------------------------------------------------|
| Linewidth | 1000 MHz | 1 MHz |
| Total output of line | 10^{-1} W | 10^{-1} W |
| Power within a useful solid angle | 10^{-2} W | 10^{-1} W |
| Irradiated area (depends on focusing) | 10 cm^2 | 10^{-4} cm^2 |
| $I(\nu)$ power density per unit frequency | $10^{-6} \text{ W}/(\text{cm}^2 \cdot \text{MHz})$ | $10^3 \text{ W}/(\text{cm}^2 \cdot \text{MHz})$ |

$$\frac{N_2}{N_1 + N_2} \approx \frac{1}{2}, \quad (9.2)$$

i.e., half the number of atoms are found in the excited state and half in the lower state. This situation is called *saturation*. (If statistical weights ($g = 2J+1$) are taken into account, the expression $g_2/(g_1+g_2)$ is obtained instead of $1/2$.) We will now calculate which values of $I(\nu)$ are required to achieve this situation. $I(\nu)$ is related to the energy density $\rho(\nu)$ through

$$I(\nu) = c\rho(\nu). \quad (9.3)$$

Using this equation and (4.27) we find the following condition for saturation at a chosen wavelength of 600 nm:

$$\begin{aligned} I(\nu) \gg c \frac{A}{B} = 16\pi^2 \frac{\hbar c}{\lambda^3} &= \frac{16 \cdot 3.14^2 \cdot 1.05 \times 10^{-34} \cdot 3 \times 10^8}{6^3 \times 10^{-21}} \\ &= 2 \times 10^{-5} \frac{\text{W}}{\text{m}^2 \cdot \text{Hz}} = 2 \times 10^{-3} \frac{\text{W}}{\text{cm}^2 \cdot \text{MHz}}. \end{aligned} \quad (9.4)$$

Thus, a laser power of the order of $\text{mW}/(\text{cm}^2 \cdot \text{MHz})$ is needed to achieve saturation. This condition is easily met, even with a continuous laser.

The first excited ${}^2P_{1/2}$ state of the sodium atom ($3p$) can only decay back to the ${}^3S_{1/2}$ ground state (the D_1 line). The natural radiative lifetime of the $3p$ ${}^2P_{1/2}$ state is 16 ns. At saturation $(1/2)(1/16 \times 10^{-9}) \simeq 3 \times 10^7$ scattered fluorescence photons per second are obtained. This means that it is in principle possible to “see” individual atoms (Sect. 9.8.3).

Two types of laser spectroscopy can be distinguished. In the first kind, the laser is adjusted to the desired wavelength. The experiment is then performed at this fixed wavelength, either by pulsing the light, or influencing the atoms or molecules in other ways. In this kind of measurement good frequency stability of the laser is desirable. In the second type of spectroscopic experiment, the laser wavelength is varied continuously. Most frequently, single-

mode operation is required. A continuous sweep without mode hopping must then be achieved.

9.1.3 Excitation Methods

Several different excitation schemes can be used in laser spectroscopy. This is illustrated in Fig. 9.1 for the case of alkali atoms.

Single-Step Excitation. Atoms are transferred directly from the ground state to the excited state using an allowed electric dipole transition. This means an S-P transition for an alkali atom.

Multi-Step Excitation. Since tunable lasers have high output powers enabling the saturation of optical transitions, stepwise excitation via short-lived intermediate states is possible. A two-step process has been indicated in the figure. For an alkali atom this may mean *S-P-D* transitions. Stepwise excitations give access to states that cannot normally be reached.

Multi-Photon Absorption. At high laser powers higher-order optical absorption processes become non-negligible. Thus, it becomes possible for an atom to simultaneously absorb two photons, thus bridging energy differences between two states without utilizing real intermediate states. The theory of two-photon absorption processes was presented by M. Goeppert-Mayer as early as 1931, but only in 1961 could such transitions be observed with lasers. The transition probability R_{gf} from the ground state g to the final state f can be expressed in matrix elements of the electric dipole operator $e\vec{r}$ involving non-resonant intermediate states i :

$$R_{gf} \propto \sum_i \left| \frac{\langle g | e\vec{r} | i \rangle \langle i | e\vec{r} | f \rangle}{\delta E_i} \right|^2 P^2, \quad (9.5)$$

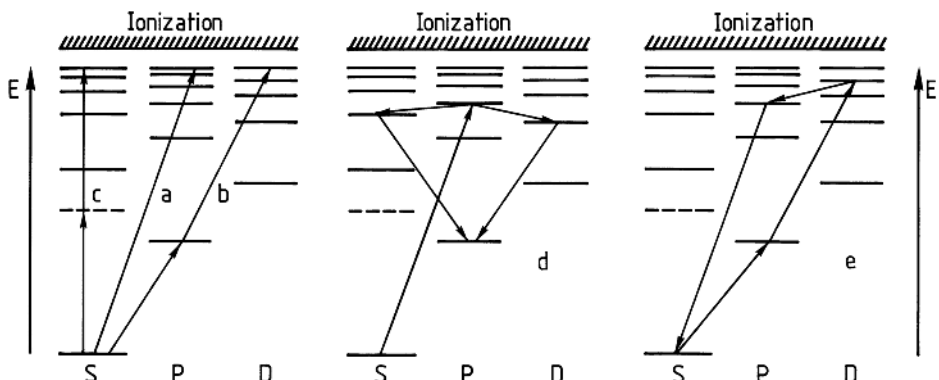


Fig. 9.1. Different schemes for excitation of an alkali atom including (a) single-step, (b) two-step, (c) two-photon, and (d, e) cascade excitation

where the summation is performed over all allowed intermediate states i . δE_i is the energy difference between the virtual and the real intermediate states i , and P is the laser power. Frequently, a single real state close to the virtual state dominates the expression. A quadratic laser power dependence is obtained. The two-photon absorption method connects states of the same parity. An S - S transition is indicated in the figure. Similarly, more than two photons can be absorbed simultaneously. For example, molecules can be made to absorb tens of IR photons in this way. Experiments of this kind will be further discussed in Sects. 9.7.3 and 10.4.2.

In the cascade decay of a laser-excited state, lower-lying states are populated as illustrated in the figure for the case of alkali atoms. This provides further possibilities for laser spectroscopy investigations.

9.1.4 Detection Methods

There are several methods of detecting whether an excited state has been populated. This is particularly true for highly excited states, i.e. *Rydberg states*, that have been the object of many laser spectroscopy investigations. Rydberg atoms are essentially hydrogen-like and some of their properties are given in Table 9.2. The spectroscopy of Rydberg states has been discussed in [9.37–9.43].

Considering these properties we will now discuss a number of detection methods.

Table 9.2. Properties of Rydberg atoms [9.1] (R : Rydberg constant, a_0 : Bohr radius, n : principal quantum number)

| Quantity | n dependence | Numerical examples for | |
|------------------------------------------------------------|------------------------------------------|---------------------------------------|-----------------------------|
| | | Na(10d) | H($n = 50$) |
| Binding energy | $-Rn^{-2}$ | 0.14 eV | 0.027 eV |
| Orbital radius | $a_0 n^2$ | $147a_0$ | $2500a_0$ |
| Geometrical cross-section | $\pi a_0^2 n^4$ | $7 \times 10^4 a_0^2$ | $6 \times 10^6 a_0^2$ |
| Dipole moment | $\propto n^2$ | $143a_0$ | |
| Polarizability | $\propto n^7$ | $210 \text{ kHz V}^{-2} \text{ cm}^2$ | |
| Radiative lifetime | $\propto n^3$ | 10^{-6} s | 10^{-3} s |
| Stark splitting in electric field $E = 1 \text{ kV/cm}$ | $\Delta w \propto n(n-1)E$ | $\sim 15 \text{ cm}^{-1}$ | $\sim 10^2 \text{ cm}^{-1}$ |
| Critical field strength E_c for field ionization | $E_c = \pi \epsilon_0 R^2 e^{-3} n^{-4}$ | $3 \times 10^6 \text{ V/m}$ | $5 \times 10^3 \text{ V/m}$ |

Fluorescence. The most direct way of detecting whether an atom has been excited to an upper state is to detect the fluorescence light released when the atom decays. The atom can return to the state from which it was excited via an allowed electric dipole transition. With increasing excitation energy the number of possible decay paths increases corresponding to many spectral lines. Since the detection must frequently be limited to a narrow wavelength band, only a small fraction of the decays will be observed. Further, the lifetime increases as n^3 . If pulsed excitation is used the detection temporal interval must be successively increased in order to be able to detect a reasonable fraction of the photons. This leads to an increase in the background signal. These factors make fluorescence detection of highly excited states less and less attractive as n increases.

Photoionization. An excited atom can be photoionized by absorbing a further photon of sufficient energy to bring the atom above the ionization limit. One way of detecting the excited atom is to detect the released electron with an electron multiplier, which is essentially a photomultiplier tube without a photocathode. For highly excited states an IR photon, e.g., from a CO₂ laser, can be used (– 0.1 eV). If a laser of sufficiently high power is used for the excitation process, ionization can occur using another photon from the laser beam. The cross-section for photoionization is low but is strongly enhanced in the presence of resonant auto-ionizing states above the ionization limit.

It is also possible to perform mass or energy analysis of the ions generated. This can be accomplished using a *time-of-flight* (TOF) spectrometer, where the ions generated are sent through an evacuated drift tube equipped with ion optics, and the arrival time at an ion detector (electron multiplier tube or a channeltron) is recorded. It is also possible to accelerate low-velocity ions in a well-defined electric field before the passage of the drift tube. Since the velocity attained depends on the mass, species identification can be performed. TOF spectrometers are discussed in [9.44].

Collisional Ionization. Highly excited atoms have a high probability of colliding because of their considerable size. Since the thermal energy of the atom ($\sim kT$) may be larger than the energy required to reach the ionization limit, there is a significant probability that a collision results in the formation of an ion. A *thermo-ionic detector* can be used to detect the presence of the ions. This technique is extremely sensitive [9.45, 9.46].

Field Ionization. Highly excited atoms are very sensitive to electrical fields. Field ionization (Sect. 2.5.2) can be brought about by populating a well-defined highly excited state using stepwise, pulsed excitation in the absence of an electric field and then applying an electric field pulse [9.47]. The electrons can be detected with a suitably located electron multiplier.

Ionization detection is further illustrated in Sect. 9.2.6.

9.1.5 Laser Wavelength Setting

Before discussing different types of laser spectroscopy experiments, we will consider the question of how the frequency of the laser is made to coincide with the absorption frequency of the atoms or molecules of interest. The problem is not at all trivial considering the sharpness of both the laser and the absorption lines, and the mode structure of both laser resonators and intracavity etalons. A high-resolution grating monochromator can be used but it is considerably more convenient to use digital laser wavelength meters. In Fig. 9.2 two systems are shown. Figure 9.2a shows a wavelength meter for continuous single-mode lasers, and Fig. 9.2b shows a system that can also operate with a pulsed laser beam.

The wavelength meter for continuous light is essentially a double Michelson interferometer (Sect. 6.2.4) in which the light from the “unknown” laser and the light from a reference laser are directed in counter-propagating paths [9.48, 9.49]. The movable mirror is a retroreflector (“corner cube”; Sect. 6.2.1) which is self-adjusting with regard to the beam direction. It can be mounted on a carriage which moves on a frictionless air track. Interference fringes from each laser are recorded at different detectors during a certain time. The optical path difference Δ can be expressed in two ways:

$$\Delta = N_\ell \lambda_\ell = N_{\text{ref}} \lambda_{\text{ref}}, \text{ i.e., } \lambda_\ell = \frac{N_{\text{ref}}}{N_\ell} \lambda_{\text{ref}}, \quad (9.6)$$

where N_{ref} and N_ℓ are the numbers of counted interference fringes for the reference laser and the unknown laser, respectively. Since the laser beams overlap in the instrument, the method is quite insensitive to air turbulence, etc. Normally, a single-mode He–Ne laser is used as the reference source. If this laser is stabilized at a saturation dip (Sect. 9.7.2), very high accuracy and stability can be obtained. It is practical to stop the fringe counting in the electronic unit when N_ℓ equals the stored digital number for the wavelength of the He–Ne laser. Then the corresponding number N_{ref} can be directly displayed as λ_ℓ , see (9.6). Since only whole fringes can be electronically counted, the accuracy can be considerably increased if the fringe counting frequency is multiplied by a factor (i.e., 10) using a *Phase-Locked Loop* (PLL).

A wavelength meter that also works for pulsed laser light employs a small spectrometer and Fabry–Pérot interferometers with different free spectral ranges [9.50]. The image plane of the spectrometer and the ring systems of the interferometers are detected by diode arrays (Sect. 6.3). Since the laser light is intense, no amplification is needed, in contrast to the case of an OMA (Sect. 6.3). The information is handled by a microprocessor which calculates the wavelength. A He–Ne laser can be used as a reference. However, if the free spectral ranges of the interferometers are constant and well known a reference laser is not needed for moderate accuracies. Several other techniques for accurate laser wavelength determination have been developed [9.51–9.53]. The accuracy of laser wavemeters has been discussed in [9.54]. Wavemeters of different constructions are now commercially available.

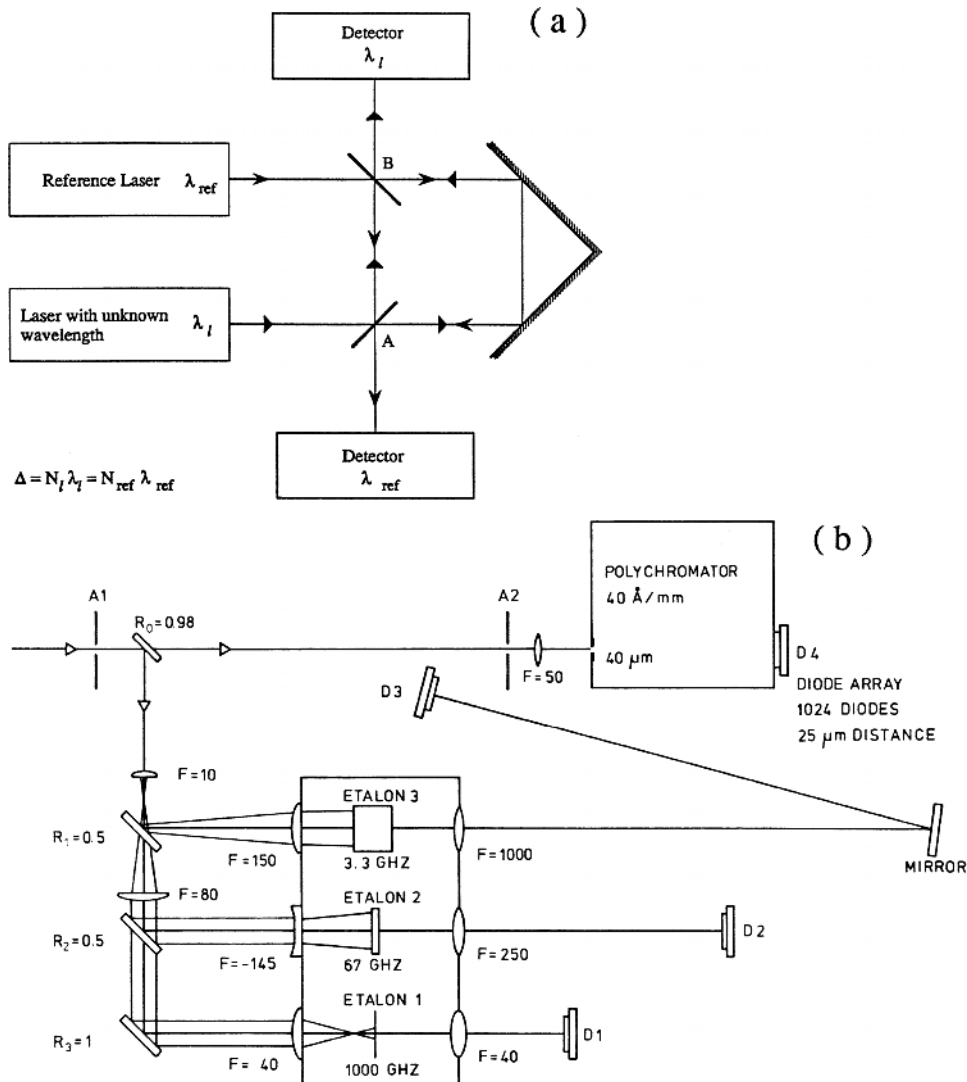


Fig. 9.2. (a) Wavelength meter for continuous lasers [9.48]. (b) Wavelength meter for pulsed or continuous lasers [9.50]

In spectroscopy using continuous laser tuning it is very important to be able to monitor the change in wavelength. For this purpose, a stable multi-pass interferometer (Sect. 6.2.3) can be used, from which the fringes are recorded together with the spectrum [9.55].

We will now consider different laser spectroscopy methods. We will first discuss techniques in which a reasonable resolution is sufficient and where relatively broadband lasers (0.01–0.001 nm) and Doppler-broadened samples

are used. We will then describe how resonance techniques can be combined with laser excitation. In the following sections, time-resolved spectroscopy will be considered. Lifetime measurements and structure determinations using such techniques will be described. In this context a comprehensive survey of methods for determining the radiative properties of atoms and molecules is made.

Extremely high laser intensities can be achieved with the pulsed systems discussed in Sect. 8.7.2. Experiments using such systems are surveyed in Sect. 9.6. A further aspect of the extreme performance achievable with laser techniques is the ultra-narrow bandwidth achievable in CW single-mode laser systems as discussed in Sect. 8.5.1. In order to benefit from this, the Doppler broadening must be eliminated. The different techniques of Doppler-free laser spectroscopy are discussed in Sect. 9.7. Finally, the ultimate resolution achievable by laser cooling and trapping techniques is discussed in Sect. 9.8.

9.2 Doppler-Limited Techniques

In this section we discuss measurement techniques in which Doppler broadening, caused by the thermal movements of the atoms or molecules, limits the achievable resolution. Lasers with a comparatively large linewidth (0.01–0.001 nm) are therefore normally employed. Experiments within this category are aimed at the determination of primary energy-level structure without regard to finer details, such as hyperfine structure. Several important analytical applications are also discussed.

9.2.1 Absorption Measurements

A tunable laser is very useful for measuring the absorption of a sample as a function of the wavelength as shown in Fig. 9.3a. In this case the laser replaces the normal light source as well as the monochromator in a spectrophotometer (Sect. 6.5.6). Because of the good geometrical properties of the laser beam it is possible to work with small samples or with long absorption paths and low concentrations. Dual-beam techniques are generally employed. With continuous lasers, lock-in techniques are used for recording. When pulsed lasers are used gated integrators (boxcar integrators; see Sect. 9.4.2) are employed. Sample and reference signals are divided for normalizing purposes. In Fig. 9.3b, a commercial diode spectrometer for the IR region is shown. In this particular case, a grating monochromator has been included to suppress unwanted laser modes.

If gaseous samples of low concentration are to be investigated a *White cell* can be used [9.56, 9.57]. This is a multi-pass device in which a well-defined beam path is obtained by repeated focusing using spherical mirrors of suitable curvature. The number of passes can easily be chosen by adjusting

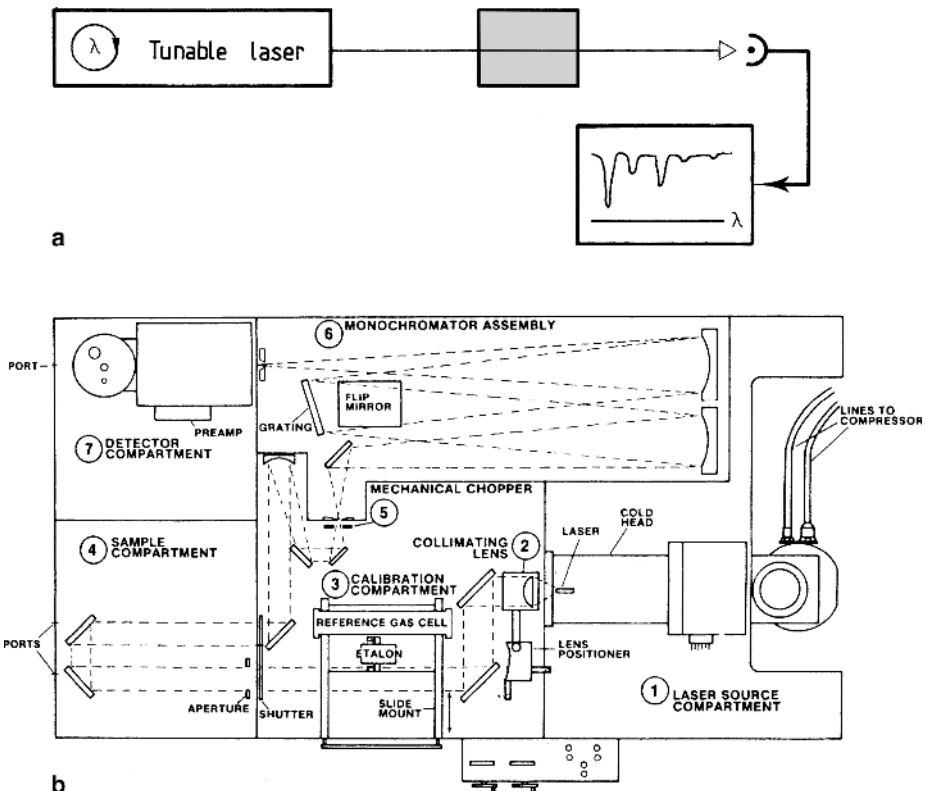


Fig. 9.3. (a) Principle of laser absorption spectroscopy. (b) A diode laser spectrometer (Courtesy: Spectra Physics)

the mirrors: 50–100 double passes can be achieved. The transmitted intensity is largely determined by the mirror reflectivities. For absorption experiments on metal atoms, for which a high temperature is required to obtain a sufficient vapour pressure (Fig. 7.2), a *heat-pipe oven* can be used [9.58, 9.59]. This consists of an evacuated metal tube, in which the central inner part is covered by a fine metal mesh. The metal is placed in the centre of the tube and a few torrs of inert gas are frequently added. The central part of the tube is resistively heated while the end parts, with optical windows, are water-cooled. A micro-climate develops in the tube and metal atoms evaporate out into the cold zones, where condensation occurs. The liquid metal is then sucked back towards the centre by surface-tension forces between the metal atoms and the mesh. The gas is fractionated so that the inner zone contains metal atoms while the windows are protected against deposits, due to metal evaporation, by the inert gas in front of them. Different aspects of laser absorption spectroscopy have been discussed in [9.60].

9.2.2 Intracavity Absorption Measurements

In the absorption measurements described above an external laser beam was used. A great increase in sensitivity can be achieved if the sample is placed inside the laser cavity [9.61–9.64]. This is due to the mode competition in a multi-mode laser. The principle of intracavity absorption measurements is given in Fig. 9.4.

A multi-mode dye laser is run in the wavelength region where the species under investigation absorbs. As an example we will consider the case of molecular iodine (I_2). If the intracavity cell is first taken out and the laser is adjusted to the desired wavelength region, laser-induced fluorescence will be observed in an external iodine cell. Normally, several molecular transitions are induced. If the intracavity iodine cell is now introduced, the fluorescence light will disappear or be strongly reduced. The reason is that in the cavity the modes that excited the molecules in the external cell will be greatly reduced in intensity compared with other modes due to the intracavity absorption. Since we have multiple passages through the internal sample and the laser is very sensitive to a small imbalance, very few molecules are needed to strongly influence the fluorescence light in the external cell. The sensitivity when using an intracavity sample is about 10^5 times greater than when an external cell is used.

A related technique, where the mode-competition in a multi-mode laser is, however, not utilized, is *cavity ring-down spectroscopy* [9.65, 9.66]. Here the damping of the laser light inside a cavity (which can also be external to the primary laser), caused by intracavity absorption by the sample is measured by observing the intensity of a small part of the light leaking through one of the cavity mirrors. If a picosecond pulse is bouncing in the cavity, it is particularly simple to observe additional passes through the cavity. If losses apart from the

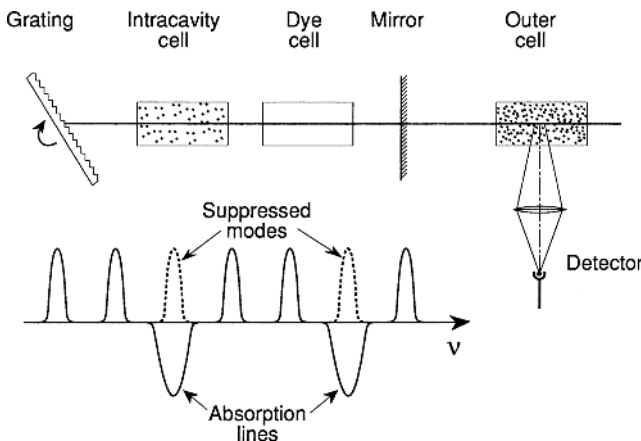


Fig. 9.4. Principle of intracavity absorption measurements

sample absorption can be kept low by using highly reflecting cavity mirrors, very long effective absorption lengths can be achieved. By tuning the laser off the absorption the effects due to the sample can be isolated.

9.2.3 Absorption Measurements on Excited States

Classical absorption measurements with a continuum light source and a photographically recording spectrograph only display absorption lines originating in the ground state or in low-lying, thermally well-populated metastable states. Through the possibility of saturating an optical transition with a laser, thus transferring essentially half the number of atoms into a short-lived

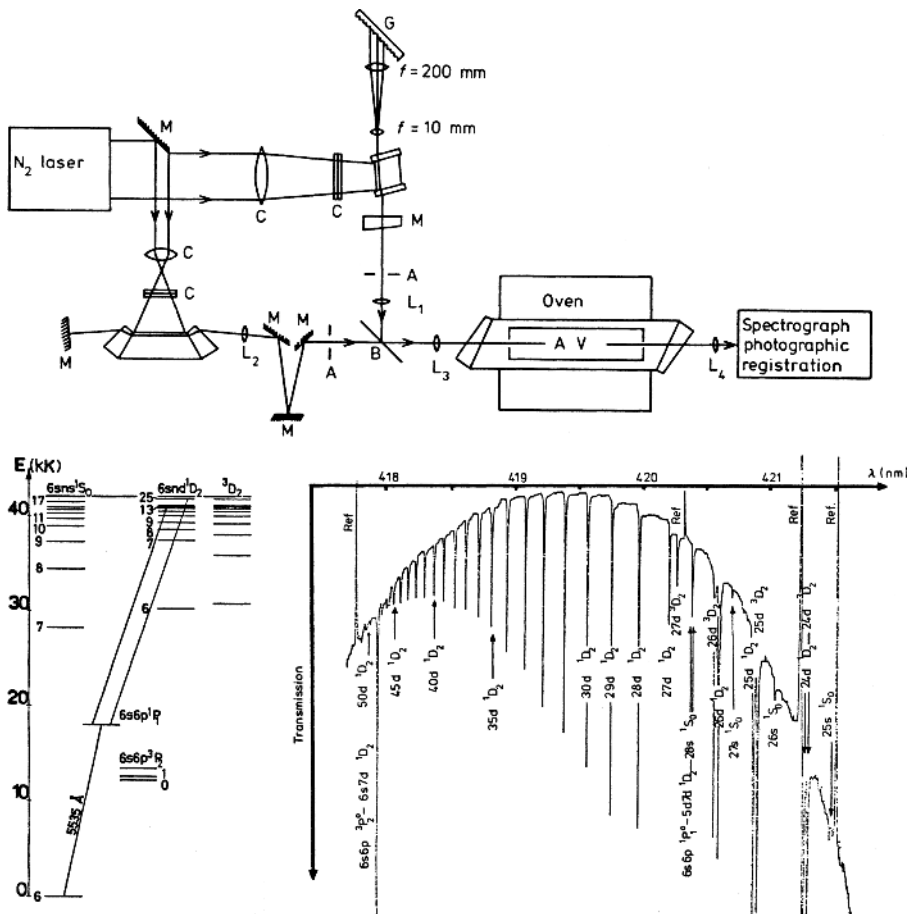


Fig. 9.5. Illustration of absorption spectroscopy from an excited state. A level scheme for Ba, an experimental set-up and a resulting absorption spectrum are shown [9.68]

excited state, it is now possible to extend absorption experiments to spectral series originating in excited states [9.67, 9.68]. In Fig. 9.5 an example for Ba is given. A nitrogen laser is used for synchronous pumping of two dye lasers. One has a narrow bandwidth and is used to saturate the $6s^2 \ ^1S_0 - 6s6p \ ^1P_1$ transition at 5535 Å. The barium vapour is contained in a heat-pipe. The second laser has a normal incidence mirror instead of a Littrow-mounted grating and it yields an intense continuum at the same time as the excited state is populated. As illustrated in the recording, light is absorbed from the continuum at wavelengths corresponding to the $6s6p \ ^1P_1 - 6sns \ ^1S_0$ and $6snd \ ^1D_2$ series. The trace in the figure has been obtained from the photographic plate using a microdensitometer.

9.2.4 Level Labelling

The analysis of molecular spectra is complicated because of the very large number of lines that is obtained simultaneously in normal excitation or absorption experiments. With narrow-band laser excitation an individual excited rotational-vibrational level can be populated selectively and only the decays originating in the excited state are observed. A similar simplification in absorption measurements is very desirable. Through the possibility of saturating optical transitions, a certain lower level can be “labelled” by depleting the population with a laser (*pump* laser). If this laser is switched on and off repetitively, all absorption lines originating in the labelled level will be modulated when induced with a second (*probe*) laser [9.69, 9.70]. A number of schemes for modulation detection are indicated in Fig. 9.6. Several schemes can be used to ascertain that absorption has occurred, as discussed

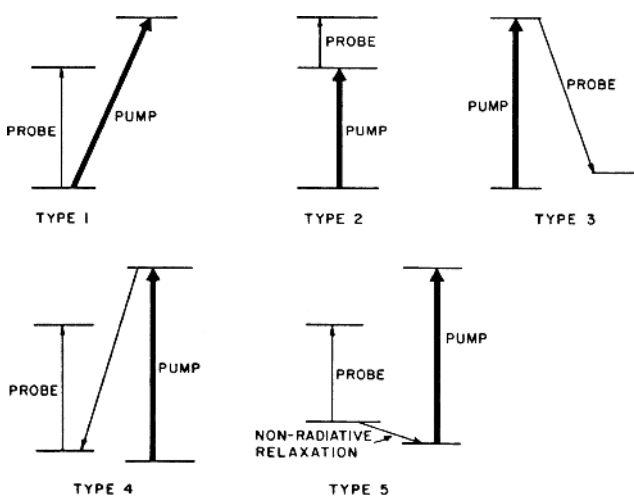


Fig. 9.6. Different schemes for level labelling [9.70]

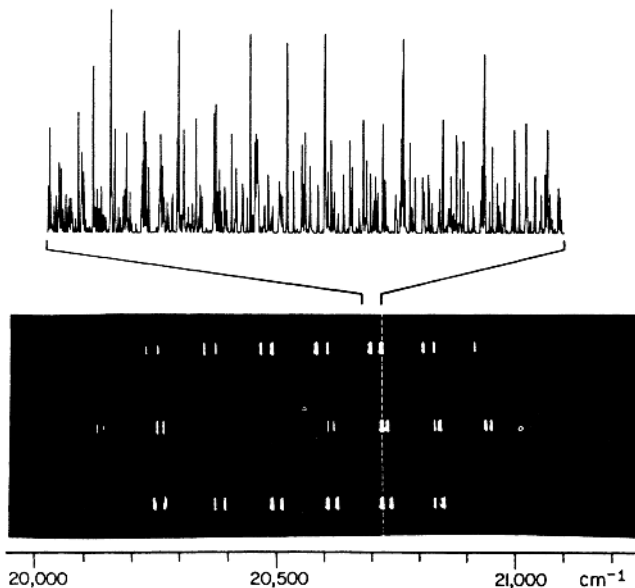


Fig. 9.7. Principles of level polarization labelling. The experimental set-up and a recording for Na_2 molecules displaying $\Delta J = +1$ and $\Delta J = -1$ transitions from the labelled level are shown [9.71]

in Sect. 9.1.4. A still more powerful technique using equipment similar to that described in the preceding section is shown in Fig. 9.7. The probe laser is a broadband laser and normally cannot illuminate the entrance slit of the recording spectrometer since it is blocked by crossed polarizers. The pump laser is circularly polarized and induces an optical anisotropy by molecular orientation of the sample, which is placed between the crossed polarizers [9.71]. For lines coupled to the oriented molecules the plane of polarization is rotated for the probe laser light and the entrance slit is illuminated. On the photographic plate all absorption lines originating in the labelled level give rise to bright lines.

9.2.5 Two-Photon Absorption Measurements

Series of levels of the kind discussed in connection with absorption measurements from excited states (Sect. 9.2.3) can also be investigated in two-photon absorption experiments. Then only a single pulsed dye laser is needed. Amplifier stages may be used to achieve sufficient power (Sect. 8.5.1). When the laser has been tuned to bridge the energy difference between the ground state and an excited state of the same parity by means of two simultaneously absorbed laser photons, this can be detected by using yet another photon to photoionize the excited atoms. The ion current can be detected by electrodes at a low dc voltage inserted into the heat-pipe oven. The ion transients are

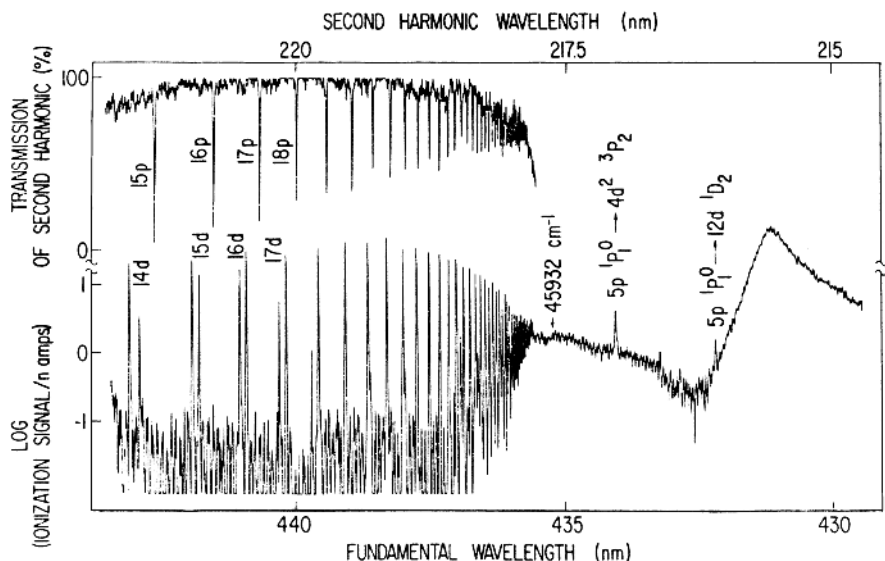
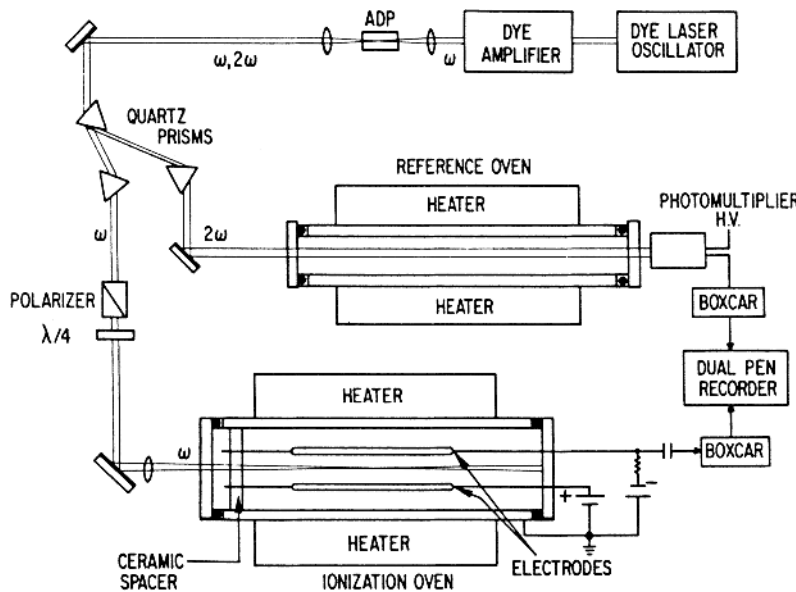


Fig. 9.8. Experimental set-up, ionization recording of two-photon transitions, and absorption recording of single-photon transitions in strontium vapour [9.72]

averaged in a boxcar integrator. In Fig. 9.8 two-photon transitions to $5sns\ ^1S_0$ and $5snd\ ^1D_2$ states in Sr are shown. Simultaneous single-photon absorption detection of $5s^2\ ^1S_0 \rightarrow 5snp\ ^1P_1$ transitions is illustrated using frequency-doubled laser radiation. In the figure the increase in ionization current above

the ionization limit of Sr is shown, as well as a dispersion-shaped broad resonance due to an autoionizing state (*Fano resonance*).

9.2.6 Opto-Galvanic Spectroscopy

In the previous section we described how *optical* resonance could be detected by direct observation of *electrical* phenomena. From this point of view we described a special type of *opto-galvanic* spectroscopy. When electrical detection of optical resonance in connection with measurements on electrical discharges or flames is performed the term *Laser-Enhanced Ionization* (LEI) spectroscopy is frequently used. In Fig. 9.9 opto-galvanic spectroscopy (LEI)

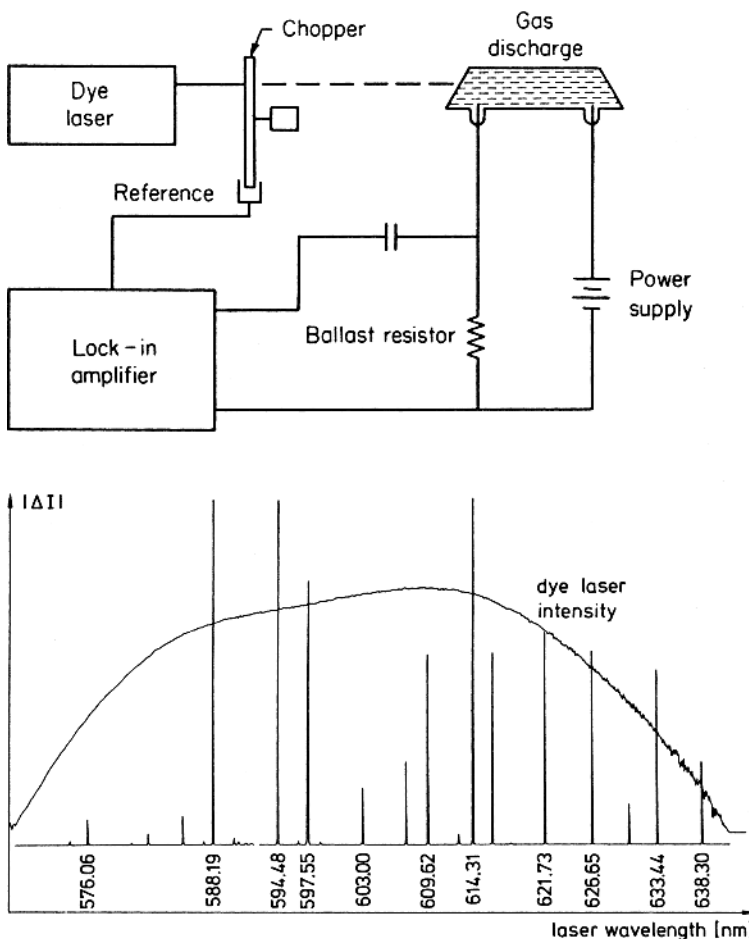


Fig. 9.9. Experimental arrangement for opto-galvanic spectroscopy on a gas discharge [9.73] and a recorded spectrum for a Ne discharge [9.1]

of a gas discharge is illustrated. The laser beam is directed into the discharge and when it is tuned to an optical transition the discharge current is changed, since the probability of collisional ionization is different for high-lying levels compared with low-lying ones. Current changes ΔI can be detected as a voltage change, $\Delta V = R\Delta I$, over a ballast resistor R in the discharge circuit. An opto-galvanic spectrum of a neon discharge is also given in the figure. The technique can conveniently be used for wavelength calibration of a tunable laser. A small part of the laser light is directed into a hollow cathode containing, e.g. thorium or uranium, which both have a large number of lines distributed over the visible and ultraviolet spectral regions [9.74]. A very simple pure electrical method of detection of the reference lines can thus be obtained. Optical resonance in radio-frequency discharges can also be detected electrically by observing an imbalance in the RF circuitry used for the oscillator.

Opto-galvanic spectroscopy of flames has important analytical applications. If an atomic absorption flame (Sect. 6.5.3) is irradiated by a tunable laser, a change in the current between two electrodes, placed in the outer parts of the flame, can be detected. A typical arrangement is shown in Fig. 9.10. A sensitivity exceeding that obtainable in atomic absorption spectroscopy (Sect. 6.5.2) can be achieved for elements seeded into the flame. Two-step excitation improves both sensitivity and background rejection [9.76]. A very high sensitivity can be obtained by evaporating the analytical sample in an electrically heated graphite oven (Sect. 6.5.4) [9.77, 9.78]. In this case laser absorption or fluorescence spectroscopy is frequently used for the detection. Tunable diode lasers are finding important applications in this context and ge-

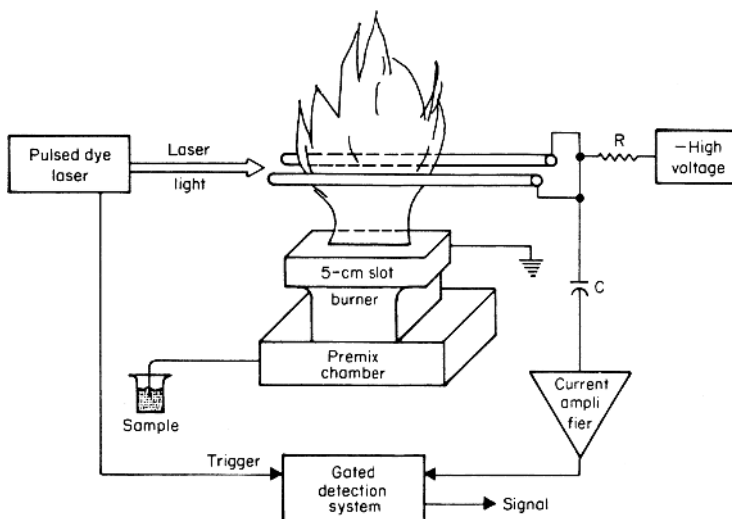


Fig. 9.10. Set-up for opto-galvanic flame spectroscopy [9.75]

nerally in analytical and fundamental spectroscopy [9.79]. The opto-galvanic technique can also be used for studying normal flame constituents such as O, H and OH [9.80].

As we have seen, collisions are important for the signal generation in LEI. In low-pressure experiments photoionization instead is the principal origin of the signal. The term *Resonance Ionization Spectroscopy* (RIS) is then frequently used. Several examples of opto-galvanic detection schemes

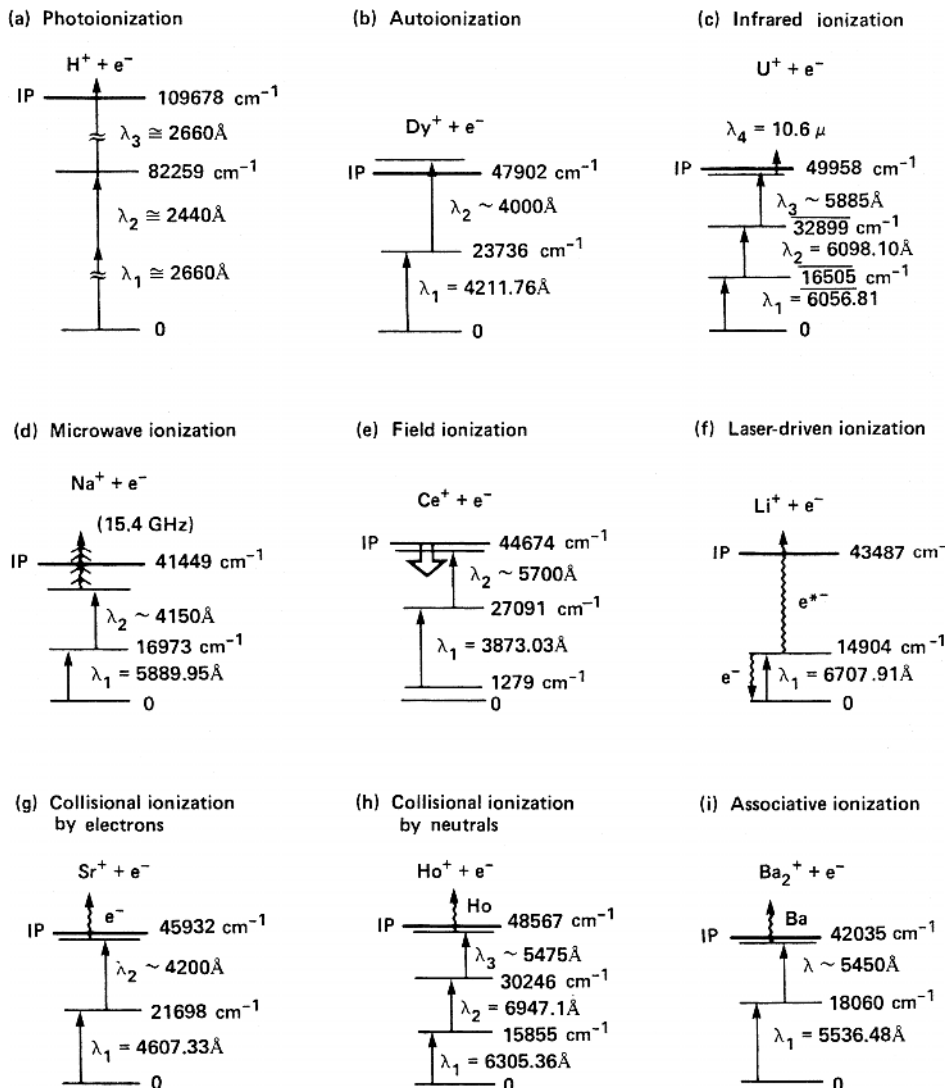


Fig. 9.11. Examples of resonance ionization pathways [9.81]

for different atoms are shown in Fig. 9.11. If multi-photon excitation of the atoms to be studied is used the technique is referred to as REMPI (*REsonance Multi-Photon Ionization*) spectroscopy. The selectivity of RIS and REMPI can be further enhanced by using a mass spectrometer to analyse the produced ions. This technique is referred to as RIMS (*Resonance Ionization Mass Spectroscopy*). The numerous aspects of opto-galvanic spectroscopy are covered in [9.81–9.91].

9.2.7 Single-Atom and Single-Molecule Detection

We have already mentioned that single atoms or ions can, in principle, be detected by the emission of a large number of photons per second at saturation. We will come back to this in Sect. 9.8.4. The resonance ionization techniques discussed in the previous section also have the potential for single-atom detection. The energy density of the laser beams is chosen in such a way that the probability of photoionization of an atom in the beam is unity. The released electron can be detected with 100% probability if the atom is located inside a proportional counter. It has been demonstrated that a single Cs atom in a background of 10^{19} Ar atoms can be detected in this way. Single-atom detection is of great interest, e.g., for studying rare reactions such as those induced by neutrinos from the sun: $^{37}\text{Cl}(\nu, e) ^{37}\text{Ar}$. Other applications include dating of the polar ice caps, studies of ocean mixing by monitoring of atmospherically produced ^{37}Ar , etc. Single-atom detection using resonant photoionization is reviewed in [9.92, 9.93]. Different techniques for ultra-sensitive atomic laser spectroscopy are discussed in [9.94–9.97]. Single-molecule detection has also been achieved using mostly fluorescence detection techniques [9.98]. The ultra-sensitive analytical methods are of great interest, e.g. in molecular biology research [9.99]. The general field of analytical laser spectroscopy is treated in [9.100–9.104].

9.2.8 Opto-Acoustic Spectroscopy

In this section we will describe another non-optical technique for the detection of optical absorption: *opto-acoustic spectroscopy*. The principle of a laser-based opto-acoustic spectrometer (spectrophone) is given in Fig. 9.12. A molecular sample at relatively high pressure is contained in a closed volume and is irradiated with a chopped cw laser beam tuned to resonance. The excited molecules are mainly de-excited radiationlessly at the prevailing pressure. The excitation energy is converted to translational energy upon collision. Thus the pressure rises and falls periodically in the cell. The pressure variations can be detected as a sound wave by a microphone mounted in the cell wall. Weak signals can be detected by lock-in techniques. If the cell is shaped as a resonant cavity for the chopping frequency, a very high sensitivity can be achieved, better than 1 ppb (1 part in 10^9) in the measurement of, for

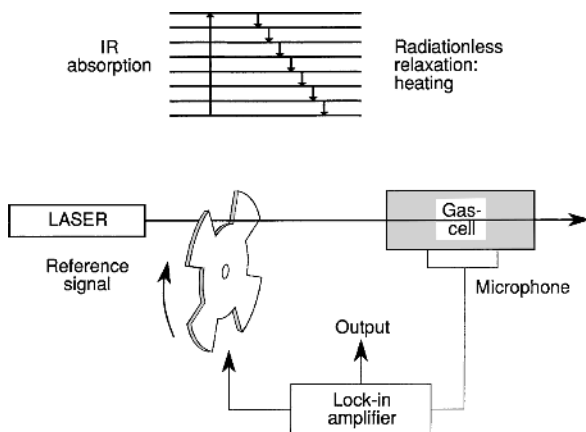


Fig. 9.12. The principle of opto-acoustic spectroscopy [9.105]

example, air pollutants. CO_2 lasers or diode lasers can be used to induce vibrational transitions. Since the detector is only sensitive to the absorbed part of the radiation, very small absorptions can be measured. This is not possible in normal optical absorption measurements, where the difference between two almost equally large quantities is to be measured. Another feature of opto-acoustic spectroscopy is that it is insensitive to stray light. The technique is discussed further in [9.106–9.112].

The absorption of solid or liquid materials can also be measured using these techniques [9.113]. The laser illuminates the sample and the heat variations are coupled to a non-absorbing gas, which is in contact with the microphone. Piezoelectrical detection can also be used with solid or liquid samples. Elastic waves in the material are then detected. In Fig. 9.13 an example of an opto-acoustic spectrum of a powder is given.

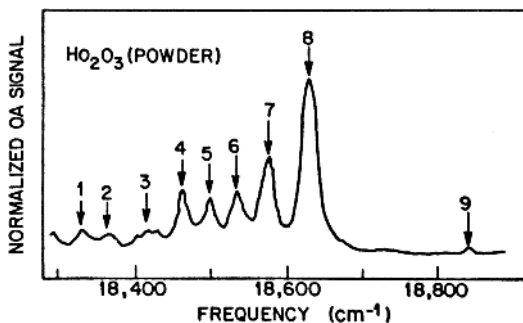


Fig. 9.13. Example of an opto-acoustic spectrum from a solid [9.113]

9.3 Optical Double-Resonance and Level-Crossing Experiments with Laser Excitation

In this section we will deal with experiments in which, similarly to the conditions in the previous sections, Doppler-broadened media and rather broadband lasers are used. In spite of this fact, a resolution is obtained that is only limited by the Heisenberg uncertainty relation. This is due to the fact that the signals are resonant in nature with half-widths limited essentially only by the lifetime of the excited state. Optical double-resonance and level-crossing experiments (Sects. 7.1.4 and 7.1.5) with laser excitation utilize the high intensity of polarized laser light in order to populate levels that are normally not accessible for investigation for intensity reasons. In particular, experiments employing stepwise excitation become possible [9.114]. For the alkali metal atoms, a large number of investigations on fine structure, hyperfine structure and the Stark effect have been performed using such techniques [9.115–9.120]. As an example, the energy-level diagram of Cs is given in Fig. 9.14. Stepwise excitation of S and D levels via the first P -doublet is illustrated in the diagram. At the early stage of development of cw dye lasers

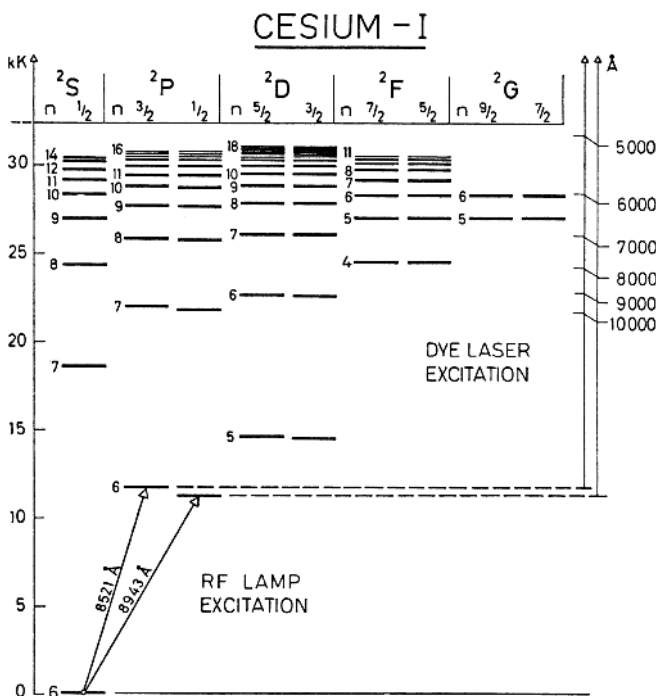


Fig. 9.14. Energy level scheme for Cs. Rf-lamp excitation of the first excited 2P states is indicated and absorption wavelengths for subsequent 2S and 2D state excitation are given [9.117]

only a narrow wavelength region in the yellow and red spectral range was available with Rhodamine dyes. Thus the spectroscopic applicability for such lasers was quite limited. However, if the laser excitation is initiated from the first P state, many highly excited states become accessible for the given spectral range. This is true not only for Cs but also for the other alkali metals. The P states can be weakly populated using the very strong resonance lines (D_1 and D_2) in the alkali atoms. A sealed RF lamp (Sect. 6.1.1) is very suitable for the efficient generation of these lines. At a vapour pressure of 10^{-3} torr strong multiple scattering is obtained in the resonance cell for these lines, and thus the average population of the P levels is increased. Re-emitted photons are reused to bring the atoms into the P state, which has a lifetime of some tens of ns. Still, only about 1 atom in 10^4 is in the P state. The RF lamp cannot, by a long way, saturate the optical transition. A multi-mode dye laser is used to induce the second excitation step. By piezo-electrically vibrating one of the laser mirrors the mode structure can, on average, be washed out and a "white" excitation is obtained. In Fig. 9.15 an experimental arrangement for optical double-resonance and level-crossing spectroscopy is shown.

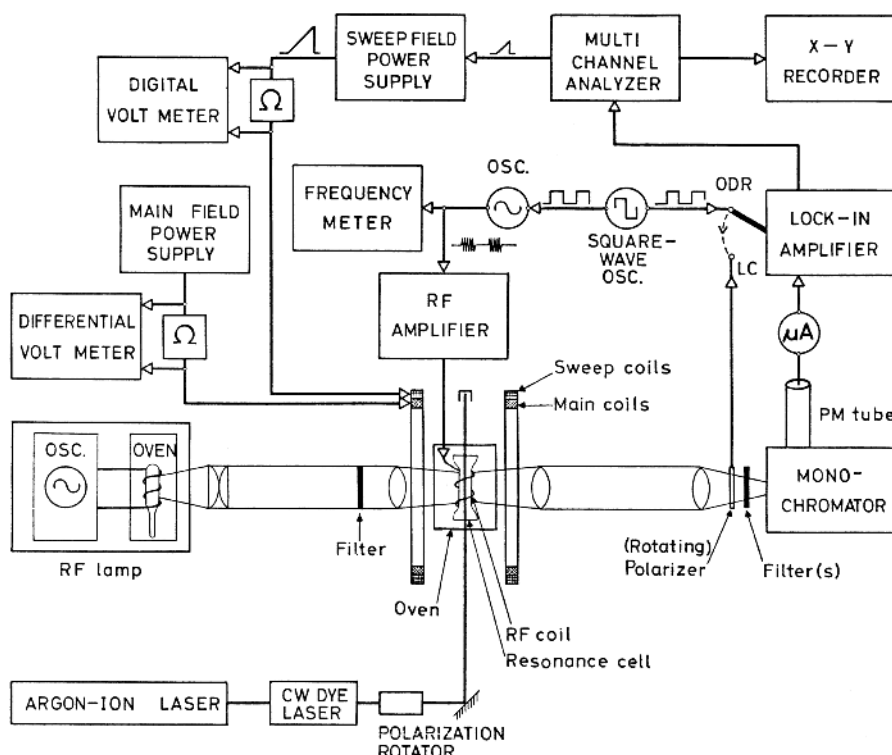


Fig. 9.15. Experimental arrangement for LC and ODR spectroscopy of excited alkali metal atom levels, populated using stepwise excitation [9.116]

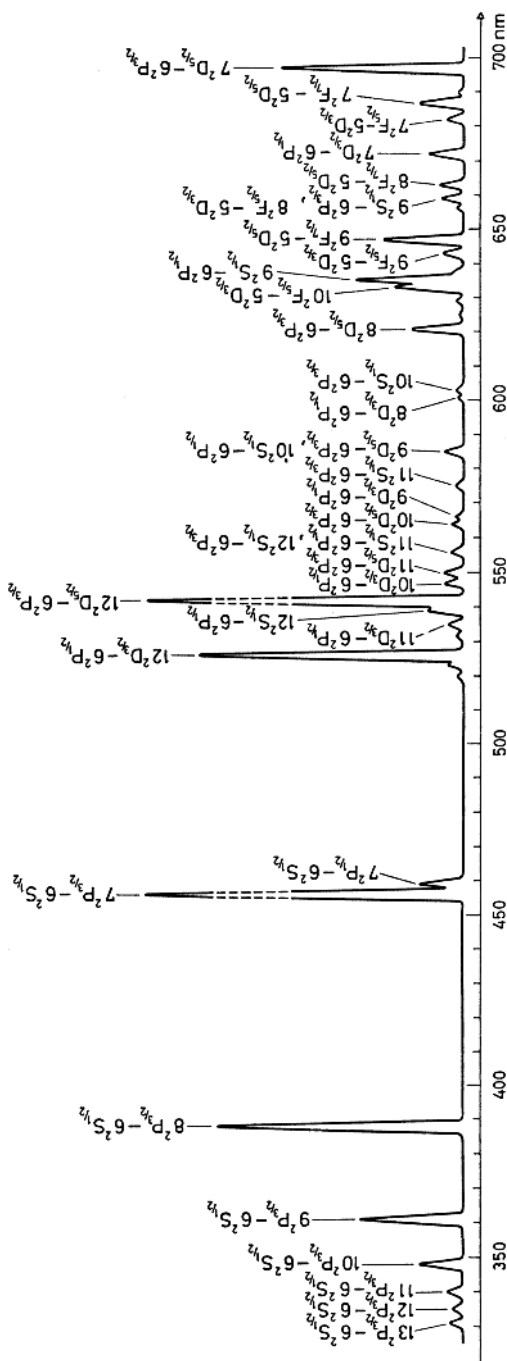


Fig. 9.16. Fluorescence spectrum from Cs atoms following stepwise excitation to the $12^2 D_{5/2}$ state [9.117]

Lock-in detection is used for signal detection and the lock-in signals are further averaged using a multichannel analyser, which has a channel advancement which is synchronized with a repetitive magnetic field sweep. In ODR experiments the RF transmission is pulse-modulated, while LC signals are detected by recording the fluorescent light intensity through a rotating linear polarizer. Normally, circularly polarized light components are obtained in the direction of the magnetic field (Fig. 4.9). The only occasion for which linearly polarized light can be obtained in the direction of the magnetic field is at a coherently excited and coherently decaying level crossing, where the σ^+ and σ^- light is phase-related and results in linearly polarized light. This light is then modulated by the rotating linear polarizer and this modulation is detected by the lock-in amplifier.

In Fig. 9.16 a fluorescence light spectrum for Cs is given as recorded with the apparatus shown in Fig. 9.15. The $12^2D_{5/2}$ state is populated by stepwise excitation. In cascade decays, as illustrated in Fig. 9.1, lower-lying P and F

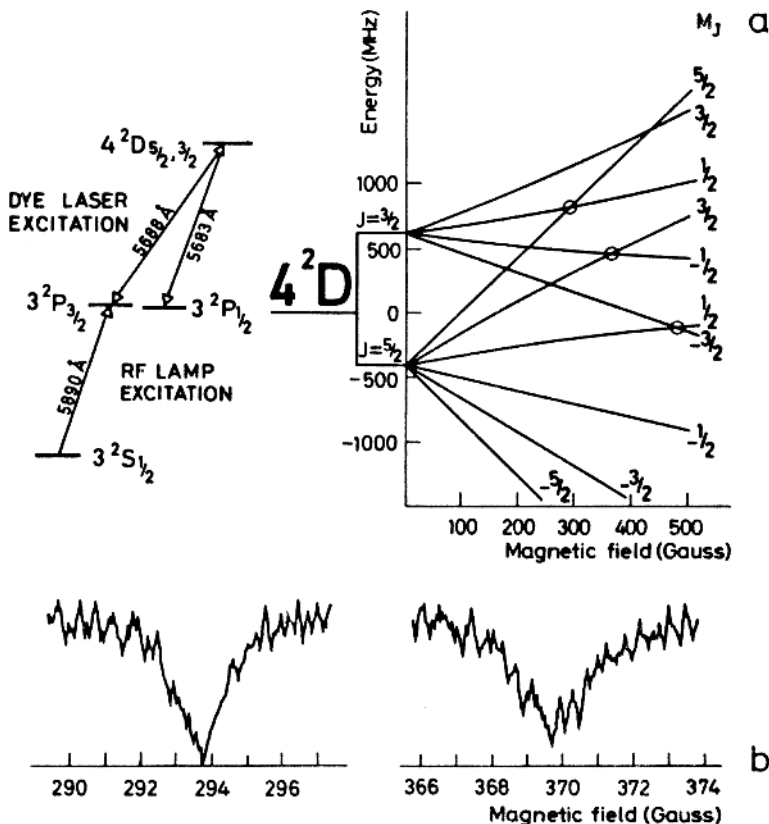


Fig. 9.17. Illustration of fine-structure measurement for an alkali metal D doublet using level-crossing spectroscopy [9.120]

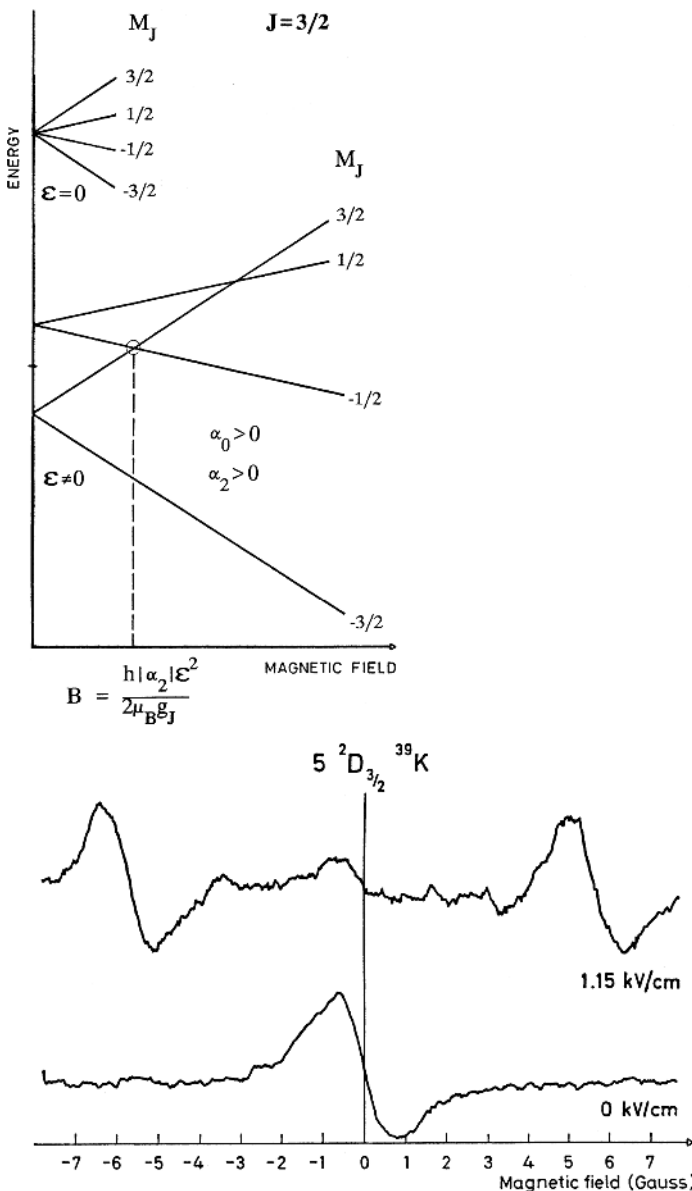


Fig. 9.18. Illustration of the determination of the tensor polarizability of an excited alkali metal D state using level-crossing spectroscopy in parallel electric and magnetic fields [9.115]

levels are populated and fluorescence lines are obtained in the blue and UV, and in the red spectral regions, respectively.

If the primary excitation is performed, e.g., with π light (Fig. 4.9) the magnetic sublevels of the $^2D_{5/2}$ state will be non-uniformly populated. The fluorescence in the different decay lines will then also be linearly polarized. Radio-frequency transitions, that are induced in the primary state or in cascade states, will give rise to a depolarization and redistribution of the light that can be detected. Thus the properties of many P , D and F states can be investigated. Examples of ODR signals in excited S states, populated by stepwise excitation, were given in Fig. 7.11.

In Chap. 7 we have discussed how hyperfine structure can be determined by level-crossing spectroscopy. Clearly, alkali atom 2D states can readily be studied using this technique after stepwise excitation. We will here instead choose an example illustrating fine-structure measurements. In Fig. 9.17 the example of the inverted sodium $4d\ ^2D_{5/2,3/2}$ state is given. From the measured level-crossing positions the fine-structure splitting can be calculated using the Breit–Rabi formula for the fine structure, (2.31).

We will conclude this section by illustrating how the tensor Stark polarizability constant can be measured using level-crossing spectroscopy. As illustrated in Fig. 9.18, for the case of the potassium $5d\ ^2D_{3/2}$ state the unknown Stark effect is measured in terms of the well-known Zeeman effect (g_J is well-defined in LS coupling). In the absence of an external electric field the normal Hanle signal (differentiated) is recorded. If, in addition, a fixed electric field \mathcal{E} is applied over the atoms, a high-field level crossing will be produced when scanning the electric field. The simple relation given in Fig. 9.18 is easily verified from (2.29) and (2.35).

9.4 Time-Resolved Atomic and Molecular Spectroscopy

In this section we study time-resolved laser spectroscopy and generally discuss radiative properties of atoms and molecules and methods of studying these properties. Since very short laser pulses with a power density sufficient to saturate optical transitions can be obtained, a large fraction of the irradiated ground-state atoms can be transferred to the excited state. Using stepwise excitation with synchronized lasers a large number of atoms can be excited into very highly excited states. When the laser pulse ceases, the exponential decay of the excited state can be monitored. Note, that primarily the population number $N(t)$ decays exponentially, i.e.,

$$N(t) = N_0 e^{-t/\tau}. \quad (9.7)$$

This decay can be monitored by observing the decay of the fluorescence light in an arbitrary spectral line originating in the state. For the light intensity $I(t)$ we have

$$I(t) \sim -\frac{dN(t)}{dt} = \frac{N_0}{\tau} e^{-t/\tau} = I_0 e^{-t/\tau}. \quad (9.8)$$

Because of the special properties of the exponential function the light decays with the same time constant τ as the population decay. The light decay can be followed by a fast detector connected to fast, time-resolving electronics. If the excited state has a substructure, e.g., because of the Zeeman effect or hyperfine structure, and an abrupt, coherent excitation is made, oscillations (quantum beats) in the light intensity will be recorded. The oscillation frequencies correspond to the energy level separations and can be used for structure determinations. We will first discuss the generation of short optical pulses and measurement techniques for fast optical transients.

9.4.1 Generation of Short Optical Pulses

Broadband flash-lamps with specially designed driving circuits can be used to produce light pulses, with a pulse length of the order of 1 ns. Synchrotron radiation can be produced as pulses of ~ 0.1 ns duration [9.121]. A suitable spectral region can be filtered out from the broadband distribution using a monochromator and can be used for exciting species with broad absorption bands, i.e., liquids and solids. For free atoms or molecules absorbing in a very narrow spectral region, the high monochromaticity of lasers is normally needed for efficient excitation. In Chap. 8 we described a variety of pulsed lasers with a pulse duration in the 3–20 ns range. The repetition rate of such lasers seldom exceeds a few hundred Hz and is frequently substantially lower (e.g., 10 Hz). Pulses at a higher repetition rate can be obtained by modulating a cw laser beam by means of a Pockels cell or a Bragg diffraction cell (acousto-optic modulation). In the latter device, an RF oscillator coupled to a piezoelectric transducer induces density variations in a crystal causing a deflection of the beam into an aperture because of grating diffraction. While a rise time below 10 ns can be achieved in this way the peak power of the pulses is, by necessity, minute. A much more efficient way of producing laser pulses of short duration and high peak power is by *mode-locking*, as discussed in Sect. 8.7.1.

9.4.2 Measurement Techniques for Optical Transients

In this subsection we discuss techniques for recording a decaying optical signal on a timescale exceeding 0.1 ns, where fast photomultiplier tubes can still be used. The corresponding electrical signal can be handled in different ways, which can conveniently be discussed with reference to Fig. 9.19.

Transient-Digitizer Technique. The most direct way of capturing the transient signal from the photomultiplier tube is to use a normal fast oscilloscope and take a photograph of the screen with open camera shutter while the electron beam, which is triggered by the laser, sweeps the screen drawing the decay curve. Clearly, it is inconvenient to further process data

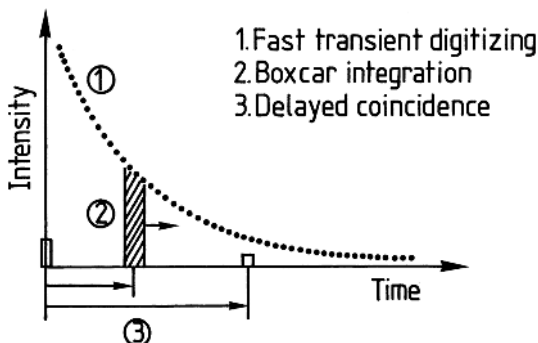


Fig. 9.19. Illustration of methods to measure optical transients

stored as photographs. A *transient digitizer* instead captures the transient digitally by successively recording the input voltage at given time intervals, e.g., 10 ns, and generating numbers that are proportional to the input voltage. The whole sequence of numbers is stored digitally and the memory can then be read out repetitively as an analogue signal at a low rate. Thus a permanent oscilloscope trace of high brightness is obtained. Alternatively, the sequence of numbers can be transferred to a computer and an arbitrary number of individual transients can then be averaged. This method of measurement is very efficient since all the signal information from each transient is captured. A time resolution of less than 1 ns can be obtained. As a result of the digitization, the data can easily be processed further.

Examples of atomic excited-state decay curves recorded with the transient digitizer technique for a sequence of states in sulphur are shown in Fig. 9.20. The lifetimes increase with a $\tau \propto n^3$ trend as expected for a Rydberg sequence (Table 9.2). Sulphur and a number of other elements evaporate as molecules, making normally employed thermal atomization techniques (Fig. 7.2) less suitable. A laser-produced plasma source, where pulses of few tens of mJ from a Q-switched laser impinge on a sample of a sulphur compound kept in a vacuum chamber is then very convenient. Other advantages are the ease with which refractory elements are vaporized and singly and doubly ionized atoms are formed. Through the laser ablation a rapidly expanding (several km/s) plume consisting of atoms and also ions is formed, and this dynamic target can be studied by firing the spectroscopic laser after an appropriate delay to ensure unperturbed conditions and correct lifetime determinations. Figure 9.21 shows a time-expanded recording related to Fig. 9.20, where the light emission from the recombining plasma is first observed. Then, after a delay of about 10 μ s the spectroscopic laser tuned to 126 nm for exciting the $7s\ ^3S_1$ state is fired and the subsequent laser-induced fluorescence is observed as a spike. This signal, on a higher resolution timescale, is included in Fig. 9.20. In the example discussed the sulphur sample was in the form of a lead sulphide powder. It was placed in a container which was shaken

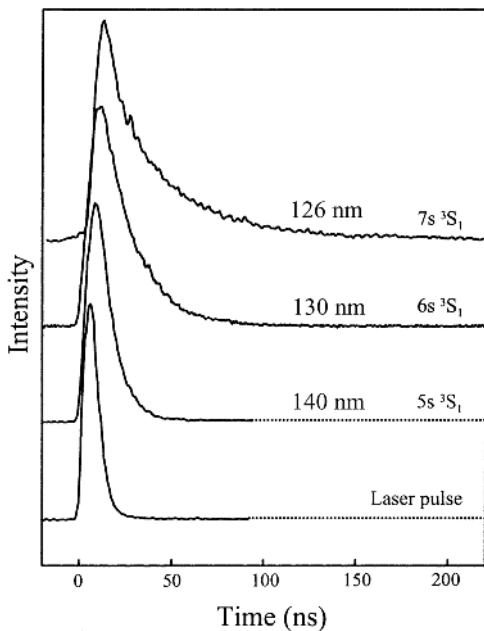


Fig. 9.20. Time-resolved laser-induced fluorescence recordings in a sequence of sulphur, employing the transient digitizer technique [9.122]

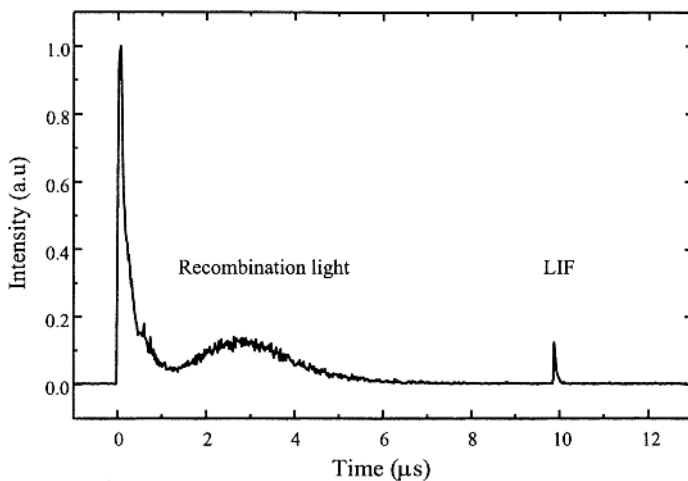


Fig. 9.21. Time-resolved recording of the light emission following laser-ablation from a sulphur target. The spike at $10\text{ }\mu\text{s}$ is the laser-induced fluorescence from the $7s\ ^3S_1$ state [9.122]

to re-prepare the surface [9.123]. Alternatively, a rotating disc made out of the element under study can be used to ensure fresh target points for the

ablation laser [9.124] or a self-healing molten target surface can be employed [9.125]. The combination of sample preparation in a laser-produced plasma and generation of UV and VUV laser light (Fig. 8.42) of short pulse duration [9.126] has recently allowed the laser techniques to be applied on a broad scale [9.127, 9.128] addressing, for example, the astrophysical needs related to the wealth of new short-wavelength data obtained for atoms and ions employing the Hubble Space Telescope.

Boxcar Technique. In a *boxcar integrator* a time window of a certain length is set for the input signal at a certain delay after the trigger signal, and the corresponding electrical charge is stored in a capacitor with a suitable time constant. Transients are repeatedly recorded and the capacitor is charged to a stationary value. The voltage over the capacitor is read out to a recorder. If the time delay is slowly increased to longer and longer values (with a speed that is compatible with the chosen discharge constant), the exponential decay will be reproduced on the recorder. An ADC (Analogue-to-Digital Converter) at the output of the boxcar integrator can be used to adapt the signal for computer processing. The boxcar technique is relatively simple, but clearly not very efficient, since only photons at a certain time delay are used while the others are discarded. In this respect, the cases of transient digitizer versus boxcar integrator, and optical multichannel analyzer versus photoelectrically recording slit monochromator are analogous. The transient digitizer, as well as the boxcar technique, normally requires strong optical transients consisting of a large number of individual photon pulses. Possible nonlinearities in the photomultiplier, which has to record very strong and very weak signals at short time intervals, constitute a limitation to both techniques as regards the recording accuracy.

Delayed-Coincidence Techniques. This method operates in the extremely low intensity regime, in which single-photon counts are recorded. The principle is illustrated in Fig. 9.22.

A single photon gives rise to an electric pulse, which in good photomultipliers has a length of only a few nanoseconds. A Time-to-Amplitude pulse-height Converter (TAC) is a critical component when using this technique. A clock is started when the excitation pulse is fired. The clock runs until the photomultiplier records the first fluorescence photon. A standard electronic pulse, the height (= voltage) of which is proportional to the time difference, is generated and is fed to a Multichannel Analyzer (MCA). An ADC at the input of the MCA converts the voltage into a channel address number, which is proportional to the pulse height. One count is then added to the contents of this channel. Since the decay is exponential, it is likely that the first photon will arrive early. It is important that the probability of two or more photons reaching the detector is kept low, since later photons cannot be recorded. In such cases small time delays would be strongly over-represented, giving rise to the so-called *pile-up* effect. If the probability of detecting a single photon is kept below 1 : 30 the pile-up correction will be

Delayed Coincidence Technique

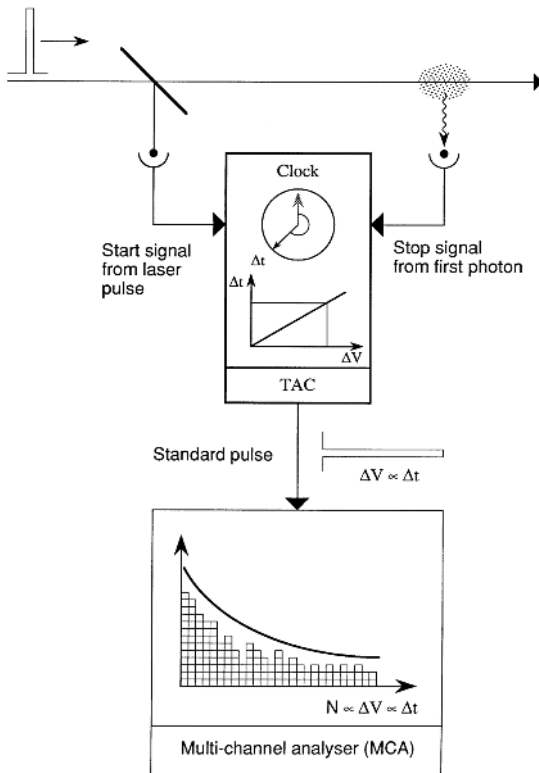


Fig. 9.22. Principle of lifetime measurements using the delayed-coincidence technique

negligible [9.129]. A histogram is then built up in the multichannel analyser. The histogram displays the exponential decay when a sufficient number of counts have been accumulated. The microscopic probability function is then converted into a macroscopic intensity function. Clearly, a high repetition rate is necessary for the excitation source in order to provide an acceptable measurement time. Thus, a pulse-modulated cw laser or a mode-locked laser is normally required. Very accurate results are obtained with this method since there are no linearity problems. It is simply a matter of *when* the photon comes, not how large the corresponding pulse is. When using high repetition rate-sources it is useful to reverse the role of the start and stop pulses so that the TAC is activated by a fluorescence photon and is stopped by the next excitation pulse. In this way dead time in the electronics is reduced. Delayed-coincidence measurements with pulse-modulated or mode-locked cw lasers have been discussed in [9.130].

In Fig. 9.23 examples of decay curves recorded using delayed-coincidence techniques with an acousto-optic modulator are shown for excited Ba states. Two-step excitation is used and only the second laser is pulse-modulated. Lifetime results are also given for the $6sns\ ^1S_0$ and $6snd\ ^1D_2$ sequences of Ba in the figure. An overall trend of $\tau \propto n_{\text{eff}}^3$ is found, but strong localized perturbations are also evident. These are due to admixtures into the wave function of a doubly excited state of the same parity, belonging to the $5d7d$ configuration. Doubly excited states have very short lifetimes in comparison with the highly excited states of the Rydberg sequences. Thus the experi-

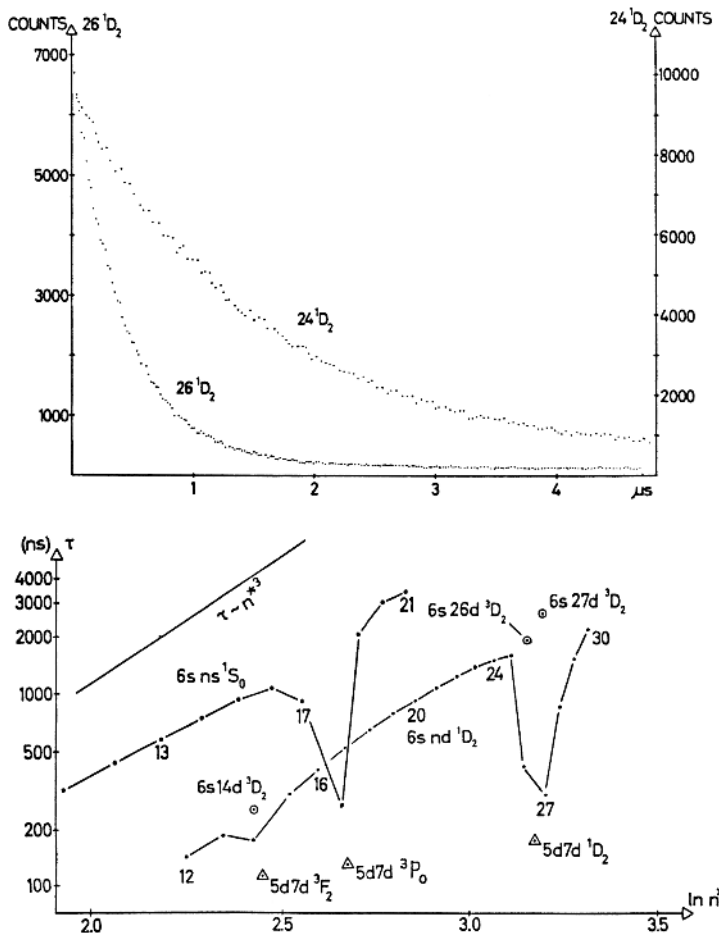


Fig. 9.23. Delayed-coincidence recordings of decay curves for excited barium $6snd\ ^1D_2$ states and plot of lifetime results for perturbed barium Rydberg state sequences. An excitation scheme can be found in Fig. 9.5 ([9.131, first Ref.] and [9.132])

mental results can be used to investigate the composition of the atomic wave functions [9.131].

While the delayed-coincidence technique (or the *time-correlated single-photon counting* technique, as it is sometimes referred to) is very fast and convenient in this type of Rydberg-state study, its inherently high precision is even more valuable in experiments designed to distinguish between very accurate theoretical methods for lifetime calculations. Very accurate lifetimes of the first excited states in lithium and sodium are of great interest in this context. Using a mode-locked CW dye laser with a cavity dumper to produce a MHz train of 6 ps-long pulses it was possible to reach a lifetime precision of about 0.5 percent for short lifetimes around 20 ns [9.133, 9.134].

Optical detection methods (streak-camera and pump-probe techniques) exist that are even faster than those discussed here. Ultrafast spectroscopy is discussed in Sect. 9.5.

9.4.3 Background to Lifetime Measurements

On several previous occasions we have discussed measurement techniques yielding information on natural radiative lifetimes. We now discuss the motivation behind such measurements. In Fig. 9.24 some important relations between radiative properties are presented.

In many contexts, transition probabilities, A_{ik} , (Sect. 4.1) are the quantities of primary interest. As we will see in the next section, relative transition probabilities, a_{ik} , can be determined by several methods. A direct, absolute determination is considerably more difficult. However, lifetimes can be used to determine the relevant constant c , used to normalize relative transition probabilities to absolute ones

$$\frac{l}{\tau_i} = \sum_k c a_{ik} = \sum_k A_{ik} . \quad (9.9)$$

There are many reasons for studying radiative properties:

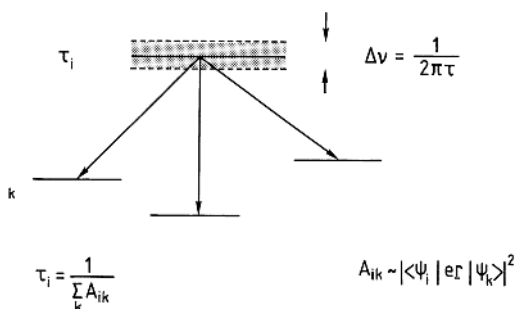


Fig. 9.24. Relations between radiative properties

1. The natural lifetime determines the *fundamental limit* of resolution $\Delta\nu_N = 1/2\pi\tau$ in spectroscopic investigations.
2. Transition probabilities can be used for sensitive *testing of atomic wave functions*. A_{ik} is related to the matrix element of the electric dipole operator $e\vec{r}$ between the two wave functions (Sect. 4.1). Note that A_{ik} is especially sensitive to the outer part of the wave function (at larger r values) because of the r weighting.
3. As we have mentioned in Sect. 6.7, transition probabilities and the related *oscillator strengths* f_{ik} are of utmost importance for *astrophysics*, e.g., for calculations of the relative abundances of the elements in the sun and stars.

The absorption oscillator strength f_{ki} is related to the corresponding transition probability A_{ik} by the following relation:

$$f_{ki} = 1.5 \frac{1}{\sigma^2} \frac{g_k}{g_i} A_{ik}, \quad (9.10)$$

where σ is the wavenumber for the transition and g_i and g_k are the statistical weights for the upper and lower states, respectively.

4. The radiative properties of atoms and ions are also of great importance in *plasma physics*, e.g., for temperature determination and for the calculation of the concentrations of different constituents. In fusion research, determination of the concentrations of contaminating species that tend to cool the plasma are of great interest. The study of the properties of refractory elements that are used for plasma confinement (Mo, Va, etc.) is especially important [9.135].
5. In *laser physics* lifetimes and transition probabilities are decisive for predictions of potential laser action in specific media.

9.4.4 Survey of Methods of Measurement for Radiative Properties

We now discuss a number of measurement techniques for radiative properties. We start with methods of lifetime determination and continue with techniques for the measurement of transition probabilities. Detailed descriptions can be found in [9.136–9.139].

Linewidth Measurements. The natural linewidth of a short-lived state is $\Delta\nu_N = 1/2\pi\tau$. If this constitutes the only broadening mechanism, the measured linewidth yields the lifetime directly. For very short lifetimes the technique is quite useful. The lifetimes of inner-shell states connected by X-ray transitions can be determined in this way (Sect. 5.2.1). Short-lived states for external electrons can also be determined from the linewidth if the Doppler effect is totally eliminated and a single-mode laser of small linewidth is employed [9.140].

ODR and LC. Here the natural radiative width is also determined directly. The contribution from Doppler broadening is negligible since the measurement is performed in the radio-frequency regime ($\sim 10^7$ Hz). Thus the Doppler broadening is about 10^8 times smaller than for optical transitions. In radio-frequency measurements the lifetime is given by $\tau = 1/\pi\Delta\nu$ in the limit of vanishing RF field strengths. At higher field strengths a broadening of the signal occurs, since the perturbation is no longer negligible. In level-crossing experiments the lifetime is directly obtained from high-field crossing signals. If $I = 0$ or $I = J$, the Hanle signal is also easy to analyse, since only signal contributions of the same half-width occur ($d\nu/dB$ is the same for all contributing level pairs; $g_F = g_J/2$ for all F if $I = J$; see (7.33) and (2.45)). In the general case a superposition of signal contributions of different intensities and half-widths has to be analysed [9.141].

Beam-Foil Techniques. The beam-foil method has been discussed in Sect. 6.1. It is a very general method for measuring lifetimes of atoms and ions. However, the non-selective excitation, leading to cascading decays, places heavy demands on the data analysis and sometimes a detailed study of the different cascade channels is necessary for reliable lifetime evaluations. While the nonselective excitation frequently constitutes a problem, it is also an advantage of the method since a multitude of excited states are populated. For measurements of multiply charged ions in particular, the technique provides unique measurement possibilities where other techniques are not applicable.

Beam-Laser Techniques. By exchanging the exciting foil in the beam-foil technique for a focused laser beam, selective excitation can be obtained and the problem of cascades is eliminated [9.142]. By directing the laser beam at a certain angle θ with respect to the ion beam considerable Doppler shifts in the interaction with the fast beam are obtained. The relativistically correct formula for the interaction wavelength λ_i , experienced by the ions that are illuminated by a laser of wavelength λ_ℓ is given by

$$\lambda_i = \lambda_\ell \frac{\sqrt{1 - v^2/c^2}}{1 - (v/c) \cos \theta}. \quad (9.11)$$

For $v/c = 1/100$ we note that Doppler shifts of tens of Å (see also Fig. 6.93) are easily accomplished by varying θ . Measurements of this kind are illustrated in Fig. 9.25. A fixed-frequency laser (e.g., an Ar^+ laser) can be used owing to the possibility of Doppler tuning. The first experiments of this kind were performed for the resonance line of $\text{Ba}^+ 6s\ ^2S_{1/2} \rightarrow 6p\ ^2P_{3/2}$ at 4554 Å. The 4545 Å Ar^+ line could be utilized by choosing $\theta = 23^\circ$ for an ion velocity of 0.63×10^6 m/s.

The lithium and sodium transitions discussed above were later studied with a precision of a fraction of one percent [9.143]. A charge-exchange cell containing alkali vapour was used in the fast ionic beam to generate the

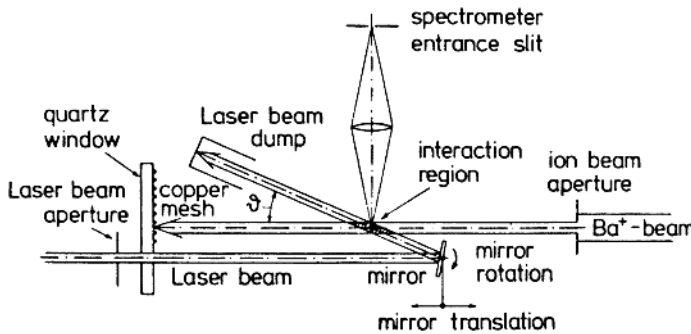


Fig. 9.25. Lifetime measurement with the beam-laser technique using Doppler tuning [9.142]

neutral species. Theoretical calculations can accurately reproduce the experimental results [9.144]. Since the transition wavelengths for ions of different charge states rapidly shift into the ultraviolet and VUV regions, due to the electronic shell contraction, and as cw lasers are scarce at such wavelengths, the applicability of this high-precision technique is unfortunately limited.

Time-Resolved Spectroscopy with Pulsed Lasers. We have recently discussed these techniques in the sections above.

Time-Resolved Spectroscopy with Pulsed Electron Beam Excitation. Abrupt excitation of atoms and molecules can be accomplished with a pulsed electron beam. In the same way as for the beam-foil interaction, non-selective excitation is obtained. One of the most efficient variations of this technique is the *high-frequency deflection* method [9.145–9.147], which is illustrated in Fig. 9.26. An electron beam of high power (~ 20 keV, 0.5 A) is deflected using RF deflection plates, as in an oscilloscope. The beam is swept over a slit and the repetition rate and pulse length can easily be selected. Delayed-coincidence techniques (Sect. 9.4.2) are used to record the decay. Because of the high light intensity obtained with this technique a high-resolution monochromator (with a narrow slit) can be used for the detection. This is of great importance, particularly in studies of molecules, for which individual rotational-vibrational lines can be isolated without blending. For molecules, cascade problems are frequently less severe than for atoms. Lifetime results for the CH molecule are shown in the figure illustrating the shortening of lifetimes for higher rotational levels due to predissociation at potential curve crossings.

Phase-Shift Method. In the phase-shift method atoms or molecules are excited by a sinusoidally modulated light or electron beam, as illustrated in Fig. 9.27. Fluorescence light is recorded with a photomultiplier tube. This light will thus also be modulated, but because of the delay in the excited state a phase-shift is introduced [9.149]. At the same time, the contrast in

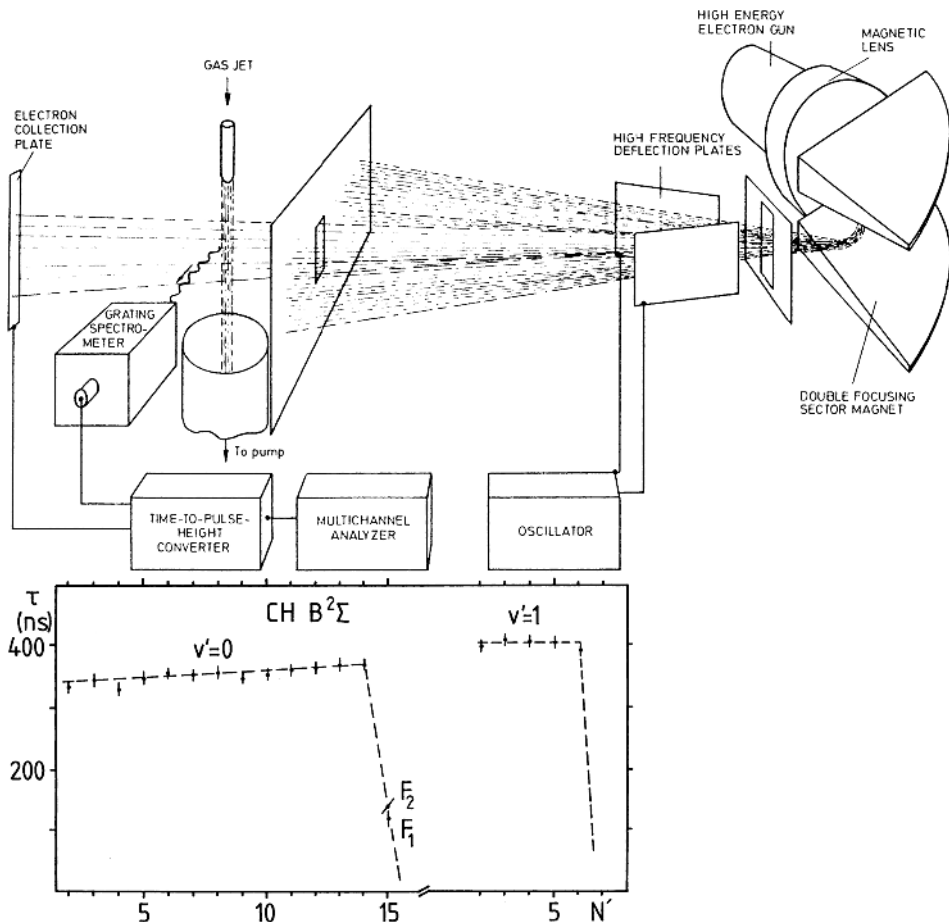


Fig. 9.26. The principle of the high-frequency deflection method for lifetime measurements, and experimental lifetime data for the CH radical [9.145, 9.148]

the modulation is reduced. If light is used for the excitation, the phase shift can be determined by comparison with the signal that is obtained when stray light is sent directly into the detector by inserting a small scattering object into the light beam at the point of interaction. If the exciting light is described by the expression

$$I_{\text{exc}} = I_0(1 + a \sin \Omega t) \cos \omega t, \quad (9.12)$$

it can be shown, by integrating the exponential decays from the different excitation function time elements, that the fluorescence light intensity is given by

$$I_{\text{fl}} = b I_0 \left(1 + \frac{a}{\sqrt{1 + \Omega^2 \tau^2}} \sin(\Omega t + \phi) \right) \cos \omega t \quad (9.13)$$

Phase-shift method

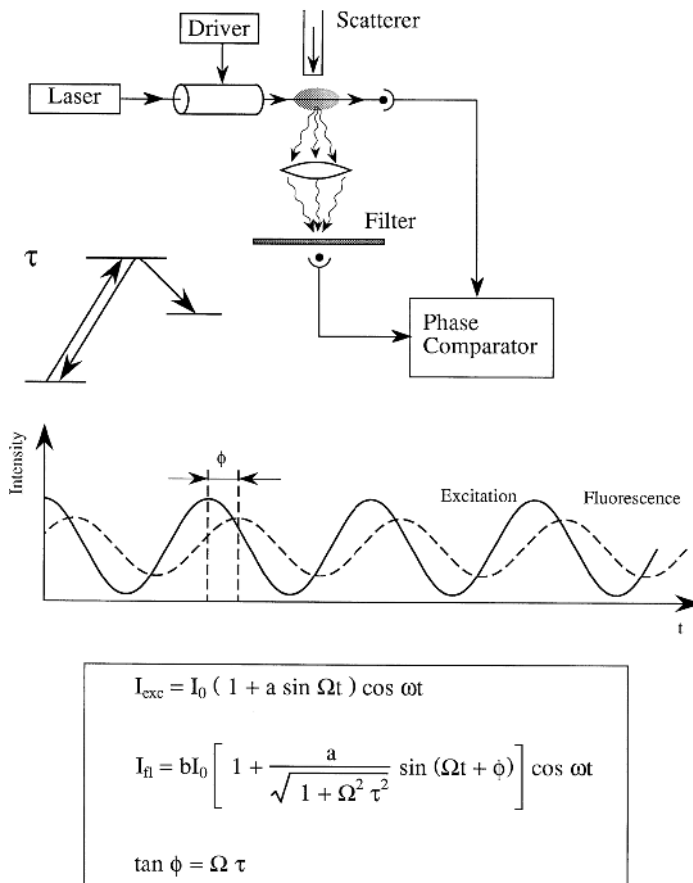


Fig. 9.27. The principle of lifetime measurements by the phase-shift method

with

$$\tan \phi = \Omega \tau. \quad (9.14)$$

If multiple-scattering processes occur, an erroneously long lifetime will be obtained, as for several of the above-mentioned methods. The opposite effect is obtained if, in addition to the fluorescence light, non-shifted stray light from the modulated light source is recorded. If the modulation is not perfectly sinusoidal, the first Fourier component can be isolated and the phase shift for this component will still yield the lifetime.

We now turn to the determination of transition probabilities.

The Emission Method. If the effective temperature in local thermodynamic equilibrium is known, the relative strength of spectral lines from a light

source can be used to calculate *relative transition probabilities*. Clearly, corrections for the wavelength-dependence of the spectrometer transmission and the photomultiplier sensitivity must be applied. This can be done by replacing the actual light source by a standard tungsten lamp (Planck radiator) with a known emissivity. A large number of elements have been investigated by *Corliss* and *Bozman* using a standardized arc discharge [9.150]. Actually, absolute values are given, but a correction factor of up to 5, as determined from normalizing lifetime measurements, must frequently be applied.

The Hook Method. The hook method is based on the Kramer–Kronig dispersion relation, which relates the refractive index of a gas to transition probabilities [9.151, 9.152]. At the same time as atoms in a vapour absorb at

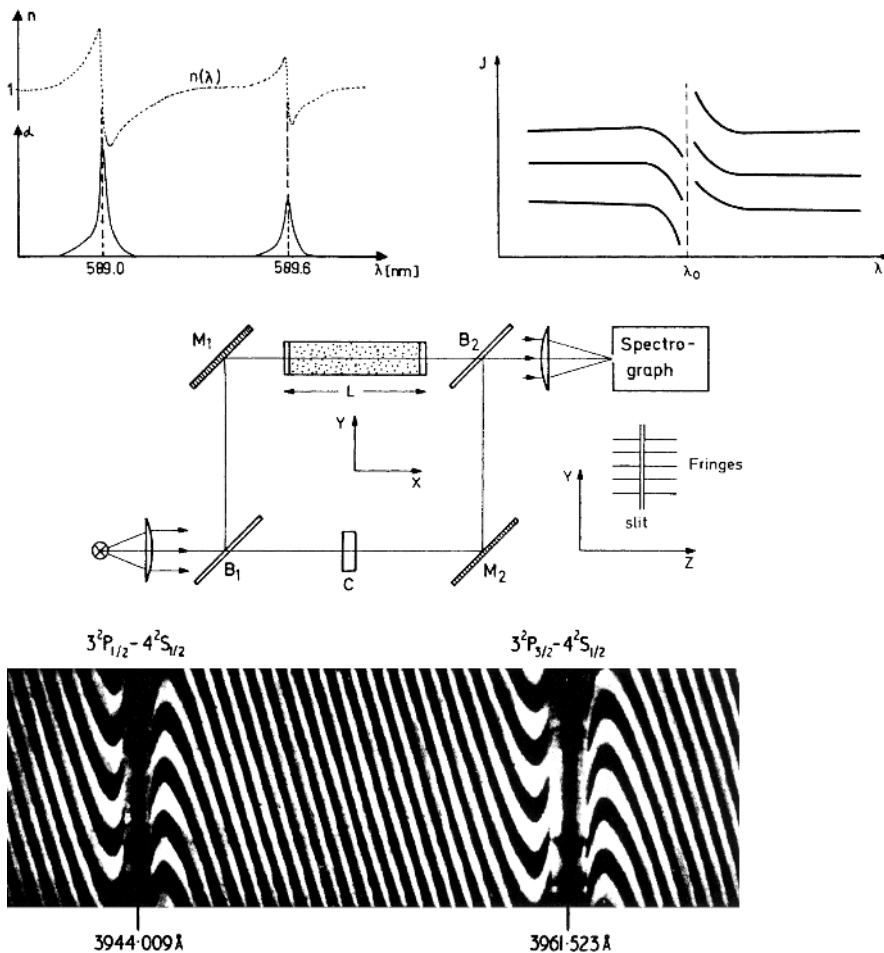


Fig. 9.28. Illustration of oscillator strength measurements [9.1]. An experimental recording for the AlI resonance doublet is included

the transition frequency, an anomalous dispersion is obtained. (The increase in refractive index of transparent materials towards the UV region is related to the UV absorption of the material, see Figs. 6.18 and 6.48.) In Fig. 9.28 the relation between the absorption and dispersion at the sodium D lines is illustrated. In the hook method, light from a continuum source is sent through a Mach-Zehnder interferometer, where a heat-pipe oven containing the metal vapour is inserted in one arm. The interference pattern is imaged as a function of wavelength through a spectrometer on a photographic plate. The abrupt change in refractive index at a line gives rise to the “hooks” in the recording. It can be shown, that the product of the atomic density and the transition probability is proportional to Δ^2 , where Δ is the hook separation. By measuring absorption as well as dispersion, absolute transition probabilities can in principle be determined.

At first it might seem surprising that transition probabilities, related to the natural radiative lifetime and its corresponding small Heisenberg broadening can be measured in the presence of the much larger Doppler broadening. However, the technique is pursued for high atomic densities where the hooks occur some 0.1 nm from the line centre, as seen in Fig. 9.28. At this large distance from the centre the influence of the Doppler broadening, described by a swiftly falling Gaussian function (6.6) is negligible compared to the influence of the Lorentzian function (4.40) due to the natural lifetime, although the halfwidth of the Gaussian is typically 100 times larger than for the Lorentzian. However, a Lorentzian has a much slower fall-off than a Gaussian.

The Hook method yields very accurate, reliable relative transition probabilities. A laser-based related technique, the “inverse Hook method”, has also been introduced [9.153].

9.4.5 Quantum-Beat Spectroscopy

We have already discussed quantum-beat spectroscopy (QBS) in connection with beam-foil excitation (Fig. 6.6). There the case of abrupt excitation upon passage through a foil was discussed. Here we will consider the much more well-defined case of a pulsed optical excitation. If two close-lying levels are populated simultaneously by a short laser pulse, the time-resolved fluorescence intensity will decay exponentially with a superimposed modulation, as illustrated in Fig. 6.6. The modulation, or the quantum beat phenomenon, is due to interference between the transition amplitudes from these coherently excited states. Consider the simultaneous excitation, by a laser pulse, of two eigenstates, 1 and 2, from a common initial state i . In order to achieve coherent excitation of both states by a pulse of duration Δt , the Fourier-limited spectral bandwidth $\Delta\nu \simeq 1/\Delta t$ must be larger than the frequency separation $(E_1 - E_2)/h = \omega_{12}/2\pi$. If the pulsed excitation occurs at time $t = 0$, the wave function of the excited state can be written as a linear superposition of the eigenstates

$$|\psi(0)\rangle = \sum_k a_k |\phi_k(0)\rangle, \quad (9.15)$$

where the coefficients a_k are probability amplitudes for finding the atom in level k . Due to the exponential decay to the final level f , the time-dependent wave function is given by

$$|\psi(t)\rangle = \sum_k a_k |\phi_k(0)\rangle \exp(-iE_k t/\hbar) e^{-t/2\tau}. \quad (9.16)$$

The time-dependent fluorescence light intensity from the excited states is determined by the transition matrix element, (see (4.28) and (7.26)).

$$I(t) = C |\langle \phi_f | \vec{e}_g \cdot \vec{r} | \psi(t) \rangle|^2, \quad (9.17)$$

where \vec{e}_g is the polarization vector for the detected light. Inserting (9.16) in (9.17) for the case of two sublevels yields

$$I(t) = C e^{-t/\tau} (A + B \cos \omega_{12} t) \quad (9.18)$$

with

$$A = a_1^2 |\langle \phi_f | \vec{e}_g \cdot \vec{r} | \phi_1 \rangle|^2 + a_2^2 |\langle \phi_f | \vec{e}_g \cdot \vec{r} | \phi_2 \rangle|^2, \quad (9.19)$$

$$B = 2a_1 a_2 |\langle \phi_f | \vec{e}_g \cdot \vec{r} | \phi_1 \rangle| |\langle \phi_f | \vec{e}_g \cdot \vec{r} | \phi_2 \rangle|. \quad (9.20)$$

We note, that a modulation is obtained ($B \neq 0$) only if the matrix elements for the transitions $1 \rightarrow f$ and $2 \rightarrow f$ are non-zero at the same time. A quantum-mechanical interpretation of the beats is based on the observation that it is impossible to determine whether the atom decayed via the transition $1 \rightarrow f$ or $2 \rightarrow f$. The total probability amplitude is therefore the sum of the two corresponding amplitudes; the observed intensity is the square of this sum and the cross-term gives rise to interference. If it had been possible to detect the transitions separately (spectrally, or by means of the polarizations), then the interference would have been lost. The situation here is analogous to that in Young's double-slit experiment. If attempts are made to determine through which of the slits the photon passes, the interference is lost. Note the very close relationship between quantum-beat spectroscopy and level-crossing spectroscopy. If time integration of the QBS phenomenon is performed, the LC phenomenon is obtained, for which continuous excitation and detection are used. Quantum beats are induced by a tunable laser with a short pulse duration (~ 5 ns). If very fast beats are to be studied, the pulse must be correspondingly shorter (in order to obtain Fourier components spectrally overlapping both levels or, expressed differently, to ensure a sufficiently small initial spread in the wave function phase factors). With a mode-locked laser, pulse lengths of the order of 1 ps or shorter can be obtained (Sect. 8.7).

In Fig. 9.29 an example of Zeeman quantum beats is shown. The geometries for excitation and detection are the same as for a recording of the Hanle effect (Sect. 7.1.5). The signal is also a $\Delta M = 2$ phenomenon. Zeeman quantum beats can also be explained semiclassically using the same model as

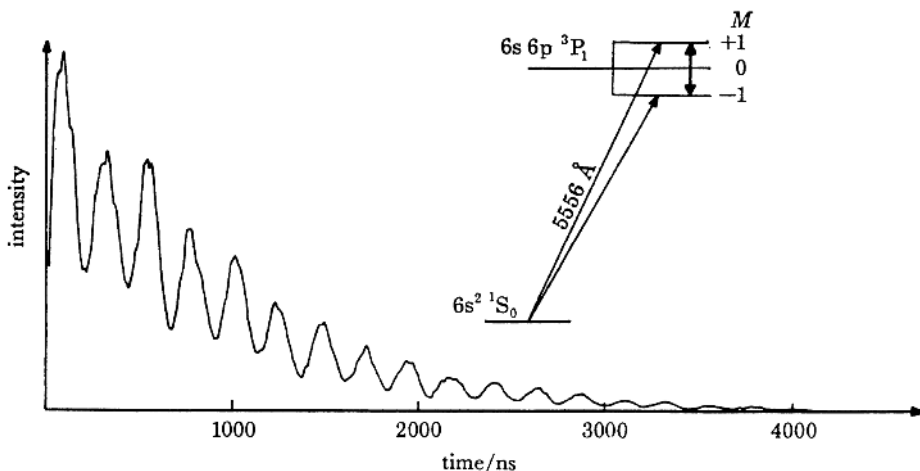


Fig. 9.29. Zeeman quantum beats for the resonance line in ytterbium [9.154]

was used for the Hanle effect (Fig. 7.15). The linearly polarized light (which has a σ^+ as well as a σ^- nature, Fig. 4.9) induces an oscillating *electric dipole* in the electron cloud, which will radiate with a dipole distribution, shrinking with a time constant of τ . Since the atom has a *magnetic dipole moment*, it will Larmor precess (Sect. 2.3.1) in the external magnetic field and a radiation lobe will be turned in towards the detector twice every full revolution. The excited atom is a microscopic “light-house”. The Hanle effect is the part of the Zeeman quantum beat that “survives” the time integration because of the common initial condition and slow lobe rotation in the field region of the Hanle effect. The situation is illustrated in Fig. 7.15. For high fields the lobes pass in and out of the detector direction many times during the decay of the dipolar distribution. Thus, the fraction of time the detector is illuminated will become essentially independent of the field strength and the signal levels off.

From the semiclassical picture it is also evident that the phase of the beat signal is changed by 180° if the linear polarizer for the case of signal detection in the direction of the magnetic field is turned by 90° (this corresponds to a sign change of the Hanle effect). Because of the phase inversion it is possible to eliminate the primary exponential decay by subtracting two signals of equal unmodulated light intensity but recorded for perpendicular detection polarizer settings. When pure exponentials are desirable for lifetime evaluation, a sufficiently high magnetic field can be applied, corresponding to frequencies well above the cut-off frequency of the detection system, to wash out the quantum beats.

Although the general features of the quantum-beat phenomenon can be understood in a simple semiclassical model, a full quantum-mechanical de-

scription is required for calculating the correct relation between B and A in (9.18) to determine the beat contrast in the decay curve. Quantum-beat spectroscopy has been discussed in detail in [9.155, 9.156].

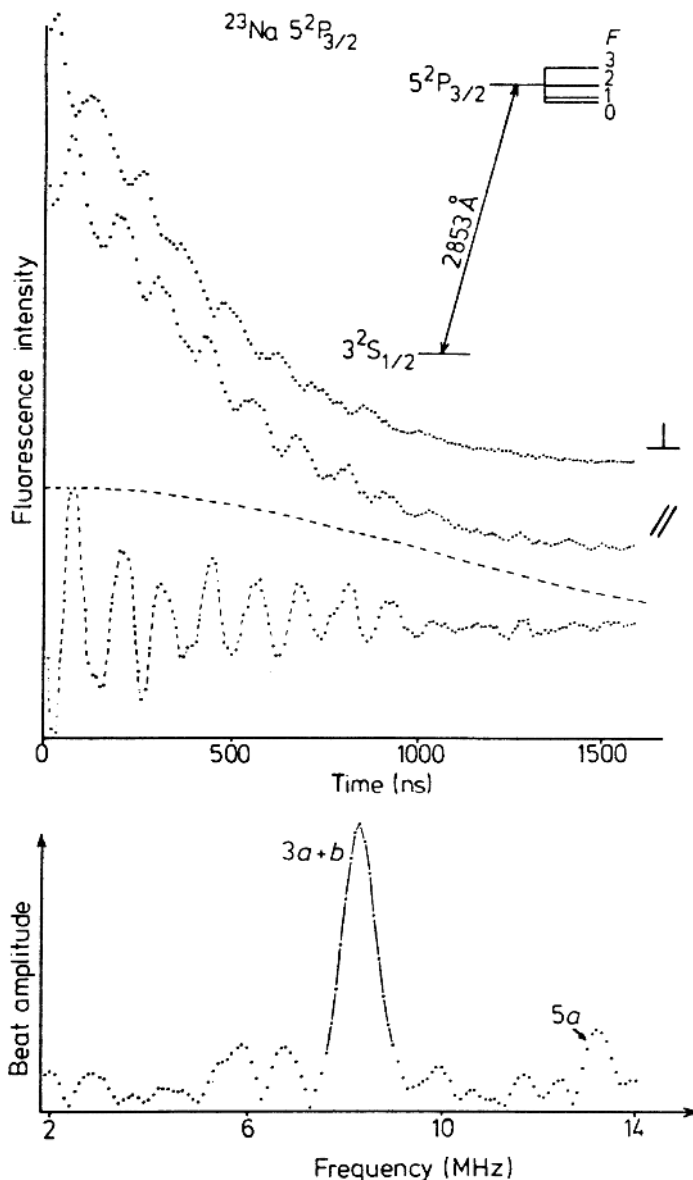


Fig. 9.30. Hyperfine quantum beats for a $^2P_{3/2}$ state in ^{23}Na recorded for two different polarizer settings [9.157]

Fine- and hyperfine splittings also give rise to quantum-beat signals. For example, the hfs beats can be understood semiclassically by considering the radiating electronic shell precessing at hyperfine frequency in the internal field due to the nucleus. $\Delta F = 1$ and $\Delta F = 2$ beats can be obtained in zero magnetic field. In Fig. 9.30 hfs quantum-beat signals corresponding to two polarizer settings are given. It can be shown that the beat amplitude is proportional to $3 \cos^2 \theta - 1$, where θ is the angle between the polarizers in the exciting and detection beams. (Thus, by making $\theta = \arccos(1/\sqrt{3}) \simeq 54.7^\circ$ ("magic angle") it is possible to suppress beats all together.) When many beat frequencies occur simultaneously, they can be isolated by a Fourier transformation from the time to the frequency domain. In Fig. 9.31 an example of hfs beats from the two stable gallium isotopes is shown and a corresponding Fourier transform is also given.

Quantum-beat spectroscopy as well as level-crossing and optical double resonance measurements using pulsed lasers are powerful techniques for high-resolution investigation of small energy intervals in a very wide wavelength region [9.159]. This is because pulsed lasers can be shifted to UV/VUV or IR wavelengths using nonlinear optical techniques (Sect. 8.6).

As a final point in this section, we discuss the question of increasing the spectral resolution beyond the natural radiation width $\Delta\nu_N = 1/2\pi\tau$. Different experiments have been performed, in which the observation after pulsed

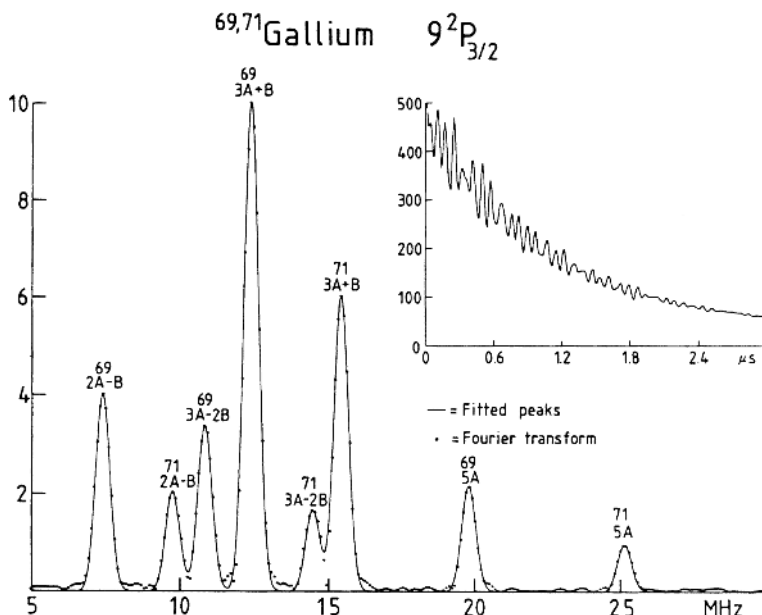


Fig. 9.31. Superimposed hyperfine quantum beats for the two stable gallium isotopes (both $I = 3/2$) and the corresponding Fourier transform displaying the beat frequencies [9.158]

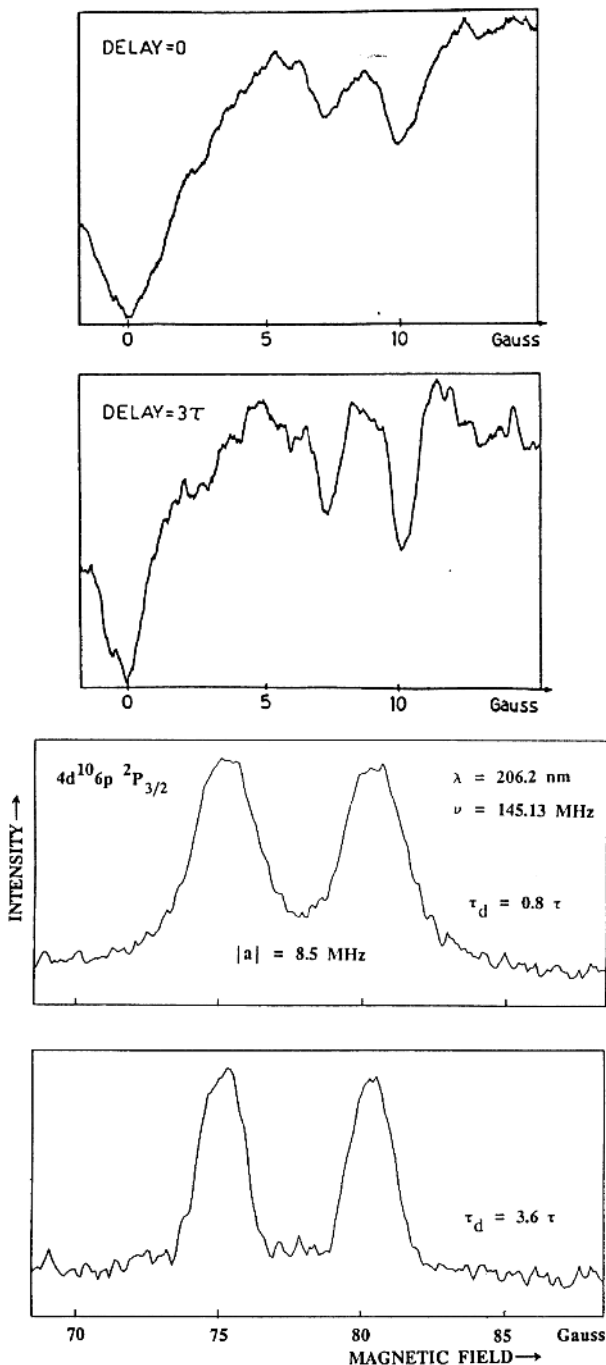


Fig. 9.32. Illustration of the influence on level-crossing (*upper part*) and optical double-resonance signals (*lower part*) due to the restriction of the recording to “old atoms” [9.164, 9.162]

excitation is limited to “old” atoms, i.e., the detection system is activated after a certain delay such that only the atoms that have survived longest in the statistical process will contribute to the signal [9.160–9.164]. Normally, the whole exponential decay is utilized and in the integration from 0 to ∞ a Lorentzian of half-width $1/2\pi\tau$ is obtained in frequency space (Fig. 4.4). The Breit formula (7.25) describing the level-crossing phenomenon has been obtained through such a complete integration. Lorentzian crossing signals are then obtained. If the integration is performed from a delayed time T to infinity, oscillations in the signal wings are obtained but the central peak becomes narrower. The same is true for quantum-beat signals, for which the Fourier transform also narrows when integration is performed after a time delay. Clearly, a very strong loss in intensity is obtained. For example, after 4τ the intensity has been reduced to 1% of the original intensity. Thus it is not at all clear that the information content has been improved by restricting the observation to “old” atoms. In special cases, e.g., if the signals are non-symmetric or overlapping, reduced systematic errors can be obtained if the linewidth is reduced in spite of the significant loss in intensity.

Examples of recordings where the detection time interval has been manipulated are shown in Fig. 9.32. In the upper part of the figure the influence on overlapping level-crossing signals (improved resolution) is seen for the case of the $9d\ ^2D_{3/2}$ state of ^{133}Cs , reached by stepwise excitations [9.164]. The sublevel system corresponding to this recording is of the type shown in Fig. 7.16, although the nuclear spin is now $I = 7/2$. Time-gated recordings of Paschen–Back region optical double-resonance signals are shown in the lower part of the figure for the case of the $4d^{10}6p\ ^2P_{3/2}$ state of silver [9.162]. The situation is similar to the one depicted in Fig. 7.11, although now with nuclear spin $I = 1/2$, resulting in $2I + 1 = 2$ RF signals. Since natural silver consists of two spin-1/2 isotopes, ^{107}Ag and ^{109}Ag , of about equal abundance and with magnetic moments differing by only 15 percent, each of the two signals actually consist of two closely overlapping contributions.

9.5 Ultrafast Spectroscopy

While the previous section mostly focused on time-resolved studies on the nanosecond timescale we will now describe how ultrafast processes, occurring on the pico- or femtosecond scale, can be investigated. Such fast phenomena mostly occur in the liquid or solid state and frequently are connected with energy transfer. Important and much-studied processes of this kind include photosynthesis, involving different light-harvesting antenna pigments, and the visual process, involving rhodopsin and other complex molecules. Ultrafast techniques also allow a detailed study of fundamental chemical reactions leading to dissociation or the formation of new molecules. Mode-locked lasers provide the necessary short pulse lengths (Sect. 8.7). Frequently, more energy than that directly available from mode-locked CW lasers is needed, e.g.,

for white-light generation (see below). Then the chirped-pulse amplification (CPA) technique can be employed (Sect. 8.7.2). Intermediate pulse-energy systems operating at 1–10 kHz repetition rate (employing Nd:YLF amplifier pump lasers) are then preferred to 10 Hz Nd:YAG-pumped high-energy systems, since photochemical decomposition of the samples studied must be avoided. We will now discuss ultrafast measurement techniques and consider some examples of ultrafast chemistry studies. General references to the field are given in [9.165–9.184].

9.5.1 Ultrafast Measurement Techniques

Boxcar integrators and transient digitizers discussed in Sect. 9.4.2 have a time resolution down to 0.5 ns or slightly better, also matching the rise time of the fastest photomultipliers available for optical measurements. The delayed-coincidence technique can be pushed further, to the tens of ps regime. This is because the clock triggering can be set to occur at a constant fraction of the full amplitude of a single-photon waveform using special *constant-fraction discriminator* electronics to eliminate time jitter due to statistical variations in the amplitude of photomultiplier photon signals. For faster measurements streak camera or autocorrelation techniques can be employed.

Streak Cameras. For the recording of very fast phenomena a *streak camera* can be used [9.185]. The principle is illustrated in Fig. 9.33. The incoming transient light impinges on a photo-cathode. The released electrons are accelerated, focused and deflected by plates subjected to a rapidly rising voltage. The deflected electron beam hits a microchannel plate (Sect. 6.3) in which

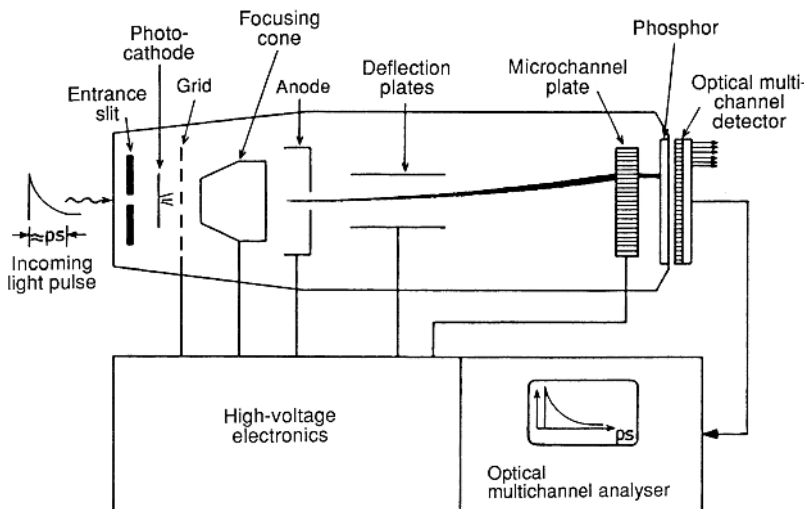


Fig. 9.33. The construction of a streak camera

every electron gives rise to an electron burst. The temporal electron distribution gives rise to a streak of light on a phosphor screen. The intensity on the screen is proportional to the time-resolved light intensity. The streak is read off by a sensitive optical multichannel system (Sect. 6.3) and the intensity is displayed on an oscilloscope or relayed to a computer. By proper choice of cathode material the streak camera can be operated for visible and UV wavelengths (see Fig. 6.36) or even X-ray wavelengths. In the latter case normally thin cathodes made of CsI are employed. Since no window materials exist the interface between the camera and the experiment must be a vacuum. Time resolutions down to 0.5 ps can be achieved.

Autocorrelators. Autocorrelators work on the principle of “probing light by light”. The general idea in these types of measurement is given in Fig. 9.34. First we consider the case of studying the shape of ultrashort laser pulses. The incoming train of pulses is divided up in a beam splitter and part of the light is passed through a fixed delay line, while the other part is passed through a variable delay line. Pulses from the two arms are merged at below a certain angle into a thin nonlinear crystal where phase-matching for frequency doubling in the bisectrix direction occurs if the two pulses arrive simultaneously. It can be shown, that for Gaussian-shaped pulses the generated UV intensity as a function of the temporal delay (the time) follows a curve with a half-width which is a factor of $\sqrt{2}$ broader than that of the incoming pulses. In autocorrelators of this kind symmetrical curves are always obtained. Thus, it is not possible to separately monitor the leading and the

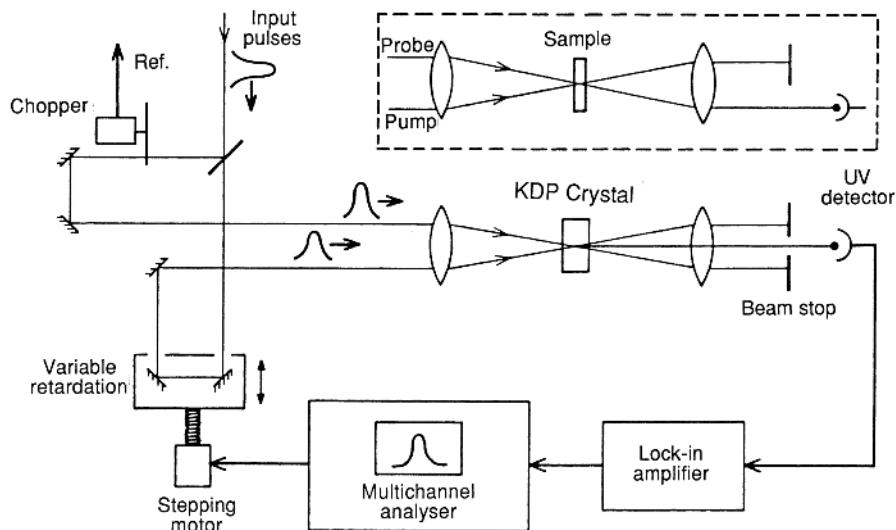


Fig. 9.34. The principle of pump-probe experiments using picosecond pulses (*insert*) and pulse-length determinations using autocorrelation with frequency doubling

trailing edges of a pulse. If a third-order process is used, e.g., a frequency-doubled pulse is correlated with the pulse itself using frequency tripling, it is possible to unravel the true shape of the pulse. By employing broad beams and an imaging detector it is possible to capture the temporal shape of individual pulses using geometrical delays across the detector.

Autocorrelators are very useful for optimizing the adjustments of ultrafast laser systems. This is particularly necessary when dealing with terawatt laser systems for high-power laser/matter interaction studies. Here the presence of an intensity pedestal around the main short pulse can be very detrimental. Generally speaking, it is very desirable to have *transform-limited* Gaussian-shaped temporal pulses, where the spectral contents is described by the Fourier transform; also a Gaussian. In complex laser amplification systems the oscillator pulse is frequently distorted temporally by the fact that not all the frequency components building up the short pulse are amplified equally, mainly due to the limited spectral region where the amplification medium has gain (gain narrowing) and due to possible spectral clipping in the wavelength-dispersion arrangement of a CPA system. These modifications in the spectral content by necessity lead to modifications in the amplified pulse temporal behaviour after compression, e.g., the occurrence of an intensity pedestal. To allow a full characterization and manipulation of a pulse it is necessary to monitor the temporal as well as the spectral contents and their interplay. Several methods have been developed for the purpose, e.g., the *frequency-resolved optical gating* (FROG) technique and the *spectral phase interferometry for direct electric-field reconstruction* (SPIDER) technique [9.186].

Pump-Probe Techniques, White-Light and Terahertz-Radiation Generation. Pump-probe techniques are more general schemes, in which the temporal resolution comes from the short pulse duration and the possibility of defining temporal intervals by the corresponding spatial translations in optical delay lines (light travels 0.3 mm in 1 ps). Autocorrelators, as discussed above, operate on these principles, but the concept can be extended to the study of liquid or solid samples as indicated in the insert of Fig. 9.34. A *pump* pulse tuned to a certain frequency provides a partial depletion of the lower level, which is observed as a loss of absorption in the *probe* pulse. The two pulses can be of different frequency if a primary short-pulse laser pumps a secondary source to generate new wavelengths by nonlinear optical methods or laser action. By delaying the probe pulse progressively it is possible to see how fast the hole is filled in by *relaxation* processes. Alternatively, the excited-state population can be probed by letting the second pulse ionize or transfer the remaining atoms/molecules and then integrating the resulting signal using detectors and electronics that do not need to be ultrafast.

Optical parametric oscillators (OPOs) (Sect. 8.6) are very useful widely tunable secondary sources of ultrafast pulses that find a wide applicability in pump-probe experiments. Two independent OPOs, which are pumped by the same laser for automatic synchronization and minimal temporal jitter, are

particularly useful. In other experiments it is very convenient to monitor the action of a wavelength-selected pump pulse by a *white-light continuum* probe pulse [9.187]. If a beam of high-power pulses is focused onto a transparent solid or liquid (water is frequently used), a beam of “white” laser light will emerge. The reason for this white-light generation is self-phase modulation of the optical waves due to the rapid change in the nonlinear refractive index (8.20) of the medium in the rising and falling edges of the intense pulses. This fast refractive index change corresponds to the generation of new wavelength components as evidenced in a Fourier transformation from the time to the frequency domain. A very strong frequency broadening occurs, resulting in intense light covering the whole visible spectrum. The duration of this continuum is about the same as the generating pulse. The probe light can be dispersed by a grating (resulting in some temporal stretching) and imaged by a CCD detector. A white light lidar system has recently been constructed [9.187].

Broadband radiation in the THz frequency region can also be generated using ultrashort laser pulses. *Terahertz time-domain spectroscopy* utilizes pump-probe techniques as well. If charged short antenna rods of a length of typically $50\text{ }\mu\text{m}$ are connected photoconductively by impacts from a train of intense laser pulses of ultrashort duration, broadband bursts of terahertz radiation (5 THz–100 GHz; $60\text{--}3000\text{ }\mu\text{m}$) are generated [9.188, 9.189]. This radiation can be collected by a mirror and sent through a sample, followed by radiation collection and detection in a THz detector, as illustrated in Fig. 9.35. The detector consists of a similar arrangement to the transmitting antenna and generates a signal only when it is made conducting by the impact of a gating pulse derived from the short-pulse laser. By sweeping an optical delay line between transmitter and receiver at a typical velocity of 30 cm/s ($v/c = 10^{-9}$) a time-resolved signal down-converted to the kHz region can be recorded as the beat note between the primary THz radiation and the Doppler-shifted detector-gating radiation. THz radiation penetrates most dry materials such as plastics, paper and cardboard but is strongly absorbed in water (cf. Fig. 7.24) and other polar solvents, and is totally blocked by metals.

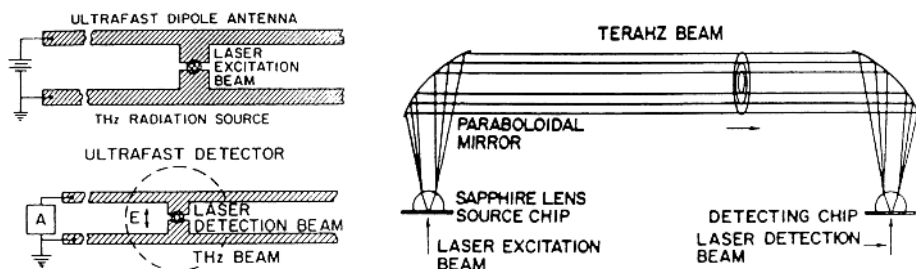


Fig. 9.35. Set-up for terahertz spectroscopy, and transmitter and receiving antennas [9.189, 1st reference]

Molecules in the gas phase absorb on rotational or vibrational-rotational transitions. These features allow applications such as luggage inspection and spectroscopic gas analysis. THz techniques can also be implemented for object imaging. THz technology and applications are discussed in [9.190].

9.5.2 Molecular Reaction Dynamics (Femtochemistry)

One of the most exciting possibilities of ultrafast laser techniques is to follow the course of fundamental chemical reactions on the relevant timescale at which they occur. Previously, it was only possible to know the individual states of molecules A and B before reacting and the final state of the compound molecule AB. In contrast, the details of the chemical reaction can now be followed on a femtosecond scale with information on how chemical bonds are formed and broken. In particular, the existence of *transition states* has been demonstrated. This new field of science is frequently referred to as *femtochemistry* [9.191–9.204], for which *A. Zewail* was awarded a Nobel prize in chemistry (1999).

The study of the dissociation of sodium iodide (NaI) into sodium and iodine can serve as an example showing the power of ultrafast spectroscopy. A short pump pulse excites the molecule, which has an equilibrium separation of 0.28 nm, to a higher state as indicated in Fig. 9.36. Here the molecule starts to vibrate. At a nucleus separation of 0.69 nm there is a large probability that the molecule falls back to the ground state (when the internuclear distance diminishes) or, alternatively, dissociates into free Na and I atoms (when the internuclear distance increases). The molecular dissociation process, depicted in the experimental recordings included in the figure, can be monitored by a femtosecond probe pulse tuned to excite the upper-state molecules from the potential bottom to a still more excited molecular state (maximum signal). When the atoms move apart, the energy level moves upward and the molecule tunes out of resonance (minimum signal). The periodic release of dissociation products can be monitored if the probe pulse is tuned instead to the sodium D-line. The build-up in Na atom concentration through periodic additions of Na pulses can also be seen in the figure [9.202].

An important question in chemistry is why certain bonds are more reactive than others and what happens if there are two equivalent bonds in a molecule subject to photodissociating light. Will the bonds break simultaneously or sequentially? In a study of tetrafluorodiiodoethane, $C_2I_2F_4$, it was found that the dissociation, freeing I atoms, is sequential; the first stage occurring about 200 fs after the pump pulse and the second one after about 20 ps (100 times longer) [9.203].

A further type of reaction, which can be studied by femtosecond spectroscopy, is photoisomerisation, i.e., the optically induced transformation of one molecular structure into another. When *cis*-stilbene is excited by a femtosecond pulse, the central double bond is weakened allowing a rotation of the benzene rings to yield the *trans*-stilbene configuration (Fig. 9.37). The

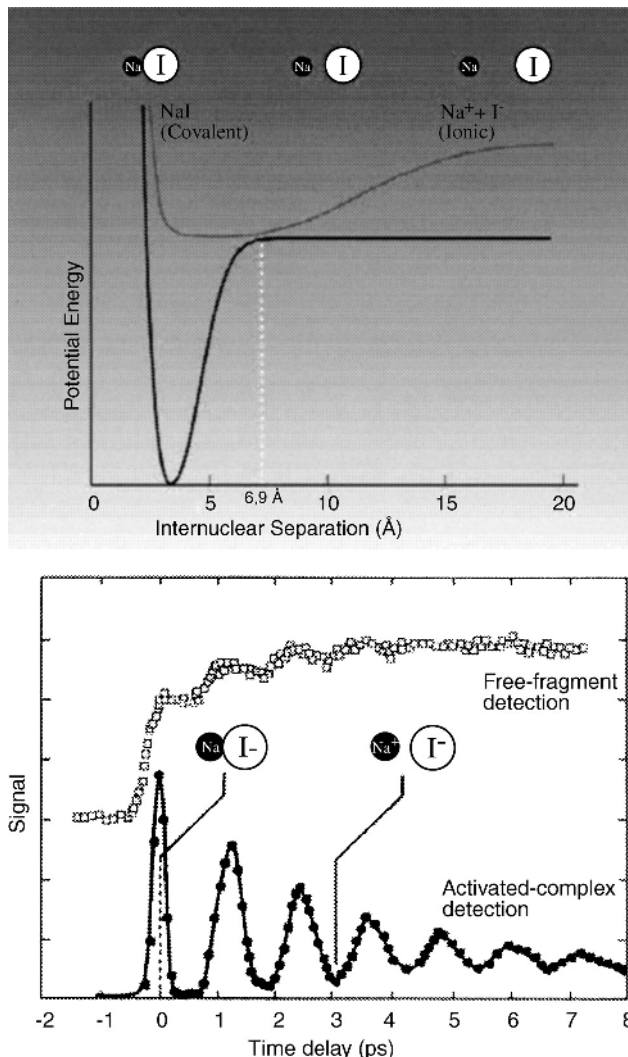


Fig. 9.36. Photodissociation of NaI by a short pulse. The energy-level structure is shown and experimental curves showing excited-state molecular vibration and the periodic release of sodium atoms are shown (Adapted from [9.202])

process occurs in 300 fs [9.204]. Similar molecular twisting occurs in a timescale of 200 fs in retinal, which is part of the rhodopsin molecule active in the light absorption in the vision process. The schematic construction of a light-harvesting photosynthetic pigment are included in Fig. 9.37.

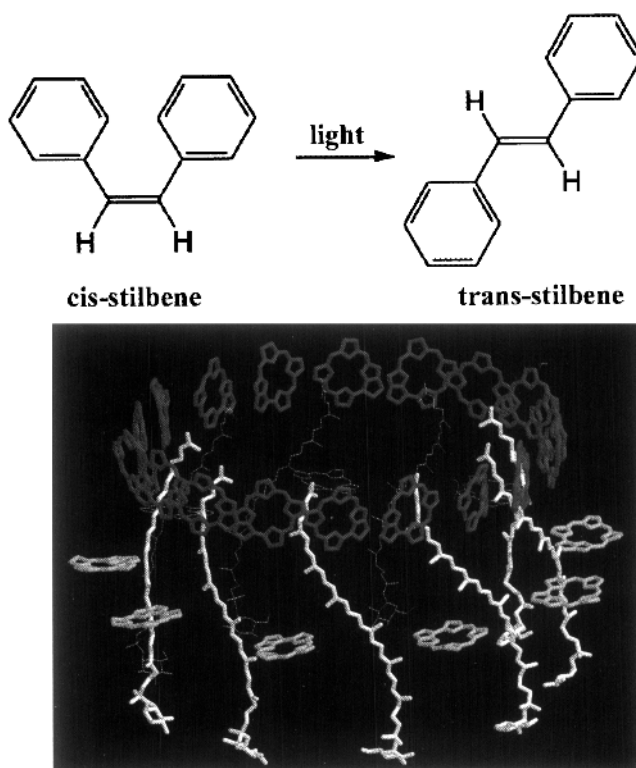


Fig. 9.37. Photoisomerisation of stilbene (*upper part*), and the structure of a light-harvesting photosynthetic pigment (including chlorophyll and carotenoid building blocks) (*lower part*; Courtesy: V. Sundström)

9.5.3 Coherent Control

Normally, only the frequency and the intensity of a light field are considered in the interaction of radiation with matter. With the availability of short-pulse radiation with well-defined phase properties it has become possible to interact coherently with matter, opening up new possibilities of controlling chemical reactions and light-matter interactions. We will here consider two aspects of this quickly evolving field: coherent chemistry and interference effects profoundly changing the absorptive properties of matter.

Coherent Chemistry. Short-pulse laser radiation normally leads to broad and rather unspecific excitation of vibrational modes (See also Sect. 10.4). By tailoring the pulses, which typically would have a pulse length of 100 fs, by sending them into a pulse shaper, certain modes can be enhanced and others be suppressed. In particular, discrimination between chiral molecules (right- or left-handed) otherwise performing in an identical way could be considered. A pulse shaper is a stretcher-like arrangement (Sect. 8.7.2) with

an electro-optical or liquid-crystal modulator between the gratings to modify the frequency contents. The modulator can be operated in a learning loop to achieve optimum spectral modification for enhancing selected spectral features. By strongly driving certain vibrations it might become possible to perform selective chemistry (Sect. 10.4) [9.205, 9.206].

Electromagnetically Induced Transparency and Lasing Without Inversion. The traditional requirement for population inversion in order to achieve gain in a laser has recently been challenged. As a matter of fact, it is possible to eliminate the lower state absorption by simultaneously pumping two suitably chosen transitions, for which a quantum-mechanical interference brings about an elimination of the absorption. The phenomenon is called *electromagnetically induced transparency* (EIT) [9.207] and forms the basis for various theoretical predictions of the *lasing without inversion* phenomenon [9.208–9.213], which has also been experimentally demonstrated. The phenomenon is of particular interest for achieving powerful X-ray lasing with lower pulsed pumping requirements, although a lot of the work in this field actually has been performed with narrow-band CW lasers.

The electromagnetically induced transparency leads to a very steep change in the index of refraction around the nominal transition frequency (see also Fig. 9.28). Still, the value is all the time close to 1, meaning that the phase velocity is very close to the speed of light in vacuum. However, a pulse of light contains different Fourier components which develop slightly different phase velocities and thus get out of phase with each other, leading to the pulse envelope travelling much more slowly than the individual frequency components. The pulse speed, or the group velocity, is inversely proportional to the slope of $n(\omega)$, and light velocities as low as 10 m/s have been observed in certain experiments while light has been brought to a full stop in others [9.214]. Using light beams propagating at low velocities means that very long interaction times become possible, possibly enabling nonlinear optics to be performed at the single-photon level [9.215].

9.6 High-Power Laser Experiments

High-power, short-pulse lasers, as described in Sect. 8.7.2, have made possible new types of basic physics experiments, and applications are also emerging. Extremely high focused intensities can be obtained with the new types of sources. To get a feeling for the numbers involved we note that if 1 TW laser radiation is focused down to a $10\text{ }\mu\text{m}$ diameter spot size, a power density of about 10^{18} W/cm^2 is obtained, corresponding to an optical electric field strength of about $3 \times 10^{10}\text{ V/cm}$. In comparison, it could be noted that an electron in the ground state of hydrogen experiences a Coulomb field of about $5 \times 10^9\text{ V/cm}$. Thus, instead of being a small perturbation to the atomic potential, as discussed in Chap. 4, the field interaction now becomes the

dominant one, posing new challenges to theoretical atomic physics. General overviews of this swiftly developing field are given in [9.216–9.233].

9.6.1 Above Threshold Ionization (ATI)

The process of regular photoionization was considered in Sect. 9.1.4. The electron released in the photoionization attains a kinetic energy which equals the excess energy of the photon above the ionisation limit I_p . Frequently, a multi-photon process is needed to attain sufficient energy for ionization. If the power of the ionizing field is increased and the energy of the electrons released is measured, e.g., by a time-of-flight spectrometer, several peaks separated by the laser photon energy are observed, as shown in Fig. 9.38 [9.234, 9.216]. The electron can pick up the total energy of several photons up to a maximum number determined by the power of the laser light. The

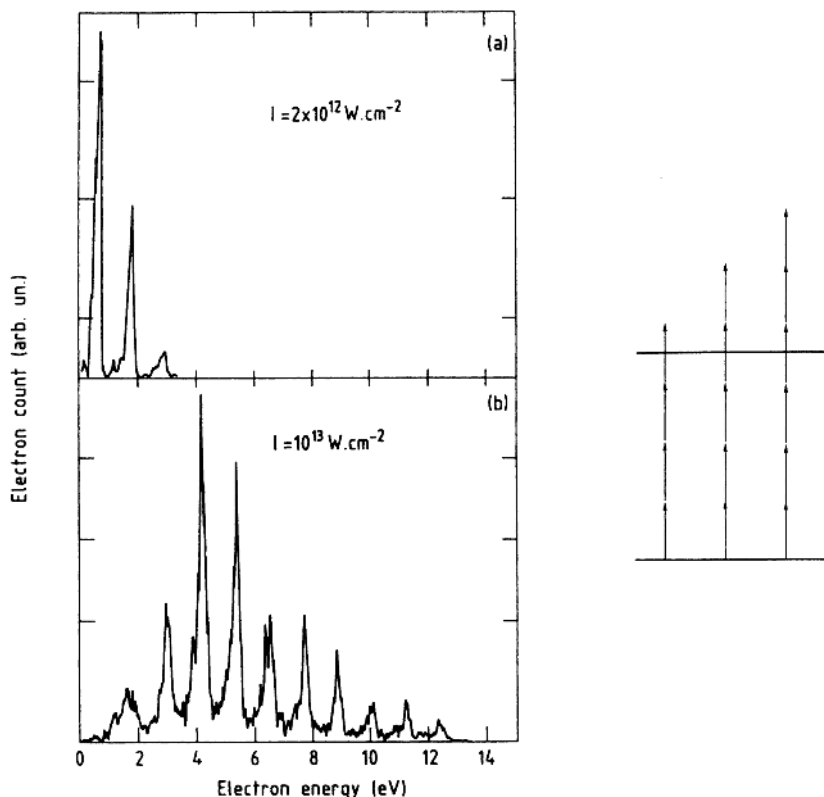


Fig. 9.38. ATI spectra for xenon atoms irradiated with intense pulses from a Nd:YAG laser (1064 nm, 1.1 eV). (a) Electron energy spectrum obtained for $I = 2 \times 10^{12} \text{ W/cm}^2$, (b) corresponding spectrum for $I = 10^{13} \text{ W/cm}^2$. The insert shows a schematic view of the lower-power process (From [9.216])

strongly nonlinear process, which is schematically depicted in the insert of Fig. 9.38, is referred to as *Above Threshold Ionisation* (ATI). For not-too-high intensities (Fig. 9.38a) it can be described by perturbation theory and extensions thereof. Each peak corresponds to a certain order of perturbation theory, and the strength of the peaks correspondingly falls off quickly. However, if the intensity is increased (Fig. 9.38b) we see a completely different behaviour, indicating the breakdown of perturbation theory. New theory developments thus became necessary [9.234–9.240]. The oscillation (*quiver*) energy U_p of the external weakly bound electrons in the oscillating field E becomes non-negligible. U_p is frequently referred to as the *ponderomotive potential*:

$$U_p = \overline{mv^2}/2 = e^2 E^2 / 4m\omega^2 \quad (9.21)$$

(e and m are the electronic charge and mass, respectively, and ω is the angular frequency of the light field $E \sin \omega t$; the mean value of $\cos^2 \omega t$, occurring in the calculation, is $1/2$). To free an electron from the atom the additional energy of U_p is needed; thus the ionization potential I_p is effectively increased by this amount. Thus, a shift by U_p in the kinetic energy of the released electron is observed.

For even higher intensities and, in particular, when short pulses are employed, a strong AC Stark effect due to the electric field in the pulse is obtained. In the rising electric field of the laser pulse, real atomic energy levels are swept into resonance, temporarily increasing the ionization yield [9.241]. This gives a stronger weight to certain energies in the monitored spectrum, which starts to display features related to the atomic bound states, as shown in Fig. 9.39.

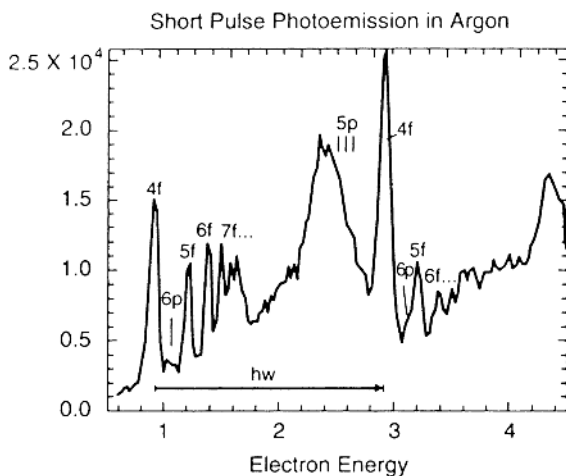


Fig. 9.39. ATI spectrum for Ar atoms recorded for 616 nm (2 eV) pulses with a pulse length of 0.2 ps [9.241]

When molecules are subjected to high-power laser radiation, ionization occurs, but of course so too does violent photodissociation. When a lot of electrons are removed, the remaining highly charged atoms cannot stay together; a *Coulomb explosion* occurs. High-power dissociation processes are discussed in [9.242–9.246].

9.6.2 High Harmonic Generation

When a high-power laser beam is focused onto a gas jet of inert gas atoms, odd high harmonics are generated [9.247, 9.248]. Even harmonics are not obtained due to symmetry considerations. The process clearly is in competition with the ATI phenomenon just discussed. High-harmonic generation is now relatively well understood [9.249] and overviews are given in, for example, [9.250, 9.251]. The first step is a tunnelling of an external electron through the barrier due to the Coulomb field combined with the electric field of the laser light. The situation is similar to the one shown in Fig. 2.14. The electron is accelerated in the optical field and is then forced back towards the nucleus when the field switches direction. Passing in the vicinity of the nucleus, it recombines with the ion and harmonic radiation is emitted, as schematically shown in Fig. 9.40 [9.252]. The highest order harmonics are obtained for the light inert gases such as He and Ne, but the most efficient generation of lower harmonics is in the heavy gases such as Kr and Xe. Experimental recordings of high harmonics are shown in Fig. 9.41 [9.253]. The shortest wavelength obtained through high-harmonic conversion using pulse lengths around 100 fs is of the order of 7 nm. Thus, the 109th harmonic for a titanium sapphire laser at 806 nm [9.254], the 143rd harmonic for a Nd:Glass system at 1053 nm [9.255] and the 37th harmonic of a KrF laser at 248 nm [9.256] have been achieved. Using ultrashort pulses with pulse lengths below 10 fs employing titanium sapphire technology it has become possible to reach the water window [9.257, 9.258] (see also Sect. 5.1.3), corresponding to harmonic orders of about 200. The reason that the water-window could be reached with short-pulse lasers but not with the longer pulses is that an ultrafast rise

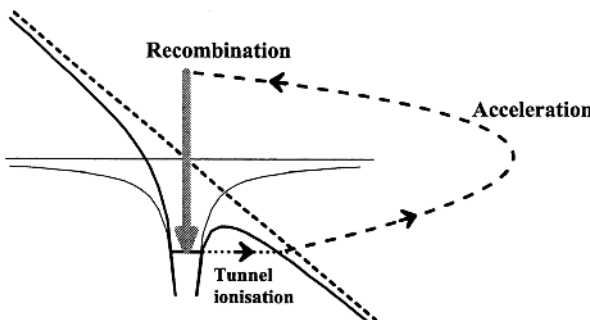


Fig. 9.40. Schematic description of high-harmonic generation in atoms [9.252]

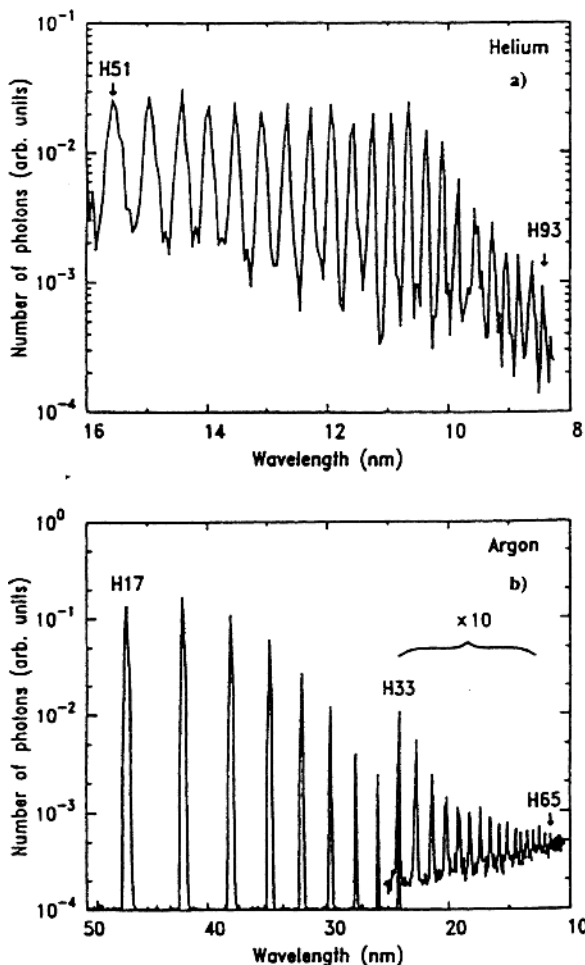


Fig. 9.41. Harmonics from He and Ar pulsed jets when the focused laser intensity was approximately 10^{15} W/cm^2 [9.253]

time leaves less time for competing ionization. Much effort has been put into understanding the high-frequency cut-off for the harmonics. Considering the single-atom response only, the cut-off is given by [9.249]

$$E_{\text{cut-off}} = I_p + 3.2 U_p, \quad (9.22)$$

where I_p is the ionization potential and U_p is the ponderomotive potential. Experimentally an earlier cut-off is observed [9.253]. This is because of phase mismatch in the collective generation by an ensemble of atoms. Also this effect is now well understood.

In order to develop high harmonics into an attractive general purpose source of spectroscopic radiation it is necessary to optimize the generation

efficiency with regard to focus geometry, gas density, etc., and many studies along these lines, as well as for the temporal and spatial characterization, have been performed [9.259–9.261]. It should be noted that short-pulse harmonics are for Fourier-transform reasons by necessity broad, putting limitations on the spectral resolution.

The harmonics are particularly attractive in terms of the radiation peak power, which can be 10^5 times higher than for synchrotron undulators. Thus, it should open the way for nonlinear laser spectroscopy in the short-wavelength (10 nm) regime. A competing technology requiring much larger installations is *Self Amplified Spontaneous Emission used for Free-Electron-Laser* action (SASE-FEL) [9.262].

Harmonics are tunable when the primary laser radiation is obtained from a tunable laser, such as a titanium-doped sapphire laser. However, the need for wavelength-dependent adjustments in the CPA chain can make the tuning

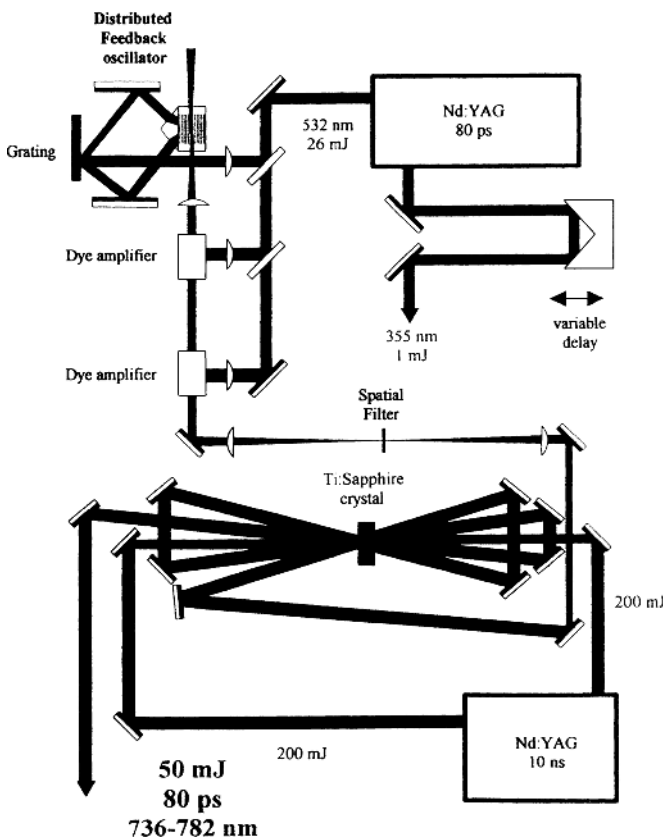


Fig. 9.42. Lay-out of a spectroscopic high-peak-power, fully tunable combined dye/Ti:S laser system, suitable for the generation of narrow-band, tunable harmonics [9.263, 9.264]

procedure tedious. The laser system illustrated in Fig. 9.42 is easier to tune [9.263, 9.264]. A *distributed feedback dye laser* (DFDL) oscillator [9.265] is used, where the wavelength selection is performed by changing the angles of the two short-pulse Nd:YAG pumping beams, changing the separation of the gain regions set up by constructive light interference in the dye. Fine tuning can be achieved by changing the temperature of the dye. Two dye amplifier cells and a multi-pass titanium-sapphire final amplifier are used to boost the 30 ps pulses to power density levels close to the material damage limit. Since the CPA techniques are not used, the entire system tunes easily together with the DFDL oscillator. The peak power is still enough for this system to generate low harmonics (7th - 21st) in a jet of Kr or Xe. In this way a very interesting fully tunable laser source for the XUV region has been achieved, featuring a high spectral resolution feasible with pulse-lengths of tens of ps rather than tens of fs.

As discussed in Sect. 9.4.3, experimentally determined radiative properties of free atoms and ions are of great interest for testing atomic theories, and more practically, for astrophysics, plasma and laser physics. With the availability of the Hubble Space Telescope the VUV spectral region, out of reach for terrestrial observation, has become accessible and there is a great need for accurate data in the short-wavelength region. The most straightforward way to measure excited-state lifetimes is to perform a selective laser excitation and then observe the exponential decay of the light intensity from the excited state [9.127]. Such measurements are described in Sect. 9.4.2. The VUV region can be assessed by stimulated Raman scattering or by four-wave mixing. Narrow-band harmonic generation as discussed here gives access to even shorter wavelengths (the XUV region). The available energy for the excitation is low, and direct fluorescence light observation is not possible. Instead, a more efficient detection method using a pump/probe scheme (Sect. 9.5.1) can be used to follow the decay. Such a technique using optical delays of the probe beam also eliminates problems with limited time response for the detection system. As an example, a measurement of the radiative lifetime of the $2p\ ^1P_1$ states of helium is chosen [9.264]. The experimental set-up used is shown in Fig. 9.43. To excite the $2p$ state (with a transition energy of 21 eV, i.e. 58.4 nm), the DFDL in Fig. 9.42 was tuned to 760 nm and the 13th harmonic was selected with a normal-incidence spherical grating. Helium atoms were excited and the number of excited atoms was probed by photoionization using a temporally delayed pulse, chosen to be the second or the third harmonic of the Nd:YAG pump laser. The resulting ions were detected by a microchannel plate detector after passage through a time-of-flight (TOF) spectrometer that was tuned to the helium mass. An experimental decay curve for the $2p$ state is given in Fig. 9.44. The techniques can also be extended to the study of radiative properties of simple molecules with absorption in the VUV spectral region and also to perform non-linear laser spectroscopy [9.266].

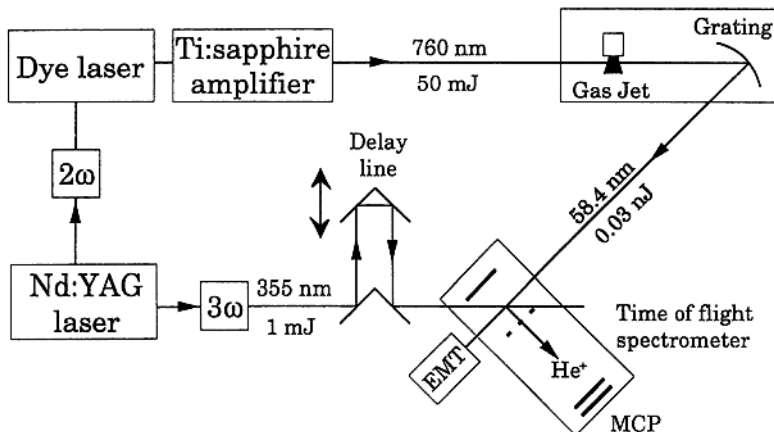


Fig. 9.43. Set-up for delayed photoionization measurements on helium atoms, excited by high-harmonic radiation [9.264]

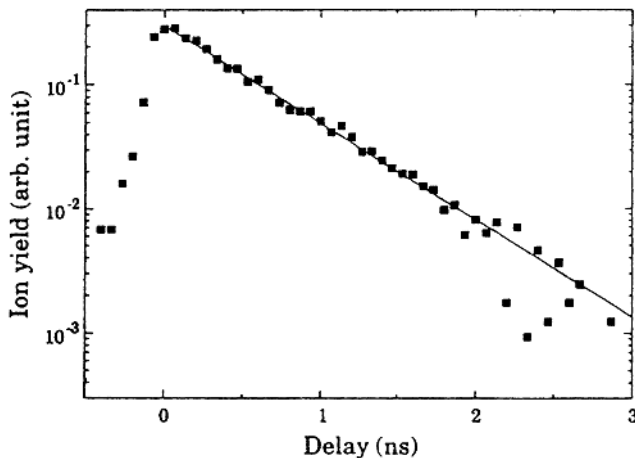


Fig. 9.44. Experimental decay curve for the $2p\ ^1P_1$ state of He [9.264]

The tunability of such a system could also be utilized for measuring autoionisation widths of Rydberg states of molecules [9.267]. More fundamentally, similar techniques, emphasizing a maximal resolution, have been used for studies of the He atom, yielding accurate Lamb-shift data [9.268].

Photoionization experiments are conveniently performed with monochromatized synchrotron radiation. However, if a high temporal resolution is required, harmonics provide unique possibilities, as recently demonstrated [9.269].

Harmonics constitute a source of coherent XUV radiation that can be utilized for interferometric measurements of electron densities in plasmas,

which cannot be studied with visible radiation because of strong refraction and absorption by the plasma. A very high temporal resolution is obtained using short-pulse high harmonics [9.270].

An interesting aspect of high-order harmonics is the potential possibility of generating a train of attosecond pulses [9.271], recognising the conceptual similarity between the energetically equidistant high-order harmonics and the cavity modes in a CW laser, which can be locked together for femtosecond pulse generation (Sect. 8.7.1). The challenge is to assure phase-locking and to isolate individual attosecond pulses, and different approaches have been suggested and demonstrated [9.272]. Pulses of a duration of about 10^{-16} s (100 as, corresponding to the classical orbiting time of a ground-state hydrogen electron or the vibrational time period in small molecules) should be achievable, opening up a new field of ultrafast spectroscopy. Measuring techniques on this timescale need to be developed. It is interesting to note that attosecond pulse generation requires a very wide bandwidth, about 20 eV (see (8.19)), which can be understood from the Heisenberg uncertainty relation or, more technically, from the mathematical properties of the Fourier transform. Such a wide frequency range is only available in the high-frequency domain, well beyond the visible region ($\nu = 5 \times 10^{14}$ Hz).

9.6.3 X-Ray Laser Pumping

Achieving population inversion in the X-ray regime is difficult because of the strong probability of spontaneous emission for such frequencies (8.1). As mentioned in Chap. 8, soft X-ray lasing was first demonstrated in neon-like selenium, yielding emission at about 21 nm [9.273]. Since then an intense research activity has been pursued [9.274] involving mainly *collisional and recombination schemes*. Initially, very large lasers with low repetition rates had to be used for achieving X-ray lasing. The shortest wavelength achieved so far is 3.5 nm for collisional pumping of nickel-like gold [9.275]. The neon-like zinc laser at 21.2 nm is particularly efficient and easy to operate, and has been employed in applications [9.276].

The development of high-repetition-rate and moderate pulse-energy systems as described in Sect. 8.7.2 has opened the possibility of achieving more practical soft X-ray lasers. Special attention has been given to *optical field-ionization* (OFI) schemes [9.277] using gaseous media. Detailed spectroscopy of laser-produced plasmas is needed for locating gain line candidates. The experimental set-up is then very similar to the one used in the studies of high-harmonic generation. Search for gain can be performed by observing the emission of the laser-produced gas plasma in the forward direction and in a perpendicular direction. Gain is manifested by stronger forward emission for certain lines and has been identified, e.g. for ionized nitrogen and oxygen [9.278, 9.279]. Particularly spectacular is the demonstration of strong amplification in Xe^{8+} at about 42 nm [9.280], as illustrated in Fig. 9.45. Efficient soft X-ray laser emission in neon-like argon at 46.9 nm has also been achieved

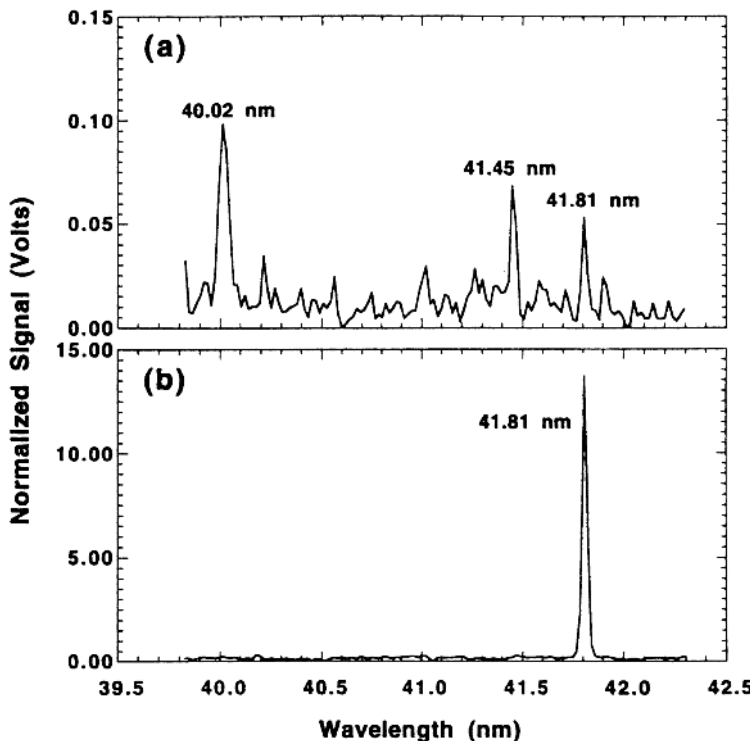


Fig. 9.45. Emission lines of Xe^{8+} for gas pressures of 3 and 12 torr, respectively (note the x100 change in scale). The strong amplification of spontaneous emission at about 42 nm is clearly demonstrated [9.280]

using a strong capillary electrical discharge in argon gas [9.281]. Recent progress in the field of X-ray lasers is comprehensively covered in the proceedings of the International Conferences on X-ray Lasers [9.282–9.286].

9.6.4 Broadband X-Ray Generation

By focusing sub-picosecond terawatt pulses on solid targets consisting of atoms with a high nuclear charge Z , intense X-ray radiation can be obtained. An experimental set-up for such experiments is shown in Fig. 9.46. In contrast to the situation when nanosecond pulses are employed, there is no time for the formation of an expanding plasma that would shield off the main part of the impinging pulse. Thus, femtosecond laser pulses may lead to the formation of a solid-density plasma. The plasma radiates at all wavelengths, from microwaves to hard X-rays. It has been shown that photon energies of the order of MeV can be obtained [9.287, 9.288]. The measurement of the spectrum poses difficult problems since the radiation is produced in ultrashort (10^{-12} s), extremely intense bursts followed by intermissions that

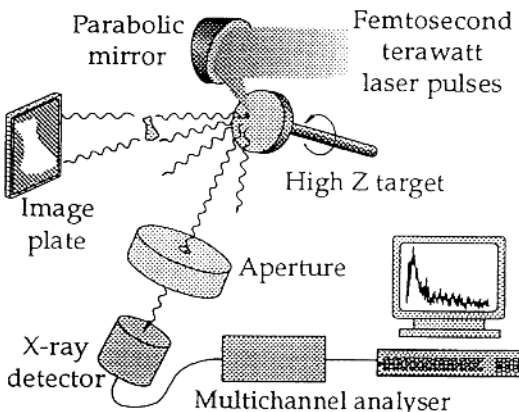


Fig. 9.46. Experimental set-up for the generation of ultrashort broadband hard X-ray radiation [9.293]

are typically 10^{11} times longer. Thus, solid-state detectors, developed for low-intensity conventional X-ray and γ -ray spectroscopy are hampered by heavy pile-up problems. By using energy-dispersive detectors in Compton-scattering geometry or specially developed X-ray spectrometers it is still possible to characterize the spectrum [9.289, 9.290], which consists of a broad continuum with superimposed characteristic lines. The new X-ray source has special properties and can have medical applications, as already discussed in Sect. 5.1.3. Imaging on standard radiological image plates using a laser-driven X-ray source has been demonstrated [9.288, 9.291].

Differential absorption radiography using monochromatic X-rays above and below the K absorption edge of a contrast agent such as iodine (33 keV) has been demonstrated (Fig. 5.13) using synchrotron radiation for angiographic applications [9.292]. Such measurements using the characteristic lines from Gd and W targets bridging the K-edge (at 50 keV) of gadolinium have also been demonstrated [9.293].

The extremely short duration of the X-ray burst can be utilized for gated viewing through tissue in order to eliminate Compton-scattered X-rays blurring the image. While multiple scattering is massive in the optical regime, calling for the development of reduced-scattering methods for optical mammography as will be discussed in Sect. 10.5.4, elimination of the less prominent X-ray scattering, particularly for thick tissue imaging, can be advantageous from a dose-reduction point of view [9.294]. Monte Carlo simulations on X-ray transport through tissue in tissue give insight in the process, and experiments employing an X-ray streak camera for one-dimensional imaging through thick tissue phantoms clearly demonstrate the gating effect [9.295]. In Fig. 9.47, the shadow of a small lead object is recorded time-resolved through water layers of increasing thickness. It can be clearly seen that a sharp shadow is obtained using the “ballistic” X-rays, even when

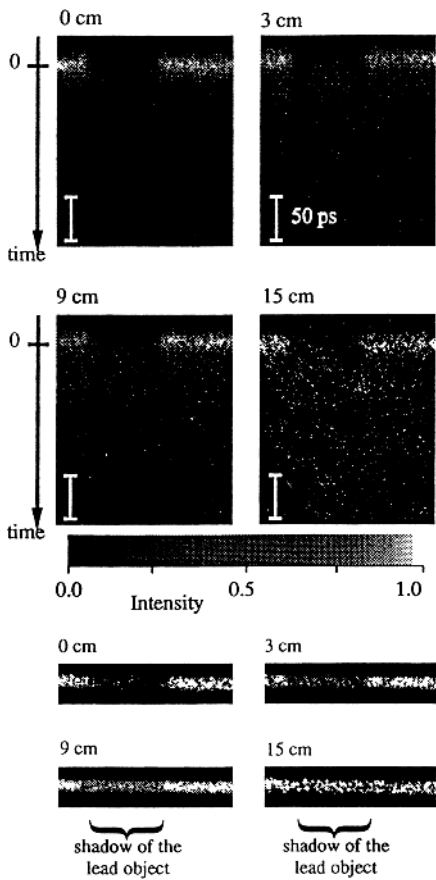


Fig. 9.47. Gated viewing recordings of a small lead object using short-pulse X-ray bursts passing through water layers of different thicknesses. In the lower part of the figure time-integrated representations are shown, clearly demonstrating the loss of contrast for thicker samples [9.295]

imaging through 15 cm of water, while the time-integrated images in the lower part of the figure show a strong loss of contrast. Scattering reduction is particularly valuable in volume tomography and the gating principle has also been demonstrated for the tomographic case [9.296]. The future of these techniques will be strongly coupled to the potential development of efficient gateable imaging X-ray detectors. The radiotoxic equivalence between a given dose (Grays) of conventionally produced X-rays and a corresponding dose of laser-produced X-rays, having 10^{10} higher peak power, has been established in cell culture experiments [9.297].

Short pulses of softer X-rays of, for example, 3 keV energy are very attractive for time-resolved diffraction studies of complex molecules and solids [9.298]. The duration of laser-produced X-rays is much shorter (1 ps) than

what is available from synchrotrons (100 ps) and a lot of work has been invested in developing laser-based time-resolved diffraction [9.299] and combined synchrotron/laser approaches [9.300].

9.6.5 Relativistic Effects and Laser Accelerators

When the ponderomotive energy of an electron in a laser field is of the order of 1 MeV, the speed of the electron becomes a substantial fraction of that of light and relativistic effects start to occur [9.301]. The relativistic effects cause a self-focusing of a high-power laser beam, which produces a plasma in a gas target. A plasma column can be a useful source of X-ray laser radiation [9.302]. The intense fields in the optical pulse cause acceleration effects and various schemes for laser particle acceleration have been proposed, including *wake-field acceleration* [9.303]. Acceleration of an electron to an energy of 50 MeV in a distance of just 1 mm has been demonstrated, suggesting that laser techniques will find important applications in future accelerator technology. A further strongly relativistic effect of high power laser beams is the creation of matter (production of electron–positron pairs). The required power density would be of the order of 10^{30} W/cm^2 for production in vacuum.

9.6.6 Laser-Nuclear Interactions and Laser-Driven Fusion

We have seen that intense laser radiation can induce hard X-rays and accelerate particles to high energies. Thus it is not unexpected that even nuclear reactions can be induced. A number of such experiments have recently been made [9.304]. In particular, laser-accelerated protons can be used to produce short-lived isotopes of great importance for nuclear medical-imaging techniques such as *Single Photon Emission Computed Tomography* (SPECT) and *Positron Emission Tomography* (PET). The protons might also be used for direct tumour irradiation [9.305].

Gamma-ray laser action is a further related field which has attracted much efforts [9.306]. Laser-driven (inertial confinement) fusion using the largest laser installation is a huge research field for laser-nuclear interaction [9.307]. The laser energy requirements for “conventional” laser-driven deuterium-tritium fusion seem to be difficult to reach. This has stimulated the development of a modified concept, the “*fast igniter*” scheme, where an extremely intense (petawatt) laser pulse is fired into the pre-compressed plasma [9.308].

9.7 High-Resolution Laser Spectroscopy

In this section we will describe a number of high-resolution methods, in which the extremely narrow linewidth of single-mode lasers is utilized. Various

ways of eliminating Doppler broadening have been investigated leading to the development of Doppler-free laser spectroscopic techniques. The effective linewidth that is experimentally obtained is determined by a number of effects:

- The natural radiation width.
- Residual Doppler broadening, in particular the second-order Doppler effect (due to the time dilatation effect $(1 - v^2/c^2)^{1/2}$ in (9.11), which is present irrespective of the direction of motion.
- The laser linewidth.
- The transit time broadening, due to the finite time that an atom dwells in the laser beam because of its motion (see also Sect. 7.1.2).

We will first describe spectroscopy on *collimated atomic beams* and on *kinematically compressed ion beams*. Two groups of nonlinear spectroscopic techniques will be discussed: *saturation techniques* and *two-photon absorption techniques*. We will also deal with the optical analogy to the Ramsey fringe technique (Sect. 7.1.2). In a subsequent section (Sect. 9.8) laser cooling and atom- and ion-trap techniques will be discussed. Here, the particles are basically brought to rest, eliminating the Doppler as well as the transit broadening effects.

9.7.1 Spectroscopy on Collimated Atomic and Ionic Beams

As we have already noted (Sect. 6.1.1), a well-collimated atomic beam displays a very small absorption width perpendicular to the atomic beam. As shown in Fig. 9.48, the collimation ratio C for an atomic beam is defined as

$$C = s/d. \quad (9.23)$$

The residual (first-order) Doppler broadening $(\Delta\nu_D)_{\text{res}}$ for a collimated atomic beam is given by

$$(\Delta\nu_D)_{\text{res}} \simeq \frac{\Delta\nu_D}{C\sqrt{2}}, \quad (9.24)$$

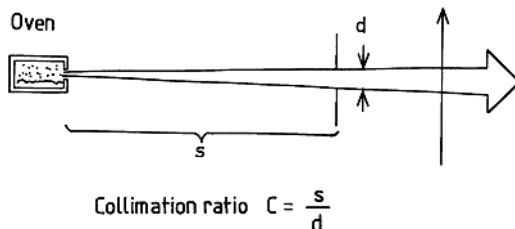


Fig. 9.48. Definition of the collimation ratio

where $\Delta\nu_D$ is the normal Doppler broadening. High-resolution spectroscopy can be performed by irradiating such a beam at right angles with a narrow-band, single-mode laser. With a collimation ratio of 100 a typical residual Doppler broadening of 5 MHz is obtained.

The atomic-beam technique is a very versatile one. Atomic beams can be produced for essentially any element, whereas conventional cell techniques are limited to a temperature interval up to about 1000 °C. Besides reducing the Doppler width, collisional effects are significantly reduced with the atomic-beam technique compared with cells. The possibility of utilizing spatially separated interaction regions along the beam is also valuable in certain cases. We note that the most probable velocity v of a thermal atomic beam emerging from an oven is

$$v = \sqrt{\frac{3RT}{M}}, \quad (9.25)$$

where T is the absolute temperature, M the mass number and R the gas constant. This formula results in typical thermal velocities of about 300 m/s. Typical mean free paths between collisions with residual gas in the vacuum system are about 10 m at 10^{-5} torr. There are several methods for detecting the narrow resonance induced by the laser. In Fig. 9.49 a few methods are illustrated:

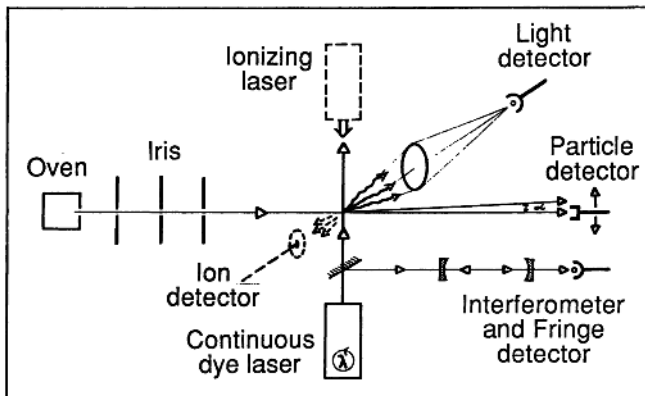


Fig. 9.49. Laser spectroscopy with a collimated atomic beam. Three different detection methods are illustrated

Detection Through Fluorescence. The most direct way to study optical resonance is to observe the *fluorescence light* that is released after the excitation. In Fig. 9.50 a schematic spectrum for the D_2 line in ^{23}Na is shown ($3s^2S_{1/2} \rightarrow 3p^2P_{3/2}$). Two well-separated component groups corresponding to the ground-state hyperfine splitting occur. The components corresponding to the small excited-state splittings are well resolved and the a and b constants

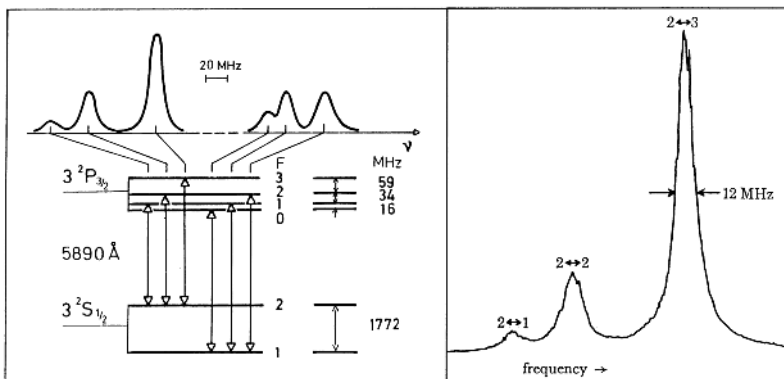


Fig. 9.50. Schematic representation of the hyperfine structure in the sodium D_2 line. An experimental curve from a well-collimated sodium beam is included [9.154]

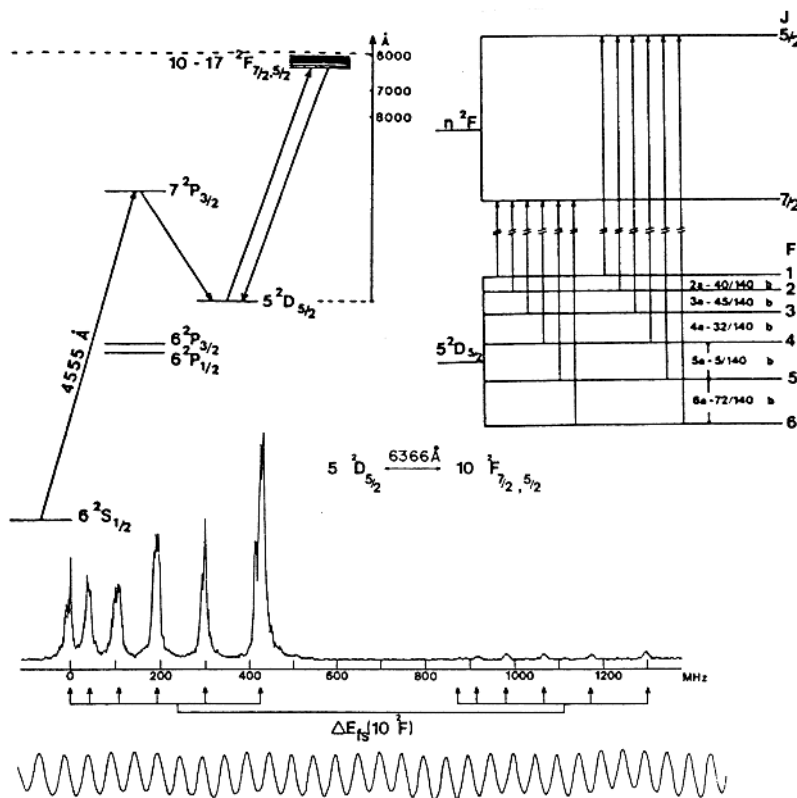


Fig. 9.51. Recording of a D-F cesium transition obtained in a collimated atomic beam experiment using stepwise excitations [9.309]

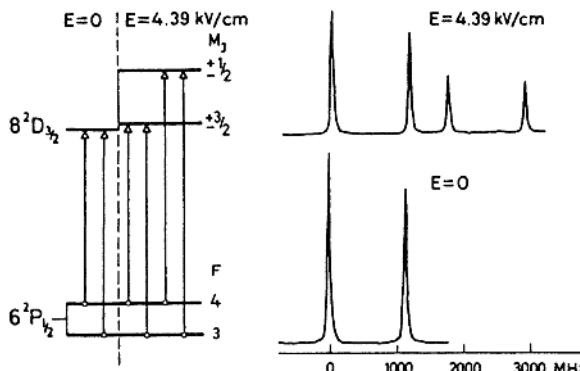


Fig. 9.52. Stark-effect determination in the transition in $6^2P_{1/2} - 8^2D_{3/2}$ ^{133}Cs . The lower state has too low a polarizability to be affected by the electric field [9.118, 9.310]

for the hyperfine structure can be evaluated. The natural radiation width corresponding to $\tau = 16\text{ ns}$ for the $3p^2P_{3/2}$ state is 10 MHz . As can be seen from the inserted experimental curve, such a linewidth can be approached. In Fig. 9.51 a further example of this type of spectroscopy is given. Here a broadband cw laser has been used to populate the rather long-lived $5d^2D_{5/2}$ ($\tau \sim 1\mu\text{s}$) state in ^{133}Cs in the cascade decay of the primary excited $7p^2P_{3/2}$ state. A narrow-band laser is swept through the components of the $5d^2D_{5/2} \rightarrow 10f^2F_{7/2,5/2}$ transition. The inverted hyperfine structure of the lower state and the inverted fine structure (evident from the intensity ratio between the low- and high-frequency groups) of the highly excited state are shown. The hyperfine structure of the F-state is too small to be resolved.

An example of the Stark effect is given in Fig. 9.52. Note, that while only the tensor Stark interaction constant α_2 (Sect. 2.5.2) can be determined in an LC experiment (Sect. 7.1.5; Fig. 9.18), the scalar interaction constant α_0 can be obtained in this type of experiment as well as α_2 . In the same way, isotope shifts can be measured by direct optical high-resolution methods while resonance methods and quantum-beat spectroscopy can only be used for measurements of splittings within the *same atom*.

Detection by Photoionization. In this method the atomic beam is simultaneously irradiated by a narrow-band laser and an intense laser. The latter has a sufficient photon energy to photoionize the atoms that are transferred to the excited state, while ground-state atoms cannot be ionized. The photoelectrons are detected in an electron multiplier, which is constructed like a photomultiplier tube but without a photocathode. For the case of very long-lived Rydberg atoms, field ionization can also be applied as an efficient detection method. During a period of $10\mu\text{s}$ atoms move several mm, and it is possible to physically separate a field-free laser interaction region from the field-ionization region [9.311].

Detection by the Recoil Effect. When an atom absorbs a photon impinging perpendicularly to the direction of flight of the atom the photon momentum

$$p = h\nu/c \quad (9.26)$$

is transferred to the atom. For a sodium atom absorbing a D-line quantum the transverse velocity change is about 3 cm/s. The atom is then deflected by an angle given by

$$\alpha \simeq p/mv \simeq 10^{-5} \text{ rad}, \quad (9.27)$$

where m and v are the mass and the velocity of the atom, respectively. If the atom is de-excited by stimulated emission, the absorbed perpendicular momentum is cancelled by the recoil of the atom when the stimulated photon is emitted in the same direction as the incoming light. On the other hand, if spontaneous decay occurs, the direction of the recoil will be randomized. Thus, on average, a transverse momentum is transferred to the atomic beam, which is deflected and also broadened. At optical resonance the intensity at a particle detector placed in the path of the original atomic beam is reduced. The deflection of the beam depends on the intensity of the laser and the length of the interaction region. Deflections are normally small ($\sim 1^\circ$). In principle, isotopes can be separated in this way by isotope-selective excitation. However, more efficient methods have been developed (Sect. 10.4.2). Beam deflection under the influence of resonance radiation was demonstrated as early as in 1933 using classical lamps [9.312]. Beam deflection due to laser radiation is much more efficient [9.313].

The mechanical influence of light on atoms and particles was noticed early on when observing the comet tails pointing away from the sun. Particle acceleration with laser light was also considered early on [9.314]. Cooling and trapping with laser light is discussed in Sect. 9.8.

Detection by Magnetic Deflection. In one version of this kind of experiment the atomic beam in an ABMR apparatus (Sect. 7.1.2) is irradiated by a sharply tuned laser in the C region. At optical resonance, a flop-in signal is obtained due to the pumping of atoms with $\mu_{\text{eff}} < 0$ into states with $\mu_{\text{eff}} > 0$. A single inhomogeneous magnetic field, e.g., from a sextupole magnet, can also be used for non-optical signal detection. The atomic beam emerging from the source is perpendicularly irradiated by the laser beam before it enters the sextupole magnet, which focuses $\mu_{\text{eff}} < 0$ atoms and deflects $\mu_{\text{eff}} > 0$ atoms. The focused atoms hit the detector, which can be the entrance slit of a mass spectrometer. Such a detection system is particularly valuable when dealing with small amounts of radioactive atoms. When the laser beam pumps atoms from one F-state into another in a field-free region, a flop-in (increase) or a flop-out (decrease) signal is recorded, depending on which Paschen-Back group a particular F-level communicates with. In Fig. 9.53 an example of this type of experiment for radioactive alkali metal elements is shown. Extensive

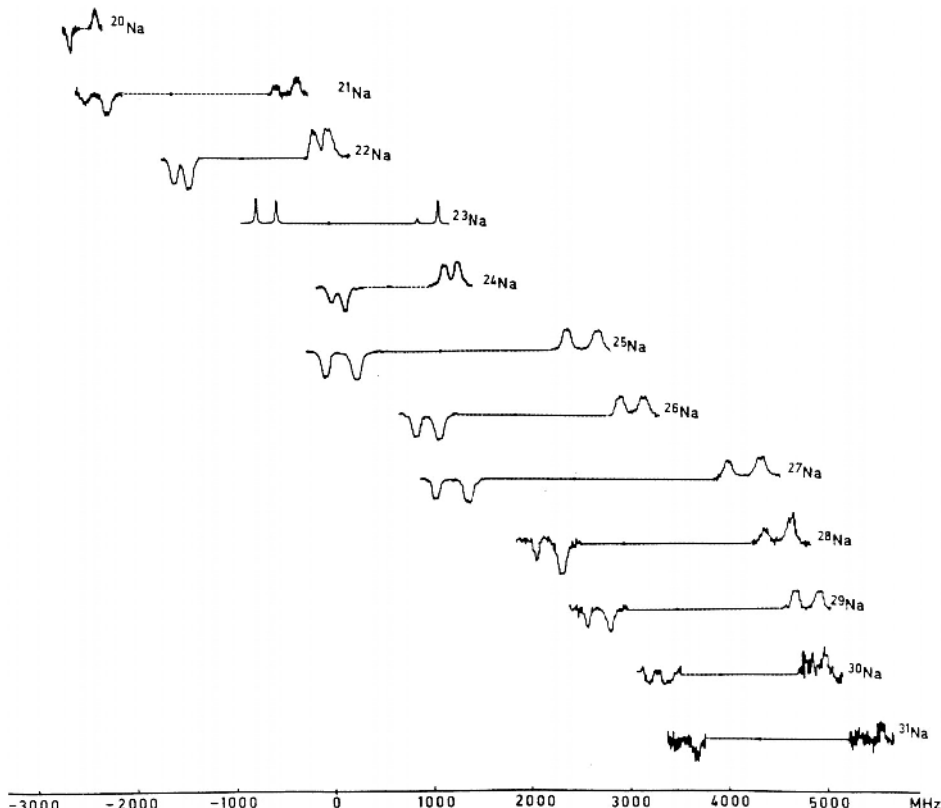


Fig. 9.53. Recordings illustrating hfs and isotopic shifts between different isotopes of sodium. The recordings were made on collimated beams and detection by magnetic deflection was used [9.315]

measurements of short-lived radioactive isotopes of the alkali metal elements, including francium, have been performed [9.316, 9.317].

As we have seen, magnetic deflection can be used for the detection of optical resonance. However, laser beams can also be used to replace the inhomogeneous A and B magnets in ABMR (Fig. 7.5). The laser is then tuned to substantially reduce the population of a particular F-level while the atoms are in the A region. A beam from the same laser is used in the B region, where the fluorescence induced by the beam is monitored. Here the light is reduced as a result of the low F-state population. However, if $\Delta F = \pm 1$ transitions from neighbouring, well-populated levels are induced in the C region, the population of the state initially chosen is increased, which is observed in the B region as an increase in the fluorescence light [9.318]. With the A and B magnets retained, laser-induced fluorescence can be used to detect the transmitted atoms [9.319].

We conclude this section by describing the special conditions pertaining to spectroscopy on fast ion beams. As we have noted in connection with beam-foil spectroscopy, the transverse Doppler broadening of an ion beam is substantial due to the high ion velocities. Thus, high-resolution spectroscopy cannot be accomplished by perpendicular laser beam radiation. However, it is possible to obtain a high resolution by directing the laser beam along the ion beam, which at first sight might seem very surprising. The effect is due to a *kinematic compression*, which occurs in the ion acceleration process [9.320, 9.321]. For a particle in movement the non-relativistic kinetic energy is given by

$$E = \frac{1}{2}mv^2. \quad (9.28)$$

By differentiating we obtain

$$\Delta E = mv\Delta v. \quad (9.29)$$

For a given energy spread ΔE of the ions, which is mainly due to the thermal velocity spread in the ion source, we obtain, since ΔE is the same after the acceleration,

$$\Delta v \propto 1/v. \quad (9.30)$$

The velocity spread Δv that gives rise to the Doppler broadening is thus inversely proportional to the ion velocity. At $v = 0.001 c$, which should be compared with the thermal value of $v \simeq 300 \text{ m/s}$, we have a reduction of the Doppler width by a factor of 1000. This technique can also be applied to neutral atoms. An ion beam can be neutralized by sending it through a charge-exchange gas. Many studies of isotope shifts and hfs have been performed for longitudinally excited fast beams. In particular, short-lived radioactive nuclei have been studied. Reviews of determinations of nuclear properties using various laser spectroscopic techniques are given, in [9.322–9.327].

Recently, ion storage rings with high intensity beams have become available and are used for spectroscopic studies. Lifetime measurements of ions in long-lived metastable states can be performed, taking advantage of the small losses resulting from collisions with the residual gas [9.328]. Also, multiply charged ions and molecular ions can be investigated. Many types of collision experiments (ion–atom, ion–ion, ion–electron) of theoretical and astrophysical interest can be performed [9.329]. As one molecular example, the study of dissociative recombination in the astrophysically very important ion H_3^+ could be mentioned [9.330]. The particle energy spread present in normal storage rings can be strongly reduced by colinear interaction with a strongly monochromatic electron beam (*electron cooler*), and by laser interaction it is also possible to cool ionic beams, i.e. reduce the energy spread [9.331]. If the energy spread between the ions is eliminated, the electrostatic forces between the ions will start to dominate and the ionic beam can be expected to “crystallize” [9.332] (*Wigner crystal*; see also Sect. 9.8.3).

In connection with the laser spectroscopy of ionic beams it should be noted that *negative ions* can also be investigated [9.333]. Positive ions in an accelerated beam are subjected to a charge-exchange process in a cell filled with cesium vapour and electrons are picked up. Negatively charged systems are weakly bound by forces which are due to polarization effects and are particularly suited for studying *electron correlation* effects. The shallow box-like potential can generally only bind a ground state, and for many atomic species not even one state is formed, i.e., the ion does not exist. Negative ions can only be studied by breaking them up by absorption of photons of sufficiently high energy to remove one of the electrons (*photo-detachment*). The binding energy is thus determined by observing at what wavelength the onset of the photo-detachment process occurs. Thus it has been found that bound states exist for Li^- , Be^- , O^- and Rb^- , for example. Ca^- was long believed not to exist, until it was finally found that an extremely weakly bound state (24.55(10) meV) did exist [9.334]. A particularly efficient method for detecting the process is to excite the negative ion to an excited state of the neutral atom, followed by a second excitation to a Rydberg state. After field ionization (Sects. 2.5.2 and 9.1.4) the positive ion is detected in a mass spectrometer [9.335].

9.7.2 Saturation Spectroscopy and Related Techniques

We discussed earlier how a multi-mode laser reacts in the presence of an intracavity absorption cell (Sect. 9.2.2). We now consider the corresponding situation when the laser is forced to run in a single-cavity mode through the action of an intracavity etalon (Fig. 9.54). The atoms or molecules in the intracavity absorption cell have a Doppler broadening of the order of 1000 MHz. Different velocity groups of the atoms are responsible for the absorption in the different parts of the absorption curve. The narrow-band laser light will be absorbed at two different positions in the Doppler profile, symmetrically placed around the peak. Light moving to the right is absorbed at one position,

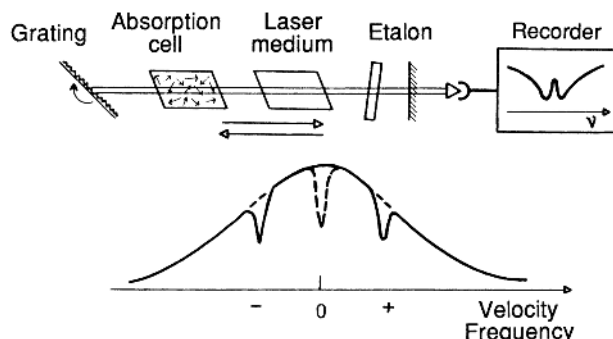


Fig. 9.54. Inverted Lamb-dip Spectroscopy

while light moving to the left is absorbed at the other position. Through the action of the intense light, essentially half the number of the atoms with the corresponding velocity will leave the ground state; “holes” are burnt in the velocity distribution (saturation, Sect. 9.1.2). If the laser is tuned towards the centre of the Doppler-broadened absorption line, the output power of the laser will drop successively. When the laser is tuned exactly to the peak of the absorption curve, both laser beams will be absorbed at the same position (atoms moving perpendicularly to the laser beam are affected). Since light of *one* direction of propagation can saturate the transition for the particular velocity group, the total absorption will *decrease* when light of *both* directions of propagation interacts with the same atoms. Compared with the situation just before the laser tuning had reached the line centre only half the number of atoms are available as ground-state absorbers. The output power of the laser will be significantly *increased* at the centre of the absorption line. The width of the corresponding signal is no longer limited by the Doppler broadening. We note that the reason why the signal at the line centre is obtained is that the absorption is *nonlinear*, due to the saturation phenomenon. If the laser intensity is weak and we are far from saturation, very weak hole burning occurs and we have the *linear* absorption situation. Then no narrow signal is observed at the line centre, since the absorptions add linearly at the line center as well as off the line centre. In contrast, the *inverted Lamb-dip* experiment [9.336] we have just described constitutes an example of *nonlinear laser spectroscopy*. The *normal Lamb-dip* effect [9.337], which is closely related to the above described process, produces a *decrease* in the output power of a single-mode gas laser (without absorption cell) when the frequency is tuned to the centre of the laser gain profile. The decrease occurs since only one population-inverted velocity group is available at the line centre, whereas two velocity groups contribute to the amplification off the line centre. The sharp Lamb dip or inverted Lamb dip can be used for frequency stabilization of a laser. The output power is sensed and a servo system adjusts the length of the cavity. A small modulation is introduced into the length regulation and the derivative of the light intensity is monitored using lock-in techniques. Thus the servo system adjustment can be performed with the correct phase. In this way a He–Ne laser can be stabilized on an I_2 absorption line at 6328 Å or a methane line at 3.39 μm . The frequency of the He–Ne transitions, and some I_2 lines, has been measured directly with the Cs clock as the reference, using a special technique employing ultrafast mixing photodetectors and several intermediate stabilized lasers [9.338–9.341] (see also [9.400]). Further, the wavelength of the stabilized light has been determined with high precision using interferometric techniques. The orange (Doppler broadened) line at 6058 Å from ^{86}Kr , which until recently defined the metre, has been used as the reference. By multiplying frequency and wavelength, a very accurate value for the velocity of light could be calculated. A best value of $c = 299\,792\,458\,\text{m/s}$ has been established from measurements at different laboratories. An error is

associated with this result, mainly reflecting the uncertainty in the definition of the metre, which has posed a significant problem. At the meeting of “Conférence Internationale des Poids et des Mesures” in 1983, it was decided that the metre should be directly connected to the much more precise time (second) definition by *defining* the velocity of light as the above-mentioned value (it no longer has an error) resulting in a definition of the metre as the distance light travels in vacuum during 1/299 792 458 s [9.342, 9.343]. Thus, one basic unit definition has effectively been eliminated and length is now expressed in terms of time. For practical purposes, secondary standards must, of course, be used, and the most obvious ones are the Lamb-dip stabilized laser lines used in the process of establishing the above-mentioned value of c . Authorized data for a few lines are given in Table 9.3. Lamb-dip studies of transitions in gas lasers have been performed for a long time. With the advent of the dye laser a renewed interest in spectroscopy utilizing saturation effects has evolved. The first saturation spectroscopy experiments using a tunable narrow-band laser were performed by Hänsch, Schawlow and co-workers [9.344, 9.345] and by Bordé [9.346]. The atomic sample is normally placed outside the cavity for practical reasons. An experimental set-up for studying the sodium D_1 line ($3s\ ^2S_{1/2} \rightarrow 3p\ ^2P_{1/2}$) is shown in Fig. 9.55.

The primary laser beam is divided into two beams using a partially reflecting mirror (beam splitter). The two beams then pass the sodium vapour cell in opposite directions and with overlapping paths. One of the beams, the saturating beam or *pump beam*, has a high intensity while the other, the detection or *probe beam*, is weak. The intensity of the probe beam is measured after passing through the cell. When the laser is tuned towards the centre of the Doppler-broadened absorption line, the strong laser beam saturates the transition for atoms in a certain velocity group. At the same time, the probe beam experiences an increasing absorption. When the laser is tuned to the line centre, the probe beam “detects” the hole that has been burnt by the saturating beam and thus its transmission is increased. In order to isolate the part of the signal that depends on the saturation (*the Doppler-free signal*) a lock-in amplifier, which is synchronized with a light-chopper in the saturating beam, is used. The lock-in amplifier records the amplitude of the ac component that can be obtained when the saturating beam is switched on

Table 9.3. Secondary length standards based on saturation spectroscopy using He–Ne laser oscillations locked to molecular absorption lines [9.343]

| Transition | Frequency | Wavelength |
|------------------------------------------------------------|--------------------|--------------------|
| $\text{CH}_4, \nu_3, \text{P}(7), \text{comp. } F_2^{(2)}$ | 88 376 181 608 kHz | 3 392 231 397.0 fm |
| $^{127}\text{I}_2, 17-1, \text{P}(62), \text{comp. o}$ | 520 206 808.51 MHz | 576 294 760.27 fm* |
| $^{127}\text{I}_2, 11-5, \text{R}(127), \text{comp. i}$ | 473 612 214.8 MHz | 632 991 398.1 fm |
| $^{127}\text{I}_2, 9-2, \text{R}(47), \text{comp. o}$ | 489 880 355.1 MHz | 611 970 769.8 fm |

* Frequency doubled 1.15 μm He–Ne transition

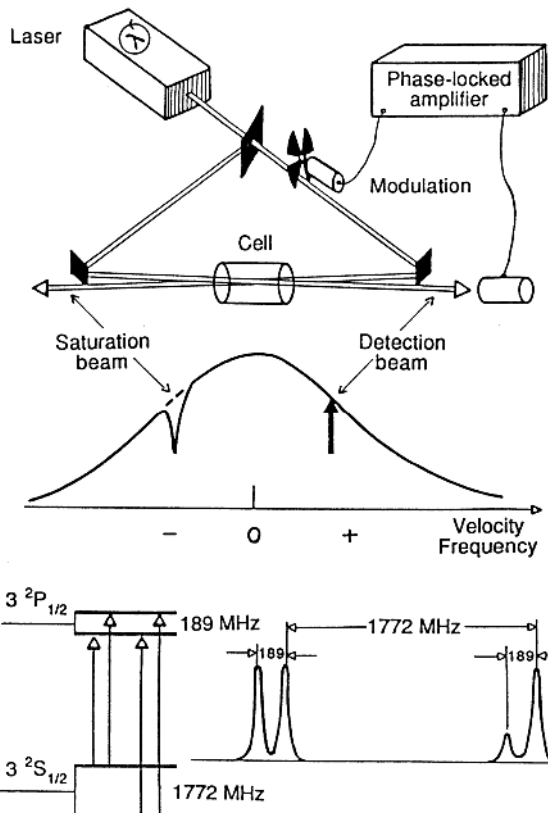


Fig. 9.55. Set-up for saturation spectroscopy of the sodium D_1 line [9.345]. A schematic spectrum is also shown where “cross-over resonances” (Fig. 9.58) have been omitted

and off. Out in the line wings the two beams interact with completely different velocity groups and therefore the transmission of the probe beam does not depend on the presence or not of a saturating beam. However, at the line centre the transmission strongly depends on whether a hole has been burnt or not and therefore an ac signal is obtained at the chopper frequency. Information is then transferred from one beam to the other, counter-propagating one with the atoms as the transfer medium. In the lower part of Fig. 9.55 the Doppler-free structure of the D_1 line is schematically shown when the laser is tuned through the line. The Doppler-free signal is given by the expression

$$S(\nu) = f(I/I_{\text{sat}}) \frac{1}{1 + [(\omega - \omega_0)/\gamma_s]^2}, \quad (9.31)$$

where the signal amplitude f depends on the pump-beam intensity in relation to I_{sat} , which is the intensity required to saturate the transition.

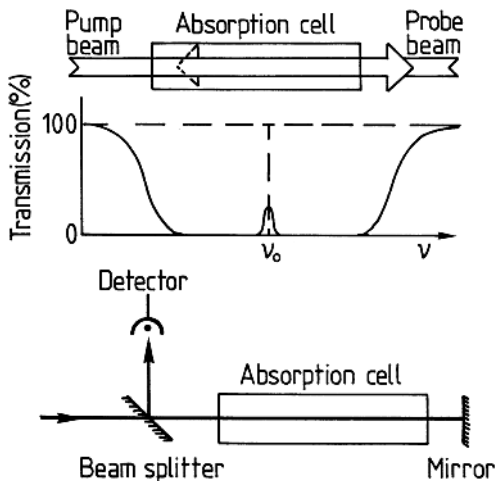


Fig. 9.56. High-contrast transmission spectroscopy [9.347]

The half-width of the signal increases with pump beam intensity according to

$$\gamma_s = \frac{1}{2} \gamma_0 \left(1 + \sqrt{1 + I/I_{\text{sat}}} \right), \quad (9.32)$$

where

$$\gamma_0 = \pi \Delta \nu_N. \quad (9.33)$$

A particularly simple form of saturation spectroscopy is obtained if a sample that is sufficiently dense to completely block a probe beam is used. Only at the line centre does the bleached path induced by a strong counterpropagating pump beam allow the probe beam to emerge from the cell and hit the detector. A simple set-up and a schematic curve are shown in Fig. 9.56 for this type of high-contrast transmission spectroscopy [9.347].

In normal saturation spectroscopy the detector essentially “looks” straight into the laser and a substantial absorption is needed in order to observe a signal. This means that only strong spectral lines, originating in well-populated states, can be investigated by this method. In cases where less favourable conditions prevail, the so-called *polarization spectroscopy* method can instead be used [9.348]. The experimental set-up is shown in Fig. 9.57.

The set-up is similar to the one used in normal saturation spectroscopy but the probe beam is now blocked by crossed polarizers that are placed at opposite sides of the absorption cell. The polarizer in front of the cell is used to increase the linear polarization of the laser beam, which is frequently already well polarized. A matched pair of polarizers (frequently Glan-Thompson prisms, Fig. 6.46) can have a rejection ratio of 10^6 to 10^7 in the crossed position. The pump beam is circularly polarized and induces an anisotropy

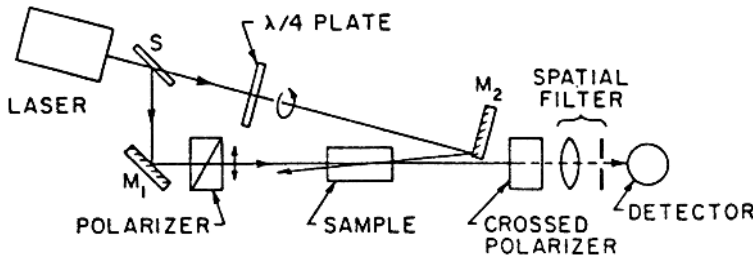


Fig. 9.57. Arrangement for polarization spectroscopy [9.348]

in the gas for the affected velocity group. At the line centre these atoms can, considered as an optically active medium, turn the plane of polarization so that probe beam light can pass the analysing polarizer (Sect. 9.2.4). If the relative orientation of the polarizer is off set by a small angle θ , a constant background results, but at the same time signal amplification is also obtained. It can be shown that the intensity of the polarization spectroscopy signal is given by

$$I = I_0 \left(\theta^2 + \frac{1}{2} \theta s \frac{x}{1+x^2} + \frac{1}{16} s^2 \frac{1}{1+x^2} \right), \quad (9.34)$$

where s is a factor that depends on the degree of saturation, which in turn is determined by the transition probability and the laser spectral power density. The variable x is proportional to the laser frequency detuning from the line centre. For completely crossed polarizers ($\theta = 0$) the signal is a Lorentzian, while the admixture of a dispersion-shaped curve increases with θ . The amplitude of the dispersion curve increases but so does the background θ^2 . Thus, there exists a small angle θ for which the signal-to-noise ratio has an optimum value. The dispersion-shaped signal can be very useful for locking a laser onto an atomic transition. A change in signal sign is obtained at the line centre without a need for frequency modulation of the laser.

One interesting application of Doppler-free laser spectroscopy is precision determination of the Rydberg constant, which has been performed by Hänsch, Schawlow and co-workers [9.349–9.351], and others [9.352–9.354]. The Rydberg constant can be evaluated if an accurate wavelength determination is performed for a suitable line in hydrogen [9.355, 9.356]. A large number of evaluations have been performed by conventional spectroscopy on the red Balmer line H_α at 6563 Å. The very large Doppler broadening (~ 6000 MHz) of the very light element hydrogen presents a significant problem because of the wide overlap of the fine structure components. In Fig. 9.58 the fine structure of the H_α line and a theoretically calculated Doppler-broadened line are shown. In the lower part of the figure the Doppler-free structure obtained by saturation spectroscopy is shown. The Lamb-shift can be directly observed. The individual positions of the components can now be well established and the uncertain deconvolution procedure that previously had to be used can

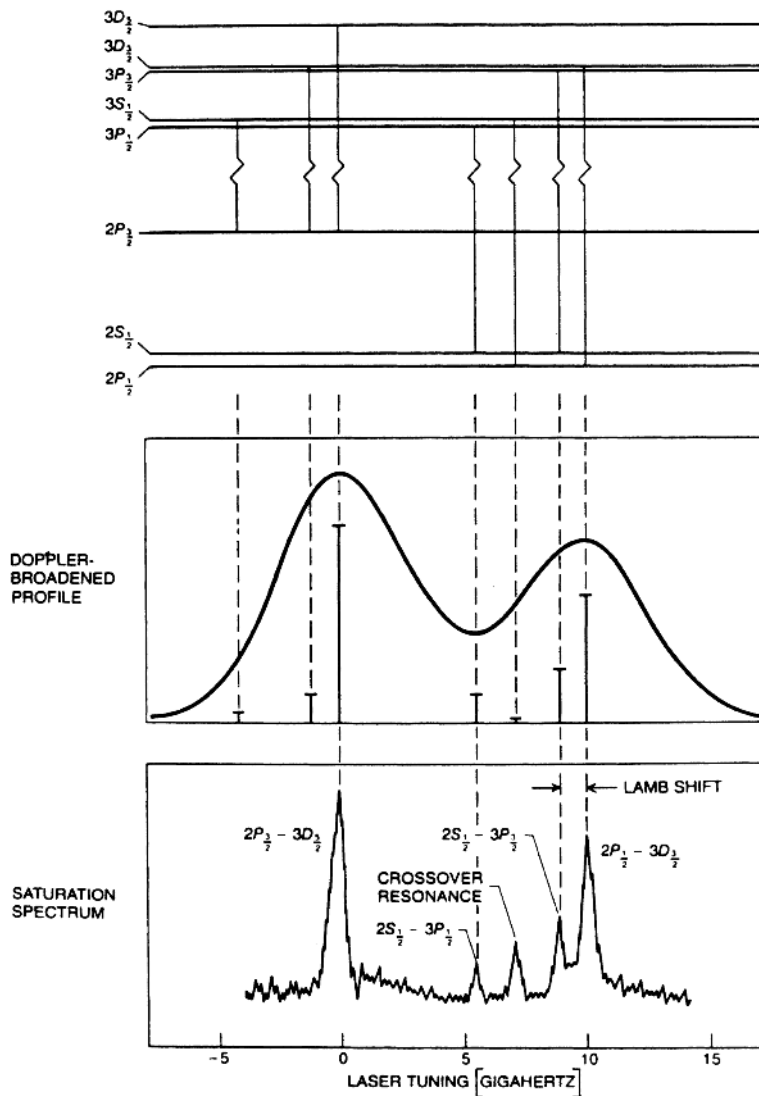


Fig. 9.58. Saturation spectroscopy recording of the H_{α} line of hydrogen [9.349]

now be eliminated. In this way, the Rydberg constant can be determined much more accurately than before. The presently recommended value for the Rydberg constant obtained is

$$R_y = 109\,737.3156855(8) \text{ cm}^{-1}.$$

A fascinating aspect of precision spectroscopy is that the constancy of the natural constants will ultimately be challenged!

In Fig. 9.58 a so-called *cross-over resonance* is shown. This is an inherent phenomenon in saturation spectroscopy and occurs when two lower- or upper-state sublevels have transitions to a common level in the other state. The two oppositely propagating laser beams can then interact at frequencies half-way between the normal resonances. Then atoms moving with a certain velocity along the laser beams are utilized [9.357, 9.358].

An experimental set-up similar to the one used in polarization spectroscopy is employed in experiments testing atomic manifestations of *parity violation* in the electro-weak interaction. [9.359–9.361]. The experiments are important for testing the *Standard Model* in elementary particle physics. Right-left asymmetries in atomic physics are of the order of $1 : 10^6$. A small optical rotation detectable using crossed polarizers is induced by interference between neutral weak and electromagnetic interactions in atoms. The most accurate experiments deal with heavy elements such as mercury, thallium, lead and bismuth [9.362, 9.363]. Another way of probing the parity violation is to observe the strength of certain forbidden transitions, notably the $7\ ^2S - 6\ ^2S$ transition in cesium [9.364]. The interaction between the neutral intermediate vector boson Z^0 with the electron violates parity and mixes a tiny amount (10^{-11}) of the P state into the S state, making the highly forbidden transition slightly allowed by electric dipole interaction. By applying a weak electric field the transition can be made more probable through the induced state mixing. A multiplicative interference term occurring between the two interactions amplifies the electro-weak interaction term of interest. For the interpretation of the nuclear effect an accurate atomic physics calculation has to be performed. This is more feasible for the alkali metal element cesium than for the heavier atoms [9.365]. The strength of the parity violation is now accurately measured in terms of the “weak charge” parameter Q with result $Q = -72.2(3)$, in good agreement with the theoretical value of -73.2 . By attaining an even higher accuracy, experimentally and theoretically, manifestations of further neutral vector bosons or of a nuclear *anapole moment* might be detectable [9.366].

In connection with this discussion of fundamental interactions we note that, besides hydrogen, there are numerous simple systems for which precision spectroscopic measurements can provide accurate tests of the QED theory and reveal effects beyond the Standard Model [9.367]. Positronium ($e^+ - e^-$) and muonium ($\mu^+ - e^-$) are hydrogen-like systems for which precise Lamb-shift and $g-2$ experiments have been performed. Precision spectroscopic studies on anti-hydrogen (antiproton–positron), once achievable, would certainly be extremely interesting in revealing possible asymmetries between the “world” and an “anti-world” [9.368].

Returning to the field of saturation spectroscopy we note, that it is also possible to observe Doppler-free saturation signals in cell experiments without detecting the intensities of the transmitted beams. Fluorescence, opto-galvanic and opto-acoustic detection can all be used. However, since the

signal information is no longer carried by a well-defined probe beam, which is coupled to the pump beam only at the line centre, a double-modulation technique must generally be employed in order to isolate the Doppler-free signal from the Doppler-broadened one. This is because a modulation of the pump beam at frequency f_1 clearly causes a huge Doppler-broadened signal at frequency f_1 in these alternative detection schemes. If the oppositely directed beam (which in this case has an intensity similar to that of the pump beam) is modulated at a different frequency f_2 , a modulation of the signal will also occur at this frequency. Clearly, these modulations are normally quite independent of each other since they are coupled to different velocity groups. However, at the line centre the two modulations interact due to the nonlinear response of the medium resulting from the saturation. Thus, for the same reason that frequency sum and difference generation occurs in nonlinear crystals (Sect. 8.6), signals at the frequencies $(f_1 + f_2)$ and $(f_1 - f_2)$ will arise at the line centre in these *intermodulated* experiments. In Fig. 9.59 arrangements for intermodulated fluorescence [9.369] and intermodulated opto-galvanic spectroscopy [9.370] are shown. Doppler-free signals can also be obtained using RF opto-galvanic spectroscopy [9.371] where amplitude variations in the RF oscillator driving a discharge in the sample are utilized. Doppler-free acousto-optic intermodulated spectroscopy is described in [9.372].

The need for intermodulation in the experiments discussed above arises from the fact that the beams are amplitude modulated. By instead utilizing beam overlap modulation, e.g., by reflecting the laser beam back through the cell from a vibrating mirror, both beams are present at all times and no modulation is normally obtained. However, when one beam is swept to overlap the other, the nonlinear interaction at the line centre changes the total signal at the vibration frequency f or $2f$, depending on the sweep geometry [9.373]. By combining the saturation spectroscopy techniques discussed above with rotating polarizers instead of choppers in the laser beams, problems due to $(f_1 + f_2)$ and $(f_1 - f_2)$ frequency generation caused by nonlinearities in the detectors, rather than true signals, can be eliminated. The technique is then called POLINEX (POLarization INtermodulated EXcitation) spectro-

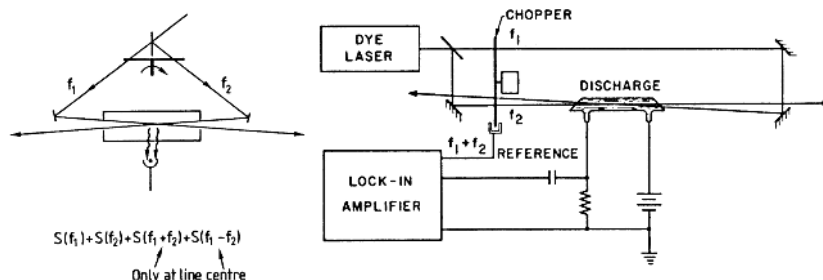


Fig. 9.59. Experimental arrangements for intermodulated fluorescence spectroscopy (left) and intermodulated opto-galvanic spectroscopy (right) [9.370]

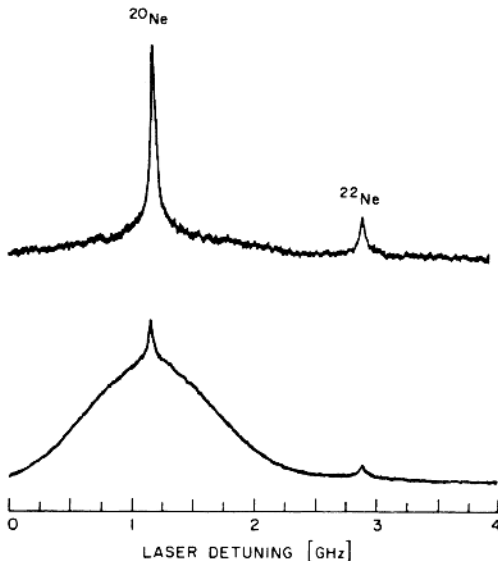


Fig. 9.60. Comparing recordings of the 5882 Å Ne line using POLINEX (*upper curve*) and intermodulated fluorescence spectroscopy [9.374]

scopy [9.374]. The polarization methods also have an additional advantage of being largely insensitive to velocity-changing collisions, which can cause broad signal pedestals under the narrow signals even if lock-in detection at the frequencies $(f_1 + f_2)$ or $(f_1 - f_2)$ is performed. (The collisions tend to spread the “hole” over a larger frequency range). Since the orientation of the atoms induced by the polarized light is normally changed by collisions, the POLINEX signal, which is sensitive to polarization rather than to light intensity, will essentially only exhibit the narrow signal contribution. The effect is illustrated in Fig. 9.60, in which the reduction in collisional effects is shown for a Ne transition.

9.7.3 Doppler-Free Two-Photon Absorption

We have already discussed the two-photon absorption process [9.375] (Sect. 9.1.3). Normally, the signals are Doppler broadened, and high resolution is not obtained even if narrow-band lasers are used. However, a very important observation was made as early as 1970 by *Chebotayev* and co-workers [9.376]. The Doppler broadening can be eliminated if the two photons are extracted in such a way that one is supplied from one of two counter-propagating laser beams and one from the other beam. For a certain atom with a velocity component v along one direction of propagation, the energy interval ΔE can be bridged by two Doppler-shifted contributions

$$\Delta E = h\nu(1 + v/c) + h\nu(1 - v/c) = 2h\nu. \quad (9.35)$$

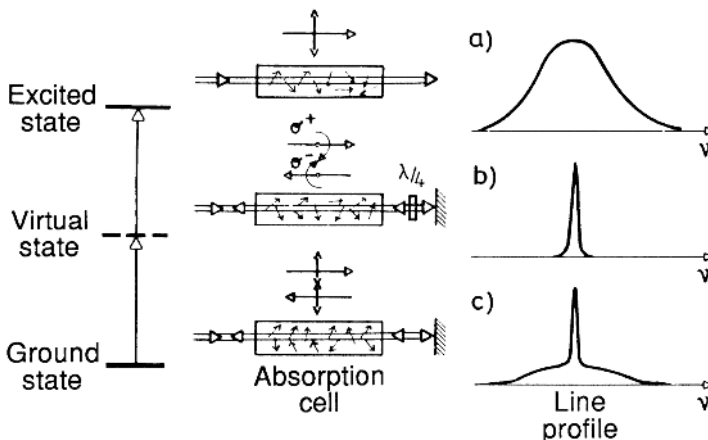


Fig. 9.61. Two-photon absorption spectroscopy signals for different laser beam arrangements

Thus, the first-order Doppler shift in one absorption is exactly cancelled by the corresponding shift in the second absorption. Since the velocity is eliminated, *all* irradiated atoms can contribute to the signal and not just a certain velocity group, as in saturation techniques. In S-S transitions we have the selection rules $\Delta F = 0$, $\Delta M = 0$ for the two-photon transition between the two states of equal parity. By making both laser beams either right-hand circularly polarized or left-hand circularly polarized it is possible to ensure that the two photons come from different laser beams ($\Delta M = +1$ and $\Delta M = -1$ make effectively $\Delta M = 0$). In Fig. 9.61 this case is shown (Fig. 9.61b) as well as the case of a Doppler-broadened signal, which is obtained if only one laser beam (unpolarized or linearly polarized) is used (Fig. 9.61a). If two such oppositely propagating beams are used, a Doppler-free as well as a Doppler-broadened contribution will be obtained (Fig. 9.61c). Early experimental observations of Doppler-free signals were made by several groups [9.377–9.379]. Doppler-free two-photon absorption has been used in a large number of atomic level investigations. For highly excited states, thermionic diode detection is frequently employed. States up to $n = 500$ have been reached in stepwise excitations [9.380]. As an example, a recording is shown in Fig. 9.62. Systematic studies of alkali metal atoms [9.381–9.383] and alkaline earth atoms have been performed. For the alkaline earth atoms the data obtained in two-photon and stepwise excitation experiments on sequences of Rydberg states have been analysed using multichannel quantum defect theory [9.384–9.387].

We will also discuss another series of investigations on hydrogen initiated by Hänsch and co-workers, which is of fundamental importance [9.388–9.391, 9.396]. The experiment deals with the determination of the Lamb shift in the ground state ($n = 1$) (Fig. 9.63). In contrast to the situation

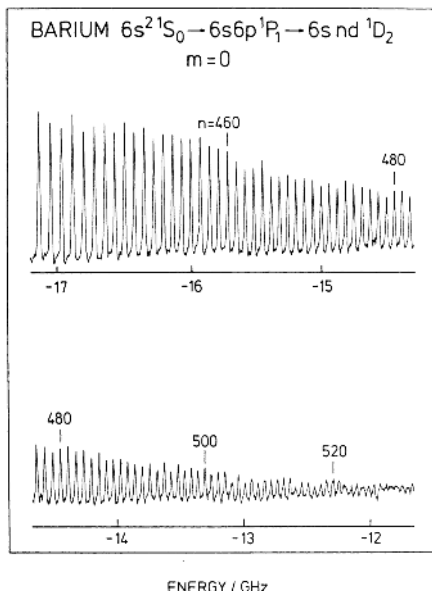


Fig. 9.62. Doppler-free spectrum for high-lying Rydberg states in Ba [9.380]

for the $n = 2$ state, in which the position of the $2s\ ^2S_{1/2}$ state can easily be related to the $2p\ ^2P_{1/2}$ state position, there is no neighbouring state for the ground state. However, its energy position is still affected by QED effects, and in order to measure these, reference to the $n = 2 \leftrightarrow n = 4$ transition (H_β) can be made. The simple Balmer–Rydberg formula states that the $n = 2 \leftrightarrow n = 4$ interval should be $1/4$ of the $n = 1 \leftrightarrow n = 2$ interval. Because of fine structure, relativistic and QED effects (the Lamb shift is the ground state QED effect which is to be determined) the simple energy interval relation does not hold exactly. Starting from a primary narrow-band laser at 4860 \AA it is possible to simultaneously measure the H_β -line using polarization spectroscopy and the $n = 1 \leftrightarrow n = 2$ transition with two-photon spectroscopy, and compare the signal positions for the Lamb-shift determination. Sometimes well-known lines from Te_2 molecules are used as reference lines. These molecules have many transitions in the blue spectral region which can be used as wavelength standards [9.392] in the same way as I_2 lines are used at longer wavelengths [9.393]. Light from the 4860 \AA laser is amplified with pulsed amplifier stages pumped by a pulsed excimer laser and the pulses are frequency-doubled to 2430 \AA in a nonlinear crystal. The two-photon transitions between $n = 1$ and $n = 2$ are monitored using the Lyman line at 1216 \AA , which is obtained after collisional transfer in the discharge from the $2s\ ^2S_{1/2}$ to the $2p\ ^2P_{1/2}$ state. The two-photon signals have a larger linewidth than the polarization spectroscopy signals because of the Fourier broadening of the pulsed amplification (pulse length 10 ns

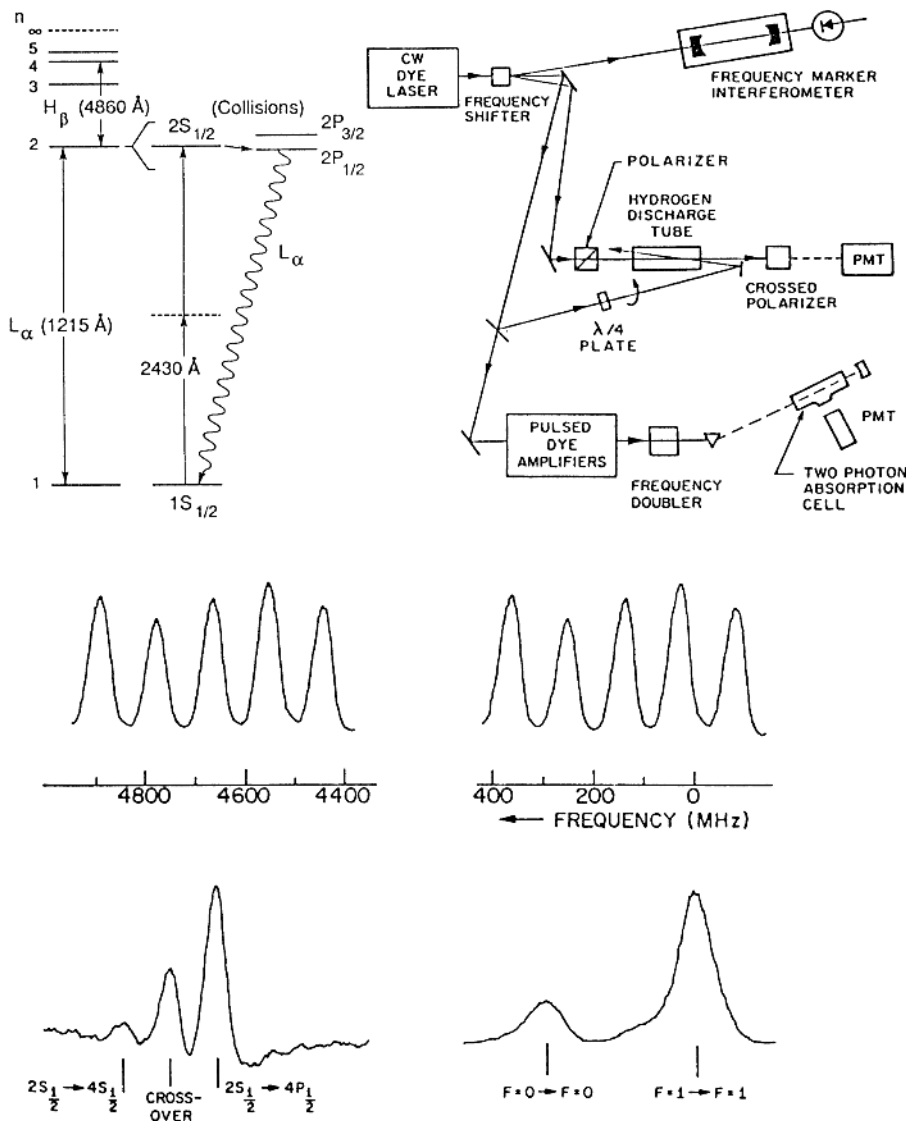


Fig. 9.63. Experimental arrangement and recorded signals for simultaneous saturation spectroscopy ($2s$ - $4p$) and two-photon absorption spectroscopy ($1s$ - $2s$) in atomic hydrogen [9.388]

$\rightarrow \Delta\nu \simeq 1/10^{-8} \text{ Hz} = 100 \text{ MHz}$). The measurement yields a Lamb shift of the $1s$ state of about 8170 MHz (best value is 8172.876(29) MHz [9.396]), which is in close agreement with the theoretical predictions. Since the natural life-time of the $2s$ state is about 10^{-1} s , extremely narrow lines should, in principle, be attainable. Narrow-band 243 nm radiation has been genera-

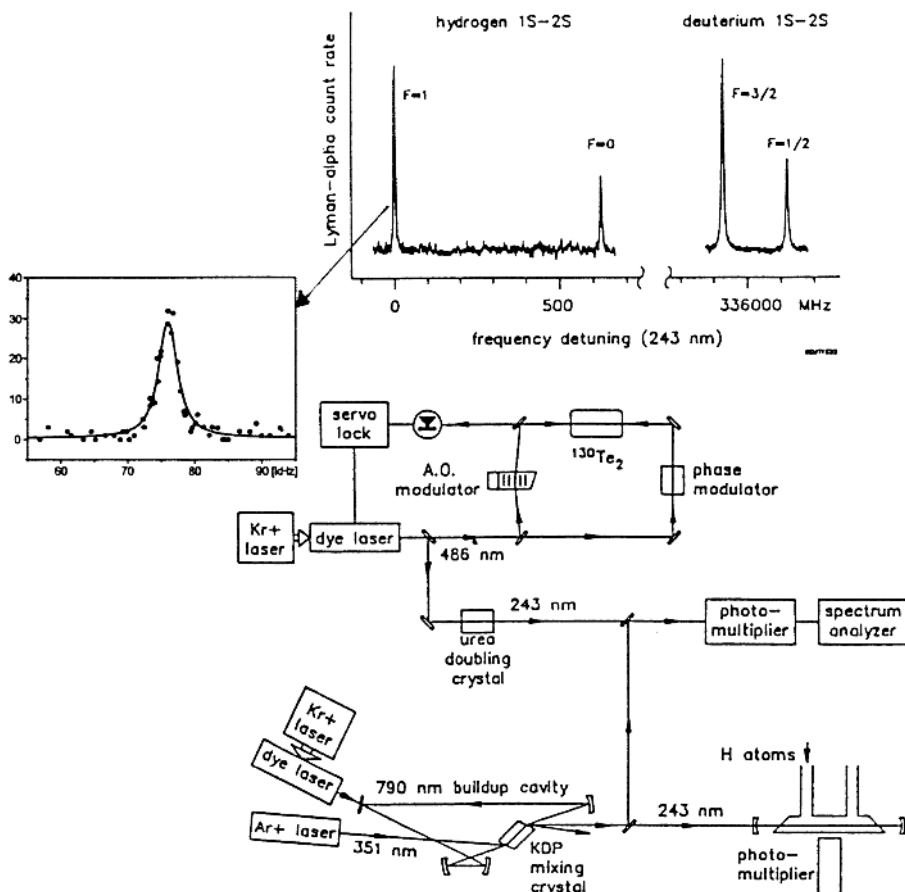


Fig. 9.64. Recording of the $1s-2s$ transition in atomic hydrogen and deuterium using CW high resolution lasers [9.390, 9.391 first ref.]. As an insert a very recent, narrow-linewidth recording of one of the hyperfine transitions is shown [9.396]

ted using cw frequency-mixing techniques, yielding a resolution of $1 : 10^{10}$ [9.390, 9.394, 9.395].

An example of high-resolution spectroscopy for hydrogen and deuterium is given in Fig. 9.64. Many groups have been very active in the field of precision hydrogen spectroscopy [9.397–9.399]. Frequently, combinations of atomic states and utilization of simple relationships between transition frequencies as given by the Balmer–Rydberg formula have been utilized [9.351].

To relate optical frequencies to the cesium time standard remains a very important issue in precision metrology. In this context the development of the optical-frequency-comb technique using mode-locked lasers has been very important [9.400].

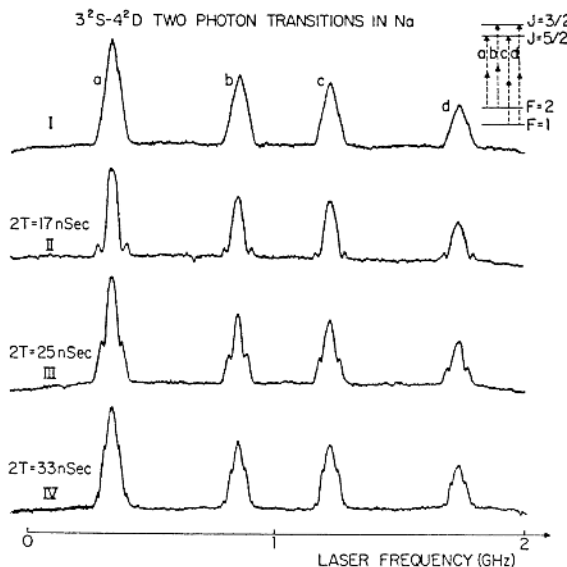
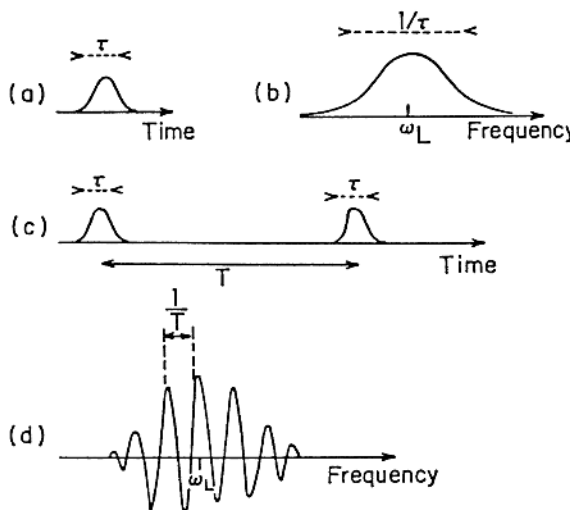


Fig. 9.65. Illustration of the optical Ramsey fringe technique in the time domain [9.401]

We conclude this section by discussing techniques which can be considered to be optical analogues of the Ramsey fringe technique, first introduced for the RF region (Sect. 7.1.2). We first consider the case of two-photon spectroscopy with a pulsed laser. In Fig. 9.65 (top) the inevitable Fourier broadening of a short pulse is illustrated.

However, by applying a further pulse after a delay T , a sharp interference pattern in the two-photon signal can be obtained. It is important that the signal is Doppler-free so that the phase memory from the first pulse is not lost through the velocity spread. Ordinary signals and Ramsey fringes for the two-photon transitions $3s\ ^2S_{1/2} \rightarrow 4d\ ^2D_{3/2,5/2}$ in ^{23}Na are shown in the figure [9.401]. The signals display the hyperfine structure of the ground state (1772 MHz, Fig. 9.55) and the inverted fine structure of the excited state (1028.8 MHz, see also Fig. 9.17). The sharpness in the interference pattern can be increased using multiple pulses [9.402]. An analogy with the interference from a double slit and from a grating illuminates this effect.

Recently, a similar technique has also been demonstrated using a train of femtosecond pulses [9.403]. The possibility of using multi-pulse interference effects of the Ramsey type for high-resolution laser spectroscopy is particularly interesting for the VUV, XUV and soft X-ray regions, where narrow-band CW coherent sources are absent. High-harmonic generation (Sect. 9.6.2) is of particular interest in this context, especially since the radiation has been shown to have a high degree of coherence [9.270]. As discussed earlier, high-resolution spectroscopy of internal structures over difficult wavelength ranges can also be performed using quantum-beat spectroscopy or optical double resonance and level-crossing spectroscopy using pulsed sources, for which nonlinear conversion can readily be performed [9.159].

The optical Ramsey effect has also been demonstrated for the case of saturation spectroscopy with cw laser beams [9.404]. An atomic beam is crossed by counter-propagating laser beams at three different locations along the atomic beam. In this way the transit-time broadening can be strongly reduced, which was the original reason for introducing the technique in the RF regime. The technique has primary importance in connection with the establishment of ultra-stable laser secondary wavelength standards. A special variety of the Ramsey fringe technique using a “fountain” of very slow atoms has also been proposed and demonstrated [9.405].

9.8 Cooling and Trapping of Ions and Atoms

9.8.1 Introduction

In principle, lasers can be stabilized to a linewidth in the sub-Hz region. If transitions between the ground state and long-lived metastable states with a lifetime of the order of 1 ms are utilized, the natural radiation width will be very small (100 Hz). On the other hand, transit-time broadening can be substantial. The transit time of a thermal atom through a 3 mm laser beam is about 10^{-5} s, which corresponds to a broadening of about 10 kHz. As we have seen, this effect can be reduced by employing the Ramsey fringe technique. A remaining fundamental broadening is the second-order Doppler effect, related to the relativistic Lorenz contraction. The effect amounts to about 100 Hz

in the visible region. Obviously, in order to achieve an optimal resolution the atoms must be brought to rest. Spectroscopy on a sample of ultracold atoms or ions can provide extremely small linewidths and extreme precision in measurements of fundamental nature (Rydberg constant, Lamb shift, fine-structure constant, isotropy of space etc.). New types of atomic clocks with unprecedented precision (fractions of a Hz on a visible transition at about 10^{15} Hz) are also possible. Finally, at very low temperatures, sufficiently dense atomic samples can “condense” into a new state of matter, a *Bose condensate*.

Slowing down the velocity of atoms, ions or molecules thermodynamically corresponds to cooling. Cooling can be achieved using laser light. Basically, the transfer of the momentum of the photon ($p = h\nu/c$) is utilized as suggested in 1975 by *Hänsch and Schawlow* [9.406] and *Wineland and Dehmelt* [9.407]. The mechanical influence of light on atoms and other particles was demonstrated early on (Sect. 9.7.1). The motion of atoms in a beam can be decreased by directing a laser beam against the atoms. For each head-on absorption process, the velocity of a sodium atom is reduced by 3 cm/s. By absorbing (and emitting) photons some 20 000 times they can be brought to rest. Clearly the fact that the atoms shift out of resonance with the counter-propagating single-mode laser beam as they slow down is a problem. *Letokhov* and co-workers suggested that the laser frequency be shifted downwards to counteract the Doppler shift [9.408]. A small “package” of atoms could be cooled down to 1.5 K without shifting the frequency [9.409]. A more efficient way was proposed and demonstrated by *Phillips* and co-workers [9.410]. By using the combined effect of optical pumping into the highest m quantum state (Sect. 7.1.3) and Zeeman tuning in a magnetic field of decreasing strength along the beam path, the atoms can be kept in resonance (Fig. 9.66). The techniques described above only affect the longitudinal velocity of the beam. In order to bring atoms or ions to a “complete” rest all velocity components must be removed. This can be achieved if the atoms or ions are confined in a trap. An electrically charged particle can be trapped in a potential

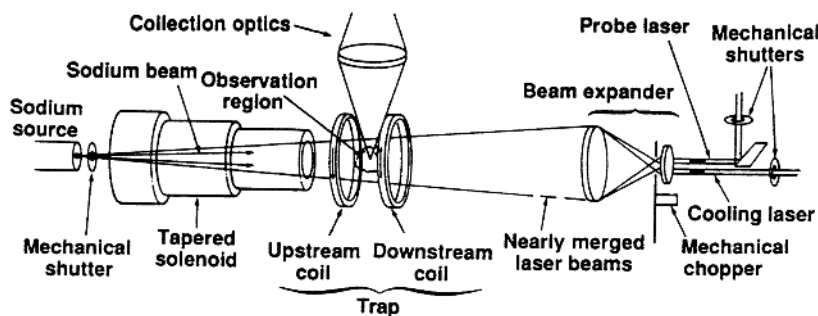


Fig. 9.66. Arrangement for cooling atoms in a beam using a Zeeman slower. In the middle of the figure a magnetic trap is shown [9.411]

generated by static or oscillating electromagnetic fields, while the trapping of neutrals is more complicated.

9.8.2 Ion Traps

Many different types of ion trap exist. Already in the 1930s the *Penning* trap had been developed, basically as a means of making more sensitive ionization gauges for vacuum measurements [9.412]. In a discharge through a low-pressure gas, the electron paths can be considerably prolonged by applying a strong magnetic field, in which the charged particles spiral. An optimized Penning trap consists of two hyperbolically shaped pole caps held at the same potential and a hyperbolically shaped ring forming the other electrode placed symmetrically between the caps. (See Fig. 9.67a). The potential field tends to stabilize the charged particles between the caps in the z direction but they are unstable in the x - y plane. The magnetic field in the z direction makes them spiral back and forth between the end caps with a given rotation frequency, which is close to the *cyclotron resonance* frequency

$$\omega_c = qB/m, \quad (9.36)$$

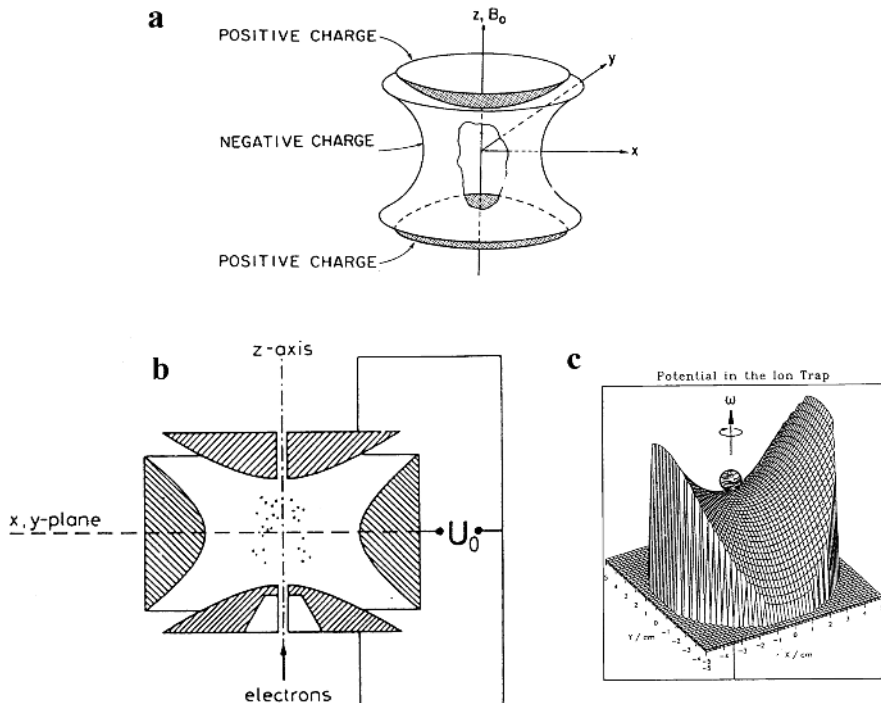


Fig. 9.67. (a) Penning and (b) Paul traps for ions. A mechanical analogue of the Paul trap is also included (c) [9.416].

where q is the particle charge, m its mass and B the applied magnetic field. This equation suggests that the mass of an ion can be measured very exactly in an ion trap [9.413, 9.414].

In the *Paul trap* (the RF quadrupole trap), the static magnetic field is removed and the dc electric supply for the Penning trap is replaced by an RF electric field (Fig. 9.67b), which supplies a dynamic stabilization [9.415, 9.416]. This can be seen in a mechanical analogue (Fig. 9.67c, [9.416]). The trap forms a saddle-shaped surface on which a small steel ball is placed. The ball is stabilized in one dimension but will slide down in the other dimension. If now the saddle surface is rotated around a vertical axis, the ball is prevented from falling down. The depth of the trapping potential is substantial (\approx eV).

9.8.3 Basic Laser Cooling in Traps

By irradiating an ion or atom in a trap with laser radiation tuned to the low-frequency side of the Doppler curve of the transition, the velocity of the ion will be successively slowed down [9.406] (Fig. 9.68). Because of the detuning of the laser, a photon can only be absorbed when the ion is moving against the laser beam. The absorption of the momentum of the photon will slow down the ion. The decay photon can be emitted in any direction. After some time, the ion will have been brought to a very low velocity. Two counter-propagating beams of the same frequency can be used for simultaneously cooling particles moving in opposite directions. The intuitive velocity limit would correspond to the atomic recoil energy due to a photon emission, which in thermodynamical language corresponds to the *recoil limit temperature* T_R :

$$T_R = p^2/4mk, \quad (9.37)$$

where p is the photon momentum (9.26).

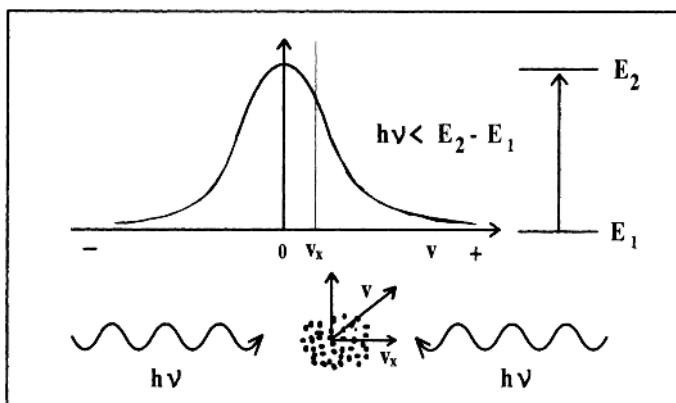


Fig. 9.68. The principle of laser cooling

The recoil velocity for a sodium atom is, as mentioned above, about 0.03 m/s , which would in thermodynamic language correspond to a temperature of about $2\text{ }\mu\text{K}$. However, the statistical nature of absorption and emission in a gas of atoms or ions leads to a certain heating of the gas and a corresponding Doppler width, which is of the order of few hundred μK . This is referred to as the *Doppler limit* for the cooling temperature T_D , which can be expressed as

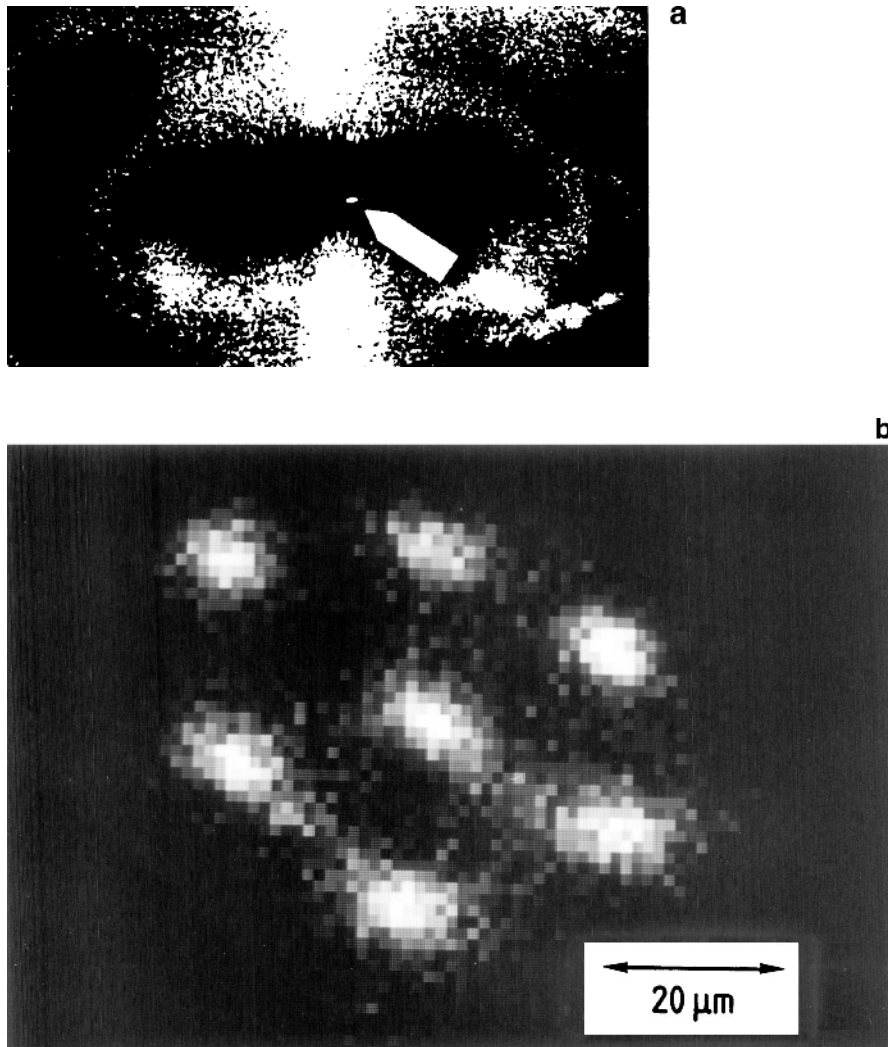


Fig. 9.69. (a) Photograph of the fluorescence light from a single barium ion kept in an RF trap [9.418]. (b) Recording of the fluorescence of seven stored magnesium ions exhibiting “crystallization” behaviour [9.419]

$$T_D = \hbar/2\tau k. \quad (9.38)$$

Efficient cooling of ions was first achieved in 1978 [9.417, 9.418]. A photograph of a single Ba^+ ion is shown in Fig. 9.69a. In Fig. 9.69b the “crystallization” of a few Mg^+ ions in a trap is illustrated. The ions are cooled to such a low velocity that the electrostatic forces between them dominate and an ordered arrangement (“Wigner crystal”, [9.420]) is obtained [9.419]. Arrangements of cooled ions exhibit interesting properties that are discussed in [9.421]. Linear arrangements of ions have been discussed in connection with *quantum computing* [9.422]. The field of ion physics in traps is covered in [9.423, 9.424].

9.8.4 Trapped Ion Spectroscopy

Laser spectroscopy on a trapped and cooled ion can yield an extreme spectral resolution in transitions to long-lived (metastable) upper states. A new problem then has to be dealt with, connected with the low fluorescence yield of such highly forbidden transitions. A technique in which a strong transition is used for the detection of the forbidden transition has been proposed and demonstrated [9.425, 9.426]. The technique, which is applicable to a single atom or ion, is illustrated in Fig. 9.70 for the case of a Hg ion. “Strong” fluorescence light induced by a laser tuned to the strong $5d^{10}6p\ 2P_{1/2} - 5d^{10}6s\ 2S_{1/2}$ fully allowed transition at 194 nm is normally detected. If another laser is tuned through the extremely narrow resonance of the (electric-dipole) “forbidden” $5d^{10}6s\ 2S_{1/2} - 5d^96s^2\ 2D_{5/2}$ transition, a resonant transfer of the ion to the metastable state (“shelving”) is detected through the abrupt disappearance of the fluorescent light in the strong transition (“quantum jump”). Experimental recordings of this phenomenon are included in Fig. 9.70, as are ultra-high resolution scans of the “forbidden” transition.

9.8.5 Atom Cooling and Trapping

Since atoms are neutral it is obviously much more difficult to trap them. One way to prepare an ensemble of cold atoms in a small volume is to use six laser beams, pairwise in opposite directions and along three orthogonal directions. With the laser beams all derived from the same laser, tuned to the low-frequency side of the atomic transitions, the movement in all three directions can be cooled. The atoms experience a viscous force in the opposite direction to their flow direction, leading to a confinement of slow atoms in the region where the laser beams overlap (“optical molasses”). It is not a true trap, since the forces are not position-dependent. Using this technique sodium atoms were cooled to about $240\ \mu\text{K}$ by *Chu* and collaborators [9.428], corresponding to the Doppler limit, (9.38). Further cooling was thought to be impossible until *Phillips* and collaborators showed (using different methods to determine the temperature, including studying the expansion of the cooled cloud) that the actual temperature was much lower, only about $40\ \mu\text{K}$ [9.429].

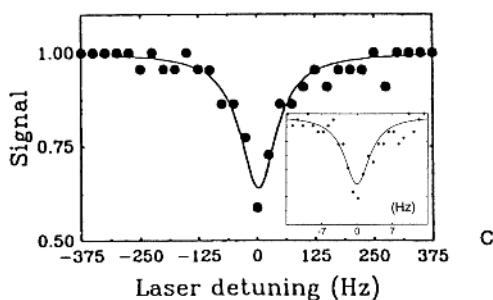
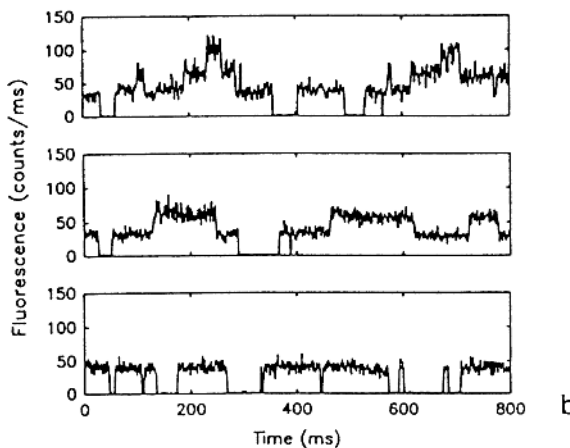
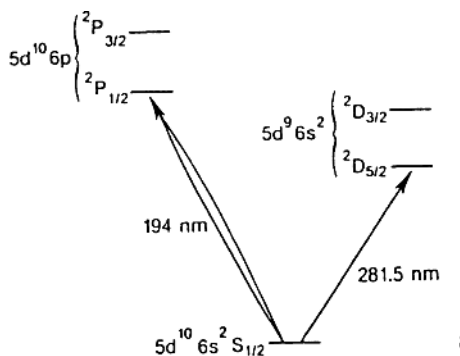


Fig. 9.70. (a) Energy levels for Hg^+ , with the “strong” transition at 194 nm and the “weak” transition at 281.5 nm indicated. (b) Fluorescence light recording at 194 nm illustrating quantum jumps in 3 ions (top), two ions (middle) and one ion (bottom) [9.426]. (c) An experimental scan of the “weak” transition using an electro-optically stabilized laser is shown, featuring a linewidth of 86 Hz. This corresponds to a spectroscopic resolution of $1 : 10^{15}$. The insert shows an even narrower linewidth [9.427]

This surprising phenomenon was soon explained by *Cohen-Tannoudji and Dalibard* as the result of a combination of spatially varying energy level shifts due to the laser light (dynamic Stark effect; Sect. 9.6.1) and optical repumping [9.430, 9.431]. Light shifts are naturally explained in the *dressed atom* theory developed by Cohen-Tannoudji since the 1960s [9.432, 9.433]. The atom loses energy by climbing the energy hill, and is then repumped to the valley without gaining velocity. Then the atom starts a new climb slowing down further. (See Fig. 9.71). The mechanism is called *Sisyphos cooling*, with reference to an unrewarded stone-roller in Greek mythology, who experienced that the stone he had rolled up to the mountain top always rolled down again. In a more detailed explanation two counter-propagating and perpendicularly polarized laser beams are seen to result in a light field, the polarization of which changes spatially from right-hand circularly polarized to linearly polarized to left-hand circularly polarized for movements of $\lambda/8$. Since the selection rules between ground- and excited-state sublevels depend on the polarization, the atoms will be repumped between ground-state sublevels with different light shifts. It can be shown that the repumping is most probable from an energetically up-shifted level to a down-shifted level. The same effect can be described in terms of *Raman cooling*, formulated and demonstrated by *Chu* and co-workers [9.434]. A common feature in laser cooling is that the energy is dissipated in emissions of blue-shifted photons. In order to truly trap atoms different techniques have been suggested. Unfortunately, atomic traps are always shallow (the potential depth is only a few meV). In order to trap atoms they have to be precooled, e.g. by using a Zeeman slower as discussed above. The simplest form of a trap is just a focused laser beam, as proposed by

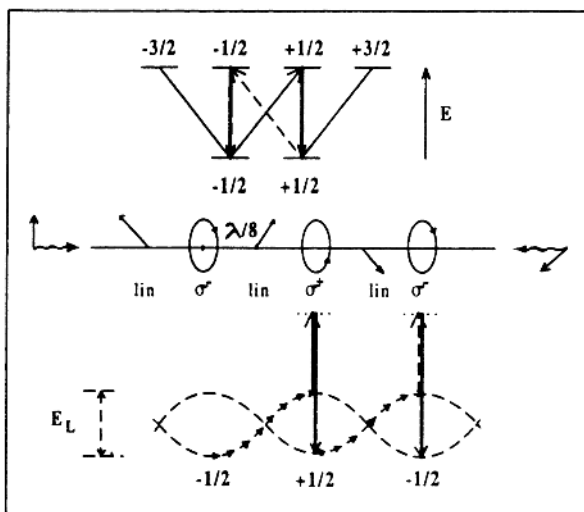


Fig. 9.71. Illustration of the principles of Sisyphos cooling (Adapted from [9.431])

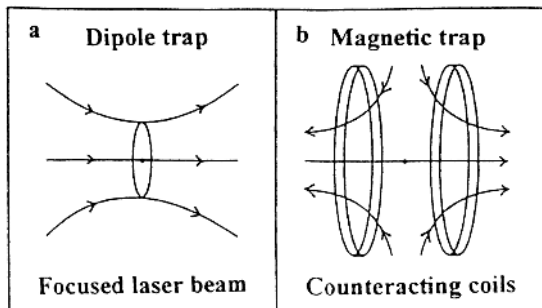


Fig. 9.72. Atomic traps based in a focused laser beam (a) and magnetic confinement (b)

Ashkin [9.435] and illustrated in Fig. 9.72a. Optical forces for confining had already been suggested by *Letokhov* [9.436]. An atom feels a force directed towards the volume of highest light intensity because of a dipole force (the light-induced electric dipole feels the electric force gradient).

Pure magnetic traps were developed by *Paul* and collaborators [9.437] and by *Phillips* and collaborators, following a suggestion by *Pritchard* [9.438]. Basically, two magnetic coils acting with the fields against each other was used, creating a strong magnetic gradient, which is felt by the magnetic atoms (see Fig. 9.72b). It became the first atomic trap to be realized [9.438], and it was performed on a Zeeman-slowed sample of sodium atoms, as indicated in Fig. 9.66. In both the electric and magnetic traps the gradient forces expressed in ((7.10), (7.11)) and discussed in connection with Figs. 7.4, 7.5, 7.7 and 8.2 are at work. In order to obtain a deeper trap for neutral atoms a combination of magnetic field coils and laser beams, the so called *magneto-optical trap* (MOT) was developed [9.439]. The MOT uses a combination of a weak magnetic field, growing from the centre outwards, and circularly polarized light, as shown in Fig. 9.73. Polarization considerations and selection rules in combination with the position-dependent energy level tuning act in such a way that atoms which move away from the centre of the trap feel on the average a recoil-based force directed towards the centre.

9.8.6 Sub-Recoil Cooling

Emission processes always lead to a photon-related recoil velocity for an atom. Thus, in the quest for still lower temperatures it is necessary to ascertain that an atom, which for some reason is brought to a standstill, can be exempt from further interaction with the light. This is possible if the atom is placed in a so-called *dark state* [9.440]. If the atom is in a coherent superposition of two ground-state sublevels, from which the transition amplitudes exhibit a total destructive interference, a dark state is achieved (See also Sect. 9.5.3). It can be shown that for counter-propagating beams with circular polariza-

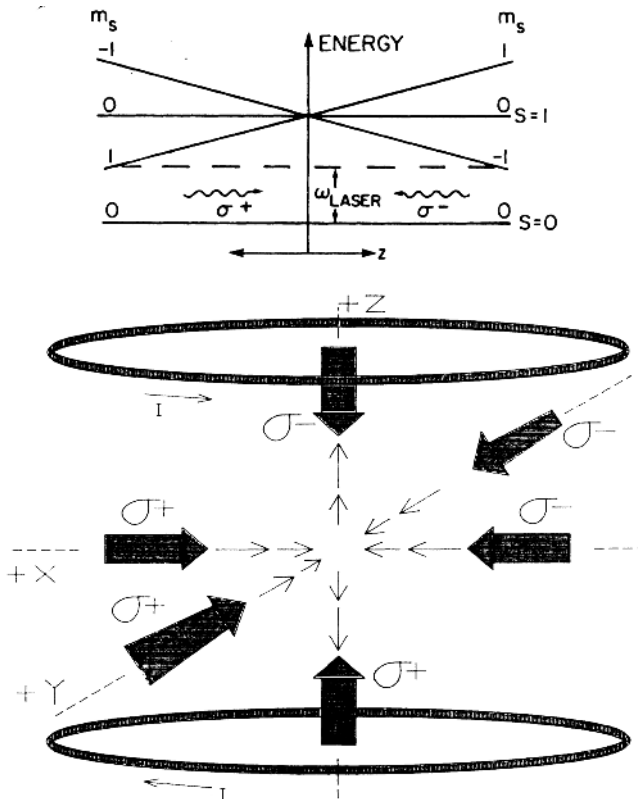


Fig. 9.73. Principle of a magneto-optical trap (MOT) [9.439]

tion only atoms with zero velocity are exempt from the absorption/emission process. Using this type of phenomenon, cooling even below the recoil limit has also been achieved by so-called *velocity selective coherent population trapping* (VSCPT) [9.441]. Temperatures as low as 5 nK have been achieved by Cohen-Tannoudji and collaborators for metastable helium atoms, for which $T_D = 23 \mu\text{K}$ and $T_R = 4 \mu\text{K}$. Two- and three-dimensional VSCPT cooling was also achieved [9.442]. The dark state can be seen as a superposition of quantum-mechanical wave packets, describing an atom which simultaneously moves in six perpendicular directions with speeds corresponding to a single-photon recoil. When the laser beams are shut off and the position of the atom is measured, the wave function collapses and the atom is found in one of six possible positions. Raman cooling is a further method of achieving sub-recoil temperatures [9.443].

Laser cooling and trapping are further discussed in [9.444]. The 1997 Nobel prize in physics was awarded to Chu, Cohen-Tannoudji and Phillips for their contributions to the development of cooling and trapping of atoms.

9.8.7 Atom Optics

A beam of slow atoms can be manipulated in many ways. This is performed within the field of atom optics [9.445–9.447]. An atomic beam can be bent or focused using laser fields. An atomic beam can also be reflected at an optical surface using the evanescent optical field from a laser beam reflected from the other side of the surface. The atom version of the Young double-slit experiment has been performed, even with monochromatic thermal atoms, showing clearly the existence of matter waves [9.448]. Beam splitters for slow atomic beams can be optically achieved to build atomic interferometers based on de Broglie wave interference. The thermal de Broglie wavelength

$$\lambda_{dB} = h/p_{th} = h/(2\pi mkT)^{1/2} \quad (9.39)$$

attains considerable values for slow atoms. Atom interferometers with slow atoms allow very accurate measurement of gravity (down to few parts in a billion) and possible space-time fluctuations [9.449]. Even atom holography has been achieved [9.450].

By using oppositely directed pairs of laser beams with carefully controlled relative phases it is possible to set up an optical lattice using the light shifts present in Sisyphos cooling. Atoms are cooled and confined into the periodic lattice points [9.451, 9.436, 9.435]. Such a lattice, with a period corresponding to optical wavelengths, can scatter laser beams in the same way as a normal crystal lattice (with typically 0.3 nm spacing) scatters X-rays (Bragg and Laue diffraction) (see Sect. 5.1.1).

Cooled atoms enable fundamental experiments in collision physics [9.452]. When the particles move very slowly, scattering can be described accurately by theory. The study of collisions is also important since they constitute a loss mechanism in laser cooling. On the other hand, collisions are necessary to achieve the evaporative cooling needed for Bose–Einstein condensation (see below).

Cooling has also been achieved for molecules without laser techniques, but employing interaction with cold helium gas or by using a pulsed electric field [9.453]. Clearly, many fundamental studies can be performed on well-prepared samples of cooled molecules.

Laser cooling and trapping, and atomic optics constitute important aspects of the mechanical effects of light on atoms. Several other such effects exist and have been explored. Studied phenomena include light diffusive pulling [9.454], light-induced drift and the optical piston [9.455].

9.8.8 Bose–Einstein Condensation and “Atom Lasers”

In sufficiently cold and dense atomic samples, where the thermal de Broglie wavelength becomes comparable to the mean separation between the atoms, so-called *Bose–Einstein condensation* (BEC) can occur. In this case the atomic matter waves overlap and the indistinguishability of atoms becomes

important. Then a gas of boson particles will condense into the lowest energy level, in a phase-transition process as predicted by Einstein, based on earlier work by the Indian physicist Bose [9.456]. A coherent matter wave is obtained with obvious fundamental interest. The condensation is a macroscopic quantum phenomenon like superfluidity or superconductivity, where electrons (fermions) couple to Cooper pairs, which behave like bosons. Photons are also bosons, and their Bose–Einstein condensation is the normal laser action, where all photons are in the same coherent state.

A crucial step for achieving BEC for free atoms was to combine laser cooling with evaporative cooling [9.457]. Such non-optical cooling by evaporation just means that the most energetic (fastest) atoms will escape from the trap more quickly than the colder ones, effectively lowering the temperature through thermalizing collisions. It was developed for the cooling of hydrogen, which cannot easily be optically cooled since the resonance line (Lyman- α) is at 121.6 nm. By a combination of very efficient laser cooling in a MOT with evaporative cooling, BEC was achieved in 1995 by *Cornell, Wieman* and collaborators [9.458] and by *Ketterle* and collaborators [9.459] for the case of ^{87}Rb and ^{23}Na , respectively. The final requirement was to tighten a final leak in a trap due to spin flips into a repelled state occurring around zero magnetic field. The stored atoms could be kept away from such field regions either by a blue-detuned focused beam repelling the atoms or by a rotating magnetic field moving the hole away from the atoms. Evaporative cooling removes the fastest atoms from the trap. An RF field is used to flip the atoms by Zeeman-level transitions into a state in which they are repelled out of the trap. In this way warm atoms are “skimmed off”. The magnetic field is zero at the trap centre and increases outwards. By properly adjusting the RF frequency the flip region can be moved. Sufficiently fast atoms can only reach the higher field region, where they are flipped. The condensate is imaged by laser-induced fluorescence or absorption imaging using a CCD camera. The process is illustrated for the case of ^{87}Rb in Fig. 9.74. The images show clouds of atoms 6 ms after the trap has been switched off. Clouds just before condensation, at the beginning of condensation and at full condensation are shown. The temperature of the Bose condensate is of the order of 10^{-9} K. Images can also be formed through the dispersive scattering of off-resonant light. The primary laser light is blocked in a Fourier plane of the imaging system. This latter method is non-intrusive and does not heat or influence the condensate.

A Bose condensate can be seen as a coherent matter wave with a very long de Broglie wavelength. The coherence can be observed by letting two expanding Bose condensates interfere, producing sharp fringes [9.461]. By switching out part of a condensate repeatedly using RF pulses and letting the atoms fall by gravity, pulses of coherent matter, a pulsed atom laser (“boser”), can be attained (see Fig. 9.75 [9.462]). Quasi-CW boser waves have also been achieved, and atom “amplification” has been observed [9.463]. The

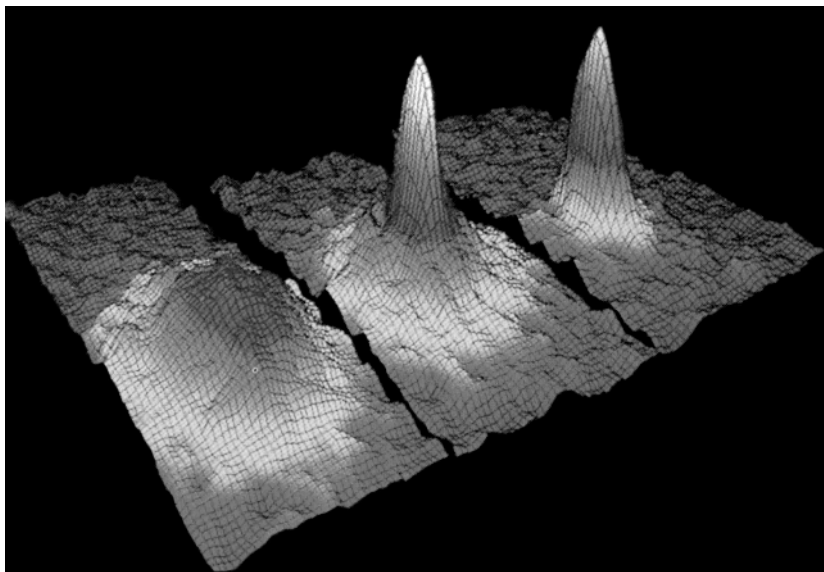


Fig. 9.74. Illustration of Bose-Einstein condensation in rubidium atoms [9.460]

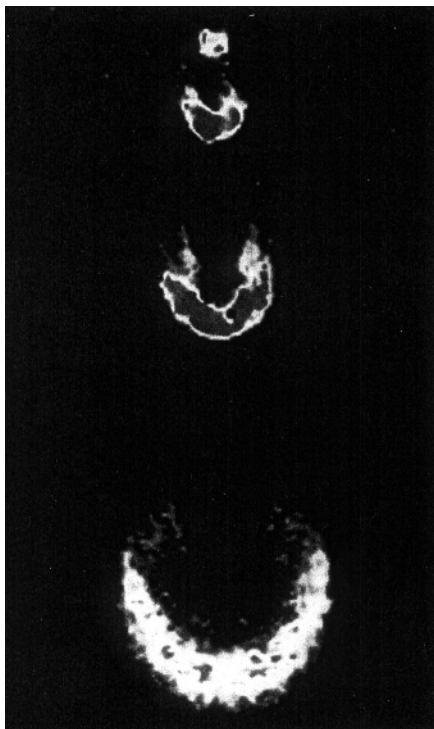


Fig. 9.75. Pulses of coherent matter waves generated from a Bose-Einstein condensate [9.462]

applications of such sources in atomic engineering and nanofabrication could be numerous. The field of BEC has attracted very high scientific interest with numerous theoretical and experimental activities [9.464]. Among the achievements the demonstration of the corresponding phenomena for coherent matter waves as observed in normal nonlinear optics could be mentioned (degenerate four-wave mixing) [9.465].

In 1998 BEC in spin-polarized hydrogen, the most long-running candidate, was also achieved [9.466] using an efficient combination of magnetic trapping and evaporative cooling [9.457].

9.8.9 Ultracold Fermionic Gases

Whereas integer-spin atoms can be made to pile up in the lowest energy state, resulting in Bose–Einstein condensation, half-integer spin atoms (fermions) cannot do so because of the Pauli exclusion principle. Instead the atoms can be brought to fill all the lowest energy states up to the Fermi level, in the same way that electrons do in a solid. While the transition into the BEC region is abrupt, as discussed above, the crossover into the *fermionic degenerate state* is more gradual. However, the phenomenon in strongly cooled fermionic gases has been clearly demonstrated [9.467]. It manifests itself in the suppression of inelastic collisions and of spontaneous emission rates, both caused by the full occupancy of the lowest-lying energy states. A major problem to be overcome was that normal evaporative cooling and subsequent rethermalization is ineffective due to the inelastic-collision suppression discussed above. This could be overcome by using a cold mixture of ${}^{40}\text{K}$ ($I = 4$) atoms in different magnetic substates of the $F = 9/2$ ground-state hyperfine level. A particularly interesting possibility for the future might be the formation of Cooper pairs (bosons) just as for normal superfluidity, resulting in the condensation of the original fermionic gas into a superfluid.

10. Laser-Spectroscopic Applications

In the previous chapter we have seen how lasers can be used in a multitude of ways to gain basic information on atomic and molecular systems. Thus, the laser has had a considerable impact on basic research, and its utility within the field of applied spectroscopy is just as great. We shall discuss here some applications of considerable interest. Previously, we have mainly chosen examples of atomic rather than molecular spectroscopy, but in this chapter we shall mainly discuss applied molecular spectroscopy. First we will describe the *diagnostics of combustion processes* and then discuss *atmospheric monitoring* by laser techniques. Different aspects of *laser-induced fluorescence* in liquids and solids will be considered with examples from the environmental, industrial and medical fields. We will also describe *laser-induced chemical processes* and *isotope separation with lasers*. Finally, *spectroscopic aspects of lasers in medicine* will be discussed. Applied aspects of laser spectroscopy have been covered in [10.1, 10.2].

10.1 Diagnostics of Combustion Processes

10.1.1 Background

Research in the field of combustion has been intensified recently because of the appreciation of the need for efficient combustion combined with low pollution. In order to obtain a deeper understanding of combustion processes it is necessary to perform the study at a molecular level. Laser spectroscopic techniques provide unique possibilities for non-intrusive measurements on the extremely aggressive media that burning or exploding gases constitute. Because of the unique properties of laser beams, both high spatial and temporal resolution can be achieved. Before we describe some measurement techniques we will give an elementary background to combustion processes [10.3, 10.4].

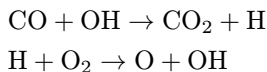
A detailed understanding of combustion must start with simple processes such as hydrogen, methane or acetylene combustion in oxygen or air. Normal liquid hydrocarbons are considerably more complex and wood or coal combustion can hardly be attacked at a molecular level. Below we give some “effective” chemical reactions leading to a transformation of fuel and oxidant

Table 10.1. Some effective chemical reactions in fuel combustion

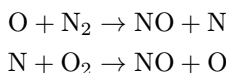
| Flame | Effective reactions | Temperature [K] | Energy release [J/g] |
|-----------------------------------------------|-----------------------------------------------------------------------------------------|--------------------|-------------------------|
| H ₂ /O ₂ | 2H ₂ + O ₂ → 2H ₂ O | 3100 | 24 000 |
| CH ₄ /O ₂ | CH ₄ + 2O ₂ → CO ₂ + 2H ₂ O | 3000 | 10 000 |
| C ₂ H ₂ /O ₂ | 2C ₂ H ₂ + 5O ₂ → 4CO ₂ + 2H ₂ O | 3300 | 12 000 |

into carbon dioxide and water. The processes are strongly exothermic, which is, of course, a common feature of combustion processes (Table 10.1).

Combustion occurs with a large number of intermediate steps, and even simple processes, such as the ones listed in Table 10.1, occur through dozens of coupled elementary reactions. With computer simulations it is possible to describe the interaction between the reactions, and concentration profiles can be calculated. In order to perform the computer calculations it is necessary to know the rate constants for the individual elementary reactions. Comparisons between theory and experiments are best made for a flat, premixed flame, which in its central part can be considered to have only one-dimensional (vertical) variation, allowing computer calculations to be performed comparatively easily. The most important reactions are included in the computer description. In Fig. 10.1 experimental and theoretically calculated concentration curves are given for the case of low-pressure ethane/oxygen combustion. As examples of important elementary processes we give the reactions



Reactive molecular fragments or radicals, such as OH, H and O, are very important in combustion. The combustion zone of a stoichiometric CH₄/O₂ flame contains about 10% OH, and 5% each of H and O. In the second of the two reactions given above the number of radicals is doubled. A fast increase in radical formation frequently leads to explosive combustion. Because of the high reactivity of radicals they cannot be measured by probe (extraction tube) techniques, since wall reactions immediately eliminate them. Thus, laser techniques are particularly valuable for radical monitoring. Pollution formation in flames should also be considered. Nitrogen and sulphur oxides, incompletely burnt hydrocarbons and soot particles form important pollutants. It is of the utmost importance to understand which elementary reactions form and eliminate pollutants. The formation of nitric oxide is reasonably well understood. At temperatures above 2000 K the nitrogen in the air is attacked:



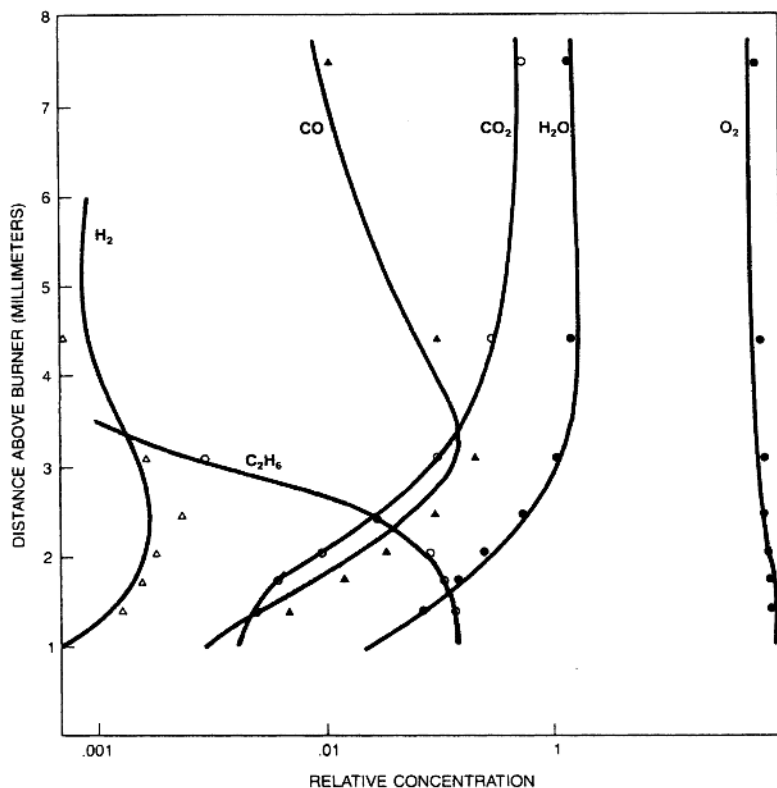
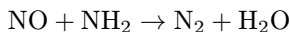
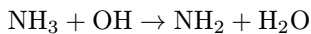


Fig. 10.1. Experimental and theoretical concentration profiles for an ethane/oxygen flame [10.3, first ref.] (Copyright 1982 by Scientific American, Inc. All rights reserved)

The two reactions constitute the so-called Zeldovich mechanism. NO is then oxidized to the toxic NO₂ by the oxygen in the air. NO can be eliminated from the post flame gases by the addition of NH₃. The following reactions occur [10.5]



In the case of sulphur oxide, SO, it is immediately further oxidized to SO₂ in the flame. It seems that a reduction of SO₂ can only be obtained by using low-sulphur fuels. SO₂ and NO₂ are further oxidized to H₂SO₄ and HNO₃ in the atmosphere with subsequent acid rain formation.

Soot formation is the subject of many studies [10.6]. Soot formation is enhanced at high fuel/air mixing ratios (rich flames) when using hydrocarbons with comparatively little hydrogen, and for bad mixing conditions. Since available fuels will become successively poorer in hydrogen, soot formation will

become an increasing problem. The chemistry of soot formation is not well understood. Many processes, including polymerization of simple hydrocarbons to heavier ones and reactions with polyaromatic hydrocarbons, may be important. Basic flame combustion has been described in [10.3, 10.4, 10.7, 10.8] and emission and absorption spectroscopy of flames discussed in [10.9].

Laser techniques have a great potential for studies of microscopic as well as macroscopic combustion in flames and engines. Combustion diagnostics with lasers has been discussed in several book reviews [10.10–10.15]. We will here give examples of measurements of concentrations and temperature (flame kinetics) using fluorescence, Raman and coherent Raman techniques. In practical combustion systems turbulence is extremely important and we will also briefly discuss laser techniques for flow and turbulence measurements.

10.1.2 Laser-Induced Fluorescence and Related Techniques

In laser-induced fluorescence (LIF) experiments a laser is normally tuned to an allowed dipole transition from a lower to an upper state of the species under consideration, and the fluorescence light that is emitted during the subsequent decay is observed. We will start this section by considering the corresponding spontaneous emission process. At the high temperatures in a flame, upper levels become thermally populated and a natural emission giving the flame its colour occurs. In Fig. 10.2 part of the emission spectrum from a C_3H_8 /air Bunsen-burner flame is shown, featuring strong bands due to the radical C_2 . This emission was described by Swan as early as 1857 in one of the earliest molecular spectroscopy experiments. C_2 is responsible for the blue-green light from the lower parts of hydrocarbon flames. Schematic energy-level diagrams for C_2 and OH with the wavelengths of the individual bandheads are depicted in Fig. 10.3. Hydrocarbon flames also exhibit strong bands due to the CH (~ 390 and 430 nm, especially in the flame front) and the OH radicals (~ 300 nm). In sooty flames the strong yellow light is due to incandescence of soot particles.

LIF yields a much more well-defined emission situation than the one pertaining to thermal emission. Different aspects of the use of LIF for combustion studies are treated in [10.18, 10.19]. For quantitative LIF measurements it is necessary to consider and control the quenching of the fluorescence due to collisional, radiationless transitions. The quenching can be represented by a term Q to be accounted for on equal footing with A (describing spontaneous emission). The observed light intensity will be strongly reduced due to the strong but rather unpredictable degree of quenching. Equation (9.1), describing saturation must now be written

$$\frac{N_2}{N_1 + N_2} = \frac{1/2}{1 + \frac{A+Q}{2B\rho(\nu)}}. \quad (10.1)$$

Since Q is frequently 10^3 times larger than A , a very high spectral energy density $\rho(\nu)$ is needed to obtain saturation with a laser beam. However,

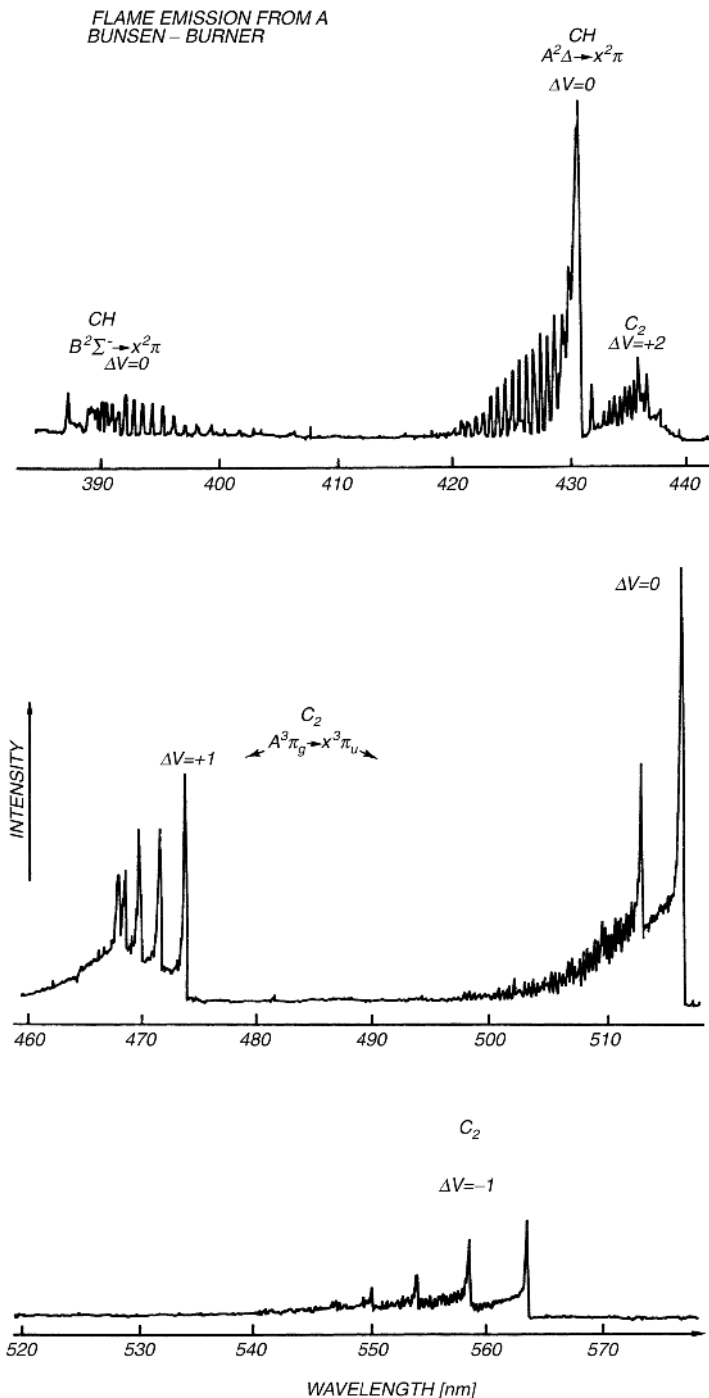


Fig. 10.2. Emission from a propane/air Bunsen-burner flame [10.16]

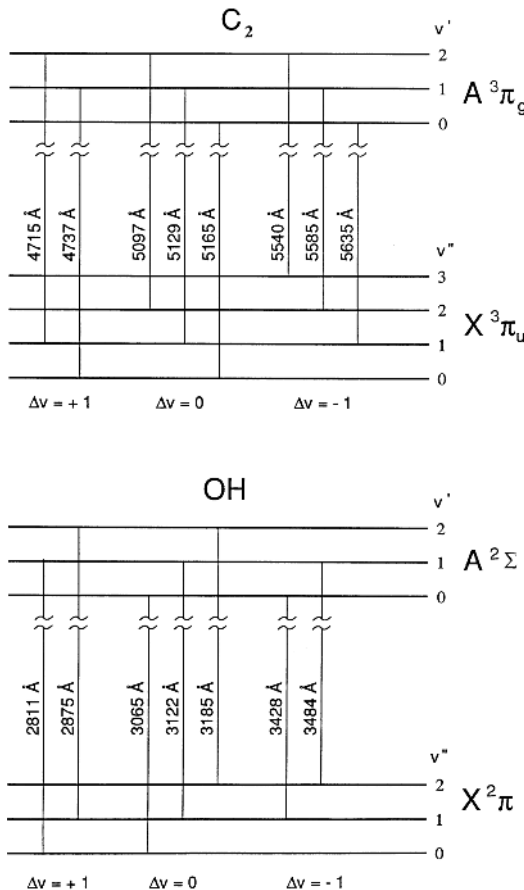


Fig. 10.3. Energy level schemes for the C₂ and OH molecules [10.17]

this can often be achieved and then the maximum fluorescence intensity is obtained despite the quenching, which no longer influences the measurement. Alternatively, the degree of quenching can be measured directly using time-resolved fluorescence spectroscopy. This is possible since the lifetime τ is shortened from its natural value $1/A$ to $1/(A + Q)$. With a prior knowledge of the low-pressure “true” lifetime the observed value immediately yields the quenching at the particular pressure. Clearly, the quenched lifetimes are normally very short and have to be measured with picosecond laser techniques (Sect. 9.5) [10.20–10.22].

An experimental set-up for studying LIF in flames is shown in Fig. 10.4. The output of a Nd:YAG pumped dye laser can be frequency doubled and, if needed, the doubled output can be mixed with residual 1.06 μm radiation to achieve still shorter wavelengths. The beam is directed through the flame and the fluorescence can be spectrally analysed with the spectrometer shown in

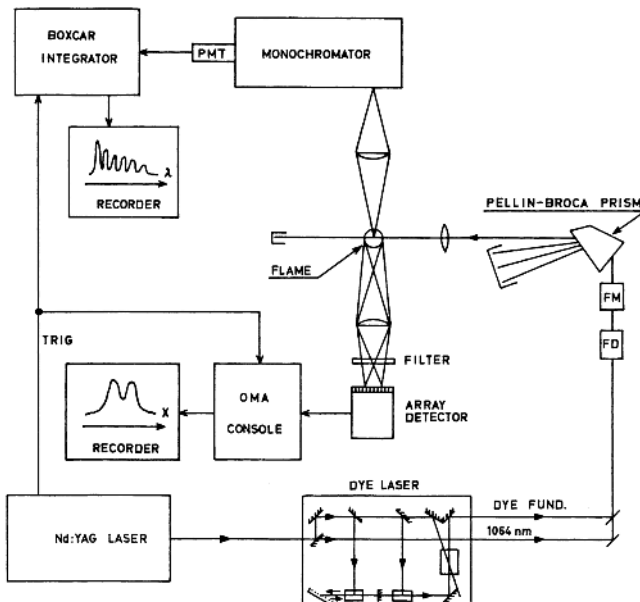


Fig. 10.4. Set-up for spectrally resolved and imaging laser-induced fluorescence studies [10.23]

the upper part of the figure. The figure also shows how a diode-array detector can be used to obtain a one-dimensional image of the distribution of a radical across a flame [10.24]. The streak of LIF is imaged onto the detector, which is gated by the laser firing. Figure 10.5 shows distributions of OH fluorescence at various heights in a CH_4/O_2 flame. A single 10 ns pulse is used for each recording.

Using two-dimensional CCD detectors, LIF imaging of full sections through flames can be performed [10.25, 10.26]. Then a thin sheet of laser light is formed by employing a combination of cylindrical and spherical lenses, and the cross-section with the flame is imaged at right angles on the gated and intensified imaging detector. Many flame species, including OH, C, CN, CH and NO have been studied using single-photon LIF. Several important flame species (such as H, C, N and O) have their single-photon excitation in the VUV region, where the flame gases absorb and tunable lasers are not readily available. It is then possible to use two-photon or even three-photon excitation (Sect. 9.1.3). In Fig. 10.6 an excitation scheme and in Fig. 10.7 (trace a) a 2-photon LIF spectrum for oxygen atoms in a $\text{C}_2\text{H}_2/\text{O}_2$ welding torch are shown. The collisional transfer from the triplet to the quintet system in O should be especially noted. (The absence of free oxygen atoms in room air is illustrated in Fig. 10.7 (trace b)).

If the two-photon transition is pumped sufficiently hard, strong amplified spontaneous emission is obtained in the forward direction [10.28]. (The

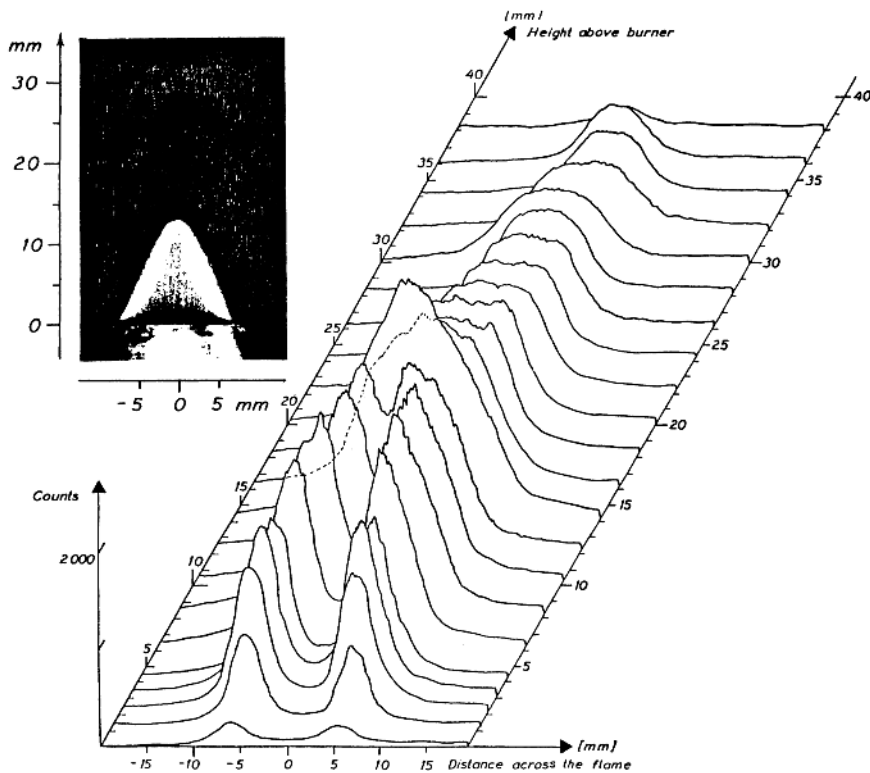


Fig. 10.5. Spatial distributions of the OH radicals in a CH_4/O_2 flame [10.24]. The excitation wavelength was 281 nm and the detection wavelength 308 nm

spectra in Fig. 10.7 are recorded in the perpendicular direction). The laser-like emission can also be used for diagnostics purposes, although quantitative information is difficult to extract.

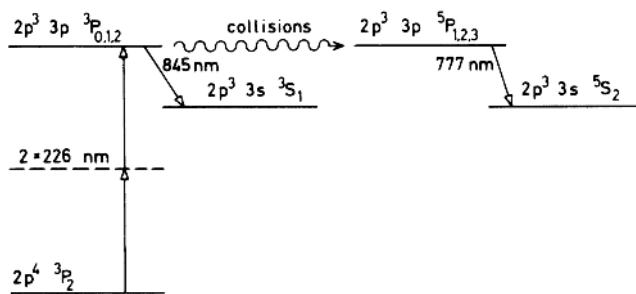


Fig. 10.6. Two-photon excitation scheme for oxygen atoms [10.27]

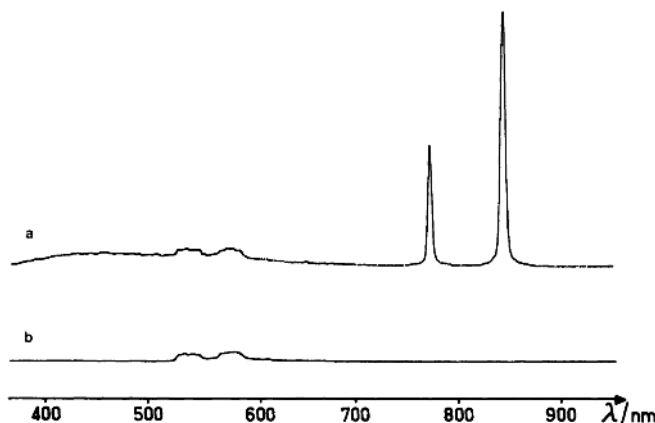


Fig. 10.7. Laser-induced fluorescence spectrum for oxygen atoms in a C_2H_2 welding torch [10.27]

Hydrogen atoms can be detected observing H_α or H_β emission from the $n = 3$ or 4 levels following two-photon [10.29] or three-photon excitation [10.30] or stepwise excitations [10.31]. CO and NH_3 molecules are also best detected using two-photon excitation [10.32]. The excitation of flame species to an upper level can also be detected by other means. Optogalvanic spectroscopy (Sect. 9.2.6) [10.33, 10.34] and photoacoustic spectroscopy (Sect. 9.2.8)[10.35] employing pulsed lasers have been used. The former method is not non-intrusive in nature because of the need for electrodes. The latter technique utilizes the local pressure increase following excitation, and a microphone close to the flame is used for detection. Spatial resolution is limited since the signal is collected along the laser beam. Ordinary absorption measurements clearly constitute the best examples of such line-of-sight measurements. Diode lasers, as well as dye lasers, have been used successfully in flame absorption measurements [10.36]. Polarization spectroscopy (Sect. 9.7.2), which is a special kind of absorption technique, has also been used for combustion diagnostics [10.37]. With tomographic techniques, similar to those used in medical X-ray imaging [10.38], spatially resolved information can be obtained from integrated absorption measurements in different directions through a gas flow or a flame [10.39]. By using tomography three-dimensional information can also be obtained utilizing thermal flame emission [10.40] and interferometry [10.41].

Laser beam deflection can also be used to detect optical resonance. In the region of optical excitation the index of refraction of the gas changes and a probing laser beam (frequently a He-Ne laser beam) crossing the excited region will be deflected [10.42].

10.1.3 Raman Spectroscopy

The laser combustion diagnostics techniques discussed so far utilized resonant processes, whether it be single- or multi-photon excitation, fluorescence or stimulated emission. We will now consider non-resonant processes of Raman nature. Because of its insensitivity to quenching (the lifetime of the virtual state is $\sim 10^{-14}$ s), Raman spectroscopy is of considerable interest for quantitative measurements on combustion processes. Further, important flame species such as O₂, N₂ and H₂ that do not exhibit IR transitions (Sect. 4.2.2) can be readily studied with the Raman technique. However, because of the inherent weakness of the Raman scattering process (Sect. 4.3) only non-luminous (non-sooting) flames can be studied.

Extractive Raman measurements on stable flame species can readily be performed. Here gases are transferred from the flame through a thin tube to the scattering cell of a laser Raman gas analysing system. In Fig. 10.8 Stokes Raman spectra, obtained using an Ar⁺ laser operating on the 488 nm line are shown for the lower and upper part of a C₃H₈/air Bunsen-burner flame are shown. The conversion of fuel and O₂ into CO₂ and H₂O, constituting the overall combustion process, is clearly demonstrated. The H₂O signal is prevented from increasing by a water vapour condenser in the gas feed-line. Soot particles, which give rise to a broadband LIF background, are also filtered away. The lower trace also displays signals due to CO and H₂, gases that will mostly burn up higher up in the flame. The weak signals in the shoulder of the strong Rayleigh line in the lower trace are due to pure rotational Raman transitions in the H₂ molecule, which, because of its small mass, has an exceptionally large rotation constant B (Sect. 3.2). The main hydrocarbon signal at about 570 nm has many components corresponding to slightly different C–H stretch vibrational frequencies. They occur at a Raman shift around 2960 cm^{−1} (Table 6.4). The corresponding IR transitions occur around 3.4 μ m. Overtone and combination bands are also observed at smaller Raman shifts.

Using pulsed lasers and gated detection electronics, Raman measurements can also be performed for major species in flames that do not contain too many particles. Temperature measurements can then also be made using the Stokes/anti-Stokes signal asymmetry or the occurrence of slightly displaced Stokes hot-bands as discussed in Sect. 4.4.1. Flame Raman Spectroscopy is discussed in further detail in [10.43, 10.44].

10.1.4 Coherent Anti-Stokes Raman Scattering

The CARS process has been described previously (Sect. 8.6). CARS spectroscopy is of particular interest for combustion diagnostics because of the strong signal available as a new laser beam emerging from the irradiated gas sample. Thus CARS is largely insensitive to the strong background light that characterizes practical combustion systems such as industrial flames and internal

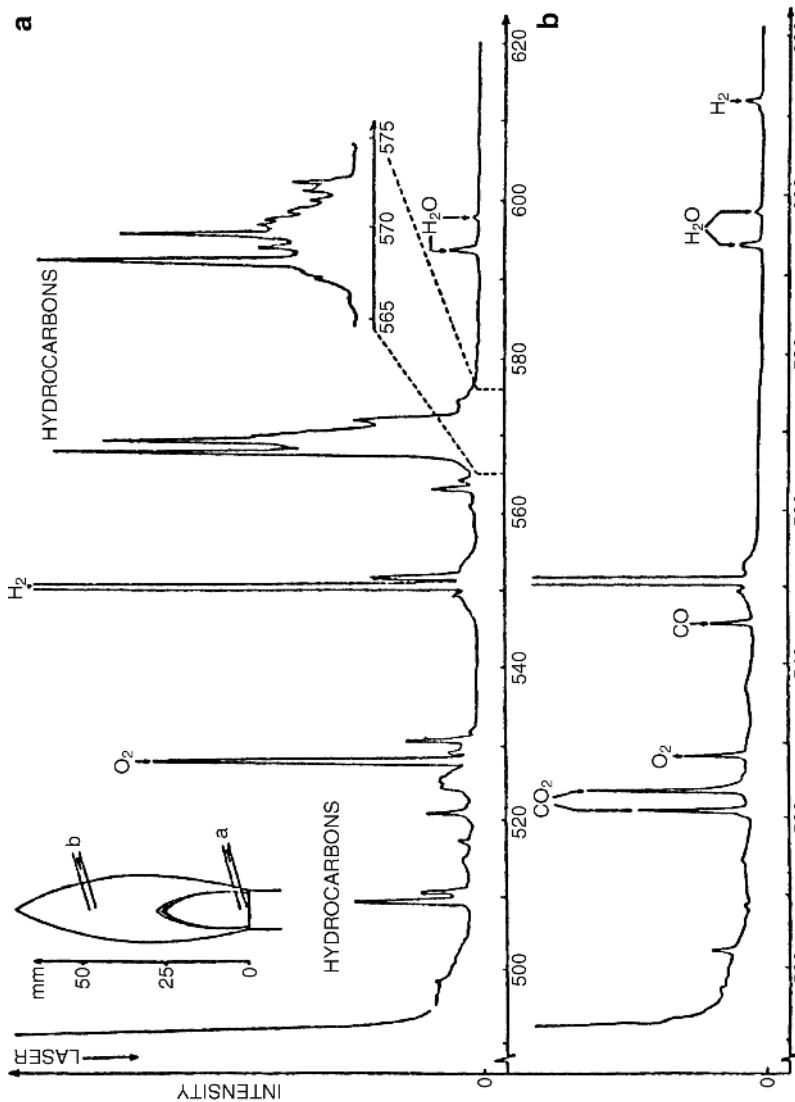


Fig. 10.8. Raman spectra of extracted flame gases at two different heights (a), (b) in a Bunsen burner flame [10.16]

combustion engines. We recall that the spectroscopic information is contained in the third-order susceptibility term $\chi^{(3)}$. This term is given by the sum of a complex resonant term (proportional to the concentration of the studied molecule) and a non-resonant background term. Thus, when the expression $|\chi^{(3)}|^2$ governing the signal strength is formed (8.13) interference between the resonant signal and the background occurs, resulting in asymmetric signals, very much like the case of polarization spectroscopy, see (9.34). For a molecule with vibrational and rotational levels, whose populations are temperature

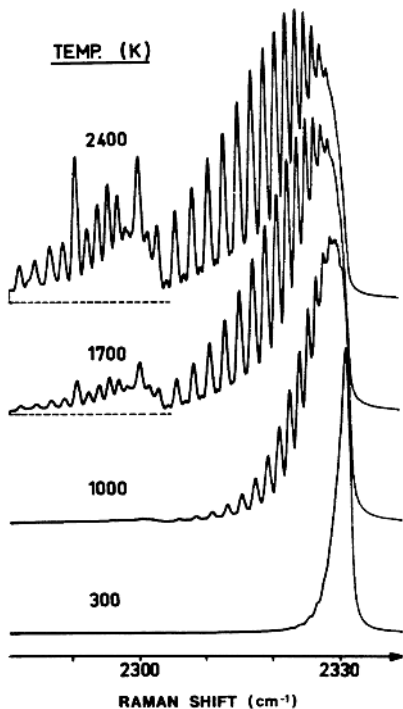


Fig. 10.9. Theoretically calculated CARS curves for N_2 molecules at different temperatures [10.45]

dependent, there are many close-lying resonances and the signal shape has to be calculated with a computer program. In Fig. 10.9 theoretical curves for the N_2 molecule are shown for different temperatures. The occurrence of the first hot-band and the gradual widening of the vibrational peaks due to increasing rotational level population can clearly be seen for increasing temperatures. Figure 10.10 shows experimental spectra for a CH_4/air flame and for room temperature air recorded with a set-up of the type shown in Fig. 10.11.

The BOXCARS phase-matching scheme (Fig. 8.47) is implemented for the pump beams at ω_p and the Stokes beam at ω_s in the arrangement shown in Fig. 10.11. After frequency doubling, the main part of the Nd:YAG laser output is used to pump the dye laser that generates the tunable ω_s beam, while the rest is used for the pump beam. The anti-Stokes beam at $\omega_{\text{AS}} = 2\omega_p - \omega_s$ which emerges when $\omega = \omega_p - \omega_s$ matches a rotational-vibrational transition for the molecule, is detected after proper spectral isolation from the strong pump beam. When the dye laser is slowly tuned through the signal region with the laser continuously firing, curves such as the ones shown in Fig. 10.10 are recorded using a gated boxcar integrator. The resolution in the

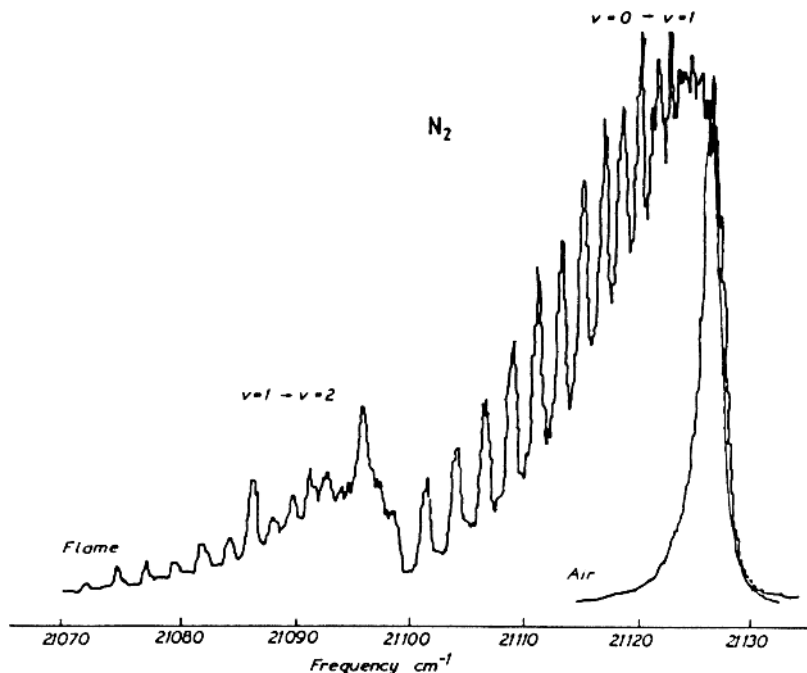


Fig. 10.10. Experimental CARS recordings for room-temperature N_2 molecules and for N_2 molecules in a flame [10.45]

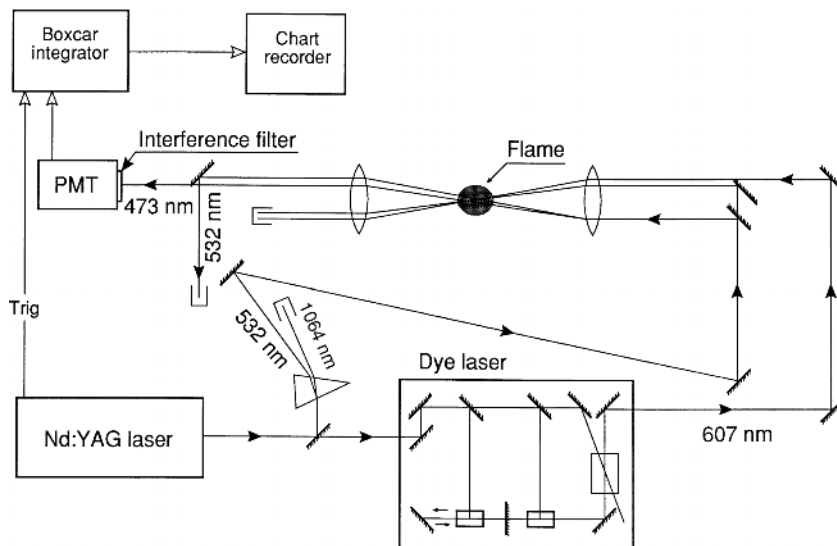


Fig. 10.11. Experimental set-up for CARS spectroscopy using the BOXCARS phase matching scheme [10.17]

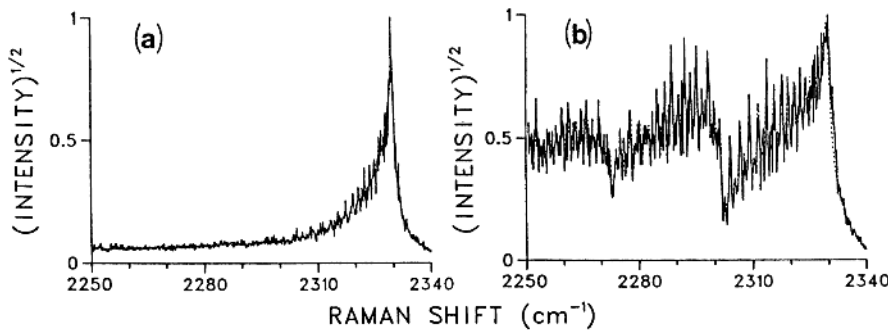


Fig. 10.12. N_2 CARS spectrum from a firing engine [10.47]: (a) 10 degrees after ignition, 7.1 atm; (b) 40 degrees after ignition, 15.6 atm

spectrum is given by the (small) laser linewidths and not by the resolution of a spectrometer, as in normal spontaneous Raman spectroscopy.

Because of the highly nonlinear nature of the CARS process (the signal is proportional to the square of the molecular number density and to $P_p^2 P_s$, see (8.13)), signal averaging does not yield a true value for rapidly varying, turbulent media. It is thus desirable to be able to perform the measurement using a single laser pulse. This is possible using an amplified broadband dye laser (Sect. 9.2.3) for the Stokes beam, which, in conjunction with a narrow-band pump-laser beam, will cover all the difference frequencies $\omega_p - \omega_s$ of interest for a specific molecular spectrum. The anti-Stokes signal frequency components are then all generated simultaneously through the action of the third-order susceptibility $\chi^{(3)}$. A gated and intensified linear diode array is used to capture the single-pulse spectrum. The technique can be used for measurements in specially adapted internal combustion engines. The laser firing can be strobed on a particular crank angle and the temperature at various time intervals can then be determined [10.46, 10.47]. An experimental spectrum from N_2 molecules in an internal combustion engine is shown in Fig. 10.12. CARS techniques have also been applied to full-scale coal furnaces [10.48] and other practical combustors [10.49, 10.50]. CARS is especially useful for remote thermometry but species concentrations can also be determined, especially for major species. CARS techniques have been discussed in more detail in [10.44, 10.45, 10.51]. For minor species, LIF is frequently the most suitable technique. Since the LIF signals also depend on the temperature-dependent distribution of population on levels, the temperature can also be determined in such experiments if excitations from two metastable levels with different energies are used (two-line fluorescence method [10.52])

Recently, degenerate four-wave mixing (Sect. 8.6) has also been applied to combustion studies [10.53]. In this technique the sensitivity of LIF is combined with the advantages of a coherent signal beam characteristic to CARS.

The techniques discussed here in connection with combustion diagnostics can clearly also be used for the monitoring of other reactive media. The techniques have been found to be valuable in the characterization of *chemical vapour deposition* (CVD) processes for semiconductor fabrication [10.54]. The examples mentioned here illustrate the power of laser spectroscopic techniques in studying chemical processes. Numerous other examples of chemical applications of laser spectroscopy can be found. The field was covered in [10.2, 10.55].

10.1.5 Velocity Measurements

Laser Doppler Velocimetry (LDV) is an important non-spectroscopic laser technique for intrusion-free measurements of velocities in liquid or gaseous flows, including combustion flows. In this technique two laser beams (frequently from an Ar^+ laser) are crossed at a small angle in the medium to be studied, as shown in Fig. 10.13. A standing interference pattern with bright and dark fringes is then formed. If a small particle being carried by the flow passes the interference pattern, it will produce periodic glimpses of light that can be detected by a photomultiplier tube. The frequency f_D of the periodic signal (the Doppler burst) can be analysed by Fourier transformation, and the velocity v can then be determined since the fringe separation d is given by the laser wavelength λ and the beam-crossing angle θ . We have

$$v = \frac{\lambda f_D}{2 \sin(\theta/2)} . \quad (10.2)$$

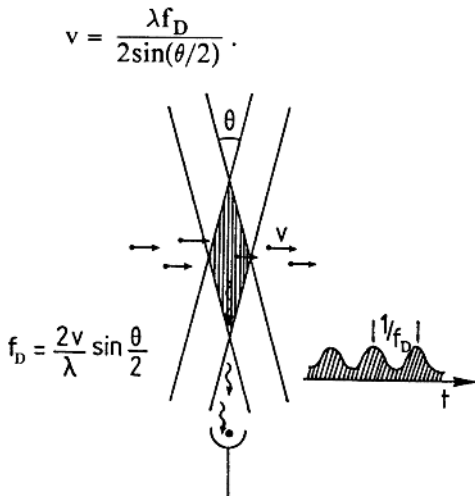


Fig. 10.13. Principle of Laser Doppler Velocimetry (LDV)

Clearly, if the particle is larger than the fringe separation, the contrast is reduced and thus LDV measurements also provide information on the particle sizes.

With one pair of crossing laser beams only one velocity component in the flow field can be determined. Furthermore, it is not possible to determine the sign of that velocity component since either flow direction produces the same Doppler burst. However, by frequency shifting one of the crossing beams with a Bragg cell (acousto-optic modulator), moving interference fringes are produced. It is then possible to decide from which direction a particle passed the interference field by noting whether the burst frequency was shifted upwards or downwards from the frequency from a fixed object. A second velocity component can be measured by using two additional laser beams propagating in a plane perpendicular to the first laser beam plane and crossing at the same point. In order to be able to distinguish the Doppler burst from this interference pattern, different wavelengths are used for the laser beams. Thus, it is customary to use the 5145 Å line of an Ar⁺ laser for one velocity component and the 4880 Å line for the other. The elastically scattered light is then detected through sharp interference filters in front of individual photomultiplier tubes. The third velocity component (in the direction of the bisectrix of the crossing laser beams) is harder to measure. However, by using three crossing beams in the same plane and extracting the information pair-wise from the central beam and one or other of the external beams, the third velocity component can be projected out, although at lower accuracy. When the scattered intensity is low, e.g. because of small particles, it is still possible to extract velocity information from the time correlation of the recorded individual photons. Special autocorrelation techniques have been developed for optimum information extraction [10.56]. It is frequently necessary to seed the flow with small particles. These particles do not necessarily truly follow the gas flow, which constitutes a complication with this technique.

We should conclude this description of LDV techniques with a comment on its common name. In our description of the technique we have not used “Doppler language” at all but rather expressed the observed phenomena in terms of a spatial interference pattern. However, we can alternatively consider the Doppler shift in the scattered light frequency caused by the motion of the particle. This shift is detected as a beat frequency against the light scattered from the other crossing beam. The beat frequency corresponds exactly to the frequency produced by a particle crossing the fringe pattern, so the two pictures are actually equivalent. LDV techniques have been discussed in detail in the monographs [10.57, 10.58].

A further class of velocity measurement techniques uses molecular “tagging”. A “package” of molecules is first tagged with a pump pulse, and the movement of the molecules is then monitored with a second laser beam [10.59].

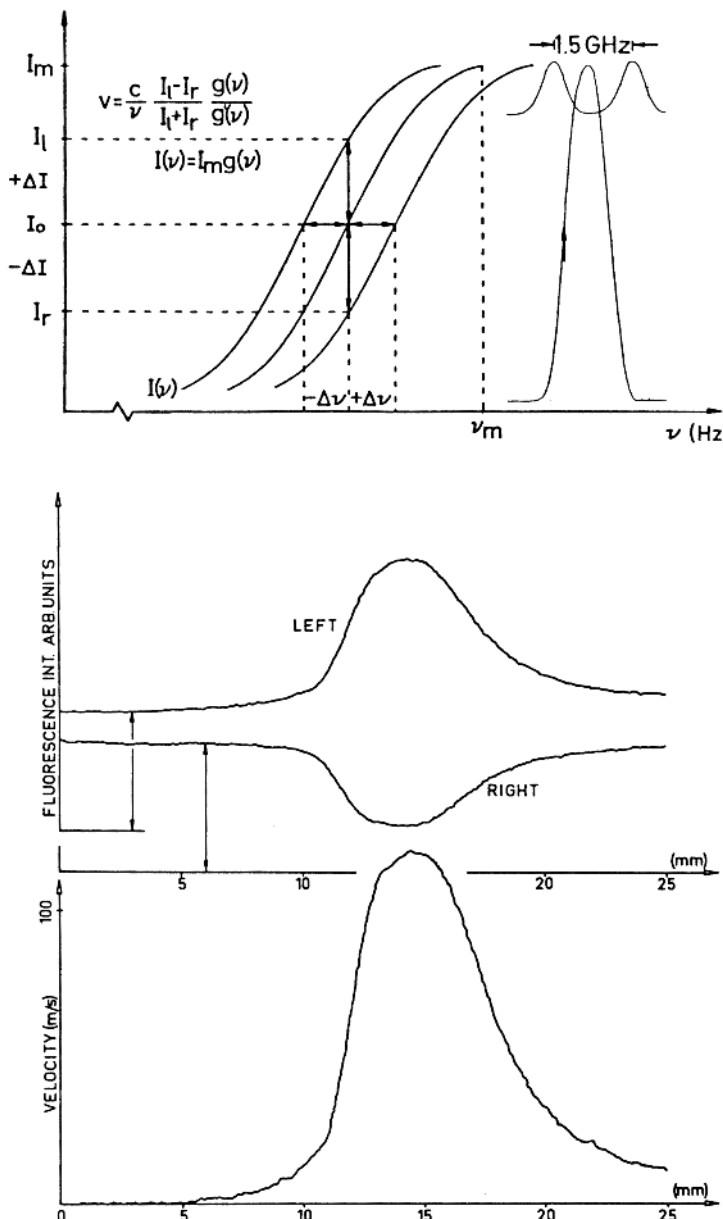


Fig. 10.14. Spectroscopic flow imaging for an I_2 seeded gas jet [10.61]

We will also consider a technique for velocity measurements which is based on Doppler shifting of absorption lines of atoms or molecules in the flow [10.60, 10.61]. The principle of the technique is illustrated in Fig. 10.14.

A narrow-band cw laser is tuned to a frequency ν in the shoulder of a Doppler-broadened absorption line, where fluorescence light of half the maximum intensity can be induced. If the gas molecules are displaced by a flow the whole Doppler-broadened profile will shift in frequency. Depending on the direction of this flow the fluorescence light intensity will increase or decrease. In order to measure the presence of a net flow, two alternating laser beams are sent through the medium in opposite directions. The fluorescence intensities are balanced out for a static gas, by adjusting the relative powers in the two beams. If the gas is moving, a modulation will be observed at the frequency of the beam direction shifting. By normalizing the signal it becomes independent of the number density of the molecules. We have

$$v = \frac{c}{\nu} \frac{I_{\text{left}} - I_{\text{right}}}{I_{\text{left}} + I_{\text{right}}} \frac{g(\nu)}{dg/d\nu}, \quad (10.3)$$

where I_{left} and I_{right} are the two detected fluorescence intensities and $g(\nu)$ is the value of the line-shape function at the chosen frequency ν .

A single-mode cw dye laser can be used for measurements of this kind. The experimental set-up is similar to the one used in Doppler-free intermodulated fluorescence measurements (Sect. 9.7.2), but now the beams are presented to the atoms/molecules one at a time. For measurements of this kind, the flow can be seeded with sodium atoms or I_2 molecules. Imaging measurement along a line can be performed using a CCD detector as illustrated in Fig. 10.14.

Laser techniques for flow measurements are discussed in [10.62]. Different types of imaging measurements of species concentrations, temperatures and flows utilizing LIF have been described in [10.23–10.27, 10.60, 10.61].

10.2 Laser Remote Sensing of the Atmosphere

Different aspects of remote sensing have been discussed in Sects. 6.6 and 7.2. In this section we will describe how laser techniques can be used for monitoring of the atmosphere and its pollutants. General information on the atmosphere and its optical properties is given in [10.63]. Laser beams are particularly useful for monitoring over large distances because of the low divergence of the beam. Typically, a divergence of 0.5 mrad is obtained, corresponding to a spot diameter of 0.5 m at a distance of 1 km. Dry air contains 78.1% N_2 and 20.9% O_2 . The rare gases Ar, Ne and He are present at levels of 9300, 18 and 5 ppm (parts per million), respectively. The CO_2 content is presently about 380 ppm, a value which increases annually by 0.5%. This may give rise to an increase in the average global temperature because of the change in the atmospheric radiation budget, the so-called extended *greenhouse effect* [10.64, 10.65]. Ordinary air also contains widely varying amounts of water vapour. The gases N_2O , H_2 , CH_4 , NO_2 , O_3 , SO_2 , CO , NH_3 , etc. are also naturally present in the atmosphere in concentrations that vary from several ppm to fractions of ppb (parts per billion). If such gases are found

in higher concentrations in the air because of human activities, they are considered as pollutants [10.66–10.69]. Measurements in the troposphere, as well as in the stratosphere, are of great interest. In the troposphere, monitoring of industrial emissions, as well as ambient air quality, is needed for environmental protection purposes. Stratospheric measurements are important, e.g. for assessing possible long-term changes in the absorption characteristics that could result in an altered radiation environment at the earth's surface (see the discussion of stratospheric ozone destruction in Sect. 6.4.5). Further, laser techniques also provide powerful means of remotely measuring meteorological conditions such as temperature, pressure, humidity, visibility and wind speed.

We will discuss two active remote-sensing techniques for the atmosphere – the *long-path absorption technique* and the *lidar technique*. However, we will first consider a passive technique, in which lasers play an important part in the detection scheme. This *optical heterodyne technique* is even more frequently used for signal recovery in connection with the active optical remote-sensing methods. The field of laser monitoring of the atmosphere is covered in several monographs and articles [10.70–10.76].

10.2.1 Optical Heterodyne Detection

Heterodyne detection is an important technique for low-noise signal recovery. Well-known in the radio-frequency region, it also has its counterpart in the optical regime. The principle of optical heterodyne detection is illustrated in Fig. 10.15. The incoming radiation is mixed in the detector with the radiation from a local oscillator, which could be a diode laser or a CO₂ laser. Beats are generated in the detector at the difference frequency between the signal frequency ν_s and the local oscillator frequency ν_L . A narrow-band electronic filter, which only transmits a fixed frequency ν_{IF} , the *intermediate frequency*, selects the beat frequency $\nu_s - \nu_L = \nu_{IF}$. ν_{IF} is chosen in the radio-frequency region in which amplification can easily be performed. When the frequency of the local oscillator is swept, the frequency of the recorded external signal is also swept and the spectrum will be recorded successively. The mixing of the signals can be described as

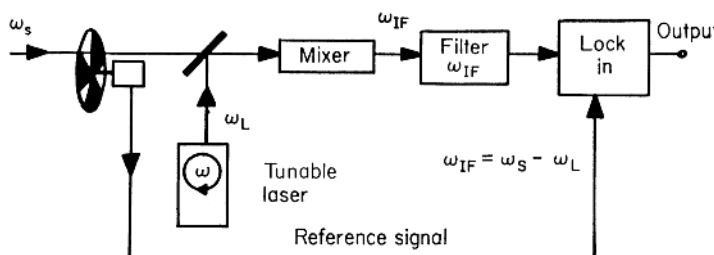


Fig. 10.15. Optical heterodyne detection [10.76]

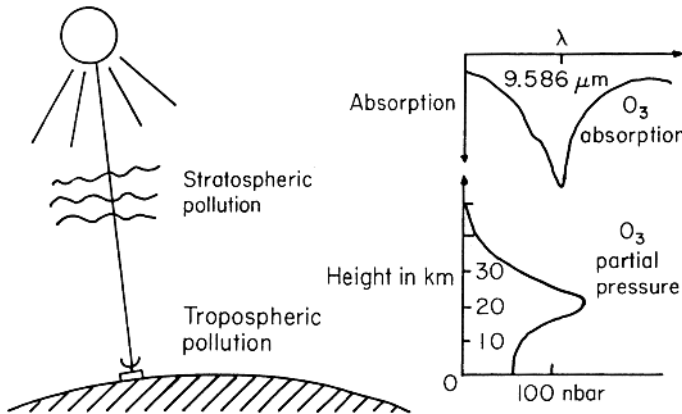


Fig. 10.16. Vertical ozone profiling (Adapted from [10.77])

$$\begin{aligned}
 I &= [A_s \sin(2\pi\nu_s t) + A_\ell \sin(2\pi\nu_\ell t)]^2 \\
 &= A_s A_\ell \sin[2\pi(\nu_s - \nu_\ell)t] + \text{terms oscillating at high frequencies.}
 \end{aligned} \tag{10.4}$$

As we can see, the amplitude of the recorded signal is proportional to that of the incoming signal A_s as well as to that of the local oscillator A_ℓ . By increasing the amplitude of the local oscillator, noise-free amplification can be achieved. Heterodyne detection is frequently referred to as *coherent detection* in contrast to *direct* detection of the incoming radiation. It is sometimes also convenient to use phase-sensitive (lock-in) detection at the frequency of a beam chopper to obtain a further increase in the signal-to-noise ratio and background rejection. An example of heterodyne detection is shown in Fig. 10.16. The sun-disc is used as a radiation source and the absorption of the earth's atmosphere is monitored. The sun-disc is tracked with a heliostat. By tuning the local diode laser oscillator through the spectral region of an ozone infrared absorption line (see also Fig. 6.52), a signal with a pressure-broadened component (Sect. 6.1.1) from tropospheric ozone and a narrow component from the stratospheric layer is recorded. The vertical ozone concentration profile can then be calculated using a mathematical deconvolution procedure.

10.2.2 Long-Path Absorption Techniques

The principle of long-path absorption techniques is illustrated in Fig. 10.17. A laser beam is transmitted continuously into the atmosphere against a corner-cube retro-reflector (Fig. 6.21) that is placed at a distance of up to 10 km. The reflected beam is received by an optical telescope that is placed at the site of the laser and is directed towards the retroreflector. The received light intensity is measured photoelectrically as a function of the laser wavelength.

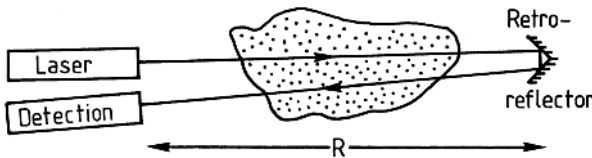


Fig. 10.17. Long-path absorption measurement of atmospheric pollutants

The absorption spectrum of the atmosphere between the laser and the retro-reflector is then recorded and the mean concentrations N_i , of pollutant molecules can be determined using the Beer–Lambert relation

$$\ln \frac{P_0(\nu)}{P_t(\nu)} = 2R \left(\sum_{i=1}^n \sigma_i(\nu) N_i + K_{\text{ext}} \right). \quad (10.5)$$

Here $P_t(\nu)$ is the received light intensity and $P_0(\nu)$ is the intensity that would have been received in the absence of atmospheric absorption. $\sigma_i(\nu)$ is the absorption cross-section for the molecules of type i . $\sigma_i(\nu)$ normally varies strongly with the wavelength while K_{ext} represents particle extinction, which is largely wavelength independent in a small wavelength region. If several molecules absorb in the same wavelength range it is necessary to perform the measurements in a sufficiently large wavelength interval, preferably with a continuously tunable laser to allow unambiguous determination of the individual molecular species. Frequently one tries to work in a wavelength region where the gas of interest is the dominant absorber. Then the measurement can conveniently be performed by rapidly switching the laser wavelength from the line centre to a nearby off-line wavelength. Clearly, it is necessary to work in a wavelength region where the dominant atmospheric absorbers CO_2 and H_2O have a low absorption (Sect. 6.4.5). Such regions can be found where the CO_2 and DF lasers emit around 10 and 4 μm , respectively. These gas lasers are normally only line-tunable and accidental wavelength coincidences are utilized. Sometimes, two lasers tuned to an on-resonance and an off-resonance frequency, respectively, are used, and rapid switching between transmission from the two lasers is performed. High-pressure CO_2 lasers and diode lasers are continuously tunable. The long-path absorption technique is used mainly for monitoring gases such as C_2H_4 (ethylene), $\text{C}_2\text{H}_3\text{Cl}$ (vinyl chloride) O_3 and CO utilizing suitably located vibrational transitions. Results from a measurement of NO across a major road are shown in Fig. 10.18. Clearly, these kinds of long-path absorption measurements are closely related to those performed using classical light sources (*differential optical absorption spectroscopy, doas*, Fig. 6.74). Diode laser spectroscopy for atmospheric measurements is discussed in [10.79].

The IR region can also be reached by difference-frequency generation between two diode lasers operating in the red and near-IR regions [10.80]. For increased efficiency, a periodically poled lithium niobate (PPLN) crystal (Sect. 8.6) can be used. A set-up for such measurements is shown in Fig. 10.19

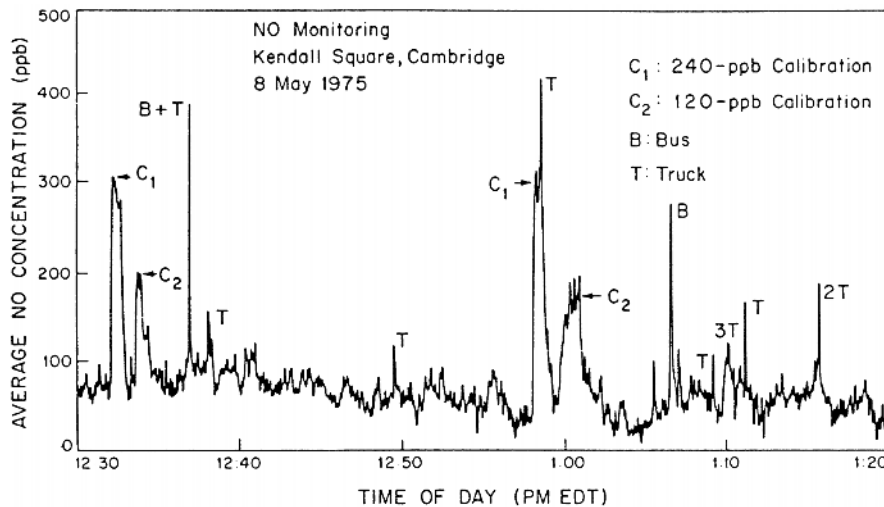


Fig. 10.18. Long-path absorption measurement of the NO concentration across a major road [10.78]

where the three available frequencies ω_1 , ω_2 and $\omega_1 - \omega_2$ are each resonant with an atmospheric species, O₂ at 760 nm, H₂O at 980 nm and CH₄ at 3.4 μ m [10.81]. The three species are simultaneously monitored over a 15 m open-air path through the laboratory. Included in the figure is a demonstration of the evacuation by the room ventilation system down to ambient levels following a methane release from a pressurised tank. An isolated CH₄ line at 2928 cm⁻¹ belonging to the *P*-branch of the ν_3 fundamental band was monitored in the measurements.

By sum-frequency mixing of the outputs from a blue and a red diode laser, the UV region can be reached as illustrated in Fig. 10.20. Measurements on the 254 nm mercury line are demonstrated for a low-pressure cell containing a mercury droplet and after letting atmospheric pressure air into the cell. Individual isotopic lines exhibiting only Doppler broadening merge together under the influence of pressure broadening [10.82]. The UV region can also be reached by frequency quadrupling a high-power near-IR laser in two successive frequency-doubling stages with nonlinear crystals in enhancement cavities [10.83].

The recordings in Figs. 10.19 and 10.20 were obtained by averaging a large number of fast sweeps. In this way the detrimental influence of atmospheric turbulence, etc. can be eliminated, as in doas measurements. If the optical absorption is very small an increased signal-to-noise ratio can be obtained if a modulation technique is employed. If the modulation frequency imposed on the diode-laser drive current is low compared to the absorption linewidth, the driver wavelength is modulated and the signal can be picked up by a lock-in amplifier as illustrated in Fig. 10.21a. The technique is referred to

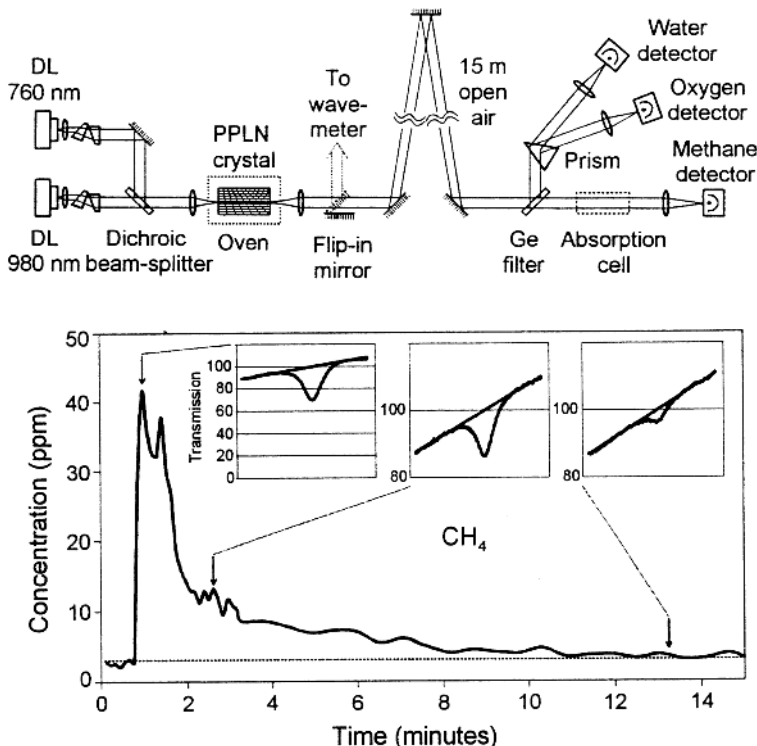


Fig. 10.19. Set-up for difference-frequency generation using two diode lasers. Arrangements for simultaneous long-path absorption monitoring of water vapour, molecular oxygen and methane are shown. Included in the figure is also the dynamics of the evacuation of a methane release into the laboratory [10.81]

as *wavelength modulation spectroscopy* (WMS). If the modulation frequency is increased to be of the order of one MHz the lock-in amplifier is replaced by a combination of a mixer and a phase shifter (Fig. 10.21b). The phase-sensitive detection can be performed at the modulation frequency (ν_m) and the signal close to the derivative is obtained or at $2\nu_m$, where the signal resembles the second derivative. An example of a recording where the modulation frequency was 5 MHz is included in Fig. 10.20 (curve (d) in the right part of the figure). If the modulation frequency is comparable to the pressure-broadened linewidth (few GHz) a more natural view of the modulation process is to consider the occurrence of an upper and a lower sideband around the single-frequency optical carrier. The phases of the sidebands are locked to the carrier, and there is a 180 degree phase shift between the two sidebands. The beat notes (at the modulation frequency) between the upper sideband and the carrier, on the one hand, and the lower sideband and the carrier, on the other hand, will normally cancel out at the detector because

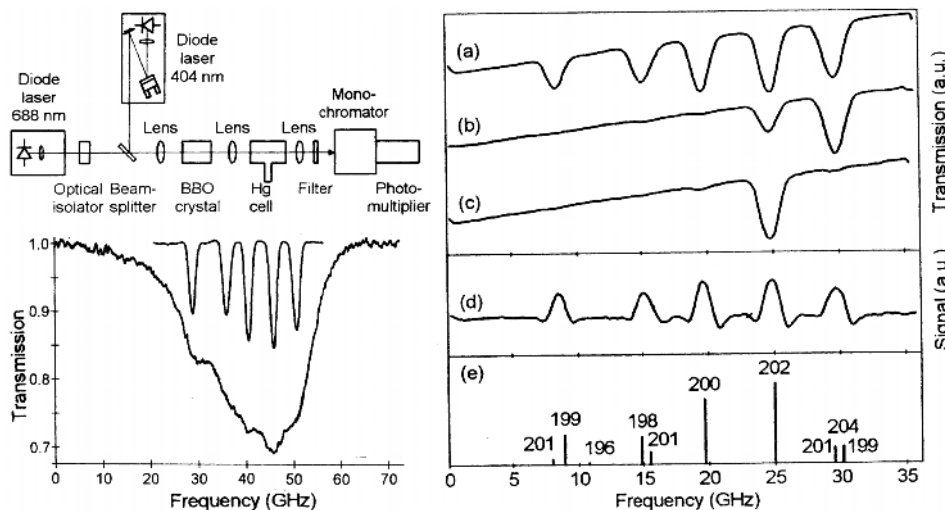


Fig. 10.20. Set-up for sum-frequency generation between a blue and a red diode laser to achieve the 254 nm mercury line (*upper left*). The mercury absorption spectra recorded at low pressure for natural isotopic mixture (*a*) and isotopically enriched samples; ^{204}Hg in (*b*) and ^{202}Hg in (*c*), are also included in the *right part* of the figure, together with designations and relative strengths of natural Hg line components (*e*). Finally, in the *lower left part* of the figure the pressure-broadened line of mercury in atmospheric air is shown together with a low-pressure spectrum [10.82]

of the phase shift. If, however, one of the side bands is attenuated by the presence of an absorbing species, a high-frequency beat is obtained. It is demodulated down to DC in a mixer, which can be seen to have the role of a high-frequency lock-in amplifier. The technique is referred to as *frequency-modulation spectroscopy* (FMS) and is illustrated in Fig. 10.22. In a variety of this technique, *two-tone frequency modulation spectroscopy* (TTFMS), the diode laser is simultaneously modulated at two high frequencies, separated by, for example 10 MHz. It can be shown, that the absorptive signal can be picked up at the 10 MHz frequency, which is electronically more convenient for detection.

It has been shown that FM techniques are capable of measuring absorption signals down to the shot-noise limit (caused by the number fluctuations for the discrete photons), which frequently means, that absorptive signals of 1 part in 10^6 or 10^7 are detectable. Frequency modulation spectroscopy is described and discussed in [10.85].

In a variant of the long-path absorption technique, radiation from a diode laser or a light-emitting diode is transmitted fibre-optically to remotely located multi-pass absorption cells (Sects. 6.5.6, 9.2.1) and the partially absorbed beam is sent back to the measurement system also using fibre-optics. Using such a system, which operates at short IR wavelengths (1 to $2\text{ }\mu\text{m}$) at which

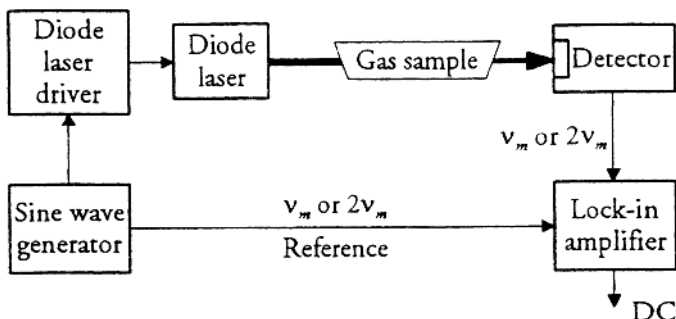
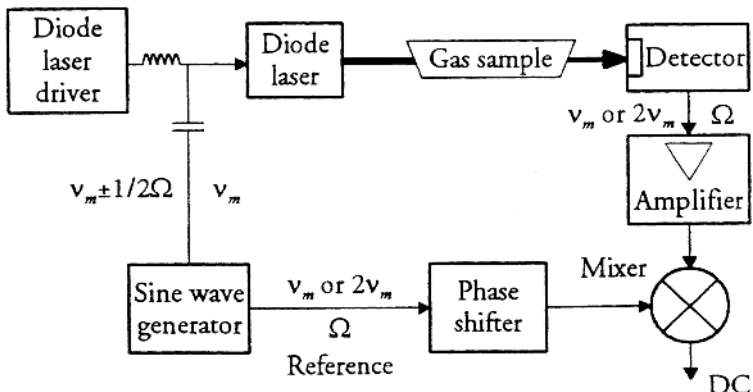
a) Low frequency modulation ($v_m < 100$ kHz)b) High frequency modulation ($v_m > 100$ kHz)

Fig. 10.21. Arrangements for frequency modulation spectroscopy with diode lasers. In (a) low frequencies are employed and the term wavelength modulation spectroscopy pertains. In (b) high frequencies are used and discrete components replace the lock-in amplifier [10.84]

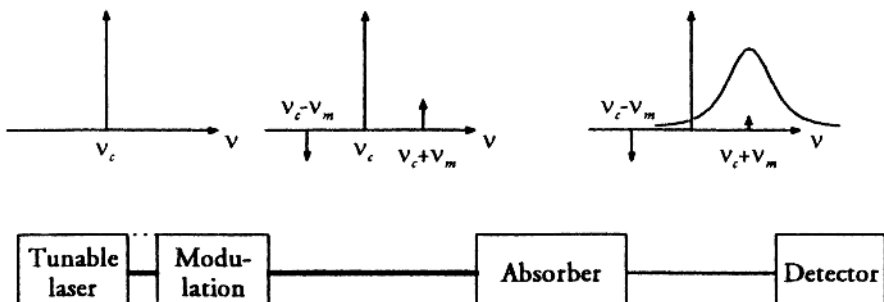


Fig. 10.22. Sideband generation in high-frequency modulation spectroscopy and resulting imbalance when one of the sidebands is absorbed by a gas [10.84]

optical fibres transmit well (Fig. 8.34), many points can be monitored from a central system with laser and computer facilities [10.86].

10.2.3 Lidar Techniques

Lidar, which is an acronym for *Light detection and ranging*, is a measurement technique in which pulsed laser radiation is transmitted into the atmosphere and back-scattered light is detected at a certain time delay in a radar-like fashion. The principle of lidar (also called laser radar) is illustrated in Fig. 10.23. Laser light that is back-scattered from a distance R arrives at the lidar receiver at a time $t = 2R/c$ after the transmission of the pulse. The velocity of light, c , is 300 m/μs. Range-resolved information can be obtained from the time delay, and the range resolution ΔR , is given by the duration of the laser pulse t_p : $\Delta R = t_p c/2$. (The range resolution may be further impaired due to the finite electronic response of the detection system.)

The most common use of the lidar techniques is for ranging, where the distance to a target is measured. Laser *range finders* have many applications, many of which are of a military nature. However, the technique is also used in land surveillance and in a number of interesting scientific contexts. A distinction is made between cooperative and non-cooperative targets, the former being equipped with reflectors to ease the procedure. Using high-repetition rate systems employing mirror scanning it is possible to map out the geometry of complex volumes such as grottoes, underground storage rooms and mines, e.g. for volume assessment. Satellite ranging is performed from a global network of stations equipped with picosecond laser transmitters and moderate-size receiving telescopes. Satellite ranging is important for orbit tracking, but a large number of very interesting geodetic results are also obtained. The technique allows to establish a very accurate reference frame for the surface definition. Precision data from the network include the following findings: there are tidal effects in the solid earth crust amounting to few cm, the average sea surface is changing by 2 mm/y, the motion of the centre of gravity of the earth is constrained within a roughly 1 cm diameter sphere relative to the fixed network of stations, tectonic plates are moving relative to each other at speeds ranging from a few mm to several cm/y, the length of the day varies, but on average is getting longer by about 2 ms/century, and the poles (instantaneous spin axis) wander within a 14 m diameter circle about its nominal position. Lunar ranging measurements using retroreflectors left on the lunar surface by astronauts or placed on unmanned moon landers have a precision of about 2 cm and reveal that the moon is moving away from the earth at a rate of 3.9 cm/y. Finally, in a laser time-transfer experiment involving ground based and airborne atomic clocks and precision satellite ranging to the aircraft over a period of approximately 30 hours, a 47 ns time differential was observed in agreement with general relativistic predictions of the effect of gravity and aircraft velocity on the rate of atomic clocks [10.87].

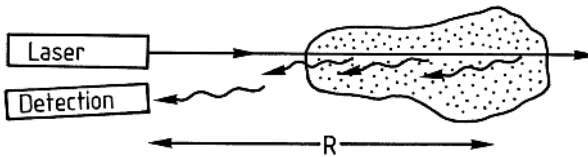


Fig. 10.23. The principle of lidar

Back-scattering is not only obtained from solid targets but also from particles and molecules in the atmosphere. The scattering is of the same kind as the common one involving the sun's radiation (Fig. 4.21). We obtain continuous laser ranging from small targets distributed along the path of the laser beam as illustrated in Fig. 10.23. The intensity of the received lidar signal is given by the general lidar equation

$$P(R, \Delta R) = CWN_b(R)\sigma_b(R)\sigma_b \frac{\Delta R}{R^2} \exp \left\{ -2 \int_0^R [\sigma(\nu)N(r) + K_{\text{ext}}(r)] dr \right\}, \quad (10.6)$$

where C is a system constant, W is the transmitted pulse energy and $N_b(R)$ is the number density of scattering objects with back-scattering cross-section σ_b . The exponential factor describes the attenuation of the laser beam and the back-scattered radiation due to the presence of absorbing molecules of concentration $N(r)$ and absorption cross-section $\sigma(\nu)$, and due to attenuating particles with wavelength-independent extinction coefficient K_{ext} . A single absorbing molecular species is assumed. The product $N_b(R)\sigma_b$ in the lidar equation determines the strength of the back scattering, which can be caused by several processes. It can be due to *fluorescence* from atoms or molecules that are resonantly excited by the laser light. At high pressures, i.e. in the troposphere, radiationless transitions due to collisions strongly quench the fluorescence light (Sect. 10.1.2). On the other hand, fluorescence detection is very efficient for the monitoring of mesospheric constituents. There are layers of Li, Na, K and Ca atoms in the mesosphere at a height of about 100 km. These layers of atoms, which are produced mainly through evaporation of meteorites impinging on the atmosphere, have been mapped out very successfully with ground-based fluorescence lidar systems operating with tunable dye lasers [10.88].

As discussed in connection with astronomical imaging (Sect. 6.7), sodium fluorescence lidars have found important application for providing *laser guide-stars* for allowing an effective use of adaptive optics to enhance image quality through the turbulent atmosphere [10.89].

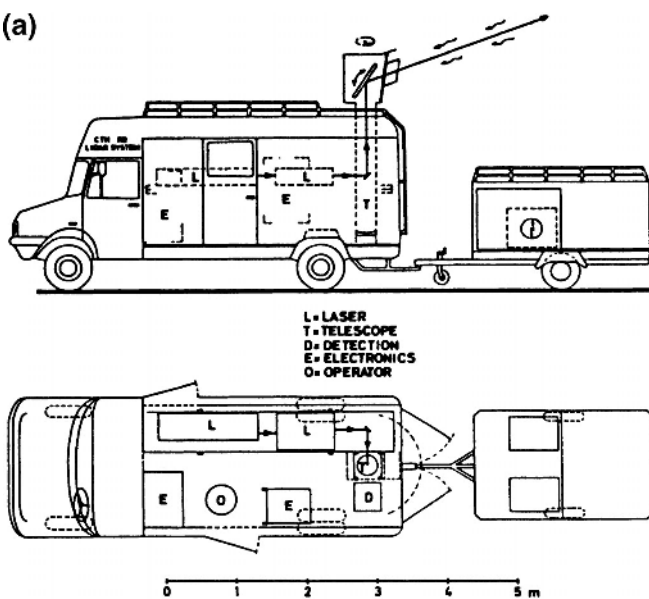
The back scattering can be caused by the *Raman* process. Because of the weakness of this kind of scattering, high-power laser beams are normally required even for the monitoring of major atmospheric species. Here light back scattered with a characteristic Stokes frequency shift is detected. The

technique has been used for vertical monitoring of water vapour profiles and for temperature measurements. Temperature can be retrieved by observing the pure rotational or the rotational-vibrational lines from the major constituents N_2 and O_2 [10.90] using two narrow-band filters located at different positions in the line distributions. The line intensities are affected by the temperature as discussed in connection with Figs. 4.15, 4.18 and 4.20, and from the intensity ratio from the two detection channels the temperature can be obtained after calibration. The water vapour Raman signal [10.91] is normally referenced to the well predictable N_2 signal to get the mixing ratio. Atmospheric visibility can also be assessed by measuring signals from N_2 molecules that are recorded with reduced intensity because of mist and fog particles. Slant visibility measurements are of great importance, e.g. at airports.

The strongest back-scattering process in the atmosphere is Mie scattering from particles (see Sect. 4.5). Since this form of scattering is elastic, no information is obtained on the chemical composition of the particles. Such information can be obtained using very high-power laser pulses which, through focusing, can induce air breakdown (laser sparks) at distances up to 100 m. The emission spectrum from the spark carries information on vaporized particles. LIBS (*Laser Induced Breakdown Spectroscopy*) is also a powerful laboratory technique [10.92]. The intensity of the Mie-scattered light depends on the number density, size, shape, refractive index and absorption properties of the particles (Sect. 4.5). Thus, a quantitative analysis requires a calibration, whereas relative particle spatial distributions can be obtained more directly. Since particle back scattering frequently dominates strongly over particle extinction K_{ext} , the range-resolved lidar signal directly maps out the particle distribution $N_b(r)$.

The construction of a lidar system is illustrated in Fig. 10.24. A Nd:YAG laser is used, either directly or after frequency conversion in a dye laser, to produce pulses that are transmitted into the atmosphere via a planar first-surface aluminized mirror. The same mirror is used for directing back-scattered light down into a fixed Newtonian telescope. In the focal plane of the telescope there is a polished metal mirror with a small hole, which defines the field-of-view of the telescope. For a telescope with a focal length of 1 m, a 1 mm hole corresponds to a telescope field-of-view of 1 mrad, which matches typical laser beam divergences. In order to suppress background light it is essential that the telescope only observes regions from which laser photons can be back scattered. The light passing the aperture is detected by a photomultiplier tube, while all the other light is directed into a TV camera which produces a picture of the target area, except for the laser beam region, which is seen as a black spot. The detected lidar signal is transferred to a transient digitizer (Sect. 9.4.2) and is read out to a computer system. The computer is used for controlling the planar mirror, the laser wavelength, etc. and also performs signal averaging and necessary processing

(a)



(b)

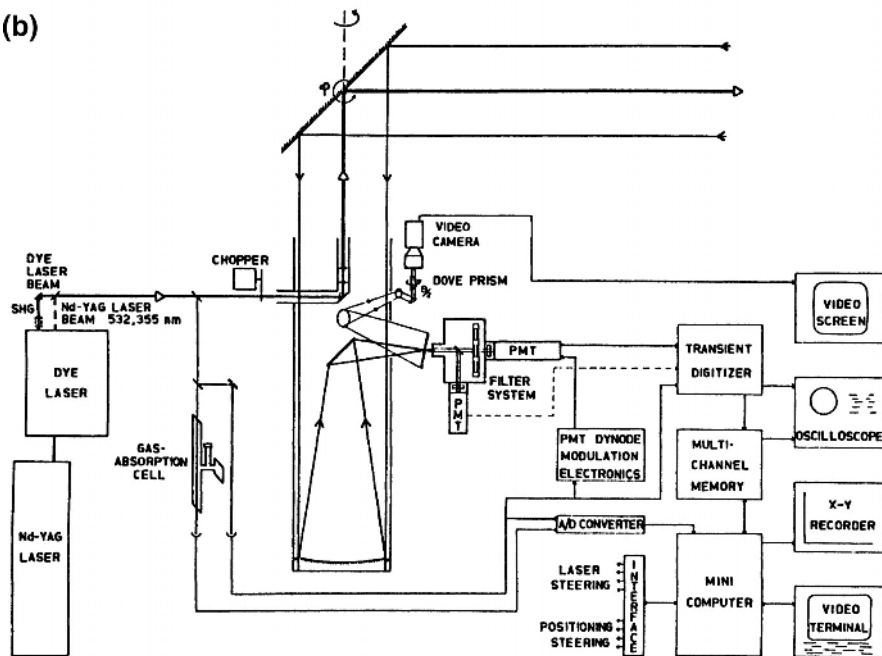


Fig. 10.24. Construction of a mobile lidar system. (a) General lay-out; (b) optical and electronic systems [10.93]

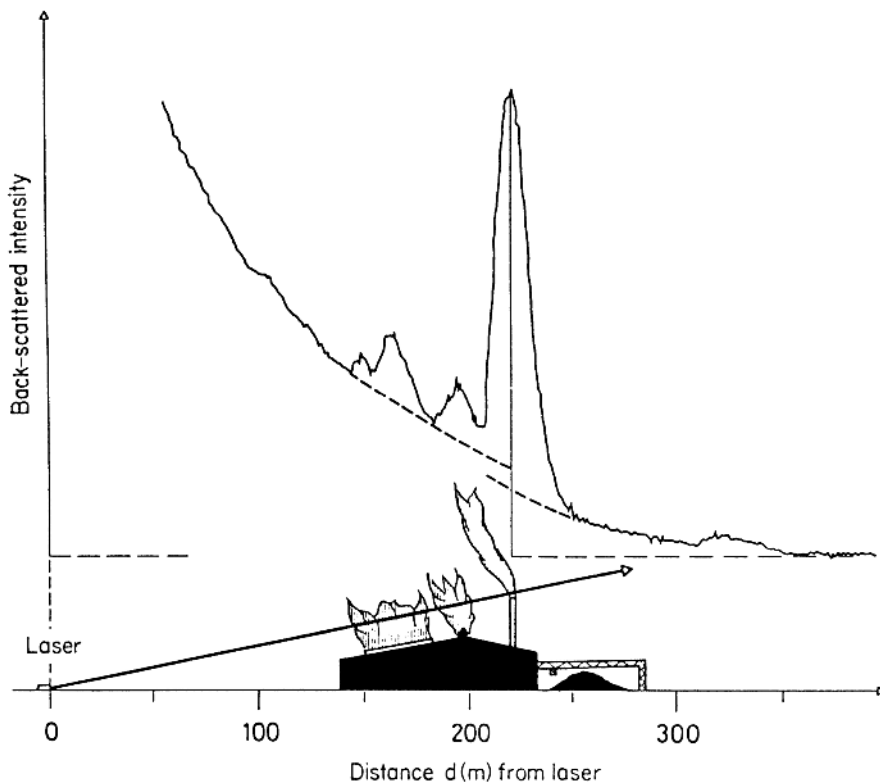


Fig. 10.25. Lidar particle monitoring [10.94]

of the lidar signals. Particle monitoring with lidar techniques is illustrated in Fig. 10.25. Increased back scattering is monitored from particle plumes while a smoothly falling $1/R^2$ intensity is obtained from the uniform background particle distribution in the atmosphere.

In order to measure the concentration of gaseous pollutants with lidar techniques, resonance absorption can be used in a similar way to the long-path-absorption method that was described above. However, in the lidar technique no retroreflector is required and the scattering from particles is utilized to generate a reflected signal. The particles serve as a “distributed mirror”. The differential absorption at close-lying wavelengths of molecules in the atmosphere is used. The method, which is called DIAL (*Differential Absorption Lidar*), is useful for qualitative as well as quantitative range-resolved measurements of air pollutants. The principles are illustrated in Fig. 10.26. For the sake of argument we consider an atmosphere with a uniform particle distribution and with two localized clouds of absorbing gas molecules. Lidar curves are recorded at a frequency ν_1 of strong specific absorption and at a nearby reference frequency ν_2 . For atmospheres with typical particle size

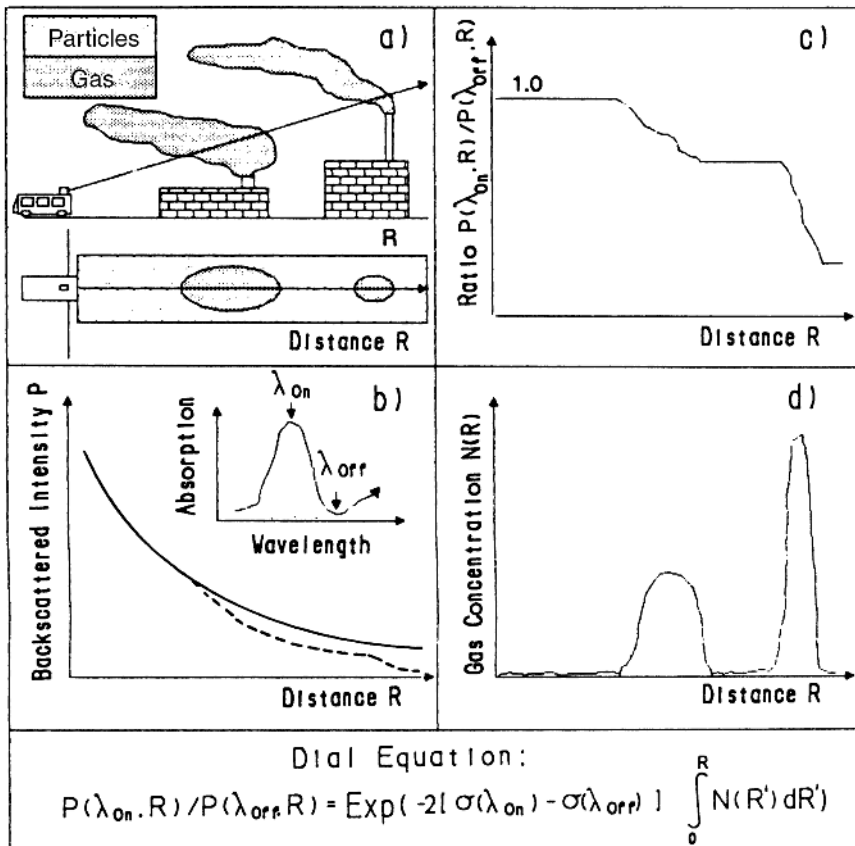


Fig. 10.26. Illustration of the DIAL principle [10.95]

distributions, σ_b and K_{ext} will not change in the small frequency range, since the oscillatory behaviour that is characteristic of uniform particles will be washed out. If the particle extinction K_{ext} is small, the recorded curves for both frequencies will have a simple $1/R^2$ dependence for the region preceding the first gas cloud. For the non-absorbing frequency the lidar curve continues with a $1/R^2$ intensity fall-off even through the gas clouds, while intensity reductions occur in the on-resonance lidar curve at the site of the gas clouds. If no gas had been present, both curves would have had the same appearance. The presence of an absorbing gas is best illustrated if the two curves are divided by each other, as illustrated in the figure. Mathematically, this ratio can be formed by dividing the expressions for the lidar equation (10.6) for the two frequencies ν_1 and ν_2

$$\frac{P_{\nu_1}(R, \Delta R)}{P_{\nu_2}(R, \Delta R)} = \exp \left\{ -2[\sigma(\nu_1) - \sigma(\nu_2)] \int_0^R N(r) dr \right\}. \quad (10.7)$$

As can be seen, all unknown parameters such as $N_b(r)$, σ_b and $K_{\text{ext}}(r)$ are eliminated upon division and only the absorption cross-sections at the two frequencies have to be known from laboratory measurements for an evaluation of the gas concentration $N(r)$ as a function of the distance R . It can also be seen that the method does not even require a uniform particle distribution, since any bumps in the curves due to particle clouds would be cancelled out. This is important since gaseous pollutants and particles frequently occur together.

In Fig. 10.27 the absorption spectrum for SO_2 in the wavelength region around 300 nm is shown. Similar spectra have already been illustrated in the doas recordings shown in Figs. 6.74 and 6.75. In practical DIAL measurements the wavelength is changed between 300.0 nm and 299.3 nm every other laser pulse and the corresponding lidar curves are added in separate computer registers to attain a sufficient signal-to-noise ratio. SO_2 monitoring of an industrial plume, also containing particulate emissions, is illustrated in Fig. 10.28a,b. The effective elimination of the extended particle back scattering in the plume is clearly seen in the divided signal curve, where only the step due to the SO_2 contents is observed, surrounded by horizontal portions of the curve corresponding to no SO_2 contents. By combining evaluated range-resolved concentration curves, a plume concentration cross-section can be obtained. The concentration values (g/m^3) are multiplied with the area elements

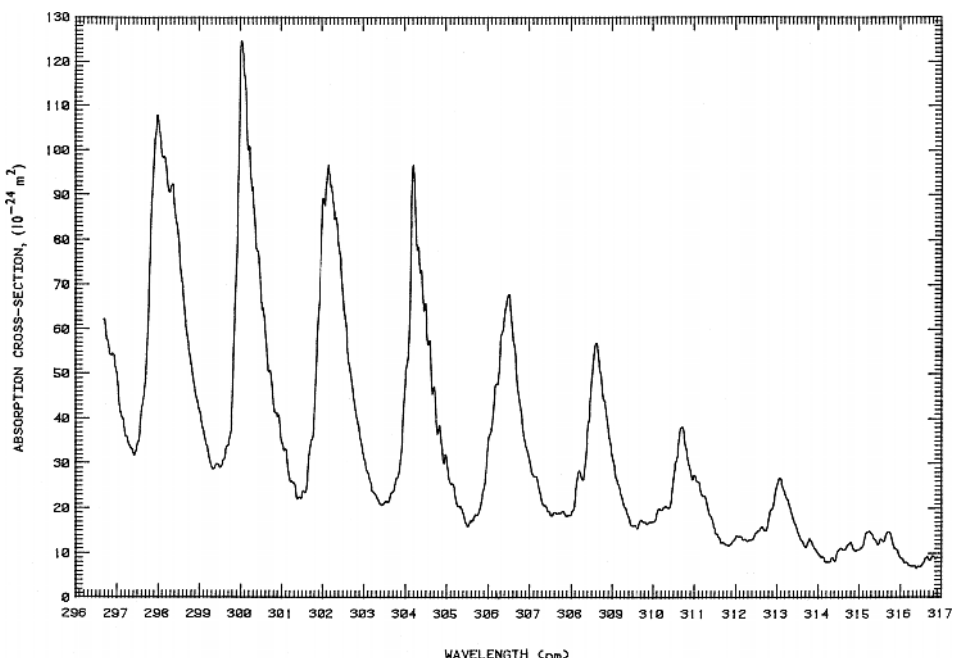


Fig. 10.27. SO_2 absorption spectrum [10.96]

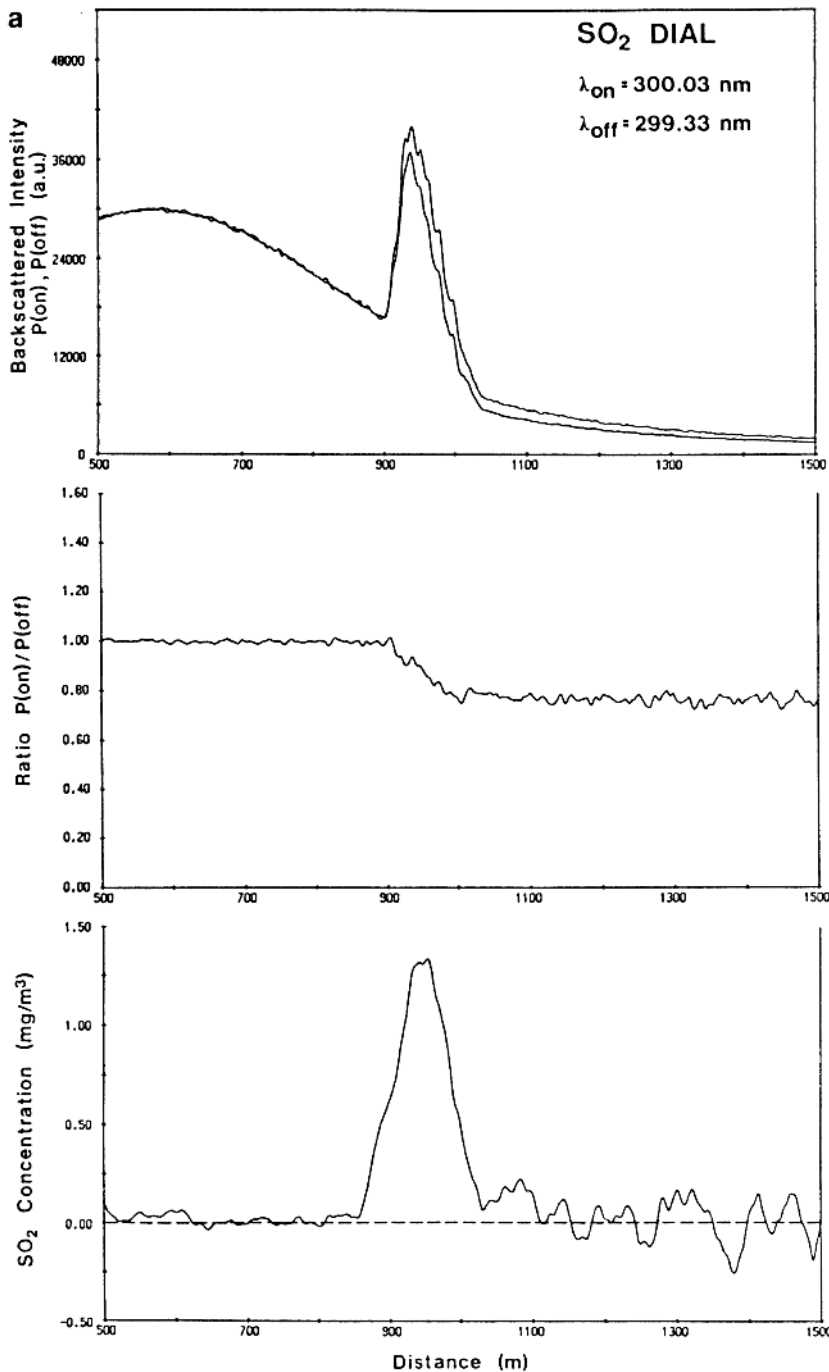


Fig. 10.28a. SO₂ DIAL measurement. The R^{-2} dependence has been suppressed by using a reduced amplification at short ranges [10.95]

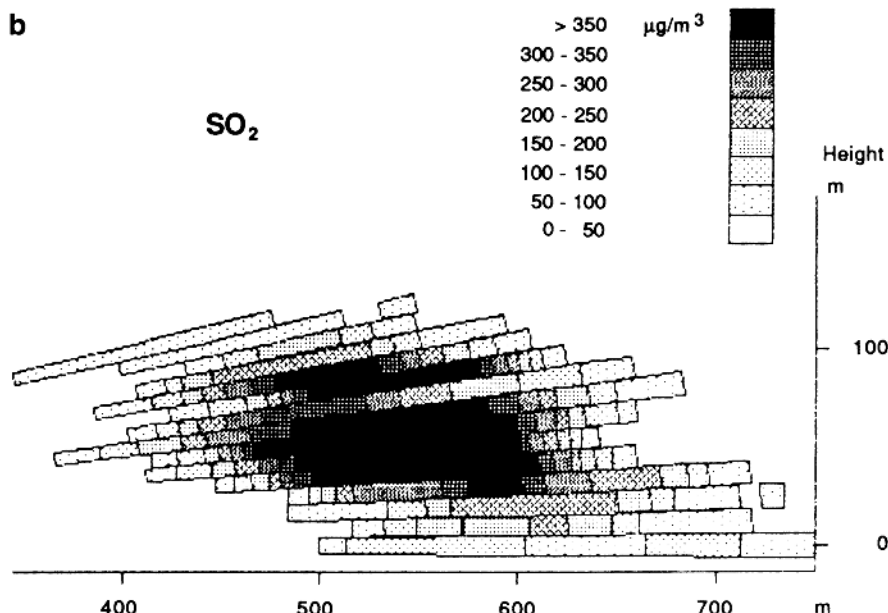


Fig. 10.28b. Mapping of a cross-section of an SO_2 plume from a paper mill obtained by DIAL measurements. By multiplying the integrated SO_2 content by the wind velocity normal to the vertical section a total flow of 230 kg/h of SO_2 was found [10.95]

(m^2) over the cross section area to yield the integrated value (g/m). Finally, by multiplying with the perpendicular wind velocity component (m/s), the total flux of SO_2 (g/s) is obtained as the environmentally most relevant parameter [10.97].

Sulphur dioxide emissions from volcanoes can be measured by performing traverses with a vertically sounding lidar [10.98, 10.99]. Such shipborne measurements are illustrated for the Italian volcano Stromboli in Fig. 10.29. Lidar measurements can be used for comparisons with more commonly employed passive measurements with doas or correlation techniques (Figs. 6.75 and 6.76). The passive measurements on high-lying plumes require corrections due to sunlight scattering inside and below the plume. For low-altitude plumes with few scattering particles, e.g., Mt. Stromboli (920 m), the down-welling sky radiation mostly originates above the plume, and a simple evaluation of the gas contents using the Beer–Lambertian law can be performed. This is to be contrasted to the complicated situation pertaining to Mt. Etna (3340 m), for example.

Mercury is a further gas which can have a geophysical origin apart from anthropogenic ones. It is the only pollutant which is present in the atmosphere in atomic form. Compared to molecules with a multitude of rotational-vibrational transitions, mercury in contrast exhibits only a single

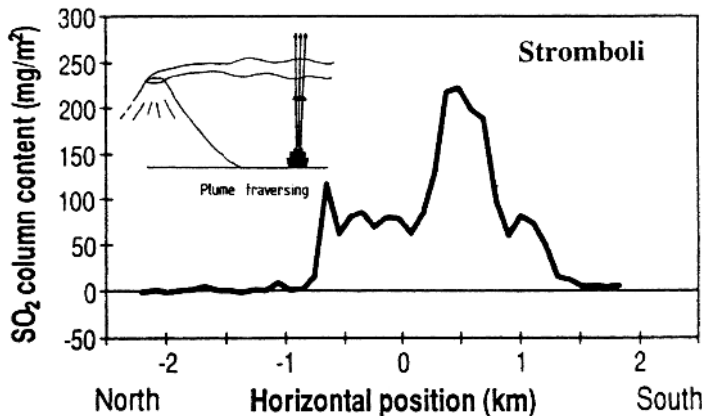


Fig. 10.29. Illustration of shipborne DIAL monitoring of the SO₂ emission of Mt. Stromboli. By multiplying the integrated overhead SO₂ burden by the wind velocity a flux of 6 metric tonnes per hour was obtained [10.98]

pressure-broadened resonance line (built up from a number of isotopic and hyperfine components; see Fig. 10.20) with a high oscillator strength (transition probability) at about 254 nm. This means that very low atmospheric concentrations (ppt:s; parts per trillion, instead of ppb:s or ppm:s) can be detected [10.100]. Mercury can, because of its high vapour pressure (Fig. 7.2) be used as a geophysical tracer gas with certain relations to geothermal energy [10.101, 10.102], ore deposits and mining [10.103], and possibly to seismic activities. A DIAL mapping of the mercury concentration around a cooling tower at a geothermal power station is shown in Fig. 10.30. Environmental mercury pollution is discussed in [10.104].

Nitrogen oxide (NO), mostly due to automotive traffic, and the subsequently formed nitrogen dioxide (NO₂) can readily be measured by DIAL techniques [10.105]. A sharp bandhead around 226 nm is utilized for attaining the characteristic differential absorption for NO, while NO₂ can be measured in a wide range of blue wavelengths [10.106]. The monitoring of hydrocarbons and carbon monoxide (CO) requires IR wavelengths (e.g. see Figs. 10.19 and 6.68). Emissions from petrochemical industries and leaks from natural gas pipe lines are important targets for hydrocarbon monitoring around 3.4 μ m [10.107].

The requirements for very sharp and well-defined laser frequencies when using the DIAL technique can be relaxed by using a gas correlation lidar technique [10.108], where the back-scattered radiation from a broadband transmitter is split up in two channels; one supplied with a cell filled with optically thick gas which only passes the off-resonance components for the signal, and one channel where the total signal (on and off) is detected. If the cell gas is present in the atmosphere, a differential lidar effect is obtained using many absorption lines simultaneously (compare Fig. 6.77). This technique

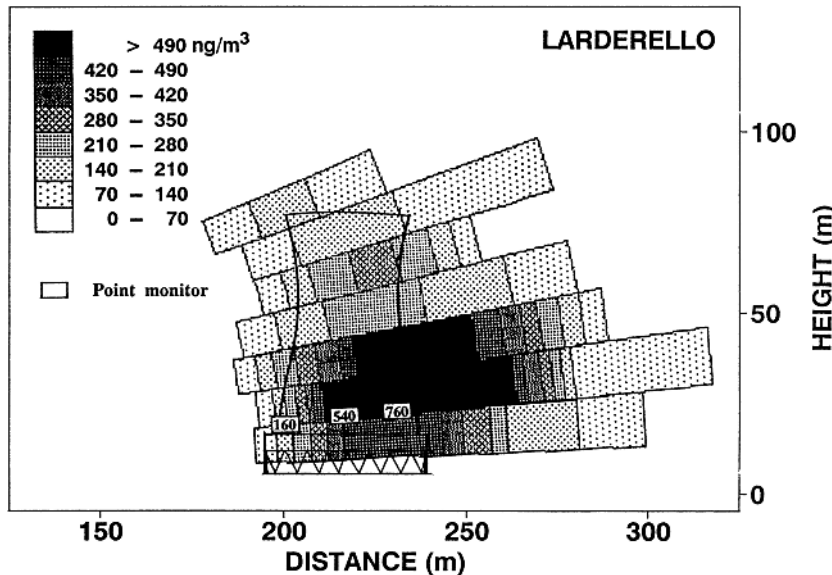


Fig. 10.30. Atomic mercury distribution around a cooling tower of an Italian geothermal power plant. The numbers given at certain locations are reference values measured with the standard gold amalgamation technique [10.102]

has been demonstrated for Hg [10.108] and CH₄ [10.109] lidar detection. Industrial emission control using lidar techniques is discussed in [10.110].

Ozone is a particularly important gas in relation to global environmental issues. It can be monitored by DIAL around 300 nm. Water vapour vertical profiles can also be measured. Ground-based and airborne lidar systems are being used in extensive studies of these gases [10.111]. Furthermore, many lidar stations monitor the stratospheric dust layers due to volcanic eruptions (e.g., Mt. Helens 1980, El Chichon 1982, Pinatubo 1991) [10.112]. The dust cloud movements provide an important insight into upper atmosphere dynamics. Dust particles, water vapour, ozone, carbon dioxide and other greenhouse gases all influence the global heat balance. (The year 1816 is frequently referred to as “the year without a summer”, due to heavy emissions from Mt. Tambora, Indonesia, which blew up on 5 April 1815.)

Atmospheric wind velocities can also be measured by lidar techniques. Apart from the obvious interests for general meteorology there are several important air-traffic applications. Clear-air turbulence causes unexpected problems for airliners in flight, and a minute of early warning from an on-board forward-looking wind lidar system is useful. Shear winds resulting in a sudden height drop along projected landing approach lines are dangerous and have caused accidents. The appearance of a pair of strongly rotating swirls persisting for minutes in the wake behind a landing airliner can cause problems to smaller airplanes. The Doppler shift in the back-scattered ra-

diation is used in a similar way to that discussed in connection with the velocity measurements in Sect. 10.1.5. If a narrow-band lidar transmitter is used, it is possible to distinguish between a sharp Mie-scattering peak, which moves corresponding to the particle flow, and a Doppler-broadened Rayleigh scattering component due to the fast thermal motion of the molecules. The envelope (a few GHz broad) also shifts corresponding to the wind displacement in a similar way to that discussed in connection with Fig. 10.14. In order to detect the movement, sharp transmission Fabry-Pérot transmission filters are placed around the Mie and/or Rayleigh distributions to observe the increase or decrease in the intensity in split detection channels. This is the so-called *edge technique* [10.113]. Clearly, the etalons used for the interferometer must be very accurately temperature stabilized to avoid drifts. It can then be an advantage to use atomic or molecular absorption filters [10.114] and observe the Doppler distribution slide up or down the sharp absorption edges. A related technique for velocity measurements in combustion flows utilizing thermal emission lines that are more or less absorbed by blocking atomic line gas filters has been proposed [10.115].

A different approach to atmospheric wind velocity measurements is to utilize coherent detection in narrow-bandwidth IR lidar systems. If the scattering aerosol particles in the atmosphere are moving, a Doppler shift in the received signal leads to a corresponding difference-frequency beat when mixed with a CW local oscillator signal (*coherent* detection; see Sect. 10.2.1). Frequently, the local oscillator also seeds the pulsed lidar transmitter to give it a sharp and well-defined frequency. The beat-frequency spectrum yields information on radial wind speed and turbulence. Ranges of tens of kilometres have been attained with coherent wind lidar systems [10.116]. In order to obtain all wind vector components the laser beam is frequently scanned over the surface of a cone. This scenario is particularly relevant for airborne or spaceborne large-area coverage.

Lidar systems have been tested from space utilizing the Shuttle vehicle [10.117]. Primarily, Mie scattering lidar measurements of particles and cloud structures have been performed. Several space lidar projects are being planned [10.118]. Global wind mapping is the single most important task for a continuously monitoring space system.

10.3 Laser-Induced Fluorescence and Raman Spectroscopy in Liquids and Solids

Laser-induced fluorescence (LIF) in liquids and solids can be used for diagnostic purposes in many contexts. Most substances have broad absorption bands in the UV region and a pulsed UV laser is frequently most useful for inducing fluorescence. The nitrogen laser ($\lambda = 337\text{ nm}$) is a simple and practical source for such measurements. Other useful laser systems are tripled Nd:YAG

lasers ($\lambda = 355$ nm), excimer lasers (XeCl, $\lambda = 308$ nm; KrF, $\lambda = 249$ nm) or blue diode lasers. Liquids and solids exhibit broad fluorescence emission bands [10.119–10.123]. As already discussed for dyes, sharp emission features are lost because of rotational quenching and mutual interactions between the molecules. Vibrational Raman spectra, on the other hand, exhibit quite sharp lines. Raman spectroscopy is a powerful tool for studying liquids and surface layers on solids. In this section we shall describe a few applications of LIF and Raman spectroscopy of liquids and solids. We will first consider *hydrospheric remote sensing* and *vegetation monitoring* and will then discuss *monitoring of surface layers*.

10.3.1 Hydrospheric Remote Sensing

The increasing pollution of seas and inland waters calls for efficient methods of aquatic pollution monitoring. Oil spills cause drastic damage to the environment. For marine monitoring, airborne surveillance systems are the most useful ones. All-weather capability generally calls for a microwave-based system. Fluorescence can be monitored at a distance with a modified lidar set-up and an airborne laser fluorosensor can be a valuable complement to a SLAR system (Sect. 7.2) for characterizing detected oil-slicks. Clearly, it is necessary to perform laboratory measurements on the substances of interest in order to obtain the basic information necessary for a field system. A laboratory set-up for LIF studies is shown in Fig. 10.31. Either a scanning monochromator connected to a boxcar integrator is used, or better, an optical multichannel analyser (Fig. 6.38). In Fig. 10.32 LIF spectra for different substances in the aquatic environment are shown for N_2 -laser excitation. A crude-oil spectrum is shown featuring a broad and strong fluorescence distribution. Oil products fluoresce quite strongly because of their aromatic hydrocarbon content, e.g. anthracene and naphthalene. Refined products fluoresce even more strongly with the peak fluorescence shifted to shorter wavelengths, while heavy residual oils, such as asphalt, fluoresce weakly and mainly towards longer wavelengths. A spectrum of sea water is also shown with a prominent sharp signal due to the OH stretch Raman mode of H_2O . The broad blue fluorescence is due to organic water pollution. The spectrum

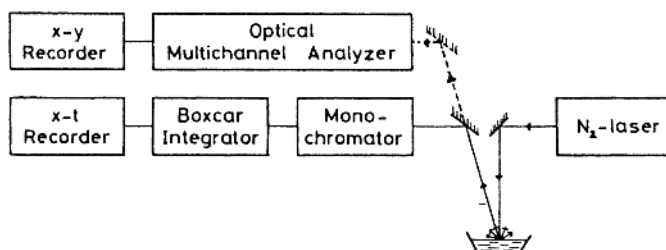


Fig. 10.31. Laboratory set-up for LIF measurements [10.124]

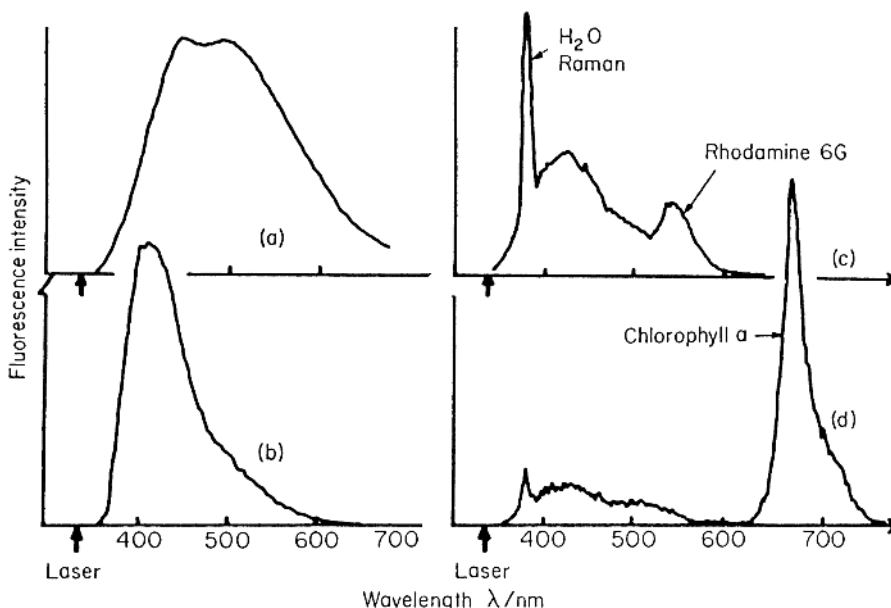


Fig. 10.32. LIF spectra for aquatic substances. (a) Crude oil, Abu Dhabi; (b) river water down-stream from a sulphite pulp mill; (c) sea water containing $3\text{ }\mu\text{g/l}$ Rhodamine 6G dye. The Raman peak from water is exhibited, too; (d) the green algae *Chlorella ovalis* Butcher in sea water [10.124]

also shows a fluorescence peak from a tracer dye that has been added to the water. Such dyes can be used to tag a “package” of water allowing studies of flow patterns in aquatic systems. A concentration as low as $1\text{ }\mu\text{g/l}$ is sufficient for such fluorescence tracing. Included in Fig. 10.32 is a spectrum from river water, polluted by lignine sulphonate from a pulp mill and a spectrum of water containing microscopic green algae. The prominent peak at 685 nm is due to the chlorophyll-*a* pigment that is present in all plants [10.125]. LIF can be used to study algal blooms, induced by eutrophication in seas and lakes. Airborne oil monitoring systems have been constructed [10.126]. Oil slicks are detected by an increase in the blue fluorescence at the same time as the water Raman signal disappears because of full absorption in the oil layer.

An airborne lidar system operating in the blue-green transmission window of water (Fig. 6.54) can be used for measurements of water depth [10.127]. The principle of such measurements is given in Fig. 10.33. The speed of light in water is about $0.75c$. A laser with a short pulse length must be used. Water is strongly attenuating and in order to enhance the weak bottom echo with respect to the strong surface echo a polarization scheme can be used. If the laser pulse is linearly polarized the surface echo remains largely polarized whereas the bottom echo is almost completely depolarized. Thus, by using a crossed

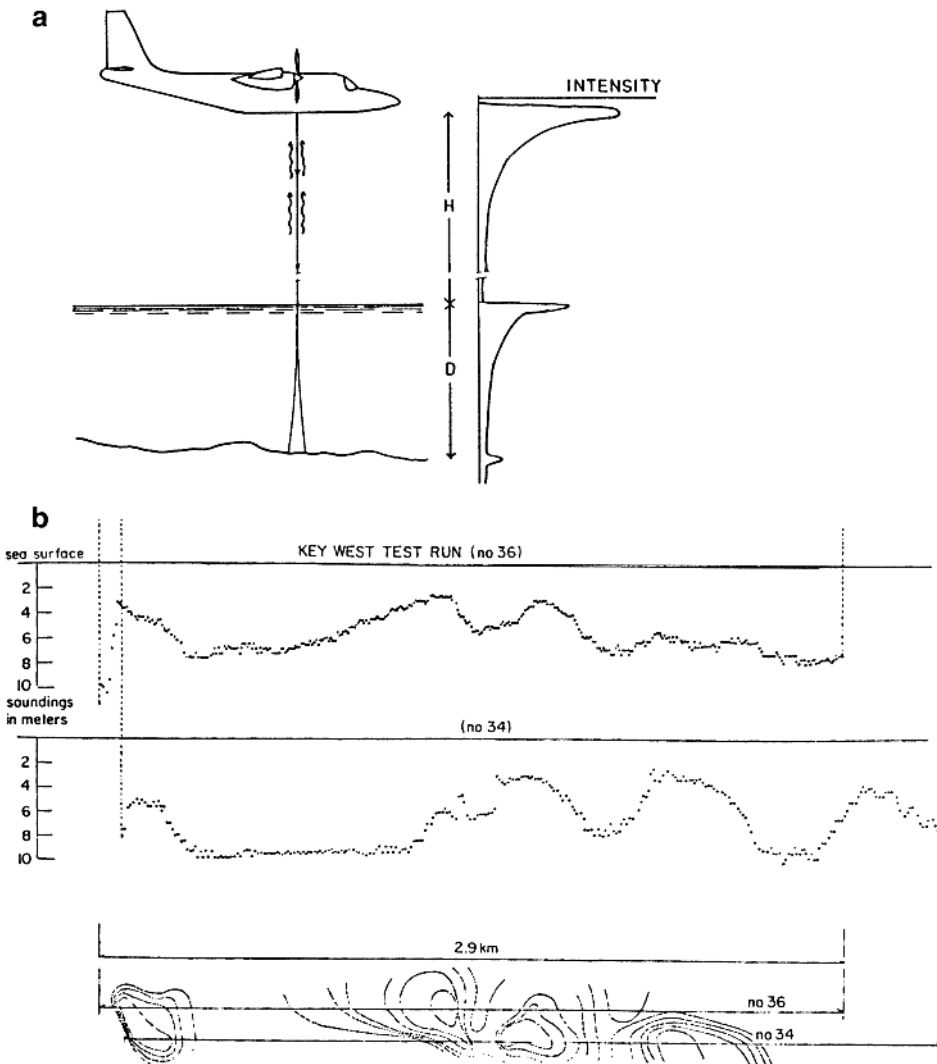


Fig. 10.33. (a) Principle of airborne laser bathymetry [10.127] (last Ref.). (b) Results from lidar bathymetry in shallow waters [10.127] (first Ref.)

linear polarizer in front of the detector a more reasonable relative strength of the two echoes is obtained. Depths down to several tens of metres can be measured by laser bathymeters of this construction. A frequency-doubled Nd:YAG laser ($\lambda = 532$ nm), a copper vapour laser ($\lambda = 510$ and 578 nm) or a Hg-Br laser ($\lambda = 520$ nm) are candidates for laser bathymeters. Space-borne green lasers are also being discussed for communication with submarines. The field of hydrospheric probing by lasers has been discussed in [10.71].

10.3.2 Vegetation Monitoring

In the same way as a UV laser beam can be directed into water to induce fluorescence for diagnostic purposes, the beam from the fluorescence lidar system can be directed onto the leaves and needles of vegetation. A measurement scenario is shown in Fig. 10.34. Frequency-tripled Nd:YAG radiation at 355 nm is directed onto the foliage of a beech tree and fluorescence is collected by the lidar system receiving telescope. After dispersion in a spectrometer, the spectrum is recorded on a gated and image-intensified detector. The microchannel plate of the intensifier is activated at a delay after the laser is fired, corresponding to the time-of-flight from the system to the target and back. Fluorescence spectra, captured at 60 m distance, are included in the figure. In addition to the 690 nm chlorophyll peak already discussed above, a second peak at 735 nm is observed in terrestrial vegetation. When the concentration of chlorophyll in the leaves increases both peaks grow, but since the 690 nm peak occurs at a wavelength where chlorophyll absorbs, the continuing growth of this peak is suppressed. Thus, the ratio between the two peak intensities is related to the chlorophyll concentration. The blue-green fluorescence observed is due to accessory pigments and the leaf wax layer. Environmental stress can influence the shape of the fluorescence spectrum [10.125] and provide complementary information to data obtained in reflectance measurements (Sect. 6.6.2). Vegetation studies using fluorescence lidar techniques are discussed in [10.129]. A fluorescence lidar system can also be used for studies of the facades of historical buildings and monuments [10.130]. The stone surface might be corroded due to environmental pollutants and the surface may also be invaded by algae and lichen. Data from a vertical scan of the wall of a cathedral are shown in Fig. 10.35. The beam interacts with the sandstone wall. In the middle of the scan of the wall, areas with algae signatures occur [10.131].

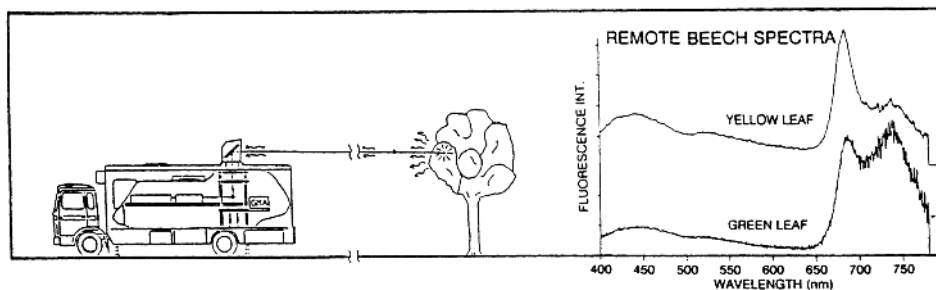


Fig. 10.34. Fluorescence lidar monitoring of vegetation. Remote fluorescence spectra from green and yellow leaves of a beech tree are included [10.128]

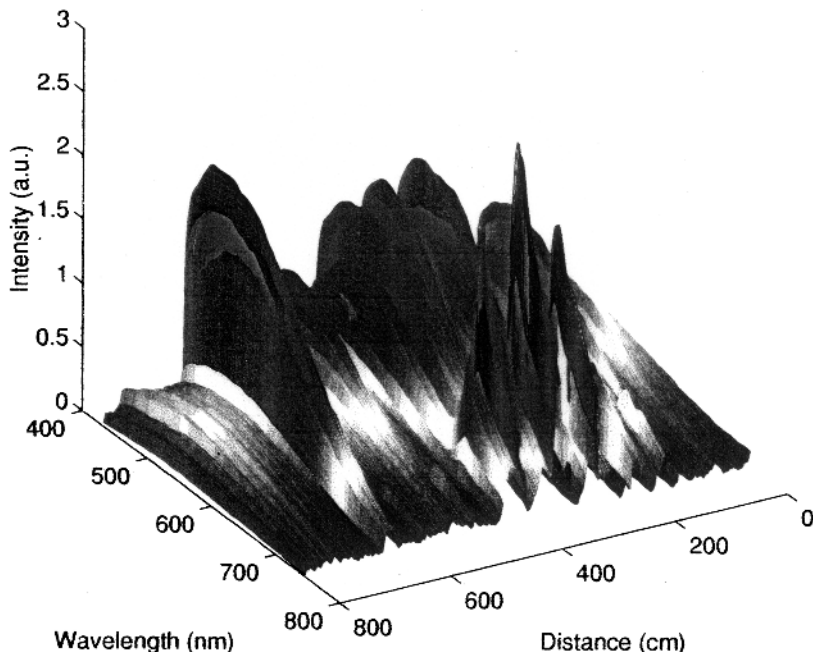


Fig. 10.35. Fluorescence spectra from a vertical scan of the facade of Lund Cathedral, Sweden. The measurement distance was about 60 m [10.131]

10.3.3 Monitoring of Surface Layers

We have already mentioned that oils strongly absorb UV light. Thus, LIF can be used for detecting very thin surface layers of oil [10.132, 10.133]. Industrially, it can be of interest to be able to establish that sheet metal components are free from oil before entering a painting shop. It is also interesting to monitor the presence of surface layers, e.g. of corrosion-protective agents. Examples of spectra of this kind are given in Fig. 10.36. Monitoring of the application of oil for rust protection during sheet metal coiling in a steel rolling mill using an industrial fluorosensor is illustrated in Fig. 10.37.

The penetration depth in organic liquids rapidly increases for longer wavelengths. By choosing a suitable excitation wavelength, sensitive measurements of film thickness can be performed in different thickness ranges. The fluorescence of organic substances can also be used for sensitive detection of signals in liquid chromatography and electrophoresis [10.134, 10.135]. A UV laser or blue laser beam can be used for exciting fluorescence at the outlet of the column, or can be used to illuminate the whole column. In the latter case the fluorescence from the different constituents moving forward in the column under the influence of an electric field can be imaged simultaneously onto a CCD detector, as illustrated in Fig. 10.38. By spectral analysis of the fluorescence from the different components, further selectivity in the

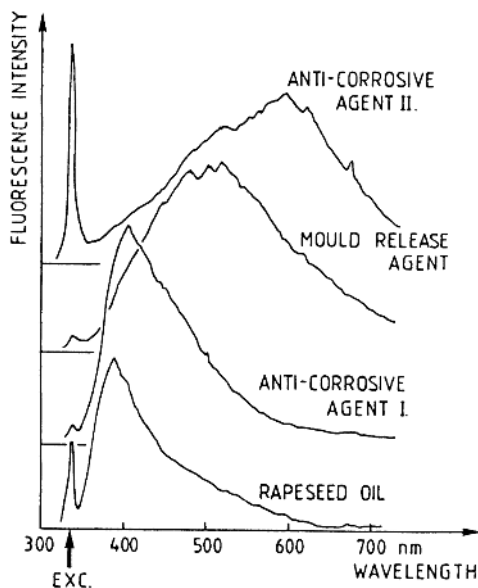


Fig. 10.36. LIF spectra of industrial surface layers. A nitrogen laser was used for the excitation [10.132]

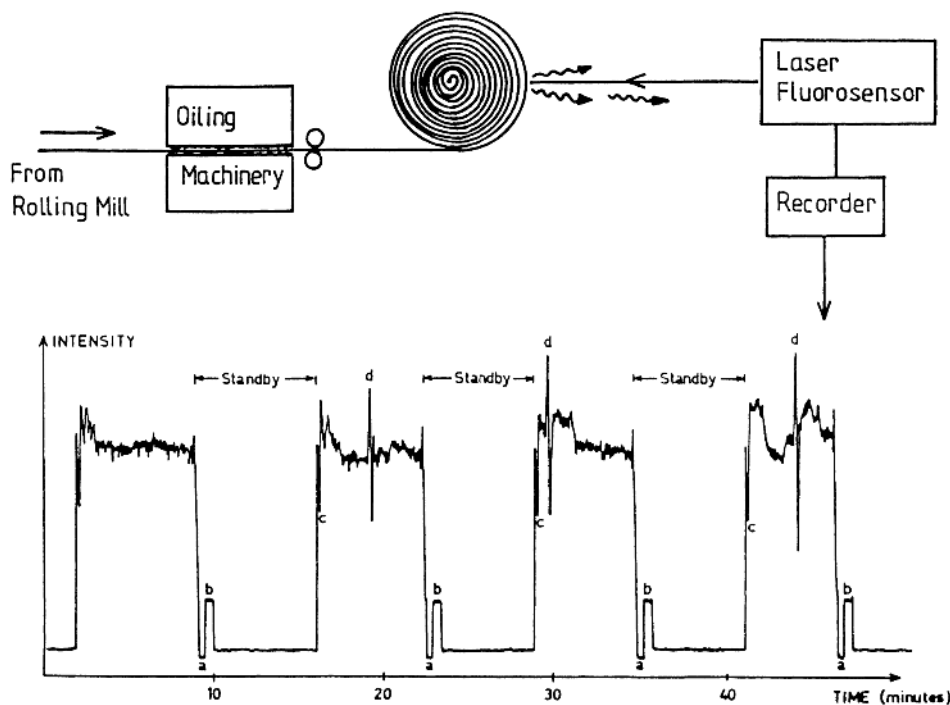


Fig. 10.37. Anti-rust oil application monitoring in a steel rolling mill [10.132]

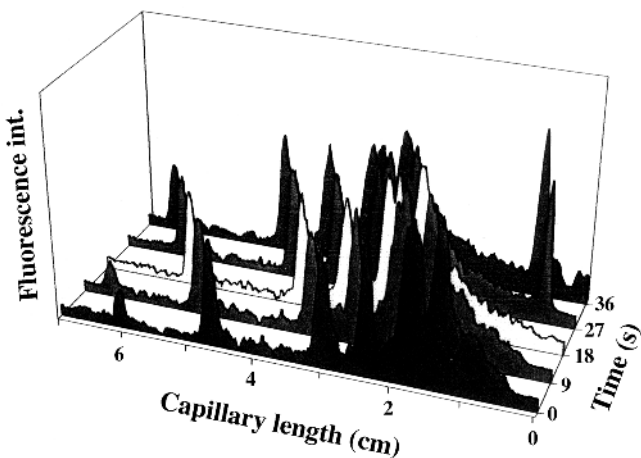
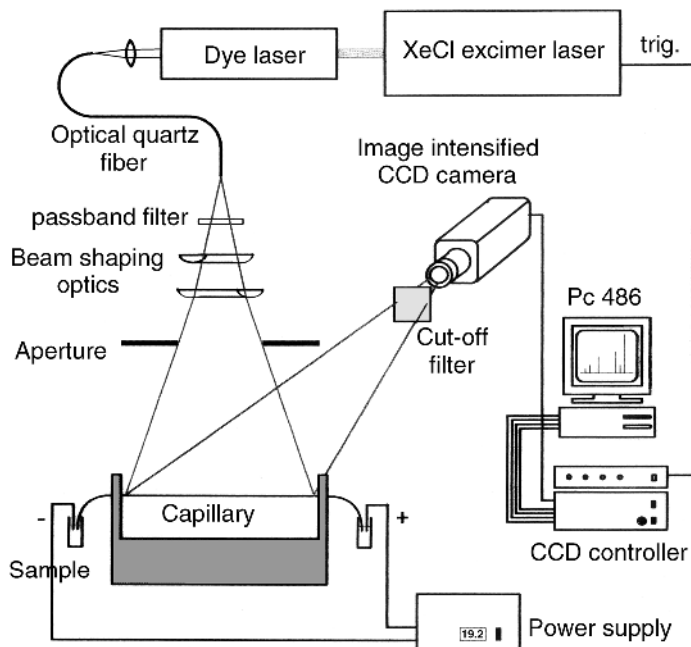


Fig. 10.38. Set-up for imaging detection of capillary electrophoretic separation. Blue light from an excimer-pumped dye laser is used to induce fluorescence from DNA fragments, which are separating in the column as visualised in read-outs (bottom) from an intensified CCD camera [10.135]

identification of individual components in complicated chromatography and electrophoresis separations can be obtained.

Fluorescence can be used in many additional analytical applications. As discussed in Sect. 10.5, it is a powerful tool in medical diagnostics of tissue. It is also used in forensic sciences, e.g. for visualisation of latent fingerprints [10.136]. More everyday applications include fluorescence "hidden" codes on bank notes, credit cards and driving licences.

Certain salts of rare earths exhibit sharp fluorescence lines when excited by UV light. It has been shown that the relative strengths of different lines and also the decay time of the fluorescence at a certain fluorescence wavelength vary strongly with temperature [10.137]. Fibre thermometers with a rare-earth-salt fibre tip have been developed. By applying thin layers of such salts to surfaces it is possible to remotely measure the temperature by LIF. This technique could be particularly valuable for hot rotating machine parts.

Surfaces of solids can also be investigated by Raman spectroscopy, which has a higher specificity than LIF. Thus, this method is well suited for studying chemical processes such as corrosion, electrochemical processes, etc. Frequently, an Ar^+ laser is used in conjunction with a double or triple monochromator for isolating the Raman signals from the very strong elastic scattering from the surface. In Fig. 10.39 a Raman spectrum illustrating sur-

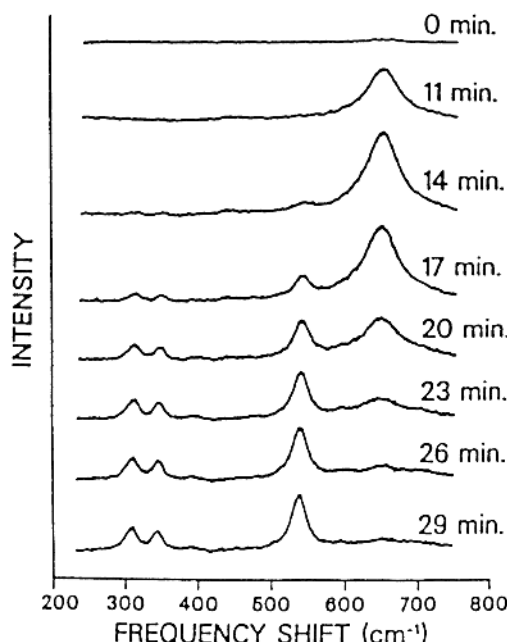


Fig. 10.39. Surface Raman spectra showing an oxidation process on a surface of a Fe/Cr/Mo alloy. Initially an Fe/Cr double oxide (spinel) is formed which is successively transformed into Cr_2O_3 [10.138]

face oxidation is shown. The Raman scattering from a surface can be strongly enhanced compared with the bulk material scattering. The enhancement is connected with periodic structures on the surface. Surface-enhanced Raman scattering has been discussed in [10.139–10.142]. Surfaces can also be studied by other optical techniques. A method in which the strength of surface frequency doubling of impinging laser light is investigated is rapidly evolving into a very powerful technique [10.143, 10.144]. An example of surface studies

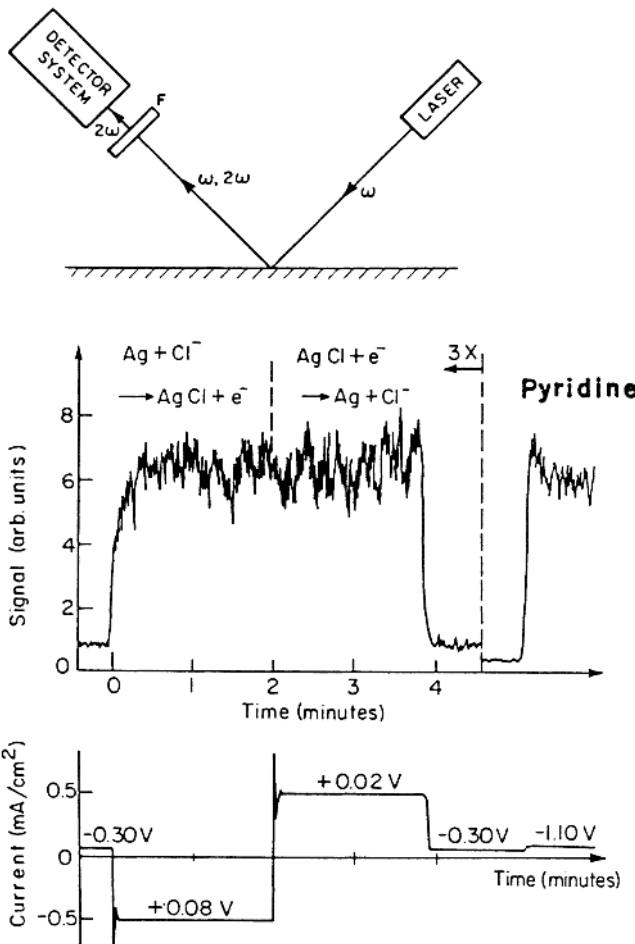


Fig. 10.40. Surface monitoring by observing the generation of frequency-doubled light. The *top* figure depicts the experimental arrangement in this type of measurements. *Below*, the electrolytic build up and removal of AgCl on an Ag electrode in a cell with KCl solution is illustrated. The second harmonic signal saturates for a single monolayer. When the last monolayer is removed following voltage reversal, the voltage changes and the signal disappears [10.144]

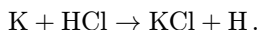
using frequency doubling is shown in Fig. 10.40. The general field of laser spectroscopy of solids was covered in [10.145, 10.146].

10.4 Laser-Induced Chemical Processes

Laser light can be used for inducing or controlling chemical processes in different ways. Photons of suitable energy can greatly increase the speed of certain reactions, leading to a significant increase in the yield of a desired substance. In this section we will discuss *laser-induced chemical processes* in general and also consider processes in which strong isotopic selectivity is obtained leading to *laser isotope separation*. The very active field of laser-induced processes is covered in a number of conference proceedings and reviews [10.147–10.155].

10.4.1 Laser-Induced Chemistry

A primary question in connection with laser-induced chemistry is whether it could be possible to selectively break chemical bonds in large molecules by irradiating the molecules at a frequency corresponding to the vibrational mode associated with that particular bond. It has been found that the energy absorbed in a particular vibrational mode is very quickly distributed over the whole molecule, resulting in an essentially thermal and unselective excitation. In order to achieve selectivity a great deal of energy must be deposited in a bond in a time shorter than 1 ps. This can be achieved using the techniques of femtochemistry (Sect. 9.5.2) and coherent control (Sect. 9.5.3). We will here consider other techniques to influence chemical reactions using laser light. By exciting a molecule to a higher vibrational level it can be made to react much faster (*chemical activation*). One example is the reaction



This reaction occurs 100 times faster if the HCl molecules are excited to $v = 1$ compared with $v = 0$. Laser radiation can also act as a catalyst in certain reactions, e.g. in the production of vinyl chloride, $\text{C}_2\text{H}_3\text{Cl}$, for the plastic industry. The process, which is basically thermal break-up of dichloroethane $\text{C}_2\text{H}_4\text{Cl}_2$ into $\text{C}_2\text{H}_3\text{Cl}$ and HCl , can be run at considerably lower temperatures in the presence of laser light. With an XeCl excimer laser (308 nm) free Cl radicals are formed that open up new reaction paths. Only one laser photon is needed to produce 10^4 vinyl chloride molecules, since a chain reaction is utilized [10.147]. Laser radiation is also very effective in many *pyrolysis reactions*. Here local heating of the reacting gases is accomplished by the laser light. As an example, the cracking of heavy hydrocarbons into lighter ones can be mentioned. In the petrochemical industry it is frequently desirable to increase the yield of ethylene C_2H_4 over methane CH_4 , since ethylene is a more desirable starting material for many petrochemical processes. Laser

pyrolysis results in a higher yield than that possible with thermal heating. Laser pyrolysis also has good potential in the production of ceramic materials. Using silane (SiH_4) as a starting product, powders of Si, Si_3N_4 or SiC can be produced, later to be sintered into ceramics.

Laser chemistry can also be used for *purifying* certain chemicals. The production of ultrapure silicon for the semiconductor industry and for producing solar cells is of special interest. For optical fibres the purest possible SiO_2 is desirable. A suitable starting material is silane gas. Arsine (AsH_3) and phosphine (PH_3) are typical impurities. On irradiation of the natural gas mixture with an ArF excimer laser ($\lambda = 193\text{ nm}$) the impurities are quickly dissociated. The technique has a good production potential and the cost for purification could be quite reasonable. Since the cost of the laser photons will always be an important factor, it is likely that laser-induced chemical processes will be advantageous, especially for producing specialized and expensive chemicals, e.g. pharmaceuticals. Photo-assisted production of vitamine D and prostaglandine has also been considered.

10.4.2 Laser Isotope Separation

Using narrow-band laser light it is possible to induce isotope-selective processes leading to isotopic separation by utilizing optical isotopic shifts [10.154, 10.155]. Enriched or separated isotopes are of great interest in many contexts. Pure radioisotopes are used in medicine. Also, stable elements, such as ^{13}C , can be used for studies of the metabolism and other biological processes. In NMR spectroscopy signals are only obtained from isotopes with a nuclear spin. For sulphur and calcium the useful isotopes ^{33}S and ^{43}Ca are naturally present only in very small concentrations. By using enriched isotopes in the building up of organic material completely new possibilities arise. Enrichment of ^{14}C from organic objects that are to be dated would mean a much higher sensitivity since the tracer element could be concentrated into a small volume allowing small detectors to be used with a resulting low background count rate. In this way the time span when dealing with the ^{14}C method could be considerably increased.

However, the greatest interest in isotope separation comes from the nuclear power industry. Production of heavy water for heavy-water reactors and separation of highly active components from the burnt-out uranium fuel are two applications. The most important aspect by far is, however, isotope separation of ^{235}U . Natural uranium contains only 0.7% ^{235}U and enrichment to about 3% is needed for use in light-water reactors. The normal separation method is diffusion of uranium hexafluoride UF_6 through porous filters. This process, which relies on the slightly different mobilities of $^{235}\text{UF}_6$ and $^{238}\text{UF}_6$, is very inefficient and the separation costs are very high and correspond to about 10% of the resulting price of the produced electricity. Several nuclear reactors are needed to provide the electricity for a typical separation plant. A technique based on high-speed gas centrifugation is now

pursued as a possible alternative. At the same time, laser techniques for uranium isotope separation are being investigated. Clearly, any technique that could reduce the separation costs would be of great interest.

Laser techniques can lead to a high degree of enrichment and may also be useful in processing uranium tailings from which most of the fissile material has already been removed. Laser isotope separation schemes based on free atoms or on UF_6 are possible. In both cases the presence of an isotopic shift is utilized. We will first consider free atoms. For heavy elements, such as uranium, the isotopic shift is only due to the volume effect (Sect. 2.8). In Fig. 10.41 the different isotopically separated components of a uranium emission line are shown for an enriched sample. The broadening in the ^{235}U line is due to unresolved hyperfine structure. The basic principle for atomic uranium separation is illustrated in Fig. 10.42. A narrow-band tunable laser selectively transfers ^{235}U atoms to an excited state. Since atomic transitions can be saturated with laser pulses (Sect. 9.1.2) a large fraction of the ^{235}U atoms are transferred to the higher state, from which they can be photoionized using a second laser pulse. The photon energy for this laser is not sufficient to photoionize ground-state atoms. The ^{235}U ions that are formed in this way are extracted to a collector plate using an electric field. A separation scheme with two selective excitation steps induced by dye lasers that are pumped by powerful copper vapour lasers has been explored for practical separation purposes [10.154]. A powerful excimer laser is used for the photoionizing step. The properties of uranium call for special evaporation techniques. It is

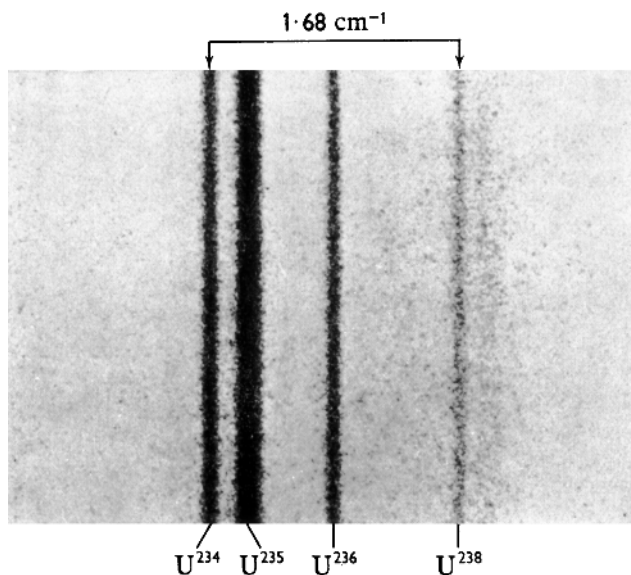


Fig. 10.41. Isotope shifts in a uranium emission line. A uranium sample enriched in ^{236}U was used in the light source [10.156]

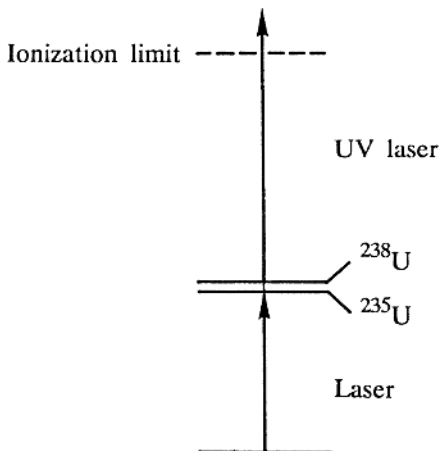


Fig. 10.42. A schematic uranium isotope separation scheme

necessary to heat the uranium to 2300 K to achieve substantial evaporation. However, molten uranium metal is extremely reactive and attacks most furnace materials. One technique which can be used to overcome this problem is local surface heating with electron guns.

Uranium isotope separation using a molecular approach is based on selective multi-photon dissociation of UF_6 . The relevant vibrational isotope shift is 0.6 cm^{-1} in the primary vibrational transition at 628 cm^{-1} ($16 \mu\text{m}$). In the development of the technique, experiments on SF_6 have been very important. The conditions are much more favourable for SF_6 than for UF_6 . The isotope shift is 17 cm^{-1} between ^{32}S and ^{34}S in the IR active vibrational mode that involves asymmetric stretching of two $S-\text{F}$ bonds. The spectrum has a typical P , Q and R branch structure and the whole region of absorption for the rotational level population distribution that is obtained at room temperature is 15 cm^{-1} . Thus, the isotopic molecules are spectroscopically totally separated. Furthermore, the vibrational transition in $^{32}\text{SF}_6$ well matches the emission of a free-running pulsed CO_2 laser.

The multi-photon dissociation process is illustrated in Fig. 10.43. Because of the anharmonicity of the vibrational potential a photon energy that is resonant in the first vibrational step will successively pull out of resonance higher up in the vibrational energy level ladder. However, the molecule can be excited in a multi-photon process (Sect. 9.1.3) until it is dissociated. SF_6 then disintegrates into SF_5 and F . By making the first step resonant for one isotopic molecule the probability of subsequent dissociation for this molecular species is significantly increased.

To carry out the corresponding process for UF_6 the availability of efficient lasers in the $16 \mu\text{m}$ region is a necessity. This has resulted in considerable effort being put into producing such lasers. An efficient way of generating laser radiation at $16 \mu\text{m}$ is to Raman shift a pulsed CO_2 laser at $10.6 \mu\text{m}$. A $16 \mu\text{m}$ beam can be produced at a 50% efficiency by stimulated Raman scattering in

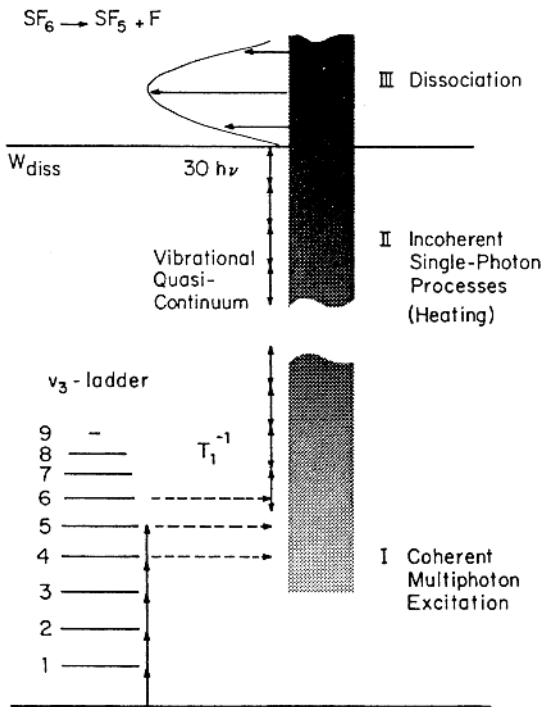
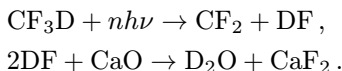


Fig. 10.43. Multi-photon dissociation process [10.157]

a multi-pass cell filled with para- H_2 . Rotational transitions in this molecule with parallel nuclear spins are used. A problem with UF_6 is that the width of the sharpest feature in the spectrum (the Q branch) is 5 cm^{-1} at room temperature, which greatly exceeds the isotope shift. Thus, the selectivity is poor. The selectivity can be increased by using two laser wavelengths in the $16 \mu\text{m}$ region. By dynamic cooling of the UF_6 gas through expansion from a supersonic nozzle, the number of populated rotational levels can be drastically reduced, leading to a much better resolution of the Q branches of the two isotopic molecules. Even then, two separate $16 \mu\text{m}$ wavelengths are advantageous and further efficiency is gained by adding excimer laser UV photons for more efficient photo-dissociation of molecules that are excited in the multi-photon process. Upon UF_6 dissociation, UF_5 molecules are formed in the form of a powder that can be collected.

For the separation of ^{13}C , multi-photon dissociation of Freon-22 (CF_2HCl) or CF_3I can be used, and macroscopic quantities are being produced utilizing CO_2 TEA lasers. Heavy water (D_2O) can also be enriched with a multi-photon process utilizing CO_2 laser radiation acting on CF_3D molecules:



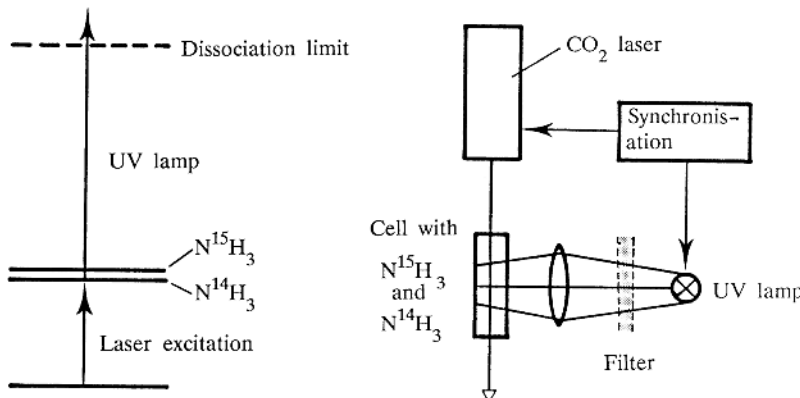
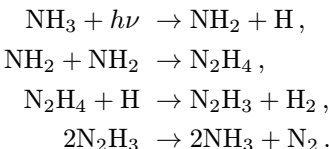


Fig. 10.44. Ammonia separation scheme

The isotope shift between CF_3D and CF_3H is large and the cross-sections for multi-photon absorption differ by a factor of 6000 between the two molecules.

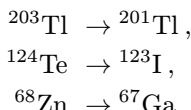
Formaldehyde, HCHO , has also been much studied. Using multi-photon processes this molecule can be used for the separation of hydrogen and carbon as well as oxygen.

Stepwise processes involving few photons can also be used for molecules. As a matter of fact, one of the first laser separations was performed in this way [10.158]. This experiment on NH_3 molecules is illustrated in Fig. 10.44. A mixture of $^{14}\text{NH}_3$ and $^{15}\text{NH}_3$ is kept in a cell and is irradiated by a pulsed CO_2 laser, which can only excite $^{14}\text{NH}_3$ vibrationally because of the isotope shift. At the same time a strong UV source, consisting of a spark discharge in air, is fired. The UV photons dissociate the vibrationally excited molecules but thanks to suitable filtering no photons with sufficient energy to dissociate ground-state molecules are available. The following reactions occur, but only for $^{14}\text{NH}_3$:

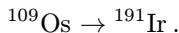


Thus, isotopically enriched $^{14}\text{N}_2$ gas has been formed in the cell. Similar processes can be used for boron and chlorine separation.

For the production of pure radioisotopes for medical use it is advantageous to induce the nuclear reactions in suitably chosen isotopically pure elements. Examples of such processes are



and



The annual world demand for such isotopes may only be of the order of 100 grams, but since conventional production methods are extremely costly, laser isotope separation might here be an attractive possibility.

10.5 Spectroscopic Aspects of Lasers in Medicine

10.5.1 Thermal Interaction of Laser Light with Tissue

Lasers are finding increasing applications in the field of medicine. Normally, the heating effect of laser beams is utilized. Raising the temperature from 37° to 44°C causes disruptions in the enzymatic and electrical activities of the cells. At 60°C protein denaturation occurs and at 100°C the cells rupture due to the boiling of the cellular fluid. Carbonization occurs at temperatures above 200°C. The laser power densities required to attain a certain temperature rise clearly depend on the absorption properties of the tissue, which are governed by the properties of water and haemoglobin. Skin absorption is largely due to the presence of melanin. The corresponding absorption curves are included in Fig. 10.45. Beams from the three most important medical laser types, the CO₂, the Nd:YAG and the Ar⁺ laser, have a surgical penetration depth of about 0.1, 4 and 1 mm, respectively, in normal tissue. Short-wavelength excimer lasers have a very low penetration depth and tissue removal is caused by ablation. Under pulsed irradiation the tissue is lifted off layer by layer. These lasers are now being extensively investigated for medical use, e.g. for corneal refractive surgery and opening of clogged blood vessels (angioplasty).

An important feature of laser beams in surgery is their ability to cut tissue and small vessels and at the same time coagulate the blood, which strongly reduces the need for blood transfusions ("the bloodless knife"). The thickness of the coagulated zone varies with the laser wavelength used. Other advantages are the sterile, contactless nature of the cutting and the minimum mechanical strain on the tissue. The last point is particularly important in neurosurgery. Lasers are also used to vaporize tumours. The laser radiation from Nd:YAG and Ar⁺ lasers can conveniently be delivered through flexible optical fibres that are highly transparent to the corresponding wavelengths. However, for CO₂ no fibres have been available until very recently, when the first fibres of limited applicability appeared. Normally, CO₂ radiation is delivered through a specially designed multi-joint arm that is terminated with a handpiece.

The strong absorption of green Ar⁺ radiation in blood can be utilized for selective coagulation of blood in small blood vessels. This is utilized in the treatment of portwine stains. This dermatological disease is caused by

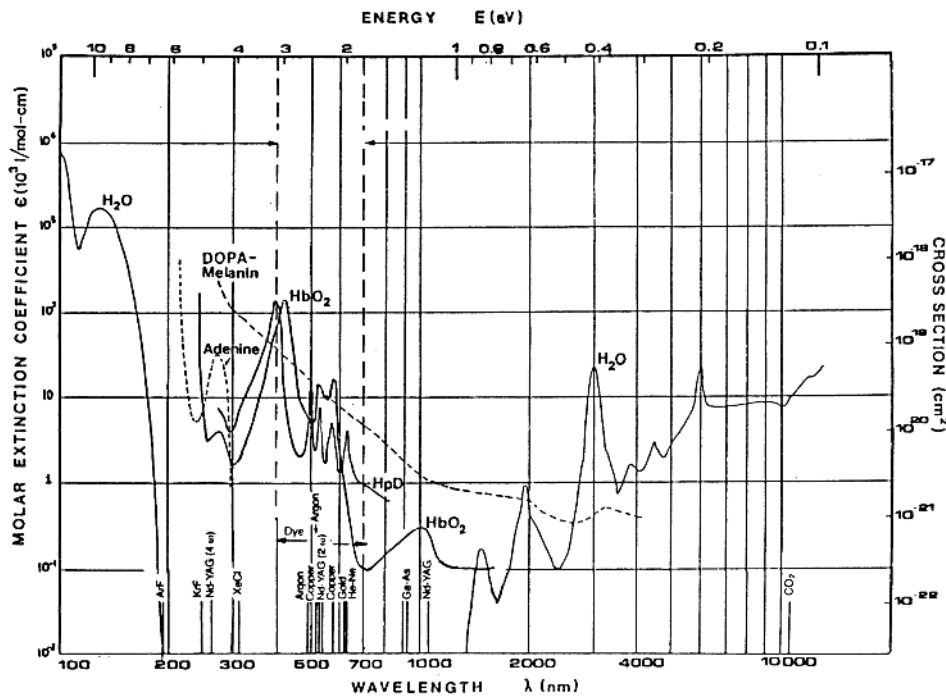


Fig. 10.45. Absorption curves for tissue constituents [10.159]

excessive growth of a network of tiny blood vessels close to the skin. The laser light penetrates the skin but is absorbed in the blood, eliminating the cause of skin discolouration.

Ar^+ lasers are also used for photo-coagulation treatment of excessive blood vessel growth in the retina of diabetes patients. This type of laser is also used for “spot welding” of the retina in cases of retinal detachment. Because of the relatively easy optical access to the interior of the eye this organ is well suited for laser treatment. The retina consists of many layers with different absorption properties. Thus, by choosing a certain wavelength an energy dose can be delivered to a particular layer with a certain selectivity. One area in the retina has very special absorption properties because of its high content of xanthophyll. The optical and spectroscopic properties of the eye largely determine the criteria for safe utilization of lasers and form the basis for legal classification of lasers. American regulations [10.160] are frequently used as a starting point in setting up national rules. The maximum permissible dose of laser light for eye exposure obviously varies strongly with wavelength. The strictest regulations apply for the wavelength region 400 to 1400 nm, in which the retina is fully exposed to the radiation. The Nd:YAG laser operating at $1.06 \mu\text{m}$ is one of the most dangerous lasers from an eye safety point of view since it penetrates into the eye, yet the presence of beams is not revealed

through scattering, since the wavelength falls in the invisible region. For wavelengths below 400 nm absorption occurs in the cornea. However, high doses of UV absorbed in the cornea cause cataracts.

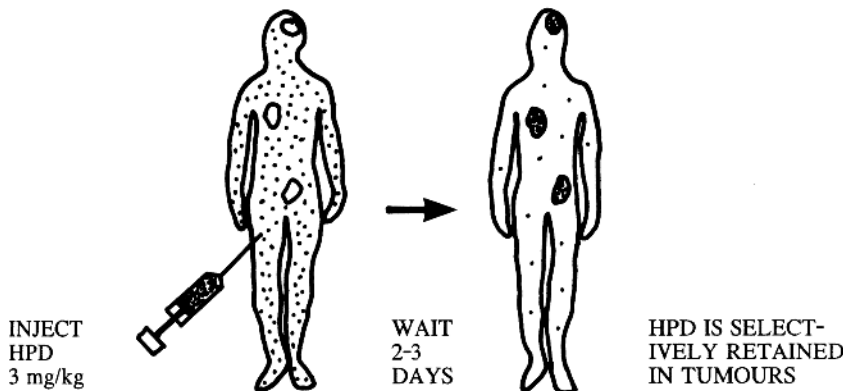
The most relaxed regulations pertain to the wavelength region above 1.4 μm where only the heat deposition in the cornea sets the limit. As a rule of thumb, safety limits are relaxed by at least a factor of 1000 when operating outside the 400–1.4 μm window. For detailed accounts of the medical use of the thermal energy in laser beams we refer the reader to [10.159, 10.161–10.163]. The somewhat related field of material processing with laser is covered extensively in [10.164].

10.5.2 Photodynamic Tumour Therapy

Apart from the surgical application of laser beams discussed above, a new interesting field of laser utilization for tumour localization and treatment is emerging. The techniques take advantage of the special properties of certain agents, e.g. hematoporphyrin derivative (HPD) [10.165–10.173]. After intravenous injection (typically 3 mg/kg bodyweight), the HPD molecules are distributed all over the body. However, after a few days the material is excreted from the body, but not from tumours, where it is selectively retained, as illustrated in Fig. 10.46. The HPD molecules themselves have no therapeutic effect but they have two important properties that can be used in connection with the selective retention just mentioned. These properties are set on a spectroscopic foundation in Fig. 10.47. The molecules have a very characteristic dual-peaked fluorescence in the red spectral region, as shown in Fig. 10.47. The excitation is most efficiently performed in the Soret band peaking at 405 nm. The violet lines of a Kr^+ laser (Sect. 8.4.5) fall conveniently in this region, but Ar^+ laser lines or the N_2 laser emission can also be used. The fluorescence can be utilized for localizing tumours [10.174–10.180], e.g. in the lung or bladder, that would otherwise not be visible in normal endoscopic investigations with viewing devices based on fibre optics.

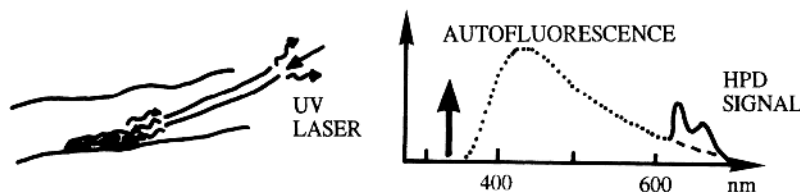
The other important property of HPD is that upon excitation and subsequent transfer to its triplet state, the HPD molecules can transfer their excitation energy to ground-state $X\ 3\Sigma_g$ oxygen molecules that are present in the tissue, as indicated in Figs. 10.46 and 10.47. The oxygen molecules are then excited from the triplet state to a singlet state, a ${}^1\Delta_g$. Singlet oxygen is known to strongly react with tissue through rapid oxidation and the tissue becomes necrotic. The process is thus of the laser-induced chemistry type (Sect. 10.4.1) and involves heating of the tissue only as a weak secondary effect. Since the process only occurs in the presence of HPD and since HPD is accumulated in tumours, selective therapy is obtained. Again, the HPD excitation most efficiently takes place in the Soret band. However, normally the absorption peak of HPD at 630 nm is preferred since tissue transmits this radiation much better as the wavelength falls outside the region of strong haemoglobin absorption (Fig. 10.45). An effective penetration depth of about

TUMOUR DETECTION AND TREATMENT USING HEMATOPORPHYRIN AND LASERS



TUMOUR DEMARCATIION CAN BE USED IN TWO WAYS:

1. TUMOUR DETECTION USING LASER-INDUCED FLUORESCENCE



**2. TUMOUR DESTRUCTION USING LASER-INDUCED CHEMISTRY
(SELECTIVE RELEASE OF SINGLET OXYGEN)**

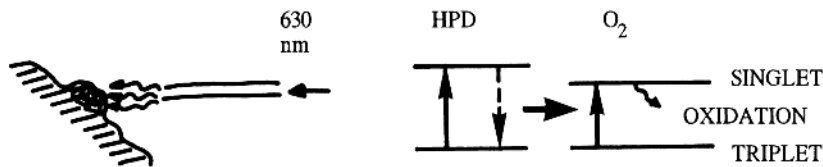


Fig. 10.46. Principle of HPD-PDT and tumour fluorescence detection [10.174]

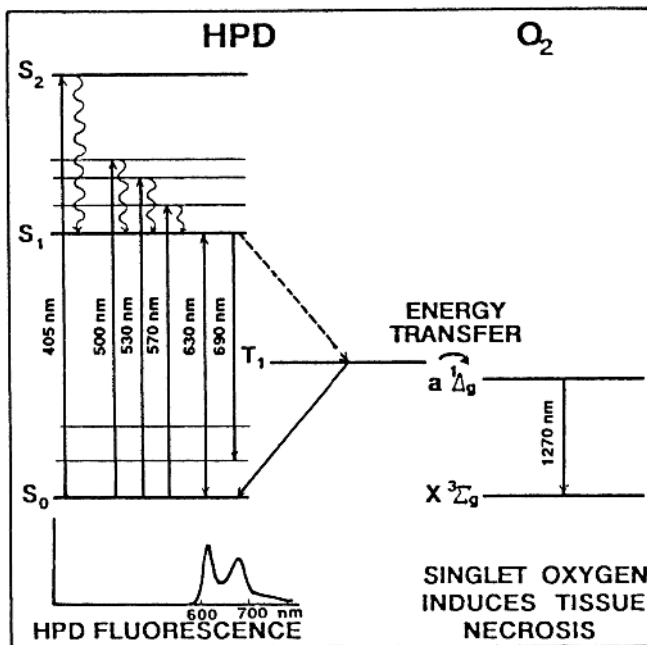


Fig. 10.47. Energy level diagrams for HPD and oxygen molecules [10.175]

0.5 cm is achieved. CW argon-ion or pulsed copper vapour laser pumping of a dye laser has normally been used to generate the 630 nm radiation but the 628 nm emission from a pulsed gold vapour laser can also be utilized. Recently, diode lasers with sufficient powers ($\sim 2\text{ W}$) have become available also in the 630 nm region and present unprecedented convenience in this type of therapy. The laser radiation can conveniently be delivered through a quartz optical fibre. For superficial tumours the radiation is applied directly to the surface and doses of tens of J/cm^2 are normally used. An example of tumour treatment is shown in Fig. 10.48, where a basal cell carcinoma was healed. The radiation can also be fibre-optically delivered through a bronchoscope or a cystoscope for lung and bladder applications, respectively. For deep-lying lesions the laser light can be transmitted fibre-optically through the lumen of a syringe needles that are inserted into the tumour mass [10.181]. A remarkable rate of success has been reported for this new type of treatment, which is normally referred to as PDT (*Photodynamic Therapy*).

The strongly increasing interest in PDT is related to the development of new, improved sensitizers. Attractive properties of a PDT substance are a high selectivity for tumour tissue versus normal ones, a well-defined chemical structure, a fast clearance from the body, and absorption at deeper red wavelengths than for HPD in order to allow thicker lesions to be treated. Additional sensitizers (with absorption wavelength) now being tested in-

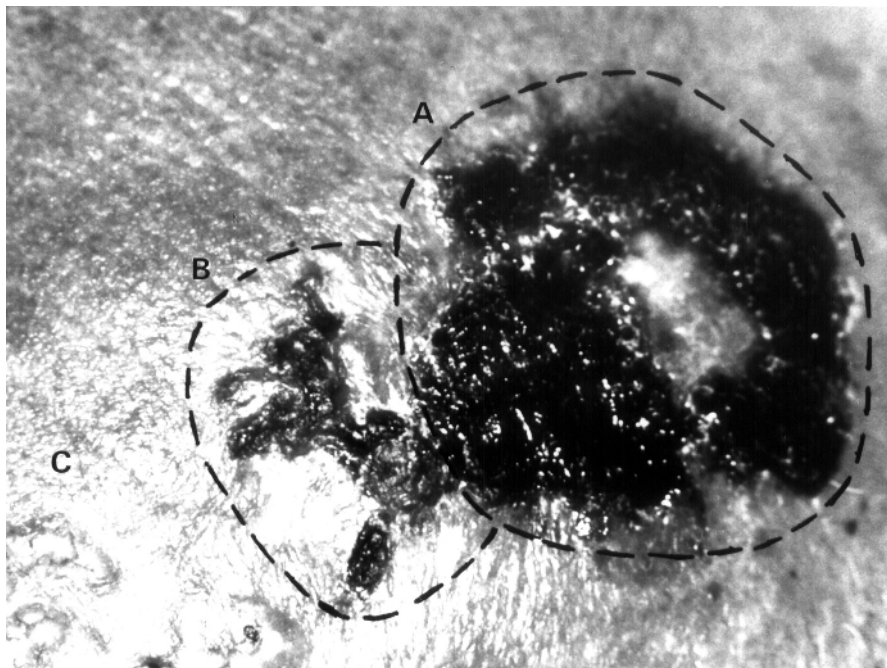


Fig. 10.48. Photograph of human basal cell cancer lesions one week after HPD-PDT. The area *A* received a uniform light dose of 60 J/cm^2 . The strong demarcation of destructed tissue from undamaged tissue due to the selective uptake of HPD in tumour cells only is evident. The area *B* received only 30 J/cm^2 . In area *C* untreated tumour parts are visible

cludes bensoporphyrin, BPD (690 nm), mono aspartyl chlorin e6, MACE (670 nm), tetra hydrophenylchlorin, THPC (650 nm), zinc phtalocyanine, ZnPC (675 nm) and tin ethyl etiopurpurin, SnET2 (660 nm).

Of special interest is δ -amino levulinic acid, ALA, which occurs naturally in the human body. It is the building stone, out of which the red blood pigment, haem, is synthesised in the haem cycle, illustrated in Fig. 10.49. In an enzymatically controlled process the strongly fluorescent and photodynamically active substance protoporphyrin IX (PpIX) is produced. After incorporation of an iron atom, haem is obtained. If ALA is administered orally or intravenously to the body in elevated concentrations, an excess concentration of PpIX is produced with selectivity to tumour tissue because of differences in enzymatic concentrations. A special feature of ALA is that it can also be administered topically, e.g. in a cream applied over skin tumours. After few hours PpIX is built up in the skin tumours because of the stronger permeability of the damaged keratin layer. The generated substance is clearly seen in fluorescence, and treatment can be performed using 635 nm radiation.

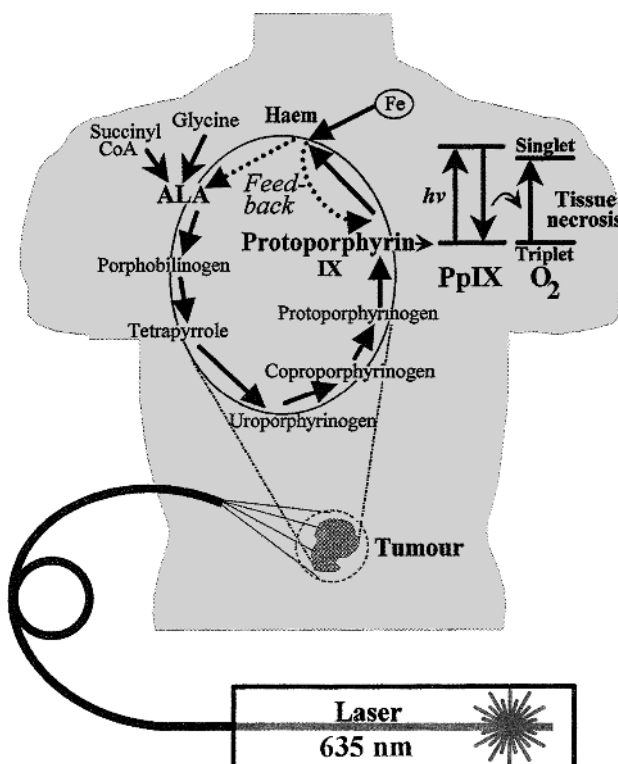


Fig. 10.49. Schematic diagram of the haem cycle, in which the haem pigment is produced from ALA (δ -amino levulinic acid). The photodynamic action of protoporphyrin IX leading to tissue necrosis is also indicated [10.182]

ALA-PDT is a very convenient treatment modality, which is now widely being used [10.183, 10.182].

10.5.3 Tissue Diagnostics with Laser-Induced Fluorescence

We will now discuss tumour diagnostics using laser-induced fluorescence. As mentioned above, the tumour-seeking agents exhibit characteristic peaks in the red spectral region. Also, the natural tissue fluorescence from the various organic compounds in the tissue, such as elastin, collagen, amino acids, etc., gives rise to a broad fluorescence distribution in the blue-green spectral region (the *autofluorescence*), and often this natural signal is also useful for tumour detection and demarcation. Especially in clinical work, tissue fluorescence is most conveniently recorded using a fibre-optic fluorosensor of the type shown in Fig. 10.50. A sealed-off nitrogen laser, emitting at 337 nm, is a very convenient excitation source. This laser typically generates 3 ns long pulses at 10 Hz, and can also be employed to pump a compact dye laser, converting the

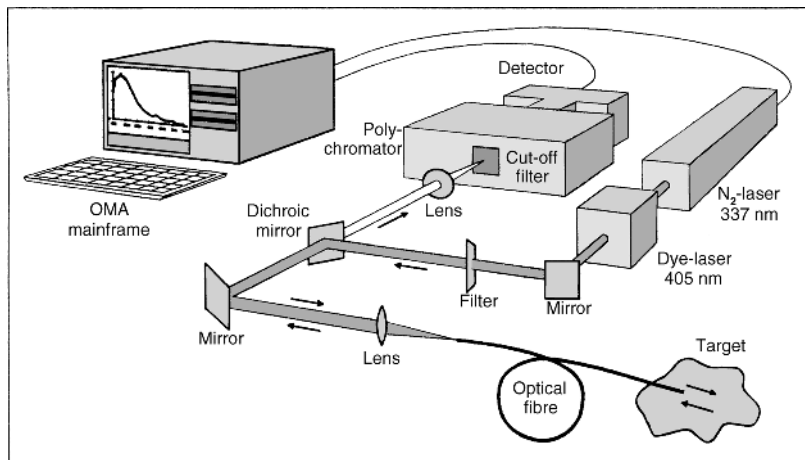


Fig. 10.50. Diagram of a laser fluorosensor based on a pulsed short-wavelength laser, fibre-optic fluorescence sampling and an optical multichannel analyzer [10.184]

pump radiation to a longer, selectable wavelength. Fluorescence is best analysed with an optical multichannel analyzer system consisting of a spectrometer equipped with an intensified CCD detector in the focal plane (see Fig. 6.38). For each exciting laser pulse the whole fluorescence spectrum is captured and can be directly displayed on a monitor and stored in a computer. The image intensifier, providing amplification of the weak light signals, is gated synchronously with the laser pulses. In this way background radiation due to daylight or operation lamps can be suppressed in the recordings.

Typical tissue spectra recorded with a fluorosensor of this kind are shown in Fig. 10.51. The sample chosen is a rat tumour in a muscle environment and spectra for tumour as well as for surrounding normal tissue are shown for two excitation wavelengths, 337 and 405 nm. The rat had been injected by a dose of HPD two days earlier. For both excitation wavelengths a broad intensity distribution extending from the blue to the near IR region is obtained. In the measurements the strong elastically scattered light from the primary laser excitation light is suppressed by a suitable filter, blocking completely towards shorter wavelengths but letting all longer wavelengths through, basically unattenuated.

In the tumour spectra we can see the characteristic dual-peaked fluorescence signal from HPD in the red wavelength region (see also Figs. 10.46 and 10.47). This signal is more prominent in the tumour than in the normal tissue because of the selective retention of the drug in tumour tissue. The blue-green autofluorescence peaks at about 470 nm. We notice that the autofluorescence is much stronger and the red HPD signal much weaker when 337 nm is chosen as the excitation wavelength. This can be understood from the absorption curves in Fig. 10.45. 405 nm corresponds to the absorption maximum (the

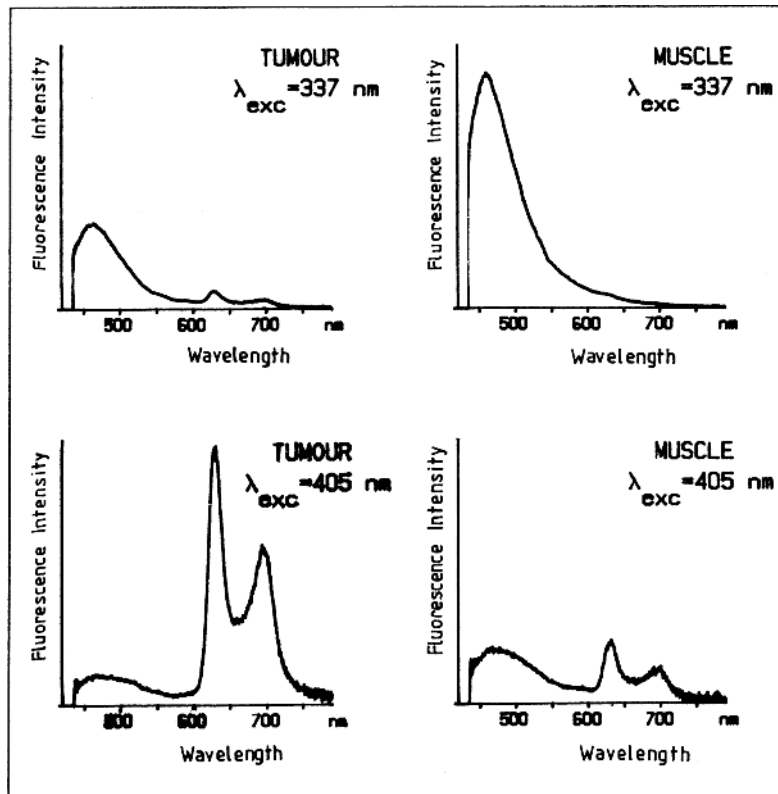


Fig. 10.51. Laser-induced fluorescence spectra for an experimental tumour (a human colon adenocarcinoma inoculated in rat muscle) and normal surrounding tissue. The rat had been injected with a dose of hematoporphyrin derivative about two days before the investigation. Two excitation wavelengths, 337 and 405 nm, are chosen to illustrate the influence of the wavelength choice [10.185]

Soret band) of the HPD molecules, and excitation here is more efficient than at 337 nm. Many chromophores contribute to the signal in the blue-green wavelength region. The absorption for most of these molecules increases for shorter wavelengths. An interesting observation relating to Fig. 10.51 is that the intensity of the autofluorescence signal is reduced in tumour tissue as compared to normal one. This seems to be due to a transformation of strongly fluorescing NADH in normal tissue to NAD^+ with a much weaker fluorescence. These observations form the basis for efficient tumour detection and demarcation using laser-induced fluorescence after injection of a tumour-seeking drug: the red fluorescence increases and the blue-green fluorescence decreases in a tumour. Both effects can be utilised in a convenient way by dividing the red signal intensity by the blue intensity. This is illustrated in Fig. 10.52 for the case of a scan through a tumour inoculated in a rat brain.

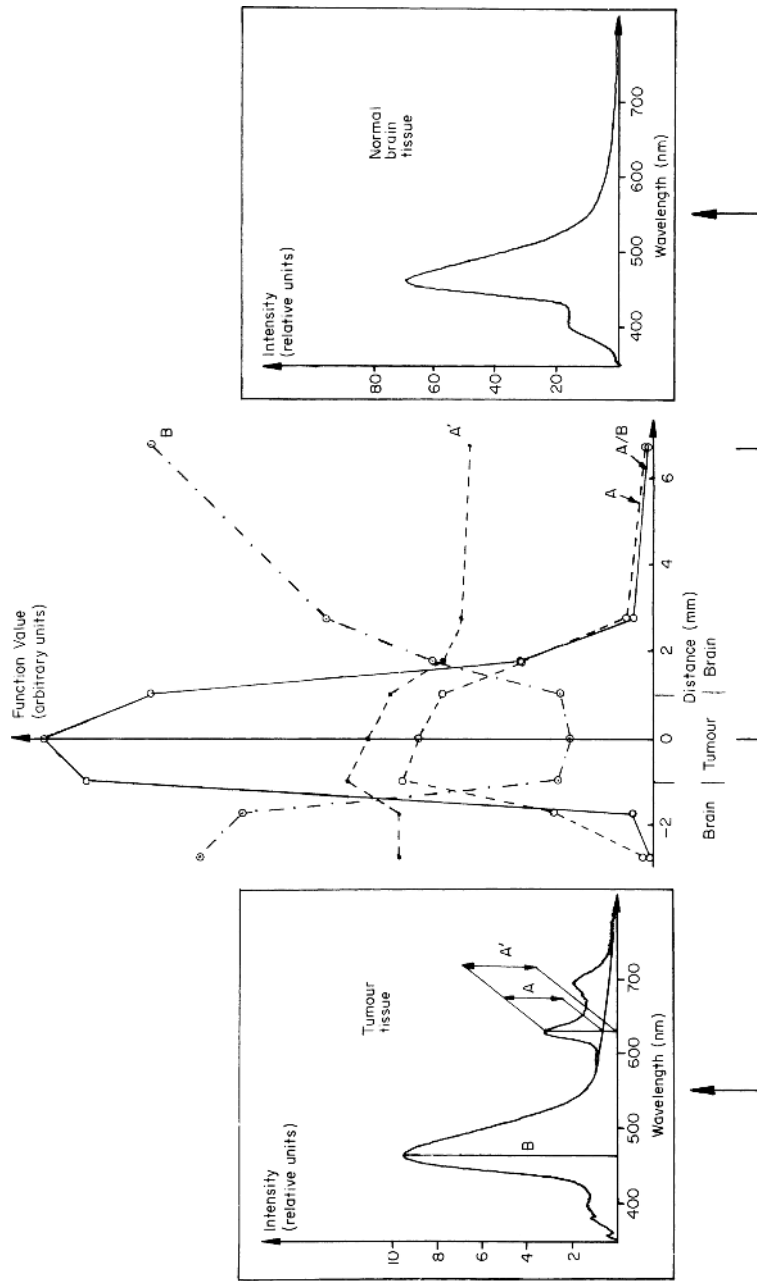


Fig. 10.52. Fluorescence spectra for a rat-brain tumour and normal brain following HPD injection. Demonstration of contrast enhancement by ratio formation [10.186].

The rat had been injected with Photofrin (1 mg/kg bodyweight) 24 hours before the animal was sacrificed and the fluorescence investigation was performed. Typical spectra for normal and tumour regions are included in the figure, with the red intensity at 630 nm denoted by A' and the blue intensity at 480 denoted by B. The background-free HPD signal at 630 nm is denoted by A. In the scan the red increase and the blue decrease in the tumour are very evident. Contrast enhancement is obtained by forming the ratio A/B. The use of such a dimensionless ratio also has other important advantages in practical clinical work, since dimensionless quantities are immune to

- distance changes between tissue and measurement equipment;
- variations in angle of incidence of radiation on tissue;
- fluctuations in illumination source and detection system efficiency.

Clearly, these observations about dimensionless quantities pertain to many other measurement situations in physics unrelated to medicine, in particular in the imaging of objects which have complex topology [10.187].

As already mentioned, laser-induced fluorescence has proven to have a considerable potential for early tumour detection and demarcation in many clinical specialities [10.180]. Since the fluorosensor fibre can be brought through the biopsy channel on clinical endoscopes, access to the surface of organs like the bronchii, the bladder, the gastrointestinal and gynaecological tracts can be obtained.

Laser-induced fluorescence can also be used for characterisation of arteriosclerosis in blood vessels. A scenario for combined diagnosis and treatment of cardiovascular disease is shown in Fig. 10.53. A fibre-optic fluorosensor characterises the vessel wall by its fluorescence, which has been found to be different for normal wall and atherosclerotic plaques [10.188–10.191]. The reason is different molecular compositions, e.g. the balance between elastin and collagen. Depending on the outcome of the spectral analysis following a diagnostic pulse, a high-energy ablation pulse from an excimer laser is released through the fibre to remove material and clear a clogged vessel. This might become a future replacement for certain bypass cardiac operations.

Differences in the spectral properties of various organic substances can be used for different kinds of diagnostics in biology and medicine [10.192]. Autofluorescence only has been used for tumour characterization [10.193–10.195] as well as for the detection of caries in teeth [10.196, 10.197]. Raman, near-IR and polarized light reflectance spectroscopy also shows substantial promise for medical diagnostics [10.198–10.200].

So far only the spectral distribution of the fluorescence light has been utilized for diagnostics. However, as discussed extensively in Sect. 9.4, the fluorescence decay time following a pulsed excitation is also a characteristic property for molecules. Differences in decay times can thus be exploited for cancer and cardiovascular disease diagnostics, as illustrated in Fig. 10.54. This type of measurement is also illustrated in Fig. 10.53, where a simple ratio between the intensity of “late” fluorescence to “early” fluorescence is

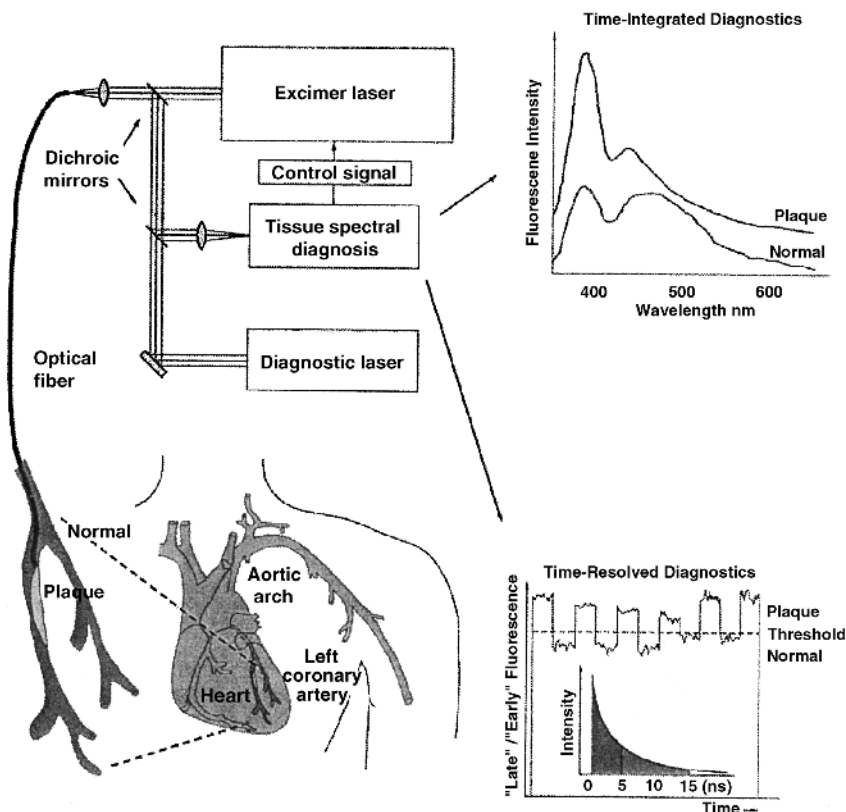


Fig. 10.53. Schematic diagram of fluorescence diagnostics and interactive laser ablation to remove plaque in clogged vessels. A fast spectral characterization of the material in front of the fibre end allows a decision on whether an ablation pulse should be fired or not [10.188]

shown to demarcate between normal tissue wall and plaque. Time-resolved fluorescence spectroscopy is generally speaking a valuable tool in biological and medical research [10.201–10.205]. General surveys of the use of laser-induced fluorescence for medical diagnostics can be found in [10.206].

The point-monitoring techniques discussed above can be extended to tissue imaging [10.207, 10.208]. A larger area is then illuminated with exciting light and fluorescence images are then recorded in selected spectral bands using a gated and image-intensified two-dimensional CCD detector [10.187, 10.207]. Contrast-enhancement mathematical operations are then performed for spatially corresponding points in the images, e.g. a ratio is formed as discussed in connection with Fig. 10.52. Alternatively, the fluorescence image for a selected wavelength band is recorded for different delays after the exciting pulse and a spatial mapping of the lifetimes can be

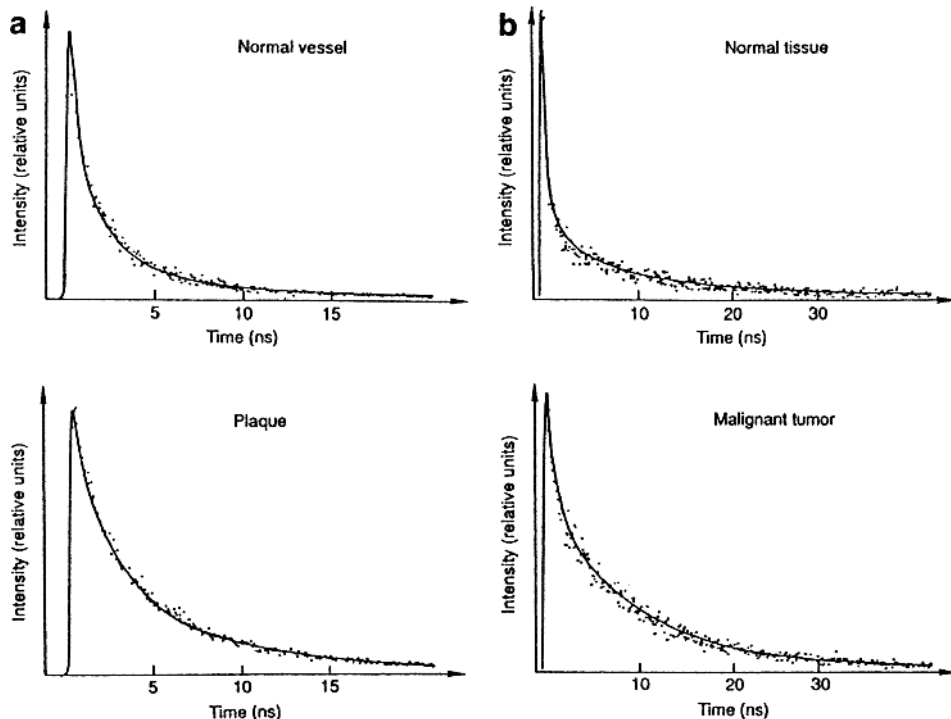


Fig. 10.54. Fluorescence-decay curves showing demarcations between normal vessel and atherosclerotic plaque (left), and normal tissue and malignant tumor (right) [10.206]

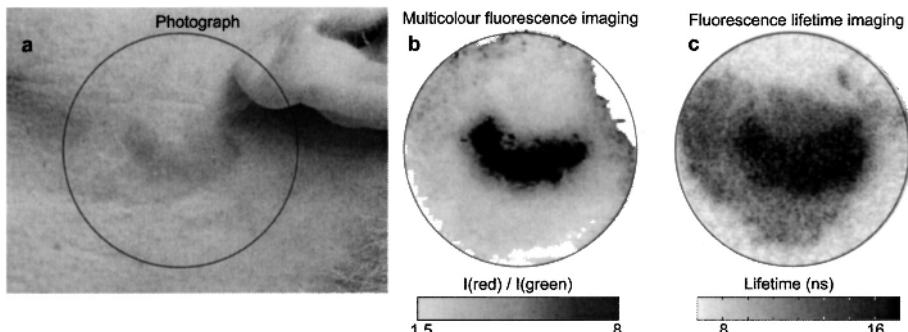


Fig. 10.55. Fluorescence imaging of a basal-cell carcinoma below the ear. The photograph (a) shows the measurement site, (b) is a multi-colour image obtained by dividing two images, recorded in the red region of sensitizer peak and for the blue autofluorescence, and (c) is a lifetime image, where the fluorescence decay time of red fluorescence light has been evaluated in each image point from gated recordings made at different time delays after the excitation [10.209]

made, discriminating certain types of tissue [10.208]. Images of both types are shown in Fig. 10.55 for the case of a human basal cell carcinoma tumour.

Similar spectral techniques as discussed for macroscopic tumour imaging can be employed for fluorescence microscopy. *Confocal and two-photon-induced fluorescence microscopy* [10.210], and imaging Fourier transform spectroscopy [10.211] are all valuable techniques for studies at the cellular level. Related to this field is the optical trapping of cells with focused laser beams (*optical tweezers*), which relies on gradient forces of the same kind as discussed in Sect. 9.8.5. Trapped cells and polymer strings can be manipulated in many ways to enable fundamental studies to be conducted [10.212].

10.5.4 Scattering Spectroscopy and Tissue Transillumination

Atmospheric light scattering has been discussed in Sects. 4.5, 4.6 and 10.2.3. If the density of scatterers is high, multiple scattering can occur, as in clouds or in dense fog. Light can also be scattered in liquids and in solids. Examples of strongly scattering media are milk and human tissue. In order to understand light propagation in tissue it is necessary to treat absorption and scattering simultaneously and on an equal footing. Clearly, no simple Beer–Lambertian law (6.45), (6.46) is valid in scattering media, since the path length is undefined. Much effort has been invested in describing the optics of scattering media [10.213, 10.214]. Analytical descriptions based on transport equations can be used or differential equations can be solved numerically. The most general way to treat the problem is by *Monte Carlo simulations*, where individual photons released by the source are followed on their way through the medium controlled by probabilistic laws for absorption and scattering in certain angles. A good understanding of human tissue optics is important for light dosimetry for PDT, for spectroscopy for the determination of the oxygenation [10.215] or the concentration of constituents such as glucose (diabetic applications) or urea (dialysis applications) in blood, or photosensitizers in tissue [10.216]. It is also important for the development of optical mammography and similar applications [10.217–10.219]. Using time-resolved spectroscopy it is possible to follow the photon paths through the tissue. Two basic geometries are illustrated in Fig. 10.56. In transillumination there is a shortest path corresponding to the very unlikely event of non-scattered radiation, giving rise to a distinct signal (*ballistic photons*). Most photons arriving at the detector come much later and only after several scattering events. If the transmitter and the detector are on the same side of the sample, all photons received must have been scattered. If the position of transmitter and receiver coalesce (laser-radar geometry), a histogram of arrival times for photons that have sampled a certain volume below the measurement point is obtained. This mode of operation is common in Doppler measurements of superficial blood flow, which we will discuss first.

A measure of the blood perfusion in tissue can be obtained by analysing the signal due to slightly Doppler-shifted photons that encountered scattering

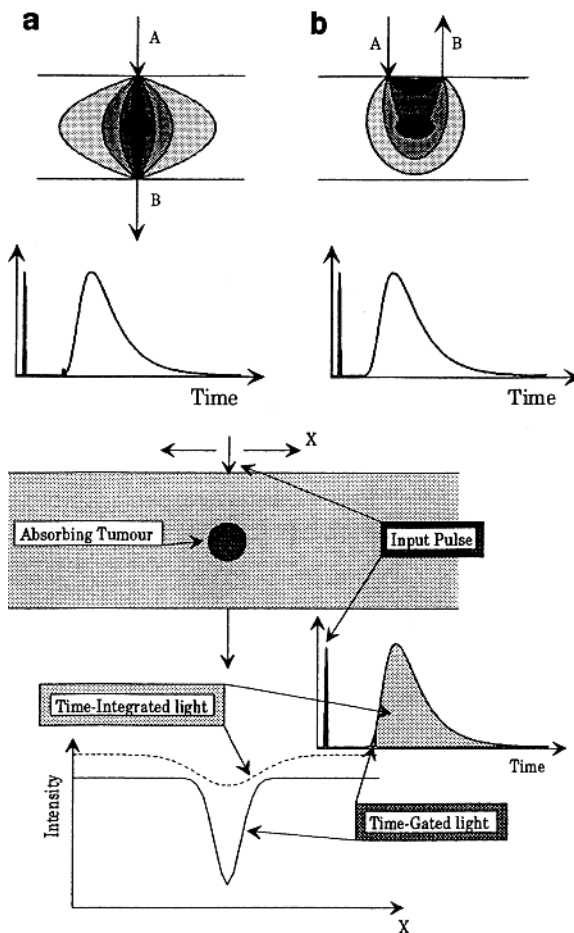


Fig. 10.56. *Top:* Geometries for time-resolved measurements on turbid media. (a) Transillumination (b) Backscattering. *Bottom:* Gated-viewing through tissue. An enhanced spatial resolution is obtained by selecting the “early” light only [10.214]

against moving red blood cells. A CW helium–neon laser operating at 633 nm, or a dark red/near IR diode laser is normally used in such measurements. The shift is governed by the Doppler formula (6.4). Light (at about 10¹⁴ Hz) which is scattered from capillary blood cells moving with a velocity of 3 mm/sec is shifted by about 1 kHz. Such small shifts can only be detected by optical heterodyne techniques (Sect. 10.2.1), where the beat signal between the light scattered from the moving objects and from the fixed tissue cells is picked up. Obviously, an objective full quantification is difficult to obtain, since a complex averaging is performed over photons scattered at different depths. Still, valuable information can be obtained, in particular for assessing reperfusion in connection with transplant surgery and for the monitoring of

wound healing. By performing sequential measurements with a system where the laser beam is scanned in a matrix pattern over the tissue it is possible to generate images of the superficial blood flow. Laser-Doppler techniques for blood perfusion monitoring are discussed in [10.220].

Complete image blurring occurs in transillumination of strongly scattering media. It is well known that red light penetrates a human hand (due to the strongly reduced absorption of haem above 600 nm; see Fig. 10.45). Nevertheless, it is impossible to see the shadows of the bones because of strong multiple scattering. Optical mammography (breast transillumination) would be attractive because of the absence of mutagenic ionizing radiation, but obviously a straightforward approach has little chance of success because of the scattering. However, the problems can be reduced by using a pulsed transmitter and time-resolving detection electronics for the transmitted light, as illustrated in the lower part of Fig. 10.56. Because of the multiple scattering, most of the photons penetrating the tissue have spent a long time in the tissue, while only very few photons arrive at the detector at the nominal propagation time without disruptions. By selecting a small detection time window and recording the very first photons, it is possible to look at just the “fastest” photons coming out of the tissue. *Gated viewing* or *conditional sampling* is performed. If an obstacle, such as a bone [10.218] or a tumour [10.219], blocks the passage, a “shadow” will be created for the selected subgroup of very early photons. For thicker samples there are no unscattered photons. Still, the first photons have been minimally scattered and produce a clearer image, as schematically shown in the figure. By performing a scan of the tissue under investigation, a transillumination image can be created. An example for a ductal carcinoma in a newly resected human

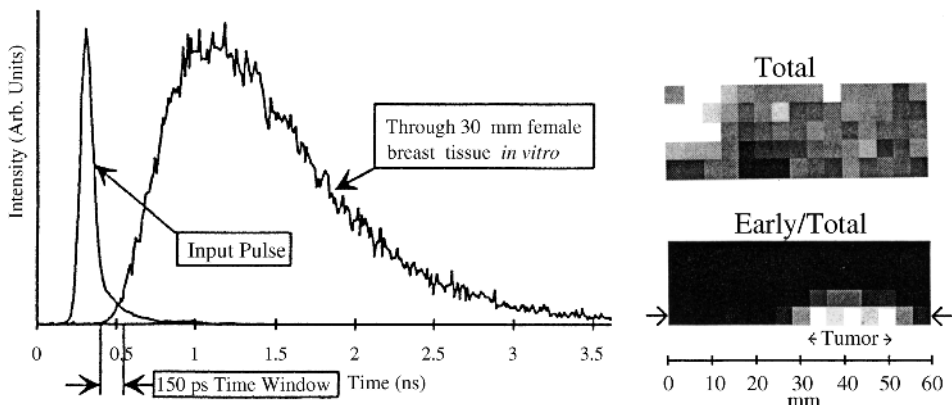
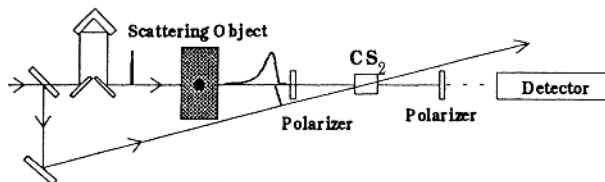


Fig. 10.57. Transillumination images of breast tissue in vitro, showing the presence of a tumour when the first part of the time-dispersion signal is utilized. Integration of the whole signal does not yield a tumour image. The early light signal has been normalized to the integrated light [10.219]

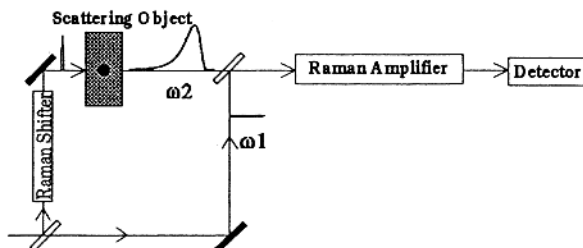
breast is shown in Fig. 10.57, where the transmitting and receiving fibres were scanned together under computer control over the tissue, which was compressed between glass plates [10.218]. A diode laser operating at 815 nm and producing 30 ps long pulses at a repetition rate of 10 MHz was used in these recordings. An example of a time dispersion curve is shown, recorded by the delayed coincidence technique (Fig. 9.22). By restricting the detection to a narrow time window around the nominal ballistic flight time it was possible to see the tumour (lower diagram), which disappears in a total light image (upper diagram). A streak camera can also be used for detecting the early photons [10.221].

In addition to these electronic gating techniques for suppressing the influence of excessive scattering in tissue, nonlinear optical phenomena can be utilized for the gating. Three techniques are illustrated in Fig. 10.58. When using an optical Kerr gate, a Kerr-active medium is utilized and, by employing a strong laser pulse, birefringence is induced to rotate the plane of polarization

Optical Kerr Gate



Stimulated Raman Amplification



Second-harmonic Cross-correlation

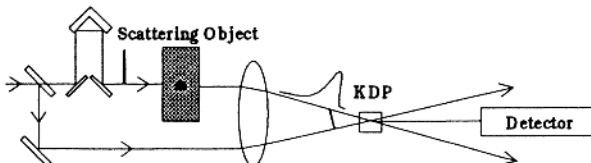


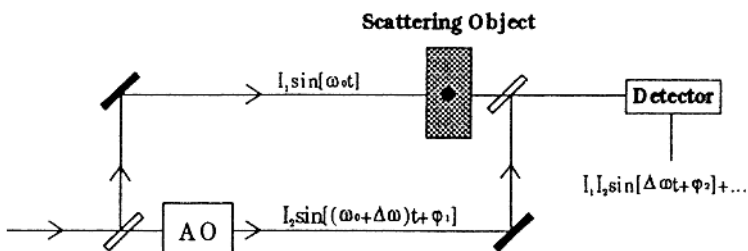
Fig. 10.58. Gated-viewing techniques using non-linear optical phenomena [10.214]

of the probing light, which is normally blocked out by crossed polarizers. By proper delay between the two pulses, derived from the same laser, it is possible to strobe on the early light [10.222]. The same result can be obtained using a Raman amplifier, which is activated by fast pump light arriving at the proper time [10.223]. Finally, using the second-harmonic cross-correlation technique (see also Fig. 9.34), the desired temporal part of the probe light can be selected [10.224].

By studying the shape of the whole time-dispersed photon distribution from a scattering medium the absorption and scattering coefficients of the medium can be evaluated. The same information can be obtained by employing a sinusoidally modulated CW laser beam and studying the phase-shift and the modulation contrast reduction in the scattered light [10.225]. This is basically the phase-shift method discussed previously in Sect. 9.4.4. Several modulation frequencies are needed to obtain the same information as in the conceptually simpler pulsed techniques.

The non-scattered part of the transmitted radiation can also be detected by *coherent* techniques, as illustrated in Fig. 10.59. Using heterodyne

Heterodyne detection



Light-in-flight Holography

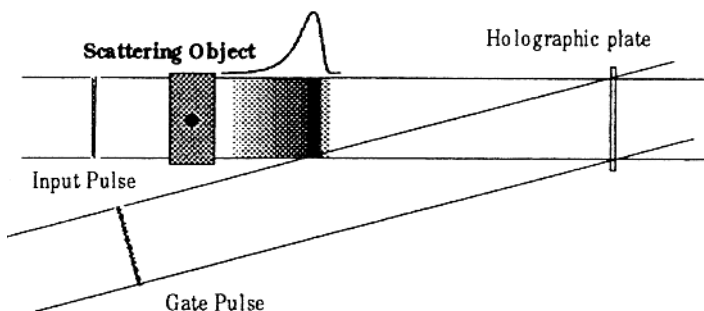


Fig. 10.59. Detection of the non-scattered part of the probe light by coherent techniques [10.214]

detection [10.226], a signal with a well-defined phase is only obtained at the intermediate frequency ($\Delta\omega$) if the probe light has not been scattered. Light-in-flight holography [10.227] is a technique, that also relies on the presence of a fixed phase relation between the probe and the reference beam, only available for the non-scattered part of the radiation [10.228]. All the techniques discussed can be used in multiple beam/detector applications to allow tomographic reconstruction of the interior of a scattering medium. Then more complex objects can be studied, such as uncompressed breasts [10.229] or human skulls (for detection of bleeding, e.g. after accidents) [10.230]. For thin objects a further, particularly simple and powerful, coherent technique can be utilized, *optical coherence tomography* [10.231]. As illustrated in Fig. 10.60,

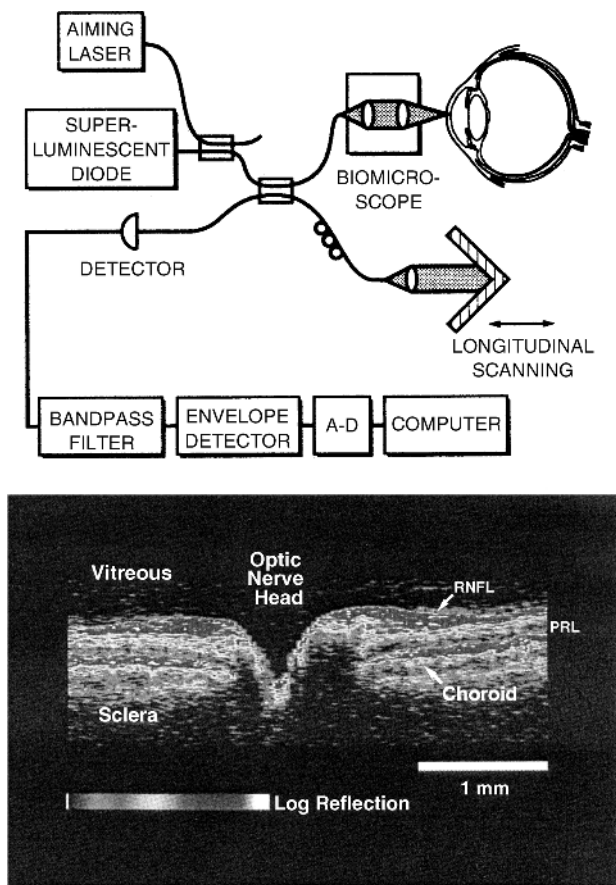


Fig. 10.60. *Top:* Set-up for *in vivo* eye optical coherence tomography using a fibre-optic Michelson interferometer. *Below:* a scan of the region around the position of the optical nerve is shown, featuring many details including the photoreceptor layer (PRL) [10.232]

a Michelson interferometer (Sect. 6.2.4), frequently arranged with fibre-optic arms, is used. The technique relies on the fact that all frequency components from a broadband CW light source interfere constructively when the interferometer arms have the same length. Thus, by scanning the length of the reference arm, light scattered at different depths in the tissue can be isolated to map out a depth profile. The broader the spectral distribution of the light source, the higher the depth resolution of the system will be. The technique has proved very successful for probing the structures of the eye (Fig. 10.60, lower part) and for mapping cross-sections of blood vessels.

Techniques developed primarily for medical applications can also find many other biological and technical applications. Thus, the time-resolved techniques using delayed-coincidence electronics have been used for studying the scattering properties of plant leaves [10.233], paper sheets [10.234], and pharmaceutical preparations [10.235].

Recently a technique for studying free gas in scattering solids and liquids was introduced [10.236]. In *gas in scattering media absorption spectroscopy* (GASMAS), single-mode laser radiation is injected into the scattering object and sharp absorptive signals in detected scattered light are observed. Free gas typically exhibits a linewidth of 0.01 nm or less, which is typically 10^4 times smaller than absorptive features in the condensed-matter matrix material. By wavelength modulation spectroscopy (Sect. 10.2.2), which is conveniently performed with diode lasers, the gas signals can be observed even in weak light which has travelled a long distance.

By performing time-resolved measurements with a pulsed laser in a similar way as discussed in connection with Fig. 10.56, it is possible to track the time history of the emerging photons and determine the mean pathlength. Thus, by combining CW and pulsed measurements performed at the same wavelength, it is possible to calculate the absolute gas concentration in the medium [10.237]. Normal molecular oxygen, featuring lines around 760 nm, is well adapted for GASMAS studies. The internal pressure in the gas pores can be assessed from the linewidth observed [10.236]. It is also possible to readily study gas diffusion through the porous medium by first subjecting the sample to, e.g., pure nitrogen gas, which penetrates the sample and displaces the oxygen. By then performing GASMAS measurements in the normal ambient atmosphere, the oxygen reinvansion of the sample can be followed. The technique has many applications, e.g., in studying building materials, surface coatings, ceramics, wood, foods, and possibly also for medical diagnostics [10.236, 10.238].

Questions and Exercises

Chapter 2

1. A closed electronic shell of an atom becomes spherically symmetric. Why?
2. Discuss the two angular momentum coupling schemes, LS and jj coupling. How can it be determined experimentally which coupling scheme is relevant for a particular atomic configuration?
3. Why do rare-earth elements (lanthanides) have similar chemical properties and sharp spectral lines even when incorporated in a crystal matrix?
4. What can be learned from measurements of
 - a) Landé g_J factors,
 - b) Stark effect constants (polarizabilities),
 - c) Magnetic hyperfine structure constants,
 - d) Isotopic shifts,
 - e) Radiative lifetimes?
5. What characterizes the Zeeman and the Paschen–Back effects, respectively? What is the meaning of the non-crossing rule?
6. Explain why the Zeeman effect is linear in the applied magnetic field B while the (non-hydrogenic) Stark effect is quadratic in the electric field E .
7. Why are there magnetic sublevels which progress with a linear energy displacement as a function of the magnetic field? Discuss the fine-structure and the hyperfine-structure cases.
8. The Stark effect:
 - a) Write down the expression for the Stark shift of a fine-structure level with quantum numbers J and m_J .
 - b) Explain the particular dependence on the electric field strength for non-hydrogenic states.
 - c) Can you see any practical application of measurements of the Stark effect?
9. In a strong electric field an atom can be ionized. Discuss this phenomenon and under what conditions it can most easily be studied.

10. The atomic hyperfine structure is due to the interaction between the nucleus and the electronic shell. Discuss the origin of the interactions and what nuclear and electronic properties are being tested. Give some example of hyperfine splitting (e.g. for a state with electronic spin $J = 3/2$ and nuclear spin $I = 3/2$) with reference to the mathematics governing the structure.
11. Discuss electrical hyperfine structure. What is its origin? What can be learned from it? Under what circumstances (quantum numbers etc.) can it be observed?
12. Hyperfine structure:
 - a) What is the typical size of atomic hyperfine structures?
 - b) Which hyperfine structure quantum numbers F are possible for a $J = 3/2$ state in an $I = 5/2$ atom?
 - c) For what types of electrons does the Fermi contact interaction yield a large contribution to the hyperfine structure?
 - d) How can an inverted hyperfine-structure level sequence occur?
 - e) How does the electric hyperfine structure show up in high-resolution spectra?
 - f) What are the requirements for the I and J quantum numbers to make an electric quadrupole interaction possible?
13. When do the normal mass isotopic shift and the volume shift dominate?

Chapter 3

14. What is the essence of the Born–Oppenheimer approximation?
15. Discuss the vibrational energy of a diatomic molecule. How can the simplest quantum-mechanical model be extended for realistic molecules? Explain how observed deviations from the simplest model can be utilized for temperature measurements in molecular gases.
16. What information about a diatomic molecule can be obtained from the rotational constant B' ?
17. Discuss how the vibrational spectrum is influenced in electronic transitions in diatomic molecules considering the Franck–Condon principle.
18. Why are electronic molecular transitions necessary in order to be able to observe band-heads (bent-over Forbrat parabolas)? What determines if a band is shaded to the red or to the violet?

Chapter 4

19. Discuss the energy-level diagram and the spectrum of the helium atom. Which types of emission lines are seen in the spectrum? The calcium atom

also has two electrons outside its closed shells. Discuss the differences between the calcium and helium spectra!

20. What is phosphorescence?
21. Discuss Rayleigh and Raman scattering.
22. When the sublevels of an excited state are statistically populated, the emitted light becomes isotropic and non-polarized. What does this mean in terms of the relation between π and σ radiation?

Chapter 5

23. Describe the physics behind the X-ray absorption spectroscopy method and discuss its refinement, EXAFS.
24. Discuss the PIXE method for chemical analysis.
25. What is common to XPS (ESCA) and Auger spectroscopy, and what is different? Discuss how the techniques can be used for identifying chemical compounds.
26. Discuss Auger electron spectroscopy. Why are the requirements for energy sharpness of the exciting X-ray radiation more relaxed than for normal electron spectroscopy (XPS)?

Chapter 6

27. What is the meaning of the two concepts homogeneous and inhomogeneous linewidths?
28. Electron synchrotrons provide radiation of great importance for spectroscopy. Describe briefly the generation process and the properties of the radiation.
29. What factors determine the resolution of the following spectroscopic instruments:
 - a) Grating spectrometer
 - b) Fabry–Pérot interferometer
 - c) Fourier transform spectrometer
30. What is the difference between an Ebert and a Czerny–Turner spectrometer?
31. Mention three different types of detectors for IR radiation.
32. Describe the construction and use of an optical multichannel analyser system with time-gating possibility.

33. How short-lived would an excited level have to be to exhibit a natural radiative width of the same order of magnitude as the Doppler width (visible light)? How does the Doppler broadening depend on the temperature and the mass of the gas particles?
34. What is the use of neutral density filters?
35. Transmission of media:
 - a) What window material is transparent at the shortest possible optical wavelengths, and what is the wavelength cut-off?
 - b) Below what wavelength can spectroscopic investigations not be performed without evacuating the air from the apparatus?
 - c) Below what wavelength can ground-based astronomers not observe the stars using optical techniques?
 - d) How far out into the IR spectral region can quartz be used as a lens material?
 - e) At what wavelength towards the UV region does the atmosphere cut off sunlight, and what molecule is responsible for the absorption?
 - f) Discuss the transmission of sea water.
36. Discuss the problems that occur when one wants to push optical spectroscopy from the visible region down towards shorter wavelengths (transmission in optical components, air etc.).
37. What practical problems might be encountered when performing satellite-based measurements of the reflectance of the Earth's surface in order to do Earth-resource inventories?
38. Spectroscopic lineshapes:
 - a) How does pressure influence the linewidth of a spectral absorption line?
 - b) Discuss briefly how a vertical atmospheric concentration profile can be obtained by satellite limb absorption measurements for a particular species?
39. Why are hollow-cathode lamps used in connection with atomic absorption spectrometry?
40. Describe the calibration procedure for atomic absorption spectrometry (establishing a calibration curve, or using the standard addition method).
41. Discuss satellite remote sensing of land and water areas using passive optical techniques.

Chapter 7

42. Precession:
 - a) Show that a quantum-mechanical magnetic moment precesses around a magnetic field.
 - b) Are there any clear manifestations of such a precession in any laser spectroscopic experiment?
 - c) The precession of a magnetic moment can be used for the detection of nuclear magnetic resonance signals. How?
43. Briefly explain the Atomic Beam Magnetic Resonance (ABMR) technique according to Rabi. Why can only certain types of magnetic resonance transitions be seen? What determines the linewidth of the transitions?
44. Briefly discuss the level-crossing spectroscopic method. The zero-field level-crossing effect is understandable also classically. How?
45. Level-crossing signals at certain magnetic fields can be used for determining hyperfine structure constants of excited states. Why is the number of detectable signals quite limited? Describe in general terms how hyperfine-structure information can be deduced from the experimental data.
46. When is it advantageous to use the level-crossing method instead of the optical double resonance technique?
47. What is the advantage of using the Fourier Transform NMR method instead of a scanning technique?
48. Discuss microwave radiometry, applied to environmental monitoring and to astronomy.
49. Discuss radio astronomy paying special attention to telescope resolution, aperture synthesis and microwave lineshapes.
50. How can a reasonable spatial resolution still be obtained when imaging in the microwave region (radar, radio astronomy)?

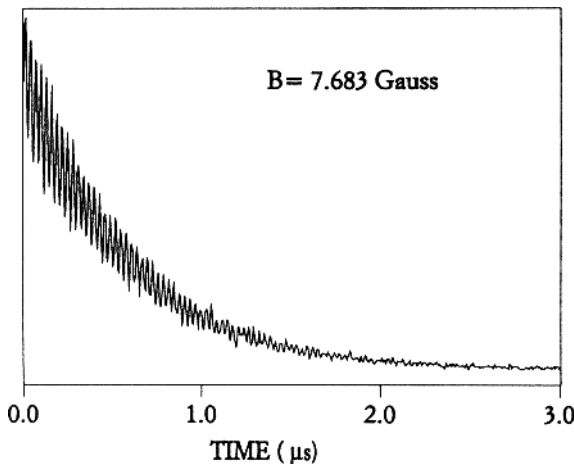
Chapter 8

51. Why is it easier to achieve a maser than an X-ray laser?
52. How does the laser process start?
53. Why is a combination of an oscillator and an amplifier preferred to a strongly pumped laser oscillator only?
54. Discuss the CO₂ laser: molecular basis, arrangement, and spectroscopic possibilities.

55. The dye laser and the titanium-doped sapphire ($\text{Ti} : \text{Al}_2\text{O}_3$) laser are both capable of generate pulsed or continuous tuneable radiation. Discuss the advantages (possibilities) and disadvantages (limitations) of the two different types.
56. Mode locking:
- Describe the generation of short laser pulses by mode locking.
 - What is the relation between mode locking and a spectroscopic grating in terms of interference?
57. Describe the general idea of chirped pulse amplification.

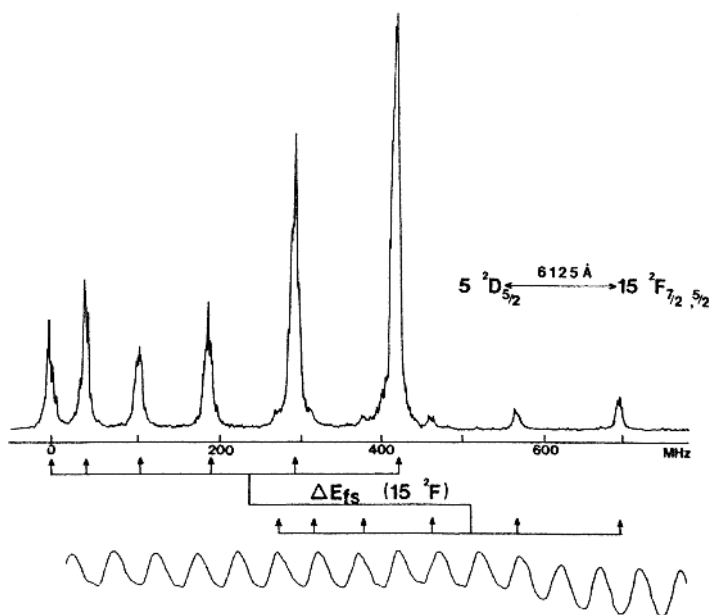
Chapter 9

58. Give some characteristics of Rydberg atoms.
59. Indicate some advantages of laser spectroscopic analytical techniques.
60. Laboratory trace gas monitoring: Discuss and compare the following methods: optoacoustic spectroscopy, cavity ring-down spectroscopy and frequency modulation spectroscopy.
61. Describe the Zeeman quantum beat method using laser excitation. If a Landé g factor of 1.500 is determined for an atomic state designated 3P_1 , how would you comment on such a result?
62. Discuss the relation between the Zeeman quantum beats and the Hanle effect.
63. In a Zeeman quantum-beat experiment of the $4p^35s\ {}^5S_2$ state in the selenium atom the excitation was performed at 207 nm from the ground state $4p^4\ {}^3P_2$ using linearly polarised light from a pulsed laser. In the decay a signal curve in an external magnetic field as illustrated below was obtained.
- Comment on the fact that the selected transition can be used for the excitation. Is this expected?
 - Evaluate the natural radiative lifetime τ and the Landé g_J factor for the state from the recording.
 - Comment on the g_J factor result. Is the result expected?
64. In Zeeman quantum-beat measurements oscillations superimposed on an exponential decay of the fluorescence light intensity are observed. In experiments on ytterbium atoms with zero nuclear spin the beat frequency for the $6s19d\ {}^1D_2$ state was 31.52 MHz for a fixed magnetic field, in which the beat frequency for the signal from the $6s6p\ {}^3P_1$ state (with known g_J value = 1.493) was 46.05 MHz. What is the g_J value of the $6s19d\ {}^1D_2$ state? Is the result expected? Discuss what can be learned from measurements of Landé g_J factors.



Qu. 63.

65. The spectrum below is recorded in fluorescence from a collimated cesium atomic beam, excited on the D-F transition by a single mode tunable dye laser. The D level is populated in cascade decay from the P state, which is excited with a broadband CW dye laser. The Fabry-Pérot fringes at the bottom correspond to a free spectral range of 50 MHz.



Qu. 65.

- a) How can it be seen from the spectrum that the magnetic dipole interaction constant (a) of the D-state is negative?
 - b) Give an approximate value for the a constant.
 - c) What is the nuclear spin of the single cesium isotope in the beam?
 - d) What is the fine-structure splitting of the F doublet (which has a negligible hyperfine structure)? Could this splitting be resolved using conventional Doppler-broadened spectroscopy?
66. Describe the saturation spectroscopy method. Why is the polarization spectroscopy version of the technique attractive? How can the technique be used to create a secondary standard for the metre unit?
67. Describe the basic physics behind high-harmonic generation in gases. Discuss some applications of such radiation.
68. Why is it interesting to study chemical reactions on the femtosecond timescale? How can such studies be achieved?
69. Discuss how fundamental information on the hydrogen atom and basic atomic theories can be obtained by simultaneously performing two Doppler-free laser spectroscopic investigations on two different energy splittings in the atom.
70. Why is it interesting from a spectroscopic point of view to be able to cool down atoms to very low translation energies (temperatures)?
71. Discuss techniques to achieve laser cooling of atoms.
72. How can a strongly forbidden atomic transition be used as a frequency standard with a strong spectroscopic signal in spite of the low transition probability (the shelving phenomenon)?
73. What is the general idea behind Bose–Einstein condensation experiments?
74. Discuss atomic optics and the concept of an atomic laser.

Chapter 10

75. Describe the CARS method and its application to combustion diagnostics.
76. How can the laser Doppler velocimetric method be used to measure flow velocities in particle-rich gas flows?
77. Describe air pollution measurements using the lidar method.
78. Why is it possible to obtain information on atmospheric gaseous pollutants using laser radar although elastic backscattering from particles is primarily observed?

79. Discuss the principles that allow laser-induced chemistry to be performed.
80. Discuss the penetration of laser light of different wavelengths into tissue and how this governs the medical applications of lasers.
81. Discuss the fluorescence diagnostics and photodynamic treatment of cancer tumours using tumour-seeking drugs and laser light.

Questions not pertaining to any special chapter

82. What spectroscopic method would you choose for the following tasks (explain)?
 - a) Determine the amount of cadmium in a blood sample from a patient.
 - b) Determine the amount of vanadium in a steel alloy.
 - c) Determine the average concentration of sulphur dioxide 5 m above street level.
 - d) Determine the amount of organic oil admixed in a sample of sea water after a tanker accident.
 - e) Determine the temperature of a welding torch flame.
 - f) Determine the water contents in newly harvested grain.
83. What spectroscopic method would you choose for the following tasks (explain)?
 - a) Determine the average concentration of atomic mercury in the smoke from a coal-fired power plant.
 - b) Determine the concentration of chlorophyll in leaves from a maple tree.
 - c) Monitor the growth of an oxide layer on a metal surface.
 - d) Determine the content of CO_2 in respiration air from a patient's lungs.
 - e) Determine if the ozone hole over Antarctica is increasing.
 - f) Determine if the red light from a piece of fireworks is due to strontium.
84. Suggest and explain (in a few words) a suitable spectroscopic method for the following tasks:
 - a) Determination of the absorption spectrum of a powder such as flour.
 - b) Measurement of the magnetic field in a Helmholtz coil system capable of producing a field strength of 0.1 Tesla.
 - c) Monitoring of thin oil films on metal surfaces.
 - d) Precision determination of the Rydberg constant.
 - e) Determination of the content of CO in the exhaust gases from a car at the car inspection station.
 - f) Determination of whether the black paints in two paintings, said to be by Rubens, are really of the same type.

85. What spectroscopic method would you choose for the following tasks (explain)?
- Determine the amount of mercury in the pikes in a lake in an industrial area.
 - Determine the concentration of sulphur dioxide 100 m above the top of the Big Ben Tower in London.
 - Determine if a sheet metal surface is really clean from press oil before it enters the painting stage at a car assembly plant.
 - Determine the amount of lead in the leaves of a tree standing close to a highway.
 - Determine if a metallic surface, prepared for fundamental surface physics research in an ultra-high vacuum system, is really clean.
 - Determine the concentration of carbon dioxide in indoor air.
86. Suggest, with a short explanation, a suitable spectroscopic method for the following tasks:
- Determination of the CO contents in car engine exhausts.
 - Determination of the total flux of SO_2 from a volcano.
 - Study of the start of corrosion/oxidation on a metal surface.
 - Determination of the Li contents in blood serum (this relates to certain psychiatric diseases).
 - Determination of the oil contents in sunflower seeds.
 - Determination of the average concentration of ozone in the stratosphere.
87. Suggest, with a short explanation, a suitable spectroscopic method for the following tasks:
- Calibration of the magnetic field in a coil designed for fields up to 0.001 Tesla (10 Gauss).
 - Determination of the gas temperature in the hot gas stream of a jet engine.
 - Detection of a major oil spill at sea.
 - Precision determination of the mass of an ion.
 - Study of the details of a molecular dissociation process.
 - Efficient detection of gas leaks in the petrochemical industry.
88. What factors determine the resolution obtainable using the following spectroscopic methods?
- Optical double resonance.
 - Optical pumping.
 - Laser saturation spectroscopy.
89. Discuss atomic clocks operating at microwave and optical frequencies (brief operating principles). Give examples of applications where a very high time precision is required.
90. Electron synchrotrons provide radiation of great importance for spectroscopy.

- a) Describe briefly the generation process and the properties of the radiation.
- b) Compare synchrotron radiation with laser radiation and give some hints when one or the other is to be preferred.
91. Discuss the medical applications of X-rays. Recently, laser-produced X-rays have been generated. What are the possible future advantages in medicine using such X-rays?
92. In certain cases the energy levels of an atom are slightly modified by the environment, which can be utilized for chemical analysis and chemical structure determinations. Discuss the following cases:
 - a) Electron spectroscopy.
 - b) Nuclear magnetic resonance spectroscopy.
93. How are picosecond laser pulses generated using mode locking? What parallels do you see between this process and the conditions for a diffraction grating, a Fabry-Pérot interferometer or a hologram?
94. Discuss hyperfine structure and isotopic shifts. What are the origins of these effects? What can be learned from these phenomena? Certain experimental techniques can be used for measuring hyperfine structures as well as isotopic shifts, while others are only useful for hyperfine-structure measurements. How does this arise?
95. Give approximate values for the following quantities (numbers without calculations are OK; numbers derived after calculations are also OK, but take more time!):
 - a) Doppler broadening of spectral lines in the visible wavelength region.
 - b) Thermal velocities of atoms/molecules at room temperature.
 - c) kT at room temperature.
 - d) Frequency of visible light.
 - e) Energy in eV for visible light.
 - f) Number of atoms/molecules per cm^3 of gas at atmospheric pressure.
 - g) Distance light travels in 1 ns.
 - h) Size in eV of vibrational splittings in simple diatomic molecules.
 - i) Energy of X-rays in eV.
 - j) Cavity mode spacing in a normal laboratory He-Ne laser.
96. Laser mode locking:
 - a) Describe the generation of short laser pulses by mode locking.
 - b) What is the relation between mode locking and a spectroscopic grating in terms of interference?
 - c) Is it possible to generate a 100 attosecond pulse (10^{-16} s) in the visible part of the spectrum?
97. Discuss the relation between the Hanle effect and Zeeman quantum beats following short laser light excitation of an ensemble of free atoms.

98. Mark with an (x) in the table below if the method listed is useful for the determination of the atomic physics properties indicated:

| | Hyperfine coupling constants a, b | Scalar polarisability α_0 | Natural lifetime τ |
|------------------------------|-------------------------------------|----------------------------------|-------------------------|
| Level-crossing spectroscopy | | | |
| Doppler-free two-photon abs. | | | |
| Quantum-beat spectroscopy | | | |
| Saturation spectroscopy | | | |

99. How can population differences be created between atomic sublevels to be used in resonance investigations of structures? Discuss three principally different methods.
100. Explain briefly why the optical Doppler effect is eliminated in the following types of experiments:
- Collimated thermal atomic-beam spectroscopy.
 - Accelerated ion-beam spectroscopy (irradiation along the beam).
 - Saturation spectroscopy.
 - Two-photon absorption spectroscopy.
 - Optical double resonance.
 - Spectroscopy on a sample of laser-cooled atoms.
101. Describe in a few words the meaning of the following concepts:
- Core polarization.
 - Bragg relation.
 - Hyperfine anomaly.
 - Equivalent width.
 - Magic angle.
 - Coherent detection.
102. Explain the meaning of the following abbreviations, and write one sentence describing each concept:
- | | |
|----------|---------|
| a) QED | g) NMR |
| b) EXAFS | h) MRI |
| c) ESR | i) DOAS |
| d) SAR | j) BEC |
| e) CARS | k) CPA |
| f) DIAL | l) VLBI |

References

Chapter 1

- [1.1] F. Cardarelli: *Scientific Unit Conversion* (Springer, Heidelberg 1998)
- [1.2] P.J. Mohr, B.N. Taylor: Adjusting the values of the fundamental constants. *Phys. Today* **3**, 29 (2001)

Chapter 2¹

- [2.1] H. Haken, H.C. Wolf: *The Physics of Atoms and Quanta*, 5th edn. (Springer, Berlin, Heidelberg 1996)
- [2.2] B. Cagnac, J.C. Pebay-Peyroula: *Modern Atomic Physics: I Fundamental Principles, II Quantum Theory and its Applications* (Wiley, New York 1975)
- [2.3] H.G. Kuhn: *Atomic Spectra*, 2nd edn. (Longmans, London 1969)
- [2.4] H.E. White: *Introduction to Atomic Spectroscopy* (McGraw-Hill, London 1934)
- [2.5] B.W. Shore, D.H. Menzel: *Principles of Atomic Spectra* (Wiley, New York 1968)
- [2.6] G.K. Woodgate: *Elementary Atomic Structure* (Oxford University Press, Oxford 1998)
- [2.7] M. Weissbluth: *Atoms and Molecules* (Academic Press, New York 1978)
- [2.8] J.C. Wilmott: *Atomic Physics* (Wiley, Chichester 1984)
- [2.9] E.U. Condon, G.H. Shortley: *The Theory of Atomic Spectra* (Cambridge University Press, Cambridge 1964)
- [2.10] E.U. Condon, H. Odabasi: *Atomic Structure* (Cambridge University Press, Cambridge 1980)
- [2.11] I.I. Sobelman: *Atomic Spectra and Radiative Transitions*, 2nd edn., Springer Ser. Atoms and Plasmas, Vol. 12 (Springer, Berlin, Heidelberg 1996)
- [2.12] G. Herzberg: *Atomic Spectra and Atomic Structure* (Dover, New York 1944)
- [2.13] R.D. Cowan: *The Theory of Atomic Structure and Spectra* (University of California Press, Berkeley 1981)

¹ Note that we make reference only to the European edition of Scientific American. The number following the slash gives the issue number. Page numbers for the American edition differ slightly.

- [2.14] H.A. Bethe, E.E. Salpeter: *Quantum Mechanics of One- and Two-Electron Atoms* (Springer, Berlin, Heidelberg 1957; Plenum/Rosetta, New York 1977)
- [2.15] C. Cohen-Tannoudji, B. Diu, F. Laloe: *Quantum Mechanics*, Vols. 1 and 2 (Wiley, New York 1977)
- [2.16] L.I. Schiff: *Quantum Mechanics* (McGraw-Hill, New York 1968)
- [2.17] A. Messiah: *Quantum Mechanics* (Wiley, New York 1962)
- [2.18] E. Merzbacher: *Quantum Mechanics*, 2nd edn. (Wiley, Orlando, FL 1970)
- [2.19] W. Greiner: *Quantum Mechanics - An Introduction*, 3rd edn. (Springer, Berlin, Heidelberg 1994)
- [2.20] F. Schwabl: *Quantum Mechanics*, 2nd edn. (Springer, Berlin, Heidelberg 1995).
- [2.21] Z.B. Rudzikas: *Theoretical Atomic Spectroscopy* (Cambridge University Press, Cambridge 1997)
- [2.22] V.P. Shevelko: *Atoms and Their Spectroscopic Properties*, Springer Ser. Atoms and Plasmas, Vol. 18 (Springer, Berlin, Heidelberg 1996)
- [2.23] I. Lindgren, I. Martinson, R. Schuch (eds.): Heavy-Ion Spectroscopy and QED Effects in Atomic Systems, *Phys. Scripta* **T46**, (1993)
- [2.24] V.W. Hughes: High-precision spectroscopy of positronium and muonium. *Adv. Quantum Chem.* **30**, 99 (1998)
- [2.25] C.E. Moore: *Atomic Energy Levels as Derived from Optical Spectra*, Circular 467, National Bureau of Standards, Volumes I-III, Reissued 1971 as NSRDS-NBS 35 Vol. I 1H–23V, Vol. II 24Cr–41Nb, Vol. III 42Mo–57La (NBS, Washington, DC 1971)
- [2.26] W.C. Martin, R. Zalubas, L. Hagan: *Atomic Energy Levels – The Rare Earth Elements*, NSRDS-NBS 60 (US Govt. Printing Office, Washington, DC 1978)
http://www.physics.nist.gov/cgi-bin/AtData/main_asd
- [2.27] S. Bashkin, J.O. Stoner: *Atomic Energy Levels and Grotrian Diagrams*, Vol. I H I – P XV (1975), Vol. I Addenda (1978), Vol. II S I – Ti XXII (1978), Vol. III V I – Cr XXIV (1981), Vol. IV Mn I–XXV (North-Holland, Amsterdam 1982)
- [2.28] B. Edlén: ‘Atomic spectra.’ In: *Handbuch der Physik*, Vol. XXVII, ed. by S. Flügge (Springer, Berlin, Heidelberg 1964)
B. Edlén: Energy structure of highly ionized atoms. (See [2.77], Pt. D, p. 271)
- [2.29] P.J. Mohr, W.L. Wiese (eds.): *Atomic and Molecular Data and their Applications* (AIP Press, New York 1998)
- [2.30] V.A. Boiko, V.G. Pal’chikov, I.Yu. Skobelev, A.Ya. Faenov: *The Spectroscopic Constants of Atoms and Ions* (CRC, Boca Raton, CA 1994)
- [2.31] G.W.F. Drake (ed.): *Atomic, Molecular and Optical Physics Reference Book* (AIP Press, New York 1996)
- [2.32] N.H. March: *Self-consistent Fields in Atoms* (Pergamon, Oxford 1978)
- [2.33] C. Froese-Fisher: *The Hartree-Fock Method for Atoms* (Wiley, New York 1977)
- [2.34] C. Froese-Fisher: Multi-configuration Hartree-Fock calculations for complex atoms. (See [2.77], Pt. C, p. 29)
- [2.35] C.F. Froese Fischer, T. Brage, P. Jönsson: *Computational Atomic Structure – An MCHF Approach* (IOP Publishing, Bristol 1997)
- [2.36] B.G. Wybourne: *Spectroscopic Properties of Rare Earths* (Wiley, New York 1965)
- [2.37] B.R. Judd: Complex atomic spectra. *Rep. Prog. Phys.* **48**, 907 (1985)

- [2.38] M.J. Seaton: Quantum defect theory. I. General formulation. Proc. Phys. Soc. London **88**, 801 (1966); II. Illustrative one-channel and two-channel problems. Proc. Phys. Soc. London **88**, 815 (1966)
- [2.39] U. Fano: Unified treatment of perturbed series, continuous spectra and collisions. J. Opt. Soc. Am. **65**, 979 (1975)
- [2.40] J.A. Armstrong, P. Esherick, J.J. Wynne: Bound, even parity $J = 0$ and 2 spectra of Ca: A multichannel quantum-defect theory analysis. Phys. Rev. A **15**, 180 (1977)
P. Esherick: Bound, even parity $J = 0$ and $J = 2$ spectra of Sr. Phys. Rev. A **15**, 1920 (1977)
M. Aymar, O. Robaux: Multichannel quantum defect analysis of the bound, even parity $J = 2$ spectra of neutral barium. J. Phys. B **12**, 531 (1979)
- [2.41] N. Ryde: *Atoms and Molecules in Electric Fields* (Almqvist & Wiksell International, Stockholm 1976)
- [2.42] J.-P. Connerade: *Highly Excited Atoms* (Cambridge University Press, Cambridge 1997)
- [2.43] T.F. Gallagher: *Rydberg Atoms* (Cambridge University Press, Cambridge 1994).
- [2.44] T.W. Ducas, M.G. Littman, R.R. Freeman, D. Kleppner: Stark ionization of high-lying states of sodium. Phys. Rev. Lett. **35**, 366 (1975)
- [2.45] T.F. Gallagher, L.M. Humphrey, R.M. Hill, S.A. Edelstein: Resolution of $[m_l]$ and $[m_j]$ levels in the electric field ionization of highly excited states of Na. Phys. Rev. Lett. **37**, 1465 (1976)
T.F. Gallagher, L.M. Humphrey, R.M. Hill, W. Cooke, S.A. Edelstein: Fine structure intervals and polarizabilities of highly excited p and d states of sodium. Phys. Rev. A **15**, 1937 (1977)
- [2.46] D. Kleppner, M.G. Littman, M.L. Zimmerman: Highly excited atoms. Sci. Am. **244**(5), 108 (1981)
- [2.47] H. Kopfermann: *Nuclear Moments* (Academic Press, New York 1958)
- [2.48] W.A. Nierenberg, I. Lindgren: In: *Alpha-, Beta-, and Gamma-Ray Spectroscopy*, ed. by K. Siegbahn (North-Holland, Amsterdam 1965) p. 1263
- [2.49] G.H. Fuller, V.W. Cohen: Nuclear spins and moments. Nuclear Data Tables A **5**, 433 (1969)
- [2.50] E. Arimondo, M. Inguscio, P. Violino: Experimental determinations of the hyperfine structure in the alkali atoms. Rev. Mod. Phys. **49**, 31 (1977)
- [2.51] I. Lindgren, A. Rosén: Relativistic self-consistent field calculations with application to hyperfine interaction. Pt. I Relativistic self-consistent fields, Pt. II Relativistic theory of atomic hyperfine interaction. Case Stud. Atom. Phys. **4**, 93 (1974), Pt. III Comparison between theoretical and experimental hyperfine structure results. Case Stud. Atom. Phys. **4**, 197 (1974)
- [2.52] S. Büttgenbach: *Hyperfine Structure in 4d- and 5d-Shell Atoms*, Springer Tracts Mod. Phys., Vol. 96 (Springer, Berlin, Heidelberg 1982)
- [2.53] I. Lindgren, J. Morrison: *Atomic Many-Body Theory*, 2nd edn., Springer Ser. Atoms and Plasmas, Vol. 3 (Springer, Berlin, Heidelberg 1987)
- [2.54] I. Lindgren: Effective operators in the atomic hyperfine interaction. Rep. Prog. Phys. **47**, 345 (1984)
- [2.55] J.R.P. Angel, P.G.H. Sandars: The hyperfine structure Stark effect, I. Theory. Proc. Roy. Soc. A **305**, 125 (1968)
- [2.56] A. Khadjavi, A. Lurio, W. Happer: Stark effect in the excited states of Rb, Cs, Cd, and Hg. Phys. Rev. **167**, 128 (1968)
- [2.57] K. Heilig, A. Steudel: Changes in mean square nuclear charge radii from optical isotope shifts. Atomic Data and Nuclear Data Tables **14**, 613 (1974)

- [2.58] K. Heilig, A. Steudel: New developments in classical optical spectroscopy. (See [2.76], Pt. A, p. 263)
- [2.59] W.H. King: *Isotope Shifts in Atomic Spectra* (Plenum, New York 1984)
- [2.60] V.W. Hughes, B. Bederson, V.W. Cohen, F.M.J. Pichanick (eds.): *Atomic Physics*, New York 1968 (Plenum, New York 1969)
- [2.61] G.K. Woodgate, P.G.H. Sandars (eds.): *Atomic Physics 2*, Oxford 1970 (Plenum, New York 1971)
- [2.62] S.J. Smith, G.K. Walters (eds.): *Atomic Physics 3*, Boulder, Colo. 1972 (Plenum, New York 1973)
- [2.63] G. zu Putlitz, E.W. Weber, A. Winnacker (eds.): *Atomic Physics 4*, Heidelberg 1974 (Plenum, New York 1975)
- [2.64] R. Marrus, M. Prior, H. Shugart (eds.): *Atomic Physics 5*, Berkeley 1976 (Plenum, New York 1977)
- [2.65] A.M. Prokhorov, R. Damburg (eds.): *Atomic Physics 6*, Riga 1978 (Plenum, New York 1979)
- [2.66] D. Kleppner, F.M. Pipkin (eds.): *Atomic Physics 7*, Cambridge, MA 1980 (Plenum, New York 1981)
- [2.67] I. Lindgren, A. Rosén, S. Svanberg (eds.): *Atomic Physics 8*, Göteborg 1982 (Plenum, New York 1983)
- [2.68] R.S. Van Dyck Jr., E.N. Fortson (eds.): *Atomic Physics 9*, Seattle 1984 (World Scientific, Singapore 1985)
- [2.69] H. Narumi, I. Shimamura (eds.): *Atomic Physics 10*, Tokyo 1986 (North-Holland, Amsterdam 1987)
- [2.70] S. Haroche, J.C. Gay, G. Grynberg (eds.): *Atomic Physics 11*, Paris 1988 (World Scientific, Singapore 1989)
- [2.71] J. Zorn, R. Lewis (eds.): *Atomic Physics 12*, Ann Arbor 1990 (Plenum, New York 1990)
- [2.72] H. Walther, T.W. Hänsch, B. Neizert (eds.): *Atomic Physics 13*, Munich 1992 (AIP Press, New York 1993)
- [2.73] D.J. Wineland, C.E. Wieman, S.J. Smith (eds.): *Atomic Physics 14*, Boulder 1994 (AIP Press, New York 1995)
- [2.74] H.B. van Linden van den Heuvell, J.T.M. Walraven, M.W. Reynolds (eds.): *Atomic Physics 15*, Amsterdam 1996 (World Scientific, Singapore 1997)
- [2.75] W.E. Baylis, G.W.F. Drake (eds.): *Atomic Physics 16*, Windsor 1998, To be published
E. Arimondo, P. De Natale, M. Inguscio (eds.): *Atomic Physics 17*, Firenze 2000 (AIP Conference Proceedings, Melville, NY 2001)
H.R. Sagdepour, D.E. Pritchard, E.J. Heller (eds.): *Atomic Physics 18*, Cambridge 2002 (World Scientific, Singapore 2003)
- [2.76] W. Hanle, H. Kleinpoppen (eds.): *Progress in Atomic Spectroscopy*, Pts. A and B (Plenum, New York 1978 and 1979)
- [2.77] H.J. Beyer, H. Kleinpoppen (eds.): *Progress in Atomic Spectroscopy*, Pts. C and D (Plenum, New York 1984 and 1987)

Chapter 3

- [3.1] C.E. Banwell, E.M. McCash: *Fundamentals of Molecular Spectroscopy*, 4th edn. (McGraw-Hill, London 1983)
- [3.2] G.B. Barrow: *The Structure of Molecules* (Benjamin, New York 1963)
- [3.3] J.I. Steinfeld: *Molecules and Radiation*, 2nd edn. (MIT Press, Cambridge, MA 1985)

- [3.4] G.W. King: *Spectroscopy and Molecular Structure* (Holt, Rinehart and Winston, New York 1964)
- [3.5] M. Weissbluth: *Atoms and Molecules* (Academic Press, New York 1978)
- [3.6] W.G. Richards, P.R. Scott: *Structure and Spectra of Molecules* (Wiley, Chichester 1985)
- [3.7] G. Herzberg: *Molecular Spectra and Molecular Structure. I. The Spectra of Diatomic Molecules* (Krieger Publ., Malabar, FL 1991)
- [3.8] G. Herzberg: *Molecular Spectra and Molecular Structure, II. Infrared and Raman Spectra of Polyatomic Molecules* (Krieger Publ., Malabar, FL 1991)
- [3.9] G. Herzberg: *Molecular Spectra and Molecular Structure. III. Electronic Spectra and Electronic Structure of Polyatomic Molecules* (Krieger Publ., Malabar, FL 1991)
- [3.10] G. Herzberg: *The Spectra and Structures of Simple Free Radicals – An Introduction to Molecular Spectroscopy* (Dover, New York 1971, 1988)
K.P. Huber, G. Herzberg: *Molecular Spectra and Molecular Structure. IV Constants of Diatomic Molecules* (Van Nostrand Reinhold, New York 1979)
H. Lefebre-Brion, R.W. Field: *Perturbations in the Spectra of Diatomic Molecules* (Academic, Orlando 1986)
- [3.11] L.M. Sverdlov, M.A. Kovner, E.P. Krainov: *Vibrational Spectra of Polyatomic Molecules* (Israel Program for Scientific Translations, Jerusalem 1974)
- [3.12] R.F. Hout Jr.: *Pictorial Approach to Molecular Structure and Reactivity* (Wiley, New York 1984)
- [3.13] R.W.B. Pearse, A.G. Gaydon: *The Identification of Molecular Spectra* (Chapman and Hall, London 1950)
- [3.14] P.J. Mohr, W.L. Wiese (eds.): *Atomic and Molecular Data and their Applications* (AIP Press, New York 1998)
- [3.15] B.S. Tsukerblat: *Group Theory in Chemistry and Spectroscopy* (Academic Press, London 1994)
- [3.16] D.C. Harris, M.D. Bertolucci: *Symmetry and Spectroscopy* (Dover, New York 1990)
- [3.17] D.M. Bishop: *Group Theory and Chemistry* (Dover, New York 1993)
- [3.18] D.A. McQuarrie: *Quantum Chemistry* (Oxford University Press, Oxford 1983) Chap. 10
- [3.19] A.C. Hurley: *Introduction to the Electron Theory of Small Molecules* (Academic Press, London 1976)
- [3.20] R. McWeeny, B.T. Pickup: Quantum theory of molecular electronic structure. *Rep. Prog. Phys.* **43**, 1065 (1980)
- [3.21] A. Hinchliffe: *Ab Initio Determination of Molecular Electronic Structure* (Hilger, Bristol 1987)
- [3.22] Ch. Jungen: *Molecular Applications of Quantum Defect Theory* (IOP Publishing, Bristol 1996)
- [3.23] R.M. Dreizler, E.K.U. Gross: *Density Functional Theory* (Springer, Berlin, Heidelberg 1990)
R.G. Parr, W.T. Yang: *Density Functional Theory of Atoms and Molecules* (Oxford Science, Oxford 1989)
- [3.24] P.v.R. Schleyer, (ed.): *Encyclopaedia of Computational Chemistry* (Wiley, New York 1998)
- [3.25] W.J. Hehre, L. Radom, P.v.R. Schleyer, J.A. Pople: *Ab Initio Molecular Orbital Theory* (Wiley, New York 1996)
- [3.26] R.F. Curl, R.E. Smalley: Probing C₆₀. *Science* **242**, 1017 (1988)
H. Kroto: Space, stars, C₆₀, and soot. *Science* **242**, 1139 (1988)

- [3.27] H. Haberland: *Clusters of Atoms and Molecules I*, Springer Series in Chemical Physics, Vol. 52 (Springer, Berlin, Heidelberg 1994)
- [3.28] H. Haberland: *Clusters of Atoms and Molecules II* (Springer Series in Chemical Physics, Vol. 56 (Springer, Berlin, Heidelberg 1994)
- [3.29] Acc. Chem. Res. **25**(3) (1992)
- [3.30] S. Iijima: Helical microtubules of graphitic carbon. Nature **354**, 56 (1991)
- [3.31] P.M. Ajayan, T.W. Ebbesen: Nanometer size tubes of carbon. Rep. Prog. Phys. **60**, 1025 (1997)
- A. Rosén: A periodic table in three dimensions: A sightseeing tour in the nanometer world. In: *Modern Trends in Atomic Physics*, Adv. Quantum Chem. **30**, 235 (1998)
- T.W. Ebbesen: *Carbon Nanotubes* (CRC Press, Boca Raton 1997)
- R. Saito, G. Dresselhaus, M.S. Dresselhaus: *Physical Properties of Carbon Nanotubes* (Imperial College Press, London 1998)

Chapter 4

- [4.1] D.J. Jackson: *Classical Electrodynamics*, 2nd edn. (Wiley, New York 1975)
- [4.2] P. Lorraine, D. Corson: *Electromagnetic Fields and Waves*, 2nd edn. (Freeman, New York 1970)
- [4.3] F.A. Hopf, G.I. Stegeman: *Applied Classical Electrodynamics*, Vol. 1: Linear Optics, Vol. 2: Non-Linear Optics (Wiley, New York 1986)
- [4.4] W. Heitler: *The Quantum Theory of Radiation*, 2nd edn. (Oxford University Press, Oxford 1944)
- [4.5] R. Loudon: *The Quantum Theory of Light*, 3rd edn. (Oxford Univ. Press, New York 2000)
- [4.6] J.N. Dodd: *Atoms and Light Interactions* (Plenum, New York 1991)
- [4.7] F.H.M. Faisal: *Theory of Multiphoton Processes* (Plenum, New York 1987)
- [4.8] H.C. van de Hulst: *Light Scattering by Small Particles* (Wiley, New York 1957)
- H.C. van de Hulst: *Multiple Light Scattering*, Vols. 1 and 2 (Academic Press, Orlando 1980)
- [4.9] B. Chu: *Laser Light Scattering*, 2nd edn. (Academic Press, New York 1991)
- [4.10] C.F. Bohren, D.R. Huffman: *Absorption and Scattering of Light by Small Particles* (Wiley, New York 1983)
- M.I. Mishchenko, L.D. Travis, J.W. Hovenier (eds.): *Conference on Light Scattering by Nonspherical Particles: Theory, Measurements, and Applications* (American Meteorological Society, Boston 1998)
- [4.11] A. Anderson (ed.): *The Raman Effect, Principles and The Raman Effect, Applications* (Dekker, New York 1971 and 1973)
- [4.12] D.A. Long: *Raman Spectroscopy* (McGraw-Hill, New York 1977)
- [4.13] J.F. Ferraro, K. Nakamoto: *Introductory Raman Spectroscopy* (Academic Press, London 1994)
- [4.14] A. Einstein: On the quantum theory of radiation. Phys. Z. **18**, 124 (1917)
- [4.15] T.F. Gallagher, W.E. Cooke: Interaction of blackbody radiation with atoms. Phys. Rev. Lett. **42**, 835 (1979)
- [4.16] J. Farley, W.H. Wing: Accurate calculation of dynamic Stark shifts and depopulation rates of Rydberg energy levels induced by blackbody radiation. Hydrogen, helium and alkali-metal atoms. Phys. Rev. A **23**, 2397 (1981)

- [4.17] D. Kleppner: Turning off the vacuum, *Phys. Rev. Lett.* **47**, 233 (1981)
R.G. Hulet, E.S. Hilfer, D. Kleppner: Inhibited spontaneous emission by a Rydberg atom. *Phys. Rev. Lett.* **55**, 2137 (1985)
W. Jhe, A. Anderson, E.A. Hinds, O. Meschede, L. Moi, S. Haroche: Suppression of spontaneous decay at optical frequencies: Test of vacuum-field anisotropy in confined space. *Phys. Rev. Lett.* **58**, 666 (1987)
- [4.18] S. Haroche, J.M. Raimond: *Advances in Atomic and Molecular Physics* 20, 350 (Academic, New York 1985)
J.A.C. Gallas, G. Leuchs, H. Walther, H. Figger: *ibid.*, p. 414
- [4.19] P. Goy, J.M. Raimond, M. Gross, S. Haroche: Observation of cavity-enhanced single-atom spontaneous emission. *Phys. Rev. Lett.* **50**, 1903 (1983)
- [4.20] D.F. Walls, G.J. Milburn: *Quantum Optics* (Springer, Berlin, Heidelberg 1994)
- [4.21] L. Mandel, E. Wolf: *Optical Coherence and Quantum Optics* (Cambridge University Press, Cambridge 1995)
- [4.22] M.O. Scully, M.S. Zubairy: *Quantum Optics* (Cambridge University Press, Cambridge 1997)
- [4.23] J.D. Harvey, D.F. Walls (eds.): *Quantum Optics IV*, Springer Proc. Phys., Vol. 12 (Springer, Berlin, Heidelberg 1986)
- [4.24] J.D. Harvey, D.F. Walls (eds.): *Quantum Optics V*, Springer Proc. Phys., Vol. 41 (Springer, Berlin, Heidelberg 1989)
- [4.25] D.F. Walls, J.D. Harvey (eds.): *Quantum Optics VI*, Springer Proc. Phys., Vol. 77 (Springer, Berlin, Heidelberg 1994)
- [4.26] E.R. Pike, S. Sarkar (eds.): *Frontiers in Quantum Optics* (Hilger, Bristol 1986)
E.R. Pike, H. Walther (eds.): *Photons and Quantum Fluctuations* (Hilger, Bristol 1988)
P. Meystre, M. Sargent III: *Elements of Quantum Optics*, 2nd edn. (Springer, Berlin, Heidelberg 1991)
- [4.27] J.H. Eberly, L. Mandel, E. Wolf (eds.): *Coherence and Quantum Optics VI* (Plenum, New York 1989)
- [4.28] J.H. Eberly, L. Mandel, E. Wolf (eds.): *Coherence and Quantum Optics VII* (Plenum, New York 1996)
- [4.29] R. Hanbury-Brown, R.Q. Twiss: Correlation between photons in two coherent beams of light. *Nature* **177**, 27 (1956)
- [4.30] L. Mandel: Fluctuations of photon beams and their correlations. *Proc. Phys. Soc.* **72**, 1037 (1958)
- [4.31] R. Glauber: The quantum theory of optical coherence. *Phys. Rev.* **130**, 2529 (1963)
R. Glauber: Coherent and incoherent states of the electromagnetic field. *Phys. Rev.* **131**, 2766 (1963)
- [4.32] H.J. Kimble, M. Dagenais, L. Mandel: Photon anti-bunching in resonance fluorescence. *Phys. Rev. Lett.* **39**, 691 (1976)
D.F. Walls: Evidence for the quantum nature of light. *Nature* **280**, 451 (1979)
R. Loudon: Non-classical effects in the statistical properties of light. *Rep. Prog. Phys.* **43**, 913 (1980)
- [4.33] P. Meschede, H. Walther, G. Müller: One-atom maser. *Phys. Rev. Lett.* **54**, 551 (1985)
- [4.34] S. Haroche, J.-M. Raimond: Cavity quantum electrodynamics. *Sci. Am.* **268**(4), 26 (1993)

- [4.35] G. Raitel, Ch. Wagner, H. Walther, L.M. Narducci, M.O. Scully: 'The micromaser: A proving ground for quantum physics.' In: *Cavity Quantum Electrodynamics* ed. by P.R. Berman (Academic Press, Boston 1994) p. 57
- [4.36] P.R. Berman (ed.): *Cavity Quantum Electrodynamics* (Academic Press, Boston 1994)
- [4.37] D. Meschede: Radiating atoms in confined space: From spontaneous emission to micromasers. *Phys. Rep.* **211**, 201 (1992)
- [4.38] H. Walther: Atoms in cavities and traps. *Adv. At. Mol. Opt. Phys.* **32**, 379 (1994)
- [4.39] K. An, J.J. Childs, R.R. Dasari, M.S. Feld: Microlaser: A laser with one atom in an optical resonator. *Phys. Rev. Lett.* **73**, 3375 (1994)
- [4.40] M.S. Feld, K.W. An: The single-atom laser. *Sci. Am.* **279**(1), 40 (1998)
- [4.41] D.F. Walls: Squeezed states of light. *Nature* **306**, 141 (1983)
- G. Leuchs: Squeezing the quantum fluctuations of light. *Contemp. Phys.* **29**, 299 (1988)
- R.E. Slusher, B. Yurke: Squeezed light. *Sci. Am.* **258**(5), 50 (1988)
- [4.42] R.E. Slusher, L.W. Hollberg, B. Yurke, J.C. Mertz, J.F. Valley: Observation of squeezed states generated by four-wave mixing in an optical cavity. *Phys. Rev. Lett.* **55**, 2409 (1985)
- L.-A. Wu, H.J. Kimble, J.L. Hall, H. Wu: Generation of squeezed states by parametric down-conversion. *Phys. Rev. Lett.* **57**, 2520 (1986)
- [4.43] H.J. Kimble, D.F. Walls (eds.): Squeezed states of the electromagnetic field. *J. Opt. Soc. Am.* **4**, 1450 (1987) (Feature Issue)
- [4.44] C. Fabre: Squeezed states of light. *Phys. Rep.* **219**, 215 (1992)
- [4.45] J. Dietrich: Realizing LIGO. *Engineering and Science* **64**(2), 8 (1998)
http://www.ligo.caltech.edu/LIGO_web/about/factsheet.html
<http://www.estec.esa.nl/spdwww/future/html/lisa.htm>
- [4.46] G. Herzberg: *Molecular Spectra and Molecular Structure, I. The Spectra of Diatomic Molecules* (Van Nostrand, Princeton, NJ 1963)
- [4.47] H. Inaba: In *Laser Monitoring of the Atmosphere*, ed. by E.D. Hinkley, *Topics Appl. Phys.*, Vol. 14 (Springer, Berlin, Heidelberg 1976)
- [4.48] C.K. Sloan: *J. Phys. Chem.* **59**, 834 (1955)
- [4.49] A. D'Alessio, A. Di Lorenzo, A.F. Serafim, F. Beretta, S. Masi, C. Venitozzi: Soot formation in methane-oxygen flames. 15th Int. Symp. on Combustion (The Combustion Institute, Pittsburgh 1975) p. 1427
- A. D'Alessio, A. Di Lorenzo, A. Borghese, F. Beretta, S. Masi: Study of the soot nucleation zone of rich methane-oxygen combustion. 16th Int. Symp. on Combustion (The Combustion Institute, Pittsburgh 1977) p. 695
- [4.50] H.M. Nussenzveig: The theory of the rainbow. *Sci. Am.* **236**/4, 116 (1977)
- [4.51] D.K. Lynch: Atmospheric haloes. *Sci. Am.* **238**(4), 144 (1978)
- A.B. Fraser, W.H. Mach: Mirages. *Sci. Am.* **234**(1), 102 (1976)
- W. Tape: The topology of mirages. *Sci. Am.* **252**(6), 100 (1985)
- D.J.K. O'Connel: The green flash. *Sci. Am.* **202**(1), 112 (1960)
- H.C. Bryant, N. Jarmie: The glory. *Sci. Am.* **231**(1), 60 (1974)
- J. Walker (ed.): *Light from the Sky*, Reprint collection (Scientific American) (Freeman, San Francisco 1980)
- R. Greenler: *Rainbows, Haloes and Glories* (Cambridge University Press, Cambridge 1980)
- D.K. Lynch, W. Livingstone: *Color and Light in Nature* (Cambridge University Press, Cambridge 1995)
- M. Mimaert: *Light and Color in the Outdoors* (Springer, Berlin, Heidelberg 1995)

- [4.52] I. Shimamura, K. Takayanagi (eds.): *Electron-Molecule Collisions* (Plenum, New York 1984)
- [4.53] G.F. Drukarev: *Collisions of Electrons with Atoms and Molecules* (Plenum, New York 1987)
- [4.54] F. Brouillard (ed.): *Atomic Processes in Electron-Ion and Ion-Ion Collisions*, NATO ASI Series, Vol. 145 (Plenum, New York 1987)
- [4.55] J.M. Bowman (ed.): *Molecular Collision Dynamics*, Topics in Current Phys., Vol. 33 (Springer, Berlin, Heidelberg 1983)
- [4.56] U. Fano, A.R.P. Rau: *Atomic Collisions and Spectra* (Academic Press, New York 1986)
- [4.57] P. Schattschneider: *Fundamentals of Inelastic Electron Scattering* (Springer, Wien 1986)
- [4.58] J. Eichler, W.E. Meyerhof: *Relativistic Atomic Collisions* (Academic Press, San Diego 1995)
- N. Anderssen, K. Bartschat: 'Complete experiments in electron-atom collisions.' In: *Advances in Atomic, Molecular, and Optical Physics*, Vol. 36, ed. by B. Bederson, H. Walther (Academic Press, San Diego 1996) p. 1
- Y. Itikawa, K. Okonu, H. Tanaka, A. Yagashita, M. Matsuzawa (eds.): *The Physics of Electronic and Atomic Collisions*. Proc. XXI Conference (AIP, Melville, NY 2000)

Chapter 5

- [5.1] B. Crasemann (ed.): *Atomic Inner-Shell Physics* (Plenum, New York 1985)
- [5.2] R. Karazija: *Introduction to the Theory of X-Ray and Electronic Spectra of Free Atoms* (Plenum, New York 1992)
- R.L. Johnson, H. Schmidt-Böcking, B.F. Sonntag (eds): *X-Ray and Inner-Shell Processes*, AIP Conf. Proc. **389** (AIP, New York 1997)
- R.W. Dunford, D.S. Gemmell, E.P. Kanter, B. Krässig, S.H. Southworth, L. Young: *X-Ray and Inner Shell Processes* (AIP, Melville, NY 2000)
- [5.3] W.C. Röntgen: Sitzungsbericht der Physikal.-Medicin. Gesellschaft 132 (Würzburg 1895): Engl. Translation: *Nature* **53**, 274 (1896)
- G. Farmelo: The discovery of X-rays. *Sci. Am.* **273**(5), 68 (1995)
- G.L. Clark: *Applied X-Rays* (McGraw-Hill, New York 1955)
- [5.5] K. Siegbahn (ed.): *Alpha-, Beta-, and Gamma-Ray Spectroscopy* (North-Holland, Amsterdam 1965)
- H.H. Johann: Die Erzeugung lichtstarker Röntgenspektren mit Hilfe von Konkavkristallen. *Z. Physik* **69**, 185 (1931)
- Y. Cauchois: Spectrographie des rayons X par transmission d'un faisceau non canalisé à travers un cristal courbé (I). *J. Phys. Rad.* **3**, 320 (1932)
- E. Förster, E.E. Fill, K. Gäbel, H. He, Th. Missalla, O. Renner, I. Ushmann, J. Wark: X-ray emission spectroscopy. *J. Quant. Spectrosc. Radiat. Transf.* **51**, 101 (1994)
- [5.6] G. Hölzer, E. Förster, M. Grätz, C. Tillman, S. Svanberg: X-ray crystal spectroscopy of sub-picosecond laser-produced plasmas beyond 50 keV, *J. X-Ray Sci. Technol.* **7**, 50 (1997)
- [5.7] P. Suortti, U. Lienert, C. Schulze: 'Bent crystal optics for high energy synchrotron radiation.' In: *X-Ray and Inner Shell Processes*, AIP Conference Proceedings Vol. 389, ed. by R.L. Johnson, H. Schmidt-Böcking, B.F. Sonntag (AIP, Woodbury 1997), p. 175

- [5.8] B. Agarwal: *X-Ray Spectroscopy*, 2nd edn., Springer Ser. Opt. Sci., Vol. 15 (Springer, Berlin, Heidelberg 1990)
- [5.9] R. Jenkins, R.W. Gould, D. Gedcke: *Quantitative X-Ray Spectrometry* (Dekker, New York 1981)
- [5.10] J.V. Gilfrich et al. (eds): *Advances in X-Ray Analysis* (Plenum, New York, several publishing years for series of books)
- [5.11] S.A.E. Johansson: Proton-induced X-ray emission spectrometry – state of the art. *Fresenius Z. Anal. Chem.* **324**, 635 (1986)
- [5.12] S. Johansson (ed.): Proc. 1st Int. PIXE Conf., Nucl. Instrum. Methods **142**, 1 (1977); Proc. 2nd Int. PIXE Conf., Nucl. Instrum. Methods **181**, 1 (1981)
- B. Martin (ed.): Proc. 3rd Int. PIXE Conf., Nucl. Instrum. Methods **231**, 1 (1984)
- H. van Rinsvelt, S. Bauman, J.W. Nelson, J.W. Winchester (eds.): Proc. 4th Int. PIXE Conf., Nucl. Instrum. Methods B **22**, 1 (1987)
- [5.13] S.A.E. Johansson, J.L. Campbell, K.G. Malmqvist (eds.): *Particle-Induced X-Ray Emission Spectroscopy (PIXE)* (Wiley, New York 1996)
- [5.14] Courtesy: J. Pallon (<http://www.fysik.lu.se/~pixejan/tycho.htm>)
- [5.15] R.W. Shaw: Air pollution by particles. *Sci. Am.* **257**(2), 84 (1987)
- T.G. Dzubiey (ed.): *X-Ray Fluorescence Analysis of Environmental Samples* (Ann Arbor Science Publ., Ann Arbor 1977)
- [5.16] J. Nordgren, L. Selander, L. Pettersson, C. Nordling, K. Siegbahn, H. Ågren: Core state vibrational excitations and symmetry breaking in the CK and OK emission spectra of CO₂. *J. Chem. Phys.* **76**, 3928 (1982)
- [5.17] B. Crasemann (ed.): *Proc. Conf. on X-ray and Atomic Inner Shell Physics*, AIP Conf. Proc. Vol. 94 (American Inst. Phys., New York 1982), especially article by C. Nordling
- [5.18] A. Meisel, G. Leonhardt, R. Szargon: *X-Ray Spectra and Chemical Bonding*, Springer Ser. Chem. Phys., Vol. 37 (Springer, Berlin, Heidelberg 1989)
- [5.19] J. Nordgren: 'Ultra-soft X-ray emission spectroscopy – a progress report.' In: *Proc. 14th Int. Conf. on X-Ray and Inner Shell Processes*. *J. Physique C* **9**, Suppl. 12 (1987)
- [5.20] J. Nordgren, C. Nordling: Ultrasoft X-ray emission from atoms and molecules. *Comments At. Mol. Phys.* **13**, 229 (1983)
- [5.21] J. Nordgren, H. Ågren: Interpretation of ultra-soft X-ray emission spectra. *Comments At. Mol. Phys.* **14**, 203 (1984)
- [5.22] J. Berkowitz: *Photoabsorption, Photoionization, and Photoelectron Spectroscopy* (Academic Press, New York 1979)
- [5.23] E.A. Stern: Structure determination by X-ray absorption. *Contemp. Phys.* **19**, 289 (1978)
- [5.24] A. Bianconi, L. Incoccia, S. Stipchich (eds.): *EXAFS and Near-Edge Structure*, Springer Ser. Chem. Phys., Vol. 27 (Springer, Berlin, Heidelberg 1983)
- [5.25] B.K. Teo: *EXAFS: Basic Principles and Data Analysis, Inorganic Chemistry Concept*, Vol. 9 (Springer, Berlin, Heidelberg 1986)
- [5.26] P.A. Lee, P.H. Citrin, B.M. Kincaid: Extended X-ray absorption fine structure – its strengths and limitations as a structural tool. *Rev. Mod. Phys.* **53**, 769 (1981)
- [5.27] R. Prinz, D. Koningsberger (eds.): *X-Ray Absorption: Principles, Applications, Techniques of EXAFS, SEXAFS and XANES* (Wiley, New York 1988)
- [5.28] J. Stöhr: *NEXAFS Spectroscopy* (Springer, New York 1992)

- [5.29] T.S. Curry III, J.E. Dowd, R.C. Murry Jr.: *Christensen's Physics of Diagnostic Radiology*, 4th edn. (Lea & Febiger, Philadelphia 1990)
E. Krestel: *Imaging Systems for Medical Diagnostics* (Siemens AG, Berlin 1990)
- [5.30] J.G. Kereiakes, S.R. Thomas, C.G. Orton (eds.): *Digital Radiography* (Plenum, New York 1986)
- [5.31] E.J. Hall: *Radiobiology for the Radiobiologist*, 4th edn. (J.B. Lippincott, Philadelphia 1988)
- [5.32] General Electric Co., Medical Systems Operations, Milwaukee, WI (1980)
- [5.33] R. Lewis: Medical applications of synchrotron radiation X-rays. *Phys. Med. Biol.* **42**, 1213 (1997)
F.A. Dilmanian, X.Y. Wu, E.C. Parsons, B. Ren, J. Kress, T.M. Button, L.D. Chapman, J.A. Coderre, P. Giron, D. Greenberg, D.J. Krus, Z. Liang, D. Marcovici, M.J. Petersen, C.T. Roque, M. Shleifer, D.N. Slatkin, W.C. Tomlinson, K. Yamamoto, J. Zhou: Single- and dual-energy CT with monochromatic synchrotron X-rays. *Phys. Med. Biol.* **42**, 371 (1997)
- [5.34] W.-R. Dix: Intravenous coronary angiography with synchrotron radiation. *Prog. Biophys. Mol. Biol.* **63**, 159 (1995)
- [5.35] T.H. Newton, D.G. Potts (eds.): *Technical Aspects of Computed Tomography* (Mosby, MI 1981)
- [5.36] R.A. Robb: *Three-Dimensional Biomedical Imaging – Principles and Practice* (VCH, New York 1994)
- [5.37] M. Murnane, H.C. Kapteyn, M.D. Rosen, R.W. Falcone: Ultrafast X-ray pulses from laser-produced plasmas. *Science* **251**, 531 (1991)
- [5.38] J.D. Kmetec, C.L. Gordon III, J.J. Macklin, B.E. Lemoff, G.S. Brown, S.E. Harris: MeV X-ray generation with a femtosecond laser. *Phys. Rev. Lett.* **68**, 1527 (1992)
- [5.39] K. Herrlin, G. Svahn, C. Olsson, H. Pettersson, C. Tillman, A. Persson, C.-G. Wahlström, S. Svanberg: Generation of X-rays for medical imaging by high-power lasers: Preliminary results. *Radiology* **189**, 65 (1993)
- [5.40] C. Tillman, A. Persson, C.-G. Wahlström, S. Svanberg, K. Herrlin: Imaging using hard X-rays from a laser-produced plasma. *Appl. Phys. B* **61**, 333 (1995)
- [5.41] L.-J. Hardell: High-speed radiography using laser-produced X-rays; Characteristics and applications, Lund Reports on Atomic Physics LRAP-217 (Lund Institute of Technology, Lund 1997)
- [5.42] C. Tillman, I. Mercer, S. Svanberg, K. Herrlin: Elemental biological imaging by differential absorption using a laser-produced X-ray source. *J. Opt. Soc. Am. B* **13**, 209 (1996)
- [5.43] C.L. Gordon III, G.Y. Yin, B.E. Lemoff, P.E. Bell, C.P.J. Barty: Time-gated imaging with an ultrashort-pulse laser-produced-plasma X-ray source. *Opt. Lett.* **20**, 1056 (1995)
- [5.44] M. Grätz, A. Pifferi, C.-G. Wahlström, S. Svanberg: Time-gated imaging in radiology: Theoretical and experimental studies. *IEEE J. Sel. Topics Quantum Electron.* **2**, 1041 (1996)
- [5.45] M.F.C. Ladd, R.A. Palmer: *Structure Determination by X-Ray Crystallography* (Plenum, New York 1993)
- [5.46] R. Jimenez, C. Rose-Petruck, T. Guo, K.R. Wilson, C.P.J. Barty: 'Time-resolved X-ray diffraction of GaAs with a 30 fs laser-driven plasma source.' In: *Ultrafast Phenomena XI* ed. by W. Zinth, J.G. Fujimoto, T. Elsaesser, D. Wiersma (Springer, Berlin, Heidelberg 1998)
M. Wulff, F. Schotte, G. Naylor, D. Bourgeois, K. Moffat, G. Mourou: Time-resolved structures of macromolecules at the ESRF: Single-pulse

- Laue diffraction, stroboscopic data collection and femtosecond flash photolysis. *Nucl. Instrum. Methods Phys. Res. A* **398**, 69 (1997)
- [5.47] M.R. Howells, J. Kirz, W. Sayre: X-ray microscopes. *Sci. Am.* **264**(2), 42 (1991)
- A.G. Michette: *Optical Systems for Soft X-Rays* (Plenum, New York 1986)
- A.G. Michette: X-ray Microscopy. *Rep. Prog. Phys.* **51**, 1525 (1988)
- A.G. Michette, G.R. Morrison, C.J. Buckley (eds.): *X-ray Microscopy III*, Springer Ser. Opt. Sci. Vol. 67 (Springer, Berlin, Heidelberg 1992)
- V.V. Aristov, A.I. Erko (eds.): *X-ray Microscopy IV* (Bogorodski Publ., Moscow Region 1995)
- G. Schmahl, D. Rudolph, J. Thieme, E. Umbach (eds.): *X-ray Microscopy V* (Springer, Heidelberg 1998)
- [5.48] L. Rymell, H.M. Hertz: Droplet target for low-debris laser-plasma soft X-ray generation. *Opt. Commun.* **103**, 105 (1993)
- L. Malmqvist, L. Rymell, H.M. Hertz: Droplet-target laser-plasma source for proximity X-ray lithography. *Appl. Phys. Lett.* **68**, 2627 (1996)
- L. Rymell: A new laser-plasma X-ray source for microscopy and lithography. PhD Dissertation, Lund Reports on Atomic Physics LRAP-214 (Lund Institute of Technology, Lund 1997)
- [5.49] J.I. Goldstein, D.E. Newbury, P. Echlin, D.C. Joy, A.D. Romig Jr., C.E. Lyman, Ch. Fiori, E. Lifshin: *Scanning Electron Microscopy and X-Ray Microanalysis* (Plenum, New York 1992)
- M.J. Dykstra: *Biological Electron Microscopy* (Plenum, New York 1992)
- [5.50] A.M. Hawryluk, R.H. Stulen (eds.): *OSA Proceedings on Soft X-ray Lithography*, Vol. 18 (Optical Society of America, Washington, DC 1993)
- G.D. Kubiak, D.R. Kania (eds.): *Extreme Ultraviolet Lithography*, OSA Trends in Optics and Photonics, Vol. 4 (OSA, Washington, DC 1996)
- [5.51] S.M. Sze: *Semiconductor Device Physics and Technology* (Wiley, New York 1985)
- W.P. Kirk, M.A. Reed (eds.): *Nanostructures and Mesoscopic Systems* (Academic Press, New York 1992)
- C. Weisbuch, B. Vinter: *Quantum Semiconductor Structures* (Academic Press, San Diego 1991)
- [5.52] B. Lindberg, R. Maripuu, K. Siegbahn, R. Larsson, C.G. Gölander, J.C. Eriksson: ESCA studies of heparinized and related surfaces. *J. Colloid Interface Sci.* **95**, 308 (1983)
- [5.53] K. Siegbahn et al. (eds.): *ESCA: Atomic, Molecular and Solid State Structure Studied by Means of Electron Spectroscopy* (Almqvist and Wiksell, Uppsala 1967)
- [5.54] H. Siegbahn, L. Karlsson: 'Photoelectron Spectroscopy.' In: *Handbuch der Physik*, Vol. 31, ed. by E. Mehlhorn (Springer, Berlin, Heidelberg 1982)
- [5.55] C.R. Brundle, A.D. Baker (eds.): *Electron Spectroscopy: Theory, Techniques and Applications*, Vols. 1–5 (Academic Press, New York 1977–84)
- [5.56] R.E. Ballard: *Photoelectron Spectroscopy and Molecular Orbital Theory* (Hilger, London 1978)
- [5.57] P. Weightman: X-ray excited Auger and photoelectron spectroscopy. *Rep. Prog. Phys.* **45**, 753 (1982)
- [5.58] K. Siegbahn: 'Some Current Problems in Electron Spectroscopy.' In: *Atomic Physics 8*, ed. by I. Lindgren, A. Rosén, S. Svanberg (Plenum, New York 1983) p. 243
- [5.59] K. Siegbahn: Photoelectron spectroscopy: retrospects and prospects. *Phil. Trans. Roy. Soc. Lond. A* **318**, 3 (1986)

- [5.60] S. Hüfner: *Photoelectron Spectroscopy*, 2nd edn., Springer Ser. Solid-State Sci., Vol. 82 (Springer, Heidelberg 1996)
- [5.61] U. Becker, D.A. Shirley (eds): *VUV and Soft X-Ray Photoionization* (Plenum, New York 1995)
- [5.62] N.V. Smith, F.J. Himpsel: 'Photoelectron Spectroscopy.' In: *Handbook of Synchrotron Radiation*, ed. by E.E. Koch (North-Holland, Amsterdam 1983)
- [5.63] J.W. Rabalais: *Principles of Ultraviolet Photoelectron Spectroscopy* (Wiley-Interscience, New York 1977)
- [5.64] S. Svensson, N. Mårtensson, E. Basilier, P.Å. Malmquist, U. Gelius, K. Siegbahn: Core and valence orbitals in solid and gaseous mercury by means of ESCA. *J. Electron. Spectrosc. Rel. Phenom.* **9**, 51 (1976)
- [5.65] K. Siegbahn: Electron Spectroscopy and molecular structure. *J. Pure Appl. Chem.* **48**, 77 (1976)
- [5.66] H. Siegbahn: Electron Spectroscopy for chemical analysis of liquids and solutions. *J. Phys. Chem.* **89**, 897 (1985)
- [5.67] L.-G. Petersson, S.-E. Karlsson: Clean and oxygen-exposed potassium studied by photoelectron Spectroscopy. *Phys. Scr.* **16**, 425 (1977)
- [5.68] R.H. Williams: Electron spectroscopy of surfaces. *Contemp. Phys.* **19**, 389 (1978)
- [5.69] K. Siegbahn: 'Electron Spectroscopy for solids, surfaces, liquids and free molecules.' In: *Molecular Spectroscopy*, ed. by A.R. West (Heyden, London 1977) Chap. 15
- [5.70] D. Briggs, M.P. Seah (eds.): *Practical Surface Analysis by Auger and X-Ray Photoelectron Spectroscopy* (Wiley, Chichester 1983)

Chapter 6

- [6.1] G.R. Harrison (ed.): *MIT Wavelength Tables* (Wiley, New York 1969)
- [6.2] F.M. Phelps III: *MIT Wavelength Tables*, Vol. 2: *Wavelengths by Element* (MIT Press, Cambridge, MA 1982)
- [6.3] R.L. Kelly, L.J. Palumbo: Atomic and ionic emission lines below 2000 Ångstroms, hydrogen through krypton. NRL Report 7599 (Naval Research Laboratory, Washington, DC 1973)
- R.L. Kelly: Atomic and ionic spectral lines below 2000 Angstroms, hydrogen through krypton. *J. Phys. Chem. Ref. Data, Suppl. No. 1 to Vol. 16* (1987)
- [6.4] J. Reader, C.H. Corliss, W.L. Wiese, G.A. Martin: *Wavelengths and Transition Probabilities for Atoms and Atomic Ions*. NSRDS-NBS 68 (US Govt. Prtg. Off., Washington, DC 1980)
- [6.5] A.R. Striganov, N.S. Sventitskii: *Tables of Spectral Lines in Neutral and Ionized Atoms* (IFI/Plenum, New York 1968)
- [6.6] A. Thorne, U. Litzén, S. Johansson: *Spectrophysics* (Springer, Berlin, Heidelberg 1999)
- B.P. Straugan, S. Walker: *Spectroscopy*, Vols. 1–3 (Chapman & Hall, London 1976)
- [6.7] P.F.A. Klinkenberg: In *Methods of Experimental Physics*, Vol. 13, *Spectroscopy* (Academic Press, New York 1976) p. 253
- [6.8] P. Bousquet: *Spectroscopy and its Instrumentation* (Hilger, London 1971)
- [6.9] J. Kuba, L. Kucera, F. Plzak, M. Dvorak, J. Mraz: *Coincidence Tables for Atomic Spectroscopy* (Elsevier, Amsterdam 1965)

- [6.10] R. Beck, W. Englisch, K. Gürs: *Tables of Laser Lines in Gases and Vapors*, 3rd edn., Springer Ser. Opt. Sci., Vol. 2 (Springer, Berlin, Heidelberg 1980)
M.J. Weber: *Handbook of Laser Wavelengths* (CRC Press, Boca Raton 1999)
- [6.11] A.C.G. Mitchell, M.W. Zemansky: *Resonance Radiation and Excited Atoms* (Cambridge University Press, Cambridge 1961)
- [6.12] I.I. Sobelmann, L.A. Vainshtein, E.A. Yukov: *Excitation of Atoms and Broadening of Spectral Lines*, 2nd edn., Springer Ser. Chem. Phys., Vol. 7 (Springer, Berlin, Heidelberg 1995)
- [6.13] B. Wende (ed.): *Spectral Line Shapes* (de Gruyter, Berlin 1981)
- [6.14] K. Burnett (ed.): *Spectral Line Shapes* (de Gruyter, Berlin 1983)
- [6.15] C.H. Corliss, W.R. Bozman: *Experimental Transition Probabilities for Spectral Lines of Seventy Elements*, NBS Monograph 53 (National Bureau of Standards, Washington, DC 1962)
- [6.16] C.H. Corliss, J.L. Tech: Revised lifetimes of energy levels in neutral iron. *J. Res. Natl. Bur. Stand. Sect. A* **80**, 787 (1976)
- [6.17] C. de Michelis, M. Mattioli: Spectroscopy and impurity behaviour in fusion plasmas. *Rep. Prog. Phys.* **47**, 1233 (1984)
- [6.18] E.T. Kennedy: Plasmas and intense laser light. *Contemp. Phys.* **25**, 31 (1984)
- [6.19] T.P. Hughes: *Plasmas and Laser Light* (Wiley, New York 1975)
- [6.20] G. Bekefi (ed.): *Principles of Laser Plasmas* (Wiley, New York 1976)
- [6.21] K. Laqua: 'Analytical Spectroscopy using Laser Atomizers.' In: *Analytical Laser Spectroscopy*, ed. by N. Omenetto (Wiley, New York 1979)
- [6.22] M.N. Rosenbluth, R.Z. Sagdeev (eds.): *Physics of Laser Plasma* (North-Holland, Elsevier, Amsterdam 1991)
- [6.23] V.S. Lisitsa: *Atoms in Plasmas* (Springer, Berlin, Heidelberg 1994)
E. Oks: *Plasma Spectroscopy*, Springer Series on Atoms and Plasmas, Vol. 9 (Springer, Berlin, Heidelberg 1995)
F.J. Wuilleumier, Y. Petroff, I. Nenner (eds.): *Vacuum Ultraviolet Radiation Physics* (World Scientific, Singapore 1993)
R.L. Johnson, H. Schmidt-Böcking, B.F. Sonntag (eds.): *X-Ray and Inner Shell Processes*, AIP Conference Proceedings Vol. 389 (AIP, Woodbury 1997)
- [6.24] N.G. Basov, Yu.A. Zakharenkov, N.N. Zorev, G.V. Sklizkov, A.A. Rupasov, A.S. Shikanov: *Heating and Compression of Thermonuclear Targets by Laser Beams* (Cambridge University Press, Cambridge 1986)
- [6.25] R.D. Cowan: Progress in the spectroscopy of highly ionized atoms and its use in plasma diagnostics. *Phys. Scr.* **24**, 615 (1981)
H.W. Drawin: Atomic physics and thermonuclear fusion research, *Phys. Scr.* **24**, 622 (1981)
R.C. Isler: Impurities in Tokamaks. *Nuclear Fusion* **24**, 1599 (1984)
E. Källne, J. Källne: X-ray spectroscopy in fusion research. *Phys. Scr.* **T17**, 152 (1987)
- [6.26] S. Bashkin: Optical spectroscopy with van de Graaff accelerators. *Nucl. Instrum. Methods* **28**, 88 (1964)
- [6.27] L. Kay: A van de Graaff beam as a source of atomic emission spectra. *Phys. Lett.* **5**, 36 (1963)
- [6.28] J.O. Stoner, J.A. Leavitt: Reduction in Doppler broadening of spectral lines in fast-beam spectroscopy. *Appl. Phys. Lett.* **18**, 477 (1971)
- [6.29] R. Hutton, L. Engström, E. Träbert: *Nucl. Instrum. Methods Phys. Res. B* **31**, 294 (1988)

- [6.30] L.J. Curtis, H.J. Berry, J. Bromander: A meanlife measurement of the $3d\ 2D$ resonance doublet in SiII by a technique which exactly accounts for cascading. *Phys. Lett. A* **34**, 169 (1971)
L.J. Curtis: In: [6.37]
- [6.31] L. Engström: CANDY, a computer program to perform ANDC analysis of cascade corrected decay curves. *Nucl. Instrum. Methods* **202**, 369 (1982)
- [6.32] I. Martinson, A. Gaupp: Atomic physics with ion accelerators – beam-foil spectroscopy. *Phys. Rep.* **15**, 113 (1974)
- [6.33] H.G. Berry, L.J. Curtis, D.G. Ellis, R.M. Schechtman: Hyperfine quantum beats in oriented ^{14}N IV. *Phys. Rev. Lett.* **35**, 274 (1975)
- [6.34] U. Fano, J.H. Macek: Impact excitation and polarization of the emitted light. *Rev. Mod. Phys.* **45**, 553 (1973)
- [6.35] W. Wittmann, K. Tillmann, H.J. Andrä, P. Dobberstein: Fine-structure measurement of ^4He by zero-field quantum beats. *Z. Physik* **257**, 279 (1972)
- [6.36] O. Poulsen, J.L. Subtil: Hyperfine structure measurement in Be III. *J. Phys. B* **7**, 31 (1974)
- [6.37] S. Bashkin (ed.): *Beam-Foil Spectroscopy*, Topics Current Phys., Vol. 1 (Springer, Berlin, Heidelberg 1976)
- [6.38] I.A. Sellin, D.J. Pegg (eds.): *Beam-Foil Spectroscopy*, Vols. 1,2 (Plenum, New York 1976)
- [6.39] S. Bashkin (ed.): *Beam-Foil Spectroscopy*. Proc. 3rd Int. Conf. on Beam-Foil Spectroscopy. *Nucl. Instrum. Methods* **110** (1973)
- [6.40] Proc. Int. Conf. on Fast Ion Beam Spectroscopy. Proc. Colloque No. 1. *J. Physique* **40** (1978)
- [6.41] E.J. Knystautas, R. Drouin (eds.): Proc. 6th Int. Conf. on Fast Ion Beam Spectroscopy. *Nucl. Instrum. Methods* **202** (1982)
- [6.42] J.D. Silver, N.J. Peacock (eds.): The Physics of Highly Ionized Atoms. *Nucl. Instrum. Methods Phys. Res. B* **9**, 359 (1985)
- [6.43] H.J. Andrä: ‘Fast Beam (Beam-Foil) Spectroscopy.’ In: *Progress in Atomic Spectroscopy*, Pt. B, ed. by W. Hanle, H. Kleinpoppen (Plenum, New York 1979) p. 829
- [6.44] D.J. Pegg: In: *Methods of Experimental Physics*, Vol. 17, ed. by P. Richard (Academic Press, New York 1980) p. 529
- [6.45] I. Martinson: Recent progress in the studies of atomic spectra and transition probabilities by beam-foil spectroscopy. *Nucl. Instrum. Methods* **202**, 1 (1982)
I. Martinson: ‘Beam-Foil Spectroscopy.’ In: *Treatise on Heavy-Ion Science*, Vol. 5, ed. by D.A. Bromley (Plenum, New York 1985)
I. Martinson: The spectroscopy of highly ionized atoms. *Rep. Prog. Phys.* **52**, 157 (1989)
- [6.46] C.L. Cocke: ‘Beam-Foil Spectroscopy.’ In: *Methods of Experimental Physics*, Vol. 13 (Academic Press, New York 1976)
- [6.47] H.G. Berry: Beam-foil spectroscopy. *Rep. Progr. Phys.* **40**, 155 (1977)
- [6.48] H.G. Berry, M. Mass: Beam-foil spectroscopy. *Ann. Rev. Nucl. Part. Sci.* **32**, 1 (1982)
- [6.49] S.M. Schaefroth, J.C. Austin (eds.): *Accelerator-Based Atomic Physics – Techniques and Applications* (AIP Press, New York 1997)
J. Schwinger: On the classical radiation of accelerated electrons. *Phys. Rev.* **75**, 1912 (1949)
R.P. Madden, K. Codling: *Phys. Rev. Lett.* **10**, 516 (1963)
K. Codling: Applications of synchrotron radiation. *Rep. Progr. Phys.* **36**, 541 (1973)

- See also O.J. Jackson: *Classical Electrodynamics*, 2nd edn. (Wiley, New York 1975)
- [6.50] D.H. Tomboulian, P.L. Hartman: Spectral and angular distribution of ultraviolet radiation from the 300 MeV Cornell synchrotron. *Phys. Rev.* **102**, 1423 (1956)
- [6.51] E. Matthias, R.A. Rosenberg, E.D. Poliakoff, M.G. White, S.-T. Lee, D.A. Shirley: Time-resolved VUV spectroscopy using synchrotron radiation: Fluorescent lifetimes of atomic Kr and Xe. *Chem. Phys. Lett.* **52**, 239 (1977)
- [6.52] T. Möller, G. Zimmerer: Time-resolved spectroscopy with synchrotron-radiation in the vacuum ultraviolet. *Phys. Scr.* **T17**, 177 (1987)
R. Rigler, O. Kristensen, J. Roslund, P. Thyberg, K. Oba, M. Eriksson: Molecular structures and dynamics: Beamline for time-resolved spectroscopy at the MAX synchrotron in Lund. *Phys. Scr.* **T17**, 204 (1987)
- [6.53] H. Motz: Undulators and free-electron lasers. *Contemp. Phys.* **20**, 547 (1979)
- [6.54] J.M.J. Madey: Stimulated emission of Bremsstrahlung in a periodic magnetic field. *J. Appl. Phys.* **42**, 1906 (1971)
D.A.G. Deacon, L.R. Elias, J.M.J. Madey, G.J. Ramian, H.A. Schwettman, T.I. Smith: First operation of free electron laser. *Phys. Rev. Lett.* **38**, 892 (1977)
- [6.55] V.L. Granatstein, C.W. Robertson (eds.): Third special issue on free electron lasers. *IEEE J. Quantum Electron.* **QE-21**, 804-1113 (1985)
- [6.56] J.M.J. Madey, A. Renieri (eds.): *Free Electron Lasers* (Conf. Proc.) (North-Holland, Amsterdam 1985)
- [6.57] F.C. Marshall: *Free Electron Lasers* (Macmillan, New York 1985)
- [6.58] H.P. Freund, R.K. Parker: Free-electron lasers. *Sci. Am.* **260**(4), 56 (1989)
- [6.59] C. Brau: *Free Electron Lasers* (Academic Press, New York 1990)
- [6.60] E.L. Saldin, E.A. Schneidmiller, M.V. Yurkov: The physics of free electron lasers: An Introduction. *Phys. Rep.* **260**, 187 (1995)
- [6.61] H.P. Freund, T.M. Antonsen Jr.: *Principles of Free-Electron Lasers*, 2nd edn. (Chapman & Hall, London 1996)
- [6.62] Proc. 17th Int. Free Electron Laser Conf., Nucl. Instrum. Methods A **375** (1996)
- [6.63] V.H. Harutunian, S.G. Oganesyan: Laser interaction – free electron interaction. *Phys. Rep.* **270**, 217 (1996)
J.M. Ortega, Y. Lapierre, B. Girard, M. Billardon, P. Elleaume, C. Baziin, M. Bergher, M. Velghe, Y. Petroff: Ultraviolet coherent generation from an optical klystron. *IEEE J. Quantum Electron.* **QE-21**, 909 (1985)
S. Werin, M. Eriksson, J. Larsson, A. Persson, S. Svanberg: First results in coherent harmonic generation using the undulator at the MAX-Lab electron storage ring. *Nucl. Instrum. Methods Phys. Res. A* **290**, 589 (1990)
- [6.64] R. Bonifacio, C. Pellegrini, I.M. Narducci: *Opt. Commun.* **50**, 373 (1984)
A VUV Free Electron Laser at the TESLA Test Facility at DESY: *Conceptual Design Report* (DESY Print, Hamburg 1995)
- [6.65] J.R. Schneider: Properties and scientific perspectives of a single-pass X-ray free-electron laser. *Nucl. Instrum. Methods Phys. Res. A* **388**, 41 (1997)
C. Joshi, T. Katsouleas (eds.): *Laser Accelerators of Particles*, AIP Conf. Proc. Vol. 130 (Am. Inst. Physics, New York 1985)
J. Wurtele (ed.): *Advanced Accelerator Concepts*, AIP Conference Proceedings Vol. 279 (AIP, Port Jefferson 1992)

- [6.66] K. Siegbahn: 'Electron spectroscopy for solids, surfaces, liquids and free molecules.' In: *Molecular Spectroscopy* (Heyden & Son, London 1983) Chap. 15, p. 227
- [6.67] C. Kunz (ed.): *Synchrotron Radiation. Techniques and Applications*, Topics Current Phys., Vol. 10 (Springer, Berlin, Heidelberg 1979)
- [6.68] H. Winich, S. Doniach (eds.): *Synchrotron Radiation Research* (Plenum, New York 1980)
- [6.69] E.E. Koch (ed.): *Handbook on Synchrotron Radiation*, Vols. 1–3, (North-Holland, Amsterdam 1983, 1986, 1987)
- [6.70] S. Ebashi, M. Koch, E. Rubinstein (eds.): *Synchrotron Radiation Research* (North-Holland, Amsterdam 1991)
M. Altarelli, F. Schachter, J. Cross: Making ultrabright X-rays. *Sci. Am.* **279**(6), 36 (1998)
- [6.71] E.J. Ansaldi: Uses of synchrotron radiation. *Contemp. Phys.* **18**, 527 (1977)
W. Jitschin: 'Inner-Shell Spectroscopy with Hard Synchrotron Radiation.' In: *Progress in Atomic Spectroscopy*, Pt. D, ed. by H.J. Beyer, H. Kleinpoppen (Plenum, New York 1987) p. 295
- [6.72] H. Winick: *Synchrotron Radiation Sources – A Technical Primer* (World Scientific, River Edge 1994)
- [6.73] H.H. Malitson: The solar energy spectrum. *Sky and Telescope* **29**(4), 162 (1965)
- [6.74] W.K. Pratt: *Laser Communication Systems* (Wiley, New York 1969)
- [6.75] S.P. Davis: *Diffraction Grating Spectrometers* (Holt, Rinehard, Winston, New York 1970)
R.A. Sawyer: *Experimental Spectroscopy* (Dover, New York 1963)
- [6.76] D.A. Skoog, D.M. West: *Principles of Instrumental Analysis* (Holt-Saunders, Philadelphia 1980)
- [6.77] M.C. Hutley: *Diffraction Gratings* (Academic Press, London 1982)
Handbook of Diffraction Gratings, Ruled and Holographic (Jobin-Yvon Optical Systems, Metuchen, NJ 1970)
- [6.78] H. Walther: Das Kernquadrupolmoment des ^{55}Mn . *Z. Physik* **170**, 507 (1962)
- [6.79] J.M. Vaughan: *The Fabry–Pérot Interferometer* (Hilger, Bristol 1989)
- [6.80] W. Demtröder: *Laser Spectroscopy*, 3rd edn. (Springer, Berlin, Heidelberg 2003)
- [6.81] J.F. James: *A Student's Guide to Fourier Transforms* (Cambridge University Press, Cambridge 1995)
R.W. Ramirez: *The FFT: Fundamentals and Concepts* (Prentice Hall, Englewood Cliffs, NJ 1985)
- [6.82] H.J. Nussbaumer: *Fast Fourier Transform and Convolution Algorithms*, 2nd edn., Springer Ser. Inf. Sci., Vol. 2 (Springer, Berlin, Heidelberg 1982)
G. Guelachvili: High accuracy Doppler-limited 10^6 samples Fourier transform spectroscopy. *Appl. Opt.* **17**, 1322 (1978)
- [6.83] S. Tolansky: *An Introduction to Interferometry* (Longmans, London 1973)
- [6.84] W.H. Steel: *Interferometry*, 2nd edn. (Cambridge University Press, Cambridge 1983)
- [6.85] P. Hariharan: *Optical Interferometry* (Academic Press, New York 1986)
- [6.86] P. Hariharan: *Basics of Interferometry* (Academic Press, London 1992)
- [6.87] R.J. Bell: *Introductory Fourier Transform Spectroscopy* (Academic Press, New York 1972)
- [6.88] P.K. Rastogi: *Holographic Interferometry* (Springer, Berlin, Heidelberg 1994)

- [6.89] D.B. Chase, J.F. Rabold (eds.): *Fourier Transform Raman Spectroscopy* (Academic Press, London 1994)
- [6.90] Th. Kreis: *Holographic Interferometry – Principles and Methods* (Akademie Verlag, Berlin 1996)
- [6.91] B.C. Smith: *Advanced Fourier Transform Infrared Spectroscopy* (Springer, Berlin, Heidelberg 1997)
- [6.92] *The Optical Industry & Systems Purchasing Directory*, 26th edn. (Laurin Publ. Co., Pittsfield, MA 1980) p. B-114
- [6.93] R.J. Keyes (ed.): *Optical and Infrared Detectors*, 2nd. edn. Topics Appl. Phys., Vol. 19 (Springer, Berlin, Heidelberg 1980)
- [6.94] R.H. Kingston: *Detection of Optical and Infrared Radiation*, Springer Ser. Opt. Sci., Vol. 10 (Springer, Berlin, Heidelberg 1979)
- [6.95] R.W. Boyd: *Radiometry and the Detection of Optical Radiation* (Wiley, New York 1983)
- [6.96] H.H. Melchior: ‘Demodulation and photodetection techniques.’ In: *Laser Handbook*, Vol. 1, ed. by T. Arecchi, E.O. Schulz-Dubois (North-Holland, Amsterdam 1972) Chap. 7
- [6.97] E.L. Dereniak, D.G. Crowe: *Optical Radiation Detectors* (Wiley, New York 1984)
- [6.98] G.H. Rieke: *Detection of Light from the Ultraviolet to the Submillimeter Region* (Cambridge University Press, Cambridge 1994)
- [6.99] E.L. Dereniak, G.D. Boreman: *Infrared Detectors and Systems* (Wiley, New York 1996)
- [6.100] R.H. Kingston: *Optical Sources, Detectors and Systems – Fundamentals and Applications* (Academic Press, New York 1995)
- [6.101] M. Lampert: The microchannel image intensifier. *Sci. Am.* **245**(5), 46 (1981)
- [6.102] Proc. Topical Meeting on Quantum-Limited Imaging and Image Processing (Optical Society of America, Washington, DC 1986)
- [6.103] C.N. Anagnostopoulos, M.M. Blouke, M.P. Lesser (eds.): *Solid State Sensor Arrays and CCD Cameras*. SPIE **2654** (1996)
- [6.104] C.D. Mackay: Charge coupled devices in astronomy. *Ann. Rev. Astron. Astrophys.* **24**, 255 (1986)
- [6.105] M.A. Stern, A. Kaiser, H.W. Mahler, E. DiBenedetto: Low-light-level image-amplifying device with full color capability. *Journal of the SMPTE* **83**, 185 (1974)
- [6.106] S. Svanberg, J. Johansson: Image registering in color at low light intensity. US Patent 5 483 379 (1996)
- [6.107] G. Blasse, B.C. Grabmaier: *Luminescent Materials* (Springer, New York 1994)
- [6.108] J. Miyahara: The imaging plate: A new radiation image sensor. *Chem. Today* **223**, 29 (1989)
- [6.109] D.H. Lumb, G.R. Hopkinson, A.A. Weels: Performance of CCDs for X-ray imaging and spectroscopy. *Nucl. Instrum. Methods* **221**, 150 (1984)
- [6.110] J.D. Cox, D.S. Langford, D.W. Williams: ‘Electronic intraoral dental imaging system employing a direct sensing CCD array.’ In: *X-ray Detector Physics and Applications II*, ed. by V.J. Orphan, SPIE **2009** (1993)
- [6.111] *The Photonics Design & Application Handbook* (Laurin Publ. Comp., Pittsfield, MA 1990)
- [6.112] G.R. Fowles: *Introduction to Modern Optics* (Holt, Rinehart and Winston, New York 1968)
- [6.113] J. Strong: *Procedures in Experimental Physics* (Prentice Hall, New York 1945)

- [6.114] M. Kasha: Transmission filters for the ultraviolet. *J. Opt. Soc. Am.* **38**, 929 (1948)
- [6.115] K. Bennett, R.L. Byer: Computer controllable wedge-plate optical variable attenuator. *Appl. Opt.* **19**, 2408 (1980)
- [6.116] C.G. Granqvist: Radiative heating and cooling with spectrally selective surfaces. *Appl. Opt.* **20**, 2606 (1981)
C.G. Granqvist: *Handbook of Inorganic Electrochromic Materials* (Elsevier, Amsterdam 1995)
- [6.117] C.G. Granqvist (ed.): *Materials Science for Solar Energy Conversion Systems* (Pergamon, Oxford 1991)
C.G. Granqvist, A. Azens, A. Hjelm, L. Kullman, G.A. Niklasson, D. Rönnow, M. Strömmme Mattsson, M. Veszelei, G. Vaivars: Recent advances in electrochromics for smart windows applications. *Solar Energy* **63**, 199 (1998)
- A.V. Dotsenko, L.B. Glebov, V.A. Tsekhomsky: *Physics and Chemistry of Photochromic Glasses* (CRC Press, Boca Raton 1998)
- [6.118] H. Bach, N. Neuroth (eds.): *The Properties of Optical Glass* (Springer, Berlin, Heidelberg 1995)
- [6.119] B. Edlén: The refractive index of air. *Metrologia* **2**, 71 (1966)
- [6.120] R. Revelle: Carbon dioxide and world climate. *Sci. Am.* **247**(5), 33 (1982)
R.A. Houghton, G.W. Woodwell: Global climatic change. *Sci. Am.* **260**(4), 18 (1989)
S.H. Schneider: The changing climate. *Sci. Am.* **261**(3), 38 (1989)
B.J. Mason: The greenhouse effect. *Contemp. Phys.* **30**, 417 (1989)
B.J. Mason: Predictions of climate changes caused by manmade emissions of greenhouse gases: A critical assessment. *Contemp. Phys.* **36**, 299 (1995)
- [6.121] J.C. Farman, B.G. Gardiner, J.D. Shanklin: Large losses of total ozone in Antarctica reveal seasonal ClO_x/NO_2 interaction. *Nature* **315**, 207 (1985)
- [6.122] R.S. Stolarski: The Antarctic ozone hole. *Sci. Am.* **258**(1), 20 (1988)
- [6.123] O.B. Toon, R.P. Turco: Polar stratospheric clouds and ozone depletion. *Sci. Am.* **264**(6), 40 (1991)
- [6.124] C.S. Zerefos, A.F. Bais: *Solar Ultraviolet Radiation, Modelling, Measurements and Effects* (Springer, Berlin, Heidelberg 1997)
- [6.125] J.H. Seinfeld: *Atmospheric Chemistry and Physics of Air Pollution* (Wiley, New York 1986)
- [6.126] R.P. Wayne: *Chemistry of Atmospheres* (Clarendon, Oxford 1985)
- [6.127] T.E. Graedel, D.T. Hawkins, L.D. Claxton: *Atmospheric Chemical Compounds: Sources, Occurrence, Bioassay* (Academic Press, Orlando 1986)
- [6.128] B.A. Thrush: The chemistry of the stratosphere. *Rep. Prog. Phys.* **51**, 1341 (1988)
T.H. Graedel, P.J. Crutzen: The changing atmosphere. *Sci. Am.* **261**(3), 28 (1989)
- [6.129] R.W. Baubel, D.B. Turner, A.C. Stern: *Fundamentals of Air Pollution*, 3rd edn. (Academic Press, London 1994)
- [6.130] W. Michaelis: *Air Pollution* (Springer, Berlin, Heidelberg 1997)
- [6.131] S.L. Valley (ed.): *Handbook of Geophysics and Space Environments* (McGraw-Hill, New York 1965)
- [6.132] M. Vergez-Deloncle: Absorption des radiations infrarouges par les gaz atmosphériques. *J. Physique* **25**, 773 (1964)
- [6.133] Hudson and Hudson (1975), quoted in [6.139]

- [6.134] L.S. Rothman, C.P. Rinsland, A. Goldman, S.T. Massie, D.P. Edwards, J.-M. Edwards, J.-M. Flaud, A. Perrin, C. Camy-Peyret, V. Dana, J.-Y. Mandin, J. Schroeder, A. McCann, R.R. Gamache, R.B. Eattson, K. Yoshino, K.V. Chance, K.W. Jucks, L.R. Brown, V. Nemtchinov, P. Varanasi: The HITRAN molecular database and HAWKS (HITRAN Atmospheric Workstation): 1996 edition. *J. Quant. Spectr. Radiat. Transfer* **60**, 665 (1998)
- P.L. Hanst: QA Soft '96, Database and quantitative analysis program for measurements of gases (Infrared Analysis Inc., Anaheim, CA 1996)
- [6.135] B.A. Thompson, P. Harteck, R.R. Reeves Jr.: Ultraviolet absorption coefficients of CO₂, CO, O₂, H₂O, N₂O, NH₃, NO, SO₂, and CH₄ between 1850 and 4000 Å. *J. Geophys. Res.* **68**, 6431 (1963)
- [6.136] W. Eppers: 'Atmospheric Transmission.' In: *Handbook of Lasers with Selected Data on Optical Technology*, ed. by R.J. Pressley (CRC Press, Cleveland 1977)
- [6.137] N.G. Jerlov: *Optical Oceanography* (Elsevier, Amsterdam 1968)
- T. Stefanick: The nonacoustic detection of submarines. *Sci. Am.* **258**(3), 25 (1988)
- [6.138] C.D. Mobley: *Light and Water – Radiative Transfer in Natural Waters* (Academic Press, London 1994)
- [6.139] R.M. Measures: *Laser Remote Sensing* (Wiley-Interscience, New York 1984)
- [6.140] D.B. Northam, M.A. Guerra, M.E. Mock, I. Itzkan, C. Deradourian: High repetition rate frequency-doubled Nd:YAG laser for airborne bathymetry. *Appl. Opt.* **20**, 968 (1981)
- [6.141] P. Armbruster, F.P. Hessberger: Making new elements. *Sci Am.* **279**(5), 50 (1998)
- S. Hofman: New elements – approaching $Z = 114$. *Rep. Prog. Phys.* **61**, 639 (1998)
- E.R. Scerri: The evolution of the periodic system. *Sci. Am.* **279**(3), 56 (1998)
- [6.142] B. Welz: *Atomic Absorption Spectroscopy* (VCH, Weinheim 1985)
- J.A. Dean, T.C. Rains (eds.): *Flame Emission and Atomic Absorption Spectrometry*, Parts 1–3 (Marcel Dekker, New York 1969, 1971, 1975)
- [6.143] C.Th.J. Alkemade, R. Herrmann: *Fundamentals of Analytical Flame Spectroscopy* (Hilger, Bristol 1979)
- [6.144] D.A. Skoog: *Principles of Instrumental Analysis*, 3rd edn. (Saunders, Philadelphia 1985)
- D.A. Skoog, M.D. West: *Fundamentals of Analytical Chemistry*, 4th edn. (Saunders, Philadelphia 1986)
- [6.145] G.D. Christian, J.E. O'Reilly (eds.): *Instrumental Analysis*, 2nd edn. (Allyn and Bacon, Boston 1986)
- [6.146] H.H. Willard, L.L. Merritt Jr., J.A. Dean, F.A. Settle Jr.: *Instrumental Methods of Analysis*, 6th edn. (Wadsworth, Belmont, CA 1981)
- [6.147] J.U. White: Long optical paths of large aperture. *J. Opt. Soc. Am.* **32**, 285 (1942)
- J.U. White: Very long paths in air. *J. Opt. Soc. Am.* **66**, 411 (1976)
- [6.148] H. Edner, A. Sunesson, S. Svanberg, L. Unéus, S. Wallin: Differential optical absorption spectroscopy system used for atmospheric mercury monitoring. *Appl. Opt.* **25**, 403 (1986)
- [6.149] J.E. Stewart: *Infrared Spectroscopy* (Marcel Dekker, New York 1970)
- [6.150] H.A. Szymanski: *Interpreted Infrared Spectra*, Vols. 1–3 (Plenum, New York 1964–67)

- [6.151] S. Hünfer: *Optical Spectra of Transparent Rare Earth Compounds* (Academic Press, New York 1978)
- [6.152] A.P.B. Lever: *Inorganic Electronic Spectroscopy*, 2nd edn. (Elsevier, Amsterdam 1984)
- [6.153] H.A. Szymanski, R.E. Erickson: *Infrared Band Handbook*, Vols. 1, 2 (IFI/Plenum, New York 1970)
- [6.154] *IUPAP Tables of Wavenumbers for the Calibration of Infrared Spectrometers* (Butterworths, London 1961) p. 560
- [6.155] B. Smith: *Infrared Spectral Interpretation* (Springer, Berlin, Heidelberg 1997)
- [6.156] R.J. Pressley (ed.): *Handbook of Lasers* (with Selected Data on Optical Technology) (CRC Press, Cleveland, Ohio 1971) p. 407
- [6.157] H.A. Szymanski (ed.): *Raman Spectroscopy* (Plenum, New York 1967)
- [6.158] A. Weber (ed.): *Raman Spectroscopy of Gases and Liquids*, Topics Current Phys., Vol. 11 (Springer, Berlin, Heidelberg 1979)
- [6.159] D.P. Strommen, K. Nakamoto: *Laboratory Raman Spectroscopy* (Wiley, New York 1984)
- [6.160] M.M. Sushchinskii: *Raman Spectra of Molecules and Crystals* (Israel Progr. for Sci. Transl., Jerusalem 1972)
- [6.161] J.F. Ferraro, K. Nakamoto: *Introductory Raman Spectroscopy* (Academic Press, London 1994)
- [6.162] H. Bergström, Lund Institute of Technology (unpublished)
- [6.163] G.L. Eesley: *Coherent Raman Spectroscopy* (Pergamon, Oxford 1981)
- [6.164] S. Svanberg: Lasers as probes for air and sea. *Contemp. Phys.* **21**, 541 (1980)
- [6.165] E. Schanda: *Physical Fundamentals of Remote Sensing* (Springer, Berlin, Heidelberg 1986)
- [6.166] S. Svanberg: 'Fundamentals of atmospheric spectroscopy.' In: *Surveillance of Electromagnetic Pollution and Resources by Electromagnetic Waves*, ed. by T. Lund (Reidel, Dordrecht 1978)
- [6.167] E.J. McCartney: *Absorption and Emission by Cases: Physical Processes* (Wiley, New York 1983)
- [6.168] C.B. Ludwig, M. Griggs, W. Malkmus, E.R. Bartle: Measurements of air pollutants from satellites, 1: Feasibility considerations. *Appl. Opt.* **13**, 1494 (1974)
- [6.169] Ph.L. Hanst, S.T. Hanst: 'Gas measurement in the fundamental infrared region.' In: *Air Monitoring by Spectroscopic Techniques* ed. by M.W. Sigrist (Wiley, New York 1994)
- [6.170] U. Platt, D. Perner, H.W. Pätz: Simultaneous measurement of atmospheric CH_2O , O_3 , and NO_2 by differential optical absorption. *J. Geophys. Res.* **84**, 6329 (1979)
- U. Platt: 'Differential optical absorption spectroscopy (DOAS).' In: *Air Monitoring by Spectroscopic Techniques*, ed. by M.W. Sigrist (Wiley, New York 1994)
- [6.171] U. Platt, D. Perner: 'Measurements of atmospheric trace gases by long path differential UV/visible absorption Spectroscopy.' In: *Optical and Laser Remote Sensing*, ed. by D.K. Killinger, A. Mooradian, Springer Ser. Opt. Sci., Vol. 39 (Springer, Berlin, Heidelberg 1983)
- [6.172] H. Edner, P. Ragnarson, S. Spännare, S. Svanberg: A differential optical absorption spectroscopy (DOAS) system for urban atmospheric pollution monitoring. *Appl. Opt.* **32**, 327 (1993); and Lund Reports on Atomic Physics LRAP-133 (Lund Institute of Technology, Lund 1992)

- [6.173] H. Edner, A. Amer, P. Ragnarson, M. Rudin, S. Svanberg: Atmospheric NH₃ Monitoring by Long-Path UV Absorption Spectroscopy. SPIE **1269**, 14 (1990)
- [6.174] H. Axelsson, H. Edner, A. Eilard, A. Emanuelsson, B. Galle, H. Kloo, P. Ragnarson: Measurements of aromatic hydrocarbons with the DOAS technique. Appl. Spectr. **49**, 1254 (1995)
- [6.175] P.V. Johnston, R.L. McKenzie: Long-path absorption measurements of tropospheric NO₂ in rural New Zealand. Geophys. Lett. **11**, 69 (1984)
- [6.176] P. Weibring, H. Edner, S. Svanberg, G. Cecchi, L. Pantani, R. Ferrara, T. Caltabiano: Monitoring of volcanic sulphur dioxide emissions using differential absorption lidar (DIAL), differential optical absorption spectroscopy (DOAS), and correlation spectroscopy (COSPEC). Appl. Phys. B **67**, 419 (1998)
- [6.177] M.M. Millan, R.M. Hoff: Dispersive correlation spectroscopy: A study of mask optimization procedures. Appl. Opt. **16**, 1609 (1977)
- [6.178] D.M. Hamilton, H.R. Varey, M.M. Millan: Atmos. Environ. **12**, 127 (1978)
- [6.179] J.A. Hodgeson, W.A. McClenney, P.L. Hanst: Science **182**, 248 (1973)
- [6.180] T.V. Ward, H.H. Zwick: Gas cell correlation spectrometer: GASPEC. Appl. Opt. **14**, 2896 (1975)
- [6.181] H.S. Lee, H.H. Zwick: Gas filter correlation instrument for the remote sensing of gas leaks. Rev. Sci. Instrum. **56**, 1812 (1985)
- [6.182] J. Sandsten, H. Edner, S. Svanberg: Gas imaging using infrared gas-correlation spectrometry. Opt. Lett. **21**, 1945 (1996)
- [6.183] J. Sandsten, P. Weibring, H. Edner, S. Svanberg: Real-time gas-correlation imaging employing thermal background radiation. Opt. Express **6**, 92 (2000). <http://www.opticsexpress.org>
- [6.184] U.N. Rao, A. Weber (eds.): *Spectroscopy of the Earth's Atmosphere and Interstellar Medium* (Academic Press, London 1992)
- [6.185] J.P. Dakin, H.O. Edwards: Gas sensor using correlation spectroscopy, compatible with fibre-optic operation. Sens. Actuators B **11**, 9 (1993)
- [6.186] J.P. Dakin, H.O. Edwards, B.H. Weigl: Progress with gas sensors using correlation spectroscopy. Sens. Actuators B **29** (1995)
- [6.187] P.H. Swain, S.M. Davis (eds.): *Remote Sensing: The Quantitative Approach* (McGraw-Hill, 1978)
- [6.188] S.C. Cox (ed.): The Multispectral Imaging Sciences Working Group: Final Report, NASA Conf. Publ. No 2260 (NASA, Washington, DC 1983); Earth Observing Systems Reports, Vol. IIc, High Resolution Imaging Spectrometry (NASA, Washington, DC 1986)
- [6.189] G. Vane (ed.): *Imaging Spectroscopy II*. Proc. SPIE-Int. Soc. Opt. Eng. **834** (1987)
- [6.190] P.N. Slater: *Remote Sensing: Optics and Optical Systems* (Addison Wesley, Reading, MA 1980)
- [6.191] A.F.H. Goertz, J. Wellman, W. Barnes: Optical remote sensing of the Earth. Proc. IEEE **73** (June 1985)
- [6.192] H.S. Chen: *Space Remote Sensing Systems* (Academic Press, Orlando 1985)
- [6.193] T.A. Croft: Nighttime images of the Earth from space. Sci. Am. **239**(1), 68 (1978)
- [6.194] S.Q. Kidder, T.H. von der Haar: *Satellite Meteorology* (Academic Press, London 1995)
- [6.195] L.R. Allen (ed.): *Thermosense XV, Proc. International Conference on Thermal Sensing and Imaging Diagnostic Applications*. Proc. SPIE Int. Soc. Opt. Eng. **1933** (1993)

- [6.190] A. Dalgarno, D. Layzer (eds.): *Spectroscopy of Astrophysical Plasmas* (Cambridge University Press, Cambridge 1987)
- [6.191] G.B. Rybicki, A.P. Lightman: *Radiative Processes in Astrophysics* (Wiley, New York 1979)
- [6.192] D.F. Gray: *The Observation and Analysis of Stellar Photospheres* (Wiley, New York 1976)
- [6.193] D. Emerson: *Interpreting Astronomical Spectra* (Wiley, Chichester 1996)
- [6.194] R. Bingham, V.N. Tsytovich: *Plasma Astrophysics* (Wiley, Chichester 1997)
- [6.195] R.H. Baker: *Astronomy* (Van Nostrand, Princeton, NJ 1964)
- [6.196] D.J. Schroeder: *Astronomical Optics* (Academic Press, San Diego 1987)
- [6.197] B. Aschenbach: X-ray telescopes. Rep. Prog. Phys. **48**, 579 (1985)
- [6.198] *The VLT Whitebook* (European Southern Observatory, Garching 1998) (also <http://www.eso.org>)
- [6.199] R.F. Griffin: *A Photometric Atlas of the Spectrum of Arcturus* (Cambridge Phil. Soc., Cambridge 1968)
- [6.200] J.M. Beckers, C.A. Bridges, L.B. Gilliam: *A High Resolution Atlas of the Solar Irradiance from 380–700 nm* (Sacramento Peak Observatory, 1983)
- [6.201] D. Dravins: In: *KOSMOS 1980* (Swedish Phys. Soc., Stockholm 1980)
- [6.202] B. Edlén: Z. Astrophysik **22**, 30 (1942)
- [6.203] B. Edlén: Forbidden lines in hot plasmas. Phys. Scr. **T8**, 5 (1984)
- [6.204] R. Giacconi: The Einstein X-ray observatory. Sci. Am. **242**(2), 70 (1980)
- [6.205] A. Vidal-Madjar, Th. Encrenaz, R. Ferlet, J.C. Henoux, R. Lallement, G. Vaudair: Galactic ultraviolet astronomy. Rep. Prog. Phys. **50**, 65 (1987)
- [6.206] S. Bowyer: Extreme ultraviolet astronomy. Sci. Am. **271**(2), 22 (1994)
- [6.207] R. Giacconi: X-ray astronomy: Past achievements and future prospects, Phys. Scr. **T61**, 9 (1996)
- [6.208] H.J. Habing, G. Neugebauer: The infrared sky. Sci. Am. **251**(5), 42 (1984)
- [6.209] J.B. Bahcall, L. Spitzer Jr.: The space telescope. Sci. Am. **247**(1), 38 (1982)
- [6.210] E.J. Chaisson: Early results from the Hubble Space Telescope. Sci. Am. **266**(6), 18 (1992)
- [6.211] D. Fischer, H. Duerbeck: *Hubble – A New Window to the Universe* (Copernicus-Springer, New York 1996)
- [6.212] P. Benvenuti, F.D. Machetto, E.J. Schreier (eds.): *Science with the Hubble Space Telescope-II* (Space Telescope Science Institute, Baltimore 1996)
- [6.213] D.S. Leckrone, S. Johansson, G.M. Wahlgren, S.J. Adelman: High resolution UV stellar spectroscopy with the HST/GHRS, challenges and opportunities for atomic physics. Phys. Scr. **T47**, 149 (1993)
- [6.214] C. Collins Peterson, J.C. Brandt: *Hubble Vision, Astronomy with the Hubble Space Telescope* (Cambridge University Press, Cambridge 1995)
- [6.215] <http://oposite.stsci.edu/> Material created with support to AURA/STScI from NASA contract NAS5-26555
- [6.216] J.W. Hardy: Adaptive optics. Sci. Am. **270**(6), 40 (1994)
- [6.217] J.M. Beckers: Adaptive optics for astronomy: Principles, performance and applications. Am. Rev. Astron. Astrophys. **31**, 13 (1993)
- [6.218] I.S. Bowen: The spectrum and composition of the gaseous nebulae. Astrophys. J. **81**, 1 (1935)
- [6.219] S. Johansson: Strong Fe II fluorescence lines in RR Tel and V1016 Cyg excited by C IV in a Bowen mechanism. Mon. Not. R. Astr. Soc. **205**, 71P (1983)

- [6.211] S. Johansson, V.S. Letokhov: Radiative cycle with stimulated emission from atoms and ions in an astrophysical plasma. *Phys. Rev. Lett.* **90**, 011101 (2003)
- [6.212] D.W. Weedman: *Quasar Astronomy* (Cambridge University Press, Cambridge 1986)
T.J.-L. Courvoisier, E.I. Robson: The Quasar 3C 273. *Sci. Am.* **264**(6), 24 (1991)
- [6.213] P.S. Osmer: Quasars as probes of the distant and early universe. *Sci. Am.* **246**(2), 96 (1982)
- [6.214] P. Murdin: The supernova in the Large Magellanic Cloud. *Contemp. Phys.* **28**, 441 (1987)
W. Hillebrandt, P. Höflich: The supernova 1987A in the Large Magellanic Cloud. *Rep. Prog. Phys.* **52**, 1421 (1989)
S. Woosley, T. Weaver: The great supernova of 1987. *Sci. Am.* **261**(2), 24 (1989)
D.N. Schramm, J.W. Truran: New physics from supernova 1987A. *Phys. Rep.* **189**, 89 (1990)
P. Murdin: *End of Fire: The Supernova in the Large Magellanic Cloud* (Cambridge University Press, Cambridge 1990)
- [6.215] R. Fosburg: The spectrum of supernova 1987A. *ESO Messenger* **47**, 32 (1987)
- [6.216] P. Andreani, R. Ferlet, R. Vidal-Madjar: *ESO Messenger* **47**, 33 (1987)
- [6.217] P. Connes, G. Michel: Astronomical Fourier spectrometer. *Appl. Opt.* **14**, 2067 (1975)
- [6.218] L.A. Soderblom, T.V. Johnson: The moons of Saturn. *Sci. Am.* **246**(1), 72 (1982)
- [6.219] T. Oen: Titan. *Sci. Am.* **246**(2), 76 (1982)
- [6.220] R.P. Laeser, W.I. McLaughlin, D.M. Wolff: Engineering Voyager 2's encounter with Uranus. *Sci. Am.* **255**(5), 34 (1986)
A.P. Ingersoll: Uranus. *Sci. Am.* **256**(1), 30 (1987)
T.J. Johnson, R.H. Brown, L.A. Soderblom: The moons of Uranus. *Sci. Am.* **256**(4), 40 (1987)
J. Kinoshita: Neptune. *Sci. Am.* **261**(5), 60 (1989)
J.N. Cuzzi, L.W. Esposito: The rings of Uranus. *Sci. Am.* **257**(1), 42 (1987)
[6.220] Sky and Telescope **73**, No. 3 (1987) (Feature issue)
Nature **321**, No. 6067 (1987) (Feature issue)
- [6.221] H. Balsiger, H. Fechtig, J. Geiss: A close look at Halley's comet. *Sci. Am.* **259**(3), 62 (1988)
- [6.221] C. Arpigny, F. Dossin, J. Manfroid, P. Magain, A.C. Danks, D.L. Lambert, C. Sterken: Spectroscopy, photometry and direct filter imagery of comet P/Halley. *ESO Messenger* **45**, 10 (1986)

Chapter 7

- [7.1] N. Ramsey: *Molecular Beams* (Clarendon, Oxford 1956; Paperback 1985)
J.M. Pendlebury, K.F. Smith: Molecular beams. *Contemp. Phys.* **28**, 3 (1987)
- [7.2] J.F. O'Hanlon: *A User Guide to Vacuum Technology*, 2nd edn. (Wiley, New York 1989)
- [7.3] J.M. Lafferty: *Foundations of Vacuum Science and Technology* (Wiley, New York 1998)

- [7.4] A.N. Nesmeyanov: *Vapor Pressure of the Elements* (Academic Press, New York 1963)
- [7.5] R.E. Honig, D.A. Kramer: *RCA Rev.* **30**, 285 (1969)
- [7.6] O. Stern, W. Gerlach: Der experimentelle Nachweis der Richtungsquantelung im Magnetfeld. Das magnetische Moment des Silberatoms. *Z. Physik* **9**, 349, 353 (1922)
- [7.7] I.I. Rabi, J.R. Zacharias, S. Millman, P. Kusch: A new method of measuring nuclear magnetic moment. *Phys. Rev.* **53**, 318 (1938)
- [7.8] N.F. Ramsey: A new molecular beamresonance method. *Phys. Rev.* **76**, 996 (1949); A molecular beam resonance method with separated oscillating fields. *Phys. Rev.* **78**, 695 (1950); Phase shifts in the molecular beam method of separated oscillating fields. *Phys. Rev.* **84**, 506 (1951)
- [7.9] M.G.H. Gustavsson, A.-M. Mårtensson-Pendrill: Four decades of hyperfine anomaly. *Adv. Quantum Chem.* **30**, 343 (1998)
- [7.10] C. Ekström, I. Lindgren: 'Atomic beam experiments at the ISOLDE facility at CERN.' In: *Atomic Physics 5*, ed. by R. Marrus, M. Prior, H. Shugart (Plenum, New York 1977) p. 201
- [7.11] C. Ekström: Spins and moments of nuclei far from stability determined by on-line atomic-beam techniques. *Adv. Quantum Chem.* **30**, 361 (1998)
- [7.12] W.J. Childs: Case Studies. *Atomic Phys.* **3**, 215 (1973)
- [7.13] S. Büttgenbach, G. Meisel, S. Penselin, K.H. Schneider: A new method for the production of atomic beams of highly refractory elements and first atomic beam magnetic resonances in Ta¹⁸¹. *Z. Physik* **230**, 329 (1970)
- [7.14] H. Rubinsztein, I. Lindgren, L. Lindström, H. Riedl, A. Rosén: Atomic beam measurements on refractory elements. *Nucl. Instrum. Methods* **119**, 269 (1974)
- [7.15] U. Brinkmann, J. Goschler, A. Steudel, H. Walther: Experimente mit Erdalkaliatomen in Metastabilen Zuständen. *Z. Physik* **228**, 427 (1969)
- [7.16] S. Garpman, G. Lidö, S. Rydberg, S. Svanberg: Lifetimes of some highly excited levels in the Pb-I spectrum measured by the Hanle method. *Z. Physik* **241**, 217 (1971)
- [7.17] S. Penselin: 'Recent developments and results of the atomic beam magnetic resonance method.' In: *Progress in Atomic Spectroscopy*, Pt. A, ed. by W. Hanle, H. Kleinpoppken (Plenum, New York 1979) p. 463
- [7.18] W.J. Childs: Overview of laser-radiofrequency double-resonance studies of atomic, molecular and ionic beams. *Phys. Rep.* **211**, 113 (1992)
- [7.19] A. Kastler: Quelques suggestions concernant la production optique et la détection optique d'une inégalité de population des niveaux de quantification spatiale des atomes. Application à l'expérience de Stern et Gerlach et à la résonance magnétique. *J. Phys. Radium* **11**, 255 (1950); Méthodes optiques d'étude de la résonance magnétique. *Physica* **17**, 191 (1951); Optical methods of atomic orientation and of magnetic resonance. *J. Opt. Soc. Am.* **47**, 460 (1957)
- [7.20] H.J. Besch, U. Köpf, E.W. Otten: Optical pumping of short-lived beta emitters. *Phys. Lett. B* **25**, 120 (1967)
- [7.21] E.W. Otten: 'Hyperfine and isotope shift measurements far from stability by optical pumping.' In: *Atomic Physics 5*, ed. by R. Marrus, M. Prior, H. Shugart (Plenum, New York 1977) p. 239
- [7.22] J. Bonn, G. Huber, H.J. Kluge, U. Köpf, L. Kugler, E.W. Otten, J. Rodrigues: 'Orientation of short-lived mercury isotopes by means of optical pumping detected by β and γ radiation.' In: *Atomic Physics 3*, ed. by S.J. Smith, G.K. Walters (Plenum, New York 1973) p. 471
- [7.23] R. Bernheim: *Optical Pumping* (Benjamin, New York 1965)

- [7.21] W. Happer: Optical pumping. *Rev. Mod. Phys.* **44**, 169 (1972)
- [7.22] G.W. Series: Thirty years of optical pumping. *Contemp. Phys.* **22**, 487 (1981)
- [7.23] M. Arditi, T.R. Carver: Optical detection of zero-field hyperfine structure in Na²³. *Phys. Rev.* **109**, 1012 (1958); Frequency shift of the zero-field hyperfine splitting of Cs¹³³ produced by various buffer gases. *Phys. Rev.* **112**, 449 (1958)
- [7.24] H.M. Goldenberg, D. Kleppner, N.F. Ramsey: Atomic hydrogen maser. *Phys. Rev. Lett.* **5**, 361 (1960)
D. Kleppner, H.M. Goldenberg, N.F. Ramsey: Properties of the hydrogen maser. *Appl. Opt.* **1**, 55 (1962)
S.B. Crampton, D. Kleppner, N.F. Ramsey: Hyperfine structure of ground state atomic hydrogen. *Phys. Rev. Lett.* **11**, 338 (1963)
- [7.25] P. Karpaschoff: *Frequency and Time* (Academic Press, London 1978)
H. Hellwig: Atomic frequency standards. *Proc. IEEE* **63**, 212 (1974)
J. Vanier, C. Audoin: *The Quantum Physics of Atomic Frequency Standards* (Hilger, Bristol 1989)
F.L. Walls: Frequency standards based on atomic hydrogen. *Proc. IEEE* **74**, 142 (1986)
D.J. Wineland: Frequency standards based on stored ions. *Proc. IEEE* **74**, 147 (1986)
Time and Frequency. Special issue of *Proc. IEEE* **79**(7) (1991)
W.M. Itano, N.F. Ramsey: Accurate measurement of time. *Sci. Am.* **269**(1), 56 (1993)
F.G. Mayor: *The Quantum Beat – The Physical Principles of Atomic Clocks* (Springer, Berlin, Heidelberg 1998)
P.F. Fisk: Trapped-ion and trapped-atom microwave frequency standards. *Rep. Prog. Phys.* **60**, 761 (1997)
- [7.26] Th.A. Herring: The global positioning system. *Sci. Am.* **274**(2) 32 (1996)
B. Hofmann-Wellenhof, H. Lichtenegger: *GPS Theory and Practice*, 4th edn. (Springer, Berlin, Heidelberg 1997)
- [7.27] G. Elgered, J.M. Johansson, B.O. Rönnäng, J.L. Davis: Measuring regional atmospheric water vapor using the Swedish permanent GPS network. *Geophys. Res. Lett.* **24**, 2663 (1997)
J.L. Davis, M.L. Cosmo, G. Elgered: ‘Using the Global Positioning System to study the atmosphere of the earth: Overview and prospects.’ In: *GPS Trends in Precise Terrestrial, Airborne, and Spaceborne Applications*, IAG Symposia, Vol. 115, ed. by G. Beutler, G.W. Hein, W.G. Melbourne, G. Seeber (Springer, Berlin 1996) p. 233
- [7.28] A. Kastler, J. Brossel: La détection de la résonance magnétique des niveaux excités: L’effet de dépolarisation des radiations de résonance optique et de fluorescence. *Comp. Rend.* **229**, 1213 (1949)
- [7.29] J. Brossel, F. Bitter: A new “double resonance” method for investigating atomic energy levels. Application to Hg ³P₁. *Phys. Rev.* **86**, 308 (1952)
- [7.30] G. Belin, I. Lindgren, I. Holmgren, S. Svanberg: Hyperfine interaction, Zeeman and Stark effects for excited states in potassium. *Phys. Scr.* **12**, 287 (1975)
- [7.31] W. Hanle: Über magnetische Beeinflussung der Polarisation der Resonanzfluoreszenz. *Z. Physik* **30**, 93 (1924); *Erg. Ex. Naturwiss.* **4**, 214 (1925)
- [7.32] F.D. Colgrove, P.A. Franken, R.R. Lewis, R.H. Sands: Novel method of spectroscopy with applications to precision fine structure measurements. *Phys. Rev. Lett.* **3**, 420 (1959)

- [7.33] G. Breit: Quantum theory of dispersion (continued). Pts. VI and VII. Rev. Mod. Phys. **5**, 91 (1933)
- [7.34] P. Franken: Interference effects in the resonance fluorescence of “crossed” excited states. Phys. Rev. **121**, 508 (1961)
- [7.35] T.G. Eck, L.L. Foldy, H. Wiedner: Observation of “anticrossings” in optical resonance fluorescence. Phys. Rev. Lett. **10**, 239 (1963)
H. Wiedner, T.G. Eck: “Anticrossing” signals in resonance fluorescence. Phys. Rev. **153**, 103 (1967)
H.J. Beyer, H. Kleinpoppen: ‘Anticrossing spectroscopy.’ In: *Progress in Atomic Spectroscopy*, Pt. A, ed. by W. Hanle, H. Kleinpoppen (Plenum, New York 1979) p. 607
- [7.36] G. Belin, S. Svanberg: Electronic g_J factors, natural lifetimes and electric quadrupole interaction in the $np\ ^2P_{3/2}$ series of the Rb I spectrum. Phys. Scr. **4**, 269 (1971)
- [7.37] R. Gupta, S. Chang, C. Tai, W. Happer: Cascade radio-frequency spectroscopy of excited S and D states of rubidium; anomalous D -state hyperfine structure. Phys. Rev. Lett. **29**, 695 (1972)
R. Gupta, W. Happer, L. Lam, S. Svanberg: Hyperfine structure measurements of excited S states of the stable isotopes of potassium, rubidium and cesium by cascade radio-frequency spectroscopy. Phys. Rev. A **8**, 2792 (1973)
- [7.38] M.E. Rose, R.L. Carovillano: Coherence effects in resonance fluorescence. Phys. Rev. **122**, 1185 (1961)
- [7.39] G. zu Putlitz: ‘Double resonance and level-crossing spectroscopy.’ In: *Atomic Physics*, ed. by V.W. Hughes, B. Bederson, V.W. Cohen, F.M.J. Pichanick (Plenum, New York 1969)
G. Moruzzi, F. Strumia (eds.): *The Hanle Effect and Level-Crossing Spectroscopy* (Plenum, New York 1991)
- [7.40] B. Budick: In: *Advances in Atomic and Molecular Physics*, ed. by R.D. Bates, I. Esterman (Academic Press, New York 1967)
- [7.41] W. Happer, R. Gupta: ‘Perturbed fluorescence spectroscopy.’ In: *Progress in Atomic Spectroscopy*, Pt. A, ed. by W. Hanle, H. Kleinpoppen (Plenum, New York 1979) p. 391
- [7.42] E. Arimondo, M. Inguscio, P. Violino: Experimental determinations of the hyperfine structure in the alkali atoms. Rev. Mod. Phys. **49**, 31 (1977)
- [7.43] P.R. Johnson, R. Pearson Jr.: *Methods in Experimental Physics*, Vol. 13, (Academic Press, New York 1976) p. 102
- [7.44] C.P. Slichter: *Principles of Magnetic Resonance*, 3rd edn. Springer Ser. Solid-State Sci., Vol. 1 (Springer, Berlin, Heidelberg 1990)
- [7.45] A.U. Rahman, M. Iqbal: *Solving Problems with NMR* (Academic Press, London 1995)
- [7.46] D.A. Skoog, D.M. West: *Principles of Instrumental Analysis* (Saunders, Philadelphia 1980)
- [7.47] R. Brewer, E.L. Hahn: Atomic memory. Sci. Am. **251**(6), 42 (1984)
- [7.48] H. Gunther: *NMR Spectroscopy – An Introduction* (Wiley, Chichester 1985)
- [7.49] D.A.R. Williams: *Nuclear Magnetic Resonance Spectroscopy* (Wiley, Chichester 1986)
- [7.50] W. Kemp: *NMR in Chemistry* (McMillan, London 1986)
- [7.51] I.L. Pykett: NMR imaging in medicine. Sci. Am. **246**(5), 54 (1982)
J. Mattson, M. Simon: *The Story of MRI* (Bar-Ilan University Press, Jericho, NY 1996)
- [7.52] D.R. Bailes, D.J. Bryant: NMR imaging. Contemp. Phys. **25**, 441 (1984)

- [7.53] R.S. MacKay: *Medical Images and Displays: Comparison of Nuclear Magnetic Resonance. Ultrasound, X-Rays and Other Modalities* (Wiley, New York 1984)
- [7.54] R.A. Robb: *Three-Dimensional Biomedical Imaging – Principles and Practice* (VCH, New York 1994)
- [7.55] C.N. Guy: The second revolution in medical imaging. *Contemp. Phys.* **37**, 15 (1996)
- [7.56] R. Kimmich: *NMR-Tomography, Diffusometry, Relaxometry* (Springer, Berlin, Heidelberg 1997)
- [7.57] M.S. Albert, G. Driehuys, W. Happer, B. Saam, C.S. Springer Jr., A. Wishniania: Biological magnetic resonanace imaging using laser-polarized Xe-129. *Nature* **370**, 199 (1994)
- W. Happer: 'Medical NMR sensing with laser polarized ^3He and ^{129}Xe .' In: *Atomic Physics Methods in Modern Research*, ed. by K. Jungmann et al. (Springer, Berlin, Heidelberg 1997) p. 121
- [7.58] M. Ebert, T. Grossmann, W. Heil, E.W. Otten, R. Surkau, M. Leduc, P. Bachert, M.V. Knopp, L.R. Schad, M. Thelen: MRI-imaging with hyperpolarized ^3He . *Lancet* **347**, 9011 (1996)
- [7.59] C.G. Aminoff, C. Larat, M. Leduc, B. Viana, D. Vivien: A powerful infrared laser for optical pumping of ^3He . *J. Lumin.* **50**, 21 (1991)
- [7.60] F.D. Colgrove, L. D Schearer, G.K. Walters: Polarization of ^3He gas by optical pumping. *Phys. Rev.* **132**, 2561 (1963)
- [7.61] M. Bouchiat, T.-R. Carver, C.M. Varnum: Nuclear polarization in ^3He gas induced by optical pumping and dipolar exchange. *Phys. Rev. Lett.* **5**, 373 (1960)
- [7.62] T.G. Walker, W. Happer: Spin-exchange optical pumping of noble-gas nuclei. *Rev. Mod. Phys.* **69**, 629 (1997)
- [7.63] J. Becker, W. Heil, B. Krug, M. Leduc, M. Meyerhoff, P.J. Nacher, E.W. Otten, Th. Prokscha, L.D. Schearer, R. Surkau: Study of mechanical compression of spin-polarized ^3He gas. *Nucl. Instrum. Methods A* **346**, 45 (1994)
- [7.64] W. Heil, H. Humblot, E.W. Otten, M. Schäfer, R. Surkau, M. Leduc: Very long relaxation times of spin-polarized ^3He in metal coated cells. *Phys. Lett. A* **201**, 337 (1995)
- [7.65] E.W. Otten: 'Interdisciplinary experiments with polarized noble gases.' In: *Atomic Physics 15*, ed. by H.B. van Linden van den Heuvell, J.T.M. Walraven, M.W. Reynolds, Amsterdam 1996 (World Scientific, Singapore 1997), p. 113
- E. Otten: 'Polarized, compressed ^3He gas and its applications.' In: *Atomic Physics Methods in Modern Research*, ed. by K. Jungmann et al. (Springer, Berlin, Heidelberg 1997) p. 105
- [7.66] P.D. Perry, Th.R. Carver, S.O. Sari, S.E. Schnatterly: Optically pumped and monitored electron-nuclear double resonance in alkali halides. *Phys. Rev. Lett.* **22**, 326 (1969)
- [7.67] R.S. Alger: *Electron Paramagnetic Resonance* (Wiley, New York 1968)
- [7.68] J.E. Wertz: *Electron Spin Resonance: Elementary Theory and Practical Applications* (Chapman and Hall, New York 1986)
- [7.69] T.K. Ishii (ed.): *Handbook of Microwave Technology*, Vols. 1, 2 (Academic Press, London 1995)
- [7.70] J.J. Davies: Optically detected magnetic resonance and its applications. *Contemp. Phys.* **17**, 275 (1976)
- [7.71] C.H. Townes, A.L. Schawlow: *Microwave Spectroscopy* (Dover, New York 1975)

- [7.72] H.W. Kroto: *Molecular Rotation Spectra* (Wiley, London 1975)
- [7.73] W. Gordy, R.L. Cook: *Microwave Molecular Spectra*, 3rd edn., Techniques of Chemistry, Vol. XVIII (Wiley, New York 1984)
- [7.74] T. Lund (ed.): Surveillance of environmental pollution and resources by electromagnetic waves. NATO Adv. St. Inst. Ser. (Reidel, Dordrecht 1978)
- [7.75] E. Schanda: *Physical Fundamentals of Remote Sensing* (Springer, Berlin, Heidelberg 1986)
- [7.76] D.T. Gjessing: Remote surveillance by electromagnetic waves for air - water - land (Ann Arbor Science, Ann Arbor 1978)
- [7.77] K.A. Browning: Uses of radar in metrology. *Contemp. Phys.* **27**, 499 (1986)
- [7.78] Ch.G. Collier: *Applications of Weather Radar Systems*, 2nd edn. (Wiley, New York 1996)
- [7.79] R.J. Doviak, D.S. Zrnic: *Doppler Radar and Weather Observation*, 2nd edn. (Academic Press, London 1993)
- [7.80] M.A. Janssens (ed.): *Atmospheric Remote Sensing by Microwave Radiometry* (Wiley, New York 1993)
- [7.81] E. Schanda: Microwave radiometry applications to remote sensing. In: [7.74]
- [7.82] E.P.W. Attema: The radar signature of natural surfaces and its application in active microwave remote sensing. In: [7.74]
- [7.83] Ch. Elachi: Radar images of the Earth from space. *Sci. Am.* **247**(6), 46 (1982)
- [7.84] W. Noack (ed.): *X-SAR Picture Book* (Springer, Berlin, Heidelberg 1996)
- [7.85] D.L. Evans, E.R. Stofan, T.J. Jones, L.M. Godwin: Earth from sky. *Sci. Am.* **271**(6), 44 (1994)
- [7.86] Courtesy: J. Askne, CTH
- [7.87] S. Haykin, E.O. Lewis, R.K. Raney, J.R. Rossiter: *Remote Sensing of Sea Ice and Icebergs* (Wiley, New York 1994)
- [7.88] A. Gustavsson, P.O. Frölin, H. Hellsten, T. Jonsson, B. Larsson, G. Stenström: *The airborne VHF SAR system CARABAS*. Proc. IEEE Geoscience Remote Sensing Symp., IGARSS'93, Tokyo, Japan, Vol. 2, pp. 558-562, August 1993
- [7.89] O.E.H. Rydbeck: 'Interstellar molecules.' In: *Kosmos 1974*, ed. by N.R. Nilsson (Swedish Phys. Soc., Stockholm 1975)
- [7.90] M. Elitzur: Physical characteristics of astronomical masers. *Rev. Mod. Phys.* **54**, 1225 (1982)
- [7.91] D.F. Dickinson: Cosmic masers. *Sci. Am.* **238**(6), 68 (1978)
- [7.92] A.W. Clegg, G.E. Nedoluka (eds.): *Astrophysical Masers* (Springer, Berlin, Heidelberg 1993)
- [7.93] M. Elitzur: Masers in the sky. *Sci. Am.* **272**(2), 52 (1995)
- [7.94] W.M. Irvine, P.F. Goldsmith, A. Hjalmarsson: 'Chemical abundances in molecular clouds.' In: *Interstellar Processes*, ed. by D.J. Hollenback, H.A. Thronson Jr. (Reidel, Dordrecht 1987)
- [7.95] G. Winnewisser, G.C. Pelz: *The Physics and Chemistry of Interstellar Molecular Clouds*, Springer Lecture Notes on Physics Vol. 459 (Springer, Berlin, Heidelberg 1995)
- [7.96] J. Lequeux, E. Roueff: Interstellar molecules. *Phys. Rep.* **200**, 241 (1991)
- [7.97] U.N. Rao, A. Weber (eds.): *Spectroscopy of the Earth's Atmosphere and Interstellar Medium* (Academic Press, London 1992)
- [7.98] A. Hewish, S.J. Bell, J.D.H. Pilkington, P.F. Scott, R.A. Collins: Observation of a rapidly pulsating radio source. *Nature* **217**, 709 (1968)
- [7.99] R.A. Hulse, J.H. Taylor: Discovery of a pulsar in a binary system. *Astrophys. J.* **195**, L51 (1975)

- [7.98] J.H. Taylor, L.A. Fowler, P.M. McCulloch: Measurements of general relativistic effects in the binary pulsar PSR 1913 + 16. *Nature* **277**, 437 (1979)
- [7.99] J. Dietrich: Realizing LIGO. *Engineering and Science* **64**(2), 8 (1998)
<http://www.ligo.caltech.edu/LIGO-web/about/factsheet.html>
<http://www.estec.esa.nl/spdwww/future/html/lisa.htm>
- [7.100] K. Rohlfs: *Tools of Radio Astronomy* (Springer, Berlin, Heidelberg 1986)
- [7.101] A.S. Webster, M.S. Longair: Millimetre and sub-millimetre astronomy. *Contemp. Phys.* **25**, 519 (1984)
- [7.102] A.C.S. Readhead: Radio astronomy and very long baseline interferometry. *Sci. Am.* **246**(6), 38 (1982)
- [7.103] A.R. Thompson, J. Moran, G.W. Swenson Jr.: *Interferometry and Synthesis in Radio Astronomy* (Wiley, New York 1986)
- [7.104] P. Morrison, J. Billingham, J. Wolfe: *The Search for Extraterrestrial Intelligence* (prepared by NASA) (Dover, New York 1979; Academic Press, New York 1986)
- [7.105] P. Horowitz, C. Sagan: Five year of project META: An all-sky narrow-band radio search for extraterrestrial signals. *Astrophys. J.* **415**, 218 (1993)
- [7.106] <http://www.nauts.com/vehicles/70s/pioneer10-11.html>

Chapter 8

- [8.1] A. Yariv: *Introduction to Quantum Electronics*, 2nd. edn. (Holt, Rinehart and Winston, New York 1976)
- [8.2] A. Yariv: *Quantum Electronics*, 3rd edn. (Wiley, New York 1989)
- [8.3] M. Sargent III, M.O. Scully, W.E. Lamb Jr.: *Laser Physics* (Addison Wesley, London 1974)
- [8.4] O. Svelto: *Principles of Lasers*, 4th edn. (Plenum, New York 1998)
- [8.5] A.E. Siegman: *Lasers* (University Science Books, Mill Valley, CA 1986)
- [8.6] H. Haken: *Laser Theory* (Springer, Berlin, Heidelberg 1983)
- [8.7] K. Shimoda: *Introduction to Laser Physics*, 2nd edn. Springer Ser. Opt. Sci., Vol. 44 (Springer, Berlin, Heidelberg 1984)
- [8.8] M. Young: *Optics and Lasers*, 3rd edn. Springer Ser. Opt. Sci., Vol. 5 (Springer, Berlin, Heidelberg 1986)
- [8.9] M.J. Weber (ed.): *CRC Handbook of Laser Science and Technology*, Vols. 1 and 2 (CRC Press, Boca Raton, FL 1982)
- [8.10] *Laser Handbook*, Vols. 1, 2, ed. by F.T. Arecchi, E.O. Schulz-Dubois (1972); Vol. 3, ed. by M.L. Stinch (1979); Vol. 4, ed. by M.L. Stinch, M. Bass (1985); Vol. 5, ed. by M. Bass, M.L. Stinch (1986) (North-Holland, Amsterdam)
- [8.11] P. Das: *Lasers and Optical Engineering* (Springer, Berlin, Heidelberg 1991)
- [8.12] W.T. Silfvast: *Laser Fundamentals* (Cambridge University Press, Cambridge 1996)
- [8.13] Ch.C. Davis: *Lasers and Electro-Optics* (Cambridge University Press, Cambridge 1996)
- [8.14] T.H. Maiman: Stimulated optical radiation in ruby. *Nature* **187**, 493 (1960)
- [8.15] A.L. Schawlow, C.H. Townes: Infrared and optical masers. *Phys. Rev.* **112**, 1940 (1958)
- [8.16] J.P. Gordon, H.J. Zeiger, Ch.H. Townes: The maser – new type of microwave amplifier, frequency standard and spectrometer. *Phys. Rev.* **99**, 1264 (1955)

- [8.17] C.H. Townes: In: *Nobel Lectures in Physics*, Vol. 4 (Elsevier, Amsterdam 1972)
- [8.18] N.G. Basov: In: *Nobel Lectures in Physics*, Vol. 4 (Elsevier, Amsterdam 1972)
- [8.19] A.M. Prokhorov: In: *Nobel Lectures in Physics*, Vol. 4 (Elsevier, Amsterdam 1972)
- [8.20] D.L. Matthews, P.L. Hagelstein, M.D. Rosen, M.J. Eckart, N.H. Ceglio, A.U. Hazi, H. Medicki, B.J. MacGowan, J.E. Trebes, B.L. Witt, E.M. Campbell, C.W. Hatcher, A.H. Hawryluk, R.L. Kaufmann, L.D. Pleasance, G. Rambach, J.H. Scofield, G. Stone, T.A. Weaver: Demonstration of a soft X-ray amplifier. *Phys. Rev. Lett.* **54**, 110 (1985); *J. Opt. Soc. Am.* **4**, 575 (1987)
- [8.21] D.L. Matthews, R.R. Freeman (eds.): The generation of coherent XUV and soft X-ray radiation. *J. Opt. Soc. Am. B* **4**, 529 (1987) (feature issue)
- [8.22] D.L. Matthews, M.D. Rosen: Soft X-ray lasers. *Sci. Am.* **256**(6), 60 (1988)
- [8.23] G. Tallents (ed.): *X-Ray Lasers*, IOP Conf. Ser. 116 (Institute of Physics Publ., Bristol 1990)
- [8.24] E.E. Fill (ed.): *X-Ray Lasers 1992*, IOP Conf. Ser. 125 (Institute of Physics Publ., Bristol 1992)
- [8.25] D.C. Eder, D.L. Matthews (eds.): *X-Ray Lasers 1994*, AIP Conf. Proc. Vol. 332 (AIP Press, New York 1994)
- [8.26] S. Svanberg, C.-G. Wahlström (eds.): *X-Ray Lasers 1996*, IOP Conf. Ser. Vol. 151 (Institute of Physics Publ., Bristol 1996)
- [8.27] Y. Kato, H. Takuma, H. Daido (eds.): *X-Ray Lasers 1998*, IOP Conf. Ser. 159 (Institute of Physics Publ., Bristol 1999)
- [8.28] H. Kogelnik, T. Li: Laser beams and resonators. *Proc. IEEE* **54**, 1312 (1966)
- [8.29] H.K.V. Lotsch: The confocal resonator system. *Optik* **30**, 1, 181, 217, 563 (1969/70)
- [8.30] N. Hodgson, H. Weber: *Optical Resonators* (Springer, Berlin, Heidelberg 1997)
- [8.31] G.D. Boyd, J.P. Gordon: Bell Syst. Tech. J. **40**, 489 (1961)
- [8.32] G.D. Boyd, H. Kogelnik: Bell Syst. Tech. J. **41**, 1347 (1962)
- [8.33] R.W. Hellwarth: 'Control of fluorescent pulsations.' In: *Advances in Quantum Electronics*, ed. by J.R. Singer (Columbia University Press, New York 1961) p. 334
- [8.34] F.J. McClung, R.W. Hellwarth: *J. Appl. Phys.* **33**, 828 (1962)
- [8.35] A. Szabo, R.A. Stein: Theory of laser giant pulsing by a saturable absorber. *J. Appl. Phys.* **36**, 1562 (1965)
- [8.36] S. Svanberg: Lasers as probes for air and sea. *Contemp. Phys.* **21**, 541 (1980)
- [8.37] W. Koechner: *Solid-State Laser Engineering*, 2nd edn. Springer Ser. Opt. Sci., Vol. 1 (Springer, Berlin, Heidelberg 1988)
- [8.38] D.C. Brown: *High-Peak-Power Nd:Glass Laser Systems*, Springer Ser. Opt. Sci., Vol. 25 (Springer, Berlin, Heidelberg 1981)
- [8.39] A.A. Kaminskii: *Laser Crystals*, 2nd edn. Springer Ser. Opt. Sci., Vol. 14 (Springer, Berlin, Heidelberg 1990)
- [8.40] D.N. Nikogosyan: *Properties of Optical and Laser Related Materials: A Handbook* (Wiley, New York 1997)
- [8.41] N. Hodgson, R. Wallenstein (eds.): *Solid State Lasers – New Developments and Applications* (Plenum, New York 1993)
- [8.42] A.F. Gibson: Lasers for compression and fusion. *Contemp. Phys.* **23**, 285 (1982)

- [8.39] R.S. Craxton, R.L. McCrory, J.M. Sources: Progress in laser fusion. *Sci. Am.* **255**(2), 60 (1986)
- [8.40] N.G. Basov, Yu.A. Zakharenkov, N.N. Zorev, G.V. Sklizkov, A.A. Rupasov, A.S. Shikanov: *Heating and Compression of Thermonuclear Targets by Laser Beams* (Cambridge University Press, Cambridge 1986)
- [8.41] J.E. Eggleston, T.J. Kane, K. Kuhn, J. Unternahrer, R.L. Byer: The slab geometry laser. *IEEE J. Quantum Electron.* **QE-20**, 289 (1984)
- [8.42] D. Findlay, D.W. Goodwin: 'The neodymium in YAG laser.' In: *Advances in Quantum Electronics*, Vol. 1, ed. by D.W. Goodwin (Academic Press, London 1970)
- [8.43] B. Zhou, T.J. Kane, G.J. Dixon, R.L. Byer: Efficient, frequency-stable laser-diode-pumped Nd:YAG laser. *Opt. Lett.* **10**, 62 (1985)
- A. Owyong, G.R. Hadley, P. Esherick: Gain switching of a monolithic single-frequency laser-diode-excited Nd:YAG laser. *Opt. Lett.* **10**, 484 (1985)
- W.R. Trutna, D.K. Donald, M. Nazarathy: Unidirectional diode-laser-pumped Nd:YAG ring laser with a small magnetic field. *Opt. Lett.* **12**, 248 (1987)
- [8.44] G.P.A. Malcolm, A.I. Ferguson: Diode-pumped solid-state lasers. *Contemp. Phys.* **32**, 305 (1991)
- [8.45] R.L. Byer, G.J. Dixon, T.J. Kane, W. Kozlovsky, B. Zhou: 'Frequency-doubled, laser diode pumped, miniature Nd:YAG oscillator – progress toward an all-solid state sub-kilohertz linewidth coherent source.' In: *Laser Spectroscopy VII*, ed. by T.W. Hänsch, Y.R. Shen, Springer Ser. Opt. Sci., Vol. 49 (Springer, Berlin, Heidelberg 1985) p. 350
- [8.46] D. Botez, D.R. Scifres (eds.): *Diode Laser Arrays* (Cambridge University Press, Cambridge 1994)
- [8.47] N.W. Carlson: *Monolithic Diode-Laser Arrays* (Springer, Berlin, Heidelberg 1994)
- [8.48] N.W. Carlson: *Diode Laser Arrays* (Springer Verlag, Heidelberg 1998)
- [8.49] C.K. Rhodes (ed.): *Excimer Lasers*, 2nd edn. Topics Appl. Phys., Vol. 30 (Springer, Berlin, Heidelberg 1984)
- [8.50] M.H.R. Hutchinson: Excimers and excimer lasers. *Appl. Phys.* **21**, 15 (1980)
- [8.51] C.K. Rhodes, H. Egger, H. Plummer (eds.): *Excimer Lasers*, Conf. Proc. Series No. 100 (Am. Inst. Phys., New York 1983)
- [8.52] Ch.E. Little: *Metal Vapour Lasers* (Wiley, New York 1998)
- I.G. Ivanov, E.L. Latush, M.F. Sem: *Metal Vapour Ion Lasers* (Wiley, New York 1996)
- I. Ivanov: *Metal Vapour Ion Lasers: Kinetic Processes and Gas Discharges* (Wiley, New York 1996)
- [8.53] A. Javan, W.R. Bennet Jr., D.R. Herriott: Population inversion and continuous optical maser oscillation in a gas discharge containing a He-Ne mixture. *Phys. Rev. Lett.* **6**, 106 (1961)
- [8.54] W.T. Silfvast, J.J. Macklin, O.R. Wood II: High-gain inner-shell photoionization laser in Cd vapor pumped by soft X-ray radiation from a laser produced plasma source. *Opt. Lett.* **8**, 551 (1983)
- W.T. Silfvast, O.R. Wood II: Photoionization lasers pumped by broadband soft-X-ray flux from laser-produced plasmas. *J. Opt. Soc. Am.* **4**, 609 (1987)
- [8.55] R.A. Lacy, A.C. Nilsson, R.L. Byer, W.T. Silfvast, O.R. Wood II, S. Svanberg: Photoionization-pumped gain at 185 nm in a laser-ablated indium plasma. *J. Opt. Soc. Am. B* **6**, 1209 (1989)

- [8.56] H.C. Kapteyn, R.W. Lee, R.W. Falcone: Observation of a short-wavelength laser pumped by Auger decay. *Phys. Rev. Lett.* **57**, 2939 (1986)
M.H. Sher, J.J. Macklin, J.F. Young, S.E. Harris: Saturation of the Xe III 109-nm laser using traveling-wave laser-produced-plasma excitation. *Opt. Lett.* **12**, 891 (1987)
- [8.57] C.C. Davis, T.A. King: 'Gaseous ion lasers.' In: *Advances in Quantum Electronics*, ed. by D.W. Goodwin (Academic Press, London 1975)
- [8.58] S.D. Smith, R.B. Dennis, R.G. Harrison: The spin-flip Raman laser. *Prog. Quantum Electron.* **5**, 205 (1977)
- [8.59] M.J. Colles, C.R. Pigeon: Tunable lasers. *Rep. Prog. Phys.* **38**, 329 (1975)
- [8.60] A. Mooradian: Tunable infrared lasers. *Rep. Prog. Phys.* **42**, 1533 (1979)
- [8.61] J. White, L. Mollenauer (eds.): *Tunable Lasers*, Topics Appl. Phys., Vol. 59 (Springer, Berlin, Heidelberg 1986)
- [8.62] F.J. Duarte: *Tunable Lasers Handbook* (Academic Press, New York 1996)
- [8.63] P.P. Sorokin, J.R. Lankard: Stimulated emission observed from an organic dye, chloro-aluminium phthalocyanine. *IBM J. Res. Dev.* **10**, 162 (1966)
- [8.64] F.P. Schäfer, W. Schmidt, J. Volze: Organic dye solution laser. *Appl. Phys. Lett.* **9**, 306 (1966)
- [8.65] B.H. Soffer, B.B. McFarland: Continously tunable narrow-band organic dye laser. *Appl. Phys. Lett.* **10**, 266 (1967)
- [8.66] T.W. Hänsch: Repetitively pulsed tunable dye laser for high resolution spectroscopy. *Appl. Opt.* **11**, 895 (1972)
- [8.67] M.G. Littman, H.J. Metcalf: Spectrally narrow pulsed dye laser without beam expander. *Appl. Opt.* **25**, 375 (1978)
I. Shoshan, U. Oppenheim: The use of a diffraction grating as a beam expander in a dye laser cavity. *Opt. Commun.* **25**, 375 (1978)
M.G. Littman: Single-mode operation of grazing incidence pulsed dye laser. *Opt. Lett.* **3**, 138 (1978)
H.S. Saikan: Nitrogen laser pumped single mode dye laser. *Appl. Phys.* **17**, 41 (1978)
M.G. Littman: Single-mode pulsed tunable dye laser. *Appl. Opt.* **23**, 4465 (1984)
- [8.68] R. Wallenstein, T.W. Hänsch: Powerful dye laser oscillator-amplifier system for high-resolution spectroscopy. *Opt. Commun.* **14**, 353 (1975)
R. Wallenstein, H. Zacharias: High-power narrowband pulsed dye laser oscillator-amplifier system. *Opt. Commun.* **32**, 429 (1980)
- [8.69] T.F. Johnston: 'Tunable dye lasers.' In: *Encyclopedia of Physical Science and Technology*, Vol. 14 (Academic Press, New York 1987)
- [8.70] T.F. Johnston, R.H. Brady, W. Proffitt: Powerful single-frequency ring dye laser spanning the visible spectrum. *Appl. Opt.* **21**, 2307 (1982)
- [8.71] O.G. Peterson, S.A. Tuccio, B.B. Snavely: CW operation of an organic dye solution laser. *Appl. Phys. Lett.* **17**, 245 (1970)
- [8.72] J. Evans: The birefringent filter. *J. Opt. Soc. Am.* **39**, 229 (1949)
F.P. Schäfer (ed.): *Dye Lasers*, 3rd edn., Topics Appl. Phys., Vol. 1 (Springer, Berlin, Heidelberg 1990)
- [8.73] M. Stuke (ed.): *Dye Lasers: 25 Years* (Springer Verlag, Berlin, Heidelberg 1992)
- [8.74] M. Maeda: *Laser Dyes* (Academic Press, Orlando 1984)
K. Brackman: Lambdachrome Laser Dyes (Lambda Physik, Göttingen 1986)
- [8.75] L.F. Mollenauer: 'Tunable lasers.' In: [8.61], Chap. 6
L.F. Mollenauer: In: [8.10], Vol. 4, Chap. 2

- [8.76] P.F. Moulton: Spectroscopic and laser characteristics of Ti:Al₂O₃. *J. Opt. Soc. Am. B* **3**, 125 (1986)
- P. Albers, E. Stark, G. Huber: Continous-wave laser operation and quantum efficiency of titanium-doped sapphire. *J. Opt. Soc. Am. B* **3**, 134 (1986)
- [8.77] Courtesy: D.T. Reid and W. Sibbett, University of St. Andrews
- [8.78] R.L. Byer (ed.): Special issue on tunable solid state lasers. *IEEE J. Quantum Electron.* **QE-21**, 1567–1636 (1985)
- B. Henderson, G.F. Imbusch: Optical processes in tunable transition-metal-ion lasers. *Contemp. Phys.* **29**, 235 (1988)
- [8.79] P. Hammerling, A.B. Budgor, A. Pinto (eds.): *Tunable Solid-State Lasers*, Springer Ser. Opt. Sci., Vol. 47 (Springer, Berlin, Heidelberg 1985)
- A.B. Budgor, L. Esterowitz, L.G. DeShazer (eds.): *Tunable Solid-State Lasers II*, Springer Ser. Opt. Sci., Vol. 52 (Springer, Berlin, Heidelberg 1986)
- [8.80] D.C. Tyle: ‘Carbon dioxide lasers.’ In: *Advances in Quantum Electronics*, Vol. 1, ed. by D.W. Goodwin (Academic Press, New York 1970)
- [8.81] W.J. Witteman: *The CO₂ Laser*, Springer Ser. Opt. Sci., Vol. 53 (Springer, Berlin, Heidelberg 1987)
- [8.82] F. O’Neill, W.T. Whitney: A high-power tunable laser for the 9–12.5 μm spectral range. *Appl. Phys. Lett.* **31**, 271 (1977)
- [8.83] R. Beck, W. Englisch, K. Gürs: *Table of Laser Lines in Gases and Vapors*, 3rd edn., Springer Ser. Opt. Sci., Vol. 2 (Springer, Berlin, Heidelberg 1978)
- [8.84] M.J. Weber: *Handbook of Laser Wavelengths* (CRC Press, Boca Raton 1999)
- [8.85] N.G. Basov, O.N. Krokhin, Y.M. Popov: Production of negative temperature states in *p-n* junctions of degenerate semiconductors. *JETP* **13**, 1320 (1961)
- R.N. Hall, G.E. Fenner, J.D. Kingsley, T.S. Soltys, E.O. Carlson: Coherent light emission from GaAs junctions. *Phys. Rev. Lett.* **9**, 366 (1962)
- M.I. Nathan, W.P. Dumke, G. Burns, F.D. Hill Jr., G.J. Lasher: Stimulated emission of radiation from GaAs *p-n* junctions. *Appl. Phys. Lett.* **1**, 62 (1962)
- T.M. Quist, R.H. Rediker, R.J. Keyes, W.E. Krag, B. Lax, A.L. McWhorter, H.J. Zeiger: Semiconductor maser of GaAs. *Appl. Phys. Lett.* **1**, 91 (1962)
- [8.86] R.M. Measures: *Laser Remote Sensing: Fundamentals and Applications* (Wiley, New York 1984)
- [8.87] Zh.I. Alferov, R.F. Kazarinov: Semiconductor laser with electric pumping. Sov. patent appl. 950 840 (1963)
- Zh.I. Alferov et al.: AlAs-GaAs heterojunction lasers with a low room-temperature threshold. *Sov. Phys. Semicond.* **3**, 1107 (1969)
- [8.88] H. Kroemer: A proposed class of heterojunction injection lasers. *Proc. IEEE* **51**, 1782 (1963)
- H.G. Grimmeiss (ed.): Heterostructures in Semiconductors. *Phys. Scr.* **T68**, Nr. 4 (1996)
- [8.89] J. Hecht: Laser Focus World, May 1992
- [8.90] Courtesy: Fiberguide Industries, Stirling, NJ, USA
- [8.91] E. Desurvire: *Erbium-Doped Fiber Amplifiers* (Wiley, New York 1994)
- [8.92] N. Holonyak Jr., S.F. Bevacqua: Coherent visible light emission from Ga(As_{1-x}P_x) junctions. *Appl. Phys. Lett.* **1**, 82 (1982)
- [8.93] S. Nakamura, G. Fasol: *The Blue Laser Diode* (Springer, Heidelberg 1997)

- [8.94] K. Iga, F. Koyama, S. Kinoshita: Surface emitting semiconductor lasers. *IEEE J. Quantum Electron.* **QE-24**, 1845 (1988)
- M. Grabherr, R. Jäger, R. Michalzik, B. Weigl, G. Reiner, K.J. Ebeling: Efficient single-mode oxide-confined GaAs VCSELs emitting in the 850 nm wavelength regime. *IEEE Photonics Technol. Lett.* **9**, 1304 (1997)
- [8.95] J. Faist, F. Capasso, D.L. Sivco, C. Sirtori, A.L. Hutchinson, A.Y. Cho: Quantum cascade laser. *Science* **264**, 553 (1994)
- F. Capasso, J. Faist, C. Sirtori, A.Y. Cho: Infrared (4–11 μm) quantum cascade lasers. *Solid State Commun.* **102**, 231 (1997)
- K. Namjou, S. Cai, E.A. Whittaker, J. Faist, F. Capasso, C. Gmachl, D.L. Sivco, A.Y. Cho: Sensitive absorption spectroscopy using room temperature distributed-feedback quantum cascade lasers. *Opt. Lett.* **23**, 219 (1998)
- [8.96] H. Kressel, J.K. Butler: *Semiconductor Lasers and Hetero junction LEDs* (Academic Press, New York 1977)
- H.C. Lasey, M.B. Panish: *Heterostructure Lasers I and II* (Academic Press, New York 1978)
- [8.97] G.P. Agarwal, N.K. Dutta: *Semiconductor Lasers* (Van Nostrand Reinhold, New York 1993)
- [8.98] G.P. Agarwal (ed.): *Semiconductor Lasers* (AIP Press, Melville, NY 1995)
- [8.99] W.W. Chow, S.W. Koch, M. Sargent III: *Semiconductor Laser Physics* (Springer, Berlin, Heidelberg 1994)
- [8.100] J.C. Camparo: The diode laser in atomic physics. *Contemp. Phys.* **26**, 443 (1985)
- [8.101] E.D. Hinkley, K.W. Nill, F.A. Blum: ‘Infrared spectroscopy with tunable lasers.’ In: *Laser Spectroscopy of Atoms and Molecules*, ed. by H. Walther, *Topics Appl. Phys.*, Vol. 2 (Springer, Berlin, Heidelberg 1976)
- [8.102] C.E. Wieman, L. Hollberg: Using diode lasers for atomic physics. *Rev. Sci. Instrum.* **62**, 1 (1991)
- K.B. MacAdam, A. Steinbach, C. Wieman: A narrow-band tunable diode laser system with grating feedback, and a saturated absorption spectrometer for Cs and Rb. *Am. J. Phys.* **60**, 1098 (1992)
- L. Ricci, M. Weidmüller, T. Esslinger, A. Herrerich, C. Zimmermann, V. Vuletic, W. König, T.W. Hänsch: A compact grating-stabilized diode laser system for atomic physics. *Opt. Commun.* **117**, 541 (1995)
- U. Gustafsson, J. Alnis, S. Svanberg: Atomic spectroscopy with violet laser diodes. *Am. J. Phys.* **68**, 660 (2000)
- [8.103] H.I. Schiff, G.I. Macay, J. Bechara: ‘The use of tunable diode laser absorption spectroscopy for atmospheric measurements.’ In: *Air Monitoring by Spectroscopic Techniques*, ed. by M.W. Sigrist, Chemical Physics Series Vol. 127 (John Wiley, New York 1994) p. 239
- P. Werle: Spectroscopic trace gas analysis using semiconductor diode lasers. *Spectrochim. Acta A* **52**, 805 (1996)
- P. Ljung, O. Axner: Measurements of rubidium in standard reference samples by wavelength-modulation diode laser absorption spectrometry in a graphite furnace. *Spectrochim. Acta B* **52**, 305 (1997)
- A. Zybin, C. Schnürer-Patschan, M.A. Bolshov, K. Niemax: Elemental analysis by diode laser spectroscopy. *Trends Anal. Chem.* **17**, 513 (1998)
- T. Imasaka: Analytical molecular spectroscopy with diode lasers. *Spectrochim. Acta Rev.* **15**, 329 (1993)
- A.W. Mantz: A review of spectroscopic applications of tunable semiconductor lasers. *Spectrochim. Acta A* **51**, 221 (1995)

- A.W. Mantz: A review of the applicability of tunable diode-laser spectroscopy at high sensitivity. *Microchem. J.* **50**, 351 (1994)
- [8.104] T.F. Johnston Jr., T.J. Johnston: 'Angle matched doubling in LiIO_3 intracavity to a ring dye laser.' In: *Laser Spectroscopy VI*, ed. by H.P. Weber, W. Lüthy, Springer Ser. Opt. Sci., Vol. 40 (Springer, Berlin, Heidelberg 1983) p. 417
- [8.105] B. Couillaud, L.A. Bloomfield, T.W. Hänsch: Generation of continuous-wave radiation near 243 nm by sum frequency mixing in an external ring cavity. *Opt. Lett.* **8**, 259 (1983)
- [8.106] A.S. Pine: 'IR Spectroscopy via difference-frequency generation.' In: *Laser Spectroscopy III*, ed. by J.L. Hall, J.L. Carlsten, Springer Ser. Opt. Ser., Vol. 7 (Springer, Berlin, Heidelberg 1977) p. 376
- [8.107] S. Singe: In *Handbook of Laser Science and Technology*, Vol. 3, ed. by M.J. Weber (CRC Press, Boca Raton, FL 1986)
- [8.108] D.S. Chemla, J. Zyss (eds.): *Nonlinear Optical Properties of Organic Molecules and Crystals*, Vols. 1, 2 (Academic Press, Orlando 1987)
- [8.109] R.C. Eckardt, Y.X. Fan, M.M. Fejer, W.J. Kozlovsky, C.N. Nabors, R.L. Byer, R.K. Route, R.S. Feigelson: 'Recent developments in nonlinear optical materials.' In: *Laser Spectroscopy VIII*, ed. by W. Persson, S. Svanberg, Springer Ser. Opt. Sci., Vol. 55 (Springer, Berlin, Heidelberg 1987) p. 426
- [8.110] V.G. Dmitriev, G.G. Gurzadyan, D.N. Nikogosyan: *Handbook of Nonlinear Optical Crystals*, Springer Ser. Opt. Sci., Vol. 64 (Springer, Berlin, Heidelberg 1991)
- [8.111] J. Webjörn, F. Laurell, G. Arvidsson: Blue light generated by frequency-doubling of laser diode light in a lithium niobate channel waveguide. *IEEE Photonics Technol. Lett.* **1**, 316 (1989)
- [8.112] U. Simon, S. Waltman, I. Loa, L. Hollberg, F. Tittel: *J. Opt. Soc. Am. B* **12**, 323 (1995)
- [8.113] M. Yamada, N. Nata, M. Saitoh, K. Watanabe: First-order quasi-phase matched LiNbO_3 waveguide. *Appl. Phys. Lett.* **62**, 435 (1993)
- [8.114] S.E. Harris: Tunable optical parametric oscillators. *Proc. IEEE* **57**, 2096 (1969)
- [8.115] Y.X. Fan, R.L. Byer: Progress in optical parametric oscillators. *SPIE Int. Soc. Opt. Eng.* **461**, 27 (1984)
- [8.116] R. Zerne, J. Larsson, S. Svanberg: Determination of radiative lifetimes in the $3d^{10}np\ 2P$ sequence of neutral copper by time-resolved VUV laser spectroscopy. *Phys. Rev. A* **49**, 128 (1994)
- [8.117] J. Larsson, R. Zerne, A. Persson, C.-G. Wahlström, S. Svanberg: Determination of radiative lifetimes in the $3snp\ 1P_1$ sequence of Mg I using time-resolved VUV spectroscopy. *Z. Physik D* **27**, 329 (1993)
- R. Hilbig, G. Hilber, A. Lago, B. Wolff, R. Wallenstein: Tunable coherent VUV radiation generated by nonlinear optical frequency conversion in gases. *Comments At. Mol. Phys.* **18**, 157 (1986)
- R. Hilbig, G. Hilber, A. Timmermann, R. Wallenstein: 'Generation of coherent tunable VUV radiation.' In: *Laser Spectroscopy VI*, ed. by H.P. Weber, W. Lüthy, Springer Ser. Opt. Sci., Vol. 40 (Springer, Berlin, Heidelberg, Berlin 1983) p. 387
- G. Hilber, A. Lago, R. Wallenstein: 'Generation and application of coherent tunable VUV radiation at 60 to 200 nm.' In: *Laser Spectroscopy VIII*, ed. by W. Persson, S. Svanberg, Springer Ser. Opt. Sci., Vol. 55 (Springer, Berlin, Heidelberg 1987) p. 446

- [8.118] P.P. Sorokin, J.A. Armstrong, R.W. Dreyfus, R.T. Hodgeson, J.R. Landkard, L.H. Manganaro, J.J. Wynne: 'Generation of vacuum ultraviolet radiation by non-linear mixing in atomic and ionic vapors.' In: *Laser Spectroscopy*, ed. by S. Haroche, J.C. Pebay-Peyroula, T.W. Hänsch, S.E. Harris, Lecture Notes Phys., Vol. 43 (Springer, Berlin, Heidelberg 1975) p. 46
 J.F. Rentjes: *Nonlinear Optical Parametric Processes in Liquids and Gases* (Academic Press, New York 1984)
 W. Jamroz, B.P. Stoicheff: Generation of tunable coherent vacuum-ultraviolet radiation. *Progress in Optics XX*, Vol. 325 (North-Holland, Amsterdam 1983)
- [8.119] C.R. Vidal: Coherent VUV sources for high-resolution spectroscopy. *Appl. Opt.* **19**, 3897 (1980)
- [8.120] T.J. McIlrath, R.R. Freeman (eds.): *Laser Techniques for Extreme Ultraviolet Spectroscopy*, Conf. Proc. Series, No. 90 (Am. Inst. Phys., New York 1982)
- [8.121] S.E. Harris, T.B. Lucatorto (eds.): *Laser Techniques in the Extreme Ultraviolet*, Conf. Proc. Series, No. 119 (Am. Inst. Phys., New York 1984)
- [8.122] D.T. Attwood, J. Bokor (eds.): *Short Wavelength Coherent Radiation: Generation and Application*, Conf. Proc. Series, No. 147 (Am. Inst. Phys., New York 1986)
- [8.123] R.W. Falcone, J. Kirz (eds.): *Short Wavelength Coherent Radiation: Generation and Applications* (Opt. Soc. Am., Washington, DC 1988)
 C. Yamanaka (ed.): *Short-Wavelength Lasers*, Springer Proc. Phys., Vol. 30 (Springer, Berlin, Heidelberg 1988)
- [8.124] S. Svanberg, A. L'Huillier, C.-G. Wahlström: Atomic physics using short-wavelength coherent radiation. *Nucl. Instrum. Methods Phys. Res. A* **398**, 55 (1997)
 S. Svanberg: High-power lasers and their applications. *Adv. Quantum Chem.* **30**, 209 (1998)
 U. Berzinsh, S. Svanberg: Atomic radiative lifetimes measured by pulsed laser spectroscopy in the UV/VUV spectral region. *Adv. Quantum Chem.* **30**, 283 (1998)
- [8.125] B. Ya Zeldovich, V.I. Popovichev, V.V. Ragulsky, F.S. Faizullov: Connection between the wavefronts of the reflected and exciting light in stimulated Mandelstam-Brillouin scattering. *ZhETF Pis. Red.* **15**, 160 (1972); *JETP Lett.* **15**, 109 (1972)
 O.Yu. Nosach, V.I. Popovichev, V.V. Ragulsky, F.S. Faizullov: Cancellation of phase distortions in an amplifying medium with a Brillouin mirror. *ZhETF Pis. Red.* **16**, 617 (1972); *JETP Lett.* **16**, 435 (1972)
- [8.126] R.W. Hellwarth: Generation of time-reversed wave fronts by nonlinear refraction. *J. Opt. Soc. Am.* **67**, 1 (1977)
 A. Yariv: On transmission and recovery of three-dimensional image information in optical waveguides. *J. Opt. Soc. Am.* **66**, 301 (1976)
- [8.127] B.Ya. Zel'dovich, N.F. Pilipetsky, V.V. Shkunov: *Principles of Phase Conjugation*, Springer Ser. Opt. Sci., Vol. 42 (Springer, Berlin, Heidelberg 1985)
 V.V. Shkunov, B.Ya. Zel'dovich: Optical phase conjugation. *Sci. Am.* **253**(6), 40 (1985)
 D.M. Pepper: Applications of optical phase conjugation. *Sci. Am.* **254**(1), 56 (1986)
- [8.128] H.J. Eichler, P. Gunther, D.W. Pohl: *Laser Induced Dynamic Gratings*, Springer Ser. Opt. Sci., Vol. 50 (Springer, Berlin, Heidelberg 1986)

- [8.129] M.C. Gower, D. Proch (eds.): *Optical Phase Conjugation* (Springer, Berlin, Heidelberg 1994)
- [8.130] D.T. Hon: Pulse compression by stimulated Brioullin scattering. *Opt. Lett.* **5**, 516 (1980)
- [8.131] S. Schiemann, W. Ubachs, W. Hogervorst: Efficient temporal compression of coherent ns-pulses in a compact SBS generator-amplifier setup. *IEEE J. Quantum Electron.* **33**, 358 (1997); Fourier-transform-limited laser pulses tunable in wavelength and in duration (400–2000 ps), *ibid.* **34**, 407 (1998)
- [8.132] Z.-S. Li, J. Norin, A. Persson, C.-G. Wahlström, S. Svanberg, P.S. Doidge, E. Biémont: Radiative properties of neutral germanium obtained from excited state lifetime and branching ratio measurements and comparison with theoretical calculations. *Phys. Rev. A* **60**, 198 (1999)
- [8.133] V. Wilke, W. Smidt: Tunable coherent radiation source covering a spectral range from 185–880 nm. *Appl. Phys.* **18**, 177 (1979); see also *Appl. Phys.* **18**, 235 (1979)
- [8.134] J. Paisner, S. Hargrove: ‘A tunable laser system for UV, visible, and IR regions.’ In: *Energy and Technology Review* (Lawrence Livermore Nat’l Lab., Livermore 1979)
A.P. Hickman, J.A. Paisner, W.K. Bishel: Theory of multiwave propagation and frequency conversion in a Raman medium. *Phys. Rev. A* **33**, 1788 (1986)
- [8.135] F. Moya, S.A.J. Druet, J.P. Taran: ‘Rotation-vibration spectroscopy of gases by coherent anti-Stokes Raman scattering: Application to concentration and temperature measurements.’ In: *Laser Spectroscopy*, ed. by S. Haroche, J.C. Pebay Peyroula, T.W. Hänsch, S.E. Harris (Springer, Berlin, Heidelberg 1975)
- [8.136] M. Aldén, H. Edner, S. Svanberg: Coherent anti-Stokes Raman spectroscopy (CARS) applied to combustion probing. *Phys. Scr.* **27**, 29 (1983)
- [8.137] A.C. Eckbreth: BOXCARS: Crossed beam phase-matched CARS generation in gases. *Appl. Phys. Lett.* **32**, 421 (1978)
- [8.138] N. Bloembergen: *Nonlinear Optics* (Benjamin, New York 1977)
- [8.139] Y.R. Shen: *The Principles of Nonlinear Optics* (Wiley, New York 1984)
- [8.140] M. Schubert, B. Wilhelmi: *Nonlinear Optics and Quantum Electronics, Theoretical Concepts* (Wiley, New York 1986)
- [8.141] P.N. Butcher, D. Cotter: *The Elements of Nonlinear Optics* (Cambridge University Press, Cambridge 1990)
- [8.142] R.W. Boyd: *Nonlinear Optics* (Academic Press, San Diego 1992)
- [8.143] E.G. Sauter: *Nonlinear Optics* (Wiley, New York 1996)
- [8.144] V.S. Letokhov, V.P. Chebotayev: *Nonlinear Laser Spectroscopy*, Springer Ser. Opt. Sci., Vol. 4 (Springer, Berlin, Heidelberg 1977)
- [8.145] M.D. Levenson, S. Kano: *Introduction to Nonlinear Spectroscopy*, 2nd edn. (Academic Press, New York 1988)
- [8.146] H. Mocker, R.J. Collins: Mode competition and self-locking effects in a Q-switched ruby laser. *Appl. Phys. Lett.* **7**, 270 (1965)
A.J. De Maria, D.A. Stetser, H. Heynau: Self mode-locking of lasers with saturable absorbers. *Appl. Phys. Lett.* **8**, 174 (1966)
- [8.147] E.P. Ippen, C.V. Shank, A. Dienes: Passive mode-locking of the CW dye laser, *Appl. Phys. Lett.* **21**, 348 (1972)
- [8.148] R.L. Fork, B.I. Greene, C.V. Shank: Generation of optical pulses shorter than 0.1 ps by colliding pulse mode-locking, *Appl. Phys. Lett.* **38**, 671 (1981)

- [8.149] R.L. Fork, C.H. Brito Cruz, P.C. Becker, C.V. Shank: Compression of optical pulses to six fs by using cubic phase compression, *Opt. Lett.* **12**, 483 (1987)
- [8.150] L. Xu, C. Spielmann, F. Krausz, R. Szipöcs: Ultrabroadband ring oscillator for sub-10-fs pulse generation. *Opt. Lett.* **21**, 1259 (1996)
- [8.151] D.E. Spence, P.N. Kean, W. Sibbett: 60 fs pulse generation from a self-mode-locked Ti:sapphire laser. *Opt. Lett.* **16**, 42 (1991)
- [8.152] U. Morgner, F.X. Kärtner, S.H. Cho, Y. Shen, H.A. Haus, J.G. Fujimoto, E.P. Ippen, V. Scheuer, G. Angelow, T. Tschudi: *Opt. Lett.* **24**, 411 (1999)
- [8.153] D.H. Sutter, G. Steinmeyer, L. Gallman, N. Matuschek, F. Morier-Genoud, U. Keller, V. Scheuer, G. Angelow, T. Tschudi: Semiconductor saturable-absorber mirror-assisted Kerr-lens mode-locked Ti:sapphire laser producing pulses in the two-cycle regime. *Opt. Lett.* **24**, 631 (1999)
- [8.154] A. Baltuska, Z. Wei, M.S. Pshenichnikov, D.A. Wiersma: Optical pulse compression to 5 fs at a 1-MHz repetition rate. *Opt. Lett.* **22**, 102 (1997)
- [8.155] M. Nisoli, S. De Silvestri, O. Svelto, R. Szipöcs, F. Ferencz, Ch. Spielmann, S. Sartania, F. Krausz: Compression of high-energy laser pulses below 5 fs. *Opt. Lett.* **22**, 522 (1997)
- [8.156] G.H.C. New: The generation of ultrashort laser pulses. *Rep. Prog. Phys.* **46**, 877 (1983)
- [8.157] S. de Silvestri, P. Laporta, V. Magni: Generation and applications of femtosecond laser pulses. *Europhys. News* **17**(9), 105 (1986)
- [8.158] T.F. Johnston Jr.: 'Tunable dye lasers.' In: *Encyclopedia of Physical Science and Technology*, Vol. 14 (Academic Press, New York 1987)
- [8.159] B. Couillaud, V. Fossati-Bellani: Modelocked lasers and ultrashort pulses. *Lasers & Appl.* (January 1985) pp. 79–83 and (February 1985) pp. 91–94
- [8.160] S.L. Shapiro (ed.): *Ultrashort Light Pulses*, 2nd edn. *Topics Appl. Phys.*, Vol. 18 (Springer, Berlin, Heidelberg 1984)
- [8.161] W. Kaiser (ed.): *Ultrashort Laser Pulses and Applications*, 2nd edn. *Springer Ser. Opt. Sci.*, Vol. 60 (Springer, Berlin, Heidelberg 1993)
- [8.162] P.M.W. French: The generation of ultrashort laser pulses. *Rep. Prog. Phys.* **58**, 169 (1995)
- [8.163] I.N. Duling III (ed.): *Compact Sources of Ultrashort Pulses* (Cambridge University Press, Cambridge 1995)
- [8.164] J.-C. Diels, W. Rudolph: *Ultrashort Laser Pulse Phenomena* (Academic Press, San Diego 1996)
- [8.165] C. Rullières (ed.): *Femtosecond Laser Pulses* (Springer, Berlin, Heidelberg 1998)
- [8.166] D. Strickland, G. Mourou: Compression of amplified chirped optical pulses. *Opt. Commun.* **56**, 219 (1985)
- [8.167] P. Maine, D. Strickland, P. Bado, M. Pessot, G. Mourou: Generation of ultrahigh peak power pulses by chirped pulse amplification. *IEEE J. Quantum Electron.* **QE-24**, 398 (1988)
- [8.168] S. Svanberg, J. Larsson, A. Persson, C.-G. Wahlström: Lund High-Power Laser Facility - Systems and first results, *Phys. Scr.* **49**, 187 (1994)
- [8.169] M.H.R. Hutchinson: Terawatt lasers. *Contemp. Phys.* **30**, 355 (1989)
- [8.170] M.D. Perry, G. Mourou: Terawatt to petawatt subpicosecond lasers, *Science* **264**, 917 (1994)
- [8.171] M.D. Perry, D. Pennington, B.C. Stuart, G. Tietbohl, J.A. Britten, C. Brown, S. Herman, B. Golick, M. Kartz, J. Miller, H.T. Powell, M. Vergino, V. Yanovsky: Petawatt laser pulses. *Opt. Lett.* **24**, 160 (1999)
- [8.172] M.D. Perry, R.D. Boyd, J.A. Britten, D. Decker, B.W. Shore, C. Shannon,

- E. Shults: High-efficiency multi-layer dielectric diffraction gratings. *Opt. Lett.* **20**, 940 (1995)
- [8.164] S. Backus, Ch.G. Durfee III, M.M. Murnane, H.C. Kapteyn: High power ultrafast lasers. *Rev. Sci. Instrum.* **69**, 1207 (1998)
- [8.165] C.P.J. Barty, W. White, W. Sibbett, R. Trebino (eds.): *Ultrafast Optics*. IEEE J. Sel. Top. Quantum Electron. **4**, No. 2 (1998)

Chapter 9

- [9.1] W. Demtröder: *Laser Spectroscopy*, 3rd edn. (Springer, Berlin, Heidelberg 2003)
- [9.2] A. Corney: *Atomic and Laser Spectroscopy* (Clarendon, Oxford 1977)
- [9.3] L.J. Radziemski, R.W. Solarz, J.A. Paisner (eds.): *Laser Spectroscopy and its Applications* (Dekker, New York 1987)
- [9.4] V.S. Letokhov, V.P. Chebotayev: *Nonlinear Laser Spectroscopy*, Springer Ser. Opt. Sciences, Vol. 4 (Springer, Berlin, Heidelberg 1977)
- [9.5] M.D. Levenson, S. Kano: *Introduction to Nonlinear Spectroscopy*, revised edn. (Academic Press, New York 1988)
- [9.6] Y.R. Shen: *The Principles of Nonlinear Optics* (Wiley, New York 1984)
- [9.7] M. Schubert, B. Wilhelmi: *Nonlinear Optics and Quantum Electronics, Theoretical Concepts* (Wiley, New York 1986)
- [9.8] S. Stenholm: *Foundations of Laser Spectroscopy* (Wiley, New York 1984)
- [9.9] A.L. Schawlow: Spectroscopy in a new light. *Rev. Mod. Phys.* **54**, 697 (1982)
- [9.10] N. Bloembergen: Nonlinear optics and spectroscopy. *Rev. Mod. Phys.* **54**, 685 (1982)
- [9.11] G.W. Series: Laser spectroscopy. *Contemp. Phys.* **25**, 3 (1984)
- [9.12] B. Couillaud, A. Ducasse: New methods in high-resolution laser spectroscopy, in *Progress in Atomic Spectroscopy*, Pt. C, ed. by H.J. Beyer, H. Kleinpoppen (Plenum, New York 1984) p. 57
- [9.13] R.C. Thompson: High-resolution laser spectroscopy of atomic systems. *Rep. Prog. Phys.* **48**, 531 (1985)
- [9.14] H. Walther (ed.): *Laser Spectroscopy of Atoms and Molecules*, Topics Appl. Phys., Vol. 2 (Springer, Berlin, Heidelberg 1976)
- [9.15] K. Shimoda (ed.): *High-Resolution Laser Spectroscopy*, Topics Appl. Phys., Vol. 13 (Springer, Berlin, Heidelberg 1976)
- [9.16] Y. Prior, A. Ben-Reuven, M. Rosenbluh: *Methods of Laser Spectroscopy* (Plenum, New York 1986)
- R.A. Smith (ed.): *Very High Resolution Spectroscopy* (Academic Press, London 1976)
- [9.17] A. Mooradian, T. Jaeger, P. Stokseth (eds.): Tunable Lasers and Applications, Springer Ser. Opt. Sci., Vol. 3 (Springer, Berlin, Heidelberg 1976)
- [9.18] M.D. Levenson, W.H. Yen (eds.): Lasers, Spectroscopy and New Ideas. A Tribute to A.L. Schawlow, Springer Ser. Opt. Sci., Vol. 54 (Springer, Berlin, Heidelberg 1987)
- [9.19] M.H. Mittelman: *Introduction to the Theory of Laser-Atom Interactions* (Plenum, New York 1993)
- B.W. Shore: *The Theory of Coherent Atomic Excitation. Vol. 1: Simple Atoms and Fields, Vol. 2: Multilevel Atoms and Incoherence* (Wiley, New York, 1990)

- [9.20] D.L. Andrews, A.A. Demitov: *Introduction to Laser Spectroscopy* (Plenum, New York 1995)
- [9.21] A.P. Roy (ed.): *Spectroscopy – Perspectives and Frontiers* (Narosa, New Delhi 1997)
S. Mukamel: *Principles of Nonlinear Optical Spectroscopy* (Oxford University Press, Oxford 1998)
- [9.22] C. Cohen-Tannoudji, J. Dupont-Roc, G. Grynberg: *Atom–Photon Interactions – Basic Processes and Applications* (Wiley, New York 1998)
R. Gupta: Resource letter LS-1: Laser Spectroscopy. Am. J. Phys. **59**, 874 (1991)
T.W. Hänsch, H. Walther: Laser spectroscopy and quantum optics. Rev. Mod. Phys. **71**, S242 (1999)
- [9.23] R.G. Brewer, A. Mooradian (eds.): *Laser Spectroscopy*, Proc. 1st Int. Conf., Vail 1973 (Academic Press, New York 1974)
- [9.24] S. Haroche, J.C. Pebay-Peyroula, T.W. Hänsch, S.E. Harris (eds.): *Laser Spectroscopy*, Proc. 2nd. Int. Conf., Megeve 1975, Lecture Notes Phys., Vol. 43 (Springer, Berlin, Heidelberg 1975)
- [9.25] J.L. Hall, J.L. Carlsten (eds.): *Laser Spectroscopy III*, Proc. 3rd. Int. Conf., Jackson Lake 1977, Springer Ser. Opt. Sci., Vol. 7 (Springer, Berlin, Heidelberg 1977)
- [9.26] H. Walther, K.W. Rothe (eds.): *Laser Spectroscopy IV*, Proc. 4th Int. Conf., Rottach-Egern 1979, Springer Ser. Opt. Sci., Vol. 21 (Springer, Berlin, Heidelberg 1979)
- [9.27] A.R.W. McKellar, T. Oka, B.P. Stoicheff (eds.): *Laser Spectroscopy V*, Proc. 5th Int. Conf., Jasper 1981, Springer Ser. Opt. Sci., Vol. 30 (Springer, Berlin, Heidelberg 1981)
- [9.28] H.P. Weber, W. Lüthy (eds.): *Laser Spectroscopy VI*, Proc. 6th Int. Conf., Interlaken 1983, Springer Ser. Opt. Sci., Vol. 40 (Springer, Berlin, Heidelberg 1983)
- [9.29] T.W. Hänsch, Y.R. Shen (eds.): *Laser Spectroscopy VII*, Proc. 7th Int. Conf., Maui 1985, Springer Ser. Opt. Sci., Vol. 49 (Springer, Berlin, Heidelberg 1985)
- [9.30] W. Persson, S. Svanberg (eds.): *Laser Spectroscopy VIII*, Proc. 8th Int. Conf., Åre 1987, Springer Ser. Opt. Sci., Vol. 55 (Springer, Berlin, Heidelberg 1987)
- [9.31] M.S. Feld, J.E. Thomas, A. Mooradian (eds.): *Laser Spectroscopy IX* (Academic Press, Boston 1989)
- [9.32] M. Ducloy, E. Giacobino, G. Camy (eds.): *Laser Spectroscopy X* (World Scientific, Singapore 1992)
- [9.33] L. Bloomfield, Th. Gallagher, D. Larson (eds.): *Laser Spectroscopy XI* (AIP, New York 1994)
- [9.34] M. Inguscio, M. Allegrini, A. Sasso (eds.): *Laser Spectroscopy XII* (World Scientific, Singapore 1996)
- [9.35] Z.-J. Wang, Y.-Z. Wang, Z.-M. Zhang (eds.): *Laser Spectroscopy XIII* (World Scientific, Singapore 1998)
- [9.36] R. Blatt, J. Eschner, D. Leibfried, F. Schmidt-Kaler (eds.): *Laser Spectroscopy XIV* (World Scientific, Singapore 1999)
S. Chu, V. Vutelic, A.J. Kerman, C. Chin (eds.): *Laser Spectroscopy 15* (World Scientific, Singapore 2002)
P. Hannaford, A. Siderov, H. Bachor, K. Baldwin (eds.): *Laser Spectroscopy 16* (World Scientific, Singapore 2004)
- [9.37] C.J. Latimer: Recent experiments involving highly excited atoms. Contemp. Phys. **20**, 631 (1979)

- [9.38] D. Kleppner: 'The spectroscopy of highly excited atoms.' In: *Progress in Atomic Spectroscopy*, ed. by W. Hanle, H. Kleinpoppen (Plenum, New York 1979) Pt. B, p. 713
- D. Kleppner, M.G. Littman, M.L. Zimmerman: Highly excited atoms. *Sci. Am.* **244**, 130 (1981)
- [9.39] R.F. Stebbings, F.B. Dunning (eds.): *Rydberg States of Atoms and Molecules* (Cambridge University Press, Cambridge 1983)
- [9.40] T.F. Gallagher: Rydberg atoms. *Rep. Prog. Phys.* **51**, 143 (1988)
- [9.41] T.F. Gallagher: Resonant collisional energy transfer between Rydberg atoms. *Phys. Rep.* **210**, 319 (1992)
- T.F. Gallagher: *Rydberg Atoms* (Cambridge University Press, Cambridge 1994)
- [9.42] J.-P. Connerade: *Highly Excited Atoms* (Cambridge University Press, Cambridge 1997)
- [9.43] R.R. Jones, L.D. Noordam: 'Electronic wavepackets.' In: *Progress in Atomic, Molecular, and Optical Physics*, Vol. 38, ed. by B. Bederson, H. Walther (Academic Press, San Diego 1998) p. 1
- G.M. Lankhuijzen, L.D. Noordam: 'Rydberg ionization: From field to photon.' In: *Progress in Atomic, Molecular, and Optical Physics*, Vol. 38, ed. by B. Bederson, H. Walther (Academic Press, San Diego 1998) p. 121
- [9.44] W.C. Wiley, I.H. McLaren: *Rev. Sci. Instrum.* **26**, 313 (1955)
- P. Kruit, F.H. Read: *J. Phys. E* **16**, 313 (1983)
- D.J. Trevor, L.D. van Woerkom, R.R. Freeman: *Rev. Sci. Instrum.* **60**, 1051 (1989)
- J. Spickermann, K. Martin, H.J. Räder, K. Müllen, R.-P. Krüger, H. Schlaad, A.H.E. Müller: Quantitative analysis of broad molecular weight distributions obtained by matrix-assisted laser desorption/ionisation time-of-flight mass spectrometry. *Eur. Mass Spectrom.* **2**, 161 (1996)
- [9.45] K.C. Harvey, B.P. Stoicheff: Fine structure of the n^2D series in rubidium near the ionization limit. *Phys. Rev. Lett.* **38**, 537 (1977)
- [9.46] K. Niemax: Spectroscopy using thermionic diode detectors, *Appl. Phys. B* **38**, 147 (1985)
- [9.47] T.W. Ducas, M.G. Littman, R.R. Freeman, D. Kleppner: Stark ionization of high-lying states of sodium. *Phys. Rev. Lett.* **35**, 366 (1975)
- T.F. Gallagher, L.M. Humphrey, R.M. Hill, S.A. Edelstein: Resolution of $[m_l]$ and $[m_j]$ levels in the electric field ionization of highly excited d -states of Na. *Phys. Rev. Lett.* **37**, 1465 (1976)
- T.F. Gallagher, L.M. Humphrey, R.M. Hill, W. Cooke, S.A. Edelstein: Fine structure intervals and polarizabilities of highly excited p and d states of sodium. *Phys. Rev. A* **15**, 1937 (1977)
- [9.48] F.V. Kowalski, R.T. Hawkins, A.L. Schawlow: Digital wavemeter for cw lasers. *J. Opt. Soc. Am.* **66**, 965 (1976)
- [9.49] J.L. Hall, S.A. Lee: Interferometric real time display of cw dye laser wavelengths with sub-Doppler accuracy. *Appl. Phys. Lett.* **29**, 367 (1976)
- [9.50] A. Fischer, K. Kullmer, W. Demtröder: Computer-controlled Fabry-Pérot wavemeter. *Opt. Commun.* **39**, 277 (1981)
- [9.51] L.S. Lee, A.L. Schawlow: Multi-wedge wavemeter for pulsed lasers. *Opt. Lett.* **6**, 610 (1981)
- [9.52] P. Juncar, J. Pinard: A new method for frequency calibration and laser control. *Opt. Commun.* **14**, 438 (1975)
- [9.53] T.W. Hänsch, J.J. Snyder: *Wavemeters, Dye Lasers*, 3rd edn., ed. by F.P. Schäfer, *Topics Appl. Phys.*, Vol. 1 (Springer, Berlin, Heidelberg 1990)

- [9.54] R. Castell, W. Demtröder, A. Fischer, R. Kullmer, H. Weickenmeier, K. Wikkert: The accuracy of laser wavelength meters. *Appl Phys. B* **38**, 1 (1985)
- [9.55] M. Herscher: The spherical mirror Fabry-Pérot interferometer. *Appl. Opt.* **7**, 951 (1968)
- [9.56] J.U. White: Long optical paths of large aperture. *J. Opt. Soc. Am.* **32**, 285 (1942)
- [9.57] J.U. White: Very long paths in air. *J. Opt. Soc. Am.* **66**, 411 (1976)
- [9.58] G. Yale Eastman: The heat pipe. *Sci. Am.* **218**, 38 (1968)
- [9.59] C.R. Vidal, J. Cooper: Heat pipe oven. A new well-defined metal vapor device for spectroscopic measurements. *J. Appl. Phys.* **40**, 3370 (1969)
- [9.60] H.-L. Chen: Applications of laser absorption spectroscopy. In: [9.3] p. 261
- [9.61] T.W. Hänsch, A.L. Schawlow, P. Toschek: Ultrasensitive response of a cw dye laser to selective extinction. *IEEE J. Quantum Electron.* **QE-8**, 802 (1972)
- [9.62] T.H. Harris: Laser intracavity-enhanced spectroscopy. In: [9.97] p. 343
- V.M. Baev, T.P. Belikova, E.A. Sviridenkov, A.F. Suchkov: *JETP* **74**, 21 (1978)
- [9.63] V.M. Baev, J. Eschner, E. Paeth, R. Schüler, P.E. Toschek: Intra-cavity spectroscopy with diode lasers. *Appl. Phys. B* **55**, 463 (1992)
- [9.64] W. Gurlit, J.P. Burrows, H. Burkhard, R. Böhm, V.M. Baev, P.E. Toschek: Intracavity diode laser for atmospheric field measurements. *Infrared Phys. Technol.* **37**, 95 (1996)
- [9.65] A. O'Keefe, D.A.G. Deacon: Cavity ring-down spectrometer for absorption measurements using pulsed laser sources. *Rev. Sci. Instrum.* **59**, 2544 (1988)
- R.T. Jongma, M.G.H. Boogaarts, I. Holleman, G. Meijer: Trace gas detection with cavity ring down spectroscopy. *Rev. Sci. Instrum.* **66**, 2821 (1995)
- M.D. Wheeler, S.M. Newman, A.J. Orr-Ewing and M.N.R. Ashfold: Cavity ring-down spectroscopy. *J. Chem. Soc. Faraday Trans.* **94**, 337 (1998)
- [9.66] J.J. Scherer, D. Voelkel, D.J. Rakestraw, J.B. Paul, C.P. Collier, R.J. Saykally, A. O'Keefe: Infrared cavity ringdown laser absorption spectroscopy (IR-CRLAS). *Chem. Phys. Lett.* **245**, 273 (1995)
- [9.67] D.J. Bradley, P. Ewart, J.V. Nicholas, J.R.D. Shaw: Excited state absorption spectroscopy of alkaline earths selectively pumped by tunable dye lasers. I. Barium arc spectra. *J. Phys. B* **6**, 1594 (1973)
- [9.68] J.R. Rubbmark, S.A. Borgström, K. Bockasten: Absorption spectroscopy of laser-excited barium. *J. Phys. B* **10**, 421 (1977)
- [9.69] M.E. Kaminsky, R.T. Hawkins, F.V. Kowalski, A.L. Schawlow: Identification of absorption lines by modulated lower-level population: Spectrum of Na. *Phys. Rev. Lett.* **36**, 671 (1976)
- [9.70] A.L. Schawlow: Simplifying spectra by laser level labeling. *Phys. Scr.* **25**, 333 (1982)
- [9.71] R. Teets, R. Feinberg, T.W. Hänsch, A.L. Schawlow: Simplification of spectra by polarization labeling. *Phys. Rev. Lett.* **37**, 683 (1976)
- [9.72] P. Esherick: Bound, even-parity $J = 0$ and $J = 2$ states of Sr. *Phys. Rev. A* **15**, 1920 (1977)
- [9.73] J.E.M. Goldsmith, J.E. Lawler: Optogalvanic spectroscopy. *Contemp. Phys.* **22**, 235 (1981)
- [9.74] C.J. Sansonetti, K.-H. Weber: Reference lines for dye-laser wavenumber calibration in the optogalvanic spectra of uranium and thorium. *J. Opt. Soc. Am.* **131**, 361 (1984)

- [9.75] O. Axner, I. Lindgren, I. Magnusson, H. Rubinsztein-Dunlop: Trace element determination in flames by laser-enhanced ionization spectrometry. *Anal. Chem.* **57**, 773 (1985)
- [9.76] O. Axner, H. Rubinsztein-Dunlop: Detection of trace amounts of Cr by two laser-based spectroscopic techniques: Laser-enhanced ionization in flames and laser-induced fluorescence in graphite furnace. *Appl. Opt.* **32**, 867 (1993)
- [9.77] J. Travis and G. Turk (eds.): *Laser-Enhanced Ionization Spectrometry* (Wiley, New York 1996)
- [9.77] P. Ljung, E. Nyström, J. Enger, P. Ljungberg, O. Axner: Detection of titanium in electro-thermal atomizers by laser-induced fluorescence. *Spectrochim. Acta B* **52**, 675 (1997); *B* **52**, 703 (1997)
- [9.77] P. Ljung, O. Axner: Measurements of rubidium in standard reference samples by wavelength-modulation diode laser absorption spectrometry in a graphite furnace. *Spectrochim. Acta B* **52**, 305 (1997)
- [9.78] X. Hou, S.-J.J. Tsai, J.X. Zhou, K.X. Yang, R.F. Leonardo, R.G. Michel: 'Laser-excited atomic fluorescence spectrometry: Principle, instrumentation and applications.' In: *Lasers in Analytical Spectroscopy*, ed. by J. Sneddon, T.L. Thiem, Y.-I. Lee (VCH Publishers, New York 1997)
- [9.79] A. Zybin, C. Schnürer-Patschan, M.A. Bolshov, K. Niemax: Elemental analysis by diode laser spectroscopy. *Trends Anal. Chem.* **17**, 513 (1998)
- [9.79] T. Imasaka: Analytical molecular spectroscopy with diode lasers. *Spectrochim. Acta Rev.* **15**, 329 (1993)
- [9.79] A.W. Mantz: A review of spectroscopic applications of tunable semiconductor lasers. *Spectrochim. Acta A* **51**, 221 (1995)
- [9.79] A.W. Mantz: A review of the applicability of tunable diode-laser spectroscopy at high sensitivity. *Microchem. J.* **50**, 351 (1994)
- [9.79] M. Inguscio, F.S. Cataliotti, C. Fort, F.S. Pavone, M. Prevedelli: 'A new generation of light sources for applications in spectroscopy.' In: *Atomic Physics Methods in Modern Research*, ed. by K. Jungmann, J. Kowalski, I. Reinhard, F. Träger (Springer, Heidelberg, Berlin 1997)
- [9.79] C.E. Wieman, L. Hollberg: Using diode lasers for atomic physics. *Rev. Sci. Instrum.* **62**, 1 (1991)
- [9.80] F.S. Pavone: Diode lasers and their applications in spectroscopy. *Rivista del Nuovo Cimento* **19**, 1 (1996)
- [9.80] J.E.M. Goldsmith: Recent advances in flame diagnostics using fluorescence and ionization techniques. In: [9.30] p. 337
- [9.81] J.A. Paisner, R.W. Solarz: Resonance photoionization spectroscopy. In: [9.3] p. 175
- [9.82] P. Camus (ed.): Optogalvanic Spectroscopy and its Applications. *J. Physique Coll. C7*, Suppl. no. 11, Tome 44 (1983)
- [9.83] P. Hannaford: Spectroscopy with sputtered atoms. *Contemp. Phys.* **24**, 251 (1983)
- [9.84] K.C. Smith, P.K. Schenck: Optogalvanic spectroscopy of a neon discharge. *Chem. Phys. Lett.* **55**, 466 (1978)
- [9.85] V.S. Letokhov: *Laser Photoionization Spectroscopy* (Academic Press, Orlando 1987)
- [9.86] J.C. Travis, G.C. Turk, J.R. DeVoe, P.K. Schenck, C.A. van Dijk: *Prog. Anal. Atom. Spectrosc.* **7**, 199 (1984)
- [9.87] I. Magnusson, O. Axner, I. Lindgren, H. Rubinsztein-Dunlop: Laser-enhanced ionization detection of trace elements in a graphite furnace. *Appl. Spectrosc.* **40**, 968 (1986)
- [9.87] O. Axner, I. Magnusson, J. Petersson, S. Sjöström: Investigation of the

- multi-element capability of laser-enhanced ionization spectrometry in flames for analysis of trace elements in water solution. *Appl. Spectrosc.* **41**, 19 (1987)
- [9.88] N. Omenetto: 'The impact of several atomic and molecular laser spectroscopic techniques for chemical analysis.' In: *Laser Technology in Chemistry*, Special issue, ed. by H. Medin, S. Svanberg, *Appl. Phys. B* **46**, No. 3 (1988)
- [9.89] G.S. Hurst, M.G. Payne (eds.): *Resonance Ionization Spectroscopy and its Applications* 1984, Conf. Series No. 71 (Institute of Physics, Bristol 1984)
- G.S. Hurst, C. Grey Morgan (eds.): *Resonance Ionization Spectroscopy*, Conf. Series No. 84 (Institute of Physics, Bristol 1987)
- [9.90] G.S. Hurst, M.G. Payne (eds.): *Principles and Applications of Resonance Ionization Spectroscopy* (Adam Hilger, Bristol 1988)
- [9.91] H.-J. Kluge, B.A. Bushaw, G. Passler, K. Wendt, N. Trautmann: Resonance ionization spectroscopy for trace analysis and fundamental research. *Fresenius Z. Anal. Chem.* **350**, 78 (1994)
- [9.92] C.H. Chen, G.S. Hurst, M.G. Payne: 'Resonance ionization spectroscopy: Inert gas detection.' In: *Progress in Atomic Spectroscopy*, Pt. C, ed. by H.J. Beyer, H. Kleinpoppen (Plenum, New York 1984) p. 115
- [9.93] G.S. Hurst, M.G. Payne, S.D. Kramer, C.H. Chen, R.C. Phillips, S.L. Allman, G.D. Alton, J.W.T. Dabbs, R. Willis, B.E. Lehman: Method for counting noble gas atoms with isotopic selectivity. *Rep. Prog. Phys.* **48**, 1333 (1985)
- V.S. Letokhov: Detecting individual atoms and molecules with lasers. *Sci. Am.* **259**(3), 44 (1988)
- J.T. Höffges, H.W. Baldauf, T. Eichler, S.R. Helmfried, H. Walther: 'Resonance fluorescence of a single ion.' In: *Atomic Physics Methods in Modern Research*, ed. by K. Jungmann, J. Kowalski, I. Reinhard, F. Träger (Springer, Berlin, Heidelberg 1997)
- [9.94] J.A. Gelbwachs (ed.): *Laser Spectroscopy for Detection*. Proc. SPIE Int. Soc. Opt. Eng. Vol. 286 (SPIE, Washington 1981)
- [9.95] R.A. Keller: *Laser-Based Ultrasensitive Spectroscopy and Detection*. Proc. SPIE Int. Soc. Opt. Eng. Vol. 426 (SPIE, Washington 1983)
- [9.96] J.J. Snyder, R.A. Keller (eds.): *Ultrasensitive Laser Spectroscopy*, Special issue, *J. Opt. Soc. Am. B* **2**, No 9 (1985)
- [9.97] D. Kliger (ed.): *Ultrasensitive Laser Spectroscopy* (Academic Press, New York 1983)
- [9.98] M. Eigen, R. Rigler: Proc. Natl. Acad. Sci. USA **91**, 5740 (1994)
- W.E. Moerner, R.M. Dickson, D.J. Norris: 'Single-molecule spectroscopy and quantum optics in solids.' In: *Progress in Atomic, Molecular, and Optical Physics*, Vol. 38, ed. by B. Bederson, H. Walther (Academic Press, San Diego 1998) p. 193
- M. Orrit, J. Bernard, R. Brown, B. Lounis: 'Optical spectroscopy of single molecules in solids.' In: *Progress in Optics XXXV*, ed. by E. Wolf (Elsevier, Amsterdam 1996), p. 63
- Th. Basche, W.E. Moerner, M. Orritt, U.P. Wild (eds.): *Single Molecule Optical Detection, Imaging and Spectroscopy* (Wiley-VCH, Munich 1997)
- K. Kneipp, Y. Wang, H. Kneipp, L.T. Perelman, I. Itzkan, R.R. Dasari, M.S. Feld: Single molecule detection using surface-enhanced Raman scattering (SERS). *Phys. Rev. Lett.* **78**, 1667 (1997)
- K. Kneipp, H. Kneipp, I. Itzkan, R. Dasari, M.S. Feld: Surface-enhanced Raman scattering: A new tool for biomedical spectroscopy. *Current Science* **77**, 915 (1999)

- [9.99] S. Weiss: Fluorescence spectroscopy of single biomolecules. *Science* **283**, 1676 (1999) (Special Issue, March 12, 1999)
X. Sunney Xie, J.K. Trautman: Single-molecule optical studies at room temperature. *Ann. Rev. Phys. Chem.* **49**, 441 (1998)
- [9.100] N. Omenetto (ed.): *Analytical Laser Spectroscopy* (Wiley, New York 1979)
- [9.101] E.H. Piepmeier (ed.): *Analytical Applications of Lasers* (Wiley, New York 1986)
- [9.102] V.S. Letokhov (ed.): *Laser Analytical Spectrochemistry* (Hilger, Bristol 1986)
- [9.103] J. Sneddon, T.L. Thiem, Y.-I. Lee (eds.): *Lasers in Analytical Spectroscopy* (VCH Publishers, New York 1997)
- [9.104] N. Omenetto: The role of lasers in analytical atomic spectroscopy – Where, when and why. *J. Anal. At. Spectrom.* **13**, 385 (1998)
- [9.105] S. Svanberg: 'Fundamentals of atmospheric spectroscopy.' In: *Surveillance of Electromagnetic Pollution and Resources by Electromagnetic Waves*, ed. by T. Lund (Reidel, Dordrecht 1978)
- [9.106] L.B. Kreutzer: Laser optoacoustic spectroscopy. A new technique of gas analysis. *Anal. Chem.* **46**, 239A (1974)
- [9.107] A. Rosencwaig: *Photoacoustics and Photoacoustic Spectroscopy* (Wiley, New York 1980)
- [9.108] V. Letokhov, V. Zhaorov: *Laser Opto-Acoustic Spectroscopy*, Springer Ser. Opt. Sci., Vol. 37 (Springer, Berlin, Heidelberg 1986)
- [9.109] A.C. Tam: Applications of photoacoustic sensing techniques. *Rev. Mod. Phys.* **58**, 381 (1986)
- [9.110] P. Hess, J. Pelzl (eds.): *Photoacoustics and Photothermal Phenomena*, Springer Ser. Opt. Sci., Vol. 58 (Springer, Berlin, Heidelberg 1988)
- [9.111] P. Hess (ed.): *Photoacoustics* (Springer, Berlin, Heidelberg 1990)
- [9.112] M.W. Sigrist: 'Air monitoring by laser photoacoustic spectroscopy.' In: *Air Monitoring by Spectroscopic Techniques*, ed. by M.W. Sigrist (Wiley, New York 1994)
- F.G.C. Bijnen, H. Zuckermann, F.J.M. Harren, J. Reuss: Multi-component trace gas analysis by three photoacoustic cells intracavity in a CO-laser; observation of anaerobic and post-anaerobic emission of acetaldehyde and ethanol in cherry tomatoes. *Appl. Opt.* **37**, 3345 (1998)
- F.J.M. Harren: 'Photoacoustic spectroscopy in trace gas monitoring.' In: *Encyclopedia of Analytical Chemistry: Applications, Theory and Instrumentation*, ed. by R.A. Meyers (Wiley, New York 2000) p. 2203
- [9.113] C.K.N. Patel, A.C. Tam: Pulsed optoacoustic spectroscopy of condensed matter. *Rev. Mod. Phys.* **53**, 517 (1981)
- [9.114] S. Svanberg, P. Tsekleris, W. Happer: Hyperfine structure studies of highly excited D and F levels in alkali atoms using a CW dye laser. *Phys. Rev. Lett.* **30**, 817 (1973)
- S. Svanberg, P. Tsekleris: Hyperfine-structure investigation of highly excited 2D levels in ^{87}Rb and ^{133}Cs using a cw tunable laser in a two-step excitation scheme. *Phys. Rev. A* **11**, 1125 (1975)
- [9.115] G. Belin, I. Lindgren, L. Holmgren, S. Svanberg: Hyperfine interaction, Zeeman and Stark effects for excited states in potassium. *Phys. Scr.* **12**, 287 (1975)
- [9.116] G. Belin, L. Holmgren, S. Svanberg: Hyperfine interaction, Zeeman and Stark effects for excited states in rubidium. *Phys. Scr.* **13**, 351 (1976)
- [9.117] G. Belin, L. Holmgren, S. Svanberg: Hyperfine interaction, Zeeman and Stark effects for excited states in cesium. *Phys. Scr.* **14**, 39 (1976)

- [9.118] S. Svanberg: Measurement and calculation of excited alkali hyperfine and Stark parameters. In: [9.25] p. 183
- [9.119] R. Neumann, F. Träger, G. zu Putlitz: 'Laser-microwave spectroscopy.' In: *Progress in Atomic Spectroscopy*, Pt. D, ed. by H.K. Beyer, H. Kleinpopp (Plenum, New York 1987) p. 1
- T.F. Gallagher: 'Radiofrequency spectroscopy of Rydberg atoms.' In: *Progress in Atomic Spectroscopy*, Pt. D, ed. by H.K. Beyer, H. Kleinpopp (Plenum, New York 1987) p. 12
- [9.120] K. Fredriksson, S. Svanberg: Precision determination of the fine structure of the 4d state in sodium using level crossing spectroscopy. *Phys. Lett. A* **53**, 61 (1975)
- [9.121] E. Matthias, R.A. Rosenberg, E.D. Poliakoff, M.G. White, S.-T. Lee, D.A. Shirley: Time-resolved VUV spectroscopy using synchrotron radiation: Fluorescent lifetimes of atomic Kr and Xe. *Chem. Phys. Lett.* **52**, 239 (1977)
- T. Möller, G. Zimmerer: Time-resolved spectroscopy with synchrotron radiation in the vacuum ultraviolet. *Phys. Scr.* **T17**, 177 (1987)
- R. Rigler, O. Kristensen, R. Roslund, P. Thyberg, K. Oba, M. Eriksson: Molecular structure and dynamics: Beamline for time-resolved spectroscopy at the MAX synchrotron in Lund. *Phys. Scr.* **T17**, 204 (1987)
- [9.122] U. Berzinsh, Luo Caiyan, R. Zerne, S. Svanberg: Determination of radiative lifetimes of neutral sulphur by time-resolved VUV laser spectroscopy. *Phys. Rev. A* **55**, 1836 (1997)
- [9.123] Se. Johansson, A. Joueizadeh, U. Litzén, J. Larsson, A. Persson, C.-G. Wahlström, S. Svanberg, D.S. Leckrone, G.M. Wahlgren: Comparison of new experimental and astrophysical f -values for some Ru II lines, observed in HST spectra of χ Lupi. *Astrophys. J.* **421**, 809 (1994)
- [9.124] H. Bergström, G.W. Faris, H. Hallstadius, H. Lundberg, A. Persson, C.-G. Wahlström: Radiative lifetime and hyperfine-structure studies on laser-evaporated boron. *Z. Phys. D* **8**, 17 (1988)
- [9.125] R.A. Lacy, A.C. Nilsson, R.L. Byer, W.T. Silvfast, O.R. Wood II, S. Svanberg: 'Photoionization-pumped gain at 185 nm in a laser-ablated Indium plasma.' In: *Short Wavelength Coherent Radiation: Generation and Applications*, AIP Conference Proceedings No. 147, ed. by D.T. Attwood, J. Bokor (AIP, New York 1986); and *J. Opt. Soc. Am. B* **6**, 1209 (1989)
- [9.126] Z.-S. Li, J. Norin, A. Persson, C.-G. Wahlström, S. Svanberg, P.S. Doidge, E. Biémont: Radiative properties of neutral germanium obtained from excited state lifetime and branching ratio measurements and comparison with theoretical calculations. *Phys. Rev. A* **60**, 198 (1999)
- [9.127] M.B. Gaarde, R. Zerne, C. Luo, Z. Jiang, J. Larsson, S. Svanberg: Determination of radiative lifetimes of excited states in neutral gold using time-resolved VUV laser spectroscopy. *Phys. Rev. A* **50**, 209 (1994)
- R. Zerne, J. Larsson, S. Svanberg: Determination of radiative lifetimes in the $3d^{10}np\ ^2P$ sequence of neutral copper by time-resolved VUV laser spectroscopy. *Phys. Rev. A* **49**, 128 (1994)
- C. Luo, U. Berzinsh, R. Zerne, S. Svanberg: Determination of radiative lifetimes on neutral bismuth by time-resolved UV/VUV laser spectroscopy. *Phys. Rev. A* **52**, 1936 (1995)
- U. Berzinsh, S. Svanberg: Atomic radiative lifetimes measured by pulsed laser spectroscopy in the UV/VUV spectral region. *Adv. Quantum Chem.* **30**, 283 (1998)

- Z.S. Li, S. Svanberg, P. Quinet, X. Tordoir, E. Biemont: Lifetime measurements in Yb II with time-resolved laser spectroscopy. *J. Phys. B* **32**, 1731 (1999)
- Zhang Zhiguo, Z.S. Li, H. Lundberg, K.Y. Zhang, Z.W. Dai, Jiang Zhan-kui, S. Svanberg: Radiative properties of Eu II and Eu III obtained from lifetime and branching ratio measurements. *J. Phys. B* **33**, 521 (2000)
- P. Quinet, P. Palmeri, E. Biemont, Z.S. Li, Z.G. Zhang, S. Svanberg: Radiative lifetime measurements and transition probability calculations in lanthanide ions. *J. of Alloys and Compounds* **344**, 255 (2002)
- [9.128] J.C. Cooper, N.D. Gibson, J.E. Lawler: Radiative lifetimes in Cr I by laser-induced fluorescence. *J. Quant. Spectrosc. Radiat. Transfer* **58**, 85 (1997)
- G.M. Wahlgren, S.G. Johansson, U. Litzén, N.D. Gibson, J.C. Cooper, J.E. Lawler, D.S. Leckrone, R. Engleman Jr.: Atomic data for the Re II resonance multiplet and its application to astrophysics. *Astrophys. J.* **475**, 380 (1997)
- [9.129] P.B. Coates: The correction for photon "pile-up" in the measurement of radiative lifetimes. *J. Phys. E* **1**, 878 (1968)
- [9.130] M. Gustavsson, H. Lundberg, L. Nilsson, S. Svanberg: Lifetime measurements for excited states of rare-earth atoms using pulse-modulation of a cw dye laser beam. *J. Opt. Soc. Am.* **69**, 984 (1979)
- J. Carlsson: Accurate time-resolved laser spectroscopy on sodium and bismuth atoms. *Z. Phys. D* **9**, 147 (1988)
- [9.131] K. Bhatia, P. Grafström, C. Levinson, H. Lundberg, L. Nilsson, S. Svanberg: Natural radiative lifetimes in the perturbed $6s\text{nd}$ 1D_2 sequence of barium. *Z. Physik A* **303**, 1 (1981)
- T.F. Gallagher, W. Sandner, K.A. Safinya: Probing configuration interaction of the Ba $5d7d$ 1D_2 state using radiofrequency spectroscopy and lifetime measurements. *Phys. Rev. A* **23**, 2969 (1981)
- M. Aymar, R.-J. Champeau, C. Delsart, J.C. Keller: Lifetimes of Rydberg levels in the perturbed $6s\text{nd}$ $^{1,3}D_2$ series of barium I. *J. Phys. B* **14**, 4489 (1981)
- [9.132] S. Svanberg: Perturbations in Rydberg sequences probed by lifetime, Zeeman-effect and hyperfine structure measurements. In: [9.27] p. 301
- [9.133] J. Carlsson, L. Sturesson: Accurate time-resolved laser spectroscopy on lithium atoms. *Z. Phys. D* **14**, 281 (1989)
- [9.134] J. Carlsson: Accurate time-resolved laser spectroscopy on sodium and bismuth atoms. *Z. Phys. D* **9**, 147 (1988)
- J. Carlsson, P. Jönsson, L. Sturesson, C. Froese Fischer: Multi-configuration Hartree-Fock calculations and time-resolved laser spectroscopy studies of hyperfine structure constants in sodium. *Phys. Scr.* **46**, 394 (1992)
- [9.135] C. De Michelis, M. Mattioli: Spectroscopy and impurity behaviour in fusion plasmas. *Rep. Prog. Phys.* **47**, 1233 (1984)
- R.C. Isler: Impurities in Tokomaks. *Nuclear Fusion* **24**, 1599 (1984)
- [9.136] R.E. Imhof, F.H. Read: Measurements of lifetimes of atoms, molecules and ions. *Rep. Prog. Phys.* **40**, 1 (1977)
- [9.137] P. Erman: 'Time-resolved spectroscopy of small molecules.' In: *Specialists Periodical Reports, Molecular Spectroscopy*, Vol. 6, Chap. 5 (The Chemical Society, London 1979) p. 174
- [9.138] J.N. Dodd, G.W. Series: 'Time-resolved fluorescence spectroscopy.' In: *Progress in Atomic Spectroscopy*, Pt. A, ed. by W. Hanle, H. Kleinpoppen (Plenum, New York 1978) p. 639
- W.L. Wiese: 'Atomic transition probabilities and lifetimes.' In: *Progress*

- in *Atomic Spectroscopy*, Pt. B, ed. by W. Hanle, H. Kleinpoppen (Plenum, New York 1979) p. 1101
- [9.139] M.C.E. Huber, R.J. Sandeman: The measurement of oscillator strengths. *Rep. Prog. Phys.* **49**, 397 (1986)
- [9.140] O. Poulsen, J.L. Hall: Spectroscopic investigation in ^{209}Bi I using tunable-cw-dye-laser spectroscopy. *Phys. Rev. A* **18**, 1089 (1978)
- [9.141] S. Svanberg: Natural radiative lifetimes of some excited Bi I levels belonging to the $6p^27s$ and the $6p^26d$ configurations measured by the Hanle method. *Phys. Scr.* **5**, 73 (1972)
- [9.142] H.J. Andrä, A. Gaupp, W. Wittmann: New method for precision lifetime measurements by laser excitation of fast-moving atoms. *Phys. Rev. Lett.* **31**, 501 (1973)
- [9.143] A. Gaupp, P. Kuske, H.J. Andrä: Accurate lifetime measurements of the lowest $^2P_{1/2}$ states in neutral lithium and sodium. *Phys. Rev. A* **26**, 3351 (1982)
- C.E. Tanner, A.E. Livingston, R.C. Rafac, F.G. Serpa, K.W. Kukla, H.G. Berry, L. Young, C.A. Kurtz: *Phys. Rev. Lett.* **69**, 2765 (1992)
- [9.144] T. Brage, C. Froese Fischer, P. Jönsson: Effects of core-valence and core-core correlation on the line strength of the resonance lines in Li I and Na I. *Phys. Rev. A* **49**, 2181 (1994)
- C.E. Tanner: 'Precision measurements of atomic lifetimes.' In: *Atomic Physics XIV*, ed. by D.J. Wineland, C.E. Wieman, S.J. Smith (AIP Publ., New York 1995) p. 150
- [9.145] P. Erman, J. Brzozowski, B. Sigfridsson: Gas excitations using high-frequency deflected electron beams: A convenient method for determinations of atomic and molecular lifetimes. *Nucl. Instrum. Methods* **110**, 471 (1973)
- [9.146] P. Erman: High-resolution measurements of atomic and molecular lifetimes using the high-frequency deflection technique. *Phys. Scr.* **11**, 65 (1975)
- [9.147] P. Erman: Astrophysical applications of time-resolved molecular spectroscopy. *Phys. Scr.* **20**, 575 (1979); Studies of perturbations using time resolved techniques. *Phys. Scr.* **25**, 365 (1982)
- [9.148] J. Brzozowski, P. Bunker, N. Elander, P. Erman: Predissociation effects in the A, B, and C states of CN and the interstellar formation rate of CH via inverse predissociation. *Astrophys. J.* **207**, 414 (1976)
- [9.149] J.K. Link: Measurement of the radiative lifetimes of the first excited states of Na, K, Rb, and Cs by means of the phase-shift method. *J. Opt. Soc. Am.* **56**, 1195 (1966)
- P.T. Cunningham, J.K. Link: Measurement of lifetimes of excited states of Na, Tl, In, Ga, Cu, Ag, Pb, and Bi by the phase-shift method. *J. Opt. Soc. Am.* **57**, 1000 (1967)
- L. Armstrong Jr., S. Ferneuil: Theoretical analysis of the phase shift measurement of lifetimes using monochromatic light. *J. Phys. B* **8**, 546 (1975)
- [9.150] C.H. Corliss, W.R. Bozman: Experimental transition probabilities for spectral lines of seventy elements. NBS Monograph 53 (National Bureau of Standards, Washington, DC 1962)
- [9.151] W. Marlow: Hakenmethode. *Appl. Opt.* **6**, 1715 (1967)
- [9.152] N.P. Penkin: 'Experimental determination of electronic transition probabilities and the lifetimes of the excited atomic and ionic states.' In: *Atomic Physics 6*, ed. by R. Damburg (Plenum, New York 1979) p. 33

- [9.153] W.A. van Wijngaarden, K.D. Bonin, W. Happer: Inverse hook method for measuring oscillator strengths for transitions between excited atomic states. *Hyperfine Interact.* **38**, 471 (1987)
- [9.154] S. Svanberg: Atomic spectroscopy by resonance scattering. *Philos. Trans. R. Soc. London A* **293**, 215 (1979)
- [9.155] J.N. Dodd, G.W. Series: 'Time-resolved fluorescence spectroscopy.' In: *Progress in Atomic Spectroscopy*, Pt. A, ed. by W. Hanle, H. Kleinpoppen (Plenum, New York 1978) p. 639
- [9.156] S. Haroche: Quantum beats and time-resolved fluorescence spectroscopy. In: [9.15] p. 253
- [9.157] P. Grundevik, H. Lundberg, A.-M. Mårtensson, K. Nystrom, S. Svanberg: Hyperfine-structure study in the P sequence of ^{23}Na using quantum-beat spectroscopy. *J. Phys. B* **12**, 2645 (1979)
- [9.158] G. Jönsson, C. Levinson, L Lindgren, A. Persson, C.G. Wahlström: Experimental and theoretical studies of the $4s^2 np \ ^2P$ sequence in neutral gallium. *Z. Phys. A* **322**, 351 (1985)
- [9.159] J. Bengtsson, J. Larsson, S. Svanberg, C.-G. Wahlström: Hyperfine-structure study of the $3d^{10} 5p \ ^2P_{3/2}$ level of neutral copper using pulsed level-crossing spectroscopy at short wavelengths. *Phys. Rev. A* **41**, 233 (1990)
J. Bengtsson, J. Larsson, S. Svanberg, C.G. Wahlström: High-resolution pulsed laser spectroscopy in the UV/VUV spectral region. In: [9.31] p. 86
S. Svanberg: 'High-resolution laser spectroscopy in the UV/VUV spectral region.' In: *Applied Laser Spectroscopy*, ed. by M. Inguscio, W. Demtröder (Plenum, New York 1990)
G.J. Bengtsson, P. Jönsson, J. Larsson, S. Svanberg: Time-resolved spectroscopic studies of the $7p \ ^2P$ states of neutral silver following VUV excitation, *Z. Physik D* **22**, 437 (1991)
- [9.160] J. Larsson, S. Svanberg: High-resolution VUV spectroscopy using pulsed laser sources. *Appl. Phys. B* **59**, 433 (1994)
- [9.161] D.P. O'Brien, P. Meystre, H. Walther: 'Subnatural linewidths in atomic spectroscopy.' In: *Advanced Atomic and Molecular Physics*, Vol. 21, ed. by D.R. Bates, B. Bederson (Academic Press, Orlando 1985)
H. Figger, H. Walther: Optical resolution beyond the natural linewidth: A level-crossing experiment on the $3 \ ^2P_{3/2}$ level of sodium using a tunable dye laser. *Z. Phys.* **267**, 1 (1974)
- [9.162] P. Schenk, R.C. Hilborn, H. Metcalf: Time-resolved fluorescence from Ba and Ca excited by a pulsed tunable dye laser. *Phys. Rev. Lett.* **31**, 189 (1974)
- [9.163] J. Bengtsson, J. Larsson, S. Svanberg: Hyperfine structure and radiative lifetime determination for the $4d^{10} 6s \ ^2P$ states of neutral silver using pulsed laser spectroscopy. *Phys. Rev. A* **42**, 545 (1990)
- [9.164] F. Shimizu, K. Shimizu, Y. Gomi, H. Takuma: Direct observation of hyperfine splittings of the $^7\text{Li} \ ^2P_{3/2}$ state by subnatural linewidth spectroscopy. *Phys. Rev. A* **35**, 3149 (1987)
- [9.165] J. Larsson, L. Sturesson, S. Svanberg: Manipulation of level-crossing signals using narrow-band or pulsed laser excitation. *Phys. Scr.* **40**, 165 (1989)
- [9.166] S.L. Shapiro (ed.): *Ultrashort Light Pulses*, 2nd edn. *Topics Appl. Phys.*, Vol. 18 (Springer, Berlin, Heidelberg 1984)
W. Kaiser (ed.): *Ultrashort Laser Pulses and Applications*, 2nd edn. Springer Ser. Opt. Sci., Vol. 60 (Springer, Berlin, Heidelberg 1993)
C.V. Shank, E. Ippen, S.L. Shapiro: *Picosecond Phenomena*, Springer Ser. Chem. Phys., Vol. 4 (Springer, Berlin, Heidelberg 1978)

- [9.167] R.M. Hochstrasser, W. Kaiser, C.V. Shank: *Picosecond Phenomena II*, Springer Ser. Chem. Phys., Vol. 14 (Springer, Berlin, Heidelberg 1980)
- [9.168] K. Eisenthal, R.M. Hochstrasser, W. Kaiser, A. Lauberau (eds.): *Picosecond Phenomena III*, Springer Ser. Chem. Phys., Vol. 23 (Springer, Berlin, Heidelberg 1982)
- [9.169] D. Auston, K. Eisenthal (eds.): *Ultrafast Phenomena IV*, Springer Ser. Chem. Phys., Vol. 38 (Springer, Berlin, Heidelberg 1984)
- [9.170] A. Siegman, G. Fleming (eds.): *Ultrafast Phenomena V*, Springer Ser. Chem. Phys., Vol. 46 (Springer, Berlin, Heidelberg 1986)
- [9.171] P.F. Barbara, W.H. Knox, G.A. Mourou, A.H. Zewail (eds.): *Ultrafast Phenomena VI* (Springer Berlin, Heidelberg 1988)
- [9.172] P.F. Barbara, W.H. Knox, G.A. Mourou, A.H. Zewail (eds.): *Ultrafast Phenomena VII* (Springer Berlin, Heidelberg 1990)
- [9.173] P.F. Barbara, W.H. Knox, G.A. Mourou, A.H. Zewail (eds.): *Ultrafast Phenomena VIII* (Springer, Berlin, Heidelberg 1993)
- [9.174] P.F. Barbara, W.H. Knox, G.A. Mourou, A.H. Zewail (eds.): *Ultrafast Phenomena IX*, Springer Ser. Chem. Phys., Vol. 60 (Springer, Berlin, Heidelberg 1994)
- [9.175] P.F. Barbara, J.G. Fujimoto, W.H. Knox, W. Zinth (eds.): *Ultrafast Phenomena X*, Springer Ser. Chem. Phys., Vol. 62 (Springer, Berlin, Heidelberg 1996)
- [9.176] T. Elsaesser, J.G. Fujimoto, D.A. Wiersmaa, W. Zinth (eds.): *Ultrafast Phenomena XI* (Springer, Berlin, Heidelberg 1998)
- [9.177] T. Elsaesser, S. Mukamel, M.M. Murnane, N.F. Scherer (eds.): *Ultrafast Phenomena XII* (Springer, Berlin, Heidelberg 2001)
- [9.178] D.R. Miller, M.M. Murnane, A.M. Weiner (eds.): *Ultrafast Phenomena XIII* (Springer, Berlin, Heidelberg 2003)
- [9.179] J.C. Diels, W. Rudolph: *Ultrashort Laser Pulse Phenomena* (Academic Press, New York 1996)
- [9.180] T. Baumert, G. Gerber: Femtosecond spectroscopy of molecules and clusters. *Adv. At. Mol. Opt. Phys.* **35**, 163 (1995)
- [9.181] Th. Elsaesser, M. Woerner: Femtosecond infrared spectroscopy of semiconductors and semiconductor nanostructures. *Phys. Rep.* **321**, 253 (1999)
- [9.182] O. Svelto, S. De Silvestri, G. Denardo (eds.): *Ultrafast Processes in Spectroscopy* (Plenum, New York 1996)
- [9.183] E. Schreiber: *Femtosecond Real-Time Spectroscopy of Small Molecules and Clusters* (Springer, Berlin, Heidelberg 1998)
- [9.184] R. Schinke: *Photodissociation Dynamics* (Cambridge University Press, Cambridge 1993)
- [9.185] G.D. Billings, K.V. Mikkelsen: *Introduction to Molecular Dynamics and Chemical Kinetics* (Wiley, London 1996)
- [9.186] J.W. Hepburn, R.E. Continetti, M.A. Johnson (eds.): *Laser Techniques for State-Selective and State-to-State Chemistry IV*, Proc. SPIE Int. Soc. Opt. Eng. **3271** (1997)
- [9.187] J. Hoff, J. Deisenhofer: Photophysics of photosynthesis. *Phys. Rep.* **287**, 1 (1997)
- [9.188] S. Letzring: Buying and using a streak camera. *Lasers & Appl.* (March 1983) p. 49
- [9.189] R. Trebino, D.J. Kane: Using phase retrieval to measure the intensity and phase of ultra-short pulses: Frequency-resolved optical gating. *J. Opt. Soc. Am. A* **10**, 1101 (1993)
- [9.190] D.J. Kane, R. Trebino: Characterization of arbitrary femtosecond pulses

- using frequency-resolved optical gating. *IEEE J. Quantum Electron.* **QE-29**, 571 (1993)
- R. Trebino, K.W. DeLong, D.N. Fittinghoff, D.N. Sweetser, M.A. Krumbugel, B.A. Richman, D.J. Kane: Measuring ultra-short laser pulses in the time-frequency domain using frequency-resolved optical gating. *Rev. Sci. Instrum.* **68**, 3277 (1997)
- A. Baltuska, M. Pschenichnikov, D.A. Wiersma: Amplitude and phase characterization of 4.5 fs pulses by frequency-resolved optical gating. *Opt. Lett.* **23**, 1474 (1998)
- S. Linden, H. Giessen, J. Kuhl: XFROG, A new method for amplitude and phase characterization of weak ultrashort pulses. *Phys. Status Solidi* **206**, 119 (1998)
- C. Iaconis, I.A. Walmsley: Spectral phase interferometry for direct electric-field reconstruction of ultrashort optical pulses. *Opt. Lett.* **23**, 792 (1998)
- [9.187] R.R. Alfano (ed.): *The Supercontinuum Laser Source* (Springer-Verlag, New York 1989)
- H. Wille, M. Rodriguez, J. Kasparian, D. Mondelain, J. Yu, A. Mysyrowicz, R. Sauerbrey, J.P. Wolf, L. Wöste: Teramobile: A mobile femtosecond-terawatt laser and detection system. *Eur. Phys. J. AP* **20**, 183 (2002)
- [9.188] P.R. Smith, D.A. Auston, M.C. Nuss: Subpicosecond photoconducting dipole antennas. *IEEE J. Quantum Electron.* **QE-24**, 255 (1988)
- [9.189] M. van Exter, Ch. Fattiger, D. Grischkowsky: High-brightness terahertz beams characterized with an ultrafast detector. *Appl. Phys. Lett.* **55**, 337 (1989)
- D. Grischkowsky, S. Keiding, M. van Exter, Ch. Fattiger: Far-infrared time-domain spectroscopy with terahertz beams of dielectrics and semiconductors. *J. Opt. Soc. Am. B* **7**, 2006 (1990)
- [9.190] M. van Exter, D. Grischkowsky: Characterization of an optoelectronic terahertz beam system. *IEEE Trans. Microwave Theory Tech.* **38**, 1684 (1990)
- L. Xu, X.-C. Zhang, D.H. Auston: Terahertz beam generation by femtosecond optical pulses in electro-optic materials. *Appl. Phys. Lett.* **61**, 1784 (1992)
- R.A. Cheville, D. Grischkowsky: Far-infrared terahertz time-domain spectroscopy of flames. *Opt. Lett.* **20**, 1646 (1995)
- B.B. Hu, M.C. Nuss: Imaging with terahertz waves. *Opt. Lett.* **20**, 1716 (1995)
- D.M. Mittleman, R.H. Jacobsen, M.C. Nuss: T-ray imaging. *IEEE J. Sel. Topics Quantum Electron.* **2**, 679 (1996)
- P.Y. Han, G.C. Cho, X.C. Zhang: Time-domain transillumination of biological tissues with terahertz pulses. *Opt. Lett.* **24**, 242 (2000)
- P.H. Siegel: Terahertz technology. *IEEE MTT* **50**, 910 (2002)
- R.M. Woodward, W.P. Wallace, R.J. Pye, B.E. Cole, D.D. Arnone, E.H. Linfield, M. Pepper: Terahertz pulse imaging of ex vivo basal cell carcinoma. *J. Invest. Derm.* **120**, 72 (2003)
- C. Zandonella: Terahertz imaging: T-ray specs. *Nature* **424**, 721 (2003)
- [9.191] A.H. Zewail: Laser femtochemistry. *Science* **242**, 1645 (1988)
- A.H. Zewail: The birth of molecules. *Sci. Am.* **263**(6), 40 (1990)
- [9.192] M. Dantus, M.J. Rosker, A.H. Zewail: Real-time femtosecond probing of "transition states" in chemical reactions. *J. Chem. Phys.* **87**, 2395 (1987)
- M.J. Rosker, M. Dantus, A.H. Zewail: Femtosecond real-time probing of reactions. I. The technique. *J. Chem. Phys.* **89**, 6113 (1988)

- M.J. Rosker, M. Dantus, A.H. Zewail: Femtosecond real-time probing of reactions. II. The dissociation reaction of ICN. *J. Chem. Phys.* **89**, 6128 (1988)
- [9.193] A.H. Zewail: Femtochemistry. *J. Phys. Chem.* **97**, 12 427 (1993)
- S. Pedersen, J.L. Herek, A.H. Zewail: The validity of the “diradical hypothesis”: Direct femtosecond studies of the transition-state structures. *Science* **266**, 1359 (1994)
- A.H. Zewail: *J. Phys. Chem.* **100**, 12 701 (1996)
- H. Ihee, V. Lobastov, U. Gomez, B. Goodson, R. Srinivasan, C.-Y. Ruan, A.H. Zewail: Direct imaging of transient molecular structures with ultrafast diffraction. *Science* **291**, 385 (2001)
- S.K. Pal, J. Peon, A.H. Zewail: Biological water at the protein surface dynamical solvation probed directly with femtosecond resolution. *Proc. Natl. Acad. Sci.* **99**, 1763 (2002)
- [9.194] Proc. Femtosecond Chemistry – The Berlin Conference: *J. Phys. Chem.* **97**, 12 424–12 649 (1993) Special issue
- [9.195] A.H. Zewail (ed.): *Femtochemistry: Ultrafast Dynamics of the Chemical Bond*, Vols. 1 and 2 (World Scientific, Singapore 1994)
- [9.196] J. Manz, L. Wöste (eds.): *Femtosecond Chemistry*, Vol. 1 and 2 (VCH, Weinheim 1995)
- [9.197] P. Brumer, M. Shapiro: Laser control of chemical reactions. *Sci. Am.* **272**(3), 34 (1995)
- [9.198] M.A. El-Sayed, I. Tanaka, Y. Molin: *Ultrafast Processes in Chemistry and Photobiology* (Blackwell Science, Oxford 1995)
- [9.199] M. Chergui (ed.): *Femtochemistry: Ultrafast Chemical and Physical Processes in Molecular Systems* (World Scientific, Singapore 1996)
- [9.200] V. Sundström (ed.): *Femtochemistry and Femtobiology: Ultrafast Reaction Dynamics at Atomic-Scale Resolution* (World Scientific, Singapore 1997)
- [9.201] D.L. Andrews: *Lasers in Chemistry*, 3rd edn. (Springer Verlag, Heidelberg 1997)
- [9.202] M.J. Rosker, T.S. Rose, A.H. Zewail: Real-time dynamics of photo-fragment-trapping resonances on dissociative potential energy surfaces. *Chem. Phys. Lett.* **146**, 175 (1988)
- [9.203] L.R. Khundkar, A.H. Zewail: Picosecond photofragment spectroscopy. IV. Dynamics of consecutive bond breakage in the reaction $C_2F_4I_2 \rightarrow C_2F_4 + 2I$. *J. Chem. Phys.* **92**, 231 (1990)
- [9.204] S. Pedersen, L. Banares, A.H. Zewail: Femtosecond vibrational transition state dynamics in a chemical reaction. *J. Chem. Phys.* **97**, 8801 (1992)
- [9.205] M. Shapiro, P. Brumer: Coherent and incoherent laser control of photochemical reactions. *Int. Rev. Phys. Chem.* **13**, 187 (1994)
- [9.206] C.J. Bardeen, V.V. Yakolev, K.R. Wilson, S.D. Carpenter, P.M. Weber, W.S. Warren: *Chem. Phys. Lett.* **280**, 151 (1997)
- T.C. Weinacht, J. Ahn, P.H. Bucksbaum: Controlling the shape of a quantum wavefunction. *Nature* **397**, 233 (1999)
- J. Ahn, T.C. Weinacht, P.H. Bucksbaum: *Science* **287**, 463 (2000)
- [9.207] S.E. Harris: Electromagnetically induced transparency. *Physics Today* **50**, No 7, 36 (1997)
- O. Kocharovskaya: Amplification and lasing without inversion. *Phys. Rep.* **219**, 175 (1992)
- G. Alzetta, A. Gozzini, L. Moi, G. Orriols: *Nuovo Cimento B* **36**, 5 (1976)
- [9.208] O.A. Kocharovskaya, Y.I. Khanin: Coherent amplification of ultrashort pulse in the three-level medium without population inversion. *JETP Lett.* **48**, 630 (1988)

- [9.209] S.E. Harris: Lasers without inversion: Interference of lifetime-broadened resonances. *Phys. Rev. Lett.* **62**, 1033 (1989)
- [9.210] M.O. Scully, S.-Y. Zhu, A. Gavridiles: Degenerate quantum-beat laser: Lasing without inversion and inversion without lasing. *Phys. Rev. Lett.* **62**, 2813 (1989)
- [9.211] P. Mandel: Lasers without inversion: A useful concept? *Contemp. Phys.* **34**, 235 (1993)
- [9.212] O. Kocharovskaya: From lasers without inversion to gamma lasers? *Laser Physics* **5**, 284 (1995)
- O. Kocharovskaya, R. Kolesov, Yu. Rostovtsev: Lasing without inversion: a new path to gamma-ray laser. *Laser Physics* **9**, 745 (1999)
- [9.213] J. Gao, C. Guo, X. Guo, G. Jin, P. Wang, J. Zhao, H. Zhang, Y. Jiang, D. Wang, D. Jiang: Observation of light amplification without population inversion. *Opt. Commun.* **93**, 323 (1992)
- A. Nottelman, C. Peers, W. Lange: Inversionless amplification of picosecond pulses due to Zeeman coherence. *Phys. Rev. Lett.* **70**, 1783 (1993)
- E.S. Fry, X. Li, D. Nikonov, G.G. Padmabandu, M.O. Scully, A.V. Smith, F.K. Tittel, C. Wang, S.R. Wilkinson, S.-Y. Zhu: Atomic coherence effect within the sodium D line: Lasing without inversion via population trapping. *Phys. Rev. Lett.* **70**, 3235 (1993)
- W.E. van der Veer, R.J.J. van Dienst, A. Dönszelmann, H.B. van Linden van den Heuvell: Experimental demonstration of light amplification without population inversion. *Phys. Rev. Lett.* **70**, 3243 (1993)
- A.S. Zibrov, M.D. Lukin, D.E. Nikonov, L. Hollberg, M.O. Scully, V.L. Veltchansky, H.G. Robinson: Experimental demonstration of laser oscillation without population inversion via quantum interference in Rb. *Phys. Rev. Lett.* **75**, 1499 (1995)
- G.G. Padmabandu et al.: Laser oscillation without population inversion in a sodium atomic beam. *Phys. Rev. Lett.* **76**, 2053 (1996)
- J.A. Kleinfeld, A.D. Streater: Gain and coherence effects induced by strong cw-laser coupling in potassium-rare-gas mixtures. *Phys. Rev. A* **53**, 1839 (1996)
- C. Fort, F.S. Cataliotti, T.W. Hänsch, M. Inguscio, M. Prevedelli: Gain without inversion on the cesium D₁ line. *Opt. Commun.* **139**, 31 (1997)
- [9.214] A. Kaspari, M. Jain, G.Y. Jin, S.E. Harris: Electromagnetically induced transparency: Propagation dynamics. *Phys. Rev. Lett.* **74**, 2447 (1995)
- O. Schmidt, R. Wynands, Z. Hussein, D. Meschede: Steep dispersion and group velocity below c/3000 in coherent population trapping. *Phys. Rev. A* **53**, R27 (1996)
- L. Vestergaard Hau, S.E. Harris, Z. Dutton, C.H. Behroozi: Light speed reduction to 17 metres per second in an ultracold atomic gas. *Nature* **397**, 594 (1999)
- M.M. Kash, V.A. Sautenkov, A.S. Zibrov, L. Hollberg, G.R. Welch, M.D. Lukin, Y. Rostovtsev, E.S. Fry, M.O. Scully: Ultraslow group velocity and enhanced nonlinear optical effects in a coherently driven hot atomic gas. *Phys. Rev. Lett.* **82**, 5229 (1999)
- D.-F. Phillips, A. Fleischhauer, A. Mair, R.L. Walsworth, M.D. Lukin: Storage of light in atomic vapor. *Phys. Rev. Lett.* **86**, 783 (2001)
- C. Liu, Z. Dutton, C.H. Behroozi, L.V. Hau: Observation of coherent optical information storage in an atomic medium using halted light pulses. *Nature* **409**, 490 (2001)
- [9.215] S.E. Harris, L. Vestergaard Hau: Nonlinear optics at low light levels. *Phys. Rev. Lett.* **82**, 4611 (1999)

- A.S. Zibrov, M.D. Lukin, M.O. Scully: Nondegenerate parametric self-oscillation via multiwave mixing in coherent atomic media. *Phys. Rev. Lett.* **83**, 4049 (1999)
- M.D. Lukin, A. Imamoglu: Nonlinear optics and quantum entanglement of ultraslow single photons. *Phys. Rev. Lett.* **84**, 1419 (2000)
- [9.216] G. Mainfray, P. Agostini (eds.): *Multiphoton Processes* (CEA, Paris 1991)
- [9.217] M. Gavrila (ed.): *Atoms in Intense Laser Fields* (Academic Press, Boston 1992)
- [9.218] B. Piraux, A. L'Huillier, K. Rzazewski (eds.): *Super-Intense Laser-Atom Physics*, NATO ASI Ser. Vol. 316 (Plenum, New York 1993)
- [9.219] N.B. Delone, V.P. Krainov: *Multiphoton Processes in Atoms*, Vol. 13 (Springer Verlag, Heidelberg 1994)
- [9.220] S. Svanberg, J. Larsson, A. Persson, C.-G. Wahlström: Lund high power laser facility - Systems and first results. *Phys. Scr.* **49**, 187 (1994)
- [9.221] H.G. Muller, M.V. Fedorov (eds.): *Super-Intense Laser-Atom Physics IV* (Kluwer, Dordrecht 1996)
- [9.222] P. Gibbon, E. Förster: Short-pulse laser-plasma interactions. *Plasma Phys. Control. Fusion* **38**, 769 (1996)
- [9.223] P. Lambropoulos, H. Walther (eds.): *Multiphoton Processes 1996* (IOP Publishing, Bristol 1997)
- L.F. DiMauro, R.R. Freeman, K. Kulander: *Multiphoton Processes: ICOP XIII* (AIP, Melville, NY 2000)
- [9.224] P. Lambropoulos, H. Walther (eds.): *Multiphoton Physics*, IOP Conf. Ser., Vol. 154 (IOP Publishing, Bristol 1997)
- [9.225] S. Svanberg, A. L'Huillier, C.-G. Wahlström: Atomic physics using short-wavelength coherent radiation. *Nucl. Instrum. Methods A* **398**, 55 (1997)
- [9.226] M. Protopapas, C.H. Keitel, P.L. Knight: Atomic physics with super-high intensity lasers. *Rep. Prog. Phys.* **60**, 389 (1997)
- [9.227] N.H. March: *Atoms and Molecules in Intense Fields* (Springer Verlag, Heidelberg 1997)
- [9.228] L. Di Mauro, M. Murnane, A. L'Huillier (eds.): *Applications of ol. High-field and Short Wavelength Sources* (Plenum, New York 1998)
- [9.229] E. Turcu, B. Dance: *X-rays from Laser Plasmas* (Wiley, Chichester 1998)
- [9.230] D. Giulietti, L.A. Gizzii: X-ray emission from laser-produced plasmas. *Riv. Nuovo Cimento* **21**, 1 (1998)
- [9.231] M. Lontano, G. Mourou, F. Pegoraro, E. Sindroni (eds.): *Superstrong Fields in Plasmas*, AIP Conf. Proc. **426** (AIP, New York 1998)
- [9.232] F.H.M. Faisal: *Theory of Multiphoton Processes* (Plenum, New York 1987)
- [9.233] P. Mulser: *High Power Laser-Matter Interaction* (Springer, Berlin, Heidelberg 1999)
- [9.234] P. Agostini, F. Fabre, G. Mainfray, G. Petite, N. Rahman: Free-free transitions following six-photon ionization of xenon atoms. *Phys. Rev. Lett.* **42**, 1127 (1979)
- [9.235] J.H. Eberly, J. Javanainen, K. Rzazewski: Above-threshold ionization. *Phys. Rep.* **204**, 331 (1991)
- [9.236] L.F. DiMauro, P. Agostini: Ionization dynamics in strong laser fields. *Adv. At. Mol. Opt. Phys.* **35**, 79 (1995)
- [9.237] H.G. Muller, P. Agostini, G. Petite: Multiphoton Ionization. In: [9.217] p. 1.
- [9.238] H.M. van Linden van den Heuvel, H.G. Muller: In: *Multiphoton Processes, Studies in Modern Optics*, Vol. 8, ed. by S.J. Smith, P.L. Knight (Cambridge University Press, Cambridge 1988)

- [9.239] P.B. Corkum, N.H. Burnett, F. Brunel: Above-threshold ionization in the long-wavelength limit. *Phys. Rev. Lett.* **62**, 1259 (1989)
- [9.240] K.C. Kulander: Time-dependent theory of multiphoton ionization of xenon. *Phys. Rev. A* **38**, 778 (1988)
- [9.241] R.R. Freeman, P.H. Bucksbaum, H. Milchberg, S. Darack, D. Schumacher, M. Geusic: Above-threshold ionization with subpicosecond laser pulses. *Phys. Rev. Lett.* **59**, 1092 (1987)
- [9.242] L.J. Fransinski, K. Codling, P.A. Hatherly: *Science* **246**, 973 (1989)
- [9.243] R. Schinke: *Photodissociation Dynamics* (Cambridge University Press, Cambridge 1993)
- [9.244] K. Codling, L.J. Frasinski: Coulomb explosion of simple molecules in intense laser fields. *Contemp. Phys.* **35**, 243 (1994)
- [9.245] L.J. Fransinski, P.A. Hatherly, K. Codling, M. Larsson, A. Persson, C.-G. Wahlström: Multielectron dissociative ionization of CO₂ in intense laser fields. *J. Phys. B* **27**, L109 (1994)
- [9.246] S. Hunsche, T. Starczewski, A. L'Huillier, A. Persson, C.-G. Wahlström, B. van Linden van den Heuvell, S. Svanberg: Ionization and fragmentation of C₆₀ via multiphoton-multiplasmon excitation. *Phys. Rev. Lett.* **77**, 1966 (1996)
- [9.247] A. McPherson, G. Gibson, H. Jara, U. Johann, T.S. Luk, I.A. McIntyre, K. Boyer, C.K. Rhodes: Studies of multi-photon production of vacuum-ultraviolet radiation in rare gases. *J. Opt. Soc. Am. B* **4**, 595 (1987)
- [9.248] M. Ferrey, A. L'Huillier, X.F. Li, L.A. Lompré, G. Mainfray, C. Manus: Multiple-harmonic conversion of 1064 nm radiation in rare gases. *J. Phys. B* **21**, L31 (1988)
- [9.249] J.L. Krause, K.J. Schaefer, K.C. Kulander: High-harmonic generation from atoms and ions in the high intensity regime. *Phys. Rev. Lett.* **68**, 3535 (1992)
- [9.250] A. L'Huillier, T. Auguste, Ph. Balcou, B. Carré, P. Monot, P. Salières, C. Altucci, M. Gaarde, J. Larsson, E. Mevel, T. Starczewski, S. Svanberg, C.-G. Wahlström, R. Zerne, K.S. Budil, T. Ditmire, M.D. Perry: High-order harmonics: a coherent source in the XUV range, *J. Nonlinear Opt. Phys. Mater.* **4**, 647 (1995)
- [9.251] A. L'Huillier: Generation and application of high-order harmonics: 'An alternative coherent short-pulse XUV source.' In: *X-Ray Lasers 1996*, IOP Conference Series **151**, ed. by S. Svanberg, C.-G. Wahlström (IOP Publishing, Bristol 1996)
- [9.252] C. Lyngå: PhD Dissertation (Lund Institute of Technology, Lund 1999)
- [9.253] C.-G. Wahlström, J. Larsson, A. Persson, T. Starczewski, S. Svanberg, P. Salières, P. Balcou, A. L'Huillier: High-order harmonic generation in rare gases with an intense short-pulse low-frequency laser. *Phys. Rev. A* **48**, 4709 (1993)
- [9.254] J.J. Macklin, J.M. Kmetec, C.L. Gordon III: High-order harmonic generation using intense femtosecond pulses. *Phys. Rev. Lett.* **70**, 766 (1993)
- [9.255] A. L'Huillier, Ph. Balcou: High-order harmonic generation in rare gases with a 1 ps 1053 nm laser. *Phys. Rev. Lett.* **70**, 774 (1993)
- [9.256] S.G. Preston, A. Sanpera, M. Zepf, W.J. Blyth, C.G. Smith, J.S. Wark, M.H. Key, K. Burnett, M. Nakai, D. Neely, A.A. Offenberger: High-order harmonics of 248.6 nm KrF laser from helium and neon ions. *Phys. Rev. A* **53**, 31 (1996)
- [9.257] Z. Chang, A. Rundquist, H. Wang, M.M. Murnane, H. Kapteyn: Generation of coherent soft X-rays at 2.7 nm using high harmonics. *Phys. Rev. Lett.* **79**, 2967 (1997)

- [9.258] Ch. Spielmann, N.H. Burnett, S. Sartarnia, R. Koppnitsch, M. Schnürer, C. Kan, M. Lenzner, P. Wobrauscheck, F. Krausz: Generation of coherent X-rays in the water window using 5 femtosecond laser pulses. *Science* **278**, 661 (1997)
- [9.259] T. Starczewski, J. Larsson, C.-G. Wahlström, M.H.R. Hutchinson, J.E. Muffett, R.A. Smith, J.W.G. Tisch: Time-resolved harmonic generation in an ionizing gas. *J. Phys. B* **27**, 3291 (1994)
C. Altucci, T. Starczewski, C.-G. Wahlström, E. Mevel, B. Carré, A. L'Huillier: Influence of atomic density in high-order harmonic generation. *J. Opt. Soc. Am. B* **13**, 148 (1996)
- [9.260] J.M. Schins, P. Breger, P. Agostini, R.C. Constantinescu, H.G. Muller, A. Bouhal, G. Grillon, A. Antonetti, A. Mysyrowicz: Cross-correlation measurements of femtosecond extreme-ultraviolet high-order harmonics. *J. Opt. Soc. Am. B* **13**, 197 (1996)
- [9.261] P. Salières, A. L'Huillier, Ph. Antoine, M. Lewenstein: 'Study of the spatial and temporal coherence of high-order harmonics.' In: *Progress in Atomic, Molecular, and Optical Physics*, Vol. 41, ed. by B. Bederson, H. Walther (Academic Press, San Diego 1999) p. 84
L. Roos, M.B. Gaarde, A. L'Huillier: Tailoring harmonic radiation to different applications using a genetic algorithm. *J. Phys. B* **34**, 5041 (2001)
R. López-Martens, J. Mauritsson, A. Johansson, J. Norin, A. L'Huillier: Time-frequency characterization of high-order harmonic pulses. *Eur. Phys. J. D* (2003), to appear
- [9.262] R. Bonifacio, C. Pellegrini, I.M. Narducci: Collective instabilities and high-gain regime in a free electron laser. *Opt. Commun.* **50**, 373 (1984)
B.H. Wiik: The TESLA project: an accelerator facility for basic science. *Nucl. Instrum. Methods Phys. Res. A* **398**, 1 (1997)
- [9.263] C. Lyngå, F. Ossler, T. Metz, J. Larsson: A laser system providing radiation tunable from 35 nm to 2 μ m. *Appl. Phys. B* **72**, 913 (2001)
- [9.264] J. Larsson, E. Mevel, R. Zerne, A. L'Huillier, C.-G. Wahlström, S. Svanberg: Two-colour time-resolved spectroscopy of helium using high-order harmonics. *J. Phys. B* **28**, L53 (1995)
- [9.265] C.V. Shank, J.E. Bjorkholm, H. Kogelnik: Distributed feedback dye laser. *Appl. Phys. Lett.* **18**, 395 (1972)
F. Schäfer, W. Schade, B. Garbe, V. Helbig: Temperature-tuned distributed feedback dye laser with high repetition rate. *Appl. Opt.* **29**, 3950 (1990)
G.J. Bengtsson, K. Hansen, J. Larsson, W. Schade, S. Svanberg: Determination of radiative lifetimes in neutral nitrogen using short laser pulses from a distributed feedback dye laser. *Z. Physik D* **22**, 397 (1991)
- [9.266] P. Cacchiani, W. Ubachs, P.C. Hinnen, C. Lyngå, A. L'Huillier, C.-G. Wahlström: Lifetime measurements of the $E^1\Pi$, $v = 0$ and $v = 1$ states of $^{12}\text{C}^{16}\text{O}$, $^{13}\text{C}^{16}\text{O}$ and $^{13}\text{C}^{18}\text{O}$. *Astrophys. J.* **499**, L223 (1998)
- [9.267] D. Dechamps, L. Roos, C. Delfin, A. L'Huillier, C.-G. Wahlström: Two- and three-photon ionization of rare gases using femtosecond harmonic pulses generated in a gas medium. *Phys. Rev. A* **64**, 031404/1-4 (2001)
P. Erman, A. Karawajczyk, E. Rachlew-Källne, E. Mevel, R. Zerne, A. L'Huillier, C.-G. Wahlström: Autoionization width of the NO Rydberg-valence state complex in the 11–12 eV region. *Chem. Phys. Lett.* **239**, 6 (1995)
- [9.268] K.S.E. Eikema, W. Ubachs, W. Wassen, W. Hogervorst: First laser excitation of the ^4He $1\ 1^1S - 2\ 1^1P$ resonance line at 58 nm. *Phys. Rev. Lett.* **71**, 1690 (1993)

- W. Hogervorst, K.S.E. Eikema, W. Ubachs, W. Vassen: In: *Laser Spectroscopy*, ed. by M. Inguscio, M. Allegrini, A. Sasso (World Scientific, Singapore, 1996) p. 92
- K.S.E. Eikema, W. Ubachs, W. Vassen, W. Hogervorst: Precision spectroscopy on the Lyman- α transitions of H and He. In *Laser Physics at the limit*; eds. H. Figger, D. Meschede, C. Zimmerman (Springer Verlag, Berlin, Heidelberg 2002) p. 107
- [9.269] R. Haight, J. Bokor, J. Stark, R.H. Storz, R.R. Freeman, P.H. Bucksbaum: Picosecond time-resolved photoemission study of the InP (110) surface. *Phys. Rev. Lett.* **54**, 1302 (1985)
- R. Haight, D.R. Peale: Antibonding state on the Ge(111)As surface: spectroscopy and dynamics. *Phys. Rev. Lett.* **70**, 3979 (1993); *Rev. Sci. Instrum.* **65**, 1853 (1994)
- R. Haight: Electron dynamics at surfaces. *Surf. Sci. Rep.* **21**, 275 (1995)
- R. Haight, P.F. Seidler: High resolution atomic core level spectroscopy with laser harmonics. *Appl. Phys. Lett.* **65**, 517 (1994)
- H.S. Karlsson, G. Ghiaia, U.O. Karlsson: A system for time- and angle-resolved photo-electron spectroscopy based on an amplified titanium:sapphire laser system. *Rev. Sci. Instrum.* **67**, 3610 (1996)
- S. Sorensen, O. Björneholm, S. Buil, D. Deschamps, T. Kihlgren, A. L'Huillier, J. Norin, G. Öhrwall, S. Sundin, S. Svensson, C.-G. Wahlström: Femtosecond pump-probe photoelectron spectroscopy of predissociative Rydberg states in acetylene. *J. Chem. Phys.* **112**, 8038 (2000)
- [9.270] R. Zerne, C. Altucci, M. Bellini, M.B. Gaarde, T.W. Hänsch, A. L'Huillier, C.-G. Wahlström: Phase-locked high-order harmonic sources. *Phys. Rev. Lett.* **79**, 1006 (1997)
- M. Bellini, C. Lyngå, A. Tozzi, M.B. Gaarde, T.W. Hänsch, A. L'Huillier, C.-G. Wahlström: Temporal coherence of ultrashort high-order harmonic pulses. *Phys. Rev. Lett.* **81**, 297 (1998)
- D. Deschamps, C. Lyngå, J. Norin, A. L'Huillier, C.-G. Wahlström, J.-F. Hergott, H. Merdji, P. Salières, M. Bellini, T.W. Hänsch: Extreme ultraviolet interferometry measurements with high-order harmonics. *Opt. Lett.* **25**, 135 (2000)
- [9.271] G. Farkas, C. Toth: Proposal for attosecond light pulse generation using laser-induced multiple-harmonic conversion processes in rare gases. *Phys. Lett. A* **168**, 447 (1992)
- [9.272] S.E. Harris, J.J. Macklin, T.W. Hänsch: Atomic scale temporal structure inherent to high-order harmonic generation. *Opt. Commun.* **100**, 487 (1993)
- P.B. Corkum, N.H. Burnett, M.Y. Ivanov: Subfemtosecond pulses. *Opt. Lett.* **19**, 1870 (1994)
- P. Antoine, A. L'Huillier, M. Lewenstein: Attosecond pulse trains using high-order harmonics. *Phys. Rev. Lett.* **77**, 1234 (1996)
- I.P. Christov, N.H. Murnane, H.C. Kapteyn: High-harmonic generation of attosecond pulses in the "single-cycle" regime. *Phys. Rev. Lett.* **78**, 1251 (1997)
- E. Constant, V.D. Tatanukhin, A. Stolow, P.B. Corkum: Methods for the measurement of the duration of high-harmonic pulses. *Phys. Rev. A* **56**, 3870 (1997)
- N.A. Papadogiannis, B. Witzel, C. Kalpouzos, D. Charalambidis: Observation of attosecond light localization in higher order harmonic generation. *Phys. Rev. Lett.* **83**, 4289 (1999)

- P.M. Paul, E.S. Toma, P. Breger, G. Mullot, F. Augé, Ph. Balcou, H.G. Muller, and P. Agostini: Observation of a train of attosecond pulses from high harmonic generation. *Science* **292**, 1689 (2001)
- M. Drescher, M. Hentschel, R. Kienberger, G. Tempea, C. Spielmann, G.A. Reider, P.B. Corkum, F. Krausz: X-ray pulses approaching the attosecond frontier. *Science* **291**, 1923 (2001)
- M. Hentschel, R. Kienberger, Ch. Spielmann, G.A. Reider, N. Milosevic, T. Brabec, P.B. Corkum, U. Heinzmann, M. Drescher, F. Krausz: Attosecond metrology. *Nature* **414**, 511 (2001)
- M. Drescher, M. Hentschel, R. Kienberger, M. Uiberacker, V. Yakovlev, A. Scrinzi, Th. Westerwalbesloh, U. Kleineberg, U. Heinzmann, F. Krausz: Time resolved atomic inner-shell spectroscopy. *Nature* **419**, 803 (2002)
- D. Charalambidis, N.A. Papadogiannis, P. Tzallas, G.D. Tsakiris, K. Witte: Recent developments in attosecond pulse train metrology. *Phys. Scr.* **T105**, 23 (2003)
- A. Baltuska, Th. Udem, M. Uiberacher, H. Hentschel, E. Goulielmakis, Ch. Gohle, R. Holzwarth, V.S. Yakovlev, A. Scrinzi, T.W. Hänsch, F. Krausz: Attosecond control of electronic processes by intense light fields. *Nature* **421**, 611 (2003)
- P.H. Bucksbaum: Attophysics: Ultrafast control. *Nature* **421**, 593 (2003)
- [9.273] D.L. Matthews, P.L. Hagelstein, M.D. Rosen, M.J. Eckart, N.M. Ceglio, A.U. Hazi, H. Medecki, B.J. MacGowan, J.E. Trebes, B.L. Whitten, E.M. Campbell, C.W. Hatcher, A.M. Hawryluk, R.L. Kauffman, L.D. Pleasance, G. Rambach, J.H. Scofield, G. Stone, T.A. Weaver: Demonstration of a soft X-ray amplifier. *Phys. Rev. Lett.* **54**, 110 (1985)
- [9.274] R.C. Elton: *The Physics of X-Ray Lasers* (Academic Press, New York 1990)
- J.J. Rocca, P.L. Hagelstein (eds.): *Soft X-ray Lasers and Applications*, Proc. SPIE Int. Soc. Opt. Eng. **2520** (SPIE, Bellingham 1995)
- J.J. Rocca, L.B. Da Silva (eds.): *Soft X-Ray Lasers and Applications II*, Proc. SPIE Int. Soc. Opt. Eng. **3156** (SPIE, Bellingham 1997)
- [9.275] B.J. MacGowan, L.B. Da Silva, D.J. Fields, C.J. Keane, J.A. Koch, R.A. London, D.L. Matthews, S. Maxon, S. Mrowka, A.L. Osterheld, J.H. Scofield, G. Smimkaveg, J.E. Trebes, R.S. Walling: *Phys. Fluids B* **4**, 2326 (1992)
- [9.276] B. Rus, A. Clarillon, B. Gauthé, P. Goedtkindt, P. Jaeglé, G. Jamelot, A. Klisnick, A. Sureau, P. Zeitoun: Observation of intense soft-X-ray lasing at the $J = 0$ to $J = 1$ transition in neonlike zinc. *J. Opt. Soc. Am. B* **11**, 564 (1994)
- F. Albert, Ph. Zeitoun, P. Jaeglé, D. Joyeux, M. Boussoukaya, A. Clarillon, S. Hubert, G. Jamelot, A. Klisnick, D. Phalippou, D. Ros, A. Zeitoun-Fakiris: Metal-surface mapping by means of soft-x-ray interferometry. *Phys. Rev. B* **60**, 11 089 (1999)
- [9.277] Y. Nagata, K. Midorikawa, M. Obara, H. Tashiro, K. Toyoda: Soft-X-ray amplification of the Lyman- α transition by optical-field-induced ionization. *Phys. Rev. Lett.* **71**, 3774 (1993)
- [9.278] B.N. Chichkov, A. Egbert, H. Eichmann, C. Momma, S. Nolte, B. Wellegehausen: Soft-x-ray lasing to the ground states in low-charged oxygen ions. *Phys. Rev. A* **52**, 1629 (1995)
- [9.279] E. Fill, S. Borgström, J. Larsson, T. Starczewski, C.-G. Wahlström, S. Svanberg: XUV spectra of optical-field ionized plasmas. *Phys. Rev. E* **51**, 6016 (1995)
- S. Borgström, E. Fill, T. Starczewski, J. Steingruber, S. Svanberg,

- C.-G. Wahlström: Time-resolved X-ray spectroscopy of optical-field-ionized plasmas. *Laser Part. Beams* **13**, 459 (1995)
- [9.280] B.E. Lemoff, G.Y. Yin, C.L. Gordon III, C.P.J. Barty, S.E. Harris: Demonstration of a 10 Hz femtosecond-pulse-driven XUV laser at 41.8 nm in Xe IX. *Phys. Rev. Lett.* **74**, 1574 (1995)
- [9.281] J.J. Rocha, V.N. Shlyapstev, F.G. Tomasel, O.D. Cortazar, D. Hartshorn, J.L.A. Chilla: Demonstration of a discharge-pumped table-top soft-X-ray laser. *Phys. Rev. Lett.* **73**, 2192 (1994)
- [9.282] G. Tallents (ed.): *X-Ray Lasers*, IOP Conf. Ser. Vol. 116 (Institute of Physics Publ., Bristol 1990)
- [9.283] E.E. Fill (ed.): *X-Ray Lasers 1992*, IOP Conf. Ser. Vol. 125 (Institute of Physics Publ., Bristol 1992)
- [9.284] D.C. Eder, D.L. Matthews (eds.): *X-Ray Lasers 1994*, AIP Conf. Proc. Vol. 332 (AIP Press, New York 1994)
- [9.285] S. Svanberg, C.-G. Wahlström (eds.): *X-Ray Lasers 1996*, IOP Conf. Ser. Vol. 151 (Institute of Physics Publ., Bristol 1996)
- [9.286] Y. Kato, H. Takuma, H. Daido (eds.): *X-Ray Lasers 1998*, IOP Conf. Ser. Vol. 159 (Institute of Physics Publ., Bristol 1999)
- G. Jamelot, C. Möller, A. Klisnick (eds.): *X-Ray Lasers 2000* (EDP Sciences, Les Ulis 2001)
- J.J. Rocca, J. Dunn, S. Suckewer (eds.): *X-Ray Lasers 2002*, AIP Conf. Proc. Vol. 641 (AIP Press, New York 2002)
- [9.287] J.D. Kmetec, C.L. Gordon III, J.J. Macklin, B.E. Lemoff, G.S. Brown, S.E. Harris: MeV X-ray generation with a femtosecond laser. *Phys. Rev. Lett.* **68**, 1527 (1992)
- [9.288] K. Herrlin, G. Svanhn, C. Olsson, H. Pettersson, C. Tillman, A. Persson, C.-G. Wahlström, S. Svanberg: Generation of X-rays for medical imaging by high-power lasers: Preliminary results. *Radiology* **189**, 65 (1993)
- [9.289] C. Tillman, S. Johansson, B. Erlandsson, M. Grätz, B. Hemdal, A. Almén, S. Mattson, S. Svanberg: High-resolution spectroscopy of laser-produced plasmas in the photon energy range above 10 keV. *Nucl. Instrum. Methods A* **394**, 387 (1997)
- [9.290] G. Hölzer, E. Förster, M. Grätz, C. Tillman, S. Svanberg: X-ray crystal spectroscopy of sub-picosecond laser-produced plasmas beyond 50 keV. *J. X-Ray Sci. Technol.* **7**, 50 (1997)
- [9.291] C. Tillman, A. Persson, C.-G. Wahlström, S. Svanberg, K. Herrlin: Imaging using hard X-rays from a laser-produced plasma. *Appl. Phys. B* **61**, 333 (1995)
- A. Sjögren, M. Harbst, C.-G. Wahlström, S. Svanberg, C. Olsson: High-repetition-rate, hard x-ray radiation from a laser-produced plasma: Photon yield and application considerations. *Rev. Sci. Instr.* **74**, 2300 (2003)
- [9.292] R. Lewis: Medical applications of synchrotron radiation X-rays. *Phys. Med. Biol.* **42**, 1213 (1997)
- F.A. Dilmanian, X.Y. Wu, E.C. Parsons, B. Ren, J. Kress, T.M. Button, L.D. Chapman, J.A. Coderre, P. Giron, D. Greenberg, D.J. Krus, Z. Liang, D. Marcovici, M.J. Petersen, C.T. Roque, M. Shleifer, D.N. Slatkin, W.C. Tomlinson, K. Yamamoto, J. Zhou: Single- and dual-energy CT with monochromatic synchrotron X-rays. *Phys. Med. Biol.* **42**, 371 (1997)
- [9.293] C. Tillman, I. Mercer, S. Svanberg, K. Herrlin: Elemental biological imaging by differential absorption using a laser-produced X-ray source. *J. Opt. Soc. Am. B* **13**, 209 (1996)

- [9.294] C.L. Gordon III, G.Y. Yin, B.E. Lemoff, P.E. Bell, C.P.J. Barty: Time-gated imaging with an ultrashort-pulse laser-produced-plasma X-ray source. *Opt. Lett.* **20**, 1056 (1995)
- [9.295] M. Grätz, A. Pifferi, C.-G. Wahlström, S. Svanberg: Time-gated imaging in radiology: Theoretical and experimental studies. *IEEE J. Sel. Topics Quantum Electron.* **2**, 1041 (1996)
- [9.296] M. Grätz, L. Kiernan, C.-G. Wahlström, S. Svanberg: Time-gated X-ray tomography. *Appl. Phys. Lett.* **73**, 2899 (1998)
- M. Grätz, L. Kiernan, K. Herrlin: Time-gated imaging in planar and tomographic X-ray imaging. *Med. Phys.* **26**, 438 (1999)
- [9.297] C. Tillman, G. Grafström, A.-Ch. Jonsson, B.-A. Jönsson, I. Mercer, S. Mattson, S.-E. Strandh, S. Svanberg: Survival of mammalian cells exposed to ultrahigh dose rates from a laser-produced plasma X-ray source. *Radiology* **213**, 860 (1999)
- [9.298] P.M. Renzepis, J.R. Helliwell (eds.): *Time-Resolved Diffraction* (Oxford University Press, Oxford 1997)
- J. Wark: Time-resolved X-ray diffraction. *Contemp. Phys.* **37**, 205 (1996)
- [9.299] C. Rischel, A. Rousse, I. Uschmann, O.-A. Albouy, J.-P. Geindre, P. Audebert, J.C. Gauthier, E. Förster, J.-L. Martin, A. Antonetti: Femtosecond time-resolved X-ray diffraction from laser-heated organic films. *Nature* **370**, 480 (1997)
- R. Jimenez, C. Rose-Petrucci, T. Guo, K.R. Wilson, C.P.J. Barty: 'Time-resolved X-ray diffraction of GaAs with a 30 fs laser driven plasma source.' In: *Ultrafast Phenomena XI*, ed. by W. Zinth, J.G. Fujimoto, T. Elsaesser, D. Wiersma (Springer, Berlin, Heidelberg 1998)
- A. Rousse, C. Rischel, S. Fourmaux, I. Uschmann, S. Sebban, G. Grillon, Ph. Balcou, E. Förster, J.P. Geindre, P. Audebert, J.C. Gauthier, D. Hulin: *Nature* **410**, 65 (2001)
- O. Synnergren, M. Harbst, T. Missalla, J. Larsson, G. Katona, R. Neutze, R. Wouts: Projecting picosecond lattice dynamics through X-ray topography. *Appl. Phys. Lett.* **80**, 3727 (2002)
- [9.300] L. Larsson, Z. Chang, E. Judd, P.J. Schuck, P.H. Bucksbaum, R.W. Lee, H.A. Padmore, R.W. Falcone: Ultrafast structural changes measured by time-resolved X-ray diffraction. *Appl. Phys. A* **66**, 587 (1998)
- M. Wulff, F. Schotte, G. Naylor, D. Bourgeois, K. Moffat, G. Mourou: Time-resolved structures of macromolecules at the ESRF: Single-pulse Laue diffraction, stroboscopic data collection and femtosecond flash photolysis. *Nucl. Instrum. Methods Phys. Res. A* **398**, 69 (1997)
- D.A. Reis, M.F. DeCamp, P.H. Bucksbaum, R. Clarke, E. Dufresne, M. Hertlein, R. Merlin, R. Falcone, H. Kapteyn, M.M. Murnane, J. Larsson, Th. Missalla, J.S. Wark: Probing impulsive strain propagation with X-ray pulses. *Phys. Rev. Lett.* **86**, 3072 (2001)
- J. Larsson, A. Allen, P.H. Bucksbaum, R.W. Falcone, A. Lindenberg, G. Naylor, T. Misalla, D.A. Reis, K. Scheidt, A. Sjögren, P. Sondhauss, M. Wulff, J.S. Wark: Pico-second X-ray diffraction studies in laser-excited acoustic phonons in InSb. *App. Phys. A* **75**, 467 (2002)
- [9.301] D. Umstadter, T.B. Norris (eds.): *Feature Issue on Optics of Relativistic Electrons*. *IEEE J. Quantum Electron.* **33**, 1877 (1997)
- D. Umstadter, S.-Y. Chen, R. Wagner, A. Maksimchuk, G. Sarkisov: Non-linear optics in relativistic plasmas. *Opt. Express* **2**, 282 (1998)
- [9.302] J. Fan, T.R. Clark, H.M. Milchberg: Generation of a plasma waveguide in an elongated, high repetition rate gas jet. *Appl. Phys. Lett.* **73**, 3064 (1998)

- [9.303] E. Esarey, P. Sprangle, J. Krall, A. Ting: Overview of plasma-based accelerator concepts. *IEEE Trans. Plasma Sci.* **PS-24**, 252 (1996)
 R. Wagner, S.-Y. Chen, A. Maksimchuk, D. Umstadter: Electron acceleration by a laser wakefield in a relativistically self-guided channel. *Phys. Rev. Lett.* **78**, 3125 (1997)
 A. Maksimchuk, S. Gu, K. Filippo, G. Mourou, D. Umstadter: Observation of high-energy proton beam in interaction of high-intensity subpicosecond laser pulse with thin foil. *APS Div. of Plasma Physics Meeting, Seattle 1999* (AIP News Update **457**, Nov. 15 1999)
 S. Karsch, S. Düsterer, H. Schwoerer, F. Ewald, D. Habs, M. Hegelich, G. Pretzler, A. Pukhov, K. Witte, R. Sauerbrey: High-intensity laser induced ion acceleration from heavy water droplets. *Phys. Rev. Lett.* **91**, 015001 (2003)
- [9.304] S. Matinyan: Lasers as a bridge between atomic and nuclear physics. *Phys. Rep.* **298**, 199 (1998)
 G. Pretzler, A. Saemann, A. Pukov, D. Rudolph, T. Schätz, U. Schramm, P. Thirolf, D. Habs, K. Eidmann, G.D. Tsakiris, J. Meyer-ter-Vehn, K.J. Witte: Neutron production by 200 mJ ultrashort laser pulses. *Phys. Rev. E* **58**, 2 (1998)
 K. Ledingham, P.A. Norreys: Nuclear physics merely using a light source. *Contemp. Phys.* **40**, 367 (1999)
 G. Gahn, G.D. Tsakiris, G. Pretzler, K.J. Witte, C. Delfin, C.-G. Wahlström, D. Habs: Generating positrons with femtosecond-laser pulses. *Appl. Phys. Lett.* **77**, 2662 (2000)
 A. Andreev et al.: Excitation and decay of low-lying nuclear states in a dense plasma produced by a subpicosecond laser pulse. *J. Exp. Theor. Phys.* **91**, 1163 (2000)
 H. Schwoerer, F. Ewald, R. Sauerbrey, J. Galy, J. Magill, V. Rondinella, R. Schenkel, T. Butz: Fission of actinides using a tabletop laser. *Europhys. Lett.* **66**, 47 (2003)
- [9.305] P.A. Norreys et al.: *Phys. Plasmas* **6**, 2150 (1999)
 M. Chown: A cheap proton source could transform radiotherapy. *New Scientist*, Dec. 4, 1999
- [9.306] G.C. Baldwin, J.C. Solem: *Rev. Mod. Phys.* **69** 1085 (1997)
 V.S. Letokhov: in *Frontiers in Laser Spectroscopy*, Proceedings of the Les Houches Summer Schools, Vol. 2, ed. by R. Ballian, S. Haroche, S. Liberman (North-Holland, Amsterdam 1977)
 C.B. Collins, F. Davanloo, M.C. Yosif, R. Dussart, J.M. Hicks, S.A. Karamian, C.A. Ur, I.I. Popescu, V.I. Kirischuk, J.J. Carroll, H.E. Roberts, P. McDaniel, C.E. Crist: Accelerated emission of gamma rays from the 31 yr isomer ^{178}Hf induced by X-ray irradiation. *Phys. Rev. Lett.* **82**, 695 (1999)
 O. Kocharovskaya, R. Kolesov, Yu. Rostovtsev: Lasing without inversion: a new path to gamma-ray laser. *Laser Physics* **9**, 745 (1999)
- [9.307] W.J. Hogan (ed.): *Energy from Inertial Fusion* (IAEA, Vienna 1995)
- [9.308] M. Tabak, J. Hammer, M.E. Glinsky, W.L. Kruer, S.C. Wilks, J. Woods-worth, E.M. Campbell, M.D. Perry: Ignition and high gain with ultrapowerful lasers. *Phys. Plasmas* **1**, 1626 (1994)
- [9.309] M.D. Perry, D. Pennington, B.C. Stuart, G. Tietbohl, J.A. Britten, C. Brown, S. Herman, B. Golick, M. Kartz, J. Miller, H.T. Powell, M. Vergino, V. Yanovsky: Petawatt laser pulses. *Opt. Lett.* **24**, 160 (1999)
 K. Fredriksson, H. Lundberg, S. Svanberg: Fine- and hyperfine structure investigation in the $5D - nF$ series of cesium. *Phys. Rev. A* **21**, 241 (1980)

- [9.310] K. Fredriksson, L. Nilsson, S. Svanberg: Stark interaction for alkali atoms (unpublished report, 1980)
- [9.311] M.A. Zaki Ewiss, W. Hogervorst, W. Vassen, B.H. Post: The Stark effect in the $6snf$ Rydberg series of barium. *Z. Phys. A* **322**, 211 (1985)
- [9.312] R. Frisch: Experimenteller Nachweis des Einsteinschen Strahlungsrückstosses. *Z. Physik* **86**, 42 (1933)
- [9.313] J.-L. Piqué, J.-L. Vialle: Atomic-beam deflection and broadening by recoils due to photon absorption or emission. *Opt. Commun.* **5**, 402 (1972)
R. Schieder, H. Walther, L. Wöste: Atomic beam deflection by the light of a tunable dye laser. *Opt. Commun.* **5**, 337 (1972)
- [9.314] A.P. Kazantzev: Acceleration of atoms by a resonant field. *Sov. Phys. JETP* **36**, 1628 (1973)
- [9.315] F. Touchard, J.M. Serre, S. Büttgenbach, P. Guimbal, R. Klapisch, M. de Saint Simon, C. Thibault, H.T. Duong, P. Juncar, S. Liberman, J. Pinard, J.-L. Vialle: Electric quadrupole moments and isotopic shifts of radioactive sodium isotopes. *Phys. Rev. C* **25**, 2756 (1982)
- [9.316] S. Liberman: High resolution laser spectroscopy of radioactive atoms. In: [9.30] p. 162
- [9.317] H.T. Duong, P. Juncar, S. Liberman et al.: First observation of the blue optical lines of francium. *Europhys. Lett.* **3**, 175 (1987)
S.V. Andreev, V.S. Letokhov, V.I. Mishin: Laser resonance photoionization spectroscopy of Rydberg levels in Fr. *Phys. Rev. Lett.* **59**, 1274 (1987)
- [9.318] W. Ertmer, B. Hofer: Zero-field hyperfine structure measurements of metastable states $3d^2 4s\ ^4F_{3/2,9/2}$ of ^{45}Sc using laser fluorescence atomic-beam-magnetic-resonance technique. *Z. Phys. A* **276**, 9 (1976)
S.D. Rosner, R.A. Holt, T.D. Gaily: Measurement of the zero-field hyperfine structure of a single vibration-rotation level of Na_2 by a laser-fluorescence molecular-beam-resonance technique. *Phys. Rev. Lett.* **35**, 785 (1975)
- [9.319] P. Grundevik, M. Gustavsson, I. Lindgren, G. Olsson, L. Robertsson, A. Rosén, S. Svanberg: Precision method for hyperfine structure studies in low-abundance isotopes: The quadrupole moment of ^{43}Ca . *Phys. Rev. Lett.* **42**, 1528 (1979)
- [9.320] W.H. Wing, G.A. Ruff, W.E. Lamb, J.J. Spezeski: Observation of the infrared spectrum of the hydrogen molecular ion HD^+ . *Phys. Rev. Lett.* **36**, 1488 (1976)
- [9.321] S.L. Kaufmann: High resolution laser spectroscopy in fast beams. *Opt. Commun.* **17**, 309 (1976)
- [9.322] E.W. Otten: 'Hyperfine and isotope shift measurements.' In: *Atomic Physics 5*, ed. by R. Marrus, M. Prior, H. Shugart (Plenum, New York 1977)
- [9.323] P. Jaquinot, R. Klapisch: Hyperfine spectroscopy of radioactive atoms. *Rep. Prog. Phys.* **42**, 773 (1979)
- [9.324] R. Neugart, S.L. Kaufman, W. Klempt, G. Moruzzi: High resolution spectroscopy in fast beams. In: [9.25] p. 446
R. Neugart: 'Collinear fast-beam laser spectroscopy.' In: *Progress in Atomic Spectroscopy*, Pt. D, ed. by H.K. Beyer, H. Kleinpoppen (Plenum, New York 1987) p. 75
- [9.325] H.J. Kluge: 'Optical spectroscopy of shortlived isotopes.' In: *Progress in Atomic Spectroscopy*, Pt. B, ed. by W. Hanle, H. Kleinpoppen (Plenum, New York 1979) p. 727
- [9.326] H.J. Kluge: *Hyperfine Interact.* **24–26**, 69 (1985)
H. H Stroke: 'Isotopic shifts.' In: *Atomic Physics 8*, ed. by I. Lindgren, A. Rosen, S. Svanberg (Plenum, New York 1983) p. 509

- [9.327] S. Svanberg: Laser spectroscopy applied to the study of hyperfine interactions. *Hyperfine Interact.* **15/16**, 111 (1983)
- [9.328] H.T. Schmidt, P. Forck, M. Grieser, D. Habs, J. Kenntner, G. Miersch, R. Repnow, U. Schramm, T. Schussler, D. Schwam, A. Wolf: *Phys. Rev. Lett.* **72**, 1616 (1994)
S. Mannervik, L. Broström, J. Lidberg, L.O. Norlin, P. Royen: Strong hyperfine induced quenching of a metastable state in Xe^+ observed by hyperfine selective laser probing of a stored ion beam. *Phys. Rev. Lett.* **76**, 3675 (1996)
J. Lidberg, A. Al-Khalidi, L.-O. Norlin, P. Royen, X. Tordoir, S. Mannervik: Lifetime of the metastable $3d\ ^2D_{3/2}$ and $3d\ ^2D_{5/2}$ levels in Ca^+ measured by laser probing of a stored ion beam. *J. Phys. B* **32**, 757 (1999)
- [9.329] M. Larsson: Atomic and molecular physics with ion storage rings. *Rep. Prog. Phys.* **58**, 1267 (1995)
Th.U. Kühl: 'Storage ring laser spectroscopy.' In: *Progress in Atomic, Molecular, and Optical Physics*, Vol. 40, ed. by B. Bederson, H. Walther (Academic Press, San Diego 1999) p. 114
P.H. Mokler, Th. Stöhlker: 'The physics of highly charged heavy ions revealed by storage/cooler rings.' In: *Progress in Atomic, Molecular, and Optical Physics*, Vol. 37, ed. by B. Bederson, H. Walther (Academic Press, San Diego 1996) p. 297
- [9.330] M. Larsson, H. Danared, J.R. Mowat, P. Sigray, G. Sundström, L. Broström, A. Filevich, A. Källberg, S. Mannervik, K.G. Rensfelt, S. Datz: Direct high-energy neutral-channel dissociative recombination of cold H_3^+ in an ion storage ring. *Phys. Rev. Lett.* **70**, 430 (1993)
S. Datz, G. Sundström, Ch. Biedermann, L. Broström, H. Danared, S. Mannervik, J.R. Mowat, M. Larsson: Branching processes in the dissociative recombination of H_3^+ . *Phys. Rev. Lett.* **74**, 896 (1995)
- [9.331] G. Budker: In: *Proc. Int. Symp. on Electron and Positron Storage Rings*, ed. by H. Zyngier, E. Cremieux-Alcan (Presses Universitaire, Saclay 1966)
G. Budker et al.: In *Proc. IV All-Union Meeting on Accelerators of Charged Particles*, IEEE Trans. Nucl. Sci. **VS-22**, 2093 (1975)
H. Danared, G. Andler, L. Bagge, C.J. Herrlander, J. Hilke, J. Jeansson, A. Källberg, A. Nilsson, A. Paál, K.-G. Rensfelt, U. Rosengård, J. Starker, M. af Ugglas: Electron cooling with an ultracold electron beam. *Phys. Rev. Lett.* **72**, 3775 (1994)
S. Schröder, R. Klein, N. Roos, M. Gerhard, R. Grieser, G. Huber, A. Karafillides, M. Krieg, N. Schmidt, T. Kuhl, R. Neumann, V. Balykin et al.: First laser cooling of relativistic ions in a storage ring. *Phys. Rev. Lett.* **64**, 2901 (1990)
J.S. Hangst, M. Kristensen, J.S. Nielsen, O. Poulsen, J.P. Schiffer, P. Shi: Laser cooling of a stored ion beam to 1 mK. *Phys. Rev. Lett.* **67**, 1238 (1991)
- [9.332] D.M. Maletic, A.G. Ruggiero (eds.): *Crystalline Beams and Related Issues* (World Scientific, Singapore 1996)
- [9.333] L.H. Andersen, T. Andersen, P. Hvelplund: Studies of negative ions in storage rings. *Adv. At. Mol. Opt. Phys.* **38**, 155 (1998)
D. Hanstorp: An ion beam apparatus for collinear photodetachment experiments. *Nucl. Instrum. Methods B* **100**, 165 (1995)
D. Hanstorp, G. Haefliger, A.E. Klinkmüller, U. Ljungblad, U. Berzinsh, I.Yu. Kiyani, D.J. Pegg: 'Two-electron dynamics in photodetachment.' In: *Modern Trends in Atomic Physics*, *Adv. Quantum Chem.* **30**, 311 (1998)

- [9.334] D. Hanstorp, P. Devynck, W.G. Graham, J.R. Peterson: Observation of metastable autodetaching Ca^- . *Phys. Rev. Lett.* **63**, 368 (1989)
- [9.335] V.V. Petrunin, J.D. Voldstad, P. Balling, P. Kristensen, T. Andersen, H.K. Haugen: Resonant ionization spectroscopy of Ba^- metastable and stable ions. *Phys. Rev. Lett.* **75**, 1911 (1995)
- [9.336] P.H. Lee, M.L. Skolnick: Saturated neon absorption inside a 6328 Å laser. *Appl. Phys. Lett.* **10**, 303 (1967)
- [9.337] W.E. Lamb Jr.: Theory of the optical laser. *Phys. Rev. A* **134**, 1429 (1964)
- [9.338] W.R. Rowley, B.W. Jolliffe, K.C. Schotton, A.J. Wallard, P.T. Woods: Laser wavelength measurements and the speed of light. *Opt. Quantum Electron.* **8**, 1 (1976)
- [9.339] J.L. Hall: Stabilized lasers and precision measurements. *Science* **202**, 147 (1978)
- [9.339] K.M. Evenson, D.A. Jennings, F.R. Peterson, J.S. Wells: Laser frequency measurements: A review, limitations, extension to 197 THz (1.5 mm). In: [9.25] p. 57
- [9.340] D.A. Jennings, F.R. Petersen, K.M. Evenson: Direct frequency measurement of the 260 THz (1.15 μ) ^{20}Ne laser: And beyond. In: [9.26] p. 31
- [9.340] D.A. Jennings, C.R. Pollock, F.R. Petersen, R.E. Drullinger, K.M. Evenson, J.S. Wells: Direct frequency measurement of the I_2 stabilized He-Ne 473 THz (633 nm) laser. *Opt. Lett.* **8**, 136 (1983)
- [9.341] R.G. DeVoe, R.G. Brewer: Laser frequency division and frequency stabilization. *Phys. Rev. A* **30**, 2827 (1984)
- [9.341] R.G. DeVoe, C. Fabre, K. Jungmann, J. Hoffnagle, R.G. Brewer: Precision optical-frequency difference measurements. *Phys. Rev. A* **37**, 1802 (1988)
- [9.342] T. Wilkie: Time to remeasure the metre. *New Scientist* (Oct. 27, 1983)
- [9.343] Documents concerning the new definition of the metre. *Metrologia* **19**, 163 (1984)
- [9.344] M.D. Levenson, A.L. Schawlow: Hyperfine interactions in molecular iodine. *Phys. Rev. A* **6**, 10 (1972)
- [9.345] T.W. Hänsch, I.S. Shahin, A.L. Schawlow: High resolution saturation spectroscopy of the sodium D line with a pulsed tunable dye laser. *Phys. Rev. Lett.* **27**, 707 (1971)
- [9.346] C. Bordé: Spectroscopie d'absorption saturée de diverses molécules au moyen des lasers à gas carbonique et à prooxyde d'azote. *C. R. Acad. Sci. B* **271**, 371 (1970)
- [9.347] S. Svanberg, G.-Y. Yan, T.P. Duffey, A.L. Schawlow: High-contrast Doppler-free transmission spectroscopy. *Opt. Lett.* **11**, 138 (1986)
- [9.347] S. Svanberg, G.-Y. Yan, T.P. Duffey, W.-M. Du, T.W. Hänsch, A.L. Schawlow: Saturation spectroscopy for optically thick atomic samples. *J. Opt. Soc. Am. B* **4**, 462 (1987)
- [9.348] C. Wieman, T.W. Hänsch: Doppler-free laser polarization spectroscopy. *Phys. Rev. Lett.* **36**, 1170 (1976)
- [9.349] T.W. Hänsch, I.S. Shahin, A.L. Schawlow: Optical resolution of the Lamb shift in atomic hydrogen. *Nature* **235**, 56 (1972)
- [9.349] T.W. Hänsch, M.H. Nayfeh, S.A. Lee, S.M. Curry, I.S. Shahin: Precision measurement of the Rydberg constant by laser saturation spectroscopy of the Balmer- α line in hydrogen and deuterium. *Phys. Rev. Lett.* **32**, 1336 (1974)
- [9.350] J.E.M. Goldsmith, E.W. Weber, T.W. Hänsch: New measurement of the Rydberg constant using polarization spectroscopy of H. *Phys. Rev. Lett.* **41**, 1525 (1978)

- [9.351] K. Pachucki, D. Leibfried, M. Weitz, A. Huber, W. König, T.W. Hänsch: Theory of the energy levels and precise two-photon spectroscopy of atomic hydrogen and deuterium. *J. Phys. B* **29**, 177 (1996)
- [9.352] P. Zhao, W. Lichten, J.C. Bergquist, H.P. Layer: Remeasurement of the Rydberg constant. *Phys. Rev. A* **34**, 5138 (1986)
- [9.353] P. Zhao, W. Lichten, H. Layer, J. Bergquist: New value for the Rydberg constant from the hydrogen Balmer- β transition. *Phys. Rev. Lett.* **58**, 1293 (1987)
- [9.354] F. Biraben, J.C. Garreau, L. Julien: Determination of the Rydberg constant by Doppler-free two-photon spectroscopy of hydrogen Rydberg states. *Europhys. Lett.* **2**, 925 (1986); and in [9.30] p. 8
- [9.355] T.W. Hänsch, A.L. Schawlow, G.W. Series: The spectrum of atomic hydrogen. *Sci. Am.* **240**(3) 72 (1979)
- G.W. Series (ed.): *The Spectrum of Atomic Hydrogen: Advances* (World, Scientific, Singapore 1988)
- G.F. Bassani, M. Inguscio, T.W. Hänsch (eds.): *The Hydrogen Atom* (Springer, Berlin, Heidelberg 1989)
- B. Cagnac, M.D. Plimmer, L. Julien, F. Biraben: The hydrogen atom, a tool for metrology. *Rep. Prog. Phys.* **57**, 853 (1995)
- B. Cagnac: 'Two-photon method for metrology in hydrogen.' In: *Atomic Physics Methods in Modern Research*, ed. by K. Jungmann, J. Kowalski, I. Reinhard, F. Träger (Springer Verlag, Heidelberg, Berlin 1997)
- [9.356] A.I. Ferguson, J.M. Tolchard: Laser spectroscopy of atomic hydrogen. *Contemp. Phys.* **28**, 383 (1987)
- [9.357] H.R. Schlossberg, A. Javan: Saturation behaviour of a Doppler-broadened transition involving levels with closely spaced structure. *Phys. Rev.* **150**, 267 (1966)
- [9.358] T.W. Hänsch, P. Toschek: Theory of a three-level gas laser amplifier. *Z. Physik* **236**, 213 (1970)
- [9.359] M.A. Bouchiat, L. Pottier: An atomic preference between left and right. *Sci. Am.* **250**(6), 76 (1984)
- M.-A. Bouchiat, L. Pottier: Optical experiments and weak interactions. *Nature* **234**, 1203 (1986)
- M.-A. Bouchiat, C. Bouchiat: Parity violation in atoms. *Rep. Prog. Phys.* **60**, 1352 (1997)
- [9.360] E.D. Commins: Parity violation in atoms. In: [9.30] p. 43
- [9.361] T.P. Emmons, E.N. Fortson: 'Parity conservation in atoms.' In: *Progress in Atomic Spectroscopy*, Pt. D, ed. by H.K. Beyer, H. Kleinpoppen (Plenum, New York 1987) p. 237
- D.N. Stacey: 'Parity non-conservation in atoms.' In: *Atomic Physics 13*, ed. by H. Walther, T.W. Hänsch, B. Neizert (AIP Publishing, New York 1993) p. 46
- [9.362] P.A. Vetter, D.M. Meekhof, P.K. Majumder, S.K. Lamoreaus, E.N. Fortson: Precise test of electroweak theory from a new measurement of parity nonconservation in atomic thallium. *Phys. Rev. Lett.* **74**, 2658 (1995)
- [9.363] M.J.D. MacPherson, K.P. Zetie, R.B. Warrington, D.N. Stacey, J.P. Hoare: Precise measurement of parity nonconserving optical rotation at 876 nm in atomic bismuth. *Phys. Rev. Lett.* **67**, 2784 (1991)
- [9.364] M.C. Noecker, B.P. Masterson, C.E. Wieman: Precision measurement of parity nonconservation in atomic cesium: A low-energy test of the electro-weak theory. *Phys. Rev. Lett.* **61**, 310 (1988)

- C.S. Wood, S.C. Bennett, D. Cho, B.P. Masterson, J. L Roberts, C.E. Tanner, C.E. Wieman: Measuerement of parity nonconservation and an anapole moment in cesium. *Science* **275**, 1759 (1997)
- S.C. Bennett, C.E. Wieman: *Phys. Rev. Lett.* **82**, 2484 (1999); *ibid.* **83**, 889 (1999)
- [9.365] S.A. Blundell, W.R. Johnson, J. Sapirstein: High-accuracy calculation of the $6\text{ S}_{1/2}$ - $7\text{ S}_{1/2}$ parity-nonconserving transition in atomic cesium and implications for the standard model. *Phys. Rev. Lett.* **65**, 1411 (1990); *Phys. Rev. A* **43**, 3407 (1991)
- A.C. Hartley, E. Lindroth, A. Mårtensson-Pendrill: Parity nonconservation and electric dipole moments in caesium and thallium. *J. Phys. B* **23**, 3417 (1990)
- [9.366] Ya.B. Zel 'Dovich: Electromagnetic interaction with parity violation. *Sov. Phys. JETP* **6**, 1184 (1968)
- V.F. Dmitriev, I.B. Kriplovich, V.B. Telitsin: Nuclear anapole moments in single-particle approximation. *Nucl. Phys. A* **577**, 691 (1994)
- C. Bouchiat, C.A. Piketty: Nuclear spin dependent parity violating electron-nucleus interaction in heavy atoms. The anapole moment and the perturbation of the hadronic vector neutral current by the hyperfine interaction. *Phys. Lett. B* **269**, 195 (1991)
- W.C. Haxton, C.E. Wieman: Atomic parity nonconservation and nuclear anapole moments. *Ann. Rev. Nucl. Part. Sci.*; *Annual Reviews* 2001, 261 (2001)
- [9.367] V.W. Hughes: 'High precision atomic spectroscopy of muonium and simple muonic atoms.' In: *Atomic Physics Methods in Modern Research*, ed. by K. Jungmann, J. Kowalski, I. Reinhard, F. Träger (Springer Verlag, Heidelberg, Berlin 1997)
- V.W. Hughes: High-precision spectroscopy of positronium and muonium. *Adv. Quantum Chem.* **30**, 99 (1998)
- D. Taqqu, F. Biraben, C.A.N. Conde, T.W. Hänsch, F.J. Hartmann, P. Hauser, P. Indelicato, P. Knowles, F. Kottmann, F. Mulhauser, C. Petitjean, R. Pohl, P. Rabinowitz, R. Rosenfelder, J.M.F. Santos, W. Scott, L.M. Simons, J.F.C.A. Veloso: Laser spectroscopy of the Lamb shift in muonic hydrogen. *Hyperfine Interact.* **119**, 317 (1999)
- [9.368] J. Eades (ed.): *Proceedings of the Antihydrogen Workshop, July 1992*, *Hyperfine Interact.* **76** (1993)
- G. Gabrielse, D.S. Hall, A. Khabbaz, T. Roach, P. Yesley, C. Heimann, H. Kalinowsky, W. Jhe: 'Comparing the antiproton and the proton and progress towards antihydrogen.' In: *Atomic Physics 15*, ed. by H.B. van Linden van den Heuvell, J.T.M. Walraven, M.W. Reynolds (World Scientific, Singapore 1997) p. 446
- K.S.E. Eikema, J. Walt, T.W. Hänsch: Continuous wave coherent Lyman-alpha radiation. *Phys. Rev. Lett.* **83**, 3828 (1999)
- M. Amoretti et al.: Production and detection of cold antihydrogen atoms. *Nature* **419**, 456 (2002)
- G. Gabrielse, N.S. Bowen, P. Oxley, A. Speck, C.H. Storry, J.N. Tan, M. Wessels, D. Grzonka, W. Oelert, G. Schepers, T. Sefwick, J. Walz, H. Pittner, T.W. Hänsch, E.A. Hessels: Background-free observation of cold antihydrogen with field-ionization analysis of its states. *Phys. Rev. Lett.* **89**, 213 401 (2002)
- [9.369] M.S. Sorem, A.L. Schawlow: Saturation spectroscopy in molecular iodine by intermodulated fluorescence. *Opt. Commun.* **5**, 148 (1972)

- [9.370] J.E. Lawler, A.I. Ferguson, J.E.M. Goldsmith, D.J. Jackson, A.L. Schawlow: Doppler-free intermodulated optogalvanic spectroscopy. *Phys. Rev. Lett.* **42**, 1046 (1979)
- [9.371] D.R. Lyons, A.L. Schawlow, G.-Y. Yan: Doppler-free radiofrequency optogalvanic spectroscopy. *Opt. Commun.* **38**, 35 (1981)
- [9.372] E.E. Marinero, M. Stuke: Doppler-free optoacoustic spectroscopy. *Opt. Commun.* **30**, 349 (1979)
- [9.373] T.P. Duffey, D. Kammen, A.L. Schawlow, S. Svanberg, H.-R. Xia, G.-G. Xiao, G.-Y. Yan: Laser spectroscopy using beam overlap modulation. *Opt. Lett.* **10**, 597 (1986)
- [9.374] T.W. Hänsch, D.R. Lyons, A.L. Schawlow, A. Siegel, Z.-Y. Wang, G.-Y. Yan: Polarization intermodulated excitation (POLINEX) spectroscopy of helium and neon. *Opt. Commun.* **37**, 87 (1981)
- [9.375] M. Goeppert-Mayer: Über Elementarakte mit zwei Quantensprüngen. *Ann. Phys.* **9**, 273 (1931)
- [9.376] L.S. Vasilenko, V.P. Chebotayev, A.V. Shishaev: Line shape of a two-photon absorption in a standing-wave field in a gas. *JETP Lett.* **12**, 113 (1970)
- [9.377] F. Biraben, B. Cagnac, G. Grynberg: Experimental evidence of two-photon transition without Doppler broadening. *Phys. Rev. Lett.* **32**, 643 (1974)
- [9.378] G. Grynberg, B. Cagnac: Doppler-free multiphoton spectroscopy. *Rep. Prog. Phys.* **40**, 791 (1977)
- [9.379] N. Bloembergen, M.D. Levenson: Dopplerfree two-photon absorption spectroscopy. *Phys. Rev. Lett.* **31**, 645 (1974)
- [9.380] T.W. Hänsch, K.C. Harvey, G. Meisel, A.L. Schawlow: Two-photon spectroscopy of Na $3s - 4d$ without Doppler broadening using a cw dye laser. *Opt. Commun.* **11**, 50 (1974)
- [9.381] H. Rinneberg, J. Neukammer, G. Jönsson, H. Hieronymus, A. König, K. Vietzke: High- n Rydberg atoms and external fields. *Phys. Rev. Lett.* **55**, 382 (1985)
- [9.382] J. Neukammer, H. Rinneberg, K. Vietzke, A. König, H. Hieronymus, M. Kohl, H.-J. Grabka: Spectroscopy of Rydberg atoms at $n \simeq 500$: Observation of quasi-Landau resonances in low magnetic fields. *Phys. Rev. Lett.* **59**, 2947 (1987)
- [9.383] B.P. Stoicheff, E. Wineberger: Doppler-free two-photon absorption spectrum of rubidium. *Can. J. Phys.* **57**, 2143 (1979)
- [9.384] C.-J. Lorenzen, K. Niemax, L.R. Pendrill: Precise measurements of ^{39}K nS and nD energy levels with an evacuated wavemeter. *Opt. Commun.* **39**, 370 (1981)
- [9.385] K.-H. Weber, C.J. Sansonetti: Accurate energies of nS , nP , nF and nG levels of neutral cesium. *Phys. Rev. A* **35**, 4650 (1987)
- [9.386] M.J. Seaton: Quantum defect theory. *Rep. Prog. Phys.* **46**, 167 (1983)
- [9.387] E. Matthias, H. Rinneberg, R. Beigang, A. Timmermann, J. Neukammer, K. Lücke: 'Hyperfine structure and isotope shifts in alkaline earth atoms.' In: *Atomic Physics 8*, ed. by I. Lindgren, A. Rosén, S. Svanberg (Plenum, New York 1983) p. 543
- [9.388] H. Rinneberg: 'Rydberg series of two-electron systems studied by hyperfine interactions.' In: *Progress in Atomic Spectroscopy*, Pt. D, ed. by H.K. Beyer, H. Kleinpoppen (Plenum, New York 1987) p. 157
- [9.389] M. Aymar: Rydberg series of alkaline-earth atoms Ca through Ba. The interplay of laser spectroscopy and multi-channel quantum defect theory. *Phys. Rep.* **110**, 163 (1984)

- [9.387] W. Hogervorst: Laser spectroscopy of Rydberg states of two-electron atoms. *Comments At. Mol. Phys.* **13**, 69 (1983)
- [9.388] C. Wieman, T.W. Hänsch: Precision measurement of the $1S$ Lamb shift and the $1S-2S$ isotope shift of hydrogen and deuterium. *Phys. Rev. A* **22**, 192 (1980)
- [9.389] E.A. Hildum, U. Boesl, D.H. McIntyre, R.G. Beausoleil, T.W. Hänsch: Measurements of the $1s - 2s$ frequency in atomic hydrogen. *Phys. Rev. Lett.* **56**, 576 (1986)
- [9.390] R.G. Beausoleil, D.H. McIntyre, C.J. Foot, E.A. Hildum, B. Couillaud, T.W. Hänsch: Continous wave measurement of the $1S$ Lamb shift in atomic hydrogen. *Phys. Rev. A* **35**, 4878 (1987); *ibid. A* **39**, 4591 (1989)
- C. Zimmermann, R. Kallenback, T.W. Hänsch: High-resolution spectroscopy of the hydrogen $1s - 2s$ transition in an atomic beam. *Phys. Rev. Lett.* **65**, 571 (1990)
- [9.391] T.W. Hänsch, R.G. Beausoleil, B. Couillaud, C. Foot, E.A. Hildum, D.H. McIntyre: High resolution laser spectroscopy of atomic hydrogen. In: [9.30] p. 2
- F. Schmidt-Kaler, D. Leibfried, S. Seel, C. Zimmermann, W. König, M. Weitz, T.W. Hänsch: High-resolution spectroscopy of the hydrogen $1s - 2s$ transition in an atomic hydrogen and deuterium. *Phys. Rev. A* **51**, 2789 (1995)
- A. Huber, B. Gross, M. Weitz, T.W. Hänsch: High-resolution spectroscopy of the $1S-2S$ transition in atomic hydrogen. *Phys. Rev. A* **59**, 1844 (1999)
- M. Niering, R. Holzwarth, R. Reichert, P. Pokasov, Th. Udem, M. Weitz, T.W. Hänsch, P. Lemonde, G. Santarelli, M. Abgrall, P. Laurent, C. Salomon, A. Clairon: Measurement of the hydrogen $1S-2S$ transition frequency by phase coherent comparison with a microwave cesium fountain clock. *Phys. Rev. Lett.* **84**, 5496 (2000)
- [9.392] J. Cariou, P. Luc: *Atlas du Spectre d'Absorption de la Molécule de Tellure* (Laboratoire Aime' Cotton, CNRS II, Orsay 1980)
- [9.393] S. Gersternkorn, P. Luc: *Atlas du Spectre d'Absorption de la Molecule d'Iode 14 800–20 000 cm⁻¹* (Editions du CNRS, Paris 1978)
- [9.394] C.J. Foot, B. Couillaud, R.G. Beausoleil, T.W. Hänsch: Continous two-photon spectroscopy of hydrogen $1s - 2s$. *Phys. Rev. Lett.* **54**, 1913 (1985)
- [9.395] M.G. Boshier, P.E.G. Baird, C.J. Foot, E.A. Hinds, M.D. Plimmer, D.N. Stacey, J.B. Swan, D.A. Tate, D.M. Warrington, G.K. Woodgate: Precision cw laser spectroscopy of hydrogen and deuterium. In: [9.30] p. 18
- [9.396] Th. Udem, A. Huber, B. Gross, J. Reichert, M. Prevedelli, M. Weitz, T.W. Hänsch: Phase-coherent measurement of the hydrogen $1S-2S$ transition frequency with an optical frequency interval divider chain. *Phys. Rev. Lett.* **79**, 2646 (1997)
- [9.397] B. de Beauvoir, F. Nez, L. Juilien, B. Cagnac, F. Biraben, D. Touahri, L. Hilico, O. Acef, A. Clarion, J.J. Zondy: Absolute frequency measurement of the $2S-8S/D$ transitions in hydrogen and deuterium: New determination of the Rydberg constant. *Phys. Rev. Lett.* **78**, 440 (1997)
- [9.398] P. Zhao, W. Lichten, H.P. Layer, J.C. Bergquist: Absolute wavelength measurements and fundamental atomic physics. In: [9.30] p. 12
- [9.399] S. Bourzeix, B. de Beauvoir, F. Nez, M.D. Plimmer, F. de Tomasi, L. Juilien, F. Biraben: High resolution spectroscopy of the hydrogen atom: Determination of the $1S$ Lamb shift. *Phys. Rev. Lett.* **76**, 384 (1996)
- [9.400] M. Kourogi, B. Widiyatomoko, Y. Takeuchi, M. Ohtsu: Limit of optical-frequency comb generation due to material dispersion. *IEEE J. Quantum Electron.* **QE-31**, 2120 (1995)

- S.A. Diddams, L.S. Ma, J. Ye, J.L. Hall: Broadband optical frequency comb generation with a phase-modulated parametric oscillator. *Opt. Lett.* **24**, 1747 (1999)
- Th. Udem, J. Reichert, R. Holzwarth, T.W. Hänsch: Absolute optical frequency measurement of the Cs D₁ line with a mode-locked laser. *Phys. Rev. Lett.* **82**, 3568 (1999)
- R. Holzwarth, Th. Udem, T.W. Hänsch, J.C. Knight, W.J. Wadsworth, P.St.J. Russel: Optical frequency synthesizer for precision spectroscopy. *Phys. Rev. Lett.* **85**, 2264 (2000)
- Th. Udem, S.A. Diddams, K.R. Vogel, C.W. Oates, E.A. Curtis, W.D. Lee, W.M. Itano, R.E. Drullinger, J.C. Bergquist, L. Hollberg: Absolute frequency measurements of the Hg⁺ and Ca optical clock transitions with a femtosecond laser. *Phys. Rev. Lett.* **86**, 4996 (2001)
- S. Bize, S.A. Diddams, U. Tanaka, C.E. Tanner, W.H. Oskay, R.E. Drullinger, T.E. Parker, T.P. Heavner, S.R. Jefferts, L. Hollberg, W.H. Itano, J.C. Bergquist: Testing the stability of fundamental constants with the ¹⁹⁹Hg⁺ single-ion optical clock. *Phys. Rev. Lett.* **90**, 150 802 (2003)
- T.W. Hänsch: Laser frequency combs and ultraprecise spectroscopy. In P. Hannaford, A. Siderov, H. Bachor, K. Baldwin (eds.): *Laser Spectroscopy 16* (World Scientific, Singapore 2004)
- [9.401] M.M. Salour, C. Cohen-Tannoudji: Observation of Ramsey's interference fringes in the profile of Doppler-free two-photon resonances. *Phys. Rev. Lett.* **38**, 757 (1977)
- [9.402] R. Teets, J. Eckstein, T.W. Hänsch: Coherent two-photon excitation by multiple light pulses. *Phys. Rev. Lett.* **38**, 760 (1977)
- [9.403] M. Bellini, A. Bartoli, T.W. Hänsch: Two-photon Fourier spectroscopy with femtosecond light pulses. *Opt. Lett.* **22**, 540 (1997)
- [9.404] J.C. Bergquist, S.A. Lee, J.L. Hall: Saturated absorption with spatially separated laser fields: Observation of optical "Ramsey" fringes. *Phys. Rev. Lett.* **38**, 159 (1977); and in [9.25] p. 142
- [9.405] R.G. Beausoleil, T.W. Hänsch: Two-photon optical Ramsey spectroscopy of freely falling atoms. *Opt. Lett.* **10**, 547 (1985)
- R.G. Beausoleil, T.W. Hänsch: Ultra-high-resolution two-photon optical Ramsey spectroscopy of an atomic fountain. *Phys. Rev. A* **33**, 1661 (1986)
- M.A. Kasevich, E. Riis, S. Chu, R.G. DeVoe: RF spectroscopy in an atomic fountain. *Phys. Rev. Lett.* **63**, 612 (1989)
- B. Gross, A. Huber, M. Niering, M. Weitz, T.W. Hänsch: Optical Ramsey spectroscopy of atomic hydrogen. *Europhys. Lett.* **44**, 186 (1998)
- [9.406] T.W. Hänsch, A.L. Schawlow: Cooling of gases by laser radiation. *Opt. Commun.* **13**, 68 (1975)
- [9.407] D. Wineland, H. Dehmelt: Proposed $10^{14} \Delta\nu \ll \nu$ laser fluorescence spectroscopy on Tl⁺ mono-ion oscillator III. *Bull. Am. Phys. Soc.* **20**, 637 (1975)
- [9.408] V.S. Letokhov, V.G. Minogin, B.D. Pavlik: Cooling and trapping of atoms and molecules by a resonant laser field. *Opt. Commun.* **19**, 72 (1976)
- V.S. Letokhov: Laser control of atomic motion: Velocity selection, cooling and trapping. *Comments At. Mol. Phys.* **6**, 119 (1977)
- V.S. Letokhov, V.G. Minogin, B.D. Pavlik: Cooling and capture of atoms and molecules by a resonant light field. *Sov. Phys. JETP* **45**, 698 (1977)
- V.I. Balykin, V.S. Letokhov, V.I. Mishin: Cooling of sodium atoms by resonant laser emission. *JETP Lett.* **29**, 560 (1979)
- V.I. Balykin, V.S. Letokhov, V.I. Mishin: Cooling of sodium atoms by resonant laser emission. *Sov. Phys. JETP* **51**, 692 (1980)

- S.V. Andreev, V.I. Balykin, V.S. Letokhov, V.G. Minogin: Radiative slowing and reduction of the energy spread of a beam of sodium atoms to 1.5 K in an oppositely directed laser beam. *JETP Lett.* **34**, 442 (1982)
- [9.410] J. Prodan, A. Migdal, W.D. Phillips, I. So, H. Metcalf, J. Dalibard: Stopping atoms with laser light. *Phys. Rev. Lett.* **54**, 992 (1985)
- W. Phillips, J. Prodan, H. Metcalf: Laser cooling and electromagnetic trapping of neutral atoms. *J. Opt. Soc. Am. B* **2**, 1751 (1985)
- H. Metcalf, W.D. Phillips: Laser cooling of atomic beams: *Comments. At. Mol. Phys.* **16**, 79 (1985)
- W.D. Phillips, H. Metcalf: Laser deceleration of an atomic beam. *Phys. Rev. Lett.* **48**, 596 (1982)
- J.V. Prodan, W.D. Phillips, H. Metcalf: Laser production of very slow monoenergetic atomic beam. *Phys. Rev. Lett.* **49**, 1149 (1982)
- [9.411] W.D. Phillips, P.L. Gould, P.D. Lett: Cooling, stopping and trapping atoms. *Science* **239**, 877 (1988)
- [9.412] F.M. Penning: *Physica* **3**, 873 (1936)
- J.R. Pierce: *Theory and Design of Electron Beams* (van Nostrand, New York 1949), Chap. 3
- [9.413] I. Bergström, C. Carlberg, R. Schuch (eds.): *Trapped Charged Particles and Related Fundamental Physics*. *Phys. Scr.* **T59** (1995)
- C. Carlberg et al.: SMILETRAP – A wide range high-precision mass spectrometer. *IEEE Trans. Instrum. Meas.* **44**, 553 (1995)
- F. DiFilippo, V. Natarajan, M. Bradley, F. Palmer, D.E. Pritchard: ‘Accurate atomic mass measurements from Penning trap comparisons of individual ions.’ In: *Atomic Physics XIV*, ed. by D.J. Wineland, C.E. Wieman, S.J. Smith (AIP Publ., New York 1995) p. 149
- M.P. Bradley, J.V. Porto, S. Rainville, J.K. Thompson, D.E. Pritchard: *Phys. Rev. Lett.* **83**, 4510 (1999)
- [9.414] G. Bollen et al.: ISOLTRAP: A Penning trap system for accurate on-line mass determinations of short-lived isotopes. *Nucl. Instrum. Methods A* **368**, 675 (1996)
- [9.415] W. Paul, H.P. Reinhard, U. von Zahn: Das elektrische Massenfilter als Massenspektrometer und Isotopen trenner. *Z. Physik* **152**, 143 (1958)
- [9.416] W. Paul: ‘Electromagnetic traps for charged and neutral particles.’ In: *Nobel Lectures in Physics 1981–1990*, ed. by G. Ekspong (World Scientific, Singapore 1993), p. 601
- H.G. Dehmelt: ‘Experiments with an isolated subatomic particle at rest.’ In: *Nobel Lectures in Physics 1981–1990*, ed. by G. Ekspong (World Scientific, Singapore 1993), p. 583
- [9.417] D.J. Wineland, R.E. Drullinger, F.L. Walls: Radiation pressure cooling of bound resonant absorbers. *Phys. Rev. Lett.* **40**, 1638 (1978)
- W. Neuhauser, M. Hohenstatt, P. Toschek, H. Dehmelt: Optical-sideband cooling of visible atom cloud confined in parabolic well. *Phys. Rev. Lett.* **41**, 233 (1978)
- D.J. Wineland, W.M. Itano: Spectroscopy of a single Mg^+ ion. *Phys. Lett. A* **82**, 75 (1981)
- [9.418] W. Neuhauser, M. Hohenstatt, P. Toschek, H. Dehmelt: Localized visible Ba^+ mono-ion oscillator. *Phys. Rev. A* **22**, 1137 (1980)
- [9.419] F. Diedrich, E. Peik, J.M. Chen, W. Quint, H. Walther: Observation of a phase transition of stored laser-cooled ions. *Phys. Rev. Lett.* **59**, 2931 (1987); and *Phys. Blätter* **44**, 12 (1988); *Nature* **334**, 309 (1988)
- [9.420] E.P. Wigner: *Trans. Faraday Soc.* **34**, 678 (1938)

- [9.421] D.J. Wineland, J.C. Bergquist, W.M. Itano, J.J. Bollinger, C.H. Manney: Atomic-ion Coulomb cluster in an ion trap. *Phys. Rev. Lett.* **59**, 2935 (1987)
 J. Hoffnagle, R.V. DeVoe, L. Reyna, R.G. Brewer: Order-chaos transition of two trapped ions. *Phys. Rev. Lett.* **61**, 255 (1988)
 R.G. Brewer, J. Hoffnagle, R.G. DeVoe, L. Reyna, W. Henshaw: Collision-induced two-ion chaos. *Nature* **344**, 305 (1990)
- [9.422] D.J. Wineland, C. Monroe, D.M. Meekhof, B.E. King, D. Leibfried, W.M. Itano, J.C. Bergquist, D. Berkeland, J.J. Bollinger, J. Miller: Coherent quantum state manipulation of trapped atomic ions. *Adv. Quantum Chem.* **30**, 41 (1998)
 A. Steane: Quantum computing. *Rep. Prog. Phys.* **61**, 117 (1998)
 H.J. Kimble, C.J. Hood, T.W. Lynn, H. Mabuchi, D.W. Vernooy, J. Ye: The quantum internet, in [9.36] p. 80
- [9.423] D.A. Church: Collision measurements and excited-level lifetime measurements on ions stored in Paul, Penning and Kingdon ion traps. *Phys. Rep.* **228**, 253 (1993)
 H.A. Klein: 'Ion Traps.' In: *Experimental Methods in the Physical Sciences*, Vol. 29A, ed. by F.B. Dunning, R.G. Hulet (Academic Press, San Diego 1995) p. 349
 J.I. Cirac, A.S. Parkins, R. Blatt, P. Zoller: Nonclassical states of motion in ion traps. *Adv. At. Mol. Opt. Phys.* **37**, 238 (1996)
 J.I. Cirac, A.S. Parkins, R. Blatt, P. Zoller: 'Nonclassical states of motion in ion traps.' In: *Progress in Atomic, Molecular, and Optical Physics*, Vol. 37, ed. by B. Bederson, H. Walther (Academic Press, San Diego 1996) p. 238
- [9.424] P.F. Fisk: Trapped-ion and trapped-atom microwave frequency standards. *Rep. Prog. Phys.* **60**, 761 (1997)
 K. Gibble, S. Chu: Future slow-atom frequency standards. *Metrologia* **29**, 201 (1992)
 Ch. Monroe, J. Bollinger: Atomic physics in ion traps. *Physics World* (March 1997) p. 37
 M. Roberts, P. Taylor, G.P. Barwood, P. Gill, H.A. Klein, W.R.C. Rowley: Observation of an electric octupole transition in a single ion. *Phys. Rev. Lett.* **78**, 1876 (1997)
 B.E. Young, F.C. Cruz, W.M. Itano, J.C. Bergquist: Visible laser with subhertz linewidths. *Phys. Rev. Lett.* **82**, 3799 (1999)
- [9.425] H.G. Dehmelt: Proposed $10^{14}\Delta\nu > \nu$ laser fluorescence spectroscopy on Ti^+ mono-ion oscillator II. *Bull. Am. Phys. Soc.* **20**, 60 (1975)
- [9.426] Th. Sauter, W. Neuhauser, R. Blatt, P.E. Toschek: Observation of quantum jumps. *Phys. Rev. Lett.* **57**, 1696 (1986); see also *Phys. Scr.* **T22**, 129 (1988) and [9.30] p. 121
 J.E. Bergquist, R.G. Hulet, W.M. Itano, D.J. Wineland: Observation of quantum jumps in a single atom. *Phys. Rev. Lett.* **57**, 1699 (1986); see also *Phys. Scr.* **T22**, 79 (1988) and [9.30] p. 117
 W. Nagourney, J. Sandberg, H. Dehmelt: Shelved optical electron amplifier Observation of quantum jumps. *Phys. Rev. Lett.* **56**, 2797 (1986); see also [9.30] p. 114
 W. Nagourney: The mono-ion oscillator: An approach to an ideal atomic spectrometer. *Comments At. Mol. Phys.* **21**, 321 (1988)
- [9.427] J.C. Bergquist, F. Diedrich, W.M. Itano, D.J. Wineland: Hg^+ single ion spectroscopy. In: [9.31] p. 274

- B.C. Young, R.J. Rafac, J.A. Beall, F.C. Cruz, W.M. Itano, D.J. Wineland, J.C. Bergquist: Hg^+ optical frequency standard: Recent progress. In: [9.36] p. 61; *Physics Today* **3**, 37 (2001)
- [9.428] S. Chu, L. Hollberg, J.E. Bjorkholm, A. Cable, A. Ashkin: Three-dimensional viscous confinement and cooling of atoms by resonance radiation pressure. *Phys. Rev. Lett.* **55**, 48 (1985)
- [9.429] P.D. Lett, R.N. Walls, Ch.I. Westbrook, W.D. Phillips, P.L. Gould, H.J. Metcalf: Observation of atoms laser cooled below the Doppler limit. *Phys. Rev. Lett.* **61**, 169 (1988)
- [9.430] J. Dalibard, C. Cohen-Tannoudji: Dressed-atom approach to atomic motion in laser light: the dipole force revisited. *J. Opt. Soc. Am. B* **2**, 1707 (1986)
- [9.431] J. Dalibard, C. Cohen-Tannoudji: Laser cooling below the Doppler limit by polarization gradients: simple theoretical models. *J. Opt. Soc. Am. B* **6**, 2023 (1989)
- [9.432] C. Cohen-Tannoudji: Thesis (Paris 1962); *Ann. Phys.* **7**, 423 and 469 (1962)
C. Cohen-Tannoudji: in *Cargese Lectures in Physics*, ed. by Levy (Gordon & Breach, 1968)
- [9.433] C. Cohen-Tannoudji, J. Dupont-Roc, G. Grynberg: *Atom-Photon Interactions – Basic Processes and Applications*, Chap. VI (Wiley, New York 1992)
- [9.434] P.J. Ungar, D.S. Weiss, E. Riis, S. Chu: Optical molasses and multilevel atoms: Theory. *J. Opt. Soc. Am.* **6**, 2058 (1989)
- [9.435] A. Ashkin: Trapping of atoms by resonance radiation pressure. *Phys. Rev. Lett.* **40**, 729 (1978)
S. Chu, J.E. Bjorkholm, A. Ashkin, A. Cable: Experimental observation of optically trapped atoms. *Phys. Rev. Lett.* **57**, 314 (1986)
- [9.436] V.S. Letokhov: Narrowing of the Doppler width in a standing light wave. *JETP Lett.* **7**, 272 (1968)
- [9.437] K.-J. Kugler, W. Paul, U. Trinks: A magnetic storage ring for neutrons. *Phys. Lett. B* **72**, 422 (1978)
- [9.438] D.E. Pritchard: Cooling neutral atoms in a magnetic trap for precision spectroscopy. *Phys. Rev. Lett.* **51**, 1336 (1983)
A.L. Midgall, J.V. Prodan, W.D. Phillips, T.H. Bergemann, H.J. Metcalf: First observation of magnetically trapped neutral atoms. *Phys. Rev. Lett.* **54**, 2596 (1985)
- [9.439] E.L. Raab, M.G. Prentiss, A.E. Cable, S. Chu, D.E. Pritchard: Trapping of neutral sodium atoms with radiation pressure. *Phys. Rev. Lett.* **59**, 2631 (1987)
- [9.440] G. Alzetta, A. Gozzini, L. Moi, G. Orriols: *Nuovo Cimento B* **36**, 5 (1976)
E. Arimondo, G. Orriols: *Lett. Nuovo Cimento* **17**, 333 (1976)
- [9.441] A. Aspect, E. Arimondo, R. Kaiser, N. Vansteenkiste, C. Cohen-Tannoudji: Laser cooling below the one-photon recoil energy by velocity-selective coherent population trapping. *Phys. Rev. Lett.* **61**, 826 (1988)
- [9.442] J. Lawall, F. Bardou, B. Saubamea, K. Shimizu, M. Leduc, A. Aspect, C. Cohen-Tannoudji: Two-dimensional subrecoil laser cooling. *Phys. Rev. Lett.* **73**, 1915 (1994)
- [9.443] J. Lawall, S. Kulin, B. Saubamea, N. Bigelow, M. Leduc, C. Cohen-Tannoudji: Three-dimensional laser cooling of helium beyond the single-photon recoil limit. *Phys. Rev. Lett.* **75**, 4194 (1995)
M. Kasevich, S. Chu: Laser cooling below a photon recoil with three-level atoms. *Phys. Rev. Lett.* **69**, 1741 (1992)

- N. Davidson, H.J. Lee, M. Kasevich, S. Chu: Raman cooling of atoms in two and three dimensions. *Phys. Rev. Lett.* **72**, 3158 (1994)
- H.J. Lee, C.S. Adams, M. Kasevich, S. Chu: Raman cooling of atoms in an optical dipole trap. *Phys. Rev. Lett.* **76**, 2658 (1996)
- [9.444] A. Bárány, A. Kerek, M. Larsson, S. Mannervik, L.-O. Norlin (eds.): Workshop and symposium on the physics of low-energy stored and trapped particles. *Phys. Scr.* **T22**, 1 (1988)
- P. Meystre, S. Stenholm (eds.): The mechanical effects of light. *J. Opt. Soc. Am. B* **2**, 1706-1860 (1985) (special issue)
- S. Stenholm: Light forces put a handle on the atom: To cool and trap atoms by laser light. *Contemp. Phys.* **29**, 105 (1988)
- V.G. Minogin, V.S. Letokhov: *Laser Light Pressure on Atoms* (Harwood, London 1987)
- W.D. Phillips, H.J. Metcalf: Cooling and trapping of atoms. *Sci. Am.* **256**(3), 36 (1987)
- P.L. Gould, P.D. Lett, W.D. Phillips: New measurements with optical molasses. In: [9.30] p. 64
- D.J. Wineland, W.M. Itano, J.C. Bergquist, J.J. Bollinger: Trapped Ions and Laser Cooling, NBS Technical Note 1086 (NBS, Washington, DC 1985)
- D.J. Wineland, W.M. Itano, R.S. VanDyck Jr.: 'High-resolution spectroscopy of stored ions.' In: *Advances in Atomic and Molecular Physics*, Vol. 19, ed. by O.R. Bates, B. Bederson (Academic Press, New York 1983)
- D.J. Wineland, W.M. Itano, J.C. Bergquist, J.J. Bollinger, J.D. Prestige: 'Spectroscopy of stored ions.' In: *Atomic Physics 9*, ed. by R.S. Van Dyck Jr., E.N. Fortson (World Scientific, Singapore 1985) p. 3
- S. Stenholm: The semiclassical theory of laser cooling. *Rev. Mod. Phys.* **58**, 699 (1986)
- C.J. Foot: Laser cooling and trapping of atoms. *Contemp. Phys.* **32**, 369 (1991)
- S. Chu: Laser trapping of neutral particles. *Sci. Am.* **266**(2), 48 (1992)
- C. Cohen-Tannoudji: Laser cooling and trapping of neutral atoms: Theory. *Phys. Rep.* **219**, 153 (1992)
- M. Metcalf, P. van der Straten: Cooling and trapping of neutral atoms. *Phys. Rep.* **244**, 203 (1994)
- H. Walther: Atoms in cavities and traps. *Adv. At. Mol. Opt. Phys.* **32**, 379 (1994)
- N.R. Newbury, C. Wieman: Resource Letter TNA-1: Trapping of neutral atoms. *Am. J. Phys.* **64**, 18 (1996)
- E. Arimondo: 'Coherent population trapping in laser spectroscopy.' In: *Progress in Optics XXXV*, ed. by E. Wolf (Elsevier, Amsterdam 1996) p. 259
- A. Ashkin: Optical trapping and manipulation of neutral particles using lasers. *Proc. Natl. Acad. Sci. USA* **94**, 4853 (1997)
- M. Metcalf, P. van der Straten: *Laser Cooling and Trapping* (Springer, Berlin, Heidelberg 1999)
- [9.445] V.I. Balykin, V.S. Letokhov, Yu.B. Ovchinnikov, A.I. Sidorov: Focusing of an atomic beam and imaging of atomic sources by means of a laser lens based on resonance-radiation pressure. *J. Mod. Opt.* **35**, 17 (1988)
- V.I. Balykin, V.S. Letokhov, V.G. Minogin: Laser control of the motion of neutral atoms and optical atomic traps. *Phys. Scr.* **T22**, 119 (1988)
- I. Balykin, V.S. Letokhov: Laser optics on neutral atomic beams. *Phys. Today* (April 1989) p. 23

- [9.446] K. Cloppenburg, G. Hennig, A. Mihm, H. Wallis, W. Ertmer: Optical elements for manipulating atoms. In: [9.30] p. 87
- [9.447] C.S. Adams: Atomic optics. *Contemp. Phys.* **35**, 1 (1994)
 C.S. Adams, M. Sigel, J. Mlynek: Atom optics. *Phys. Rep.* **240**, 143 (1994)
 K. Sengslock, W. Ertmer: Laser manipulation of atoms. *Adv. At. Mol. Opt. Phys.* **35**, 1 (1995)
 V.V. Balykin: 'Atom waveguides.' In: *Progress in Atomic, Molecular, and Optical Physics*, Vol. 41, ed. by B. Bederson, H. Walther (Academic Press, San Diego 1999) p. 182
- [9.448] P.E. Moskowitz, P.L. Gould, S.R. Atlas, D.E. Pritchard: Diffraction of an atomic beam by standing-wave radiation. *Phys. Rev. Lett.* **51**, 370 (1983)
 P.L. Gould, G.A. Ruff, D.E. Pritchard: Diffraction of atoms by light: The near-resonant Kapitza-Dirac effect. *Phys. Rev. Lett.* **59**, 827 (1986)
 O. Carnal, J. Mlynek: Young's double-slit experiment with atoms: A simple atom interferometer. *Phys. Rev. Lett.* **66**, 2689 (1991)
 D.K. Keith, C.E. Ekstrom, Q.A. Turchette, D.E. Pritchard: An interferometer for atoms. *Phys. Rev. Lett.* **66**, 2693 (1991)
 F. Riehle, Th. Kistlers, A. White, J. Helmecke, Ch.J. Bordé: Optical Ramsey spectroscopy in a rotating frame: Sagnac effect in a matter-wave interferometer. *Phys. Rev. Lett.* **67**, 177 (1991)
 M. Kasevich, S. Chu: Atomic interferometry using stimulated Raman transitions. *Phys. Rev. Lett.* **67**, 181 (1991)
 C.S. Adams, O. Carnal, J. Mlynek: Atom interferometry. *Adv. At. Mol. Opt. Phys.* **34**, 1 (1994)
 P. Berman (ed.): *Atom Interferometry* (Academic Press, New York 1997)
- [9.449] I. Percival: Atom interferometry, spacetime and reality. *Physics World* (March 1997)
 T.L. Gustavson, P. Broyer, M.A. Kasevich: Precision rotation measurements with an atomic interferometer gyroscope. *Phys. Rev. Lett.* **78**, 2046 (1997)
 A. Peters, K.Y. Chung, S. Chu: Measurement of gravitational acceleration by dropping atoms. *Nature* **400**, 849 (1999)
 M. Arndt, O. Nairz, J. Voss-Andreae, C. Keller, G. van der Zouw, A. Zeilinger: *Nature* **401**, 680 (1999)
- [9.450] J. Fujita, M. Morinaga, T. Kishimoto, M. Yasuda, S. Matsui, F. Shimizu: Manipulation of an atomic beam by a computer-generated hologram. *Nature* **380**, 691 (1996)
 M. Morinaga, M. Yasuda, T. Kishimoto, F. Shimizu: Holographic manipulation of a cold atomic beam. *Phys. Rev. Lett.* **77**, 802 (1996)
 F. Shimizu, J. Fujita, S. Mitake, T. Kishimoto: Holography with cold atoms. In: [9.36] p. 227
- [9.451] C.I. Westbrook, R.N. Watts, C.E. Tanner, S.L. Rolston, W.D. Phillips, P.D. Lett, P.L. Gould: Localization of atoms in a three-dimensional standing wave. *Phys. Rev. Lett.* **65**, 33 (1990)
 P.S. Jessen, C. Gerz, P.D. Lett, W.D. Phillips, S.L. Rolston, R.J.C. Spreeuw, C.I. Westbrook: Observation of quantized motion of Rb atoms in an optical field. *Phys. Rev. Lett.* **69**, 49 (1992)
 A. Hemmerich, T.W. Hänsch: Two-dimensional atomic crystal bound by light. *Phys. Rev. Lett.* **70**, 410 (1993)
 D. Grynberg, B. Lounis, P. Verkerk, J.-Y. Courtois, C. Salomon: Quantized motion of cold cesium atoms in two- and three-dimensional optical potentials. *Phys. Rev. Lett.* **70**, 2249 (1993)

- A. Kastberg, W.D. Phillips, W.S.L. Rolston, R.J.C. Spreeuw, P.S. Jessen: Adiabatic cooling of cesium to 700 nK in an optical lattice. *Phys. Rev. Lett.* **74**, 1542 (1995)
- [9.452] P.L. Gould, P.D. Lett, P.S. Julienne, W.D. Phillips, H.R. Thorsheim, J. Weiner: Observation of associative ionization of ultracold laser-trapped sodium atoms. *Phys. Rev. Lett.* **60**, 788 (1988)
- P.D. Lett, P.S. Jessen, W.D. Phillips, S.L. Rolston, C.I. Westbrook, P.L. Gould: Laser modification of ultracold collisions: Experiment. *Phys. Rev. Lett.* **67**, 2139 (1991)
- J. Weiner: Advances in ultracold collisions: Experimentation and theory. *Adv. At. Mol. Opt. Phys.* **35**, 45 (1995)
- [9.453] J.D. Weinstein, R. deCarvalho, T. Guillet, B. Friedrich, J.M. Doyle: Magnetic trapping of calcium monohydride molecules at millikelvin temperatures. *Nature* **395**, 148 (1998)
- H.L. Bethlem, G. Berden, G. Meijer: Decelerating neutral dipolar molecules. *Phys. Rev. Lett.* **83**, 1558 (1999)
- [9.454] S.N. Atutov, S.P. Podjachev, A.M. Shalagin: Diffusion pulling of Na vapor into the light beam. *Opt. Commun.* **57**, 236 (1986)
- [9.455] Kh. Gel'mukhanov, A.M. Shalagin: Sov. Phys.-JETP **51**, 839 (1980)
- E.R. Eliel: Light-induced drift. *Adv. At. Mol. Opt. Phys.* **31**, 199 (1993)
- H.G.C. Werij, J.P. Woerdman, J.J.M. Beenakker, I. Kuscer: Demonstration of a semipermeable optical piston. *Phys. Rev. Lett.* **52**, 2237 (1984)
- G. Nienhuis: Theory of light-induced drift and the optical piston. *Phys. Rev. A* **31**, 1636 (1985)
- [9.456] S.N. Bose: *Z. Phys.* **26**, 178 (1924)
- A. Einstein: *Sitzungsber. Preuss. Akad. Wiss.* **1924**, 261 (1924); *ibid.* **1925**, 3 (1925)
- [9.457] H.F. Hess: Evaporative cooling of magnetically trapped and compressed spin-polarized hydrogen. *Phys. Rev. B* **34**, 3476 (1986)
- H.F. Hess, G.P. Kochanski, J.M. Doyle, N. Masuhara, D. Kleppner, T.J. Greytak: Magnetic trapping of spin-polarized atomic hydrogen. *Phys. Rev. Lett.* **59**, 672 (1987)
- N. Masuhara, J.M. Doyle, J.C. Sandberg, D. Kleppner, T.J. Greytak, H.F. Hess, G.P. Kochanski: Evaporative cooling of spin-polarized atomic hydrogen. *Phys. Rev. Lett.* **61**, 935 (1988)
- [9.458] M.H. Anderson, J.R. Ensher, M.R. Matthews, C.E. Wieman, E.A. Cornell: Observation of Bose-Einstein condensation in a dilute atomic vapor. *Science* **269**, 198 (1995)
- [9.459] K.B. Davies, M.O. Mewes, M.R. Andrews, N.J. van Druten, D.S. Durfee, D.N. Kurn, W. Ketterle: Bose-Einstein condensation in a gas of sodium atoms. *Phys. Rev. Lett.* **75**, 3969 (1995)
- [9.460] Physics Today (August 1995) p. 17
- [9.461] M.R. Andrews, C.G. Townsend, H.-J. Miesner, D.S. Durfee, D.M. Kurn, W. Ketterle: Observation of interference between two Bose condensates. *Science* **275**, 637 (1997)
- [9.462] M.-O. Mewes, M.R. Andrews, D.M. Kurn, D.S. Durfee, C.G. Townsend, W. Ketterle: Output coupler for Bose-Einstein condensed atoms. *Phys. Rev. Lett.* **78**, 582 (1997)
- [9.463] I. Bloch, T.W. Hänsch, T. Esslinger: Atom laser with a cw output coupler. *Phys. Rev. Lett.* **82**, 3008 (1999)
- W. Hagley, L. Deng, M. Kozuma, J. Wen, M.A. Edwards, K. Helmersson, S.L. Rolston, W.D. Phillips: A well-collimated quasi-continuous atom laser. *Science* **283**, 1706 (1999)

- S. Inouye, T. Pfau, S. Gupta, A.P. Chikkatur, A. Gorlitz, D.E. Pritchard, W. Ketterle: Phase-coherent amplification of atomic matter waves. *Nature* **402**, 641 (1999)
- A.P. Chikkatur, Y. Shin, A.E. Leanhardt, D. Kielpinski, E. Tsikata, T.L. Gustavson, D.E. Pritchard, W. Ketterle: A continuous source of Bose-Einstein condensed atoms. *Science* **296**, 2193-2195 (2002)
- [9.464] C.C. Bradley, C.A. Sackett, J.J. Tollett, R.G. Hulet: Evidence for Bose-Einstein condensation in an atomic gas with attractive interactions. *Phys. Rev. Lett.* **75**, 1687 (1995)
- C.C. Bradley, C.A. Sackett, R.G. Hulet: Bose-Einstein condensation of lithium: Observation of a limited condensate number. *Phys. Rev. Lett.* **78**, 985 (1997)
- A. Griffin, D.W. Snoke, S. Stringari (eds.): *Bose-Einstein condensation* (Cambridge University Press, Cambridge 1995)
- Ch. Townsend, W. Ketterle, S. Stringari: Bose-Einstein condensation. *Physics World* (March 1997) p. 29
- W. Ketterle, M.R. Andrews, K.B. Davies, D.S. Durfee, D.M. Korn, M.-O. Mewes, N.J. van Druten: Bose-Einstein condensation of ultra-cold atomic gases. *Phys. Scr.* **T66**, 31 (1996)
- K. Burnett: Bose-Einstein condensation with evaporatively cooled atoms. *Contemp. Phys.* **37**, 1 (1996)
- W. Ketterle, N.J. Druten: Evaporative cooling of trapped atoms. *Adv. At. Mol. Opt. Phys.* **37**, 181 (1996)
- W. Ketterle, N.J. van Druten: 'Evaporative cooling.' In: *Progress in Atomic, Molecular, and Optical Physics*, Vol. 37, ed. by B. Bederson, H. Walther (Academic Press, San Diego 1996) p. 181
- E.A. Cornell, C.E. Wieman: The Bose-Einstein condensate. *Sci. Am.* **278**(3), 26 (1998)
- A.S. Parkins, D.F. Walls: The physics of trapped dilute-gas Bose-Einstein condensates. *Phys. Rep.* **303**, 1 (1998)
- B.P. Anderson, M.A. Kasevich: *Science* **282**, 1686 (1998)
- M.R. Matthews, B.P. Anderson, P.C. Haljan, D.S. Hall, C.E. Wieman, E.A. Cornell. *Phys. Rev. Lett.* **83**, 2498 (1999)
- C. Raman, M. Köhl, R. Onofrio, D.S. Durfee, C.E. Kuklewicz, Z. Hadzibabic, W. Ketterle: *Phys. Rev. Lett.* **83**, 2502 (1999)
- S.L. Cornish, N.R. Claussen, J.L. Roberts, E.A. Cornell, C.E. Wieman: Stable ^{85}Rb Bose-Einstein condensates with widely tunable interactions. *Phys. Rev. Lett.* **85**, 1795 (2000)
- E.A. Cornell, C.E. Wieman: Nobel Lecture: Bose-Einstein condensation in a dilute gas, the first 70 years and some recent experiments. *Rev. Mod. Phys.* **74**, 875 (2002)
- W. Ketterle: Nobel Lecture: When atoms behave like waves: Bose-Einstein condensation and the atom laser. *Rev. Mod. Phys.* **74**, 1131 (2002)
- G. Modugno, G. Ferrari, G. Roati, R. Brecha, A. Simoni, M. Inguscio: Bose-Einstein condensation of potassium by sympathetic cooling. *Science* **294**, 1320 (2001)
- W. Hänsel, P. Hommelhoff, T.W. Hänsch, J. Reichel: Bose-Einstein condensation on a microelectronic chip. *Nature* **413**, 498 (2001)
- M. Greiner, O. Mandel, T. Esslinger, T.W. Hänsch, I. Bloch: Quantum phase transition from a superfluid to a Mott insulator in a gas of ultracold atoms. *Nature* **415**, 39 (2002)
- M. Greiner, O. Mandel, T.W. Hänsch and I. Bloch: Collapse and revival of the matter wave field of a Bose-Einstein condensate. *Nature* **419**, 51 (2002)

- J.R. Abo-Shaeer, C. Raman, J.M. Vogels, W. Ketterle: Observation of vortex lattices in Bose–Einstein condensates. *Science* **292**, 476 (2001)
- E.A. Donley, N.R. Claussen, S.L. Cornish, J.L. Roberts, E.A. Cornell, C.E. Wieman: Dynamics of collapsing and exploding Bose–Einstein condensates. *Nature* **412**, 295 (2001)
- E.A. Donley, N.R. Claussen, S.T. Thompson, C.E. Wieman: Atom-molecule coherence in a Bose–Einstein condensate. *Nature* **417**, 529 (2002)
- K. Dieckmann, C.A. Stan, S. Gupta, Z. Hadzibabic, C. Schunck, W. Ketterle: Decay of ultracold fermionic lithium gas near a Feshbach resonance. *Phys. Rev. Lett.* **89**, 203 201 (2002)
- A.E. Leanhardt, A.P. Chikkatur, D. Kielpinski, Y. Shin, T.L. Gustavson, W. Ketterle, D.E. Pritchard: Propagation of Bose–Einstein condensates in a magnetic waveguide. *Phys. Rev. Lett.* **89**, 040401 (2002)
- T.L. Gustavson, A.P. Chikkatur, A.E. Leanhardt, A. Görlitz, S. Gupta, D.E. Pritchard, W. Ketterle: Transport of Bose–Einstein condensates with optical tweezers. *Phys. Rev. Lett.* **88**, 020401 (2002)
- J.R. Anglin, W. Ketterle: Bose–Einstein condensation of atomic gases. *Nature* **416**, 211 (2002)
- P. Engels, I. Coddington, P.C. Haljan, V. Schweikhard, E.A. Cornell: Observation of long-lived vortex aggregates in rapidly rotating Bose–Einstein condensates. *Phys. Rev. Lett.* **90**, 170 405/1-4 (2003)
- A.E. Leanhardt, Y. Shin, A.P. Chikkatur, D. Kielpinski, W. Ketterle, D.E. Pritchard: Bose–Einstein condensates near a microfabricated surface. *Phys. Rev. Lett.* **90**, 100 404 (2003)
- [9.465] L. Deng, E.W. Hagley, J. Wen, M. Trippenbach, Y. Band, P.S. Julienne, J.E. Simsarian, K. Helmerson, S.L. Rolston, W.D. Phillips: Four-wave mixing with matter waves. *Nature* **398**, 218 (1999)
- S.L. Rolston: Linear and non-linear atom optics with Bose–Einstein Condensates. In: [9.36] p. 120
- [9.466] W.C. Stwalley, L.H. Nosanow: Possible "new" quantum systems. *Phys. Rev. Lett.* **36**, 910 (1976)
- I.F. Silvera, J.T.M. Walraven: Stabilization of atomic hydrogen at low temperature. *Phys. Rev. Lett.* **44**, 164 (1980)
- D.G. Fried, T.C. Killian, L. Willmann, D. Landhuis, S.C. Moss, D. Kleppner, T.J. Greytak: Bose–Einstein condensation of atomic hydrogen. *Phys. Rev. Lett.* **81**, 3811 (1999)
- [9.467] B. DeMarco, D.S. Jin: Onset of Fermi degeneracy in a trapped atomic gas. *Science* **285**, 1703 (1999)
- G. Modugno, G. Roati, F. Riboli, F. Ferlaino, R. Brecha, M. Inguscio: Collapse of a degenerate Fermi gas, *Science* **297**, 2240 (2002)
- S. Gupta, Z. Hadzibabic, M.W. Zwierlein, C.A. Stan, K. Dieckmann, C.H. Schunck, E.G.M. van Kempen, B.J. Verhaar, W. Ketterle: Rf spectroscopy of ultracold fermions. *Science* **300**, 1723 (2003)

Chapter 10

- [10.1] L.J. Radziemski, R.W. Solarz, J.A. Paisner (eds.): *Laser Spectroscopy and its Applications* (Dekker, New York 1987)
- [10.2] H. Medin, S. Svanberg (eds.): Laser Technology in Chemistry, Special issue. *Appl. Phys. B* **46**, No. 3 (1988)

- [10.3] W.C. Gardiner Jr.: The chemistry of flames. *Sci. Am.* **246**(2), 86 (1982)
W.C. Gardiner Jr. (ed.): *Combustion Chemistry* (Springer, Berlin, Heidelberg 1984)
- [10.4] J. Walker: The physics and chemistry underlying the infinite charm of a candle flame. *Sci. Am.* **238**(4), 154 (1978)
A.M. Kanury: *Introduction to Combustion Phenomena* (Gordon and Breach, New York 1975)
W.C. Strahle: *An Introduction to Combustion* (Gordon and Breach, Langhorne 1993)
- [10.5] G. Cox: *Combustion Fundamentals of Fire* (Academic Press, London 1995)
M. Gehring, K. Hoyermann, H. Schacke, J. Wolfrum: Direct studies of some elementary steps for the formation and destruction of nitric oxide in the H – N – O system. 14th Symp. on Combustion (Combustion Institute, Pittsburgh, PA 1973)
- [10.6] H. Bockhorn (ed.): *Soot Formation in Combustion Mechanisms and Models*, Springer Series in Chemical Physics, Vol. 59 (Springer-Verlag, Berlin, Heidelberg 1994)
B.S. Haynes: 'Soot and hydrocarbons in combustion.' In: *Fossil Fuel Combustion*, ed. by W. Bartok, A.F. Sarofim (Wiley, New York 1991) Chap. 4.
- [10.7] A.G. Gaydon, H.G. Wolfhard: *Flames, their Structure, Radiation and Temperature* (Chapman and Hall, New York 1979)
- [10.8] J. Wolfrum: Chemical kinetics in combustion systems: The specific effect of energy, collisions, and transport processes. 20th Symp. on Combustion (Combustion Institute, Pittsburgh, PA 1985)
- [10.9] A.C. Gaydon: *The Spectroscopy of Flames* (Chapman and Hall, New York 1974)
- [10.10] D.R. Crosley (ed.): *Laser Probes for Combustion Chemistry*, ACS Symp. Ser. Vol. 134 (Am. Chem. Soc., Washington 1980)
- [10.11] A.C. Eckbreth, P.A. Bonczyk, J.F. Verdiuk: Combustion Diagnostics by Laser Raman and Fluorescence Techniques. *Prog. Energy Comb. Sci.* **5**, 253 (1979)
- [10.12] J.H. Bechtel, C.J. Dasch, R.E. Teets: 'Combustion research with lasers.' In: *Laser Applications*, ed. by R.K. Erf, J.F. Ready (Academic Press, New York 1984)
J.H. Bechtel, A.R. Chraplyvy: Proc. IEEE **70**, 658 (1982)
- [10.13] T.D. McCay, J.A. Roux (eds.): Combustion diagnostics by nonintrusive methods. *Progr. Astronautics and Aeronautics*, Vol. **92** (1983)
- [10.14] A.C. Eckbreth: *Laser Diagnostics for Combustion Temperature and Species* (Gordon & Breach, Amsterdam 1996)
- [10.15] K. Iinuma, T. Asanuma, T. Ohsawa, J. Doi (eds.): *Laser Diagnostics and Modelling of Combustion* (Springer, Berlin, Heidelberg 1987)
- [10.16] M. Aldén, H. Edner, S. Svanberg, T. Höglberg: Combustion studies with laser techniques, Göteborg Institute of Physics Reports GIPR-206 (Chalmers University of Technology, Göteborg 1980)
- [10.17] M. Aldén, H. Edner, G. Holmstedt, T. Höglberg, H. Lundberg, S. Svanberg: Relative distribution of radicals and temperature in flat flames, studied by laser-induced fluorescence and BOXCARS spectroscopy. Lund Reports on Atomic Physics LRAP-1 (Lund Institute of Technology, Lund 1981)
- [10.18] D.R. Crosley, G.P. Smith: Laser-induced fluorescence spectroscopy for combustion diagnostics. *Opt. Eng.* **22**, 545 (1983)
K. Schofield, M. Steinberg: Quantitative atomic and molecular fluorescence in the study of detailed combustion processes. *Opt. Eng.* **20**, 501 (1981)

- [10.19] R. Lucht: Applications of laser-induced fluorescence spectroscopy for combustion and plasma diagnostics. In: [10.1] p. 623
- [10.20] N.S. Bergano, P.A. Janimaagi, M.M. Salour, J.H. Bechtel: Picosecond laser spectroscopy measurement of hydroxyl fluorescence lifetime in flames. *Opt. Lett.* **8**, 443 (1983)
- [10.21] S. Agrup, F. Ossler, M. Aldén: Measurement of collisional quenching of hydrogen atoms in an atmospheric pressure hydrogen/oxygen flame by picosecond laser-induced fluorescence. *Appl. Phys. B* **61**, 479 (1995)
F. Ossler, J. Larsson, M. Aldén: Measurement of the effective lifetime of O atoms in atmospheric premixed flames. *Chem. Phys. Lett.* **250**, 287 (1996)
F. Ossler, T. Metz, L. Martinsson, M. Aldén: Two-dimensional visualization of fluorescence lifetimes by use of a picosecond laser and a streak camera. *Appl. Opt.* **37**, 2303 (1998)
- [10.22] F.C. Bormann, T. Nielsen, M. Burrows, P. Andresen: Single-pulse, collision-insensitive picosecond planar laser-induced fluorescence of OH A $^2\sum^+(v' = 2)$ in atmospheric pressure flames. *Appl. Phys. B* **62**, 601 (1996)
F.C. Bormann, T. Nielsen, M. Burrows, P. Andresen: Picosecond planar laser-induced fluorescence measurements of OH A $^2\sum^+(v' = 2)$ lifetime and energy transfer in atmospheric pressure flames. *Appl. Opt.* **36**, 6129 (1997)
- [10.23] M. Aldén, H. Edner, P. Grafström, H.M. Hertz, G. Holmstedt, T. Högberg, H. Lundberg, S. Svanberg, S. Wallin, W. Wendt, U. Westblom: 'Imaging measurements of species concentrations, temperatures and velocities in reactive flows using laser-induced fluorescence.' In: *Lasers 86*, ed. by K.M. Corcoran, D.M. Sullivan, W.C. Stwalley (STS Press, McLean, VA. 1985) p. 209
- [10.24] M. Aldén, H. Edner, G. Holmstedt, S. Svanberg, T. Högberg: Single-pulse laser-induced OH fluorescence in an atmospheric flame, spatially resolved with a diode array detector. *Appl. Opt.* **21**, 1236 (1982)
- [10.25] M.J. Dyer, D.R. Crosley: Two-dimensional imaging of OH laser-induced fluorescence in a flame. *Opt. Lett.* **7**, 382 (1982)
G. Kychakoff, R.D. Howe, R.K. Hanson, J.C. McDaniel: Quantitative visualization of combustion species in a plane. *Appl. Opt.* **21**, 3225 (1982)
G. Kychakoff, R.D. Howe, R.K. Hanson: Quantitative flow visualization technique for measurements in combustion gases. *Appl. Opt.* **23**, 704 (1984)
G. Kychakoff, K. Knapp, R.D. Howe, R.K. Hanson: Flow visualization in combustion gases using nitric oxide fluorescence. *AIAA J.* **22**, 153 (1984)
G. Kychakoff, R.D. Howe, R.K. Hanson, M.C. Drake, R.W. Pitz, M. Lapp, C.M. Penney: Visualization of turbulent flame fronts with planar laser-induced fluorescence. *Science* **224**, 382 (1984)
- [10.26] R.K. Hanson: Combustion diagnostics: 'Planar imaging techniques.' In: *Proc. 21st Symp. on Combustion*, Munich 1986 (The Combustion Institute Pittsburgh, PA 1986)
B. Hiller, R.K. Hanson: Simultaneous planar measurements of velocity and pressure fields in gas flows using laser-induced fluorescence. *Appl. Opt.* **27**, 33 (1988)
R.K. Hanson, J.M. Seitzman, P.H. Paul: Planar laser-induced fluorescence imaging of combustion gases. *Appl. Phys. B* **50**, 441 (1990)
V. Sick, J. Wolfrum: 'Applied laser spectroscopy in combustion devices.' In: *Atomic Physics Methods in Modern Research*, ed. by K. Jungmann, J. Kowalski, I. Reinhard, F. Träger (Springer, Heidelberg, Berlin 1997)

- U. Westblom, M. Aldén: Simultaneous multiple-species detection in a flame using laser-induced fluorescence. *Appl. Opt.* **28**, 2592 (1989)
- C. Véret (ed.): *Flow Visualization IV* (Springer, Berlin, Heidelberg 1987)
- [10.27] M. Aldén, H. Edner, P. Grafström, S. Svanberg: Two-photon excitation of atomic oxygen in a flame. *Opt. Commun.* **42**, 244 (1982)
- M. Alden, H.M. Hertz, S. Svamberg, S. Wallin: Imaging laser-induced fluorescence of oxygen atoms in a flame. *Appl. Opt.* **23**, 3255 (1984)
- [10.28] M. Aldén, U. Westblom, J.E.M. Goldsmith: Two-photon-excited stimulated emission from atomic oxygen in flames and cold gases. *Opt. Lett.* **14**, 305 (1989)
- J.E.M. Goldsmith: Two-photon-excited stimulated emission from atomic hydrogen in flames. *J. Opt. Soc. Am. B* **6**, 1979 (1989)
- [10.29] R.P. Lucht, J.P. Salmon, G.B. King, D.W. Sweeney, N.M. Laurendeau: Two-photon-excited fluorescence measurement of hydrogen atoms in flames. *Opt. Lett.* **8**, 365 (1983)
- [10.30] M. Aldén, A.L. Schawlow, S. Svanberg, W. Wendt, P.-L. Zhang: Three-photon excited fluorescence detection of atomic hydrogen in an atmospheric pressure flame. *Opt. Lett.* **9**, 211 (1984)
- [10.31] J.E.M. Goldsmith: Two-step saturated fluorescence detection of atomic hydrogen in flames. *Opt. Lett.* **10**, 116 (1985)
- J.E.M. Goldsmith, R.J.M. Anderson: Imaging of atomic hydrogen in flames with two-step saturated fluorescence detection. *Opt. Lett.* **11**, 67 (1985)
- [10.32] M. Aldén, S. Wallin, W. Wendt: Applications of two-photon absorption for detection of CO in combustion gases. *Appl. Phys. B* **33**, 205 (1984)
- U. Westblom, M. Aldén: Laser-induced fluorescence detection of NH₃ in flames with the use of two-photon excitation. *Appl. Spectrosc.* **44**, 881 (1990)
- [10.33] J.E.M. Goldsmith: Resonant multiphoton optogalvanic detection of atomic hydrogen in flames. *Opt. Lett.* **7**, 437 (1982)
- J.E.M. Goldsmith: Recent advances in flame diagnostics using fluorescence and ionization techniques. In: [10.34], p. 337
- P.J.H. Tjossem, T.A. Cool: *Chem. Phys. Lett.* **100**, 479 (1983)
- [10.34] W. Persson, S. Svanberg (eds.): *Laser Spectroscopy VIII*, Springer Ser. Opt. Sci., Vol. 55 (Springer, Berlin, Heidelberg 1987)
- [10.35] K. Tennal, G.J. Salomo, R. Gupta: Minority species concentration measurements in flames by the photoacoustic technique. *Appl. Opt.* **21**, 2133 (1982)
- A.C. Tam: Applications of photoacoustic sensing techniques. *Rev. Mod. Phys.* **58**, 381 (1986)
- [10.36] R.K. Hanson, P.A. Kuntz, C.H. Kruger: High-resolution spectroscopy of combustion gases using a tunable IR diode laser. *Appl. Opt.* **16**, 2045 (1975)
- K. Knapp, R.K. Hanson: Spatially resolved tunable diode-laser absorption measurements of CO using optical Stark shifting. *Appl. Opt.* **22**, 1980 (1983)
- I. Linnerud, P. Kaspersen, T. Jaeger: Gas monitoring in the process industry using diode lasers. *Appl. Phys. B* **67**, 297 (1998)
- M.P. Arroyo, S. Langlois, R.K. Hanson: Diode-laser absorption technique for simultaneous measurements of multiple gasdynamic parameters in high-speed flows containing water vapor. *Appl. Opt.* **33**, 3296 (1994)
- [10.37] K. Nyholm, R. Maier, C.G. Aminoff, M. Kaivola: Detection of OH in flames by polarization spectroscopy. *Appl. Opt.* **32**, 919 (1993)

- K. Nyholm, R. Fritzon, M. Aldén: Two-dimensional imaging of OH in flames by use of polarization spectroscopy. *Opt. Lett.* **18**, 1672 (1993)
- B. Löfstedt, R. Fritzon, M. Aldén: Investigation of NO detection in flames by the use of polarization spectroscopy. *Appl. Opt.* **35**, 2140 (1996)
- K. Nyholm, R. Fritzon, N. Gregoriev, M. Aldén: Two-photon induced polarization spectroscopy applied to the detection on NH₃ and CO molecules in cold flows and flames. *Opt. Commun.* **114**, 76 (1995)
- [10.38] Special Issue on Computerized Tomography. *Proc. IEEE* **71**, 291 (March 1983)
- Special Issue on Industrial Applications of Computed Tomography and NMR Imaging. *Appl. Opt.* **24**, 23 (1985)
- T.H. Newton, D.G. Potts (eds.): *Technical Aspects of Computed Tomography* (Mosby 1991)
- [10.39] K.E. Bennett, G.W. Faris, R.L. Byer: Experimental optical fan beam tomography. *Appl. Opt.* **23**, 2678 (1984)
- P. Kauranen, H.M. Hertz, S. Svanberg: Tomographic imaging of fluid flows by the use of two-tone frequency modulation spectroscopy. *Opt. Lett.* **19**, 1489 (1994)
- [10.40] H.M. Hertz, G.W. Faris: Emission tomography of flame radicals. *Opt. Lett.* **13**, 351 (1988)
- [10.41] H.M. Hertz: Experimental determination of 2-D flame temperature fields by interferometric tomography. *Opt. Commun.* **54**, 131 (1985)
- [10.42] A. Rose, G.J. Salamo, R. Gupta: Photoacoustic deflection spectroscopy: A new species-specific method for combustion diagnostics. *Appl. Opt.* **23**, 781 (1984)
- H. Sonntag, A.C. Tam: Time-resolved flow-velocity and concentration measurements using a travelling thermal lens. *Opt. Lett.* **10**, 436 (1985)
- G.W. Faris, R.L. Byer: Beam-deflection optical tomography. *Opt. Lett.* **12**, 72 (1987)
- G.W. Faris, R.L. Byer Beam-deflection optical tomography of a flame. *Opt. Lett.* **12**, 155 (1987)
- [10.43] M. Lapp, C.M. Penney: 'Raman measurements on flames.' In: *Advances in Infrared and Raman Spectroscopy*, ed. by R.J.H. Clark, R.E. Hester (Heyden, London 1977)
- [10.44] R.W. Dibble, A.R. Masri, R.W. Bilger Combust. Flame **67**, 189 (1987)
- J.J. Valentini: Laser Raman techniques. In: [10.1] p. 507
- W. Reckers, L. Huwel, G. Grunewald, P. Andresen: Spatially resolved multispecies and temperature analysis in hydrogen flames. *Appl. Opt.* **32**, 907 (1993)
- [10.45] M. Aldén, H. Edner, S. Svanberg: Coherent anti-Stokes Raman spectroscopy (CARS) applied in combustion probing. *Phys. Scr.* **27**, 29 (1983)
- [10.46] D. Klick, K.A. Marko, L. Rimai: Broadband single-shot CARS spectra in a fired internal combustion engine. *Appl. Opt.* **20**, 1178 (1981)
- G.C. Alessandretti, P. Violino: Thermometry by CARS in an automobile engine. *J. Phys. D* **16**, 1583 (1983)
- M. Richter, B. Axelsson, M. Aldén, G. Josefsson, L.-O. Carlsson, M. Dahlberg, J. Nisbet, H. Simonsen: Investigation of the fuel distribution and the in-cylinder flow field in a stratified charge engine using laser techniques and comparison with CFD-Modelling. SAE Technical Paper Series 1999-01-3540 (SAE International, Warrendale, PA 1999)
- [10.47] L.A. Rahn, S.S. Johnston, R.L. Farrow, P.L. Mattern: 'CARS thermometry in an internal combustion engine.' In: *Temperature*, Vol. 5, ed. by J.F. Schooley (AIP, New York 1982)

- [10.48] M. Aldén, S. Wallin: CARS Experiment in a full-scale ($10 \times 10 \text{ m}^2$) industrial coal furnace. *Appl. Opt.* **24**, 3434 (1985)
- [10.49] B. Attal, M. Pealat, J.P. Taran: *J. Energy* **4**, 135 (1980)
- [10.50] A.C. Eckbreth: CARS thermometry in practical combustors. *Combust. Flame* **39**, 133 (1980)
- [10.51] A.C. Eckbreth, P.W. Schreiber: 'Coherent anti-Stokes Raman spectroscopy (CARS): Applications to combustion and gas-phase diagnostics.' In: *Chemical Applications of Non-Linear Raman Spectroscopy*, ed. by A.B. Harvey (Academic Press, New York 1981)
- R.J. Hall, A.C. Eckbreth: 'Coherent anti-Stokes Raman Spectroscopy (CARS): Application to combustion diagnostics.' In: *Laser Applications*, Vol. 5, ed. by J.F. Ready, R.K. Erf (Academic Press, New York 1984)
- [10.52] H. Haragushi, B. Smith, S. Weeks, D.J. Johnson, J.D. Winefoder: Measurement of small volume flame temperature by the two-line atomic fluorescence method. *Appl. Spectrosc.* **31**, 156 (1977)
- R.G. Jolik, J.W. Daily: Two-line atomic fluorescence temperature measurements in flames: An experimental study. *Appl. Opt.* **21**, 4158 (1982)
- M. Aldén, P. Grafström, H. Lundberg, S. Svanberg: Spatially resolved temperature measurements in a flame using laser-excited two-line atomic fluorescence and diode-array detection. *Opt. Lett.* **8**, 241 (1983)
- [10.53] J. Pender, L. Hesselink: Phase conjugation in a flame. *Opt. Lett.* **10**, 264 (1985)
- P. Ewart, S.V. O'Leary: Detection of OH in a flame by degenerate four-wave mixing. *Opt. Lett.* **11**, 279 (1986)
- G. Hall, B.J. Whitaker: Laser-induced grating spectroscopy. *J. Chem. Soc. Faraday Trans.* **90**, 1 (1994)
- B. Yip, P.M. Danehy, R.K. Hanson: Degenerate four-wave mixing temperature measurements in a flame. *Opt. Lett.* **17**, 751 (1992)
- P. Ewart, P.G.R. Smith, R.G. Williams: Imaging of trace species distributions by degenerate four-wave mixing: Diffraction effects, spatial resolution, and image referencing. *Appl. Opt.* **36**, 5959 (1997)
- [10.54] R.M. Osgood, S.R.I. Brueck, H.R. Schlossberg (eds.): *Laser Diagnostics and Photochemical Processing for Semiconductor Devices* (North-Holland, Amsterdam 1983)
- D. Bäuerle (ed.): *Laser Processing and Diagnostics*, Springer Ser. Chem. Phys., Vol. 39 (Springer, Berlin, Heidelberg 1984)
- D. Bäuerle, K.L. Kompa, L.D. Laudé (eds.): *Laser Processing and Diagnostics II* (Physique, Les Ulis 1986)
- D. Bäuerle: *Laser Processing and Chemistry*, 2nd edn. (Springer, Berlin, Heidelberg 1996)
- L.D. Laudé, D. Bäuerle, M. Wautelet (eds.): *Interfaces under Laser Irradiation*, NATO ASI Series (Nijholl, Dordrecht 1987)
- W.G. Breiland, M.E. Coltrin, P. Ho (eds.): *Laser-Based Studies of Chemical Vapor Deposition*, Proc. SPIE-Int. Soc. Opt. Eng. **385**, 146 (1983)
- [10.55] K.L. Kompa, J. Wanner: *Laser Applications in Chemistry* (Plenum, New York 1984)
- V.S. Letokhov (ed.): *Laser Analytical Spectrochemistry* (Hilger, Bristol 1986)
- T.R. Evans (ed.): *Applications of Lasers to Chemical Problems* (Wiley, New York 1982)
- S. Svanberg: Laser spectroscopy applied to energy, environmental and medical research. *Phys. Scr.* **T23**, 281 (1988); *Appl. Phys. B* **46**, 271 (1988)

- [10.56] E.R. Pike, H.Z. Cummins (eds.): *Photon Correlation and Light Beating Spectroscopy* (Plenum, New York 1974)
- [10.57] L.E. Drain: *The Laser Doppler Technique* (Wiley, Chichester 1980)
- [10.58] E. Durst, A. Melling, J.H. Whitelaw: *Principles and Practice of Laser-Doppler Anemometry*, 2nd edn. (Academic Press, London 1981)
- [10.59] C.J. Dasch, J.A. Sell: Velocimetry in laminar and turbulent flows using the photothermal deflection effect with a transient grating. *Opt. Lett.* **11**, 603 (1986), and references therein
R. Miles, C. Cohen, J. Connors, P. Howard, S. Huang, E. Markovitz, G. Russel: Velocity measurements by vibrational tagging and fluorescent probing of oxygen. *Opt. Lett.* **12**, 861 (1987)
- [10.60] B. Hiller, J.C. McDaniel, E.C. Rea Jr., R.K. Hanson: Laser-induced fluorescence technique for velocity field measurements in subsonic gas flows. *Opt. Lett.* **8**, 474 (1983)
- [10.61] U. Westblom, S. Svanberg: Imaging measurements of flow velocitites using laser-induced fluorescence. *Phys. Scr.* **31**, 402 (1985)
U. Westblom, A. Aldén: Spatially resolved flow velocity measurement using laser-induced fluorescence from a pulsed laser. *Opt. Lett.* **14**, 9 (1989)
- [10.62] A.M.P.K. Taylor: *Instrumentation for Flows with Combustion* (Academic Press, London 1993)
L. Laching, G. Wigley: *Optical Diagnostics for Flow Processes* (Plenum, New York 1995)
- R.J. Adrian, D.F.G. Durao, F. Durst, M.V. Heitor, M. Maeda, J.H. Whitelaw (eds.): *Developments in Laser Techniques and Fluid Mechanics* (Springer, Berlin, Heidelberg 1997)
- [10.63] E.J. McCartney: *Absorption and Emission by Atmospheric Gases* (Wiley, New York 1983)
E.J. McCartney: *Optics of the Atmosphere; Scattering by Molecules and Particles* (Wiley, New York 1976)
L.S. Rothman, C.P. Rinsland, A. Goldman, S.T. Massie, D.P. Edwards, J.-M. Edwards, J.-M. Flaud, A. Perrin, C. Camy-Peyret, V. Dana, J.-Y. Mandin, J. Schroeder, A. McCann, R.R. Gamache, R.B. Eattson, K. Yoshino, K.V. Chance, K.W. Jucks, L.R. Brown, V. Nemtchinov, P. Varanasi: The HITRAN molecular database and HAWKS (HITRAN Atmospheric Workstation): 1996 edition. *J. Quant. Spectrosc. Radiat. Transfer* **60**, 665 (1998)
- P.L. Hanst: QA Soft '96, Database and quantitative analysis program for measurements of gases (Infrared Analysis Inc., Anaheim, CA 1996)
- [10.64] W. Bach, J. Pankrath, W. Kellogg (eds.): *Man's Impact on Climate* (Elsevier, Amsterdam 1979)
- [10.65] R. Revelle: Carbon dioxide and world climate. *Sci. Am.* **247**(2), 33 (1982)
S.H. Schneider: Climate modeling. *Sci. Am.* **256**(5), 72 (1987)
R.A. Houghton, G.W. Woodwell: Global climatic change. *Sci. Am.* **260**(4), 18 (1989)
S.H. Schneider: The changing climate. *Sci. Am.* **261**(3), 38 (1989)
B.J. Mason: The greenhouse effect. *Contemp. Phys.* **30**, 417 (1989)
B.J. Mason: Predictions of climate changes caused by manmade emissions of greenhouse gases: A critical assessment. *Contemp. Phys.* **36**, 299 (1995)
C.S. Zerefos, A.F. Bais: *Solar Ultraviolet Radiation, Modelling, Measurements and Effects* (Springer, Berlin, Heidelberg 1997)
- [10.66] T.E. Graedel, D.T. Hawkins, L.D. Claxton: *Atmospheric Chemical Compounds: Sources, Occurrence, Bioassay* (Academic Press, Orlando 1986)

- [10.67] R.M. Harrison, R. Perry (eds.): *Handbook of Air Pollution Analysis*, 2nd edn. (Chapman and Hall, London 1986)
 R.W. Baubel, D.B. Turner, A.C. Stem: *Fundamentals of Air Pollution*, 3rd edn. (Academic Press, London 1994)
 W. Michaelis: *Air Pollution* (Springer, Berlin, Heidelberg 1997)
- [10.68] R.P. Wayne: *Chemistry of Atmospheres* (Clarendon, Oxford 1985)
- [10.69] J.H. Seinfeld: *Atmospheric Chemistry and Physics of Air Pollution* (Wiley, New York 1986)
- [10.70] D.A. Killinger, A. Mooradian (eds.): *Optical and Laser Remote Sensing*, Springer Ser. Opt. Sci., Vol. 39 (Springer, Berlin, Heidelberg 1983)
- [10.71] R.M. Measures: *Laser Remote Sensing - Fundamentals and Applications* (Wiley, New York 1984)
- [10.72] E.D. Hinkley (ed.): *Laser Monitoring of the Atmosphere*, Topics Appl. Phys., Vol. 14 (Springer, Berlin, Heidelberg 1976)
- [10.73] V. Zuev, I. Naats: *Inverse Problems of Lidar Sensing of the Atmosphere*, Springer Ser. Opt. Sci., Vol. 29 (Springer, Berlin, Heidelberg 1983)
- [10.74] R.M. Measures: In: *Analytical Laser Spectroscopy*, ed. by N. Omenetto (Wiley, New York 1979)
 D.K. Killinger, N. Menyuk: Laser remote sensing of the atmosphere. *Science* **235**, 37 (1987)
 W.B. Grant: Laser remote sensing techniques. In: [10.1] p. 565
 T. Kobayashi: Techniques for laser remote sensing of the environment. *Remote Sens. Rev.* **3**, 1 (1987)
 R.M. Measures (ed.): *Laser Remote Chemical Analysis* (Wiley-Interscience, New York 1988)
 E. Zanzottera: Differential absorption lidar techniques in the determination of trace pollutants and physical parameters of the atmosphere. *Crit. Rev. Anal. Chem.* **21**, 279 (1990)
 S. Svanberg: 'Environmental monitoring using optical techniques.' In: *Applied Laser Spectroscopy*, ed. by M. Inguscio, W. Demtröder (Plenum, New York 1990)
 C.Y. She: Remote measurements of atmospheric parameters: New applications of physics with lasers. *Contemp. Phys.* **31**, 247 (1990)
 S. Svanberg: 'Atmospheric pollution monitoring using laser lidars.' In: *Optoelectronics for Environmental Sciences*, ed. by Martellucci and A.N. Chester (Plenum Press, New York 1990) p. 3
 S. Svanberg: 'Differential absorption lidar (DIAL).' In: *Air Monitoring by Spectroscopic Techniques*, ed. by M. Sigrist, (Wiley, New York 1994)
 S. Martellucci, A.N. Chester (eds.): *Optoelectronics for Environmental Science* (Plenum, New York 1991)
 M.W. Sigrist (ed.): *Air Monitoring by Spectroscopic Techniques* (Wiley, New York 1994)
 A. Ansmann, R. Neuber, P. Rairoux, U. Wandinger (eds.): *Advances in Atmospheric Remote Sensing with Lidar* (Springer, Heidelberg 1997)
- [10.75] S. Svanberg: Lasers as probes for air and sea. *Contemp. Phys.* **21**, 541 (1980)
 [10.76] S. Svanberg: 'Fundamentals of atmospheric spectroscopy.' In: *Surveillance of Environmental Pollution and Resources by Electromagnetic Waves*, ed. by T. Lund (Reidel, Dordrecht 1978)
- [10.77] R.T. Menzies, R.K. Seals Jr.: *Science* **197**, 1275 (1977)
- [10.78] E.D. Hinkley: Laser spectroscopic instrumentation and techniques: Long path monitoring by resonance absorption. *Opt. Quantum Electron.* **8**, 155 (1976)

- [10.79] H.I. Schiff, G.I. Macay, J. Bechara: 'The use of tunable diode laser absorption spectroscopy for atmospheric measurements.' In: *Air Monitoring by Spectroscopic Techniques*, ed. by M.W. Sigrist, Chemical Physics Series Vol. 127 (John Wiley, New York 1994) p. 239
- P. Werle: Spectroscopic trace gas analysis using semiconductor diode lasers. *Spectrochim. Acta A* **52**, 805 (1996)
- A.A. Kostarov, R.F. Curl, F.K. Tittel, G. Gmachl, F. Capasso, D.L. Sivco, J.N. Baillargeon, A.L. Hutchinson, A.Y. Cho: Methane concentration and isotopic composition measurements with a quantum-cascade laser. *Opt. Lett.* **24**, 1762 (1999)
- [10.80] U. Simon, C.E. Miller, C.C. Bradley, R.G. Hulet, R.F. Curl, F.K. Tittel: Difference frequency generation in AgGaS_2 using single-mode diode laser pump sources. *Opt. Lett.* **18**, 1062 (1993)
- Th. Töpfer, K.P. Petrov, Y. Mine, D. Jundt, R.F. Curl, F.K. Tittel: Room-temperature mid-infrared laser sensor for trace gas detection. *Appl. Opt.* **36**, 8042 (1997)
- M. Seiter, M.W. Sigrist: Compact gas sensor using a pulsed difference-frequency laser spectrometer. *Opt. Lett.* **24**, 110 (1999)
- [10.81] U. Gustafsson, J. Sandsten, S. Svanberg: Simultaneous detection of methane, oxygen and water vapour utilizing near-infrared diode lasers in conjunction with difference-frequency generation. *Appl. Phys. B* **71**, 853 (2000)
- [10.82] J. Alnis, U. Gustafsson, G. Somesfalean, S. Svanberg: Sum-frequency generation with a blue diode laser for mercury spectroscopy at 254 nm. *Appl. Phys. Lett.* **76**, 1234 (2000)
- [10.83] C. Zimmermann, V. Vuletic, A. Hemmerich, T.W. Hänsch: All solid state laser source for tunable blue and ultraviolet radiation. *Appl. Phys. Lett.* **66**, 238 (1995)
- [10.84] U. Gustafsson: PhD Thesis (Lund Institute of Technology, Lund 2000)
- [10.85] G.C. Bjorklund: Frequency modulation spectroscopy: a new method for measuring weak absorptions and dispersions. *Opt. Lett.* **6**, 15 (1980)
- N.H. Tran, R. Kachru, P. Pillet, H.B. van Linden van den Heuvell, T.F. Gallagher, J.P. Watjen: Frequency modulation spectroscopy with a pulsed dye laser: Experimental investigations of sensitivity and useful features. *Appl. Opt.* **23**, 1353 (1984)
- M. Gehrtz, G.C. Bjorklund, E.A. Whittaker: Quantum-limited laser frequency modulation spectroscopy. *J. Opt. Soc. Am. B* **2**, 1810 (1985)
- G.R. Janik, C.B. Carlisle, T.F. Gallagher: Two-tone frequency modulation spectroscopy. *J. Opt. Soc. Am. B* **3**, 1070 (1986)
- C.B. Carlisle, D.E. Cooper: Tunable-diode-laser frequency modulation spectroscopy using balanced homodyne detection. *Opt. Lett.* **14**, 1306 (1989)
- F.S. Pavone, M. Inguscio: Frequency- and wavelength-modulation spectroscopies: comparison of experimental methods using an AlGaAs diode laser. *Appl. Phys. B* **56**, 118 (1993)
- V.G. Avetisov, P. Kauranen: High-resolution absorption measurements using two-tone frequency-modulation spectroscopy with diode lasers. *Appl. Opt.* **36**, 4043 (1997)
- [10.86] U. Gustafsson, G. Somesfalean, J. Alnis, S. Svanberg: Frequency modulation spectroscopy with blue diode lasers, *Appl. Opt.* **39**, 3774 (2000)
- M.C. Alarcon, H. Ito, H. Inaba: All-optical remote sensing of city gas through CH_4 gas absorption employing a low-loss optical fibre link and an

- InGaAsP light emitting diode in the near-infrared region. *Appl. Phys. B* **43**, 79 (1987)
- [10.87] J.J. Degnan, NASA Goddard Space Flight Centre, CLEO Europe, Sept. 13–18 and Glasgow 1998
- J.J. Degnan: ‘Satellite laser ranging and very long baseline interferometry.’ In: *Encyclopedia of Earth Sciences*, Vol. 2, ed. by M. Kauffman (Simon and Schuster Macmillan, New York 1996) p. 935
- J.J. Degnan: ‘Millimeter accuracy satellite laser ranging: A review.’ In: *Contributions of Space Geodesy to Geodynamics: Technology*, ed. by D.E. Smith, D.L. Turcotte, AGU Geodynamics Series, Vol. 25 (1993) p. 133
- [10.88] M.L. Chanin: Rayleigh and resonance sounding of the stratosphere and mesosphere. In: [10.70] p. 192
- C. Granier, G. Megie: Daytime lidar measurement of the mesospheric sodium layer. *Planet. Space Sci.* **30**, 169 (1982)
- C. Granier, J.P. Jegou, G. Megie: Resonant lidar detection of Ca and Ca⁺ in the upper atmosphere. *Geophys. Res. Lett.* **12**, 655 (1985)
- K.H. Fricke, U. von Zahn: Mesopause temperatures derived from probing the hyperfine structure of the D₂ resonance line of sodium by lidar. *J. Atmos. Terr. Phys.* **47**, 499 (1985)
- U. von Zahn, P. von der Gathen, G. Hansen: Forced release of sodium from upper atmosphere dust particles. *Geophys. Res. Lett.* **14**, 76 (1987)
- L.A. Thompson, C.S. Gardner: Laser guidestar experiment at Mauna Kea Observatory for adaptive imaging in astronomy. *Nature* **328**, 229 (1987)
- C.Y. She, J.R. Yu: Simultaneous three-frequency Na lidar measurements of radial wind and temperature in the mesopause region. *Geophys. Res. Lett.* **21**, 1771 (1994)
- M. Alpers, J. Hoffner, U. von Zahn: Upper atmosphere Ca and Ca⁺ at mid-latitudes. *Geophys. Res. Lett.* **22**, 263 (1995)
- U. von Zahn, J. Hoffner: Mesopause temperature profiling by potassium lidar. *Geophys. Res. Lett.* **23**, 141 (1996)
- [10.89] W. Happer, G. MacDonald, C. Max, F.J. Dyson: Atmospheric-turbulence compensation by resonant optical backscattering from the sodium layer in the upper atmosphere. *J. Opt. Soc. Am. A* **11**, 263 (1994)
- M.J. Beran, J. Oz-Vogt: ‘Imaging through turbulence in the atmosphere.’ In: *Progress in Optics XXXIII*, ed. by E. Wolf (Elsevier, Amsterdam 1994) p. 321
- M.C. Roggemann, B.M. Welsh, R.Q. Fugate: Improving the resolution of ground-based telescopes. *Rev. Mod. Phys.* **69**, 437 (1997)
- [10.90] Y.F. Arshinov, S.M. Bobrovnikov, V.E. Zuev, V.M. Mitev: Atmospheric temperature measurements using a pure rotational Raman lidar. *Appl. Opt.* **22**, 2984 (1983)
- D. Nedeljkovic, A. Hauchecorne, M.L. Chanin: Rotational Raman lidar to measure the atmospheric temperature from the ground to 30 km. *IEEE Trans. Geosci. Remote Sens.* **31**, 90 (1993)
- A. Behrendt, J. Reichart: Atmospheric temperature profiling in the presence of clouds with a pure rotational Raman lidar by use of an interference-filter-based polychromator. *Appl. Opt.* **39**, 1372 (2000)
- [10.91] J. Reichardt, U. Wandinger, M. Serwasi, C. Weitkamp: Combined Raman lidar for aerosol, ozone and moisture measurements. *Opt. Eng.* **35**, 1457 (1996)
- [10.92] L.J. Radziemski, T.R. Loree, D.A. Cremers, N.M. Hoffman: Time-resolved laser-induced breakdown spectrometry of aerosols. *Anal. Chem.* **55**, 1246 (1983)

- J.A. Millard, R.H. Dalling, L.J. Radziemski: Time-resolved laser-induced breakdown spectrometry for the rapid determination of beryllium in beryllium-copper alloys. *Appl. Spectrosc.* **40**, 491 (1986)
- D.J. Cremers, L.J. Radziemski: Laser plasmas for chemical analysis. In: [10.1] p. 351
- [10.93] K. Fredriksson, B. Galle, K. Nyström, S. Svanberg: Mobile lidar system for environmental probing. *Appl. Opt.* **20**, 4181 (1981)
- [10.94] K. Fredriksson, I. Lindgren, S. Svanberg, G. Weibull: Measurements of the emission from industrial smoke stacks using laser radar techniques. Göteborg Institute of Physics Reports GIPR-121 (CTH, Göteborg 1976)
- [10.95] H. Edner, K. Fredriksson, A. Sunesson, S. Svanberg, L. Unéus, W. Wendt: Mobile remote sensing system for atmospheric monitoring. *Appl. Opt.* **26**, 4330 (1987)
- [10.96] D.J. Braxton: Measurement of the SO₂ absorption spectrum between 297 and 316 nm using a tunable dye laser. Lab. Note No. RD/L/N 184/79 (Central Electricity Res. Labs., Leatherhead 1979)
- D.J. Braxton: Sulphur dioxide absorption cross-section measurement from 290 nm to 317 nm. *Appl. Opt.* **20**, 3774 (1981)
- [10.97] P. Weibring, M. Andersson, H. Edner, S. Svanberg: Remote monitoring of industrial emissions by combination of lidar and plume velocity measurements. *Appl. Phys. B* **66**, 383 (1998)
- [10.98] H. Edner, P. Ragnarson, S. Svanberg, E. Wallinder, R. Ferrara, R. Cioni, B. Raco, G. Taddeucci: Total fluxes of sulphur dioxide from the Italian volcanoes Etna, Stromboli and Vulcano measured by differential absorption lidar and passive differential optical absorption spectroscopy. *J. Geophys. Res.* **99**, 18 827 (1994)
- [10.99] P. Weibring, H. Edner, S. Svanberg, G. Cecchi, L. Pantani, R. Ferrara, T. Caltabiano: Monitoring of volcanic sulphur dioxide emissions using differential absorption lidar (DIAL), differential optical absorption spectroscopy (DOAS), and correlation spectroscopy (COSPEC). *Appl. Phys. B* **67**, 419 (1998)
- P. Weibring, J. Swartling, H. Edner, S. Svanberg, T. Caltabiano, D. Condarelli, G. Cecchi, L. Pantani: Optical monitoring of volcanic sulphur dioxide emissions – Comparison between four different remote sensing techniques, *Opt. Lasers Eng.* **37**, 267 (2002)
- S. Svanberg: Geophysical gas monitoring using optical techniques: Volcanoes, geothermal fields and mines. *Opt. Lasers Eng.* **37**, 245 (2002)
- [10.100] H. Edner, G.W. Faris, A. Sunesson, S. Svanberg: Atmospheric atomic mercury monitoring using differential absorption lidar techniques. *Appl. Opt.* **28**, 921 (1989)
- R. Ferrara, B.E. Maseri, H. Edner, P. Ragnarson, S. Svanberg, E. Wallinder: Mercury emissions into the atmosphere from a chlor-alkali complex measured with the lidar technique. *Atmos. Environ.* **26A**, 1253 (1992)
- [10.101] H. Edner, G.W. Faris, A. Sunesson, S. Svanberg, J.Ö. Bjarnason, K.H. Sigurdsson, H. Kristmansdottir: Lidar search for atomic mercury in Icelandic geothermal fields. *J. Geophys. Res.* **96**, 2977 (1991)
- [10.102] H. Edner, P. Ragnarson, S. Svanberg, E. Wallinder, A. De Liso, R. Ferrara, B.E. Maseri: Differential absorption lidar mapping of atmospheric atomic mercury in Italian geothermal fields. *J. Geophys. Res.* **97**, 3779 (1992)
- [10.103] H. Edner, P. Ragnarson, S. Svanberg, E. Wallinder, R. Ferrara, B.E. Maseri, R. Bargagli: Atmospheric mercury mapping in a cinnabar mining area. *Sci. Total Environ.* **133**, 1 (1993)

- R. Ferrari, B.M. Maserti, M. Andersson, H. Edner, P. Ragnarson, S. Svanberg, A. Hernandez: Atmospheric mercury concentration and fluxes in the Almaden district (Spain). *Atmos. Environ.* **32**, 3897 (1998)
- [10.104] R. Ebinghaus, R.R. Turner, L.D. de Lacerda, O. Vasiliev, W. Salomons (eds.): *Mercury Contaminated Sites* (Springer, Berlin, Heidelberg 1999)
- [10.105] M. Aldén, H. Edner, S. Svanberg: Laser monitoring of atmospheric NO using ultraviolet differential-absorption techniques. *Opt. Lett.* **7**, 543 (1982)
- [10.106] K.W. Rothe, U. Brinkmann, H. Walther: *Appl. Phys.* **3**, 115 (1974)
W.R. Grant, R.D. Hake Jr., E.M. Liston, R.C. Robbins, E.K. Proctor Jr.: Calibrated remote measurement of NO₂ using the differential absorption backscatter technique. *Appl. Phys. Lett.* **24**, 550 (1974)
- [10.107] T.D. Gardiner, R.A. Robinson, M.J.T. Milton, P.T. Woods: Infrared differential absorption lidar for trace gas measurement. *Proc. Int. Laser Sensing Symposium*, Fukui, Japan, September 6–8 1999, p. 173
P. Weibring, J.N. Smith, H. Edner, S. Svanberg: Differential absorption lidar system based on a frequency agile optical parametric oscillator for multi-component chemical analysis of gas mixtures. *Proc. Int. Laser Radar Conference*, Vichy, France, July 10–14 (2000)
P. Weibring, H. Edner, S. Svanberg: Versatile mobile lidar system for environmental monitoring. *Appl. Opt.* **42**, 3583 (2003)
- [10.108] H. Edner, S. Svanberg, L. Unéus, W. Wendt: Gas correlation lidar. *Opt. Lett.* **9**, 493 (1984)
- [10.109] A. Minato, T. Kobayashi, N. Sugimoto: Laser long-path absorption technique for measuring methane using gas correlation method. *J. Appl. Phys.* **37**, 3610 (1998)
- [10.110] H. Edner, P. Ragnarson, E. Wallinder: Industrial emission control using lidar techniques. *Environ. Sci. Technol.* **29**, 330 (1995)
- [10.111] J. Pelon, G. Megie: Ozone monitoring in the troposphere and lower stratosphere: Evaluation and operation of a ground-based lidar station. *J. Geophys. Res.* **87**, 4947 (1982)
G.J. Megie, G. Ancellet, J. Pelon: Lidar, measurements of ozone vertical profiles. *Appl. Opt.* **24**, 3454 (1985)
O. Uchino, M. Tokunaga, M. Maeda, Y. Miyazoe: Differential absorption-lidar measurement of tropospheric ozone with excimer-Raman hybrid laser. *Opt. Lett.* **8**, 347 (1983)
O. Uchino, M. Maeda, H. Yamamura, M. Hirono: Observation of stratospheric vertical ozone distribution by a XeCl lidar. *J. Geophys. Res.* **88**, 5273 (1983)
J. Werner, K.W. Rothe, H. Walther: Monitoring of the stratospheric ozone layer by laser radar. *Appl. Phys. B* **32**, 113 (1983)
- E.V. Browell et al.: Ozone and aerosol distributions and air mass characteristics over the south Atlantic basin during the burning season. *J. Geophys. Res.* **101**, 24 043 (1996)
- [10.112] M.P. McCormick: Lidar measurements of Mount St. Helens effluents. *Opt. Eng.* **21**, 340 (1982)
M.P. McCormick, T.J. Swisser, W.H. Fuller, W.H. Hunt, M.T. Osborn: Airborne and ground-based lidar measurements of the El Chichon stratospheric aerosol from 90° N to 56° S. *Geofisica Internacional* **23-2**, 187 (1984)
M.R. Rampino, S. Self: The atmospheric effects of El Chichon. *Sci. Am.* **250**(1), 34 (1984)

- E.E. Uthe: Application of surface-based and airborne lidar systems for environmental monitoring. *J. Air Pollut. Control Assoc.* **33**, 1149 (1983)
- G. Fiocco, D. Fua, G. Visconti (eds.): *The Mount Pinatubo Eruption – Effects on the Atmosphere and Climate*. NATO ASI Series, Vol. 142 (Springer, Heidelberg 1996)
- [10.113] C.L. Korb, B.M. Gentry, C.Y. Weng: Edge technique: Theory and application to the lidar measurement of atmospheric wind. *Appl. Opt.* **31**, 4202 (1992)
- C. Flesia, C.L. Korb: Theory of the double-edge molecular technique for Doppler lidar wind measurement. *Appl. Opt.* **38**, 432 (1999)
- [10.114] J.S. Friedman, C.A. Tepley, P.A. Catleberg, H. Roe: Middle-atmospheric Doppler lidar using an iodine-vapour edge filter. *Opt. Lett.* **22**, 1648 (1997)
- [10.115] P. Kauranen, S. Andersson-Engels, S. Svanberg: Spatial mapping of flame radical emission using a spectroscopic multi-colour imaging system. *Appl. Phys. B* **53**, 260 (1991)
- [10.116] R.M. Huffaker, R.M. Hardesty: Remote sensing of atmospheric wind velocities using solid-state and CO₂ coherent laser systems. *Proc. IEEE* **84**, 181 (1996)
- J.M. Vaughan: Coherent laser spectroscopy and Doppler LIDAR sensing in the atmosphere. *Phys. Scr. T78*, 73 (1998)
- [10.117] D.M. Winkler, R.C. Couch, M.P. McCormick: *Proc. IEEE* **84**, 164 (1996)
- D.M. Winkler, M.P. McCormick: Aerosol and cloud sensing with the Lidar in Space Technology experiment (LITE). *SPIE* **2310**, 98 (1994)
- E.V. Browell, S. Ismail, W.B. Grant: Differential absorption lidar (DIAL) measurements from air and space. *Appl. Phys. B* **67**, 399 (1998)
- [10.118] Y. Sasano, K. Asai, N. Sugimoto, Y. Kawamura, K. Tatsumi, T. Imai: NASDA mission demonstration satellite lidar project and science. *Proc. SPIE-Int. Soc. Opt. Eng.* **3504**, 2 (1998)
<http://essp.gsfc.nasa.gov/picasso-cena/index.html>
- [10.119] D.H. Hercules (ed.): *Fluorescence and Phosphorescence Analysis* (Interscience, New York 1966)
- P. Pringsheim: *Fluorescence and Phosphorescence* (Interscience, New York 1949)
- [10.120] J.B. Birks: *Photophysics of Aromatic Molecules* (Wiley, New York 1970)
- [10.121] I. Berlman: *Handbook of Fluorescence Spectra of Aromatic Molecules*, 2nd edn. (Academic Press, New York 1971)
- [10.122] J.R. Lakowicz: *Principles of Fluorescence Spectroscopy* (Plenum, New York 1983)
- E.L. Wehrly (ed.): *Modern Fluorescence Spectroscopy*, Vols. 1 and 2 (Plenum, New York 1976)
- [10.123] J.R. Lakowicz (ed.): *Topics in Fluorescence Spectroscopy* (Plenum, New York 1994)
- J.R. Lakowicz (ed.): *Topics in Fluorescence Spectroscopy, Vol. 1: Techniques, Vol. 2: Principles, Vol. 3: Biochemical Applications, Vol. 4: Probe Design and Chemical Sensing, Vol. 5: Nonlinear and Two-Photon-Induced Fluorescence* (Plenum, New York 1991–1997)
- O.S. Wolfbeis (ed.): *Fluorescence Spectroscopy, New Methods and Applications* (Springer-Verlag, Heidelberg 1992)
- [10.124] L. Celander, K. Fredriksson, B. Galle, S. Svanberg: Investigation of laser-induced fluorescence with application to remote sensing of environmental parameters. *Göteborg Institute of Physics Reports GIPR-149* (CTH, Göteborg 1978)

- S. Svanberg: 'Environmental diagnostics.' In: *Trends in Physics*, ed. by M.M. Woolfson (Hilger, Bristol 1978) p. 119
- [10.125] Govindjee, R. Govindjee: The absorption of light in photosynthesis. *Sci. Am.* **231**(6), 68 (1974)
- D.C. Youvan, B.L. Marrs: Molecular mechanisms of photosynthesis. *Sci. Am.* **256**(6), 42 (1987)
- H.K. Lichtenhhaler, U. Rinderle: The role of chlorophyll fluorescence in the detection of stress conditions in plants. *CRC Crit. Rev. Anal. Chem.* **19**, Suppl. 1, S29 (1988)
- A.J. Hoff, J. Deisenhofer: Photophysics of photosynthesis. *Phys. Rep.* **287**, 1 (1997)
- A.R. Young, L.O. Björn, J. Moan, W. Nultsch (eds.): *Environmental UV Photobiology* (Plenum, New York 1993)
- K.C. Smith (ed.): *The Science of Photobiology*, 2nd edn. (Plenum, New York 1989)
- F.E. Hoge, R.N. Swift: Airborne simultaneous spectroscopic detection of laser-induced water Raman backscatter and fluorescence from chlorophyll *a* and other naturally occurring pigments. *Appl. Opt.* **20**, 3197 (1981)
- F.E. Hoge, R.N. Swift, J.K. Yungel: Active-passive airborne ocean color measurement 2: Applications. *Appl. Opt.* **25**, 48 (1986)
- [10.126] R.A. O'Neill, L. Buja-Bijunas, D.M. Rayner: Field performance of a laser fluorosensor for the detection of oil spills. *Appl. Opt.* **19**, 863 (1980)
- G.A. Capelle, L.A. Franks, D.A. Jessup: Aerial testing of a KrF laser-based fluorosensor. *Appl. Opt.* **22**, 3382 (1983)
- H. Amann: Laser spectroscopy for monitoring and research in the ocean. *Phys. Scr.* **T78**, 68 (1998)
- [10.127] H.H. Kim: Airborne laser bathymetry. *Appl. Opt.* **16**, 45 (1977)
- J. Banic, S. Sizgoric, R. O'Neill: Airborne scanning lidar bathymeter measures water depth. *Laser Focus* **23**(2), 40 (1987)
- K. Fredriksson, B. Galle, K. Nyström, S. Svanberg, B. Öström: Underwater laser-radar experiments for bathymetry and fish-school detection. *Göteborg Institute of Physics Reports GIPR-162* (CTH, Göteborg 1978)
- [10.128] H. Edner, J. Johansson, S. Svanberg, E. Wallinder: Fluorescence lidar multicolor imaging of vegetation. *Appl. Opt.* **33**, 2471 (1994)
- [10.129] S. Svanberg: Fluorescence lidar monitoring of vegetation status. *Phys. Scr.* **T58**, 79 (1995)
- S. Svanberg: 'Laser fluorescence spectroscopy in environmental monitoring.' In: *Optoelectronic for Environmental Science*, S. Martellucci, ed. by A.N. Chester (Plenum Press, New York 1990) p. 15
- J. Johansson, M. Andersson, H. Edner, J. Mattsson, S. Svanberg: Remote fluorescence measurements of vegetation spectrally resolved and by multi-colour fluorescence imaging. *J. Plant Physiology* **148**, 632 (1996)
- T. Fujii (ed.): *Recent Advances in Laser Remote Sensing* (Marcel Dekker 2003)
- [10.130] V. Raimondi, G. Cecchi, L. Pantani, R. Chiari: Fluorescence lidar monitoring of historical buildings. *Appl. Opt.* **37**, 1089 (1996)
- P. Weibring, M. Andersson, G. Cecchi, H. Edner, J. Johansson, L. Pantani, V. Raimondi, B. Sundnér, S. Svanberg: A preliminary experiment on the remote sensing of historical monuments by fluorescence lidar. *Proc. SPIE-Int. Soc. Opt. Eng.* **3222**, 372 (1997)
- [10.131] P. Weibring, Th. Johansson, H. Edner, S. Svanberg, B. Sundnér, V. Raimondi, G. Cecchi, L. Pantani: Fluorescence lidar imaging of historical monuments. *Appl. Opt.* **40**, 6111 (2001)

- D. Lognoli, G. Cecchi, L. Pantani, V. Raimondi, R. Chiari, Th. Johansson, P. Weibring, H. Edner, S. Svanberg: Fluorescence lidar imaging of the Parma Cathedral and Batistery, *Appl. Physics B* **76**, 1 (2003)
- [10.132] S. Montán, S. Svanberg: A system for industrial surface monitoring utilizing laser-induced fluorescence. *Appl. Phys. B* **38**, 241 (1985)
- [10.133] S. Montán, S. Svanberg: Industrial applications of laser-induced fluorescence. *L.I.A. ICALEO* **47**, 153 (1985)
- P.S. Andersson, S. Montán, S. Svanberg: Remote sample characterization based on fluorescence monitoring. *Appl. Phys. B* **44**, 19 (1987)
- [10.134] E.S. Yeung: In: *Adv. Chromatography*, Vol. 23 (Dekker, New York 1984) Chap. 1
- E.S. Yeung: In: *Microcolumn Separations: Columns, Instrumentation and Ancillary Techniques*, ed. by M.V. Novotny, D. Ishii (Elsevier, Amsterdam 1985) p. 135
- E. Gassman, J.E. Kuo, R.N. Zare: Electrokinetic separation of chiral compounds. *Science* **230**, 813 (1985)
- M.C. Roach, P.H. Gozel, R.N. Zare: Determination of methotrexate and its major metabolite, 7-hydroxymethotrexate, using capillary zone electrophoresis and laser-induced fluorescence detection. *J. Chromatography* **426**, 129 (1988)
- J.P. Landers: *Handbook of Capillary Electrophoresis*, 2nd edn. (Springer-Verlag, Heidelberg 1996)
- [10.135] S. Nilsson, J. Johansson, M. Mecklenburg, S. Birnbaum, S. Svanberg, K.-G. Wahlund, K. Mosbach, A. Miyabayashi, P.-O. Larsson: Real-time fluorescence imaging of capillary electrophoresis: Separation of nucleic acids. *J. Cap. Elec.* **22**, 46 (1995)
- [10.136] E.R. Menzel: Detection of latent fingerprints by laser-excited luminescence. *Anal. Chem.* **61**, 557A (1989)
- E.R. Menzel: *Laser Detection of Fingerprints*, 2nd edn. (Marcel Dekker, New York 1999)
- E.R. Menzel: 'Fluorescence in forensic science.' In: *Encyclopedia of Analytical Chemistry* (Wiley, New York 2000)
- [10.137] J.S. McCormack: Remote optical measurements of temperature using fluorescent materials. *Electron. Lett.* **17**, 630 (1981)
- K.T.V. Grattan, Z.Y. Zhang: *Fibre-Optic Fluorescence Thermometry* (Chapman & Hall, London 1995)
- [10.138] J.C. Hamilton, R.J. Anderson: In situ Raman spectroscopy of Fe–18Cr–3Mo(100) surface oxidation. Sandia Combustion Research Program Annual Rept. (Sandia, Livermore, CA 1984)
- [10.139] M. Fleischmann, P.J. Hendra, A.J. McQuillan: Raman spectra of pyridine absorbed at a silver electrode. *Chem. Phys. Lett.* **26**, 163 (1974)
- [10.140] R.K. Chang, T.E. Furtak: *Surface-Enhanced Raman Scattering* (Plenum, New York 1982)
- [10.141] M. Moskovits: Surface-enhanced spectroscopy. *Rev. Mod. Phys.* **57**, 783 (1985)
- [10.142] A. Otto, I. Mrozek, H. Grabhorn, W. Akemann: Surface-enhanced Raman scattering. *J. Phys. Cond. Matter* **4**, 1143 (1992)
- K. Kneipp, H. Kneipp, I. Itzkan, R. Dasari, M.S. Feld: Surface-enhanced Raman scattering: A new tool for biomedical spectroscopy. *Current Science* **77**, 915 (1999)
- W. Suetaka: *Surface Infrared and Raman Spectroscopy* (Plenum, New York 1995)
- [10.143] Y.R. Shen: *Annu. Rev. Mater. Sci.* **16**, 69 (1986)

- [10.144] Y.R. Shen: 'Applications of optical second-harmonic generation in surface science.' In: *Chemistry and Structure at Interfaces*, ed. by R.B. Hall, A.B. Ellis (Verlag-Chemie, Weinheim 1986) p. 151
- [10.145] W. Yen, P.M. Selzer (eds.): *Laser Spectroscopy of Solids*, 2nd edn. Topics Appl. Phys., Vol. 49 (Springer, Berlin, Heidelberg 1989)
W.M. Yen (ed.): *Laser Spectroscopy II*, Topics Appl. Phys., Vol. 65 (Springer, Berlin, Heidelberg 1989)
- [10.146] F.R. Aussemegg, A. Leitner, M.E. Lippitsch (eds.): *Surface Studies with Lasers*, Springer Ser. Chem. Phys., Vol. 33 (Springer, Berlin, Heidelberg 1983)
- [10.147] K. Kleinermanns, J. Wolfrum: Laser Chemistry – What is Its Current Status?, Angew. Chem. Int. Ed. Engl. **26**, 38 (1987)
- [10.148] A.M. Ronn: Laser chemistry. Sci. Am. **240**(5), 102 (1979)
D.L. Andrews: *Lasers in Chemistry*, 3rd edn. (Springer, Berlin, Heidelberg 1997)
P. Brumer, M. Shapiro: Laser control of chemical reactions. Sci. Am. **272**(3), 34 (1995)
S. Svanberg: Chemical sensing with laser spectroscopy, Sensors and Actuators B **33**, 1 (1996)
- [10.149] V.S. Letokhov: *Nonlinear Laser Chemistry*, Springer Ser. Chem. Phys., Vol. 22 (Springer, Berlin, Heidelberg 1983)
- [10.150] E. Grunvald, D.F. Dever, P.M. Keeher: *Megawatt Infrared Laser Chemistry* (Wiley, New York 1978)
- [10.151] A. Zewail (ed.): *Advances in Laser Chemistry*, Springer Ser. Chem. Phys., Vol. 3 (Springer, Berlin, Heidelberg 1978)
- [10.152] V.S. Letokhov: Laser-induced chemistry – basic nonlinear processes and applications. In: [10.2] p. 237
- [10.153] R.L. Woodin, A. Kaldor (eds.): *Applications of Lasers to Industrial Chemistry*. Proc. SPIE-Int. Soc. Opt. Eng. **458** (SPIE, Bellingham, WA 1984)
- [10.154] J.A. Paisner, R.W. Solarz: Resonance photoionization spectroscopy. In: [10.1] p. 175
J.A. Paisner: Atomic vapor laser isotope separation. In: [10.2] p. 253
- [10.155] V.S. Letokhov: Laser separation of isotopes. Annu. Rev. Phys. Chem. **28**, 133 (1977)
V.S. Letokhov: Laser isotope separation. Nature **277**, 605 (1979)
J.L. Lyman: Laser-induced molecular dissociation. Applications in isotope separation and related processes. In: [10.1] p. 417
- [10.156] P.T. Greenland: Laser isotope separation. Contemp. Phys. **31**, 405 (1990)
H.G. Kuhn: *Atomic Spectra* (Longmans, London 1962)
- [10.157] N. Bloembergen, E. Yablonovitch: 'Collisionless multiphoton dissociation of SF₆: A statistical thermodynamic process.' In: *Laser Spectroscopy III*, ed. by J.L. Hall, J.L. Carlsten, Springer Ser. Opt. Sci., Vol. 7 (Springer, Berlin, Heidelberg 1977)
- [10.158] R.V. Ambartsumian, V.S. Letokhov, G.N. Makarov, A.A. Puretsky: Laser separation of nitrogen isotopes. JETP Lett. **17**, 63 (1973); JETP Lett. **15**, 501 (1972)
- [10.159] J.-L. Boulnois: Photophysical processes in recent medical laser developments: A review. Lasers Med. Sci. **1**, 47 (1986)
J.-L. Boulnois: 'Photophysical processes in laser-tissue interactions.' In: *Laser Applications in Cardiovascular Diseases*, ed. by R. Ginsburg (Futura, New York 1987)
- [10.160] D. Sliney, M. Wolbarsht: *Safety with Lasers and Other Optical Sources* (Plenum, New York 1980)

- ANSI: Laser Standards designed Z 136.1 - 1973 (American National Standards Institute, Washington 1983)
- B. Anderberg, M.L. Wolbarsht: *Laser Weapons – Dawn of a New Military Age* (Plenum, New York 1992)
- [10.161] L. Goldman (ed.): *The Biomedical Laser: Technology and Clinical Applications* (Springer, Berlin, Heidelberg 1981)
- [10.162] S. Martellucci, A.N. Chester: *Laser Photobiology and Photomedicine* (Plenum, New York 1985)
- A.N. Chester, S. Martellucci, A.M. Scheggi (eds.): *Laser Systems for Photobiology and Photomedicine* (Plenum, New York 1991)
- [10.163] M.L. Wolbarsht: *Laser Applications in Medicine and Biology* (Plenum, New York 1991)
- M.W. Berns: Laser surgery. *Sci. Am.* **264**(6), 58 (1991)
- A. Katzir: *Lasers and Optical Fibers in Medicine* (Academic Press, San Diego 1993)
- A.J. Welch, M. van Gemert: *Optical-Thermal Response of Laser-Irradiated Tissue* (Plenum, New York 1995)
- J.D. Bronzino (ed.): *The Biomedical Engineering Handbook* (CRC Press, Boca Raton 1995)
- M. Niemz: *Laser-Tissue Interactions* (Springer, Berlin, Heidelberg 1996)
- T. Karu: *The Science of Low Power Laser Therapy* (Gordon & Breach/IPD 1998)
- [10.164] M. v. Allmen, A. Blatter: *Laser-Beam Interactions with Materials*, 2nd edn. (Springer, Berlin, Heidelberg 1995)
- D. Elliott: *Ultraviolet Laser Applications and Technology* (Academic Press, New York 1995)
- J. Mazumder, A. Kar: *Theory and Application of Laser Chemical Vapor Deposition* (Plenum, New York 1995)
- D. Bäuerle: *Laser Processing and Chemistry*, 2nd edn. (Springer, Berlin, Heidelberg 1996)
- W.W. Duley: *UV Lasers: Effects and Applications in Material Science* (Cambridge University Press, Cambridge 1996)
- J.C. Miller, R.F. Haglund: *Laser Ablation and Desorption* (Academic Press, San Diego 1998)
- [10.165] J.A. Parrish, T.F. Deutsch: Laser photomedicine. *IEEE J. Quantum Electron.* **QE-20**, 1386 (1984)
- [10.166] T.J. Dougherty: In: *CRC Critical Reviews in Oncology/Hematology*, ed. by S. Davis (CRC, Boca Raton, FL 1984)
- [10.167] Y. Hayata, T.J. Dougherty (eds.): *Lasers and Hematoporphyrin Derivative in Cancer* (Ikaku-shoin, Tokyo 1983)
- [10.168] R. Pratesi, C.A. Sacchi (eds.): *Lasers in Photomedicine and Photobiology*, Springer Ser. Opt. Sci., Vol. 22 (Springer, Berlin, Heidelberg 1980)
- [10.169] A. Andreoni, R. Cubeddu (eds.): *Porphyrins in Tumor Phototherapy* (Plenum, New York 1984)
- [10.170] Ch.J. Gomer (ed.): Proc. Clayton Foundation Conf. on Photodynamic Therapy (Childrens Hospital, Los Angeles 1987)
- [10.171] S.L. Marcus: 'Photodynamic therapy: Clinical status, potential and needs.' In: *Photodynamic Therapy of Human Cancer*, ed. by C. Gomer (SPIE Press, Bellingham 1990) p. 1
- [10.172] L.I. Grossweiner: *The Science of Phototherapy* (CRC Press, Boca Raton 1994)

- [10.173] T.J. Dougherty, C.J. Gomer, B.W. Henderson, G. Jori, D. Kessel, M. Korbelik, J. Moan, Q. Peng: Photodynamic therapy, *J. Nat. Cancer Inst.* **90**, 889 (1998)
- [10.174] S. Svanberg: Medical diagnostics using laser-induced fluorescence. *Phys. Scr.* **T17**, 469 (1987)
- [10.175] S. Svanberg: Medical applications of laser spectroscopy. *Phys. Scr.* **T26**, 90 (1989)
- [10.176] A.E. Profio, D.R. Doiron, O.J. Balchum, G.C. Huth: Fluorescence bronchoscopy for localization of carcinoma in Situ. *Med. Phys.* **10**, 35 (1983)
- [10.177] H. Kato, D.A. Cortese: Early detection of lung cancer by means of hematoporphyrin derivative fluorescence and laser photoradiation. *Clinics in Chest Medicine* **6**, 237 (1985)
- [10.178] J.H. Kinsey, D.A. Cortese: Endoscopic system for simultaneous visual examination and electronic detection of fluorescence. *Rev. Sci. Instrum.* **51**, 1403 (1980)
- [10.179] P.S. Andersson, S.E. Karlsson, S. Montán, T. Persson, S. Svanberg, S. Tapper: Fluorescence endoscopy instrumentation for improved tissue characterization. *Med. Phys.* **14**, 633 (1987)
- [10.180] L. Baert, R. Berg, B. Van Damme, M.A. d'Hallewin, J. Johansson, K. Svanberg, S. Svanberg: Clinical fluorescence diagnosis of human bladder carcinoma following low-dose photofrin injection. *J. Urology* **41**, 322 (1993)
- S. Andersson-Engels, J. Johansson, U. Stenram, K. Svanberg, S. Svanberg: Malignant tumor and atherosclerotic plaque diagnosis using laser-induced fluorescence. *IEEE J. Quantum Electron.* **QE-26**, 2207 (1990)
- C. Eker, S. Montán, E. Jamarillo, K. Koizumi, C. Rubio, S. Andersson-Engels, K. Svanberg, S. Svanberg, P. Slezak: Clinical spectral characterization of colonic mucosal lesions using autofluorescence and δ -aminolevulinic acid sensitization. *Gut* **44**, 511 (1999)
- A.E. Profio: 'Endoscopic fluorescence detection of early lung cancer.' In: *Optical Methods for Tumor Treatment and Early Diagnosis: Mechanisms and Techniques*, ed. by T.J. Dougherty, Proc. SPIE-Int. Soc. Opt. Eng. **1426**, 44 (1991)
- S. Andersson-Engels, J. Johansson, S. Svanberg: Medical diagnostic system based on simultaneous multi-spectral fluorescence imaging. *Appl. Opt.* **33**, 8022 (1994)
- G.A. Wagnières, W.M. Star, B.C. Wilson: In vivo fluorescence spectroscopy and imaging for oncological applications. *Photochem. Photobiol.* **68**, 603 (1998)
- S. Andersson-Engels, G. Canti, R. Cubeddu, C. Eker, C. af Klinteberg, A. Pifferi, K. Svanberg, S. Svanberg, P. Taroni, G. Valentini, I. Wang: Spectroscopic characterization of basal cell carcinomas of the skin with multi-colour and lifetime fluorescence imaging. To be published
- [10.181] T.J. Dougherty, R.E. Thoma, D.G. Boyle, K.R. Weishaupt: Interstitial photoradiation therapy for primary solid tumors in pet cats and dogs. *Cancer Research* **41**, 401 (1981)
- C.P. Lowell, D.V. Ash, I. Driver, S.B. Brown: Interstitial photodynamic therapy. Clinical experience with diffusing fibres in the treatment of cutaneous and subcutaneous tumours. *Br. J. Cancer* **67**, 1398 (1993)
- S.F. Purkiss, R. Dean, J.T. Allardice, M. Grahn, N.S. Williams: An interstitial light delivery system for photodynamic therapy within the liver. *Lasers Med. Sci.* **8**, 253 (1993)
- M. Stenberg, M. Soto Thompson, Th. Johansson, S. Pålsson, C. af Klinteberg, S. Andersson-Engels, S. Svanberg, K. Svanberg: Interstitial photody-

- namic therapy - diagnostic measurements and treatment of rat malignant experimental tumours. SPIE **4161** (2000)
- [10.182] K. Svanberg, T. Andersson, D. Killander, I. Wang, U. Stenram, S. Andersson-Engels, R. Berg, J. Johansson, S. Svanberg: Photodynamic therapy of non-melanoma malignant tumours of the skin utilizing topical δ -amino levulinic acid sensitization and laser irradiation. British J. of Dermatology **130**, 743 (1994)
- [10.183] J.C. Kennedy, R.H. Potter, D.C. Pross: Photodynamic therapy with endogenous protoporphyrin IX: Basic principles and present clinical experience. J. Photochem Photobiol. **6**, 143 (1990)
- J.C. Kennedy, R. Pottier: Endogenous protoporphyrin IX, a clinically useful photosensitizer for photodynamic therapy. J. Photochem. Photobiol. B **14**, 275 (1992)
- I. Wang, N. Bendsoe, C. af Klinteberg, A.M.K. Enejder, S. Andersson-Engels, S. Svanberg, K. Svanberg: Photodynamic therapy versus cryosurgery of basal cell carcinomas; Results of a Phase III clinical trial. Brit. J. Derm., in press
- I. Wang, B. Bauer, S. Andersson-Engels, S. Svanberg, K. Svanberg: Photodynamic therapy utilizing topical δ -amino levulinic acid sensitization and laser irradiation. Acta Ophtal. Scand. **77**, 182 (1999)
- Q. Peng, T. Warloe, K. Berg, J. Moan, M. Kongshaug, K.-E. Giercksky, J.M. Nesland: 5-aminolevulinic acid-based photodynamic therapy: clinical research and future challenges. Cancer **79**, 2282 (1997)
- [10.184] S. Andersson-Engels, Å. Elner, J. Johansson, S.-E. Karlsson, L.G. Salford, L.-G. Strömblad, K. Svanberg and S. Svanberg: Clinical recordings of laser-induced fluorescence spectra for evaluation of tumour demarcation feasibility in selected clinical specialities. Lasers Med. Sci. **6**, 415 (1991)
- C. af Klinteberg, A.M.K. Nilsson, I. Wang, S. Andersson-Engels, S. Svanberg, K. Svanberg: Laser-induced fluorescence diagnostics of basal cell carcinomas of the skin following topical ALA application. Proc. SPIE-Int. Soc. Opt. Eng. **2926** (1996)
- [10.185] S. Montán: On the use of laser-induced fluorescence in medical and industrial applications, PhD dissertation, Lund Reports on Atomic Physics LRAP-75 (Lund Institute of Technology, 1987)
- [10.186] S. Andersson-Engels, A. Brun, E. Kjellén, L.G. Salford, L.-G. Strömblad, K. Svanberg, S. Svanberg: Identification of brain tumours in rats using laser-induced fluorescence and haematoporphyrin derivative. Laser Med. Sci. **4**, 241 (1989)
- [10.187] P.S. Andersson, S. Montán, S. Svanberg: Multi-spectral system for medical fluorescence imaging. IEEE J. Quantum Electron. **QE-23**, 1798 (1987)
- [10.188] S. Svanberg: New developments in laser medicine. Phys. Scr. **T72**, 69 (1997)
- [10.189] C. Kittrell, R.L. Willett, C. de los Santon-Pacheo, N.B. Ratliff, J.R. Kramer, E.G. Malk, M.S. Feld: Diagnosis of fibrous arterial atherosclerosis using fluorescence. Appl. Opt. **24**, 2280 (1985)
- R.M. Cothren, G.B. Hayes, J.R. Kramer, B. Sachs, C. Kittrell, M.S. Feld: Lasers Life Sci. **1**, 1 (1986)
- [10.190] P.S. Andersson, A. Gustafson, U. Stenram, K. Svanberg, S. Svanberg: Monitoring of human atherosclerotic plaque using laser-induced fluorescence. Lasers Med. Sci. **2**, 261 (1987)
- S. Andersson-Engels, A. Gustafson, J. Johansson, U. Stenram, K. Svanberg, S. Svanberg: Laser-induced fluorescence used in localizing atherosclerotic lesions. Laser Med. Sci. **4**, 171 (1989)

- S. Andersson-Engels, J. Johansson, S. Svanberg: The use of time-resolved fluorescence for diagnosis of atherosclerotic plaque and malignant tumours. *Spectrochim. Acta A* **46**, 1203 (1990)
- S. Andersson-Engels, A. Gustafson, J. Johansson, U. Stenram, K. Svanberg, S. Svanberg: An investigation of possible fluorophores in human atherosclerotic plaque. *Lasers Life Sci.* **5**, 1 (1992)
- [10.191] J.M. Isner, R.H. Clarke: The current status of lasers in the treatment of cardiovascular disease. *IEEE J. Quantum Electron.* **QE-20**, 1406 (1984)
- J.M. Isner, P.G. Steg, R.H. Clarke: Current status of cardiovascular laser therapy. *IEEE J. Quantum Electron.* **QE-23**, 1756 (1987)
- M.R. Prince, T.F. Deutsch, M.M. Mathews-Roth, R. Margolis, J.A. Parrish, A.R. Oseroff: Preferential light absorption in atheromas in vitro: Implications for laser angioplasty. *J. Clin. Invest.* **78**, 295 (1986)
- [10.192] S. Udenfriend: *Fluorescence Assay in Biology and Medicine*, Vol. I (1962), Vol. II (1969) (Academic Press, New York)
- K.P. Mahler, J.F. Malone: Digital fluorescence: A new development in medical imaging. *Contemp. Phys.* **27**, 533 (1986)
- G.M. Barenboim, A.N. Domanskii, K.K. Turovov: *Luminescence of Biopolymers and Cells* (Plenum, New York 1969)
- D.M. Kirschenbaum (ed.): *Atlas of Protein Spectra in the Ultraviolet and Visible Regions*, Vol. 2 (IFI/Plenum, New York 1974)
- [10.193] R.R. Alfano, B.T. Darayash, J. Cordero, P. Tomashevsky, F.W. Longo, M.A. Alfano: Laser-induced fluorescence spectroscopy from native cancerous and normal tissue. *IEEE J. Quantum Electron.* **QE-20**, 1507 (1984)
- R.R. Alfano, G.C. Tang, A. Pradhan, W. Lam, D.S.J. Choy, E. Opher: Fluorescence spectra from cancerous and normal human breast and lung tissues. *IEEE J. Quantum Electron.* **QE-23**, 1806 (1987)
- R. Richards-Kortum, R.P. Rava, R.E. Petras, M. Fitzmaurice, M.V. Sivak, M.S. Feld: Spectroscopic diagnosis of colonic dysplasia. *Photochem. Photobiol.* **53**, 777 (1991)
- [10.194] Y.M. Ye, Y.L. Yang, Y.F. Li, F.M. Li: Characteristic autofluorescence for cancer diagnosis and the exploration of its origin. *Proc. CLEO '85* (Baltimore, MD)
- [10.195] S. Montán: Diploma paper, Lund Reports on Atomic Physics LRAP-19 (Lund University, Lund 1982)
- P.S. Andersson, E. Kjellén, S. Montán, K. Svanberg, S. Svanberg: Auto-fluorescence of various rodent tissues and human skin tumour samples. *Lasers Med. Sci.* **2**, 41 (1987)
- J. Hung, S. Lam, J.C. LeRiche, B. Palcic: Autofluorescence of normal and malignant bronchial tissue, *Lasers Surg. Med.* **11**, 99 (1991)
- B. Palcic, S. Lam, J. Hung, C. Mac Aulay: Detection and localization of early lung cancer by imaging techniques. *Chest* **99**, 742 (1991)
- [10.196] R.R. Alfano, W. Lam, H.J. Zarrabi, M.A. Alfano, J. Cordero, D.B. Tata, C.E. Swenberg: Human teeth with and without caries studied by laser scattering, fluorescence and absorption spectroscopy. *IEEE J. Quantum Electron.* **QE-20**, 1512 (1984)
- [10.197] F. Sundström, K. Fredriksson, S. Montán, U. Hafström-Björkman, J. Ström: Laser-induced fluorescence from sound and carious tooth substance: Spectroscopic studies. *Swed. Dent. J.* **9**, 71 (1985)
- [10.198] J.J. Baraga, M.S. Feld, R.P. Rava: Rapid near-infrared Raman spectroscopy of human tissue with a spectrograph and CCD detector. *Appl. Spectrosc.* **46**, 187 (1992)

- J.J. Baraga, M.S. Feld, R.P. Rava: In situ histochemistry of human artery using near-infrared Fourier transform Raman spectroscopy (Proc. Natl. Acad. Sci. USA 1992)
- T.J. Römer, J.F. Brennan III, M. Fitzmaurice, M.F. Feinstein, G. Deinum, J.L. Myles, J.R. Kramer, R.S. Lees, M.S. Feld: Histopathology of human coronary atherosclerosis by quantifying its composition with Raman spectroscopy. *Circulation* **97**, 878 (1998)
- [10.199] A.M.K. Nilsson, D. Heinrich, J. Olajos, S. Andersson-Engels: Near-infrared diffuse reflection and laser-induced fluorescence spectroscopy for myocardial tissue characterisation. *Spectrochim. Acta A* **53**, 1901 (1997)
- [10.200] J.J. Baraga, M.S. Feld, R.P. Rava: Infrared attenuated total reflectance of human artery: a new modality for diagnosing atherosclerosis. *Lasers Life Sci.* **5**, 13 (1992)
- I.J. Bigio, T.R. Loree, T. Shimada, K. Story-Held, R.D. Glickman, R. Conn: Optical diagnostics based on elastic scattering: recent clinical demonstrations with the Los Alamos Biopsy System. *Proc. SPIE-Int. Soc. Opt. Eng.* **2081** (1994)
- V. Backman, R. Gurjar, K. Badizadegan, I. Itzkan, R. Dasari, L.T. Perelman, M.S. Feld: Polarized light scattering spectroscopy for quantitative measurements of epithelial cellular structure *in situ*. *IEEE JSTQE Las. Med. Biol.* **5** (1999)
- L.T. Perelman, V. Backman, M. Wallace, G. Zonios, R. Manoharan, A. Nusrat, S. Shields, M. Seiler, C. Lima, T. Hamano, I. Itzkan, J. Van Dam, J.M. Crawford, M.S. Feld: Observation of periodic structure in reflectance from biological tissue: A new technique for measuring nuclear size distributions. *Phys. Rev. Lett.* **80**, 627 (1998)
- [10.201] S.R. Meech, C.D. Stubbs, D. Phillips: The application of fluorescence decay measurements in studies of biological systems. *IEEE J. Quantum Electron. QE-20*, 1343 (1984)
- [10.202] M. Yamashita, M. Nomura, S. Kobayashi, T. Sato, K. Aizawa: Picosecond time-resolved fluorescence spectroscopy of hematoporphyrin derivative. *IEEE J. Quantum Electron. QE-20*, 1363 (1984)
- V.S. Letokhov (ed.): *Laser Picosecond Spectroscopy and Photochemistry of Biomolecules* (Hilger, Bristol 1987)
- [10.203] L. Stryer: The molecules of visual excitation. *Sci. Am.* **257**(1), 32 (1987)
- [10.204] D.B. Tata, M. Foresti, J. Cardero, P. Thomachefsky, M.A. Alfano, R.R. Alfano: Fluorescence polarization spectroscopy and time-resolved fluorescence kinetics of native cancerous and normal rat kidney tissues. *Biophys. J.* **50**, 463 (1986)
- [10.205] S. Andersson-Engels, J. Johansson, S. Svanberg: The use of time-resolved fluorescence for diagnosis of atherosclerotic plaque and malignant tumours. *Spectrochim. Acta A* **46**, 1203 (1990)
- [10.206] S. Andersson-Engels, J. Johansson, K. Svanberg, S. Svanberg: Fluorescence diagnostics and photochemical treatment of diseased tissue using lasers. Pt. I, *Anal. Chem.* **61**, 1367A (1989); Pt. II, *ibid.* **62**, 19A (1990)
- S. Andersson-Engels, J. Johansson, U. Stenram, K. Svanberg, S. Svanberg: Malignant tumor and atherosclerotic plaque diagnostics using laser-induced fluorescence. *IEEE J. Quantum Electron. QE-26*, 2207 (1990)
- [10.207] S. Andersson-Engels, C. af Klinteberg, K. Svanberg, S. Svanberg: In vivo fluorescence imaging for tissue diagnosis. *Phys. Med. Biol.* **42**, 815 (1997)
- K. Svanberg, I. Wang, S. Colleen, I. Idvall, C. Ingvar, R. Rydell, D. Jocham, H. Diddens, S. Bown, G. Gregory, S. Montán, S. Andersson-Engels,

- S. Svanberg: Clinical multi-colour fluorescence imaging of malignant tumours – Initial experience. *Acta Radiol.* **38**, 2 (1998)
- [10.208] R. Cubeddu, P. Taroni, G. Valentini, G. Canti: Use of time-gated fluorescence imaging for diagnosis in biomedicine. *J. Photochem. Photobiol. B* **12**, 109 (1992)
- R. Cubeddu, A. Pifferi, P. Taroni, G. Valentini, G. Canti: Tumor detection in mice by measurement of fluorescence decay time matrices. *Opt. Lett.* **20**, 2553 (1995)
- S. Andersson-Engels, G. Canti, R. Cubeddu, Ch. Eker, C. af Klinteberg, A. Pifferi, K. Svanberg, S. Svanberg, P. Taroni, G. Valentini, I. Wang: Preliminary evaluation of two fluorescence imaging methods for the detection and the delineation of basal cell carcinomas of the skin. *Lasers Surg. Med.* **26**, 76 (2000)
- [10.209] C. af Klinteberg, I. Wang, I. Karu, Th. Johansson, N. Bendsoe, K. Svanberg, S. Andersson-Engels, S. Svanberg, G. Canti, R. Cubeddu, A. Pifferi, P. Taroni, G. Valentini: Diode laser-mediated ALA-PDT guided by laser-induced fluorescence imaging. Unpublished.
- [10.210] J.R. Lakowicz: *Principles of Fluorescence Microscopy* (Plenum, New York 1983)
- B. Herman, J.J. Lemasters (eds.): *Optical Microscopy – Emerging Methods and Applications* (Academic Press, San Diego 1993)
- R.H. Webb: Confocal optical microscopy. *Rep. Prog. Phys.* **59**, 427 (1996)
- [10.211] Z. Malik, D. Cabib, R.A. Buckwald, Y. Garini, D. Soenkeson: A novel spectral imaging system combining spectroscopy with imaging – Applications for biology. *Proc. SPIE-Int. Soc. Opt. Int.* **2329**, 180 (1994)
- Z. Malik, G. Kostenich, C. Rothmann, I. Barshack, A. Orenstein: Imaging of human skin lesions using multipixel Fourier transform spectroscopy. *Lasers Med. Sci.* **13**, 12 (1998)
- [10.212] A. Ashkin, J.M. Dziedzic, J.E. Bjorkholm, S. Chu: Observation of a single-beam gradient force optical trap for dielectric particles. *Opt. Lett.* **11**, 288 (1986)
- K. Svoboda, S. Block: Biological applications of optical forces. *Ann. Rev. Biophys. Biomol. Struct.* **23**, 247 (1994)
- K. Visscher, S.P. Gross, S.M. Block: Construction of multiple-beam optical traps with nanometer resolution position sensing. *IEEE J. Sel. Top. Quantum Electron.* **2**, 1066 (1996)
- A. Ashkin: Optical trapping and manipulation of neutral particles using lasers. *Proc. Natl. Acad. Sci. USA* **94**, 4853 (1997)
- S. Chu et al.: *Science* **280**, 1253 (1998), *Science* **282**, 95 (1998), *Nature* **394**, 52 (1998)
- M.W. Berns: Laser scissors and tweezers. *Sci. Am.* **278**(4), 52 (1998)
- M.E.J. Friese, T.A. Nieminen, N.R. Heckenberg, H. Rubinsztein-Dunlop: Alignment and spinning of laser-trapped microscopic particles. *Nature* **394**, 348 (1998)
- [10.213] A. Ishimaru: *Wave Propagation and Scattering in Random Media* (Academic Press, New York 1978)
- B. Chance, J.S. Leigh, H. Miyake, D.S. Smith, S. Nioka, R. Greenfeld, M. Finander, K. Kaufmann, W. Levy, M. Young, P. Cohen, H. Yoshioka, R. Boretsky: Comparison of time-resolved and -unresolved measurements of deoxyhemoglobin in the brain. *Proc. Natl. Acad. Sci. USA* **85**, 4971 (1988)
- B. Chance (ed.): *Photon Migration in Tissue* (Plenum, New York 1989)
- M.S. Patterson, B.C. Wilson, D.R. Wyman: The propagation of optical

- radiation in tissue. Models for radiation transport and their application. *Lasers Med. Sci.* **6**, 155 (1991)
- S.L. Jacques: Time-resolved propagation of ultrashort pulses within turbid tissues. *Appl. Opt.* **28**, 2223 (1989)
- B. Chance, G. Müller (eds.): *Optical Tomography*, (SPIE, Bellingham 1993)
- G. Müller, B. Chance, R. Alfano, S. Arridge, J. Beuthan, E. Gratton, M. Kaschke, B. Masters, S. Svanberg, P. van der Zee (eds.): *Medical Optical Tomography, Functional Imaging and Monitoring*, SPIE Institute Series, Vol. **11** (SPIE, Bellingham 1993)
- B.J. Tromberg, L.O. Svaasand, T.-T. Tsay, R.C. Haskell: Properties of optical density waves in multiple-scattering media. *Appl. Opt.* **32**, 607 (1993)
- S. Andersson-Engels, R. Berg, S. Svanberg: Effects of optical constants on time-gated transillumination of tissue and tissue-like media. *J. Photochem. Photobiol.* **16**, 155 (1992)
- R. Berg, S. Andersson-Engels, C. af Klinteberg, S. Svanberg: In: *OSA Proc. in Optical Imaging and Photon Migration*, Vol. 21 (OSA, Washington DC, 1993) p. 126
- A.H. Gandjbakhche, G.H. Weiss: 'Random walk and diffusion-like models of photon migration in turbid media.' In: *Progress in Optics XXXIV*, ed. by E. Wolf (Elsevier, Amsterdam 1995) p. 333
- C. Lindquist, A. Pifferi, R. Berg, S. Andersson-Engels, S. Svanberg: Reconstruction of diffuse photon-density wave interference in turbid media from time-resolved transmittance measurements. *Appl. Phys. Lett.* **69**, 1674 (1996)
- J.C. Hebden, S.R. Arridge, D.T. Delpy: Optical imaging in medicine: I. Experimental techniques. *Phys. Med. Biol.* **42**, 825 (1997)
- [10.214] R. Berg, S. Andersson-Engels, S. Svanberg: 'Time-resolved transillumination imaging.' In: G. Müller, B. Chance, R. Alfano, S. Arridge, J. Beuthan, E. Gratton, M. Kaschke, B. Masters, S. Svanberg, P. van der Zee (eds.): *Medical Optical Tomography, Functional Imaging and Monitoring*, SPIE Institute Series, Vol. **11** (SPIE, Bellingham 1993) p. 397
- [10.215] J.P. Payne, J.W. Severinghaus (eds.): *Pulse Oximetry* (Springer, Heidelberg 1986)
- M. Cope, D.T. Delpy: System for long-term measurement of cerebral blood and tissue oxygenation on newborn infants by near-infrared transillumination. *Med. Biol. Eng. Comp.* **26**, 289 (1988)
- [10.216] J.W. Hall, A. Pollard: Near-infrared spectroscopic determination of serum total proteins, albumin, globulins and urea. *Clin. Biochem.* **26**, 483 (1993)
- Y. Mendelson, A.C. Clermont, R.A. Peura, B.-C. Lin: Blood glucose measurement by multiple attenuated total reflection and infrared absorption spectroscopy. *IEEE Trans. Biomed. Eng.* **37**, 458 (1990)
- S. Andersson-Engels, R. Berg, A. Persson, S. Svanberg: Multispectral tissue characterization using time-resolved detection of diffusely scattered white light. *Opt. Lett.* **18**, 1697 (1993)
- [10.217] K.M. Yoo, B.B. Das, R.R. Alfano: Imaging of a translucent object hidden in highly scattering medium from the early portion of the diffuse component of a transmitted ultrafast laser pulse. *Opt. Lett.* **17**, 958 (1992)
- J.C. Hebden, R.A. Kruger, K.S. Wong: Time-resolved imaging through a highly scattering medium. *Appl. Opt.* **30**, 788 (1991)
- B. Chance, K. Kang, L. He, J. Weng, E. Sevick: Highly sensitive object location in tissue models with linear in-phase and anti-phase multi-element

- optical arrays in one and two dimensions. *Proc. Natl. Acad. Sci. USA* **90**, 3423 (1995)
- S.G. Demos, R.R. Alfano: Temporal gating in highly scattering media by the degree of optical polarization. *Opt. Lett.* **21**, 161 (1996)
- K. Michielsen, H. De Raedt, J. Przeslawski, N. Garcia: Computer simulation of time-resolved optical imaging of objects hidden in turbid media. *Phys. Rep.* **304**, 89 (1998)
- [10.218] S. Andersson-Engels, R. Berg, S. Svanberg, O. Jarlman: Time-resolved transillumination for medical diagnostics. *Opt. Lett.* **15**, 1179 (1990)
- [10.219] R. Berg, O. Jarlman, S. Svanberg: Medical transillumination imaging using short pulse diode lasers. *Appl. Opt.* **32**, 574 (1993)
- [10.220] P.Å. Öberg: Laser-Doppler flowmetry. *Critical Reviews in Biomedical Engineering* **18**, 125 (1990)
- A.P. Shepherd, P.Å. Öberg (eds.): *Laser Doppler Blood Flowmetry* (Kluwer Academic Publishers, Boston 1990)
- K. Wårdell, A. Jacobsson, G.E. Nilsson: Laser Doppler perfusion imaging by dynamic light scattering. *IEEE Trans. Biomed. Eng.* **40**, 309 (1993)
- M.L. Arildsson, K. Wårdell, G.E. Nilsson: Higher order moment processing of laser Doppler perfusion signals. *J. Biomed. Opt.* **2**, 358 (1997)
- [10.221] R.R. Alfano, P.P. Ho, K.M. Yoo: Photons for prompt tumour detection. *Phys. World* **5**, 37 (1992)
- [10.222] L. Wang, Y. Liu, P.P. Ho, R.R. Alfano: Photons for prompt tumour detection. *Proc. SPIE-Int. Soc. Opt. Eng.* **1431**, 97 (1991)
- [10.223] M.D. Duncan, R. Mahon, L.L. Tankersley, R. Reintjes: Time-gated imaging through scattering media using stimulated Raman amplification. *Opt. Lett.* **16**, 1868 (1991)
- [10.224] K.M. Yoo, Q. Xing, R.R. Alfano: Imaging objects hidden in highly scattering media using femtosecond second-harmonic-generation cross-correlation time gating. *Opt. Lett.* **16**, 1019 (1991)
- [10.225] J.R. Lakowicz, G. Laczo, I. Gryczynski, H. Szmacinski, W. Wiczk, M.L. Johnson: Frequency-domain fluorescence spectroscopy: Principles, biochemical applications and future developments. *Ber. Bunsenges. Phys. Chem.* **93**, 316 (1989)
- J. Fishkin, E. Gratton, M.J. van de Ven, W. W Mantulin: Diffusion of intensity-modulated near-infrared light in turbid media. *Proc. SPIE-Int. Soc. Opt. Eng.* **1431**, 122 (1991)
- M. Kaschke, H. Jess, G. Gaida, J.-M. Kaltenbach, W. Wrobel: 'Transillumination imaging of tissue by phase-modulation techniques.' In: *Advances in Optical Imaging and Photon Migration*, ed. by R.R. Alfano. *Proc. OSA* **21**, 88 (1994)
- [10.226] M. Toida, T. Ichimura, H. Inaba: The first demonstration of laser computed tomography achieved by coherent detection imaging method for biomedical applications. *IEICE Trans.* **E74**, 1692 (1991)
- [10.227] N. Abramson: Light-in-flight recording: High-speed holographic motion pictures of ultrafast phenomena. *Appl. Opt.* **22**, 215 (1983)
- [10.228] K.G. Spears, J. Serafin, N.H. Abramson, X. Zhu, H. Bjelkhagen: Chrono-coherent imaging for medicine. *IEEE Trans. Biomed. Eng.* **36**, 1210 (1989)
- H. Chen, Y. Chen, D. Dilworth, E. Leith, J. Lopez, J. Valdmanis: Two-dimensional imaging through diffusing media using 150 fs gated electronic holography techniques. *Opt. Lett.* **16**, 487 (1991)
- [10.229] J.H. Hoogenraad, M.B. van der Mark, S.B. Colak, G.W. t'Hooft, E.S. van der Linden: 'First results from the Phillips optical mammoscope.' In: *Photo-*

- ton Propagation in Tissue*, ed. by D.A. Benaron, B. Chance, M. Ferrari. Proc. SPIE-Int. Soc. Opt. Eng. **3194**, 184 (1998)
- B.W. Pogue, M. Testorf, U.L. Osterberg, K.D. Paulsen: Instrumentation and design of a frequency-domain diffuse optical tomography imager for breast cancer detection. Opt. Express **1**, 391 (1997). <http://pubs.osa.org/oarchive/source/2827.htm>
- [10.230] J.P. van Houten, D.A. Benaron, S. Spilman, D.K. Stevenson: Imaging brain injury using time-resolved near infrared light scanning. Pediatr. Res. **39**, 470 (1996)
- [10.231] D. Huang, E.A. Swanson, C.P. Lin, J.S. Schuman, W.G. Stinton, W. Chang, M.R. Hee, T. Flotte, K. Gregory, C.A. Puliafito, J.G. Fujimoto: Optical coherence tomography. Science **254**, 1178 (1991)
- E.A. Swanson, D. Huang, M.R. Hee, J.G. Fujimoto, C.P. Lin, C.A. Puliafito: High-speed optical coherence domain reflectometry. Opt. Lett. **17**, 151 (1992)
- M.R. Hee, J.A. Izatt, J.M. Jacobson, J.G. Fujimoto: Femtosecond transillumination optical coherence tomography. Opt. Lett. **18**, 950 (1993)
- M.R. Hee, J.A. Izatt, E.A. Swanson, D. Huang, C.P. Lin, J.S. Schuman, C.A. Puliafito, J.G. Fujimoto: Optical coherence tomography of the human retina. Arch. Ophthalmol. **113**, 325 (1995)
- G.J. Tearney, M.E. Brezinski, B.M. Bouma, S.A. Boppart, C. Pitris, J.F. Southern, J.G. Fujimoto: In vivo endoscopic optical biopsy with optical coherence tomography. Science **276**, 2037 (1997)
- J.A. Izatt, M.D. Kulkarni, K. Kobayashi, M.V. Sivak, J.K. Barton, A.J. Welsch: Optical coherence tomography for biodiagnosis. Opt. Photonics News **8**, 41 (1997)
- A.M. Kowalievicz, T. Ko, I. Hartl, J.G. Fujimoto, M. Pollnau, R.P. Salathé: Ultrahigh resolution optical coherence tomography using a superluminescent light source. Opt. Express **10**, 349 (2002)
- W. Drexler et al.: Enhanced visualization of macular pathology with the use of ultra-high resolution optical coherence tomography. Arch. Ophtalmol. **121**, 695 (2003)
- [10.232] E.A. Swanson, J.A. Izatt, H.M. Hee, D. Huang, C.P. Lin, J.S. Schuman, C.A. Puliafito, J.G. Fujimoto: In vivo retinal imaging by optical coherence tomography. Opt. Lett. **18**, 1864 (1993)
- [10.233] J. Johansson, R. Berg, A. Pifferi, S. Svanberg, L.O. Björn: Time-resolved studies of light propagation in *Crassula* and *Phaseolus* leaves. Photochem. Photobiol. **69**, 242 (1999)
- [10.234] J. Carlsson, P. Hellentin, L. Malmqvist, A. Persson, W. Persson, C.-G. Wahlström: Time-resolved studies of light propagation in paper. Appl. Opt. **34**, 1528 (1995)
- [10.235] J. Johansson, S. Folestad, M. Josefson, A. Sparén, C. Abrahamsson, S. Andersson-Engels, S. Svanberg: Time-resolved NIR/VIS spectroscopy for analysis of solids: Pharmaceutical tablets. Appl. Spectr. **56**, 725 (2002)
- [10.236] M. Sjöholm, G. Somesfalean, J. Alnis, S. Andersson-Engels, S. Svanberg: Analysis of gas dispersed in scattering media. Opt. Lett. **26**, 16 (2001)
- [10.237] G. Somesfalean, M. Sjöholm, J. Alnis, C. af Klinteberg, S. Andersson-Engels, S. Svanberg: Concentration measurement of gas imbedded in scattering media by employing absorption and time-resolved laser spectroscopy. Appl. Opt. **41**, 3538 (2003)
- [10.238] J. Alnis, B. Anderson, M. Sjöholm, G. Somesfalean, S. Svanberg: Laser spectroscopy on free molecular oxygen dispersed in wood materials. Appl. Phys. B (2003), in press

Index

- Ablation, 451
- ABMR, 189
- Above threshold ionization, 340, 341
- Absolute binding energies, 79
- Absorbance, 149
- Absorption, 44, 51, 138, 151, 157
 - intracavity, 296, 359
 - long-path, 407
- Absorption coefficient, 164, 454
- Absorption cross-section, 408
- Absorption edge, 80
- Abundances, 176, 319
- AC Stark effect, 341
- Accessory pigments, 429
- Accidental coincidences, 98, 181
- Acid rain, 145, 391
- Acousto-optic modulator, 317, 404
- Acousto-optical spectrometers, 223
- Adaptive optics, 180, 415
- ADC, 77, 315
- Advantage
 - Felgett, 127
 - Jaquinot, 128
- Air, 144, 406
- Air pollution, 79, 145
 - particulate, 78, 407
- Airy distribution, 123, 234
- ALA, 446
- Alexander's dark band, 69
- Algae, 427, 429
- Alignment, 105
- Alkali atoms, 7, 306
- Alkaline-earth atoms, 11, 297, 300
- Alveoles, 79
- Ammonia maser, 228
- Amplified spontaneous emission, 241
- Analogue-to-digital converter, 77, 315
- Anapole moment, 366
- Angiography, 349
- Angioplasty, 441
- Angular distributions, 53, 55, 198, 201
- Angular frequency, 8
- Anisotropy, 198, 364, 375
- Anomalous dispersion, 325
- Antenna, 219
- Antenna pigments, 331
- Anti-crossing, 206
- Anti-glare, 140
- Anti-hydrogen, 366
- Anti-reflection layers, 135
- Anti-Stokes, 62, 273
- Anti-Stokes component, 63, 274
- Aperture synthesis, 223
- Apodization, 127
- Archaeology, 78
- Astronomical observations, 147, 176
- Astrophysical spectroscopy, 176, 222, 319
- Astrophysics, 319
- Atherosclerotic plaques, 451
- ATI, 340, 341
- Atmosphere, 144, 406
- Atmospheric absorption, 144, 146, 164, 200, 218
- Atmospheric chemistry, 145
- Atom optics, 384
- Atomic absorption method, 152
- Atomic beam, 189
 - collimated, 352
 - lamp, 102
- Atomic clocks, 199, 223, 229, 360, 379, 414
- Attosecond pulses, 347
- Auger effect, 95
- Auger electron spectroscopy, 95
- Autocorrelation, 223
- Autocorrelation technique, 404
- Autocorrelator, 333
- Autofluorescence, 447
- Avalanche diodes, 130
- B-integral, 284
- Back-projection, 214

- Ballast resistor, 302
- Ballistic photons, 454
- Band head, 57
- Bands, 60
- Bathymeters, 428
- Bathymetry, 148
- BBO, 263
- Beam-foil light source, 102
- Beam-foil method, 102, 320
- Beam-laser technique, 320
- Beam overlap modulation, 367
- Beer–Lambert law, 149, 164, 409, 422
- Binding energy, 86
- Birefringent, 141
- Birefringent Lyot filter, 251
- Black-body emitter, 106
- Black-body radiation, 49, 223
- Black holes, 226
- Blaze angle, 118
- Bloch equations, 210
- Blood perfusion, 454, 456
- Blood vessels, 451, 460
- Blumlein circuit, 241
- Bohr atomic model, 73
- Bohr magneton, 8
- Bolometer, 129
- Boltzmann constant, 46
- Boltzmann distribution, 59, 209, 218
- Boltzmann law, 46, 151
- Born–Oppenheimer approximation, 32
- Bose condensate, 375
- Bose–Einstein condensation, 384
- Boser, 385
- Bowen mechanism, 181
- Boxcar integrator, 294, 315, 400
- BOXCARS, 274, 400
- Bragg cell, 278
- Bragg diffraction, 74, 312, 384
- Bragg geometry, 74
- Bragg relation, 74, 87
- Bragg scattering, 271
- Breit formula, 204, 331
- Breit–Rabi formula, 20, 27
- Bremssstrahlung, 71
- Brewster angle, 69, 141, 233, 251
- Broadening
 - Doppler, 98
 - Holtsmark, 100
 - homogeneous, 98
 - inhomogeneous, 98
 - Lorentz, 100
 - pressure, 100, 165, 218
 - Stark, 100
- transit time, 352, 374
- Buckminsterfullerene, 39
- Buffer gas, 199
- Burners, 155
- CaF₂, 143
- Calcium, 15
- Capillary waves, 219
- Caries, 451
- Carrier, 411
- CARS, 273, 398
- Cascade impactors, 79
- CAT, 214
- Cavity, 50, 232
- Cavity-dumping, 278
- Cavity round-trip time, 277
- CCD, 133
- Central field, 5
- Central-field approximation, 11
- Ceramic materials, 436
- Channeltron, 291
- Charge-exchange process, 359
- Chemical activation, 435
- Chemical analysis, 148
 - ESCA, 90, 94
 - laser methods, 296, 301, 304, 334, 336, 392, 406, 425, 430, 435
 - NMR, 211
 - optical methods, 148
 - X-ray methods, 77
- Chemical shift, 81, 90
- Chemical vapour deposition, 403
- Chernobyl reactor accident, 174
- Chiral molecules, 338
- Chirped-pulse amplification, 282
- Chlorofluoro-carbons, 145
- Chlorophyll, 429
- Chlorophyll-*a*, 427
- Chromatography, 430
- Chromophores, 449
- Clear sky, 113
- Clear-air turbulence, 424
- Clusters, 39
- Co:MgF₂, 257
- Coherence, 230
 - spatial, 230
 - temporal, 230
- Coherence length, 230
- Coherent, 228
- Coherent anti-Stokes Raman scattering, 273, 398
- Coherent chemistry, 338
- Coherent control, 338, 435
- Coherent detection, 408, 425

- Coherent excitation, 204
 Coherent superposition, 105
 Coherent technique, 458
 Cold atoms, 379
 Colliding pulse, 279
 Collimation ratio, 352
 Collision
 – velocity-changing, 368
 Collisional effects, 353
 Collisions, 52, 70, 100, 197, 199, 304, 384, 385
 Colour night vision, 134
 Combustion, 389
 Combustion engines, 402
 Comet, 184, 356
 Comparator, 128
 Complex index of refraction, 66
 Compressor, 283
 Computer-Aided Tomography, 214
 Cone, 133
 Configuration, 11, 209
 Confocal microscopy, 454
 Confocal parameter, 233
 Constant-fraction discriminator, 332
 Continuum light source, 136, 158, 166
 Contrast agents, 82, 214
 Contrast enhancement, 451
 Conversion factors, 3
 Cooling, 374, 375
 – evaporative, 385
 – Raman, 381
 – Sisyphos, 381
 – sub-recoil, 382
 Cooper pairs, 385, 387
 Core, 7
 Core polarization, 10
 Correlation spectrometers, 168
 Correlations, 29
 Corrosion, 430
 COT, 251
 Coulomb explosion, 342
 Coulomb field, 30
 Covalent bonds, 31
 CPA, 282
 Cross-correlation technique, 333, 458
 Cross-over resonance, 366
 Cross-section, 65, 69
 Crystal, 263, 267
 Crystal field, 216, 236
 Crystallization, 378
 Curve of growth, 177
 CVD, 403
 Cyclotron resonance, 376
 Cylindrical symmetry, 32, 33
 Czerny–Turner, 120
 Dark current, 129
 Dark state, 382
 de Broglie wavelength, 384, 385
 Deconvolution, 165, 364
 Degenerate four-wave mixing, 271
 Delay line, 333
 Delayed coincidence technique, 315, 321, 457, 460
 δ -amino levulinic acid, 446
 Delves cup, 156
 Dephasing time, 213
 Detectors, 128
 – array, 132
 – mercury cadmium telluride (HgCdTe), 130
 – thermo-ionic, 291
 Deuterium lamp, 158
 DFWM, 271
 Diagnostic radiology, 82
 Diagonalization, 28, 195
 DIAL, 418
 Diatomic molecules, 31
 Dielectric layers, 135
 Dielectric properties, 220
 Difference-frequency generation, 265, 409
 Differential absorption lidar, 418
 Differential imaging, 83
 Differential optical absorption spectroscopy, 166
 Dimensionless quantities, 451
 Diode array, 89
 Dipole transitions, 51
 Discharge
 – channel, 242
 – electrical, 242
 – gas, 100
 – lamp, 101
 – spark, 100
 Dispersion, 114, 325
 – group-velocity, 280
 Dispersion curve, 206, 364
 Dissociation, 336
 Dissociation energy, 36, 38
 Divergence, 233
 Doas, 166, 409
 Dobson instruments, 145
 Doppler
 – effect, 99
 – width, 99
 Doppler broadening, 99, 294, 352

- Doppler burst, 403
 Doppler effect, 374
 Doppler limit, 378
 Doppler measurements, 454
 Doppler shift, 220, 225, 320, 424
 Doppler width, 244
 Double Fresnel rhomb, 142
 Doubly refractive materials, 263
 Dressed atom, 381
 Drift tube, 291
 Dry ice, 129
 Dye, 246
 Dyes
 – bleachable, 238
 Dynamic Stark effect, 381
 Dynodes, 129
- Ebert–Fastie, 120
 Edge technique, 425
 Effective charges, 92
 Effective magnetic moment, 192
 Einstein coefficients, 46
 EIT, 339
 Elastic rotator, 36
 Electric dipole moment, 21, 61
 Electric dipole operator, 45
 Electric dipole transitions, 51
 Electric field gradient, 26
 Electric hyperfine structure, 25
 Electro-weak interaction, 366
 Electrochromic films, 140
 Electromagnetically induced transparency, 339
 Electron configuration, 11
 Electron cooler, 358
 Electron correlation, 359
 Electron microscopy, 84
 Electron multiplier, 355
 Electron-nuclear double-resonance, 217
 Electron spectroscopy for chemical analysis, 86, 94
 Electron spin resonance, 216
 Electron synchrotrons, 108
 Electron tunneling, 342
 Electron tunnelling, 22
 Electronic magnetic moment, 27
 Electrons
 – equivalent, 14
 – non-equivalent, 14
 Electrophoresis, 430
 Electrostatic analyser, 87
 Electrostatic velocity analyser, 105
 Elementary reactions, 390
- Endohedral fullerenes, 39
 ENDOR, 217
 Energy-dispersive system, 74, 76
 Environmental applications, 78, 144, 162, 218, 389, 406, 425
 Equivalent electrons, 16
 Equivalent width, 176
 ESCA, 71, 86, 94, 111
 ESO, 180
 ESR, 216
 Etalon, 234, 245, 249
 Eulerian formulae, 43
 EXAFS, 81, 113
 Extended X-ray absorption fine structure, 81
 External fields, 17
 Extraordinary beam, 141
 Extraterrestrial intelligence, 226
 Eye exposure, 442
 Eye safety, 442
- F-centre, 255
 Facades, 429
 Fano resonance, 301
 Fast igniter, 351
 FEL, 111
 – SASE, 111, 344
 Femtochemistry, 336, 435
 Fermat principle, 121
 Fermi contact interaction, 25
 Fermi Golden Rule, 45
 Fermi level, 81
 Fermionic degenerate state, 387
 Fibre amplifier, 261
 FID, 212
 Field ionization, 22, 291, 359
 Filter
 – coloured glass, 135
 – interference, 134
 Filters
 – absorption, 138
 – atomic absorption, 425
 – gas, 425
 – liquid, 138
 – neutral-density, 139
 Fine-focusing, 89
 Fine-structure constant, 19
 Fine-structure splitting, 9
 Finesse, 123, 126
 Fingerprints, 433
 First-order perturbation theory, 9
 Flame, 154, 302, 390
 Flash-lamp, 237, 246, 248
 Flop-in, 193

- Flop-out, 193
- Fluorescence, 291
 - intermodulated, 367
- Fluorescence light, 52, 353
- Fluorescence microscopy, 454
- Fluorescent lamp, 134
- Fluorosensor, 451
- Flux, 422
- FMS, 412
- Forbidden transition, 53, 178, 366, 379
- Forensic science, 78, 433
- Forrat parabola, 58
- Fountain, 374
- Four-wave mixing, 267, 345, 402
- Fourier analysis, 49, 230
- Fourier broadening, 373
- Fourier components, 339
- Fourier transform, 49, 127, 212, 223, 276, 277, 344, 347
- Fourier transform NMR, 212
- Fourier transformation, 329, 335, 403
- Fovea, 133
- Franck–Condon principle, 60
- Fraunhofer line, 166
- Free induction decay, 212
- Free spectral range, 123
- Freons, 145
- Frequency-comb technique, 372
- Frequency doubling, 262
- Frequency mixing, 265, 267
- Frequency standard, 196, 199, 372
- Fresnel reflection, 140
- FROG, 334
- FT-NMR, 212
- Fundamental constants, 3
- Fundamental frequencies, 38
- Fundamental modes, 257
- Garnet, 239
- Gas centrifugation, 436
- Gas correlation
 - spectrometer, 169
- Gas correlation imaging, 169
- Gated viewing, 456
- Gaussian, 99, 233, 281, 325, 333
- Geiger counter, 75
- Geiger–Muller detector, 196
- Geophysical tracer gas, 423
- Geothermal energy, 423
- Ghost lines, 118
- Giant pulse, 237
- g_J factor, 18, 201
- Glass, 143
- Global positioning system, 200
- Glucose, 454
- GPS, 200
- Graphite oven, 156, 302
- Grating, 117, 280
 - concave, 79, 119
 - echelle, 119
 - holographic, 118
 - replica, 118
- Grating spectrometers, 117
- Gravitational radiation, 226
- Gravitons, 226
- Gravity-wave detection, 51
- Gray wedge, 169
- Grays, 350
- Grazing incidence, 119, 249
- Green flash, 69
- Greenhouse effect, 406
- Ground configurations, 12
- Group theory, 38, 236
- Group velocity dispersion, 280
- Haloes, 69
- Hamiltonian, 5, 10, 43
- Hanle effect, 206, 327
- Hanle signal, 320
- Harmonic oscillator, 37, 48
- Heat-pipe, 299
- Heat-pipe oven, 295, 325
- Heisenberg relation, 50
- Heisenberg uncertainty principle, 199
- Heisenberg uncertainty relation, 48, 88, 187, 193, 306, 347
- Helium, 14
- Hematoporphyrin derivative, 443
- Hermitian, 45
- Hetero-nuclear, 34
- Heterodyne detection, 130, 407, 459
- High-frequency deflection, 321
- High harmonic generation, 342
- High-power decoupling, 212
- Highly ionized atoms, 100, 178
- Highly ionized spectra, 102
- Hollow cathode, 100, 152
- Hologram, 127
- Holography, 246, 384
- Homo-nuclear molecules, 32, 56
- Homogeneous
 - broadening, 49
- Hook method, 324
- Hot band, 63, 398
- HPD, 443
- HST, 179
- Hubble Space Telescope, 179, 315, 345

- Human eye, 133, 262, 442, 459
- Hund coupling cases, 36
- Hydrogen, 5, 224
- Hydrogen maser, 199
- Hydrospheric remote sensing, 147, 218, 426
- Hyperfine anomaly, 195
- Hyperfine structure, 23, 106, 125, 194, 199, 201, 208, 311, 328, 354, 372
- Hyperspectral
 - imaging, 173
- ICP, 157
- Idler, 267
- IFEL, 111
- Image intensifier, 132, 429, 448
- Image plates, 82, 134, 349
- Image processing, 173
- Imaging
 - astronomical, 415
 - lung, 214
 - medical, 82, 349, 351, 453
 - spectrometer, 173
 - tissue, 452
- Imaging spectrometers, 133
- Independent particle model, 11
- Indium antimonide, 130
- Indium arsenide, 130
- Inductively coupled plasma, 157
- Inelastic scattering, 62
- Inertial confinement, 351
- Inhomogeneous
 - broadening, 49
- Inhomogeneous electric field, 229
- Inhomogeneous magnetic field, 189, 192
- Inner electrons, 71
- Interaction constant
 - electric quadrupole, 25
 - magnetic dipole, 23
- Intercombination lines, 53
- Interference, 121, 134, 338, 339, 366, 374, 399
- Interferogram, 126
- Interferometer, 223
 - atom, 384
 - confocal, 124
 - Fabry–Pérot, 121, 251, 292
 - Mach–Zehnder, 325
 - Michelson, 231, 292, 460
 - multi-pass, 125
- Interferometry
 - radio, 223
- Intermediate coupling, 17, 21
- Intermediate fields, 27
- Intermediate frequency, 407
- Intermediate vector boson, 366
- Intermodulated, 367
- Internal combustion engines, 399, 402
- Interstellar gas, 223
- Interstellar molecules, 224
- Interval rule, 16
 - Landé, 24, 26
- Intracavity, 265, 359
- Invar spacers, 124
- Inverse free-electron laser, 111
- Inverse Hook method, 325
- Inversion, 57
- Inversion layer, 165
- Inverted fine structure, 10, 309, 355
- Inverted hyperfine structure, 24, 355
- Iodine, 82, 370, 406
- Ionic bonds, 31
- Ionization
 - collisional, 291
 - field, 22, 291
 - Penning, 244
 - photo-, 291
- Isotope shift, 29, 438
- Isotopic selectivity, 435
- IUE, 179
- jj coupling, 16, 21
- K-absorption edge, 82, 349
- Kayser, 3
- KDP, 263
- Kerr effect, 237, 281
- Kerr gate, 457
- Kinematic compression, 358
- KPB, 263
- Kramer–Kronig dispersion relation, 324
- Lamb dip, 360
 - inverted, 360
 - normal, 360
- Lamb shift, 50, 346, 364, 369, 371
- Λ doubling, 36, 224
- Lamp, 102
 - deuterium, 108
 - discharge, 102, 288
 - hollow-cathode, 100, 152
 - RF, 101, 307
 - xenon and mercury, 108
- Landé formula, 21
- Landé g_J factor, 18, 201
- Landé interval rule, 15, 24
- LANDSAT, 164, 172

- Langmuir–Taylor detector, 195
- Laplace operator, 5
- Larmor frequency, 207
- Larmor precession, 8, 188, 212
- Laser, 227
 - 4-level, 238
 - ablation, 313
 - accelerators, 351
 - alexandrite, 256
 - amplifier, 239
 - argon-ion, 244
 - chemical, 259
 - CO, 259
 - CO₂, 257
 - Colour-centre, 255
 - cooling, 377
 - copper vapour, 242
 - crystals, 240
 - diffraction-limited, 233
 - diode, 262
 - distributed feedback dye, 345
 - dye, 246
 - emerald, 256
 - excimer, 242
 - femtosecond, 281
 - fixed-frequency, 236
 - Forsterite, 257
 - free-electron, 111
 - He–Ne, 243
 - helium–cadmium, 244
 - heterojunction, 259
 - HF, 259
 - krypton-ion, 245
 - LISAF, 257
 - LNA, 214
 - Nd-glass, 239
 - Nd:YAG, 239
 - Nd:YVO₄, 246
 - nitrogen, 241, 447
 - quantum cascade, 262
 - ring, 254
 - Ruby, 236
 - semiconductor, 259
 - spin-flip Raman, 246
 - super-radiant, 241
 - three-level, 237
 - Ti:sapphire, 281
 - Ti³⁺:Al₂O₃, 257
 - tunable, 246
 - vertical cavity surface emitting, 262
 - waveguide, 259
 - X-ray, 229, 347
- Laser beam deflection, 397
- Laser doppler velocimetry, 403
- Laser-driven fusion, 102, 351
- Laser-enhanced ionization, 301
- Laser guide star, 181, 415
- Laser-induced chemical processes, 435
- Laser-induced chemistry, 435, 443
- Laser-induced fluorescence, 392, 425, 447
- Laser isotope separation, 435, 436
- Laser-nuclear interactions, 351
- Laser-produced plasma, 313
- Laser radar, 414
- Laser-spectroscopic applications, 389
- Lasers in medicine, 441
- Lasing without inversion, 339
- Lattice, 384
- Laue diffraction, 384
- Laue geometry, 74
- LBO, 246
- LCAO method, 32
- LDV, 403
- Lead sulphide (PbS) cell, 130
- LEI, 301
- Level crossing, 203, 306
- Level inversion, 10
- Level labelling, 298
- LIBS, 416
- Lidar, 414
- Lidar equation, 419
- LIF, 392, 425, 447
- LiF, 143
- Lifetime, 48, 203, 318, 345
- Lifetime measurements, 318
- Light diffusive pulling, 384
- Light-induced drift, 384
- Light shift, 199, 381
- Light sources, 97
 - continuum, 98, 106, 297
 - line, 97, 98, 230
- Limb absorption, 165, 218
- Limb emission, 218
- LiNbO₃, 265
- Liquid-crystal modulator, 339
- Liquid nitrogen, 129, 237
- Liquids, 209
- Lithium niobate, 265
- Lithographic applications, 262
- Littrow
 - mount, 115, 119, 248
 - prism, 115
- Local oscillator, 407, 425
- Lock-in amplifier, 152, 304, 361, 410, 412

- Lock-in detection, 209, 309, 408
 Lock-in detector, 169
 Lock-in techniques, 294
 Longitudinal relaxation time, 210
 Lorentz condition, 43
 Lorentzian, 49, 100, 206, 209, 210, 325, 331, 364
 LS coupling, 11, 21, 53
 Luggage inspection, 336
 Lunar ranging, 414
- Magic angle, 213, 329
 Magnetic dipole interaction constant, 23, 24
 Magnetic dipole moment, 23
 Magnetic dipole transitions, 188
 Magnetic field measurements, 199, 213
 Magnetic hyperfine structure, 23
 Magnetic moment, 8, 18, 211
 Magnetic resonance, 187, 188
 – atomic-beam, 189
 Magnetic resonance imaging, 214
 Magnetization, 211
 Magnetometers, 199
 Magnification radiography, 83
 Mammography, 82, 454
 Maser, 222, 224, 228
 Mass effect, 29
 Mass spectra, 39
 Mass spectrometric studies, 39
 Maxwell distribution, 99
 MBE, 259
 MCA, 315
 Mechanical moment, 8
 Medical imaging, 82, 349, 351, 453
 Mercury, 108, 422
 Mesosphere, 415
 Metal coatings, 137
 Metal-organic chemical vapour deposition, 259
 Metastable, 297, 402
 Metastable levels, 196
 Metastable states, 82, 358, 379
 Meteorites, 415
 Meteorological conditions, 163
 Michelson
 – interferometer, 171, 231, 292, 460
 Microbeam, 78
 Microchannel plate, 89, 132, 332, 429
 Microdensitometer, 101, 128, 298
 Microphone, 304, 397
 Microwave radiometry, 218
 Microzone plate, 84
- Mie scattering, 65, 416
 Mirages, 69
 Mirrors, 135
 – chirped, 280
 Mixer, 407, 411
 Mixing ratios, 391
 MOCVD, 259
 Mode hopping, 234
 Mode-locking, 276
 Modes, 38, 232
 Molecular beam epitaxy, 259
 Molecular structure, 31
 Moment
 – electric quadrupole, 25
 – magnetic dipole, 23
 Moment of inertia, 35
 Monochromator, 111, 114
 – double, 119
 Monopole interaction, 25
 Monte Carlo simulations, 349, 454
 Moon, 113, 414
 Morse potential, 36
 Moseley's law, 73
 MOT, 382
 MQD'T, 17
 MRI, 214
 MSS, 172
 Multi-channel analyser, 77
 Multi-element analysis, 77, 157
 Multi-mode operation, 234
 Multi-pass cell, 159, 439
 Multi-photon absorption, 289
 Multi-photon process, 340, 438
 Multi-spectral aerial photography, 171
 Multi-spectral scanning, 172
 Multichannel analyzer, 315
 Multichannel quantum defect theory, 17, 369
 Multilayer techniques, 126, 135
 Multiplicity, 11, 33
 Multipole fields, 47
 Muonium, 6, 366
- Nadir, 218
 Natural lifetime, 44, 48, 79, 319
 Natural linewidth, 319
 Natural radiation width, 48, 98, 201, 204, 329, 352
 Nd:YAG, 239
 Nd:YLF, 240
 Near-edge X-ray absorption fine structure, 81
 Negative ions, 359
 Nephelometry, 66

- Nernst glower, 108, 159
 Neutron stars, 225
 NEXAFS, 81
 Night vision, 133
 NMR, 211
 Non-crossing rule, 21, 206
 Nonharmonicity, 63
 Nonlinear index of refraction, 284
 Nonlinear optical effects, 262
 Nonlinear optics, 262, 339
 Normal structure, 24
 Nuclear magnetic resonance, 211
 Nuclear magneton, 23
 Nuclear moments, 25, 26, 195, 211
 Nuclear orientation, 198
 Nuclear physics, 78, 351
 Nuclear spin, 23, 192, 196, 198, 211
- O branch, 65
 Oblate shape, 25
 OFI, 347
 Oil, 219
 Oil slicks, 427
 Oil spills, 426
 Old atoms, 331
 OMA, 132
 OPO, 267
 Optical coherence tomography, 459
 Optical components, 134
 Optical density, 139, 140, 150
 Optical double resonance, 200, 306
 Optical fibre, 261, 414, 445
 Optical field-ionization, 347
 Optical klystron, 111
 Optical mammography, 456
 Optical materials, 143
 Optical molasses, 379
 Optical multichannel analyser, 132
 Optical parametric amplifier, 267
 Optical parametric oscillator, 267
 Optical phase conjugation, 272
 Optical piston, 384
 Optical pumping, 197, 214
 Optical remote sensing, 162
 Optical retarder plates, 142
 Optical spectroscopy, 97
 Optical tweezers, 454
 Ordinary beam, 141
 Organic dye, 246
 Orientational energy, 9, 19, 23
 Oscillator strengths, 319
 Overlapping orders, 119, 124
 Overtones, 56
- Ozone depletion, 145
 Ozone hole, 145
 Ozone layer, 144
- P branch, 57
 Paramagnetic ions, 214
 Paramagnetic substances, 217
 Parity, 51
 Parity violation, 366
 Particle, 66, 404, 418
 Particle-induced X-ray emission, 77
 Paschen–Back effect, 19, 27, 194
 Paschen–Back region, 21, 28, 217, 331
 Pauli principle, 11, 14, 32, 387
 PDT, 445
 Pedestal, 284, 368
 Periodic poling, 267
 Periodic table, 148
 Periodically poled lithium niobate, 409
 PET, 351
 Petrochemical industries, 423
 Phase control, 253
 Phase-locked loop, 292
 Phase matching, 263, 274, 333
 Phase memory, 204
 Phase shift, 122, 284, 411
 Phase-shift method, 321, 458
 Phosphor screen, 89
 Phosphorescence, 52
 Photo-detachment, 359
 Photocell, 129
 Photochemistry, 242, 435, 443
 Photochromism, 140
 Photoconducting detectors, 130
 Photodissociation, 342
 Photodynamic tumour therapy, 443, 445
 Photoelectric effect, 73, 129
 Photoelectric recording, 101
 Photoelectron spectroscopy, 71, 85
 Photographic plate, 128
 Photoionization, 303, 345, 355, 437
 Photoisomerisation, 336
 Photomultiplier tube, 129
 Photon anti-bunching, 50
 Photon echoes, 213
 Photon momentum, 356
 Photosynthetic pigment, 337
 Picosecond pulses, 278
 Pile-up effect, 315
 PIXE, 77
 Planck distribution, 230
 Planck radiation law, 46
 Planck radiator, 324

- Planetary atmospheres, 184
 Plant leaves, 460
 Plasma, 319
 – laser-produced, 102, 314
 – solid-density, 348
 Plasmons, 95
 PLL, 292
 PMMA, 85
 PMT, 129
 Pockels cell, 283, 312
 Pockels effect, 237
 Point groups, 38
 Polarizability constants, 263
 – scalar, 22
 – tensor, 22
 Polarization, 54, 141, 233
 Polarization spectroscopy, 399
 Polarization tensor, 61
 Polarized, 69
 Polarizers, 141
 – Glan–Taylor, 141
 – Glan–Thompson, 141
 – polyvinyl film, 142
 Polarizing beam-splitter, 142
 POLINEX, 367
 Pollutants, 418
 Pollution, 390
 Polyatomic molecules, 37
 Ponderomotive potential, 341
 Population inversion, 228
 Portwine stains, 441
 Positron, 351
 Positronium, 6, 366
 Powder, 305
 ppb, 148
 PPLN, 409
 ppm, 148
 ppt, 148
 Precess, 26, 33, 187
 Precession, 19
 Precessional motion, 8
 Pressure shifts, 200
 Primary rainbow, 66
 Prism, 114, 280
 – Amici (roof), 116
 – corner-cube, 117
 – dove, 117
 – Glan–Thompson, 141, 363
 – Pellin–Broca, 116
 – penta, 116
 – right-angle, 115
 – straight-view, 116
 Prism spectrometers, 114
 Prisms, 115
 Probe, 298, 334, 361
 Prolate shape, 25
 Protoporphyrin IX, 446
 Pulsars, 225
 Pulse compression, 279
 Pulse shaper, 338
 Pump, 298, 334, 361
 Pump-probe technique, 334
 Purification, 436
 Push-broom, 133
 Pyroelectric, 130
 Pyrolysis, 435
 Q branch, 60, 64
 Q-switching, 237
Q-value, 50
 QBS, 325
 QCL, 262
 QED, 6, 45, 49, 370
 Quadrupole interaction, 25
 Quantum chemistry, 39
 Quantum computing, 50, 379
 Quantum cryptography, 50
 Quantum defect, 7
 Quantum efficiency, 129
 Quantum electrodynamics, 6, 18, 45
 Quantum jump, 379
 Quantum-mechanical squares, 9, 19
 Quantum number
 – azimuthal, 5
 – effective, 7
 – principal, 5
 Quantum optics, 50
 Quartz, 143
 Quasars, 183, 226
 Quasi-phase-matching, 267
 Quenching, 69, 216, 392
 Quiver energy, 341
 R branch, 57
 Radar, 218
 Radar systems, 218
 Radiation
 – resonance, 41
 Radiation process, 41
 Radiation source
 – natural, 113
 – Planck, 113
 Radicals, 217, 390
 Radio astronomy, 222
 Radio-frequency spectroscopy, 187
 Radio-frequency transition, 311
 Radio telescopes, 222

- Radioactive atoms, 198, 356
 Radioactive isotopes, 195, 357
 Radioactive nuclei, 358
 Radiography, 82
 Rainbow, 66
 Rainbow angle, 68
 Rainfall, 218
 Raman cooling, 383
 Raman effect, 62
 Raman scattering, 61
 – surface-enhanced, 434
 Raman shifting, 273
 Raman spectroscopy, 160, 162, 398
 Ramsey fringe method, 193, 197, 374
 Range finders, 414
 Ranging, 414
 Rayleigh scattering, 61, 425
 Reaction dynamics, 336
 Recoil effect, 356
 Recoil energy, 86
 Recoil limit, 377
 Recombination, 347
 Red shifts, 183
 Reduced mass, 29, 35, 37
 Reflective remote sensing, 171
 Refocusing, 103
 Refractive surgery, 441
 Refractory elements, 196, 313
 Regen(erative) amplifier, 283
 Relativistic, 351, 414
 Relativistic effects, 108, 109
 Relativistic Lorenz contraction, 374
 Relativistically, 320
 Relativity, 226
 Relaxation, 89, 199, 246, 334
 Relaxation processes, 200
 Remote sensing, 218, 406
 – atmospheric, 148
 – hydrospheric, 426
 REMPI, 304
 Resolution, 222
 Resolving power, 114
 Resonance, 44
 Resonance ionization mass spectroscopy, 304
 Resonance multi-photon ionization, 304
 Resonance radiation, 52
 Resonance Raman effect, 162
 Resonator, 231
 Retardation, 122
 Retina, 133, 442
 Retroreflector, 117, 292, 408
 Rhodopsin, 331, 337
 Rigid rotator, 36
 RIMS, 304
 Ring-laser cavity, 253
 RIS, 303
 Rod, 133
 Rotational constant, 57
 Rotational energy, 35
 Rotational quantum number, 55
 Rotational transitions, 55
 Rowland circle, 79, 87, 89, 119
 Rydberg atoms, 22, 355
 Rydberg constant, 5, 364, 365
 Rydberg sequences, 317
 Rydberg states, 50, 290, 369
 S branch, 65
 Sample boat, 156, 157
 SAR, 220
 SASE-FEL, 111, 344
 Satellites, 163, 179, 200, 218, 220, 414
 Saturable absorber, 237, 278
 Saturation, 287
 Saturation technique, 352
 SBS, 271
 Scenes, 173
 Schawlow–Townes limit, 234
 Schrödinger equation, 5, 32, 41
 Scintillation counter, 75
 Sea clutter, 219
 Sea ice, 219
 Second-order Doppler effect, 352, 374
 Secondary rainbow, 66
 Selection rules, 47, 51–53, 56, 57, 193
 Self-conjugating crystal, 271
 Self-consistent field, 17, 92
 Self-phase modulation, 280, 281, 335
 Self-terminating, 241
 Sensitizers, 445
 Sensor, 163
 Separation plant, 436
 Sextupole magnet, 196, 356
 Seya–Namioka, 120
 Shake-up lines, 89
 Shear winds, 424
 Shelving, 50, 379
 Shielding, 211
 Side looking airborne radar, 218
 Si(Li) detector, 78
 Single-atom detection, 304
 Single-mode dye laser, 254
 Single-mode operation, 234
 Single-mode oscillation, 245
 Single-molecule detection, 304
 Single-photon counting, 318

- Singlet oxygen, 443
- Singlet system, 247
- Slab, 239
- Slant visibility, 416
- SLAR, 218, 426
- Sliding spark, 100
- Smart-window technology, 140
- Solar corona, 178
- Solids, 209
- Solvation energy, 94
- Solvents, 159
- Soot, 391
- Soot particles, 390
- Soret band, 443
- Space quantization, 19, 189
- Specific mass effect, 29
- SPECT, 351
- Spectral resolution instruments, 114
- Spectrometer
 - Fourier transform, 126
 - mass, 304
 - time-of-flight, 340, 345
- Spectroscopy
 - atomic absorption, 152
 - cavity ring-down, 296
 - coherent Raman, 162
 - differential optical absorption, 409
 - flame emission, 151
 - frequency-modulation, 412
 - γ -ray, 349
 - high-contrast transmission, 363
 - laser, 287
 - laser induced breakdown, 416
 - level-crossing, 203
 - opto-acoustic, 304
 - opto-galvanic, 301, 367, 397
 - photoacoustic, 397
 - polarization, 363
 - quantum-beat, 106, 325
 - resonance ionization, 303
 - saturation, 359
 - time-resolved, 311
 - two-tone frequency modulation, 412
 - ultra-sensitive, 304
 - ultrafast, 331
 - vacuum, 144
 - wavelength modulation, 411
 - X-ray, 349
 - X-ray absorption, 79
- Spectrum
 - beam-foil, 103
 - photoelectron, 89
 - X-ray emission, 72
- X-ray fluorescence, 74
- Speed of light, 339, 427
- Spherically symmetric, 7
- SPIDER, 334
- Spin echo, 213
- Spin-exchange collisions, 214
- Spin-orbit interaction, 9, 15, 89
- Spin-spin interactions, 211
- Spontaneous emission, 45
- SPOT, 164, 173
- Sputtering, 100
- Squeezed state, 50
- SST, 145
- Standard addition method, 155
- Standard model, 366
- Standard solutions, 155
- Star spectra, 176
- Stark effect, 21
 - linear, 21
 - scalar, 21
 - tensor, 21
- Stellar atmosphere, 177
- Stern-Gerlach experiment, 192
- Stimulated Brillouin scattering, 271
- Stimulated emission, 44, 227
- Stimulated Raman scattering, 273, 345, 438
- Stokes, 62, 273
- Stokes component, 63
- Stokes shifting, 60
- Storage rings, 109, 358
- Straggling, 105
- Stratosphere, 218
- Stratospheric dust, 424
- Stratospheric ozone destruction, 407
- Stray light, 119
- Streak camera, 133, 332, 349, 457
- Stretcher, 282
- Submarines, 148
- Sum-frequency mixing, 410
- Sun, 113
- Supercavity, 126
- Superconducting coils, 211
- Superconductivity, 385
- Superfluidity, 385, 387
- Supernova, 183
- Supersonic nozzle, 439
- Supersonic transport, 145
- Surface, 94, 96, 426, 429, 430
- Surface spectroscopy, 93–95, 430
- Susceptibilities, 263
- Swath, 172
- Swirls, 424

- Symmetry properties, 38
- Synchronous pumping, 278
- Synchrotron radiation, 81, 108, 312
- Synthetic aperture radar, 220
- TAC, 315
- Tag, 427
- Tagging, 404
- TEA Laser, *see* Laser
- Telecommunication, 261
- Telescopes, 176
- TEM₀₀, 232
- Temperature, 63, 174, 183, 416, 433
- Temperature measurements, 59, 63, 398, 433
- Tensor Stark interaction, 21, 355
- Terahertz-radiation generation, 334
- Terms, 11
- Texture, 173
- Thermal interaction, 441
- Thermal velocities, 102
- Thermocouple, 129
- Thermodynamic equilibrium, 46, 227, 323
- Thermometers, 433
- Thermometry, 402
- Thermovision, 169, 176
- Theta pinch, 102
- Time dilatation, 352
- Time-of-flight spectrometer, 291
- Time-resolved diffraction studies, 84
- Time-resolved experiments, 109, 350
- Time-to-amplitude pulse-height converter, 315
- Tissue diagnostics, 447
- Tokamak, 102
- Tomographic, 214, 397
- Tomographic reconstruction, 83
- Tracer dye, 427
- Transform-limited, 334
- Transient digitizer, 312, 416
- Transit-time broadening, 193, 374
- Transition
 - radiationless, 247
- Transition probabilities, 22, 42, 100, 318, 324
- Transition states, 336
- Transmission medium, 144
- Transverse relaxation time, 210
- Trap
 - ion, 376
 - magneto-optical, 382
 - Paul, 377
- Penning, 376
- quadrupole, 377
- Trapping, 374
- Triplet molecules, 251
- Triplet state, 247
- TTFMS, 412
- Tumour, 214, 351, 443
 - localization, 176
- Tungsten
 - lamps, 106, 158
- Turbidimetry, 66
- Turbulence, 165, 180, 182, 410, 425
- Turbulent, 402
- Two-photon absorption, 289, 352, 368
- Two-photon transitions, 43
- Ultracold fermionic gases, 387
- Undulators, 111
- Universal distribution function, 109
- Unpaired electron, 25
- Unstable resonator, 239
- Vacuum state, 46, 49
- Vacuum techniques, 189
- Vacuum wavelengths, 144
- Valence orbitals, 90
- Van der Waals molecules, 31
- Vapour pressure, 189, 197
- Variance, 48
- VCSEL, 262
- Vector potential, 43
- Vegetation monitoring, 171, 426, 429
- Velocity, 455
- Velocity measurements, 403
- Velocity of light, 360
- Very long base line interferometry, 223
- Vibrational energy, 36
- Vibrational–rotational Raman spectra, 64
- Vibrational transitions, 56
- Virtual levels, 62, 290
- VLBI, 223
- VLT, 180
- VLW, 148
- Volcanic plume, 168
- Volcanoes, 422
- Volume effect, 29
- Voyager missions, 184
- VSCPT, 383
- VUV, 179, 271, 345
- Wake-field acceleration, 351
- Water depth, 427
- Water pollution, 426

- Water window, 84, 342
Wavelength-dispersive, 74
Wavemeter, 292
Weather radar station, 218
Whisk-broom, 172
White cell, 159, 294
White excitation, 307
White-light continuum, 335
White-light generation, 332, 334
Wien displacement law, 106
Wigglers, 111
Wigner crystal, 358, 379
Wind velocities, 424
Wolf-Rayet stars, 178
- X-ray
– continuum, 80
– laser-produced, 350
– laser pumping, 347
– lithography, 84
– microscopy, 84
– photoionization, 244
- X-ray fluorescence, 73
X-ray imaging, 134
X-ray microscopy, 84
X-ray monochromatization, 87
X-ray photoemission spectroscopy, 86
X-ray spectroscopy, 71
XANES, 81
XPS, 71, 86
XUV, 109, 119, 345
- Young's double-slit experiment, 69, 204, 231, 326, 384
- Zeeman effect, 19, 26, 27, 184, 193, 311
Zeeman quantum beats, 326
Zeeman region, 20
Zeeman slower, 375
Zeldovich mechanism, 391
Zenith, 218
Zero-point energy, 37
Zodiacal light, 113

The New Springer Global Website

Be the first to know

- ▶ Benefit from new practice-driven features.
 - ▶ Search all books and journals – now faster and easier than ever before.
 - ▶ Enjoy big savings through online sales.
- springeronline.com – the innovative website with you in focus.

springeronline.com

The interactive website for all Springer books and journals

010048x



Springer